Transactions of the ASME®

Transactions of the ASME, Journal of Heat Transfer (ISSN 0022-1481) is published quarterly (Feb., May, Aug., Nov.) for $160.00 per year by The American Society of Mechanical Engineers, 345 East 47th Street, New York, NY 10017. Second class postage paid at New York, NY and additional mailing offices. POSTMASTER: Send address changes to Transactions of the ASME, Journal of Heat Transfer, c/o THE AMERICAN SOCIETY OF MECHANICAL ENGINEERS, 22 Law Drive, Box 2300, Fairfield, NJ 07007-2300.
CHANGES OF ADDRESS must be received at Society headquarters seven weeks before they are to be effective. Please send old label and new address.
PRICES: To members, $36.00, annually; to nonmembers, $160.00. Add $15.00 for postage to countries outside the United States and Canada.

INDEXED by Applied Mechanics Reviews and Engineering Information, Inc.

Journal of Heat Transfer

Published Quarterly by The American Society of Mechanical Engineers

VOLUME 112 • NUMBER 3 • AUGUST 1990

ANNOUNCEMENTS

TECHNICAL PAPERS

TECHNICAL NOTES

1987 Max Jakob Memorial Award Lecture

Dynamics and Stability of Thin Heated Liquid Films

S. G. Bankoff
Chemical Engineering Department,
Northwestern University,
Evanston, IL 60208

This review covers the dynamics and tendency toward rupture of thin evaporating liquid films on a heated surface. Very large heat transfer coefficients can be obtained. The applications include various boiling heat transfer and film cooling devices. A relatively new area for study is heat transfer through ultrathin films, which are less than 100 nm in thickness, and hence subject to van der Waals and other long-range molecular forces. Some recent work employing lubrication theory to obtain an evolution equation for the growth of a surface wave is described. Earlier phenomenological work is briefly discussed, as well as the connection between forced-convection subcooled nucleate boiling and thin-film heat transfer.

1 Introduction

Thin evaporating liquid films provide excellent cooling of hot solid surfaces. The surface temperature is generally very close to the saturation temperature, and if the film is thin enough very large temperature gradients normal to the surface can be sustained. Indeed, if the surface temperature were the local saturation temperature, and if the film vapor pressure were the same as the vapor pressure of bulk liquid at the same surface temperature, heat transfer coefficients on the order of 60 MW/m^2K could be realized for a water film 10 nm thick on a smooth solid surface. Such enormous coefficients are not realizable, because of surface nonequilibrium, the reduction of vapor pressure owing to long-range molecular forces, and the general impossibility of supplying makeup liquid continuously to such a thin, rapidly evaporating film. However, as can be readily realized, even much thicker films can give excellent heat transfer.

Heat transfer applications for thin films abound. Capillary phase-change devices, such as heat pipes, sweat coolers, grooved evaporators, and other enhanced heat transfer surface devices, depend on the formation of thin-film regions owing to capillary action. In boiling heat transfer, there is a thin liquid microlayer underneath bubbles growing on a solid surface, whose evaporation contributes to the overall heat transfer. Indeed, in the evaporative cooling of three-dimensional, heat-generating structures, such as microelectronics arrays, it is difficult to distinguish between thin-film heat transfer and boiling heat transfer. It is well known that droplet condensation, which results when very thin films of condensate rupture and roll up upon a poorly wetted wall, is much more efficient than film condensation on well-wetted surfaces. Cooling by somewhat thicker liquid films, such as film cooling of turbine blades, falling films on heated surfaces, and evaporating annular flows, have all been extensively studied. In each case the tendency of films to rupture and premature formation of dry regions are important areas for study.

However, in this review we concentrate on ultrathin films, which may be defined as liquid films that are thick enough to be treated by continuum mechanics, but thin enough so that long-range molecular forces are significant in determining their dynamics. This corresponds roughly to films thicker than a few molecular diameters, but less than 100 nm. For these films inertial effects are negligible; gravitational effects for horizontal, or near-horizontal, films can also be neglected; and lubrication theory, which assumes small dimensionless wave numbers, is a powerful tool for analysis. It is then possible to develop one or more partial differential equations for the film thickness as a function of time and position, depending on the number of components in the liquid. For a pure liquid, subject only to surface tension and van der Waals forces, the nonlinear evolution equation was developed by Williams and Davis (1982). It is possible thereby to follow the nonlinear growth of a surface wave all the way down to near-rupture. At this point the theory breaks down, because inertial effects become significant (Burelbach et al., 1988). At rupture itself, contact lines appear and the wettability, signified by the contact angle, is an important variable. No analytical theory to date has been successful in describing this transition, although several phenomenological theories have been proposed (Chung and Bankoff, 1980a, 1980b; Tung and Bankoff, 1982).

Even thicker, evaporating (condensing) films, such as those draining down heated (cooled) walls, may become locally ultrathin, and hence subject to the above stability considerations. Wettability effects can influence the stability to rupture of these films through the sign of the Hamaker constant (Hamaker, 1937), which in turn determines whether the extra body force is stabilizing or destabilizing. The linear and nonlinear stability of surface waves on these thicker films, which may be several millimeters in mean thickness, has been extensively studied. The linear theory was developed by Benjamin (1957) and Yih (1963), while the nonlinear theory, utilizing long-wave expansions, has been treated by Benney (1966), Gjevik (1970), Krantz and Goren (1970), and Homsy (1974). The connection of the film thickness evolution equation to the Kuramoto–Sivashinsky equation, which appears in various problems of chemical physics, was pointed out by Sivashinsky and Michelson (1980). In the case of evaporating films draining down a heated inclined or vertical wall, there is an extra normal surface stress term owing to phase change at the surface (Bankoff, 1971).

A related topic is the enhanced heat transfer that may be possible in the neighborhood of a contact line. For a perfectly wetting (zero contact angle) evaporating liquid, there is no contact line *per se*, but only an interline region where the macroscopic film (or drop edge) merges into an adsorbed precursor film, which may be only a few molecules thick.

Contributed by the Heat Transfer Division and presented at the National Heat Transfer Conference, Houston, Texas, July 24–27, 1988. Manuscript received by the Heat Transfer Division July 25, 1989; revision received February 25, 1990. Keywords: Evaporation, Phase-Change Phenomena, Thin Film Flow.

However, the extensive studies of Wayner (Renk et al., 1978; Renk and Wayner, 1979; Wayner, 1979, 1980, 1982; Park and Wayner, 1987), as well as of Moosman and Homsy (1980), will not be reviewed here, since they do not deal with the stability or rupture of these thin evaporating films.

Finally, the connection between subcooled, forced-convection nucleate boiling and thin-film heat transfer will be reviewed. This is a high-flux mode of heat transfer in which the bubbles grow and collapse while remaining attached to the heating surface. One component of this heat transfer is latent heat transfer in which evaporation of a thin film of liquid at the bubble base and condensation of vapor at the colder polar bubble cap occur simultaneously. The bubble thus functions as a minute heat pipe. After nearly forty years, the relative importance of this mode compared to direct solid–liquid heat transfer in this type of high-flux heat transfer is still uncertain (Section 2).

The combination of very high heat fluxes attainable without excessive surface temperatures, coupled with the tendency for very thin films to break up owing to a variety of destabilizing effects, such as thermocapillarity, vapor recoil, and van der Waals attractions, make the study of the stability and rupture of these thin films attractive. Section 2 of this review covers some ideas concerning long-range molecular forces, and their incorporation into the conservation equations. Section 3 deals with general equations for conservation of mass, momentum, and energy of a thin heated film, together with associated boundary conditions. In section 4 these are specialized to an evaporating thin film on a horizontal surface, subject to van der Waals forces. Various special cases of this general problem are briefly considered, including temperature-dependent viscosity. Section 5 deals with evaporating liquid films draining down an inclined wall where inertial and gravitation effects are important. Section 6 deals with thin films in subcooled nucleate boiling, and Section 7 concludes with some brief remarks.

2 Long-Range Molecular Forces

Long-range molecular or ionic forces can significantly affect the properties and behavior of thin liquid films on a solid substrate. These may be classified as follows: van der Waals forces, which exist between neutral atoms or molecules; ionic forces, which arise from the mutual repulsion of ionic double layers; and structural or solvation forces, owing to surface hydration, surface adsorption, and/or the repulsion of large molecules when their centers of mass are brought too close to each other. Thin liquid films have been the subject of extensive investigations over many years. For a general background the reader is referred to recent reviews and books by de Gennes (1985), Israelachvili (1985), Derjaguin and Churaev (1986), Derjaguin et al. (1987), Hirasaki (1988), and Ivanov (1988).

We begin with a brief discussion of van der Waals (vdW) forces, since these are central to the equations governing the motions of very thin films of nonionic (organic) liquids. These are long-range attractive forces between any two molecules or atoms separated by a distance that is large compared to their own dimensions. These arise from dipole–dipole interaction (Keesom forces), dipole–induced dipole interaction (Debye forces), and induced dipole–induced dipole interaction (London dispersion forces). In each case the free energy of interac-

Nomenclature

Note: the same symbol is used for dimensional and scaled (dimensionless) quantities

- a = amplification factor in streamwise direction, equation (41)
- A = Hamaker constant, equation (1a)
- c = complex wave speed
- C = capillary number, equation (29)
- D = vapor–liquid density ratio
- E = evaporation number, equation (22)
- g = acceleration due to gravity
- h = film thickness
- H = mean surface curvature
- k = wavenumber, or liquid thermal conductivity
- L = latent heat
- M = Marangoni number, equation (31)
- M_W = molecular weight
- n = refractive index
- $\mathbf{n}$ = unit normal vector
- J = evaporative mass flux
- K = nonequilibrium surface parameter, equation (26)
- p = pressure
- Pr = Prandtl number
- q_w = wall heat flux
- R_g = gas constant
- Re = Reynolds number based on average velocity
- S = surface tension number, equation (28)
- t = time
- $\mathbf{t}$ = unit tangential vector
- T = temperature
- $\hat{T}$ = scaled time, equation (35b)
- u = velocity component parallel to wall
- U = average velocity parallel to wall
- $\mathbf{v}$ = velocity vector
- V = viscosity-temperature number, equation (36)
- w = velocity component normal to wall
- x = coordinate parallel to wall
- X = scaled coordinate, equation (35a)
- y = circumferential coordinate, equation (41)
- z = coordinate perpendicular to wall
- α = accommodation coefficient; dimensionless wave number
- α_v = temperature coefficient of viscosity
- β = vapor recoil number, equation (39)
- γ = temperature coefficient of surface tension
- δ = thickness of adsorbed layer
- η = amplitude of steady-state circumferentially periodic surface wave, equation (41)
- θ = angle of inclination
- κ = thermal diffusivity
- μ = viscosity
- ν = kinematic viscosity; principal absorption frequency
- ρ = density
- σ = surface tension
- ϕ = long-range molecular force potential function
- φ = dimensionless perturbation stream function
- ω = interaction energy per unit area

Superscripts

- (I) = interface
- (v) = vapor
- $\bar{}$ = base state

Subscripts

- av = average
- D = film disappearance
- E = evaporation
- g = gas
- l = liquid
- s = saturation
- w = wall
- 0 = reference condition or zeroth-order quantity
- 1, 2, 3 = solid substrate, overlying gas phase, thin liquid film

tion varies as the inverse sixth power of the separation distance. Higher-order terms arising from multipole interactions can be neglected at distances greater than about 1 nm. In addition, there are electrostatic interactions in aqueous thin films arising from the repulsion of double layers of ions. With polar solvents, such as water, there are also solvation forces, and with macromolecules in concentrated solutions or adsorbed at interfaces, structural, or steric forces. Solvation and steric forces are short-range forces that are powerful enough to affect the local physical properties, such as liquid viscosity, species diffusivity, surface tension, and surface viscosity, particularly in films a few nanometers thick. Such films are beyond the scope of this review.

These are two approaches to calculating the van der Waals interaction energy between macroscopic bodies (Nir and Vassilieff, 1988). In one approach (Hamaker, 1937) the pairwise interactions are integrated over all space, assuming their additivity. A more general theory (Lifshitz, 1955; Dzyaloshinskii et al., 1959) is more complicated, but can account for many-body effects.

The negative gradient of this interaction energy in the direction normal to the surface of the film represents an excess pressure (called by Derjaguin (1955) the disjoining pressure), compared to that of the bulk liquid at the same temperature and surrounding pressure. The modern general theory for the attractive force per unit area for two similar bodies of large extent, separated by a small gap, was given by Lifshitz (1955), using the methods of quantum electrodynamics. The extension to thin liquid films between two dissimilar bodies was given by Dzyaloshinskii et al. (1959). The general formula is quite complex, involving an infinite sum of integrals over all frequencies of the complex dielectric susceptibilities of all three media evaluated on the imaginary frequency axis. However, the limiting cases, where the gap thickness h is small or large compared to the principal absorption wavelengths, lead to simpler expressions in which the force per unit area is proportional to h^{-3} and h^{-4}, respectively. This shift in exponent is related to electromagnetic retardation, owing to the finite speed of light. As shown by Parsegian and Ninham (1971) and Park and Wayner (1987), the van der Waals forces can be obtained directly from the theory of Dzyaloshinskii et al. if the zero-frequency dielectric constants, the major absorption peaks in the frequency spectrum, and the indices of refraction, which can be obtained from spectroscopic optical data, are known. In actuality, the effective exponent of the film thickness varies smoothly from -3 to -4 as the film thickness increases through the range of about 30 to 80 nm. The agreement of the two theories in the limiting cases is good when the only interactions are the London dispersion forces, but not when the Debye and Keesom contributions of polar materials have to be taken into account.

Approximate formulae (Israelachvili, 1985; Hirasaki, 1988) can be derived for the composite Hamaker constant of a thin liquid film 3 lying on a solid substrate 1 with an overlying gas phase 2. This leads to the following expressions for films thin enough for retardation effects to be negligible:

$$A = A_{\nu=0} + A_{\nu>0} \tag{1a}$$

$$A_{\nu=0} = \frac{3}{4} kT \left(\frac{\epsilon_1 - \epsilon_3}{\epsilon_1 + \epsilon_3}\right)\left(\frac{\epsilon_2 - \epsilon_3}{\epsilon_2 + \epsilon_3}\right) \tag{1b}$$

$$A_{\nu>0} \approx \frac{3\hbar\nu_e}{8\sqrt{2}} \frac{(n_1^2 - n_3^2)(n_2^2 - n_3^2)}{(n_1^2 + n_3^2)^{1/2}(n_2^2 + n_3^2)^{1/2}\{(n_1^2 + n_3^2)^{1/2} + (n_2^2 + n_3^2)^{1/2}\}} \tag{1c}$$

Here, for the ith phase, n_1 is the refractive index in the visible part of the spectrum, ϵ_i is the zero-frequency dielectric constant, k is the Boltzmann constant, $\hbar$ is the Planck constant, and ν_e is the principal electronic absorption or ionization frequency, assumed in this approximation to be the same for each material. The first term in equation (1*a*) corresponds to the (zero-frequency) Keesom and Debye forces of polar molecules, while the second term corresponds to the London dispersion forces. Under the assumptions of pairwise additivity and of the interactions of two different media being the geometric mean of the interactions of each medium with itself, an alternative approach to calculating the composite Hamaker constant is

$$A = (A_{11}^{1/2} - A_{33}^{1/2})(A_{22}^{1/2} - A_{33}^{1/2}) \tag{2}$$

A_{ii} is the Hamaker constant for the ith phase separated from itself by a vacuum gap. Equation (2) shows that the composite Hamaker constant of the film is negative if the Hamaker constant of the liquid lies between those of the solid and the gas. The interaction free energy per unit area is given by

$$\omega(h) = -A/12\pi h^2 \tag{3}$$

where h is the local film thickness, assumed to be slowly varying over the surface. For $A<0$ this corresponds to an increase in free energy as the two interfaces are brought from an infinite separation to the thickness of the film. Thus, the disjoining pressure is positive, and hence stabilizing. One can model this force as a surface pressure, appearing only in the surface boundary condition. This leads to a modified Young–Laplace equation for the equilibrium between the two fluids separated by a curved interface, when one of the fluids is a layer thin enough for long-range molecular or ionic forces to be effective. Alternatively (Ruckenstein and Jain, 1974), one can define a potential function ϕ, which is the negative of the disjoining pressure and which depends only on the local film thickness. We employ this approach here.

If there is an adsorbed layer of material 4 and thickness δ on the solid substrate, the interaction energy, under the same assumptions (Vincent, 1973), is given by

$$\omega(h) = \frac{(A_{11}^{1/2} - A_{44}^{1/2})(A_{22}^{1/2} - A_{33}^{1/2})}{12\pi(\delta + h)^2} + \frac{(A_{44}^{1/2} - A_{33}^{1/2})(A_{22}^{1/2} - A_{33}^{1/2})}{12\pi h^2} \tag{4}$$

It is tempting to try to apply this formula to adsorbed monomolecular layers, but the theory breaks down for such short-range interactions. We also confine ourselves to nonionic liquids, although a fairly simple approximate theory for the long-range contribution of the repulsion of diffuse double layers of ions is available (for an up-to-date review of Gouy–Chapman theory and Debye–Huckel theory, see Grimson et al. (1988)). In general, electrical double layer interactions in aqueous solutions are repulsive, and hence stabilizing. The effective distance of these interactions depends upon the Debye sheltering length, which depends upon the ion concentrations and charges. The equilibrium requirement of equality of chemical potential leads to variations in both surfaces of charge and potential as the film thins. Two limiting cases are those of constant surface electrical potential and constant surface electrical charge. Hirasaki (1988) has computed interaction energies for the two limiting cases for various ratios of the electrical potential of the two surfaces at infinite separation.

3 Governing Equations for an Evaporating Thin Film

We consider now the motion of an ultrathin liquid film lying on a flat horizontal solid surface (Fig. 1). The normal coordinate z is taken to be zero at the solid surface. The general equations are given by Atherton and Homsy (1976), but for simplicity only two-dimensional disturbances are considered here. The liquid is assumed to be Newtonian and in-

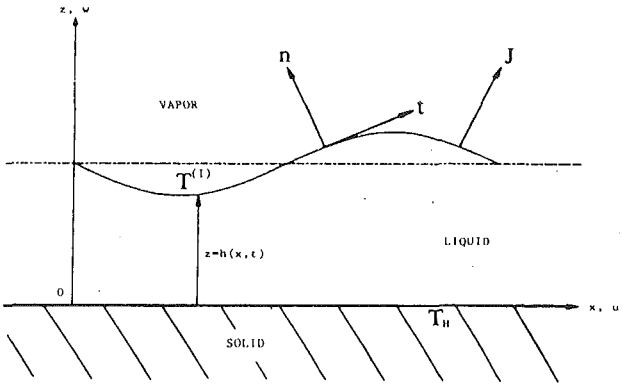

Fig. 1 Sketch of evaporating (condensing) liquid film on hot (cold) horizontal solid surface

compressible. The Navier–Stokes equations for the liquid now include the long-range molecular force potential function ϕ

$$\rho(\mathbf{v}_t + \mathbf{v}\cdot\nabla\mathbf{v}) = -\nabla(p+\phi+\rho g\sin\theta) + \mu\nabla^2\mathbf{v} \tag{5}$$

where ρ is the liquid density, μ is the dynamic viscosity, and θ is the angle of inclination of the flat solid surface to the horizontal. Here p denotes the pressure in the liquid, and $\mathbf{v}$ is the liquid velocity vector with components u and w in the x and z directions, respectively.

The continuity and energy equations in the liquid are

$$\nabla\cdot\mathbf{v} = 0 \tag{6}$$

and

$$T_t + \mathbf{v}\cdot\nabla T = \kappa\nabla^2 T \tag{7}$$

respectively, where κ is the thermal diffusivity and T is the temperature. At the heated solid boundary, $z=0$, the velocity vanishes, and the temperature or heat flux is prescribed. At the interface, $z=h(x,\ t)$, the vapor–liquid jump conditions (Slattery, 1972) are, for mass transport:

$$J = \rho(\mathbf{v}-\mathbf{v}^{(I)}) \tag{8a}$$

$$\mathbf{n} = \rho^{(v)}(\mathbf{v}^{(v)}-\mathbf{v}^{(I)})\cdot\mathbf{n} \tag{8b}$$

and for energy transport:

$$J\left\{L+\frac{1}{2}[(\mathbf{v}^{(v)}-\mathbf{v}^{(I)})]^2-\frac{1}{2}[(\mathbf{v}-\mathbf{v}^{(I)})\cdot\mathbf{n}]^2\right\} =$$

$$-k\nabla T\cdot\mathbf{n}+k^{(v)}\nabla T^{(v)}\cdot\mathbf{n} \tag{9}$$

where $\mathbf{v}^{(v)}$ is the vapor velocity, $\mathbf{v}^{(I)}$ is the velocity of the interface, L is the latent heat of vaporization, $T^{(v)}$ is the vapor temperature, and k and $k^{(v)}$ are the thermal conductivities of the liquid and vapor, respectively. The normal-stress boundary condition is

$$J(\mathbf{v}-\mathbf{v}^{(v)})\cdot\mathbf{n}-(\mathbf{T}-\mathbf{T}^{(v)})\cdot\mathbf{n}\cdot\mathbf{n} = 2H\sigma(T) \tag{10}$$

where $\mathbf{T}$ and $\mathbf{T}^{(v)}$ are the stress tensors of the liquid and vapor, respectively, and the mean curvature H of the interface is defined by

$$2H = \nabla\cdot\mathbf{n} \tag{11}$$

The tangential-stress boundary condition is

$$J(\mathbf{v}-\mathbf{v}^{(v)})\cdot\mathbf{t}-(\mathbf{T}-\mathbf{T}^{(v)})\cdot\mathbf{n}\cdot\mathbf{t} = -\nabla\sigma\cdot\mathbf{t} \tag{12}$$

where $\mathbf{n}$ and $\mathbf{t}$ are the unit normal and tangential vectors to the interface.

Surface tension is represented by a linear equation of state

$$\sigma = \sigma_o - \gamma(T^{(I)}-T_s) \tag{13}$$

where σ_o is the surface tension at the reference temperature T_s, taken as the saturation temperatrure at the system pressure. For nearly all common liquids, $\gamma = -d\sigma/dT$ is positive. There is no slip at the gas-liquid interface, so that

$$(\mathbf{v}-\mathbf{v}^{(v)})\cdot\mathbf{t} = 0 \tag{14}$$

The linearized constitutive equation

$$J = \left(\frac{\alpha\rho^{(v)}L}{T_s^{3/2}}\right)\left(\frac{M_w}{2\pi R_g}\right)^{1/2}(T^{(I)}-T_s) \tag{15}$$

is derived from kinetic theory. It relates the mass flux J at the interface to the local surface temperature $T^{(I)}$, where M_w is the molecular weight, R_g is the universal gas constant, and α is the accommodation coefficient.

Finally, appropriate initial conditions must also be specified for the film thickness and the velocity and temperature fields, as well as boundary conditions for the velocity and temperature at the liquid–solid interface. These boundary conditions can be simplified by noting that the vapor–liquid density and viscosity ratios are small, except close to the critical pressure. Hence, terms containing the vapor density or viscosity can be neglected, except that the vapor velocity is retained in equation (10), since this gives the effect of vapor recoil. A "one-sided" model of film evaporation is thus obtained.

4 Horizontal Evaporating Film

Burelbach et al. (1988) considered the nonlinear stability and rupture of a liquid film evaporating (condensing) on a hot (cold) horizontal surface, where the local film thickness is small enough that long-range molecular forces are significant. This means that, at least locally, the film thickness is less than 100 nm. This is a nonlinear problem of ultrathin film heat transfer with mass transfer. This class of stability problems appears to be relatively new to the heat transfer community. The basic technique, which was introduced by Williams and Davis (1982) for an isothermal, nonevaporating film, can be applied to a number of related problems.

The idea is to develop a nonlinear partial differential equation for the film thickness, $h(x,\ t)$, from the surface kinematic condition, which is the jump mass balance of equation (8*b*). Equation (8*a*) states that the normal component of the velocity of the liquid at the surface relative to that of the surface itself, multiplied by the liquid density, is equal to the mass flux J across the surface. Because the film is so thin, lubrication theory can be applied, which, like boundary-layer theory, assumes slow variations of all dependent variables in directions parallel to the wall. For these very thin films, inertial effects do not appear at lowest order. The length scale is thus the initial film thickness h_0, while a viscous velocity scale ν/h_0 and a viscous time scale h_0^2/ν are appropriate. The pressure and mass flux are made dimensionless with respect to these scales, and the temperature excess over saturation is made dimensionless with respect to $(T_w - T_s)$, the temperature difference between the wall and the saturation temperature.

Retaining the same symbols throughout for the corresponding dimensionless quantities, equations (5) and (6) become

$$\mathbf{v}_t + \mathbf{v}\cdot\nabla\mathbf{v} = -\nabla p - \nabla\phi + \nabla^2\mathbf{v} \tag{16}$$

and

$$\nabla\cdot\mathbf{v} = 0 \tag{17}$$

where the dimensionless potential function ϕ for unretarded van der Waals forces is

$$\phi = Ah^{-3} \tag{18}$$

and A is now a dimensionless Hamaker constant. The scaled energy equation is

$$\mathrm{Pr}(T_t + \mathbf{v}\cdot\nabla T) = \nabla^2 T \tag{19}$$

where Pr is the Prandtl number

$$\mathrm{Pr} = \nu/\kappa \tag{20}$$

An initially small surface perturbation is assumed, and the nonlinear growth is followed all the way to presumed rupture. We note that the unperturbed state is time dependent. The linear stability theory thus leads to an ordinary differential equation for the normal mode amplitude rather than an algebraic dispersion equation (Burelbach, 1988). The basic state is a flat evaporating interface. In addition to a viscous time scale, h_0^2/ν, there is an evaporative time scale, which is a measure of the time to evaporate the film to dryness

$$t_E = h_0^2 L/k\Delta T \tag{21}$$

where L is the latent heat of evaporation. For slow evaporation, the ratio of the viscous to evaporative time scales, termed the evaporation number

$$E = \frac{k\Delta T}{\rho\nu L} \tag{22}$$

is a small parameter. Since the velocity field in the basic state is zero, time is rescaled on the evaporative scale to retain the effect of mass loss in the kinematic boundary condition. The dependent variables are expanded in powers of E, and substituted in the temperature equation and boundary conditions. The resulting leading-order basic-state solution is

$$\bar{h} = -K + (K^2 + 2K + 1 - 2Et)^{1/2} \tag{23}$$

$$\bar{T} = 1 - (K^2 + 2K + 1 - 2Et)^{1/2} z \tag{24}$$

$$\bar{J} = (K^2 + 2K + 1 - 2Et)^{-1/2} \tag{25}$$

where $\bar{h}$, $\bar{T}$, and $\bar{J}$ are the nondimensional, time-dependent film thickness, temperature profile, and surface mass flux, respectively, and

$$K = \left(\frac{kT_s^{3/2}}{\alpha h_o \rho^{(v)} L^2}\right)\left(\frac{2\pi R_g}{M_w}\right)^{1/2} \tag{26}$$

The parameter K measures the degree of nonequilibrium at the evaporating interface. $K=0$ corresponds to the quasi-equilibrium limit where the interfacial temperature is constant and equal to the saturation value, $T=0$. $K^{-1}=0$ corresponds to the nonvolatile case in which the evaporative mass flux J is zero.

The nonuniformities at early and late times can be removed by the introduction of boundary layers in O(E) neighborhoods near $t=0$ and $t=t_D$. Multiple scales and matched asymptotics may then be used to find the inner solutions. Details are given by Burelbach (1988) and Burelbach et al. (1988). The initial temperature field adjusts in a time of O(E) to the linear (quasi-steady) profile, and negligible evaporation occurs during this adjustment period. A late-time analysis yields a solution that breaks down at higher order. However, since disturbances grow or decay much faster than the basic-state film thickness goes to zero, this late limitation does not seriously affect the analysis.

We assume that the dependent variables vary slowly along the plate and in time, so that lubrication theory may be used. Such an approximation excludes those small time intervals near $t=t_D$ and $t=0$ where the basic state may be nonuniform in time; inside these regions the temperature profile or the film thickness change rapidly.

For the long-wave nonlinear stability analysis, the dimensionless wavenumber k is a small parameter. After rescaling the independent variables (x, z, t) to immobilize the basic-state free surface, and expanding the dependent variables in powers of k, a sequence of boundary-value problems with periodic end conditions is obtained. The zeroth-order system contains the dimensionless velocity components, u_o and w_o, as well as dimensionless temperature and pressure, T_o and p_o. Burelbach et al. (1987, 1988) solved for these variables in terms of the dimensionless film thickness h, and then eliminated the velocities from the one-sided surface kinematic

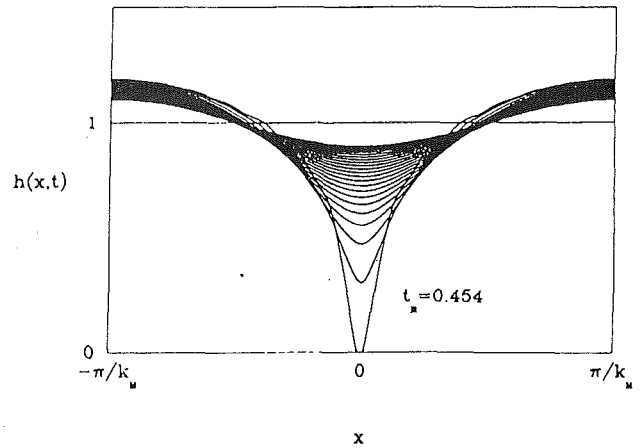

Fig. 2 Dimensionless evaporating film thickness profile over one wavelength. Dimensionless time steps $\Delta t = 0.0001$; 30 spatial nodes. Quasi-equilibrium evaporation ($K=0$); no Marangoni effects ($M=0$). Van der Waals ($A=1$), mass loss ($E=0.1$), surface tension ($S=1/3$), and vapor recoil ($E_2/D=1$) effects taken into account. Dimensionless rupture time $t_R=0.454$.

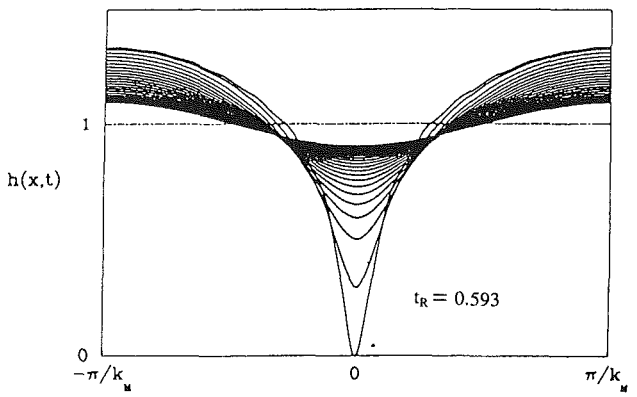

Fig. 3 Dimensionless condensing film thickness profile over one wavelength. Same as in Fig. 2, except that $E=-0.1$. Dimensionless rupture time $t_R=0.593$.

condition, equation (8*a*), obtaining a nonlinear evolution equation for the film thickness:

$$h_t + E(h+K)^{-1} + S(h^3 h_{xxx})_x + \{[Ah^{-1} + E^2 D^{-1}(h+K)^{-3}h^3 + KMP^{-1}(h+K)^{-2}h^2]h_x\}_x = 0 \tag{27}$$

The second term represents mass loss due to evaporation, while the remaining terms take into account the effects of surface tension, van der Waals forces, vapor recoil pushing down on the film surface, and surface-tension variation, in that order. To retain all these effects, it was assumed that Ak, Dk^{-3}, Ek^{-1}, Mk and Sk^3 are all 0(1). This will rarely, if ever, be the case, so that a simpler equation is usually obtained. The nondimensional surface tension S in equation (27) is defined as

$$S = \frac{\sigma_o h_o^2}{3\rho\nu^2} \tag{28}$$

while the capillary number C is given by

$$C = \frac{\gamma\Delta T}{\sigma_o} \tag{29}$$

The parameter D is proportional to the ratio of the vapor to liquid densities

$$D = \frac{3\rho^{(v)}}{2\rho} \tag{30}$$

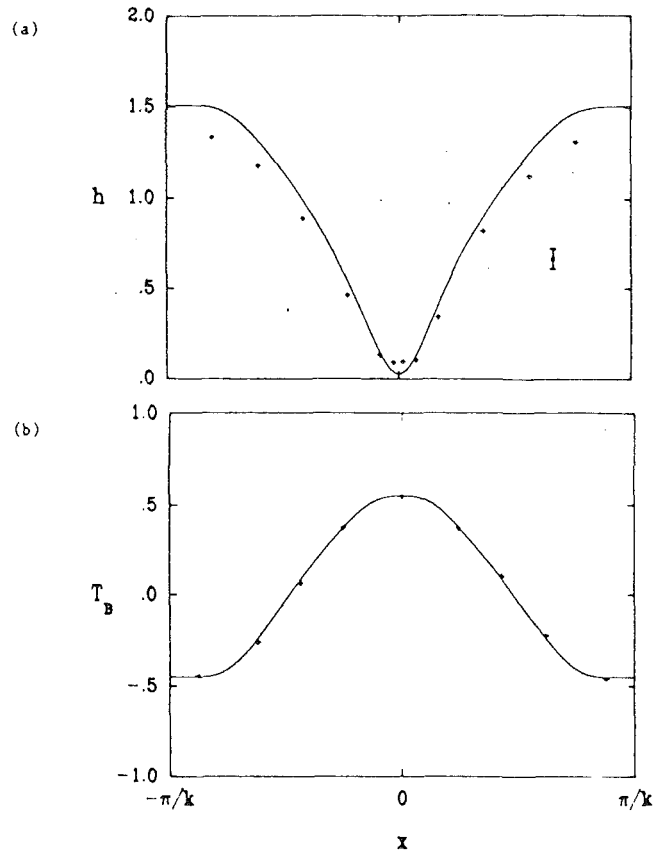

Fig. 4 (a) Measured film thickness of a silicone oil layer on a horizontal plate heated along the centerline, and cooled at two opposite edges, compared to the predicted profile. Initial thickness $h_o = 0.375$ mm. Surface tension parameter $S = 5.8 \times 10^{-4}$. (b) Scaled temperature data and the estimated temperature distribution for Run 18 (Burelbach, 1989).

while M is the Marangoni number

$$\mathrm{M} = \frac{\gamma \Delta T h_o}{2\rho\nu\kappa} \tag{31}$$

which is related to the capillary number, Prandtl number, and nondimensional surface tension (equations (28) and (29)).

For $K = 0$ (quasi-equilibrium evaporation), one obtains

$$h_t + Eh^{-1} + [(Ah^{-1} + E^2 D^{-1})h_x]_x + S(h^3 h_{xxx})_x = 0 \tag{32}$$

The parameters A and S can be removed by rescaling. One obtains the general form

$$h_{\hat{T}} + \mathbb{E}h^{-1} + [(h^{-1} + \mathbb{D})h_X]_X (h^3 h_{XXX})_X = 0 \tag{33}$$

where

$$\mathbb{E} = ES/A^2, \qquad \mathbb{D} = E^2 D^{-1} S/A^2 \tag{34a, b}$$

$$X = (A/S)^{1/2} x, \qquad \hat{T} = (A^2/S)t, \tag{35a, b}$$

As shown in Figs. 2 and 3, for evaporation ($E = 0.1$) the dimensionless rupture time is $t_R = 0.454$, while under the same conditions, except for condensation ($E = -0.1$), $t_R = 0.593$. In both cases the long-range forces contribute strongly to the growth of the surface wave, as can be seen from the rapid growth of the wave, in the final stages. There is a competition between this destabilizing effect and the stabilizing effect of mass gain owing to condensation, which slows down the initial growth of the wave, but the long-range forces easily win in the end. In this case the dimensionless wavenumber $k_{\mathrm{M}} = 2^{-1/2}$, which is the fastest-growing wavenumber for the isothermal linear analysis. It is shown by Burelbach et al. (1988) that the often-employed quasi-steady linear analysis, assuming a frozen base state compared to the rate of growth of the surface wave, introduces artifacts, which predict exponential growth, rather than the true algebraic growth, due to mass loss/gain.

Davis (1983) has also considered the horizontal, nonevaporating film when the solid surface temperature is nonuniform, so that the surface tension is therefore a function of position. Tan et al. (1989) derived a rupture criterion for these conditions by obtaining bounds for the dimensionless heat flux which would allow a smooth solution for the film thickness to exist. At some critical heat flux one expects a cusp to appear. Burelbach et al. (1989) performed confirmatory experiments on the dimpling and rupture of a silicone oil film on a nonuniformly heated Invar surface, which were in excellent agreement with the theory of Burelbach et al. (1988) and Tan et al. (1989) (Fig. 4). This was the first independent experimental confirmation of lubrication theory applied to nonisothermal thin films.

Reisfeld and Bankoff (1989) have extended the analysis to include a linear dependence of viscosity on temperature. If a viscosity-temperature number is defined as

$$V = (\alpha_v \Delta T)/\mu_o \tag{36}$$

where α_v is the temperature coefficient of viscosity, and μ_o is the viscosity at the reference temperature, one arrives, for $K = 0$, at an evolution equation that differs only from the constant-viscosity equation (27) by a factor V, which multiplies the spatial derivative terms. Hence, by appropriate rescaling, one recovers equation (29). More general temperature-viscosity functions can also be employed.

5 Liquid Film Draining Down a Heated Wall

For these films, whose mean thickness may be on the order of millimeters, van der Waals forces are negligible, but gravity and inertia are important. We confine ourselves here to the linear theory. Benjamin (1957) performed a power-series expansion in z of the Orr–Sommerfeld equation for the dimensionless perturbation stream function φ:

$$(D^2 - \alpha^2)^2 \varphi = i\alpha \mathrm{Re}[(U - c)(D^2 - \alpha^2)\varphi - \varphi Du] \tag{37}$$

where z is the distance from the wall, $D = d/dz$, α is now the dimensionless wavenumber, $U = U(z)$ is the steady velocity, $u = u(z)$ is the dimensionless amplitude of the two-dimensional velocity perturbation, and c is the complex wave speed. An analytical long-wave solution for the neutral stability curve was obtained. It was thus established that a free-flow down a vertical plane is unstable for all Reynolds numbers. Yih (1955, 1963) showed that the first nontrivial result is that the imaginary part of the wave speed c_i is given by

$$c_i = (6\alpha \mathrm{Re})/5 - \alpha(3 \cot \theta + \alpha^2 S \mathrm{Re})/3 \tag{38}$$

where S is again a dimensionless surface tension, α is the dimensionless wavenumber, θ is the angle of inclination with the horizontal, and Re is the Reynolds number, based on the average velocity. This shows that the neutral stability curve in the α–Re plane has a bifurcation point at $\alpha = 0$, and $\mathrm{Re}_c = (5/6) \cot \theta$, corresponding to the critical Reynolds number. Note that surface waves grow for all Reynolds numbers *above* Re_c, which is just the opposite of what one wishes if a rupture criterion is sought.

Bankoff (1971) extended the analysis to evaporating films draining down an inclined heated plate. It was assumed that the film thickness is so small, and/or the liquid thermal conductivity is so large (as in a hypothetical loss-of-flow accident in a liquid-metal fast-breeder reactor) that the Peclet number is small compared to unity. This implies that the thermal time constant of the undisturbed film is small compared to either the convective time constant or the wave period. This leads to a linear temperature profile through the liquid at all times. The evaporating interface is also assumed to be always at the saturation temperature. It is found that the neutral stability curve now depends on the dimensionless parameter

$$\beta = \frac{\rho_g}{\rho_l}\left(\frac{q_w}{L\rho_g U_{av}}\right)^2 \tag{39}$$

where ρ_g and ρ_l are the vapor and liquid densities, q_w is the wall heat flux, and U_{av} is the average unperturbed velocity. The critical Reynolds number now becomes

$$\mathrm{Re}_c = \frac{\cot\theta}{\frac{6}{5}+\frac{2}{3}\beta} \tag{40}$$

Thus, for vertical walls the flow is again always unstable. Since β is positive for either evaporation or condensation, vapor recoil effects are always destabilizing. Furthermore, there is a critical wall heat flux at which this effect becomes dominant. Subsequent investigators (Marschall and Lee, 1973; Unsal and Thomas, 1978; Spindler et al., 1978) removed the limitation of small Peclet numbers by including the perturbed energy equation, and included small effects, such as the liquid momentum flux into the interface. Spindler (1982) later considered the full stability problem, taking into account the thinning of the film as it drains down the wall, and also including the induced vapor stress.

Formation of dry spots in heated, draining, liquid films in vertical round or annular geometries was studied experimentally by Norman and McIntyre (1960), Hsu et al. (1965), Simon and Hsu (1970), and on a horizontal strip owing to thermocapillary effects, by Orell and Bankoff (1971). Sharon and Orell (1980) extended the study to the rupture of a heated film flowing along a horizontal plate. The course of thinning and rupture is influenced by contact angle effects, as well as nonlinear wave growth. Phenomenological models have therefore been developed. These depend upon one or more heuristic assumptions concerning the nature of the breakdown process, or conversely, the rewetting process. Contrary to the Yih–Benjamin traveling-wave analysis, dry patches form more readily at a given wall heat flux as the film thickness is decreased, rather than increased. Hence, while small traveling waves grow more readily above a critical Reynolds number, film rupture occurs more readily below some critical Reynolds number. Futhermore, in some still unknown way, the contact angle influences the ease of formation of a dry spot. Anshus and Ruckenstein (1975) proposed a circumferentially periodic steady-state disturbance growing in the axial downstream direction:

$$\eta = \hat{\eta}\ \exp\ [i\alpha y + ax] \tag{41}$$

They showed instability below a critical Re for nonevaporating films with zero surface shear stress.

Chung and Bankoff (1980a) extended the method to evaporating flows with surface shear stress. Multiple, closely spaced eigenvalues were found. Figure 5 shows the comparison between the predicted critical Reynolds number, using the mean amplification factor a for the first five roots, with the experimental value based on film rupture data by Chung and Bankoff (1980*a*, 1980*b*) for a Freon-113/liquid-nitrogen gas cocurrent-downward annular flow in an electrically heated, stainless-steel tube. The agreement is quite good up to a film Reynolds number of 160. The large positive value of a implies a large contact angle ($\theta \cong 80$ deg) at the point where the film thickness goes to zero. It is interesting that this purely mathematical model, which does not take into account the surface wettability, agrees qualitatively with the predictions of entirely different physical models for the same phenomena, as discussed below.

An alternative approach (Hartley and Murgatroyd, 1964) employs a heuristic energy method in which it is assumed that the film breaks up into parallel straight rivulets when the total mechanical energy (kinetic plus surface energy) of the film is equal to that of the rivulets. Still a third approach considers

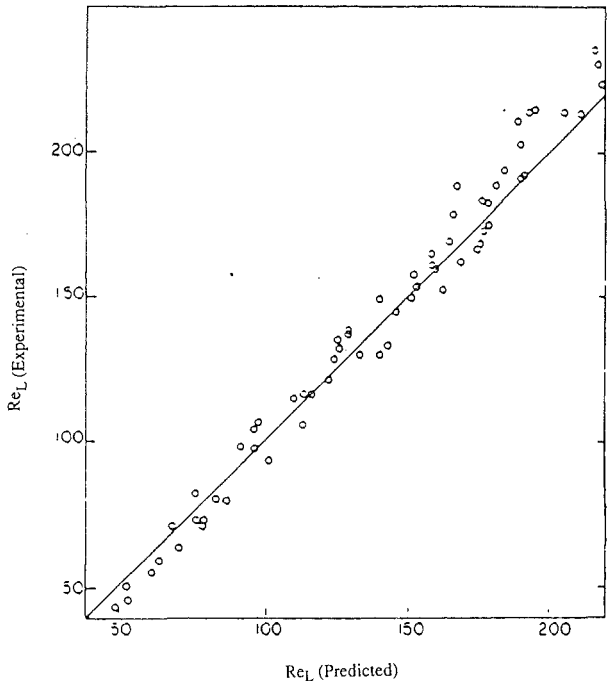

Fig. 5 Comparison of experimental values of critical liquid Reynolds number for onset of dryout of a Freon film flowing cocurrently downward with nitrogen gas in a vertical, heated stainless steel tube with predictions of steady, spatially growing wave model, equation (41)

the conditions for rewetting a dry patch on a vertical wall, based upon a force balance through a cross section of the flow through the stagnation point (Hartley and Murgatroyd, 1964; Zuber and Staub, 1966; Chung and Bankoff, 1980a). These models were successively refined to take into account thermocapillary effects, vapor recoil, and surface shear stress. Finally a fourth model was proposed by Bankoff and Tung (1982), linking the circumferential wavelength of the prerupture vertical film surface corrugations and the final rivulet system. These models have in common that a single parameter, such as the contact angle on a heated, dry surface, must be assumed in order to fit the data. In each case the contact angle is large, which agrees with the adsorption analysis of Segev and Bankoff (1980). However, the agreement with the Chung–Bankoff experimental data is again fairly good (Fig. 6), showing the surprising insensitivity of the critical conditions for film rupture to the details of the model.

6 Thin Films in Subcooled Nucleate Boiling

Perhaps the only other heat transfer mode capable of such high heat transfer rates from continuous solid surfaces is highly subcooled nucleate boiling. This was explored (Gunther and Kreith, 1950; Gunther, 1950) as a means of protecting the throat region of liquid-fueled rocket motors. Even here the overlap between boiling heat transfer and evaporative film heat transfer is considerable. For one thing, a thin film may not be stable to bubble formation as its thickness, or the heat flux, is increased. Vapor bubbles nucleate at surface cavities (Bankoff, 1957) rather than at surface projections as had been speculated in the early literature. Neutral stability for bubble growth occurs when the embryonic bubble forms a hemisphere at the circular cavity mouth. Any further growth of the bubble then proceeds spontaneously to macroscopic dimensions. For neutral stability to be maintained, the embryonic bubble must be in contact with liquid in equilibrium with it. Hsu (1962) noted that this provided a relationship between the temperature gradient in the laminar sublayer close to the wall, the bulk liquid temperature, and the mouth radius of the

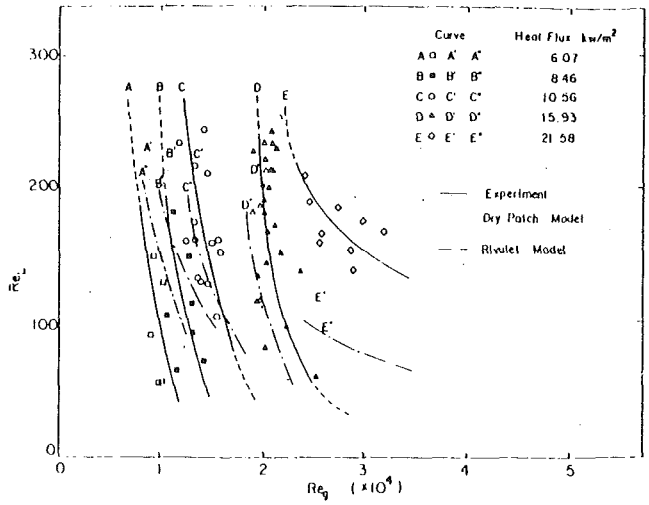

Fig. 6 Comparison of experimental data for rupture of a heated Freon film flowing downward with (a) drypatch model with effective contact angle of 110 deg and (b) rivulet model with effective contact angle of 120 deg (Chung and Bankoff, 1980b)

neutrally stable cavity. As the heat flux increases, this radius decreases. Geometric considerations also apply. The cavity must be a stable vapor trap in order to allow repetitive nucleation (Bankoff, 1958). Hence, if the thickness of the liquid layer is made small enough, very large surface heat fluxes can be sustained without boiling, particularly if vapor traps of sufficiently small mouth radius and apex angle are not available on the solid surface.

Even if for very short periods, the action of these thin evaporating films can be important. Thus, in nucleate boiling, the bubbles strongly enhance heat transfer as compared to all-liquid heat transfer, both by virtue of the latent heat content of the vapor and the stirring action of the bubbles on the surrounding liquid. In highly subcooled, forced-convection nucleate boiling, the bubbles may slide along the surface during their lifetime without ever detaching. Large surface heat transfer coefficients (of the order of 0.5 MW/m^2K) were measured by Gunther (1950).

There is still uncertainty concerning the relative importance of evaporative and nonevaporative mechanisms in this heat transfer. One possibility (Bankoff et al., 1956; Snyder, 1956; Bankoff and Mikesell, 1959; Bankoff, 1959, 1962; Robin and Snyder, 1970) is that the bubbles function as minute heat pipes with evaporation occurring at their base, and condensation at their cold polar cap. The required vapor supply would come principally from the evaporation of a thin liquid microlayer at the base of the growing-and-collapsing bubble (Moore and Mesler, 1961; Sharp, 1964; Cooper and Lloyd, 1969; Voutsinos and Judd, 1975; Judd and Hwang, 1976). On the other hand, Gunther (1950), Rohsenow and Clark (1951), and Del Valle and Kenning (1985) noted that the visible vapor volumetric flux accounts for only 1–2 percent of the total surface heat flux, and suggested that nonevaporative mechanisms, such as stirring of the wall boundary layer by the bubbles and quenching of the hot wall upon bubble collapse, are more important. Furthermore, Plesset and Prosperetti (1978) showed that a stagnant, uniform microlayer would not evaporate fast enough to supply more than about 10 percent of the total surface heat flux in the Gunther experiments. However, Koffman and Plesset (1983) later made interferometric measurements of the thickness of the thin liquid films under bubbles growing on a heated glass plate submerged in a pool of slightly subcooled water. They concluded that microlayer evaporation was significant, and might account for somewhat less than half the observed heat flux, even for stationary bubbles with small solid-wall superheat temperatures and small bulk-liquid subcooling.

Very recently, Tsung-Chang and Bankoff (1989) estimated the increase in microlayer evaporation to be greater by a factor of 0.5–3, depending on the model, for sliding bubbles (as in Gunther, 1950), compared to stationary bubbles under the same thermal conditions. Furthermore, the stability of this microlayer can be very important. On unwetted surfaces the microlayer ruptures very rapidly, and there will be a moving contact line. From potential theory there would be a logarithmic singularity in the heat flow from the solid per unit length of contact line if the solid substrate had infinite thermal conductivity, and if the vapor–liquid interface were everywhere at the saturation temperature. With water on engineering surfaces, such as stainless steel, the contact angle is generally in the range of 40–60 deg. Burelbach (1988) has shown that rupture times can be expected to be on the order of microseconds for unstable films thinner than about 10 nm. All this demonstrates that thin-film heat transfer is intertwined very closely with boiling heat transfer under large heat flux conditions in ways that are not yet completely understood.

7 Concluding Remarks

This is a promising area for further research. A number of compact, high-heat-flux devices depend on the heat transfer characteristics of thin liquid films, and a better understanding of some of the older, well-known heat transfer phenomena may also result. Nonlinear wave theory, bifurcation theory, and asymptotics can all play a role here. On the experimental side, improved techniques for measuring the thickness of very thin films, local velocities and temperatures, and contact angles are needed for development of reliable data in the ranges of interest. A considerable start has been made, but it is only a start.

Acknowledgments

This work was supported by a grant from the Office of Basic Energy Sciences, Department of Energy.

References

Anshus, B. E., and Ruckenstein, E., 1975, "The Appearance of Dry Patches on a Wetted Wall," *J. Colloid and Interface Science*, Vol. 51, pp. 12–22.

Atherton, R. W., and Homsy, G. M., 1976, "On the Derivation of Evolution Equations for Interfacial Waves," *Chem. Eng. Commun.*, Vol. 2, pp. 57–77.

Bankoff, S. G., Colahan, W. R., Jr., and Bartz, D. R., 1956, "Summary of Conference on Bubble Dynamics and Boiling Heat Transfer Held at the Jet Propulsion Laboratory," *Jet Propulsion Laboratory Memo 20–137*, California Institute of Technology, Pasadena, CA.

Bankoff, S. G., 1957, "Ebullition From Solid Surfaces in the Absence of a Pre-existing Gaseous Phase," *Trans. ASME*, Vol. 29, pp. 735–740.

Bankoff, S. G., 1958, "Entrapment of Gas in the Spreading of a Liquid Over a Rough Surface," *AIChE Journal*, Vol. 4, pp. 24–26.

Bankoff, S. G., 1959, "On the Mechanism of Highly Subcooled Nucleate Boiling," *Jet Propulsion Lab. Memo 30–38*, California Institute of Technology, Pasadena, CA.

Bankoff, S. G., and Mikesell, R. D., 1959, "Bubble Growth Rates in Highly Subcooled Nucleate Boiling," *Chem. Eng. Progress Symp. Ser. No. 29*, Vol. 55, pp. 95–102.

Bankoff, S. G., 1962, "A Note on Latent Heat Transport in Nucleate Boiling," *AIChE Journal*, Vol. 8, pp. 63–65.

Bankoff, S. G., 1971, "Stability of Liquid Flow Down a Heated Inclined Plane," *Int. J. Heat Mass Transfer*, Vol. 14, pp. 377–385.

Bankoff, S. G., and Tung, H. H., 1982, "Rivulet Formation on a Heated Wall," *Proceedings, Seventh International Heat Transfer Conference*, Munich, Federal Republic of Germany, pp. 363–367.

Benjamin, T. B., 1957, "Wave Formation in Laminar Flow Down an Inclined Plane," *J. Fluid Mech.*, Vol. 554–574.

Benney, D. J., 1966, "Long Waves on Liquid Films," *J. Math. Phys.*, Vol. 45, pp. 150–155.

Burelbach, J. P., Bankoff, S. G., and Davis, S. H., 1987, "Nonlinear Stability of Evaporating/Condensing Films," Applied Mathematics Tech. Rpt. No. 8704, Northwestern University, Evanston, IL.

Burelbach, J. P., Bankoff, S. G., and Davis, S. H., 1988, "Nonlinear Stability of Evaporating/Condensing Films," *J. Fluid Mech.*, Vol. 195, pp. 463–494.

Burelbach, J. P., 1988, Ph.D. thesis, Chemical Engineering Department, Northwestern University, Evanston, IL.

Burelbach, J. P., Bankoff, S. G., and Davis, S. H., 1990, "Steady Thermocapillary Flows of Thin Liquid Layers. II. Experiment," *Phys. Fluids A*, Vol. 2, pp. 322–333.

Chung, J. C., and Bankoff, S. G., 1980a, "Initial Breakdown of a Heated Liquid Film in Cocurrent Two-Component Annular Flow I: Small Perturbation Model," *Chem. Eng. Communications*, Vol. 4, pp. 433–453.

Chung, J. C., and Bankoff, S. G., 1980b, "Initial Breakdown of a Heated Liquid Film in Cocurrent Two-Component Annular Flow. II: Rivulet and Drypatch Models," *Chem. Eng. Communications*, Vol. 4, pp. 455–470.

Cooper, M. G., and Lloyd, A. J. P., 1969, "The Microlayer in Nucleate Boiling," *Int. J. Heat Mass Transfer*, Vol. 12, pp. 895–913.

Davis, S. H., 1983, "Rupture of Thin Liquid Films," in: *Waves on Fluid Interfaces*, R.E. Meyer, ed., Academic Press, New York, pp. 291–302.

De Gennes, P. G., 1985, "Wetting: Statics and Dynamics," *Rev. Mod. Phys.*, Vol. 57, pp. 827–863.

Del Valle, V. H., and Kenning, D. B. R., 1985, "Subcooled Flow Boiling at High Heat Flux," *Int. J. Heat Mass Transfer*, Vol. 28, pp. 1907–1925.

Derjaguin, B. V., and Churaev, N. Y., 1986, "Properties of Water Layer Adjacent to Interfaces," in: *Fluid Interfacial Phenomena*, C. A. Croxton, ed., Wiley, New York.

Derjaguin, B. V., Churaev, N. Y., and Muller, V. M., 1987, *Surface Forces*, Consultants Bureau, New York.

Derjaguin, B. V., 1955, "Definition of the Concept and Magnitude of the Disjoining Pressure and Its Role in the Statics and Dynamics of Thin Layers of Liquids," *Colloid J. U.S.S.R.*, Vol. 17, pp. 191–197.

Dzyaloshinskii, I. E., Lifshitz, E. M., and Pitaevskii, A. E., 1959, "Van der Waals Forces in a Liquid Film," *Zh. Eksper. Teor. Fiz.*, Vol. 37, pp. 229–241; *Soviet Phys. JETP*, Vol. 37, 1960, pp. 161–170.

Gjevik, B., 1970, "Occurrence of Finite-Amplitude Surface Waves on Falling Liquid Films," *Phys. Fluids*, Vol.13, pp. 1918–1925.

Grimson, M. J., Richmond, P., and Vassilieff, C. S., 1988, "Electrostatic Interactions in Thin Films," in: *Thin Liquid Films*, I. G. Ivanov, ed., Marcel Dekker, New York, Chap. 5, pp. 276–327.

Gunther, F. C., 1950, *Progress Report No. 4–75*, Jet Propulsion Laboratory, California Institute of Technology, Pasadena, CA.

Gunther, F. C., and Kreith, F., 1950, *Progress Report No. 4–120*, Jet Propulsion Laboratory, California Institute of Technology, Pasadena, CA.

Hamaker, H. C., 1937, "The London–van der Waals Attraction Between Spherical Particles," *Physica*, Vol. 4, pp. 1058–1072.

Hartley, D. E., and Murgatroyd, W., 1964, "Criteria for the Breakup of Thin Liquid Layers Flowing Over Solid Surfaces," *Int. J. Heat Transfer*, Vol. 7, pp. 1003–1015.

Hirasaki, G., 1988, "Wettability: Fundamentals and Surface Forces," SPE/DOE 1736, Soc. Petr. Engrs., Richardson, TX.

Homsy, G. M., 1974, "Model Equations for Wavy Viscous Film Flow," *Lectures in Applied Math.*, Vol. 15, pp. 191–194.

Hsu, Y. Y., 1962, "On the Size Range of Active Nucleation Cavities on a Heating Surface," ASME JOURNAL OF HEAT TRANSFER, Vol. 84, pp. 207–216.

Hsu, Y. Y., Simon, F. F., and Lad, J. F., 1965, "Destruction of a Thin Liquid Film Flowing Over a Heated Surface," *Chem. Eng. Progress Symp. Ser. No. 16*, Vol. 57, pp. 139–152.

Israelachvili, J. N., 1985, *Intermolecular and Surface Forces*, Academic Press, New York.

Ivanov, I. B., ed., 1988, *Thin Liquid Films*, Marcel Dekker, New York.

Judd, R. L., and Hwang, K. S., 1976, "A Comprehensive Model for Nucleate Pool Boiling Heat Transfer Including Microlayer Evaporation," ASME JOURNAL OF HEAT TRANSFER, Vol. 98, pp. 623–629.

Koffman, L., and Plesset, M. S., 1983, "Experimental Observation of the Microlayer in Vapor Bubble Growth on a Heated Solid," ASME JOURNAL OF HEAT TRANSFER, Vol. 105, pp. 625–632.

Krantz, W. B., and Goren, S. L., 1970, "Finite-Amplitude, Long Waves on Liquid Films Flowing Down a Plane," *Ind. Eng. Chem. Fund.*, Vol. 9, pp. 107–113.

Lifshitz, E. M., 1955, "Theory of Molecular Attractions Between Solid Bodies," *J. Exp. Theor. Phys. U.S.S.R.*, Vol. 29, p. 94; *Soviet Phys. JETP*, Vol. 7, 1958, pp. 182.

Marschall, E., and Lee, C. Y., 1973, "Stability of Condensate Flow Down a Heated Wall," *Int. J. Heat Mass Transfer*, Vol. 16, pp. 41–48.

Moore, F. D., and Mesler, R. B., 1961, "The Measurement of Rapid Surface Temperature Fluctuations During Nucleate Boiling of Water," *AIChE Journal*, Vol. 7, pp. 620–624.

Moosman, S., and Homsy, G. M., 1980, "Evaporating Menisci of Wetting Fluid," *J. Colloid Interf. Sci.*, Vol. 73, pp. 212–223.

Nir, S., and Vassilieff, C. S., 1988, "Van der Waals Interactions in Thin Films," in: *Thin Liquid Films*, I. B. Ivanov, ed., Marcel Dekker, New York, Chap. 4, pp. 208–274.

Norman, W. S., and McIntyre, V., 1960, "Heat Transfer to a Liquid Film on a Vertical Surface," *Trans. Inst. Chem. Engrs.*, Vol. 38, pp. 301–307.

Orell, A., and Bankoff, S. G., 1971, "Formation of a Dry Spot in a Liquid Film Heated From Below," *Int. J. Heat Mass Transfer*, Vol. 14, pp. 1838–1842.

Park, C. J., and Wayner, P. C., Jr., 1987, "Surface Shear Near the Contact Line of a Binary Evaporating Curved Thin Film," *AIChE Journal*, Vol. 33, pp. 1–10.

Parsegian, V. A., and Ninham, B. W., 1971, "Towards the Correct Calculation of van der Waals Interactions Between Lyophobic Colloids in an Aqueous Medium," *J. Colloid Interf. Sci.*, Vol. 37, pp. 332–341.

Plesset, M. S., and Prosperetti, A., 1978, "The Contribution of Latent Heat Transport in Subcooled Nucleate Boiling," *Int. J. Heat Mass Transfer*, Vol. 21, pp. 725–735.

Reisfeld, B., and Bankoff, S. G., 1989, "Nonlinear Stability of Thin Films With Variable Viscosity," presented at session on Fundamental Research in Fluid Mechanics: Hydrodynamic Stability and Nonlinear Transitions, AIChE Annual Mtg., San Francisco, CA.

Renk, F. J., Wayner, P. C., Jr., and Homsy, G. M., 1978, "On the Transition Between a Wetting Film and a Capillary Meniscus," *J. Colloid Interf. Sci.*, Vol. 67, pp. 408–414.

Renk, F. J., and Wayner, P. C., Jr., 1979, "An Evaporating Ethanol Meniscus: Part II, Theoretical Studies," ASME JOURNAL OF HEAT TRANSFER, Vol. 101, pp. 59–62.

Robin, T. J., Jr., and Snyder, N. W., 1970, "Bubble Dynamics in Subcooled Nucleate Boiling Based on the Mass Transfer Mechanism," *Int. J. Heat Mass Transfer*, Vol. 13, pp. 305–318.

Rohsenow, W. M., and Clark, J. A., 1951, "A Study of the Mechanism of Boiling Heat Transfer, " *Trans. ASME*, Vol. 73, pp. 609–620.

Ruckenstein, E., and Jain, R. K., 1974, "Spontaneous Rupture of Liquid Films," *J. Chem. Soc., Faraday Trans. II*, Vol. 70, pp. 132–147.

Segev, A., and Bankoff, S. G., 1980, "The Role of Adsorption in Determining the Minimum Film Boiling Temperature," *Int. J. Heat Mass Transfer*, Vol. 23, pp. 637–642.

Sharp, R. R., 1964, "The Nature of Liquid Film Evaporation in Nucleate Boiling," NASA TN D-1997.

Sharon, A., and Orell, A., 1980, "Dry Patch Formation in Liquid Films Flowing in a Heated Horizontal Channel," *Int. J. Heat Mass Transfer*, Vol. 21, pp. 547–537.

Simon, F. F., and Hsu, Y. Y., 1970, "Thermocapillary-Induced Breakdown of a Falling Liquid Film," NASA TN D-5624.

Sivashinsky, G. I., and Michelson, D. M., 1980, "On Irregular Wavy Flow of a Liquid Film Down a Vertical Plane," *Prog. Theor. Phys.*, Vol. 63, pp. 2112–2114.

Slattery, J. C., 1972, *Momentum, Energy and Mass Transfer in Continua*, McGraw-Hill, New York, Chaps. 1 and 2.

Snyder, N. W., 1956, Private Communication, Comments on pp. 13, 14, 15, 20, 21, 38 and 39 of Bankoff et al. (1956).

Spindler, B., Solesio, J. N., and Delhaye, J. M., 1978, "On the Equations Describing the Instabilities of Liquid Films With Phase Change," *Two-Phase Momentum, Heat and Mass Transfer in Chemical Process and Energy Engineering Systems*, F. Durst, G. V. Tsiklauri, and N. H. Afgan, eds., Vol. 1, pp. 339–344, Hemisphere Press, Washington, DC.

Spindler, B., 1982, "Linear Stability of Liquid Films With Interfacial Phase Change," *Int. J. Heat Mass Transfer*, Vol. 25, pp. 161–173.

Tan, M., Bankoff, S. G., and Davis, S. H., 1990, "Steady Thermocapillary Flows of Thin Liquid Layers. I. Theory," *Phys. Fluids A*, Vol. 2, pp. 313–321.

Tsung-Chang, G., and Bankoff, S. G., 1990, "On the Mechanism of Forced-Convection Subcooled Nucleate Boiling," ASME JOURNAL OF HEAT TRANSFER, Vol. 112, pp. 213–218.

Unsal, M., and Thomas, W. C., 1978, "Linearized Stability Analysis of Film Rupture," ASME JOURNAL OF HEAT TRANSFER, Vol. 100, pp. 629–634.

Vincent, B., 1973, "The van der Waals Attraction Between Colloid Particles Having Adsorbed Layers. II: Calculation of Interaction Curves," *J. Colloid Interf. Sci.*, Vol. 42.2, pp. 270–285.

Voutsinos, C. M., and Judd, R. L., 1975, "Laser Interferometric Investigation of the Microlayer Evaporation Phenomenon," ASME JOURNAL OF HEAT TRANSFER, Vol. 97, pp. 82–92.

Wayner, P. C., Jr., 1979, "Effect of Interfacial Phenomena in the Interline Region on the Rewetting of a Hot Spot," *Int. J. Heat Mass Transfer*, Vol. 22, pp. 1033–1040.

Wayner, P. C., Jr., 1980, "Interfacial Profile in the Contact Line Region of a Finite Contact Angle System," *J. Colloid Interf. Sci.*, Vol. 77, pp. 495–500.

Wayner, P. C., Jr., 1982, "Adsorption and Capillary Condensation at the Contact Line in Change of Phase Heat Transfer," *Int. J. Heat Mass Transfer*, Vol. 25, pp. 707–713.

Williams, M. B., and Davis, S. H., 1982, "Nonlinear Theory of Film Rupture," *J. Colloid Interf. Sci.*, Vol. 90, pp. 220–228.

Yih, C.-S., 1955, "Stability of Parallel Laminar Flow With a Free Surface," *Quart. Appl. Math.*, Vol. 12, pp. 434–439.

Yih, C.-S., 1963, "Stability of Liquid Flow Down an Inclined Plane," *Phys. Fluids*, Vol. 6, pp. 321–334.

Zuber, N., and Staub, F. W., 1966, "Stability of Dry Patches Forming in Liquid Films Flowing Over Heated Surfaces," *Int. J. Heat Mass Transfer*, Vol. 9, pp. 897–905.

Model Reduction of Transfer Functions Using a Dominant Root Method

J. E. Seem
Johnson Controls, Inc.,
Milwaukee, WI 53201

S. A. Klein

W. A. Beckman

J. W. Mitchell

Solar Energy Laboratory,
University of Wisconsin—Madison,
Madison, WI 53706

Transfer function methods are more efficient for solving long-time transient heat transfer problems than Euler, Crank–Nicolson, or other classical techniques. Transfer functions relate the output of a linear, time-invariant system to a time series of current and past inputs, and past outputs. Inputs are modeled by a continuous, piecewise linear curve. The computational effort required to perform a simulation with transfer functions can be significantly decreased by using the Padé approximation and bilinear transformation to determine transfer functions with fewer coefficients. This paper presents a new model reduction method for reducing the number of coefficients in transfer functions that are used to solve heat transfer problems. There are two advantages of this method over the Padé approximation and bilinear transformation. First, if the original transfer function is stable, then the reduced transfer function will also be stable. Second, reduced multiple-input single-output transfer functions can be determined by this method.

Introduction

Year-long simulations of the hourly (or shorter time period) heating and cooling loads for buildings are important for sizing heating, ventilating, and air conditioning equipment, determining the effect of a design change or retrofit on energy usage, and developing optimal control strategies. Yearly simulations require a large amount of computational effort because the solution to a long-time transient heat transfer problem must be determined. For long-time solutions, transfer function methods are more efficient than Euler, Crank–Nicolson, or other classical techniques because there is no critical time step and the internal temperature distribution is not calculated. Transfer functions relate the output of a linear, time-invariant system to a time series of current and past inputs, and past outputs. Inputs are modeled by a continuous, piecewise linear curve.

The definition of transfer function used in the field of heat transfer in buildings is different from that used in the field of automatic controls. In automatic controls a transfer function is the Laplace or z-transform of the output divided by the Laplace or z-transform of the input. In heat transfer, a transfer function is a recursive difference equation that relates the output of a linear, time-invariant system to a time series of current and past inputs, and a time series of past outputs. In this paper, the latter definition will be used. Also, this paper uses the Laplace transfer function as the definition for the Laplace transform of the output divided by the Laplace transform of the input and the z-transfer function as the z-transform of the output divided by the z-transform of the input.

Transfer functions for computing heat flow through building elements (e.g., walls, floors, roofs, partitions) are of the form

$$q_t'' = \sum_{j=0}^{n} (a_j T_{t-j\delta,o} + b_j T_{t-j\delta,i}) - \sum_{j=1}^{n} (c_j q_{t-j\delta}'') \qquad (1)$$

There are a number of methods available for calculating the transfer function coefficients in equation (1). Stephenson and Mitalas (1971) presented a method for determining transfer functions for one-dimensional heat transfer through multilayered slabs by solving the conduction equation with Laplace and z-transform theory. Hittle (1981) presented a very detailed description of the development of transfer functions for multilayered slabs. Celyan and Myers (1980) and Seem et al. (1989a) presented methods for determining transfer functions for multidimensional heat transfer by determining the exact solution to a system of ordinary differential equations.

Seem et al. (1988b) presented a method in which the transfer functions describing heat flows in building elements can be combined into a single transfer functions for an enclosure, referred to as a comprehensive room transfer function. The number of past time steps in the combined transfer function is equal to the summation of the number of past time steps for the individual transfer functions. Thus, the computational effort of performing a simulation with a comprehensive room transfer function is not significantly different from the effort required to perform a simulation with the individual transfer functions. Fortunately, model reduction methods can be used to reduce the number of significant coefficients in transfer functions.

A number of different model reduction methods have been developed by researchers in the fields of automatic controls and systems analysis. The motivation behind the development of these methods is to reduce computer time for system simulation and to make control system design and analysis easier. Shamash (1980) notes that the Padé approximation is a popular method for reducing single-input Laplace transfer functions because it requires little computational effort, cancels common factors if they exist, and matches the steady-state response of the original and reduced Laplace transfer functions for polynomial inputs. The Padé approximation requires the power series expansion of the original Laplace-transfer function to be equal to the power series expansion of the reduced Laplace-transfer function for terms of order s^0 to s^{2m}. (The number of coefficients in the reduced Laplace-transfer function is equal to $2m+1$.) There are two disadvantages of the Padé approximation. First, if the original transfer function is stable, then the reduced transfer function is not guaranteed to be stable. Second, reduced multiple-input transfer functions cannot be obtained with the Padé approximation.

Seem et al. (1989b) have used the bilinear transformation and Padé approximation to reduce single-input transfer func-

Contributed by the Heat Transfer Division and presented at the ASME Winter Annual Meeting, Chicago, Illinois, November 28–December 2, 1989. Manuscript received by the Heat Transfer Division March 6, 1989; revision received August 4, 1989. Keywords: Building Heat Transfer, Conduction, Numerical Methods.

tions. There are five main steps required to compute a reduced transfer function with m past time steps. First, z-transform theory is used to determine a z-transfer function from the original transfer function. Second, the bilinear transformation is used to transform the z-transfer function into a w-transfer function. w-transfer functions and Laplace transfer functions have similar properties because both are unstable if they have poles in the right halves of their planes. Third, the Padé approximation is used to determine a reduced w-transfer function. The Padé approximation requires the power series expansion for the reduced w-transfer function to be equal to the power series expansion of the original w-transfer function for terms of order w^0 to w^{2m}. Fourth, the bilinear transformation is used to determine a reduced z-transfer function from the reduced w-transfer function. Fifth, z-transform theory is used to transform the reduced z-transfer function into a reduced transfer function.

This paper presents a new model reduction method for reducing the number of coefficients in transfer functions used to solve heat transfer problems. There are two advantages of this method over the Padé approximation and bilinear transformation. First, if the original transfer function is stable, then the reduced transfer function will also be stable. Second, reduced multiple-input single-output transfer functions can be determined by this method.

The first section of this paper contains the development of equations for reducing single-input transfer functions. In the second section of this paper, a step-by-step procedure for reducing multiple-input transfer functions is presented. The last section of this paper contains applications of dominant root model reduction.

Reduction of Single-Input Transfer Functions

This section describes a method for determining a reduced single-input transfer function with m past time steps from a single-input transfer function with n past time steps (m is less than n). First, a derivation is presented for determining the roots of the original transfer function that have the largest effect on the transient response to a step input. (The roots of a transfer function are determined from the output coefficients.) The roots that have the largest effect on the transient response are defined as the dominant roots. The dominant root of the original transfer function are used to determine the output coefficients of the reduced transfer function. Input coefficients of the reduced transfer function are determined by using the same procedure that the Padé approximation and bilinear transformation use to determine input coefficients, i.e., the power series of the original and reduced w-transfer functions are equated for powers of w from 0 to m. The seven main steps required to determine a reduced single-input transfer function are described as follows.

Dominant Roots (Step One). This step uses z-transform theory (Jury, 1964) to determine the explicit solution of the response to a unit step input for a single-input transfer function. This explicit solution is used to determine which roots have the largest effect on the transient response to a step input, i.e., the "dominant roots."

The following single-input transfer function relates the inputs of a system to the outputs:

$$y_t = \sum_{j=0}^{n} (a_j u_{t-j\delta}) - \sum_{j=1}^{n} (b_j y_{t-j\delta}) \tag{2}$$

The z-transform of the output, $Y(z)$, is related to the z-transform of the input, $U(z)$, by the following relationship:

$$Y(z) = \frac{\sum_{j=0}^{n} (a_j z^{-j})}{\sum_{j=0}^{n} (b_j z^{-j})} U(z) = \frac{\sum_{j=0}^{n} (a_j z^{n-j})}{\sum_{j=0}^{n} (b_j z^{n-j})} \tag{3}$$

where $b_o = 1$.

The z-transform of a unit step is

$$U(z) = \frac{z}{z-1} \tag{4}$$

Substituting equation (4) into equation (3) gives

$$Y(z) = \frac{z\sum_{j=0}^{n} a_j z^{n-j}}{(z-1)\sum_{j=0}^{n} b_j z^{n-j}} \tag{5}$$

Equation (5) is the z-transform of the output when the input is a unit step. Equation (5) can be rewritten in the following form:

Nomenclature

a = input transfer function coefficient, outdoor temperature transfer function coefficient
$\bar{a}$ = input coefficient for w-transfer function
b = output coefficient for transfer function, indoor temperature coefficient for a building element transfer function
$\bar{b}$ = input coefficient for w-transfer function
c = transfer function coefficient for past heat fluxes for a building element
$\bar{c}$ = coefficient for power series expansion of w-transfer function
d = outdoor temperature coefficient for a building element transfer function, output coefficient for reduced transfer function
$\bar{d}$ = input coefficient for reduced w-transfer function
e = output coefficient for reduced transfer function
$G(w)$ = w-transfer function
$G_r(w)$ = reduced w-transfer function
$G(z)$ = z-transfer function
$G_r(z)$ = reduced z-transfer function
m = number of past time steps in reduced transfer function
n = number of past time steps in original transfer function
$N_r(w)$ = function of complex variable w
q'' = heat flux
u = input
$U(z)$ = z-transform of the input
w = complex variable that results from the bilinear transformation
y = output
$Y(z)$ = z-transform of the output
z = complex variable that results from z-transformation
β = constant that results from partial fraction expansion, equation (8)
δ = time step
λ = root, equation (6)
$\bar{\lambda}$ = dominant root
ω = quantity used to select dominant roots, equation (12)

Subscripts

i = inside
o = outside
$t\text{-}n\delta$ = input or output n time steps prior to time t

$$Y(z) = \frac{\sum_{j=0}^{n} (a_j z^{n+1-j})}{\prod_{j=0}^{n} (z-\lambda_j)} \tag{6}$$

where $\lambda_0 = 1$ and $\lambda_1, \lambda_2, \lambda_3, \ldots, \lambda_n$ are the roots of

$$z^n + b_1 z^{n-1} + b_2 z^{n-2} + \ldots + b_{n-1} z + b_n = 0 \tag{7}$$

Prandt and Wu (1983) state that a transfer function will be stable if the absolute value of every root in equation (7) is less than one. For heat transfer problems that have at least one convective or specified temperature boundary condition, the roots of equation (7) are real and between zero and one (Ceylan, 1979). Hittle (1981) shows that all the roots are distinct for partial differential equations describing heat transfer. When all roots are distinct, the response (e.g., temperature or heat flux) to a step change in an input (e.g., temperature or heat flux) is a summation of exponentials. Transfer functions generated from finite-difference/element models or from a combination of transfer functions for building elements may have multiple real roots. Seem (1987) describes a method for eliminating multiple roots in transfer functions.

When the roots are real and distinct, partial fraction expansion can be used to write the z-transform of the output as

$$Y(z) = \frac{\beta_0 z}{z-\lambda_0} + \frac{\beta_1 z}{z-\lambda_1} + \frac{\beta_2 z}{z-\lambda_2} + \ldots + \frac{\beta_n z}{z-\lambda_n} \tag{8}$$

where

$$\beta_j = \frac{\sum_{i=0}^{n} (a_i \lambda_j^{n-i})}{\prod_{\substack{i=0 \\ i \neq j}}^{n} (\lambda_j - \lambda_i)} \tag{9}$$

Transforming equation (8) back to the time domain gives

$$y_{t+k\delta} = \beta_0 + \beta_1 \lambda_1^k + \beta_2 \lambda_2^k + \ldots + \beta_n \lambda_n^k \tag{10}$$

where $k \geq 0$.

Equation (10) is the explicit solution for the response at time $k\delta$ to a step input at time zero. The response to a step input can be split into two parts: the steady-state response and the transient response. The steady-state response is β_0 and the transient response is

$$y_{t+k\delta} - \beta_0 = \beta_1 \lambda_1^k + \beta_2 \lambda_2^k + \ldots + \beta_n \lambda_n^k \tag{11}$$

The summation of the transient response from time zero to infinity is

$$\sum_{k=0}^{\infty} (y_{t+k\delta} - \beta_0) = \sum_{k=0}^{\infty} (\beta_1 \lambda_1^k + \beta_2 \lambda_2^k + \ldots + \beta_n \lambda_n^k)$$

$$= \frac{\beta_1}{1-\lambda_1} + \frac{\beta_2}{1-\lambda_2} + \ldots + \frac{\beta_n}{1-\lambda_n} \tag{12}$$

The roots with the largest effect on the transient response are the roots with the largest value of the following quantity:

$$\omega_j = \left| \frac{\beta_j}{1-\lambda_j} \right| \tag{13}$$

The dominant roots are defined as the roots with the largest effect on the transient response, i.e., the roots with the largest ω_j computed from equation (13). (The third section of this paper shows that the largest root is not always the dominant root.)

Output Coefficients of the Reduced Transfer Function (Step Two). Equations (9) and (13) can be used to determine the m dominant roots of the original transfer function. This section contains equations for determining the output coefficients from the m dominant roots.

The following equation is used to determine the numerator of the reduced z-transfer function from the m dominant roots:

$$G_r(z) = \frac{z^m \sum_{j=0}^{m} (d_j z^{-j})}{\prod_{j=1}^{m} (z-\bar{\lambda}_j)} = \frac{\sum_{j=0}^{m} (d_j z^{-j})}{\prod_{j=1}^{m} (1-\bar{\lambda}_j z^{-1})} \tag{14}$$

where $\bar{\lambda}_j =$ one of the m dominant roots; $m =$ number of past time steps in the reduced transfer function.

Multiplying the m terms together in equation (14) results in

$$G_r(z) = \frac{\sum_{j=0}^{m} (d_j z^{-j})}{\sum_{j=0}^{m} (e_j z^{-j})} \tag{15}$$

where

$$\begin{aligned}
e_0 &= 1 \\
e_1 &= -\sum_{i=1}^{m} \bar{\lambda}_i \\
e_2 &= \sum_{i=1}^{m-1} \left(\bar{\lambda}_i \sum_{j=i+1}^{m} \bar{\lambda}_j \right) \\
e_3 &= -\sum_{i=1}^{m-2} \left[\bar{\lambda}_i \sum_{j=i+1}^{m-1} \left(\bar{\lambda}_j \sum_{k=j+1}^{m} \bar{\lambda}_k \right) \right] \\
&\vdots \\
e_m &= (-1)^m \prod_{i=1}^{m} \bar{\lambda}_i
\end{aligned} \tag{16}$$

The e_j coefficients in the reduced z-transfer function, equation (15) are the output coefficients for the reduced transfer function. As an alternative to equation (16), Appendix A contains an algorithm for determining the e_j coefficients in equation (15).

This step used a subset of the roots of the original transfer function (i.e., the dominant roots) to determine the output coefficients of the reduced transfer function. Thus, if all the roots of the original transfer function are less than one in absolute value, then all the roots of the reduced transfer function will be less than one in absolute value. Recall that the transfer function is stable if all the roots are less than one in absolute value. Therefore, if the original transfer function is stable, the reduced transfer function will also be stable.

Original w-Transfer Function (Step Three). The input coefficients of the reduced transfer function are determined by equating the power series expansion of the original w-transfer function with the reduced transfer function for terms of w^0 to w^m. Step four contains equations for determining the power series expansion of the original w transfer function from the original w-transfer function. This step contains equations for determining the original w-transfer function from the original transfer function, i.e., equation (2).

To determine the original w-transfer function, $G(w)$, the bilinear transformation (Kuo, 1980)

$$z=\frac{1+w}{1-w} \tag{17}$$

is substituted into the original z-transfer function, i.e., equation (3). This results in

$$G(w)=\frac{\sum_{j=0}^{n}a_j\left(\frac{1-w}{1+w}\right)^{-j}}{\sum_{j=0}^{n}b_j\left(\frac{1-w}{1+w}\right)^{-j}}=\frac{\sum_{j=0}^{n}a_j(1-w)^j(1+w)^{n-j}}{\sum_{j=0}^{n}b_j(1-w)^j(1+w)^{n-j}} \tag{18}$$

Appendix B contains an algorithm for determining the $v_{i(j,n)}$ coefficients in the following equation:

$$(1-w)^j(1+w)^{n-j}=\sum_{i=0}^{n}(v_{i(j,n)}\ w^i) \tag{19}$$

Substituting equation (19) into equation (18) gives

$$G(w)=\frac{\sum_{j=0}^{n}a_j\left(\sum_{i=0}^{n}v_{i(j,n)}\ w^i\right)}{\sum_{j=0}^{n}a_j\left(\sum_{i=0}^{n}v_{i(j,n)}w^i\right)}=\frac{\sum_{i=0}^{n}\left(\sum_{j=0}^{n}a_jv_{i(j,n)}\right)w^i}{\sum_{i=0}^{n}\left(\sum_{j=0}^{n}b_jv_{i(j,n)}\right)w^i} \tag{20}$$

Rearranging equation (20) results in

$$G(w)=\frac{\sum_{i=0}^{n}\bar{a}_iw^i}{\sum_{i=0}^{n}\bar{b}_iw^i} \tag{21}$$

where

$$\bar{a}_i=a_jv_{i(j,n)} \tag{22}$$

$$\bar{b}_i=b_jv_{i(j,n)} \tag{23}$$

Power Series Expansion for the w-Transfer Function (Step Four). Following is a description of equations for determining the power series expansion of the original w-transfer function from the original w-transfer function. The power series expansion for the original w-transfer function is of the form

$$G(w)=\bar{c}_0+\bar{c}_1w+\bar{c}_2w^2+\bar{c}_3w^3+\ldots \tag{24}$$

The following equation results from equating equation (24) with equation (20):

$$\bar{a}_0+\bar{a}_1w+\ldots+\bar{a}_nw^n=(\bar{b}_0+\bar{b}_1w+\ldots+\bar{b}_nw^n)(\bar{c}_0+\bar{c}_1w+\bar{c}_2w^2+\ldots) \tag{25}$$

Multiplying the terms on the right-hand side of equation (25) together and combining common powers of the complex variable w results in

$$\bar{a}_0+\bar{a}_1w+\ldots+a_nw^n=\bar{b}_0\bar{c}_0+(\bar{b}_0\bar{c}_1+\bar{b}_1\bar{c}_0)w+(\bar{b}_0\bar{c}_2+\bar{b}_1\bar{c}_1+\bar{b}_2\bar{c}_2)w^2+\ldots \tag{26}$$

The coefficients for the power series expansion of $G(w)$ are determined by equating the coefficients for equal powers of w in equation (26).

$$\bar{c}_0=\frac{\bar{a}_0}{\bar{b}_0}$$

$$\bar{c}_1=\frac{\bar{a}_1-\bar{b}_1\bar{c}_0}{\bar{b}_0}$$

$$\bar{c}_2=\frac{\bar{a}_2-\bar{b}_1\bar{c}_1-\bar{b}_2\bar{c}_0}{\bar{b}_0}$$

$$\bar{c}_m=\frac{\bar{a}_m-\sum_{j=0}^{m-1}\bar{c}_j\bar{b}_{m-j}}{\bar{b}_0} \tag{27}$$

Denominator of the Reduced w-Transfer Function (Step Five). This step contains equations for determining the denominator of the reduced w-transfer function from the e_j coefficients in the reduced z-transfer function, i.e., equation (15). Step six contains the equation for determining the numerator of the reduced w-transfer function from the denominator of the reduced w-transfer function and the power series expansion of the original w-transfer function.

Substituting the bilinear transformation, equation (17), into equation (15) results in the following reduced w-transfer function:

$$G_r(w)=\frac{N_r(w)}{\sum_{j=0}^{m}\left[e_j\left(\frac{1-w}{1+w}\right)^j\right]}=\frac{[N_r(w)](1+w)^m}{\sum_{j=0}^{m}[e_j(1-w)^j(1+w)^{m-j}]} \tag{28}$$

where

$N_r(w)$ = function of complex variable w

The algorithm described in appendix B can be used to determine the $v_{i(j,m)}$ coefficients in the following equation:

$$(1-w)^j(1+w)^{m-j}=\sum_{i=0}^{m}(v_{i(j,m)}w^i) \tag{29}$$

Substituting equation (29) into equation (28) gives

$$G_r(w)=\frac{[N_r(w)](1+w)^m}{\sum_{j=0}^{m}\left[e_j\sum_{i=0}^{m}(v_{i(j,m)}w^i)\right]}=\frac{[N_r(w)](1+w)^m}{\sum_{i=0}^{m}\left[\left(\sum_{j=0}^{m}e_jv_{i(j,m)}\right)w^i\right]} \tag{30}$$

Rearranging equation (30) gives

$$G_r(w)=\frac{\sum_{i=0}^{m}\bar{d}_iw^i}{\sum_{i=0}^{m}\bar{e}_iw^i} \tag{31}$$

where

$\bar{d}_i$ = coefficients to be determined in step six

$$\bar{e}_i=\sum_{j=0}^{m}e_jv_{i(j,m)} \tag{32}$$

Numerator of Reduced w-Transfer Function (Step Six). This step describes equations for computing the numerator of the reduced w-transfer function, $G_r(w)$, from the

denominator of the reduced w-transfer function and the power series expansion of the original w-transfer function. Equating the reduced w-transfer function, equation (31), with the power series expansion of the original w-transfer function, equation (24), gives

$$\bar{d}_0+\bar{d}_1w+\bar{d}_2w^2+\ldots+\bar{d}_mw^m$$
$$=(\bar{e}_0+\bar{e}_1w+\bar{e}_2w^2+\ldots+\bar{e}_mw^m)(\bar{c}_0+\bar{c}_1w+\bar{c}_2w^2+\ldots)$$
$$=\bar{e}_0\bar{c}_0+(\bar{e}_0\bar{c}_1+\bar{e}_1\bar{c}_0)w+(\bar{e}_0\bar{c}_2+\bar{e}_1\bar{c}_1+\bar{e}_2\bar{c}_2)w^2+\ldots$$
$$+(\bar{e}_0\bar{c}_m+\bar{e}_1\bar{c}_{m-1}+\bar{e}_2\bar{c}_{m-2}+\ldots+\bar{e}_m\bar{c}_0)w^m+\ldots \quad (33)$$

The numerator coefficients $\bar{c}_0, \bar{c}_1, c_2, \ldots, \bar{c}_m$ of the reduced w-transfer function are determined by equating powers of w from zero to m in equation (33).

$$\bar{d}_0=\bar{e}_0\bar{c}_0$$

$$\bar{d}_1=\bar{e}_0\bar{c}_1+\bar{e}_1\bar{c}_0$$

$$\bar{d}_2=\bar{e}_0\bar{c}_2+\bar{e}_1\bar{c}_1+\bar{e}_2\bar{c}_0$$

•

•

•

$$\bar{d}_m=\bar{e}_0\bar{c}_m+\sum_{i=1}^{m}\bar{e}_i\bar{c}_{m-i} \quad (34)$$

Input Coefficients From the Reduced Transfer Function (Step Seven). Next, the bilinear transformation and z-transform theory will be used to determine the input coefficients of the reduced transfer function from the reduced w-transfer function. The reduced w-transfer function, $G_r(w)$, can be transformed into a reduced z-transfer function by using the bilinear transformation

$$w=\frac{z-1}{z+1}=\frac{1-z^{-1}}{1+z^{-1}} \quad (35)$$

Substituting equation (35) into equation (31) results in

$$G_r(z)=\frac{\sum_{i=0}^{m}\left[\bar{d}_i\left(\frac{1-z^{-1}}{1+z^{-1}}\right)^i\right]}{\sum_{i=0}^{m}\left[\bar{e}_i\left(\frac{1-z^{-1}}{1+z^{-1}}\right)^i\right]}=\frac{\sum_{i=0}^{m}[\bar{d}_i(1-z^{-1})^i(1+z^{-1})^{m-i}]}{\sum_{i=0}^{m}[\bar{e}_i(1-z^{-1})^i(1+z^{-1})^{m-i}]} \quad (36)$$

The algorithm described in Appendix B can be used to compute the $v_{j(i,m)}$ coefficients in the following equation:

$$(1-z^{-1})^i(1-z^{-1})^{m-i}=\sum_{j=0}^{m}v_{j(i,m)}z^{-j} \quad (37)$$

Substituting equation (37) into equation (36) gives

$$G_r(z)=\frac{\sum_{i=0}^{m}\bar{d}_i\left(\sum_{j=0}^{m}v_{j(i,m)}z^{-j}\right)}{\sum_{i=0}^{m}\bar{e}_i\left(\sum_{j=0}^{m}v_{j(i,m)}z^{-j}\right)}=\frac{\sum_{j=0}^{m}\left(\sum_{i=0}^{m}\bar{d}_iv_{j(i,m)}\right)z^{-j}}{\sum_{j=0}^{m}\left(\sum_{i=0}^{m}\bar{e}_iv_{j(i,m)}\right)z^{-j}}=\frac{\sum_{j=0}^{m}d_jz^{-j}}{\sum_{j=0}^{m}e_jz^{-j}} \quad (38)$$

where

$$d_j=\frac{\sum_{i=0}^{m}\bar{d}_iv_{j(i,m)}}{\sum_{i=0}^{m}\bar{e}_iv_{0(i,m)}} \quad (39)$$

Recall that the e_j coefficients were determined from the dominant roots, i.e., equation (16) or the algorithm in Appendix A. Transforming the reduced z-transfer function back into the time domain gives the following reduced transfer function:

$$y_t=\sum_{j=0}^{m}(d_ju_{t-j\delta})-\sum_{j=1}^{m}(e_jy_{t-j\delta}) \quad (40)$$

An example of dominant root model reduction for a single input transfer function is considered in Appendix C.

Reduction of Multiple-Input Transfer Functions

This section extends the single-input model reduction method described in the previous section to multiple-input transfer functions. First, a step-by-step procedure for reducing multiple-input transfer functions is presented. Then, a discussion of dominant root model reduction for building element transfer functions and CRTF's will be presented.

The following procedure can be used to compute reduced multiple-input transfer functions:

1 Use a root-finding procedure to determine the roots of equation (7). The roots in equation (7) are the same for all inputs because equation (7) is based upon the transfer function coefficients for outputs.

2 Use equation (9) to determine n β_j terms for every input (n is equal to the number of past time steps in the original transfer function).

3 Use equation (13) to determine the n ω_j values for every input.

4 Select the dominant roots for every input. Let m equal the total number of dominant roots for all inputs.

5 Use equation (16) or the algorithm described in Appendix A to determine the transfer function coefficients for past outputs from the m dominant roots.

6 Use z-transform theory and the bilinear transformation to determine single-input w-transfer functions for every input from the original transfer function, i.e., use equations (22) and (23) and the algorithm described in Appendix B to determine the coefficients in equation (21) for every input.

7 Use equation (27) to determine the power series expansion of the w-transfer functions for terms of order w^0 to w^m (a power series expansion must be computed for every input).

8 Use equation (32) and the algorithm described in Appendix B to determine the denominator of a reduced w-transfer function. (The denominators of all the reduced transfer functions are the same.)

9 Use equation (34) to determine the numerator of the reduced w-transfer functions from the denominator of the reduced w-transfer function and the power series expansion of the original w-transfer functions.

10 Use equation (39) to determine the coefficients for the inputs in the reduced multiple-input transfer function from the reduced single-input w-transfer functions.

When using the methods of Stephenson and Mitalas (1971), Ceylan and Myers (1980), and Hittle (1981) to determine transfer functions for building elements, the roots are determined before the output transfer function coefficients are computed. Thus, a root-finding procedure is not needed when computing reduced transfer functions for building elements, i.e., step one can be eliminated. Determining the roots of a CRTF may be a numerically difficult problem. Seem (1987) presented a method for avoiding this numerical problem.

Table 1 Transfer function coefficients for ASHRAE wall 25

j	a_j (W/m²-°C)	b_j (W/m²-°C)	c_j
0	0.0021224	−4.0930276	1.0000000
1	0.0467467	6.9131200	−1.0305444
2	0.0558484	−3.0653380	0.2012205
3	0.0071115	0.1336760	−0.0072612
4	0.0000640	−0.0002212	0.0000026

Table 2 Roots and ω_j values for ASHRAE wall 25

		ω_j	
j	λ_j	Outdoor temperature	Indoor temperature
1	0.78640705	**0.718**	0.066
2	0.19749089	0.062	**0.722**
3	0.04628098	0.019	0.002
4	0.00036547	0.002	0.004

Table 3 Reduced transfer function coefficients for ASHRAE wall 25

j	a_j (W/m²-°C)	b_j (W/m²-°C)	c_j
0	0.0136599	−4.0877158	1.0000000
1	0.0128340	6.7063322	−0.9838979
2	0.0908708	−2.7359821	0.1553082

Table 4 Reduced transfer function coefficients for ASHRAE wall 25

	Dominant root		Largest root	
j	b_j (W/m²-°C)	c_j	b_j (W/m²-°C)	c_j
0	−4.30546	1.00000	−1.64838	1.00000
1	3.75600	−0.19749	1.50217	−0.78641

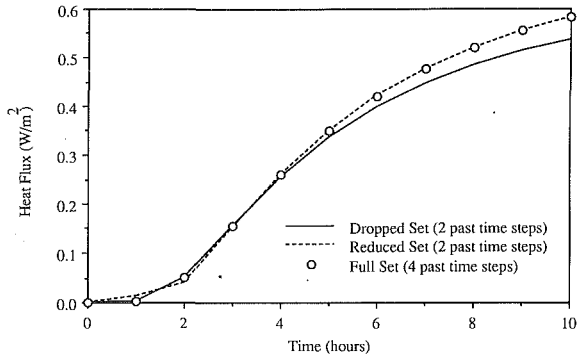

Fig. 1 Response to 1°C step change in outdoor temperature for ASHRAE wall 25

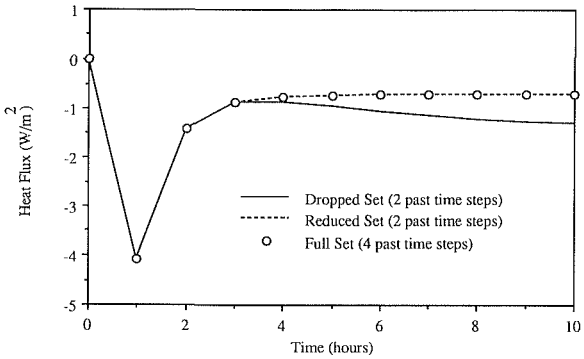

Fig. 2 Response to 1°C step change in indoor temperature for ASHRAE wall 25

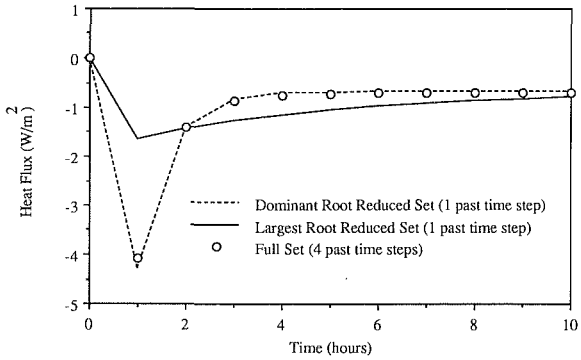

Fig. 3 Response to 1°C step change in outdoor temperature for ASHRAE wall 25

Applications

To test dominant root model reduction for building elements with a wide range of properties, reduced transfer functions for the following ASHRAE (1977) building elements were computed:

1 Exterior Wall 4 (0.1 m face brick, air space, and 0.2 m high).
2 Exterior Wall 25 (frame wall with 0.1 m brick veneer).
3 Exterior Wall 28 (metal curtain wall with 0.05 m of insulation).
4 Exterior Wall 36 (frame wall with 0.08 m insulation).
5 Exterior Wall 54 (0.1 m face brick, air space, and 0.3 m high weight concrete).

For all of the building elements tested, dominant root model reduction was used to obtain a reduced set of coefficients that closely modeled the response of the full set of coefficients.

Table 1 contains transfer function coefficients generated from Mitalas and Arsenault's (1971) program for ASHRAE wall 25. Table 2 contains the roots and values of ω_j for ASHRAE wall 25. Table 2 shows that the first root is the dominant root for a step change in the outdoor temperature and the second root is the dominant root for a step chnge in indoor temperature. These two dominant roots were used to obtain the reduced transfer function coefficients in Table 3. Figure 1 is a graph of the response to a 1°C step change in outdoor temperature for the full set of coefficients, the reduced set of coefficients, and the dropped set of coefficients, i.e., the full set of coefficients for two time steps back. Figure 2 is a similar graph for a 1°C step change in indoor temperature. Both these graphs demonstrate that the reduced set of coefficients closely match the response of the full set of coefficients and the dropped set of coefficients produces a response different from the full set of coefficients.

To demonstrate that the second root is dominant for the indoor temperature, reduced transfer functions were computed with both the largest root and the dominant root. (The largest root is the root with the largest value.) Table 4 contains these reduced transfer functions. Figure 3 is a graph of the response to a 1°C step change in temperature for the full set of coefficients and reduced sets of coefficients, which were obtained with both the dominant root and the largest root. The response for the reduced transfer function with the dominant root is much closer to the response of the full set of coefficients than the response for the reduced transfer function with the largest root.

Dominant root model reduction can also be used to determine reduced CRTF's. Seem (1987) contains the original and reduced transfer function coefficients for an eight-surface room. Figure 4 shows the response to a 1°F step change in outdoor temperature for a CRTF with 19 past time steps and a reduced CRTF with 3 past time steps. The responses for the original and reduced transfer functions are nearly identical. Seem (1987) shows similar figures for step changes in indoor temperature, solar radiation gains, and radiation gains from people, equipment and lights. These figures demonstrate that dominant root model reduction can be used to reduce signif-

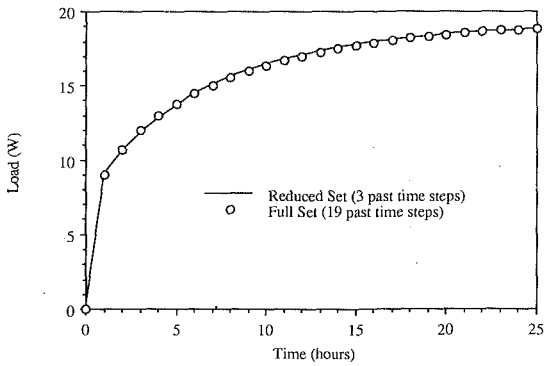

Fig. 4 Response to 1°C step change in outdoor temperature for the eight-surface room.

icantly the number of coefficients in a CRTF. Seem (1987) describes a method for determining the "correct" model order of reduced transfer functions, i.e., the minimum number of past time steps required to model the heat transfer processes accurately in a building with a reduced transfer function.

Conclusions

A new model reduction method for reducing the number of coefficients in multiple-input transfer functions with real and distinct roots has been presented in this paper. This model reduction method can be used to reduce significantly the computational effort of performing simulations of transfer functions used to solve heat transfer problems.

Acknowledgments

Financial support for this work has been provided by Lawrence Berkeley Laboratory, University of California and the Solar Heating & Cooling Research Development Branch, Office of Conservation and Solar Applications, U.S. Department of Energy.

References

ASHRAE, *Handbook of Fundamentals*, 1977, 1981, 1985, American Society of Heating, Refrigeration, and Air Conditioning Engineers, Atlanta, GA.

Ceylan, H. T., 1978, "Long-Time Solutions to Heat Conduction Transients With Time-Dependent Inputs," Ph.D. Thesis, University of Wisconsin—Madison.

Ceylan, H. T., and Myers, G. E., 1980, "Long-Time Solutions to Heat Conduction Transients With Time-Dependent Inputs," ASME JOURNAL OF HEAT TRANSFER, Vol. 102, No. 1, pp. 115–120.

Conte, S. D., and de Boor, C., 1980, *Elementary Numerical Analysis an Algorithmic Approach*, McGraw-Hill, New York.

Hittle, D. C., 1981, "Calculating Building Heating and Cooling Loads Using the Frequency Response of Multilayered Slabs," Ph.D. Thesis, E-169, U.S. Army Construction Engineering Research Laboratory, Champaign, IL.

Jury, E. I., 1964, *Theory and Application of the z-Transform Method*, Wiley, New York.

Kuo, B. C., 1980, *Digital Control Systems*, Holt, Rinehart and Winston, New York, pp. 286–287.

Mitalas, G. P., and Arseneault, J. C., 1978, "Fortran IV Program to Calculate z-Transfer Functions for the Calculation of Transient Heat Through Walls and Roofs," *Proceedings of the Conference on Use of Computer for Environmental Engineering Related to Buildings*, Gaithersburg, MD, NBS Building Science Series 39.

Pandit, S. M., and Wu, S. M., 1983, *Time Series and System Analysis With Applications*, Wiley, New York.

Sedgewick, R., 1983, *Algorithms*, Addison Wesley Publishing Company, Boston, MA.

Seem, J. E., 1987, "Modeling of Heat Transfer in Buildings," Ph.D. Thesis, University of Wisconsin—Madison.

Seem, J. E., Klein, S. A., Beckman, W. A., and Mitchell, J. W., 1989a, "Transfer Functions for Efficient Calculation of Multi-Dimensional Transient Heat Transfer," ASME JOURNAL OF HEAT TRANSFER, Vol. 111, No. 1, pp. 5–13.

Seem, J. E., Klein, S. A., Beckman, W. A., and Mitchell, J. W., 1989b, "Comprehensive Room Transfer Functions for Efficient Calculation of the Transient Heat Transfer Process in Buildings," ASME JOURNAL OF HEAT TRANSFER, Vol. 111, No. 2, pp. 264–273.

Shamash, T., 1980, "Failure of the Routh-Hurwitz Method of Reduction," *IEEE Transactions on Automatic Control*, Vol. AC-25, No. 2, pp. 313–314.

Spiegel, M. R., 1968, *Mathematical Handbook of Formulas and Tables*, Schaum's Outline Series, McGraw-Hill, New York.

Stephenson, D. G., and Mitalas, G. P., 1971, "Calculation of Heat Conduction Transfer Functions for Multi-layer Slabs," *ASHRAE Transactions*, Vol. 77, Part II, pp. 117–126.

APPENDIX A

Algorithm for Determining Output Coefficients

This appendix contains an algorithm that can be used to determine the output coefficients of the reduced transfer functions from m dominant roots of the original transfer function. The following equation relates the m dominant roots of the original transfer function with the output coefficients of the reduced transfer function:

$$\prod_{j=1}^{m} (1-\overline{\lambda_j} z^{-1}) = \sum_{j=0}^{m} e_j z^{-j} \tag{41}$$

where

$\overline{\lambda_j}$ = one of the m dominant roots

The following algorithm can be used to determine the e_j coefficients in equation (15) or equation (41):

$e_0 = 1$

$e_1 = -\overline{\lambda_1}$

For $i = 2$ to m with a step size of 1

  $e_i = 0$

  For $j = i$ to 1 with a step size of -1

    $e_j = e_j - e_{j-1}\overline{\lambda_i}$

  Next j

Next i

APPENDIX B

Extension of Pascal's Triangle

Numerical analysis textbooks (Conte and de Boor, 1980; Sedgewick, 1983) contain algorithms for multiplying polynomials. These algorithms could be used to obtain the $v_{j(i,n)}$ coefficients in the following equation:

$$(1-x)^i(1+x)^{n-i} = \sum_{j=0}^{n} v_{j(i,n)} x^j \tag{42}$$

This appendix contains a numerically efficient algorithm for determining the $v_{j(i,n)}$ coefficients in equation (42). The algorithm is numerically efficient because no multiplications or divisions are required. The following algorithm for computing the $v_{j(i,n)}$ coefficients is based upon an extension of Pascal's triangle (Spiegel, 1968):

$v_{0(i,n)} = 1$

For $k = 1$ to i with a step size of 1

  $v_{k(i,n)} = -v_{k-1(i,n)}$

  For $j = (k-1)$ to 1 with a step size of -1

    $v_{j(i,n)} = v_{j(i,n)} - v_{j-1(i,n)}$

  Next j

Next k

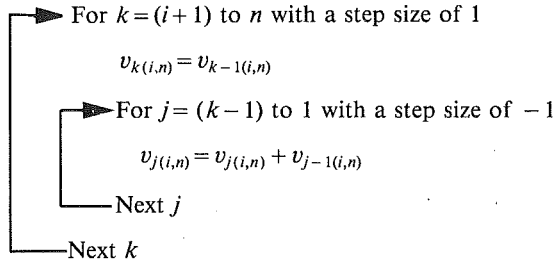

APPENDIX C

Example

To demonstrate dominant root model reduction, a reduced transfer function with one past time step (i.e., $m=1$) will be determined from a transfer function with two past time steps (i.e., $n=2$). For this example, the following transfer function will be reduced:

$$y_t=a_0u_t=a_1u_{t-\delta}+a_2u_{t-2\delta}-b_1y_{t-\delta}-b_2y_{t-2\delta}$$

$$=u_t+0.5u_{t-\delta}+0.1u_{t-2\delta}+1.1y_{t-\delta}-0.3y_{y-2\delta}$$

From equation (5), the z-transform of the output when the input is a unit step is

$$Y(z)=\frac{z(a_0z^2+a_1z+a_2)}{(z-1)(b_0z^2+b_1z+b_2)}=\frac{z(z^2+0.5z+0.1)}{(z-1)(z^2-1.1z+0.3)}$$

The quadratic equation can be used to determine the roots of equation (7).

$$\lambda_1,\ \lambda_2=\frac{-b_1\pm\sqrt{b_1^2-4b_2}}{2}$$

$$=\frac{1.1\pm\sqrt{(-1.1)^2-4(0.3)}}{2}=0.6,\ 0.5$$

Using the roots determined from the quadratic equation, the z-transform of the output can be written as

$$Y(z)=\frac{a_0z^3+a_1z^2+a_2z}{(z-\lambda_0)(z-\lambda_1)(z-\lambda_2)}=\frac{z^3+0.5z^3+0.1z}{(z-1)(z-0.6)(z-0.5)}$$

From equation (9), the β_j coefficients in equation (8) are

$$\beta_1=\frac{a_0\lambda_1^2+a_1\lambda_1+a_2}{(\lambda_1-\lambda_0)(\lambda_1-\lambda_2)}=\frac{1(0.6)^2+0.5(0.6)+0.1}{(0.6-1)(0.6-0.5)}=-19$$

$$\beta_2=\frac{a_0\lambda_2^2+a_1\lambda_2+a_2}{(\lambda_2-\lambda_0)(\lambda_2-\lambda_1)}=\frac{1(0.5)^2+0.5(0.5)+0.1}{(0.5-1)(0.5-0.6)}=12$$

Using equation (13), the following ω_j quantities can be computed for the roots:

$$\omega_1=\left|\frac{\beta_1}{1-\lambda_1}\right|=\left|\frac{-19}{1-0.6}\right|=47.5$$

$$\omega_2=\left|\frac{\beta_2}{1-\lambda_2}\right|=\left|\frac{12}{1-0.5}\right|=24$$

ω_1 is larger than ω_2, therefore the dominant root is

$$\overline{\lambda_1}=\lambda_1=0.6$$

Next, the coefficient in the denominator of the reduced z-transfer function is computed from equation (16)

$$e_1=-\overline{\lambda_1}=-0.6$$

From equation (18), the original w-transfer function is

$$G(w)=\frac{a_0(1+w)^2+a_1(1-w)(1+w)+a_2(1-w)^2}{b_0(1+w)^2+b_1(1-w)(1+w)+b_2(1-w)^2}$$

$$=\frac{(1+w)^2+0.5(1-w)(1+w)+0.1(1-w)^2}{(1+w)^2-1.1(1-w)(1+w)+0.3(1-w)^2}$$

$$=\frac{1.6+1.8w+0.6w^2}{0.2+1.4w+2.4w^2}=\frac{\bar{a}_0+\bar{a}_1w+\bar{a}_2w^2}{\bar{b}_0+\bar{b}_1w+\bar{b}_2w^2}$$

The first two terms in the power series expansion of $G(w)$ can be computed from equation (27)

$$\bar{c}_0=\frac{\bar{a}_0}{\bar{b}_0}=\frac{1.6}{0.2}=8$$

$$\bar{c}_1=\frac{\bar{a}_1-\bar{b}_1\bar{c}_0}{\bar{b}_0}=\frac{1.8-(1.4)(8)}{0.2}=-47$$

From equation (28), the reduced w-transfer function is

$$G_r(w)=\frac{N_r(w)(1+w)}{e_0(1+w)+e_1(1-w)}$$

$$=\frac{N_r(w)(1+w)}{(1+w)+(-0.6)(1-w)}$$

$$=\frac{N_r(w)(1+w)}{0.4+1.6w}=\frac{N_r(w)(1+w)}{\bar{e}_0+\bar{e}_1w}$$

The numerator coefficients of the reduced w-transfer function are determined from equation (34)

$$\bar{d}_0=\bar{e}_0\bar{c}_0=(0.4)(8)=3.2$$

$$\bar{d}_1=\bar{e}_0\bar{c}_1+\bar{e}_1\bar{c}_0=(0.4)(-47)+(1.6)(8)=-6$$

Equation (36) can be used to compute the reduced z-transfer function from the reduced w-transfer function

$$G_r(z)=\frac{\bar{d}_0(1+z^{-1})+\bar{d}_1(1-z^{-1})}{\bar{e}_0(1+z^{-1})+\bar{e}_1(1-z^{-1})}$$

$$=\frac{3.2(1+z^{-1})-6(1-z^{-1})}{0.4(1+z^{-1})+1.6(1-z^{-1})}$$

$$=\frac{-1.4+4.6z^{-1}}{1-0.6z^{-1}}$$

Transforming the reduced z-transfer function into the time domain gives

$$y_t=-1.4u_t+4.6u_{t-\delta}+0.6y_{t-\delta}$$

Hyperbolic Heat Conduction Equation for Materials With a Nonhomogeneous Inner Structure

W. Kaminski
Assistant Professor,
Institute of Chemical and Process Engineering,
Technical University of Lodz,
Lodz, Poland

The physical meaning of the constant τ in Cattaneo and Vernotte's equation for materials with a nonhomogeneous inner structure has been considered. An experimental determination of the constant τ has been proposed and some values for selected products have been given. The range of differences in the description of heat transfer by parabolic and hyperbolic heat conduction equations has been discussed. Penetration time, heat flux, and temperature profiles have been taken into account using data from the literature and our experimental and calculated results.

Introduction

The equation describing the relationship between heat flux and temperature gradient has been known since the publication of Fourier's studies concerning heat conduction (1807, 1812)

$$q = -k\nabla T \tag{1}$$

Although the Fourier equation has been used successfully, doubts have arisen since the publication of his work (Herivel, 1980).

One of the problems causing doubt was the infinite heat propagation velocity for unsteady processes resulting from the interpretation of equation (1). At first, this was only a theoretical obstacle. With the development of science and technology, particularly research on low-pressure gases, cryogenic engineering, nuclear engineering, seismology, etc., new experimental facts revealed the paradox of infinite propagation velocity. Initially, Maxwell (1867), Morse and Feshbach (1953), and then Vernotte (1958a, 1958b) and Cattaneo (1958) formulated a modified description of unsteady heat conduction

$$q + \tau\frac{\partial q}{\partial t} = -k\nabla T \tag{2}$$

$$-\nabla \cdot q = c_p\rho\frac{\partial T}{\partial t} \tag{3}$$

Equation (2) is the Cattaneo and Vernotte (CV) equation. Equations (2) and (3) lead to a description of an unsteady temperature profile in the form of the hyperbolic equation

$$c_p\rho\left(\frac{\partial T}{\partial t} + \tau\frac{\partial^2 T}{\partial t^2}\right) = k\nabla^2 T \tag{4}$$

where

$$\tau = a/c^2 \tag{5}$$

The concept of finite heat propagation velocity, leading to equation (4), was the subject of numerous studies in which its thermodynamic validity was discussed. In addition, the relationship between equation (4) and kinetic and molecular theory, together with the possibility of formulating equation (4) in another way, were considered.

The hyperbolic heat conduction equation (HHCE) was introduced to chemical and process engineering by Luikov (1966). Many papers suggested that the hyperbolic equation should be applied in heat transfer processes that take place in dissipative and dispersive systems (Antonishyn et al., 1974; Luikov, 1966; Sieniutycz, 1977; Todos et al., 1970).

Advances in research on heat transfer phenomena at a finite propagation velocity have resulted in increased interest in solutions of the hyperbolic equation (4). Analytical and numerical solutions concerning model cases are given in the literature. Approximate solutions can also be important.

2 Heat Conduction in Materials With a Nonhomogeneous Inner Structure

Materials encountered in practice, except for pure liquids, gases, and homogeneous solids, can be described as complex systems made up of solid, liquid, and gas, e.g., porous-capillary bodies, cellular systems, suspensions, pastes, etc. The cumulative effect of different transfer mechanisms, for instance, heat conduction, heat transfer by particle-to-particle contact, free convection in a closed space, radiation, etc., is often described by the heat conduction equation. The presence of moisture and its method of binding with a material play an important role in heat transfer. The thermal conductivity determined experimentally is an average value. It should be also noticed that in order to obtain a better fitting of experimental and calculated results thermal conductivity is expressed as a function of temperature, moisture content, etc. We will call these nonhomogeneous inner structure materials.

An attempt to obtain a more accurate description of heat transfer in nonhomogeneous materials leads to the application of the CV equation.

Luikov (1966) suggested that depending on process intensity, τ can range from 10^{-3} to 10^{3} s. Brazhnikov et al. (1975) give τ = 20 to 30 s for meat products. Michalowski et al. (1982) and Mitura et al. (1988) claim that for the falling drying rate period, the average value of τ is of the order of several thousand seconds. Similar data have been published elsewhere (Antonishyn et al., 1974; Raspopov, 1967; Todos et al., 1970). These seem unnaturally high.

For homogeneous substances, τ values for gases of 10^{-8} to 10^{-10} s, and for liquids and dielectric solids of 10^{-10} to 10^{-12} s, have been quoted (e.g., Sieniutycz, 1977).

The following problems arise when considering nonhomogeneous inner structure materials:

- the physical meaning of τ in the CV equation.
- methods of experimental determination of τ.
- the range in which the hyperbolic instead of the parabolic equation must be used.

The problems listed above have not previously been solved and they are the subjects of this paper.

Contributed by the Heat Transfer Division for publication in the JOURNAL OF HEAT TRANSFER. Manuscript received by the Heat Transfer Division June 7, 1988; revision received September 26, 1989. Keywords: Conduction, Porous Media, Transient and Unsteady Heat Transfer.

3 Physical Meaning of τ

Consider an electrical analogy of heat conduction at a finite wave propagation velocity (Doetsch, 1961; Lumsdaine, 1972; Ulbrich, 1961). Transfer of electrical impulses is in a cable of a given resistance R, conductance C, inductance L, and leakage conductance G. R, C, L, and G are referred to a unit length of the cable. The following system of linear partial differential equations after Doetsch (1961) describing the relationship between voltage $E(x, t)$ and current $I(x, t)$ is obtained:

$$\frac{\partial E(x, t)}{\partial x} + L\frac{\partial I(x, t)}{\partial t} + RI(x, t) = 0 \tag{6}$$

$$\frac{\partial I(x, t)}{\partial x} + C\frac{\partial E(x, t)}{\partial t} + GE(x, t) = 0 \tag{7}$$

The analogous terms for heat conduction are temperature, heat flux, thermal resistance, conductance, and inductance. Assuming thermal leakage conductance equals zero, the system of equations (6) and (7) becomes a hyperbolic equation for one-dimensional heat conduction.

Another interesting approach to the problem can be obtained on the basis of the thermodynamic theory of bodies with fading memory (Chadwick and Sneddon, 1958; Coleman and Mizel, 1963; Coleman and Gurtin, 1965, Coleman, 1970; Gurtin and Pipkin, 1968; Kalashnikova and Taganov, 1981; Kolesnikov, 1987; Luikov, 1974; Nunzioto, 1971; Shashkov and Abramienko, 1975). Such a concept was also used by Swenson (1977) who assumed that heat flux at some moment t depends both on the temperature gradient at t and on past gradients

$$q(t) = -\int_{-\infty}^{t} \lambda(t-t')\nabla T(t')dt' \tag{8}$$

When the system (body) has an extremely short memory, equation (8) combined with the heat balance equation (3) leads to the parabolic heat conduction equation (PHCE)

$$\frac{\partial T}{\partial t} = a\nabla^2 T \tag{9}$$

A subsequent extreme case occurs when the body has an extremely long memory. Then, one obtains

$$\tau\frac{\partial^2 T}{\partial t^2} = a\nabla^2 T \tag{10}$$

In an intermediate case the exponential dependence of function $\lambda(t)$ is assumed

$$\lambda(t) = \frac{k_0}{\tau}\exp\left(-\frac{t}{\tau}\right) \tag{11}$$

In the third case, equation (4) is obtained.

Finally, one should also note the analogy between hyperbolic heat conduction and fluid mechanics (Hughes, 1979). The constitutive relations for viscoelastic fluids are analogous to the CV equation. There is also similarity between the concept of heat conduction for materials with memory and the theory of fluids with memory.

On the basis of the examples presented, one can state that τ in the CV equation for nonhomogeneous inner structure materials has a different meaning from relaxation time. This parameter can be interpreted in terms of an electrical analogy. The constant τ characterizes thermal inductance, defined as the time needed for accumulating the thermal energy required for propagative transfer to the nearest element of the inner structure. In the second example τ has a meaning of the time constant of fading memory (equation (11)).

Summing up the above points, the author suggests that τ represents the interaction of structural elements in inner heat transfer. For homogeneous materials this interaction is at the molecular or crystal lattice level. Then, τ has a meaning and value of relaxation time. For nonhomogeneous inner structure materials, the structural heat transfer interaction is at a different level and τ may take a much greater value.

4 Experimental Determination of τ

The value of relaxation time for homogeneous materials may be calculated theoretically (Sieniutycz, 1977; Taitel, 1972). However, those equations are not suitable for nonhomogeneous inner structure materials. It has been suggested that τ can be determined by fitting experimental temperature data with theoretical results from the hyperbolic equation, by using τ as a variable parameter (Antonishyn et al., 1974; Raspopov, 1967; Brazhnikov et al., 1975; Michalowski et al., 1982; Mitura et al., 1988). There is no direct experimental method for determination of τ.

The evaluation of τ for nonhomogeneous inner structure materials could be carried out based on the measurement of penetration time, thermal diffusivity, and equation (5). Penetration time can be found by placing a linear heat source and temperature sensor in the material. The way this device operates is shown in Fig. 1. It consists of a linear heat source in the form of a needle containing a 0.2-mm resistance wire in 0.1-mm electrical insulation supplied by a power stabilizer. The temperature of the heater was not measured but it has been estimated to be from 12.8°C to 32.1°C higher than the

Nomenclature

a = thermal diffusivity, m^2/s
c = heat propagation velocity, m/s
c_p = specific heat, J/(kg K)
E = voltage, V
G = leakage conductance, 1 /(Ω m)
h = heat transfer coefficient, $W/(m^2 K)$
I = current, A
k = thermal conductivity, W/(m K)
L = inductance, Ω/(m s)
n = exponent
q = heat flux density, W/m^2
R = resistance, Ω/m
t = time, s
T = temperature, °C
x = distance, m
δ = thickness, m
$\lambda(\,.\,.\,)$ = memory function, W/(m s K)
μ = scaling factor
π = 3.141 . . . . .
ρ = density, kg/m^3
τ = time constant, relaxation time, s

Subscripts

p = penetration
H = heater
∞ = infinite time
0 = initial

Dimensionless numbers

Nu = $h\delta/k$ = Nusselt number
Fo = $at/(\delta/2)^2$ = Fourier number

Abbreviations

CV = Cattaneo and Vernotte
HHCE = hyperbolic heat conduction equation
PHCE = parabolic heat conduction equation

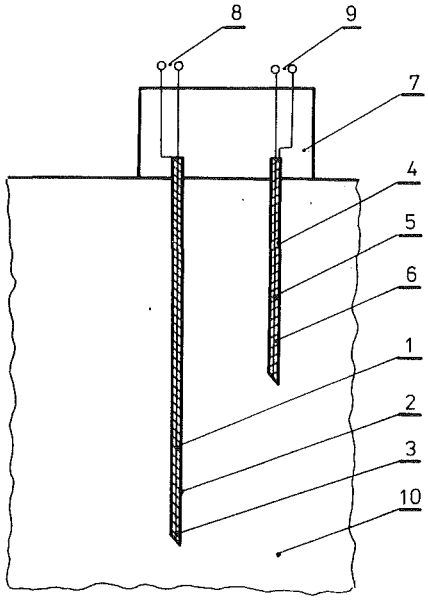

Fig. 1 Experimental device: (1) resistance wire, (2) needle, (3) electric insulation, (4) needle, (5) thermocouple, (6) insulation (7) support, (8) to power supply and stabilizer, (9) to amplifier and recorder, (10) material

Table 1 Properties of materials examined

Material	Mean particle diameter μm	Moisture content kg moisture / kg dry prod.	Bulk density kg/m³	Bed voidage %
H acid	19.3	0.129	439	72.9
$NaHCO_3$	96.4	0.185	1236	49.9
Sand	187.0	0.0098	1551	42.2
Glass ballotini	206.0	0.069	1607	36.6
Ion exchanger	602.0	0.181	862	41.1

Table 2 Thermal diffusivity, propagation velocity, and τ

Material	a 95% confid. interval	c 95% confid. interval	τ 95% confid. interval
	mm²/s	mm/s	s
H acid	0.260 ± 0.048	0.103 ± 0.006	24.5 ± 7.5
$NaHCO_3$	0.310 ± 0.041	0.104 ± 0.004	28.7 ± 5.9
Sand	0.408 ± 0.060	0.143 ± 0.012	20.0 ± 6.4
Glass ballotini	0.251 ± 0.030	0.152 ± 0.011	10.9 ± 2.9
Ion exchanger	0.220 ± 0.019	0.064 ± 0.005	53.7 ± 13.4

ambient temperature. The thermocouple is placed in the needle and parallel to the heater.

In Table 1 the properties of selected materials are presented. The measurement includes the evaluation of time delay of heat wave from the heater to the sensor. In order to determine precisely the penetration time, the thermocouple response is referred to a certain standard voltage and then amplified appreciably. The dynamics of the heater and sensor affects only the response and does not cause any additional delay. If the temperature profile caused by the linear heat source satisfied the PHCE, then the change of electrical signal of the thermocouple would be observed after 5 to 10 s, while in the experiments (the distance of the heater to the temperature sensor being 16.8 mm) the signal was observed after 100 to 200 s. Thermal diffusivity was determined by temperature measurement in unsteady conditions caused by the linear heat source (after Carslaw and Jaeger, 1959). The experimental device is the same as in Fig. 1. The measurements of both penetration time and thermal diffusivity were performed at two distances between the heater and sensor (6.8 mm, 16.8 mm) and each experiment was repeated five times. The initial temperature of the samples was kept at 20°C. The penetration time evaluated in this way and thermal diffusivity of the material allowed the constant τ to be determined for the materials. The final results and 95 percent confidence interval are presented in Table 2.

This method can be modified using a linear heat source and two temperature sensors parallel to the heater at different distances. The temperature sensed by the closer probe is with reference to the other probe and reveals a maximum. It should be noted that this maximum as calculated from PHCE and HHCE may differ significantly. From the time at which the maximum occurs, τ can be determined by solution of hyperbolic equation (4).

5 Comparison of Results Obtained Using the PHCE and HHCE Equations

Differences that may arise when considering heat transfer problems for nonhomogeneous inner structure materials as a consequence of the use of PHCE and HHCE equations are related to the following: penetration time, heat flux, and temperature profile. Of great importance is the range of sample thickness, time, and intensity of the process in which the differences in the above occur. In this section the answers to these questions are considered. The appropriateness of proposed criteria is verified by our own data, as well as those in the literature.

The PHCE and HHCE have been compared by other authors, for example: Baumeister and Hamil (1969), Chan et al. (1971), Frankel et al. (1987), Glass et al. (1986), Vick and Ozisik (1983), and Wiggert (1977), with τ as the relaxation time. Due to the dimensionless form of the data, those comparisons can also be used in the analysis of nonhomogeneous inner structure materials.

If a scaling factor is introduced into equation (4) such that $t = \mu^2 t'$, $x = \mu x'$, the HHCE solutions approach the PHCE asymptotically when $\tau/\mu^2 \ll 0(1)$, that is, for large t and x (Maurer and Thompson, 1973). However, in the literature, there is no precise determination of what large distance and time mean.

One of the basic differences between HHCE and PHCE is the penetration time. In general, the penetration time for PHCE for any sample thickness is zero. However, for comparison purposes, the asymptotic solution of the PHCE for a semi-infinite body and the penetration time are taken into account. For instance, in the studies by Lardner (1963), Vujanovic and Baclic (1976), and Vujanovic and Djukic (1972), the temperature profile is in the form

$$\frac{T(x,t)-t_0}{T_{H\infty}-T_0} = \left(1-\frac{x}{x_p(t)}\right)^n \tag{12}$$

where $x_p(t)$, called the penetration depth, is the depth reached by the heat front after a given penetration time.

If thermal diffusivity does not depend on temperature, the penetration depth can be expressed by the formula (Vujanovic and Djukic, 1972)

$$x_p(t) = \sqrt{10\,at} \tag{13}$$

The time delay in the heat wave reaching a given place is an experimental fact. Taking the concept of constant penetration velocity for HHCE, the penetration depth can be written in the form

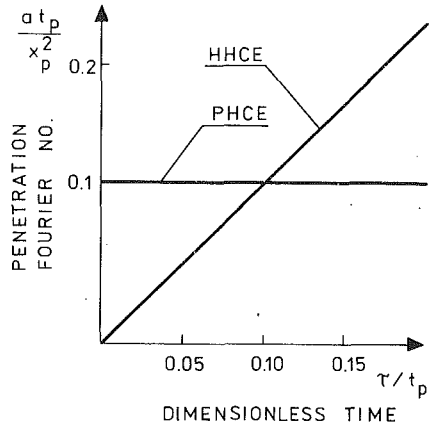

Fig. 2 Dimensionless penetration time for PHCE and HHCE

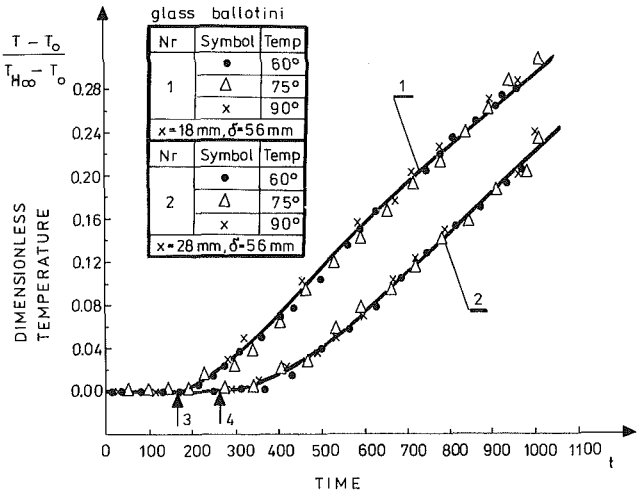

Fig. 3 Comparison of experimental and calculated values: penetration time; (1, 2) experimental and calculated values of temperature; (3, 4) penetration time for x = 18 mm and x = 28 mm layers, respectively

$$x_p(t) = ct \tag{14}$$

A comparison of equations (13) and (14) in the dimensionless form is presented in Fig. 2. Differences in the determination of the penetration time can be significant. Referring to the data presented by Kaminski (1988), the values calculated from equations (13) and (14) for a 28-mm layer of glass ballotini are 497 and 258 s, respectively, with 258 s corresponding well with the experimental data (Fig. 3). The relative magnitude of the values of penetration time calculated using HHCE and the asymptotic solution of PHCE change at a value of the dimensionless time of 0.1 (Fig. 2).

Another significant value is the heat flux defined by equation (2). This combines the heat flux, its rate of change, and temperature gradient. It has been suggested in the literature that the CV equation should be used for short duration and highly intensive processes (Antonishyn et al., 1974; Baumeister and Hamil, 1969; Chan et al., 1971; Glass et al., 1985; Lakusta and Timofeev, 1980; Taitel, 1972; Wiggert, 1977). As in the previous case, two ranges can be considered, one referring to the molecular or crystal lattice interaction and the other representing the share of complex material structure in a heat transfer process. The relative values of q and $\tau\ \partial q/\partial t$ decide whether the rate of change in heat flux affects the heat flux. The heat flux resulting from PHCE for short duration processes is higher than that observed experimentally.

Heat propagation at a finite velocity in a material of finite

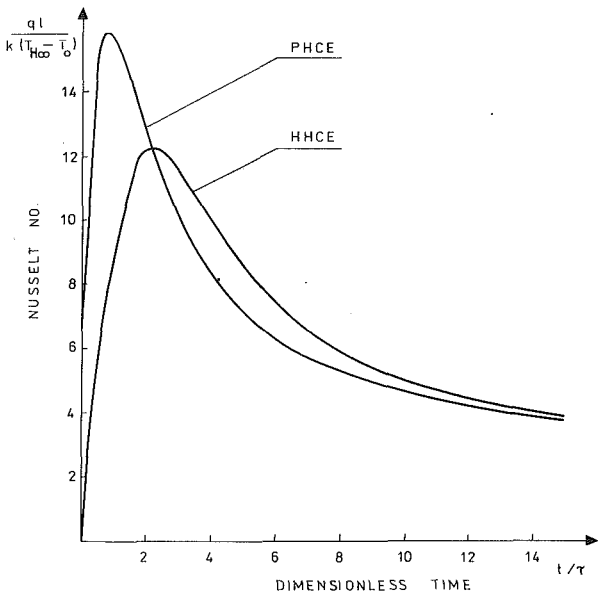

Fig. 4 Differences in heat fluxes for Fourier's and Cattaneo and Vernotte's equations

thickness can be treated as heat wave propagation in a semi-infinite medium up to the moment when the wave front meets either the boundary of the body or another front moving in another or opposite direction.

The problem to be solved is the process duration within which significant differences occur between PHCE and HHCE. Taking into account the experimental results and theoretical considerations, one can state that the largest changes take place at the moving boundary of the disturbances. In a recent study (Kaminski, 1989) the characteristic material thickness for two-sided symmetric heating was given as

$$\delta = 2\pi\sqrt{a\tau} \tag{15}$$

Therefore, it is proposed to assume a time shorter than the penetration time for the thickness $\delta/2$ as the process duration for which significant differences occur between heat fluxes resulting from the solutions of PHCE and HHCE:

$$t_p = \frac{\delta}{2c} = \pi\tau \tag{16}$$

The value calculated from equation (16) corresponds to that calculated by Baumeister and Hamil (1969), who stated that the maximum heat flux at a step change of the temperature for $x = 0$ occurs at $t = 2\tau$. The significant differences in heat flux occur in the interval $\langle 0, 3\tau\rangle$. The range of time represented by equation (16) is also in good agreement with our data (Kaminski, 1988) where heat fluxes calculated on the basis of PHCE and HHCE for a slab heated on both sides, with temperature changing from T_0 to $T_H(t)$ at the boundary, were compared. This dependence, shown in Fig. 4, is similar to that presented by Baumeister and Hamil (1969) but in our case calculations were performed for $\tau > 1$.

Substituting time by equation (16) and distance by equation (15) in the definition of Fourier number, one obtains

$$\mathrm{Fo} = \frac{at}{(\delta/2)^2} = \frac{1}{\pi} \tag{17}$$

Figure 5 presents experimental data of heat transfer from an immersed heater to the bed (after Todos et al., 1970). The boundary value of the Fourier number, represented by equation (17), and the experimental data are in very good agreement.

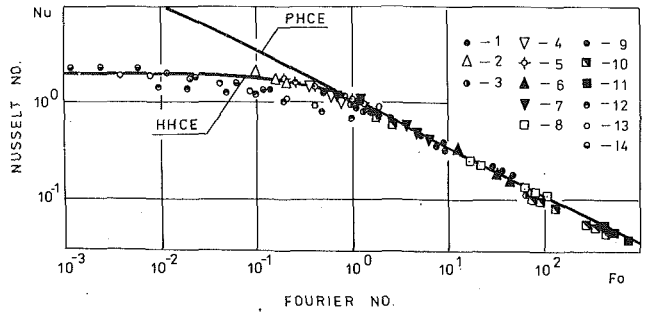

Fig. 5 Comparison of calculated and experimental data for the following systems: (1, 2) ballotini/air, (3, 4, 5) ballotini/freon 12, (6, 7) ballotini/helium, (8) Al_2O_3 powder/air, (9) Al_2O_3 powder/freon 12, (10) Al_2O_3 powder/helium, (11) mica powder/air, (12, 13, 14) slug balls/air

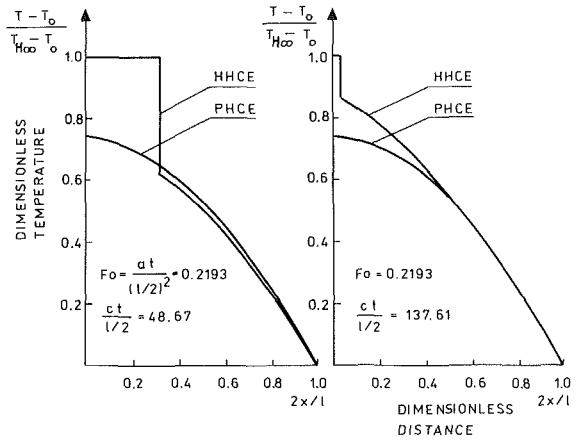

Fig. 6 Comparison of temperature profiles for PHCE and HHCE in a slab

The consequence of the differences in heat fluxes calculated on the basis of PHCE and HHCE appear as the differences of temperature profiles. The temperature profile caused by a step change at the boundary in a slab in the initial period of heat transfer, in a dimensionless system of coordinates for two values of the slab thickness, is presented in Fig. 6. The solution of HHCE for various slab thicknesses is different in spite of dimensionless data presentation and asymptotically approaches the PHCE solution after a distance and time calculated from equations (15) and (16), respectively.

6 Summary and Conclusions

In the paper a physical meaning of the constant τ in the CV equation for nonhomogeneous inner structure materials has been considered. Examples leading to the hyperbolic heat conduction equation included an electrical analogy of heat conduction at a finite propagation velocity of disturbances, bodies with fading memory. It was found that the CV equation provides a more adequate description of unsteady heat transfer processes occurring in the nonhomogeneous inner structure materials. The constant τ can be interpreted as a measure of interaction of material structure in unsteady heat transfer processes.

It is suggested that τ be determined on the basis of heat propagation velocity. The values of thermal diffusivity, propagation velocity, and τ are given for selected products.

Differences in the description of heat transfer inside the material by the HHCE and PHCE were discussed. The following terms were taken into account: penetration time, heat flux, and temperature profile. Both the literature data and our experimental and calculated results were used.

The analysis revealed that significant differences between the PHCE and the HHCE exist for the thickness $\delta/2$ determined by equation (15), which is connected with the moving heat front. The differences occur for times shorter than $\pi\tau$.

References

Antonishyn, N. V., Geller, M. A., and Parnas, A. L., 1974, "Hyperbolic Heat Conduction.Equation for a Disperse System," *Inzhenerno Fizicheskij Zhurnal*, Vol. 26, No. 3, pp. 503–508.

Baumeister, K. J., and Hamil, T. D., 1969, "Hyperbolic Heat-Conduction Equation: a Solution for the Semi-infinite Body Problem," ASME JOURNAL OF HEAT TRANSFER, Vol. 91, pp. 543–548.

Brazhnikov, A. M., Karpychev, V. A., and Luikova, A. V., 1975, "One Engineering Method of Calculating Heat Conduction Processes," *Inzhenerno Fizicheskij Zhurnal*, Vol. 28, No. 4, pp. 677–680.

Carslaw, H. S., and Jaeger, J. C., 1959, *Conduction of Heat in Solids*, Oxford University Press, London, p. 221.

Cattaneo, M. C., 1958, "Sur une forme de l'equation de la chaleur eliminant le paradoxe d'une propagation instantanee," *Comptes Rendus Hebd. Seances Acad. Sci.*, Vol. 247, No. 4, Paris, pp. 431–433.

Chadwick, P., and Sneddon, I. N., 1958, "Plane Waves in an Elastic Body Conducting Heat," *Journal of the Mechanics and Physics of Solids*, Vol. 6, pp. 223–230.

Chan, S. H., Low, M. J. D., and Mueller, W. K., 1971, "Hyperbolic Heat Conduction in Catalytic Supported Crystallites," *AIChE Journal*, Vol. 17, No. 6, pp. 1499–1501.

Coleman, B. D., 1970, "Some Recent Results in the Theory of Fading Memory," *Pure and Applied Chemistry*, Vol. 22, No. 3–4, p. 321.

Coleman, B. D., and Gurtin, M. E., 1965, "On the Growth and Decay of One-Dimensional Acceleration Waves," *Archive for Rational Mechanics and Analysis*, Vol. 19, pp. 239–265.

Coleman, B. D., and Mizel, V. J., 1963, "Thermodynamics and Departures From Fourier's Law of Heat Conduction," *Archive for Rational Mechanics and Analysis*, Vol. 13, pp. 245–261.

Doetsch, G., 1961, *Guide to the Applications of Laplace Transforms*, Van Nostrand Comp. Ltd., New York, p. 173.

Frankel, J. I., Vick, B., and Özişik, M. N., 1987, "General Formulation and Analysis of Hyperbolic Heat Conduction in Composite Media," *International Journal of Heat and Mass Transfer*, Vol. 30, No. 7, pp. 1293–1305.

Glass, D. E., Özişik, M. N., McRae, D. S., and Vick, B., 1986, "Hyperbolic Heat Conduction With Temperature-Dependent Thermal Conductivity," *Journal of Applied Physics*, Vol. 59, No. 6, pp. 1861–1865.

Glass, D. E., Özişik, M. N., and Vick, B., 1985, "Hyperbolic Heat Conduction With Surface Radiation," *International Journal of Heat and Mass Transfer*, Vol. 28, No. 10, pp. 1823–1830.

Gurtin, M. E., and Pipkin, A. C., 1968, "A General Theory of Heat Conduction With Finite Wave Speed," *Archive for Rational Mechanics and Analysis*, Vol. 31, pp. 113–126.

Herivel, J., 1980, *Joseph Fourier: face aux objections contre sa theorie de la chaleur*, Bibliotheque Nationale, Paris.

Hughes, W. F., 1979, *An Introduction to Viscous Flow*, McGraw-Hill, New York.

Kalashnikova, L. S., and Taganov, I. N., 1981, "Mass Transfer Equation for Materials With Memory," *Teoreticheskie Osnovy Khimicheskoj Tekhnologii*, Vol. 15, No. 6, pp. 914–917.

Kaminski, W., 1988, "Heat Conduction With Finite Wave Propagation Velocity for Material of Non-homogeneous Inner Structure," *Inżynieria Chemiczna i Procesowa*, Vol. 9, No. 1, pp. 81–93.

Kaminski, W., 1989, "Heat Conduction With Finite Wave Propagation Velocity," D.Sc. thesis, Lodz Technical University, No. 509/90, p. 16.

Kolesnikov, P. M., 1987, "Generalized Boundary Conditions of the Heat and Mass Transfer," *International Journal of Heat and Mass Transfer*, Vol. 30, No. 1, pp. 85–92.

Lakusta, K. V., and Timofeev, Yu. A., 1980, "Estimating the Range of the Applicability of Hyperbolic Thermal Conductivity Equation," *Inzhenerno Fizicheskij Zhurnal*, Vol. 37, No. 2, pp. 366–370.

Lardner, T. J., 1963, "Biot's Variational Principle in Heat Conduction," *AIAA Journal*, Vol. 1, No. 1, pp. 196–206.

Luikov, A. V., 1966, "Application of Irreversible Thermodynamics Methods to Investigation of Heat and Mass Transfer," *International Journal of Heat and Mass Transfer*, Vol. 9, pp. 139–152.

Luikov, A. V., 1974, "Some Problems of Heat and Mass Transfer Theory," *Inzhenerno Fizicheskij Zhurnal*, Vol. 26, No. 5, pp. 781–793.

Lumsdaine, E., 1972, "Thermal Resonance," *Mechanical Engineering News*, Vol. 9, No. 3, pp. 34–37.

Maurer, M. J., and Thompson, H. A., 1973, "Non-Fourier Effects at High Heat Flux," ASME JOURNAL OF HEAT TRANSFER, Vol. 95, pp. 284–286.

Maxwell, J. C., 1867, "On the Dynamic Theory of Gases," *Phil. Trans. R. Soc.*, Vol. 157, pp. 49–88.

Michalowski, S., Mitura, E., and Kaminski, W., 1982, "The Application of Mathematical Method to Describe the Kinetics of Drying," *Hungarian Journal of Industrial Chemistry*, Vol. 10, pp. 387–394.

Mitura, E., Michalowski, S., and Kaminski, W., 1988, "A Mathematical Model of Convection Drying in the Falling Drying Rate Period," *Drying Technology*, Vol. 6, No. 1, pp. 113–137.

Morse, M., and Feshbach, H., 1953, *Methods of Theoretical Physics*, McGraw-Hill, New York, p. 865.

Nunzioto, J. W., 1971, "On Heat Conduction in Materials With Memory," *Quarterly Journal Applied Mathematics*, Vol. 29, No. 9, pp. 187–192.

Raspopov, B. M., 1967, "Control of Some Transfer Processes," *Inzhenerno Fizicheskij Zhurnal*, Vol. 12, No. 4, pp. 444–450.

Shashkov, A. G., and Abramenko, T. N., 1975, "Heat Conduction Structure," *Inzhenerno Fizicheskij Zhurnal*, Vol. 28, No. 5, pp. 884–893.

Sieniutycz, S., 1977, "The Variational Principle of Classical Type for Noncoupled Non-stationary Irreversible Transport Processes With Convective Motion and Relaxation," *International Journal of Heat and Mass Transfer*, Vol. 20, pp. 1221–1231.

Swenson, R. J., 1977, "Generalized Heat Conduction Equation," *American Journal of Physics*, Vol. 46, No. 1, pp. 76–77.

Taitel, Y., 1972, "On the Parabolic, Hyperbolic and Discrete Formulation of the Heat Conduction Equation," *International Journal of Heat and Mass Transfer*, Vol. 15, pp. 369–371.

Todos, O. M., Antonishyn, N. V., Sumchenko, L. E., and Lushchikov, V. V., 1970, "Possibility of Description of the Process of Unsteady-State Heat Conduction of Dense Disperse Systems by Differential Equations Allowing for the Peculiarities of Phase Interaction," *Inzhenerno Fizicheskij Zhurnal*, Vol. 18, No. 5, pp. 815–822.

Ulbrich, C. W., 1961, "Exact Electrical Analogy to Vernotte Hypothesis," *Physical Review*, Vol. 123, No. 6, pp. 2001–2002.

Vernotte, P., 1958, "Les paradoxes de la theorie continue de l'equation de la chaleur," *Comptes Rendus Hebd. Seances Acad. Sci.*, Vol. 246, No. 22, Paris, pp. 3154–3155.

Vernotte, P., 1958, "La veritable equation de la chaleur," *Comptes Rendus Hebd. Seances Acad. Sci.*, Vol. 247, No. 23, Paris, pp. 2103–2105.

Vick, B., and Özişik, M., N., 1983, "Growth and Decay of a Thermal Pulse Predicted by the Hyperbolic Heat Conduction Equation," ASME JOURNAL OF HEAT TRANSFER, Vol. 105, No. 4, pp. 902–907.

Vujanovic, B., and Baclic, B., 1976, "Application of Gauss Principle of Least Constraint to the Nonlinear Heat-Transfer Problems," *International Journal of Heat and Mass Transfer*, Vol. 19, pp. 721–730.

Vujanovic, B., and Djukic, D., 1972, "On One Variational Principle of Hamilton's Type for Nonlinear Heat Transfer Problems," *International Journal of Heat and Mass Transfer*, Vol. 15, pp. 1111–1123.

Wiggert, D. C., 1977, "Analysis of Early-Time Transient Heat Conduction by Method of Characteristics," ASME JOURNAL OF HEAT TRANSFER, Vol. 99, pp. 35–40.

J. Fransaer
Research Fellow.

M. De Graef
Research Fellow.

J. Roos
Professor and Head of Department.

Department of Metallurgy and Materials Engineering,
Catholic University Leuven,
Heverlee, Belgium

The Temperature Distribution Around a Spherical Particle on a Planar Surface

The solutions for three related boundary value problems in tangent sphere coordinates are presented; two of these problems involve a conducting and a nonconducting sphere on a conducting flat surface when the field at infinity is linear. The third problem describes the potential field around a conducting sphere on an insulating surface where the field at infinity vanishes. Depending on the nature of the problem, either the Laplace equation or the Stokes stream function formalism is used. The integral solutions are rewritten as series expansions, which are numerically easier to evaluate.

1 Introduction

Knowledge of the effective conductivity of two-phase flows and heterogeneous media is required in various technological applications. In particular, the evaluation of the thermal conductivity of a dispersion of gas bubbles in a liquid is an important heat transfer problem. The problem can be divided into two related subproblems, namely, the conductivity of the three-dimensional dispersion of gas bubbles in the bulk liquid and, secondly, the influence of attached gas bubbles on the heat conducting surface. In the study of heat transfer with accompanying phase transformations from liquid to gas, the thermal conductivity of bubbles attached to a heated surface is an important variable. Increased thermal resistance is not the only thermal effect of the presence of the bubbles; bubbles also screen a portion of the heated surface, hence a gas-evolving surface may include an additional thermal resistance because the local heat flux exceeds the average heat flux. The attached bubbles increase the effective thermal resistance, which in turn adds significantly to the cost of the heat transfer operation.

A second related problem is the influence of fouling on the thermal resistance. In this work the influence of fouling is modeled by the presence of a conducting and/or a nonconducting sphere on a planar surface.

Two limiting cases were studied (the perfectly conducting and the insulating sphere) to illustrate the effect of the conductivity on the fouling of a heated surface. Expressions developed for the additional thermal resistance due to the attached particles are applicable to other physical properties, such as electrical conductivity, dielectric constants, and magnetic permeability, when the proper form of the respective property is used.

2 Review

Potential problems involving tangent sphere boundaries have received repeated attention in the literature. Such problems arise in various research fields, among others: the study of two-phase flow (Reed and Morrison, 1974), suspension mechanics (Feke, 1981), heat and mass transfer (Morrison and Reed, 1974), electrophoresis (Morrison and Stukel, 1970), electrochemistry (de Levie, 1966), and escape and coalescence of particles in filtration systems (Vreeken, 1983).

Recently this line of investigation has been applied to novel fields such as the production of state-of-the-art ceramic particles by decomposition of metallo-organic precursors (Okuyama et al., 1986). Recent shuttle experiments on the movement and removal of gas bubbles by a thermal gradient in glass samples are another example and constitute an important new application (Sheppard, 1986).

One of the first problems involving tangent sphere coordinates concerns the axisymmetric flow of an ideal fluid around two touching spherical particles. In one of the first attempts this problem was treated as a limiting case of two separated spheres for vanishing separation distance; a formal solution in spherical bicoordinates for the case of separated spheres was derived by Stimpson and Jeffery (1926). However, in order to converge, the number of terms in this series solution increases without bounds for vanishing separation. Therefore, the situation where the two spheres actually touch is not well described by this formulation. Bentwich and Miloh (1978) obtained a solution for the touching sphere case as a limiting process to the axisymmetric two-sphere configuration, but their analysis is rather cumbersome. An approximate solution by means of the image and reflection method was also presented (Brenner and Happel, 1973).

Recent work used the tangent sphere coordinates as the natural coordinate system to simplify writing the boundary conditions at the sphere surface (Witze et al., 1968); in all cases the solutions were expressed in integral form. The significance of these solutions for numerical evaluation of the results is rather limited. Because the integrand becomes increasingly oscillatory, numerical difficulties arise around the point of contact, which is precisely the area one is most interested in. In view of this, the problem is reexamined in this paper; all integrals are replaced by summations, thereby avoiding the numerical problems mentioned above.

3 Governing Equations: Tangent Sphere Coordinates

The TSC (Tangent Sphere Coordinates) system is frequently applied to problems involving two equally sized spheres; however, in this paper the special case of a sphere tangent to a plane is considered. Most practical applications involving equally sized spheres can be modeled with a sphere interacting with a plane wall.

The equations to be solved in this paper are the Laplace equation

$$\nabla^2\phi = 0$$

and the creeping irrotational flow equation

$$E^2\psi = 0$$

Contributed by the Heat Transfer Division for publication in the JOURNAL OF HEAT TRANSFER. Manuscript received by the Heat Transfer Division September 28, 1988; revision received September 18, 1989. Keywords: Conduction, Mass Transfer.

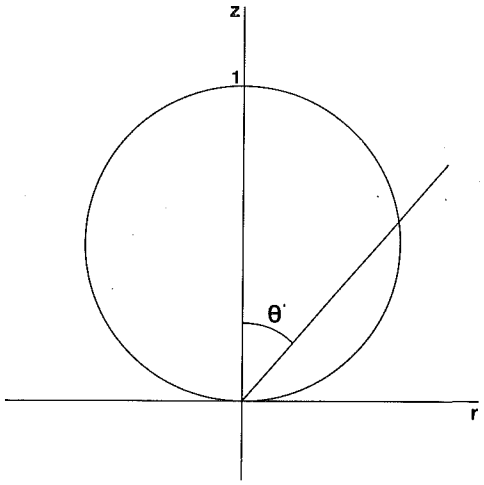

Fig. 1 Definition of the tangent sphere geometry

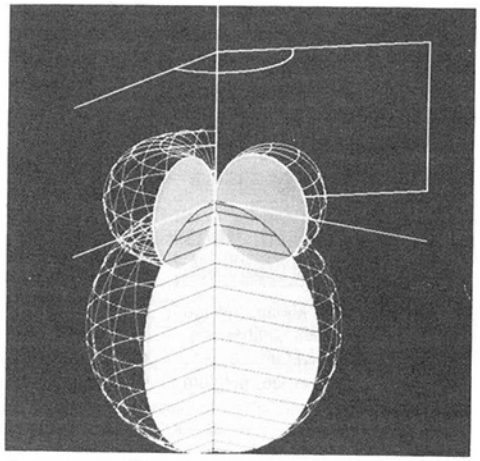

Fig. 2 Perspective drawing of the coordinate surfaces for the tangent sphere coordinate system; $\mu = \text{cst}$ represents a toroid without center opening, $\nu = \text{cst}$ represents a sphere tangent to the $z = 0$ plane, and $\phi = \text{cst}$ a half plane containing the axis of symmetry

for the geometry of Fig. 1. In order to apply the method of separation of variables, the most appropriate coordinate system is the one in which the coordinate surfaces coincide with the physical boundaries of the problem; for this problem the boundary conditions suggest the use of tangent sphere coordinates.

The TSC system is a rotational orthogonal curvilinear coordinate system, shown in Fig. 2. The coordinate surfaces are tangent spheres ($\nu = \pm\text{cst}$), toroids without center opening ($\mu = \pm\text{cst}$), and planes passing through the z axis. With reference to the cylindrical coordinate system (r, z), where the z axis coincides with the symmetry axis passing through the contact point and the sphere center, and recognizing the two-dimensional nature of the problems posed in this paper, the TSC coordinates are defined as follows:

$$r = \frac{\mu}{\mu^2 + \nu^2} \tag{1a}$$

$$z = \frac{\nu}{\mu^2 + \nu^2} \tag{1b}$$

$$\cos\theta = \frac{\nu}{(\mu^2 + \nu^2)^{1/2}} \tag{1c}$$

In this coordinate system the Laplace equation becomes

$$\nabla^2\phi = \frac{\partial}{\partial\mu}\left[\frac{\mu}{\mu^2+\nu^2}\frac{\partial\phi}{\partial\mu}\right] + \mu\frac{\partial}{\partial\nu}\left[\frac{1}{\mu^2+\nu^2}\frac{\partial\phi}{\partial\nu}\right] = 0 \tag{2a}$$

and the equation for the Stokes stream function is given by

$$E^2\psi = \mu(\mu^2+\nu^2)\left[\frac{\partial}{\partial\mu}\left(\frac{\mu^2+\nu^2}{\mu}\frac{\partial\psi}{\partial\mu}\right) + \frac{\partial}{\partial\nu}\left(\frac{\mu^2+\nu^2}{\mu}\frac{\partial\psi}{\partial\nu}\right)\right] = 0 \tag{2b}$$

The general solutions to these equations are given by

$$\phi = (\mu^2+\nu^2)^{1/2}[A\sinh(q\nu) + B\cosh(q\nu)][CJ_0(q\mu) + DY_0(q\mu)] \tag{3a}$$

and

$$\psi = \frac{\mu}{(\mu^2+\nu^2)^{1/2}}[A\sinh(q\nu) + B\cosh(q\nu)][CJ_1(q\mu) + DY_1(q\mu)] \tag{3b}$$

More information on this coordinate system can be found in Moon and Spencer's *Field Theory Handbook* (1971).

All variables in this paper are defined in dimensionless form. The distances are normalized with respect to the bubble diameter and thus $r = 1$ corresponds to a distance of one bubble diameter away from the point of contact.

4 Applications

4.1 Conducting Sphere on Conducting Surface. This first case concerns the temperature field around a spherical surface in point contact with a planar equipotential surface. Using the

Nomenclature

A, B, C, D = separation functions
r = radial position in cylindrical coordinates
z = axial position in cylindrical coordinates
q = integration variable
$\beta, \eta, \xi, \lambda$ = sums of reciprocal powers (Abramowitz and Stegun, 1965, Table 23.3, pp. 811–812)
$\Delta\phi, \Delta\phi_n$ = additional thermal resistance
θ = angle defined by equation (1) and Fig. 1
κ = conductivity
μ, ν = tangent sphere coordinates defined by equation (1)
ϕ = potential function
ϕ_0 = potential gradient at infinity
ϕ_d = disturbance potential
ψ = stream function
ψ_0 = stream function gradient at infinity
ψ_d = disturbance stream function

principle of superposition, where the field far from the sphere is linear, the total (temperature, electrostatic, . . .) potential is written as the sum of a linear term $\phi_0 z$ and a disturbance ϕ_d around the sphere

$$\nabla^2(\phi_0 z + \phi_d) = 0 \tag{4}$$

from which

$$\nabla^2 \phi_d = 0 \tag{5}$$

The boundary conditions for the disturbance are

$$\phi_d = 0 \qquad (\mu,\ \nu = 0) \tag{6a}$$

$$\phi_d = -\phi_0 z \qquad (\nu = 1) \tag{6b}$$

$$\frac{\partial \phi_d}{\partial \mu} = 0 \qquad (\mu = 0) \tag{6c}$$

The disturbance must vanish both on the plane and far away from the sphere (equation (6*a*)); equation (6*c*) expresses the rotational symmetry of the problem and equation (6*b*) matches the linear field to the disturbance on the sphere surface. The general solution given in Section 3, satisfying all boundary conditions except equation (6*b*), can be written as (Moon and Spencer, 1971)

$$\phi_d = A(q)\sinh(q\mu) J_0(q\mu)\,(\mu^2 + \nu^2)^{1/2} \tag{7}$$

where q is a continuous separation constant and J_0 is the Bessel function of the first kind (order zero). Since there are no discrete eigenvalues for q, boundary condition equation (6*b*) can be satisfied by integrating equation (7) for $\nu = 1$ over the whole semi-infinite range of q values and equating the resulting integral to the externally imposed field.

$$\frac{-\phi_0}{(1+\mu^2)^{3/2}} = \int_0^\infty A(q)\sinh(q) J_0(q\mu)\, dq \tag{8}$$

This integral equation can be solved for $A(q)$ by relying on the properties of the Hankel transform (Erdelyi et al., 1954)

$$\int_0^\infty q e^{-q} J_0(q\mu)\, dq = \frac{1}{(1+\mu^2)^{3/2}} \tag{9}$$

from which, using equation (8)

$$A(q) = -\phi_0 \frac{q e^{-q}}{\sinh(q)} \tag{10}$$

Therefore the total solution is

$$\phi = \phi_0 z - \phi_0 (\mu^2 + \nu^2)^{1/2} \int_0^\infty q e^{-q} \frac{\sinh(q\nu)}{\sinh(q)} J_0(q\mu)\, dq \tag{11}$$

Note that close to the contact point of sphere and surface (i.e., $\mu \to \infty$) the integrand is strongly oscillating and hence difficult to evaluate numerically.

The integral can be rewritten as an infinite series by expanding the $\sinh(q)$ in the denominator as follows:

$$\frac{1}{\sinh\,(q)} = 2 \sum_{n=0}^{\infty} e^{-(2n+1)q} \tag{12}$$

Introducing this expansion in the integral and regrouping terms results in

$$\sum_{n=0}^{\infty} \left[\int_0^\infty q J_0(q) e^{-[2(n+1)-\nu]q}\, dq - \int_0^\infty q J_0(q) e^{-[2(n+1)+\nu]q}\, dq \right] \tag{13}$$

Using the following integral (Watson, 1966):

$$\int_0^\infty e^{-aq} J_0(bq)\, dq = \frac{2a\Gamma(3/2)}{\sqrt{\pi}(a^2+b^2)^{3/2}} = \frac{a}{(a^2+b^2)^{3/2}} \tag{14}$$

the complete solution finally becomes

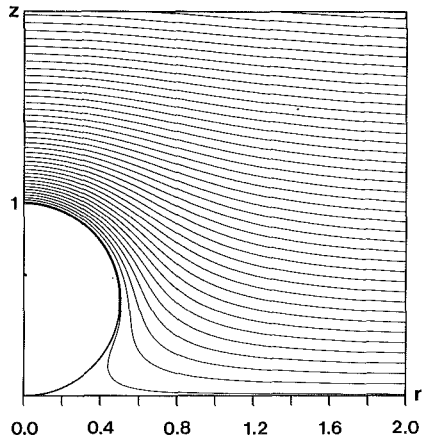

Fig. 3 Equipotential lines for a conducting sphere on a conducting surface

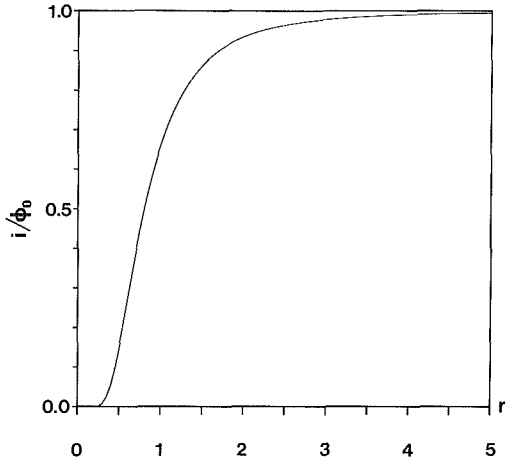

Fig. 4 Current distribution on the plane $z = 0$ versus distance from the point of tangency for the conducting sphere on a conducting surface in units of ϕ_0

$$\phi = \phi_0 z - \phi_0 (\mu^2 + \nu^2)^{1/2} \sum_{n=1}^{\infty} \left[\frac{2n-\nu}{[(2n-\nu)^2 + \mu^2]^{3/2}} - \frac{2n+\nu}{[(2n+\nu)^2 + \mu^2]^{3/2}} \right] \tag{15}$$

The equipotential lines for this problem are depicted in Fig. 3.

From this analytical solution the heat flux distribution can be derived by straightforward differentiation; for instance, the heat flux distribution on the equipotential surface is obtained by

$$\left.\frac{\partial \phi}{\partial z}\right|_{z=0} = \left.\frac{\partial \phi}{\partial \mu}\frac{\partial \mu}{\partial z}\right|_{z=0} + \left.\frac{\partial \phi}{\partial \nu}\frac{\partial \nu}{\partial z}\right|_{z=0} = \mu^2 \left.\frac{\partial \phi}{\partial \nu}\right|_{\nu=0} \tag{16}$$

Substitution of equation (15) into equation (16) results in

$$\left.\frac{\partial \phi}{\partial z}\right|_{z=0} = \phi_0 \left[1 - 2\mu^3 \sum_{n=1}^{\infty} \frac{8n^2 - \mu^2}{(4n^2+\mu^2)^{5/2}} \right] \tag{17}$$

This derivative is shown in Fig. 4 as a function of distance r from the point of tangency. This result was obtained by numerical summation of the series expansion: for large r this series converges rapidly, whereas for distances close to the contact point the number of terms increases linearly with μ.

The heat flux distribution on the sphere as a function of the angle θ (defined in Fig. 2) is given by

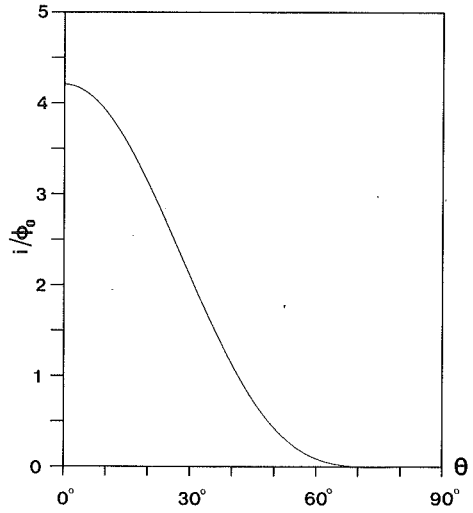

Fig. 5 Current distribution versus θ on the sphere surface in units of ϕ_0 (θ defined in Fig. 1)

$$\left.\frac{\partial\phi}{\partial\nu}\right|_{\nu=1} = 2\phi_0(1+\mu^2)^{1/2}\sum_{n=0}^{\infty}\frac{2(2n+1)^2-\mu^2}{[(2n+1)^2+\mu^2]^{5/2}} \tag{18}$$

and is shown in Fig. 5. The maximum normalized heat flux at $\mu=0$ can be rewritten as (equation (23.2.20) in Abramowitz and Stegun, 1965)

$$\left.\frac{i}{\phi_0}\right|_{\substack{\nu=1\\ \mu=0}} = 4\sum_{n=0}^{\infty}\frac{1}{(2n+1)^3} = 4\lambda(3) = 4\times 1.0517997902 \tag{19}$$

4.2 Insulating Sphere on Conducting Surface. In the former case the problem was solved using the potential function approach; in this section we sketch a second approach to the tangent sphere problem in terms of the Stokes velocity potential (Brenner and Happel, 1973). Potential problems can often be solved by either method, but usually the imposed boundary conditions decide which one is mathematically more tractable. For an insulating sphere on a conducting surface the boundary conditions cannot be expressed as a Dirichlet problem; on the nonconducting sphere surface the potential derivative has to be zero whereas on the plane surface the potential has a constant value. This mixed boundary condition can be transformed into a Dirichlet problem by computing the stream function ψ rather than the potential function ϕ. This situation represents two tangent equally sized spheres moving through a liquid. We consider the spheres to be stationary while the fluid at infinity flows in the $-z$ direction with constant velocity ψ_0. A solution reported earlier (Cooley and O'Neill, 1969) was mathematically more cumbersome because the fluid was kept stationary whereas the spheres moved with constant velocity.

The solution of this problem can be written as the superposition of the stream function far from the origin and a disturbance μ_d. The first is a uniform flow, which is a solution to the Stokes equation without any disturbance; the second is a correction due to the presence of the two tangent spheres. The boundary conditions for this disturbance can be expressed as

$$\psi_d = 0 \qquad (\mu=0) \tag{20a}$$

$$\psi_d = 0 \qquad (|\nu|=1) \tag{20b}$$

$$\psi_d \to -\frac{1}{2}r^2\psi_0 \qquad \text{for } (\mu,\nu)\to 0 \tag{20c}$$

where r is the distance to the contact point in cylindrical coordinates. The second boundary condition (20b) states that no heat flux passes through the sphere surface or, in terms of fluid mechanics, that the fluid is diverted around the spheres.

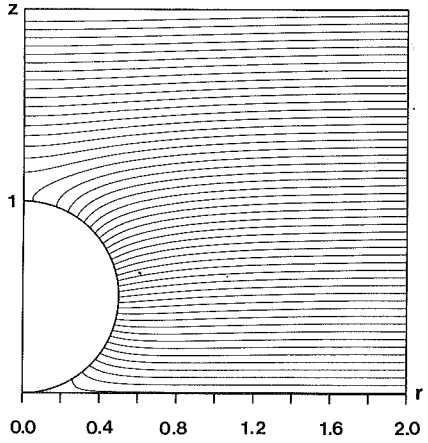

Fig. 6 Equipotential lines for an insulating sphere on a conducting surface

Expressed in integral form the total stream function becomes

$$\psi = \frac{1}{2}r^2\psi_0 - \frac{\mu}{(\mu^2+\nu^2)^{1/2}}\int_0^{\infty} J_1(q\mu)\{A(q)\sinh(q\nu)+B(q)\cosh(q\nu)\}dq \tag{21}$$

From the boundary conditions it follows that $A(q)=0$ and

$$\psi_0\frac{\mu}{2(1+\mu^2)^{3/2}} = \int_0^{\infty} B(q)\cosh(q)J_1(q\mu)dq \tag{22}$$

From the Hankel transform (Erdelyi et al., 1954)

$$\frac{a}{(a^2+b^2)^{3/2}} = \int_0^{\infty} qe^{-q|b|}J_1(qa)dq \tag{23}$$

follows

$$B(q) = \psi_0\frac{qe^q}{2\cosh(q)} \tag{24}$$

Hence, the final solution is

$$\psi = \psi_0\frac{r^2}{2} - \psi_0\frac{\mu}{2(\mu^2+\nu^2)^{1/2}}\int_0^{\infty} qe^{-q}\frac{\cosh(q\nu)}{\cosh(q)}J_1(q\mu)dq \tag{25}$$

Again this function can be expressed as a rapidly converging infinite series

$$\psi = \psi_0\frac{r^2}{2} - \psi_0\frac{\mu}{2(\mu^2+\nu^2)^{1/2}}\sum_{n=1}^{\infty}(-1)^{n-1}\left[\frac{\mu}{[(2n-\nu)^2+\mu^2]^{3/2}} + \frac{\mu}{[(2n+\nu)^2+\mu^2]^{3/2}}\right] \tag{26}$$

The equipotential lines derived from this streamfunction are depicted in Fig. 6. The normalized heat flux on the plane $z=0$ is given by

$$\left.\frac{i}{\psi_0}\right|_{z=0} = 1+\mu^3\sum_{n=1}^{\infty}(-1)^n\left[\frac{1}{(4n^2+\mu^2)^{3/2}} - \frac{3\mu^2}{(4n^2+\mu^2)^{5/2}}\right] \tag{27}$$

and is shown in Fig. 7. The maximum value of 1.027521 is reached for $r=1.065545$.

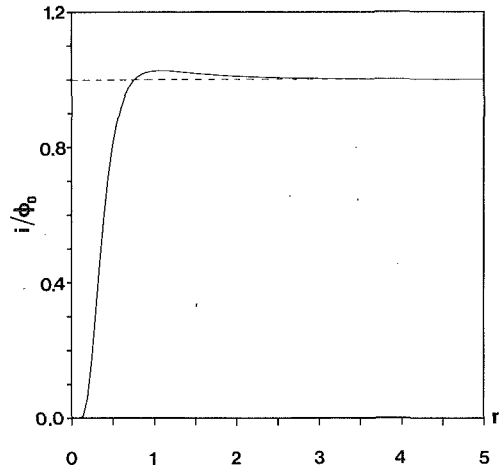

Fig. 7 Current distribution on the plane $z=0$ versus distance from the point of tangency for the insulating sphere on a conducting surface in units of ϕ_0

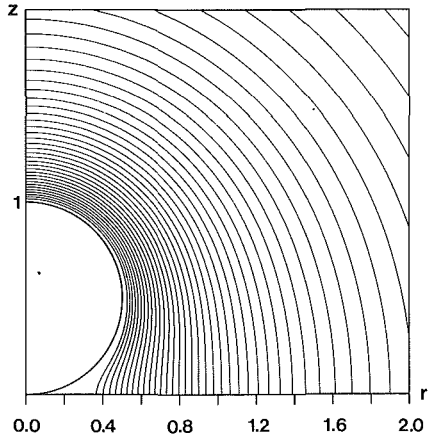

Fig. 8 Equipotential lines for conducting sphere on insulating surface

4.3 Conducting sphere on Insulating Surface. Far from the sphere the temperature goes to zero, whereas the sphere surface is at temperature ϕ_0. The boundary condition on the insulating surface can be replaced by a condition for the mirror image of the first sphere. Hence the following conditions can be formulated:

$$\phi = 0 \qquad (\mu,\ \nu \to = 0) \tag{28a}$$

$$\phi = \phi_0 \qquad (|\nu| = 1) \tag{28b}$$

$$\left.\frac{\partial \phi}{\partial z}\right|_{z=0} = 0 \qquad \text{or } \phi = \phi_0 \text{ for } \nu = -1 \tag{28c}$$

$$\left.\frac{\partial \phi}{\partial \mu}\right|_{\mu=0} = 0 \qquad \text{(rotational symmetry)} \tag{28d}$$

The general solution now is

$$\phi = [A \sinh(q\nu) + B \cosh(q\nu)][CJ_0(q\mu) + DY_0(q\mu)] \tag{29}$$

ϕ has to remain finite for $\mu = 0$, hence $D = 0$. From boundary condition equation (28b) it follows that ϕ is even in ν, hence $A = 0$. The potential can then be written in integral form as

$$\phi = (\mu^2 + \nu^2)^{1/2} \int_0^\infty A(q) J_0(q\mu) \cosh(q\nu)\, dq \tag{30}$$

Using boundary condition equation (28b) and

$$\int_0^\infty e^{-q} J_0(q\mu)\, dq = \frac{1}{(\mu^2+1)^{1/2}} \tag{31}$$

the function $A(q)$ can be determined as

$$A(q) = \phi_0 \frac{e^{-q}}{\cosh(q)} \tag{32}$$

from which the total solution follows:

$$\phi = \phi_0 (\mu^2 + \nu^2)^{1/2} \int_0^\infty e^{-q} \frac{\cosh(q\nu)}{\cosh(q)} J_0(q\mu)\, dq \tag{33}$$

This integral can again be written as an infinite series by expanding the $\cosh(q)$ in the denominator and regrouping terms:

$$\phi = \phi_0 (\mu^2 + \nu^2)^{1/2} \sum_{n=0}^{\infty} \left[\frac{1}{[(2n+\nu)^2 + \mu^2]^{1/2}} + \frac{1}{[(2n-\nu)^2 + \mu^2]^{1/2}} \right] \tag{34}$$

As in the previous section the equipotential lines were computed by numerically summing equation (34); the results are shown in Fig. 8. In contrast with the previous series equation (34) is slowly convergent: Improving the accuracy by one digit demands a tenfold increase in the number of terms. However, making use of a Kummer transform, the convergence rate can be increased by a factor 1000 (on the average). The series in equation (34) can be replaced by

$$\phi = \phi_0 (\mu^2 + \nu^2)^{1/2} \left[\frac{2}{(\mu^2+\nu^2)^{1/2}} - \ln(2) + \sum_{n=1}^{\infty} (-1)^n \left[\frac{1}{[\ ]} + \frac{1}{[\ ]} - \frac{1}{n} \right] \right] \tag{35}$$

where the brackets in the denominators refer to the corresponding terms in equation (34).

The heat flux on the sphere is given by

$$\left.\frac{\partial \phi}{\partial \nu}\right|_{\nu=1} = 2\phi_0 (1+\mu^2)^{1/2} \sum_{n=0}^{\infty} (-1)^n \frac{2n+1}{[(2n+1)^2 + \mu^2]^{3/2}} \tag{36}$$

The maximum value at the top of the sphere equals (equation (23.2.21) in Abramowitz and Stegun, 1965)

$$\left.\frac{i}{\phi_0}\right|_{\substack{\nu=1 \\ \mu=0}} = 2 \sum_{n=1}^{\infty} \frac{(-1)^n}{(2n+1)^2} = 2\beta(2) = 2 \times 0.9159655941 \tag{37}$$

5 Discussion and Conclusion

Comparing Figs. 3 and 6, it is seen that the potential fields differ substantially; however, from the point of view of the heat flux entering the tangent plane, the situations are rather similar. In either case the point of contact is screened by the sphere and the heat flux becomes effectively zero in the vicinity of the contact point. In the case of a conducting sphere on a conducting surface the normalized heat flux reaches 1 percent of its unperturbed value on the plane at a distance $r = 0.304925$ from the contact point and for an angle $\theta = 72.12$ deg on the sphere surface. Therefore, the sphere can be thought of as being equivalent to a spherical cap with a contact angle of 35.75 deg with the plane.

The thermal resistance decrease caused by a single particle of radius a is proportional to the integral of the potential disturbance over a plane parallel to the electrode (Sides and Tobias, 1980)

$$\Delta\phi = 4a^2 \int_0^\infty 2\pi r \phi_d\, dr \qquad z \gg 0 \tag{38}$$

For a conducting particle on a conducting surface this integral can be rewritten as (using equation (15))

$$\Delta\phi = \pi a^2 \phi_0 \sum_{n=1}^{\infty} \frac{1}{n^3} \frac{z}{(r^2+z^2)^{1/2}} \Big|_0^{\infty} \tag{39}$$

which after taking the limit for $z \to \infty$ becomes

$$\Delta\phi = \pi\phi_0 \xi(3) = \pi\phi_0 \times 1.202056903159 \tag{40}$$

Therefore, the thermal resistance decreases by about 20 percent. Sides and Tobias (1980) obtained a thermal resistance increase of about 10 percent for a nonconducting particle on a conducting surface: They found $\Delta\phi = \pi\phi_0 \times 0.90154$, which is equal to $\pi\phi_0\eta(3)$.

The influence of the presence of a conducting or nonconducting particle on the thermal flux reaching the planar surface disappears rapidly with increasing distance from the contact point. At a distance of more than two bubble radii, the disturbance is effectively zero. Neglecting the mutual interactions of neighboring particles, the net effect of a distribution of particles of radius a and mean number density n per unit area will be n times the effect of a single particle

$$\Delta\phi_n = n \times \Delta\phi \tag{41}$$

From this the thermal resistance can be obtained by dividing the additional thermal resistance $\Delta\phi_n$ by the conductivity κ and the unperturbed thermal flux ϕ_0

$$R = \frac{\Delta\phi_n}{\kappa\phi_0} \tag{42}$$

This result applies equally to ordered and random arrays of particles as long as the individual particles are well spaced.

Acknowledgments

The present work was carried out in the framework of the interuniversity networks for fundamental research financed by the Belgian Government (Contract UIAP No. 4). One of us (JF) would like to thank the IWONL for financial support.

References

Abramowitz, M., and Stegun, I., eds., *Handbook of Mathematical Functions*, Dover Publications Inc., New York.

Bentwich, M., and Miloh, T., 1978, "On the Exact Solution for the Two-Sphere Problems in Axisymmetrical Potential Flow," ASME *Journal of Applied Mechanics*, Vol. 45, pp. 463–468.

Brenner, H., and Happel, J., 1973, *Low Reynolds Number Hydrodynamics*, Noordhoff International Publishing, Leiden.

Cooley, M. D. A., and O'Neill, M. E., 1969, "On the Slow Motion of Two Spheres in Contact Along their Line of Centers Through a Viscous Fluid," *Proc. Camb. Phil. Soc.*, Vol. 66, pp. 407–415.

de Levie, R., 1966, "Electrochemical Response of Porous and Rough Electrodes," in: *Advances in Electrochemistry & Electrochemical Engineering*, P. Delahay and C. W. Tobias, eds., Vol. 2, pp. 329–397.

Erdelyi, A., Magnus, W., Oberhettinger, F., and Tricomi, F. G., 1954, *Tables of Integral Transforms*, Vol. II, McGraw-Hill, New York.

Feke, D. L., 1981, "Kinetics of Flow-induced Coagulation With Weak Brownian Diffusion," Ph.D. Thesis, Princeton University, Princeton, New Jersey.

Moon, P., and Spencer, D. E., 1971, *Field Theory Handbook: Including Coordinate Systems, Differential Equations, and Their Solutions*, 2nd ed., Springer Verlag, Berlin, p. 104.

Morrison, F. A., Jr., and Stukel, J. J., 1970, "Electrophoresis of an Insulating Sphere Normal to a Conducting Plane," *J. Colloid Int. Sc.*, Vol. 33, pp. 88–93.

Morrison, F. A., Jr., and Reed, L. D., 1974, "Low Knudsen Number Heat Transfer From Two Spheres in Contact," ASME JOURNAL OF HEAT TRANSFER, Vol. 96, pp. 478–482.

Okuyama, K., Kousaka, Y., Tohge, N., Yamamoto, S., Wu, J. J., Flagan, R. C., and Seinfeld, J. H., 1986, "Production of Ultra-fine Metal Oxide Aerosol Particles by Thermal Decomposition of Metal Alkoxide Vapours," *AIChE Journal*, Vol. 32, pp. 2010–2019.

Reed, L. D., and Morrison, F. A., Jr., 1974, "The Slow Motion of Two Touching Fluid Spheres Along Their Line of Centers," *Int. J. Multiphase Flow*, Vol. 1, pp. 573–584.

Sides, P. J., and Tobias, C. W., 1980, "Primary Potential and Current Distribution Around a Bubble on an Electrode," *J. Electrochem. Soc.*, Vol. 117, pp. 288–291.

Stimpson, M., and Jeffery, G. B., 1926, "The Motion of Two Spheres in a Viscous Fluid," *Proc. Royal Soc. London*, Vol. A111, pp. 110–116.

Vreeken, C., 1983, "Diepbedfiltratie met Modelsystemen," Diss. doct. Technische Wetenschappen, Technische Hogeschool, Delft, Netherlands.

Watson, G. N., 1966, *Treatise on the Theory of Bessel Functions*, 2nd ed., Cambridge University Press, Cambridge, p. 383.

Witze, C. P., Schrock, V. E., and Chambre, P. L., 1968, "Flow About a Growing Sphere in Contact With a Plane Surface," *Int. J. Heat Mass Transfer*, Vol. 11, pp. 1637–1652.

Temperature Profile in Semi-infinite Body With Exponential Source and Convective Boundary Condition

B. F. Blackwell
Sandia National Laboratory,
Aerothermodynamics Division 1553,
Albuquerque, NM 87185

An analytical solution for the temperature profile in a semi-infinite body with an exponentially decaying (with position) source and convective boundary condition is obtained using Laplace transforms. The appropriate dimensionless parameters are identified and the temperature as a function of these parameters is presented in graphic form. With cooling at the exposed surface, the maximum temperature occurs in the interior of the slab instead of at the exposed surface. The location of the temperature maximum as a function of the various system parameters is presented in graphic form. Approximate relationships are presented for small values of dimensionless time.

1 Introduction

Over the past decade, considerable interest has been shown in material processing using lasers. In particular, laser drilling, machining, and welding have been studied analytically and experimentally. Lasers are now being routinely used in some material processing industries. Dabby and Paek (1972) observed "explosive removal of material" when sufficient transmission of the laser energy past the exposed surface occurs. A possible explanation for this phenomenon is that the point of maximum temperature (before phase change occurs at the exposed surface) lies inside the body because of heat loss to the surroundings. If the material expands on changing phase, and the initial phase change occurs inside the body instead of at the exposed surface, then explosive material removal may be possible. The location of the maximum temperature is determined by a balance between the laser energy deposited within the material and heat conduction. For a given laser intensity, increasing the heat loss from the exposed surface moves the location of maximum temperature farther into the body. In fact, actively cooling the surface may be a means of enhancing the penetration rate for a given power laser. The purpose of this work is to present a model for determining the location of maximum temperature prior to the initiation of phase change.

2 Mathematical Preliminaries

The equation describing heat conduction in a constant property one-dimensional body with an energy source is

$$\rho C_p \frac{\partial T}{\partial t} = k \frac{\partial^2 T}{\partial x^2} + \dot{u}''' \tag{1}$$

For a material that absorbs the laser energy internally, the energy source terms is modeled as

$$\dot{u}''' = I_o(1-R)\mu \exp(-\mu x) \tag{2}$$

where I_o is the laser incident intensity, R is the surface reflectance, and μ is the absorption coefficient. This model assumes no spatial variation of I_o in the plane normal to the beam. Also, the problem times are sufficiently small that diffusion perpendicular to the beam (x) direction can be ignored; see Ready (1978) for a discussion of when this condition is satisfied. Approximately 95 percent of the laser energy is absorbed within a depth of $3/\mu$. For metals in which μ is of the order 10^5 cm^{-1} (Ready, 1978), 95 percent of the energy will be absorbed within 3×10^{-5} cm; for many purposes, this can be considered a skin effect. This work is directed more toward organic materials in which μ is considerably smaller and energy is deposited over a greater thickness.

The assumed initial condition is a uniform temperature

$$T(x, 0) = T_o \tag{3}$$

and the boundary conditions are

$$-k \frac{\partial T(0, t)}{\partial x} = h[T_\infty - T(0, t)] \tag{4}$$

and

$$\frac{\partial T(\infty, t)}{\partial x} = 0 \tag{5}$$

There are several analyses in the literature in which the above boundary/initial conditions are used, except the exposed face is assumed to be insulated instead of losing heat by convection; for example, see Carslaw and Jaeger (1959), p. 80. For this case, the maximum temperature will occur at the exposed surface instead of in-depth.

Defining θ as the temperature rise above the initial temperature

$$\theta = T - T_o \tag{6}$$

the energy equation and boundary conditions can be written as

$$\frac{\partial \theta}{\partial t} = \alpha \frac{\partial^2 \theta}{\partial x^2} + \frac{\dot{u}'''}{\rho C_p} \tag{7}$$

$$\theta(x, 0) = 0 \tag{8}$$

$$\frac{\partial \theta(0, t)}{\partial x} + \frac{h}{k}[T_\infty - T_o - \theta(0, t)] = 0 \tag{9}$$

$$\frac{\partial \theta(\infty, t)}{\partial x} = 0 \tag{10}$$

Contributed by the Heat Transfer Division for publication in the JOURNAL OF HEAT TRANSFER. Manuscript received by the Heat Transfer Division August 26, 1988; revision received July 15, 1989. Keywords: Conduction, Transient and Unsteady Heat Transfer.

Let $\bar{\theta}(x, s)$ denote the Laplace transform of $\theta(x, t)$ with respect to time t. Taking the Laplace transform of equation (7), one obtains

$$s\bar{\theta}(x, s) - \theta(x, 0^+) = \alpha \frac{d^2\bar{\theta}(x, s)}{dx^2} + \frac{I_o(1-R)\mu\exp(-\mu x)}{\rho C_p}\frac{1}{s} \tag{11}$$

Making use of the initial condition on θ and rearranging, equation (11) can be written as

$$\frac{d^2\bar{\theta}(x, s)}{dx^2} - \frac{s}{\alpha}\bar{\theta}(x, s) = -\frac{I_o(1-R)\mu\exp(-\mu x)}{k}\frac{1}{s} \tag{12}$$

The transformed boundary conditions become

$$\frac{d\bar{\theta}(0, s)}{dx} + \frac{h}{k}\left[\frac{(T_\infty - T_o)}{s} - \bar{\theta}(0, s)\right] = 0 \tag{13}$$

$$\frac{d\bar{\theta}(\infty, s)}{dx} = 0. \tag{14}$$

The solution to equation (12) can be written as

$$\bar{\theta}(x, s) = C_1\exp\left(\sqrt{\frac{s}{\alpha}}x\right) + C_2\exp\left(-\sqrt{\frac{s}{\alpha}}x\right) - \frac{I_o(1-R)\mu\exp(-\mu x)}{k}\frac{1}{s}\frac{1}{\mu^2 - \frac{s}{\alpha}} \tag{15}$$

In order for the temperature to remain finite at $x = \infty$, the constant C_1 must be zero. The constant C_2 can be evaluated by applying equation (13). The final solution in the transformed space is found to be

$$\bar{\theta}(x, s) = \left[\frac{\frac{h(T_\infty - T_o)}{k}\frac{1}{s} + \frac{I_o(1-R)\mu\left(\mu + \frac{h}{k}\right)}{k}\frac{1}{s}\frac{1}{\mu^2 - \frac{s}{\alpha}}}{\sqrt{\frac{s}{\alpha}} + \frac{h}{k}}\right] \exp\left(-\sqrt{\frac{s}{\alpha}}x\right) - \frac{I_o(1-R)\mu\exp(-\mu x)}{k}\frac{1}{s}\frac{1}{\mu^2 - \frac{s}{\alpha}} \tag{16}$$

In order to determine the inverse Laplace transform of equation (16) using standard Laplace transform tables, the following algebraic relationship will be helpful:

$$\frac{1}{s(\sqrt{s}-b)(\sqrt{s}+b)(\sqrt{s}+a)} = -\frac{1}{ab^2}\frac{1}{s} - \frac{1}{a(a^2-b^2)}\frac{1}{\sqrt{s}(\sqrt{s}+a)} - \frac{(a-b)}{2b^2(a^2-b^2)}\frac{1}{\sqrt{s}(\sqrt{s}-b)} + \frac{(a+b)}{2b^2(a^2-b^2)}\frac{1}{\sqrt{s}(\sqrt{s}+b)} \tag{17}$$

The following inverse Laplace transform relationships will be utilized:

$$\mathcal{L}^{-1}\left[\frac{a\exp(-\kappa\sqrt{s}}{s(\sqrt{s}+a)}\right] = -\exp(a^2t + a\kappa)\operatorname{erfc}\left(\frac{\kappa}{2\sqrt{t}} + a\sqrt{t}\right) + \operatorname{erfc}\left(\frac{\kappa}{2\sqrt{t}}\right) \tag{18}$$

$$\mathcal{L}^{-1}\left[\frac{\exp(-\kappa\sqrt{s})}{s}\right] = \operatorname{erfc}\left(\frac{\kappa}{2\sqrt{t}}\right) \tag{19}$$

$$\mathcal{L}^{-1}\left[\frac{\exp(-\kappa\sqrt{s}}{\sqrt{s}(\sqrt{s}+a)}\right] = \exp(a^2t + a\kappa)\operatorname{erfc}\left(\frac{\kappa}{2\sqrt{t}} + a\sqrt{t}\right) \tag{20}$$

$$\mathcal{L}^{-1}\left[\frac{1}{s(s-b)}\right] = \frac{1}{b}[\exp(bt) - 1] \tag{21}$$

Utilizing the above Laplace transform relationships, the inverse transform of equation (16) can be written as

$$T - T_o = (T_\infty - T_o)\left[\operatorname{erfc}\left(\frac{x}{2\sqrt{\alpha t}}\right) - \exp\left(\frac{h^2}{k^2}\alpha t + \frac{hx}{k}\right)\operatorname{erfc}\left(\frac{x}{2\sqrt{\alpha t}} + \frac{h}{k}\sqrt{\alpha t}\right)\right] + \frac{I_o(1-R)}{\mu k}\left\{\left(1 + \frac{\mu k}{h}\right)\operatorname{erfc}\left(\frac{x}{2\sqrt{\alpha t}}\right) + \frac{1}{\frac{h}{\mu k}\left(\frac{h}{\mu k} - 1\right)}\exp\left(\frac{h^2}{k^2}\alpha t + \frac{hx}{k}\right)\operatorname{erfc}\left(\frac{x}{2\sqrt{\alpha t}} + \frac{h}{k}\sqrt{\alpha t}\right)\right.$$

Nomenclature

- Bi = Biot number = $h/k\mu$
- C_p = specific heat
- erf = error function
- erfc = complimentary error function = 1 − erf
- h = convective heat transfer coefficient
- I_o = intensity of laser, energy/area
- k = thermal conductivity
- $\mathcal{L}$ = Laplace transform
- $\dot{q}''$ = heat flux
- R = surface reflectance
- s = Laplace transform variable
- t = time
- T = temperature
- T_o = initial temperature
- T_w = wall or surface temperature
- T_∞ = free-stream temperature
- $\dot{u}'''$ = energy generation rate per unit volume
- x = spatial coordinate
- α = thermal diffusivity = $k/\rho C_p$
- θ = temperature rise above initial temperature = $T - T_o$
- μ = absorption coefficient, 1/length
- ρ = density
- τ = dimensionless time = $\alpha\mu^2$t
- χ = dimensionless distance = μx
- χ^* = value of χ at maximum temperature
- ω = dimensionless energy absorption at surface = $\frac{I_o(1-R)}{h(T_\infty - T_o)}$

$$-\frac{1}{2}\left(\frac{\frac{h}{\mu k}+1}{\frac{h}{\mu k}-1}\right)\exp(\mu^2\alpha t+\mu x)\operatorname{erfc}\left(\frac{x}{2\sqrt{\alpha t}}+\mu\sqrt{\alpha t}\right)$$

$$-\frac{1}{2}\exp(\mu^2\alpha t-\mu x)\operatorname{erfc}\left(\frac{x}{2\sqrt{\alpha t}}-\mu\sqrt{\alpha t}\right)$$

$$+\exp(-\mu x)[\exp(\mu^2\alpha t)-1]\Bigg\} \tag{22}$$

The term in equation (22) multiplied by $(T_\infty - T_o)$ is the solution for a semi-infinite body with uniform initial temperature T_o, *no energy source*, and a convective boundary condition; it accounts for heat loss or gain when T_∞ and T_o are different. Even when $T_o = T_\infty$, there will still be heat loss because the energy deposition is causing the surface temperature to rise. The term in equation (22) multiplied by $I_o\,(1 - R)$ accounts for heat flow due to energy deposition.

The local heat flux can be evaluated by differentiating equation (22) with respect to x and applying Fourier's Law

$$\dot{q}''(x,t)$$

$$=h(T_\infty-T_o)\left[\exp\left(\frac{h^2}{k^2}\alpha t+\frac{hx}{k}\right)\operatorname{erfc}\left(\frac{x}{2\sqrt{\alpha t}}+\frac{h}{k}\sqrt{\alpha t}\right)\right]$$

$$+I_o(1-R)\Bigg\{-\frac{1}{\left(\frac{h}{\mu k}-1\right)}\exp\left(\frac{h^2}{k^2}\alpha t+\frac{hx}{k}\right)\operatorname{erfc}\left(\frac{x}{2\sqrt{\alpha t}}+\frac{h}{k}\sqrt{\alpha t}\right)$$

$$+\frac{1}{2}\left(\frac{\frac{h}{\mu k}+1}{\frac{h}{\mu k}-1}\right)\exp(\mu^2\alpha t+\mu x)\operatorname{erfc}\left(\frac{x}{2\sqrt{\alpha t}}+\mu\sqrt{\alpha t}\right)$$

$$-\frac{1}{2}\exp(\mu^2\alpha t-\mu x)\operatorname{erfc}\left(\frac{x}{2\sqrt{\alpha t}}-\mu\sqrt{\alpha t}\right)$$

$$+\exp(-\mu x)[\exp(\mu^2\alpha t)-1]\Bigg\} \tag{23}$$

If there is external cooling, then the maximum temperature will occur inside the body instead of at the $x=0$ surface. The position of maximum temperature will then be determined by the location where the local heat flux is zero.

There are several dimensionless groups that appear in equation (22). The main interest of this paper is for laser heating applications in which $I_o\,(1 - R)$ is large in comparison to $h(T_\infty - T_o)$. For this case, a convenient group of dimensionless variables is as follows:

$$\tau=\mu^2\alpha t \tag{24}$$

$$\chi=\mu x \tag{25}$$

$$\mathrm{Bi}=\frac{h}{\mu k} \tag{26}$$

$$\omega=\frac{I_o(1-R)}{h(T_\infty-T_o)} \tag{27}$$

Note that when $T_\infty < T_o$, then ω is negative. Cooling can still occur even if ω is positive; however, cooling does not occur until after the surface temperature exceeds T_∞. If $T_\infty = T_o$, then $\omega = \infty$ and it is not a significant dimensionless group.

Utilizing the above dimensionless variables, the temperature profile and heat flux expressions can be written as

$$\frac{T(\chi,\tau)-T_o}{\frac{I_o(1-R)}{k\mu}}$$

$$=\frac{1}{\mu\mathrm{Bi}}\left[\operatorname{erfc}\left(\frac{\chi}{2\sqrt{\tau}}\right)-\exp(\mathrm{Bi}^2\tau+\mathrm{Bi}\chi)\operatorname{erfc}\left(\frac{\chi}{2\sqrt{\tau}}+\mathrm{Bi}\sqrt{\tau}\right)\right]$$

$$+\left(1+\frac{1}{\mathrm{Bi}}\right)\operatorname{erfc}\left(\frac{\chi}{2\sqrt{\tau}}\right)$$

$$+\frac{1}{\mathrm{Bi}(\mathrm{Bi}-1)}\exp(\mathrm{Bi}^2\tau+\mathrm{Bi}\chi)\operatorname{erfc}\left(\frac{\chi}{2\sqrt{\tau}}+\mathrm{Bi}\sqrt{\tau}\right)$$

$$-\frac{1}{2}\left(\frac{\mathrm{Bi}+1}{\mathrm{Bi}-1}\right)\exp(\tau+\chi)\operatorname{erfc}\left(\frac{\chi}{2\sqrt{\tau}}+\sqrt{\tau}\right)$$

$$-\frac{1}{2}\exp(\tau-\chi)\operatorname{erfc}\left(\frac{\chi}{2\sqrt{\tau}}-\sqrt{\tau}\right)+\exp(-\chi)[\exp(\tau)-1] \tag{28}$$

and

$$\frac{\dot{q}''(\chi,\tau)}{I_o(1-R)}$$

$$=\frac{1}{\omega}\left[\exp(\mathrm{Bi}^2\tau+\mathrm{Bi}\chi)\operatorname{erfc}\left(\frac{\chi}{2\sqrt{\tau}}+\mathrm{Bi}\sqrt{\tau}\right)\right]$$

$$-\frac{1}{(\mathrm{Bi}-1)}\exp(\mathrm{Bi}^2\tau+\mathrm{Bi}\chi)\operatorname{erfc}\left(\frac{\chi}{2\sqrt{\tau}}+\mathrm{Bi}\sqrt{\tau}\right)$$

$$+\frac{1}{2}\left(\frac{\mathrm{Bi}+1}{\mathrm{Bi}-1}\right)\exp(\tau+\chi)\operatorname{erfc}\left(\frac{\chi}{2\sqrt{\tau}}+\sqrt{\tau}\right)$$

$$-\frac{1}{2}\exp(\tau-\chi)\operatorname{erfc}\left(\frac{\chi}{2\sqrt{\tau}}-\sqrt{\tau}\right)+\exp(-\chi)[\exp(\tau)-1] \tag{29}$$

The dimensionless wall temperature can be determined by evaluating equation (28) at $\chi = 0$

$$\frac{T_w-T_o}{\frac{I_o(1-R)}{k\mu}}=\frac{1}{\omega\mathrm{Bi}}[1-\exp(\mathrm{Bi}^2\tau)\operatorname{erfc}(\mathrm{Bi}\sqrt{\tau})]+\frac{1}{\mathrm{Bi}}$$

$$+\frac{1}{\mathrm{Bi}(\mathrm{Bi}-1)}\exp(\mathrm{Bi}^2\tau)\operatorname{erfc}(\mathrm{Bi}\sqrt{\tau})$$

$$-\frac{1}{2}\left(\frac{\mathrm{Bi}+1}{\mathrm{Bi}-1}\right)\exp(\tau)\operatorname{erfc}(\sqrt{\tau})+\frac{1}{2}\exp(\tau)\operatorname{erfc}\sqrt{\tau} \tag{30}$$

If $\omega = \infty$, corresponding to $T_\infty = T_o$, then the first term on the right-hand side of the equality sign in equations (28)–(30) will be zero.

If αt is sufficiently small that diffusion effects are not important, then the last term in equation (22) becomes dominant and the temperature response can be approximated by

$$T-T_o\approx\frac{I_o(1-R)\mu}{\rho C_p}\exp(-\mu x)t, \qquad \alpha t\ll 1 \tag{31}$$

where x must be sufficiently large that the presence of the

boundary condition at $x=0$ is not felt. This result is a simple statement of conservation of energy for small αt: All the energy deposited locally goes to increasing the internal energy of the solid because diffusion does not have time to take place.

A small time solution for the surface temperature can be developed from the small argument expansions for the functions exp and erfc. It can be shown that

$$\exp(z^2)\operatorname{erfc}(z) = 1 - \frac{2}{\sqrt{\pi}}z + z^2 - \frac{4}{3\sqrt{\pi}}z^3 + O(z^4) \qquad (32)$$

For $z<0.36$, the above result has a relative error less than 1 percent. The surface temperature can then be approximated by

$$\frac{T_w - T_o}{\frac{I_o(1-R)}{k\mu}} = \frac{1}{\omega}\left[\frac{2}{\sqrt{\pi}}\sqrt{\tau} - \mathrm{Bi}\tau + \frac{4}{3\sqrt{\pi}}\mathrm{Bi}^2\tau^{3/2} - \frac{\mathrm{Bi}^3}{2}\tau^2 + O(\tau^{5/2})\right]$$

$$+\tau - \frac{4}{3\sqrt{\pi}}(\mathrm{Bi}+1)\tau^{3/2} + \frac{1}{2}(\mathrm{Bi}^2+\mathrm{Bi}+1)\tau^2 + O(\tau^{5/2}) \qquad (33)$$

3 Numerical Results

This section will present numerical results in an attempt to develop an understanding of how the convective cooling and energy deposition interact. Figure 1 presents the dimensionless temperature profile for a range of dimensionless times τ and a series of dimensionless cooling parameters (Bi), all for $\omega = -10^4$. The parameter ω is the ratio of the laser energy available for absorption by the body to the convective cooling at time zero; the negative sign indicates that $T_\infty < T_o$. For Bi = 0.05, the external cooling is sufficiently small that the temperature profile resembles that for an insulated boundary condition. As either Bi or τ are increased, the effects of the convective cooling become more pronounced causing the location of the peak temperature to move away from $x = 0$. For Bi = 5.0 and $\tau = 0.01$, the exposed surface temperature is considerably below the maximum temperature.

Figure 2 presents the temperature history for several depths, various ω, and Bi = 0.5. When ω becomes sufficiently large negative, the impact of the convective cooling on the surface temperature becomes less pronounced. When the depth below the surface becomes sufficiently large, the temperature history is approximately independent of the convective cooling; in essence, the effect of the convective boundary condition has not had time to diffuse in-depth. For sufficiently large depths

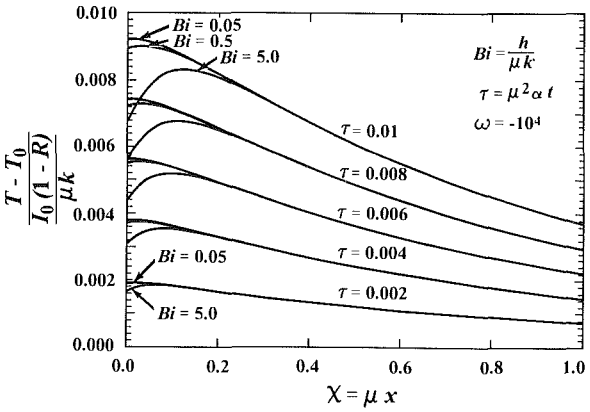

Fig. 1 Dimensionless temperature profile as a function of χ for various Bi and τ

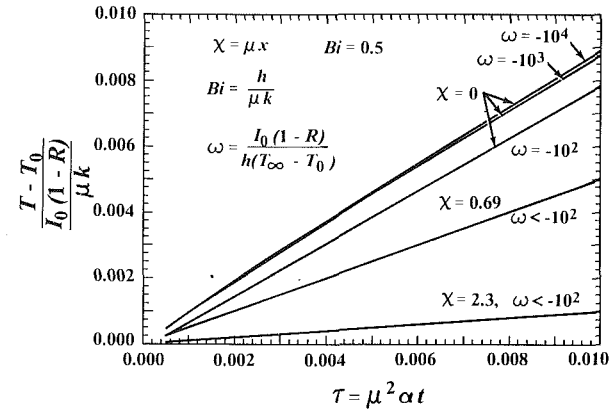

Fig. 2 Dimensionless temperature as a function of dimensionless time for various depths, ω, and for Bi = 0.5

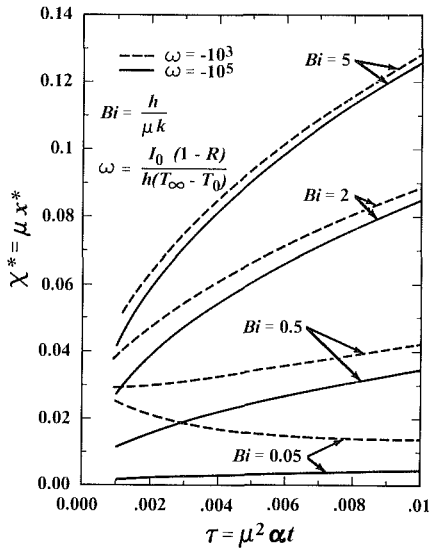

Fig. 3 Dimensionless depth at which maximum temperature occurs as a function of dimensionless time for various values of ω and Bi

below the surface, the temperature history is linear with time; for this condition, equation (31) is applicable. The surface temperature does not vary linearly with time even for small αt; see equation (33).

The depth at which a temperature maximum occurs is determined from equation (29) by setting the heat flux equal to zero. This dimensionless depth χ^* is presented in Fig. 3 as a function of dimensionless time τ for various values of the parameters ω and Bi. Increasing τ increases χ^* except for the case of small Bi and small negative values of ω, a physically uninteresting combination of parameters for this study. As $|\omega|$ increases, χ^* decreases for a given dimensionless time τ because energy is being deposited at a rate much faster than it is removed by convective cooling. For a given τ, χ^* is more sensitive to changes in Bi than changes in ω.

Figure 4 presents the dimensionless depth for the temperature maximum as a function of Bi for various values of dimensionless time τ. For Bi < 1, χ^* is approximately linear in Bi for all other parameters fixed and $\omega = -10^5$; for Bi > 1, χ^* increases more slowly than linear. This suggests a practical limit beyond which increases in Bi become insignificant. A systems analysis comparing incremental cost of cooling with increased penetration rate would be necessary to answer this question.

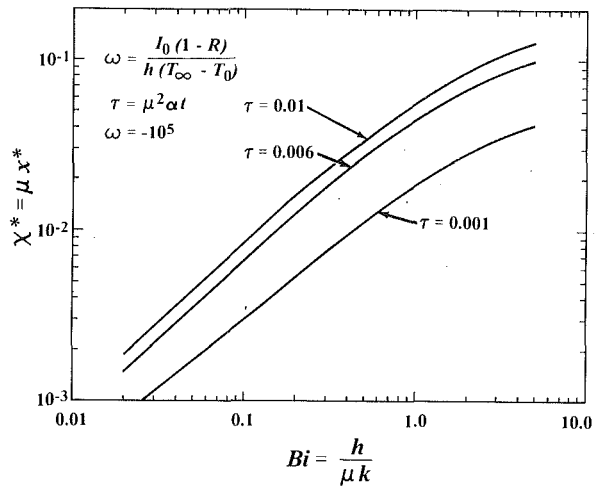

Fig. 4 Dimensionless depth at which maximum temperature occurs as a function of Bi for various dimensionless times and $\omega = -10^5$

4 Summary

Equations have been developed for the temperature response and the local heat flux for a semi-infinite body with an exponentially decaying (with position) source and convective cooling at the surface. An appropriate set of dimensionless parameters was defined. The maximum temperature occurs at an interior point and its location relative to the exposed surface increases with increased dimensionless convective cooling (Bi) and time (τ). This temperature maximum within the material (as opposed to at the exposed surface) is a possible explanation for explosive removal of material subjected to an intense laser.

Although the analysis reported here was for convective cooling of the exposed surface, radiation heat losses will be important for most materials when the surface temperature approaches realistic phase change temperatures. For applications in which radiation losses and an ablating boundary condition are important, a numerical model will be necessary. The SODDIT computer code (Blackwell, 1987) is one example of a code capable of solving moving boundary problems with exponential sources, radiation boundary conditions, and temperature-dependent thermal properties.

Acknowledgments

This work was performed at Sandia National Laboratories and supported by the US Department of Energy under Contract No. DE-AC04-76DP00789.

References

Blackwell, B. F., Douglass, R. W., and Wolf, H., 1987, "A User's Manual for the Sandia One-Dimensional Direct and Inverse Thermal (SODDIT) Code," SAND 85-2478, Sandia National Laboratories.

Carslaw, H. S., and Jaeger, J. C., 1959, *Conduction of Heat in Solids*, 2nd ed., Oxford, New York.

Dabby, F. W., and Paek, U., 1972, "High-Intensity Induced Laser Vaporization and Explosion of Solid Material," *IEEE Journal of Quantum Electronics*, Vol. QE-8, No. 2, pp. 106–111.

Ready, J. F., 1978, *Industrial Applications of Lasers*, Academic Press, New York.

P. Luchini

M. Lupo

A. Pozzi

Istituto di Gasdinamica,
University of Naples,
Naples, Italy

The Effects of Wall Thermal Resistance on Forced Convection Around Two-Dimensional Bodies

The influence of wall thermal resistance on stagnation and supersonic wedge flow is studied in this paper. The equation of heat conduction inside the wall is transformed by a suitable approximation into boundary conditions for the equations of heat transfer in the fluid, which are then solved for several situations. The method of solution is based on series expansions, the convergence of which is improved through the Padé approximation technique. The results, exact for all purposes in the entire field, are discussed in terms of the interface temperature and Nusselt number.

1 Introduction

In order to study the influence on the fluid flow of the bulk thermal resistance of a body surrounded by a fluid stream, one must deal with the coupling between the thermo-fluid-dynamic field in the fluid and the thermal field in the solid. An interesting analysis of this problem for the flat-plate case is given by Luikov (1974), but the results of that analysis are not easily applicable in practice. To simplify the problem some authors neglect axial thermal conduction; the flow along a flat plate was studied in this way, either in the case of free convection (Timm and Padet, 1985; Pozzi and Lupo, 1988a) or in the case of forced convection (Gosse, 1980; Pozzi and Lupo, 1988b), by assuming as thermal boundary condition at the fluid–solid interface one of proportionality between temperature and its normal derivative. External flows around geometries different from the flat plate do not seem to have been studied in this respect. These other geometries entail different thermal boundary conditions at the fluid–solid interface, thus giving a new mathematical and physical character to the problem.

In this paper we study the influence on the fluid flow of the bulk thermal resistance of two-dimensional sharp or blunt bodies, considering the canonical problems of stagnation flow and supersonic wedge flow in several situations, assuming isothermal and adiabatic conditions on the lower side of a strip (stagnation flow) and isothermal and adiabatic conditions on the axis of a wedge. The solution procedure is based on the extension of the method introduced by two of the present authors for the flat-plate case (Pozzi and Lupo, 1988a, 1988b), which makes use of two expansions, an initial and an asymptotic one, and of the Padé approximation technique to extend the range of convergence of these expansions. Each situation has required a different application of the method because of the different character, parabolic or elliptic, given to the equation system by the boundary conditions, which in some cases allows a similarity solution and in others does not.

2 Previous Work

In a previous paper (Pozzi and Lupo, 1988b) we studied the coupling of conduction with forced convection in flow over a constant-thickness flat plate with one side held at constant temperature, neglecting lengthwise conduction. The Padé technique of continuation of series was found in that occasion to be very effective, transforming a divergent series in a succession of rational functions, which, already for a number of terms of the order of 15, stabilized to the point that no further oscillation was recognizable within graphic accuracy, meaning that the solution of the model equations had been obtained with an accuracy certainly better than 1 percent. A comparison was made with the results of Luikov et al. (1971), as reported in Fig. 1, and Gosse (1980), Fig. 2. Let us emphasize that any discrepancy appearing in these plots can only be ascribed to differences between the models chosen by those authors and our models, because our solution of the model equations was accurate to better than 1 percent.

In this paper we analyze a number of situations of coupled heat transfer in a fluid and the adjacent solid wall that are of interest in supersonic and hypersonic flight, where care must be taken to dissipate the heat generated by friction and compression of the gas and transferred to the walls of the aircraft. A part of the analysis is based on a generalization of the previous solution to boundary-layer flow over a wedge, behind the leading shock wave, considering, however, different boundary conditions with respect to conduction in the solid. We shall study two subcases, quite different from each other: a solid wedge refrigerated, and thus held at constant temper-

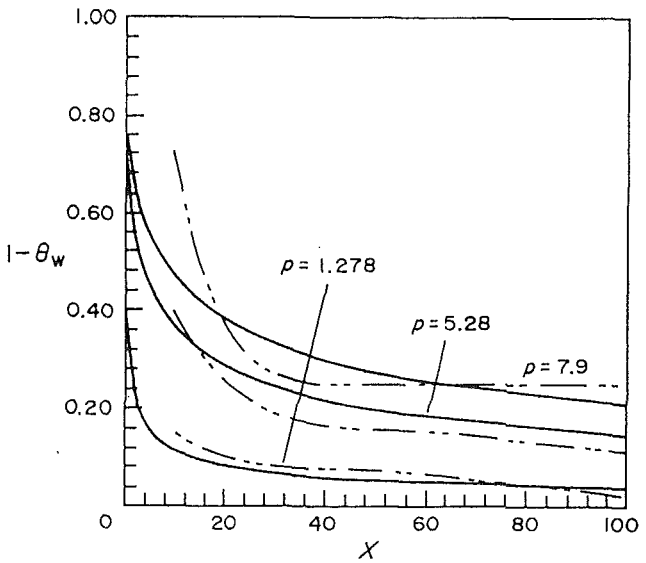

Fig. 1 Comparison between wall temperature profiles obtained for incompressible flow along a flat plate by the present authors (Pozzi and Lupo, 1988b, solid line) and those of Luikov et al. (1971, broken line). x, ϑ_w: dimensionless axial coordinate and wall temperature: p: coupling parameter = $\lambda_0 Re^{1/2}/\lambda_{s0}$.

Contributed by the Heat Transfer Division for publication in the JOURNAL OF HEAT TRANSFER. Manuscript received by the Heat Transfer Division March 6, 1989; revision received November 15, 1989. Keywords: Conjugate Heat Transfer, Forced Convection.

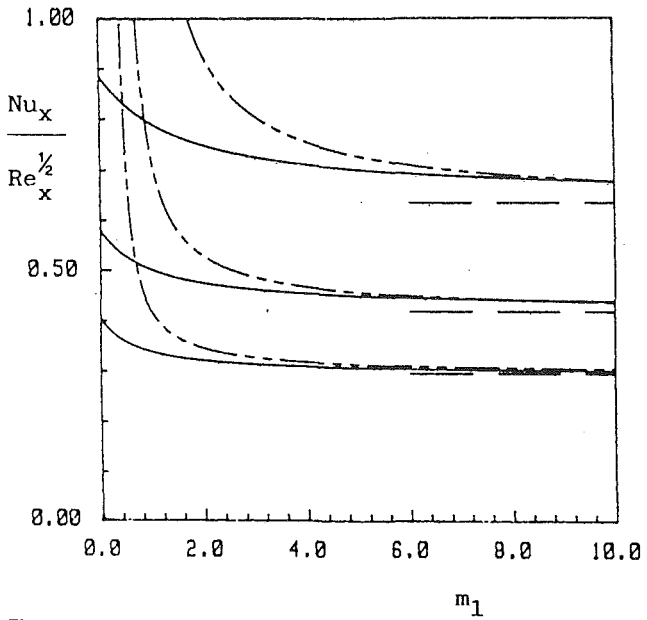

Fig. 2 Comparison between wall temperature profiles for incompressible flow along a flat plate found by the present authors (Pozzi and Lupo, 1988b, solid line) and by Gosse (1980, broken line); symbols as in Fig. 1

ature, on its axis, and a nonrefrigerated wedge, where heat is removed by axial conduction only. This case differs from the previous flat-plate analysis for the presence of heat generation within the fluid and the different thermal constraints imposed on the solid. Whereas the fluid-dynamic field in this first part does not differ from the one considered by Pozzi and Lupo (1988b), and only the thermal field is different, in the second part we shall consider a different kind of flow: flow in the proximity of a stagnation point, assuming that the wall, locally modeled as plane, is of constant thickness. Again we will study the two subcases where heat is either absorbed by a refrigerator placed on the opposite side, thus making it isothermal, or conducted away along the plate. In this case, in addition to the different situations assumed in the solid, the fluid-dynamic field is completely different from that existing beside a flat plate surrounded by a uniform stream.

Summarizing, we shall consider four cases: a constant-width slab, hit upon normally by the stream on one side and held in either isothermal or adiabatic conditions on the opposite side, and a solid wedge, surrounded by a supersonic stream that forms a shock wave at its edge and held in either isothermal or adiabatic (symmetric) conditions on its axis. These four cases are characterized each by a peculiar thermal field, with properties and functional forms very different from one another and from the cases considered in the past.

The analysis performed will allow us to evaluate the dependence of wall temperature on the thickness of the slab (both in the case of isothermal and adiabatic conditions on the far side of the slab) and on the angle of the wedge (both in the case of symmetric conditions when the wedge axis is adiabatic and in the case of refrigeration when the wedge axis is at constant temperature). Each case is characterized by nontrivial interactions between the physical parameters determining the problem and requires a description not only quantitatively but qualitatively different from the others.

3 Temperature in the Solid

The temperature in the solid is governed by the Laplace equation

$$\Delta_2 T = 0 \tag{1}$$

We shall denote quantities calculated at the fluid–solid interface by the subscript w.

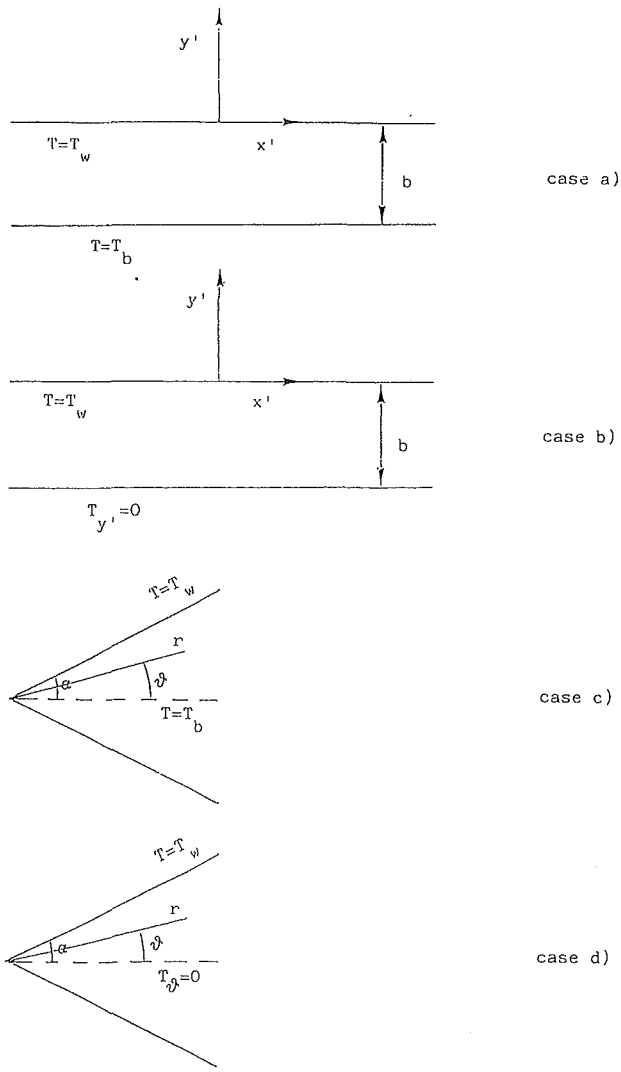

Fig. 3 Flow cases: (*a*) strip with isothermal condition on the lower side; (*b*) strip with adiabatic condition on the lower side; (*c*) wedge with isothermal condition on the axis; (*d*) wedge with adiabatic condition on the axis

When the geometry of the body is elongated, in the sense that its transverse dimension is small compared to the longitudinal one, it is possible to express heat flux at the interface in terms of T_w and its axial derivatives, as we shall do in several situations.

Let us study equation (1) in a strip of height b with two types of boundary conditions (see Fig. 3): $T = T_w(x')$ on the upper side and $T = T_b = \text{const}$ on the lower side, case (a); $T = T_w(x')$ on the upper side and $T_{y'} = 0$ on the lower side, case (b). x' and y' denote dimensional coordinates. In case (a), if L is a characteristic length in the x' direction, it is convenient to introduce the dimensionless coordinates $X = x'/L$ and $Y = y'/b$. Equation (1) may then be written as

$$T_{YY} = -(b/L)^2 T_{XX} \tag{2}$$

and the temperature may be expanded in a MacLaurin series in powers of the parameter $(b/L)^2$, if it is assumed that such a parameter is much less than 1. The leading term T^o of this expansion, governed by the equation $T^o_{YY} = 0$, is given by

$$T^o = T_w + (T_w - T_b) y'/b \tag{3}$$

Then

$$T^o_{y',w} = (T_w - T_b)/b \tag{4}$$

which is the condition already adopted by Pozzi and Lupo

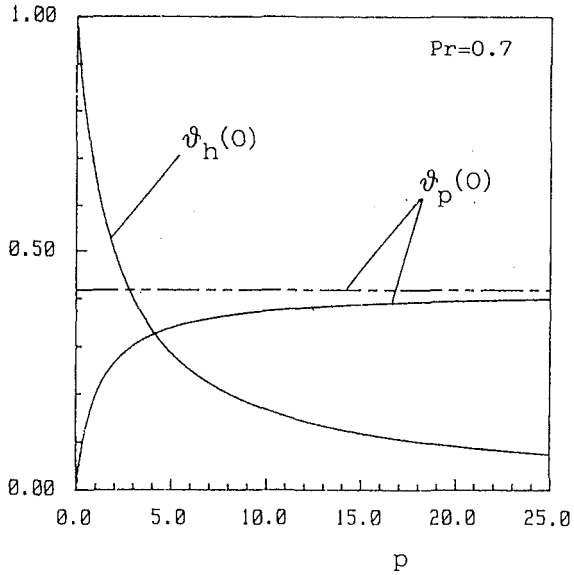

Fig. 4 Stagnation flow with isothermal condition on the lower side of the slab; constants necessary for calculation of the wall temperature, as $\vartheta_w = \vartheta_h(0) + (\gamma-1)M_\delta^2 x^2 \vartheta_p(0)$, versus coupling parameter p of equation (16)

(1988a, 1988b, 1990) in studying flow along a streamwise flat plate.

Also in case (*b*) $T_{y'}$ may be expanded in a Taylor series in terms of y'. Taking equation (1) into account one has, for the leading term,

$$T_{y',w} = -T_{x'x',w}b \tag{5}$$

which is the boundary condition to be used for the heat transfer equation in this case.

Let us now study equation (1), in polar coordinates, in a wedge of half-angle α with two types of boundary conditions (Fig. 4): $T(\alpha, r) = T_w(r)$ and $T(0, r) = T_b$ = const, case (*c*); $T(\alpha, r) = T_w(r)$ and $T_\vartheta(0, r) = 0$, case (*d*). Equation (1) in polar coordinates becomes

$$T_{\vartheta\vartheta} + r(rT_r)_r = 0 \tag{6}$$

The role of the parameter b/L is played in this case by the angle α. An analysis similar to that of case (*a*), valid for small values of α^2, leads in case (*c*) to the following temperature distribution in the solid, at leading order:

$$T = T_b + (T_w - T_b)\vartheta/\alpha \tag{7}$$

and hence one has

$$T_{n,w} = r^{-1}T_{\vartheta,w} = (T_w - T_b)/\alpha r \tag{8}$$

For case (*d*) one finds

$$T_{n,w} = r^{-1}T_{\vartheta,w} = -\alpha(rT_r)_{r,w} \tag{9}$$

These two conditions are different from equations (4) and (5), the first simply because the varying height of the wedge is taken into account, the second more profoundly.

4 Equations and Boundary Conditions for the Thermo-fluid-dynamic Field

The equations governing the thermo-fluid-dynamic field are the compressible boundary-layer equations. In the case of a perfect gas it is convenient to introduce the Stewartson–Dorodnitzin transformation (Schlichting, 1968) so that, if one assumes that $\mu\rho$ and $\lambda\rho$ are constants, these equations may be written in a simpler form. In particular, for supersonic wedge flow (constant external velocity) and for stagnation flow at small values of the abscissa x, the boundary layer equations can be reduced to the following dimensionless incompressible form (Pozzi and Lupo, 1988b, 1988c):

$$u_x + v_y = 0 \tag{10}$$

$$uu_x + vu_y = u_{yy} \tag{11}$$

$$u\vartheta_x + v\vartheta_y = \vartheta_{yy}/\mathrm{Pr} + (\gamma-1)M_o^2 u_y^2 \tag{12}$$

where u and y are the velocity components along the x and y Cartesian axes, $\vartheta = (T - T_e)/T_o$ is the dimensionless temperature and γ is the specific heat ratio. The subscript e denotes external quantities. The reference quantities are L, $L\mathrm{Re}^{-1/2}$, V_o, $V_o\mathrm{Re}^{-1/2}$, ρ_0, μ_0, and λ_0 for x, y, u, v, ρ, μ, and λ, respectively. Re and Pr are the Reynolds and Prandtl numbers and M_o is the Mach number referred to the temperature T_o. L is a characteristic length in the direction of the x axis and V_o, ρ_o, μ_o, and λ_o are the characteristic velocity, density, viscosity, and thermal conductivity of the flow.

The characteristic temperature T_o is equal to $(T_b - T_e)$ in cases (*a*) and (*c*), and is equal to the stagnation temperature in cases (*b*) and (*d*).

The boundary conditions associated with equations (10)–(12) are

$$u(x, 0) = v(x, 0) = 0 \tag{13}$$

$$u(x, \infty) = u_e/V_o; \quad \vartheta(x, \infty) = 0 \tag{14}$$

where u_e/V_o equals x for stagnation flow and 1 for supersonic wedge flow. Moreover, the coupling of the thermal field of the fluid with that of the solid requires the continuity of temperature and of heat flux at the solid–fluid interface. In dimensional form the heat-flux coupling condition may be written as

$$\lambda T_{y,w} = \lambda_{so} T_{so,n} \tag{15}$$

where λ_{so} is the thermal-conductivity coefficient of the solid and $T_{so,n}$ is the normal derivative at the wall of the temperature of the solid, which was given in the previous section in terms of the wall temperature and its derivatives.

Equations (10) and (11) may be solved independently of the energy equation (12) and the stream function ψ is obtained in similarity form (Schlichting, 1968).

The boundary conditions associated with the energy equation are $\vartheta(x, \infty) = 0$ and the coupling condition (15); this second condition, which can destroy the similarity, may be written in dimensionless form, in terms of orthogonal Cartesian coordinates whose x axis lies along the wall, as follows:

Case (a)

$$p\vartheta_{y,w} = \vartheta_w - 1; \qquad p = \mathrm{Re}^{1/2} b\lambda_o/L\lambda_{so} \tag{16}$$

Case (b)

$$p\vartheta_{y,w} = -\vartheta_{xx,w}; \qquad p = \mathrm{Re}^{1/2} L\lambda_o/b\lambda_{so} \tag{17}$$

Case (c)

$$p\vartheta_{y,w} = (\vartheta_w - 1)/x; \qquad p = \mathrm{Re}^{1/2}\alpha\lambda_o/\lambda_{so} \tag{18}$$

Case (d)

$$p\vartheta_{y,w} = -(x\vartheta_x)_{x,w}; \qquad p = \mathrm{Re}^{1/2}\lambda_o/\alpha\lambda_{so} \tag{19}$$

where p may be called the coupling parameter.

5 Method of Solution

The similarity solution for the stream function ψ such that $u = \psi_y$ and $v = -\psi_x$ has the form $\psi = x^{\delta+1/2} f(z)$, where $z = yx^{\delta-1/2}$ ($\delta = 1/2$ for stagnation flow and $\delta = 0$ for a wedge in a supersonic stream). In terms of f equation (12) becomes

$$x\vartheta_x f' - (\delta + 1/2) f\vartheta_z = \vartheta_{zz}/\mathrm{Pr} + (\gamma-1)M_0^2 x^{4\delta} f''^2 \tag{20}$$

$f(z)$ is the solution of the differential equation

$$f''' + (\delta + 1/2)ff'' + (4\delta/(1+2\delta))(1 - f'^2) = 0 \tag{21}$$

with the boundary conditions $f(0) = f'(0) = 0$, $f'(\infty) = 1$.

In terms of the variable z equations (16)–(19) may be written

Case (a)

$$p\vartheta_{z,w} = \vartheta_w - 1 \tag{22}$$

Case (b)

$$p\vartheta_{z,w} = -\vartheta_{xx,w} \tag{23}$$

Case (c)

$$p\vartheta_{z,w} = (\vartheta_w - 1)/x^{1/2} \tag{24}$$

Case (d)

$$p\vartheta_{z,w} = -x^{1/2}(x\vartheta_x)_{x,w} \tag{25}$$

We shall now determine the solutions of equation (20), which is linear, with the thermal boundary conditions at the wall–fluid interface, (22), (23), (24) or (25), by writing ϑ as the sum of ϑ_h, the solution of the homogeneous part of equation (20), and $(\gamma-1)\mathrm{M}_o^2 x^{4\delta}\vartheta_p$, a particular solution of the same equation.

In cases (*b*) and (*c*) it is convenient to solve the problem in terms of the variables z and

$$m_1 = px^{1/2+3\delta} \tag{26}$$

by expressing ϑ_h and ϑ_p by means of the following MacLaurin series in the variable m_1:

$$\vartheta_h = \sum_{i=0}^{\infty} m_1^i \vartheta_{h,i}(z) \tag{27}$$

$$\vartheta_p = \sum_{i=0}^{\infty} m_1^i \vartheta_{p,i}(z) \tag{28}$$

These series may not have an infinite convergence range; in these cases we shall use the Padé approximation technique in order to obtain a representation valid in the entire field. The four cases previously considered will now be analyzed separately and the results obtained for Pr = 0.7 will be presented.

The ordinary-differential-equation boundary value problems arising out of the analysis have been solved numerically by the "shooting" method using a standard fourth-order Runge–Kutta algorithm.

Case (a). In this case ϑ_h and ϑ_p may be obtained in a similarity form in terms of the variable z. In fact setting $\vartheta_h = \vartheta_h(z)$, one obtains from equations (20) and (22)

$$\vartheta_h''/\mathrm{Pr} + f\vartheta_h' = 0 \tag{29}$$

$$\vartheta_h(\infty) = 0; \quad p\vartheta_h'(0) = \vartheta_h(0) - 1 \tag{30}$$

for ϑ_h and

$$\vartheta_p''/\mathrm{Pr} + f''^2 - 2f'\vartheta_p + f\vartheta_p = 0 \tag{31}$$

$$\vartheta_p(\infty) = 0; \quad p\vartheta_p'(0) = \vartheta_p(0) \tag{32}$$

for ϑ_p.

The solution of equation (29) with boundary conditions (30) are given by

$$\vartheta_h(z) = \int_\infty^z \exp\left[-\mathrm{Pr}\int_0^z f dz\right] dz \Bigg/ \left[\int_\infty^0 \exp\left(-\mathrm{Pr}\int_0^z f dz\right) dz - p\right] \tag{33}$$

The curves of $\vartheta_h(0)$ and $\vartheta_p(0)$ versus p are plotted in Fig. 4. In this figure is also reported the value that $\vartheta_p(0)$ attains when $p\to\infty$ (dotted line), obtained with the adiabatic boundary condition at the interface. For $p=0$ the solution is the one corresponding to the isothermal boundary condition at the interface.

Case (b). Case (*b*) requires a procedure that respects the elliptic character of the boundary condition (23). In fact this condition couples the solution valid for small values of x with that valid for high values of x, so that the temperature at the stagnation point $\vartheta(0, 0)$ becomes an unknown. In general a problem of this kind, given its linearity, can be solved by writing ϑ in the following form:

$$\vartheta = C\vartheta_h + (\gamma-1)\mathrm{M}_\delta^2 x^2 \vartheta_p \tag{34}$$

where C is $\vartheta(0, 0)$, whose value should be calculated by requiring that the correct asymptotic behavior be obtained for $x\to\infty$.

To determine ϑ_h and ϑ_p, expressed by equations (27) and (28), we substitute equation (34) into equations (20) and (23), thus obtaining the following equations and boundary conditions.

For the homogeneous part

$$\vartheta_{h,o}''/\mathrm{Pr} + f\vartheta_{h,o}' = 0 \tag{35a}$$

$$\vartheta_{h,o}(\infty) = 0; \quad \vartheta_{h,o}(0) = 1 \tag{35b}$$

for the leading term, and

$$\vartheta_{h,i}''/\mathrm{Pr} - 2i\vartheta_{h,i}f' + f\vartheta_{h,i}' = 0 \tag{36a}$$

$$\vartheta_{h,i}(\infty) = 0; \quad \vartheta_{h,i}(0) = -\vartheta_{h,i-1}'(0)/(4i^2 - 2i) \tag{36b}$$

for $i>0$. For the particular integral

$$\vartheta_{p,o}''/\mathrm{Pr} + f''^2 - 2\vartheta_{p,o}f' + f\vartheta_{p,o}' = 0 \tag{37a}$$

$$\vartheta_{p,o}(\infty) = 0; \quad \vartheta_{p,o}(0) = 0 \tag{37b}$$

for the leading term and

$$\vartheta_{p,i}''/\mathrm{Pr} - 2(1+i)\vartheta_{p,i}f' + f\vartheta_{p,i}' = 0 \tag{38a}$$

$$\vartheta_{p,i}(\infty) = 0; \quad \vartheta_{p,i}(0) = -\vartheta_{p,i-1}'(0)/(2 + 6i + 4i^2) \tag{38b}$$

for $i>0$.

To calculate the constant C we need to determine the asymptotic solution for $x\to\infty$. This solution may be obtained by expanding ϑ_p in an asymptotic series in the variable $m_2 = 1/m_1$ and considering the leading term $h_o(z)$ of this expansion. The equation and the boundary conditions determining $h_o(z)$ are

$$h_o''/\mathrm{Pr} + f''^2 - 2h_o f' + fh_o' = 0 \tag{39a}$$

$$h_o(\infty) = 0; \quad h_o'(0) = 0 \tag{39b}$$

Now the constant C can be determined by matching the solution (34) with the asymptotic solution $(\gamma-1)\mathrm{M}_o^2 x^2 h_o(z)$ calculated, for instance, at $z=0$. One has

$$\frac{C}{(\gamma-1)\mathrm{M}_o^2} = \lim_{x\to\infty} x^2 \frac{\left[h_o(0) - \sum_{i=0}^{\infty} m_1^i \vartheta_{p,i}(0)\right]}{\sum_{i=0}^{\infty} m_1^i \vartheta_{h,i}(0)} \tag{40}$$

So far we have described the general procedure. However, in the particular case of equations (20) and (23), characterized by the appearance of x in integral powers, an exact solution having a polynomial dependence on x turns out to exist. On inserting an expression of the form $\vartheta = \vartheta_o(z) + x^2\vartheta_2(z)$ into equations (20) and (23), it may be verified that these equations are satisfied provided ϑ_o and ϑ_2 obey the equations and boundary conditions

$$\vartheta_{2zz}/\mathrm{Pr} + (\gamma-1)\mathrm{M}_0^2 f''^2 = 2\vartheta_2 f' - f\vartheta_{2zz}; \quad \vartheta_{2z,w} = 0 \tag{41a}$$

$$\vartheta_{ozz}/\mathrm{Pr} = -f\vartheta_{oz}; \quad p\vartheta_{oz,w} = -2\vartheta_{2,w} \tag{41b}$$

The same result would, of course, be recovered if equation (40) were evaluated numerically.

In Fig. 5 $p\vartheta_w/(\gamma-1)\mathrm{M}_o^2$ is plotted versus m_1 together with the function $m_1 h_o(0)$ (dotted curve) up to $m_1 = 50$, whereas in Fig. 6 $h_o(0)$ (dotted line) and $p\vartheta_w/m_1(\gamma-1)\mathrm{M}_o^2$ are plotted

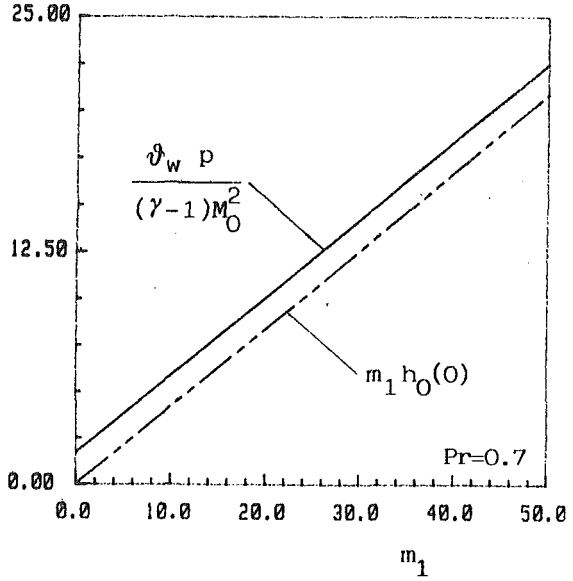

Fig. 5 Stagnation flow with adiabatic condition on the lower side of the slab. Universal plot of wall temperature, rescaled as indicated, versus generalized axial coordinate m_1 of equation (26), in the presence (——) and absence (····) of wall conduction.

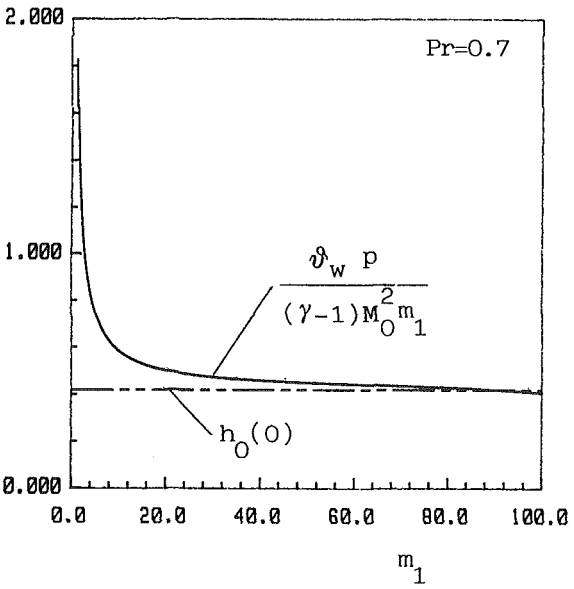

Fig. 6 Stagnation flow with adiabatic condition on the lower side of the slab: same results as in Fig. 5, plotted in a different scaling in which the dimensionless temperature is finite at infinity

versus m_1. These figures enable one to estimate the influence of the thermal resistance of the wall: $h_o(0)$ represents the temperature of the wall when it is adiabatic. For $p \to 0$ the temperature goes to infinity, owing to the elliptic character of the boundary condition (23). In fact, when the thermal resistance is small, the high values of temperature reached at high values of the abscissa strongly influence the values of the temperature all the way back to the stagnation point.

Case (c). In case (*c*) it is possible to follow a unified procedure for the determination of the equations and the boundary conditions for the terms $\vartheta_{h,i}$ and $\vartheta_{p,i}$ of expansions (27) and (28).

In fact, from equations (20) and (24) one obtains

$$\vartheta_o''/\mathrm{Pr} + f\vartheta_o' + \epsilon f''^2 = 0 \tag{42a}$$

$$\vartheta_o(0) = 1 - \epsilon; \quad \vartheta_o(\infty) = 0 \tag{42b}$$

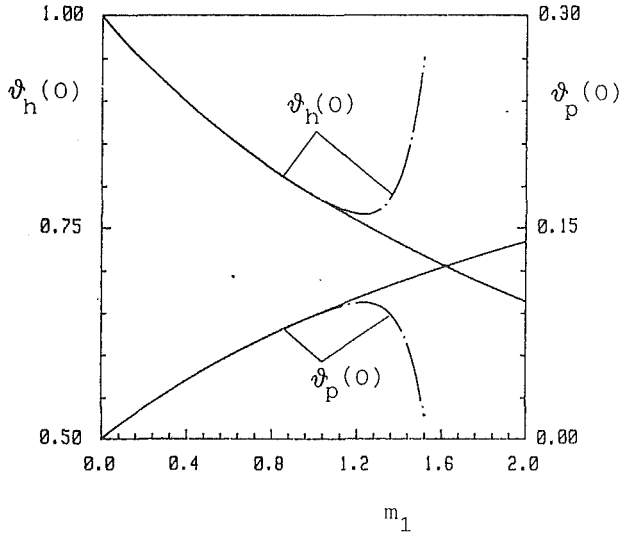

Fig. 7 Wedge flow with isothermal condition on the axis: convergence of Padé approximations (solid lines) and Taylor series (dotted lines)

for the leading term (where $\epsilon = 0$ for $\vartheta_{h,o}$ and $\epsilon = 1$ for $\vartheta_{p,o}$) and

$$\vartheta_i''/\mathrm{Pr} + f\vartheta_i' - if'\vartheta_i = 0 \tag{43a}$$

$$\vartheta_i(0) = \vartheta_{i-1}'(0); \quad \vartheta_i(\infty) = 0 \tag{43b}$$

for $i > 0$.

For the summation of series of this kind the Padé approximation technique has been suggested (Pozzi and Lupo, 1988a, 1988b, 1990). This technique, which consists of replacing a MacLaurin expansion by a sequence of rational functions, allows us to obtain a representation that is valid even when the MacLaurin series does not converge. The comparison between the MacLaurin (dash-and-dot lines) and the Padé (solid lines) representations is shown in Fig. 7 for 14-term expansions. For $0 \le m_1 \le 1$ the two representations coincide because the radius of convergence of the MacLaurin series is 1. For $m_1 > 1$ the MacLaurin curves diverge while the Padé representations still converge.

To verify the validity of the solutions given by Padé representation for ϑ_h and ϑ_p, we have studied the asymptotic behavior of these two functions. As in the previous case, we expand ϑ_h and ϑ_p in terms of the variable $m_2 = 1/m_1$ and consider the zero-order term of these expansions. It can be seen that the asymptotic solution for ϑ_h is identically zero, whereas the one for ϑ_p, denoted by $h_o(z)$, is the solution of the differential equation

$$h_o''/\mathrm{Pr} + fh_o' + f''^2 = 0 \tag{44}$$

with the boundary conditions

$$\vartheta_o'(0) = 0; \quad \vartheta_o(\infty) = 0 \tag{45}$$

The curves of $\vartheta_h(0)$ and $\vartheta_p(0)$, obtained from the Padé technique, and the asymptotic value $h_o(0)$ (dotted line) are plotted versus m_1 in Fig. 8. This figure shows that for $m_1 \to \infty$ ($x \to \infty$), ϑ_h indeed vanishes and ϑ_p tends to the asymptotic solution h_o.

We are now in a condition to draw the curve of ϑ_w and $\mathrm{Nu}/\mathrm{Re}_x^{1/2}$ along the wall. We consider a supersonic stream of Mach number M_1 and temperature T_1 that encounters a wedge aligned with the flow of half-angle $\alpha = 5$ deg. After the shock wake that forms at the front the Mach number and temperature are M_2 and T_2. As the Mach number M_o has been referred to the temperature $T_o = T_b - T_2$, we can write $M_o^2 = M_2^2/\Delta t$ where $\Delta t = (T_b - T_2)/T_2$. Therefore in case (*c*) the dimensionless temperature ϑ may be written as

$$\vartheta = \vartheta_h + ((\gamma - 1)M_2^2/\Delta t)\vartheta_p$$

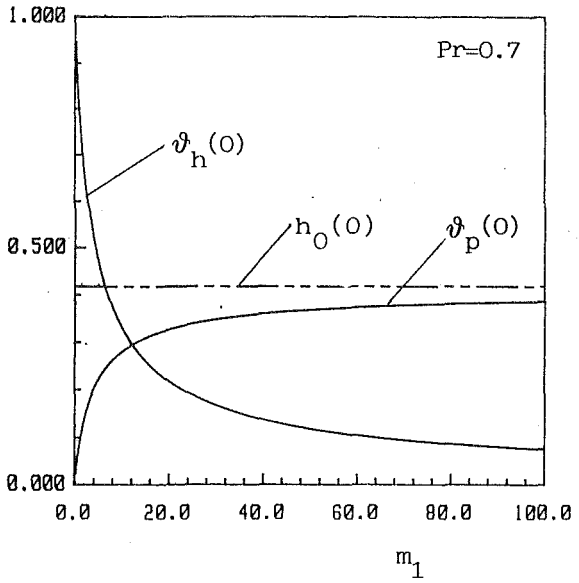

Fig. 8 Wedge flow with isothermal condition on the axis: universal plot of the functions necessary for calculation of the wall temperature as $\vartheta_w(0) = \vartheta_h(0) + (\gamma - 1)M_0^2\vartheta_p(0)$

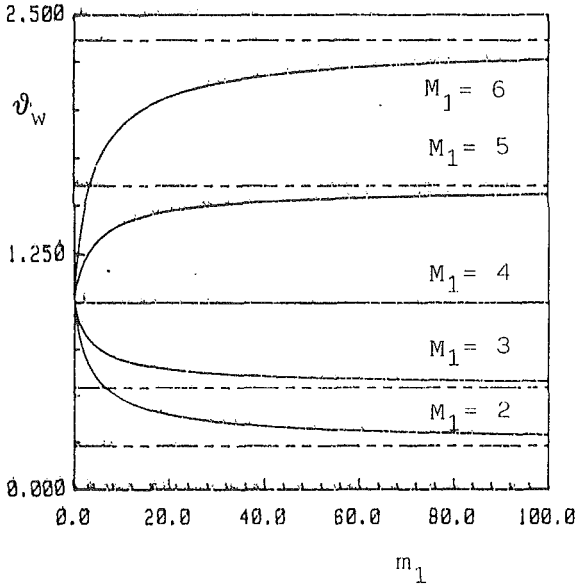

Fig. 9 Variation of wall temperature ϑ_w versus generalized axial coordinate m_1 for wedge flow with isothermal boundary condition at several Mach numbers

The curves of ϑ_w and $\mathrm{Nu}/\mathrm{Re}_x^{1/2}$ are plotted versus m_1 in Figs. 9 and 10, respectively, assuming $T_1 = 270$ K, $T_b = 1000$ K and $M_1 = 2, 3, 4, 5, 6$.

It must be noted, in Fig. 10, that $\mathrm{Nu}/\mathrm{Re}_x^{1/2}$ tends to zero for $m_1 \to \infty$, because the asymptotic solution is the one obtained with the adiabatic condition at the interface. Figure 9 shows how ϑ_w, starting from 1, reaches the adiabatic wall temperature (broken lines) at infinity, which presents the usual dependence on the Mach number. At $M_1 = 4$ the solution coincides both with the asymptotic one and with the one obtained with the isothermal condition at the interface. Under this condition the wedge is at constant temperature.

The dependence on p of the solution has been concealed by the choice of scales in Figs. 9 and 10. Changing p is equivalent to stretching the scale of m_1 in these figures; in particular for $p \to 0$ the solution corresponding to an isothermal boundary condition and for $p \to \infty$ the one corresponding to an adiabatic condition is attained.

Case (d). The solution of this case is trivial. In fact, as ϑ turns out to be a function of the variable z only, because the variable x does not appear explicitly either in the equation or in the boundary condition, the coupling condition (25) is satisfied by simply letting $\vartheta'(0) = 0$. Hence the solution of equation (20) with the boundary condition (25) is the function $\vartheta(z)$ satisfying the following equation and boundary conditions:

$$\vartheta''/\mathrm{Pr} + f\vartheta' + f''^2 = 0$$

$$\vartheta'(0) = 0; \quad \vartheta(\infty) = 0$$

The similarity solution thus obtained is at the same time adiabatic and isothermal at the wall and satisfies equation (25) for any value of p.

Notice that the accidental situation that an adiabatic solution is at the same time isothermal makes this solution valid even when no approximation is made in the treatment of the thermal field in the solid wall, as in this case temperature inside the solid is simply constant.

6 Conclusions

In this paper the coupling between the thermo-fluid-dynamic field in the fluid flowing around a body and the thermal field in the solid body itself has been studied in connection with the

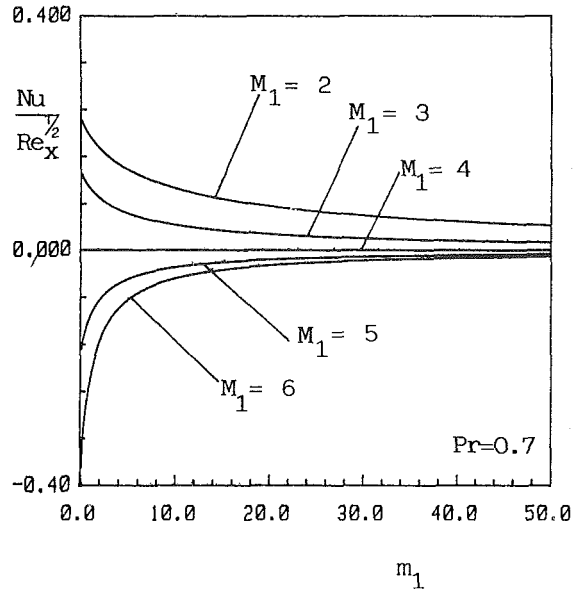

Fig. 10 Variation of local Nusselt number $\mathrm{Nu}/\mathrm{Re}_x^{1/2}$ with m_1 for wedge flow with isothermal boundary condition at several Mach numbers

problems of stagnation flow against a solid slab and supersonic flow along a wedge. Several situations have been considered: (*a*) isothermal condition on the far side of the slab, (*b*) adiabatic condition on the far side of the slab, (*c*) isothermal condition on the axis of the wedge, (*d*) adiabatic (symmetry) condition on the axis of the wedge. In all these cases the heat flux at the wall–fluid interface has been expressed in terms of T_w and its axial derivatives. These four cases encompass a wide range of mathematical and physical behavior.

From a mathematical point of view, these problems are characterized by a mixed boundary condition; in cases (*b*) and (*d*) of a kind that gives an elliptic character to the problem, and must be handled by series expansion. However, for some cases it has nevertheless been possible to obtain a closed-form solution; for the others the technique of Padé summation of series has afforded a solution, which, although calculated on a computer, is so rapidly convergent as to be exact for all practical purposes.

From a physical point of view the isothermal cases, (*a*) and (*c*), are characterized by the linear superposition of the heating (or cooling) generated in the fluid and at the far side of the wall. Each of these is influenced by the thermal coupling between the solid and fluid and contributes to determining the interface temperature. Cases (*b*) and (*d*) are characterized by the redistribution of friction heating allowed by thermal conduction inside the wall, which manifests itself through the existence, in case (*b*), of a nonzero temperature increase right at the stagnation point despite the fact that no friction heat is generated there. (In case (*d*) no redistribution takes place because the wall happens to be already isothermal.)

It is interesting to observe that the finite thermal resistance of the wall is such that the thermal field in the fluid tends to the one corresponding to an isothermal boundary condition when the boundary layer is thin (small coupling parameter p in the stagnation-point case or small x in the supersonic-wedge case) and to the one corresponding to an adiabatic boundary condition in the opposite situation. This observation was the physical basis for the series expansions chosen.

Results have been presented for $\mathrm{Pr} = 0.7$ and the influence of wall thermal resistance on the thermo-fluid-dynamic field has been discussed.

Acknowledgments

This work was financed by Ministero Pubblica Istruzione.

References

Gosse, J., 1980, "Analyse simplifiée du couplage conduction-convection pour un écoulement à couche limite laminaire sur une plaque plane," *Rev. Gén. Therm.*, Vol. 228, pp. 967–971.

Luikov, A. V., 1974, "Conjugate Convective Heat Transfer Problems," *Int. J. Heat Mass Transfer*, Vol. 17, pp. 257–265.

Luikov, A. V., Aleksashenko, V. A., and Aleksashenko, A. V., 1971, "Analytical Methods of Solution of Conjugated Problems in Convective Heat Transfer," *Int. J. Heat Mass Transfer*, Vol. 14, pp. 1047–1056.

Pozzi, A., and Lupo, M., 1988a, "The Coupling of Conduction With Laminar Natural Convection Along a Flat Plate," *Int. J. Heat Mass Transfer*, Vol. 31, pp. 1807–1814.

Pozzi, A., and Lupo, M., 1988b, "The Coupling of Conduction With Forced Convection Along a Flat Plate," *Proc. 6th UIT Nat. Conf.*, Bari, Italy, pp. 3–12.

Pozzi, A., and Lupo, M., 1990, "Variable-Property Effects in Free Convection," *Int. J. Heat Fluid Flow*, in press.

Schlichting, H., 1968, *Boundary Layer Theory*, McGraw-Hill, New York.

Timma, J., and Padet, J. P., 1985, "Etude théorique du couplage convection-conduction en convection libre laminaire sur une plaque vertical," *Int. J. Heat Mass Transfer*, Vol. 28, pp. 1097–1104.

Measurement of the Thermal Contact Conductance and Thermal Conductivity of Anodized Aluminum Coatings

G. P. Peterson
Professor of Mechanical Engineering. Mem. ASME

L. S. Fletcher
Dietz Professor of Mechanical Engineering. Fellow ASME

Department of Mechanical Engineering, Texas A&M University, College Station, TX 77843

An experimental investigation was conducted to determine the thermal contact conductance and effective thermal conductivity of anodized coatings. One chemically polished Aluminum 6061-T6 test specimen and seven specimens with anodized coatings varying in thickness from 60.9 μm to 163.8 μm were tested while in contact with a single unanodized aluminum surface. Measurements of the overall joint conductance, composed of the thermal contact conductance between the anodized coating and the bare aluminum surface and the bulk conductance of the coating material, indicated that the overall joint conductance decreased with increasing thickness of the anodized coating and increased with increasing interfacial load. Using the experimental data, a dimensionless expression was developed that related the overall joint conductance to the coating thickness, the surface roughness, the interfacial pressure, and the properties of the aluminum substrate. By subtracting the thermal contact conductance from the measured overall joint conductance, estimations of the effective thermal conductivity of the anodized coating as a function of pressure were obtained for each of the seven anodized specimens. At an extrapolated pressure of zero, the effective thermal conductivity was found to be approximately 0.02 W/m-K. In addition to this extrapolated value, a single expression for predicting the effective thermal conductivity as a function of both the interface pressure and the anodized coating thickness was developed and shown to be within ±5 percent of the experimental data over a pressure range of 0 to 14 MPa.

Introduction

Many independent parameters influence the contact conductance occurring at metallic interfaces, including the surface roughness, surface waviness, mean slope of the individual roughness asperities, mean temperature of the interface, interfacial contact pressure, loading history, and mechanical and thermophysical properties of the contacting materials (i.e., thermal expansion coefficient, thermal conductivity, the elastic modulus, and the hardness of the material) (Fletcher and Peterson, 1986). In addition to these physical properties and characteristics, the presence of grease, moisture, or oxide layers may also have a singificant effect on the overall joint conductance. In some instances, such as the design and development of thermal control systems for electronic devices where an electrically insulating coating is required, oxide layers may be intentionally applied in the form of an anodized coating.

Anodized coatings are the result of an oxidation process occurring at the surface of a material. The term "anodize" originates from the technique used to produce these layers. In the case of anodizing aluminum, an electric cell is constructed with the aluminum acting as the anode and carbon typically acting as the cathode, both immersed in an electrolytic solution. When an electric current is passed through the cell, the surface of the aluminum is converted to an aluminum oxide coating due to the chemical reaction. This oxide coating is an integral part of the aluminum material and as a result has excellent adherence characteristics.

Although anodized surfaces are in many respects mechanically similar to electroplated or vapor-deposited coatings, one significant difference exists. In electroplating or vapor deposition, the initial coating layer remains in contact with the substrate material, and thicker layers build on each previous layer. In the anodization process, the substrate material is actually converted to the oxide layer. Hence, the initial surface of the substrate is oxidized first and additional anodization proceeds from the outer surface inward. Because the initial coating forms a barrier to the flow of electricity, thicker layers require higher voltages. Presented here is a brief review of previous investigations dealing with the thermal contact conductance of coated surfaces. Also included is a description of an experimental investigation designed to determine the thermal contact conductance and effective thermal conductivity of anodized layers of varying thicknesses applied to Aluminum 6061-T6 surfaces.

Literature Review

Previous investigations of the thermal contact conductance of coatings can be divided into two major categories: metallic coatings and oxide layers. For clarity, the following summary of previous investigations of coated surfaces has been separated into these two categories.

Metallic Coatings. Several experimental and analytical investigations have studied the effect of thin metallic coatings on the thermal contact conductance at the interface of metallic surfaces. Fried and Kelley (1965) compared the measured thermal contact conductance of uncoated stainless steel surfaces in a vacuum in which one of the stainless steel surfaces had been coated with a thin layer of vapor-deposited aluminum. This comparison indicated that the overall joint conductance of uncoated junctions could be enhanced through the use of a coating material that was softer than the substrate.

Contributed by the Heat Transfer Division for publication in the JOURNAL OF HEAT TRANSFER. Manuscript received by the Heat Transfer Division June 12, 1989; revision received September 26, 1989. Keywords: Conduction, Electronic Equipment, Materials Processing and Manufacturing Processes.

Shortly after the completion of this work, Mal'kov and Dobashin (1969) compared the overall joint conductance of two uncoated stainless steel surfaces in which one of the surfaces was coated with silver. These tests, which were also conducted in a vacuum, illustrated a significant increase in the measured conductance values. This increase displayed a decreasing trend with respect to increases in the apparent interface pressure.

In a later investigation, Shah (1978) presented the results of an experimental investigation that compared the overall joint conductance of uncoated bronze surfaces with those obtained when one bronze surface had been coated with a thin layer of a tin/nickel alloy. Again it was observed that coating one surface increased the overall joint conductance significantly; however, the magnitude of this increase was found to decrease with respect to increases in the apparent interface pressure.

The analytical evaluation of the thermal contact conductance of thin metallic layers on metallic surfaces requires the simultaneous solution of three separate problems: the thermal problem in which the questions of constriction resistance and thermal behavior must be addressed; the mechanical problem in which the various physical properties such as surface hardness and elastic modulus must be addressed; and the metrological problem in which the effects of the surface characteristics such as roughness, waviness, flatness, and asperity slope must be addressed (Yovanovich, 1987).

Although not addressing all of these issues, Al-Astrabadi et al. (1980) developed an analytical model for predicting the contact conductance of tin-coated stainless steel interfaces and compared the results with those of their own experimental investigation. The resulting large variations between the predicted and measured values were partially due to the difference in the analytical method that predicted the thermal contact conductance, i.e., the constriction resistance resulting from a reduction in the actual contact area, and the experimental method, which measured the overall joint resistance, i.e., the summation of the thermal contact conductance and the bulk resistance of the metallic coating material. The thermal problem has also been addressed by Kharitonov et al. (1974) and Negus et al. (1985), while the mechanical and metrological issues have been investigated by Hegazy (1985).

Two recent investigations, one by Antonetti (1983) and one by Kang (1989) have addressed all three of these issues: the thermal problem, the mechanical analysis, and the metrological problem. In a combined analytical and experimental investigation, Antonetti (1983) investigated the thermal contact conductance of nickel surfaces coated with thin metallic layers of silver. In the analytical portion, the coated metallic interface was reduced to an equivalent uncoated metal interface by using the concepts of effective hardness, effective thermal conductivity, and an uncoated interface correlation previously developed. The predicted thermal contact conductance values were compared with the results of an experimental investigation in which several nickel surfaces were coated with varying thicknesses of vapor-deposited silver. The contact conductance was shown to increase at a relatively constant rate, approximately twice as large as that observed in the bronze or stainless steel surfaces previously reported. In addition, evidence of an optimum coating thickness was presented and it was proposed that this optimum thickness was dependent on the hardness/conductivity ratio.

The most extensive investigation of different types and thicknesses of metallic coatings was conducted by Kang et al. (1989). This study included an experimental investigation to determine the degree to which the thermal contact conductance at the interface of contacting Aluminum 6061-T6 surfaces could be enhanced through the use of vapor-deposited metallic coatings. Three different coating materials (lead, tin, and, indium) were evaluated using four different thicknesses for each coating material. The results verified the existence of an optimum coating thickness, demonstrated that the percentage increase in the overall joint conductance was strongly pressure dependent, and found that the hardness of the coating material was the most significant parameter in the ranking of the substrate and coating material combinations for the surfaces investigated.

Although these previously described investigations have helped to understand better the physical phenomena occurring at coated interfaces, the results cannot be applied directly to oxide layers because of several significant differences that exist (oxide layers are typically harder than the substrate material and tend to be brittle and uneven).

Oxide Layers. Keller et al. (1953) investigated the structural features of porous anodic oxide coatings applied to aluminum and found that the coatings consisted of closely packed hexagonal-shaped cells of oxide, each of which contains a single pore. The specific characteristics of the oxide were found to be a strong function of the forming voltage and only moderately affected by the electrolyte. Comprehensive reviews of the literature, including the thermal contact conductance behavior of oxide layers, were presented by Gale (1970) for the period through the late 1960s and through the early 1980s by Madhusudana and Fletcher (1986) and Fletcher (1988). A generally accepted conclusion of these reviews was that although oxide films may have a major effect on electrical contact resistance, these coatings do not appreciably decrease the thermal contact conductance unless they are sufficiently thick. Experiments conducted by Tsao and Heimburg (1970) on Aluminum 7075-T5 surfaces in dry air found that very thin oxide films resulted in only small reductions in the thermal contact conductance values, while thicker coatings significantly reduced these values, thereby supporting this conclusion. It was also observed in this investigation that the time of exposure to dry air decreased the thermal contact conductance while degassing of the surfaces increased the thermal contact conductance. In specimens aged in laboratory (humid) air, however, the opposite trend was noted. This anomalous behavior was thought to be due to the decrease of fracture stress of the aluminum oxide layers in the presence of adsorbed gases and moisture.

Mikic and Carnascialli (1970) developed an analytical solution for predicting the thermal behavior of metallic and oxide layers based on the premise that for a fixed geometry any increase in the thermal conductivity in the vicinity of contact

Nomenclature

h_b = conductance of the bulk material
$h_{c,1}$ = conductance between the substrate and the anodized coating
$h_{c,2}$ = conductance between the uncoated aluminum surface and the anodized coating
h_t = overall joint conductance
H_s = hardness of the substrate
k_{eff} = effective thermal conductivity
k_s = thermal conductivity of the substrate material
P = apparent contact pressure
R_b = bulk resistance of the interstitial material
$R_{c,1}$ = resistance at interface 1
$R_{c,2}$ = resistance at interface 2
R_t = total joint resistance
t = thickness
T = temperature
σ = rms surface roughness

points should reduce the value of the resistance. The results indicated that the increase in conductance due to thin layers was directly dependent on t/a and k_p/k, where t was the thickness of the coating material, a was the contact radius, k the conductivity of the substrate, and k_p the conductivity of the coating material.

The theoretical work of Kharitonov et al. (1974, 1976) also considered the effects of both oxide films and coatings of higher conductivity metals and led to the following conclusions:

1 For flat rough surfaces, a coating of a few tens of microns will noticeably reduce the thermal contact resistance.

2 For wavy surfaces the contour radius might have a value of a fraction of a millimeter, and the coating thickness mentioned in point 1 would be ineffective.

3 Since the oxide layers usually have thicknesses of 1 μm and their conductivity is smaller than that of metals by factors of 3 to 30, the conductance depends only weakly on the oxide layer.

Yip (1975) investigated oxide layers on Aluminum 6063-T6 and considered them to behave as Gaussian surfaces of uniform thickness. In this investigation, it was demonstrated that oxide coatings of sufficient thickness could cause drastic reductions in the thermal contact conductance. Experiments on three pairs of Aluminum 6061-T6 surfaces clearly demonstrated that the effect of the oxide film was more pronounced for smoother surfaces.

The resuls of previous investigators were confirmed in the experiments of Mian et al. (1979) on steel-steel (EN3B) surfaces in a vacuum, where it was found that the thickness of the oxide coatings caused a variable decrease in the overall joint conductance.

Ogden et al. (1987) conducted experimental mesurements of the thermal conductivity of thick anodized coatings using a transient measurement technique. They reported bulk conductivity values ranging from 0.61 to 1.00 W/m-K depending on the process used to produce the anodized layer.

Experimental Program

In order to determine the thermal contact conductance and effective thermal conductivity of anodized aluminum coatings in contact with metallic surfaces, an experimental investigation was conducted. One chemically polished Aluminum 6061-T6 test specimen and seven specimens with anodized coatings varying in thickness from 60.9 μm to 163.8 μm were tested while in contact with a single uncoated aluminum surface.

Specimen Preparation. A total of nine test specimens, 8 cm long and 2.54 cm in diameter, were prepared on a lathe from a single piece of Aluminum 6061-T6 bar stock. Once the test specimens had been machined to a smooth finish, three thermocouple holes were drilled (number 56 drill) to the specimen centerline at 1.27-cm intervals. The end face of each specimen was masked and then chemically polished. On seven of the specimens the end faces were anodized to thicknesses varying from 60.9 μm to 163.8 μm. Table 1 lists the coating thicknesses as determined by an eddy current tester. The remaining two specimens were left uncoated.

Once the coating process had been completed, all nine specimens were sent to Sheffield Measurements Laboratory in Dayton, OH, where the surface parameters were measued, for each finished surface, including the rms surface roughness, the average surface roughness (CLA), the rms asperity slope, the average asperity slope, and the flatness deviation. The results of these measurements are shown in Table 2.

Experimental Test Facility. The experimental test facility, shown in Fig. 1, along with the details of the facility construction, operation, and accuracy, have been reported previously by Peterson and Fletcher (1988a) and Kang et al. (1989). The experimental apparatus consisted of a vertical column composed of a guard heater, a heat source, two Aluminum 6061-T6 test specimens, a heat sink, a load cell, and a gas bellows. The two test specimens were arranged so that the anodized end face of one aluminum test specimen was in contact with the uncoated surface of the other. The heat source was a 300-W band heater attached to the lower test fixture at the base of the column. To eliminate axial heat losses in the test fixture, a guard heater was mounted below the heat source. Radial heat losses from the two aluminum test specimens were minimized by placing a radiation shield (made of sheet aluminum and asbestos) around the test column. In addition, a 200-W radiation shield heater was placed around

Table 1 Anodized coating thickness

Test Specimen	(μm)	(mils)
1	-	-
2	60.9	2.4
3	78.7	3.1
4	85.3	3.4
5	118.1	4.6
6	120.6	4.7
7	157.7	6.2
8	163.8	6.4

Table 2 Specimen surface characteristics

Test Specimen	Surface Roughness RMS (μm)	Surface Roughness CLA (μm)	Asperity Slope RMS (μm/μm)	Asperity Slope ARITH (μm/μm)	Flatness Deviation (μm)
0*	4.88	3.94	.19	.14	1.02
1	4.19	3.25	.22	.16	0.76
2	3.61	2.92	.22	.17	0.88
3	3.10	2.46	.20	.16	1.33
4	5.33	4.32	.25	.19	0.89
5	3.68	2.92	.24	.19	0.76
6	4.27	3.56	.24	.18	0.56
7	0.46	0.30	.09	.07	0.25
8	0.30	0.25	.08	.07	0.25

* Common uncoated specimen

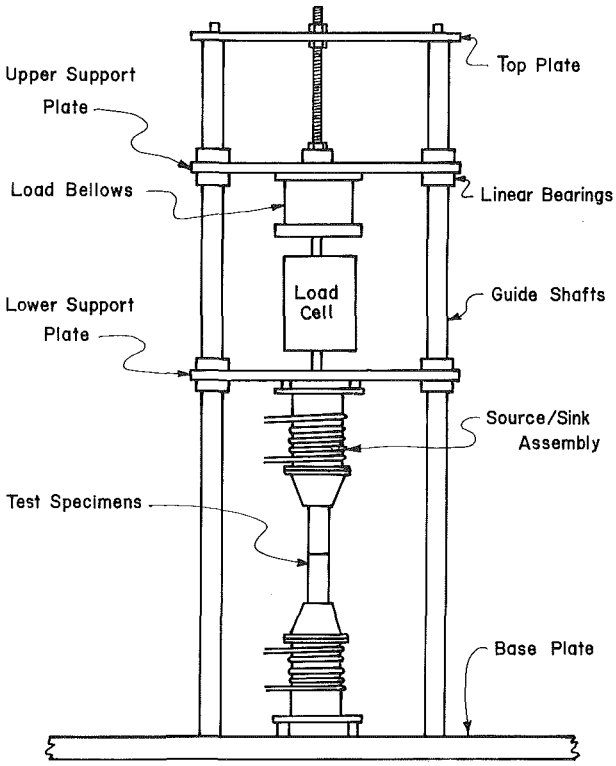

Fig. 1 Experimental test facility

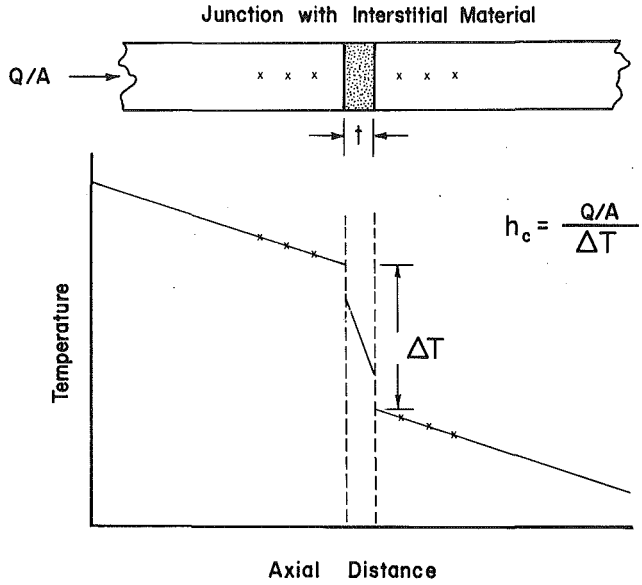

Fig. 2 Thermal contact conductance of interfaces in the presence of interstitial materials

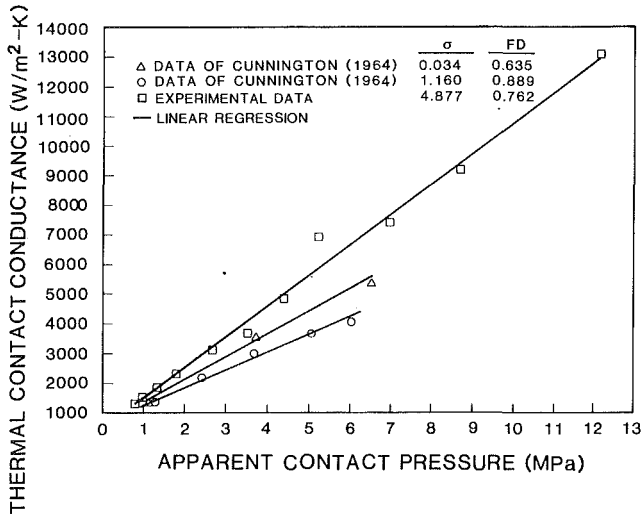

Fig. 3 Measured overall joint conductance as a function of the pressure for the uncoated surfaces in contact

the test specimens, outside of the asbestos shield. This radiation heater was maintained at a temperature equal to the mean interface temperature.

The thermal test facility was operated in a vacuum environment to reduce the effects of any interstitial fluids on the thermal measurements. A vacuum of 5×10^{-5} Torr was maintained using an Alcatel 2300C roughing pump in series with an NRC VHJ-6 oil diffusion pump. A 46×76 cm Pyrex bell jar was used to encase the thermal test facility. Four NRC model 531 thermocouple gages, in conjunction with two Bayard–Alpert ionization gage tubes and controller, were used to monitor the vacuum level.

To determine the thermal contact conductance of the interface and the effect of the anodized coating, a total of eight chromel-alumel thermocouples were used. Six thermocouples, three in each specimen, were located along the centerline of the test specimens. The remaining two thermocouples were located on the outer surface of the test specimens in order to monitor the radial temperature distribution. The thermocouples were packed tightly into the holes using powdered aluminum. Temperatures at the contact surfaces were determined by extrapolating the temperatures along the specimen centerlines, as shown in Fig. 2. The heat flux was calculated using these temperatures, the location of the thermocouples, and the previously measured thermal conductivity of the aluminum test specimens.

The uncertainties associated with these types of measurement also have been presented by Kang et al. (1989) and are composed of the uncertainty in the location of the thermocouple wells, the measurement of the temperature, and the determination of the axial heat flux. In order to determine the heat flux during the tests, it was necessary to know the variation of the thermal conductivity with respect to temperature for the Aluminum 6061-T6 material from which the test specimens were made. For this reason, prior to evaluating the thermal contact conductance, two additional test specimens were machined from the same piece of material as the anodized test specimens. These two additional test specimens were used in conjunction with a standard reference material of known thermal conductivity (NBS Electrolytic Iron) to determine the temperature dependent thermal conductivity. The data resulted in a correlation for the thermal conductivity of the Aluminum 6061-T6 test material of

$$k = 0.226T + 111.94 \quad (1)$$

where k was in W/m-K and T was in degrees Kelvin. Since all test specimens used in this investigation were made of the same bar stock, this thermal conductivity correlation was later utilized with all of the test data. Combining the uncertainty associated with the measurement of the thermal conductivity with other previously mentioned uncertainties resulted in an experimental uncertainty of the thermal contact conductance measurements ranging from ±5 percent at high heat fluxes to ±8 percent at low heat flux levels.

Experimental Procedure. Once the test specimens had been prepared and the surfaces characterized, the test specimens were cleaned with acetone and placed in contact. The resulting test column was installed in the test facility. The fixtures were visually aligned and a slight load was applied to the test column to insure that the surfaces remained in contact during the evacuation of the test chamber. The radiation shields were put in place, the chamber evacuated, and the specimens allowed to out-gas for 4–5 h.

Temperature and pressure test conditions were set by adjusting the heater to the required power and pressurizing the load bellows. Tests were conducted at a mean interface temperature of 25°C±1°C over a pressure range of approximately 0.05 to 12 MPa. Data were taken when the temperature of the test specimens did not vary more than 0.2°C over a 45-min period.

Prior to testing the two chemically polished unanodized surfaces (specimen numbers 0 and 1), the unanodized reference surface (specimen number 0) was preloaded to 15 MPa. Previous tests indicated that this procedure would prevent the deformation resulting from repeated loadings from biasing the results. The two chemically polished surfaces were then tested and used to establish a baseline thermal contact conductance value. Following this, the remaining seven anodized surfaces (specimen numbers 2 through 8) were tested in order of increasing thickness while in contact with the same unanodized reference surface.

Results and Discussion

Figure 3 illustrates the measured overall joint conductance as a function of the apparent contact pressure for the two unanodized surfaces in contact. Also shown in Fig. 3 are the results of an experimental investigation conducted by Cunnington (1968) on Aluminum 6061-T4 surfaces in contact. For comparison the surface characteristics of the tests specimens used are shown on the figure. As predicted by Pinto and Mikic

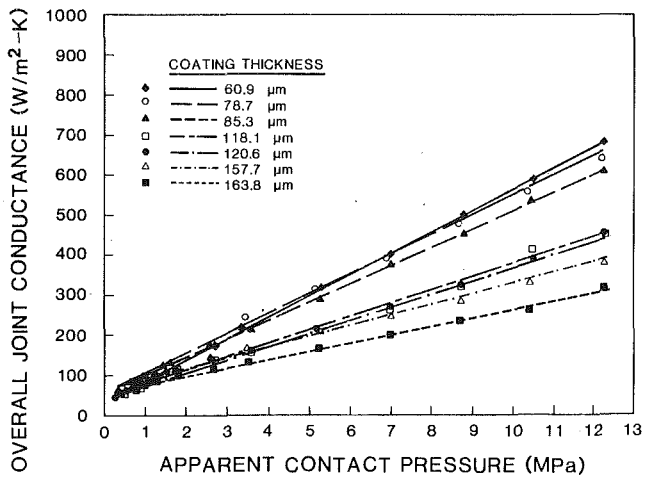

Fig. 4 Measured overall joint conductance as a function of the pressure for the seven coating thicknesses

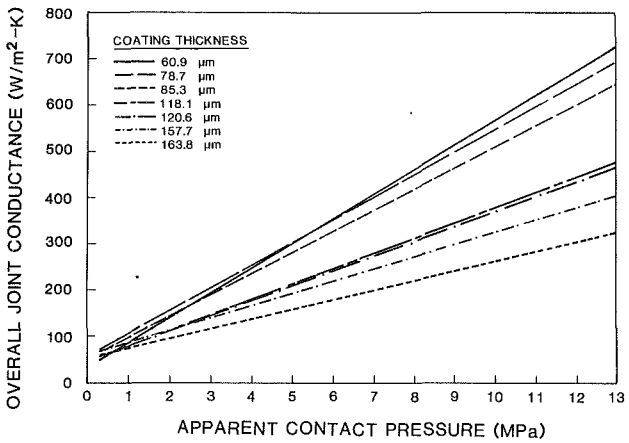

Fig. 5 Overall joint conductance as a function of pressure

(1988) and experimentally verified by Peterson and Fletcher (1988b), this comparison indicates that for very smooth surfaces, slight increases in roughness result in moderate increases in the thermal contact conductance. For all three sets of data, the overall joint conductance increased with increasing pressure.

Figure 4 illustrates the experimental results for the remaining seven anodized surfaces in contact with a common unanodized surface and shows the variation of the measured overall joint conductance, composed of the thermal contact conductance and the bulk conductance of the anodized layer, as a function of the apparent interface pressure. Using a linear regression technique, an equation for the "best fit" straight line through the data was derived for each coated sample. These equations represented a linear approximation of the overall joint conductance as a function of pressure. As in the case for the unanodized specimens, all seven of the anodized test specimens resulted in a thermal joint conductance, which decreased over the entire pressure range as the thickness increased.

By comparing the best-fit straight lines obtained for the thermal contact conductance for each of the seven anodized test specimens, it is apparent that the uncoated joint results provide the highest overall joint conductance and that increasing the thickness of the anodized coating results in a corresponding decrease. The variations in the slope of the lines are due to variations in the effective microhardness of the two surfaces in contact. For very thin anodized layers, the effective microhardness of the interface results from a combination of the uncoated aluminum surface, the relatively hard anodized surface, and the aluminum substrate. As the thickness of the anodized surface increases, the uncoated aluminum asperities do not penetrate the anodized coating and the effective microchardness results only from a combination of the uncoated aluminum surface and the relatively hard anodized surface.

In addition to determining the thermal contact conductance present at the interface of anodized Aluminum 6061-T6 and uncoated Aluminum 6061-T6 surfaces, the thermal conductivity of the anodized coating was estimated. When two surfaces in contact have a thin layer of material between them, as shown in Fig. 2, the overall joint resistance can be expressed as the summation of the two thermal contact resistances and the bulk resistance of the interfacial material

$$R_t = R_{c,1} + R_b + R_{c,2} \tag{2}$$

or in terms of the thermal conductances

$$\frac{1}{h_t} = \frac{1}{h_{c,1}} + \frac{1}{h_b} + \frac{1}{h_{c,2}} \tag{3}$$

For the case of anodized coatings, the thermal contact resistance between the anodized coating and the aluminum surface that is anodized, $h_{c,1}$, is normally considered to be zero due to the molecular bonding that occurs. This yields an expression for the overall joint conductance, which is equal to the summation of the thermal contact conductance and the bulk resistance

$$\frac{1}{h_t} = \frac{1}{h_{c,2}} + \frac{1}{h_b} \tag{4}$$

Recognizing that the bulk conductance can be expressed as a function of the thermal conductivity and the thickness yields

$$\frac{1}{h_t} = \frac{1}{h_{c,2}} + \frac{t}{k_{\text{eff}}} \tag{5}$$

Solving for the effective thermal conductivity of the coating material yields

$$k_{\text{eff}} = \frac{t}{(1/h_t - 1/h_{c,2})} \tag{6}$$

From this expression, it is apparent that if the overall joint conductance can be measured and the thermal contact conductance between the aluminum surface and the anodized surface and thickness are known, the effective thermal conductivity can be estimated.

Using the experimental data from Fig. 4 and the linear regression technique mentioned previously, expressions for the overall joint conductance as a function of thickness were developed. These expressions are compared in Fig. 5. It is important to note that the overall joint conductance illustrated in this figure is the sum of the thermal contact conductance and the bulk conductance of the anodized coating material; hence, the overall joint conductance at a thickness of zero (the Y intercept) represents the thermal contact conductance occurring at the interface of the anodized surface and the uncoated aluminum surface for a given pressure. Increasing the thickness, i.e., moving to the right, would decrease the overall joint conductance due to the added resistance of the anodized material. As expected, the thermal contact conductance values, i.e., the Y intercepts illustrated in Fig. 5, are strongly pressure dependent.

In addition to the individual expressions for the pressure-dependent thermal contact conductance as a function of pressure, a dimensionless correlation that relates dimensionless contact conductance to the dimensionless pressure was developed. This correlation can be expressed as

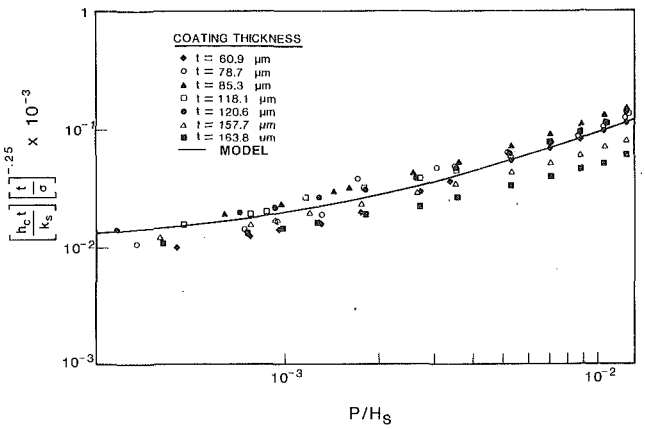

Fig. 6 Dimensionless contact conductance

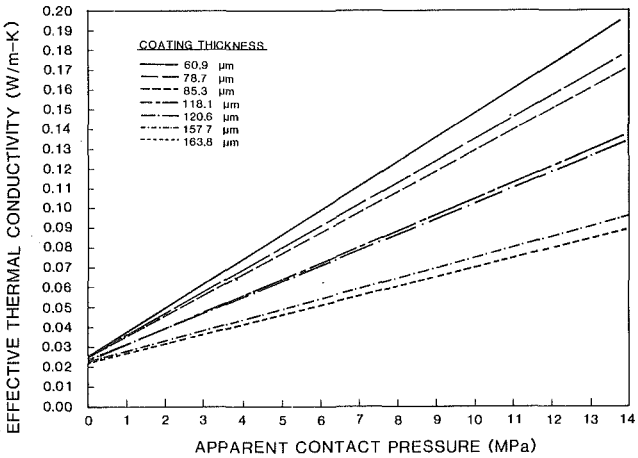

Fig. 7 Effective thermal conductivity as a function of pressure

$$\left(\frac{h_c t}{k_s}\right)\left(\frac{t}{\sigma}\right)^{0.25} = 0.83\times 10^{-2}\left(\frac{P}{H_s}\right) + 0.11\times 10^{-4} \qquad (7)$$

where h_c is in W/m^2-K, t and σ are in μm, k is in W/m-K, and both P and H_s are in Pa. As shown in Fig. 6 this dimensionless correlation predicts the thermal contact conductance for the seven coating thicknesses over a large dimensionless pressure range with a reasonable degree of accuracy.

Determination of the Effective Thermal Conductivity. Using the extrapolated values for the thermal contact conductance occurring at the interface of the anodized surface and the uncoated aluminum surface, the effective thermal conductivity of the anodized coating material can be computed as described in equation (6).

The results of this process are shown in Fig. 7, which illustrates the resulting pressure-dependent effective thermal conductivity. Because of the experimental uncertainties associated with the measured thermal contact conductance values at low pressures, only the data obtained above an apparent contact pressure of 3 MPa were used in this comparison. The uncertainty of these results would be determined by the uncertainty associated with the measurement of the thermal joint conductance discussed previously and the uncertainty associated with the measurement of the coating thickness. Combining these values yields an overall uncertainty in the effective thermal conductivity measurements of ±7 to 11 percent. These values are significantly lower than the results of the bulk thermal conductivity measurements made by Ogden et al. (1987) serving to highlight the importance of including the contact resistance in the computation of overall joint resistance.

Normally one would not expect the effective thermal conductivity to be pressure dependent; but as explained earlier, since the microhardness varies with respect to pressure, the effective thermal conductivity will also be pressure dependent. These pressure-dependent expressions for the effective thermal conductivity are listed in Table 3 for each of the different thicknesses, where P is in MPa.

Although the expressions listed in Table 3 are important, of specific interest here is the relationship between the effective thermal conductivity, and both pressure and thickness. This value can be expressed algebraically as a function of the pressure P and the thickness t as

$$k_{\text{eff}} = 0.62Pt^{-0.94} + 0.0463t^{-0.145} \qquad (8)$$

and can be used to predict the effective thermal conductivity in units of W/m-K for anodized aluminum surfaces given the pressure in MPa and the thickness in μm to within ±5 percent over a pressure range of 0 to 14 MPa.

At an interface pressure of zero, the results of this expression, 0.022 W/m-K, can be compared with the values from Fig. 4 extrapolated to a pressure of zero, 0.025 W/m-K. The similarity between these two values helps to validate the results and illustrates the accuracy of the resulting effective thermal conductivity expression.

Table 3 Computed expressions for the effective thermal conductivity for different thicknesses of anodized coatings

Thickness (μm)	Expression*
60.9	$k_{eff} = 0.0122\ P + 0.0255$
78.7	$k_{eff} = 0.0109\ P + 0.0249$
85.3	$k_{eff} = 0.0104\ P + 0.0247$
118.1	$k_{eff} = 0.0080\ P + 0.0236$
120.6	$k_{eff} = 0.0787\ P + 0.0236$
157.7	$k_{eff} = 0.0052\ P + 0.0223$
163.8	$k_{eff} = 0.0048\ P + 0.0221$

* k_{eff} in W/m-K and P in MPa

Conclusions and Recommendations

An experimental investigation was conducted to determine the thermal contact conductance and effective thermal conductivity of anodized coatings. One chemically polished Aluminum 6061 = T6 test specimen and seven specimens with anodized coatings varying in thickness from 60.9 μm to 163.8 μm were tested while in contact with a single uncoated aluminum surface. Measurements of the overall joint conductance, composed of the thermal contact conductance between the anodized coating and the uncoated aluminum surface and the bulk conductance of the coating material, indicated that the overall joint conductance decreased with increasing thickness of the anodized coating and increased with increasing interfacial load. Using the experimental data, a dimensionless expression was developed that related the overall joint conductance to the coating thickness, the surface roughness, the interfacial pressure, and the properties of the aluminum substrate.

The experimental data obtained in this investigation were used to develop a series of seven expressions, which related the overall thermal joint conductance to the coating thickness and the interfacial pressure. By subtracting the thermal contact conductance from the overall joint conductance, estimations of the effective thermal conductivity as a function of pressure were obtained for each of the seven anodized specimens. At an extrapolated pressure of zero, the effective thermal conductivity was found to be approximately 0.02 W/m-K. In addition

to this extrapolated value, an expression for predicting the effective thermal conductivity as a function of both the interface pressure and the anodized coating thickness was developed. Although the data presented in this investigation are consistent, all tests were conducted on Aluminum 6061-T6. Additional investigations should be conducted to determine whether the information gained can be extended to oxides formed on other alloys.

Acknowledgments

The authors would like to acknowledge the support of the Texas Advanced Technology Program.

References

Al-Astrabadi, F. R., O'Callaghan, P. W., and Probert, S. D., 1980, "Thermal Resistance of Contacts: Influence of Oxide Films," AIAA 15th Thermophysics Conference, Snowmass, CO, July, Paper No. AIAA-80-1467.

Antonetti, V. W., 1983, "On the Use of Metallic Coatings to Enhance Thermal Contact Conductance," Ph.D. Thesis, Mechanical Engineering Department, University of Waterloo, Waterloo, Ontario, Canada.

Cunnington, G. R., Jr., 1968, "Thermal Conductance of Filled Aluminum and Magnesium Joints in a Vacuum Environment," ASME Paper No. 64-WA/HT-40.

Fletcher, L. S., and Peterson, G. P., 1986, "The Effect of Interstitial Materials on the Thermal Contact Conductance of Metallic Junctions," *Proceedings of the Heat Transfer in Thermal Systems Seminar—Phase II*, National Cheng Kung University, Tainan, Taiwan, pp. 1-8.

Fletcher, L. S., 1988, "Recent Developments in Contact Conductance Heat Transfer," ASME JOURNAL OF HEAT TRANSFER, Fiftieth Anniversary Issue, Vol. 110, No. 4(*B*), pp. 864-870.

Fried, E., and Kelley, M. J., 1965, "Thermal Conductance of Metallic Contacts in a Vacuum," AIAA Thermophysics Specialist Conference, Monterey, CA, Sept., Paper No. AIAA-65-661.

Gale, E. H., Jr., 1970, "Effect of Surface Films on Thermal Contact Conductance: Part 1—Microscopic Experiments," ASME Paper No. 70-HT/SpT-26.

Hegazy, A. A., 1985, "Thermal Joint Conductance of Conforming Rough Surfaces: Effects of Surface Microhardness Variations," Ph.D. Thesis, Mechanical Engineering Department, University of Waterloo, Waterloo, Ontario, Canada.

Kang, T. K., 1989, "Enhancing Thermal Contact Conductance Through the Use of Thin Metallic Coatings," M. S. Thesis, Mechanical Engineering Department, Texas A&M University, College Station, TX, Aug.

Kang, T. K., Peterson, G. P., and Fletcher, L. S., 1990, "Enhancing the Thermal Contact Conductance Through the Use of Thin Metallic Coatings," ASME JOURNAL OF HEAT TRANSFER, Vol. 112, in press.

Keller, F., Hunter, M. S., and Robinson, D. L., 1953, "Structural Features of Oxide Coatings on Aluminum," *J. Electrochemical Society*, Vol. 100, No. 9, pp. 411-419.

Kharitonov, V. V., Kokrev, L. S., and Tyurin, Yu. A., 1974, "Effect of Thermal Resistance," *Soviet Atomic Energy*, Vol. 36, Apr., pp. 385-387.

Kharitonov, V. V., Kozhosev, L. S., and Tyurin, Y. A., 1976, "Effect of Thermal Conductivity of Surface Layers on Contact Thermal Resistance," *Atomanya Energiya*, Vol. 36, No. 4, pp. 308-310.

Madhusudana, C. V., and Fletcher, L. S., 1986, "Contact Heat Transfer—The Last Decade," *AIAA Journal*, Vol. 24, No. 3, pp. 510-523.

Mal'kov, V. A., and Dobashin, P. A., 1969, "The Effect of Soft-Metal Coatings and Linings on Contact Thermal Resistance," *Inzhenerno-Fizicheskii Zhurnal*, Vol. 17, No. 5, pp. 871-879.

Mian, M. N., Al-Astrabadi, F. R., O'Callaghan, P. W., and Probert, S. D., 1979, "Thermal Resistance of Pressed Contacts Between Steel Surfaces: Influence of Oxide Films," *Journal of Mechanical Engineering Science*, Vol. 21, pp. 159-166.

Mikic, B., and Carnasciali, G., 1970, "The Effect of Thermal Conductivity of Plating Material on Thermal Contact Resistance," ASME JOURNAL OF HEAT TRANSFER, Vol. 92, No. 3, pp. 475-482.

Negus, K. J., Yovanovich, M. M., and Thompson, J. C., 1985, "Thermal Constriction Resistance of Circular Contacts on Coated Surfaces: Effects of Contact Boundary Conditions," AIAA 20th Thermophysics Conference, Williamsburg, VA, June, Paper No. AIAA-85-1014.

Ogden, T. R., Rathsam, A. D., and Gilchrist, J. T., 1987, "Thermal Conductivity of Thick Anodic Oxide Coatings on Aluminum," *Materials Letters*, Vol. 5, No. 3, pp. 84-87.

Peterson, G. P., and Fletcher, L. S., 1988a, "Evaluation of the Thermal Contact Conductance Between Mold Compound and Heat Spreader Materials," ASME JOURNAL OF HEAT TRANSFER, Vol. 110, No. 4, pp. 996-999.

Peterson, G. P., and Fletcher, L. S., 1988b, "Thermal Contact Conductance in the Presence of Thin Metallic Foils," Aerospace Sciences Conference, Reno, NV, Jan., Paper No. AIAA-88-0466.

Pinto, E. J., and Mikic, B. B., 1988, "A Novel Design Concept for Reduction of Thermal Contact Resistance," *Cooling Technology for Electronic Equipment*, W. Aung, ed., Hemisphere Publishing Corporation, New York, pp. 547-562.

Shah, H. J., 1978, Personal communication of unpublished data.

Tsao, Y. H., and Heimburg, R. W., 1970, "Effects of Surface Films on Thermal Contact Conductance: Part 2—Macroscopic Experiments," ASME Paper No. 70-HT/SpT-27.

Yip, F. C., 1975, "Effect of Oxide Films on Thermal Contact Resistance," *AIAA Progress in Astronautics and Aeronautics: Heat Transfer With Thermal Control Applications*, Vol. 39, M. M. Yovanovich, ed., MIT Press, Cambridge, MA, pp. 45-46.

Yovanovich, M. M., 1987, "Theory and Applications of Constriction and Spreading Resistance Concepts for Microelectronic Thermal Management," *Proceedings of the International Symposium on Cooling Technology for Electronic Equipment*, Pacific Institute for Thermal Engineering, Honolulu, HI, Mar.

J. H. Jang[1]

A. Faghri
Brage Golding Distinguished Professor.
Department of Mechanical and Materials Engineering,
Wright State University,
Dayton, OH 45435

W. S. Chang

E. T. Mahefkey
Wright Research and Development Center,
Wright-Patterson, AFB, OH 45433

Mathematical Modeling and Analysis of Heat Pipe Start-Up From the Frozen State

The start-up process of a frozen heat pipe is described and a complete mathematical model for the start-up of the frozen heat pipe is developed based on the existing experimental data. The model is simplified and solved numerically. The two-dimensional transient model for the wall and wick is coupled with the one-dimensional transient model for the vapor flow when vaporization and condensation occur at the interface. A parametric study is performed to examine the effect of the boundary specification at the surface of the outer wall on the successful start-up from the frozen state. For successful start-up, the boundary specification at the outer wall surface must melt the working substance in the condenser before dryout takes place in the evaporator.

Introduction

The demand for an effective thermal management device for high-temperature applications, such as cooling the leading edges of re-entry vehicles and hypersonic aircraft, and a space-based power station, has stimulated the study of the start-up of frozen liquid-metal heat pipes. Also, the start-up of frozen low-temperature heat pipes is important in applications such as heat pipe heat exchangers, cooling electronic equipment, and melting snow and ice on roads and bridges.

Neal (1967) and Shlosinger (1968) performed the first experimental tests to study the start-up performance of low-temperature heat pipes with the water initially frozen. Deverall et al. (1970) also made a series of tests with water and liquid-metal heat pipes. Successful start-up from the frozen state was possible but was highly dependent on the heat rejection rate at the condenser. Tolubinsky et al. (1978) investigated the startup characteristics of sodium and potassium heat pipes. Camarda (1977) investigated the performance of a sodium heat pipe cooling a leading edge. Start-up and shutdown of a 4-m-long lithium heat pipe were studied experimentally by Merrigan et al. (1985, 1986). Ivanovskii et al. (1982) presented the vapor temperature distribution along the length of a sodium heat pipe during the start-up period. Three flow regimes in the condenser were described based on the vapor temperature: free molecular flow, intermediate, and continuum vapor flow. Unfortunately, the existing experimental data for the start-up period are in general not represented in the archival literature and lack sufficient information for comparison with numerical simulations.

Colwell et al. (1987) and Jang (1988) developed a simple mathematical model to predict the start-up behavior of a sodium heat pipe with a rectangular cross section from the frozen state. In the wall and wick structure, energy transport is described by the transient, two-dimensional heat conduction equation, and the phase change of the working substance is taken into account. In the vapor region, free molecular, choked, and continuum flows are considered and one-dimensional compressible quasi-steady state laminar flow is assumed. The numerical results obtained by using the finite-element method are in agreement with the experimental results given by Camarda (1977). Hall and Doster (1987) have also made some analyses of the start-up behavior of heat pipes.

The liquid-metal heat pipe operates at high temperatures, but may be initially at ambient temperature. In this temperature range, the working substance may be in the solid state as well as the liquid and vapor states. In the vapor space, free molecular, continuum, sonic, and supersonic flows may be encountered due to the extremely low density during the start-up of the heat pipe. These conditions may cause the failure of operation of the heat pipe and limit the performance of the heat pipe. Understanding the start-up behavior and the transient performance of the high-temperature heat pipe is therefore important and an efficient mathematical model is needed to predict this behavior.

The first part of this paper presents a complete mathematical model to describe the start-up behavior of the heat pipe from the frozen state. This model is then simplified to obtain numerical results. To the authors' knowledge, the analysis presented here is the only model that includes the effect of the transient vapor flow in the analysis of the start-up of a heat pipe from the frozen state with a two-dimensional phase-change modeling. After the mathematical models are tested separately, the models are used for a parametric study of the start-up of frozen heat pipes.

Description of Heat Pipe Start-up

Previous experimental observations suggest the following sequence of events during heat pipe start-up from the frozen state. Initially, the working substance is in the solid state and the vapor density is extremely low, so that free molecular flow conditions prevail throughout the vapor space. The input heat flux over the evaporator increases the temperature and starts to melt the frozen substance in this region. Meanwhile, the heat transport from the heated zone to the adjacent pipe proceeds quite slowly via axial conduction through the heat pipe wall, working substance, and wick structure, while the heat transfer in the vapor is almost negligible. Thus, a large temperature gradient exists between the evaporator and condenser.

When energy is continuously added to the evaporator, the frozen working substance in the evaporator is melted, so that evaporation can take place at the liquid–vapor interface and the vapor density in this region is increased. The molecular mean free path in the heated region then becomes small compared to the diameter of the vapor passage and the continuum flow regime is established, while in the cooled zone the vapor

[1]Presently with NASA Lewis Research Center, Cleveland, OH 44135-3191.

Contributed by the Heat Transfer Division for publication in the JOURNAL OF HEAT TRANSFER. Manuscript received by the Heat Transfer Division May 1, 1989; revision received November 11, 1989. Keywords: Heat Pipes and Thermosyphons, Numerical Methods, Phase-Change Phenomena.

is still in free molecular flow. In the continuum flow region, the vapor flows into the condenser section due to the large pressure gradient. During this stage, energy is mainly transferred as latent heat owing to vaporization in the heated zone and condensation in the cooled zone in the vapor space where continuum flow is established. The temperature near the evaporator remains constant and the location of the temperature gradient moves toward the end of the condenser until continuum flow is established in the entire vapor space. Cotter (1967) also described this frontal start-up mode when the vapor density is low and noncondensible gas does not exist in the vapor space.

In heat pipes with metallic working substances, the vapor densities are very small during start-up even in the continuum flow region. Thus, for relatively low values of heat input, sonic vapor velocities can be reached. Also, the vapor flow in the heat pipe is quite similar to the flow in a converging-diverging nozzle due to the vapor addition in the evaporator and the vapor removal in the condenser (Dunn and Reay, 1982). Thus, the heat transfer through the vapor space may be limited by the choked flow condition, and supersonic vapor flow and a shock front may occur in the continuum flow region in the condenser. The maximum rate of heat transfer is limited by the sonic limit, so that a high heat input in the evaporator causes the various types of start-up failure.

This process continues until the frozen working substance is completely melted and the continuum flow regime reaches the end of the heat pipe, at which time the liquid returning to the evaporator is sufficient for normal transient operation. Eventually, the heat pipe may reach a steady-state condition. The start-up process of the liquid metal heat pipe from a frozen state may be divided into several distinct periods for convenience of analysis based on the status of the working substance and the behavior of the vapor flow.

1 In the first period, no phase change takes place in the entire region, but the temperature near the heated region increases. The vapor flow is in the free molecular condition.

2 The working substance in the evaporator is in the liquid state, but evaporation does not occur at the liquid–vapor interface.

3 The liquid and solid states of the working substance exist simultaneously in the wick structure and vaporization of the working substance takes place at the liquid–vapor interface. In the vapor space, a region of continuum flow is established in the heated region and a continuum flow front moves toward the cooled end of the heat pipe. The vapor flow may be choked at the beginning of the condenser.

4 The working substance is completely melted but free molecular flow still exists in part of the vapor space.

5 Continuum flow exists over the entire heat pipe length in the vapor region but the heat pipe does not reach the steady-state condition.

6 The heat pipe then reaches the steady-state operation.

For low-temperature heat pipes, the experimental results of successful start-up from the frozen state are very rare. Deverall et al. (1970) successfully started a water heat pipe from the frozen state (208 K). The wall temperature distribution obtained is similar to that of high-temperature heat pipes. The vapor temperature was not obtained, but the vapor density is relatively high even around the melting temperature. This means that the vapor velocity is very low so that choked flow and supersonic vapor velocities may not be encountered during start-up. Unlike high-temperature heat pipes, experimental results show that the heat pipe becomes immediately active where the ice is melted, but there is still a large temperature gradient in the axial direction. The heat input at the evaporator should be low enough to return sufficient water into the evaporator for the successful start-up.

Mathematical Formulation

Consideration is given to the heat pipe wall, the wick structure with the working substance initially subcooled at a uniform temperature, and the vapor region. A schematic diagram of the physical model is shown in Fig. 1.

Heat Pipe Wall. In this region, the progress can be modeled by the heat conduction equation in a hollow cylinder. The governing equation is expressed as follows:

$$(\rho c_p)_w \frac{\partial T_w}{\partial t} = \frac{1}{r}\frac{\partial}{\partial r}\left(rK_w\frac{\partial T_w}{\partial r}\right) + \frac{\partial}{\partial x}\left(K_w\frac{\partial T_w}{\partial x}\right) \tag{1}$$

Wick Structure. Initially, the working substance is in the solid state. When heat is added to the evaporator, the frozen

Nomenclature

c_p = specific heat at constant pressure, J/kg-K
c_v = specific heat at constant volume, J/kg-K
D = diameter of the vapor space, m
E = total energy of the vapor per unit volume = ρ $[c_v T_v + 1/2(U_v^2 + V_v^2)]$
f = friction coefficient at the wall = $\tau/\rho U_v^2$
h = enthalpy, J/kg
h_c = heat transfer coefficient, W/m^2-K
h_{lv} = latent heat of vaporization, J/kg
H_{sl} = latent heat of melting per unit volume, J/m^3
k = permeability of the wick structure, m^2
K = thermal conductivity, W/m-K
L = length of the heat pipe, m
$\dot{m}_o$ = rate of evaporation or condensation per unit area, kg/m^2-s
M = molecular weight, kg/kmol
n = unit outward normal direction
P = pressure, N/m^2
q = heat flux, W/m^2
q' = new heat flux, W/m^2
q'' = new guessed heat flux, W/m^2
P_{cr} = reference pressure for the Clausius–Clapeyron relationship, N/m^2
r = coordinate in the radial direction
r_c = effective capillary radius, m
r_p = radius of curvature of the meniscus, m
Δr = radial distance between nodes, m
R_u = universal gas constant, kJ/kmol-K
R_v = radius of the vapor space, m
R_w = inner radius of the heat pipe wall, m
$\mathbf{S}$ = interface position in vector, m
t = time, s
T = temperature, K
T_c = reference temperature for convection, K
T_{cr} = reference temperature for the Clausius–Clapeyron relationship, K

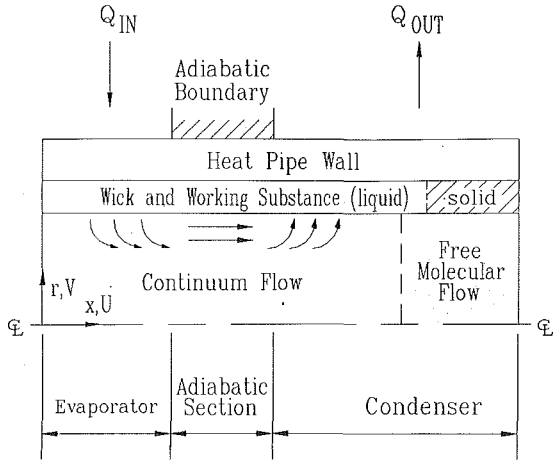

Fig. 1 Schematic diagram and coordinate configuration of the heat pipe

working substance in the heated region is melted so that the liquid and solid states of the working substance exist in the wick. Fluid motion in the liquid region may then occur due to vaporization and condensation of the working substance. The liquid flow in the wick is considered to be unsteady two-dimensional incompressible laminar flow with negligible body forces. The fluid and wick structure are assumed to be in local equilibrium and the velocities in the axial and radial directions are the local area-averaged velocities over a cross section of a finite element of the wick region instead of the pore velocity or actual velocity. Also, the wick is assumed to be isotropic and homogeneous. The governing equations for the wick region are formulated by using the principles of the conservation of mass, momentum, and energy. The viscous dissipation terms in the energy equation are neglected.

The continuity, momentum, and energy equations are

$$\frac{1}{r}\frac{\partial}{\partial r}(rV_l)+\frac{\partial U_l}{\partial x}=0 \tag{2}$$

$$\frac{1}{\epsilon}\frac{\partial V_l}{\partial t}+\frac{1}{\epsilon^2}\left(V_l\frac{\partial V_l}{\partial r}+U_l\frac{\partial V_l}{\partial x}\right)$$

$$=-\frac{1}{\rho_l}\frac{\partial P_l}{\partial r}-\frac{\nu_l V_l}{k}$$

$$+\frac{\nu_l}{\epsilon}\left[\frac{1}{r}\frac{\partial}{\partial r}\left(r\frac{\partial V_l}{\partial r}\right)-\frac{V_l}{r^2}+\frac{\partial^2 V_l}{\partial x^2}\right] \tag{3}$$

$$\frac{1}{\epsilon}\frac{\partial U_l}{\partial t}+\frac{1}{\epsilon^2}\left(V_l\frac{\partial U_l}{\partial r}+U_l\frac{\partial U_l}{\partial x}\right)$$

$$=-\frac{1}{\rho_l}\frac{\partial P_l}{\partial x}-\frac{\nu_l U_l}{k}$$

$$+\frac{\nu_l}{\epsilon}\left[\frac{1}{r}\frac{\partial}{\partial r}\left(r\frac{\partial U_l}{\partial r}\right)+\frac{\partial^2 U_l}{\partial x^2}\right] \tag{4}$$

$$(\rho c_p)_i\frac{\partial T_i}{\partial t}+V_l\frac{\partial T_i}{\partial r}+U_l\frac{\partial T_i}{\partial x}$$

$$=\frac{1}{r}\frac{\partial}{\partial r}\left(rK_i\frac{\partial T_i}{\partial r}\right)+\frac{\partial}{\partial x}\left(K_i\frac{\partial T_i}{\partial x}\right) \tag{5}$$

$$i=\begin{cases} se & \text{for solid region} \\ me & \text{for mushy region} \\ le & \text{for liquid region} \end{cases}$$

$$(\rho c_p)_i=\begin{cases} \epsilon(\rho c_p)_{fs}+(1-\epsilon)(\rho c_p)_s & \text{for solid region} \\ \epsilon H_{sl}\delta(T-T_m)+(1-\epsilon)(\rho c_p)_s & \text{for mushy region} \\ \epsilon(\rho c_p)_{fl}+(1-\epsilon)(\rho c_p)_s & \text{for liquid region} \end{cases} \tag{6}$$

When the porosity approaches unity (i.e., no wick structure exists), the permeability approaches infinity. Therefore, equations (2)–(5) can be reduced to the Navier–Stokes equation for unsteady two-dimensional incompressible laminar flow. For the steady state, equations (2)–(5) also approach a special case given by Hong et al. (1985). The expressions for the porosity and the effective thermal conductivity of the screen wicks are given by Chang (1987).

Nomenclature (cont.)

T_m = melting temperature, K
T_r = reference temperature for radiation, K
T_s = saturation temperature, K
T_{j-1} = temperature at node $j-1$ in the radial direction in the wick region, K
T_j = temperature at last node near liquid–vapor interface in the radial direction in the wick region, K
T^* = transition temperature, K
ΔT = small finite temperature interval around T_m to define mushy zone, K
U = axial velocity, m/s
V = radial velocity, m/s
$\mathbf{W}$ = net velocity vector, m/s
x = coordinate in the axial direction
α = relaxation factor
$\delta(T\text{-}T_m)$ = Dirac function
ϵ = porosity
θ = contact angle of the liquid, deg
λ = length of mean free path, m
μ = dynamic viscosity, N-s/m^2
ν = kinematic viscosity, m^2/s
ξ = emissivity
ρ = density, kg/m^3
σ = Stefan–Boltzmann constant, W/(m^2-K^4)
τ = shear stress
ω = surface tension, N/m

Subscripts

fl = working substance in the liquid state in the wick
fs = working substance in the solid state in the wick
l = liquid where there is liquid motion in the wick
le = wick region where the working substance is in the liquid state
me = wick region where the working substance is in the mushy state
o = properties at the liquid–vapor interface
s = wick structure material
se = wick region where the working substance is in the solid state
v = vapor state
w = properties at the heat pipe wall

The governing equations (2)–(5), however, are not always applicable. For example, during the second period the liquid state of the working substance exists in the wick but evaporation of the working substance at the interface is negligible. Also, the liquid layer is so thin that the effect of natural convection in the liquid region is neglected. Thus, there is no fluid motion in the liquid region, so only equation (5) without the second and third terms is applicable, and equations (2)–(4) are useful after the second period when there is liquid motion in the wick.

In addition to equations (2)–(5), coupling conditions at the liquid–solid interface are needed:

$$T_{se} = T_{le} = T_m \tag{7}$$

$$K_{se}\frac{\partial T_{se}}{\partial n} - K_{le}\frac{\partial T_{le}}{\partial n} = \epsilon H_{sl}\frac{dS}{dt} \tag{8}$$

Vapor Flow Dynamics. Initially, the entire working substance is in the solid state so that the vapor space may be nearly evacuated. As the temperature at the interface increases, the vapor density also increases. Continuum flow in the vapor space is considered to be established when the mean free path, λ, is substantially less than the minimum dimensions of the vapor flow passage (Holman, 1981), i.e.,

$$K_n \equiv \frac{\lambda}{D} \leq 0.01 \tag{9}$$

The transition temperature T^* of the vapor corresponding to the given dimension of the vapor space is expressed by using the kinetic theory of gases as follows (Jang, 1988):

$$T^* \geq \frac{\pi}{2\times 10^{-4}}\frac{M}{R_u}\left(\frac{\mu_v}{\rho_v D}\right)^2 \tag{10}$$

When the vapor temperature is greater than that calculated by equation (10), continuum flow is assumed to be established in the vapor space.

When continuum flow is established in the vapor space during start-up from the frozen state, complex flow phenomena are encountered in the continuum flow region due to the extremely low density of the vapor. The vapor pressure is low and the temperature and pressure gradients are large in the axial direction, so the vapor velocity may reach the sonic velocity, and supersonic vapor flow and a shock front may occur in the condenser. Thus, the effects of compressibility, friction at the liquid–vapor interface, and viscous dissipation in the vapor should be considered in the mathematical model. The vapor flow may be considered to be axisymmetric compressible unsteady laminar flow and the governing equations for this flow are formulated with negligible body forces and heat sources as follows. In cylindrical coordinates, the continuity, momentum, and energy equations are

$$\frac{\partial \rho_v}{\partial t} + \frac{1}{r}\frac{\partial}{\partial r}(r\rho_v V_v) + \frac{\partial(\rho_v U_v)}{\partial x} = 0 \tag{11}$$

$$\rho_v\left(\frac{\partial V_v}{\partial t} + V_v\frac{\partial V_v}{\partial r} + U_v\frac{\partial V_v}{\partial x}\right) = -\frac{\partial P_v}{\partial r} + \mu_v\left[\frac{4}{3r}\frac{\partial}{\partial r}\left(r\frac{\partial V_v}{\partial r}\right) - \frac{4}{3}\frac{V_v}{r^2} + \frac{1}{3}\frac{\partial^2 U_v}{\partial x \partial r} + \frac{\partial^2 V_v}{\partial x^2}\right] \tag{12}$$

$$\rho_v\left(\frac{\partial U_v}{\partial t} + V_v\frac{\partial U_v}{\partial r} + U_v\frac{\partial U_v}{\partial x}\right) = -\frac{\partial P_v}{\partial x} + \mu_v\left\{\frac{1}{r}\frac{\partial}{\partial r}\left[r\left(\frac{\partial V_v}{\partial x} + \frac{\partial U_v}{\partial r}\right)\right] - \frac{2}{3}\frac{\partial}{\partial x}\left[\frac{1}{r}\frac{\partial}{\partial r}(rV_v)\right] + \frac{4}{3}\frac{\partial}{\partial x}\left(\frac{\partial U_v}{\partial x}\right)\right\} \tag{13}$$

$$\rho_v C_{pv}\left(\frac{\partial T_v}{\partial t} + V_v\frac{\partial T_v}{\partial r} + U_v\frac{\partial T_v}{\partial x}\right) = \frac{1}{r}\frac{\partial}{\partial r}\left(rK_v\frac{\partial T_v}{\partial r}\right) + \frac{\partial}{\partial x}\left(K_v\frac{\partial T_v}{\partial x}\right) + \frac{\partial P_v}{\partial t} + V_v\frac{\partial P_v}{\partial r} + U_v\frac{\partial P_v}{\partial x} + \mu_v\phi \tag{14}$$

where

$$\phi = 2\left[\left(\frac{\partial V_v}{\partial r}\right)^2 + \left(\frac{V_v}{r}\right)^2 + \left(\frac{\partial U_v}{\partial x}\right)^2 + \frac{1}{2}\left(\frac{\partial V_v}{\partial x} + \frac{\partial U_v}{\partial r}\right)^2 - \frac{1}{3}(\nabla\cdot\mathbf{W})^2\right]$$

$$\nabla\cdot\mathbf{W} = \frac{1}{r}\frac{\partial}{\partial r}(rV_v) + \frac{\partial U_v}{\partial x}$$

The numerical and analytical solutions of the above equations under steady-state conditions for annular and conventional heat pipes were given by Faghri (1986) and Faghri and Parvani (1988). Transient results are needed for the start-up from the frozen condition.

Initial and Boundary Conditions. Initially, a uniform temperature for the wall, wick, and vapor regions is assumed that is less than the melting temperature of the working substance, so the entire working substance in the wick is in the solid state. The heat flux, convection, and radiation boundary conditions are applicable at the outer surface of the evaporator and condenser of the heat pipe. Both ends of the heat pipe are assumed to be insulated. When the liquid motion exists in the wick structure, the no-slip condition is used for the velocities at the interface between the heat pipe wall and the wick structure.

The boundary conditions at the liquid–vapor interface change during the start-up process. In the first and second periods, free molecular flow is prevalent in the vapor space so that heat transfer through the vapor space is negligible. Therefore, the adiabatic condition is employed at the liquid–vapor interface. When continuum flow is established in the vapor space, vaporization and condensation of the working substance at the interface is considered by using interfacial energy and mass balances. The vapor temperature at the interface is assumed to be the saturation temperature corresponding to the vapor pressure at the interface. The Clausius–Clapeyron relationship is used to obtain the saturation temperature. The continuity of the axial velocity and shear stress is also used. The pressure difference at the liquid–vapor interface induced from the action of the surface tension is given by using the Laplace and Young equation. This condition couples the liquid and vapor momentum equations at the liquid–vapor interface.

While part of the vapor space is in the continuum flow regime, free molecular flow also exists in the rest of the vapor space. Even though the heat transfer through the free molecular flow region may be negligible, the boundary conditions at the border of the two regions are needed to solve the governing equations for the continuum flow region. Since a large temperature gradient exists in the continuum flow region in the condenser during start-up, most of the vapor may be condensed at the interface. Thus, the vapor penetration in the free molecular flow region may be minimal or penetration may occur in the immediate vicinity of the interface between the continuum flow region and the free molecular flow region.

Table 1 Summary of the boundary conditions for a mathematical model of the heat pipe startup

Time	First and second periods	Third period	Fourth period	Fifth and sixth periods
Event	Heat transfer by conduction; no liquid motion; free molecular flow	Solid and liquid states; liquid motion in the wick; continuum flow in the part of the vapor space	No solid state of the working substance; liquid motion in the wick; continuum flow in the part of the vapor space	Liquid motion in the wick; continuum flow in the entire vapor space; the heat pipe approaches the steady-state operation
Location				
Outer wall surface	$K_w\frac{\partial T_w}{\partial r}=q(x,t)+h_c(T_c-T_w)+\sigma\xi(T_r^4-T_w^4)$			
Wall and wick structure interface ($r=R_w$)	$T_w=T_i$ $K_w\frac{\partial T_w}{\partial r}=K_i\frac{\partial T_i}{\partial r}$	$T_w=T_i$ $K_w\frac{\partial T_w}{\partial r}=K_i\frac{\partial T_i}{\partial r}$ $U_l=V_l=0$ for $T_i>T_m$ (liquid region)	$T_w=T_{le}$ $K_w\frac{\partial T_w}{\partial r}=K_{le}\frac{\partial T_{le}}{\partial r}$ $U_l=V_l=0$	
Liquid–vapor interface ($r=R_v$)	$\frac{\partial T_i}{\partial r}=0$	$\frac{\partial T_i}{\partial r}=0$ for $T_i<T^*$ (free moelcular flow region) $K_{le}\frac{\partial T_{le}}{\partial r}-K_v\frac{\partial T_v}{\partial r}=h_{lv}\dot{m}_o$ for $T_{le}\geq T^*$ $U_l=U_v,\quad \mu_l\frac{\partial U_l}{\partial r}=\mu_v\frac{\partial U_v}{\partial r}$ $V_l=-\frac{B\dot{m}_o}{\rho_l}=\frac{\rho_v}{\rho_l}V_v$ $P_v-P_l=\frac{2\omega}{r_p}$ $T_s=\frac{1}{\frac{1}{T_{cr}}-\frac{R_u}{Mh_{lv}}\ln\frac{P}{P_{cr}}}$	$\frac{\partial T_{le}}{\partial r}=0$ for $T_{le}<T^*$ (free molecular flow region) $K_{le}\frac{\partial T_{le}}{\partial r}-K_v\frac{\partial T_v}{\partial r}=h_{lv}\dot{m}_o$ for $T_{le}\geq T^*$ $U_l=U_v,\quad \mu_l\frac{\partial U_l}{\partial r}=\mu_v\frac{\partial U_v}{\partial r}$ $V_l=-\frac{B\dot{m}_o}{\rho_l}=\frac{\rho_v}{\rho_l}V_v$ $P_v-P_l=\frac{2\omega}{r_p}$ $T_s=\frac{1}{\frac{1}{T_{cr}}-\frac{R_u}{Mh_{lv}}\ln\frac{P}{P_{cr}}}$	$K_{le}\frac{\partial T_{le}}{\partial r}-K_v\frac{\partial T_v}{\partial r}=h_{lv}\dot{m}_o$ $U_l=U_v$ $\mu_l\frac{\partial U_l}{\partial r}=\mu_v\frac{\partial U_v}{\partial r}$ $V_l=-\frac{B\dot{m}_o}{\rho_l}=\frac{\rho_v}{\rho_l}V_v$ $P_v-P_l=\frac{2\omega}{r_p}$ $T_s=\frac{1}{\frac{1}{T_{cr}}-\frac{R_u}{Mh_{lv}}\ln\frac{P}{P_{cr}}}$
Both ends of the pipe ($x=0, L$) — Wall	$\frac{\partial T_w}{\partial x}=0$			
Both ends of the pipe ($x=0, L$) — Wick structure	$\frac{\partial T_i}{\partial x}=0$	$\frac{\partial T_i}{\partial x}=0$ $U_l=V_l=0$ for $T_i>T_m$ (liquid region)	$\frac{\partial T_{le}}{\partial x}=0$ $U_l=V_l=0$	
Both ends of the pipe ($x=0, L$) — Vapor space	No boundary condition is needed due to free molecular flow	$U_v=V_v=0$ for $T_{le}>T^*$ (continuum flow region) $\frac{\partial T_v}{\partial x}=\frac{\partial P_v}{\partial x}=\frac{\partial \rho_v}{\partial x}=0$		$U_v=V_v=0$ $\frac{\partial T_v}{\partial x}=\frac{\partial P_v}{\partial x}=\frac{\partial \rho_v}{\partial x}=0$
Centerline of the pipe ($r=0$)	No boundary condition is needed due to free molecular flow	$V_v=0$ for $T_{le}\geq T^*$ (continuum flow region) $\frac{\partial \rho_v}{\partial r}=\frac{\partial U_v}{\partial r}=\frac{\partial E_v}{\partial r}=\frac{\partial P_v}{\partial r}=0$		$V_v=0$ $\frac{\partial \rho_v}{\partial r}=\frac{\partial U_v}{\partial r}=\frac{\partial E_v}{\partial r}=\frac{\partial P_v}{\partial r}=0$

Also, the temperature in the region of free molecular flow remains unchanged except in the vicinity of the continuum flow region due to the near vacuum. Therefore, an imaginary plane, which is adiabatic and normal to the axial direction, is assumed to divide the two vapor flow regions at the point of the transition temperature. The dividing plane moves toward the cooled end of the heat pipe as the location of the transition temperature at the liquid–vapor interface moves.

The axisymmetric condition along the centerline of the heat pipe is used in the continuum flow region. The no-slip condition and the adiabatic condition at both ends of the heat pipe are also used for the velocities and temperature. The pressure and density at both ends of the heat pipe are unknown but the vapor velocity near the ends of the heat pipe is so low that the axial pressure and density gradients are assumed to be zero. All of the boundary conditions for a mathematical model of the heat pipe start-up from the frozen state are summarized in Table 1.

Simplification of the Model

The mathematical model, equations (1)–(14), for the start-up behavior of the liquid-metal heat pipe described in the previous section includes most of the physical phenomena that may occur in the heat pipe. Therefore, this model is very complex to solve numerically. The effect of some physical phenomena may be negligible, so a simplified model is derived to predict the performance of the heat pipe during the start-up period. For this purpose, assumptions are made based on the characteristics of the heat pipe and previous studies.

The density of the liquid state of the working substance is much greater than that of the vapor state, so the velocity of the working substance in the wick structure is small. The thermal conductivity of the liquid metal is large and the thickness of the wick region is very thin. It is then assumed that the effect of the liquid flow in the wick structure is negligible and the wick structure is saturated by the working substance. Thus, the heat transport through the wick structure and working substance is by conduction only but the phase change of the working substance is considered. Under these assumptions, the same governing equation is also applicable to the heat pipe wall and the wick structure by using the proper properties for each region. The governing equation is given as follows:

$$(\rho c_p)_i\frac{\partial T_i}{\partial t}=\frac{1}{r}\frac{\partial}{\partial r}\left(rK_i\frac{\partial T_i}{\partial r}\right)+\frac{\partial}{\partial x}\left(K_i\frac{\partial T_i}{\partial x}\right) \tag{15}$$

$$i=\begin{cases} w & \text{for wall region} \\ se & \text{for solid region in the wick} \\ me & \text{for mushy region in the wick} \\ le & \text{for liquid region in the wick} \end{cases}$$

The expression of $(\rho c_p)_i$ for the wick structure region is given by equation (6). The thermal conductivity K_i can be the thermal conductivity of the wall material for the wall region. When the effective thermal conductivity for the wick region is calculated by using the expression given by Chang (1987), the thermal conductivity for the working substance is substituted by the solid conductivity, liquid conductivity, or the average value of the solid and liquid conductivity of the working

substance corresponding to the solid, liquid, or mushy region, respectively.

The vapor flow is also simplified further from the two-dimensional model to a one-dimensional model since a previous study (Jang et al., 1989) shows that the one-dimensional transient compressible model described the vapor flow dynamics as well as the two-dimensional model for simulated heat pipe vapor flow. The transient compressible one-dimensional continuity, momentum, and energy equations are written as follows:

$$\frac{\partial}{\partial t}(\rho_v)+\frac{\partial}{\partial x}(\rho U_v)=\frac{4\rho_o V_o(x)}{D} \tag{16}$$

$$\frac{\partial}{\partial t}(\rho_v U_v)+\frac{\partial}{\partial x}(\rho_v U_v U_v)$$
$$+\frac{\partial}{\partial x}\left(P_v-\frac{4}{3}\mu_v\frac{\partial U_v}{\partial x}\right)=-\frac{2\rho_v U_v^2 f}{D} \tag{17}$$

$$\frac{\partial E_v}{\partial t}+\frac{\partial}{\partial x}\left(U_v(E_v+P_v)-\frac{4}{3}\mu_v\frac{\partial U_v}{\partial x}U_v-K_v\frac{\partial T_v}{\partial x}\right)$$
$$=\frac{4\rho_o V_o(x)}{D}\left(h_o(x)+\frac{V_o^2(x)}{2}\right)+\frac{2\rho_v U_v^2 f}{D}U_v \tag{18}$$

Since the governing equations are simplified, the corresponding boundary conditions are also modified to match the governing equations.

Numerical Procedure

The governing equations are solved separately for each region. When the coupling is implemented at the interface, iterations are needed. To reduce the amount of computer time, noniterative schemes are employed for each region. The well-known alternating direction implicit (ADI) method is used for the heat pipe wall and wick, and the phase change of the working substance during start-up is modeled by using the equivalent heat capacity method (Hsiao, 1985). This method approximates the rapid change of the heat capacity over the phase change temperature range, which is an artificially defined finite temperature range, ΔT, instead of using the Dirac function. In the numerical calculation, this property is evaluated based on the nodal temperatures. The implicit Beam-Warming method is used for the vapor flow dynamics. The detailed numerical method for the vapor flow in the heat pipe is described by Jang et al. (1989).

When continuum flow exists in the vapor space, equation (15) should be coupled with equations (16)-(18) by using the same boundary conditions at the interface. The coupling of the governing equations for the vapor region to those for the wall and wick regions would be achieved by using the heat flux and the saturation temperature at the interface. However, the heat flux at this interface and the saturation temperature are initially unknown, so that these boundary conditions should be assumed and iterations are needed for each time step until the coupling conditions are satisfied along the interface. The numerical procedure used for coupling is as follows:

1 It is assumed that the liquid-vapor interface temperature is the initial temperature for the first time step.

2 Solve for the temperatures in the wall and wick regions.

3 Calculate the heat fluxes q at each node of the liquid-vapor interface by using the temperatures (T_{j-1} and T_j) in the wick region

$$q=K_{le}\frac{(T_{j-1}-T_j)}{\Delta r} \tag{19}$$

4 These heat fluxes are used as the boundary conditions at the interface to solve for temperatures in the wall and wick regions.

5 Use the same heat fluxes to solve the vapor temperature and pressure for the same period at the wall and wick regions. Obtain the saturation temperature T_s by using the Clausius-Clapeyron relationship.

6 Calculate the new heat fluxes q' at the interface by using the saturation temperature T_s in the wick

$$q'=K_{le}\frac{(T_{j-1}-T_s)}{1.5\Delta r} \tag{20}$$

7 Compare the new heat fluxes q' with the old heat fluxes q at each node of the interface.

8 If the difference between the new heat flux and old heat flux is within an acceptable range, repeat steps (4) to (7) for the next time step.

9 If the difference between the new heat flux and the old heat flux is not within the acceptable range, assume new guessed heat fluxes q'' by using the relaxation method and repeat steps (4) to (7) until the comparison of the results is acceptable

$$q''=q+\alpha(q'-q) \tag{21}$$

10 Repeat steps (4) to (9) until the temperatures reach steady state.

When the coupling of the governing equations is attempted, some physical characteristics of the two regions are considered. Since the density of the vapor is much smaller than that of the liquid, the volumetric specific heat ρc_p ($=8.8$ J/m^{3}K) for the sodium vapor is much smaller than that ($=1040.1$ kJ/m^{3}K) for the liquid. Therefore, a difference between the transient response times of the vapor region and the wall and wick regions exists. The time step for the vapor space should then be much smaller than that for the wall and wick regions. The governing equations for the wall and wick regions are solved for one time step by using the heat flux assumed at the interface, and then the governing equations for the vapor space are solved by using the same heat flux at the interface and smaller time steps for the same period as the wall and wick regions.

Results and Discussion

The governing equations for the wall and wick regions and the vapor flow are solved separately, and then are coupled at the liquid-vapor interface. Therefore, the numerical methods and algorithms can be separately tested and compared to the available data. Since the working substance changes phase from the solid state to the liquid state during the start-up period from the frozen state, this effect should be incorporated into the numerical model. The solidification of sodium in a square region is chosen to verify the numerical model and algorithm for governing equation (15). The results are in agreement with available data (Rathjen and Jiji, 1971). The transient one-dimensional model for the vapor flow dynamics in the heat pipe has already been verified by Jang et al. (1989). The combined model is used to predict the performance of the liquid-metal heat pipe.

Simulation of the Heat Pipe Start-up in the Initial Stages. Previous experimental results (Deverall et al., 1970) show that successful start-up of the frozen heat pipe depends greatly on the boundary condition at the outer surface of the evaporator and condenser. For successful start-up from the frozen state, the heat input and output should melt the working substance in the condenser and allow sufficient liquid to return to the evaporator. All of the previous experimental results show the wall surface temperatures, so that even for successful start-up the status of the working substance with time is unknown. Thus, the governing equations that described the start-up behavior of a cylindrical heat pipe during the first and second periods are solved numerically to examine

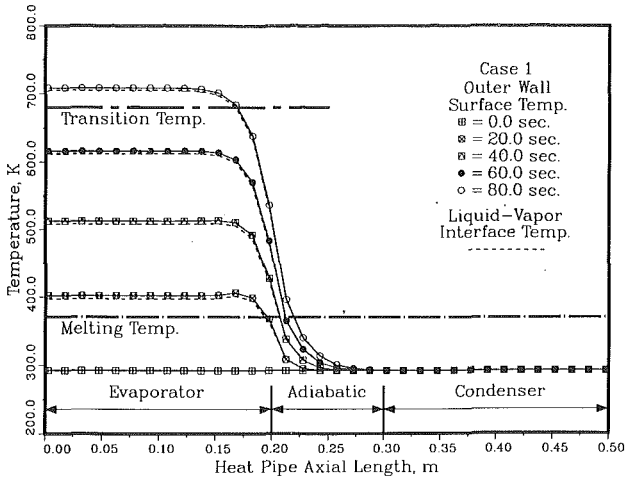

Fig. 2 Temperature distribution at the outer wall surface and liquid-vapor interface of the heat pipe wall with time for case 1

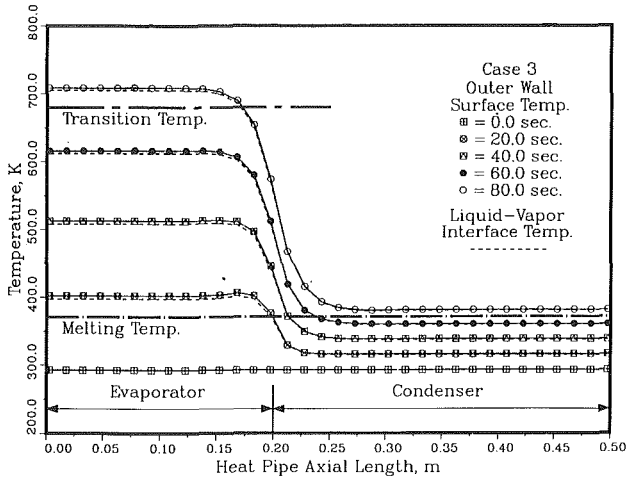

Fig. 4 Temperature distribution at the outer wall surface and liquid-vapor interface of the heat pipe wall with time for case 3

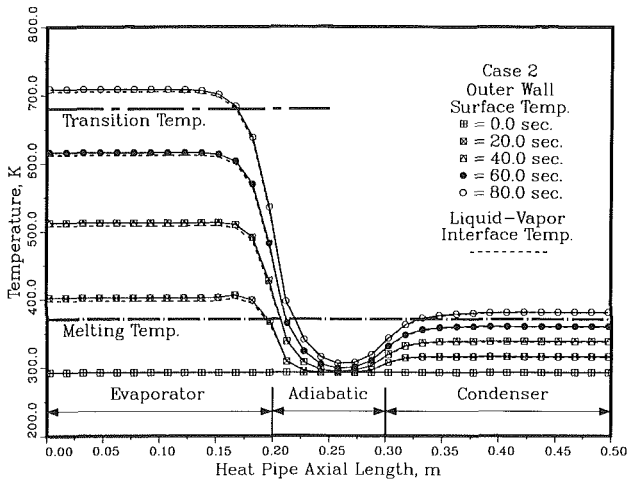

Fig. 3 Temperature distribution at the outer wall surface and liquid-vapor interface of the heat pipe wall with time for case 2

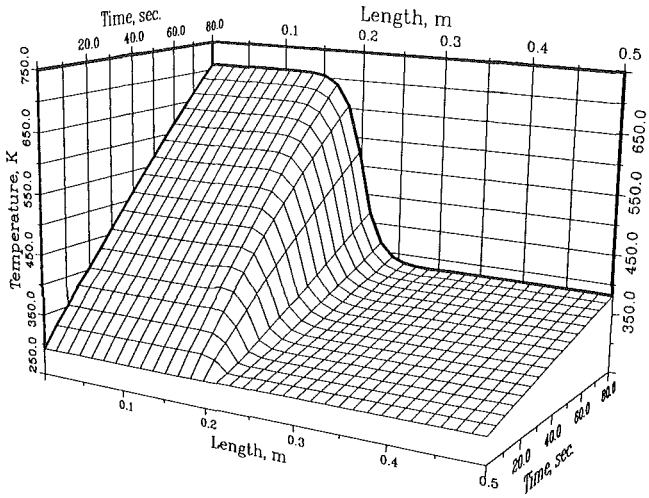

Fig. 5 Temperature distribution at the outer wall surface of the heat pipe wall with different times for case 3

the effect of the boundary conditions and to recommend the optimum boundary condition.

The physical model has evaporator, adiabatic, and condenser section lengths of 0.2, 0.1, and 0.2 m, respectively. The radius of the vapor space and the inner and outer radii of the heat pipe wall are 0.00685, 0.008, and 0.01 m, respectively. The material for the heat pipe wall and wick structure is stainless steel (AISI 316). Sodium initially in the solid state at the ambient temperature is used as the working substance. The melting temperature of sodium is 371 K and the transition temperature of 680 K is obtained by using equation (10) for the radius of the vapor space (0.00685 m) by iteration. Three different boundary condition cases are chosen for the outer surface of the heat pipe. A uniform input heat flux of 50 kW/m^2 and radiative heat output are used on the evaporator for all three cases. An emissivity of 0.9 and a radiation reference temperature of 293 K are employed. The boundary conditions at the condenser and adiabatic sections are changed while that at the evaporator remains the same for all three cases. The liquid-vapor interface is assumed to be adiabatic due to the free molecular flow in the vapor space during the initial two periods.

For case 1, only radiation is used in the condenser to reject heat. Figure 2 shows the temperature distributions at the heat pipe outer wall surface and the liquid-vapor interface. As heat is added in the evaporator, the temperature in the evaporator increases and at 20 s the working substance in the evaporator is in the liquid state. However, the temperature in the condenser is not changed from the initial temperature and in the adiabatic section the temperature in the region adjacent to the evaporator increases due to axial conduction. Additional heat input in the evaporator increases the temperature above the transition temperature in the evaporator, but the temperature in the condenser is still not changed so that a large temperature gradient exists. In the adiabatic section, part of the working substance (sodium) is in the liquid state. When the heat input is continued at the evaporator, vaporization occurs at the interface in the evaporator. However, the working substance in most of the adiabatic section and condenser is in the solid state. Therefore, the heat input in the evaporator should be small to prevent dryout of the wick structure while the working substance in the solid state is melted. Even though successful start-up may be possible for this case, the start-up progresses very slowly.

For case 2, 10 kW/m^2 is added in the condenser in addition to the radiative boundary condition to assist in the start-up of the frozen heat pipe. Figure 3 shows the temperature distributions at the outer wall surface and liquid-vapor interface. Since a small amount of heat is added in the condenser, the

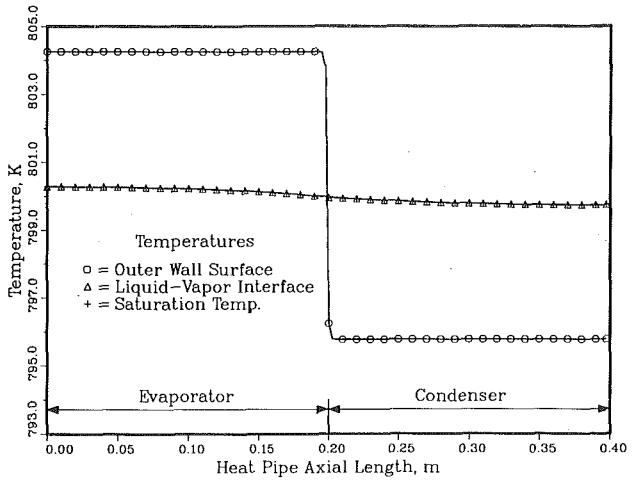

Fig. 6 Temperature distributions at the outer wall surface and liquid-vapor interface, and saturation temperature for time of 0.35

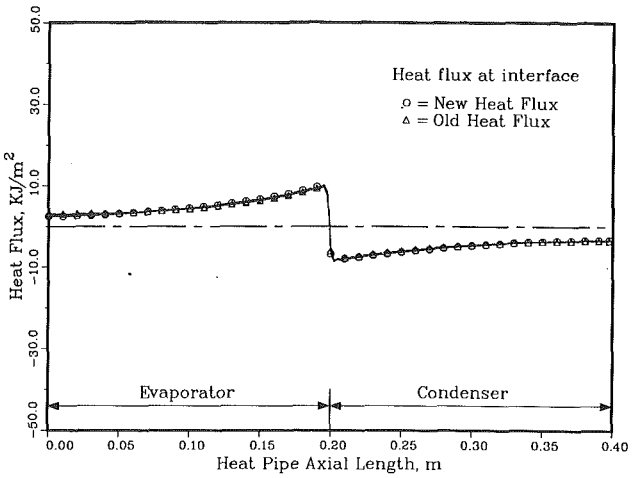

Fig. 7 Comparison of new heat flux with old heat flux at the interface for time of 0.3 s during transient continuum flow

temperature in the condenser is raised above the melting temperature. However, the temperature in the adiabatic section is still below the melting temperature. Thus, the liquid in the condenser cannot flow to the evaporator until the working substance in the adiabatic section liquefies. The temperature in the adiabatic section increases relatively faster than that for case 1 due to heat transfer at both ends of the adiabatic section. The startup period may be shorter than that for case 1.

Finally, the adiabatic section is used as part of the condenser and 10 kW/m^2 of heat is input in the condenser section. Figure 4 shows the temperature distributions at the heat pipe surface and the liquid-vapor interface and Fig. 5 shows the surface temperature at different times. Even though a large temperature gradient still exists along the axial direction, the working substance is completely melted in the entire heat pipe in 80 s. When vaporization occurs in the evaporator, the working substance can flow from the condenser to the evaporator to prevent dryout of the wick structure in the evaporator. Thus, a relatively large amount of heat can be added at the evaporator without dryout so that the start-up period is expected to be much less than those of cases 1 and 2.

Transient Heat Pipe Operation. To simulate the coupling of the governing equation for the wall and wick to that for the vapor flow, the same physical heat pipe model is used, except that the adiabatic section is eliminated. Sodium is employed as the working substance. In order to concentrate on the coupling problem, it is assumed that continuum flow is established in the entire vapor space and the working substance is in the liquid state. To yield these conditions, a uniform initial temperature of 800 K, which is greater than the transition temperature (680 K), is used for the wall, wick, and vapor regions. The external surfaces of the heat pipe wall at the evaporator and condenser are exposed to a uniform heat flux of 50 kW/m^2 and a convective boundary condition, respectively. A reference temperature of 300 K and a heat transfer coefficient of 100 W/m^{2}K are used for the convective boundary condition at the condenser section. The time step for the vapor space should be much smaller than that for the wall and wick regions, so a time step of 0.1 s is employed for the wall and wick regions and a time step of 0.1×10^{-3} s is used for the vapor flow. Twenty nodes in the radial direction and 160 nodes in the axial direction are used at the wall and wick regions. Also, 160 nodes are employed along the vapor space. A relaxation factor of $\alpha=3.0\times10^{-5}$ is used to obtain the new guessed heat flux.

Figure 6 shows the temperature distributions at the outer wall surface, liquid-vapor interface, and the saturation

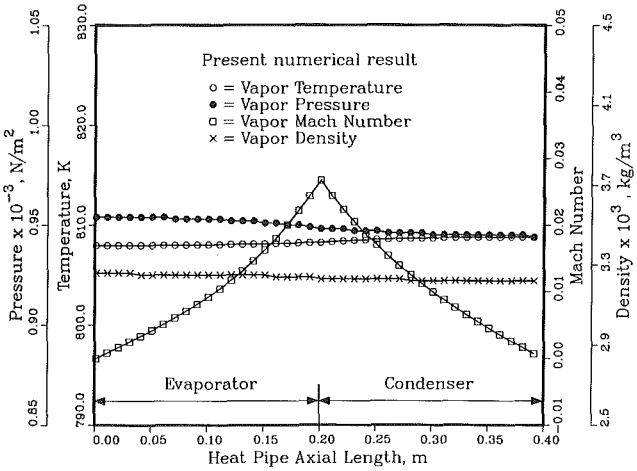

Fig. 8 Axial variations of temperature, pressure, density, and velocity for time of 0.3 s during transient continuum flow

temperature for a time of 0.3 s. The temperature distribution at the outer wall surface is uniform within each section, and near the border between the evaporator and condenser the surface temperature abruptly changes corresponding to the boundary conditions at the surface. The interface temperature matches well with the saturation temperature, which is evaluated by using the Clausius-Clapeyron relationship with the vapor pressure. The saturation temperature decreases gradually. Figure 7 shows the heat flux distribution at the interface. The new heat flux calculated converges on the old heat flux. The maximum difference between the two heat fluxes is about 10 percent. Even though the heat flux at the surface is relatively uniform, the heat flux at the interface is not uniform. Also, the heat flux at the interface is much less than that at the surface. This implies that most of the energy is used to raise the wall and wick temperature at this moment. Figure 8 shows the vapor temperature, pressure, velocity, and density distributions. The variation of the vapor temperature, pressure, and density is small. Also, a Mach number of M = 0.027 is obtained at the exit of the evaporator.

Conclusions

The start-up process of the frozen heat pipe is described based on experimental results. A complete mathematical model is developed to predict the start-up behavior of the heat

pipe from the frozen condition. A simplified model is used to obtain the numerical results. The numerical results during the first and second periods show that the heat flux distributions for the evaporator and condenser should be chosen to melt the working substance in the condenser prior to vaporization occurring in the evaporator. A small amount of heat input at the condenser helps start-up and a high heat rejection at the condenser during the start-up should be avoided. The coupling of the two-dimensional transient model for the wall and wick to the one-dimensional transient model for the vapor flow is achieved when continuum flow exists in the vapor space. During the transient operation, the heat flux distribution at the interface is quite different from that at the surface. Efforts to improve the present model will continue.

Acknowledgments

Funding for this work was provided by a joint effort of the NASA Lewis Research Center and the Thermal Energy Group of the Aero Propulsion and Power Laboratory of the U.S. Air Force under contract No. F33615-88-C-2820.

References

Camarda, C. J., 1977, "Analysis and Radiant Heating Tests of a Heat-Pipe-Cooled Leading Edge," NASA TN-8486.

Chang, W. S., 1987, "Effective Thermal Conductivity of Wire Screens," *Fundamentals of Conduction and Recent Developments in Contact Resistance*, ASME HTD-Vol. 69, pp. 64–75.

Colwell, G. T., Jang, J. H., and Camarda, C. J., 1987, "Modeling of Startup From the Frozen State," *Proc. 6th Int. Heat Pipe Conf.*, France, Vol. 1, pp. 165–170.

Cotter, T. P., 1967, "Heat Pipe Startup Dynamics," *Proc. IEEE Thermionic Conversion Specialist Conf.*, Palo Alto, CA, pp. 344–348.

Deverall, J. E., Kemme, J. E., and Florschuetz, L. W., 1970, "Sonic Limitations and Startup Problems of Heat Pipes," LA-4518.

Dunn, P. D., and Reay, D. A., 1982, *Heat Pipes*, 3rd ed., Pergamon Press, Oxford, United Kingdom.

Faghri, A., 1986, "Vapor Flow Analysis in a Double-Walled Concentric Heat Pipe," *Numerical Heat Transfer*, Vol. 10, No. 6, pp. 583–595.

Faghri, A., and Parvani, S., 1988, "Numerical Analysis of Laminar Flow in a Double-Walled Heat Pipe," *J. Thermophysics and Heat Transfer*, Vol. 2, No. 3, pp. 165–171.

Hall, M., and Doster, J., 1987, "Transient Thermohydraulic Heat Pipe Modeling," in: *Space Nuclear Power Systems*, Vol. VI, M. El-Genk, ed., Orbit Book Co., Malabar, FL.

Holman, J. P., 1981, *Heat Transfer*, 5th ed., McGraw-Hill, New York.

Hong, J. T., Tien, C. L., and Kaviany, M., 1985, "Non-Darcian Effects on Vertical-Plate Natural Convection in Porous Media With High Porosities," *Int. J. Heat Mass Transfer*, Vol. 28, pp. 2149–2157.

Hsiao, J. S., 1985, "An Efficient Algorithm for Finite-Difference Analysis of Heat Transfer With Melting and Solidification," *Numerical Heat Transfer*, Vol. 8, pp. 653–666.

Ivanovskii, M. N., Sorokin, V. P., and Yagodkin, I. V., 1982, *The Physical Principles of Heat Pipes*, Clarendon Press, Oxford, United Kingdom.

Jang, J. H., 1988, "An Analysis of Startup From the Frozen State and Transient Performance of Heat Pipes," Ph.D. Dissertation, Georgia Institute of Technology, Atlanta, GA.

Jang, J. H., Faghri, A., and Chang, W. S., 1989, "Analysis of the Transient Compressible Vapor Flow in Heat Pipes," *Proc. of 26th National Heat Transfer Conf.*, Philadelphia, PA.

Merrigan, M. A., Keddy, E. S., and Sena, J. T., 1985, "Transient Heat Pipe Investigations for Space Power Systems," LA-UR-85-3341.

Merrigan, M. A., Keddy, E. S., and Sena, J. T., 1986, "Transient Performance Investigation of a Space Power System Heat Pipe," AIAA Paper No. AIAA-86-1273.

Neal, L. G., 1967, "An Analysis and Experimental Study of Heat Pipes," TRW System Rept. No. 99900-6114-R000.

Rathjen, K. A., and Jiji, L. M., 1971, "Heat Conduction With Melting or Freezing in a Corner," ASME JOURNAL OF HEAT TRANSFER, Vol. 93, pp. 101–109.

Shlosinger, A. P., 1968, "Heat Pipe Devices for Space Suit Temperature Control," TRW System Rept. No. 06462-6005-RO-00.

Tolubinsky, V. I., Shevchuk, E. N., and Stambrovsky, V. D., 1978, "Study of Liquid-Metal Heat Pipes Characteristics at Startup and Operation Under Gravitation," *Proc. of 3rd Int. Heat Pipe Conf.*, pp. 274–282.

Steady-State Modeling and Testing of a Micro Heat Pipe

B. R. Babin
Research Assistant.
Student Mem. ASME

G. P. Peterson
Professor Mechanical Engineering.
Mem. ASME

D. Wu
Research Associate.
Mem. ASME

Mechanical Engineering Department,
Texas A&M University,
College Station, TX 77843

A combined experimental and analytical investigation was conducted to identify and understand better the phenomena that govern the performance limitations and operating characteristics of micro heat pipes—heat pipes so small that the mean curvature of the vapor—liquid interface is comparable in magnitude to the reciprocal of the hydraulic radius of the flow channel. The analytical portion of the investigation began with the development of a steady-state model in which the effects of the extremely small characteristic dimensions on the conventional steady-state heat pipe modeling techniques were examined. In the experimental portion of the investigation, two micro heat pipes, one copper and one silver, 1 mm^2 in cross-sectional area and 57 mm in length, were evaluated experimentally to determine the accuracy of the steady-state model and to provide verification of the micro heat pipe concept. Tests were conducted in a vacuum environment to eliminate conduction and convection losses. The steady-state experimental results obtained were compared with the analytical model and were found to predict accurately the experimentally determined maximum heat transport capacity for an operating temperature range of 40°C to 60°C. A detailed description of the methodology used in the development of the steady-state model along with a comparison of the predicted and experimental results are presented.

Introduction

The concept of incorporating very small "micro" heat pipes as an integral part of semiconductor devices for thermal control was first introduced by Cotter (1984). At that time, a micro heat pipe was defined as one "so small that the mean curvature of the liquid–vapor interface is necessarily comparable in magnitude to the reciprocal of the hydraulic radius of the total flow channel." Mathematically, this relationship can be expressed as

$$K \propto \frac{1}{r_h} \tag{1}$$

where K is the mean curvature of the liquid–vapor interface and r_h is the hydraulic radius of the flow channel. Assuming a constant of proportionality of one and multiplying both the mean curvature of the liquid–vapor interface and the hydraulic radius by the capillary radius r_c yields a dimensionless expression that more clearly defines a micro heat pipe as one that satisfies the condition

$$\frac{r_c}{r_h} \geq 1 \tag{2}$$

(Peterson, 1988).

In practical terms, a micro heat pipe is a wickless, noncircular channel with an approximate diameter of 100–1000 μm and a length of about 10–60 mm. Figures 1(*a*) and 1(*b*) illustrate the general size and shape of a heat pipe that satisfies the criteria set forth in equations (1) and (2). As shown, the outer dimensions of this device are 1 mm by 1 mm and the length is 57 mm.

The operation of micro heat pipes is similar to that occurring in larger more conventional heat pipes. Heat applied to the evaporator region vaporizes the liquid in the evaporator. The resulting vapor flows to the cooler end through the central portion of the heat pipe, where it condenses and releases the latent heat of vaporization. This vaporization and condensation of the working fluid causes the liquid–vapor interface to change continually along the pipe, as illustrated in Fig. 1(*b*), and results in a pressure difference between the evaporator and condenser that promotes the flow of working fluid from the condenser back to the evaporator through the triangular corner regions. These corner regions serve as liquid arteries; thus no wicking structure is required. Because of the small size

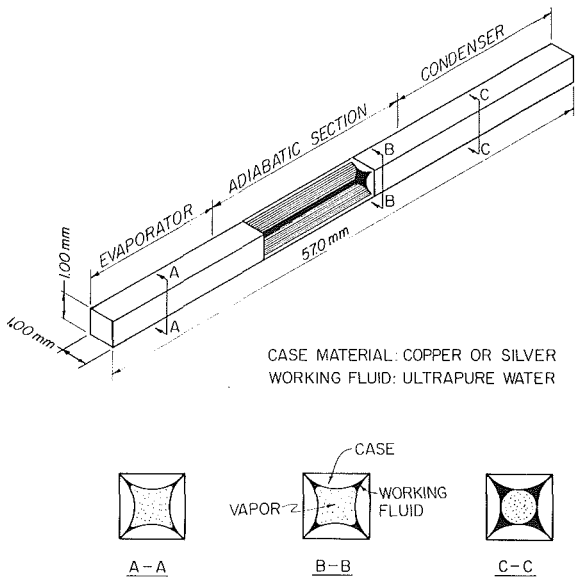

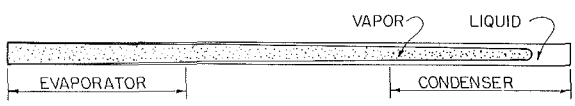

Fig. 1 Trapezoidal micro heat pipe

Contributed by the Heat Transfer Division and presented at the National Heat Transfer Conference, Houston, Texas. July 24-27, 1988. Manuscript received by the Heat Transfer Division January 20, 1989; revision received October 20, 1989. Keywords: Heat Pipes and Thermosyphons, Phase-Change Phenomena, Thermocapillary Flows.

of the heat pipe, micro heat pipes are extremely sensitive to the amount of working fluid present and care must be taken to ensure proper wetted conditions without flooding.

In order to understand better the parameters that govern the performance limitations and operating characteristics of these heat pipes, a combined analytical and experimental investigation was conducted. The objectives of this investigation were threefold; first, to verify the operation of a micro heat pipe; second, to determine whether traditional steady-state modeling techniques could be used to accurately predict the transport limits of these devices; and third, to determine the maximum heat transport capacity as a function of the physical and thermophysical properties.

Steady-State Model

Figure 2 illustrates the critical cross-sectional dimensions for the micro heat pipe studied in this investigation. Because the mean curvature of the liquid–vapor interface and the reciprocal of the hydraulic radius are of the same order of magnitude, the fundamental phenomena involved in the operation of this heat pipe may be different from those occurring in larger heat pipes. However, traditional steady-state modeling techniques can be used to formulate an initial estimate of the operational characteristics and performance limitations.

The maximum heat transport capacity of a heat pipe is governed by five different limits: the sonic limit, the entrainment limit, the boiling limit, the viscous limit, and the capillary limit. Using the techniques outlined by Chi (1976) and Dunn and Reay (1982), the sonic, entrainment, boiling, and viscous limits can be determined from

$$q_{s,m} = A_v \rho_v h_{fg} \left(\frac{\gamma_v R_v T_v}{2(\gamma_v + 1)} \right)^{1/2} \tag{3}$$

$$q_{e,m} = A_v h_{fg} \left(\frac{\sigma \rho_v}{2(r_{h,w})} \right)^{1/2} \tag{4}$$

$$q_{b,m} = \left(\frac{2\pi L_{\text{eff}} k_{\text{eff}} T_v}{h_{fg} \rho_v \ln(r_i/r_v)} \right) \left(\frac{2\sigma}{r_n} - \Delta P_{c,m} \right) \tag{5}$$

$$q_{v,m} = \frac{r_v^2 f_{fg} \rho_v P_v}{16 \mu_v L_{\text{eff}}} A_v \tag{6}$$

respectively. However, a preliminary analysis conducted by Babin et al. (1989) indicated that the heat pipe described in Figs. 1 and 2 was governed by the capillary limit for virtually all conceivable situations. For this reason, the following analysis will focus on this limit.

As is the case with larger heat pipes, the operation of micro heat pipes requires that the capillary pumping pressure be greater than the sum of all the pressure drops occurring in the flow path. This relationship can be expressed as

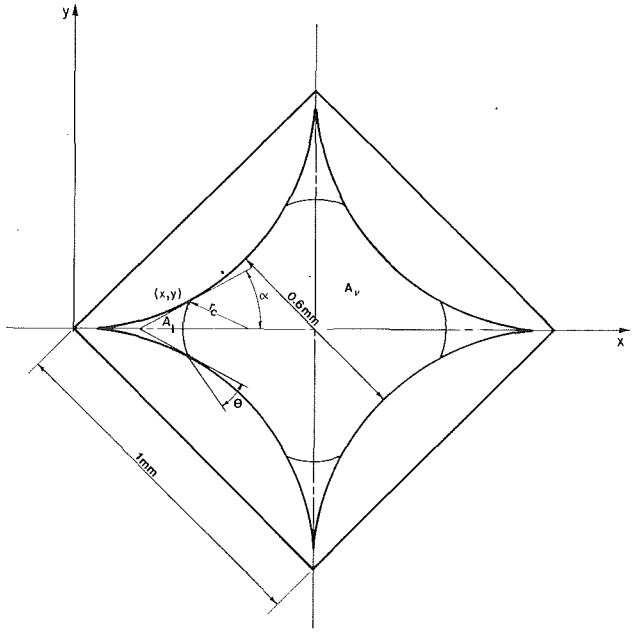

Fig. 2 Cross-sectional dimensions of the micro heat pipe

$$\Delta P_c \geq \Delta P_+ + \Delta P_\parallel + \Delta P_l + \Delta P_v \tag{7}$$

where

ΔP_c = net capillary pressure difference; ΔP_+ = radial hydrostatic pressure drop; $\Delta P_\parallel$ = axial hydrostatic pressure drop; ΔP_l = viscous pressure drop occurring in the liquid phase; ΔP_v = viscous pressure drop occurring in the vapor phase.

The conventional method for determining the capillary limitation in heat pipes has been presented by Chi (1976) and summarized by Marto and Peterson (1988). In this method each of the pressure terms in equation (7) is determined independently and then combined to yield an expression for the maximum heat transport capacity.

The net capillary pressure difference ΔP_c can be found from the LaPlace–Young equation by assuming that during steady-state operation the capillary radius of curvature in the condenser section approaches infinity. This allows the capillary pressure to be defined as a function of the surface tension σ,

Nomenclature

A = cross-sectional area
C = constant, defined in equation (18)
D = pipe diameter
f = friction factor
h_{fg} = latent heat of vaporization
$h(z/L)$ = fraction of axial heat transport
$H(L)$ = integrated value of $h(z/L)$
k = thermal conductivity
K = permeability, curvature
K' = shape factor
L = length
$\dot{m}$ = mass flow rate
M = Mach number
P = pressure
q = heat transfer
r = radius
R = gas constant
Re = Reynolds number
T = temperature
w = vapor velocity
α = half included angle
δ = average film thickness
γ = specific heat ratio
ϵ = wick porosity
θ = liquid wetting angle
μ = viscosity
ρ = density
σ = liquid surface tension
ϕ = tilt angle
ω = groove width

Subscripts

a = adiabatic
b = boiling
c = capillary, condenser
e = evaporator, entrainment
eff = effective
h = hydraulic
l = liquid
m = mean, maximum
n = nucleation
s = sonic
w = wick
v = vapor, viscous
$\parallel$ = axial
$+$ = radial

the wetting angle θ, and the radius of curvature of the liquid–vapor interface in the evaporator, r_{ce}, or

$$\Delta P_c = (2\sigma/r_{ce}) \cos \theta \tag{8}$$

The corner regions of the micro heat pipe can be approximated by a triangular groove and hence the capillary radius can be found as

$$r_{ce} = \omega/\cos \alpha \cos \theta \tag{9}$$

where ω is the groove width and α is half of the included angle.

The radial and axial hydrostatic pressure drops are the result of the body forces and can be expressed as

$$\Delta P_{+} = \rho_l g D_v \cos (\phi) \tag{10}$$

$$\Delta P_{\parallel} = \rho_l g L_p \sin (\phi) \tag{11}$$

respectively, where D_v is the vapor space diameter, L_p is the overall length of the heat pipe, and ϕ is the angle measured between the heat pipe and a line normal to the gravitational force.

The liquid pressure drop, ΔP_l, can be found by evaluating the shear forces at the liquid–solid and liquid–vapor interfaces. These forces inhibit the return of the liquid through the corner regions and can be found by integrating the pressure gradient over the length of the heat pipe. For constant heat addition and heat rejection, this yields

$$\Delta P_l = -\left(\frac{\mu_l}{K A_l h_{fg} \rho_l}\right) L_{\text{eff}} q_c \tag{12}$$

where K and L_{eff} are the permeability and the effective length, expressed as

$$K = \frac{2\epsilon (r_{h,l})^2}{(f_l \text{Re}_l)} \tag{13}$$

and

$$L_{\text{eff}} = 0.5 L_e + L_a + 0.5 L_c \tag{14}$$

respectively.

Determination of the vapor pressure drop in heat pipes is complicated by the compressibility of the vapor phase and the mass addition and removal in the evaporator and condenser. Performing a mass balance in the adiabatic region of the heat pipe ensures that for continued operation, the liquid mass flow rate and vapor mass flow rate must be equal. Because of the large difference in the density of these two phases, the velocity of the vapor phase must necessarily be significantly higher than the velocity of the liquid phase. For this reason, in addition to the pressure gradient resulting from frictional drag, the pressure gradient due to variations in the dynamic pressure must also be considered. Both Chi (1976) and Dunn and Reay (1983) have addressed this problem and found that upon integration of the vapor pressure gradient, the dynamic pressure effects cancel, resulting in an expression for the vapor pressure drop of

$$\Delta P_v = \left(\frac{C(f_v \text{Re}_v)\mu_v}{2(r_{h,v})^2 A_v \rho_v h_{fg}}\right) L_{\text{eff}} q_c \tag{15}$$

where the friction factor f_v and the constant C, which depends on the Mach number, can be determined once the local axial Reynolds number, defined as

$$\text{Re}_v = \frac{2(r_{h,v})q}{A_v \mu_v h_{fg}} \tag{16}$$

and the local Mach number, defined as

$$\text{M}_v = \frac{q}{A_v \rho_v h_{fg} (R_v T_v \gamma)} 0.5 \tag{17}$$

are known. Previous investigations summarized by Kraus and Bar-Cohen (1983) have demonstrated that for different sets of conditions, these values are

$$\text{Re}_v \le 2300, \quad \text{M}_v \le 0.2 \tag{18}$$

$$(f_v \text{Re}_v) = 16$$

$$C = 1.00$$

$$\text{Re}_v \le 2300, \quad \text{M}_v > 0.2 \tag{19}$$

$$(f_v \text{Re}_v) = 16$$

$$C = C_1 = \left[1 + \left(\frac{\gamma - 1}{2}\right) \text{M}_v^2\right]^{0.5}$$

$$\text{Re}_v > 2300, \quad \text{M}_v \le 0.2 \tag{20}$$

$$(f_v \text{Re}_v) = 0.038$$

$$C = C_2 = \left(\frac{2 r_{h,v} q}{A_v h_{fg} \mu_v}\right)^{0.75}$$

$$\text{Re}_v > 2300, \quad \text{M}_v > 0.2 \tag{21}$$

$$(f_v \text{Re}_v) = 0.038$$

$$C = C_1 C_2$$

Because the equations used to evaluate both the Reynolds number and the Mach number are functions of the heat transport capacity, it is necessary first to assume the vapor flow is laminar, substitute the individual pressure drop expressions into equation 1, and then calculate the maximum heat transport capacity $q_{c,m}$. Once this has been accomplished, the initial assumption of laminar vapor flow can be checked and the capillary limit found iteratively.

An alternative method for determining the capillary limitation was presented by Cotter (1984) when the concept of a micro heat pipe was first introduced. This method began with the momentum equation, which for steady-state parallel flow simplifies to

$$\mu \left(\frac{\partial^2 w}{\partial x^2} + \frac{\partial^2 w}{\partial y^2}\right) = \frac{dP}{dz} \tag{22}$$

Assuming uniform cross-sectional area and no-slip conditions at the boundaries, this expression can be transformed to

$$\frac{\delta w'}{\delta x'^2} + \frac{\delta w'}{\delta y'^2} = -1 \tag{23}$$

where x', y', and w' are given by

$$x = A^{0.5} x', \quad y = A^{0.5} y', \quad w = \frac{A}{\mu} \frac{dP}{dz} w' \tag{24}$$

Substituting these variables into the local mass flow equation

$$\dot{m} = \rho \int\int w dx dy \tag{25}$$

yields

$$\dot{m} = -\frac{K' \rho A^2}{8\pi\mu} \frac{dP}{dz} \tag{26}$$

where K' is a shape factor given by

$$K' = 8\pi \int\int w' dx' dy' \tag{27}$$

Values for K' have been developed by Cotter (1984) and are presented in Table 1.

Solving for the pressure differential in both the vapor and liquid cases and substituting yields

$$\frac{8\pi V_v \dot{m}_v}{K_v' A_v^2} = \frac{8\pi V_1 \dot{m}_1}{K_l' A_l^2} - \left(\frac{d}{dz}\right) \left(\frac{\sigma}{r_m}\right) \tag{28}$$

Realizing that for steady state, the local liquid and vapor mass flow rates are equal in magnitude and proportional to the local heat flux, the mass flow rate can be expressed as

$$\dot{m}_v(z) = -\dot{m}_l(z) = \frac{\dot{q}}{h_{fg}} h(z/L) \tag{29}$$

Table 1 Flow shape factor values

Shape	K'
Circle	1.000
Regular hexagon	0.964
Square	0.883
Triangle, 60-60-60	0.725
Triangle, 45-45-90	0.656
Triangle, 30-60-90	0.597

Table 2 Micro heat pipe dimensions

Length	0.05 m
Condenser length	0.0127 m
Evaporator length	0.0127 m
ω	0.000133 m
α	0.5854 rad

Table 3 Dimensionless constants

$H(L))$	0.5
K_l'	0.600
K_v'	0.975
β	2.044

where $h(z/L)$ is a function that expresses the distribution of the evaporator heat flux and $A(z)$ is the total area, expressed as

$$A(z) = A_l(z) + A_v(z) \tag{30}$$

At this point it is convenient to relate A_l and R with a geometrically determined dimensionless variable β by the equation

$$A_l = \beta^2 r^2 \tag{31}$$

Substituting equations (29)–(31) into equation (28), and solving, results in a first-order ordinary differential equation, which relates the radius of curvature to the axial position along the pipe, or

$$\frac{dr}{dz} = \frac{8\pi q r_m h(z/L)}{\sigma h_{fg}} \left(\frac{V_v}{K_v'(A - \beta^2 r_m)^2} + \frac{V_l}{K_l' \beta^4 r_m^4} \right) \tag{32}$$

If the cross-sectional area A is assumed constant, this equation is separable and therefore solvable, hence

$$q_{\max} = \left(\frac{0.16\beta(K_l' K_v')^{0.5}}{8\pi H(L)} \right) \left(\frac{\sigma h_{fg}}{V_l} \right) \left(\frac{V_l}{V_v} \right)^{0.5} \left(\frac{A^{0.75}}{L_p} \right) \tag{33}$$

where $H(L)$ is the integral of $h(z/L)$ over the length of the pipe.

Discussion of the Steady-State Modeling Results

In order to compare the previously described limitations, a computer model was developed. This model was used to determine the five limits previously mentioned, as a function of the operating temperature. The nomenclature used in the calculation of these limits along with the cross-sectional dimensions are illustrated in Fig. 2. The calculation of Cotter's capillary limit required several additional dimensionless constants. These were obtained from the original paper and for completeness are presented in Table 3. It should be noted that for both capillary limits, the heat pipes were assumed to have been charged with 0.0032 g of distilled, deionized water.

As illustrated in Fig. 3, both the conventional method and Cotter's method indicate that the capillary limit is the controlling factor in determining the maximum heat transport capacity of the micro heat pipe described in Figs. 1 and 2.

A few basic assumptions are shared in the development of the two methods used to calculate the capillary limit. These are:

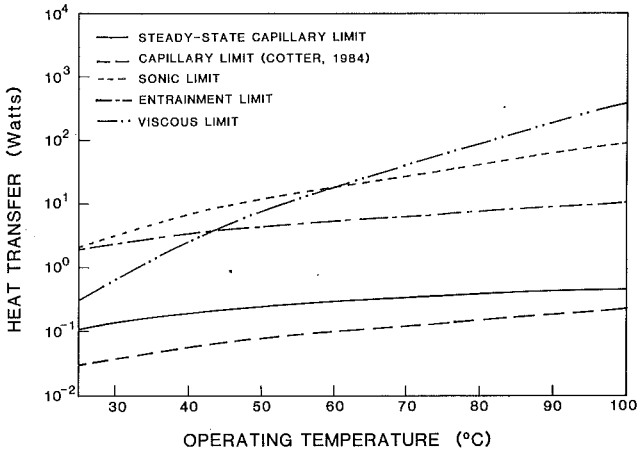

Fig. 3 Limitations of the trapezoidal micro heat pipe with water at a horizontal orientation

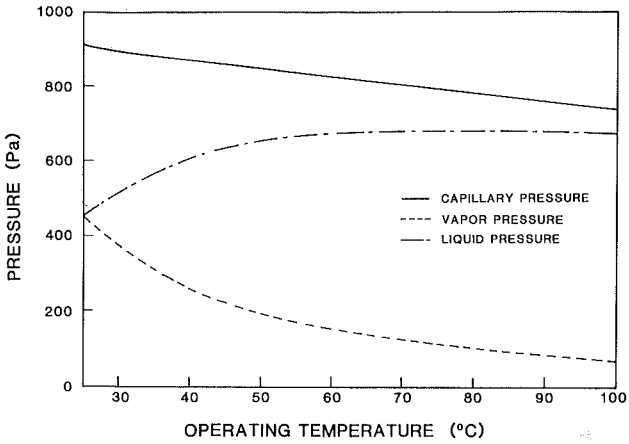

Fig. 4 Evaluation of the pressure components as a function of the operating temperature for the trapezoidal heat pipe with water at a horizontal orientation

- The heat pipe is properly charged.
- The length-to-diameter ratio is much greater than one.
- The cross-sectional area is relatively constant.
- The vapor and liquid temperatures are equal.

Further, the method proposed by Cotter (1984) assumes:

- Gravity is negligible.
- The local axial heat transfer is specified.
- The liquid–vapor interface velocity is zero.
- The vapor flow regime is both laminar and incompressible.

To determine the significance of the gravitational forces, Figs. 4, 5, and 6 are provided. For the case of a horizontal heat pipe with water as the working fluid, Fig. 4, the gravitational effects are clearly negligible. However, when the temperature is held constant and the tilt angle is varied, Fig. 5, the gravitational effects become significant. Figure 6 illustrates how the performance of the micro heat pipe as predicted by the conventional method diminishes with increasing adverse tilt. Together, these three figures indicate that gravity has a significant effect on the capillary limit and cannot be neglected.

The assumption that the local axial heat transport is specified results in the parameter, $H(L)$, which must be known a priori to predict the maximum transport capacity. In this sense, it behaves as a correction factor, which can be varied to simulate the experimental results better. Figure 7 illustrates the effect of this parameter on the capillary limit, as predicted by Cotter (1984). As shown, variation of this parameter results in a significant change in the predicted transport capacity, with a

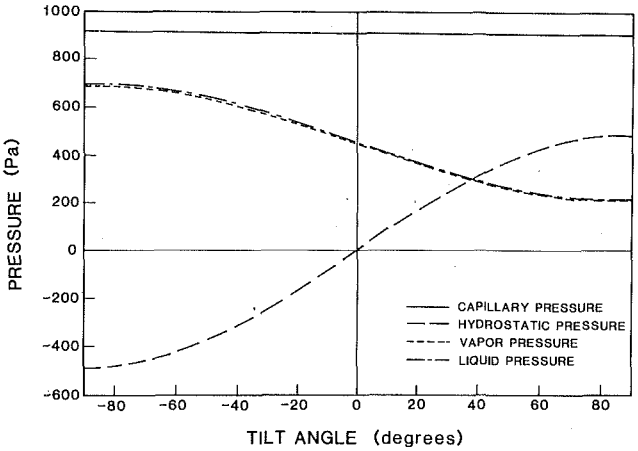

Fig. 5 Evaluation of the pressure components as a function of the tilt angle for the trapezoidal heat pipe with water at 25°C

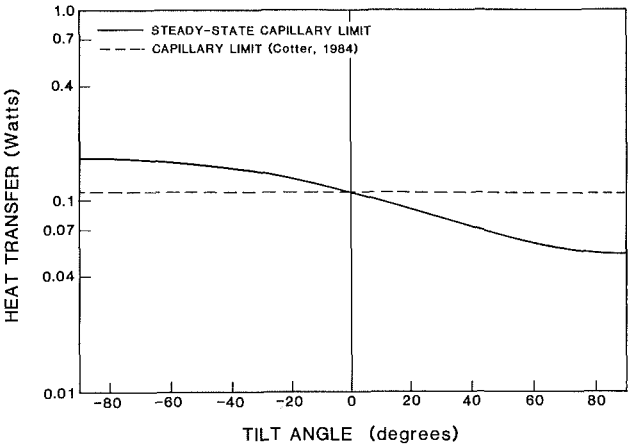

Fig. 6 Comparison of the capillary limits as a function of the tilt angle for the trapezoidal heat pipe with water at 25°C

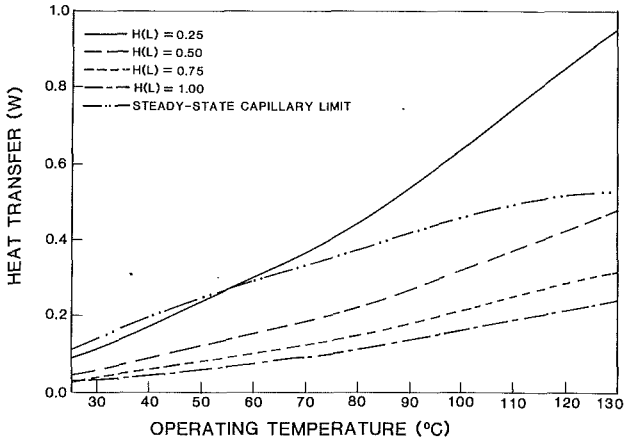

Fig. 7 Effect of variations in the local axial heat flux model (Cotter, 1984) on the maximum heat transport capacity

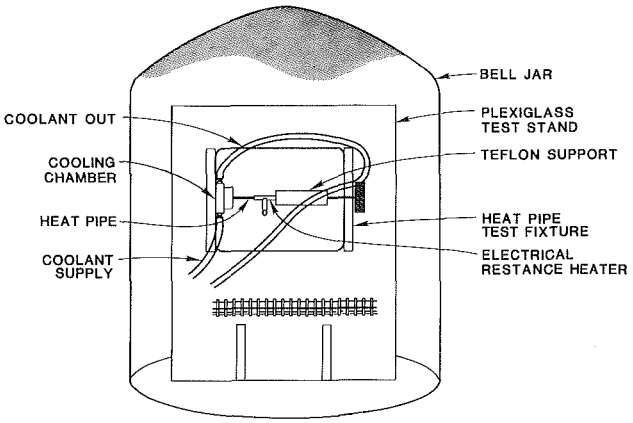

Fig. 8 Experimental test facility

value of 0.25 resulting in the closest correlation between the two techniques at operating temperatures below 60°C.

The remaining two assumptions made in the model developed by Cotter (1984) have little effect on the predicted capillary limit. The first of these, that the liquid-vapor interface velocity is zero, introduces some error; however, because the vapor velocity is relatively low the error is small. The second, the assumption that the vapor flow regime is both laminar and incompressible, was found to be both reasonable and appropriate for all the cases evaluated.

Experimental Program

To determine the accuracy of the modeling techniques, verify the micro heat pipe concept, and determine the maximum heat transport capacity, two test pipes were constructed, one from silver and one from copper. Both test pipes were charged with 0.0032 g of distilled, deionized water and were evaluated experimentally. In addition, two uncharged test pipes, one each of copper and silver, were evaluated to determine the amount of heat conducted through the wall to establish a baseline value for evaluating the improvement in performance due to the vaporization and condensation of the working fluid.

Description of Experimental Apparatus. A test facility consisting of five subsystems—the test stand, a variable heat source, a constant-temperature cooling source, a data acquisition system, and a vacuum system—was constructed for the experimental investigation. The test stand, shown in Fig. 8, was constructed from Plexiglas and provided a means for rotating the test pipes through an angle of 360 deg. In this way, tests could be conducted at tilt angles that both helped and hindered the return of liquid back to the evaporator. The test stand also supported an aluminum cooling chamber, which surrounded the condenser region of the heat pipe. A circulating bath provided a constant-temperature ethyl-glycol solution to the cooling chamber, where it flowed over the condenser portion of the heat pipe at a constant rate of approximately 10 liters/min. The evaporator portion of the heat pipe was surrounded by a copper heat spreader, 0.635 cm in diameter and 1.27 cm in length. Heat was supplied by a 5-W electric resistance heater mounted on the surface of the heat spreader and the power was monitored by measuring the voltage and current to the heater.

Two separate techniques were used to monitor the temperature distribution of the heat pipe. The first of these consisted of a series of Chromel-Alumel (AWG 36) thermocouples. Three thermocouples were attached to the outer surface of the heat pipe at equidistant positions on the evaporator: one at the end of the pipe, one at the end of the evaporator, and one midway between. Three additional thermocouples were used, one on the outer surface of the condenser, one on the outer surface of the adiabatic section, and one at the inlet to the cooling chamber.

The second technique used to monitor the temperature distribution was an infrared thermal measurement system. A Hughes Probe Eye TVS Model 3000 Infrared Camera in conjunction with an RGB monitor and a real time recorder were used to observe the temperature profile of the test pipe during both startup and steady-state operation. Using this system, the

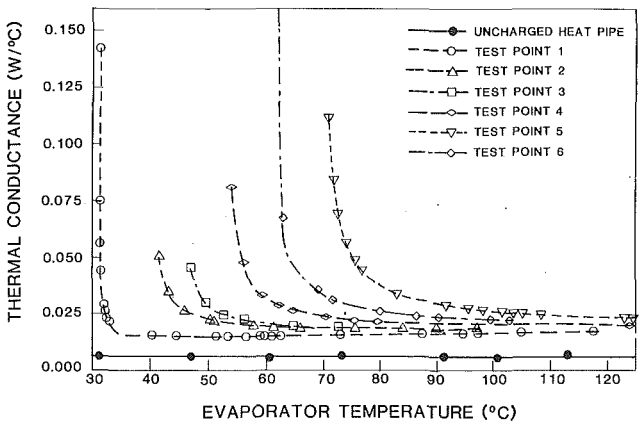

Fig. 9 Measured thermal conductance of a trapezoidal micro heat pipe as a function of the evaporator temperature (copper, 0.0032 g charge)

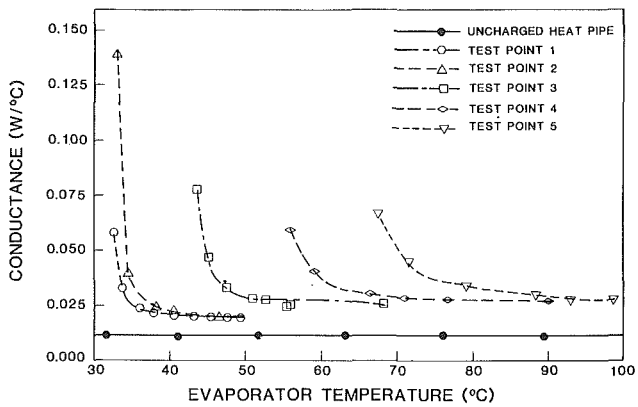

Fig. 10 Measured thermal conductance of a trapezoidal micro heat pipe as a function of the evaporator temperature (silver, 0.0032 g charge)

temperature distribution along the heat pipe could be measured with an accuracy of $\pm 0.1°C$.

To reduce any heat losses through convection, the tests were conducted in a vacuum of $> 10^{-2}$ Torr. The entire test facility was encased in a stainless steel vacuum chamber equipped with a single crystal silicon window to allow observation with the thermal measurement system. A mechanical roughing pump in series with an oil diffusion pump was used to obtain the required vacuum.

Experimental Procedure. The heat pipe was first instrumented with the thermocouples and all surfaces were painted with a flat black paint of known emissivity to enhance the infrared resolution. The test fixture was placed in the vacuum chamber and the constant temperature bath adjusted to the desired temperature. The bell jar was lowered, the vacuum pump was turned on, and the test facility was allowed to outgas for a minimum of twelve hours.

When the desired vacuum had been obtained, the input heat flux was increased in small increments until the desired operating temperature had been reached. Preliminary tests indicated that a time of approximately 20 min. was necessary for the heat pipe, cooling chamber, and heat spreader to reach steady state. Once steady state had been reached, the temperature data as measured by both the infrared camera and the thermocouples were recorded along with the time, data, power level, and coolant bath temperature.

To obtain the data for the next successive power level, the heat flux was incremented and the temperature of the coolant bath adjusted in order to maintain a constant vapor temperature as measured by the thermocouple attached to the outer surface of the adiabatic section. This procedure was followed until the conductance of the heat pipe, defined as the measured input power divided by the measured temperature difference between the evaporator and the condenser sections, approached a constant value and was then repeated for each new operating temperature.

Discussion of Results

Figure 9 illustrates the results obtained for a copper heat pipe of the dimensions shown in Figs. 1 and 2, operating in a horizontal orientation and charged with 0.0032 g of water. The heat pipe was evaluated at a total of six operating temperatures, 30.8°C, 39.5°C, 43.8°C, 51.6°C, 58.9°C, and 67.6°C, one operating temperature for each set of test points. As shown, the thermal conductance of the pipe decreased rapidly with respect to the evaporator temperature and asymptotically approached a constant value somewhat above the values obtained for an uncharged pipe. With the exception of the slightly decreasing difference between the ultimate conductance value of the test pipe and the conductance of the uncharged pipe, this behavior is precisely what would be expected for a heat pipe in which the evaporator is slowly drying out. Increases in the input power initially cause the liquid meniscus to recede into the liquid channels located in the corners of the heat pipe. This results in a decrease in the radius of curvature of the liquid–vapor meniscus, a corresponding decrease in the cross-sectional area of the liquid, and hence, a slight increase in the evaporator temperature. The receding of the meniscus continues with increasing power, until dryout of the evaporator occurs.

The slightly decreasing difference between the ultimate conductance value of the test pipe and the conductance of the uncharged pipe results from an increase in the effective size of the evaporator. Prior to dryout, all the vaporization occurs in the evaporator region. Once dryout begins, the temperature of the heat pipe wall in the adiabatic section increases and a small part of what was formerly the adiabatic section begins to act as an evaporator. As the power continues to increase, the dryout in the evaporator spreads and the portion of the adiabatic section that behaves as an evaporator expands. In the extreme case where complete dryout of the evaporator section occurs, a large portion of the adiabatic section may behave as an evaporator and may even begin to dry out at the end farthest from the condenser.

Figure 10 illustrates the results for the various test points obtained for a silver heat pipe of the same dimensions, charged with 0.0032 g of water. The test conditions were similar; however the operating temperatures at which the silver heat pipe was evaluated were 31.8°C, 32.3°C, 42.0°C, 52.2°C, and 62.8°C. As shown, the trends and tendencies are all similar to those of the copper pipe tested.

In order to compare the results of the experimental investigation with those predicted by the analytical model, it was necessary to develop a method for determining the point at which dryout begins. The experimental data presented in Figs. 9 and 10 clearly display a change in the operation of the two test pipes as the operating temperature and power levels were increased. After reviewing the experimental data, an attempt was made to identify and quantify better the onset of dryout. Because, as discussed previously, there was no clearcut division between the evaporator and condenser, this proved to be quite difficult.

Several strategies were employed, including development of a mathematical method for determining the maximum curvature for each operating temperature. The final approach used was to select a region on both sides of the point of maximum curvature, that is a range around the point at which the most rapid change of the conductance occurs with respect to evaporator temperature. This range was assumed to be the region

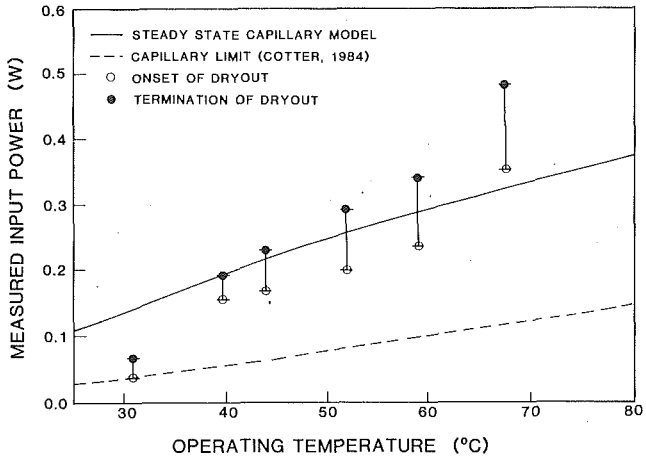

Fig. 11 Comparison of the maximum heat transport capacity of a trapezoidal micro heat pipe as a function of the operating temperature (copper, 0.0032 g charge)

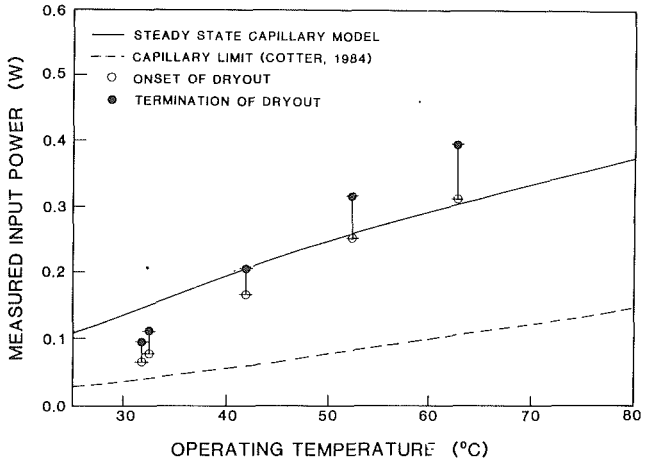

Fig. 12 Comparison of the maximum heat transport capacity of a trapezoidal micro heat pipe as a function of the operation temperature (silver, 0.032 g charge)

over which dryout occurred. The initial point, which will be referred to as the onset of dryout, was identified as that point where the slope of a line tangent to the curve was 60 deg. The termination of dryout was assumed to occur at that point where slope of the tangent line was 30 deg. Although this would appear to be a large range, in reality it is probably reasonably close to the actual behavior, since dryout is a gradual process and unlike the sonic or boiling limit, develops quite slowly.

Figures 11 and 12 illustrate the results of this process and compare the measured input power to the heat pipe evaporator, with the maximum heat transfer capacity as predicted by the conventional model for the copper and silver test pipes, respectively. As shown, at low operating temperatures, the steady-state capillary model overpredicts the experimentally determined maximum heat transport capacity by approximately 15 percent for both the copper and silver test pipes. Between operating temperatures of 40°C and 60°C, the model predicts dryout with a reasonable degree of accuracy, and above 60°C the model slightly underpredicts dryout.

If the corners of the trapezoidal heat pipe are assumed to be in the shape of equilateral triangles, $H(L)$ is 0.5, and the maximum heat transport capacity can be determined using the model developed by Cotter (1984). As shown, the limit as predicted by the Cotter model is significantly lower than those obtained experimentally. It should be noted that variations in the value of $H(L)$ can significantly affect the maximum heat transport capacity, as shown previously in Fig. 7 with values of $H(L)$ of 0.25 or 1.00, either improving the accuracy of the prediction or underestimating even further the power at which dryout occurs, respectively.

Conclusions

The steady-state experimental results obtained in this investigation provide experimental verification of the trapezoidal micro heat pipe concept and indicate that the steady-state model can be used to predict accurately the level of performance. Although additional work is required to determine the reasons for the difference in slope of the predicted and measured heat transport limits, the steady-state model can also be used to assess accurately the effects of variations in the physical geometry, the type of working fluid, and the power levels. While predicting the trend correctly, the Cotter model requires that accurate estimations of the value of $H(L)$ be known in advance. Because of the high conductivity associated with heat pipes, it is recommended that values of $H(L)$ equal to or greater than 0.5 should be used.

Since variations in the way the dryout phenomenon is defined can significantly increase or decrease the experimentally determined values, the discrepancy between the measured and predicted values may in part be due to the technique used to define dryout. As a result, the perceived accuracy of the models is strongly dependent upon the way dryout is defined. To resolve this problem, it is necessary to understand the dryout phenomenon better and define more clearly when it begins and how it proceeds.

Although the two analytical models developed have been shown to predict the steady-state performance limitations and operational characteristics with a reasonable degree of accuracy, no experimental data on the transient operational characteristics were obtained. In addition, several factors that significantly affect both the steady-state and transient behavior require continued study.

Acknowledgments

Funding for this investigation was provided by the Itoh Research and Development Corp., Osaka, Japan, the Texas Higher Education Coordinating Board (ATP), and the TAMU Center for Space Power, under Contract No. RF 2005-5. The authors would like to acknowledge Dr. J. E. Beam for his support and guidance throughout the completion of this work.

References

Babin, B. R., Peterson, G. P., and Wu, D., 1989, "Analysis and Testing of a Micro Heat Pipe During Steady-State Operation," presented at the ASME National Heat Transfer Conference, Philadelphia, PA, Aug. 5–8, Paper No. 89-HT-17.

Chi, S. W., 1976, *Heat Pipe Theory and Practice*, McGraw-Hill, New York.

Cotter, T. P., 1984, "Principles and Prospects of Micro Heat Pipes," *Proc. 5th Int'l. Heat Pipe Conf.*, Tsukuba, Japan, pp. 328–335.

Dunn, P. D., and Reay, D. A., 1982, *Heat Pipes*, 3rd ed., Pergamon Press, New York.

Kraus, A. D., and Bar-Cohen, A., 1983, *Thermal Analysis and Control of Electronic Equipment*, McGraw-Hill, New York.

Marto, P. J., and Peterson, G. P., 1988, "Chapter 4—Application of Heat Pipes to Electronics Cooling," *Advances in Thermal Modeling of Electronic Components and Systems*, A. Bar-Cohen and A. D. Kraus, eds., Hemisphere, Washington, DC, pp. 283–336.

Peterson, G. P., 1988, "Investigation of Miniature Heat Pipes," Final Report, Wright Patterson AFB, Contract No. F33615-86-C-2733, Task 9.

Rice, G., and Fulford, D., 1987, "Influence of a Fine Mesh Screen on Entrainment in Heat Pipes," *Proc. 6th Int'l. Heat Pipe Conf.*, Genoble, France, pp. 168–172.

Experimental Investigation of a Flexible Bellows Heat Pipe for Cooling Discrete Heat Sources

B. R. Babin
Research Assistant.
Student Mem. ASME

G. P. Peterson
Professor of Mechanical Engineering,
Mem. ASME

Texas A&M University,
College Station, TX 77843

A computer model was developed to aid in the design of a flexible bellows heat pipe for cooling small discrete heat sources or arrays of small heat sources. This model was used to evaluate the operational characteristics and performance limitations of these heat pipes and to formulate and optimize a series of conceptual designs. Three flexible bellows heat pipes approximately 40 mm in length and 6 mm in diameter were constructed and tested using three different wick configurations. The test pipes were found to be boiling limited over most of the operating temperature range tested. Heat fluxes in excess of 200 W/cm^2 were obtained and thermal resistance values of less than 0.7 °C/W were measured. Although the computer model slightly underestimated the experimentally determined transport limit for one of the wicking configurations, the remaining transport predictions were consistently within 8 percent of the experimental values.

Introduction

Frequently it is necessary to cool small discrete heat sources or an array of small heat sources without allowing the heat sources to come into direct contact with the cooling fluid. In many such applications, it may be possible to utilize the high effective thermal conductivity of a heat pipe to provide the thermal connection between the heat source and the coolant. Figure 1 illustrates an example of this type of application. The heat pipe shown utilizes a flexible metal bellows to make the device more compliant, a radial condenser to maximize the heat rejection area, and an axial evaporator to reduce the overall size. The overall thermal resistance of this device is comprised of the internal resistance of the heat source, the contact resistance between the heat source and the bellows heat pipe, the resistance of the heat pipe, and the convective resistance between the condenser portion of the heat pipe and the coolant.

In addition to a high thermal conductivity, these flexible bellows heat pipes offer several other advantages. First, the inherent flexibility of the bellows portion of the heat pipe compensates for any misalignment between the heat source and the heat pipe evaporator. Second, because the operating temperature of the heat pipe controls the internal pressure and hence the axial force exerted on the heat source, higher thermal power levels result in higher contact pressures. These higher contact pressures improve the contact at the heat source/heat pipe interface and therefore decrease the contact resistance.

In order to understand better and hence improve the performance characteristics and operating limits of this type of device, three small heat pipes with flexible bellows sections were designed, constructed, and evaluated. To assist in the design of the test pipes, an analytical model was developed using traditional steady-state modeling techniques.

Analysis

When heat is applied to the evaporator end of a heat pipe, the liquid is vaporized and the resulting vapor flows to the opposite end of the pipe due to the high pressure caused by the increase in temperature. On reaching the cooler condenser portion of the heat pipe, the vapor condenses and releases the latent heat of vaporization. The liquid then returns to the evaporator region through the wick due to the pressure imbalance between the liquid vapor interface at the condenser and the evaporator. This process continues until the pressure imbalance is insufficient to cause the return of the liquid to the evaporator. This so-called capillary limit along with the viscous, sonic, boiling, and entrainment limits must all be evaluated in order to determine the maximum transport capacity for a given heat pipe (Kraus and Bar-Cohen, 1983).

Using the techniques presented by Chi (1976) and summarized by Marto and Peterson (1988), a computer model capable of determining the maximum heat transport capacity for a small flexible bellows heat pipe was developed. Because the maximum heat transport capacity is a function of the capillary, boiling, entrainment, sonic, and viscous limitations, the model evaluated each of these limits individually while varying the physical parameters, tilt angle, working fluid, wicking structure, and operating temperature. In this manner, the effects of design modifications could be evaluated and the steady-state operational characteristics and transport limits improved.

Transport Limitations. For continuous operation, the net capillary pressure difference across the liquid–vapor interface in a heat pipe must be greater than the pressure losses throughout the liquid and vapor flow paths. This relationship, as presented by Chi (1976), can be expressed as

$$\Delta P_c \geq \Delta P_+ + \Delta P_\parallel + \Delta P_l + \Delta P_v \tag{1}$$

where ΔP_c = net capillary pressure difference; ΔP_+ = normal hydrostatic pressure drop; $\Delta P_\parallel$ = axial hydrostatic pressure drop; ΔP_l = viscous pressure drop occurring in the liquid phase; ΔP_v = viscous pressure drop occurring in the vapor phase.

Substituting the relationships for each pressure term and simplifying yields an expression for the capillary limited heat flux of

$$q_{c,m} = \frac{\left(\frac{2\sigma}{r_{ce}}\right) - \rho_l g (d_v \cos \Psi - L \sin \Psi)}{\mu_l \left(\frac{L_{\text{eff}}}{K_{wa} A_{wa} \lambda \rho_l} + \frac{1}{4\pi K_{we} \rho_l \delta_w \lambda}\right) + \left(\frac{C(f_v \text{Re}_v)\mu_v}{2(r_{h,v})^2 A_v \rho_v \lambda}\right)} \tag{2}$$

(Peterson, 1988).

Aside from the retention of liquid in the convolutions of the bellows, which increases the amount of liquid charge re-

Contributed by the Heat Transfer Division for publication in the JOURNAL OF HEAT TRANSFER. Manuscript received by the Heat Transfer Division January 20, 1989; revision received October 20, 1989. Keywords: Heat Pipes and Thermosyphons, Phase-Change Phenomena, Thermocapillary Flows.

quired, the presence of the bellows has little effect on the operation or transport limitations of the heat pipe. Hence, the liquid friction factor in the bellows region (which in the experimental tests discussed later was always lined with two layers of wire mesh) was assumed to be similar to that of a cylinder of the same diameter, lined with a wire mesh wicking material. The remaining characteristics, such as the permeability K, the capillary radius r_{ce}, and the flow regime constant C, can be determined as outlined by Chi (1976) and Dunn and Reay (1982).

During steady-state operation, the liquid mass flow rate must equal the vapor mass flow rate and while the liquid flow regime is always laminar, the vapor flow may be either laminar or turbulent. Therefore it was necessary to determine the vapor flow regime as a function of the heat flux. This was accomplished by evaluating the local axial Reynolds and Mach numbers, both of which are functions of the axial heat transport capacity. Assuming laminar vapor flow, equation (2) was solved for the maximum heat capacity $q_{c,m}$. This value was used to compute the vapor Reynolds number and Mach number to determine the validity of the original assumption. This iterative approach, covered in more detail by Chi (1976), was used to determine the capillary limitation as a function of the operating temperature.

Once the capillary limit has been determined, values for the sonic, entrainment, and boiling limits were evaluated from

$$q_{s,m} = A_v \rho_v \lambda \left(\frac{\gamma_v R_v T_v}{2(\gamma_v + 1)} \right)^{1/2} \tag{3}$$

$$q_{e,m} = A_v \lambda \left(\frac{\sigma \rho_v}{2(r_{h,w})} \right)^{1/2} \tag{4}$$

$$q_{b,m} = \left(\frac{A_v k_{\text{eff}} T_v}{\lambda \rho_v \delta} \right) \left(\frac{2\sigma}{r_n} - \Delta P_{c,m} \right) \tag{5}$$

respectively. Again, because the bellows was lined with a screen wick material, the presence of the bellows convolutions had little effect on these limits.

Effective Thermal Resistance. The temperature difference between the evaporator and condenser of a heat pipe is of interest in determining its suitability for a particular application. This temperature difference can be found by evaluating the overall thermal resistance of the heat pipe, which as shown in Fig. 1 is made up of nine internal resistances. A study by Asselman and Green (1973) demonstrated the significance of each of these resistances and indicated that because of the relative magnitudes, several can be neglected.

For the heat pipe investigated here, the resistance of the vapor in the adiabatic section, R_{va}, is so low compared to the axial resistance of the pipe wall, R_{pa}, and the resistance of the liquid/wick combination, R_{wa}, that it can be considered a closed circuit and negligible. The resistances of the liquid/vapor interfaces at the evaporator and the condenser, R_{ie} and R_{ic}, respectively, are also negligible. This leaves the resistance of the pipe wall at the evaporator and condenser, R_{pe} and R_{pc}, and the resistance of the liquid/wick combination at the evaporator and condenser, R_{we} and R_{wc}, acting in series to comprise the total resistance of the heat pipe. These four terms can be evaluated as follows:

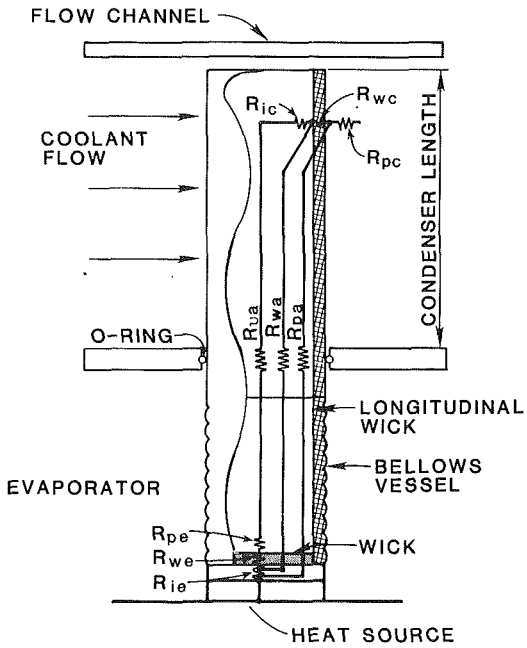

Fig. 1 Flexible bellows heat pipe

$$R_{pe} = \frac{\delta}{k_p A_e} \tag{6}$$

$$R_{we} = \frac{\delta_w}{k_e A_e} \tag{7}$$

$$R_{wc} = \frac{\ln(d_o/d_i)}{2\pi L_c k_c} \tag{8}$$

$$R_{pc} = \frac{\ln(d_o/d_i)}{2\pi L_c k_p} \tag{9}$$

where the thermal conductivities of the evaporator and condenser wicks, k_e and k_c, respectively, are calculated by the

Nomenclature

A = area, m^2
C = constant, defined in text
d = diameter, m
f = drag coefficient
k = thermal conductivity, W/m-K
K = wick permeability, m^2
L = length, m
M = Mach number
P = pressure, Pa
q = heat flow rate, W
R = thermal resistance, K/W; or universal gas constant, J/kg-K
Re = Reynolds number
r = radius, m
T = temperature, K
γ = specific heat ratio
δ = evaporator wick thickness, m
λ = latent heat of vaporization, J/kg
μ = dynamic viscosity, kg/m-s
ρ = density, kg/m^3
σ = surface tension, N/m
Ψ = angle of inclination, deg or rad

Subscripts

a = adiabatic section, air, axial
b = boiling
c = capillary, capillary limitation, condenser section
e = entrainment, evaporator section
eff = effective
h = hydraulic
i = inner
l = liquid
m = maximum
n = nucleation
o = outer
p = pipe
r = radial
s = sonic or sphere
w = sire spacing, wick
v = vapor
$\parallel$ = axial hydrostatic pressure
$+$ = normal hydrostatic pressure

techniques outlined by Chi (1976). Once the total resistance has been calculated, the temperature difference between the evaporator and the condenser can be determined from

$$\Delta T = Rq_m \tag{10}$$

The computer model combined equations (1)–(10) and was used to determine the optimum physical dimensions, working fluid, and wicking structure of a flexible bellows heat pipe, given the approximate heat source size and operating temperature range.

Experimental Investigation

Using the computer model described above, three small flexible heat pipes similar to that shown in Fig. 1 were designed, constructed, and tested. Four candidate working fluids were considered: ammonia, water, acetone, and methanol. The three test pipes were constructed sequentially, with information from the computer model and previous experimental tests used to improve the design and performance of each of the subsequent test pipes. Although the modeling results indicated that ammonia offered the highest heat transport capacity (Peterson, 1988), water was selected as the working fluid for all three test pipes due to the lower vapor pressures.

Test Article Description. The overall size, shape, and construction techniques were similar for all three test pipes, and each utilized an axial evaporator and a circumferential condenser. The first test pipe, shown in Fig. 2, was 6.27 mm in diameter and 38.2 mm in length. Heat addition to the evaporator portion of the test pipe occurred through the end face, while heat rejection occurred radially in the circumferential wick. The evaporator wick was constructed from two 4.76-mm-dia disks cut from 200 mesh copper wire screen and placed in one end of the bellows vessel. A rectangular piece of 200 mesh copper wire screen 15 mm × 38.3 mm was cut and rolled into a cylinder two layers thick. This cylinder formed the longitudinal wick in both the bellows (adiabatic) and the condenser sections.

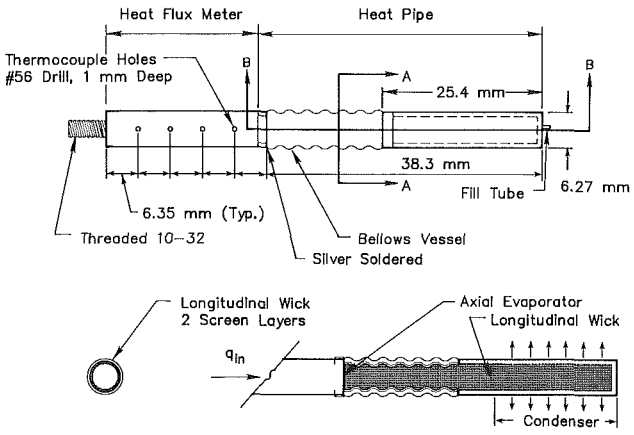

Fig. 2 Size and shape of the first test pipe

The bellows vessel used in the first test pipe had an outer diameter of 6.27 mm, an inner diameter of 4.76 mm, was 12.9 mm long, and had a maximum extension of 1.6 mm. It was constructed from Nickel 200 with a wall thickness of 43.18 μm and maximum rated pressure of 0.20 MPa. The spring rate as specified by the manufacturer was 0.0357 kg/mm ± 30 percent.

Once the condenser and heat flux meter, which were made from a single piece of oxygen-free copper rod, had been machined and the wick cut to the proper size, one end of the bellows vessel was silver soldered to the heat flux meter. After cleaning and assembling the components, the other end of the bellows vessel was silver soldered to the condenser portion of the heat pipe. Following assembly, the heat pipe was rinsed several times with acetone and once in a solution of 50 percent phosphoric acid and 50 percent nitric acid. After this final rinse, the heat pipe was vacuum baked, evacuated, and charged with the proper amount of fluid through a small fill tube located in the end of the condenser. The fill tube then was sealed by crimping and soldering.

An indicated in Table 1, the second and third test pipes were larger in both inner and outer diameters, and slightly longer in overall length than the first. In addition, the bellows vessels used for these two test pipes were slightly larger and were constructed from Stainless Steel 304 and had a thin layer of vapor-deposited copper on the inside surfaces to retard the formation of noncondensible gases. This resulted in a wall thickness of 101.6 μm and maximum rated pressure of 0.40 MPa. The spring rate as specified by the manufacturer was 0.086 kg/mm ± 20 percent.

The longitudinal wicking structure for both the second and third test pipes was constructed in a manner similar to that described for the first test pipe; however, two layers of 100 mesh copper wire screen were used. Other than the size difference, the other major difference was in material from which the evaporator wicks were constructed. For the second and third test pipes a sintered copper powder was used instead of a screen mesh. The physical properties for all the wicking materials used in the three test pipes are listed in Table 2.

Test Facility. The experimental test facility, shown in Fig. 3, consisted of five subsystems: the test pipe, a heat source, a heat sink, a temperature measurement system, and a vacuum system. The test pipe was mounted on a frame constructed of

Table 1 Heat pipe dimensions

Test article	Heat pipe: Overall length	Heat pipe: Outer diameter	Heat pipe: Inner diameter	Bellows: Length	Bellows: Outer diameter	Bellows: Inner diameter	Bellows: Wall thickness	Bellows: Spring constant
1	38.3 mm	6.27 mm	4.76 mm	12.9 mm	6.27 mm	4.76 mm	43.18 μm	0.357 kg/mm
2	38.1 mm	7.94 mm	6.16 mm	12.7 mm	7.94 mm	6.16 mm	101.6 μm	0.086 kg/mm
3	38.1 mm	7.94 mm	6.16 mm	12.7 mm	7.94 mm	6.16 mm	101.6 μm	0.086 kg/mm

Table 2 Properties of the wick

Test article	Wick	Wire diameter	Powder size	Porosity (percent)	Permeability ($m^2 \times 10^{-10}$)	Pore radius ($m \times 10^4$)
1	Evaporator	0.053 mm	--	0.65	5.43	6.35
	Condenser	0.053 mm	--	0.65	5.43	6.35
2	Evaporator	--	−100 +325	0.5	0.1	0.40
	Condenser	0.109 mm	--	0.65	2.09	1.30
3	Evaporator	--	−140 +170	0.5	0.06	0.98
	Condenser	0.109 mm	--	0.65	2.09	1.30

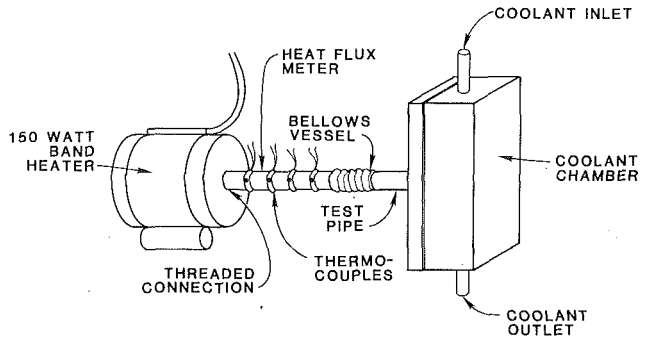

Fig. 3 Experimental test facility

Lexan and capable of being adjusted to provide 180 deg of rotation. Heat was provided by a 100-W electrical resistance band heater attached to the outer surface of a 2.54-cm-dia heat block 2.54 cm long. Input power to the electrical resistance heater was monitored by two multimeters, which measured the voltage and current.

To eliminate the thermal contact resistance between the evaporator end of the heat pipe and the heat source, the evaporator and the heat source were connected by a heat flux meter constructed from a piece of copper rod the same diameter as the heat pipe and 37 mm long. The evaporator wick and bellows vessel were mounted directly on one end of the heat flux meter and the other end was threaded to fit into the heat block. Four Chromel-Alumel (AWG 36) thermocouples were peened into 1-mm-deep holes located at 6.35-mm intervals along the surface of the heat flux meter. To improve the measurement accuracy of the thermocouples, each thermocouple was wrapped around the outer surface one time. Using the known thermal conductivity of the copper rod and the measured temperatures, both the axial heat flux and the evaporator temperature could be calculated.

The condenser portion of the heat pipe was cooled by a water-glycol solution flowing through a constant-temperature circulating bath with a nominal flow rate of 10 liters/min. In order to monitor the condenser temperature, a thermocouple was attached to the end of the heat pipe condenser with a thermally conductive epoxy. Once assembled and instrumented, the condenser portion of the heat pipe was inserted into a coolant chamber with internal dimensions of approximately 16 mm × 25.4 mm. A 2-mm Vitron O-ring was used to seal between the heat pipe and the coolant chamber and prevented the heat pipe from making direct contact with the coolant chamber. Throughout the tests, the temperature and flow rate of the constant-temperature circulating bath were adjusted so that the external condenser temperature, as measured by the thermocouple located at the end of the condenser, was 25°C.

In addition to the four thermocouples on the heat flux meter and the one at the end of the condenser, two thermocouples were attached to the test pipe, one on the external surface of the bellows vessel and one on the external surface of the heat pipe at the inlet to the condenser.

A computerized data acquisition system was used to monitor both the power and the temperature distribution during the tests. Prior to testing, the thermocouples and data acquisition system were verified at the freezing point and atmospheric boiling point of water and found to be accurate to within ±0.1 K. This information when combined with the instrumentation and placement error of the thermocouples resulted in an experimental uncertainty of ±8 percent for the thermal conductance of the heat pipe.

During the course of the experimental program, several series of tests were conducted at a vacuum of less than 5×10^{-3} Torr to determine the effect of convection losses from the outside of the test pipe and heat flux meter. There was a

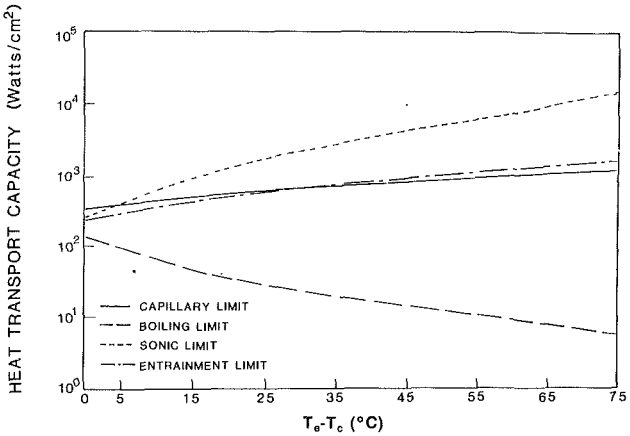

Fig. 4 Predicted limitation of the first test pipe as constructed

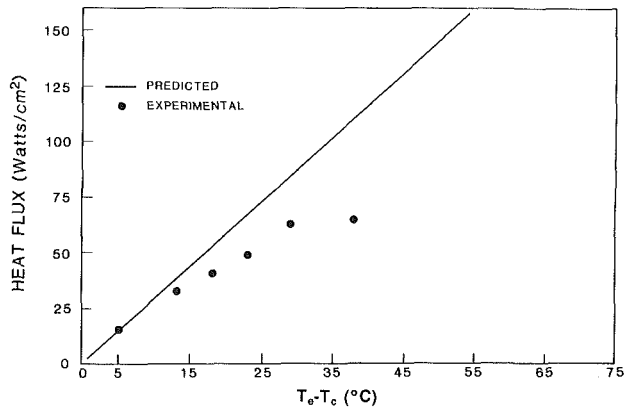

Fig. 5 Comparison of the measured and predicted transport capacity of the first test pipe

difference of less than 4 percent between the tests conducted in a vacuum and those conducted with the heat pipe insulated and in an atmospheric environment. Because of the complexity of the vacuum tests, the remaining data, and hence all of the data presented here, were collected in an atmospheric environment.

Experimental Procedure. After mounting a test pipe on the fixture and attaching the heater, thermocouples, and coolant chamber, tests were conducted at horizontal, 45 deg-evaporator down and 90 deg-evaporator down, orientations. With a step size of approximately 5 W, measurements were taken at eight-hour intervals in order to allow the heat pipe to reach steady-state conditions. The temperature and flow rate of the circulating bath were adjusted to maintain a condenser temperature of 25°C. Power levels adequate for a temperature drop across the heat pipe of approximately 85°C were tested.

Each of the three test pipes was evaluated using a condenser length of 1.27 cm. On completion of these tests, the second test pipe was re-evaluated with a condenser length of 2.54 cm to determine the effect of condenser length on both the maximum transport capacity and the overall thermal resistance.

Discussion of Results

Figure 4 illustrates the predicted heat transport capacity and associated limitations for the first heat pipe in a horizontal orientation with water as the working fluid. As illustrated, the test pipe is entirely boiling limited and the maximum transport capacity occurs at the minimum evaporator temperature. Figure 5 compares the predicted heat transport capacity and the results of the experimental tests. As shown, the results follow a trend similar to that predicted, up to an evaporator temperature of approximately 55°C. Additional testing indicated that some degradation of the wicking structure and/or working

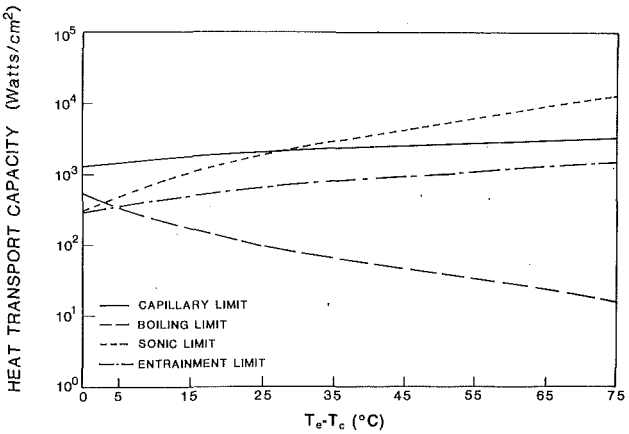

Fig. 6 Predicted limitations of the first test pipe with sintered powder evaporator wick (not constructed)

fluid occurred at this point. This degradation along with formation of a small amount of noncondensible gas was believed to be the reason for the decrease in the correlation between the measured and predicted values. Further tests were unable to reproduce the initial results and substantiated this hypothesis.

Using the computer model described earlier, each of the physical parameters was varied individually over a wide range of operating temperatures. The results of this procedure indicated that because of the smaller pore size, the sintered evaporator wick could significantly increase the power level at which boiling occurred. Figure 6 illustrates the predicted limits for a heat pipe with the same dimensions as the first test pipe, but with a sintered evaporator wick. Although as shown, this heat pipe is still predominantly boiling limited, the level at which boiling occurs has been substantially increased. By comparing Figs. 4 and 6, it is apparent that use of the sintered powder wick significantly increases the maximum heat transport capacity. In addition, results from the computer model indicated that replacing the original 200 mesh screen longitudinal wick with one constructed from 100 mesh would also improve the performance due to decreased pressure losses. Both of these changes were implemented for the second and third test pipes.

Figure 7(*a*) illustrates a comparison of the predicted and measured results for the second test pipe with both 1.27-cm and 2.54-cm condenser lengths. As shown, for the 1.27-cm condenser length, the model predicts the transport capacity to within ± 5 percent over an evaporator temperature range of 25°C to 40°C. At approximately 40°C the measured transport capacity starts to diverge from the predicted value significantly and at approximately 44°C, a very small increase in the input heat flux results in a significant increase in the evaporator temperature. Initially, this rapid increase in evaporator temperature was believed to be an anomaly; however, additional tests indicated that both the magnitude and location of this phenomenon were repeatable for increasing heat flux. Because this rapid change was not apparent when the heat flux was incrementally reduced, this phenomenon or "knee" was assumed to be the result of nucleate bubble formation occurring in the evaporator wick. Once formed, these bubbles partially block off a portion of the liquid return, decreasing the effective area of the wick and hence decreasing the heat transport capacity. Additional increases in the evaporator temperature result in a continued increase in the heat transport capacity, with a significantly higher temperature difference between the evaporator and the condenser. The same trends are apparent in the tests conducted with a condenser length of 2.54 cm; however, both the predicted transport capacity, shown as the dashed line, and the measured values, shown as the solid circles, were

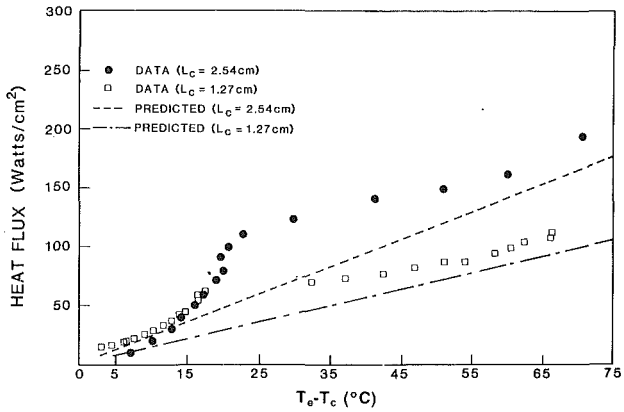

Fig. 7(*a*) Comparison of the measured and predicted transport capacity of the second test pipe at no tilt

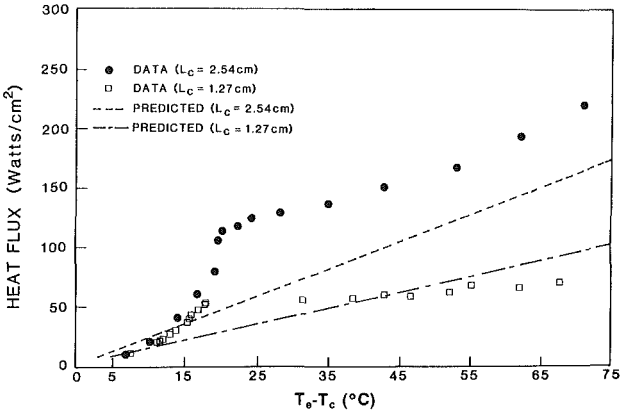

Fig. 7(*b*) Comparison of the measured and predicted transport capacity of the second test pipe at 45 deg

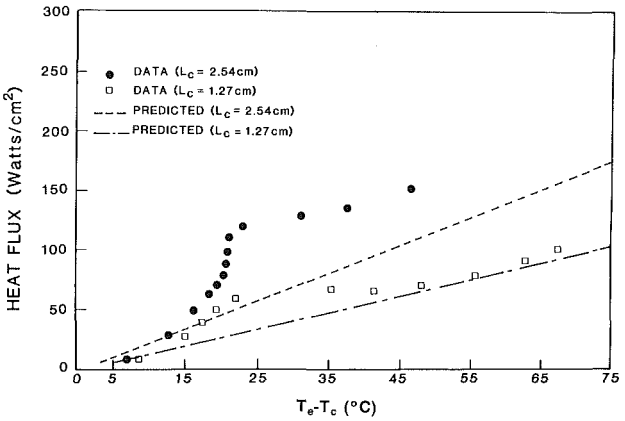

Fig. 7(*c*) Comparison of the measured and predicted transport capacity of the second test pipe at 90 deg

substantially higher than those obtained for the 1.27-cm-long condenser.

Figures 7(*b*) and 7(*c*) illustrate the results for the same test pipe at tilt angles of 45 and 90 deg (evaporator down). As was the case for the horizontal pipe, the knee was present for all three tilt configurations and the longer condenser resulted in a significant increase in the transport limit. By comparing Figs. 7(*a*), 7(*b*), and 7(*c*), it is apparent that there is very little change in the predicted transport capacity due to the changes in the tilt. Comparing the experimental results obtained for tilts of 0 and 45 deg also indicates little change in the measured transport capacity; however, a significant increase in the maximum heat transport capacity can be seen between the 45 and 90 deg tilt angles. This increase is believed to be the result of enhanced liquid flow back to the evaporator.

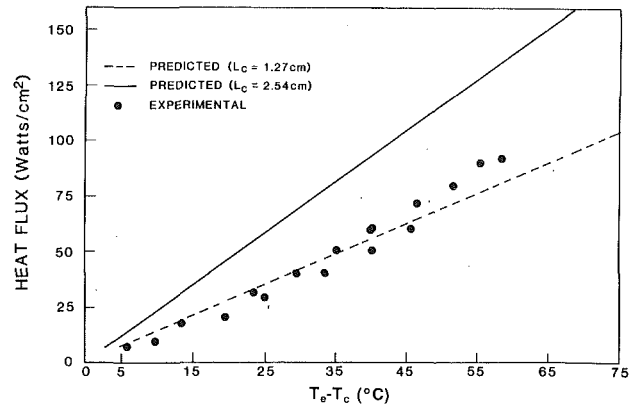

Fig. 8(*a*) Comparison of the measured and predicted transport capacity of the third test pipe at no tilt

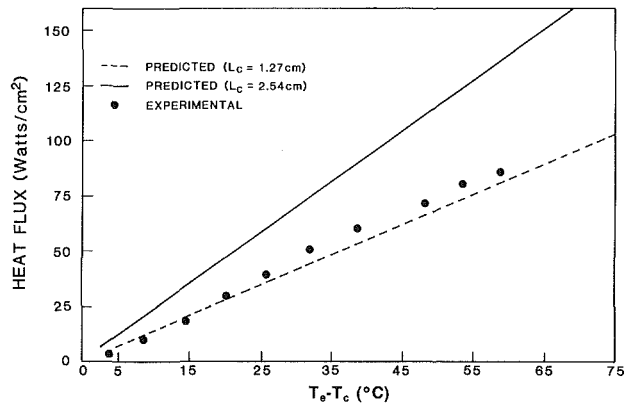

Fig. 8(*b*) Comparison of the measured and predicted transport capacity of the third test pipe at 45 deg

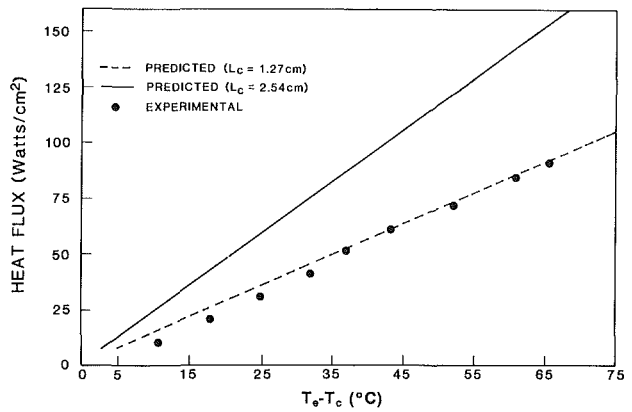

Fig. 8(*c*) Comparison of the measured and predicted transport capacity of the third test pipe at 90 deg

Although not shown, the results of the model indicated that the relationship of the various heat transport limitations for the second test pipe were similar to that of the first (see Fig. 4), and that the heat pipe was boiling limited over a majority of the operating temperature range. Because unlike the sonic and capillary limit, the boiling limit does not present a definitive physical limit, but only predicts the point at which the first nucleate bubble is formed, continued operation is possible and will result in a higher temperature drop due to an increased thermal resistance. As shown in Figs. 7(*a*), 7(*b*), and 7(*c*), the effect of this theoretical boiling limit is apparent in that the experimentally determined limits for all three tilt angles were significantly higher than those predicted by the model.

In a further effort to improve and understand the heat transport capacity, additional modifications to the evaporator wick were made and a third test pipe was constructed. As shown in Tables 1 and 2, the third test pipe was similar to the second in both size and construction with the exception of the size of the copper powder from which the evaporator wick was made. In the second test pipe the evaporator wick was made from a powder size of -100 to $+325$ mesh, while for the third test pipe a powder mesh size of -140 to $+170$ was used. This modification resulted in the elimination of those pores in both the upper and lower size ranges and an overall increase in the average pore size in the evaporator wick.

In Figs. 8(*a*), 8(*b*), and 8(*c*), the predicted limits for the third test pipe with condenser lengths of both 1.27 cm and 2.54 cm are compared with the experimental data with a condenser length of 1.27 cm. Because of damage to the third test pipe, data for a condenser length of 2.54 cm were not obtained. These comparisons indicate several significant results. First, the characteristic shape of the data is different in that no knee is apparent. In keeping with the previous explanation, it would appear that the increase in the mean pore size resulted in a lower required evaporator temperature to reach the onset of nucleate bubble formation, i.e., the partial blockage of the evaporator wick occurred throughout the entire range tested. Second, both the predicted and experimental results at operating temperatures greater than 60°C were greater than those in either the first or second test pipes due to increases in the boiling limit.

Conclusions

This investigation was initially undertaken to verify the bellows heat pipe concept, develop a model that could be used to predict and optimize the performance of such a device, and determine the validity of the model. A total of three pipes were tested with the design of each successive test pipe increasing the maximum heat transport capacity and providing additional information with which to verify the accuracy of the model. The results of the investigation indicate that the flexible bellows heat pipe does in fact operate as intended and that the operation can be accurately predicted. In addition, a device capable of transporting in excess of 200 W/m^2 with a temperature drop of 65°C and a thermal resistance of approximately 0.7°C/W was constructed and tested.

The experience gained through this investigation can be used to support the design and testing of additional laboratory test elements and prototypes; analyze the effect of varying the source and sink temperatures on the thermal performance of the system; determine the effect of varying the physical dimensions and wick type, material, and shape on the transport limitations of the heat pipe; and aid in the design of future flexible bellows heat pipes. Although all of the objectives set forth in this investigation were attained, the effect of particle size on the nucleation radius and hence, its effect on the boiling limit within sintered heat pipe wicking structures, requires additional investigation.

References

Asselman, G. A., and Green, D. B., 1973, "Heat Pipes," *Phillips Technical Review*, Vol. 16, pp. 169–186.

Chi, S. W., 1976, *Heat Pipe Theory and Practice*, McGraw-Hill, New York.

Dunn, P. D., and Reay, D. A., 1982, *Heat Pipes*, 3rd ed., Pergamon Press, New York.

Kraus, A. D., and Bar-Cohen, A., 1983, *Thermal Analysis and Control of Electronic Equipment*, McGraw-Hill, New York.

Marto, P. J., and Peterson, G. P., 1988, "Chapter 4—Application of Heat Pipes to Electronics Cooling," *Advances in Thermal Modeling of Electronic Components and Systems*, A. Bar-Cohen and A. D. Kraus, eds., Hemisphere, Washington, DC, pp. 283–336.

Peterson, G. P., 1988, "Analytical Development and Computer Modeling of a Bellows Type Heat Pipe for Cooling of Electronic Components," *Heat Transfer Engineering*, Vol. 9, No. 3, pp. 101–109.

Effect of Entrainment on the Heat Transfer to a Heated Circular Air Jet Impinging on a Flat Surface

R. J. Goldstein

K. A. Sobolik[1]

W. S. Seol

Mechanical Engineering Department,
University of Minnesota,
Minneapolis, MN 55455

An experimental investigation is described that characterizes the convective heat transfer of a heated circular air jet impinging on a flat surface. The radial distributions of the recovery factor, the effectiveness, and the local heat transfer coefficient are presented. The recovery factor and the effectiveness depend on the spacing from jet exit to the impingement plate, but do not depend on jet Reynolds number. The effectiveness does not depend on the temperature difference between the jet and the ambient. A correlation is obtained for the effectiveness. The heat transfer coefficient is independent of the temperature difference between the jet and the ambient if it is defined with the difference between the heated wall temperature and the adiabatic wall temperature.

Introduction

The high heat transfer rates that can occur in the stagnation region of impinging jets has led to their use in a wide variety of applications. These include cooling of gas turbine components, drying of paper, textiles, and film materials, and tempering of glass. Also, impinging jets are being considered for cooling electronic components.

Although many studies of jet impingement have been made, most have involved jets of the same temperature as the ambient fluid. However, if the temperature of the (air) jet is different from the ambient (air) temperature, entrainment of ambient air into the jet complicates the description of the heat transfer. Only a few studies have involved entrainment effects. Bouchez and Goldstein (1975) measured the effectiveness of a single circular jet interacting with a crossflow for two jet-exit-to-impingement-plate separations ($L/D = 6$, 12) and a range of blowing rates. Effectiveness, a concept used in film cooling, was used to characterize the entrainment. Folayan and Whitelaw (1977) investigated the effectiveness of a slot jet for a variety of jet-to-plate spacings ($2 \leq L/D \leq 12$) and impingement angles. Striegl and Diller (1984a, 1984b) carried out experimental and analytical studies of thermal entrainment for a single turbulent plane jet. Hollworth and Wilson (1984) measured the effectiveness of a single circular jet for many jet-to-plate separations up to 15 jet diameters. In the same apparatus, Hollworth and Gero (1985) investigated local heat transfer. A study by Florschuetz and Su (1987) determined the effectiveness and heat transfer with an array of impinging jets in a crossflow. The definition of effectiveness used by these researchers varies.

In this study the entrainment effect for a single circular impinging air jet has been investigated. The ratio of the jet-to-plate spacing to the jet diameter is varied between 2 and 12. The relationship between the effectiveness distribution and the mass flow rate is determined. The jet Reynolds number is varied between 61,000 and 124,000 to determine the effect of mass flow rate. A jet Reynolds number of 124,000 corresponds to a Mach number of 0.47 in the present study.

Experimental Apparatus and Measurement Procedure

The experimental apparatus is similar to those described by Goldstein and Behbahani (1982) and Goldstein et al. (1986). Only a brief description of the apparatus is presented here; a complete description is given by Butler (1984).

Air is supplied by a compressor at a pressure of 830 ± 10 kPa (8.3 ± 0.1 bar). A filter removes oil from the air flow. A regulating valve is used to reduce the pressure fluctuations caused by the pumping and bleeding strokes of the compressor. A series of needle valves in parallel allows the mass flow rate to be controlled. A calibrated standard sharp edge orifice is used to measure the total mass flow rate. Downstream from the orifice is a heated duct section where the temperature of the air is controlled. The air is then introduced to a long straight pipe (4.09 cm i.d.) held normal to the test plate. The jet total temperature is measured with a thermocouple housed in a thin-walled aluminum tube and located at the centerline of the delivery pipe about 15.24 cm upstream of the jet exit. The delivery pipe is insulated with fiberglass. Attached to this tube is the jet exit assembly.

The exit assembly, shown in Fig. 1, consists of an aluminum upper bracket, a brass spacer, and an aluminum nozzle. The upper bracket is attached to the delivery pipe and a piece of plexiglass that aids in holding the delivery pipe in place. The spacer is threaded into the bracket, and the nozzle is threaded into the spacer. Spacers of different lengths are used to provide the desired spacing between the nozzle exit and the test plate. The quarter ellipse nozzle is designed according to the ASME power test code (1959).

The test plate (Fig. 1) is designed to provide a known heat flux and allow measurement of the wall temperature at various locations. It includes a thin textolite plate with a 5.0 cm styrofoam backing. Twenty-one stainless steel strip heaters, 0.0254 mm thick and 5.08 cm wide, are bonded to the surface with silicone rubber. Sixty-three 30-gage iron-constantan thermocouples are embedded in the test plate. Copper oxide is used as a cement and an electrical insulator between the heating foils and the thermocouples.

Two runs are always done consecutively: The first is to measure the recovery factor; the second is to determine either the effectiveness or the heat transfer coefficient distribution.

In each test run, the mass flow rate is adjusted to give the desired Reynolds number. To measure the recovery factor, the air flow is heated so that the jet total temperature is within 0.1°C of the ambient temperature. After steady state is reached, the temperature distribution on the test plate is measured. If the effectiveness distribution is to be measured, the air flow is heated 2°C to 20°C above the ambient temperature and allowed to stabilize. Then the wall temperature distribution is measured. If the heat transfer coef-

[1]Present address: Sandia National Laboratory, Albuquerque, NM.

Contributed by the Heat Transfer Division for publication in the JOURNAL OF HEAT TRANSFER. Manuscript received by the Heat Transfer Division February 27, 1989; revision received September 18, 1989. Keywords: Forced Convection, Jets.

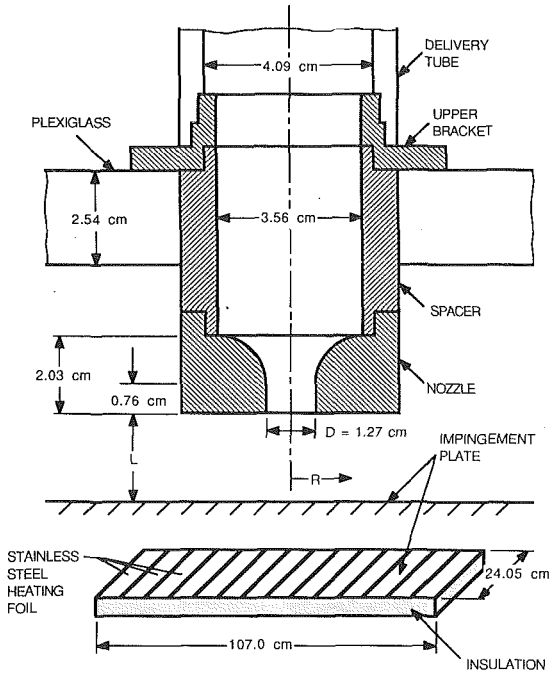

Fig. 1 Jet nozzle and impingement plate

ficient distribution is to be measured, the air flow is heated to provide the desired jet total temperature. Then, the wall temperature distribution is measured after the power is supplied to the heater foils. Steady state is usually reached in approximately 2 h.

Conduction in the test plate causes a small error in the effectiveness values. However, it was neglected since the correction for the conduction error was found to be not more than 0.5 percent (Butler, 1984). The wall heat flux was corrected for the conduction and radiation losses, which were found to be negligibly small. Typical values of each correction are 1.5 W/m^2 and 4.5 W/m^2, respectively, for the total wall heat flux of 3200 W/m^2.

Results and Discussion

The convective heat transfer coefficient can be defined as the wall heat flux divided by the difference between the temperature of the surface and some characteristic temperature of the fluid, usually the free-stream temperature. Bouchez (1973) and Kieger (1981) have shown that the use of jet total temperature as the reference results in a heat transfer coefficient that is dependent on the wall heat flux, whereas the

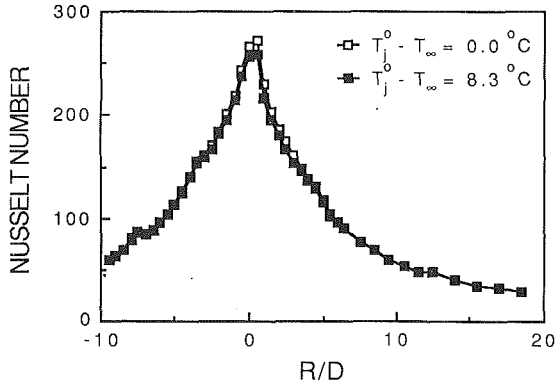

Fig. 2 Radial distribution of the local Nusselt number: independence of $T_j^o - T_\infty$, $L/D = 8$, and Re = 89,000

use of adiabatic wall temperature results in a heat transfer coefficient that is independent of the wall heat flux. The definitions

$$h = \frac{q_c}{T_w - T_{aw}} \tag{1}$$

and

$$\mathrm{Nu} = \frac{hD}{k_a} \tag{2}$$

have been used for the present study.

Figure 2 demonstrates that Nusselt number defined by equations (1) and (2) is also independent of the difference between the temperature of the jet and the ambient temperature. This is to be expected for an essentially constant property flow due to the linearity of the energy equation. This has been also observed by Hollworth and Gero (1985). Therefore, the heat transfer coefficients for impinging jets (with $T_j^o = T_\infty$), which most jet impingement studies (for example, Goldstein and Behbahani, 1982) have involved, may be used for heated (or cooled) impinging jets, if the distribution of adiabatic wall temperature is known.

The adiabatic wall temperature is dependent upon many quantities, including the jet to impingement plate spacing, the mass flow rate of the jet, the temperature of the jet, the ambient temperature, etc. To express the adiabatic wall temperature in dimensionless form, the concept of effectiveness has been adopted from film cooling. The impingement cooling/heating effectiveness, which is slightly different from the film cooling effectiveness, is defined by

Nomenclature

C_p = specific heat
D = jet exit diameter = 12.7 mm in present study
h = heat transfer coefficient = $q_c/(T_w - T_{aw})$
k_a = thermal conductivity
L = jet exit to plate distance
Nu = local Nusselt number = hD/k_a
q_c = convective wall heat flux
R = radial distance from geometric center of jet, shown as greater or less than zero on the measurement line
Re = jet Reynolds number = $u_j D/\nu$
r = recovery factor
$$= \frac{T_r - T_j^s}{T_d} = 1 + \frac{T_r - T_j^o}{T_d}$$
T_{aw} = adiabatic wall temperature
T_d = jet dynamic temperature = $u_j^2/2C_p$
T_j^o = jet total temperature
T_r = recovery temperature = T_{aw} when $T_j^o = T_\infty$
T_j^s = jet static temperature
T_w = wall temperature
T_∞ = ambient temperature
u_j = average jet exit velocity
η = effectiveness defined as
$$\eta = \frac{T_{aw} - T_r}{T_j^o - T_\infty}$$
η^* = effectiveness defined as
$$\eta^* = \frac{T_{aw} - T_\infty}{T_j^o - T_\infty}$$
ν = viscosity of air

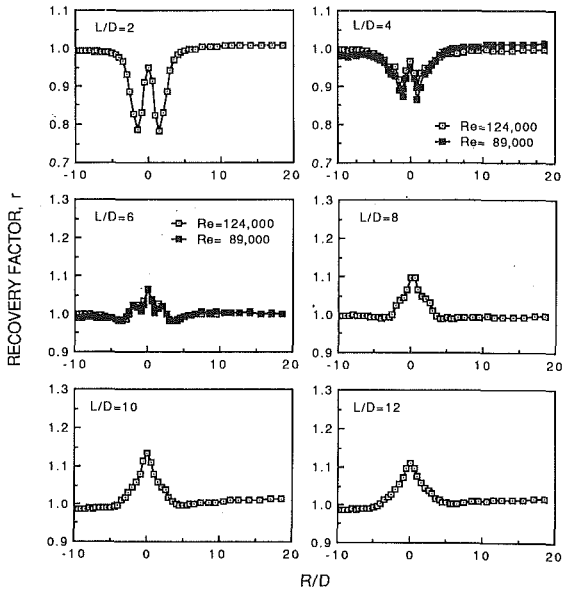

Fig. 3 Radial distribution of the recovery factor for various jet-to-plate spacings; Re = 124,000

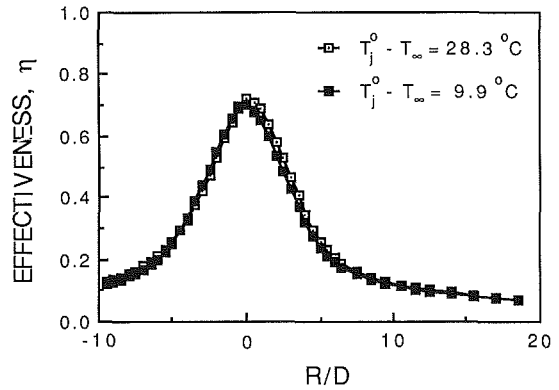

Fig. 4 Radial distribution of the effectiveness: independence of $T_j^o - T_\infty$, $L/D = 8$, and Re = 124,000

$$\eta = \frac{T_{aw} - T_r}{T_j^o - T_\infty} \tag{3}$$

where the recovery temperature T_r is defined as the adiabatic wall temperature under the special condition that the ambient and the jet total temperatures are equal (i.e., $T_j^o = T_\infty$). Note that $(T_{aw} - T_r)$ goes to zero when $(T_j^o - T_\infty)$ goes to zero.

To express the recovery temperature in a dimensionless form, the recovery factor is defined by

$$r = \frac{T_r - T_j^s}{T_d} = 1 + \frac{T_r - T_j^o}{T_d} \tag{4}$$

Recovery factor distributions for jet-to-plate separations L/D of 2, 4, 6, 8, 10, and 12 are shown in Fig. 3. The jet centerline is located at $R/D = 0$. As illustrated for $L/D = 4$ and $L/D = 6$, the recovery factor is essentially independent of the mass flow rate of the jet, which has been already noted by Goldstein et al. (1986). Small variations in temperature with time cause the difference in the wall jet region, since the recovery factor is very sensitive to any difference between the jet total temperature and the ambient temperature.

The recovery factor varies from 0.8 to 1.2 in the impingement region; in the wall jet region it is very close to unity as the recovery temperature T_r approaches the ambient temperature $T_\infty (\approx T_j^o)$. The occurrence of significant local minima (at $R/D \approx 1.5$) in the recovery factor at small jet-to-plate spacings

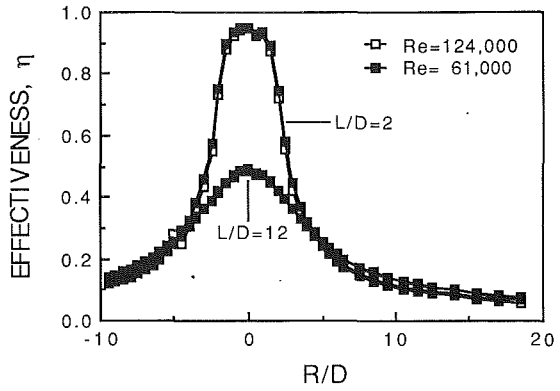

Fig. 5 Radial distribution of the effectiveness: independence of Re

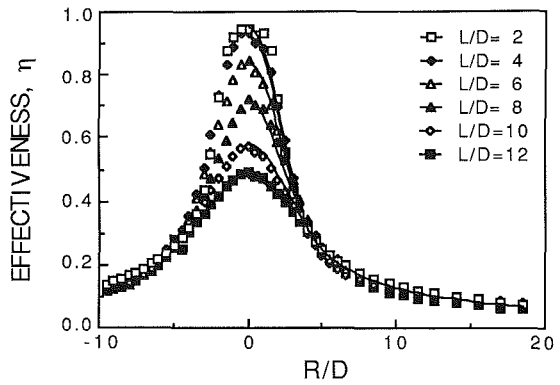

Fig. 6 Comparison of correlation with the measured effectiveness for various jet-to-plate spacings; Re = 124,000

($L/D \leq 4$) can be attributed to energy separation in the highly curved flow (Goldstein et al., 1986; Eckert, 1987). The fact that the recovery temperature T_r in the impingement region is larger than the jet total temperature T_j^o (i.e., $r \geq 1.0$) for large jet-to-plate spacings ($L/D \geq 6$) may be due to the heating of jet flow by the entrainment of warmer[2] ambient air (Goldstein and Behbahani, 1982; Goldstein et al., 1986; Gardon and Cobonpue, 1962).

Figure 4 shows that the effectiveness is independent of the temperature difference between the jet flow and the ambient. Figure 5 shows that the effectiveness is also independent of the mass flow rate of the jet (Re) in the range studied. Hollworth and Wilson (1984) found that the radial distribution of dimensionless adiabatic wall temperature is essentially similar regardless of the jet exit velocity and the temperature mismatch $(T_j^o - T_\infty)$. Florschuetz and Su (1987) also found that the effectiveness is independent of jet Reynolds number for an array of jets in a crossflow.

Effectiveness distributions are shown in Fig. 6 for jet-to-plate spacings, L/D, of 2, 4, 6, 8, 10, and 12. The effectiveness depends on L/D in the impingement region, while in the wall jet region, it is relatively independent of L/D. The impingement point ($R/D = 0$) effectiveness decreases with increasing jet-to-plate spacing. For $L/D = 2$, the effectiveness at the impingement point is close to one ($\eta = 0.95$) and the shape of the distribution curve is fairly flat near the jet centerline ($\eta = 0.92$ at $R/D = 1$). Thus, the thermal entrainment of the ambient air into the jet core is negligible for small jet-to-plate spacing. The effectiveness distribution for $L/D = 4$ is very similar to that for $L/D = 2$. The peak effectiveness for $L/D = 4$ is only 0.02 less than that for $L/D = 2$. This implies that the jet core is still

[2]For $T_j^o = T_\infty$, the static temperature of the jet is lower than the ambient temperature by the dynamic temperature of the jet.

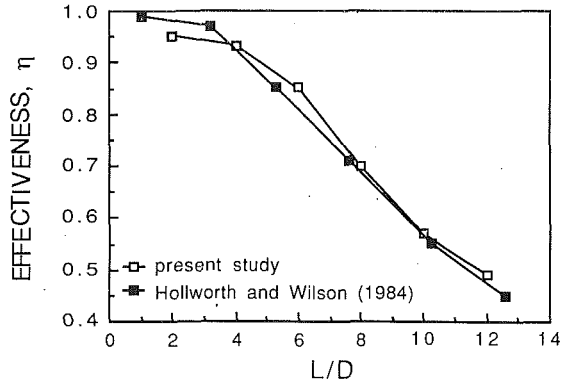

Fig. 7 Variation of the effectiveness with jet-to-plate spacing at $R/D = 0$: present study ($T_j^o - T_\infty = 2 \sim 20°C$, $u_j = 164$ m/s); Hollworth and Wilson ($T_j^o - T_\infty = 30°C$, $u_j = 125$ m/s)

almost unaffected by the entrainment of the ambient air. However, the curve of effectiveness versus radius near the jet centerline is not flat, showing greater penetration of the ambient air into the jet core. For $L/D > 4$, the thermal entrainment is important even at the centerline of the jet. The effect of thermal entrainment becomes greater with increasing jet-to-plate distance, resulting in decreasing effectiveness. The peak effectiveness at $L/D = 12$ is 0.49.

The effectiveness data in the range of the present study are satisfactorily correlated by:

$$\eta = 0.35 + 0.6e^{-0.01(L/D-2)^{2.2} - 0.1(R/D)^{2.5}} \quad (5)$$

when $0 \le R/D \le 3.5$, and

$$\eta = 1.193(R/D)^{-0.98} \quad (6)$$

(or approximately $\eta = 1.25(R/D)^{-1}$) when $R/D \ge 3.5$. The solid lines in Fig. 6 show this correlation.

The experimental uncertainties are calculated using the method of Kline and McClintock (1953); the uncertainty of an expression is calculated from the square root of the sum of the squares of the uncertainties of separate terms in the expression. The uncertainty of the recovery factor is not more than 1.5 percent, that of the effectiveness is not more than 4.3 percent, and that of the Nusselt number is not more than 5.9 percent in this experiment.

Figure 7 shows a comparison of the impingement-point effectiveness for various jet-to-plate spacings from the present study and from Hollworth and Wilson (1984). The agreement is generally good. Hollworth and Wilson used a different definition of effectiveness

$$\eta^* = \frac{T_{aw} - T_\infty}{T_j^o - T_\infty} \quad (7)$$

The difference in definition contributes to the discrepancy between the two curves. Also, a square-edged orifice was used by Hollworth and Wilson, whereas a quarter ellipse nozzle was employed for the present study.

Summary and Conclusions

The recovery factor shows no dependence upon the mass flow rate of the jet. There exist significant local minima in recovery factor near the impingement point ($R/D \approx 1.5$) for small jet-to-plate spacings ($L/D \le 4$), apparently due to energy separation. The impingement region recovery factor is larger than unity for large jet-to-plate spacings ($L/D \ge 6$) due to the heating of jet flow by the entrainment of "warmer" ambient air.

The concept of film cooling effectiveness has been adopted to express the adiabatic wall temperature in a dimensionless form. The impingement cooling/heating effectiveness is independent not only of the temperature difference between the jet and the ambient but also of the mass flow rate of the jet. The effectiveness decreases with increasing jet-to-plate spacing near the impingement region, while it is independent of L/D in the wall jet region.

The heat transfer coefficient is independent of the relative magnitude of the jet temperature and the ambient temperature, if the adiabatic wall temperature is used as a reference temperature in the definition of heat transfer coefficient. Therefore, the heat transfer coefficients for impinging jets with $T_j^o = T_\infty$, which have been extensively studied, may be used for jets with $T_j^o \ne T_\infty$ if the local adiabatic wall temperature (effectiveness) is known. In the present study, the adiabatic wall temperature distribution is presented in the form of the effectiveness for various jet-to-plate separations.

Acknowledgments

Support for the conduct of this study from the Engineering Research Program of the US Department of Energy is gratefully acknowledged.

References

ASME, 1959, *Fluid Meter, the Theory and Application*, Report of ASME Research Committee of Fluid Meters, New York, pp. 46–47.

Bouchez, J. P., 1973, "Heat Transfer to an Impinging Circular Jet in a Crossflow," Ph. D. Thesis, Department of Mechanical Engineering, University of Minnesota, Minneapolis, MN.

Bouchez, J. P., and Goldstein, R. J., 1975, "Impingement Cooling From a Circular Jet in a Cross Flow," *International Journal of Heat and Mass Transfer*, Vol. 18, pp. 719–730.

Butler, K. A., 1984, "Effect of Entrainment on the Heat Transfer Between a Flat Surface and Impinging Circular Air Jets," M.S. Thesis, Department of Mechanical Engineering, University of Minnesota, Minneapolis, MN.

Eckert, E. R. G., 1987, "Cross Transport of Energy in Fluid Streams," *Thermo- and Fluid Dynamics*, Vol. 21, No. 2–3, pp. 73–81.

Florschuetz, L. W., and Su, C. C., 1987, "Effects of Cross Flow Temperature on Heat Transfer Within an Array of Impinging Jets," ASME JOURNAL OF HEAT TRANSFER, Vol. 109, pp. 74–82.

Folayan, C. O., and Whitelaw, J. H., 1977, "Impingement Cooling and Its Application to Combustor Design," ASME—JSME *Joint Gas Turbine Congress*, Tokyo, Japan, Paper No. 7.

Gardon, R., and Cobonpue, J., 1962, "Heat Transfer Between a Flat Plate and Jets of Air Impinging on It," *International Developments in Heat Transfer*, Proc. 2nd International Heat Transfer Conference, ASME, New York, pp. 454–460.

Goldstein, R. J., and Behbahani, A. I., 1982, "Impingement of a Circular Jet With and Without Cross Flow," *International Journal of Heat and Mass Transfer*, Vol. 25, pp. 1377–1382.

Goldstein, R. J., Behbahani, A. I., Heppelmann, K., and Kieger, K. K., 1986, "Streamwise Distribution of the Recovery Factor and the Local Heat Transfer Coefficient to an Impinging Circular Air Jet," *International Journal of Heat and Mass Transfer*, Vol. 29, pp. 1227–1235.

Hollworth, B. R., and Wilson, S. I., 1984, "Entrainment Effects on Impingement Heat Transfer: Part I—Measurements of Heated Jet Velocity and Temperature Distributions and Recovery Temperatures on Target Surface," ASME JOURNAL OF HEAT TRANSFER, Vol. 106, pp. 797–803.

Hollworth, B. R., and Gero, L. R., 1985, "Entrainment Effects on Impingement Heat Transfer: Part II—Local Heat Transfer Measurements," ASME JOURNAL OF HEAT TRANSFER, Vol. 107, pp 910–916.

Kieger, K. K., 1981, "Local and Average Heat Transfer From a Flat Surface to a Single Circular Jet of Air Impinging on It," M.S. Thesis, Department of Mechanical Engineering, University of Minnesota, Minneapolis, MN.

Kline, S. J., and McClintock, F. A., 1953, "Describing Uncertainties in Single Sample Experiments," *Mechanical Engineering*, Vol. 75, No. 1.

Striegl, S. A., and Diller, T. E., 1984a, "The Effect of Entrainment Temperature on Jet Impingement Heat Transfer," ASME JOURNAL OF HEAT TRANSFER, Vol. 106, pp. 27–33.

Striegl, S. A., and Diller, T. E., 1984b, "Analysis of the Effect of Entrainment Temperature on Jet Impingement Heat Transfer," ASME JOURNAL OF HEAT TRANSFER, Vol. 106, pp. 804–810.

Mixed Convection Heat Transfer With Longitudinal Fins in a Horizontal Parallel Plate Channel: Part I—Numerical Results

J. R. Maughan[1]

F. P. Incropera

Heat Transfer Laboratory,
School of Mechanical Engineering,
Purdue University,
West Lafayette, IN 47907

Numerical calculations for laminar, fully developed mixed convection in a longitudinally finned horizontal channel have been performed for two sets of boundary conditions: (i) an isothermal, heated bottom plate with an isothermal, cooled top plate, and (ii) a uniform heat flux at the bottom surface with an adiabatic upper surface. Heat transfer and the strength of the buoyancy-driven secondary flow increase with increasing Rayleigh number and fin height. Fin spacing affects heat transfer through changes in the axial velocity distribution, the strength of the secondary flow, and the heated surface area, with decreased spacing acting to inhibit secondary flow. For the uniform heat flux condition and a small available pressure drop, close fin spacing can significantly reduce the channel flow rate and increase maximum plate temperatures.

Introduction

Heat transfer enhancement is a subject of considerable interest in the design of thermal systems. Traditionally, extended surfaces like fins and ribs have been used to augment heat transfer by adding additional surface area and encouraging mixing. However, mixed convection and buoyancy-driven secondary flows also enhance heat transfer above forced convection levels, and it is of interest to determine whether the combination of extended surfaces and mixed convection yields levels of heat transfer enhancement unattainable when either mechanism acts independently. The objective of this study is to determine whether longitudinal fins attached to the heated bottom surface of a parallel plate channel can enhance secondary flows and heat transfer and how such enhancement is affected by Rayleigh number, fin height, and fin spacing.

Previous studies of mixed convection with fins have been limited to numerical simulations. Acharya and Patankar (1981) considered laminar mixed convection in a horizontal, shrouded longitudinal fin array with and without a fin tip to shroud clearance. Reporting results in terms of the ratio Nu/Nu_f, where Nu_f is the forced convection Nusselt number of the same geometry, they concluded that heat transfer is enhanced with tip clearance. This conclusion, however, can be misleading, since they neglected to report values of the forced convection Nusselt number for each tip clearance. An earlier work, which considered forced convection for this situation (Sparrow et al., 1978), indicated that increasing tip clearance can significantly reduce forced convection heat transfer, in some cases by a factor of 10. This decrease is due to the reduced mass flow between fins, as the fluid follows the path of least resistance closer to the shroud, and suggest that increasing tip clearance may actually decrease mixed convection heat transfer. Furthermore, because the Grashof number was based on the height of the fin and not the combined lengths of the fin and the shroud clearance, which more directly influences the scale of convection, the results must not be interpreted as implying that heat transfer enhancement in a channel of fixed height increases with decreasing fin length. Additional numerical investigations of laminar mixed convection with fins were performed by Prakash and Renzoni (1985) for a vertical annulus and by Mirza and Soliman (1985) for a horizontal tube. Results suggest that buoyancy effects increase heat transfer above that associated with forced convection, but that enhancement levels decrease with increasing fin length.

The foregoing investigations suggest that, while the additional area provided by extended surfaces increases heat transfer, the effect on buoyancy can act to augment or to diminish enhancement. The purpose of this research is to investigate these effects numerically in a horizontal channel heated from below. Related experimental results are reported in a companion paper (Maughan and Incropera, 1990).

Analysis

Two separate boundary conditions were considered for fully developed flow in a channel with longitudinal fins aligned in the flow direction (Fig. 1): a heated isothermal bottom plate with a cooled isothermal top plate, and a uniform axial heat flux on the bottom surface with an adiabatic upper surface.

Isothermal Plates. For steady, laminar, fully developed, incompressible flow between isothermal plates, the nondimensional governing equations are

$$\frac{\partial u^*}{\partial x^*}+\frac{\partial v^*}{\partial y^*}=0 \tag{1}$$

$$u^*\frac{\partial u^*}{\partial x^*}+v^*\frac{\partial u^*}{\partial y^*}=\frac{\partial^2 u^*}{\partial x^{*2}}+\frac{\partial^2 u^*}{\partial y^{*2}}-\frac{\partial p^*}{\partial x^*} \tag{2}$$

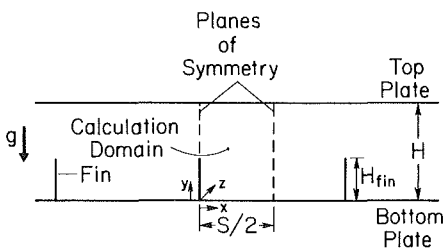

Fig. 1 Geometry and calculation domain for numerical solution

[1]Present address: General Electric Corporate Research and Development, Schenectady, NY 12301.

Contributed by the Heat Transfer Division for publication in the JOURNAL OF HEAT TRANSFER. Manuscript received by the Heat Transfer Division May 9, 1989; revision received October 16, 1989. Keywords: Finned Surfaces, Mixed Convection, Natural Convection.

$$u^*\frac{\partial v^*}{\partial x^*}+v^*\frac{\partial v^*}{\partial y^*}=\frac{\partial^2 v^*}{\partial x^{*2}}+\frac{\partial^2 v^*}{\partial y^{*2}}-\frac{\partial p^*}{\partial y^*}+Gr\Theta_T \quad (3)$$

$$u^*\frac{\partial w^*}{\partial x^*}+v^*\frac{\partial w^*}{\partial y^*}=\frac{\partial^2 w^*}{\partial x^{*2}}+\frac{\partial^2 w^*}{\partial y^{*2}}+1 \quad (4)$$

$$u^*\frac{\partial \Theta_T}{\partial x^*}+v^*\frac{\partial \Theta_T}{\partial y^*}=\frac{1}{\mathrm{Pr}}\left[\frac{\partial^2 \Theta_T}{\partial x^{*2}}+\frac{\partial^2 \Theta_T}{\partial y^{*2}}\right] \quad (5)$$

where

$$x^*=\frac{x}{H} \qquad y^*=\frac{y}{H} \quad (6a)$$

$$u^*=\frac{u}{\nu/H} \qquad v^*=\frac{v}{\nu/H} \qquad w^*=\frac{\mathrm{w}}{-\frac{dp}{dz}\frac{H^2}{\mu}} \quad (6b)$$

$$p^*=\frac{P}{\rho(\nu/H)^2} \quad (6c)$$

$$\Theta_T=\frac{T-T_{\mathrm{top}}}{T_{\mathrm{bot}}-T_{\mathrm{top}}} \quad (6d)$$

and the temperature difference associated with the Grashof number is $\Delta T=(T_{\mathrm{bot}}-T_{\mathrm{top}})$. Constant fluid properties are assumed, and the Boussinesq approximation is used to model the buoyancy force in the y-momentum equation. Pressure gradients in the momentum equations have been separated into two components. A pressure gradient in the longitudinal direction, $\partial p/\partial z$, drives the main flow, while pressure gradients in the cross-stream plane, $\partial p/\partial x$ and $\partial p/\partial y$, drive secondary flows. Because of the relatively weak buoyancy-driven flow, $\partial p/\partial z \gg \partial p/\partial x$, $\partial p/\partial y$, and the axial and cross-stream momentum equations are not coupled through pressure effects. A nondimensional fin spacing $A=S/2H$ represents the aspect ratio of the calculation domain and of the vortices that form between fins, while the parameter $F=H_{\mathrm{fin}}/H$ represents the relative fin height. The fin is presumed to have zero thickness but to be perfectly conducting and hence to have a temperature everywhere equal to that of the bottom plate. This assumption is reasonable for the low heat transfer coefficients associated with gas flows.

Thermal boundary conditions used in solving equations (1)-(5) include the prescription of a uniform temperature for the bottom and fin surfaces ($\Theta_T=1$), a uniform temperature at the top surface ($\Theta_T=0$), and a zero temperature gradient ($\partial\Theta_T/\partial x^*=0$) at the planes of symmetry. Hydrodynamic boundary conditions correspond to customary zero slip, impermeable wall, and symmetry requirements.

The average Nusselt number across the width of the cell and the height of the fin is defined as

$$\overline{\mathrm{Nu}}_{fd}=\bar{h}\frac{H}{k}=\frac{q'}{(S/2)(T_{\mathrm{bot}}-T_{\mathrm{top}})}\frac{H}{k} \quad (7)$$

which may be expressed as

$$\overline{\mathrm{Nu}}_{fd}=-\frac{1}{A}\left[\int_0^A \frac{\partial \Theta_T}{\partial y^*}dx^*+\int_0^F \frac{\partial \Theta_T}{\partial x^*}dy^*\right] \quad (8)$$

where the subscript indicates fully developed conditions and the bar emphasizes that the Nusselt number is spanwise averaged. The Nusselt number is based on the fixed area of the base (per unit length) $S/2$, and not on the surface area of the base and the fin, $(S/2)+H_{\mathrm{fin}}$. Hence, as the fin height F is varied from 0 (no fins) to 1 (no fin tip clearance), the effect on the heat transfer rate is proportionally reflected in the Nusselt number. Furthermore, since the Nusselt number is based on the unit cell of the calculation domain, fin configurations with different aspect ratios A can be directly compared without considering the number of fins per unit width.

Isoflux Plates. For the uniform heat flux boundary condition, the continuity and momentum equations (equations (1)-(4)) are the same, except that $\mathrm{Gr}\Theta_T$ is replaced with $\mathrm{Gr}^*\Theta_q$, where

$$\Theta_q=\frac{T-T_{\mathrm{in}}}{q''H/k} \quad (9)$$

and q'' is the heat flux applied at the bottom plate. Furthermore, since the fully developed condition for a uniform heat flux boundary condition is associated with a linear axial temperature gradient, the energy equation contains an additional source term and becomes

Nomenclature

A = aspect ratio of calculation domain and vortices between fins $= S/2H$
f = friction factor $= -(dp/dz)H/(\rho\bar{w}^2/2)$
$f\cdot\mathrm{Re}$ = friction factor/Reynolds number product
F = relative fin height $= H_{\mathrm{fin}}/H$
g = accelaration due to gravity
Gr = Grashof number $= g\beta\Delta TH^3/\nu^2$
Gr* = modified Grashof number = Gr Nu
h = heat transfer coefficient $= q''/\Delta T$
H = channel height
H_{fin} = fin height
k = thermal conductivity
L = channel length
$\overline{\mathrm{Nu}}$ = spanwise-averaged Nusselt number
p = pressure
Δp = channel pressure drop
P = nondimensional pressure drop $= -\Delta p/[(\alpha\mu/2H^2)(L/H)^2]$
Pr = Prandtl number $= \nu/\alpha$
q' = heat rate per length
q'' = heat rate per area, heat flux
Ra = Rayleigh number = GrPr
Ra* = modified Rayleigh number = Gr*Pr
Re = Reynolds number $= \bar{w}H/\nu$
S = separation between fins
T = temperature
u, v, w = spanwise, vertical, and axial velocities
$\bar{w}$ = mean axial velocity
x, y, z = spanwise, vertical, and axial coordinates
z^* = nondimensional axial distance $= z/H$ Re Pr
α = thermal diffusivity
β = coefficient of thermal expansion
Θ_q = nondimensional temperature for isoflux plate
Θ_T = nondimensional temperature for isothermal plates
ν = kinematic viscosity
ρ = density

Subscripts

b = bulk value (bulk temperature)
bot = bottom plate
f = forced convection value
fd = fully developed
in = inlet value
L = value at channel length
max = maximum value
out = outlet value
top = top plate

$$u^*\frac{\partial\Theta_q}{\partial x^*}+v^*\frac{\partial\Theta_q}{\partial y^*}=\frac{1}{\mathrm{Pr}}\left[\frac{\partial^2\Theta_q}{\partial x^{*2}}+\frac{\partial^2\Theta_q}{\partial y^{*2}}\right]-\frac{1}{\mathrm{Pr}}\frac{w^*}{\bar{w}^*}. \tag{10}$$

Although equation (10) applies for a uniform heat flux in the axial direction, the condition of a spanwise uniform temperature along the bottom surface (including the fin) is again employed ($\Theta_q=1$). This boundary condition is realistic for many situations where plate conduction reduces temperature gradients in the spanwise direction, while temperature gradients are sustained in the flow direction because of the continuous energy input. The top surface is specified as adiabatic ($\partial\Theta_q/\partial y^*=0$), and the Nusselt number is defined as

$$\overline{\mathrm{Nu}}_{fd}=\frac{q''H}{(T_{\mathrm{bot}}-T_b)k}=\frac{1}{\Theta_{q,\,\mathrm{bot}}-\Theta_{q,\,b}} \tag{11}$$

where $\Theta_{q,\,b}$ is the local bulk temperature.

In contrast to fully developed flow between isothermal plates, the flow rate can be important for uniform heating because it affects the axial temperature gradient and ultimately the plate temperature. Hence, the channel pressure drop is of interest and can be determined from the nondimensional friction factor/Reynolds number product

$$f\cdot\mathrm{Re})_{fd}=-\frac{dp/dz}{(\rho\bar{w}^2)/2}\frac{\rho\bar{w}H}{\mu}=\frac{2}{\bar{w}^*} \tag{12}$$

Note that, for isothermal plates, the u^*, v^*, and Θ fields are entirely independent of the axial flow, while for the isoflux plates they depend only on the axial velocity profile, and not on the magnitude of the velocities. Hence the secondary flow, $\overline{\mathrm{Nu}}_{fd}$, and $f\cdot\mathrm{Re})_{fd}$ are all independent of the axial flow rate (Reynolds number), as long as the flow remains laminar.

Solution Technique and Verification

The governing equations were solved using the SIMPLER routine (Patankar, 1980). Uniform grid deployment was used, since it was not known beforehand what the vortex structures of the various configurations would be. The grid deployment and calculation procedure were verified by comparing forced convection values of $f\cdot\mathrm{Re})_{fd}$ and $\overline{\mathrm{Nu}}_{fd}$ to known analytical solutions. The number of nodes was increased until, for a 25×25 deployment, computed and exact values agreed to within 0.5 percent for three standard cases ($F=0$, $A=F=1$ and $A=0.5$, $F=1$). Forced convection Nusselt numbers for the unfinned condition also agreed to within 0.1 percent with analytical values for the isothermal and isoflux boundary conditions. Furthermore, replacing the uniform grid with a power law grid, which concentrated nodes near the fin surface and tip, changed $\overline{\mathrm{Nu}}_{fd}$ and $f\cdot\mathrm{Re})_{fd}$ by less than 1 percent for $\mathrm{Ra}=0$, $F=0.8$, and $A=1.0$. The 25×25 grid was further verified by investigating the sensitivity of computed results to the grid resolution and noting that, for $\mathrm{Ra}=6000$ and the unfinned condition ($F=0$), increasing the grid to 35×35 changed the Nusselt number by only 0.6 percent. Mixed convection calculations of $\overline{\mathrm{Nu}}_{fd}$ for the unfinned, isothermal condition agreed to within 1 percent with the predictions of Hwang and Cheng (1971) for $A=1.0$ and $\mathrm{Ra}=10^4$. Finally, isoflux computations of $\overline{\mathrm{Nu}}_{fd}/\overline{\mathrm{Nu}}_{f,fd}$ for $\mathrm{Ra}^*=2.5\times10^4$, $F=1.0$, and $A=0.25$ agreed to within 1 percent with results reported by Acharya and Patankar (1981) for equivalent conditions.

Results

All computations were performed for air ($\mathrm{Pr}=0.7$), with the fin height F ranging from 0 to 0.8 and 0 to 1.0 for the isothermal and isoflux cases, respectively. The fin spacing A ranged from 0 to 2.0, and the Rayleigh number ranged from 0 to 1.0×10^4 and 0 to 2.5×10^4 for the isothermal and isoflux conditions, respectively. Higher Rayleigh numbers were not modeled due to concern for the existence of unsteady or turbulent flow and the possible violation of planes of symmetry imposed in the model. Because of the node placement and control volume formulation, values of F were restricted to control cell boundaries. The approximate or nominal values reported ($F=0$, 0.2, 0.4, 0.6, 0.8, 1.0) correspond to actual values of $F=0$, 0.217, 0.435, 0.609, 0.826, and 1.0, respectively.

Isothermal Plates. Figure 2 demonstrates the influence of fin height F and fin spacing A on the Nusselt number for $\mathrm{Ra}=0$ and $\mathrm{Ra}=10^4$. For fully developed forced convection ($\mathrm{Ra}=0$) heat transfer is by conduction alone, and the unfinned condition (either $A\to\infty$ or $F=0$) yields a Nusselt number of unity. Fins clearly increase conduction heat transfer, and $\overline{\mathrm{Nu}}_{f,fd}$ increases as the fins approach the top surface (increasing F) or as more fins are added to the surface (decreasing A). For $A=0$, there is no fin separation, and the net effect is one of raising the bottom plate closer to the top. For this limiting case, it is easily shown that $\overline{\mathrm{Nu}}_{f,fd}=1/(1-F)$. Note that the limiting values of $\overline{\mathrm{Nu}}_{f,fd}$ appearing in the figure correspond to the actual, rather than nominal, values of F.

Calculations for $\mathrm{Ra}=10^4$ show that, for all fin heights, close fin spacing impedes secondary flow and there is no difference between $\overline{\mathrm{Nu}}_{fd}$ and $\overline{\mathrm{Nu}}_{f,fd}$ for small values of A. As A increases, however, secondary flows develop, and the subsequent heat transfer enhancement is evident. The secondary flow in Fig. 2 has a very simple structure and consists of a single vortex, with warm fluid rising up the fin surface. As with forced convection, increasing the fin height increases heat transfer. Of particular interest is the maximum Nusselt number exhibited by the mixed convection calculations, which occurs for a fin spacing of $A\approx0.7$. For $\mathrm{Ra}=10^4$, this fin aspect ratio gives the best compromise between enhancement due to the surface area of the fins and enhancement due to the stronger vortices accompanying larger fin separations.

Numerical predictions are most valuable when they are viewed with the limitations of the model assumptions in mind. In addition to the unsteady flow, which is expected for $\mathrm{Ra}>10^4$, large aspect ratios ($A>1.0$) might result in two or more vortices due to transitions that the model equations may or may not be able to predict. The model may also be invalid for short, closely spaced fins, where vortices are likely to form above the fins, perhaps spanning several fins and crossing supposed lines of symmetry.

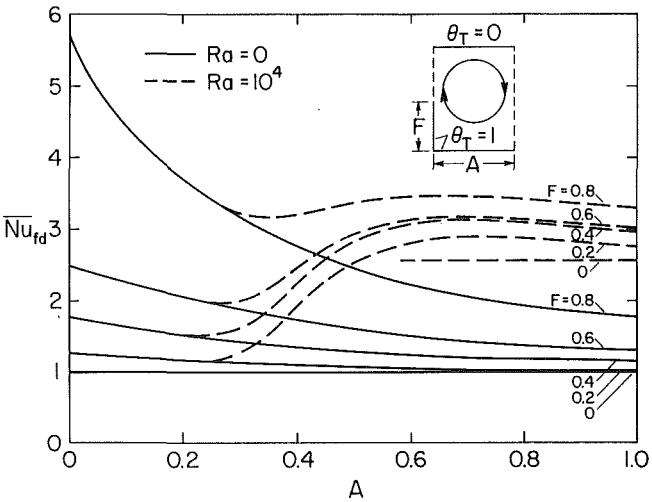

Fig. 2 Effect of fin height and spacing on Nusselt number for $\mathrm{Ra}=0$ and $\mathrm{Ra}=10^4$ (isothermal plates)

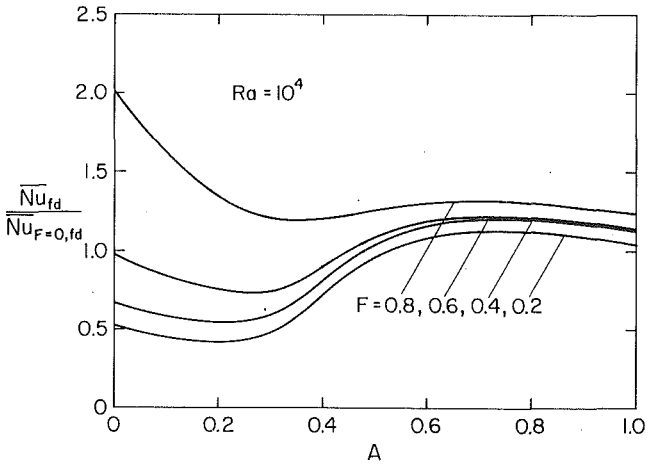

Fig. 3 Effect of fin height and spacing on mixed convection heat transfer enhancement relative to unfinned conditions (isothermal plates)

An unfinned surface with $Ra = 10^4$ also drives a secondary flow, with experiments (Ostrach and Kamotani, 1975; Maughan and Incropera, 1989) indicating a flow structure consisting of square convection cells ($A = 1.0$). Calculations for $F = 0$ and $A = 1.0$ at $Ra = 10^4$ (Fig. 2) predict a secondary flow with a single vortex (a square convection cell) and a Nusselt number of 2.675. Hence, for $Ra = 10^4$, a good comparison of fin performance is not $\overline{Nu}_{fd}/\overline{Nu}_{f,fd}$, but $\overline{Nu}_{fd}/\overline{Nu}_{F=0,fd}$ ($\overline{Nu}_{fd}/2.675$), which directly indicates the increase in heat transfer due to the addition of the fin. Such a comparison (Fig. 3) shows that, while secondary flows rising from fins may drive Nusselt numbers three times larger than those for unfinned forced convection, for $A > 0.5$, Nusselt numbers are only 10 to 30 percent larger than those for unfinned mixed convection. Hence, mixed convection heat transfer with fins is not significantly enhanced relative to mixed convection from an unfinned surface. In fact, for $A < 0.5$, use of the fins with $0.2 < F < 0.6$ is predicted to diminish, rather than enhance, heat transfer because of the reduced tendency for secondary flows to form with close fin spacings.

An additional perspective on the effect of fins is provided by Fig. 4, where results are shown for $F = 0.4$ and a range of fin spacings and Rayleigh numbers. In addition, the calculations for the unfinned surface have been included. As before, Nusselt numbers for forced convection ($Ra = 0$) steadily increase as the fin spacing (A) decreases. With buoyancy, close fin spacings show little or no enhancement with increasing Rayleigh number because fin surface friction prevents the establishment of secondary flows. Significant enhancement begins for $A \gtrsim 0.3$, as vortices develop, and enhancement begins at lower Rayleigh numbers as fin spacing increases.

Figure 4 points out the opposing influences of viscous and buoyancy forces on the Nusselt number. The fin spacing required for maximum heat transfer depends on the Rayleigh number. For low Rayleigh numbers, there is little buoyancy to overcome friction, and weak secondary flows do little for heat transfer enhancement. Hence, it is best to take advantage of conduction with many fins. As the Rayleigh number increases above about 2000, strong buoyancy forces exist for $A = 1.0$, and this fin spacing gives higher heat transfer up to $Ra \approx 8000$. Above $Ra \approx 8000$, there is sufficient buoyancy to permit a reduction in fin spacing, and $A = 0.75$ yields better performance. Notice again, however, that the fins do not perform much better than the unfinned surface.

As previously mentioned, one area of model uncertainty concerns the question of extra vortices for larger fin spacings. This effect is demonstrated in Fig. 5 for $A = 2.0$ and $F = 0.4$. Converged solutions were obtained with one, two, or three

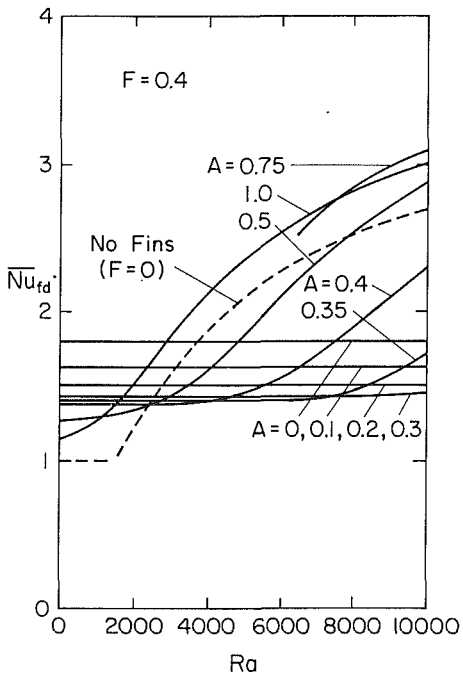

Fig. 4 Effect of Rayleigh number and fin spacing on Nusselt number for $F = 0.4$ (isothermal plates)

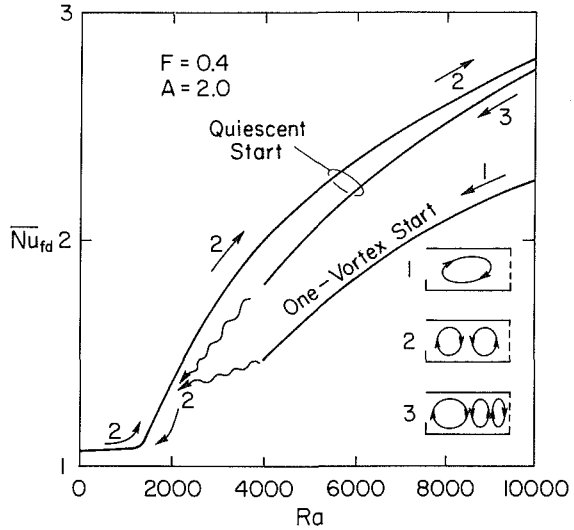

Fig. 5 Multiple numerical solutions for $A = 2.0$ and $F = 0.4$

vortices, depending on the Rayleigh number and the prescribed initial velocity distribution. For $Ra \leq 2000$ a two-vortex solution always resulted, and if the Rayleigh number was steadily increased above this value, while using the last converged two-vortex solution as an initial condition, the two-vortex form of the secondary flow was preserved. On the other hand, if calculations were begun at $Ra = 10{,}000$ with the initial u and v fields set to zero, a three-vortex solution resulted, and persisted until the Rayleigh number dropped below 4000, where the solution would transit to the two-vortex result. Initializing calculations at $Ra = 10{,}000$ with a one-vortex velocity field resulted in a converged one-vortex solution, which, if used as an initial condition for a lower Rayleigh number calculation, preserved the one-vortex solution until the Rayleigh number dropped below 4000. Such multiple solutions are consistent with the numerical results of Fung et al. (1987) and the experimental work of Walden et al. (1987). The presence of fins in a channel would strongly influence the flow

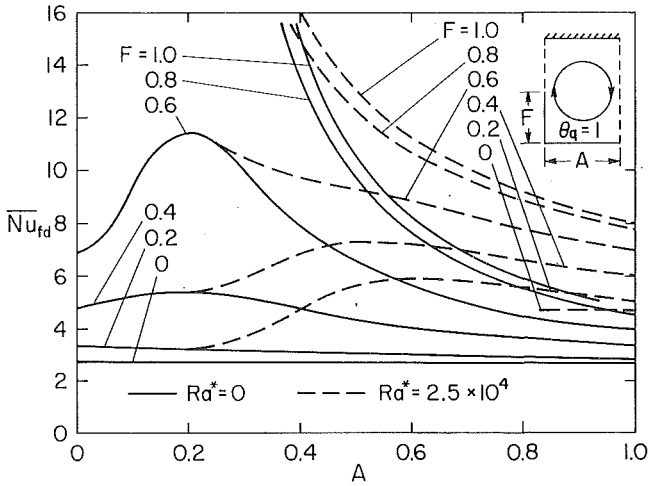

Fig. 6 Effect of fin height and spacing on Nusselt number for Ra* = 0 and Ra* = 2.5 × 10^4 (uniform heat flux)

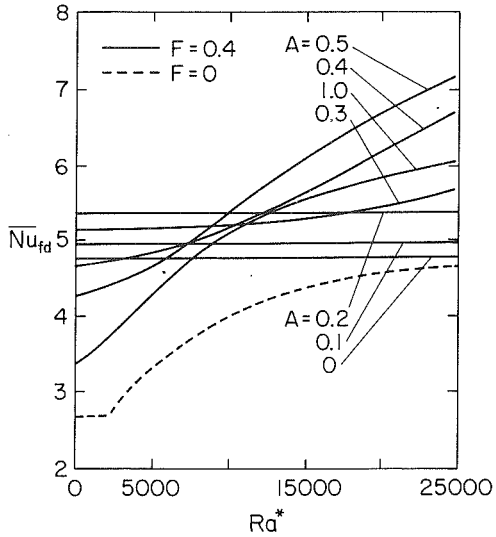

Fig. 7 Effect of Rayleigh number and fin spacing on Nusselt number (uniform heat flux)

structures, and actual fully developed conditions may depend on channel upstream conditions and/or previous heating conditions. Although theory alone cannot predict with certainty which flow and heat transfer condition will result, in related experiments (Maughan and Incropera, 1990), the two-vortex system was seen for all Rayleigh numbers at $A = 2.0$.

Isoflux Plate. The effect of fins on a channel heated uniformly from below is shown in Fig. 6 for $Ra^* = 0$ and $Ra^* = 2.5 \times 10^4$. For $A = 0$, there is no separation between the fins, and the effect is simply to reduce the effective height of the channel. For this limiting case, the fully developed forced convection temperature and velocity profiles can be determined from the one-dimensional governing equations, and from an analytical solution the Nusselt number, based on the full height of the channel, can be expressed by

$$\overline{Nu}_{f,\,fd} = \frac{-\frac{1}{36}F^6 + \frac{1}{6}F^5 - \frac{5}{12}F^4 + \frac{5}{9}F^3 - \frac{5}{12}F^2 + \frac{1}{6}F - \frac{1}{36}}{\frac{13}{1260}F^7 - \frac{13}{180}F^6 + \frac{13}{60}F^5 - \frac{13}{36}F^4 + \frac{13}{36}F^3 - \frac{13}{60}F^2 + \frac{13}{180}F - \frac{13}{1260}} \tag{13}$$

With $F = 0$, this equation reduces to $\overline{Nu}_{f,fd} = 2.692$, and as $F \to 1.0$, $\overline{Nu}_{f,fd} \to \infty$.

For the forced convection results, flow begins to move between the fins with increasing A, and the additional area causes the heat transfer coefficient to rise to a local maximum. This effect was not apparent for the isothermal case, since conditions were entirely conduction dominated and fluid movement between the fins was irrelevant. A further increase in fin spacing, however, causes the Nusselt number to decrease gradually, as there is less surface area per unit width of the plate. Thus, for each fin height, there is an optimum fin spacing from the standpoint of forced convection heat transfer. Note again that heat transfer improves as the fin height increases. Fins approaching or touching the top surface cause significant enhancement by forcing all the flow into the channels formed by the fins.

Calculations for mixed convection at $Ra^* = 2.5 \times 10^4$ again show that small fin spacings prevent secondary flow from enhancing heat transfer. When the secondary flow is able to develop, appreciable enhancement follows and, for lower fin heights, the Nusselt number exceeds the previous forced convection peak, resulting in a new maximum and an optimal fin spacing. As with the isothermal plates, the secondary flow for $A \leq 1.0$ consisted of a single vortex with fluid rising up the heated fin. Calculations for $F = 0$ and $Ra^* = 2.5 \times 10^4$ were performed with $A = 1.0$ and predict the Nusselt number for mixed convection from an unfinned surface.

Figure 7 indicates the effect of the modified Rayleigh number on heat transfer for $F = 0.4$. For $0 \leq A \leq 0.2$, there is little heat transfer enhancement over the prescribed Rayleigh number range. Consistent with Fig. 6, the forced convection Nusselt number ($Ra^* = 0$) has its maximum value at $A \approx 0.2$. Mixed convection results for $A \geq 0.3$ show enhancement with increasing Rayleigh number due to the onset and strengthening of the secondary flow. The optimum fin spacing (in terms of heat transfer alone) depends on the value of Ra*, with $A \approx 0.2$ preferred for $Ra^* < 1.0 \times 10^4$ and with $A \approx 0.5$ for larger values of the Rayleigh number.

Since pressure drop and flow rate can be of concern for a uniform heat flux condition, a complete evaluation of the fins should consider the increased pressure drop. In general, the effect of fin height and spacing on $f \cdot Re)_{fd}$ is similar to the effect on $\overline{Nu}_{fd}$. However, $f \cdot Re)_{fd}$ results are not presented directly. Instead a more complete assessment of fin performance is made by evaluating the ratio of heat transfer enhancement to the increased pressure drop, in each case comparing finned and unfinned results at the same modified Rayleigh number. Hence, the parameter of interest is $[(\overline{Nu}_{fd}/\overline{Nu}_{F=0,fd})/(f \cdot Re_{fd})/(f \cdot Re)_{F=0,fd}]$ and, as shown in Fig. 8, large Nusselt numbers associated with close fin spacings are also associated with large pressure drops, thereby diminishing the advantage of the fins. Larger fin spacings, on the other hand, carry a lower pressure drop penalty and result in a net advantage from the fins. The increase, however, is modest, ranging from just a few percent for short fins to only about 25 percent for fins extending to the very top.

As pointed out by Lau and Mahajan (1988) for turbulent flow, tightly spaced fins could so severely restrict the flow that, for uniform heat flux, a large increase in the bulk

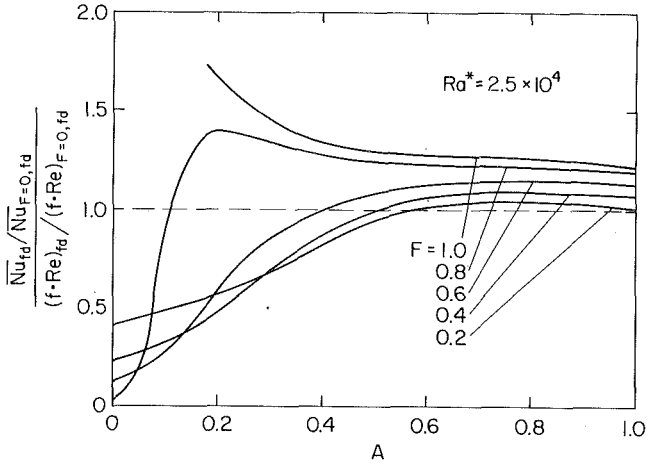

Fig. 8 Effect of fin height and spacing on heat transfer enhancement relative to pressure losses (uniform heat flux)

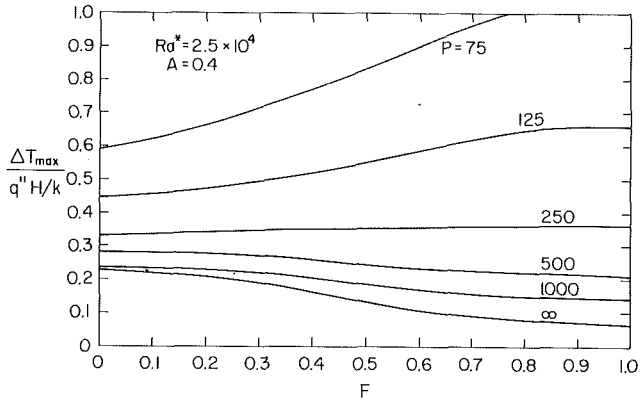

Fig. 9 Effect of available pressure drop on the plate maximum temperature

temperature would result. Hence, rather than fins decreasing plate temperatures through higher Nusselt numbers, plate temperatures could actually increase because of the reduced flow rate that would be associated with the restriction of a fixed pressure drop. To investigate this possibility, consider a fixed pressure drop Δp for fully developed flow through a channel of length L and height H. To determine the maximum plate temperature, which occurs on the heated surface at $z = L$, an energy balance is first used to express the rise in the bulk temperature of the fluid passing through the channel as

$$\frac{T_{b,\,\mathrm{out}} - T_{b,\,in}}{q'' H/k} = \frac{\alpha L}{H^2 \bar{w}} = z_L^* \tag{14}$$

where z_L^* is a nondimensional channel length. Defining a nondimensional pressure drop P and substituting from equation (14), it follows that

$$\frac{T_{b,\,\mathrm{out}} - T_{b,\,\mathrm{in}}}{q'' H/k} = z_L^* = \frac{f\cdot \mathrm{Re})_{fd}}{P} \tag{15}$$

Since the plate temperature at $z = L$ exceeds the outlet bulk temperature by the amount $(T_{\mathrm{bot},\,z=L} - T_{b,\,\mathrm{out}}) = q'' h$, or $(T_{\mathrm{bot},\,z=L} - T_{b,\,\mathrm{out}})/(q'' H/k) = 1/\mathrm{Nu}_{fd}$, equation (15) yields a maximum excess plate temperature of

$$\frac{T_{\mathrm{bot},\,z=L} - T_{\mathrm{in}}}{q'' H/k} = \frac{\Delta T_{\max}}{q'' H/K} = \frac{f\cdot \mathrm{Re})_{fd}}{P} + \frac{1}{\overline{\mathrm{Nu}}_{fd}} \tag{16}$$

where it is tacitly assumed that the temperature rise in the thermal entry region is small. Equation (16) implies that, once the value of P has been established by prescribing the channel geometry, fluid, and available pressure drop Δp, the maximum plate temperature is entirely a function of $\overline{\mathrm{Nu}}_{fd}$ and $f\cdot \mathrm{Re})_{fd}$, which in turn depend only on the Rayleigh number and fin geometry.

Figure 9 shows the effect of fin height on the maximum plate temperature for $A = 0.4$ and $\mathrm{Ra}^* = 2.5 \times 10^4$. When judged in terms of $\Delta T_{\max}/(q'' H/k)$, fin effectiveness depends on the available pressure drop. If large pressure drops are allowed, fins are advantageous and the maximum plate temperature decreases with increasing F. On the other hand, for small pressure drops, plate temperatures increase with increasing F. The optimum condition is therefore either no fins or the longest possible fins, depending on the available pressure drop.

For many cooling situations, sufficient pumping power is readily available, and fins will always be advantageous. There is, however, an important class of flows where pressure drop is a concern, namely those driven by natural draft, where buoyancy forces themselves, either within the channel or elsewhere, are the only mechanism for moving fluid between the plates. With no external source of power, flow rates in this type of situation are very sensitive to the channel pressure drop, and the presence of fins could detract from overall system performance.

Summary

For fully developed, laminar, forced convection flow in a horizontal channel with an isothermally heated bottom plate and an isothermally cooled upper plate, calculations revealed that fins significantly enhance heat transfer by providing additional surface area for conduction. Enchancement increases with fin height and decreasing fin spacing. For mixed convection, buoyancy forces induce a secondary flow in the form of longitudinal vortices that further increases heat transfer. However, because the strength of the secondary flow decreases with decreasing fin spacing, there is an optimum spacing that maximizes the Nusselt number. Computations for fully developed flow in a channel heated uniformly from below and well insulated from above revealed similar trends. In addition, it was demonstrated that, for a fixed pressure drop, the addition of fins can increase maximum plate temperatures by restricting the flow rate and causing a rapid rise in bulk temperature. This effect is most pronounced in situations where throughflow is driven by a natural draft.

Acknowledgments

Support of this work by the National Science Foundation under Grant No. CBT-8316580 is gratefully acknowledged. One author (J.R.M.) is also grateful for fellowships provided by the Chevron Corporation, NL Industries Foundation, the Shell Foundation, and the Ingersoll Rand Corporation.

References

Acharya, S., and Patankar, S. V., 1981, "Laminar Mixed Convection in a Shrouded Fin Array," ASME Journal of Heat Transfer, Vol. 103, pp. 559-565.

Fung, L., Nandakumar, K., and Masliyah, J. H., 1987, "Bifurcation Phenomena and Cellular Pattern Evolution in Mixed Convection Heat Transfer," *Journal of Fluid Mechanics*, Vol. 177, pp. 339-357.

Hwang, G. J., and Cheng, K. C., 1971, "A Boundary Vorticity Method for Finite Amplitude Convection in Plane Poiseuille Flow," *Developments in Mechanics*, Proceedings of the 12th Midwestern Mechanics Conference, Vol. 6, pp. 207-220.

Lau, K. S., and Mahajan, R. L., 1988, "Convective Heat Transfer From Longitudinal Fin Arrays in the Entry Region of Turbulent Flow," ASME Paper No. 88-WA/EEP-1.

Maughan, J. R., and Incropera, F. P., 1990, "Mixed Convection Heat Transfer With Longitudinal Fins in a Horizontal Parallel Plate Channel: Part II—Experimental Results," ASME Journal of Heat Transfer, Vol. 112, this issue.

Mirza, S., and Soliman, H. M., 1985, "The Influence of Internal Fins on

Mixed Convection Inside Horizontal Tubes," *International Communications in Heat and Mass Transfer*, Vol. 12, pp. 191–200.

Ostrach, S., and Kamotani, Y., 1975, "Heat Transfer Augmentation in Laminar Fully Developed Channel Flow by Means of Heating From Below," ASME JOURNAL OF HEAT TRANSFER, Vol. 97, pp. 220–225.

Patankar, S. V., 1980, *Numerical Heat Transfer and Fluid Flow*, Hemisphere Publishing Corporation, New York.

Prakash, C., and Renzoni, P., 1985, "Effect of Buoyancy on Laminar Fully Developed Flow in a Vertical Annular Passage With Radial Internal Fins," *International Journal of Heat and Mass Transfer*, Vol. 28, pp. 995–1003.

Sparrow, E. M., Baliga, B. R., and Patankar, S. V., 1978, "Forced Convection Heat Transfer From a Shrouded Fin Array With and Without Tip Clearance," ASME JOURNAL OF HEAT TRANSFER, Vol. 100, pp. 572–579.

Walden, R. W., Kolodner, P., Passner, A., and Surko, C. M., 1987, "Heat Transport by Parallel-Roll Convection in a Rectangular Container," *Journal of Fluid Mechanics*, Vol. 185, pp. 205–234.

Mixed Convection Heat Transfer With Longitudinal Fins in a Horizontal Parallel Plate Channel: Part II—Experimental Results

J. R. Maughan[1]

F. P. Incropera

Heat Transfer Laboratory,
School Of Mechanical Engineering,
Purdue University,
West Lafayette, IN 47907

Experiments have been performed to investigate the effects of longitudinal fins on laminar mixed convection in airflow between parallel plates, with the bottom plate heated isothermally and the top plate cooled isothermally. In addition to the unfinned condition, nondimensional fin spacings in the range $0.25 < A < 2.0$ were considered for relative fin heights of $F = 0.5$ and 0.9 and for the Rayleigh number range $760 < Ra < 29700$. For fully developed flow over the unfinned surface, square longitudinal vortices ($A = 1.0$) were observed for $Ra > Ra_c$ and persisted until $Ra \approx 20{,}000$. While data for closely spaced fins showed considerable enhancement at lower Rayleigh numbers due to the additional surface area, the development of vigorous secondary flow was delayed. Hence, for fully developed conditions and $F = 0.5$, Nusselt numbers for the finned surface were, in some instances, lower than those for mixed convection without fins. Results are compared to previous numerical predictions, and it is shown that agreement is good until the flow violates modeling assumptions of steady, symmetric flow between fins.

Introduction

Concerns about providing adequate cooling of printed circuit boards have recently motivated experiments on the use of longitudinal fins to enhance forced convection heat transfer between parallel plates. Lau and Mahajan (1988) considered the effect of shroud clearance and fin height on convection for turbulent flow in the entry region of a fin array heated uniformly from below. Results indicated that, for a constant mass flow rate and fin height, performance of the finned array decreased with increasing tip clearance. This effect can be attributed to a lower average flow velocity and an increased tendency for fluid to bypass the region between fins. They further noted that, for no tip clearance and the same flow rate, tall and short fins had comparable performance because the additional surface area of the fins was offset by a lower flow velocity. A correlation was developed to predict the performance of different fin heights, spacings, and thicknesses for fully developed, turbulent forced convection. Experiments on turbulent flow in fin arrays were also reported by Kadle and Sparrow (1986).

Experiments on mixed convection in horizontal tubes with longitudinal internal fins were performed by Rustum and Soliman (1988). Results compared well with previous numerical predictions and showed that fins delayed the development of buoyancy-driven flows. Enhancement due to secondary flows increased rapidly with Rayleigh number.

In a companion to this paper (Maughan and Incropera, 1990), the effect of longitudinal fins on laminar mixed convection between horizontal plates was considered numerically. For a channel of fixed height, the effects of Rayleigh number, fin height, and fin spacing were investigated for fully developed flow in a channel heated uniformly from below and for flow between isothermal plates. Results showed that, while forced convection heat transfer increased with increasing fin height and decreasing fin spacing, closely spaced fins inhibited secondary flows and the attendant heat transfer enhancement. Hence, in some cases, there was an optimum fin spacing, which represented a compromise between the additional surface area of many fins and the strong secondary flow associated with fewer fins. In this paper, the effects of fin height, fin spacing, and Rayleigh number on laminar mixed convection are investigated experimentally.

Experimental Apparatus and Procedure

The situation currently under consideration is laminar airflow in a finned parallel plate channel heated isothermally from below and cooled isothermally from above (Fig. 1). Air from the blower was metered and conditioned before passing through a channel of width 308 mm, height 20 mm, and test section length 914 mm. Two Reynolds numbers were emphasized: $Re = 10$, which quickly yields fully developed conditions, and $Re = 1000$, which provides an extended thermal entry region. The entrance section was sufficiently long to provide hydrodynamically fully developed flow at the start of the heated section for both Reynolds numbers. Flow visualization

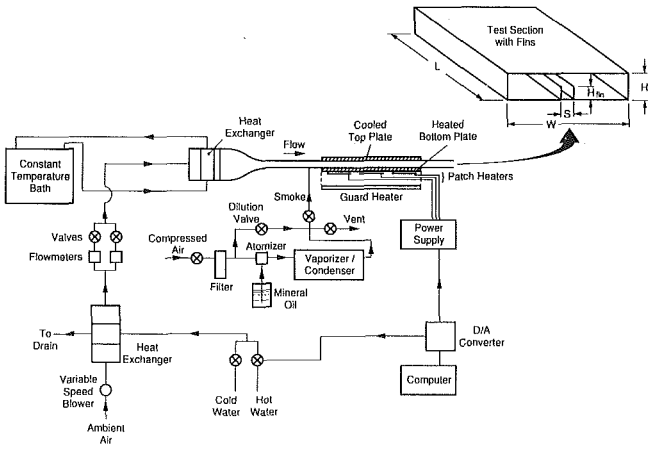

Fig. 1 Schematic of air flow channel

[1]Present address: General Electric Corporate Research and Development, Schenectady, NY 12301.

Contributed by the Heat Transfer Division for publication in the JOURNAL OF HEAT TRANSFER. Manuscript received by the Heat Transfer Division May 9, 1989; revision received October 16, 1989. Keywords: Finned Surfaces, Mixed Convection, Natural Convection.

was accomplished by introducing a uniform sheet of smoke into the flow at the bottom surface, just before the heated test section. Additional details of the smoke injection and channel construction are reported by Maughan and Incropera (1989).

A uniform surface temperature at the bottom of the test section was maintained with a 3.2-mm-thick copper plate heated by three independently controlled patch heaters. Bottom plate temperatures were in the range 20–80°C. Acting on input from eight thermocouples in the copper plate, the data acquisition computer controlled power dissipation in each patch heater to hold the plate at the prescribed temperature. Isothermal conditions were maintained to within 1 percent of the temperature difference between the top and bottom plates, except for the leading edge, which was 3 and 7 percent cooler for $\mathrm{Re} = 10$ and $\mathrm{Re} = 1000$, respectively. Conduction losses were minimized by circulating fluid through grooves machined in an aluminum plate placed below the heater assembly. The temperature of the fluid was held at that measured just below the patch heaters. A similar aluminum plate formed the top surface of the test section and was held at the fluid inlet temperature, 20°C. All surfaces were checked for flatness and were carefully cleaned and polished. The rigidity of each plate was maintained with three lengths of angle iron.

Fins were attached to the heated surface by machining longitudinal grooves 0.79 mm wide and 1.59 mm deep into the copper with centers spaced 10 mm apart. The fins were cut from 0.81-mm-thick aluminum stock, whose length corresponded to that of the copper heater (914 mm), and were sheared to the width necessary to provide fin heights of 10 and 18 mm. Initially, the grooves were filled with a mixture of spackling paste and thermally conductive silicon paste. When fins were used, the paste was removed from the desired slots, the fin edges were coated with conducting paste, and the fins were press fitted into the length of the slots. This procedure maintained the necessary fin rigidity and alignment and provided the capability to add, change, or remove fins to produce the various configurations of interest. Calculations showed that the departure from isothermal conditions caused by the filled grooves was less than 1 percent. Moreover, experiments on a fin prototype indicated that the contact resistance was about 1 percent of the total fin resistance and that fin efficiencies of approximately 98 percent could be expected. Average fin tip temperatures, $(T_{tip} - T_{top})/(T_{bot} - T_{top})$, measured during the experiments were 0.976 and 0.954 for $\mathrm{Re} = 10$ and $\mathrm{Re} = 1000$, respectively.

The average Nusselt number for the heated bottom plate is defined as

$$\overline{\mathrm{Nu}} = \frac{q_{conv}}{A_s(T_{bot} - T_{top})} \tag{1}$$

where the bar indicates that the Nusselt number is averaged over the entire surface of the plate. The top and bottom surface temperatures are measured directly from thermocouples in the plates, and properties are evaluated at $T_{avg} = (T_{bot} + T_{top})/2$. Convection heat transfer from the bottom plate, q_{conv}, was determined from an energy balance

$$q_{tot} = q_{conv} + q_{rad} + q_{insul} + q_{span} + q_{up} + q_{down} \tag{2}$$

where conduction losses have been divided into four components: downward through the insulation, out the sides of the plate (spanwise), and in the upstream and downstream directions.

The total dissipated energy was found by applying Ohm's law, $q = V^2/R$, at each patch heater. The voltage drop was measured during the experiment, while the electrical resistance was measured before the experiment. Although each heater had a different resistance, the value was found to be independent of temperature. Radiation losses were determined from the assumption of isothermal, gray, diffuse, parallel, plates. Because the emissivity of the polished copper and aluminum surfaces is low (~ 0.05), radiation losses never exceeded 5 percent of the total power dissipation. Although heat losses through the insulation were rendered small by the guard heater, spanwise losses, which occur primarily due to conduction up the sidewall from the heated copper to the cooled aluminum, accounted for 10 to 30 percent of the power dissipation. Since thermocouple measurements showed that the temperature distribution in the sidewall could be well predicted with the appropriate form of the fin equation, spanwise losses from the sides of the copper plate were calculated from

$$q_{span} = 2\sqrt{hk_w}tL\left(\frac{\Theta_{bot}\cosh(mH) - \Theta_{top}}{\sinh(mH)}\right) \tag{3}$$

Heat transfer from the leading and trailing edges was approximated by the expression for an infinite fin

$$q_{down} = W\sqrt{hk_w}t(T_{bot} - T_{out}) \tag{4a}$$

Nomenclature

A = aspect ratio of calculation domain and vortices between fins $= S/2H$
A_s = unfinned surface area of heated plate $= WL$
F = nondimensional or relative fin height $= H_{fin}/H$
g = acceleration due to gravity
h = heat transfer coefficient
H = channel height or plate separation
H_{fin} = fin height
k = thermal conductivity
L = channel length
m = fin parameter $= (h/k_w t)^{1/2}$
$\overline{\mathrm{Nu}}$ = plate-averaged Nusselt number, equation (1)
$\overline{\mathrm{Nu}}_{tot}$ = Nusselt number based on total area of plate and fins
q'' = heat rate per area, heat flux
q = heat rate
R = electrical resistance of patch heater
Ra = Rayleigh number $= g\beta\Delta TH^3/\nu\alpha$
Ra* = modified Rayleigh number = RaNu
Ra_c = critical Rayleigh number = 1708
Re = Reynolds number $= \bar{w}H/\nu$
S = separation between fins
t = thickness of side wall
T = temperature
T_{avg} = average temperature $= (T_{bot} + T_{top})/2$
V = heater voltage drop
$\bar{w}$ = mean axial velocity
W = width of plate
α = thermal diffusivity
β = coefficient of thermal expansion
Θ = excess temperature $= T - T_{avg}$
ν = kinematic viscosity
ρ = density

Subscripts

bot = bottom plate
conv = convection
down = downstream direction
f = forced convection value
fd = fully developed value
in = inlet value
insul = insulation
out = outlet value
rad = radiation
span = spanwise
tip = fin tip
top = top plate
tot = total
up = upstream direction
w = side wall

$$q_{up} = W\sqrt{h_{up}k_w t}(T_{bot} - T_{in}) \quad (4b)$$

where $h_{up} = 5$ W/m^2•K is the approximate heat transfer coefficient on the bottom of the channel upstream of the heater plate. The heat transfer coefficient on the side wall and beyond the trailing edge was assumed to be the same as that inside the channel. Each of these losses accounted for approximately 2 percent of the total power dissipation.

Following procedures outlined by Moffat (1988), the uncertainty in the Nusselt number was estimated to range from 7 to 17 percent. The estimate accounts for uncertainties associated with component measurements, as well as for uncertainties related to assumptions used in correcting for conduction and radiation losses. The largest uncertainties are associated with operating conditions corresponding to small temperature differences ($\Delta T \sim 2$°C), for which spanwise losses are most significant. Although the uncertainty in the Reynolds number is approximately 2 percent for Re = 1000 and 25 percent for Re = 10, the larger value associated with the smaller Reynolds number has no effect on related fully developed conditions. A 15 percent uncertainty in the Rayleigh number is mainly associated with measuring and maintaining the channel height. All properties were evaluated at the average plate temperature, $(T_{top} + T_{bot})/2$, which has an important bearing on the Rayleigh number, since the thermal diffusivity and kinematic viscosity of air vary by approximately 30 percent over the temperature range from 20 to 80°C.

Results and Discussion

Along with the unfinned condition, measurements were taken with 4, 7, 15, and 29 fins ($A = 2.0$, 1.0, 0.5, and 0.25) and for fin heights of 10 and 18 mm ($F = 0.5$ and 0.9). The temperature difference between plates ranged from 1 to 60°C ($760 < \mathrm{Ra} < 29{,}700$). Plate-averaged results for Re = 10 are representative of fully developed conditions because, at this low flow rate, the secondary flow developed very rapidly and appeared fully established within 50 mm of the leading edge. Although the value of the (laminar) Reynolds number has no effect on fully developed conditions (Ostrach and Kamotani, 1975), some throughflow was necessary for flow visualization. Nusselt number measurements at Re = 1000 are also plate averaged. At this Reynolds number, the test section is in the thermal entry region.

Results are shown in Figs. 1–6, where experimental results are shown with open symbols and curves are drawn through the data. Nusselt numbers for the unfinned surface and Re = 10 (Fig. 2) correspond (within experimental uncertainty) to the fully developed value of $\mathrm{Nu}_{f,fd} = 1$ for $0 < \mathrm{Ra}_c < 1708$. Above Ra_c, a sharp increase in Nu marks thermal instability and the establishment of secondary flow. Data for Re = 10 show good agreement with the fully developed flow correlation proposed by Ostrach and Kamotani (1975):

$$\mathrm{Nu}_{fd} = 1 + \frac{8.30 \times 10^{-4}(\mathrm{Ra} - 1708)}{\sqrt{1 + 1.45 \times 10^{-4}(\mathrm{Ra} - 1708)^{4/3}}} \quad (5)$$

Equation (5) is shown in the figures with a dashed line. In the thermal entry region (Re = 1000), data below Ra ≈ 17,000 show no Rayleigh number dependence and agree well with the analytical prediction of $\overline{\mathrm{Nu}}_f = 3.35$ for pure forced convection (Lundberg et al., 1963). Data at larger Rayleigh numbers show enhancement due to secondary flows.

The effects of fins on fully developed mixed convection are shown in Fig. 3(*a*). At the lowest Rayleigh numbers, heat transfer is conduction dominated and a larger number of fins (smaller fin spacing A) yields higher Nusselt numbers. Because convection in a fluid heated from the side is not associated with a threshold of instability, some of the finned plate results show a Rayleigh number dependence as Ra → 0, indicating a

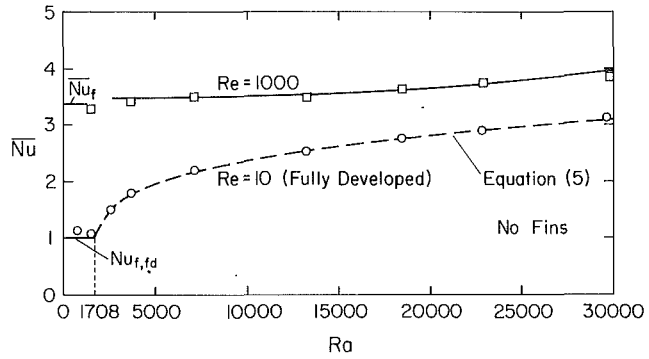

Fig. 2 Effect of Rayleigh number on Nusselt number for the unfinned condition

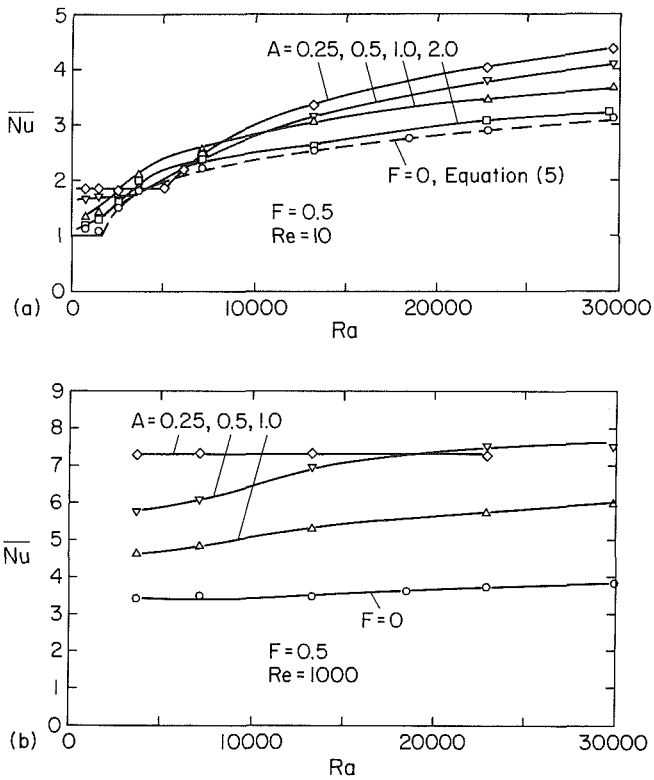

Fig. 3 Effect of fin spacing and Rayleigh number on Nusselt number for $F = 0.5$ and (*a*) Re = 10, (*b*) Re = 1000

weak secondary flow. As the Rayleigh number increases, the fin spacing influences the interaction between buoyancy and viscous forces, with closer fin spacings requiring a higher Rayleigh number to drive a strong secondary flow. Hence, in a moderate Rayleigh number region, a greater number of fins is not necessarily better. For example, in the range $3000 < \mathrm{Ra} < 8000$, fins with $A = 1.0$ give the highest heat transfer rate, outperforming surfaces with two and four times as many fins. Similarly, at Ra = 5000, the closest fin spacing ($A = 0.25$) has the worst performance, providing a lower Nusselt number than even an unfinned surface at the same Rayleigh number. Although buoyancy forces eventually become strong enough to drive vigorous secondary flows for each configuration, the figure illustrates that extended surfaces do not always provide heat transfer enhancement under mixed convection conditions.

Data for the thermal entry region (Fig. 3*b*) reveal similar trends. Fins increase heat transfer for forced convection (small Rayleigh number) by providing additional surface area. As the Rayleigh number increases, plates with larger fin spacings

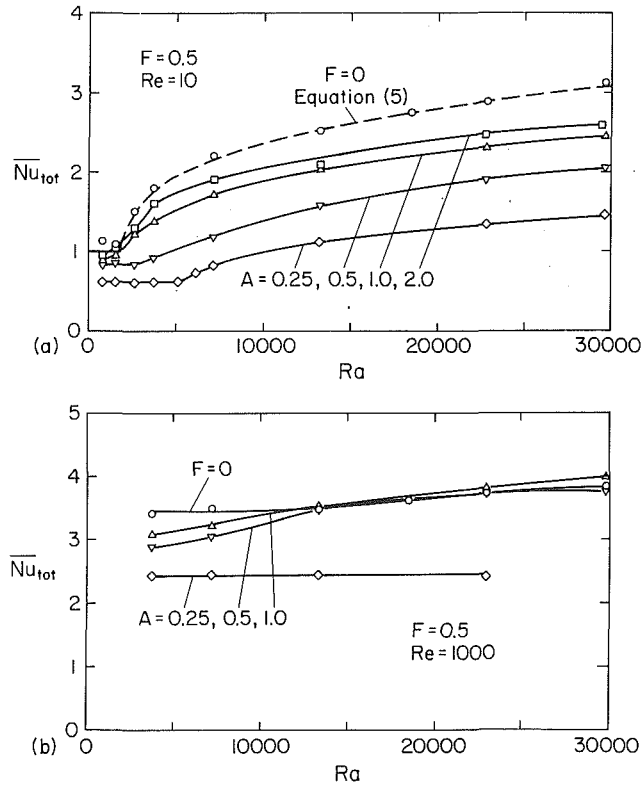

Fig. 4 Effect of fin spacing and Rayleigh number on Nusselt number based on total surface area for $F = 0.5$ and (a) Re = 10, (b) Re = 1000

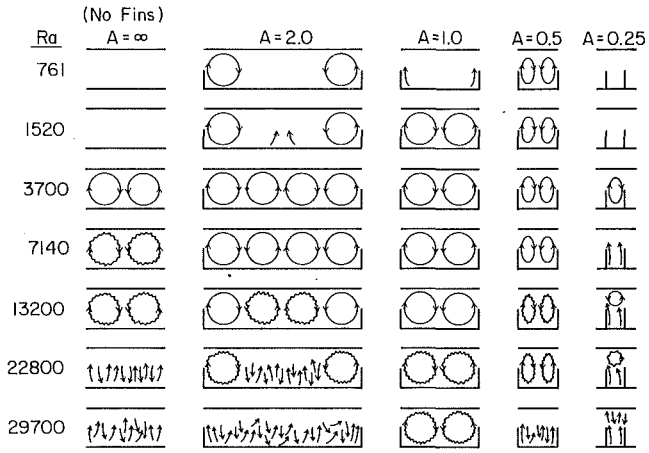

Fig. 5 Schematics of secondary flow for $F = 0.5$ and $Re = 10$

develop secondary flows with attendant heat transfer enhancement, while the closely spaced fins ($A = 0.25$) inhibit secondary flow. As a result, beyond Ra ≈ 19000 the surface with $A = 0.5$ outperforms that for which $A = 0.25$.

Since the Nusselt number $\overline{Nu}$ has been defined to provide a direct measure of the heat transfer rate and is therefore based on the fixed area of the bottom plate, A_s, it does not reveal the actual average convection coefficient on the heat transfer surfaces. However, by multiplying the measured Nusselt number by the factor $A/(A+F)$, a Nusselt number based on the total heat transfer surface area of the channel, $\overline{Nu}_{tot}$, is obtained and indicates whether use of the fins increases or decreases the average heat transfer coefficient on the surfaces. Figure 4 clearly indicates that, while fins increase the total heat transfer rate, they reduce the average heat transfer coefficient below values associated with an unfinned surface. This form of the Nusselt number gives additional physical insight into the effects of the fins but disguises the overall contribution of the extended surfaces.

Flow visualization for each condition was performed by introducing a layer of smoke into the channel upstream of the test section and by observing the secondary flow structures from the end of the channel. Illumination was provided by two fluorescent lamps through the transparent sidewalls. Although this technique allowed the general flow structure to be seen, the upper aluminum plate, small channel height, and large number of fins made photography difficult. Hence, aspects of the secondary flows are more effectively communicated through the end view sketches of Fig. 5, which correspond to fully developed conditions (Re = 10). Since the flows developed very quickly at this low Reynolds number, the same flow structure existed over essentially the entire plate. The existence of longitudinal vortices is indicated by a circular or elliptic cell, which is wavy if the vortices were unsteady and irregular. Series of arrows are used to indicate the vigorous mixing associated with random ascending and descending plumes that did not exhibit any particular larger, more coherent structure. Most flows (except for $A = 0.25$) were symmetric about the plane midway between fins.

The leftmost column of sketches shows the effect of Rayleigh number on secondary flow between unfinned plates. As expected from the heat transfer data, no secondary flow was evident for the lowest Rayleigh numbers, but higher values were associated with pairs of counterrotating vortices, each having an aspect ratio of $A \approx 1.0$. For Ra > 7000, the vortices became unsteady and developed waves and irregularities. Eventually, near Ra = 20,000, a regular cell structure was no longer evident, and the random unsteady mixing of rising and descending plumes closely resembled turbulent free convection.

In contrast to the unfinned condition, the widely spaced fins of $A = 2.0$ exhibited secondary flow at even the lowest Rayleigh number. One vortex was apparent on both sides of a fin, and, in all likelihood, an additional vortex was also present but was too weak to entrain a visible amount of smoke from the bottom surface. At higher Rayleigh numbers, this second vortex was also visible. As the Rayleigh number approached 13,000, the vortices farthest from the fins became unstable and were no longer evident at Ra = 22,800. At the highest Rayleigh number, the only consistent structure was a strong plume rising along the side of each fin. Note that, although computations predicted that either one, two, or three pairs of vortices are possible for $A = 2.0$ (Maughan and Incropera, 1989), the only laminar flow structure seen for $A = 2.0$ consisted of two pairs.

For fins with $A = 1.0$, vortices with $A = 1.0$ persisted throughout the range of Rayleigh numbers. For $A = 0.5$, conditions were similar to those for $A = 1.0$, except that vortices had an aspect ratio of $A = 0.5$. Apparently, these smaller convection cells are less stable than cells with $A = 1.0$, because by Ra = 30,000 a regular vortex structure was no longer evident.

The weak flow structure for $A = 0.25$ was difficult to see because of the closely spaced fins. When the structure was visible (Ra = 3700), however, it consisted of a single vortex between two fins, and not a vortex pair. Because this vortex was extremely weak, the heat transfer data (Fig. 3*a*) do not show any appreciable enhancement. An increase in the Rayleigh number above about 5500 did, however, create a buoyancy force strong enough to drive a plume up both sides of the fin, flushing out the weak vortex. It is at this point that the heat transfer data began to show enhancement. With further increase in the Rayleigh number to approximately 13,000, a vortex briefly became apparent above the fins, before decaying into random mixing.

Data for $F = 0.9$ (Fig. 6) show trends similar to those iden-

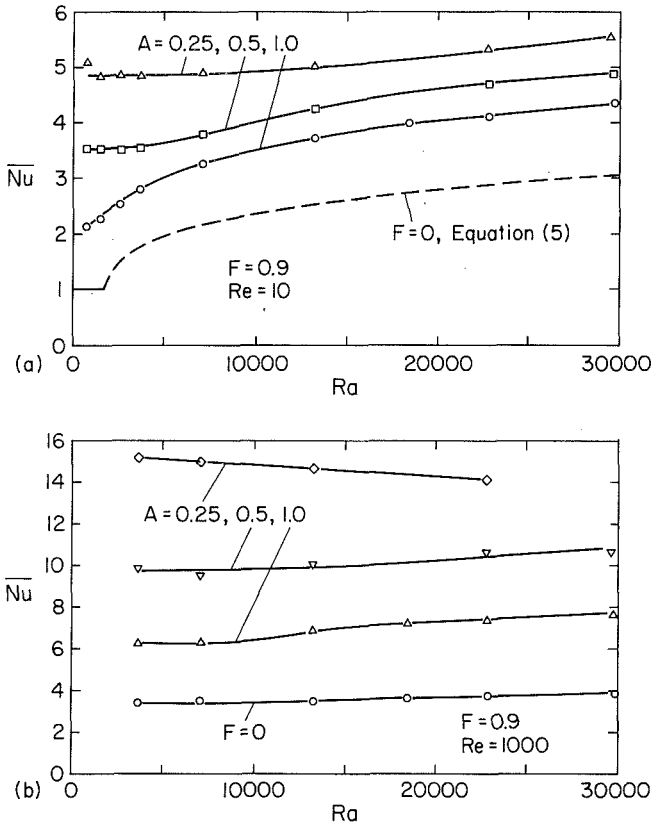

Fig. 6 Effect of fin spacing and Rayleigh number on Nusselt number for $F = 0.9$ and (a) Re = 10, (b) Re = 1000

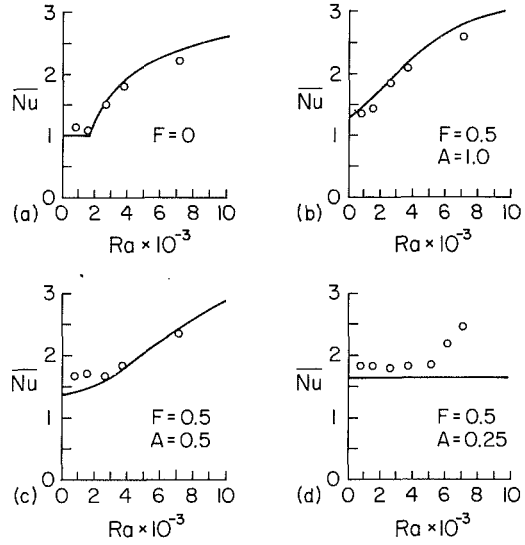

Fig. 7 Comparison of numerical predictions (solid curves) with experimental results (symbols) for Re = 10: (a) an unfinned surface, and (b, c, d) finned surfaces

tified for $F = 0.5$. Levels of enhancement, however, are higher than for $F = 0.5$ and the closer fin spacings always increase heat transfer. Both effects may be attributed to the additional surface area and to the greater role of conduction directly to the top cooled surface.

The experimental data for $F = 0.5$ are compared to earlier numerical predictions (Maughan and Incropera, 1990) in Fig. 7. Because the predictions are for fully developed flow, only results for Re = 10 are shown. Both the experiments and computations exhibit the onset of instability at Ra = 1708 for an unfinned plate and the lack thereof for a finned surface. Enhancement due to both additional surface area and secondary flow is apparent and further demonstrates the tradeoff between the effect of conduction for close fins and additional fluid motion for fins spaced more widely.

For $F = 0$ (no fins), the agreement is good until the Rayleigh number approaches 10,000, where the computations overpredict the experimental data. Flow visualization showed that vortices above $Ra \approx 7000$ were slightly unstable and by 13,000 were quite irregular. Hence, computations were performed beyond the range of applicability for the steady, laminar flow model.

For $F = 0.5$ and $A = 1.0$ and 0.5, there is again reasonable agreement between the predictions and the data. However, for $F = 0.5$ and $A = 0.25$ the data are underpredicted at the lower Rayleigh numbers. While this result may be partially caused by experimental error and modeling uncertainty, it is more likely that the experimental and numerical geometries are mismatched. Computations of the Nusselt number for close fin spacings are very sensitive to the fin height, and it is possible that during the heating and cooling of the plate, the fins worked their way slightly up the grooves and were effectively longer than originally intended. This effect would be hardly noticeable in the data if the plate had just a few fins, but could make a difference as the number of fins increases. For $A = 0.25$, a shift in the fin height as small as 5 percent (1 mm) could result in nearly a 20 percent increase in the Nusselt number (Maughan and Incropera, 1990).

Of greater interest is the large discrepancy between the data and the predictions for $A = 0.25$ and $Ra > 5000$. Such a deviation indicates an abrupt breakdown in correspondence between theory and experiment and is attributed to the mixing and vortices, which begin between and above the fins and violate planes of symmetry imposed in the model. This mixing enhances heat transfer and causes the measurements to exceed the predictions.

Although a direct comparison between these data and the earlier predictions of Acharya and Patankar (1981) is not possible, because the calculations model an axially uniform heat flux, the measurements for $A = 0.25$ nevertheless have important implications relevant to the assumptions used in numerical modeling. The experiments indicate that the assumption of a symmetric plane between fins breaks down near Ra = 5000, before any appreciable mixed convection enhancement. For a uniform heat flux condition with $\overline{Nu} = 1.66$, this Rayleigh number corresponds to $Ra^* \approx 8000$, or $Gr^+ = 178$ in terms of the nomenclature used by Acharya and Patankar (1981). The implication is that, for $A = 0.25$ and $F = 0.5$, this numerical model is not valid beyond $Gr^+ = 178$. However, because their computations were assumed to be limited only by the existence of laminar flow, results were presented for values of Gr^+ up to 10^7, which yielded $Nu/Nu_f = 24$. In contrast, the experiments of this study show that the assumption of symmetry between fins is a more restrictive aspect of modeling mixed convection between closely spaced fins.

Summary

Several aspects of mixed convection in a longitudinally finned, parallel plate channel have been considered experimentally for relative fin heights of $F = 0.5$ and 0.9 and for a range of fin spacings and Rayleigh numbers. No secondary flow was evident for fully developed conditions on the unfinned plate until the Rayleigh number exceeded the critical value of 1708. Beyond that point, regular longitudinal vortices formed and persisted until decaying into turbulence for $Ra \gtrsim 20{,}000$. Although fins on the lower heated surface generally enhanced heat transfer by increasing the heated surface area, they were also found to weaken the vortices and

delay enhancement due to vigorous secondary flows. As a result, some finned data exhibited lower Nusselt numbers than the corresponding unfinned condition. This effect was most pronounced for smaller fin heights.

Flow visualization showed that the fins had a stabilizing effect on the vortices. The convection cells were most stable for a fin aspect ratio of $A = 1$ and persisted through $\mathrm{Ra} = 29{,}700$. These experiments furthermore showed that vortices with $A = 1$ form between fins spaced with $A = 2$.

Agreement between the measurements of this study and numerical predictions for fully developed mixed convection was generally good. However, sharp disagreement was found for $F = 0.5$, $A = 0.25$, and $\mathrm{Ra} > 5000$. This was attributed to vortices that formed above the fins and violated planes of symmetry assumed in the model.

Acknowledgments

Support of this work by the National Science Foundation under Grant No. CBT-8316580 is gratefully acknowledged. One author (J.R.M.) is also grateful for fellowships provided by the Chevron Corporation, NL Industries Foundation, the Shell Foundation, and the Ingersoll Rand Corporation.

References

Acharya, S., and Patankar, S. V., 1981, "Laminar Mixed Convection in a Shrouded Fin Array," ASME JOURNAL OF HEAT TRANSFER, Vol. 103, pp. 559–565.

Kadle, D. S., and Sparrow, E. M., 1986, "Numerical and Experimental Study on Turbulent Heat Transfer and Fluid Flow in Longitudinal Fin Arrays," ASME JOURNAL OF HEAT TRANSFER, Vol. 108, pp. 16–23.

Lau, K. S., and Mahajan, R. L., 1988, "Convective Heat Transfer From Longitudinal Fin Arrays in the Entry Region of Turbulent Flow," ASME Paper No. 88-WA/EEP-1.

Lundberg, R. E., Reynolds, W. C., and Kays, W. M., 1963, "Heat Transfer With Laminar Flow in Concentric Annuli With Constant and Variable Wall Temperature and Heat Flux," NASA TN-D-1975.

Maughan, J. R., and Incropera, F. P., 1989, "Regions of Heat Transfer Enchancement for Laminar Mixed Convection in a Parallel Plate Channel," *International Journal of Heat and Mass Transfer*, in press.

Maughan, J. R., and Incropera, F. P., 1990, "Mixed Convection Heat Transfer with Longitudinal Fins in a Horizontal Parallel Plate Channel: Part I—Numerical Results," ASME JOURNAL OF HEAT TRANSFER, Vol. 112, this issue.

Moffat, R. J., 1988, "Describing the Uncertainties in Experimental Results," *Experimental Thermal and Fluid Science*, Vol. 1, pp. 3–17.

Ostrach, S., and Kamotani, Y., 1975, "Heat Transfer Augmentation in Laminar Fully Developed Channel Flow by Means of Heating From Below," ASME JOURNAL OF HEAT TRANSFER, Vol. 97, pp. 220–225.

Rustum, I. M., and Soliman, H. M., 1988, "Experimental Investigation of Laminar Mixed Convection in Tubes With Longitudinal Internal Fins," ASME JOURNAL OF HEAT TRANSFER, Vol. 110, pp. 366–372.

Convection in the Cavity Formed Between Two Cylindrical Rollers

P. A. Litsek

A. Bejan
J. A. Jones Professor of Mechanical Engineering. Fellow ASME

Department of Mechanical Engineering and Materials Science, Duke University, Durham, NC 27706

This paper describes the flow and temperature distribution in the hourglass-shaped cavity formed between two rollers and two parallel runner surfaces. The cavity fluid is heated uniformly over the roller surfaces, and cooled along the two runners, which are modeled as isothermal. The focus is on the characteristics of the flow (the Reynolds number effect) and the temperature distribution in the fluid, especially at the roller surface. These features are determined numerically. The results document the extent to which the Reynolds number, Prandtl number, geometric aspect ratio, and viscous dissipation number influence the steady-state temperature of the roller surface. It is shown that at Reynolds numbers greater than 100, the cooling effect that the cavity fluid provides to the roller approaches the behavior anticipated based on laminar forced-convection boundary layer theory.

1 Introduction

The objective of this study is to document the convective-cooling capability of the fluid trapped in the space between two cylindrical rollers in a roller bearing. This convection mechanism is relevant to the problem of controlling the temperature of the roller and the thin film of lubricant that coats it.

The heat transfer configuration addressed in this study is outlined in Fig. 1. There are four important regions around the periphery of each roller, namely, two regions of rolling contact heating, and two lateral regions over which the rollers are being cooled by the surrounding fluid. In order to calculate the steady-state average temperature of the roller, the designer must know not only the fraction of the rolling-contact heating effect absorbed by the roller, but also the proper heat transfer coefficient (h) for the convection effect provided by the surrounding fluid. Until now, the h value had to be assumed in order to analyze the steady-state temperature distribution around the roller (e.g., Gecim and Winer, 1984, 1986).

The point-heating aspect of the rolling contact problem — that is, the partition of the heating effect between two bodies in thermal contact — has been studied extensively [see, for example, Blok (1937, 1987), Jaeger (1942), Schneider et al. (1977), and Yuen (1985)]. The convection-cooling aspect, or the flow and heat transfer characteristics of the hourglass-shaped cavity formed between two rollers, has not been documented until now.

2 Mathematical Formulation

Consider the cavity formed between two consecutive cylindrical rollers and their runners, and assume that this cavity is filled with a single-phase fluid (Fig. 1). The rollers rotate clockwise with the angular speed ω, while the runners travel horizontally and without slip. The runner velocity U is equal to ωR, where R is the roller radius. The contour of the fluid cavity and the centers of the two rollers are stationary with respect to the observer. The cavity geometry is described fully by the roller radius R and the center-to-center distance L.

The fluid that fills the cavity is modeled as Newtonian, and the fluid properties are assumed constant. It is understood that the fluid (lubricant) has a viscosity that varies with the temperature, if the temperature variation across the cavity is sufficiently large. In the present case the viscosity is assumed constant for the sake of simplicity, as this is the first study of the roller-cavity convection phenomenon.

The fluid is set in motion by the tangential movement of all the walls of the cavity. Note that the tangential velocity along each wall is equal to U. The cavity fluid is heated by the two roller surfaces, which "unload" into the fluid the heat input they receive while sweeping through their respective points of rolling contact. In the real system, the distribution of heat flux over the surface of the roller is the result of the interaction between the unsteady conduction process that develops inside the roller (immediately under the surface), and the forced-convection flow that develops on the fluid side of the roller surface. This interaction is complicated, especially since its most basic components have not been studied in full.

This is why the approach used in the past and followed in this study consists of decoupling the roller conduction problem from the cavity convection problem by making a suitable assumption regarding the thermal boundary condition at the roller surface. For example, when the focus was on the conduction and temperature distribution beneath the roller surface, Gecim and Winer (1984, 1986) accounted for the cavity flow by assuming a certain (constant) heat transfer coefficient on the fluid side of the roller surface.

In the present study the focus is on the cavity flow; therefore, decoupling can be achieved by assuming that the heat flux through the roller surface q'' is constant and known. The integral of q'' over half of the roller circumference, $q''\pi R$,

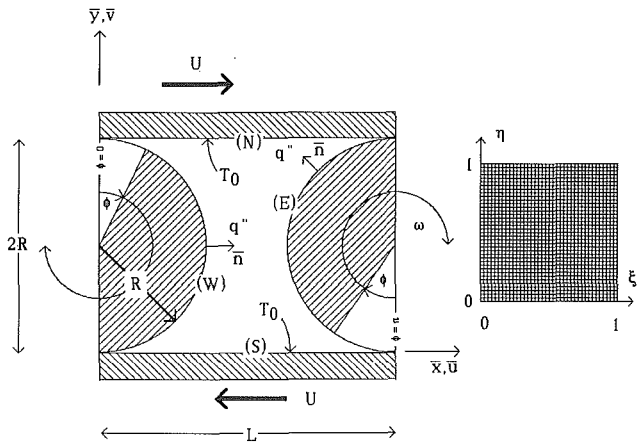

Fig. 1 The fluid cavity formed between two consecutive rollers and two runners

Contributed by the Heat Transfer Division for publication in the JOURNAL OF HEAT TRANSFER. Manuscript received by the Heat Transfer Division March 24, 1989; revision received August 8, 1989. Keywords: Enclosure Flows, Forced Convection, Rotating Flows.

represents the heat input (per unit length normal to Fig. 1) received by the roller from the respective upstream point of rolling contact. The establishment of steady-state temperatures in the cavity fluid is modeled by assuming that the fluid is cooled while in contact with the two runner surfaces. The latter are modeled as isothermal (T_0). Worth noting is that this last assumption effects the decoupling of the cavity convection problem from the conduction processes that take place inside the runners.

In the study that follows, we pursue two fundamental aspects of this problem: (*i*) the flow field and its dependence on parameters such as the Reynolds number, and (*ii*) the temperature field and, especially, the temperature distribution along the roller surfaces. The latter provides an answer to the question of how hot the roller surface must become in order to dispose of the imposed heat flux q'' when the thermal resistance separating the roller from the outside world is dominated by the resistance between the roller surface and the fluid that fills the cavity.

The dimensionless forms of the vorticity, stream function, and energy equations in the two-dimensional geometry of Fig. 1 are

$$\frac{\partial w}{\partial t} + u\frac{\partial w}{\partial x} + v\frac{\partial w}{\partial y} = \frac{1}{\mathrm{Re}}\nabla^2 w \tag{1}$$

$$\nabla^2\psi = -w \tag{2}$$

$$\frac{\partial T}{\partial t} + u\frac{\partial T}{\partial x} + v\frac{\partial T}{\partial y} = \frac{1}{\mathrm{Re\ Pr}}\nabla^2 T + \frac{\alpha}{\mathrm{Re\ Pr}}\Phi \tag{3}$$

where Φ is the dimensionless viscous dissipation function

$$\Phi = 2\left[\left(\frac{\partial u}{\partial x}\right)^2 + \left(\frac{\partial v}{\partial y}\right)^2\right] + \left(\frac{\partial u}{\partial y} + \frac{\partial v}{\partial x}\right)^2 \tag{4}$$

The symbols used in these equations are defined in the Nomenclature; in particular, the Reynolds, Prandtl, and "dissipation" numbers are defined respectively by

$$\mathrm{Re} = \frac{UR}{\nu}, \quad \mathrm{Pr} = \frac{\nu}{\alpha_{th}}, \quad \alpha = \frac{U^2\mu}{k\Delta T} \tag{5}$$

in which the dissipation number α should not be confused with the fluid thermal diffusivity α_{th}. The α notation for the dissipation number is borrowed from the field of tribology; in heat transfer, the alternative symbol is ϵ. Worth noting is that the ratio $\alpha/\mathrm{Re\ Pr}$ is the same as Ec/Re, where Ec is the Eckert number. The relationships between the dimensionless variables of equations (1)–(4) and their dimensional counterparts (denoted by *overbars*) are

$$x = \frac{\bar{x}}{R}, \qquad y = \frac{\bar{y}}{R} \tag{6}$$

$$u = \frac{\bar{u}}{U}, \qquad v = \frac{\bar{v}}{U} \tag{7}$$

$$T = \frac{\bar{T} - T_0}{\Delta T}, \qquad t = \frac{\bar{t}}{R/U} \tag{8}$$

where ΔT is a temperature difference scale proportional to the roller heat flux

$$\Delta T = \frac{q''R}{k} \tag{9}$$

According to this notation and the angular position ϕ defined in Fig. 1, the no-slip velocity boundary conditions along the four walls are (note the north, east, south, and west labeling of the four walls)

$$\begin{aligned} &u_N = 1, && v_N = 0, && 0 < x < \frac{L}{R} \\ &u_E = \cos\phi, && v_E = -\sin\phi, && \pi < \phi < 2\pi \\ &u_S = -1, && v_S = 0 && 0 < x < \frac{L}{R} \\ &u_W = \cos\phi, && v_W = -\sin\phi, && 0 < \phi < \pi \end{aligned} \tag{10}$$

The angle ϕ increases in the clockwise direction, starting from $\phi = 0$ at the top of each roller. The corresponding heat flux and temperature conditions are

Nomenclature

D_x, D_y = dimensionless quantities, equations (17)
h = heat transfer coefficient, W/m^{2}K
J = Jacobian, equation (16)
k = fluid thermal conductivity, W/mK
L = distance between the centers of two consecutive rollers, m
n = dimensionless distance normal to roller surface, Fig. 1
nx, ny = number of grid points in the horizontal and vertical directions, respectively
Nu = Nusselt number, equation (23)
Pr = Prandtl number, equation (5)
q'' = roller surface heat flux, W/m^2
R = roller radius, m
Re = Reynolds number, equation (5)
$R_{T,\max}$ = relative change in the roller maximum temperature, equation (25)
t = dimensionless time
T = dimensionless excess temperature above T_0
T_{avg} = dimensionless average roller surface temperature
$T_{\max}$ = dimensionless maximum roller surface temperature
T_0 = temperature of the runner surface, K, Fig. 1
ΔT = temperature difference scale, K, equation (9)
u = dimensionless horizontal fluid velocity, Fig. 1
U = peripheral speed of all four walls, m/s, Fig. 1
v = dimensionless vertical fluid velocity, Fig. 1
w = dimensionless vorticity function
x = dimensionless horizontal coordinate
y = dimensionless vertical coordinate
α = viscous dissipation number, equation (5)
α_{th} = fluid thermal diffusivity, m^2/s
β = geometric parameter, equation (15)
γ = geometric parameter, equation (15)
η = transformed vertical coordinate, Fig. 1
$\Delta\eta$ = vertical grid spacing
θ = geometric parameter, equation (15)
μ = fluid viscosity, Ns/m^2
ν = kinematic viscosity, m^2/s
ξ = transformed horizontal coordinate, Fig. 1
$\Delta\xi$ = horizontal grid spacing
σ = geometric parameter, equation (16)
τ = geometric parameter, equation (16)
ϕ = angular position, rad, Fig. 1
Φ = viscous dissipation function, s^{-2}, equation (4)
ψ = dimensionless streamfunction
ω = angular speed, rad/s, Fig. 1
$(\bar{\ })$ = dimensional variables
$()_{N,E,S,W}$ = north, east, south, west

Table 1 Accuracy test for determining the proper grid size (Re = 400, $L/R = 2.5$)

Grid size	ψ_{min}	ψ_{max}
9 × 9	−0.029064	0.029064
19 × 19	−0.037581	0.092112
29 × 29	−0.044186	0.100085
39 × 39	−0.048136	0.102759
51 × 51	−0.049225	0.102815

$$T_N = 0, \quad \left(\frac{\partial T}{\partial n}\right)_E = -1$$
$$T_S = 0, \quad \left(\frac{\partial T}{\partial n}\right)_W = -1 \tag{11}$$

where n represents the dimensionless position ($\bar{n}/R$) in the radial direction. Note that n points into the fluid (Fig. 1).

The problem stated above was mapped onto the rectangular domain (ξ, η) shown on the right side of Fig. 1. The details of the mathematical transformation $(x, y) \rightarrow (\xi, \eta)$ are omitted here for the sake of conciseness, and because they can be found in Thompson et al. (1977). We report only the final form of the transformed vorticity, stream function, and energy equations

$$\frac{\partial w}{\partial t} + \left(\frac{\partial \psi}{\partial \eta}\frac{\partial w}{\partial \xi} - \frac{\partial \psi}{\partial \xi}\frac{\partial w}{\partial \eta}\right)\frac{1}{J} = \left(\theta\frac{\partial^2 w}{\partial \xi^2} - 2\beta\frac{\partial^2 w}{\partial \xi\,\partial \eta} + \gamma\frac{\partial^2 w}{\partial \eta^2} + \sigma\frac{\partial w}{\partial \eta} + \tau\frac{\partial w}{\partial \xi}\right)\frac{1}{J^2 \mathrm{Re}} \tag{12}$$

$$\theta\frac{\partial^2 \psi}{\partial \xi^2} - 2\beta\frac{\partial^2 \psi}{\partial \xi\,\partial \eta} + \gamma\frac{\partial^2 \psi}{\partial \eta^2} + \sigma\frac{\partial \psi}{\partial \eta} + \tau\frac{\partial \psi}{\partial \xi} = -J^2 w \tag{13}$$

$$\frac{\partial T}{\partial t} + \left(\frac{\partial \psi}{\partial \eta}\frac{\partial T}{\partial \xi} - \frac{\partial \psi}{\partial \xi}\frac{\partial T}{\partial \eta}\right)\frac{1}{J} = \left(\theta\frac{\partial^2 T}{\partial \xi^2} - 2\beta\frac{\partial^2 T}{\partial \xi\,\partial \eta} + \gamma\frac{\partial^2 T}{\partial \eta^2} + \sigma\frac{\partial T}{\partial \eta} + \tau\frac{\partial T}{\partial \xi}\right)\frac{1}{J^2\,\mathrm{Re\,Pr}} + \frac{\alpha}{\mathrm{Re\,Pr}}\Phi(\xi, \eta) \tag{14}$$

where

$$\theta = x_\eta^2 + y_\eta^2, \quad \beta = x_\eta x_\xi + y_\eta y_\xi, \quad \gamma = x_\xi^2 + y_\xi^2 \tag{15}$$

$$\sigma = \frac{y_\xi D_x - x_\xi D_y}{J}, \quad \tau = \frac{x_\eta D_y - y_\eta D_x}{J},$$
$$J = x_\xi y_\eta - x_\eta y_\xi \tag{16}$$

$$D_x = \alpha x_{\xi\xi} - 2\beta x_{\xi\eta} + \gamma x_{\eta\eta},$$
$$D_y = \alpha y_{\xi\xi} - 2\beta y_{\xi\eta} + \gamma y_{\eta\eta} \tag{17}$$

$$\Phi(\xi, \eta) = \frac{1}{J^2}\left\{2\left[(y_\eta u_\xi - y_\xi u_\eta)^2 + (-x_\eta v_\xi + x_\xi v_\eta)^2\right] + (y_\eta v_\xi - y_\xi v_\eta - x_\eta u_\xi + x_\xi u_\eta)^2\right\} \tag{18}$$

and where $(\,)_\xi = \partial(\,)/\partial\xi$ and $(\,)_\eta = \partial(\,)/\partial\eta$. The transformed boundary conditions for stream function, vorticity, and temperature are

$$\psi_N = 0, \; w_N = \frac{-u_N y_\eta \Delta\eta - \psi(\xi, ny-1)}{\frac{1}{2}\Delta\eta^2}, \; T_N = 0 \tag{19}$$

$$\psi_E = 0, \quad w_E = \frac{(-u_E y_\xi + v_E x_\xi)\Delta\xi - \psi(nx-1, \eta)}{\frac{1}{2}\Delta\xi^2},$$
$$\left(\frac{\partial T}{\partial \xi}\right)_E = \frac{J q'' + T_\eta(y_\xi \sin\phi - x_\xi \cos\phi)}{(y_\eta \sin\phi - x_\eta \cos\phi)} \tag{20}$$

Table 2 Test for determining the largest acceptable iteration error for the flow solution (Re = 400, $L/R = 3$)

Iteration error	ψ_{min}	ψ_{max}
0.1	−0.063709	0.044785
0.01	−0.055634	0.198967
0.001	−0.054882	0.221568
0.0001	−0.054769	0.229749

$$\psi_S = 0, \quad w_S = \frac{u_S y_\eta \Delta\eta - \psi(\xi, 2)}{\frac{1}{2}\Delta\eta^2}, \quad T_S = 0 \tag{21}$$

$$\psi_W = 0, \quad w_W = \frac{(-u_W y_\xi - v_W x_\xi)\Delta\xi - \psi(2, \eta)}{\frac{1}{2}\Delta\xi^2},$$
$$\left(\frac{\partial T}{\partial \xi}\right)_W = \frac{-J q'' + T_\eta(y_\xi \sin\phi - x_\xi \cos\phi)}{(y_\eta \sin\phi - x_\eta \cos\phi)} \tag{22}$$

In the above equations, $\psi(nx-1, \eta)$, $\psi(2, \eta)$, $\psi(\xi, ny-1)$, and $\psi(\xi, 2)$ are the values of the stream function at a grid point adjacent to the east, west, north, and south boundaries, respectively.

3 Numerical Method

Equations (12)–(14) were solved using standard finite-difference techniques. Even though the focus of this study is on steady-state solutions, numerical stability considerations led to the decision to base the present calculations on the unsteady-state equations. For this, a proper time step size had to be used, and the size of this step depended on the grid fineness, the Reynolds number, and the Prandtl number.

The vorticity equation (12) was solved using the A.D.I. method described by Beam and Warming (1980). The stream function equation was solved using the successive overrelaxation method. The geometric parameters listed in equations (15)–(17) were calculated numerically. Computational time was saved by using the following methods for speeding up the convergence:

(*i*) The converged solution for Re = 1 was used as initial condition for the next case (Re = 10), and so on;

(*ii*) An even better initial guess for flow and temperature fields was made by interpolating the converged solution obtained using a coarser grid; and

(*iii*) The vorticity equation was solved three to four times more frequently than the stream function equation.

The grid size was determined based on the accuracy tests sampled in Table 1. These tests correspond to the largest Reynolds number of the flows considered in this study (Re = 400). The ψ values listed in the table represent the minimum and maximum stream function values calculated inside the fluid cavity. Table 1 shows that the 39 × 39 grid is adequate; therefore, this grid was chosen for all the numerical results described in this paper (see also the right side of Fig. 1).

The test of whether the present solutions represent steady-state solutions is illustrated in Table 2, again for the large Reynolds number case of Re = 400. In the case of the flow solution, the maximum acceptable difference between the current solution and the solution at the preceding iteration (the iteration error) was found to be less than 10^{-4}. The acceptable iteration error for the temperature solution was less than 10^{-6}.

The numerical code developed in this manner was finally tested to see whether it can reproduce classical numerical solutions that have been reported in the literature. Figure 2 shows the flow solution obtained with the present code for the "driven-cavity" problem, in which only the upper wall of the cavity moves to the right with the constant speed U. Table 3 compares this solution with Burggraf's results for the same problem (Burggraf, 1966), in terms of the minimum stream function

Table 3 Comparison between the present solution for the driven-cavity problem (Fig. 2) and the solution reported by Burggraf (1966); the numbers in the center and right columns represent the values of ψ_{min}

Re	Present results	Burggraf (1966)
1	−0.09920	−0.0998
10	−0.09989	−0.1000
100	−0.10123	−0.1015
400	−0.10184	−0.1017

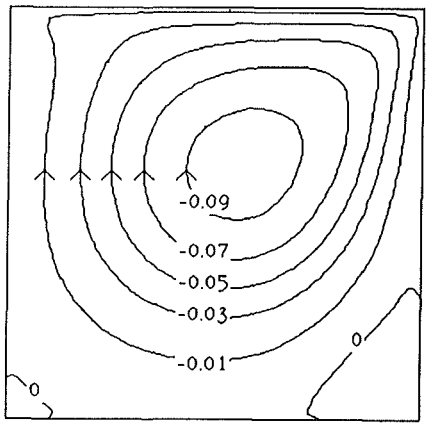

Fig. 2 Streamlines of the flow inside a square cavity whose upper wall moves to the right with the constant speed U (Re = 400)

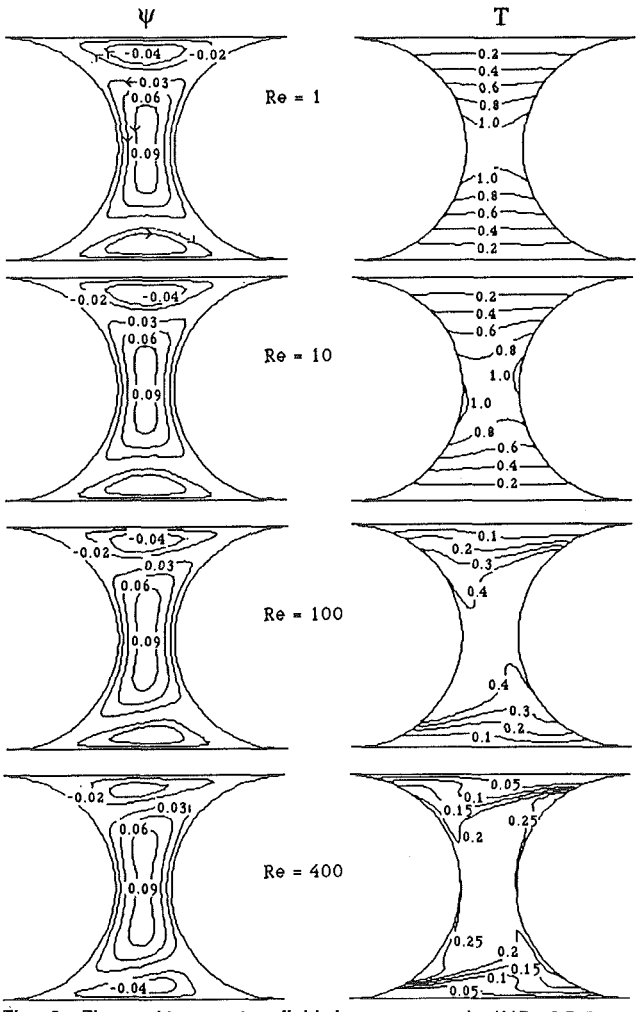

Fig. 3 Flow and temperature fields in a narrow cavity (L/R = 2.5, Pr = 1, α = 0)

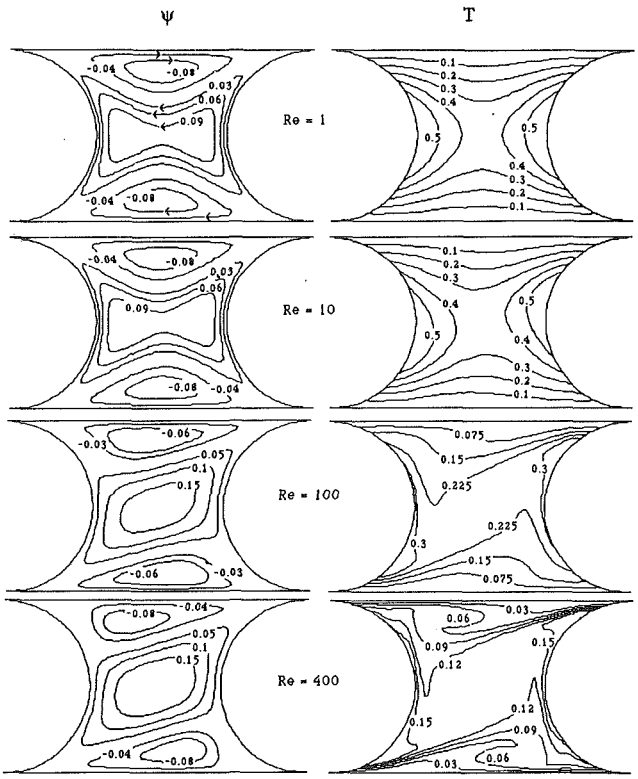

Fig. 4 Flow and temperature fields in a wide cavity (L/R = 3.5, Pr = 1, α = 0)

value in the eye of the cavity-size roll (Fig. 2). The present code reproduces Burggraf's results very well over the entire Reynolds number range covered by this study.

4 Results and Discussion

The main features of the flow driven by the two rollers are illustrated on the left side of Figs. 3 and 4. The flow consists of three counterrotating cells. At low Reynolds numbers, the flow pattern is almost symmetric about the vertical midplane of the cavity. As Re increases, the cells become tilted as their edges are sucked into the two low-pressure corners of the hourglass-shaped cavity (i.e., into the upper-right and lower-left corners). At the same time, the four walls of the cavity become lined by distinct boundary layers. Regardless of the Reynolds number, the flow pattern retains its centro-symmetry property, that is, the symmetry of two points marked equidistantly on a line that passes through the geometric center of the cavity.

The right sides of Figs. 3 and 4 contain the corresponding patterns of isotherms. These patterns were calculated for the benchmark case of Pr = 1 and α = 0 (zero frictional heating effect). The transition from a temperature field dominated by conduction at low Reynolds numbers (Re = 1) to one with distinct thermal boundary layers at high Reynolds numbers (Re = 400) is evident. The temperature field has the same symmetry properties as the flow field discussed in the preceding paragraph. Noteworthy is the nearly isothermal state of the fluid engaged in the central cell of the three-cell flow pattern. This feature is accentuated at high Reynolds numbers, because of the thinness of the boundary layers.

The effect of the roller-to-roller spacing on the flow and temperature fields can be seen by comparing Figs. 3 and 4. When the aspect ratio L/R increases and Re remains constant, the boundary layers lose some of their sharpness; this trend will be reflected in a slight decrease of the overall Nusselt number, as shown in Fig. 5, which is described next.

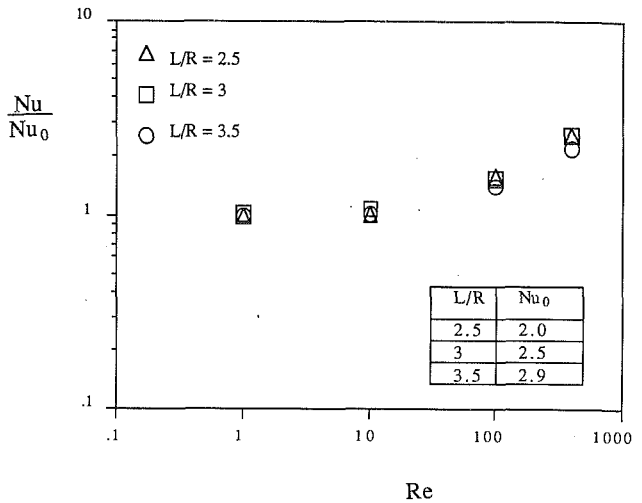

Fig. 5 Reynolds number effect on the overall Nusselt number (Pr = 1, $\alpha = 0$)

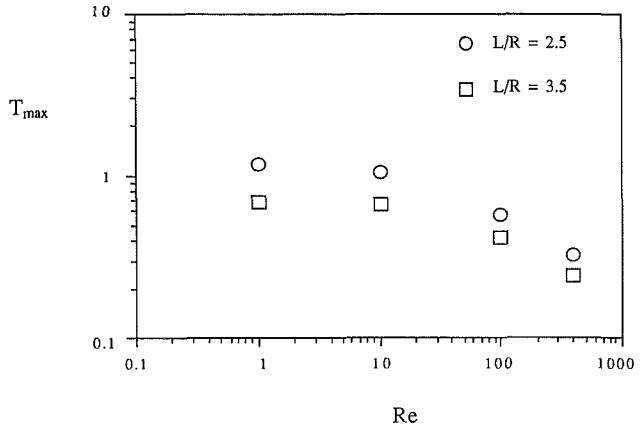

Fig. 6 Maximum temperature recorded at a point on the surface of the roller (Pr = 1, $\alpha = 0$); see also Fig. 7

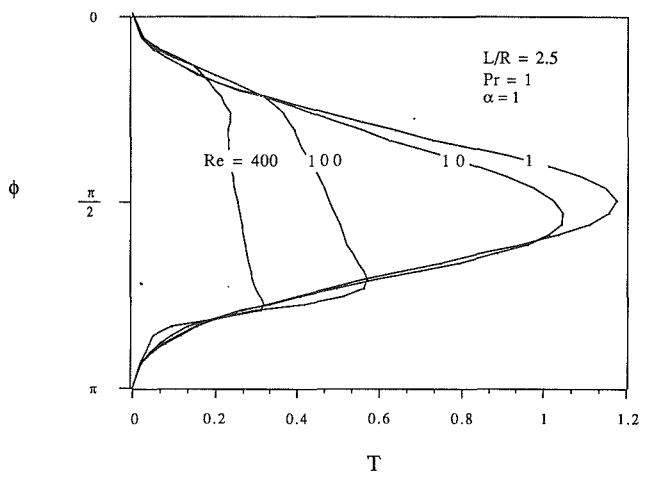

Fig. 7 Distribution of temperature over the surface of the left roller (the west wall of the fluid cavity), and the effect of the Reynolds number (Pr = 1, $\alpha = 0$, $L/R = 2.5$)

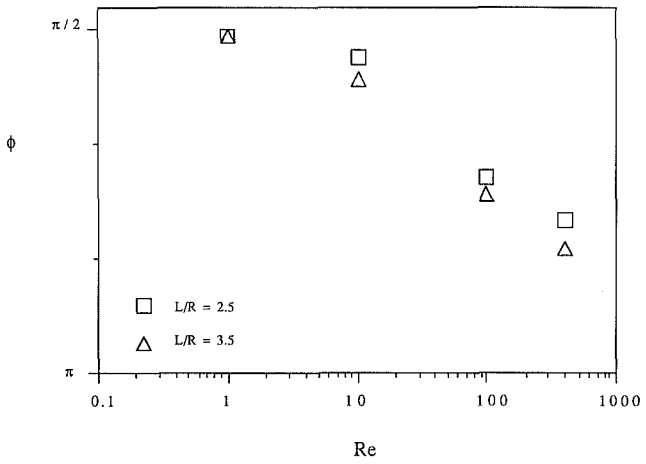

Fig. 8 Location of the point of maximum temperature on the surface of the left roller (the west wall of the fluid cavity), and the effect of Re and L/R (Pr = 1, $\alpha = 0$)

The heat transport capability of the cavity flow is described by the overall Nusselt number based on the average temperature difference between the roller surface and the runners $(\bar{T}_{avg} - T_0)$

$$\mathrm{Nu} = \frac{q''R}{k(\bar{T}_{avg} - T_0)} \tag{23}$$

In view of the dimensionless temperature definition (equations (8) and (9)), the overall Nusselt number is equal to the inverse of the average dimensionless temperature of the roller surface $T_{avg} = (\bar{T}_{avg} - T_0)/\Delta T$,

$$\mathrm{Nu} = \frac{1}{T_{avg}} \tag{24}$$

If the heat flux q'' is fixed, large Nu values mean low roller surface temperatures, i.e., effective cooling.

Figure 5 shows the effect of the Reynolds number on the ratio $\mathrm{Nu}/\mathrm{Nu}_0$, where Nu_0 represents the Nusselt number in the no-flow (pure conduction limit). The $\mathrm{Nu}/\mathrm{Nu}_0$ ratio is the factor by which the heat transfer (or the thermal contact) is enhanced by the convection effect of the cavity-driven flow. This factor increases noticeably as the Reynolds number increases. The geometric aspect ratio has a relatively weaker effect: $\mathrm{Nu}/\mathrm{Nu}_0$ decreases slightly as L/R increases, that is as the cavity becomes wider and the thermal boundary layers become less sharp.

Another measure of the effectiveness of the convection cooling effect contributed by the circulating cavity flow is the maximum temperature $(\bar{T}_{max})$ that occurs at a certain spot on the surface of the roller. Figure 6 shows the maximum dimensionless temperature $T_{max} = (\bar{T}_{max} - T_0)/\Delta T$, and the manner in which this parameter is influenced by Re and L/R. The maximum temperature decreases as both Re and L/R increase.

The Reynolds number effect on the maximum roller temperature is illustrated further in Fig. 7, which shows the actual distribution of temperature over the surface of the left (west) wall of the cavity. The point of maximum temperature migrates toward the lower 1/4 of the west wall as Re increases. At the same time, the T values of the roller surface become smaller and more uniform. The migration of the hot spot is recorded in Fig. 8. This figure shows also that the hot-spot migration toward the lower end is accentuated in cases where the aspect ratio L/R is large.

It is worth keeping in mind that the occurrence of a maximum temperature at a certain location ϕ on the roller surface is the result of the constant-flux model assumed for the roller surface, and the constant temperature model assumed for the runners. Reasons for these assumptions were given at the start of section 2. In an actual system with little viscous dissipation, the hot spot will occur in the vicinity of the two lines of rolling contact, $\phi = 0$ and $\phi = \pi$.

The preceding results were all obtained by setting Pr = 1. The effect of the Prandtl number on the temperature field is illustrated in Fig. 9, which shows the hot spot temperature as a function of both Re and Pr. When the Reynolds number is held fixed, the hot-spot temperature decreases with the in-

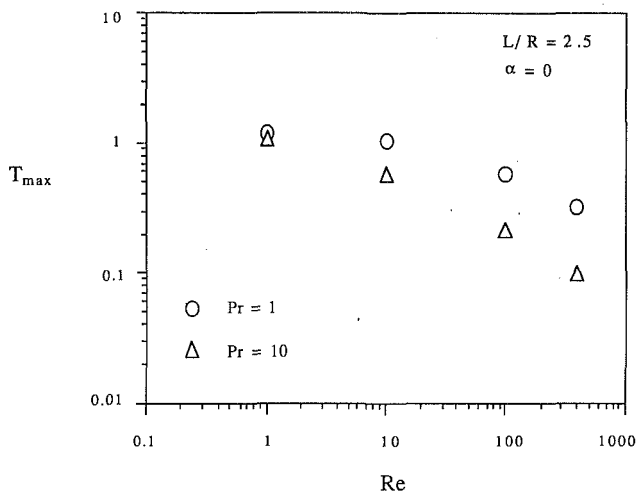

Fig. 9 Effect of the Prandtl number on the roller hot-spot temperature ($L/R = 2.5$, $\alpha = 0$)

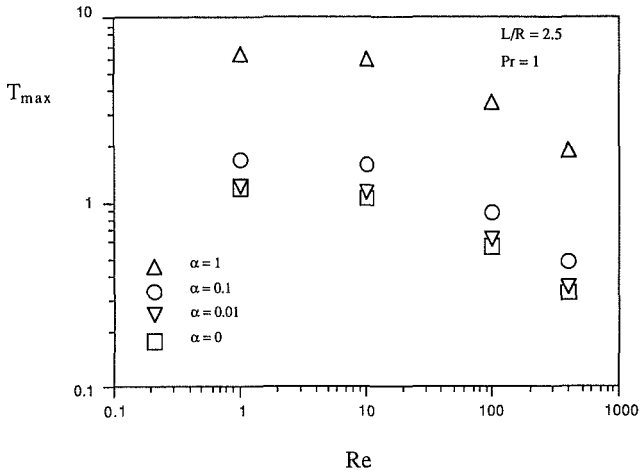

Fig. 10 Effect of the dissipation number α on the maximum roller-surface temperature ($L/R = 2.5$, Pr = 1)

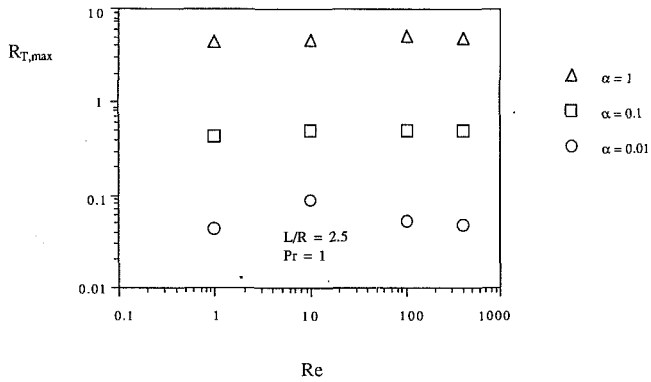

Fig. 11 Relative increase in T_{max} due to a finite dissipation number, equation (25) ($L/R = 2.5$, Pr = 1)

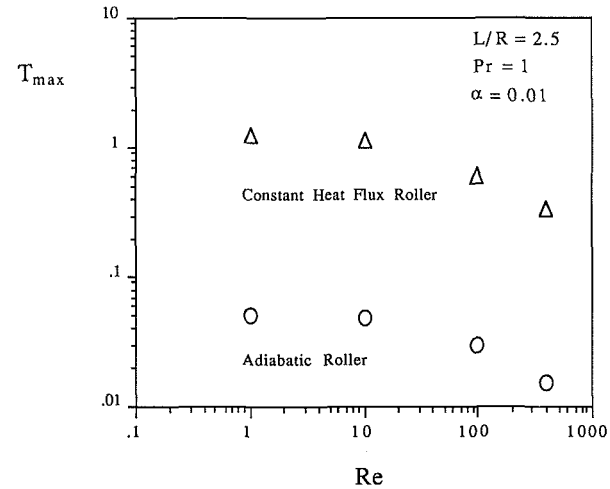

Fig. 12 Effect of volumetric viscous heating on the maximum temperature of the roller surface ($\alpha = 0.01$, $L/R = 2.5$, Pr = 1)

creasing Prandtl number. This Pr effect is due to the proportionality that exists between Nu and $Pr^{1/3}$ in forced-convection laminar boundary layer heat transfer (see Section 5). Lubricants have Prandtl numbers higher than 10, which is the highest Pr value considered in this study. The present numerical results and the Nu ~ $Pr^{1/3}$ proportionality are sufficient for anticipating the Nusselt numbers at higher Prandtl numbers, as shown later in Fig. 13.

The assumption of zero frictional heating ($\alpha = 0$) was relaxed during the numerical runs summarized in Figs. 10–12. The first of these figures shows the effect of the dissipation number α on the hot-spot (maximum) temperature of the roller surface: T_{max} increases monotonically as α increases, especially when α exceeds 0.01.

A peculiar aspect of the effect of α on T_{max} is identified in Fig. 11. This figure shows the *relative* increase in T_{max}, namely, the ratio

$$R_{T,max} = \frac{T_{max}(\alpha) - T_{max}(\alpha = 0)}{T_{max}(\alpha = 0)} \tag{25}$$

We learn from Fig. 11 that the relative increase in T_{max} due to a finite α value (relative to the T_{max} value in the absence of viscous dissipation) is practically independent of the Reynolds number. The effect of the Prandtl number on the relative increase in maximum temperature remains to be investigated.

When the dissipation number α is finite, the cavity fluid is subjected to two heating effects, the roller-surface heat flux q'' and the volumetric heating due to viscous dissipation. The volumetric heating effect was studied separately (isolated from the q'' effect) in Fig. 12, which shows the maximum roller surface temperature when that surface is adiabatic ($q'' = 0$). The behavior of T_{max} is qualitatively the same as in Fig. 10; however, the T_{max} values are smaller than in the case where the roller also heats the fluid (Fig. 10).

5 Conclusion

In summary, the chief conclusion of this study is that the flow driven by two consecutive cylindrical rollers can have a sizable impact on the peripheral heat transfer coefficient or overall Nusselt number (e.g., Fig. 5). In the absence of significant viscous dissipation in the cavity fluid ($\alpha = 0$), the parameters that influence the overall Nusselt number the most are the Reynolds number and the Prandtl number.

The Re and Pr effects on the overall Nusselt number can be anticipated theoretically in the limit of sufficiently large Reynolds numbers. Figures 3 and 4 show that when Re increases the rollers become coated with progressively thinner thermal boundary layers. The isotherm patterns show further that these boundary layers are bordered by a nearly isothermal and stagnant fluid, which occupies the core region of the hourglass-shaped cavity. It follows that in the boundary layer regime the overall Nusselt number must scale as (see, for example, Bejan, 1984)

$$\text{Nu} \sim \text{Re}^{1/2}\,\text{Pr}^{1/3} \tag{26}$$

in which Pr is of order 1 or greater, and both Nu and Re are based on the longitudinal dimension of the heated wall. In the

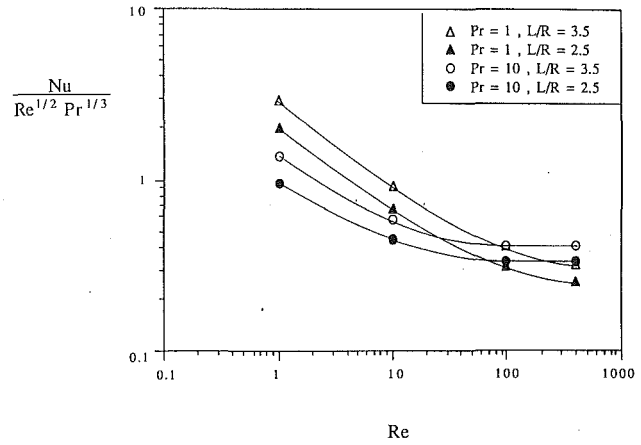

Fig. 13 Emergence of the boundary-layer Nu scaling (26) as Re increases ($\alpha = 0$)

present problem, the longitudinal length scale is R; therefore, the roles of the Nu and Re groups in equation (26) can be played by the Nusselt and Reynolds numbers defined by equations (23) and (5), respectively.

The validity of the trend anticipated in equation (26) is tested in Fig. 13. The figure summarizes the Nu calculations accumulated during this study, and projects them on the plane of $Nu / Re^{1/2} Pr^{1/3}$ versus Re. It is clear that the group listed on the ordinate approaches a plateau as the Reynolds number increases (i.e., as the boundary layers become distinct). Furthermore, the ordinate group reaches a plateau sooner (at a lower Re) when the Prandtl number is greater than 1, that is, when the thermal boundary layers are thinner than the velocity boundary layers. These features confirm the validity of equation (26) at Reynolds number above approximately 100. The crossover of the curves is an interesting effect that deserves further study.

The engineering contribution of this study is that it shows how to estimate the heat transfer coefficient labeled h in analytical studies of conduction in the shaft (Gecim and Winer, 1984, 1986). The heat transfer coefficient can be calculated using the Nu data of Fig. 13, for which the Nusselt number definition (23) reads, alternatively, $Nu = hR/k$. This calculation is correct only in an order of magnitude sense, because of all the simplifying assumptions made in the two-dimensional model of Fig. 1.

One modeling assumption that could be changed in a future study of convection between consecutive rollers is the constant-flux boundary condition on the two roller surfaces. An alternative would be to assume that the two rollers are isothermal. In this case, one would have to discard the assumption that the two runners are isothermal, and deal with the conduction processes in the runners, in the wake of each line of rolling contact.

Acknowledgments

The authors acknowledge the support received from Duke University. The numerical work was conducted using the Cornell National Supercomputer Facility, a resource of the Center for Theory and Simulations in Science and Engineering (Cornell Theory Center), which receives major funding from the National Science Foundation and IBM corporation, with additional support from New York State and members of the Corporate Research Institute. P. A. Litsek acknowledges also the support received from his home company, Promon Engenharia, S. A., and A. Bejan acknowledges the support received from the National Science Foundation through grant No. CBT-8711369.

References

Beam, R., and Warming, R. F., 1980, "Alternating Direction Implicit Methods for Parabolic Equations With a Mixed Derivative," *SIAM — Journal on Science and Statistical Computation*, Vol. 1, pp. 131–159.

Bejan, A., 1984, *Convection Heat Transfer*, Wiley, New York, pp. 38, 56.

Blok, H., 1937, "Theoretical Study of Temperature Rise at Surfaces of Actual Contact Under Oiliness Conditions," *Proc. Gen. Disc. on Lubrication*, IMechE, Vol. 2, pp. 222–235.

Blok, H., 1987, "Thermo-Tribology — Fifty Years On," *Proc. IMechE*, Vol. C248/87, pp. 1–8.

Burggraf, O. R., 1966, "Analytical and Numerical Studies of the Structure of Steady Separated Flows," *Journal of Fluid Mechanics*, Vol. 24, pp. 113–151.

Gecim, B., and Winer, W. O., 1984, "Steady Temperature in a Rotating Cylinder Subject to Surface Heating and Convective Cooling," ASME *Journal of Tribology*, Vol. 106, pp. 120–127.

Gecim, B., and Winer, W. O., 1986, "Steady Temperatures in a Rotating Cylinder — Some Variations in the Geometry and Thermal Boundary Conditions," ASME *Journal of Tribology*, Vol. 108, pp. 446–454.

Jaeger, J. C., 1942, "Moving Sources of Heat and the Temperature at Sliding Contacts," *J. Proc. R. Soc. N. S. W.*, Vol. 76, pp. 203–224.

Schneider, G. E., Strong, A. B., and Yovanovich, M. M., 1977, "Transient Thermal Response of Two Bodies Communicating Through a Small Circular Contact Area," *International Journal of Heat and Mass Transfer*, Vol. 20, pp. 301–308.

Thompson, J. F., Thames, F. C., and Mastin, W., 1977, "Boundary-Fitted Curvilinear Coordinate Systems for Solution of Partial Differential Equations on Fields Containing Any Number of Arbitrary Two-Dimensional Bodies," NASA Report No. CR-2729, July.

Yuen, W. Y. D., 1985, "On the Heat Transfer of a Moving Composite Strip Compressed by Two Rotating Cylinders," ASME JOURNAL OF HEAT TRANSFER, Vol. 107, pp. 541–548.

Natural Convection From a Heat Source in a Top-Vented Enclosure

T. A. Myrum
Mechanical Engineering Department,
Louisiana State University,
Baton Rouge, LA 70803
Mem. ASME

Natural convection from a heated disk situated at the bottom of a top-vented enclosure was studied experimentally. The experiments were performed in water ($Pr \cong 5$) for parametric variations of the vent opening size, inner enclosure height, and disk-to-enclosure-wall tempearture difference (Rayleigh number). For comparison purposes, baseline data were obtained for an unvented enclosure and for the "infinite" case (no enclosure). The heat transfer data were supplemented by cross-vent temperature measurements and by flow visualization using the thymol-blue electrochemical technique. The experiments demonstrated that, for the range of parameters considered, the average Nusselt numbers could be correlated using a single correlation to within 8 percent. It was also found that the presence of the enclosure (vented or unvented) acted to reduce the Nusselt number, especially at the lower Rayleigh numbers. Flow visualization experiments revealed an unstable flow pattern in the vicinity of the vent that fluctuated in a nonperiodic manner between four basic modes. Temperature measurements revealed asymmetric mean cross-vent temperature profiles, with the mean temperature level increasing with decreasing vent size. The intensity of the temperature fluctuations in the vent opening also increased with decreasing vent size.

Introduction

The study of natural convection from a heat source located at the bottom of a top-vented enclosure and of the resulting flow patterns within the enclosure and through the vent has a number of applications. One application involves the basic flow phenomena that arise during the venting procedures employed by firefighters while combating room or building fires. Another application involves the fluid motion through apertures connecting the rooms in buildings. Street drains partially filled with water that is warmer than the ambient air represent yet another application. This is especially important if a highly volatile toxic liquid or gas that is lighter than air finds its way into the drainage system.

Essentially, this problem involves a combination of three basic natural convection situations. These are: heat transfer for a hot upfacing horizontal surface, natural convection in enclosures, and a buoyancy-driven exchange through the vent between the heavier (cold) ambient fluid and the lighter (warm) enclosure fluid. All of these basic problems have been studied to some extent in the past.

Townsend (1959) performed extensive temperature measurements in air above a heated horizontal plate that formed the floor of an open-topped box. Husar and Sparrow (1968) studied the patterns of natural convection adjacent to a horizontal heated surface and found that the fluid moves inward from the edges of the surface along horizontal paths that are straight and parallel until the flow is engulfed by an upward moving plume. Sparrow et al. (1970) observed the periodic generation of thermals in the warm region above a heated horizontal plate. Goldstein et al. (1973) obtained average results for the mass transfer, using the naphthalene-sublimation technique, from circular, square, and rectangular planforms. A universal correlation for all three forms was obtained.

An excellent review of natural convection in enclosures and partial enclosures is given by Gebhart et al. (1988). Of particular interest are the studies of Torrance et al. (1969) and Torrance and Rockett (1969). In the former, experiments involving a heat source situated at the bottom of an unvented enclosure filled with air were performed, while the latter was a numerical study of the same situation.

To examine buoyancy-driven exchange through an aperture in a horizontal partition with a heavy fluid above the partition and a lighter fluid below it, Brown (1962) performed a theoretical and experimental study for air. The experiments involved imposing a temperature difference across the partition. Results were obtained for a Grashof number, based on the partition thickness, ranging from 3×10^3 to 4×10^7, and a ratio of partition thickness to the side of the square L/S ranging from 0.0825 to 0.66. The results were presented in the traditional Nusselt-versus-Grashof number format.

Epstein (1988) observed that Brown's results could be recast into a single functional relationship between the exchange flow rate and $\Delta\rho/\rho$, L/S, and S, where $\Delta\rho$ and ρ are the density difference across the partition and the mean density, respectively. From this relationship, it was concluded that the exchange flow rate increases with increasing L/S.

Epstein (1988) also measured the exchange flow rate through circular and square openings in a horizontal partition, where the density-driven (bidirectional) flow exchange was obtained by using brine above the partition and fresh water below it. Results were obtained for a single opening with a ratio of the opening length (in the direction normal to the flow) to opening diameter L/D ranging from 0.01 to 10.0. As L/D was increased, four different flow regimes were observed, with the competition between two of these flow regimes resulting in a peak in the exchange flow rate. The flow behavior for two openings in the partition was also considered. Both bidirectional and unidirectional flow was observed in each of the openings.

The present paper is the result of an experimental study of the heat transfer from a heat source situated at the bottom of a top-vented enclosure and of the resulting fluid flow through the vent opening. The experimental setup consisted of an isothermal-walled circular enclosure, with a circular, isothermal heat source forming the central core of the floor of the enclosure. A circular hole through the center of the top wall of the enclosure served as the vent. In this configuration, fluid simultaneously enters and exits the enclosure through the vent opening. Experiments were performed for parametric varia-

Contributed by the Heat Transfer Division for publication in the JOURNAL OF HEAT TRANSFER. Manuscript received by the Heat Transfer Division February 13, 1989; revision received November 22, 1989. Keywords: Enclosure Flows, Flow Instability, Natural Convection.

tions of the vent opening size and inner enclosure height in order to examine the effect of the presence of the vent on the fluid flow and heat transfer. For each configuration defined by these geometric parameters, the heat-source-to-enclosure-wall temperature difference (i.e., the Rayleigh number) was varied by an order of magnitude. Baseline results were also obtained for an unvented enclosure and for the source situated in a "infinite" fluid environment (no enclosure) for purposes of comparison.

The heat transfer experiments involved the determination of average Nusselt numbers for the heat source and the measurement of the cross-vent mean temperature profile as well as cross-vent distribution of the fluctuating temperature intensity. Water ($\mathrm{Pr} \cong 5$) was used as the working fluid.

Flow visualization experiments were performed using the thymol-blue method, an electrochemical flow visualization technique. These were intended to reveal the flow patterns within the enclosure and in the vicinity of the vent opening. Various modes of flow were observed and documented for certain operating conditions.

Experiments

Test Section. The experiments were performed in distilled water with an apparatus whose essential features are exhibited in Fig. 1. As seen in the figure, the main components are a top-vented cylindrical enclosure and a heat source, mounted flush with the bottom bounding surface of the enclosure.

The heat source was a 2.611-cm-long, 3.404-cm-dia hollowed-out copper cylinder with a 0.315-cm-high, 0.282-cm-long step machined at its upper end. It was heated by means of a heater core, a hollow aluminum cylinder pressed into the hollowed-out portion of the copper cylinder. Twenty equally spaced grooves were machined into both the inner and outer surfaces of the aluminum cylinder to accommodate Teflon-coated electrical resistance wire (0.0762-mm-dia chromel). Power was supplied to the source using a d-c power supply capable of supplying power to within 0.1 percent of its set-point value.

The temperature of the source was obtained from a number of 0.0762-mm chromel-constantan thermocouples (sensitivity = 60 μV/°C) that had been precalibrated to within 1 μV prior to installation. As seen in the figure, there were three thermocouple junctions located near the top surface. These were actually located 0.0254 cm below the surface. The outputs were arithmetically averaged to give the mean surface temperature, which was used in the computation of the Rayleigh and average Nusselt numbers. The remaining thermocouples in the source were used in conjunction with the thermocouples in the Polystyrene (see Fig. 1) to estimate the heat conduction through the polystyrene. A 0.0508-mm-thick piece of contact paper was affixed to the upper face of the polystyrene to protect the thermocouples and to provide a hydrodynamically smooth surface.

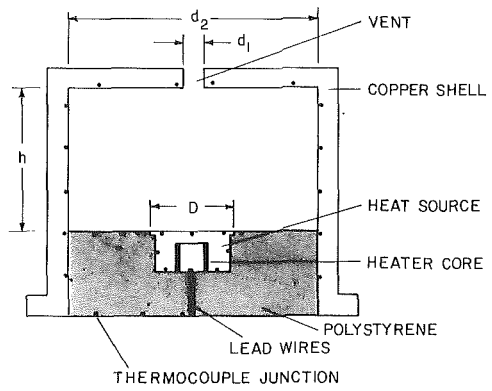

Fig. 1 Side view of the top-vented cylindrical enclosure

The cylindrical side wall of the enclosure was fabricated from a hollow copper cylinder finished to a length of 15.83 cm, an inside diameter d_2 of 15.60 cm, and an outside diameter of 16.67 cm. A 0.64-cm-thick, 17.08-cm-dia copper disk was used to close the top of the enclosure. All of the inner copper surfaces, including the surface of the heat source, were polished with 600-grit lapping compound to ensure hydrodynamically smooth surfaces.

A single circular hole was cut through the center of the disk to vent the enclosure. Four different hole diameters were used, starting with the smallest. They were: $d_1 = 1.270$, 3.192, 5.080, and 7.620 cm, respectively. The hole size was changed by enlarging the existing hole to the next largest diameter. It should be pointed out that prior to venting the enclosure, several data sets were obtained for the unvented case, i.e., $d_1 = 0$.

Test Environment. In order to obtain realistic natural convection heat transfer and flow results, the experiments had to be performed in a disturbance-free environment. To this end, a system of two water-filled tanks, one within the other; was employed. The inner tank provided a quiescent fluid environment for the test section, while the outer tank was used to set the temperature level in the inner tank. Both tanks were rectangular clear plexiglass tanks, with respective dimensions of

Nomenclature

A = wetted surface area of the heat source
D = diameter of the wetted surface of the heat source
d_1 = diameter of the vent opening
d_2 = inner diameter of the enclosure
f = frequency
g = acceleration of gravity
H = dimensionless inner enclosure height = h/d_1
h = inner enclosure height
$\bar{h}$ = average heat transfer coefficient, equation (1)
I = relative intensity of the fluctuating temperature at a given cross-vent position
k = thermal conductivity of water
Nu = average Nusselt number = $\bar{h}D/4k$
Pr = Prandtl number
Q = rate of heat transfer from the heat source
Ra = Rayleigh number, equation (2)
S = power spectral density of the dimensionless temperature fluctuations
T = instantaneous temperature in the vent opening
T_C = temperature of the enclosure wall
T_H = surface temperature of the heat source
T_m = time-averaged temperature at a given cross-vent position
T_∞ = ambient temperature
Y = dimensionless cross-vent position = y/d_1
y = cross-vent position
β = coefficient of thermal expansion
θ = dimensionless instantaneous temperature = $(T - T_\infty)/(T_H - T_\infty)$
θ_m = dimensionless mean temperature = $(T_m - T_\infty)/(T_H - T_\infty)$
ν = kinematic viscosity

$74 \times 43 \times 46$ cm and $102 \times 66 \times 51$ cm (length $\times$ width $\times$ height).

The test section of Fig. 1 was positioned at the center of the inner tank on a PVC ring so that the top of the apparatus was 18.7 cm below the water level.

A temperature controller/circulator was installed in the region between the inner and outer tanks. Both the inner and outer tanks were closed at the top using 3.81-cm-thick closed-pore polystyrene sheets to avoid heat and evaporation losses. The outer tank was also insulated using 3.81-cm-thick closed-pore polystyrene sheets.

The temperature uniformity in the test environment was monitored using three precalibrated 0.0762-mm chromel-constantan thermocouples located about 25 cm away from the test section. The three thermocouples were located along a vertical line at 10, 30, and 60 cm above the floor of the test section, respectively. Two additional thermocouples (0.0762-mm chromel and constantan) were also used to monitor the temperature of the outer bath.

Auxiliary Apparatus. In order to examine the effect of the presence of the enclosure on the heat transfer results, a data set was obtained without the enclosure. This setup consisted of a heat source located at the center of a rectangular piece of 3.81-cm-thick polystyrene so that its upper surface was flush with that of the polystyrene. This was accomplished by pressing the fully assembled bottom plug (see Fig. 1), including the heat source, into a hole bored through the center of the polystyrene sheet so that the upper surfaces of the plug, heat source, and sheet were all flush.

Once assembled, the sheet, including the fully assembled bottom plug, was positioned in the inner tank so that its upper surface, which now formed the floor of the tank, was 28 cm below the water level. Hereafter, this case will be referred to as the "infinite" case.

Experimental Procedure for Heat Transfer Runs. Several sets of data runs were performed during the experimental program. Each data set was characterized by a preselected vent diameter d_1 and consisted of three data subsets, except for the set for the largest vent diameter, which only consisted of two. A data subset was characterized by a preselected inner enclosure height h (see Fig. 1). For each data subset, the power input of the heat source (i.e., the source-to-enclosure temperature difference ΔT) was varied.

At the start of each data subset, the inner enclosure height was set and verified with a dial-gage-equipped caliper accurate to within 0.025 mm. Then, the test section was filled with water, making sure to avoid the formation of unwanted air pockets in the test section. Next, the test section was placed atop the PVC ring and leveled.

Prior to the initiation of the data subset, it was necessary for the temperatures in the inner and outer tanks to equilibrate. Temperature equilibrium between the two was verified from the thermocouples situated in the respective tanks. This step was to ensure that no extraneous buoyancy-induced flows existed in the test environment. Another prerequisite imposed at the beginning of each data run was that of uniform temperature throughout the inner tank.

Once thermal equilibrium between the inner and outer tanks was achieved, the lowest power setting was dialed in (i.e., the lowest ΔT). After the steady-state condition was attained (i.e., the variation in the ΔT was 0.3 percent in 60 min), the bath was stirred to ensure temperature uniformity. It took about one hour for steady state to be established and an additional hour for the stirring-induced disturbances to completely die away.

The steady-state condition just referred to was actually a quasi-steady state. It was observed that during a 60-min interval, the maximum temperature variation in the inner tank and the region between the two tanks ranged from 4.7 percent of the ΔT at the lowest power input to 0.4 percent of the ΔT at the highest power input.

At the end of the second waiting period, the test environment temperatures, heat source temperatures, enclosure wall temperatures, and polystyrene disk temperatures were read using a digital multimeter with a $1 = \mu$V resolution and accuracy of $\pm$ 2 counts in the smallest readable increment. The same meter was used to read the heater voltage and current to four or five significant figures depending on the power input. Three sets of readings were taken at intervals of 15 min. Then, the next highest heater power was set, "steady state" was achieved, the test environment stirred, and after an hour's wait, a new data run was completed. This was repeated until the highest power level was reached (i.e., a ΔT of about 10°C).

At the end of each data subset, the test section was removed from the inner tank and a new h value was set. Then, the aforementioned procedure was repeated. After all the h values of the data set were visited, the bottom plug was removed and the existing vent diameter was enlarged, thus setting the stage for a new data set.

Procedure for Studying the Vent Temperature Behavior. At the completion of the data run corresponding to the highest power setting (the last run of the data set), a thermocouple probe was inserted vertically through the test environment and into the vent so that the junction was positioned halfway between the inner and outer surface of the top wall (the temperature measurements were only performed at the highest ΔT). The probe consisted of a thermocouple (0.0762-mm chromel and constantan) threaded through a straight brass tube (0.0794-cm i.d.). The upper end of the tube was attached to a two-dimensional (horizontal and vertical) traversing mechanism (accurate to 0.064 cm) located atop the inner tank. All told, a total of seven locations were visited at each enclosure height for all of the vent diameters but the largest, where no data were obtained. The thermocouple emfs were read for 4 min at a sampling rate 1.0 Hz using a datalogger with an accuracy of ± 5 μV.

Flow Visualization. In order to understand the general nature of the flow in the vicinity of the vent, flow visualization experiments were conducted. To this end, the thymol-blue method of Baker (1966) was employed. This is an electrochemical technique where the fluid undergoes a change in color in response to a change in pH brought about by an imposed d-c voltage. The generated tracer fluid is neutrally buoyant and precisely follows the flow. To enable the generation of the tracer fluid, three substances were added to the water in the inner tank: a pH indicator (thymol blue), a base (sodium hydroxide), and an acid (hydrochloric acid). Because of these additional substances, the flow visualization experiments were performed separately from the heat transfer runs. However, the same experimental procedure was followed.

To implement the flow visualization technique, two electrodes are placed in the solution, and a small d-c voltage is induced between them to change the pH of the solution in the vicinity of the negative electrode (the cathode) which produces the tracer fluid. Therefore, the flow patterns of interest can be studied by placing the cathode in a suitable location.

Two different cathode arrangements were employed to study the behavior of the flow through the vent, a single-wire arrangement and a cross-wire arrangement. The respective cathode arrangements were situated immediately above the vent opening.

Photographs were taken of the flow field using a 50-mm Cannon lens utilizing Kodak TMAX 400 black and white film. Motion pictures were also taken of the flow field using a Sony video cassette recorder. A slit cut into the insulation of the

outer tank facilitated the photographic documentation of the flow field. Another slit cut in the insulation of the opposite wall allowed light from a 150-W floodlight to enter the inner tank. The light was diffused through onion skin paper.

Data Reduction. The main objective of the data reduction was to implement the dimensionless groups commonly used for natural convection. These are the Nusselt and Rayleigh numbers for the heat source (an upward-facing heated disk). The Nusselt number was evaluated from

$$\mathrm{Nu} = \bar{h}D/4k, \qquad \bar{h} = Q/A(T_H - T_C) \tag{1}$$

where Q is the rate of convective heat transfer from the source, A is the wetted surface area of the source, and D (see Fig. 1) is the diameter of the wetted surface. The number 4 in the Nusselt number expression arises from the fact that the characteristic length used for correlating natural convection results for hot upfacing surfaces has been implemented. This is from the work of Goldstein et al. (1973), where the characteristic length is defined as the exposed surface area divided by the perimeter corresponding to the exposed surface.

The temperature T_H corresponds to the average temperature of the exposed surface of the heat source and was obtained by arithmetically averaging the outputs of the three thermocouples located near the upper surface of the source. Unless stated otherwise, T_C is the arithmetic average of the temperatures recorded from the individual thermocouples embedded in the top and side walls of the copper shell. Only those thermocouples corresponding to the portion of the side wall wetted by the fluid within the enclosure were included in the averaging process (see Fig. 1). The maximum deviation from the average value for T_C was 2.5 percent of the heat-source-to-enclosure temperature difference, $\Delta T = (T_H - T_C)$. However, the typical standard deviation from the mean was only about 0.7 percent of the ΔT. As for T_H, the maximum deviation never exceeded 0.3 percent of the ΔT. Based upon the accuracy of the multimeter, it was determined, using the uncertainty analysis of Kline and McClintock (1953), that the uncertainty in the temperature measurements were 0.03°C and that of the ΔT was 0.06°C.

Two-dimensional finite difference heat conduction calculations demonstrated that the heat losses through the polystyrene fell within the experimental uncertainty. Therefore, Q was taken to be the electrical power supplied to the source without correction. The calculations used the temperatures along the top and bottom surfaces of the polystyrene, the average temperature of the heat source, and the enclosure wall temperatures as inputs.

The Rayleigh number was based on the same characteristic length that was used to compute the Nusselt number and was calculated from

$$\mathrm{Ra} = [g\beta(T_H - T_C)(D/4)^3/\nu^2]\,\mathrm{Pr} \tag{2}$$

where all of the thermophysical properties were evaluated at the film temperature $(1/2)(T_H - T_C)$.

Results and Discussion

The presentation of results will commence with an examination of the effect of the vent opening size and the enclosure height on the average Nusselt number. This will be followed in sequence by a presentation and discussion of the flow visualization results. Then, the temperature behavior in the vent opening will be addressed.

Average Heat Transfer Results. In Figs. 2 and 3, the effect of the vent opening size on the average Nusselt number is shown for the smallest and largest dimensionless enclosure heights ($H = h/d_2$), respectively. Representative uncertainties and reproducibilities for these data are given in Table 1. The uncertainties were determined using the uncertainty analysis of Kline and McClintock (1953), and the reproducibilities were determined from a set of auxiliary experiments performed at a later date.

In both figures, average Nusselt number results are displayed for five different dimensionless vent diameters: $d_1/d_2 = 0$ (no vent), 0.0814, 0.201, 0.326, and 0.489. The dashed line passing through the data points in each figure was obtained from a least-squares fit of the data for all the diameters in the corresponding figures. Relations for the dashed lines are also given in the figure. These are: $\mathrm{Nu} = 0.310[\mathrm{Ra}]^{0.277}$ and $\mathrm{Nu} = 0.274[\mathrm{Ra}]^{0.288}$ for $H = 0.327$ and 0.716, respectively.

A least-squares fit, $\mathrm{Nu} = 0.326[\mathrm{Ra}]^{0.272}$, was also obtained for the intermediate dimensionless height, $H = 0.521$. It should

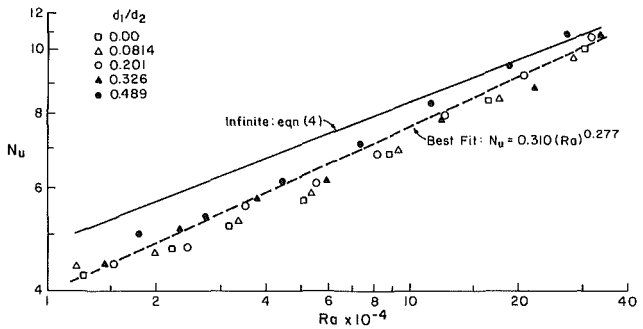

Fig. 2 Effect of vent diameter on the average Nusselt number at $H = 0.327$

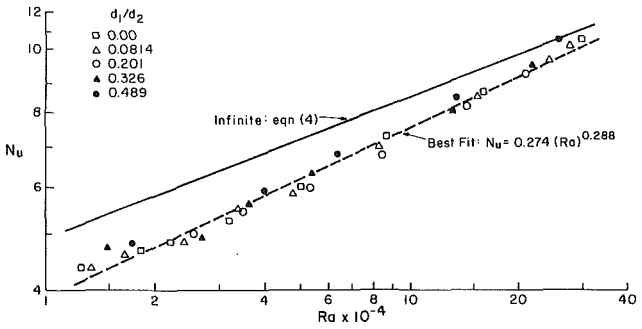

Fig. 3 Effect of vent diameter on the average Nusselt number at $H = 0.716$

Table 1 Representative uncertainties and reproducibilities

	Uncertainty (percent)		Uncertainty (percent)	Reproducibility (percent)
$\mathrm{Ra} \times 10^{-4}$	Ra	Nu	Nu	Nu
1.32	11	5.06	3.4	3.8
2.71	5.7	5.65	1.6	
4.84	3.3	6.47	0.9	
8.16	2.0	7.49	0.5	3.8
14.4	1.2	8.70	0.3	
23.5	0.8	10.0	0.2	
36.0	0.5	11.3	0.2	2.0

be pointed out, however, that there were no data obtained for $d_1/d_2 = 0.489$ at this enclosure height.

The relations just presented fit the bulk of the corresponding data (i.e., better than 95 percent of the data) to within 7 percent, and the standard error (i.e., the rms of the difference between the calculated and actual valves) in the Nusselt number is 0.2 for $H = 0.521$ and 0.716 and 0.3 for $H = 0.327$. The fact that the data for all of the vent opening sizes $0 \le d_1/d_2 \le 0.489$ fit a single correlation to within a reasonable degree of error at each enclosure height suggests, for the range of vent sizes and Rayleigh numbers $(1.2 \times 10^4 \le \mathrm{Ra} \le 36 \times 10^4)$ considered, that the Nusselt number is virtually independent of the vent opening size.

In addition, comparisons between the Nusselt numbers calculated from the respective correlations indicate that the calculated Nusselt numbers are well within 2 percent of each other. Since the correlations are obtained at different enclosure heights, it can be concluded that for the range of dimensionless enclosure heights, $0.327 \le H \le 0.716$, and Rayleigh numbers considered, there is virtually no effect of the enclosure height on the Nusselt number. This is because the thermal and momentum boundary layers above the heat source are much smaller than even the smallest enclosure height. Therefore, the heat source is totally oblivious to the presence of the top wall of the enclosure or the vent.

In view of the foregoing, it was decided to obtain a correlation for all of the experimental data. The resulting correlation is

$$\mathrm{Nu} = 0.303[\mathrm{Ra}]^{0.279} \tag{3}$$

This correlation is valid for $1.2 \times 10^4 \le \mathrm{Ra} \le 36 \times 10^4$, $0 \le d_1/d_2 \le 0.489$, and $0.327 \le H \le 0.716$. The standard error in the calculated Nusselt number is 0.3, and 98 percent of the values calculated from equation (3) lie within 8 percent of the experimental results.

Also included in Figs. 2 and 3 is a solid line. This is for the infinite case and was obtained from a least-squares fit through the measured data for the infinite case. The equation of the line is given by

$$\mathrm{Nu}_\infty = 0.542[\mathrm{Ra}]^{0.239} \qquad (1.2 \times 10^4 \le \mathrm{Ra} \le 36 \times 10^4) \tag{4}$$

The maximum deviation between the line and the measured data is 1.4 percent, while the standard error is 0.043. It should be noted that for this case, the temperature T_C used in computing the Nusselt and Rayleigh numbers is the temperature of the test environment rather than that of the test section wall.

It is noteworthy that Nusselt numbers given by equation (4) are 9 to 12 percent below those given by the textbook correlation (Incropera and DeWitt, 1985, p. 433), for a hot upfacing horizontal surface.

Attention will now be focused on the effect of the presence of the enclosure on the average Nusselt number. This will be accomplished by comparing the results for the enclosure (equation (3)) to those for the infinite case. First it can be seen in Figs. 2 and 3 that the presence of the enclosure acts to reduce the Nusselt number. This is particularly true at the lowest Rayleigh number $(\mathrm{Ra} = 1.2 \times 10^4)$, where the results calculated from equation (3) are about 20 percent lower than those for the infinite case equation (4)). However, it is seen that this large difference decreases with increasing Rayleigh number. In fact, at the highest Rayleigh number (34×10^4), the difference between the results calculated from equations (3) and (4) is only 7.5 percent.

The abovedescribed behavior can be rationalized as follows: In general, the temperature difference between the heat source and the average temperature of the infinite fluid environment (i.e., the test environment) is greater than that between the heat source and the average temperature of the fluid contained in the enclosure. This is because the heat capacity of the infinite environment is about 220 times greater than that of the enclosure environment and can absorb a larger amount of heat without a corresponding temperature increase than the enclosure environment. Therefore, the heat transfer is generally greater for the infinite case. However, as the Rayleigh number is increased, the thermal boundary layer above the heat source thins out. As the thinning process progresses, the heat source becomes increasingly less aware of what is going on around it, thus causing the enclosure to behave like an infinite environment.

It should be mentioned that Torrance et al. (1969) studied natural convection in unvented enclosures containing air. After taking into account the property variation due to temperature and recasting the heat transfer data in terms of the Nusselt and Rayleigh numbers defined in (1) and (2), respectively, it was found that for Rayleigh numbers between 1.5×10^4 and 2.6×10^4, Torrance's Nusselt numbers were about 40 percent greater than those calculated from equation (3). The uncertainty in Torrance's data was between 10 and 20 percent.

Flow Visualization Results. The flow visualization experiments were performed at the intermediate dimensionless enclosure height ($H = 0.521$) for Rayleigh numbers of 3.7×10^4, 7×10^4, and 3×10^5 and $d_1/d_2 = 0.0814$, 0.201, and 0.326. During the experiments, it was found that the flow patterns above the vent opening were unstable and quite complex. However, it was found that for all the vent opening sizes considered, the flow fluctuated between four distinct modes in a nonperiodic manner.

Figure 4 is a photograph of mode I flow, which is a symmetric flow consisting of outflow at the center of the opening and inflow near both edges. This flow pattern was witnessed at all of the Rayleigh numbers considered. Due to their inferior quality, photographs of the remaining three modes have been omitted. However, the distinguishing characteristics of these modes, along those of the mode I flow, are shown in Fig. 5, which is based on photographs, videotapes, and personal observations of the flow.

As seen in Fig. 5, mode II flow consists of all outflow along a single vent diameter. However, in order to satisfy mass conservation, this flow was simultaneously accompanied by mode I flow along another vent diameter. Like mode I flow, mode II flow occurred at all three Rayleigh numbers. Mode III flow occurred only at the two highest Rayleigh numbers and was characterized by an inflow near one of the edges of the opening and in outflow across the rest of the opening. The inflow was observed to shift from one side to the other in a nonperiodic fashion. Sudden and occasional bursts of downflow at the center of the opening, accompanied by

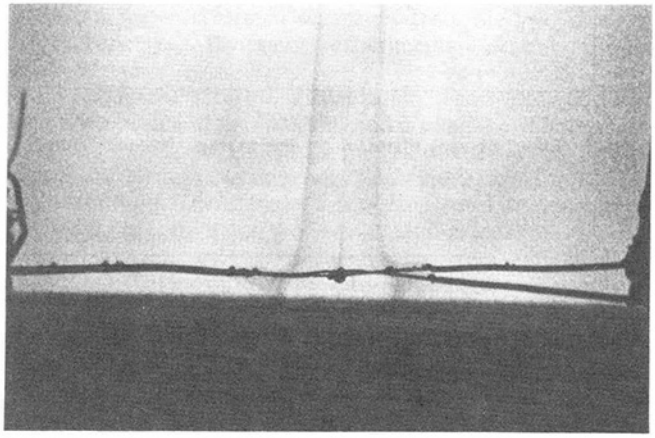

Fig. 4 Photograph of mode I flow for $H = 0.521$, $d_1/d_2 = 0.201$, and $\mathrm{Ra} = 3.7 \times 10^4$

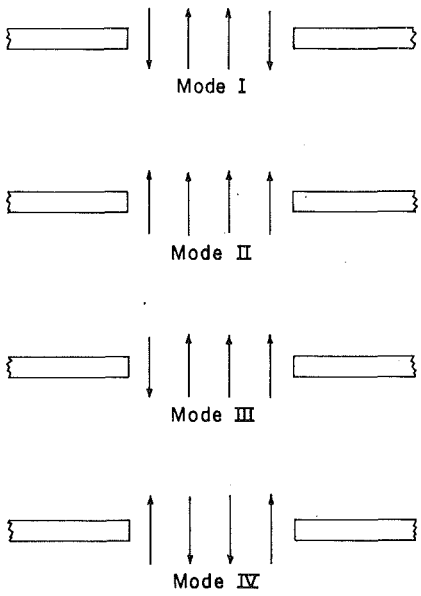

Fig. 5 Portrayal of the four modes of flow observed in the vicinity of the vent opening

upflows near both edges of the opening, typified mode IV flow. It was only observed at the largest Rayleigh number.

Although the flows were qualitatively the same for the three vent sizes studied, there were some specific differences between the flows at the largest vent opening and at the two smaller openings. These differences will now be discussed for the largest Rayleigh number ($\mathrm{Ra} = 3 \times 10^5$).

At the largest diameter, no dominant mode emerged. Rather, the flow mainly oscillated in a random fashion among modes I, III, and IV. In contrast, at the two smaller diameters, modes I and III were the dominant modes, with mode IV occurring only occasionally. It should be mentioned that mode II flow rarely occurred at the largest Rayleigh number.

It was also observed that the exchange flow (outflow or inflow) was strongest for the smallest diameter and became weaker with increasing diameter. Epstein (1988), who studied buoyancy-driven flows through vents in horizontal partitions, documented that for the range of vent sizes considered here, the exchange flow rate (inflow or outflow) increases with decreasing diameter for a fixed partition thickness.

Temperature Results. As mentioned earlier, temperature measurements were performed at various locations along a single vent diameter in order to understand the flow behavior in the vent better. In the following presentation, all of the reported temperature information is for the largest Rayleigh number ($\mathrm{Ra} \cong 3 \times 10^5$) of each data set and corresponds to an axial vent location that is exactly midway between the inner and outer surfaces of the top wall of the test section. Because of an apparatus malfunction, no temperature data are reported for the maximum vent diameter. Hereafter, the dimensionless vent diameter corresponding to the next largest diameter (i.e., $d_1/d_2 = 0.326$) will be referred to as the maximum dimensionless diameter.

As for the uncertainty in the temperature measurement, the uncertainty analysis of Kline and McClintock (1953) revealed that the uncertainty in the temperature measurement was about ± 0.8 percent of the difference between the heat source and test environment temperatures, $(T_H - T_\infty)$. In addition, comparisons between a set of vent temperature data sampled at 2.7 Hz, the maximum sampling rate available, and 1 Hz revealed that the 1-Hz sampling rate was sufficient to resolve the fluctuating temperatures in the vent. The flow visualizations also indicated that a relatively slow sampling rate was adequate.

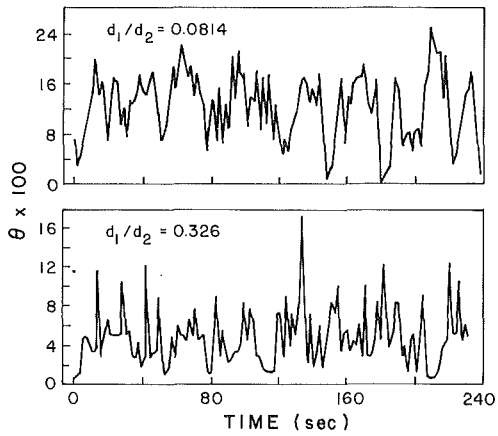

Fig. 6 Instantaneous temperature behavior at the axis of the vent for $\mathrm{Ra} = 3.0 \times 10^5$, $H = 0.327$

Figure 5 portrays the instantaneous temperature behavior at the central axis of the vent for the maximum ($d_1/d_2 = 0.326$) and minimum dimensionless vent diameters at the smallest dimensionless enclosure height. In the figure, the instantaneous dimensionless temperature, $\theta = (T - T_\infty)/(T_H - T_\infty)$, is plotted against time, where respectively T, T_∞, and T_H are the instantaneous flow temperature, the test environment temperature, and the heat source temperature. A time-temperature plot was obtained for every temperature measurement location at every enclosure height and vent diameter considered.

An inspection of the figure reveals that the peak-to-peak temperature fluctuations are larger for the smaller diameter, with the maximum peak-to-peak fluctuation being about 1.5 times greater for the smaller diameter. It is also seen that the temperature approaches and sometimes equals that of the test environment, especially at the larger diameters considered.

The fact that the instantaneous temperature often approaches the temperature of the test environment at the vent axis is attributed to mode IV flow (or a sudden burst of downflow at the vent center). Figure 6 indicates that this phenomenon is much more likely to occur at the larger diameter. Indeed, mode IV flow occurred more often at the largest diameter than at the smallest. This may be attributed to the fact that the outflow at the center of the opening appeared to be much stronger for the smaller diameter.

Before presenting the rest of the temperature results, it is observed that the temperatures in Fig. 5 fluctuate about a mean value that is essentially independent of time. This justifies the use of a time-averaged mean temperature in succeeding figures. Since the mean temperature is independent of time, the ergodic hypothesis was invoked, and the mean temperature in succeeding figures corresponds to the arithmetic average (or ensemble average) of all of the temperature measurements performed at a given location.

In order to understand better the relationhip between the unstable flow pattern and the temperature behavior in the vent opening, the power spectrum of the dimensionless temperature fluctuations was obtained. This information is displayed in Fig. 7 for the smallest and largest openings at the smallest enclosure height. For each vent opening, a power spectrum is shown for three different locations along the vent diameter. The Y value in each figure denotes the dimensionless location and is given by $Y = y/d_1$, where y is the distance from one of the edges.

An inspection of the figure shows that the largest temperature disturbances occur for the smallest diameter near

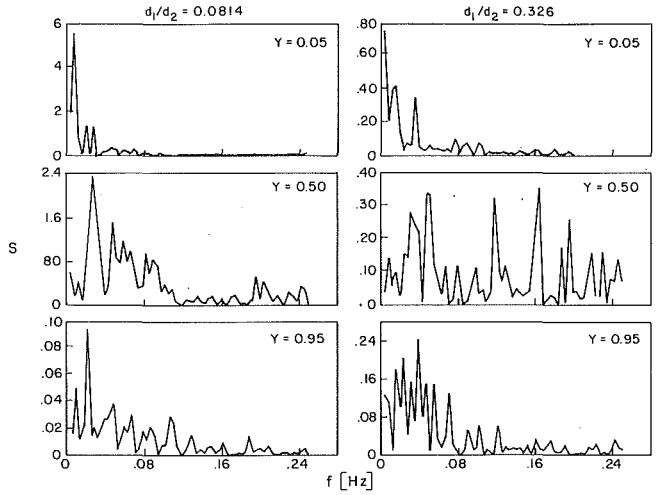

Fig. 7 Power spectra of the dimensionless temperature fluctuations at various locations along the vent diameter for Ra = 3 x 10^5 and $H = 0.327$

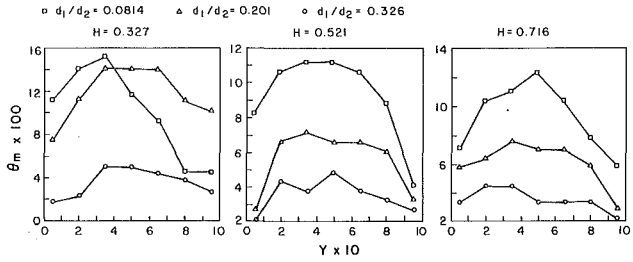

Fig. 8 Effect of vent diameter on the mean temperature distribution across the vent at different enclosure heights for Ra = 3.0 x 10^5

one of the vent edges, with these disturbances occurring at a frequency of about 0.01 Hz. Because relatively cool inflows were observed more often near the vent edges than at the center, especially for the smallest opening size, this is attributed to occasional bursts of warm outflow near the edge.

At the center of the vent the magnitude of the maximum amplitude is about half that at $Y=0.05$ and occurs at a frequency of about 0.03 Hz. Since warm outflow was observed to occur most often at the center of the opening, the large disturbances are the result of sudden bursts of cool inflow (mode IV) at the center of the vent.

As for the other edge of the vent ($Y=0.95$), the magnitudes of the disturbances are negligible compared to those at the other Y values. Because inflows are more likely to occur near the edge, the absence of any large disturbances indicates isothermal inflow with no flow reversals.

For the largest vent size, the magnitudes corresponding to the peaks in the power spectrum for $Y=0.05$ and 0.5 are much smaller than those at the same Y values for the smallest vent size, which indicates that the temperature disturbances are much smaller. Since flow reversals were observed along the diameter of the largest opening, this indicates that the disturbances (peaks in the power spectrum) associated with flow reversals are much smaller for the largest opening. This is believed to be the result of the lower flow rates observed for the largest opening.

Of particular interest is a comparison between the power spectrums for the two vent sizes at the center of the vent ($Y=0.5$). It is seen that the peaks are distributed over a number of frequencies for the larger opening, as opposed to the peaks being concentrated at the lower end of the spectrum for the smallest opening. This supports the observation that inflow occurred more frequently at the center of the largest opening than at the smallest.

Figure 8 displays the effect of the vent opening size on the mean temperature distribution for the three enclosure heights. In the figure, the dimensionless mean temperature, $\theta_m=(T_m-T_\infty)/(T_H-T_\infty)$, is plotted against the dimensionless distance Y, where T_m is the arithmetic average of all of the temperature measurements performed (240 measurements in 4 min) at the desired vent location.

An inspection of the figure reveals that the temperature profiles are asymmetric, with the temperatures at locations on one side of the symmetry axis ($Y=0.5$) being greater than those at corresponding locations on the other side. At the larger diameters ($d_1/d_2=0.201$ and 0.326), the higher temperatures occur on either side of the axis, while at the smallest diameter, they seem to prefer one side to the other.

The asymmetric behavior can be attributed to the mode III flow pattern, which was characterized by a single inflow leg shifting randomly from one side of the vent to the other. It was observed, during a 30-min observation period, that the relatively cool inflow leg preferred one side of the vent to the other. Although the results for the smallest vent opening size suggest that the preferred location always occurs at the same side, it is believed that the selection of a preferred side is a random event, as attested to by the results for the other vent opening sizes.

It is now appropriate to relate the temperature distribution for $d_1/d_2=0.0814$ at $H=0.327$ to the behavior observed in Fig. 7. The relatively high temperature near the one edge ($Y=0.05$) can be directly linked to the high amplitudes at low frequencies in Fig. 7 for this Y value. That is, the high temperature is due to low-frequency bursts of warm upflow. As for $Y=0.95$, the low temperature can be linked to the low amplitudes in Fig. 7 for this Y value and confirms that the flow is a cool inflow.

Figure 8 reveals that for any given temperature distribution, the minimum temperature (or temperatures) occurs near the edge (or edges) of the vent. This tends to agree with the observations that the cool inflow prefers the region near the edge (or edges) of the opening. It is also noticed that the temperature typically increases with decreasing vent size, with the largest increases occurring in the central portion of the opening. Note, in particular, the distinct profile evolution with decreasing vent size at $H=0.521$ and 0.716.

The temperature increases at the center of the opening with decreasing vent size because the exchange flow rate is increasing. As pointed out earlier for the larger vent size, the weaker flow at the center permits flow reversals (i.e., bursts of cool inflow) to occur more frequently than for the smaller diameters. This acts to reduce the mean temperature at the center. The lower flow rate also provides more time for molecular diffusion to occur between the cold and hot fluids. Therefore, the temperature profile is more uniform and the thermal disturbances are smaller than for the smaller diameters where the exchange flow rates are higher.

Figure 9 displays the distribution of the relative intensity of the temperature fluctuations, $I=\{[(T-T_m)^2]_m\}^{1/2}/(T_H-T_\infty)$, for each vent diameter at each vent height. In the expression for I

$$[(T-T_m)^2]_m=(1/N)\sum_{i=1}^{N}(T_i-T_m)^2 \tag{5}$$

where N is the total number of temperature readings (240) at a given vent location and T_i is the ith temperature measurement. Again, the ergodic hypothesis has been used.

An overview of the figure reveals that the intensity level generally increases with decreasing vent opening size, especially as the vent size is decreased from the largest diameter to the intermediate diameter. In addition, at the smallest diameter, the disturbances in the flow undergo rapid growth at a small distance from one or both of the vent edges. This is due to the

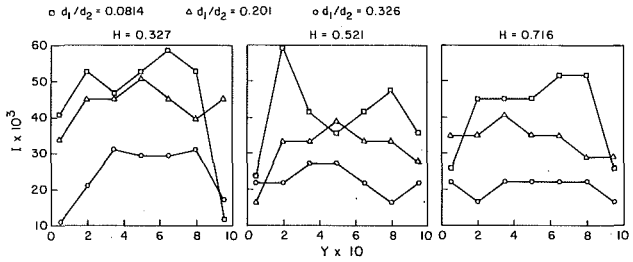

Fig. 9 Cross-vent distributions of the intensity of the dimensionless temperature fluctuations for various vent diameters and enclosure heights at Ra = 3 x 10^5

presence of a shear layer, which separates the outflow from the inflow.

Of particular interest is the behavior at the smallest enclosure height ($H=0.327$) for the minimum vent size. At $Y=0.95$ it is seen that the disturbance level is quite small. As pointed out earlier, this is a region of cool inflow with no bursts of outflow. At $Y=0.05$, it is seen that the disturbance level is quite high. This is the result of low-frequency bursts of warm outflow near this edge.

For the largest diameter, the disturbance level is fairly uniform at the largest and intermediate enclosure heights. In contrast, at the smallest height, the disturbances undergo considerable amplification at a small distance from the respective edges.

As for the intermediate diameter, the distributions exhibit larger disturbance amplification at short distances from the vent edge than those for the largest diameter at the intermediate enclosure height. On the other hand, at the smallest height the disturbance amplification is much less pronounced at the intermediate diameter than at the largest.

Conclusions

The present investigation studied the natural convection heat transfer from a heat source that was mounted flush with the bottom bounding surface of a top-vented enclosure. The behavior of the flow through the vent and of the temperatures in the vent opening was also examined.

Average Nusselt numbers were experimentally obtained for parametric variations of the dimensionless vent opening size and the enclosure height. For each geometric configuration defined by these parameters, the heat-source-to-enclosure-wall temperature difference was varied by an order of magnitude, while the Prandtl number of the working fluid (water) was maintained at a nominal value of 5. For comparison purposes, baseline data were obtained for the corresponding unvented enclosure and for the "infinite" case (no enclosure). Flow visualization experiments were conducted to reveal the fluid patterns in the vicinity of the vent. Information on the mean temperature and the intensity and spectra of the temperature fluctuations was obtained by measuring the instantaneous temperature at various locations across the diameter of the vent opening.

The experiments demonstrated that for the range of enclosure heights, vent diameters, and Rayleigh numbers considered, the effect of height and vent size had virtually no effect on the average Nusselt number. It was found that for the range of parameters considered, the average Nusselt number could be correlated to within ±8 percent using a single correlation (equation (3)). It was also found that the presence of the enclosure (vented or unvented) acted to reduce the Nusselt number, especially at the lowest Rayleigh numbers.

Flow visualization experiments revealed an unstable flow pattern in the vicinity of the vent that fluctuated between four basic modes in a nonperiodic manner. Mode I was a symmetric flow pattern consisting of an outflow at the center of the vent opening and an inflow near the edges of the opening. It was observed at all of the Rayleigh numbers considered. Mode II was also observed at all of the Rayleigh numbers, and it consisted of all outflow along one of the vent diameters. This was simultaneously accompanied by mode I flow along another vent diameter. Mode III flow occurred only at higher Rayleigh numbers and was characterized by an inflow near one of the edges of the opening and outflow across the rest of the opening. The inflow was observed to shift from one side of the opening to the other in a nonperiodic fashion. Sudden and occasional bursts of downflow at the center of the opening accompanied by upflows near both sides of the opening at the largest Rayleigh number typified mode IV flow.

The temperature measurements demonstrated that the mean cross-vent temperature distributions were asymmetric. Furthermore, the mean temperature level was quite sensitive to changes in the size of the vent opening, with the mean temperature increasing with decreasing vent size. The level of the temperature disturbances also increased with decreasing vent size. These disturbances were observed to undergo large amplification at a short distance from the edge of the opening, with the most pronounced amplifications occurring at the smallest vent size.

Acknowledgments

The author is grateful to Mr. Shahid Siddiqui and Mr. Shailendra Inamdar for their assistance in conducting the experiments.

References

Baker, D. J., 1966, "A Technique for the Precise Measurement of Small Fluid Velocities," *J. Fluid Mech.*, Vol. 26, pp. 573-575.

Brown, W. G., 1962, "Natural Convection Through Openings in Partitions—2," *Int. J. Heat Mass Transfer*, Vol. 5, pp. 869-878.

Epstein, M., 1988, "Buoyancy-Driven Exchange Flow Through Small Openings in Horizontal Partitions," ASME JOURNAL OF HEAT TRANSFER, Vol. 110, pp. 885-893.

Gebhart, B., Jaluria, Y., Mahajan, R. L., and Sammakia, B., 1988, *Buoyancy-Induced Flows and Transport*, Hemisphere Publishing Corp., New York.

Goldstein, R. J., Sparrow, E. M., and Jones, D. C., 1973, "Natural Convection Mass Transfer Adjacent to Horizontal Plates," *Int. J. Heat Mass Transfer*, Vol. 16, pp. 1025-1035.

Husar, R. B., and Sparrow, E. M., 1968, "Patterns of Free Convection Flow Adjacent to Horizontal Heated Surfaces," *Int. J. Heat Mass Transfer*, Vol. 11, pp. 1206-1208.

Incropera, F. P., and DeWitt, D. P., 1985, *Fundamentals of Heat and Mass Transfer*, 2nd ed., Wiley, New York.

Kline, S. J., and McClintock, F. A., 1953, "Estimating the Uncertainty in Single-Sample Experiments," *Mechanical Engineering*, Jan.

Sparrow, E. M., Husar, R. B., and Goldstein, R. J., 1970, "Observations and Other Characteristics of Thermals," *J. Fluid Mech.*, Vol. 41, pp. 793-800.

Torrance, K. E., Orloff, L., and Rockett, J. A., 1969, "Experiments on Natural Convection in Enclosures With Localized Heating From Below," *J. Fluid Mech.*, Vol. 36, pp. 21-31.

Torrance, K. E., and Rockett, J. A., 1969, "Numerical Study of Natural Convection in an Enclosure With Localized Heating From Below—Creeping Flow to the Onset of Laminar Instability," *J. Fluid Mech.*, Vol. 36, pp. 33-54.

Townsend, A. A., 1959, "Temperature Fluctuations Over a Heated Horizontal Surface," *J. Fluid Mech.*, Vol. 5, pp. 209-241.

D. A. Olson[1]
Graduate Student,
Department of Mechanical Engineering.
Assoc. Mem. ASME

L. R. Glicksman
Professor,
Department of Architecture and Mechanical Engineering.
Mem. ASME

H. M. Ferm[2]
Graduate Student,
Department of Mechanical Engineering.

Massachusetts Institute of Technology,
Cambridge, MA 02139

Steady-State Natural Convection in Empty and Partitioned Enclosures at High Rayleigh Numbers

Steady-state natural convection, which occurs in building enclosures (Rayleigh numbers of 10^{10}), was studied experimentally in a full-scale room and in a 1:5.5 small-scale physical model containing R114 gas. The model was geometrically similar, had the same Rayleigh number, and had the same dimensionless end wall temperatures as the full-scale room. Configurations were tested with the enclosure empty, with a vertical partition extending from the floor to midheight, and with the vertical partition raised slightly off the floor. For isothermal opposing end walls at different temperatures, excellent agreement was found between the full-scale room and the scale model in flow patterns, velocity levels, temperature distributions, and heat transfer, even though the radiation heat transfer was not scaled between the two models.

Introduction

This paper addresses the problem of how to accurately scale natural convection that occurs in enclosures of a size resulting in Rayleigh number (Ra) of order 10^{10}. The application of interest is the flow patterns and temperature distributions set up by natural convection within buildings. The primary objective is to verify that one can experimentally reproduce the phenomena using a dense refrigerant gas (R114) in a 1:5.5 scale physical model. Small-scale model studies of building enclosures offer an attractive means of testing new or existing designs for thermal comfort, indoor air quality, and energy use prior to constructing the actual facility. Scaling studies can test a range of conditions much faster and more cheaply than can the monitoring of actual buildings. The present scaling technique is evaluated by comparing experimental results of the physical scale model with measurements on a full-scale room at the same geometry, Ra, and Prandtl number (Pr). Whenever possible, results obtained in this study are compared with physical scale models using water, which have matched the geometry and Ra of a full-scale room, but not the other scaling paramenters (detailed later). A second objective of the work is to further the understanding of natural convection in an enclosure at high Ra. The work reported in this paper is based on the theses of Olson (1986) and Ferm (1985).

Scaling Parameters. The enclosure studied was a rectangular space one third as high as it was long, and one half as wide as it was long (see Fig. 1), which represented a "typical" building space. For this work, well-defined simple thermal boundary conditions were used: The opposing end walls were heated and cooled isothermally at steady state. The ceiling, floor, and side walls were well insulated. A vertical partition was placed midway between the hot and cold end walls, extending from the floor halfway to the ceiling and from one side wall to the other. The enclosure was also tested empty with the partition absent. The heated and cooled vertical surfaces were of low emissivity to facilitate measurement of the convective heat flux. The ceiling and floor were high-emissivity surfaces, common for building materials.

Nondimensionalization of the mass, momentum, and energy equations (Olson, 1986) indicates that the appropriate scaling parameters for the empty enclosure, when radiation is neglected, are: aspect ratios $A_L = H/L$ and $A_W = H/W$; the Rayleigh number based on enclosure height and the temperature difference between the heated and cooled end walls; and the Prandtl number. To scale the thermal effect of the partition, the ratio of heat conducted through the partition to heat convected from a vertical wall must be matched (Nansteel and Greif, 1981). This scaling parameter is expressed as a conductance ratio $k^* = k_p H_p/(kt_p \mathrm{Nu})$. k_p, H_p, and t_p are, respectively, the thermal conductivity, height, and thickness of the partition. Nu is the vertical end wall Nusselt number, of order 100 (Siebers et al., 1985). For geometric scaling of the partition, the partition size and location should be matched.

Because of the high emissivity of the ceiling and floor (~ 1), radiation heat transfer between them can be significant. The scaling parameter that estimates this effect is a ratio comparing the ceiling/floor radiation to heat convection from a vertical wall. Expressed as a conductance ratio, this is $k_r = 4\sigma T_m^3 LF/(k\mathrm{Nu})$, with F the radiation view factor. If $k_r > 1$, radiation is likely to be significant. A final radiation scaling parameter results from considering the attenuation of radiation heat transfer due to an absorbing or emitting gas. Although dry air is transparent, humid air is somewhat absorbent, while the scaling gas used in the present experiments, R114, is an absorber/emitter (Simpson and Plyer, 1953). The attenuation parameter can be expressed as a ratio of the height of the enclosure to the attenuation length. Or, the optical depth $H_o = aH$, where a equals the mean absorption coefficient. If H_o is 0, the fluid is transparent, and if $H_o >> 1$, the fluid is opaque.

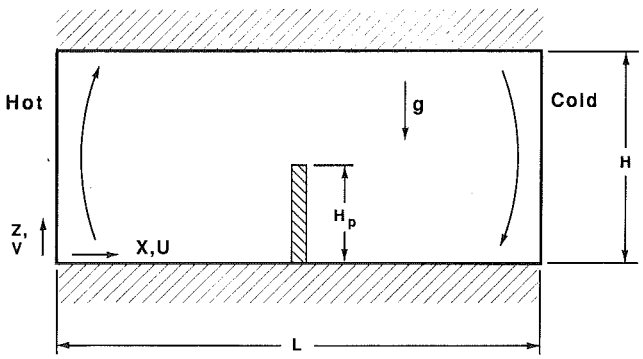

Fig. 1 Enclosure geometry

[1]Currently at National Institute of Standards and Technology, Boulder, CO 80304.

[2]Currently at CUH2A, Princeton, NJ 08540.

Contributed by the Heat Transfer Division for publication in the JOURNAL OF HEAT TRANSFER. Manuscript received by the Heat Transfer Division November 18, 1988; revision received August 21, 1989. Keywords: Building Heat Transfer, Modeling and Scaling, Natural Convection.

For an air-filled building interior of height 3 m and end-wall temperature difference of 10°C, Ra is 10^{10} and Pr is 0.7. The aspect ratio A_L is typically 0.1–1.0 in most building interiors. A partition conductance k^* is 0.1–0.5, and the radiation scaling parameters have values k_r of 10–20, and H_o of 0–0.25.

Literature Review. Natural convection in partitioned or empty enclosures at Ra ~ 10^{10}, with hot and cold opposing vertical end walls, has been the subject of many studies recently. For those that attempt to scale the flow in building enclosures, none (including the present work) have matched all the scaling parameters mentioned above. With water as the scaling fluid, the model can be 1/8 as large as full scale, the aspect ratios and Ra of room air can be matched, but Pr is 3–7, k_r is 0.03 (radiation heat transfer small compared to convection heat transfer), and $H_o >> 1$ (radiation that is emitted is highly attenuated). At a very small aspect ratio, Bejan et al. (1981) observed laminar boundary layers on the vertical surfaces (water, $\text{Ra} = 2 \times 10^9$, $A_L = 0.0625$). In the core, the flow was horizontal with a thin laminar layer flowing along the ceiling from the hot end to the cold end and along the floor from the cold to the hot. Secondary horizontal flow was observed in the core, moving in the opposite direction to the layers circulating the enclosure closest to the ceiling and floor. The vertical temperatures were linearly stratified in the core.

Bohn et al. (1984) also used water to study a cubical enclosure ($A_L = 1$) at Ra up to 6×10^{10}. The side walls were heated and cooled, along with the end walls. The secondary horizontal flow patterns seen by Bejan et al. (1981) were not observed, and at the highest Ra numbers the vertical boundary layers appeared wavy, indicating the possible onset of instability or transition to turbulence. Nansteel and Greif (1981) (for $A_L = 1/2$, water, $\text{Ra} = 10^{10}$) observed only laminar vertical boundary layers and no secondary horizontal flows. Anderson et al. (1985) tested water in a cubical enclosure at Ra about 10^{10} with a heated floor in addition to hot and cold vertical walls. A horizontal flow pattern similar to that seen by Bejan et al. (1981) was observed along the floor (flow moving from the cold to hot wall closest to the floor, and returning to the cold wall directly above the floor layer). A secondary pattern was not observed along the ceiling, which was adiabatic. In all of these cases, an experiment at full scale with air was not performed to confirm the appropriateness of the scale model for simulating air circulation in rooms.

Turbulent vertical boundary layer flow has been reported in high aspect ratio enclosures by Cowan et al. (1982) (water, $A_L = 1.5$–61), Cheesewright and Zial (1986) (air, $A_L = 6$), Elder (1965) (water, $A_L = 10$–30), and Giel and Schmidt (1986). With a narrow slot, the vertical boundary layers can interact strongly with the core region, producing turbulent motions in the core in addition to the turbulent vertical boundary layers. The aspect ratios are much higher than those expected for building enclosures; hence the results can not be taken as conclusive that turbulence will occur in buildings.

For enclosures with partitions, some experimental work has used refrigerant 12 and 114 gases, which match the geometry, Ra, and Pr of air and match the radiation parameters more closely than does water ($H_o \sim 7$ and k_r is 5 to 10). Weber and Kearney (1980), among others, have conducted scale model experiments with doorway-type partitions using refrigerant 12, measuring heat transfer between the zones of the enclosure and temperature distributions. Flow visualization was not done.

Partition studies using water most closely resemble the geometry of the present study. Nansteel and Greif (1981) ($A_L = 0.5$, $\text{Ra} = 10^{10}$, $\text{Pr} = 3.5$) tested a configuration with opposing hot and cold end walls, and with the partition extending down from the ceiling to various depths. Lin and Bejan (1983) ($A_L = 0.5$, $\text{Ra} = 10^9$–10^{10}, $\text{Pr} = 7$) tested a configuration with water in which the partition rested on the floor and extended up to various heights. In both water experiments, the vertical boundary layers were laminar. In the case of Nansteel and Greif (1981), the flow rises up the hot wall and breaks away from the hot wall at the depth of the partition, flowing horizontally toward the partition. Once past the partition the flow rises to the ceiling, flows to the cold wall, down the cold wall, and returns along the floor to the hot wall.

In summary, the past scale model studies for both empty and partitioned enclosures have not been conducted with all the relevant scaling parameters matching those of real building enclosures. With the parameters deviating from the values in buildings, it has not been shown whether the model results properly scale to the full scale. This work will directly compare a physical scale model using R114 gas to a full-scale room in terms of flow patterns, temperature distributions, and heat transfer to determine the accuracy of the scaling method.

Experimental Apparatus

Two experimental facilities were used in the investigation and are described below. One was an actual full-scale room, and the other was the small-scale model of it. Table 1 lists the relative values of the scaling parameters for air, R114, and typical water models.

Full-Scale Room. The air-filled reference facility was a rectangular room 2.5 m high, 3.9 m wide, and 7.9 m long

Nomenclature

a = mean radiation absorption coefficient
A_L = height-to-length aspect ratio = H/L
A_W = height-to-width aspect ratio = H/W
F = view factor from ceiling to all vertical walls plus floor
g = acceleration of gravity
H = height of enclosure
H_o = optical depth
H_p = height of partition
k = thermal conductivity
k_p = partition thermal conductivity
k^* = partition conductance = $k_p H_p/(k t_p \text{Nu})$
k_r = ceiling/floor radiation to wall convection = $4\sigma T_m^3 LF/(k\text{Nu})$
L = length of enclosure
Nu = Nusselt number = $Q/[Wk(T_H - T_C)]$
Pr = Prandt number = ν/α
Q = vertical wall heat transfer
Ra = Rayleigh number = $g\beta(T_H - T_C)H^3/\nu\alpha$
T = temperature
T_C = cold wall temperature
T_H = hot wall temperature
T_m = mean enclosure temperature = $(T_H + T_C)/2$
t_p = thickness of partition
U = horizontal velocity
V = vertical velocity
V_c = characteristic velocity = $[g\beta(T_H - T_m)H]^{1/2}$ = $[g\beta(T_m - T_C)H]^{1/2}$
W = width of enclosure
X = horizontal coordinate
Z = vertical coordinate
α = thermal diffusivity
β = coefficient of thermal expansion
ϵ = emissivity
θ = dimensionless temperature = $(T - T_C)/(T_H - T_C)$
ν = kinematic viscosity
σ = Stefan-Boltzmann constant

Table 1 Comparison of scaling parameter values between full-scale air enclosure, scale model R114 enclosure, and typical water enclosures

Dimension or scaling parameter	Actual enclosure values Air	R114	Typical values,* water
Height, H, m	2.5	0.47	0.3
Rayleigh number, Ra	$2.0\text{–}3.1\times10^{10}$	$1.3\text{–}3.4\times10^{10}$	$\sim10^{10}$
Prandtl number, Pr	0.7	0.8	3.5–7
Aspects ratios			
Height/length, A_L	0.32	0.35	0.1–10
Height/length, A_W	0.64	0.69	0.1–10
Partition conductance, k^*	0.4	0.3	0.01–25
Optical depth, H_o	0–0.25	6.5	$>>>1$
Ceiling-floor radiation to wall convection, k_r	20	10	0.03

*Nansteel and Greif (1981), Bohn et al. (1984), Anderson et al. (1985)

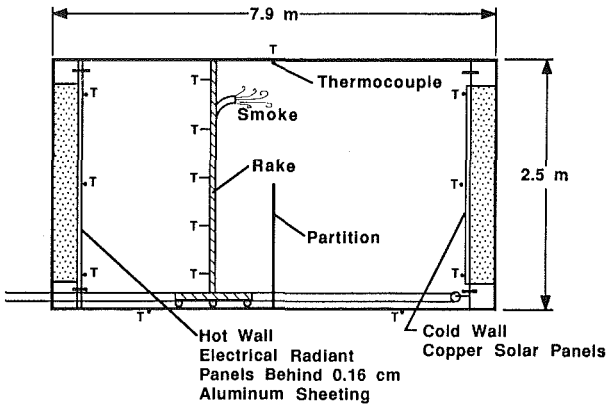

Fig. 2 Side view of full-scale air facility

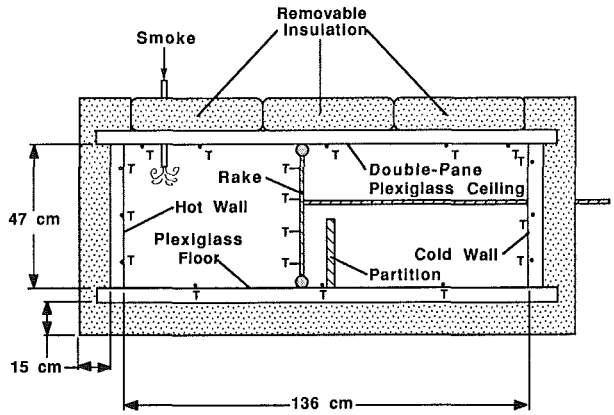

Fig. 3 Side view of small-scale R114 experimental apparatus

(Ferm, 1985); thus A_L is 0.32 and A_W is 0.64 (see Fig. 2). The effective insulating values of the floor, walls, and ceiling were R3.0, R2.8, and R11.5 (m^2-°C/W). The inner-facing surfaces of the floor, ceiling, and side walls were, respectively; black roofing paper, polyurethane foam, and fiberglass board ($\epsilon\sim1$ for all). Electric radiant heating panels were mounted on the inner wall surface of one 3.9-m-wide wall, with 1.6-mm-thick aluminum sheeting attached to the heating panels to provide an isothermal, reflective surface ($\epsilon=0.05$). The opposing 3.9-m-wide end wall was cooled by copper solar collector panels, also mounted on the inner surface ($\epsilon=0.12$). Chilled water was pumped from a storage reservoir through the collector panels. The heater power dissipation was measured for the hot wall heat transfer, and the cold wall water enthalpy rise was measured for the cold wall heat transfer. Conduction and radiation losses were estimated at 30 percent. The temperatures of the end walls were constant to within ±1°C. The partition was constructed from 2.5-cm-thick, aluminum foil-faced polyurethane insulation panel, k^* of 0.4. It extended from the floor halfway to the ceiling, and was placed midway between the hot and cold walls.

The temperatures of the air in the full-scale room were measured with a vertical array of 0.5-mm-dia type-T thermocouples mounted on a movable post. The post was located midway between the two side walls and could be moved from the hot to the cold wall from outside the room. Temperatures were also measured in the hot and cold wall boundary layers at the midplane between the side walls. Radiation errors to the temperature probes were estimated as 1.6 percent of T_H-T_C or less than 0.3°C. For flow visualization, wood smoke was generated outside the facility, cooled and filtered, and injected into the room. The smoke was illuminated by a plane of light generated by a slide projector. A black and white video system using a low-light-level camera was used to record the smoke motions. Small windows in the side walls, 30 cm by 60 cm, permitted recording with the camera and viewing the flow patterns.

Physical Scale Model. The ratio of the scale model to the full scale was 1:5.5. Refrigerant gas R114 was chosen because of its high density, low cost, low toxicity, and 3.3°C boiling point at 1 atm. The inner dimensions of the scale model were 47 cm high, 68 cm wide, and 136 cm long, making $A_L=0.35$ and $A_W=0.69$ (Fig. 3). Each vertical wall consisted of three vertical sections of 0.6-cm-thick aluminum plates ($\epsilon=0.05$). Foil-faced polyurethane strips insulated the wall sections and the assembled wall from the floor and ceiling, eliminating direct conduction from the ceiling to the floor. Electric resistance strip heaters were attached to the back side of one end wall to generate a hot wall. Copper cooling tubes were soldered to the back side of the opposing end wall to form a cold wall. Water was circulated from a refrigerated reservoir through the tubes to cool the wall. End wall temperatures were constant to ±0.5°C. Cooling and heating flux to the vertical walls was measured in the same manner as for the full-scale room, with conduction and radiation losses at 10 percent. The ceiling was a double-pane plexiglass window with a 2.5-cm-thick gap between the panes ($\epsilon\sim1$). The floor was also made of plexiglass ($\epsilon\sim1$). The walls, ceiling, and floor were surrounded with 15 cm of rigid polyurethane boards (R7.5 m^2-°C/W). The partition was made of a 1.6-cm-thick polyurethane insulation panel, so that k^* equaled 0.3.

Wall surface temperatures were measured with 0.25-mm-dia type T thermocouples mounted in small holes embedded in the aluminum. Temperatures in the interior were measured with a movable rake of 25 thermocouples (type T, 0.08-mm-dia) that could be moved horizontally from end wall to end wall. Another thermocouple probe was mounted on the end of a 1.2-cm tube, which penetrated the test cell through the ceiling and could be traversed vertically. End-wall boundary layer

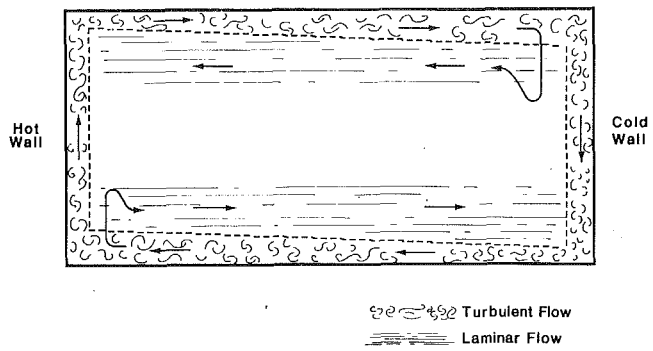

Fig. 4 Flow pattern in the empty enclosure for the small-scale model and the full-scale room

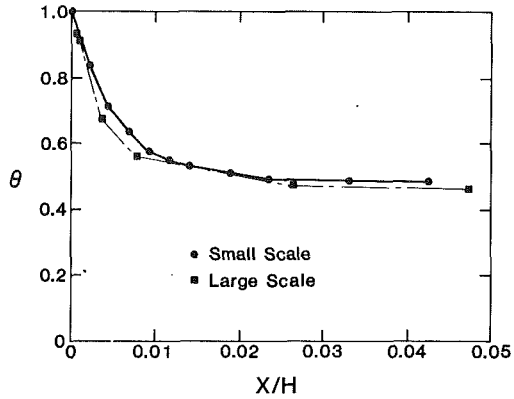

Fig. 5 Comparison of small-scale and full-scale hot wall boundary layer temperatures at $Z/H = 0.5$. Full scale: $Ra = 3.1 \times 10^{10}$, $T_H = 29.3°C$, $T_C = 10.9°C$; small scale: $Ra = 3.4 \times 10^{10}$, $T_H = 36.1°C$, $T_C = 6.1°C$.

temperatures were measured at midheight with probes that could be traversed across the boundary layer (but not vertically). The hot wall probe was mounted on a fork assembly, which eliminated conduction errors, and was made of 0.025-mm-dia type T thermocouple wire, bead size approximately 0.075 mm. The frequency response of this probe was about 10 Hz. The opposing cold end wall boundary layer temperature was measured with a thermocouple of bead size 0.25 mm mounted on a similar fork assembly attached to the interior rake. Radiation errors to the probes were estimated as 0.6 percent of $T_H - T_C$, or less than 0.2°C.

Flow motions in the scale model were made visible by injecting ammonium chloride (NH_3Cl) into the enclosure and illuminating the smoke with a planar light source. The smoke was generated (Kotrappa and Bhanti, 1967) by passing R114 gas into a 250-ml jar of concentrated HCl, then into a 250-ml jar of concentrated ammonia where the smoke was produced. The smoke-laden R114 gas was then discharged into the enclosure with neutral buoyancy. Illumination and videorecording of the flow motions was done through the ceiling after removing the top pieces of insulation.

Experimental Procedure. Experiments with the enclosure empty were conducted first on the full-scale room and the small-scale model, then the partition was added to both facilities. The averages of the hot and cold wall temperatures were held as close as possible to the ambient temperature in the surrounding room (±1-2°C). Steady-state conditions were achieved after about 10–12 h of maintaining constant hot and cold wall temperatures. Temperatures were measured of the gas in the core and next to the vertical walls, and heat flux at the hot and cold walls was measured. Smoke was then injected into the enclosures, and the flow motions were recorded on videotape. In order to generate a flow condition with Ra of 2×10^{10}, the temperature difference between the hot and cold walls was approximately 12°C and 20°C for the full-scale and scale model, respectively. At that setting, about 200 W of heat was transferred by natural convection in the full scale, and 20 W was exchanged in the scale model.

Experimental Results–Empty Enclosure

Empty enclosure experiments were performed over a range of Rayleigh numbers, from 1.3×10^{10} to 3.4×10^{10} for the scale model and 2.0×10^{10} to 3.1×10^{10} for the full-scale room. The range in Ra was generated by changing the temperature difference between the hot and cold walls.

Flow Patterns. The flow pattern of an empty enclosure is shown schematically in Fig. 4, and was qualitatively identical in the full-scale room and the scale model. Thicknesses of flow layers are drawn approximately to scale. The main characteristics of the flow were turbulent boundary layers on the vertical hot and cold walls, and two horizontal flow loops, one near the ceiling and one near the floor. No motion was detectable in the central core, extending from about 40 and 60 percent of the enclosure height.

The vertical boundary layer width was about 2–5 percent of the enclosure height, estimated visually by locating the edge of the turbulence. Eddies on the order of the boundary layer width were easily discernable, and appeared random. There was no regular waviness to the flow, which would have indicated laminar instability or transition instead of full turbulence. An approximate vertical boundary layer velocity for the small scale was 15 cm/s; it was about 30 cm/s for the full scale. When normalized to a characteristic buoyant velocity $V_c = [g\beta(T_H - T_m)H]^{1/2}$, the velocities are both about 0.4 to within experimental uncertainty (±40 percent).

Once the hot boundary layer reached the ceiling, it turned the corner and flowed along the ceiling toward the cold wall, increasing in thickness and slowing down with distance, looking very much like a wall jet. This primary ceiling jet was noticeably thicker than the vertical boundary layers. Upon reaching the top of the cold wall, part of the flow reversed direction and formed a secondary flow, proceeding all the way back to the hot wall directly beneath the ceiling jet. The flow that formed the reverse layer surged part way down the cold wall, to a Z/H depth of 0.6–0.7, before turning up to form the reverse layer. Entrainment of some of the flow into the cold wall boundary layer was visible. This horizontal flow loop was contained within the top half of the core; the primary jet thickness when it reached the cold wall was 10–20 percent of the enclosure height. A similar two-layer strucutre occurred near the floor with a primary flow and reverse secondary flow, driven by the cold wall boundary layer.

The velocities of the full-scale room and scale model in the horizontal layers also agreed to within experimental uncertainty when scaled to a buoyant velocity. At X/L of 0.8 in the primary ceiling layer, U/V_c was 0.08. A large eddy structure was also noticeable in the primary horizontal jets closest to the ceiling and floor. Based on the jet thickness and velocity estimated from the flow motions, the Reynolds numbers were on the order of 1000, above the limit for laminar flow for an isolated jet (10–30, according to Bejan, 1984). The secondary flows appeared laminar. The internal Froude number of the primary jet, based on the peak temperature of the jet minus the temperature at the jet boundary and the jet velocity and thickness, was greater than 1 but less than 10. This would indicate that the jet was driven by its initial momentum rather than by gravity, but buoyancy may be important in damping the turbulence and affecting the jet growth with distance.

The reason a secondary flow forms is believed to be the following. The momentum-driven horizontal jet entrains fluid as it flows along the ceiling. When it reaches the cold wall, the

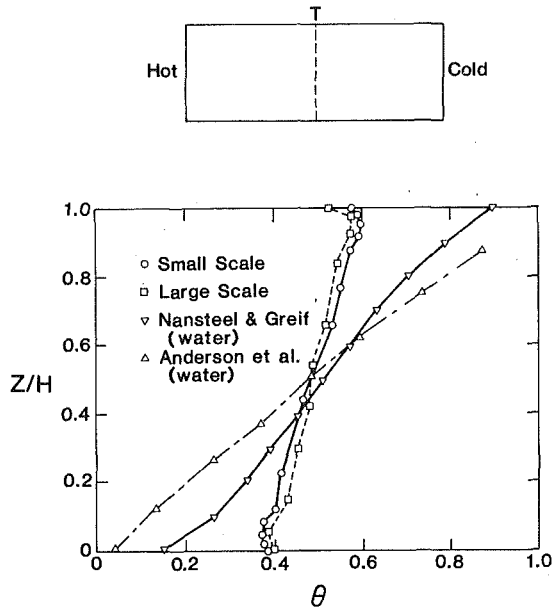

Fig. 6 Comparison of core vertical temperature profiles at $X/L = 0.5$ in the empty enclosure for small-scale, full-scale, and water experiments. Small scale: $Ra = 2.2 \times 10^{10}$, $T_H = 34.1°C$, $T_C = 13.6°C$; full scale: $Ra = 2.6 \times 10^{10}$, $T_H = 35.3°C$, $T_C = 19.9°C$.

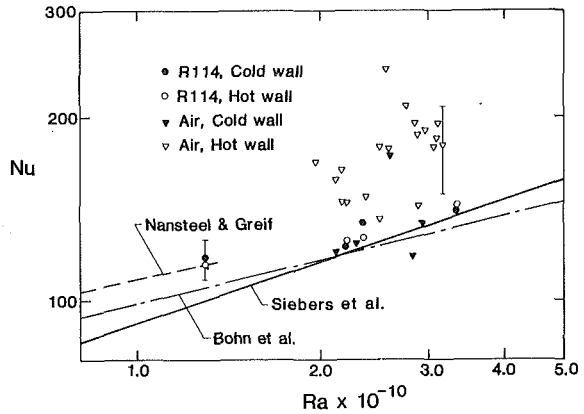

Fig. 7 Comparison of empty enclosure heat transfer of this work with past water studies and an isolated turbulent vertical wall

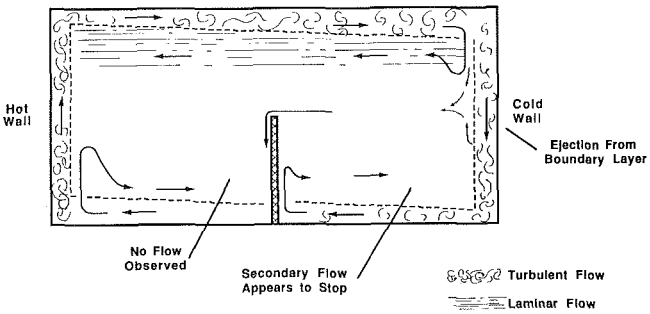

Fig. 8 Flow pattern with a partition on the floor for the small scale

mass flow is too great for the jet to be entrained entirely into the cold wall boundary layer. After turning downward, the outer portion of the jet loses little if any heat to the cold wall. The outer jet loses momentum as it flows down the wall due to the upward buoyant force; this buoyant force is present since the jet is hotter than the core. When the vertical momentum is zero, the flow reverses direction and is accelerated upward by the buoyant force. As it flows back to the hot wall, it serves as a source of entrainment for the primary jet and for the upper regions of the hot wall boundary layer.

The flow patterns in the full-scale air and scale model R114 tests at Ra of 10^{10} can be compared with the results in water experiments. Secondary flows of this type were not observed in the $A_L = 1/2$–1 experiments with vertical heated and cooled walls and an adiabatic ceiling and floor (Bohn et al., 1984; Nansteel and Greif, 1981). The secondary flow was seen in a very low aspect ratio enclosure (Bejan et al., 1981). The secondary flow was also seen at an aspect ratio of 1, along the floor only, when the floor was heated along with a vertical wall (Anderson et al., 1985). This suggests the floor and ceiling boundary conditions may affect the internal core flow pattern. In the full-scale air and small-scale R114 tests reported in the present work, radiation heat exchange between the ceiling and floor likely adds heat to the floor layer in the same manner as does external addition of heat in the experiment of Anderson et al. (1985). In all the water experiments, the horizontal flows were laminar, and the vertical boundary layers were laminar or at most of the verge of transition (Bohn et al., 1984).

Temperature Distributions. Dimensionless temperatures in the hot wall boundary layer for the full-scale room with air and the R114 scale model at Ra about 3×10^{10} are compared in Fig. 5. Measurements were made halfway between the floor and ceiling ($Z/H = 0.5$) and midway between the adiabatic side walls. The agreement in boundary layer temperature profiles was quite good. The major temperature decrease occurred for $X/H < 0.01$, which physically is 0.5 cm for the scale model and 2.5 cm for the full-scale room. Large temperature fluctuations of the order 20–30 percent of $T_H - T_m$ were observed in the small-scale vertical wall boundary layers, which also confirms their turbulent nature.

Away from the boundary layers on the hot and cold vertical walls, the core temperatures were nearly constant at fixed elevation, and decreased approximately linearly vertically from the ceiling to the floor. The vertical temperature profile is shown in Fig. 6 at a location halfway between the hot and cold walls. The vertical position is on the vertical axis. The agreement between the scale model ($Ra = 2.2 \times 10^{10}$) and the full-scale results ($Ra = 2.6 \times 10^{10}$) was quite good. Shown for comparison are results from two water experiments: Nansteel and Greif (1981) ($Ra = 0.8 \times 10^{10}$, $A_L = 0.5$), and Anderson et al. (1985) ($Ra \sim 10^{10}$, $A_L = 1.0$). In both cases the water experiments showed much larger temperature stratification than the two gas experiments.

It is hypothesized that radiation exchange between the ceiling and floor for the gas experiments may explain the lower levels of stratification when compared to the water experiments, for which radiation heat exchange was absent. Heat from the ceiling jet should be transferred by convection to the ceiling, transferred by thermal radiation from the ceiling to the floor, and then by convection from the floor to the floor jet. With gas emission, it could also be radiated directly from the ceiling jet to the core and floor jet. This vertical transfer within the core would lower temperatures near the ceiling and increase temperatures near the floor, reducing stratification. Based on measured ceiling and floor temperatures and ignoring gas emission or attenuation, the amount of the vertical wall heat flow estimated to be radiated from the ceiling to the floor was 77 percent for the R114 scale model and 62 percent for the air large scale.

Heat Transfer. Heat transfer measurements for the scale model and full-scale room are presented as Nusselt number as a function of Rayleigh number in Fig. 7 for both the hot and cold walls. Also shown are correlations from Bohn et al. (1984), $Nu = 0.31 Ra^{1/4}$, and Nansteel and Greif (1981), $Nu = 0.60 Ra^{0.226}$ for enclosure flows, and from Siebers et al. (1985) for an isolated vertical wall turbulent boundary layer,

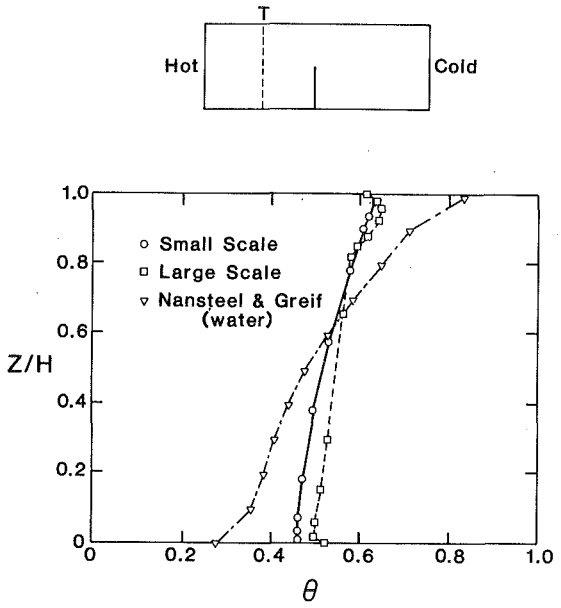

Fig. 9 Comparison of core vertical temperature profiles at $X/L = 0.25$ for the floor partition in the small scale ($Ra = 2.5 \times 10^{10}$, $T_H = 30.9°C$, $T_C = 10.4°C$), full scale ($Ra = 3.3 \times 10^{10}$, $T_H = 38.1°C$, $T_C = 18.4°C$), and water experiments (Nansteel and Greif, $Ra = 0.8 \times 10^{10}$)

$Nu = 0.050Ra^{1/3}$. Nu and Ra are based on the temperature difference between the hot and cold walls (for Siebers et al., Nu and Ra are based on twice the wall-to-ambient temperature difference for an equivalent comparison to the other data). The experimental uncertainty is shown by the vertical line, approximately 10 percent for the scale model and 30 percent for the full scale. The scale model hot and cold wall and the full-scale cold wall heat transfer data agreed well, and show the expected trend of the increasing Nu with increasing Ra. The full-scale hot wall data appeared to be systematically higher than the other data, although not much beyond the uncertainty band.

Experimental Results—Enclosures With Partitions

Two enclosure configurations with the partition were studied on both the full-scale room and the small scale R114 model. These were: (1) *Floor Partition.* The partition was placed midway between the hot and cold walls, extending across the width of the enclosure and from the floor to midheight ($Z/H = 0.5$). (2) *Raised Partition.* The partition was placed in the same location, but was raised so that the bottom edge was at Z/H of 0.12, and the top edge location was 0.62. In the small scale, experiments were conducted over a range of Rayleigh numbers from 1.1×10^{10} to 3.6×10^{10} for the floor partition, and at a single Rayleigh number ($Ra = 2.4 \times 10^{10}$) for the raised partition. Experiments were conducted at a single Rayleigh number for the full scale.

Flow Patterns With a Floor Partition. Figure 8 shows the flow pattern observed with the partition resting on the floor for the small scale, which was qualitatively the same as that observed in the full scale. The turbulent vertical boundary layer flow and the horizontal flow loop along the ceiling were very similar to the flow pattern in the empty enclosure; however, the flow pattern along the floor was quite different. Along the floor, the partition blocked the floor jet, causing it to climb about halfway up the partition (to $Z/H \sim 0.25$) before reversing back to the cold wall.

At an elevation of $Z/H = 0.5$, a laminar layer of fluid flowed horizontally from near the cold wall toward the partition, spilled over the partition like a waterfall, and fell vertically downward to the floor on the hot wall side of the partition. The velocity of this layer was about 1–2 cm/s in the small scale, comparable to velocities in the ceiling secondary flow, and was on the order of 1–4 cm thick. It appeared to be formed by fluid ejected from the boundary layer at elevation $Z/H = 0.5$. After the flow spilled over the partition and to the floor, it moved from the partition toward the hot wall. This floor flow surged up the hot wall in a fashion similar to what occurred in the empty enclosure, then fell down and formed a return layer heading back to the partition.

This flow pattern can be compared to the patterns obtained in water by Nansteel and Greif (1981), which were described earlier, with a partition extending from the ceiling downward to a range of depths ($A_L = 0.5$, $Ra \sim 10^{10}$). Partitions conductances of k^* about 25 (conducting) and k^* about 0.01 (adiabatic) were tested (recall $k^* = 0.3$ for the R114 model, and $k^* = 0.4$ for the full scale). Assuming symmetry, the floor flow in the water experiment should be comparable with the ceiling flow in the present work, and the ceiling flow for the water experiment should be comparable to the floor flow in the present work. The vertical boundary layers were laminar or in transition for water, while they were turbulent for R114 and air. A horizontal reverse flow in the region unimpeded by the partition (along the floor for the water experiment) was not reported, while it was clearly present along the ceiling for air and R114. In the water experiment, nearly all the hot boundary layer broke off to flow toward the partition, whereas in the present work, the boundary layer was observed to continue along the vertical wall.

Core Temperatures With a Floor Partition. Figure 9 compares core temperatures on the hot side of the floor partition configuration for the dense gas small scale ($Ra = 2.5 \times 10^{10}$), the air large scale ($Ra = 3.3 \times 10^{10}$), and the water model of Nansteel and Greif (1981) ($Ra = 0.8 \times 10^{10}$, $k^* = 0.01$). Temperature profiles were taken midway between the wall and the partition, at $X/L \sim 0.25$. Since the water model had a partition extending from the ceiling, symmetry has been assumed in the temperature distribution, and their profiles have been inverted for comparison. The agreement in temperatures between the small and large scale was good. The water experiment temperatures were much warmer in the top half of the core and significantly cooler in the lower half of the core. Absence of radiation exchange between the ceiling and floor in the water model is a possible explanation for the larger stratification.

Figure 10 compares core temperatures on the cold wall side of the floor partition (X/L of 0.75) for the large scale ($Ra = 2.8 \times 10^{10}$), small scale with R114 ($Ra = 2.5 \times 10^{10}$), and water model of Nansteel and Greif (1981) ($Ra = 0.8 \times 10^{10}$). The agreement between the small and large scale was again quite good, while the water temperatures were much colder in the lower part of the core and warmer in the upper part of the core than the temperatures for the gas experiments.

For the air and R114 experiments, the temperature profiles in the top half of the enclosure were identical to those with no partition. The partition had no effect on the temperatures in the top half of the enclosure because the flow pattern was unaffected by the presence of the partition. However, in the lower half of the enclosure, the floor partition caused a temperature difference across the partition, due to the cold floor jet being blocked by the partition.

Flow Patterns With a Raised Partition. The flow pattern observed on the small scale with a raised partition is shown in Fig. 11. As in the empty enclosure and the floor partition experiments, the vertical boundary layers were turbulent and the horizontal flow loop along the ceiling was unaffected by the partition. The flow along the floor resembled the empty enclosure pattern, and was quite different from the floor flow

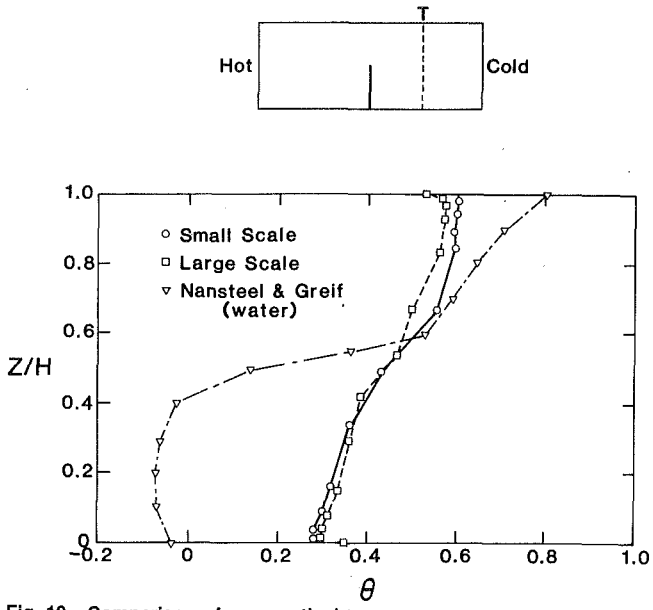

Fig. 10 Comparison of core vertical temperature profiles at $X/L = 0.75$ for the floor partition in the small scale ($Ra = 2.5 \times 10^{10}$, $T_H = 30.9°C$, $T_C = 10.4°C$), full scale ($Ra = 2.8 \times 10^{10}$, $T_H = 38.5°C$, $T_C = 21.7°C$), and water experiments (Nansteel and Greif, $Ra = 0.8 \times 10^{10}$)

pattern observed with the partition directly on the floor. The gap below the partition was approximately the thickness of the floor jet, hence it passed beneath the partition with little change in thickness or velocity. The primary effect of the partition of the flow pattern was to block the secondary flow along the floor, preventing it from returning back to the cold wall. On the cold side of the partition, a small amount of the primary floor jet was blocked by the partition, forming a return layer that was not observed close to the cold wall.

Experiments on the full-scale enclosure with a raised partition revealed flow patterns very similar to those of the small scale. Similar features were turbulent vertical boundary layers, a horizontal flow loop near the ceiling, and the floor jet which passed underneath the partition. Similar experiments using water were not found in the literature.

Core Temperatures With a Raised Partition. Core temperature profiles for the small and large-scale models when the partition was raised were in good agreement. These profiles were nearly identical to those in the empty enclosure, due to the similarity in flow pattern between the two configurations.

Heat Transfer With Partitions. A compilation of heat transfer results for the small-scale hot wall and cold wall, including the empty enclosure, the raised partition, and the floor partition, is shown in Fig. 12. Data are plotted as Nu versus Ra. Also shown are two correlations representing the best fit of the water data from Nansteel and Greif (1981), one for the conducting partition, $k^* = 25$ ($Nu = 0.501 Ra^{0.226}$) and the other for the adiabatic partition, $k^* = 0.01$ ($Nu = 0.439 Ra^{0.226}$). A raised partition for the small scale did not reduce the heat transfer from the empty enclosure value, which is consistent with the temperature data and flow patterns. When the partition extended to the floor and blocked the floor jet, the heat transfer was reduced by 10–15 percent below the empty enclosure values. The R114 scale model floor partition data agree fairly well with the conducting partition correlation of Nansteel and Greif (1981). Full-scale heat transfer in the partition tests agreed with the empty enclosure to within the experimental uncertainty, which was 30 percent. If a similar 10–15 percent reduction in heat transfer were present in the large scale due to the partition, it would not be apparent from the measurements due to the uncertainty.

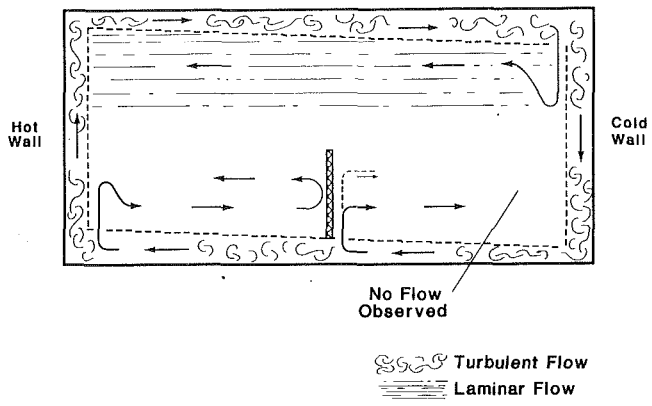

Fig. 11 Flow pattern with a partition raised off the floor for the small scale

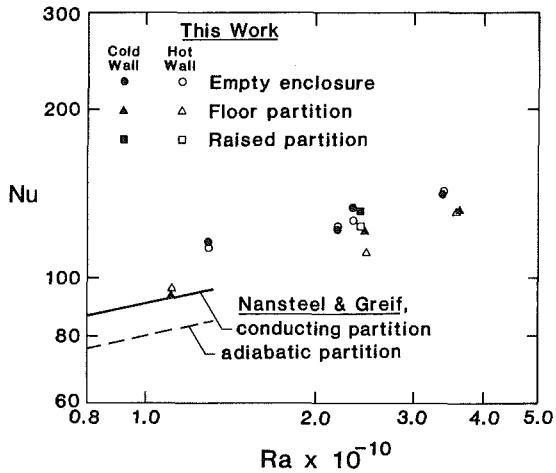

Fig. 12 Comparison of heat transfer data for all R114 small-scale experiments (empty enclosure, floor partition, and raised partition) with a ceiling partition in water (Nansteel and Greif)

Conclusions

In this paper we attempted to show that the natural convection that occurs in a building enclosure due to differentially heated and cooled vertical walls can be simulated accurately in a 1:5.5 scale model containing R114 gas. This method involves matching the geometry, Ra, and Pr of the full-sized enclosure, but neglecting to perfectly match the radiation absorption or ratio of convection to radiation conductance. Empty enclosures and enclosures with vertical partitions extending partway across the interior were tested on a full-sized room and on the reduced scale model. Because of the agreement in flow patterns, temperatures, and heat transfer, we conclude that an R114 scale model can be used confidently to study and simulate natural convection flows in buildings. Although the radiation is not perfectly scaled, it is similar enough not to alter the results between the air and R114 models.

The major flow features of the empty enclosure were turbulent boundary layers on the vertical walls, and horizontal recirculating cells in the core. The use of partitions that extend from midheight to the floor caused only a modest decrease in hot-to-cold wall heat transfer, but they changed the circulation patterns and core temperature substantially.

In comparing results of this work with previous studies using water as the scaling fluid, significant differences were found both in temperature profiles and flow patterns. Water experiments at the same geometry and Ra tend to have higher thermal stratification, reduced flow recirculation, and laminar flow in regions where turbulence is found on the full scale. It has been speculated that the absence of radiation in the water

experiments may contribute to the different flow patterns and thermal stratification.

References

Anderson, R. S., Fisher, E. M., and Bohn, M. S., 1985, "Thermal Stratification in Direct Gain Passive Heating Systems With Variable Heating of the Floor and One Vertical Wall," *Proceedings of the 10th National Passive Solar Energy Conference*, pp. 82–87.

Bejan, A., 1984, *Convection Heat Transfer*, Wiley, New York.

Bejan, A., Al-Homoud, A. A., and Imberger, J., 1981, "Experimental Study of High-Rayleigh-Number Convection in a Horizontal Cavity With Different End Temperatures," *Journal of Fluid Mechanics*, Vol. 109, pp. 283–299.

Bohn, M. S., Kirkpatrick, A. T., and Olson, D. A., 1984, "Experimental Study of Three Dimensional Laminar Convection at High Rayleigh Number," ASME JOURNAL OF HEAT TRANSFER, Vol. 106, pp. 339–345.

Cheesewright, R., and Zial, S., 1986, "Distributions of Temperature and Local Heat-Transfer Rate in Turbulent Natural Convection in a Large Rectangular Cavity," *Proceedings of the 8th International Heat Transfer Conference*, Vol. 4, pp. 1465–1470.

Cowan, G. H., Lovegrove, P. C., and Quarini, G. L,. 1982, "Turbulent Natural Convection Heat Transfer in Vertical Single Water-Filled Cavities," *Proceedings of the 7th International Heat Transfer Conference*, pp. 195–203.

Elder, J. W., 1965, "Turbulent Free Convection in a Vertical Slot," *Journal of Fluid Mechanics*, Vol. 23, Part 1, pp. 99–111.

Ferm, H. M., 1985, "Measurements and Analysis of Natural Convection in Building Enclosures," S. M. Thesis, Massachusetts Institute of Technology, Cambridge, MA.

Kotrappa, P., and Bhanti, D. P., 1967, "Smoke Puff Generator for Room Air Movement Studies," *American Industrial Hygiene Association Journal*, March–April, pp. 171–174.

Lin, N. N., and Bejan, A., 1983, "Natural Convection in a Partially Divided Enclosure," *Int. J. Heat Mass Transfer*, Vol. 26, No. 12, pp. 1867–1878.

Nansteel, M. W., and Greif, R., 1981, "Natural Convection in Undivided and Partially Divided Rectangular Enclosures," ASME JOURNAL OF HEAT TRANSFER, Vol. 103, pp. 623–629.

Olson, D. A., 1986, "Scale Model Studies of Natural Convection in Enclosures at High Rayleigh Number," Ph.D. Thesis, Massachusetts Institute of Technology, Cambridge, MA.

Siebers, D. L., Moffat, R. F., and Schwindt, R. G., 1985, "Experimental Variable Properties Natural Convection From a Large, Vertical, Flat Surface," ASME JOURNAL OF HEAT TRANSFER, Vol. 107, pp. 124–132.

Simpson, D., and Plyler, E. K., 1953, "Infrared Spectra of Pentachlorofluoroethane, 1,2-Dichlorotetrafluoroethane, and 1-Bromo-2-fluoroethane," *Journal of Research of the National Bureau of Standards*, Vol. 50, No. 5, pp. 223–225.

Weber, D. D., and Kearney, R. J., 1980, "Natural Convective Heat Transfer Through an Aperture in Passive Solar Heated Buildings," LA-UR-80-2328.

Investigation of Natural Convection in Partially Divided Rectangular Enclosures Both With and Without an Opening in the Partition Plate: Measurement Results

K. S. Chen
Professor.

A. C. Ku
Professor.

C. H. Chou
Graduate Student.

Department of Mechanical Engineering,
National Sun Yat-Sen University,
Kaoshiung, Taiwan

Experimental results are presented for steady natural convection in a two-dimensional, partially divided, rectangular enclosure, in which two of the vertical walls were maintained at different uniform temperatures and the top and bottom walls were insulated. The partition plate was adiabatic, and the experiment was carried out both with and without an opening in the partition. Rayleigh numbers ranging from 10^6 to 10^8 and opening ratios of 0, 1/8, and 1/4 were investigated for an enclosure aspect ratio (length/height) of 2 and Prandtl number of 7 (for water). Local velocity and temperature measurements were made with a laser-Doppler velocimeter and thermocouple probes. Flow visualization using colored dye was also performed. Results show that there was a recirculation zone in the upper and left quadrant of the enclosure when there was no opening in the partition plate. With an opening in the partition, the recirculation zone was absent and the heat transfer rate increased. An unopened partial obstruction would reduce the heat transfer rate by an amount of 12 to 30 percent depending on the Rayleigh number. However, the opening seems to have little effect on the velocity and temperature profiles of the left-moving fluid on the bottom wall. A correlation of the Nusselt number is derived, which shows that the heat transfer rate increases as the Rayleigh number or opening ratio increases.

1 Introduction

Thermally driven convective motion in enclosures with differentially heated vertical walls occurs in numerous situations and has attracted the attention of scientists and engineers of various disciplines. Depending on the magnitude of the geometric and dynamic parameters, applications can include heat transfer across thermopane windows, solar collectors, fire spread and energy transfer in rooms and buildings, cooling of nuclear reactors, and the growth of single crystals from crucible melts; see Ostrach (1972), Catton (1978), and Simpkins and Chen (1985).

In many circumstances, a partial obstruction extending downward from the ceiling or upward from the floor is also important. This geometry corresponds to a printed circuit board in an electronic cabinet, or a ceiling beam in a room, and has received attention recently; see Emery (1969), Bauman et al. (1980), Bajorek and Lloyd (1982), Chang et al. (1982), Nansteel and Greif (1981, 1984), Lin and Bejan (1984), Jetli et al. (1986), Shaw et al. (1987), and Zimmerman and Acharya (1987). These works have demonstrated that heat transfer between two heated side walls is reduced when a partial partition is present. Flow visualization by Nansteel and Greif (1981, 1984) shows that a weak recirculation zone in the upper quadrant near the hot wall is responsible for reducing the heat transfer across the enclosure. This suggests that if a slot or an opening is located in the partition plate, the recirculation zone may disappear and the heat transfer may increase.

In this study, results are presented of an experimental investigation on how an opening in the partition in a two-dimensional rectangular enclosure (Fig. 1) affects the natural convection heat transfer. The experiment was carried out in an enclosure with an aspect ratio of $A = L/H = 2$, and a partition ratio of $A_p = h/H = 1/2$, with isothermal vertical side walls and an insulated floor and ceiling. The opening is in the middle of the partition and has opening ratios of $A_o = s/h = 0$, 1/8, and 1/4. Water was used as the working fluid for Rayleigh numbers ranging from 10^6 to 10^8. Velocity and temperature profiles of the fluid in the enclosures at various vertical planes were measured with a laser-Doppler velocimeter and thermocouple probes, from which heat transfer between the vertical side walls was derived. The basic flow structure was observed by using dye-injection flow visualization.

It is noted that in this range of aspect ratio and Rayleigh number, results without an opening in the partition ($A_o = 0$) are also new. The power law correlation was obtained giving the dependence of the Nusselt number on the opening ratio and Rayleigh number. Extrapolation of the correlation equation for $A_o = 0$ compares fairly well with the data obtained by Nansteel and Greif (1981).

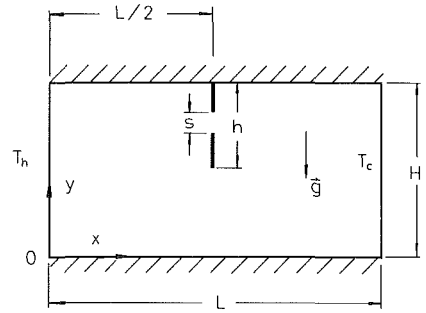

Fig. 1 Partially divided enclosure with an opening in the partition plate

Contributed by the Heat Transfer Division for publication in the JOURNAL OF HEAT TRANSFER. Manuscript received by the Heat Transfer Division October 27, 1988; revision received October 12, 1989. Keywords: Natural Convection.

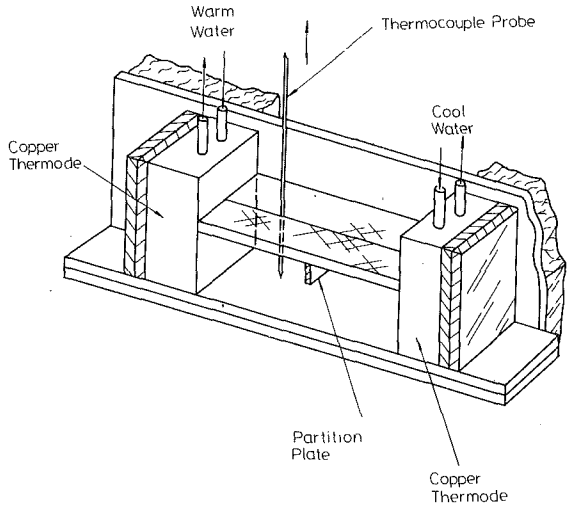

Fig. 2 Schematic of the test apparatus

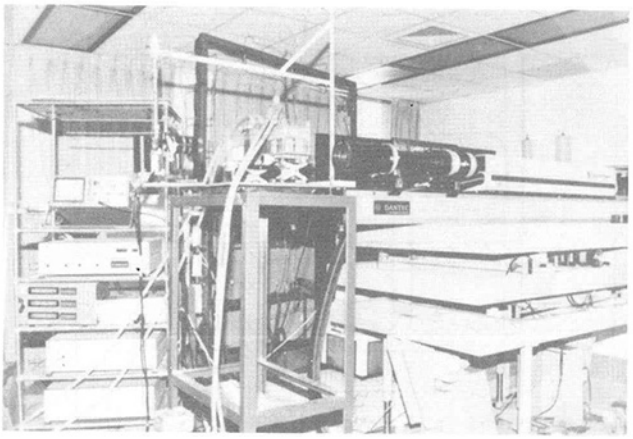

Fig. 3 Photograph of the laser-Doppler velocimeter and test apparatus

2 Experimental Apparatus

The test section consisted of a rectangular channel made of quartz glass 4.8 mm thick. The channel was 600 mm long, 110 mm wide, and 81 mm high. Inside the channel two copper thermodes formed the vertical walls, which could be adjusted longitudinally to alter the enclosure length; see Fig. 2. Plexiglass with a thickness of 3 mm served as the insulated top wall. The partition plate was made of 1.5-mm transparent plastic and was attached to the top wall with glue. A rectangular slot or opening with opening size $s = 4$ and 8 mm was cut into the middle of the partition. Investigation was also carried out without an opening in the partition.

Water of a constant temperature was pumped from two thermostatically controlled circulators to each of the thermodes, thus creating a temperature difference across the enclosure. The inlet and outlet temperatures and the front surface temperature of each thermode were measured with copper-constantan thermocouples. During the experiment the laboratory temperature varied by about 1°C over the 4-h period in which data were recorded. Prior to the measurements, the apparatus had typically been in operation for about 2 h. In all measurements the wall temperature ranged from 5 to 55°C while the Pr of the water ranged from 3 to 11. However, all data were normalized based on the fluid properties at $T_\infty = 20$°C (e.g., Pr = 7.0 for water).

Local temperature measurements of the fluid were recorded at various x planes with a chromel-alumel thermocouple probe made of 1.0-mm-thick wire. The probe was mounted on an electromechanical traversing assembly and inserted vertically downward into the enclosure through holes at the top of the enclosure. All thermocouple probes were connected to an HEW 3088 data logger with automatic ambient compensation. Calibration of the thermocouples in a well-mixed ice bath showed a maximum error of about 0.5°C.

Measurements of the horizontal velocity component across the enclosure height at various x planes were made with a one-component LDV system operating in a forward-scattering, dual-beam mode. The principal components used in the system were a Spectra-Physics 3 W argon-ion laser (green light), a Dantec 55X series optical module (including a 40 MHz Bragg cell), an RCA photomultiplier, a frequency shifter, and a frequency tracker. The laser and optical components were mounted on an optical table, which was equipped with x-, y-, and z-traversing mechanisms. The movement of the table in each direction was controlled by an a-c motor, which was interfaced to a 16-bit personal computer for data acquisition, storage, and reduction. The traversing distance in each direction was measured by a Mitutoyo optical scale with readings in ±0.005 mm increments. A 310-mm focus length achromat, which had a waist diameter of approximately 0.1 mm, formed the probe volume. The test section was mounted on two micro-adjustable jacks on a separate table. Figure 3 is a photograph of the LDV system and the test apparatus. Calibration of the LDV system was performed by comparing the output signal recorded from a stationary scatter with the signal obtained directly from the differential signal of the optical-electronic shifter. These calibrations were typically in agreement to with 5 Hz, corresponding to a velocity of 10 μm/s. A minimum of 500 frequency samples was

Nomenclature

A = aspect ratio = L/H
A_o = opening ratio = s/h
A_p = partition ratio = h/H
g = gravitational acceleration
H = enclosure height, see Fig. 1
h = height of partition plate, see Fig. 1
k = thermal conductivity of the fluid
L = enclosure length, see Fig. 1
Nu_H = Nusselt number = $qH/k(T_h - T_c)$
Ra_H = Rayleigh number = $g\beta(T_h - T_c)H^3/(\nu\alpha)$
Pr = Prandtl number = ν/α
q = total heat transfer rate per unit depth from the hot or cold wall
s = opening size, see Fig. 1
T = temperature
T_c = temperature of cold wall
T_h = temperature of hot wall
u = horizontal velocity component
u^* = nondimensional horizontal velocity component = uH/α
x = horizontal coordinate
x^* = nondimensional horizontal coordinate = x/H
y = vertical coordinate
y^* = nondimensional vertical coordinate = y/H
α = thermal diffusivity of the fluid
β = thermal expansion coefficient of the fluid
θ = dimensionless temperature = $(T - T_c)/(T_h - T_c)$
μ = dynamic viscosity of the fluid
ν = kinematic viscosity = ν/ρ
ρ = fluid density

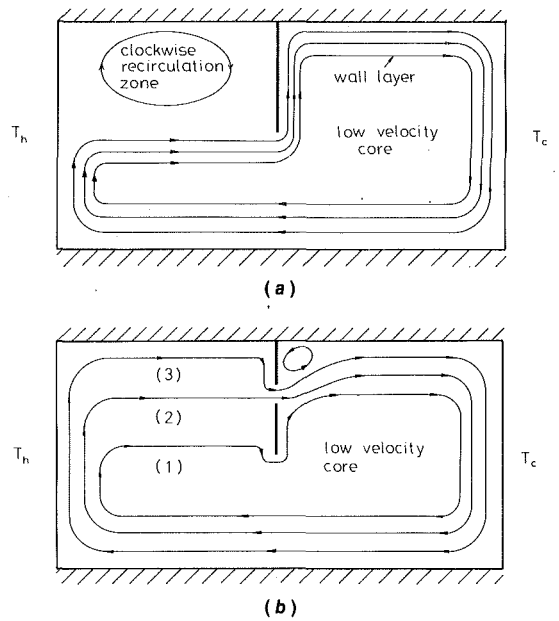

Fig. 4 Flow pattern in a partially divided enclosure at $10^6 \le Ra_H \le 10^8$ for (a) $A_o = 0$, (b) $A_o > 0$

recorded for each measurement from which an ensemble average was calculated. Note that for the measurement errors of 1.5 percent in temperature and 1 percent in velocity, the uncertainty analysis (see Kline, 1985, and Chou, 1988) shows that the error for the derived Nusselt number Nu_H (see equation (2)) is about 3 percent.

3 Results and Discussion

The laminar flow patterns observed for $A = 2$ and $A_p = 1/2$ both with and without an opening in the partition are shown in Figs. 4(*a*) and 4(*b*). The flow pattern shown in Fig. 4(*a*) is basically the same as those observed by Nansteel and Greif (1981) in the range of $10^9 \le Ra_H \le 10^{10}$. In general, the flow was composed of three regions: a region of peripheral boundary-type flow, a relatively inactive core region, and a weak clockwise recirculation zone in the upper left-hand quadrant of the enclosure. However, the flow pattern shown in Fig. 4(*b*) is quite different from that shown in Fig. 4(*a*). When there was an opening in the partition, the upward-moving flow along the hot wall divided into three streams. These were (1) a weak lower stream, (2) a middle main stream, and (3) an upper stream. The lower stream (1) separated from the hot wall at a height $y/H \simeq 1/2$, moved almost horizontally, and turned around the bottom of the partition. The middle main stream (2) separated from the hot-side wall at a height $y/H \simeq 3/4$ and flowed through the opening. The upper stream (3) flowed along the hot wall, turned along the top wall, and moved downward through the opening. These three streams merged on the other side of the partition and moved along the cold wall and the floor, recirculating back to the hot wall. A small vortex was observed on the upper right-hand corner of the partition plate and was noticeable at high Ra_H.

The nondimensional horizontal velocity profiles for $A = 2$, $A_p = 1/2$, and $Ra_H = 10^6$ at the vertical planes $x/H = 0.25$, 0.75, 1.1, 1.25, and 1.75 are shown in Figs. 5, 6, and 7 for $A_o = 0$, 1/8, and 1/4, respectively. Notice that the plane $x/H = 1.1$ is the vertical plane just on the right-hand side of the partition plate. From Fig. 5 (no opening) it can be seen that there is weak recirculation in the upper left-hand quadrant ($x/H = 0.25$ and 0.75 and $y/H \ge 0.6$). Below $y/H \simeq 0.6$, the flow moves horizontally toward the bottom of the partition and turns upward there. The thickness of the bottom fluid

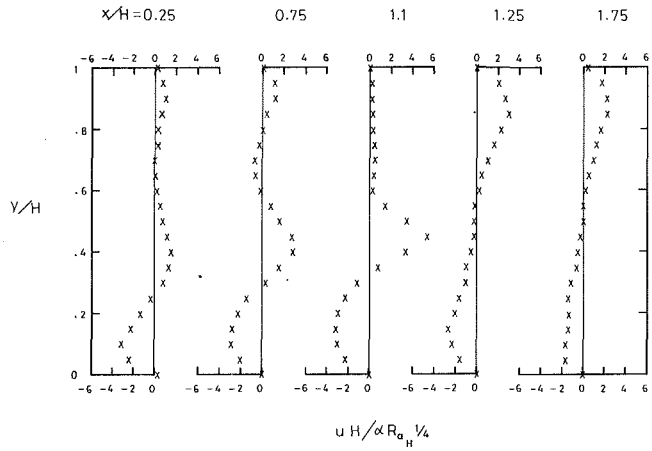

Fig. 5 Velocity profiles: $Ra_H = 10^6$, $A = 2$, $A_p = 1/2$, and $A_o = 0$

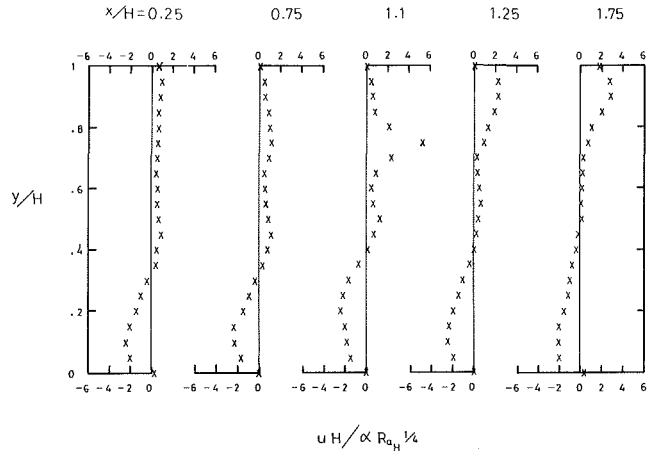

Fig. 6 Velocity profiles: $Ra_H = 10^6$, $A = 2$, $A_p = 1/2$, and $A_o = 1/8$

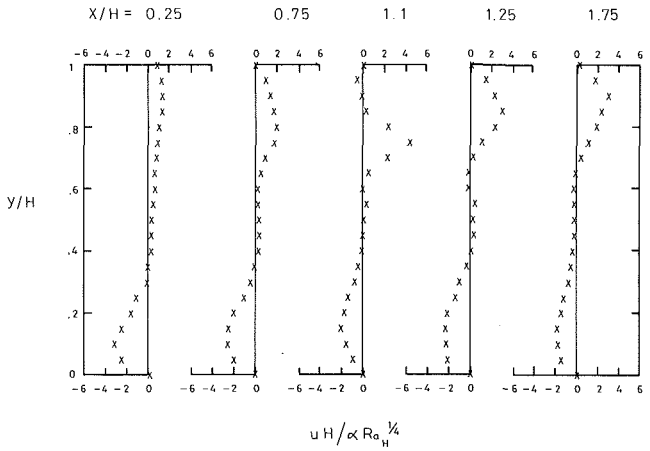

Fig. 7 Velocity profiles: $Ra_H = 10^6$, $A = 2$, $A_p = 1/4$, and $A_o = 1/4$.

layer decreases as the fluid flows from the cold wall ($x/H = 2.0$) to the hot wall ($x/H = 0$). For example, the thickness (y/H) is 0.55, 0.5, 0.3, 0.26, and 0.25, respectively, at planes of $x/H = 1.75$, 1.25, 1.1, 0.75, and 0.25. For the small opening ratio $A_o = 1/8$ shown in Fig. 6, we see that there is no recirculation in the upper left-hand quadrant of the enclosure. The fluid moves through the opening to the other side of the partition and the horizontal component of the velocity at plane $x/H = 1.1$ has a maximum value at the center of the opening ($y/H = 0.75$). Note that when the partition

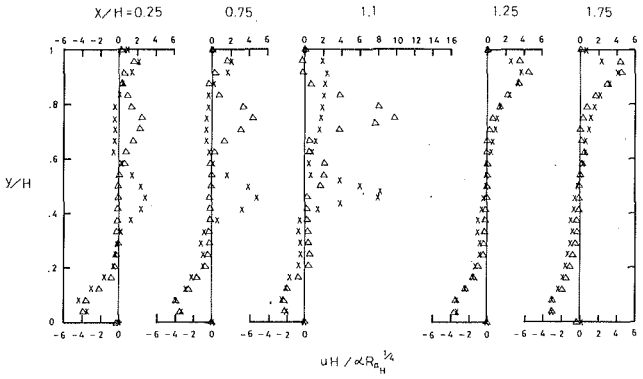

Fig. 8 Comparison of velocity profiles between $A_o = 0$ (×) and 1/4 (△) at $Ra_H = 10^8$, $A = 2$, and $A_p = 1/2$

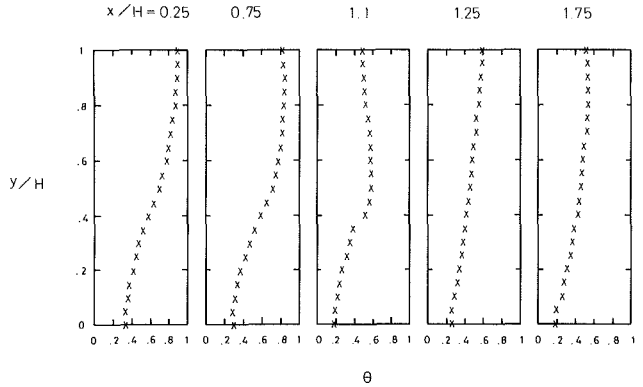

Fig. 9 Temperature profiles: $Ra_H = 10^6$, $A = 2$, $A_p = 1/2$, and $A_o = 0$

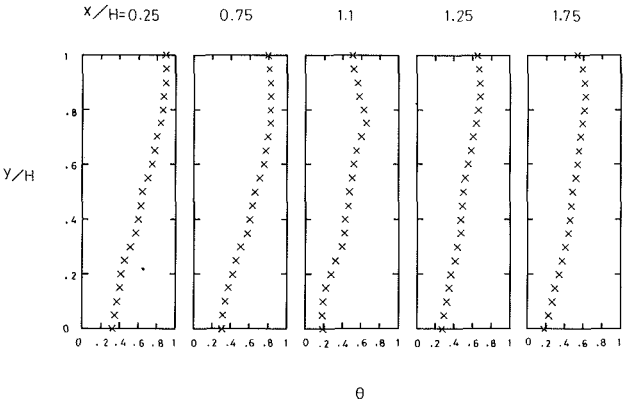

Fig. 10 Temperature profiles: $Ra_H = 10^6$, $A = 2$, $A_p = 1/2$, and $A_o = 1/8$

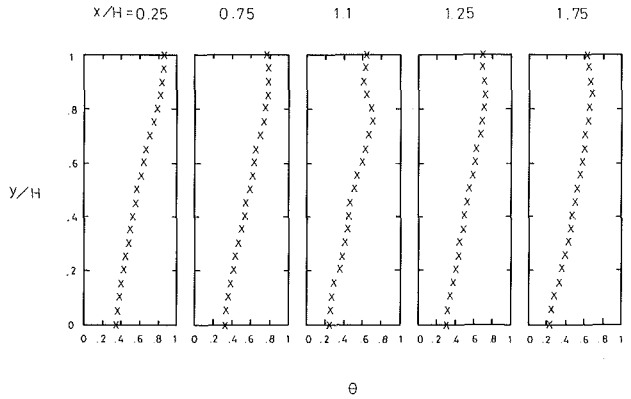

Fig. 11 Temperature profiles: $Ra_H = 10^6$, $A = 2$, $A_p = 1/2$, and $A_o = 1/4$

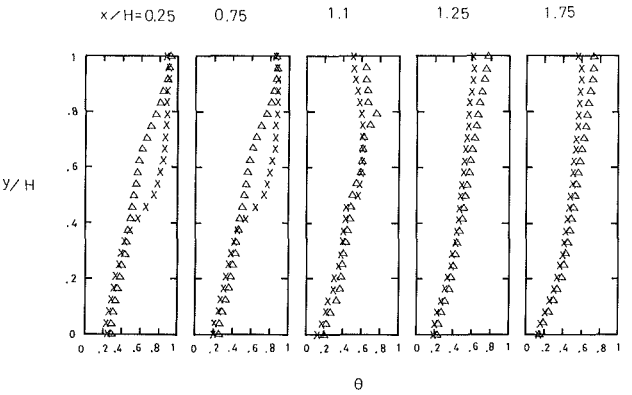

Fig. 12 Comparison of temperature profiles between $A_o = 0$ (×) and 1/4 (△) at $Ra_H = 10^8$, $A = 2$, and $A_p = 1/2$

plate is without an opening the maximum velocity at the plane $x/H = 1.1$ is at $y/H \simeq 0.45$ below the bottom of the partition (Fig. 5). However, the left-moving fluid layers adjacent to the bottom wall are not significantly affected by whether or not the partition has an opening. The horizontal velocity profiles for a large opening ratio ($A_o = 1/4$) are shown in Fig. 7. These velocity profiles are basically the same as for the small opening ($A_o = 1/8$). However, the maximum velocity at the plane $x/H = 1.1$ becomes smaller when the opening ratio becomes larger.

Figure 8 shows the velocity profiles for $A = 2$, $A_o = 1/2$, and $Ra_H = 10^8$ at various x planes for the cases both with an opening ($A_o = 1/4$) and without an opening ($A_o = 0$) in the partition plate. It is seen that hot fluid flows from the left half to the right half mainly through the opening for $A_o = 1/4$, but passes around the partition tip for $A_o = 0$. However, the velocity profiles at planes $x/H = 1.25$ and 1.75 are quite similar, and the opening seems to have little effect on the bottom fluid layer.

The nondimensional vertical temperature profiles for $A = 2$, $A_p = 1/2$, and $Ra_H = 10^6$ at various x planes are shown in Figs. 9, 10, and 11 for $A_o = 0$, 1/8, and 1/4, respectively. Inspection of these figures reveals that because the hotter fluid flows through the opening for $A_o = 1/8$ and 1/4 the peak temperature of the plane $x/H = 1.1$ appears at the center of the opening, but for $A_o = 0$ the peak value is at the bottom of the partition. Figure 12 shows the temperature profiles for $A_o = 0$ and 1/4 at $A = 2$, $A_p = 1/2$, and $Ra_H = 10^8$. It is seen from Fig. 12 that in the left-upper quadrant, because the hot fluid was trapped, temperatures for $A_o = 0$ were higher than those for $A_o = 1/4$. However, due to the flowing of the hotter fluid through the opening, temperatures in the right-upper quadrant for $A_o = 1/4$ were higher than those for $A_o = 0$.

The net heat transfer in the x direction per unit depth can be computed in terms of the Nusselt number defined by

$$\mathrm{Nu}_H = \frac{qH}{k(T_h - T_c)} = \int_0^1 u^*\theta dy^* + \int_0^1 \frac{\partial\theta}{\partial x^*}\, dy^* \qquad (1)$$

at any x plane. The first term on the right-hand side of the above equation represents the convective heat flux and the second term represents the conduction heat flux. From the temperature measurements shown in Figs. 9–12 the heat flux due to conduction is very small as compared with the heat flux due to convection; the temperature profiles of planes $x/H = 0.25$ and 0.75 were quite similar. If the second term on the right-hand side of equation (1) is negligible, then Nu_H can be determined by

$$\mathrm{Nu}_H = \int_0^1 u^*\theta dy^* \qquad (2)$$

Table 1 Nu_H calculated from equation (2) at various vertical planes

	A_o=0		A_o=1/8		A_o=1/4	
x/H \ Ra_H	10^6	10^8	10^6	10^8	10^6	10^8
0.25	6.98	26.6	7.36	28.45	7.8	30.26
0.75	6.96	26.58	7.35	28.44	7.8	30.24
1.1	6.82	26.52	7.19	28.1	7.65	29.98
1.25	6.96	26.58	7.29	28.25	7.7	30.07
1.75	6.92	26.6	7.31	28.38	7.72	30.17

from the velocity distributions and temperature measurements described previously. Table 1 lists the values of Nu_H calculated from equation (2) at various x planes. It is seen from Table 1 that the maximum value of Nu_H occurs at the plane $x/H=0.25$, and the minimum value occurs at the plane $x/H=1.1$. However, at any fixed Ra_H, the deviation of Nu_H between any two planes is within 3 percent. Thus, in the present study, Nu_H is determined from the equation (2) evaluated at the plane $x/H=0.25$. The results of Nu_H versus Ra_H are presented in Fig. 13, from which the following correlation can be derived:

$$Nu_H = 0.123 Ra_H^{0.289} (1 - s/2h)^{-1.26} \quad (3)$$

for $A=2$, $A_p=1/2$, $10^6 \le Ra_H \le 10^8$, and $0 \le s/h \le 1/4$. The root-mean-square deviation of the data from the correlation is 3.5 percent. These results show that Nu_H increases as the Ra_H and opening ratio ($A_o = s/h$) increase. The dashed lined in Fig. 13 is the correlation curve according to (see Blythe et al., 1983)

$$Nu_H = 0.32 Ra_H^{1/4} \quad (4)$$

for $A=2$, $Pr \gg 1$, and $A_p=0$ (no partition). It is seen that an unopened partial partition ($A_o=0$) would reduce the heat transfer rate by an amount of 12 to 30 percent depending on the Ra_H. Notice that the data obtained by Nansteel and Greif (1981) in a water-filled partially divided enclosure without an opening in the partition for $4.33 \times 10^9 \le Ra_H \le 1.275 \times 10^{10}$ (in the present notation) are also presented in Fig. 13. It is seen that extrapolation of equation (3) for $A_o = s/h = 0$ compares reasonably well (within 8.5 percent deviation) with the data of Nansteel and Greif (1981). Although not reported in this study, numerical simulation by Chou (1988) shows that the maximum deviation of numerically calculated Nu_H from the present work is within 10 percent.

4 Conclusion

The nonintrusive velocity measurements together with the locally recorded temperature distributions in a water-filled, partially divided enclosure, both with and without an opening in a nonconducting partition plate, have revealed that the opening in the partition has the effect of increasing heat transfer by allowing the flow of the entrapped hot fluid (that would exist in an unopened, partially divided enclosure) through the opening. Results show that an unopened partial obstruction would reduce the heat transfer rate by an amount of 12–30 percent depending on the Rayleigh number. However, the opening seems to have little effect on the velocity and temperature profiles of the bottom fluid layer. A correlation of the Nusselt number, which depends on the Rayleigh number and aspect ratio, is given and shows that the heat transfer rate increases with increasing opening ratio and Rayleigh number. It should be noted that further study is needed to determine the effect of A_p or a conducting partition on the heat transfer inside the enclosure.

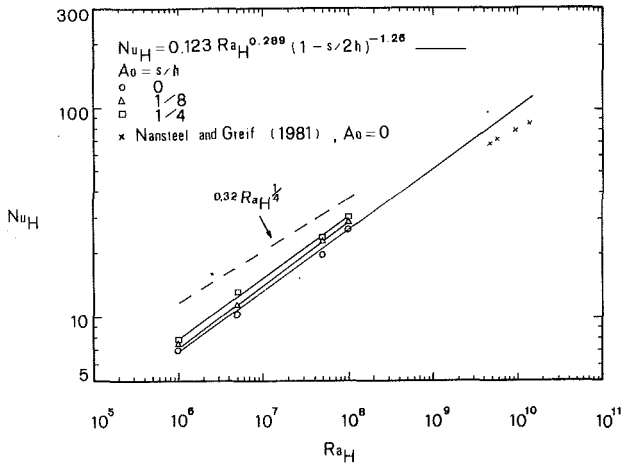

Fig. 13 Heat transfer results and correlation

Acknowledgments

The authors thank Professor R. Greif at the University of California at Berkeley for encouraging us to do this work. This work was partially supported by the National Science Council in Taiwan under Grant No. NSC-75-0401-E110-01.

References

Bajorek, S. M., and Lloyd, J. R., 1982, "Experimental Investigation of Natural Convection in Partitioned Enclosures," ASME JOURNAL OF HEAT TRANSFER, Vol. 104, pp. 527–532.

Bauman, F., Gagil, A., Kammerud, R., and Greif, R., 1980, "Buoyancy Driven Convection in Rectangular Enclosures: Experimental Results and Numerical Calculations," ASME Paper No. 80-HT-66.

Blythe, P. A., Daniels, P. G., and Simpkins, P. G., 1983, "Thermal Convection in a Cavity: The Core Structure Near the Horizontal Boundaries," *Proc. Roy. Soc. London*, Vol. A387, pp.367–388.

Catton, I., 1978, "Natural Convection in Enclosures," *Proc. 6th Int. Heat Transfer Conf.*, Vol. 6, pp. 13–31.

Chang, L. C., Lloyd, J. R., and Yang, K. T., 1982, "A Finite Difference Study of Natural Convection in Complex Enclosures," *Proc. 7th Int. Heat Transfer Conf.*, Munich, Federal Republic of Germany, pp. 183–188.

Chou, C. H., 1988, "An Experimental and Numerical Investigation of Natural Convection in Partially Divided Rectangular Enclosures With or Without an Opening in the Partition Plate," M. S. Thesis, Inst. of Mech. Engng., NSYSU, Kaohsiung, Taiwan.

Emery, A. F., 1969, "Exploratory Studies of Free Convection Heat Transfer Through an Enclosed Vertical Liquid Layer With a Vertical Baffle," ASME JOURNAL OF HEAT TRANSFER, Vol. 19, pp. 163–165.

Jetli, R., Acharya, A., and Zimmerman, E., 1986, "Influence of Baffle Location on Natural Convection in a Partially Divided Enclosure," *Num. Heat Transfer*, Vol. 10, pp. 521–536.

Kline, S. J., 1985, "The Purpose of Uncertainty Analysis," ASME *Journal of Fluids Engineering*, Vol. 107, pp. 153–161.

Lin, N. N., and Bejan, A., 1984, "Natural Convection in Undivided and Partially Divided Enclosures," *Int. J. Heat Mass Transfer*, Vol. 26, No. 12, pp. 1867–1878.

Nansteel, W. M., and Greif, R., 1981, "Natural Convection in Undivided and Partially Divided Rectangular Enclosures," ASME JOURNAL OF HEAT TRANSFER, Vol. 103, pp. 623–629.

Nansteel, W. M., and Greif, R., 1984, "An Investigation of Natural Convection in Enclosures With Two- and Three-Dimensional Partitions," *Int. J. Heat Mass Transfer*, Vol. 27, No. 4, pp. 561–571.

Ostrach, S., 1972, "Natural Convection in Enclosures," *Adv. in Heat Transfer*, Vol. 8, pp. 161–227.

Shaw, H. J., Chen, C. K., and Cleaver, J. W., 1987, "Cubic Spline Numerical Solution for Two-Dimensional Natural Convection in a Partially Divided Enclosure," *Num. Heat Transfer*, Vol. 12, pp. 439–455.

Simpkins, P. G., and Chen, K. S., 1985, "Natural Convection in Horizontal Containers With Application to Crystal Growth," in: *Natural Convection: Fundamentals and Applications*, S. Kakac, W. Aung, and R. Viskanta, eds., pp. 1010–1039, Hemisphere Corp.

Zimmerman, E., and Acharya, S., 1987, "Free Convection Heat Transfer in a Partially Divided Vertical Enclosure With Conduction End Walls," *Int. J. Heat Mass Transfer*, Vol. 30, No. 2, pp. 319–331.

Mixed Convection Transport From an Isolated Heat Source Module on a Horizontal Plate

B. H. Kang

Y. Jaluria

S. S. Tewari

Department of Mechanical and Aerospace Engineering, Rutgers, The State University of New Jersey, New Brunswick, NJ 08903

An experimental study of the mixed convective heat transfer from an isolated source of finite thickness, located on a horizontal surface in an externally induced forced flow, has been carried out. This problem is of particular interest in the cooling of electronic components and also in the thermal transport associated with various manufacturing systems, such as ovens and furnaces. The temperature distribution in the flow as well as the surface temperature variation are studied in detail. The dependence of the heat transfer rate on the mixed convection parameter and on the thickness of the heated element or source, particularly in the vicinity of the source, is investigated. The results obtained indicate that the heat transfer rate and fluid flow characteristics vary strongly with the mixed convection variables. The transition from a natural convection dominated flow to a forced convection dominated flow is studied experimentally and the basic characteristics of the two regimes determined. This transition has a strong influence on the temperature of the surface and on the heat transfer rate. As expected, the forced convection dominated flow is seen to be significantly more effective in the cooling of a heat dissipating component than a natural convection dominated flow. The location of the maximum temperature on the module surface, which corresponds to the minimum local heat transfer coefficient, is determined and discussed in terms of the underlying physical mechanisms. The results obtained are also compared with these for an element of negligible thickness and the effect of a significant module thickness on the transport is determined. Several other important aspects of fundamental and applied interest are studied in this investigation.

Introduction

A large number of practical situations involve mixed convective heat transfer in which neither the forced nor the natural convection effects are dominant and both modes are significant (Jaluria, 1980). Such circumstances arise when a fluid flows over a heated surface at a relatively low velocity. The effect of the incorporation of both transport mechanisms on the heat transfer rate is particularly important in the design of thermal systems, such as electronic circuitry and furnaces. These examples are considered by Steinberg (1980), Kraus and Bar-Cohen (1983), and Jaluria (1984). In many such applications an externally induced air flow is employed for the cooling of isolated heat sources, such as heaters or electronic components. Of particular interest is the effect of the wake generated by a heat module on the thermal field near the module since the heat transfer is determined by the temperature in the adjacent fluid. This, in turn, determines the surface temperature of the module for a given heat input. Therefore, it is important to investigate the resulting thermal field and its dependence on physical parameters, such as the external velocity, energy input, and the height of the heat source module in such problems.

In recent years, considerable work has been done on the heat transfer from an isolated heat source located on a surface. The heat transfer from a source located in the natural convection wake arising from an upstream heat source has been investigated experimentally and theoretically by Milanez and Bergles (1986), Goel and Jaluria (1986), Pera and Gebhart (1975), and Jaluria (1982a). Recently, numerical (Afrid and Zebib, 1989) and experimental (Park and Bergles, 1987) studies have been carried out on the natural convective cooling of single and multiple heated, rectangular modules mounted on a vertical wall. Even though natural convective cooling is still used in many small systems, an externally induced flow must be employed in higher power dissipating systems. In response to the cooling needs of the latter category of the systems, considerable attention has been given recently to forced convection cooling. Zebib and Wo (1986) studied forced air cooling in a constricted channel, using finite difference methods. Davalath and Bayazitoglu (1987) and Than and Bayazitoglu (1988) also studied forced convective cooling of multiple rectangular blocks with uniformly distributed heat flux. However, much less attention has been directed at the corresponding mixed convection flow, resulting from the addition of a specified flow velocity to an existing natural convection flow. Some theoretical work has been done on the mixed convection flow over a single heat source. Kennedy and Zebib (1983) presented numerical and experimental results on the buoyancy effects in a laminar horizontal channel flow with an isolated heat source on the lower or upper wall. The effect of an externally induced flow on the heat transfer rate from a single heat source has also been investigated (Jaluria, 1982b; Rao et al., 1984). A few experimental and numerical studies have been carried out on the thermal interaction between two finite-sized heat sources by Tewari et al. (1987) and Jaluria (1986). In all these investigations, the heat source was mounted flush on the surface, i.e., with essentially negligible thickness. Not much work has been done on the mixed convective flow over a rectangular heated module of significant thickness. Recently, a numerical study on the mixed convection cooling of multiple heated blocks, located in a channel formed by insulated parallel plates, was presented by Bayazitoglu and Davalath (1989). The flow field and the

Contributed by the Heat Transfer Division and presented at the 25th AIChE/ASME National Heat Transfer Conference, Houston, Texas, July 1988. Manuscript received by the Heat Transfer Division September 12, 1988; revision received October 10, 1989. Keywords: Conjugate Heat Transfer, Electronic Equipment, Mixed Convection.

resulting heat transfer rates, in terms of the local and average Nusselt numbers, were determined.

The present study is directed at the mixed convection heat transfer from an isolated heat source module, whose thickness is varied and which is mounted on a thin horizontal surface, well insulated at the back surface. The physical model and the coordinate system considered are shown in Fig. 1. The surface and the heat source module are taken as wide in the transverse direction so that a two-dimensional flow situation is obtained. The temperature distribution in the flow and at the surface are obtained experimentally. The effects of the externally induced flow velocity, heat input, and the thickness of the heat source module on the heat transfer rate and on the thermal field, particularly in the vicinity of the source, are studied in detail.

Experimental Arrangement

An essential feature of the experimental setup is a low-speed wind tunnel, with a test section 61 cm × 46 cm in cross-sectional area and 150 cm in length. These dimensions ensure that a test placed inside the test section is far from the walls and is, thus, free of the wall effects. A schematic diagram of the experimental arrangement is shown in Fig. 2. A variable-velocity flow, ranging from zero to 50 cm/s in the test section, is obtained by means of a blower, whose flow rate can be varied. A considerable effort was directed at the design of the diffuser and the associated flow arrangement, in order to obtain a uniform flow with a very small turbulence level, i.e., less than 5 percent intensity. The flow from the blower enters the test section through a honeycomb section and a fine-mesh polymer screen to ensure a fairly uniform flow with negligible turbulence in the test section. The uniformity of the flow and the turbulence level were checked by extensive hot-wire anemometry measurements. It was found that, over the range of experimental conditions considered, the straighteners at the diffuser exit and the honeycomb at the duct entrance did not introduce significant turbulence. In general, the turbulence intensity was found to be in the range of 3–5 percent.

The heat source module consists of a highly polished stainless steel foil (0.03 mm thick), wrapped over two vertical side surfaces and the horizontal top surface of a stack of several bakelite strips (2.2 cm wide, 1.5 mm thick, and 40 cm long). A thermally conducting epoxy cement was employed to ensure good contact between the foil and the bakelite strips.

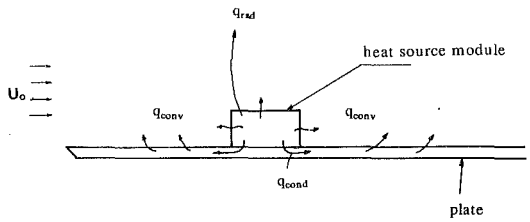

(a) Physical model.

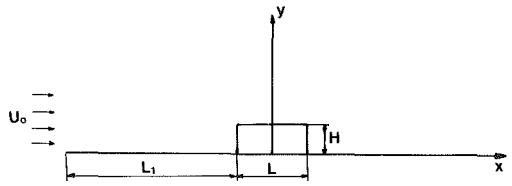

(b) Coordinate system.

Fig. 1 Physical model and the coordinate system

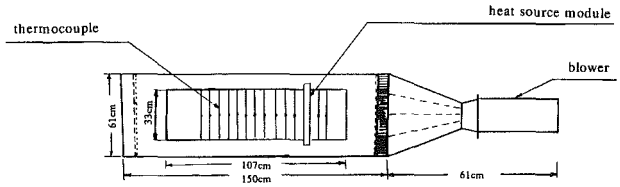

TOP VIEW

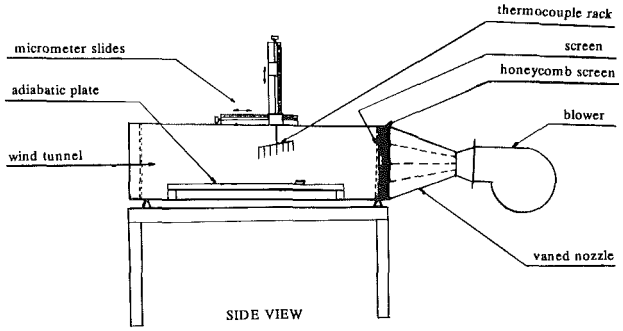

SIDE VIEW

Fig. 2 Experimental arrangement

Nomenclature

g = gravitational acceleration
Gr = Grashof number, defined in equation (2)
h = convective heat transfer coefficient
H = thickness of the heated module
k = thermal conductivity of the fluid
L = width of the heated module, shown in Fig. 1
L_1 = distance from the leading edge of the plate to the heat source module
Nu = local Nusselt number, defined in equations (3) and (4)
$\overline{\text{Nu}}$ = mean Nusselt number, defined in equation (6)
q = heat flux input at the source module surface
q_{cond} = conductive heat flux from the heat source to the horizontal plate
q_{conv} = convected heat flux from the heat source to the flow
q_{rad} = radiated heat flux from the heat source to the ambient
Re = Reynolds number, defined in equation (2)
s = distance along the module, shown in Fig. 9
T = local temperature
T_a = ambient temperature
T_s = local surface temperature
ΔT_m = temperature rise, above T_a, at a location due to heat input by the module
U_0 = externally induced flow velocity
x = distance along the surface from the midpoint of the bottom of the module, shown in Fig. 1
X = dimensionless x coordinate, defined in equation (1)
y = distance from the plate surface, shown in Fig. 1
Y = dimensionless y coordinate, defined in equation (1)
β = coefficient of thermal expansion of the fluid
θ = dimensionless local temperature, defined in equation (1)
θ_s = dimensionless surface temperature
ν = kinematic viscosity of the fluid

The thickness of the module could be varied by changing the number of strips in the stack. The stainless steel foil is electrically heated to provide a uniform heat flux input condition over the module surface. The desired voltage across the heating foil is obtained by means of a variable autotransformer whose output voltage could be varied. Several tests were undertaken to ensure that a very good contact existed between the foil and the strips and that the electrical properties of the foil remained essentially unchanged, to yield a constant surface heat flux condition.

The heat source module is mounted firmly on a horizontal plate by means of a specially designed clamp and the entire assembly is placed in the test section of the wind tunnel. The plate is made of three thin masonite boards, separated by 6-mm air gaps to reduce the transverse conductive heat loss. With this arrangement, the conduction through the air gaps was estimated to be less than 10 percent of the total electrical heat input by Tewari et al. (1987). Radiative losses are also kept low by employing a polished stainless steel foil. The emissivity of stainless steel foil was experimentally found to be of order 0.1 by Goel and Jaluria (1986). The radiation heat loss to the ambient was calculated to be less than 3 percent of the total electrical power dissipation for the heat flux range considered here, using a simple analytical model. At the low velocities considered here, the leading edge of the plate did not generate a significant disturbance. However, a sharp leading edge was employed to ensure that such disturbances would be negligible. End plates were employed to eliminate the lateral flow over the test state.

The electric power dissipation in the foil is obtained by measuring the voltage drop across the strip and the current through it by means of a precision digital voltmeter and an ammeter, respectively. Three high-temperature heat flux gages are mounted at the backside of the top surface of the heating foil and two each at the backside of the right and left sides of the heating foil. Since these heat flux gages measure the conductive heat flux from the foil to the test plate, the measured heat flux is subtracted from the uniform heat flux input due to the electric power dissipation in the strip to obtain the local convective flux from the foil to the flow. In addition to these gages, high-sensitivity heat flux gages are also mounted at various locations on the horizontal plate in order to obtain the local convective heat flux from the plate. The experimental error in these measurements was estimated to be less than ± 5 percent of the measured values, as was also confirmed by the repeatability of the results. Similar arrangements have been used by the present investigators in earlier studies (Tewari et al., 1987). Clearly, there are many other important considerations that have to be taken into account for accurate results. These are omitted here for brevity and may be obtained from the various references mentioned earlier.

Wide ranges of the heat input and flow velocity were investigated. In practical devices, such as electronic circuitry, the flow regime may vary from pure natural to forced convection. However, our interest in this paper was directed at the mixed convection regime and the parametric values considered are applicable to typical medium-sized systems, such as a small computer system cooled by a fan.

The surface temperature is measured by individual, calibrated, copper-constantan thermocouples, made of 0.025-mm-dia wires and attached to the surface by means of a high thermal conductivity cement. The temperatures in the flow are measured by a set of seven thermocouples, made of 0.05-mm-dia copper-constantan wires. These thermocouples are mounted on a rack. The thermocouples are staggered in the direction of the flow in order to avoid interference between them. The entire thermocouple rack is mounted on a pair of precision micrometer slides, which provide the desired horizontal and vertical positioning of the rack. The thermocouple signals were measured by means of an Apple microcomputer based data acquisition system (Omega Whitebox). The data processing and graphing was done on a Sun computer system. The error in the temperature measurements was estimated to be within about $\pm$ 1 percent of the measured values.

Experimental Results and Discussion

The basic physical parameters in the problem under consideration are the heat flux input q, the width L, and the thickness H of the heat source module, the distance L_1 from the leading edge of the plate to the heat source module, and the external flow velocity U_0 (see Fig. 1). As mentioned earlier, the free-stream turbulence was negligible in this study. Thus, the resulting local temperature T may be presented in functional form as

$$T=f(L_1, L, H, q, U_0)$$

The relevent dimensionless quantities may be derived from these physical variables, as given below. The distance of the module from the leading edge of the plate, L_1, is taken at a fixed value of $L_1/L=8$ here, for convenience, in the presentation of the results. Clearly, L_1/L or L_1/H is an important parameter in the flow if the heat source module is placed near the essentially leading edge of the plate. However, the basic trends were observed to remain unchanged with varying values of L_1/L, over the range 6 to 10, in the experiments. Also L is kept constant at 2.2 cm as a characteristic dimension. The coordinate system employed is shown in Fig. 1. The results are presented in terms of the dimensionless temperature, $\theta=f(\mathrm{Gr}, \mathrm{Re}, H/L)$, and the dimensionless coordinate distance X and Y for a uniform heat flux q at heated region, defined as

$$\theta=\frac{(T-T_a)}{q(L+2H)/k}\mathrm{Gr}^{1/5}, \qquad X=\frac{x}{L}, \qquad Y=\frac{y}{L} \tag{1}$$

where

$$\mathrm{Gr}=\frac{g\beta q(L+2H)L^3}{k\nu^2}, \qquad \mathrm{Re}=U_0\frac{L}{\nu} \tag{2}$$

Similar normalization has been employed in several earlier studies such as those by Jaluria (1982a) and Goel and Jaluria (1986). Here, T is the local temperature, T_a the ambient temperature, k the thermal conductivity of air, x the physical distance measured from the center of the bottom surface of the source, y the normal distance from the plate, g the magnitude of the gravitational acceleration, β the fluid coefficient of thermal expansion, ν the kinematic viscosity, Gr the Grashof number, and Re the Reynolds number. The heat input into the heated element, Q, is given by $q(L+2H)$. Therefore, the characteristic temperature difference in this formulation becomes $[q(L+2H)/k]$ instead of T_s-T_a, where T_s is the surface temperature, for the isothermal case. The typical temperature difference (T_s-T_a) ranged from 40–90°C. Properties of the fluid were evaluated at the film temperature, $[(T_s)_{\max}+T_a]/2$. Various values of the Grashof number, the Reynolds number, and the module thickness were used to obtain a range of experimental results in the laminar region. It was found that the results were well correlated in terms of the above dimensionless variables.

Figures 3(*a–c*) show the effect of the Reynolds number Re on the thermal boundary layer. In this figure, isothermal lines are shown for a fixed Grashof number, $\mathrm{Gr}=2.6\times10^6$, and three values of the Reynolds number, Re = 830, 435, and 350. For Re = 830, the thermal boundary layer thickness increases over the module and then becomes essentially constant downstream of the module. Similar trends have been observed in forced convective flow over heated blocks (Davalath and Bayazitoglu, 1987). However, for Re = 435 and 350, the ther-

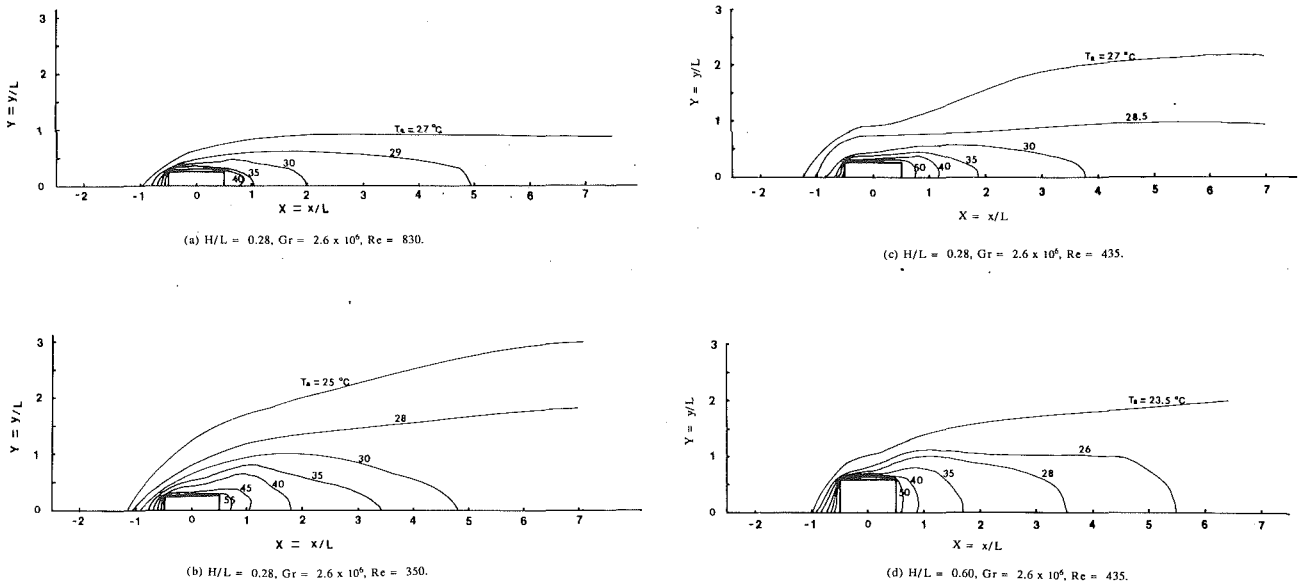

Fig. 3 Distribution of isotherms in the flow

mal boundary layer thickness keeps on increasing gradually downstream of the module because of the wake effect in the flow. The observation can be attributed to the fact that the thermal buoyancy force is normal to the external flow direction. In addition, the buoyancy force is relatively strong for these smaller values of Re, 350 and 435, at a fixed Gr. The effect of the module thickness of the thermal boundary layer thickness is seen from Figs. 3(c) and 3(d). The Grashof and Reynolds numbers are kept constant. The boundary layer thickness at $H/L=0.6$ is found to change more rapidly near the source than at $H/L=0.28$ because a thicker module has a stronger influence on the distortion of the external flow and on the resulting temperature distribution in the flow over the module. These figures also indicate the thermal field due to the heat source. The upstream penetration and the downstream spread and decay of thermal effects are clearly seen. Flow visualization by means of smoke was also attempted and the flow pattern near the source was observed. It was found that the measured thermal field, as shown in Fig. 3, is a good qualitative representation of the observed flow and its dependence on Gr and Re. Thus, Fig. 3 indicates the basic characteristics of the flow around the module. Similar trends are observed by Afrid and Zebib (1987) and Bayazitoglu and Davalath (1989).

Figure 4 shows the variation of the temperature in the flow with the dimensionless distance Y from the surface, at various X locations. The results are shown for $H/L=0.28$, $\mathrm{Gr}=2.6\times10^6$, and $\mathrm{Re}=435$ in Fig. 4(a). As seen in this figure, a sharp temperature gradient occurs at the location directly above the heated strip ($X=0$). The temperature gradients decrease rapidly as flow proceeds downstream ($X=0.6$ and $X=2.0$). It is interesting to note that the temperature gradient at an upstream location of $X=-0.6$ is higher than that obtained at the downstream location at $X=0.6$. This implies that the flow upstream of the module is considerably affected and that the convective heat transfer rates at corresponding downstream locations near the module are smaller. Figure 4(b) shows the temperature variation for $H/L=0.6$. As can be seen in this figure, the temperature profiles are not significantly different from those for a thinner source, but the temperatures near the surface at $X=0.6$ are much higher than those obtained at $X=0.6$ for $H/L=0.28$. This indicates that a smaller convective heat transfer rate is achieved downstream ($X=0.6$) with a thicker module.

The variation of the surface temperature distribution is shown for various externally induced flows at $H/L=0.28$ and

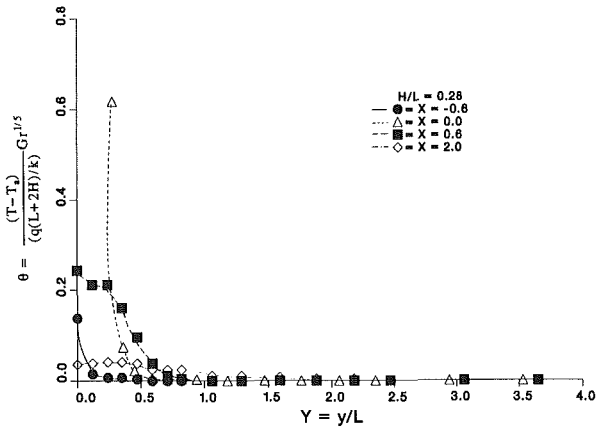

(a) H/L = 0.28, Gr = 2.6 x 10⁶, Re = 435.

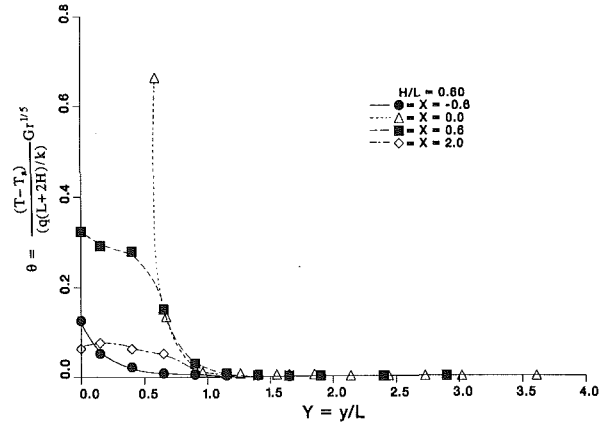

(b) H/L = 0.60, Gr = 2.6 x 10⁶, Re = 435.

Fig. 4 Measured temperature profiles in the flow

$\mathrm{Gr}=2.6\times10^6$ in Fig. 5. The heat source module is located from $X=-0.5$ to $X=0.5$. It is seen that the surface temperature starts rising gradually upstream of the heat source due to the longitudinal conductive transport in the plate, and then rises sharply in the neighborhood of the heat source module. In the case of natural convection ($\mathrm{Re}=0$), the max-

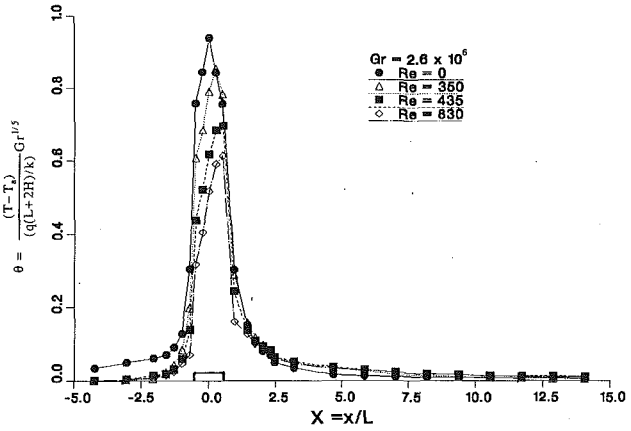

Fig. 5 Surface temperature distribution for $H/L = 0.28$ at $Gr = 2.6 \times 10^6$ and different values of Re

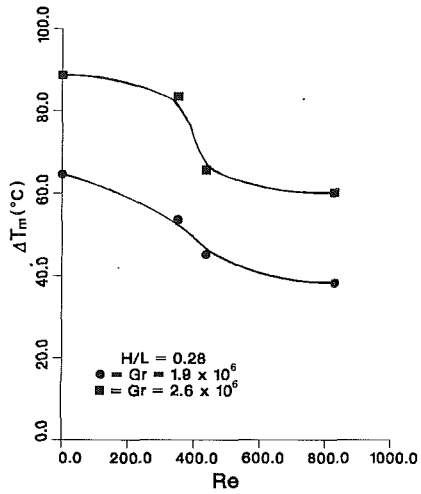

Fig. 6 Physical surface temperature rise above the ambient temperature for $H/L = 0.28$

imum surface temperature is observed at $X = 0$. At $Re = 350$ and 435, the location of the maximum temperature is found to shift to $X = 0.25$. The temperature maximum is at $X = 0.5$ for $Re = 830$. This maximum temperature is followed by a rapid drop in the vicinity of the module. A gradual temperature decay arises farther downstream. The surface temperature at the upstream location ($X < -0.5$) for mixed convection is seen to be lower than that for natural convection. However, the surface temperature for mixed convection is seen to be higher than that for natural convection at the downstream location ($X > 1$).

In the pure natural convection case, the wake over the heated module is essentially a vertically rising plume and, therefore, the locations far downstream are not affected. The plate surface is then essentially heated by longitudinal conduction of thermal energy from the module. However, in the mixed convection mode, the wake from the heat module is bent in the downstream direction due to the external flow. Thus, the downstream locations come under the effect of the wake. This implies that the combined effect of the convective heat transfer from the wake to the surface and the conduction from the module produces a relatively higher surface temperature at downstream locations in the mixed convection mode. It is also found that the surface temperature variation in natural convection is symmetric, as expected. The surface temperature distribution is gradually shifted downstream as the Reynolds number is increased.

The location of the maximum temperature and the magnitude of the temperature rise, $\Delta T_m = (T_s)_{max} - T_a$, are very important parameters in the design of a thermal system, such as an electronic component cooling system. Here, the subscript max represents the maximum value that arises. The reliability and operation of electronic components depend on the maximum temperature attained by the component. The location of the maximum temperature depends on the mixed convection parameter, $Gr/Re^{5/2}$, which represents the ratio of the buoyancy to the inertia force. This parameter arises in other mixed convection flows with a uniform heat flux condition (Jaluria, 1980). The maximum surface temperature is observed at the middle of the top face ($X = 0$) of the heat source module for natural convection. However, as the mixed convection parameter is decreased, or the forced convection effects increased, this location moves to the right corner of the top face and finally to the right face of the module. It is found that the maximum surface temperature occurs at about the right corner of the top face at $Re = 350$, at about the top corner of the right face at $Re = 435$, and around the middle of the right face at $Re = 830$. These observations are for $Gr = 2.5 \times 10^6$ at $H/L = 0.28$. The corresponding mixed convection parameter, $Gr/Re^{5/2}$, is 1.09 for $Re = 350$ and 0.63 for

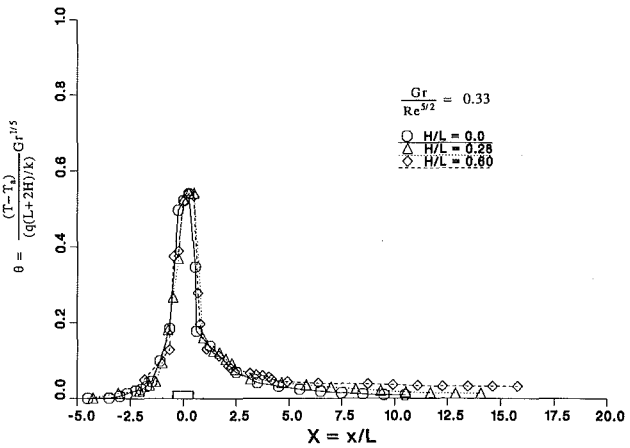

Fig. 7 Effect of the heat source module thickness on the surface temperature variation at $Re = 435$ and $Gr = 1.3 \times 10^6$

$Re = 435$. Similarly, this location moves from the right face of the module to the top face as Grashof number is increased with a fixed Reynolds number.

Additional experiments indicated that the critical value of the mixed convection parameter for this shift in the maximum surface temperature location occurs between $Gr/Re^{5/2} = 0.9$ and 1.1. The results imply that the flow is a natural convection dominated one when $Gr/Re^{5/2}$ is larger than 1.1, and a forced convection dominated one when $Gr/Re^{5/2}$ is smaller than 0.9. The temperature rise for $H/L = 0.28$ is shown in Fig. 6. The rapid change in the temperature rise is seen in the Reynolds number range of 300–400. This is probably a consequence of the transition from a natural convection dominated flow to a forced convection flow. The temperature rise is seen to increase as the Grashof number is increased. The physical temperature rise ΔT_m is employed here to eliminate the effect of Gr, which is used in the definition of the dimensionless temperature and to indicate the physical range of values obtained.

The surface temperature distribution was measured for three values of the heat source module thickness, H/L, at $Re = 435$ and $Gr = 1.3 \times 10^6$. As can be seen in Fig. 7, trends similar to those shown in Fig. 5 were observed. As the thickness H/L is increased, the surface temperature increases downstream due to a perturbation to the flow. Because of the nondimensionalization employed here, the Grashof number is based on the characteristic temperature difference, $q(L+2H)/k$. Therefore, for a given Grashof number, the

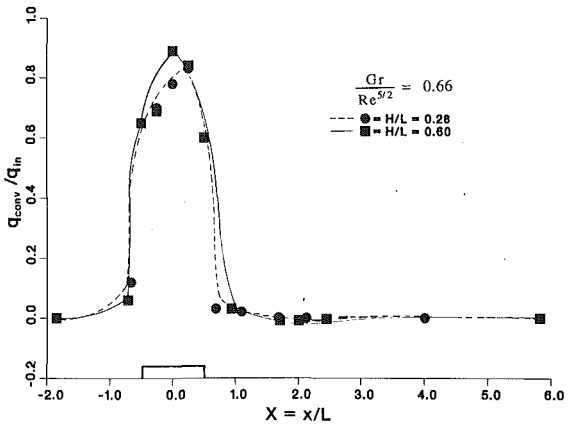

Fig. 8 Surface heat flux distribution at Re = 435 and Gr = 2.6 × 10^6

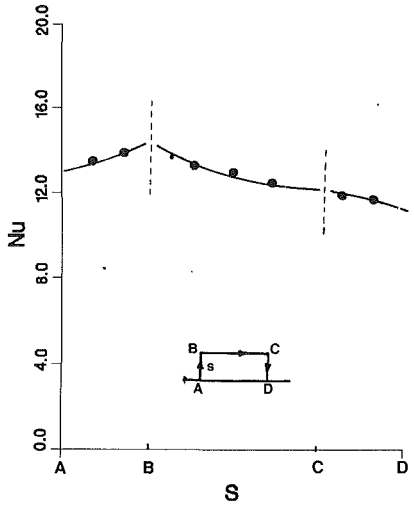

Fig. 9 Variation of the local Nusselt number Nu along the heat source module surface for *H/L* = 0.60 at Re = 435 and Gr = 2.6 × 10^6

total energy input at the module surface, $q(L+2H)$, is unchanged, even though the heat flux q at the module surface decreases with an increase in the module thickness. Thus, the thickness has little influence on the maximum value of the surface temperature variation. This explanation is further supported by the measurement of the variation of the local heat flux input into the fluid with the longitudinal distance X.

The variation of the convective heat flux measured by the heat flux gages is shown in Fig. 8. As seen in this figure, the convected energy ratio (q_{conv}/q) is somewhat increased near the heat source module with an increase in the module thickness. While the idealized variation is the step change in the heat flux over the heat module surface, the heat flux variation is found to be spread out over a much larger distance. This implies that the longitudinal conduction effect is very significant even though the plate is relatively thin and well insulated at the back surface. A similar effect has been observed in pure natural convection (Goel and Jaluria, 1986). More heat is convected upstream (around $X=-1$) of the heat module than is convected downstream (around $X=1.0$). This indicates that most of the conducted heat to the plate upstream of the source is convected to the fluid due to the external flow. A small negative value in the measured heat flux variation is observed in the range $X=1.0$–2.0 for $H/L=0.60$. A possible explanation for this observation is that conduction effects dominate near the module, so that the plate region near the module gets heated up. However, the heated air flows downstream due to buoyancy leading to the air temperature near the plate becoming higher than the surface temperature in the region $X=1.0$–2.0. Still farther downstream, the adiabatic condition at the surface is closely maintained.

The local Nusselt number Nu along the surface of the module may be expressed in terms of the measured gradient at the module surface or of the measured surface heat flux and the surface temperature. Thus,

$$\mathrm{Nu}=\frac{hL}{k}=$$

$$\frac{-\left.\frac{\partial T}{\partial y}\right|_w}{T_s-T_a}L=\frac{q_{conv}L}{(T_s-T_a)k} \qquad \text{(top face of the module)} \quad (3)$$

$$\mathrm{Nu}=\frac{-\left.\frac{\partial T}{\partial x}\right|_w}{T_s-T_a}L$$

$$=\frac{q_{conv}L}{(T_s-T_a)k} \qquad \text{(left and right faces of the module)} \quad (4)$$

Here, the subscript w represents the relevant wall or surface. Also,

$$q_{conv}=q-q_{cond} \qquad (5)$$

Here, q is the surface heat flux supplied by the electrical power. The heat flux conducted from the module to the test plate, q_{cond}, is measured by the heat flux gages mounted on the backside of the heating strip in the module. The temperature gradients at the surface are obtained by using a second-order least-square curve fit to the measurement temperature profiles. The local Nusselt numbers obtained by these two methods were found to agree closely with each other. The mean Nusselt number $\overline{\mathrm{Nu}}$ for each surface is calculated as

$$\overline{\mathrm{Nu}}=\frac{1}{A}\int_A \mathrm{Nu}\,dA \qquad (6)$$

where A is the corresponding surface area of the module exposed to air.

Since the uncertainty in each physical measurement was estimated, an uncertainty analysis for the experimental results is performed by the technique suggested by Moffat (1982, 1985). For instance, a simple determination of the relative uncertainty in the local Nusselt number, $\delta\mathrm{Nu}/\mathrm{Nu}$, can be obtained using equations (3) or (4).

$$\frac{\delta\mathrm{Nu}}{\mathrm{Nu}}=\left[\left(\frac{\delta q_{conv}}{q_{conv}}\right)^2+\left(\frac{\delta T_s}{T_s-T_a}\right)^2+\left(\frac{\delta T_a}{T_s-T_a}\right)^2+\left(\frac{\delta L}{L}\right)^2+\left(\frac{\delta k}{k}\right)^2\right]^{1/2} \qquad (7)$$

Since the error of the thermal conductivity, k, was estimated to be ±2.5 percent under the experimental conditions considered, the relative uncertainty in the local Nusselt number Nu was calculated to be 6 percent using equation (7). Similarly, the relative uncertainties in Re and Gr were calculated to be 5 and 7 percent using equation (2), respectively.

The variation of the local Nusselt number Nu with the location on the heat source module with $H/L=0.6$ is shown in Fig. 9 at Re = 435 and Gr = 2.6×10^6. The s coordinate employed for the local Nusselt number distribution includes both the vertical and the horizontal surfaces of the module. Comparisons are made with analytical solutions for forced convection cases over a semi-infinite flush heat source with constant heat flux (Kays and Crawford, 1980) and with the available numerical results associated with laminar forced flow over a forward-facing step (Baron et al., 1986). A quantitative com-

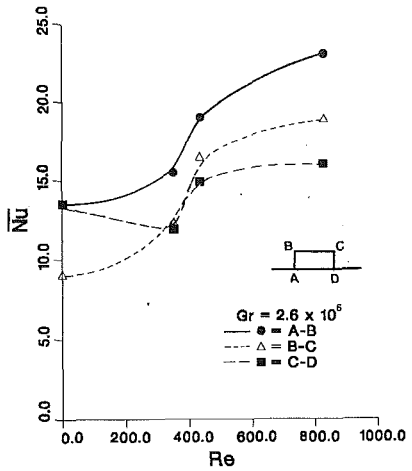

Fig. 10 Variation of the mean Nusselt number $\overline{Nu}$ with Re for $H/L = 0.28$ at $Gr = 2.6 \times 10^6$

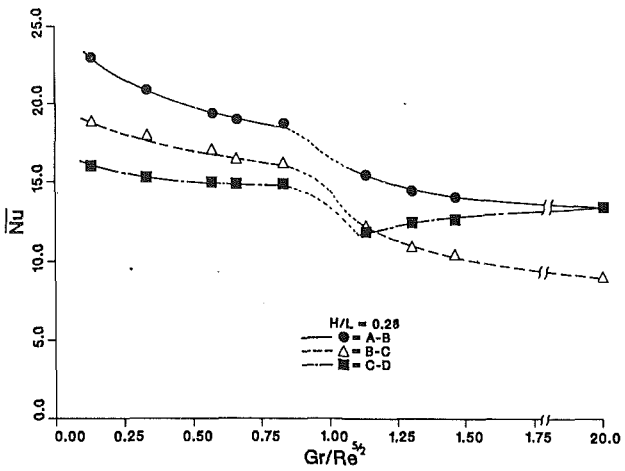

Fig. 12 Variation of the mean Nusselt number $\overline{Nu}$ with $Gr/Re^{5/2}$ for $H/L = 0.28$.

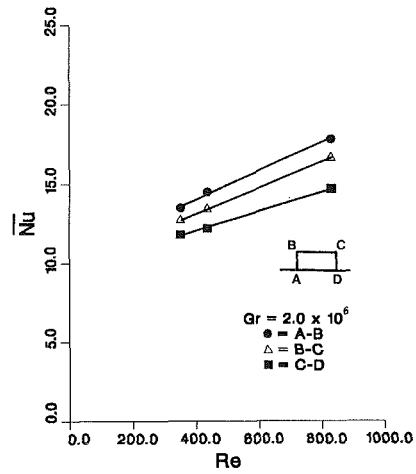

Fig. 11 Variation of the mean Nusselt number $\overline{Nu}$ with Re for $H/L = 0.60$ at $Gr = 2.0 \times 10^6$

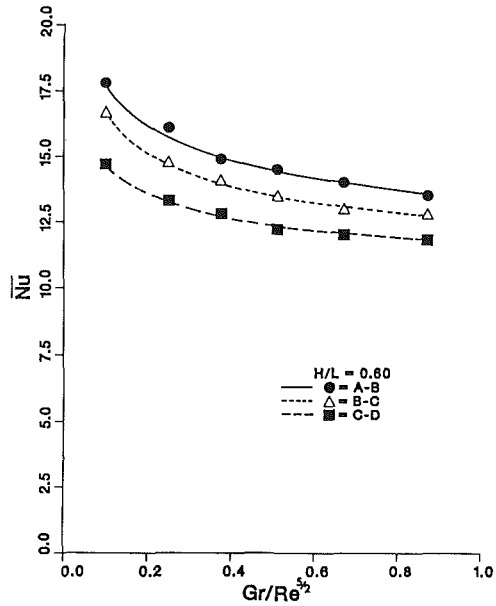

Fig. 13 Variation of the mean Nusselt number $\overline{Nu}$ with $Gr/Re^{5/2}$ for $H/L = 0.60$.

parison is not possible, but similar trends are observed qualitatively. The heat transfer rate is seen to increase up to the top corner of the left face of the module (B in Fig. 9). A maximum in the heat transfer rate is observed near this corner, followed by a gradual decay. While a recirculating flow occurs behind the module, no recirculation was observed ahead of the module for Reynolds numbers less than 1000 (Davalath and Bayazitoglu, 1987). As the air flow turns around the left top corner of the module without recirculation, the Nusselt number reaches a maximum, since a secondary boundary layer begins at the leading edge of the top face of the module.

The mean Nusselt number $\overline{Nu}$ for $H/L = 0.28$ is shown in Fig. 10 at $Gr = 2.6 \times 10^6$. The experimental value of the mean Nusselt number in natural convection is found to be higher than the calculated value from the empirical expression given by Steinberg (1980) by about 10 percent for the vertical surfaces (right and left faces of the module) and by about 20 percent for the horizontal surface (top face of the module). While the formulae given by Steinberg (1980) are based on an isolated vertical or horizontal surface, the geometry in this experiment has a combination of the vertical and horizontal surfaces. In this configuration, each surface influences the buoyancy force due to the other surfaces. This results in an increase in the heat transfer rate, above the individual surface results. In mixed convection, the mean Nusselt numbers at the left face and at the top face of the module increase with an increasing Reynolds number. This change is seen to be rapid in the Reynolds number range of $Re = 350$–430. This is the transition region from a natural convection dominated flow to a forced convection dominated flow.

The above transition in the flow has a big influence on the heat transfer rate. For the right face of the module (surface C–D), the mean Nusselt number decreases with an increase in the Reynolds number in the natural convection dominated region. A rapid increase is observed during the transition, followed by a gradual increase in the forced convection dominated regions. This result indicates that a flow velocity that puts the flow in the forced convection dominated region, just outside the transition region, is recommended. This is because a small increase in the velocity in the transition region changes the heat transfer rate by a relatively large amount. It is also interesting to note that while the mean Nusselt number for the right face of the module (surface C–D) is higher than that for the top face (surface B–C) in a natural convection dominated flow, it becomes gradually lower than the mean Nusselt number for the top face as the flow undergoes transition to a forced convection dominated circumstance.

Figure 11 shows the variation of the mean Nusselt number for $H/L = 0.60$ and $Gr = 2.0 \times 10^6$. The region investigated is found to be a forced convection dominated one. The trends observed are found to be similar to those at $H/L = 0.28$ in the forced convection dominated region. The mean value of the

Nusselt number at the left face of the module (surface A–B) is always found to be the largest among the three faces for both cases of $H/L = 0.28$ and 0.60 since this surface A–B is facing the external flow. This implies that it is advantageous, in cooling, if the surface with a higher heat flux dissipation in the module is positioned facing the external flow, when the heat fluxes at the various module surfaces are not equal.

The variation of the mean Nusselt number $\overline{Nu}$ with $Gr/Re^{5/2}$ for $H/L = 0.28$ and $H/L = 0.60$ is shown in Figs. 12 and 13, respectively. As seen in Fig. 12, the mean Nusselt number for each surface changes rapidly over the transition range of $Gr/Re^{5/2} = 0.9$ to 1.1. It is found, by comparing Figs. 12 and 13, that the mean Nusselt number for $H/L = 0.28$ is higher than that for $H/L = 0.60$, for a given mixed convection parameter, $Gr/Re^{5/2}$. This is expected since the total heat input into the module surface at $H/L = 0.28$ is 40 percent higher than that at $H/L = 0.60$ for the same Grashof number, with a fixed Reynolds number.

An attempt was made to correlate the extensive data taken to obtain the dependence to the mean Nusselt number $\overline{Nu}$ on $Gr/Re^{5/2}$. The correlation between $\overline{Nu}$ and $Gr/Re^{5/2}$ can be expressed for surfaces A–B, B–C, and C–D (Fig. 9), respectively, as:

for $H/L = 0.28$ and $0 < Gr/Re^{5/2} < 0.9$:

$$\overline{Nu} = 20.10\left(\frac{Gr}{Re^{5/2}}\right)^{-0.069}; \quad \overline{Nu} = 17.29\left(\frac{Gr}{Re^{5/2}}\right)^{-0.047}; \quad \overline{Nu} = 15.20\left(\frac{Gr}{Re^{5/2}}\right)^{-0.026}; \tag{8}$$

for $H/L = 0.28$ and $Gr/Re^{5/2} > 1.1$:

$$\overline{Nu} = 14.83\left(\frac{Gr}{Re^{5/2}}\right)^{-0.033}; \quad \overline{Nu} = 11.50\left(\frac{Gr}{Re^{5/2}}\right)^{-0.080}; \quad \overline{Nu} = 12.25\left(\frac{Gr}{Re^{5/2}}\right)^{0.033}; \tag{9}$$

for $H/L = 0.60$ and $0 < Gr/Re^{5/2} < 0.9$:

$$\overline{Nu} = 13.28\left(\frac{Gr}{Re^{5/2}}\right)^{-0.129}; \quad \overline{Nu} = 12.45\left(\frac{Gr}{Re^{5/2}}\right)^{-0.126}; \quad \overline{Nu} = 11.52\left(\frac{Gr}{Re^{5/2}}\right)^{-0.105}; \tag{10}$$

The correlation coefficients for the above equations that provide a best fit to the experimental results were calculated to be larger than 0.98. This implies a fairly good representation of the data by means of these equations, for the experimental conditions considered.

All the experimental results presented in this paper compare favorably with earlier numerical and experimental work. Unfortunately, a quantitative comparison is not possible because of lack of data for the particular configuration and parametric ranges considered. However, comparisons could be made for the pure natural convection and forced convection cases, with flush-mounted sources. Fairly good agreement with the earlier experimental work was obtained. Most of the numerical work has assumed adiabatic conditions at the surface, without considering the conjugate transport that exists in practice. Therefore, only a qualitative comparison could be made, indicating similar trends. Clearly, additional numerical work is needed on this problem to provide a better understanding of the basic processes involved and to help in the design of the relevant thermal systems.

Conclusions

An experimental study of the mixed convective heat transfer from a thermal source module mounted on a horizontal insulated plate has been carried out. The heat source and the plate are taken as large in the transverse direction so that the flow may be assumed to be two dimensional. The effects of the mixed convection parameter and of the module thickness on the thermal field and on the heat transfer were investigated in detail.

The thermal boundary layer thickness is seen to increase with a decrease in the Reynolds number and with an increase in the module thickness. This is related to the temperature profiles in the flow. However, the thickness of the module has little influence on the surface temperature distribution. This temperature distribution is shifted gradually downstream as the Reynolds number is increased. It was also found that, even though most of the energy input was eventually lost to the air, the longitudinal conduction in the plate spreads out the region over which the energy input occurs and, thus, affects the resulting local transport substantially.

The locations of the maximum temperature and the temperature rise are affected greatly by the mixed convection parameter, $Gr/Re^{5/2}$. A transition from a natural convection dominated flow to a forced convection dominated flow is observed between the mixed convection parameter values $Gr/Re^{5/2} = 0.9$ and 1.1. The maximum surface temperature occurs at the top face of the module in the natural convection dominated flow and at the right face of the module in the forced convection dominated flow. The temperature rise is found to increase with a decrease in the Reynolds number and with an increase in the Grashof number. The maximum local heat transfer rate is obtained at the left top corner of the module because of the beginning of a secondary boundary layer at this point. As expected, the heat transfer rates in the forced convection dominated flow are found to be much higher than those in the natural convection dominated flow.

Acknowledgments

The authors acknowledge the support of the National Science Foundation through Grant No. CBT-84-15364 for this work.

References

Afrid, M., and Zebib, A., 1989, "Natural Convection Cooling of Heated Components Mounted on a Vertical Wall," *Numerical Heat Transfer*, Vol. 15, pp. 243–259.

Baron, A., Tsou, F.-K., and Aung, W., 1986, "Flow Field and Heat Transfer Associated With Laminar Flow in a Forward-Facing Step," *Proceedings of the 8th International Heat Transfer Conference*, San Francisco, CA, Hemisphere Pub. Corp., New York, Vol. 2, pp. 1077–1082.

Bayazitoglu, Y., and Davalath, J., 1989, "Combined Forced and Free Convection Cooling of Heated Blocks," AIAA Paper No. 89-0425.

Carey, V. P., and Mollendorf, J. C., 1977, "The Temperature Field Above a Concentrated Heat Source on a Vertical Adiabatic Surface," *International Journal of Heat and Mass Transfer*, Vol. 20, pp. 1059–1067.

Davalath, J., and Bayazitoglu, Y., 1987, "Forced Convection Cooling Across Rectangular Blocks," ASME JOURNAL OF HEAT TRANSFER, Vol. 109, pp. 321–328.

Goel, S., and Jaluria, Y., 1986, "Thermal Transport From an Isolated Heated Source on a Vertical or Inclined Surface," *Proceeding of the 8th International Heat Transfer Conference*, San Francisco, CA, Hemisphere Pub. Corp., New York, Vol. 3, pp. 1341–1346.

Jaluria, Y., and Gebhart, B., 1977, "Buoyancy-Induced Flow Arising From a Line Thermal Source on an Adiabatic Vertical Surface," *International Journal of Heat and Mass Transfer*, Vol. 20, pp. 153–157.

Jaluria, Y., 1980, *Natural Convection Heat and Mass Transfer*, Pergamon Press, United Kingdom.

Jaluria, Y., 1982a, "Buoyancy-Induced Flow Due to Isolated Thermal Sources on a Vertical Surface," ASME JOURNAL OF HEAT TRANSFER, Vol. 104, pp. 223–227.

Jaluria, Y., 1982b, "Mixed Convection in a Wall Plume," *Computers and Fluids*, Vol. 10, pp. 95–105.

Jaluria, Y., 1984, "Numerical Study of the Thermal Processes in a Furnace," *Numerical Heat Transfer*, Vol. 7, pp. 211–224.

Jaluria, Y., 1986, "Mixed Convection Flow Over Localized Multiple Thermal Sources on a Vertical Surface," *Physics of Fluids*, Vol. 29, pp. 934–940.

Kays, W., and Crawford, M., 1980, *Convective Heat and Mass Transfer*, McGraw-Hill, New York.

Kennedy, K. J., and Zebib, A., 1983, "Combined Free and Forced Convection Between Horizontal Parallel Planes: Some Case Studies," *International Journal of Heat and Mass Transfer*, Vol. 26, pp. 471–474.

Kraus, A. D., and Bar-Cohen, A., 1983, *Thermal Analysis Control of Electronic Equipment*, Hemisphere Pub. Corp., New York.

Milanez, L. F., and Bergles, A. E., 1986, "Studies on Natural Convective Heat Transfer From Thermal Sources on a Vertical Surface," *Proceedings of the 8th International Heat Transfer Conference*, San Francisco, CA, Hemisphere Pub. Corp., New York, Vol. 3, pp. 1347–1352.

Moffat, R. J., 1982, "Contributions to the Theory of Single-Sample Uncertainty Analysis," ASME *Journal of Fluids Engineering*, Vol. 104, pp. 250–260.

Moffat, R. J., 1985, "Using Uncertainty Analysis in the Planning of an Experiment," ASME *Journal of Fluids Engineering*, Vol. 107, pp. 173–178.

Park, K.-A., and Bergles, A. E., 1987, "Natural Convection Heat Transfer Characteristics of Simulated Microelectronic Chips," ASME JOURNAL OF HEAT TRANSFER, Vol. 109, pp. 90–96.

Pera, L., and Gebhart, B., 1975, "Laminar Plume Interactions," *Journal of Fluid Mechanics*, Vol. 68, pp. 259–271.

Rao, K. V., Armaly, B. F., and Chen, T. S., 1984, "Analysis of Laminar Mixed Convection Plumes Along Vertical Adiabatic Surfaces," ASME JOURNAL OF HEAT TRANSFER, Vol. 106, pp. 552–557.

Sparrow, E. M., Patankar, S. V., and Abdel-Washed, R. M., 1978, "Development of Wall and Free Plumes Above a Heated Vertical Plate," ASME JOURNAL OF HEAT TRANSFER, Vol. 100, pp. 184–190.

Steinberg, D. S., 1980, *Cooling Techniques for Electronic Equipment*, Wiley, New York.

Tewari, S., Jaluria, Y., and Goel, S., 1987, "Natural and Mixed Convective Transport From Finite-Size Heat Sources on a Flat Plate in Cooling of Electronic Equipment," ASME HTD-Vol. 89, pp. 1–9.

Than, H. T., and Bayazitoglu, Y., 1988, "An Experimental Study of Forced Cooling Over Heated Rectangular Blocks," *Proceedings of the 1st World Conference on Experimental Heat Transfer, Fluid Mechanics, and Thermodynamics*, Dubrovnik, Yugoslavia, pp. 1228–1234.

Zebib, A., and Wo, Y. K., 1986, "A Two-Dimensional Conjugate Heat Transfer Model for Forced Air Cooling of an Electronic Device," *Proceedings IEEE Electronic Packaging Conference*, Orlando, FL.

Theory of Heat Transfer From a Surface Covered With Hair

A. Bejan
J. A. Jones Professor of Mechanical Engineering, Department of Mechanical Engineering and Materials Science, Duke University, Durham, NC 27706
Fellow ASME

This paper describes the fundamental mechanisms of heat transfer through a surface covered with perpendicular hair strands of uniform density. An air flow parallel to the skin seeps through the spaces created between the hair strands. It is shown that the total heat transfer rate from the surface is due to two contributions: (i) the heat conducted through the hair strands, which act as fins, and (ii) the heat convected from the bare portions of the skin. When the air flow is slow enough to conform to the Darcy regime, there exists an optimum hair strand diameter for which the total heat transfer rate is minimum. The optimum diameter increases as the square root of the length swept by the air flow, that is the linear size of the body of the animal covered with hair.

1 Introduction

Like everything else that we see from the first moments of conscious life, hair and fur are things that we take for granted. Their purpose seems obvious not only with respect to our own needs, but also for the survival of numerous other species.

The insulating effect of hair can be reasoned away through the argument that when the hair strands are sufficiently dense they trap a blanket of air in the tight spaces created between the strands. Well known for its low thermal conductivity, this air blanket insulates the warm skin against the colder atmosphere.

The hair-covered surface is considerably more interesting when approached from the point of view—the function—of the individual hair strand. The thermal conductivity of hair material (roughly that of human skin, 0.37 W/m K; see Incropera and DeWitt, 1985) is 14 times greater than that of ambient air (0.026 W/m K). It seems that one effect of the hair strands is to "extend" the warm surface into the cold atmosphere, in the same way that a population of cylindrical spines (pin fins) extends the heat transfer surface of a heat exchanger. This finning effect is, most certainly, an unwanted byproduct of the true function of the hair strands, which is to slow down the breeze that would otherwise blow by.

The objective of this paper is to describe the fundamental heat transfer mechanism of a surface covered with hair, particularly the competition between the detrimental augmentation effect provided by the hair strands, and the beneficial insulation effect provided by the trapped air. The hairy surface has a complicated geometry; therefore a great effort will be made to simplify the surface model and the ensuing analysis, in order to be able actually to "see" the heat transfer contributions made by the hair strands and the bare portions of the skin surface.

2 Model

The most essential features of the geometry of an actual surface covered with hair are retained in the model presented in Fig. 1. The skin surface is connected to a large number of perpendicular strands of hair, the density of which is assumed constant

$$n = \frac{\text{number of strands of hair}}{\text{unity area of skin surface}} \tag{1}$$

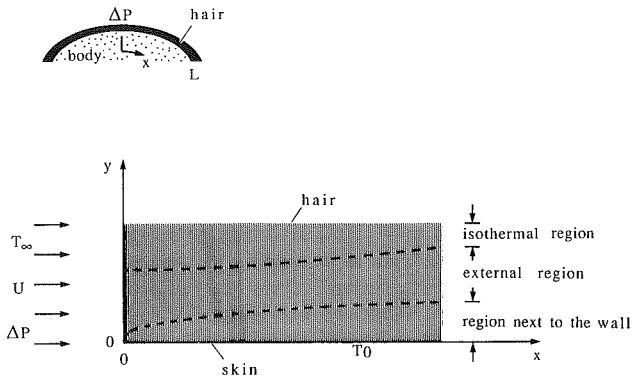

Fig. 1 Two-dimensional model for flow and hair growth near the skin

The hair population density n is related to the porosity of the "hair + air" medium that resides above the skin

$$\phi = \frac{\text{air volume}}{\text{total volume}} = 1 - nA_s \tag{2}$$

Each strand of hair is modeled as a cylinder with the cross section A_s. A more specific strand-shape model (namely, cylinder with circular cross section) will be adopted in section 6.

Parallel to the skin surface, and through the porous structure formed by the parallel hair strands, flows a uniform stream of air of velocity U. This stream is driven longitudinally by the dynamic pressure rise formed over that portion of the animal's body against which the ambient breeze stagnates. The longitudinal length L swept by the air flow is a measure of the linear size of the animal. The constant air velocity U is a quantity averaged over the volume occupied by air. It is assumed that the strand-to-strand distances are small enough (or that the "pore" Reynolds number is small; see the end of section 6) so that the air flow behaves according to the Darcy law, with apparent slip at the skin surface.

This flow model is the simplest of the flows identified in previous studies of forced convection in porous media (Vafai and Tien, 1981; Vafai, 1984; Poulikakos and Renken, 1987; Poulikakos and Kazmierczak, 1987; Renken and Poulikakos, 1988). The new features of the present system are the phenomenon of transverse conduction along the hair strands, and the absence of local thermal equilibrium. These features are described next.

At every point in the two-dimensional (x, y) space occupied by the porous medium described above, we distinguish two temperatures: the temperature of the solid structure (the local hair strand), T_s, and the temperature of air that surrounds the

Contributed by the Heat Transfer Division for publication in the JOURNAL OF HEAT TRANSFER. Manuscript received by the Heat Transfer Division March 2, 1989; revision received December 6, 1989. Keywords: Finned Surfaces, Forced Convection, Porous Media.

strand, T_a. Both T_s and T_a are functions of x and y. The transfer of heat from the skin to the atmosphere is driven by the overall temperature difference $(T_0 - T_\infty)$, where T_0 is the skin temperature and T_∞ the uniform temperature of the ambient air that enters the porous structure. The temperature of the interstitial air, T_a is equal to the constant temperature T_∞ in the entry plane $x = 0$.

The local strand and air temperatures (T_s, T_a) can be determined by solving the two equations that govern the conservation of energy at every point (x, y). For the solid structure, the appropriate energy equation is the classical conduction equation for a fin (in this case, a single strand of hair)

$$k_s A_s \frac{\partial^2 T_s}{\partial y^2} - h p_s (T_s - T_a) = 0 \tag{3}$$

The thermal conductivity of the strand, k_s, and the perimeter-averaged heat transfer coefficient, h, are both constant. It is shown later that the constancy of h is a result of the assumed low Reynolds number of the air flow that seeps through the hair strands.

The second energy conservation statement refers to the air space alone, in which (ρc_P) and k_a are the heat capacity and thermal conductivity of air

$$\rho c_P U \frac{\partial T_a}{\partial x} = k_a \frac{\partial^2 T_a}{\partial y^2} + n p_s h (T_s - T_a) \tag{4}$$

On the left-hand side of this equation, we see only one convection term, because the air-space-averaged velocity U points strictly in the x direction. The first term on the right-hand side of the equation accounts for air conduction in the transverse direction (y). By not writing the longitudinal conduction term $k_a \partial^2 T_a / \partial x^2$, we are assuming that the flow region in which the effect of transverse air conduction is important is thin. This air thermal boundary layer will be analyzed starting with equation (17).

The last term in equation (4) accounts for the "volumetric heat source" effect that is due to the contact between the air stream and the local (warmer) hair strand. Note the multiplicative role of the strand density n in the makeup of this term: The product (np_s) represents the total contact area between hair and air, expressed per unit of air volume. The heat source term of equation (4) is the air-side reflection of the heat sink term (the second term) encountered in the fin conduction equation (3).

In an air region that is sufficiently close to the skin, the air stream is warmed up mainly by contact with the skin, i.e., not by the contact with the near-skin area of the hair strands. Consequently, in equation (4) the heat source term $np_s h(T_s - T_a)$ can be neglected, as in the analysis of section 4. On the other hand, sufficiently far from the skin, the most of the heating of the air stream is effected by the hair strands that impede the flow. In the energy balance of this external flow we can neglect the vertical conduction term of equation (4). Put another way, the external region is one where the interstitial air is practically isothermal in the y direction, and in contact with relatively warmer hair strands. This is why in that region the $k_a \partial^2 T_a / \partial y^2$ term of equation (4) can be neglected while retaining the $np_s h(T_s - T_a)$ term.

3 The External Region

We begin with the analysis of the external flow region, for which equation (4) assumes the simpler form

$$\rho c_P U \frac{\partial T_a}{\partial x} = n p_s h (T_s - T_a) \tag{5}$$

Nomenclature

A_s = cross-sectional area of hair strand, m^2
b = dimensionless factor, equation (A.1)
B = modified conductivity ratio, equation (18)
c_P = air specific heat at constant pressure
C = dimensionless group, equation (33)
D = diameter of hair strand, m
D_h = hydraulic diameter of air space, m, equation (40)
$\tilde{D}$ = dimensionless strand diameter, equation (46)
$\tilde{D}_{opt}$ = optimum strand diameter, equation (48)
f = friction factor, equation (41)
h = strand-air heat transfer coefficient, W/m^2K
k_a = air thermal conductivity, W/m K
k_s = strand thermal conductivity, W/m K
k_z = Kozeny constant, equation (39)
K = permeability, m^2
L = length swept by air flow, m
$\tilde{L}$ = dimensionless length, equation (46)
n = number of hair strands per unit area, m^{-2}
N_r = number of tube rows
Nu = overall Nusselt number, equation (32)
Nu_{min} = minimum Nusselt number, equation (49)
p_s = perimeter of strand cross section, m
ΔP = pressure difference that drives the air flow, N/m^2
Pr = Prandtl number
q_1 = heat transfer rate through one hair strand, W
q' = total heat transfer rate through hair-covered surface, W/m
q'_a = heat transfer rate through all the bare portions of the skin, W/m
q''_a = heat flux through a bare portion of the skin, W/m^2
q'_s = heat transfer rate contributed by all the hair strands, W/m
Re_D = Reynolds number $= UD/\nu$
T = temperature, K
T_a = air temperature, K
T_s = hair strand temperature, K
T_∞ = ambient air temperature, K
u_{max} = maximum fluid velocity between cylinders in crossflow, m/s
U = velocity averaged over the air space, m/s
x = longitudinal coordinate, m
X_t = transversal center-to-center spacing between cylinders
X_l = longitudinal center-to-center spacing between rows
y = transversal coordinate, m
α = thermal diffusivity, m^2/s
δ = conduction penetration length along the hair strand
δ_0 = thickness of air boundary layer
η = dimensionless transversal coordinate, equation (8)
θ_a = dimensionless air temperature, equation (9)
θ_s = dimensionless strand temperature, equation (9)
θ_0 = dimensionless temperature at the interface between the inner and outer regions
μ = viscosity of air, kg/m s
ν = kinematic viscosity of air, m^2/s
ξ = dimensionless longitudinal coordinate, equation (8)
ξ_L = value of ξ at $x = L$
ρ = air density, kg/m^3
ϕ = porosity

Equations (5) and (3) can be nondimensionalized

$$\frac{\partial^2\theta_s}{\partial\eta^2}=\theta_s-\theta_a \tag{6}$$

$$\frac{\partial\theta_a}{\partial\xi}=\theta_s-\theta_a \tag{7}$$

by defining the following variables:

$$\xi=\frac{x}{\rho c_P U/np_s h} \qquad \eta=\frac{y}{(k_s A_s/hp_s)^{1/2}} \tag{8}$$

$$\theta_s=\frac{T_s-T_\infty}{T_0-T_\infty} \qquad \theta_a=\frac{T_a-T_\infty}{T_0-T_\infty} \tag{9}$$

Noteworthy among these is the definition of η, in which the transverse length scale $(k_s A_s/hp_s)^{1/2}$ is the classical conduction penetration length along a one-dimensional fin.

The boundary conditions that apply to equations (6) and (7) are the statement that the entering air stream is isothermal (T_∞)

$$\theta_a=0 \quad \text{at} \quad \xi=0 \tag{10}$$

and the "fin" conditions for each strand of hair

$$\theta_s=1 \quad \text{at} \quad \eta=0 \tag{11}$$

$$\theta_s\to 0 \quad \text{at} \quad \eta\to\infty \tag{12}$$

A closed-form solution to the external region problem (6)–(12) can be obtained based on the integral method, in which the only additional assumption concerns the shape of the θ_s and θ_a profiles. Noting that at the $\xi=0$ entrance to the porous medium the exact θ_s solution to equation (6) is of the type $\exp(-\eta)$, it makes sense to choose exponential profiles for the two unknown temperature distributions

$$\theta_s=\exp\left[-\frac{\eta}{\delta(\xi)}\right] \tag{13}$$

$$\theta_a=\theta_0(\xi)\exp\left[-\frac{\eta}{\delta(\xi)}\right] \tag{14}$$

The unknown functions $\delta(\xi)$ and $\theta_0(\xi)$ are the dimensionless thermal penetration distance along the hair strand, and the dimensionless air temperature as $\eta\to 0$ (that is, at the interface between the external region and the near-skin thermal boundary layer analyzed in section 4). Note that the profile (13) satisfies the fin boundary conditions (11) and (12): The second of these conditions states that the strand of hair is consistently longer than the distance to which conduction penetrates along the strand. The validity of the assumption that the external region is considerably thicker than the region next to the wall is discussed later in conjunction with equation (36).

The functions δ and θ_0 are determined by substituting expressions (13) and (14) into the two equations obtained by integrating equations (6) and (7) from $\eta=0$ to $\eta=\infty$. The algebra associated with this operation and the application of the $\xi=0$ condition (10) can be omitted. The end results are stated implicity by

$$\frac{1}{2}(\delta^2-1)+\ln\delta=\xi \tag{15}$$

$$\theta_0=1-\frac{1}{\delta^2} \tag{16}$$

Figure 2 shows that δ increases monotonically in the downstream direction. When the dimensionless coordinate ξ is smaller than 1, the thermal penetration distance δ is approximately equal to 1. At longitudinal positions where ξ is greater than 1, the length of conduction penetration along the hair strand increases approximately as $(2\xi)^{1/2}$. The monotonic relationship between δ and ξ implies that θ_0 approaches the value 1 as ξ increases. This behavior corresponds to the case where the hair-covered surface is so long that the permeating air stream has had enough time to warm up to the temperature of the surface (T_0).

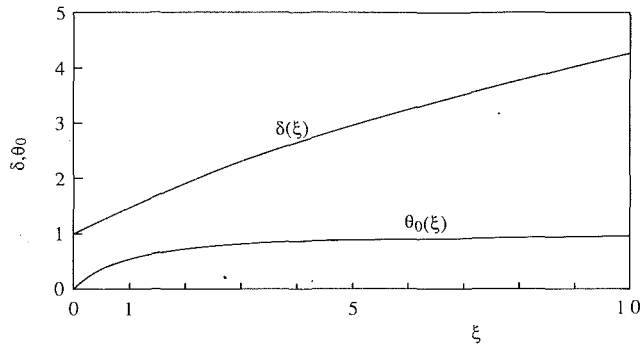

Fig. 2 Thermal penetration distance along the hair strand (δ), and air temperature at the interface between the outer and inner regions (θ_0)

4 The Region Next to the Wall

The decrease in air temperature between the surface of the skin ($\theta_a=1$) and the highest air temperature featured in the analysis of the external region (θ_0) is smoothed by a thermal boundary layer in which the convection term of equation (4) is balanced by the transverse diffusion term. Therefore, neglecting the last term in equation (4), and using the dimensionless notation (8) and (9), the equation for θ_a is

$$B\frac{\partial\theta_a}{\partial\xi}=\frac{\partial^2\theta_a}{\partial\eta^2} \tag{17}$$

where the dimensionless group B is defined as

$$B=nA_s\frac{k_s}{k_a}=(1-\phi)\frac{k_s}{k_a} \tag{18}$$

The value of B is greater than 1, because the conductivity ratio k_s/k_a is a large number. The boundary conditions that apply to equation (17) are the entrance condition (10) coupled with two conditions in the transverse direction

$$\theta_a=1 \quad \text{at} \quad \eta=0 \tag{19}$$

$$\theta_a\cong\theta_0 \quad \text{when} \quad \eta B^{1/2}\gg 1 \tag{20}$$

Writing $\delta_0(\xi)$ for the dimensionless thickness of the near-skin boundary layer, an integral solution to the problem (17)–(20) can be determined by assuming a θ_a profile shape that satisfies the transverse boundary conditions (19) and (20), as well as the entrance conditions (10). These conditions are met by the exponential profile

$$\theta_a=(1-\theta_0)\exp\left(-\frac{\eta}{\delta_0}B^{1/2}\right)+\theta_0 \tag{21}$$

which satisfies the entrance condition if $\delta_0=0$ at $\xi=0$. Integrating equation (17) from $\eta=0$ to a sufficiently large η such that $\eta B^{1/2}\gg 1$, and using the θ_a profile (21), we obtain

$$\frac{d}{d\xi}\left(\frac{\delta_0}{\delta^2}\right)=\frac{1}{\delta^2\delta_0} \tag{22}$$

Eliminating ξ between equations (22) and (15), and integrating from the entrance position ($\delta=1$, $\delta_0=0$) yields, finally,

$$\delta_0=(\delta^2-1)^{1/2}\left(\frac{3}{2}\delta^2+\frac{1}{2}\right)^{1/2} \tag{23}$$

In combination with the $\delta(\xi)$ expression listed in equation (15), this last result delivers the relationship between the thickness of the region next to the wall and the longitudinal position. Figure 3 shows the manner in which the δ_0 thickness increases

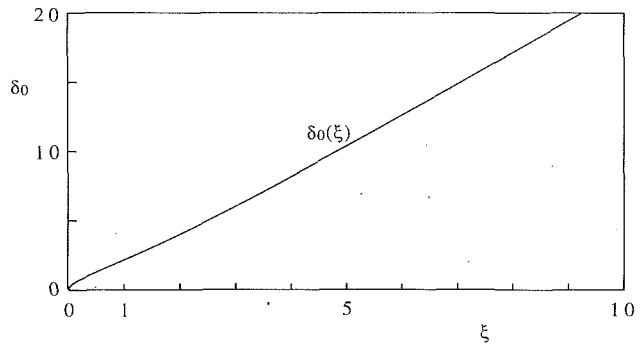

Fig. 3 Thickness of the air boundary layer (δ_0)

in the downstream direction. The small-ξ asymptote of this function is $\delta_0 = (2\xi)^{1/2}$.

It is worth noting that the above solution for the air temperature in the region next to the wall has a counterpart in Vafai and Thiyagaraja's (1987) extensive study of interface heat transfer in porous media. That solution can be seen by setting $\Omega = B$, $A = 1$, and $p = 0$ in Vafai and Thiyagaraja's equation (34). The integral solution developed in equations (23) and (15) is accurate enough for the heat transfer objectives of the present study, especially if we consider the simplified, approximate character of the model of Fig. 1, and the permeability model that will be adopted in section 6.

5 The Heat Transfer Rate

Consider now the total heat transfer rate q' through the two-dimensional skin patch of length L shown in Fig. 1. The heat transfer rate q' is expressed per unit length in the direction normal to Fig. 1. This quantity is due to two contributions, the heat transfer rate through the strands of hair, q_s', and the direct convection between the skin and the air stream that flows in the x direction, q_a':

$$q' = q_s' + q_a' \tag{24}$$

The heat transfer rate contributed by all the hair strands is given by the integral

$$q_s' = \int_0^L q_1 n \, dx \tag{25}$$

in which q_1 is the heat current through one hair strand located at x,

$$q_1 = A_s k_s \left(-\frac{\partial T_s}{\partial y} \right)_{y=0} \tag{26}$$

Combining equations (25) and (26) with the θ_s definition (9) and the θ_s solution (13) and (15) leads to

$$q_s' = (T_0 - T_\infty) \left(\frac{k_s A_s}{h p_s} \right)^{1/2} \rho c_P U \int_0^{\xi_L} \frac{d\xi}{\delta(\xi)} \tag{27}$$

where ξ_L is the value reached by ξ at $x = L$.

The heat transfer contribution made by all the bare portions of the skin is

$$q_a' = \int_0^L q_a'' \phi \, dx \tag{28}$$

in which q_a'' is the local heat flux between the skin and the air that seeps through the strands of hair

$$q_a'' = k_a \left(-\frac{\partial T_a}{\partial y} \right)_{y=0} \tag{29}$$

In combination with θ_a definition (9) and the θ_a solution (14)–(16), (21), and (23), the q_a' integral can be rewritten as

$$q_a' = \frac{k_a (T_0 - T_\infty)}{(k_s A_s h p_s)^{1/2}} B^{1/2} \frac{\phi}{n} \rho c_P U \int_0^{\xi_L} \frac{1 - \theta_0(\xi)}{\delta_0(\xi)} d\xi \tag{30}$$

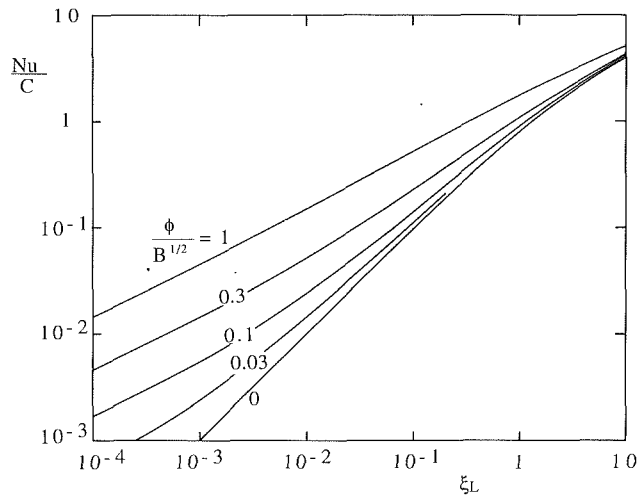

Fig. 4 Overall Nusselt number function Nu(C, ξ_L, $\phi/B^{1/2}$)

The total heat transfer rate q' obtained by adding equations (27) and (30) can be summarized as

$$\mathrm{Nu} = C \left[\delta(\xi_L) - \frac{1}{\delta(\xi_L)} + \frac{\phi}{B^{1/2}} \int_0^{\xi_L} \frac{1 - \theta_0(\xi)}{\delta_0(\xi)} d\xi \right] \tag{31}$$

where

$$\mathrm{Nu} = \frac{q'}{k_a (T_0 - T_\infty)} \tag{32}$$

$$C = \frac{U}{\alpha} \left(\frac{k_s A_s}{h p_s} \right)^{1/2} \tag{33}$$

The behavior of the overall Nusselt number Nu is presented in Fig. 4. The ratio Nu/C depends only on ξ_L and the group $\phi/B^{1/2}$. The latter is a number smaller than 1 because the B number is greater than 1. Figure 4 shows that the group $\phi/B^{1/2}$ has a noticeable effect when the abscissa parameter is small. In this limit, equation (31) assumes the much simpler form

$$\mathrm{Nu} \cong C \left[\xi_L + \frac{\phi}{B^{1/2}} (2\xi_L)^{1/2} \right] \qquad (\xi_L < 1) \tag{34}$$

In the opposite limit, the Nu function behaves as

$$\mathrm{Nu} \cong C \left[(2\xi_L)^{1/2} + 1.22 \frac{\phi}{B^{1/2}} \right] \qquad (\xi_L > 1) \tag{35}$$

The theory constructed in this paper is based on the assumption that the external region (section 3) is thicker than the region next to the wall (section 4). In dimensionless terms, this requirement reads

$$\delta(\xi_L) > \frac{\delta_0(\xi_L)}{B^{1/2}} \tag{36}$$

or, after using the δ and δ_0 solutions developed already,

$$\xi_L < \frac{B}{2}, \quad \text{when} \quad \xi_L < 1 \tag{37}$$

$$\xi_L < \frac{B}{3}, \quad \text{when} \quad \xi_L > 1 \tag{38}$$

Since B is expectedly greater than 3, the last inequality ($\xi_L < B/3$) is more general, and sums up the requirement expressed by the inequality (36). This is why the abscissa range of Fig. 4 was not extended above $\xi_L = 10$.

While comparing the thicknesses of the external region and the region next to the wall, one may be tempted to compare directly the δ values of Fig. 2 with the δ_0 values of Fig. 3. Such

a comparison would be incorrect, because the dimensionless thickness of the region next to the wall is $\delta_0/B^{1/2}$, not δ_0 [examine the argument of the exponential on the right-hand side of equation (21)].

6 Discussion

The merit of the preceding analysis is that it reduces the total heat transfer rate to a dimensionless expression that reveals the smallest number of dimensionless groups that influence q', or its dimensionless counterpart Nu. The drawback of the function $\mathrm{Nu}(C, \xi_L, \phi/B^{1/2})$ is that it obscures the influence that a physical feature of the system might have on the total heat transfer rate. The air velocity U, for example, appears in the construction of both C and ξ_L. The hair strand diameter D does not appear explicitly: Its effect is conveyed through A_s, p_s, and h.

The air seepage velocity U is not a known ("given") feature of the system. The magnitude of U depends, most certainly, on the flow conditions prevailing above the hair-strand tops, and on the geometric features (ϕ, D, L) of the hair population. For this reason, it is interesting to inquire further into the relationship between Nu and the known physical features of the system.

The model on which this discussion is based consists of four assumptions. First, it is assumed that each hair strand is a circular cylinder of diameter D, therefore

$$A_s=\frac{\pi}{4}D^2, \quad \text{and} \quad p_s=\pi D \tag{39}$$

Second, it is assumed that the air flow obeys Darcy's law

$$\phi U=\frac{K}{\mu}\frac{\Delta P}{L} \tag{40}$$

in which ϕU is the longitudinal velocity averaged over the entire volume (air + strands). In the present problem, the pressure gradient $\Delta P/L$ is "given," because it is controlled by the external flow (wind) that blows against the body of the animal. In the air region situated beyond the tips of the hair strands, the pressure gradient is maintained by the air flow, as this sweeps the curved body of the animal in the x direction (see the upper-left insert of Fig. 1). In an order of magnitude sense, the pressure rise ΔP (the pressure at the "entrance" to the problem of Fig. 1) is the same as the stagnation pressure of the external air flow. Later, in equations (48), the group $(\Delta P/\rho)^{1/2}$ will be used as reference velocity for the nondimensionalization of the physical dimensions of the system.

Third, it is assumed that the permeability of the porous medium (hair + air) obeys a relationship of the Kozeny type (Cheng 1985)

$$K=\frac{\phi^3 D^2}{k_z(1-\phi)^2} \tag{41}$$

in which the Kozeny constant k_z is a number of order 10^2. It is known that equation (41) holds very well for a porous matrix composed of identical spheres. In the appendix, it is shown that equation (41) is an adequate approximation of the permeability of a bank of cylinders in crossflow, i.e., of a porous matrix similar to the one constituted by the hair strands.

Fourth, for lack of a specific correlation linking the strand–air heat transfer coefficient (h) to the strand diameter (D) and the matrix porosity (ϕ), h will be approximated based on the analogy between friction and heat transfer. With regard to the flow through the matrix formed by parallel strands of hair, it can be shown that the hydraulic diameter of the air space is

$$D_h=\frac{\phi}{1-\phi}D \tag{42}$$

The friction factor f that corresponds to the K model (41) is

$$f=\frac{\Delta P}{\dfrac{4L}{D_h}\dfrac{1}{2}\rho U^2}=\frac{k_z}{2\mathrm{Re}_D}\frac{1-\phi}{\phi} \tag{43}$$

in which $\mathrm{Re}_D=UD/\nu$. According to the Colburn analogy between heat transfer and friction we write, approximately,

$$\frac{h}{\rho c_P U}\sim\frac{f}{2}\mathrm{Pr}^{-2/3} \tag{44}$$

Finally, using equations (43) and (44), and noting that in the case of air $\mathrm{Pr}\sim 1$, we deduce that

$$h\sim\frac{k_z}{4}\frac{1-\phi}{\phi}\frac{k_a}{D} \tag{45}$$

It is reassuring that the same order-of-magnitude conclusion is reached by recalling that in small-Re_{D_h} duct flow the heat transfer coefficient always scales as k_a/D_h (Bejan, 1984, p. 85).

In view of equations (39), (40), and (45), the C and ξ_L groups of the Nu solution assume forms that highlight the effects of hair diameter, porosity, and skin length

$$C\cong k_z^{-3/2}\left(\frac{k_s}{k_a}\right)^{1/2}\left(\frac{\phi}{1-\phi}\right)^{5/2}\frac{\tilde{D}^3}{\tilde{L}} \tag{46}$$

$$\xi_L\cong k_z^2\frac{(1-\phi)^4}{\phi^3}\frac{\tilde{L}^2}{\tilde{D}^4} \tag{47}$$

where $\tilde{D}$ and $\tilde{L}$ are two dimensionless numbers

$$\tilde{D}=\frac{D}{\nu}\left(\frac{\Delta P}{\rho}\right)^{1/2} \quad \text{and} \quad \tilde{L}=\frac{L}{\nu}\left(\frac{\Delta P}{\rho}\right)^{1/2} \tag{48}$$

The small-ξ_L asymptote (34) of the Nusselt number now reads

$$\mathrm{Nu}=\left(k_z\frac{k_a}{k_s}\right)^{1/2}\frac{(1-\phi)^{3/2}}{\phi^{1/2}}\left[\frac{\tilde{L}}{\tilde{D}}+\frac{\phi^{5/2}}{k_z(1-\phi)^2}\left(\frac{2}{B}\right)^{1/2}\tilde{D}\right] \tag{49}$$

This expression shows that a change in the strand diameter induces changes of opposite signs in the two terms listed in the square brackets. The overall Nusselt number reaches a minimum when $\tilde{D}$ assumes the optimum value

$$\tilde{D}_{\mathrm{opt}}\cong\left(\frac{k_z^2 k_s}{2k_a}\right)^{1/4}\left(\frac{1-\phi}{\phi}\right)^{5/4}\tilde{L}^{1/2} \tag{50}$$

The minimum Nu that corresponds to $\tilde{D}=\tilde{D}_{\mathrm{opt}}$ is

$$\mathrm{Nu}_{\min}\cong\left(32\frac{k_s}{k_a}\right)^{1/4}\phi^{3/4}(1-\phi)^{1/4}\tilde{L}^{1/2} \tag{51}$$

The effect of strand diameter and porosity on heat transfer is visible in closed form in equations (49)–(51). The minimum heat transfer rate (51) increases with the square root of the linear size of the body covered with hair, $\tilde{L}^{1/2}$. The optimum hair strand diameter (50) is also proportional to $\tilde{L}^{1/2}$.

The porosity has a somewhat less certain effect, in view of the approximate character of the Kozeny-type model adopted in equations (41)–(45). The optimum hair strand diameter (50) decreases as the porosity ϕ increases. The corresponding minimum Nusselt number (51) attains a maximum at an intermediate porosity level, $\phi=3/4$, and decreases rapidly as ϕ increases above 3/4.

Also noteworthy is the $\tilde{D}_{\mathrm{opt}}\sim\tilde{L}^{1/2}$ proportionality, or the conclusion that the optimum strand diameter does not increase as rapidly as the linear size of the animal. In the case of natural convection heat transfer, the optimum hair strand diameter increases as the surface height raised to the power 1/4 (Bejan, 1990). Without access to a compilation of animal hair-size measurements, it can be argued that this conclusion is supported at least qualitatively by visual observations of hair-strand sizes in mammals. It seems that in going from the rat to the buffalo the body length increases by two to three orders of magnitude, while the hair-strand diameter increases by a smaller factor.

Table A.1 Porosities and Kozeny constants for Darcy flow across the tube bundles documented by Mueller (1985), Fig. 10, p. 4-100

Configuration	X_t	X_l	ϕ	b	k_z
Staggered	1.25	1.083	0.42	73.4	119
Aligned	1.25	1.25	0.497	51	159
Staggered	1.50	1.299	0.597	22.4	90
Aligned	1.50	1.25	0.651	18.2	132

The behavior of the Nusselt number at large ξ_L values is not nearly as interesting. Substituting the new notation (46)-(48) into equation (35), we obtain

$$\mathrm{Nu} \cong \left(\frac{2k_s}{k_z k_a}\right)^{1/2} \frac{\phi}{(1-\phi)^{1/2}} \tilde{D} + \frac{1.22}{k_z^{3/2}} \frac{\phi^{7/2}}{(1-\phi)^3} \frac{\tilde{D}^3}{\tilde{L}} \tag{52}$$

Both terms on the right-hand side of equation (52) increase when $\tilde{D}$ increases. The length $\tilde{L}$ affects only the heat transfer contribution made by the bare portions of the skin.

The preceding discussion was based on a porous medium model according to which the air flow conforms to the Darcy regime, that is when the "pore" Reynolds number UD_h/ν does not exceed a number of order 10. In terms of the dimensionless variables defined in this section, the pore Reynolds number criterion reads

$$\tilde{L} > \frac{\tilde{D}^3}{10k_z} \left(\frac{\phi}{1-\phi}\right)^3 \tag{53}$$

Acknowledgments

This work was supported by the National Science Foundation through grant No. CBT-8711369. Dr. P. A. Litsek numerically evaluated the integral listed in equation (30).

References

Bejan, A., 1984, *Convection Heat Transfer*, Wiley, New York, p. 85.

Bejan, A., 1990, "Optimum Hair Strand Diameter for Minimum Free-Convection Heat Transfer From a Surface Covered With Hair," *Int. J. Heat Mass Transfer*, Vol. 33, pp. 206-209.

Cheng, P., 1985, "Geothermal Heat Transfer," in: *Handbook of Heat Transfer Applications*, 2nd ed., W. M. Rohsenow, J. P. Hartnett, and E. N. Ganic, eds., McGraw-Hill, New York, Chap. 11.

Eidsath, A., Carbonell, R. G., Whitaker, S., and Herrmann, L. R., 1983, "Dispersion in Pulsed Systems III—Comparison Between Theory and Experiments for Packed Beds," *Chem. Eng. Sci.*, Vol. 38, pp. 1803-1816.

Happel, J., 1959, "Viscous Flow Relative to Arrays of Cylinders," *AIChE J.*, Vol. 5, pp. 174-177.

Incropera, F. P., and DeWitt, D. P., 1985, *Fundamentals of Heat and Mass Transfer*, 2nd ed., Wiley, New York, pp. 766-767.

Mueller, A. C., 1985, "Process Heat Exchangers," in: *Handbook of Heat Transfer Applications*, 2nd ed., W. M. Rohsenow, J. P. Hartnett, and E. N. Ganic, eds., McGraw-Hill, New York, Chap. 4, part 2.

Poulikakos, D., and Kazmierczak, M., 1987, "Forced Convection in a Duct Partially Filled With a Porous Material," ASME JOURNAL OF HEAT TRANSFER, Vol. 109, pp. 653-662.

Poulikakos, D., and Renken, K., 1987, "Forced Convection in a Channel Filled With a Porous Medium Including the Effects of Flow Inertia, Variable Porosity and Brinkman Friction," ASME JOURNAL OF HEAT TRANSFER, Vol. 109, pp. 880-888.

Renken, K. J., and Poulikakos, D., 1988, "Experiment and Analysis of Forced Convective Heat Transport in a Packed Bed of Spheres," *Int. J. Heat Mass Transfer*, Vol. 31, pp. 1399-1408.

Vafai, K., 1984, "Convective Flow and Heat Transfer in Variable Porosity Media," *J. Fluid Mech.*, Vol. 147, pp. 233-259.

Vafai, K., and Thiyagaraja, R., 1987, "Analysis of Flow and Heat Transfer at the Interface Region of a Porous Medium," *Int. J. Heat Mass Transfer*, Vol. 30, pp. 1391-1405.

Vafai, K., and Tien, C. L., 1981, "Boundary and Inertia Effects on Flow and Heat Transfer in Porous Media," *Int. J. Heat Mass Transfer*, Vol. 24, pp. 195-203.

APPENDIX

Low Reynolds Number Flow Across a Tube Bundle, Viewed as Darcy Flow Through a Porous Medium

The following analysis refers to the friction-factor information listed for tube bundles in crossflow in Fig. 10, pp. 4-100, by Mueller (1985). In the low Reynolds number limit, each friction factor curve is fitted well by the relation

$$f = \frac{b}{\rho u_{\max} D/\mu} \tag{A.1}$$

where D is the cylinder diameter, $u_{\max}$ is the maximum fluid velocity, and b is a dimensionless constant determined graphically and listed in Table A.1. The friction factor is defined as

$$f = \frac{\Delta P}{2N_r\, \rho u_{\max}^2} \tag{A.2}$$

in which ΔP is the pressure drop imposed across the bundle, and N_r is the number of rows. Eliminating f and ΔP between equations (40), (A.1), and (A.2) leads to a formula for the equivalent porous-medium permeability of the bundle

$$K = \frac{\phi U}{u_{\max}} \frac{L}{N_r} \frac{D}{2b} \tag{A.3}$$

Since ϕU is the volume-averaged velocity through the entire space, the maximum velocity can be approximated by writing

$$u_{\max} \cong \frac{\phi U}{X_t - 1} \tag{A.4}$$

The dimensionless number X_t is defined such that $X_t D$ represents the center-to-center distance between two adjacent cylinders, in the direction normal to the flow. Furthermore, if $X_l D$ is the center-to-center distance in the flow direction, then $L/N_r = X_l D$, and equation (A.3) reduces to

$$K \cong \frac{1}{2b} (X_t - 1)\, X_l D^2 \tag{A.5}$$

This result validates the $K \sim D^2$ scaling that was assumed in the analysis starting with equation (41). In order to evaluate the approximate value of the constant k_z, we must first estimate the porosity of the bundle. When the tubes are aligned such that their centers form squares, $X_l = X_t$ and

$$\phi = 1 - \frac{\pi/4}{X_t^2} \tag{A.6}$$

When the rows are staggered, the figure formed by the centers of the closest cylinders is an equilateral triangle, $X_l = 0.886\, X_t$, in which case

$$\phi = 1 - \frac{\pi/4}{0.866 X_t^2} \tag{A.7}$$

The Kozeny constant k_z can now be evaluated by eliminating K between equations (41) and (A.5)

$$k_z = \frac{2b}{(X_t - 1)X_l} \frac{\phi^3}{(1-\phi)^2} \tag{A.8}$$

The rightmost column of Table A.1 shows that the resulting k_z values are consistently of order 10^2.

The preceding analysis relied on the best known experimental friction factor data for flow across tube bundles, in order to demonstrate the validity of the permeability model adopted in equation (41). Additional support for this model is provided by approximate analytical (Happel, 1959) and numerical calculations (Eidsath et al., 1983) of low Reynolds number flows across regular arrays of cylinders.

Variation of Heat and Mass Transfer Coefficients During Drying of Granular Beds

J. A. Rogers

M. Kaviany

Department of Mechanical Engineering and Applied Mechanics, University of Michigan, Ann Arbor, MI 48109

During convective drying of initially fully saturated granular beds, the solid matrix is gradually exposed to the ambient air, resulting in heat transfer to both the liquid and solid. In an attempt to examine the heat and mass transfer processes occurring on the surface and to examine the influence of particle size and Bond number on the drying rate, experiments are performed in which granular beds constructed of spherical particles (which range from $d = 0.2$ mm to $d = 25.4$ mm) are convectively dried. For beds constructed of very small particles ($d = 0.2$ mm, $Bo = 0.0035$) the surface areas of the liquid and solid are difficult to estimate due to the random arrangement of the particles. The experimental results confirm existing knowledge that the evaporation rate is nearly constant during the funicular state of drying. For beds constructed of large particles ($d = 25.4$ mm, $Bo = 21.7$) an estimate of the surface areas of the liquid and solid reveals that the surface areas and the evaporation rate are highly dependent on surface saturation, contact angle, and surface tension. The results indicate that heat transfer from the solid to the liquid is significant and that the heat and mass transfer processes are not analogous.

1 Introduction

In drying of nonhygroscopic granular beds during the period when the liquid phase is continuous (funicular state), the liquid moves to the surface by capillary pressure. The gravity field may hinder or assist this flow depending on the orientation of the mass transfer surface. For beds constructed of small particles (low permeability) it has been observed that the evaporation rate during the funicular state of drying is rather constant (Plumb et al., 1985) while the surface saturation decreases (the surface saturation is defined as the fraction of void space occupied by the liquid on the surface[1]). Van Brakel and Heertjes (1979) and Schlünder (1988) suggest that a constant drying rate for media with low permeabilities will be observed if the vapor concentration boundary layer thickness formed above the mass transfer surface is larger than the pore size. A constant drying rate can also be explained by redistribution of the liquid on the surface such that the surface area of the liquid remains constant.

For beds constructed of large particles, experimental evaporation rate results and an exact knowledge of the exposed liquid and solid surface areas are needed to determine the heat and mass transfer coefficients. While the former is easily obtained, the surface areas, except in some simple cases (e.g., Prata and Sparrow, 1985; Saez, 1983) are difficult to determine due to the lack of simplifying symmetry (a complete solution of the Young–LaPlace equation is a difficult task). For large particles, with the normal vector of the mass transfer surface opposing the gravity vector, liquid coverage can extend beyond that predicted by the static Young–LaPlace formulation (due to the presence of microlayers). This increases in liquid (and decrease in solid) surface area is significantly influenced by the evaporation rate. For the case of a heated surface partially covered by a liquid, Renk and Wayner (1979) (for fluids with zero contact angle) and Mirzamoghadam and Catton (1988) (for various fluids), show that:

(*a*) The menisci for evaporating (dynamic) liquid layers are different from those for the static layers (described by the static Young–LaPlace formulation). This is due to Marangoni convection (for large systems) and the presence of microlayers (evaporating thin layers) and monolayers (nonevaporating thin layers).

(*b*) The evaporation rate near the contact line (or interline) is significant.

(*c*) The meniscus contour depends on the evaporation rate.

(*d*) The evaporation rate depends on the inclination angle of the solid surface.

Solev'yev and Kovalev (1986) analyzed high heat flux heating of a porous layer and they show that the heat transfer coefficient increases with the heat flux due to an increase in the meniscus curvature.

In this study the evaporation rate from a granular bed was measured for various particle sizes ($0.0014 \leq Bo \leq 21.7$, where Bo is the Bond number and is the ratio of gravity force to capillary force). The results for the particles with the large diameters, along with an estimate of the liquid and solid surface areas (using the Young–LaPlace formulation) for the large-diameter particles, were used to determine the heat and mass transfer coefficients.

2 Experiment

2.1 Apparatus. Air was drawn over the granular bed through a plexiglass channel as shown in Fig. 1(*a*). The cross section of the channel is 16.5 × 7.6 cm. The air was heated using a 1500-W heater placed at the entrance to the channel. A passive mixer was used to homogenize the temperature field and was followed by a porous insert to homogenize the velocity field. The velocity field above the packed bed was measured with a previously calibrated hot-wire anemometer. The spherical particles were placed in a variable depth, open-top Plexiglas box with an inside cross section of 15 × 15 cm. Table 1 gives the particle diameters and the experimental conditions. Particles with $d > 3$ mm were made of Plexiglas and the others were made of glass. The larger spheres were packed regularly (one on top of the other with the centers passing through the vertical line) and the bed had a porosity of 0.476; while for $d \leq 3$ mm the packing was random and the bed had a porosity of about 0.40. The granular bed was lowered to a digital scale

[1]The surface is envisioned as a few particles thick for low-permeability, randomly packed beds, and as one particle thick for high-permeability, regularly packed beds.

Contributed by the Heat Transfer Division for publication in the JOURNAL OF HEAT TRANSFER. Manuscript received by the Heat Transfer Division July 21, 1988; revision received October 2, 1989. Keywords: Mass Transfer, Packed and Fluidized Beds, Porous Media.

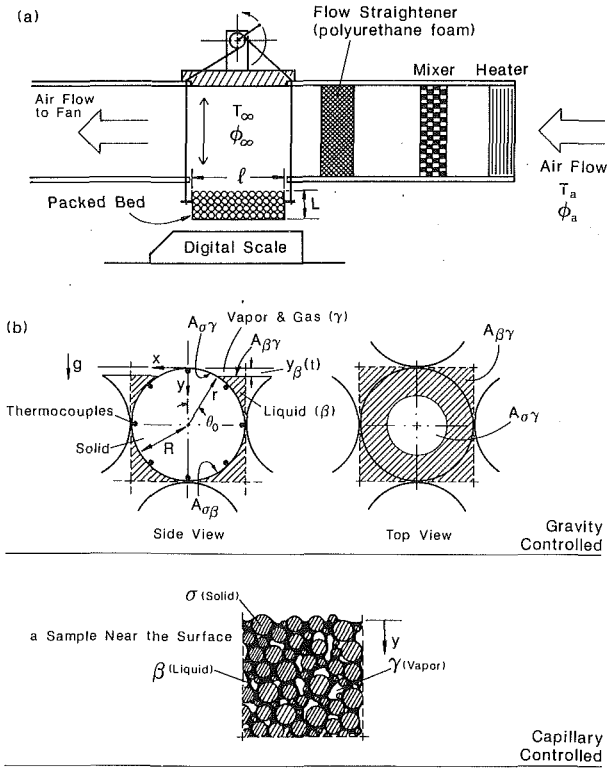

Fig. 1 *(a)* **A schematic of the apparatus, *(b)* schematic of beds with capillary- and gravity-controlled liquid motion**

(accurate to ± 0.1 g) every 20 minutes for mass measurement. Thermocouples (accurate to ± 0.05 °C) were placed in various locations, and for d = 25.4 mm several of them were placed within each particle (as shown in Fig. 1(*b*)). It should be noted that the solid surface temperature was measured by two thermocouples, one attached to the particle surface with a high-conductivity epoxy and the other embedded in the particle approximately 1 mm from the surface.

Table 1 Experimental conditions

d (mm)	Bo	u_∞ (m/s)	Re_l	Re_d	T_a (°C)	ϕ_a	T_∞ (°C)	ϕ_∞
0.2	0.00135	4.0	32000	42	24	0.38	60	0.05
1.	0.0337	4.0	32000	210	24	0.36	60	0.06
3.	0.302	4.0	32000	630	24	0.38	55	0.07
6.35	1.36	4.0	32000	1333	24	0.38	60	0.05
12.7	5.43	4.0	32000	2667	23	0.55	55	0.10
25.4	21.72	4.0	32000	5333	24	0.35	56	0.07

2.2 Measurement. The granular bed was initially filled with distilled water and allowed to reach equilibrium with the room temperature. The fan and heater were then turned on and temperatures were measured every two minutes using a Hewlett-Packard data acquisition/data processing system. Every 20 minutes the fan was turned off for 30 seconds to lower the granular bed for mass measurements.

The relative humidity in the room was measured using a mechanical meter that is accurate to 1 percent and then validated using a rotating hygrometer. The measured room temperature T_a and relative humidity ϕ_a and the measured channel temperature T_∞ were used to determine the channel relative humidity ϕ_∞ from the psychrometric chart. Since the humidity ratio of the heated air equals that of the ambient air, ϕ_∞ was found from the intersection of the humidity ratio line with the dry bulb temperature T_∞. The wet bulb temperature of the surface and the channel vapor density were found from available tables and the psychrometric chart.

The contact angles γ_c for the Plexiglas–water–air system and the glass–water–air system were measured using the sessile drop method. A drop of the liquid was placed on a horizontal, flat Plexiglas (or glass) plate and the angle of the intersection between the drop edge and the solid surface was observed and measured. The angle was observed by a microscope and the process was repeated many times. The contact angle for the Plexiglas–water–air mixture was found to be 55 ± 5 deg, while the contact angle for the glass–water–air system ranged from 0 deg for clean, smooth glass to as much as 30 deg for contaminated glass.

Nomenclature

A = surface area, m^2
Bo = Bond number = $g\rho_\beta R^2/\sigma$
c = specific heat at constant pressure, J/kg-K
d = particle diameter, m
D = binary mass diffusion coefficient, m^2/s
h_h = heat transfer coefficient, W/m^2-K
h_m = mass transfer coefficient, m/s
h_{fg} = heat of evaporation, J/kg
k = thermal conductivity, W/m-K
K = permeability, m^2
l = bed length, m
L = bed depth, m
Le = Lewis number = D/α_γ
m = mass, kg
$\dot{m}$ = mass transfer rate, kg/s
M = molecular weight, kg/kg-mole
$\overline{M}$ = mixture molecular weight, kg/kg-mole
N = number of particles in bed
Nu_l = Nusselt number = $h_h l/k$
$P_{\beta R}$ = liquid pressure, Pa
Pr = gas Prandtl number = ν_γ/α_γ
Q = heat transfer rate, W
Re_l = Reynolds number = $u_\infty l/\nu_\gamma$
r = radial position, m
R = radius of particle, m
s = saturation
Sc = Schmidt number = ν/D
Sh = Sherwood number = $h_m l/D$
t = time, s
T = temperature, °C
u = velocity, m/s
V = volume, m^3
x, z = coordinate axis, m
y = coordinate axis along gravity, m
α = thermal diffusivity, m^2/s
γ = contact angle, deg
δ = offset from centerline
ϵ = porosity
θ = angular position, rad
μ = dynamic viscosity kg/m-s
ν = kinematic viscosity = μ/ρ, m^2/s
ρ = density, kg/m^3
σ = surface tension, N/m
ϕ = relative humidity

Superscripts

$\bar{}$ = average
$''$ = per unit area

Subscripts

a = room
c = contact
cyl = cylinder
d = based on d
e = evaporation
H_2O = water
i = initial
im = immobile
l = based on l
m = modified
sat = saturation
sc = subcooling
sph = sphere
st = starting point
wb = wet bulb
β = liquid
γ = gas
σ = solid
∞ = in channel
1 = surface

The liquid surface was seeded with metal flakes for the particles with $d = 25.4$ mm in a separate experiment (because the flakes influence the evaporation rate). These flakes revealed the presence of motion on the liquid surface (either Marangoni convection or shear-driven motion).

3 Analysis

3.1 Gravity-Controlled Liquid Motion. The drying behavior of granular beds is divided into two categories, gravity-controlled and capillary-controlled. Although surface tension and contact angle play a significant role in the drying rate of granular beds with Bo $>$ 1, the drying of these granular beds is deemed gravity-controlled (while granular beds with Bo $<$ 1 are considered capillary-controlled).

Geometric Parameters. An estimate of the liquid surface area can be derived for a system in which the spherical particles (arranged regularly) are represented as equivalent cylinders. Experimental observations indicated that the liquid surface is not planar and therefore surface tension and the contact angle are important parameters when determining the exposed liquid and solid surface areas. It was not possible to measure the surface areas accurately, therefore the Young–LaPlace equation for static menisci is used to compute the meniscus contours and surface areas. The menisci between the spherical particles are three-dimensional and the solution of the Young–LaPlace equation for this case proved very difficult; therefore, the equivalent cylinder model is introduced to reduce the problem to a two-dimensional one. It is important to note that the capillary pressure and meniscus profiles for the actual surface are very different than for the model surface; however, the model is derived specifically to compute the surface areas and is not expected to predict other parameters accurately.

A planar liquid surface location y_β is calculated for the spherical particles using the experimentally determined evaporation rate. Figure 1(*b*) gives a schematic of the planar areas. The modeling is performed such that the planar liquid surface area at any y_β and surface saturation for the cylinder model is equal to that for the spheres. The meniscus contours for these cylinders are determined using the Young–LaPlace formulation. The liquid surface contour and area are calculated for elapsed times up to $y_\beta = R$, i.e., when the planar liquid surface reaches the center of the first row of spheres. For longer elapsed times the liquid surface area is calculated assuming a planar surface.

There are N spheres in the bed, and one of the top spheres is described by $x^2 + (y-R)^2 + z^2 = R^2$. The volume exposed to the gaseous phase is

$$V_{\sigma\gamma} = N\pi \int_0^{y_\beta} [R^2 - (y_\beta - R)^2]dy = N\pi y_\beta^2 R - N\pi y_\beta^3/3 \quad (1)$$

where y_β is the location of the liquid–gas interface. The volume of evaporated liquid at any time is

$$V_{\beta,e} = \frac{m_i - m}{\rho_\beta} \quad (2)$$

where $V_{\beta,e}$ and $V_{\sigma\gamma}$ are related through $4NR^2y_\beta = V_{\sigma\gamma} + V_{\beta,e}$, which can be written as

$$\pi y_\beta^2 R - \pi \frac{y_\beta^3}{3} + \frac{V_{\beta,e}}{N} - 4R^2 y_\beta = 0 \quad (3)$$

Equation (3) is solved for $y_\beta(t)$, where $V_{\beta,e}(t)$ is found for equation (2) using the experimentally measured evaporation rate.

Once y_β is known, the two-dimensional meniscus contour is determined as follows. First a simpler surface model is assumed so that the effects of surface tension and contact angle on the areas for heat transfer can be considered. For any y_β in this model there is a corresponding amount of liquid surface area in each cell (see Fig. 1*b*).

The average width of liquid surface area in each cell (or the average distance between the exposed portions of the two spheres) is found from

$$\bar{x}_{sph} = 2R - \frac{1}{R}\int_{-R}^{R} [R^2 - (y_\beta - R)^2 - z^2]^{1/2}\, dz \quad (4)$$

where the average width is assumed to be $2R$ if the sphere is not exposed.

For the same y_β a pair of identical cylinders (shown in Fig. 4) can be found that have the same liquid surface area between them. The left cylinder is described by

$$(y-R)^2 + x^2 = R_{cyl}^2 \quad (5)$$

and the right cylinder by

$$(y-R)^2 + (x-2R)^2 = R_{cyl}^2 \quad (6)$$

Then, for a given y_β, the average distance between the exposed portions of the cylinders is

$$\bar{x}_{cyl} = 2R - 2\,[R_{cyl}^2 - (y_\beta - R)^2]^{1/2}$$

Equating the two average distances, one obtains

$$\bar{x}_{cyl} = \bar{x}_{sph} = 2R - 2\,[R_{cyl}^2 - (y_\beta - R)^2]^{1/2}$$

or

$$R_{cyl} = \left[\frac{1}{4}(\bar{x}_{sph} - 2R)^2 + (y_\beta - R)^2\right]^{1/2} \quad (7)$$

where $\bar{x}_{sph}$ is found from equation (4). Assuming the liquid–vapor interface is quasi-steady, one can then use the Young–LaPlace equation to find the static meniscus shape and the position of interface for the equivalent cylinder surface (Saez, 1984)

$$\frac{R_{cyl}\, y''_{\beta m}}{(1 - y'^2_{\beta m})^{3/2}} = \frac{P_{\beta R}\, R_{cyl}}{\sigma_{\beta\gamma}} - \mathrm{Bo}\left(1 - \frac{y_{\beta m}}{R_{cyl}}\right) \quad (8)$$

with initial conditions

$$x_{\beta m} = x_{st}$$

$$y_{\beta m} = y_{st} = -\sqrt{R_{cyl}^2 - x_{st}^2} + R$$

$$\left.\frac{dy_{\beta m}}{dx_{\beta m}}\right|_{x_{st}} = \tan\left(\gamma_c + \left.\frac{dy}{dx}\right|_{x_{st}}\right)$$

where dy/dx is determined from equation (5). Here, primes indicate differentiation with respect to x. $P_{\beta R}$ is the pressure of the liquid at a distance R from the x axis and is the sum of the gas interfacial pressure, the capillary pressure, and the hydrostatic pressure. Its value is found by iteration for each surface saturation.

For this particular case $R - \delta = R_{cyl}$, where δ is the cylinder offset (Fig. 4). For a given R_{cyl}, contact angle, Bond number, and $P_{\beta R}$, there is a corresponding surface saturation S_1 (defined as the volume of liquid present at any time in the first layer of spheres divided by the initial, fully saturated volume of liquid in the first layer) and meniscus surface area $A_{\beta\gamma}$. Equation (8) is integrated using a fourth-order Runge–Kutta method (as an initial value problem), as suggested by Saez (1984). The straightforward boundary-value technique, which is generally second-order accurate, is not suitable. Following the method suggested by Saez (1984) the starting point on the left cylinder x_{st} and the corresponding y_{st} for a given contact angle, are guessed and the profile is computed by marching in x until $y_{\beta m}$ reaches the right cylinder. At the intersection, the angle of intersection (i.e., contact angle) is checked against the prescribed value, and if they do not agree a new x_{st} is chosen. The program iterates on x_{st} until convergence is found (the angle of intersection is within 10^{-2} rad of the prescribed contact

angle). This is done for various values of y_β, y_{st} and $A_{\beta\gamma}$ are then determined as functions of y_β.

Another method is also used to solve for the heat transfer areas. This method does not assume a planar liquid interface when solving for the equivalent cylinder radii. Equation (1) is modified by the addition of a volume correction factor

$$V_{\sigma\gamma} = N\pi y_\beta^2 R - N\pi \frac{y_\beta^3}{3} + \delta V \tag{1'}$$

where δV is a volume correction term to account for meniscus curvature. This factor is iterated on until equations (3), (7), and (8) are solved simultaneously. Comparisons between this method and the previous method showed that a maximum increase of 10 percent in the liquid surface area and a maximum decrease of 10 percent in the solid surface area. In most cases the difference was much less.

Once y_{st} is known, the exposed solid surface area $A_{\sigma\gamma}$ can be found from

$$A_{\sigma\gamma} = 2\pi R^2 N \int_0^{\theta_0} \sin\theta d\theta$$

where $\theta_0 = \cos^{-1}\left(\frac{R - y_{st}}{R}\right)$ is the location of the liquid-vapor interface (shown in Fig. 1*b*). The particle area in contact with the liquid is $A_{\sigma\beta} = 4\pi R^2 N - A_{\sigma\gamma}$.

Conduction Through the Solid. Diffusion of heat through particles is determined using a distributed formulation based on an axisymmetric temperature field in the particle, i.e.,

$$\frac{1}{r^2}\frac{\partial}{\partial r} r^2 \frac{\partial T}{\partial r} + \frac{\partial^2 T}{r^2 \partial\theta^2} = \frac{1}{\alpha_\sigma}\frac{\partial T}{\partial t} \tag{10}$$

with boundary conditions

$$T = \overline{T}_\sigma \quad \text{for} \quad r = R, \quad 0 \le \theta \le \theta_0$$
$$T = \overline{T}_\beta \quad \text{for} \quad r = R, \quad \theta_0 \le \theta \le \pi$$

where $\overline{T}_\sigma$ and T_β are the area-averaged measured solid and liquid temperatures. Initial conditions are given as

$$T = T_i \quad \text{for} \quad 0 \le r \le R, \quad 0 \le \theta \le \pi$$

The heat transfer from the solid to liquid is

$$Q_{\sigma\beta} = -2\pi R^2 k_\sigma N \int_{\theta_0}^{\pi} \left(\frac{\partial T}{\partial r}\right)_R \sin\theta \, d\theta \tag{11}$$

and from the gaseous phase to the solid is

$$Q_{\sigma\gamma} = -2\pi R^2 k_\sigma N \int_0^{\theta_0} \left(\frac{\partial T}{\partial r}\right)_R \sin\theta \, d\theta \tag{12}$$

An explicit finite-volume formulation is used to solve equation (10). The solutions are verified using a progressively smaller grid size until the solution no longer changes ($\Delta r = 0.05R$ and $\Delta\theta = 0.05\pi$ emerged as an economical, and yet sufficiently accurate, selection for $\frac{t\alpha_\beta}{R^2} > 0.1$).

Subcooling of Liquid. Initially heat is needed to raise the temperature of the bed from its initial value to the wet bulb value. Since the thermal diffusivity of Plexiglas is nearly the same as that for water ($\rho_\sigma = 1200 \frac{\text{kg}}{\text{m}^3}$, $c_\sigma = 1465$ J/kg-K, $k_\sigma = 0.2$ W/m-K), the heat absorbed by the water during the early stages is determined using the available results for the heat transfer during a sudden rise in surface temperature, i.e.,

$$Q_{sc} = k_\beta A_{\beta\gamma}(T_{\beta,1} - T_i)/(\pi\alpha_\beta t)^{1/2} \tag{13}$$

Average Heat and Mass Transfer Coefficients. For comparison with experimental results, the results for flow over semi-infinite planar surfaces are used (Incropera and Dewitt, 1981), i.e.,

$$\text{Nu}_l = 0.644\ \text{Re}_l^{1/2}\ \text{Pr}^{1/3} \quad \text{laminar flow} \tag{14}$$

$$\text{Nu}_l = 0.037\ \text{Re}_l^{4/5}\ \text{Pr}^{1/3} \quad \text{turbulent flow} \tag{15}$$

The average heat transfer coefficient is

$$h_h = \frac{\text{Nu}\, k_\gamma}{l} \tag{16}$$

and the average mass transfer coefficient is determined from h_h, by applying analogy between heat and mass transfer (Bird et al., 1966; Incropera and Dewitt, 1981):

$$h_m = \frac{h_h M_{H_2O}}{\rho_{\text{sat}} M c_\gamma \text{Le}^{2/3}} \tag{17}$$

where c_γ and Le are evaluated at the film temperature and concentration. Both h_h and h_m are also determined from the experimental results

$$h_h = \frac{Q}{\Delta T\, A_{\sigma\gamma}}, \qquad h_m = \frac{\dot{m}}{\Delta_{\rho\gamma}\, A_{\sigma\gamma}} \tag{18}$$

The total heat transfer to the liquid is balanced by the energy going into mass transfer and the heat being used to raise the temperature of the bed

$$Q_t = \dot{m}h_{fg} + Q_{sc} = Q_{\beta\gamma} + Q_{\sigma\beta} = h_{h\beta}A_{\beta\gamma}(T_\infty - \overline{T}_{\beta,1}) + Q_{\sigma\beta} \tag{19}$$

Then

$$Q_{\beta\gamma} = Q_t - Q_{\sigma\beta} = h_{h\beta} A_{\beta\gamma}(T_\infty - \overline{T}_{\beta,1}) \tag{20}$$

The heat transfer coefficient for the solid surface is found from

$$Q\sigma\gamma = h_{h\sigma} A_{\sigma\gamma}(T_\infty - \overline{T}_{\sigma,1}) \tag{21}$$

Finally,

$$h_m = \frac{\dot{m}}{(\rho_{\gamma,1} - \rho_{\gamma,\infty})A_{\beta\gamma}} \tag{22}$$

It should be mentioned that the liquid surface temperature may not be uniform, as assumed here, and buoyancy and surface tension driven flows may become significant. The extent of these motions is determined by the geometry, the liquid Grashof number $g\beta\Delta TR^3/\nu^2$, the liquid Marangoni number $(\partial\sigma/\partial T)(\Delta TR/\alpha\mu)$, and the liquid Prandtl number ν/α. For $R = 10$ mm, and $\Delta T = 5°$C, and water as the fluid, these values are approximately 10^5, 10^5, and 7, respectively. The critical values of Grashof and Marangoni numbers, for the transition from the conduction regime to the convection regime, are not available for this geometry. Some comparisons with two-dimensional square cavity results are made by Kaviany (1989).

3.2 Capillary Controlled Liquid Motion. For the small particles, the flow of liquid through the bed, under negligible gravitational effect, is given as (Whitaker, 1974; Kaviany and Mittal, 1987)

$$u_\beta = \frac{1}{1 - s_{im}} \frac{\epsilon^{3/2}\sigma K^{1/2}}{\mu_\beta} sK_{r\beta} \frac{df}{dS}\frac{\partial s}{\partial y} \tag{23}$$

where $K_{r\beta} = S^3$ is the relative permeability of the liquid. The function f, which shows the dependence of the capillary pressure on the local saturation and does not include the influence of the contact angle, is given as $f = 1.42(1-S) - 2.12(1-S)^2 + 1.26(1-S)^3$, where $S = (s - s_{im})/(1 - s_{im})$, and s_{im} is the immobile saturation, taken as 0.05 (Udell, 1985).

The saturation equation (conservation of mass) is given as

$$\frac{1}{1 - s_{im}} \frac{\epsilon^{3/2} s K^{1/2}}{\mu_\beta} \frac{\partial}{\partial y}\left(sK_{r\beta}\frac{df}{dS}\frac{\partial s}{\partial y}\right) = \epsilon \frac{\partial s}{\partial t} \tag{24}$$

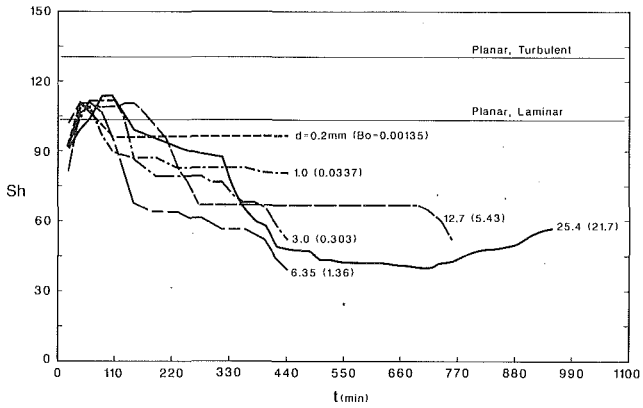

Fig. 2 Variation of dimensionless mass flow rates with respect to time for various particle diameters

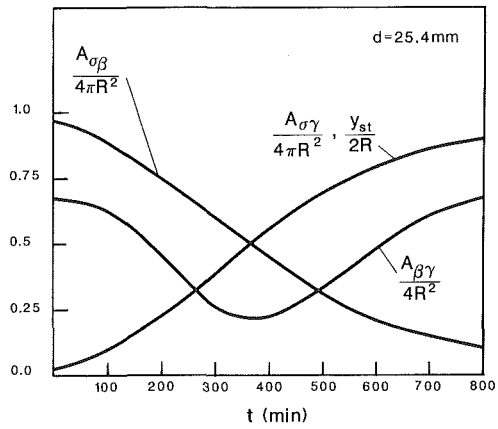

Fig. 3 Variation of the normalized liquid displacement and various normalized liquid surface areas with respect to time for d = 25.4 mm

where the effect of internal evaporation/condensation, vapor storage, and convection are neglected due to the relatively low temperatures in the bed. The initial and boundary conditions are

$$s(y, t = 0) = 1, \quad \frac{\partial s}{\partial y}(y = L, t) = 0,$$

$$u_\beta(y = 0, t) = \frac{\dot{m}''}{\rho_\beta} = \frac{1}{1 - s_{im}} \frac{\epsilon^{3/2}\sigma K^{1/2}}{\mu_\beta} s(0, t) K_{r\beta} \frac{df}{dS} \frac{\partial s}{\partial y}(0, t)$$

where $\dot{m}''$ is specified from the experimental results.

The saturation equation subject to the above conditions is solved numerically using the second-order accurate, finite-difference approximations. The computations are stopped when $\partial s/\partial y$ at the surface becomes very large such that the surface saturation vanishes, i.e., dry patches appear (Kaviany and Mittal, 1987). For the d = 0.2 mm size particles, the predicted and measured permeability are in good agreement ($K = 5 \times 10^{-11}$ m^2) and the measured absolute porosity is 0.4.

4 Results and Discussion

The dimensionless mass transfer rate (Sherwood number) with respect to time for the various particle sizes used is shown in Fig. 2. The vapor density on the surface is evaluated at T_{wb} instead of at the measured surface temperature (which is initially lower than T_{wb}) causing an increase in the value of Sherwood number. The predictions for planar, fully liquid covered surfaces (turbulent and laminar flow) are also given. In the initial period of drying, when the liquid surface is nearly planar, the experimental results are close to the prediction for laminar flow over a flat plate, i.e., equation (14). For beds constructed of small particles ($d \leq 3$ mm), the surfaces for heat and mass transfer and also the concentration and temperature fields (in the air) are similar at the start, and heat and mass transfer are expected to be analogous. This study indicates that for beds made of large particles the analogy does not exist, even at early times. For capillary-controlled liquid motion, i.e., d = 0.2 mm, the mass transfer reaches a plateau characteristic of the funicular state (when the liquid phase in the bed is continuous). On the other hand, for the gravity-controlled liquid motion (e.g., d = 25.4 mm), the mass transfer rate depends strongly on the position of the liquid–solid interface. The results suggest that the liquid motion can be categorized as

Bo $<$ 0.1 capillary controlled

Bo $>$ 1.0 gravity controlled

4.1 Gravity-Controlled Liquid Motion. The variations in the location of the surface of the liquid and in the surface areas with respect to time are shown in Fig. 3 for particles with d = 25.4 mm. The surface area of the liquid undergoes a minimum at t = 375 min., when $y_\beta = R$.

The liquid–solid interface, y_{st}, is determined from the two-dimensional surface model described earlier and the Young–LaPlace equation for Bo = 21.7 and γ_c = 55 deg. y_{st} is determined from the Young–LaPlace equation only for surface saturations greater than 0.5 (i.e., where the liquid reaches the centerline). When the liquid surface is below the centerline y_{st} is assumed to equal y_β. Figure 4 shows the computed meniscus profiles for this case and for Bo = 0 (i.e., negligible gravity forces) and γ_c = 0. The planar menisci are also plotted for comparison. Figure 5 shows the variation in liquid surface area (for a given surface saturation) as a function of the contact angle and Bond number. The results indicate that the liquid surface area between the particles is highly dependent on the contact angle; the surface area decreases as the contact angle increases. The surface area is also somewhat dependent on the Bond number, with the γ_c = 0 case being the most sensitive.

The average measured liquid and solid temperatures as well as the measured channel air temperature for d = 25.4 mm are shown in Fig. 6(a). The solid surface temperature is determined by area averaging the temperature of the exposed surface, and the liquid surface temperature is measured by a traversing probe that tracks the liquid surface. Figure 6(b) shows the variations of the various heat transfer components with respect to time. As expected, the sub-cooling heat transfer, given by equation (13), is significant only in the very early stages (the first hour), and thus Q_t is larger than $\dot{m}h_{fg}$ at early times.

Figure 6(c) shows the heat and mass transfer coefficients calculated with equations (17)–(22) using the areas given in Fig. 3 and the temperatures given in Fig. 6(a). The results indicate that heat transfer coefficients initially take on values around 27 W/m^{2}K, which is above the laminar and turbulent values found in the literature. This is expected since the bed of the surface is not smooth (due partly to waves). The heat transfer coefficient to the solid $h_{h\sigma}$ increases initially and drops off drastically at t = 50 min, while the heat transfer coefficient to the liquid $h_{h\beta}$ increases slowly and then decreases markedly at t = 310 min. In general, the increase in the heat transfer coefficients is not expected because the vortices that appear in the indentations that form on the surface as the liquid recedes reduce the transfer rates (Kaviany, 1989). In addition, $h_{h\sigma}$ is expected to decrease rather gradually until $y_{st} = R$, where it should drop significantly and $h_{h\beta}$ is expected to decrease faster than $h_{h\sigma}$ (because the solid is protruding). The difference be-

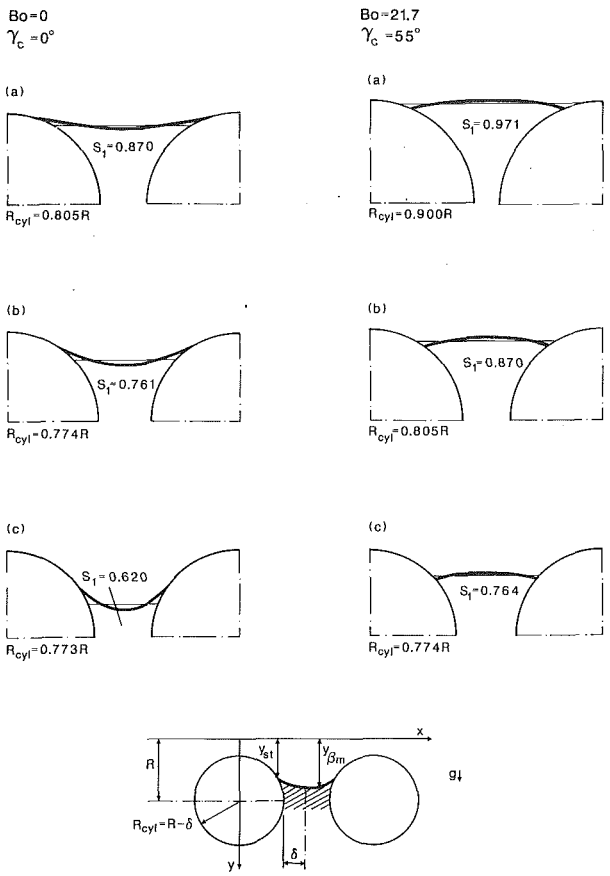

Fig. 4 Meniscus contour between cylinders for Bo = 0 and a surface saturation of 0.870, 0.761, and 0.620, and for Bo = 21.7 and a surface saturation of 0.971, 0.870, and 0.764

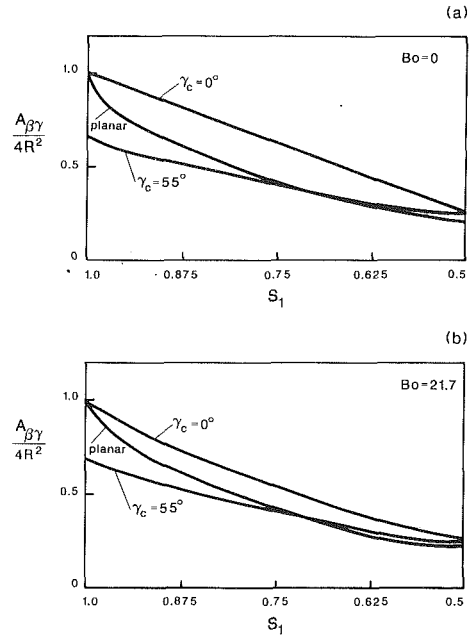

Fig. 5 (*a*) Variation of the normalized liquid surface area with respect to surface saturation for Bo = 0 and various contact angles, and (*b*) for Bo = 21.7 and various contact angles

tween the expected and observed trends for the heat transfer coefficients is attributed to the errors in the predictions of the solid and liquid surface areas (since the surface is treated as cylinders instead of spheres). Rings formed between the spheres as the liquid recedes increase the liquid surface area and decrease the solid surface area. Hence, the liquid surface area is underestimated and the solid surface area is overestimated.

The difference between the mass transfer coefficient determined from the experimental results and that calculated from the heat transfer coefficient (by assuming heat and mass transfer are analogous) indicate that analogy does not exist for d = 25.4 mm. At early times (t < 60 min) a significant amount of the heat is transferred to the subcooled liquid (as seen in Fig. 6*b*), thus destroying the analogy. At longer times (t > 60 min) a significant amount of the heat transferred to the liquid is through the solid particles, once again destroying the analogy. On the microscopic level the results shown in Fig. 6(*c*) are explained as follows. As the liquid surface recedes dry patches appear on the surface of the bed, and the dry air above the patches allows for lateral diffusion of the water vapor to begin. Although the heat transfer coefficient is decreasing (due to the vortices forming in the indentations on the surface, Kaviany, 1989) the effective mass transfer coefficient increases because of the added lateral diffusion. This trend continues until the liquid interface recedes below the neck (when y_β = R) where a large decrease in the heat transfer coefficient to the liquid overcomes the effects of the added diffusion, and the mass transfer coefficient begins to decrease.

4.2 Capillary-Controlled Liquid Motion. For d = 0.2 mm the surface (considered a few layers of particles thick) remains wet throughout the recorded experiment. It is assumed that the capillary pressure and relative permeabilities can be modeled as described earlier and that there is no internal evaporation/condensation: the surface saturation can then be determined using the measured mass transfer rates. Figure 7 gives the variation in surface saturation with respect to time up to the critical time (i.e., the first appearance of dry patches). The period after the critical time is called the pendular state and is marked by a continuous rise in the surface temperature (above the wet bulb temperature). Since the numerical integration of the saturation equation requires very small time steps, the computations are done for a smaller permeability of $K = 10^{-11}$ m^2 instead of the measured $K = 5 \times 10^{-11}$ m^2. Therefore, the predicted critical time is smaller than what would have been obtained using the actual permeability (Kaviany and Mittal, 1987).

An estimate of the liquid surface area for the very small particles is difficult because the random packing of the particles does not lend itself to analysis. However, the constant evaporation rate despite the continuous (almost linear) decrease in the surface saturation (along with the nearly constant surface temperature) suggests that the liquid surface area does not influence the transfer rate. It has been suggested that the lateral diffusion of vapor is not influenced by the surface saturation because the linear dimensions of the wet patches and surface roughnesses are much smaller than the boundary-layer thicknesses.[2] A model based on a surface with alternating wet and dry patches proposed by van Brakel and Heertjes (1979) and van Brakel (1975) suggests that such a surface can produce a constant drying rate with decreasing surface saturation, although no detailed proof based on the fundamentals of transport has been given.

5 Summary

In an attempt to (*a*) examine the influence of particle size and Bond number on the drying rate, and (*b*) show the extent of lack of analogy between interfacial heat and mass transfer

[2]For yet smaller particles (when the ratio of the roughness to the boundary-layer thickness is very small) the surface can be envisioned as protuberances within which the vapor transport is by molecular diffusion. The surface transfer rates are then the same as that for a planar surface covered by a thin layer of liquid (and in equilibrium with thin vapor layer at the wet bulb temperature (Ibrahim and Grosberg, 1978)).

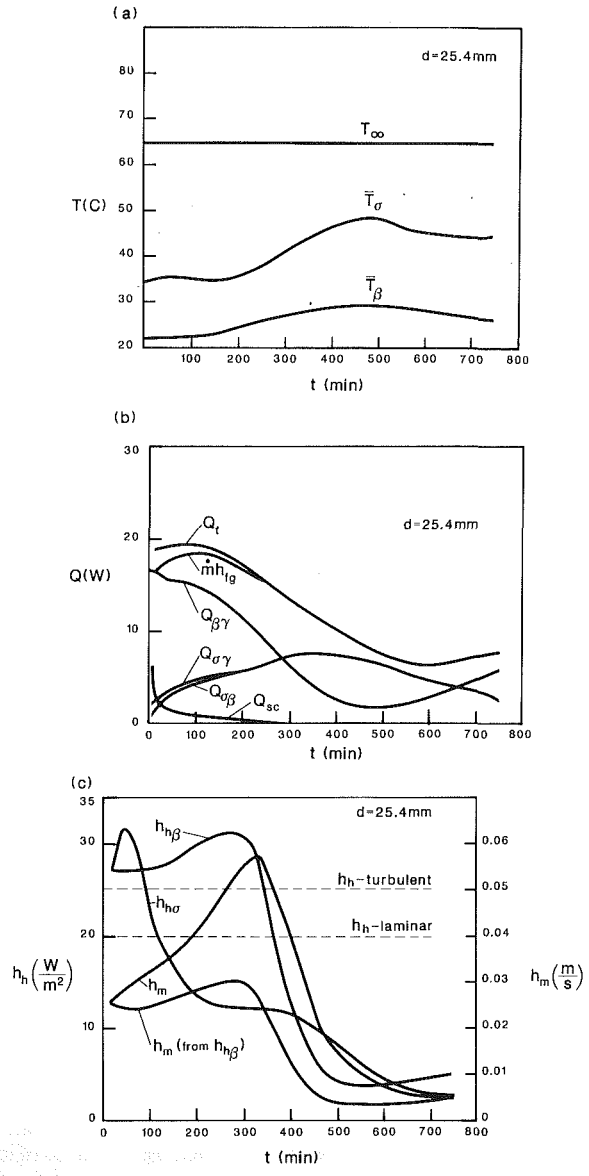

Fig. 6 ***(a)*** **Measured variation in the average channel, solid surface, and liquid surface temperatures, (*b*) variation in the various components of the heat transfer, (*c*) variations of the computed heat and mass transfer coefficients, for d = 25.4 mm**

in drying processes, experiments were performed using a variety of particle sizes that cover the range of nearly capillary-driven liquid flow (Bo < 0.1) to nearly gravity-driven liquid flow (Bo > 1.0).

For large particles (d = 25.4 mm, Bo = 21.7), the liquid and solid areas needed for the determination of the heat and mass transfer coefficients were estimated with the Young-LaPlace static formulation and the results show that (*a*) heat and mass transfer coefficients for the liquid surface initially increase and then decrease as the liquid surface recedes, while the heat transfer coefficient for the solid surface decreases monotonically (except for a short initial period) and (*b*) an analogy does not exist between heat and mass transfer.

For small particles (d = 0.2 mm, Bo = 0.0035), the calculation of the surface areas is very difficult because of the random arrangement of the particles in the bed. Since the temperature and concentration boundary-layer thicknesses are much larger than the particle size (surface roughness is on the order of the particle size) the transfer rates for surface saturation less than unity do not depend on the surface saturation (Schlünder, 1988). This is true up until the surface exhibits intermittent dry patches and the drying rate begins to fall.

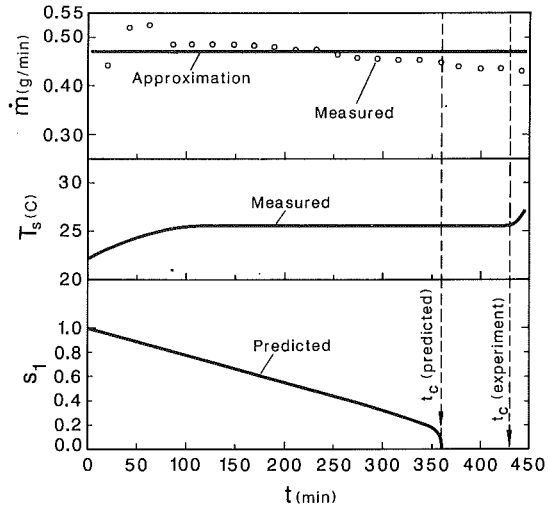

Fig. 7 Variation of the mass transfer rate, surface temperature, and surface saturation for d = 0.2 mm (capillary-controlled liquid motion)

References

Bird, R. B., Stewart, W. E., and Lightfoot, E. N., 1960, *Transport Phenomena*, Wiley, New York, p. 647.

Ibrahim, S. A., and Grosberg, P., 1978, "The Convective Drying of Single Sheets of Fabrics," *J. Text. Inst.*, Vol. 7, pp. 220–227.

Incropera, F. P., and Dewitt, D. P., 1981, *Fundamentals of Heat Transfer*, Wiley, New York, p. 299.

Johnson, R., and Dettre, R., 1965, "The Temperature Dependence of Wettability of Hexadecane on Fluoro Polymer," *Journal of Colloid Science*, Vol. 20, pp. 173–176.

Kaviany, M., 1989, "Forced Convection Heat and Mass Transfer From a Partially Liquid Covered Surface," *Numerical Heat Transfer*, Vol. 15A, pp. 445–469.

Kaviany, M., and Mittal, M., 1987, "Funicular State in Drying of a Slab," *Int. J. Heat and Mass Transfer*, Vol. 30, pp. 1407–1418.

Mirzamoghadam, A. V., and Catton, I., 1988, "Holographic Interferometry Investigation of Enhanced Tube Meniscus Behavior," ASME JOURNAL OF HEAT TRANSFER, Vol. 110, pp. 208–213.

Plumb, O. A., Spolek, G. E., and Olmstead, B. A., 1985, "Mass Transfer in Wood During Drying," *Int. J. Heat Mass Transfer*, Vol. 28, pp. 1669–1678.

Prata, A. T., and Sparrow, E. M., 1985, "Forced Convection Evaporation From a Cavity Containing a Liquid Whose Surface is Curved by Capillarity: Computations in Interlocking Rectangular and Cylindrical Domains," *Numerical Heat Transfer*, Vol. 8, pp. 667–688.

Renk, F. J., and Wayner, P. C., 1979, "An Evaporating Ethanol Meniscus, Part I: Experimental Studied; Part II: Analytical Studies," ASME JOURNAL OF HEAT TRANSFER, Vol. 101, pp. 55–62.

Saez, E. A., 1984, "Hydrodynamics and Lateral Thermal Dispersion for Gas-Liquid Concurrent Flow in Packed Beds," Ph.D. Thesis, University of California—Davis.

Schlünder, E. U., 1988, "On the Mechanism of the Constant Drying Rate Period and Its Relevance to Diffusion Controlled Catalytic Gas Phase Reactions," *Chem. Eng. Science*, Vol. 43, pp. 2685–2688.

Solev'yev, S. L., and Kovalev, S. A., 1986, "Heat Transfer in Evaporation From the Surface of a Capillary-Porous Body," *Heat Transfer—Soviet Research*, Vol. 18, pp. 44–49.

Udell, K. S., 1985, "Heat Transfer in Porous Media Considering Phase Change and Capillarity—The Heat Pipe Effect," *Int. J. Heat Mass Transfer*, Vol. 28, pp. 485–495.

van Brakel, J., 1975, "Porespace Models for Transport Phenomena in Porous Media; Review and Evaluation With Special Emphasis on Capillary Liquid Transport," *Powder Technology*, Vol. 11, pp. 205–236.

van Brakel, J., and Heertjes, P. M., 1979, "On the Period of Constant Drying Rate," *Proceedings of First International Symposium on Drying*, pp. 70–75.

Whitaker, S., 1977, "Simultaneous Heat, Mass and Momentum Transfer in Porous Media: A Theory of Drying," *Advances in Heat Transfer*, Vol. 13, pp. 119–203.

Flow Transitions in Buoyancy-Induced Non-Darcy Convection in a Porous Medium Heated From Below

N. Kladias[1]

V. Prasad
Mem. ASME

Department of Mechanical Engineering,
Columbia University,
New York, NY 10027

Thermoconvective instabilities in horizontal porous layers heated from below are studied numerically by employing the Brinkman–Forchheimer extended Darcy formulation. The onsets of stable and oscillatory convection are found to be strong functions of the governing parameters: fluid Rayleigh and Prandtl numbers, Darcy number, and conductivity ratio. The effects of porosity and specific heat ratio are pronounced only in the fluctuating convection regime. At the onset, the oscillatory convection is highly periodic, but with an increase in convective motions the disorder increases monotonically and the fluctuations become highly random. These results do not confirm the possibility of reverse transition from a more-disordered to a less-disordered state as predicted by the Darcy model (Kimura et al., 1986). The applicability of Darcy formulation is thus highly restricted in the case of a Bénard convection problem. In a randomly oscillating convective state, the heat transfer rate varies substantially with time.

Introduction

The convective instability of a horizontal porous layer subjected to a destabilizing temperature gradient has been investigated extensively by several authors in the past (see Combarnous and Bories, 1975; Cheng, 1978; Catton, 1985). It has been reported that the onset of convection takes place at a critical modified Rayleigh number, $Ra_c^* = 4\pi^2$. However, when Ra* is increased beyond a value between 240 and 280, the convective motion changes in character and becomes oscillatory (Combarnous and Bories, 1975). To define the critical conditions for the onset of oscillatory convection, Caltagirone (1975) performed a stability analysis and numerical study, which predicted the onset of fluctuations at Ra* = 389 for unicellular flow in a square cell.

Horne and O'Sullivan (1974) observed that the flow displays a periodically oscillatory behavior, generating "tongues" of fluid in the descending and ascending columns of the flow. They further noted that at low Ra* the convective flow begins in the most favorable mode for that value of Ra* that is unicellular; this mode dominates the later development of the flow until fluctuations occur as an attempt by the system to form a more favorable steady multicellular pattern, which is repressed by the dominant circulation. In a later study, Horne and O'Sullivan (1978) investigated the significance of cyclic "triggering" in the evolution of fluctuating convection in a rectangular porous cell by comparing the behavior of confined and unconfined flows. The similarity of the flows observed suggests that the oscillatory flow arises from the instability of the thermal boundary layer. In both cases, the frequency of oscillatory flow was proportional to $Ra^{*-3/2}$.

Schubert and Straus (1979) have shown that there exist four transitions in time-dependent convection in porous media. At the onset (Ra* between 380 and 400), the oscillatory flow is periodic with a single basic frequency. However, as Ra* increases the periodic state evolves to a quasi-periodic situation (at Ra* between 480 and 500) with two basic frequencies. Then, with increasing Ra*, a reverse transition occurs to a periodic state at a value somewhere between 530 and 650. In a follow-up study, Kimura et al. (1986) reported that the second periodic flow evolves to a chaotic non-periodic flow regime at a modified Rayleigh number that lies between 850 and 1000. The time dependence of the chaotic state arises from the random generation of tonguelike disturbances within the horizontal thermal boundary layers, and the transition to chaotic regime destroys the centro-symmetric property of convection.

It is important to note that all the abovementioned studies have been based on the Darcy flow model where Ra* appears as the only governing parameter. However, it is now widely realized that the Darcy model is applicable only under special circumstances, and a generalized model for accurate prediction of convection in porous media must include Forchheimer's inertia term and Brinkman's viscous diffusion term.

Rudraiah and co-workers (1980, 1984) were probably the first to consider the Darcy–Brinkman model for studying Bénard convection in porous media, and to recognize the importance of Darcy numbers other than Ra* in producing the instability. Kvernvold and Tyvand (1979) employed a second-order dispersion model to demonstrate the effect of Darcy number. Georgiadis and Catton (1986) obtained solutions for the Darcy–Brinkman–Forchheimer (DBF) model and noted that the divergence in heat transfer results is primarily due to inertia effects. They extensively studied the possibility of multiple wavenumbers in the form of competing patterns and used a maximum entropy production criterion to select a suitable wavenumber for a given Ra*. Their numerical solutions compared reasonably well with the experimental data of Jonsson and Catton (1987) and Combarnous (1970).

We have also conducted a series of studies of Bénard convection in porous media by employing the DBF model (Kladias and Prasad, 1987, 1988) and argued strongly in favor of considering the fluid Rayleigh and Prandtl numbers as independent parameters to analyze the non-Darcy convection (also see Prasad et al., 1988). Our numerical solutions for the unicellular

[1]Present address: Webster Research Center, Xerox Corporation, North Tarrytown, NY 10591.

Contributed by the Heat Transfer Division for publication in the JOURNAL OF HEAT TRANSFER. Manuscript received by the Heat Transfer Division April 16, 1989; revision received October 26, 1989. Keywords: Flow Instability, Natural Convection, Porous Media.

flow initiated in a square cell show that the critical Rayleigh number, $Ra_{f,c}$, for the onset of convection is a strong function of the fluid Prandtl number, the porous matrix structure properties (Da and Fs), and the conductivity ratio. In the stable convection regime, the heat transfer rate increases with the Rayleigh number, the Prandtl number, and the Darcy number while the conductivity ratio has the opposite effect. These results demonstrate the existence of an asymptotic convection regime where the porous media solutions are independent of the permeability of the porous matrix or Da. The objective of the present work is to extend our previous studies and examine the effect of grain size and its thermophysical properties as well as the effect of the fluid properties on oscillatory behavior of convective flows in horizontal porous layers heated from below.

Mathematical Model and Numerical Analysis

For a porous medium of uniform porosity, the mathematical background is identical to that of Kladias and Prasad (1988) and only a brief description will be given here. The conservation equations for mass, momentum, and energy based on the Brinkman-Forchheimer extended Darcy flow model for an isotropic, fluid-saturated porous medium may be written as

$$\nabla \cdot \mathbf{V} = 0 \tag{1}$$

$$\frac{\rho_f}{\epsilon}\frac{\partial \mathbf{V}}{\partial t'} + \frac{\rho_f}{\epsilon^2}(\mathbf{V}\cdot\nabla)\mathbf{V} = -\nabla p + \rho_f \mathbf{g} - \frac{\mu}{K}\mathbf{V} - \frac{\rho_{fb}}{K}|\mathbf{V}|\mathbf{V} + \mu'\nabla^2\mathbf{V} \tag{2}$$

$$(\rho c)_m \frac{\partial T}{\partial t'} + (\rho c)_f \mathbf{V}\cdot\nabla T = k_m \nabla^2 T \tag{3}$$

The equations may be rendered dimensionless by employing the following scales: H for length; $(T_h - T_c)$ for temperature; α_f/H for velocity; H^2/α_f for time; and $\alpha_f\mu/K$ for pressure.

For a two-dimensional flow, the dimensionless form of equations (1)–(3) may then be transformed into the stream function–vorticity form

$$\nabla^2 \psi = \zeta \tag{4}$$

$$\frac{\mathrm{Da}}{\mathrm{Pr}_f}\left\{\frac{1}{\epsilon}\frac{\partial \zeta}{\partial t} + \frac{1}{\epsilon^2}\left(u\frac{\partial \zeta}{\partial X} + v\frac{\partial \zeta}{\partial Y}\right)\right\} = \mathrm{Ra}_f \mathrm{Da}\frac{\partial \theta}{\partial X} - \zeta - \frac{\mathrm{Fs}}{\mathrm{Pr}_f}|\mathbf{V}|\zeta - \frac{\mathrm{Fs}}{\mathrm{Pr}_f}\left\{v\frac{\partial |\mathbf{V}|}{\partial X} - u\frac{\partial |\mathbf{V}|}{\partial Y}\right\} + \Lambda\,\mathrm{Da}\left\{\frac{\partial^2 \zeta}{\partial X^2} + \frac{\partial^2 \zeta}{2Y^2}\right\} \tag{5}$$

$$S\frac{\partial \theta}{\partial t} + u\frac{\partial \theta}{\partial X} + v\frac{\partial \theta}{\partial Y} = \frac{1}{\lambda}\left(\frac{\partial^2 \theta}{\partial X^2} + \frac{\partial^2 \theta}{\partial Y^2}\right) \tag{6}$$

Evidently, free convection in porous media is governed by the following dimensionless parameters:

Ra_f and Pr_f: functions of only fluid properties

Da, Fs, and ϵ: depend generally on grain size and matrix structure

λ, Λ, and S: functions of both solid and fluid properties

As discussed in detail in our recent papers (Kladias and Prasad, 1988; Prasad et al., 1988), this allows us to examine the true effects of fluid and solid properties. It should be noted that the modified Rayleigh number can be expressed as

$$\mathrm{Ra}^* = \lambda\,\mathrm{Ra}_f\mathrm{Da} \tag{7}$$

and the modified Prandtl number as

$$\mathrm{Pr}^* = \lambda \mathrm{Pr}_f \tag{8}$$

In the present study, the Ergun model has been used to describe the porous matrix structure, which yields:

$$\mathrm{Da} = \frac{\epsilon^3}{150(1-\epsilon)^2}\frac{d^2}{H^2} \tag{9}$$

$$\mathrm{Fs} = \frac{1.75}{150(1-\epsilon)}\frac{d}{H} = C(\epsilon)\mathrm{Da}^{0.5} \tag{10}$$

The geometric configuration considered for the present study is a two-dimensional square cavity ($H = W$), which is isothermally heated from below and cooled at the top, the side

Nomenclature

b = porous matrix structure property associated with inertia term, m
c = isobaric specific heat, J/kg-K
C = constant in equation (10) $= 0.55$ for $\epsilon = 0.4$
d = characteristic particle dimension, m
Da = Darcy number $= K/H^2$
Fs = Forchheimer number $= b/H$
$\mathbf{g}$ = body force vector, m/s^2
H = height of porous layer, m
k = thermal conductivity, W/m-K
k_m = stagnant thermal conductivity of fluid-saturated porous medium, W/m-K
K = permeability of porous medium, m^2
Nu = local Nusselt number, equation (14)
$\overline{\mathrm{Nu}}$ = overall Nusselt number, equation (13)
$\overline{\mathrm{Nu}}_f$ = overall Nusselt number based on k_f $(= \lambda\overline{\mathrm{Nu}})$
p = dimensionless pressure, Pa
Pr* = modified Prandtl number $= \nu/\alpha_m$
Pr_f = fluid Prandtl number $= \nu/\alpha_f$
Ra_f = fluid Rayleigh number $= g\beta H^3(T_h - T_c)/\nu\alpha_f$
Ra* = Darcy-modified Rayleigh number $= g\beta KH(T_h - T_c)/\nu\alpha_m$
S = specific heat ratio $= (\rho c)_m/(\rho c)_f$
t = dimensionless time
T = temperature, K
T_h = temperature at heated surface, K
T_c = temperature at cooled surface, K
u, v = dimensionless velocity in x and y directions
$\mathbf{V}$ = filtration velocity vector, m/s
$\underline{\mathbf{V}}$ = dimensionless velocity vector $= V/(\alpha_f/H)$
W = width of porous layer, m
X, Y = dimensionless distance in x and y directions $= x/H$ and y/H
α = thermal diffusivity of fluid $= k/\rho c$, m^2/s
α_m = thermal diffusivity of porous medium $= k_m/(\rho c)_f$, m^2/s
β = isobaric coefficient of thermal expansion of fluid, 1/K
ϵ = porosity
ζ = dimensionless vorticity $= \partial v/\partial X - \partial u/\partial Y$
θ = dimensionless temperature $= (T - T_c)/(T_h - T_c)$
λ = conductivity ratio $= k_f/k_m$
Λ = viscosity ratio $= \mu'/\mu$
μ = dynamic viscosity of fluid, kg/m-s
μ' = apparent dynamic viscosity for Brinkman's term, kg/m-s
ν = kinematic viscosity of fluid, m^2/s
ρ = density, kg/m^3
τ = period of oscillation
ψ = dimensionless stream function

Subscripts

c = critical value for the onset of convection
f = fluid
m = fluid-saturated porous medium
s = solid
w = wall

walls being adiabatic. The relevant hydrodynamic and thermal boundary conditions are:

$$u = v = \psi = 0 \text{ on all boundaries} \quad (11a)$$

$$\theta = 1, \quad Y = 0; \quad \theta = 0, \quad Y = 1; \text{ and } \partial\theta/\partial X = 0, \quad X = 0 \text{ and } 1 \quad (11b)$$

Thom's first-order vorticity boundary condition is derived from the zero tangential velocity condition as

$$\zeta_w = 2\psi_{w+1}/(\Delta n)^2 \text{ on all walls} \quad (12)$$

where Δn is the grid size normal to the wall. It should be noted that a higher-order representation of ζ_w is inappropriate for the present problem since the velocity peaks lie very close to the wall.

To obtain numerical solutions, and ADI procedure, described by Kladias and Prasad (1988), has been employed to perform the time integration for vorticity and temperature equations (5) and (6), while the stream function equation (4) is solved by the Gauss-Seidel SOR iterative scheme at each time step. In the present study, a nonvarying 61×61 grid field is used.

An initial sinusoidal perturbation of temperature field is introduced to drive the solution (Caltagirone, 1975). The iterative convergence of the stream function is checked by obtaining the fractional difference between the values of ψ obtained from two successive iterations, which is less than 10^{-3}. Solutions are considered to be steady when the fractional change in ζ and θ between two time steps are both less than 10^{-4} at all nodes in the computational domain. Generally, very small time steps (of the order of 10^{-3}-10^{-5}) are used to achieve the desired accuracy and the numerical stability. The present discretization scheme of the governing equations is formally second-order accurate for the stable convection solutions and does not suffer from the artificial diffusion errors.

The average Nusselt number at any Y location is obtained as:

$$\overline{\text{Nu}} = \int_0^1 \text{Nu}(X, Y)\, dX \quad (13)$$

where the local Nusselt number

$$\text{Nu} = \lambda v \theta - \partial\theta/\partial Y \quad (14)$$

The details of this numerical scheme, as well as an excellent agreement with the Darcy flow solutions (within 0.55 percent) of Caltagirone (1975) and Schubert and Straus (1979) and non-Darcy results (within 3.7 percent) of Georgiadis and Catton (1986), are discussed in our earlier paper (Kladias and Prasad, 1988) and will be omitted here for brevity.

Convective Flow Regimes

The present numerical solutions support the existence of four flow regimes: (*i*) conduction, (*ii*) stable convection, (*iii*) periodic oscillatory convection, and (*iv*) random (nonperiodic) oscillatory convection. In this section, we shall discuss these regimes as a function of fluid Rayleigh number Ra_f for fixed values of other parameters, such as Pr_f, Da, λ, etc.

Conduction Regime. In this regime, the perturbation introduced by initial conditions in the form of sinusoidal waves diminishes and the system reverts to the pure conduction state. The saturating fluid is stationary, and the Nusselt number $\overline{\text{Nu}}_m$ is unity. The onset of convection takes place at a critical Rayleigh number, $\text{Ra}_{f,c}$, which is equal to $4\pi^2/\lambda\text{Da}$ (Darcy model) only under special circumstances. Otherwise, $\text{Ra}_{f,c}$ strongly depends on Da, Fs, Pr_f, and λ (Kladias and Prasad, 1988). The dependence of $\text{Ra}_{f,c}$ on Da is clearly demonstrated in Fig. 1 for $\lambda = \text{Pr}_f = 1$.

Stable Convective Regime. Beyond $\text{Ra}_f > \text{Ra}_{f,c}$, the initial perturbation yields a stable solution for the convective flow

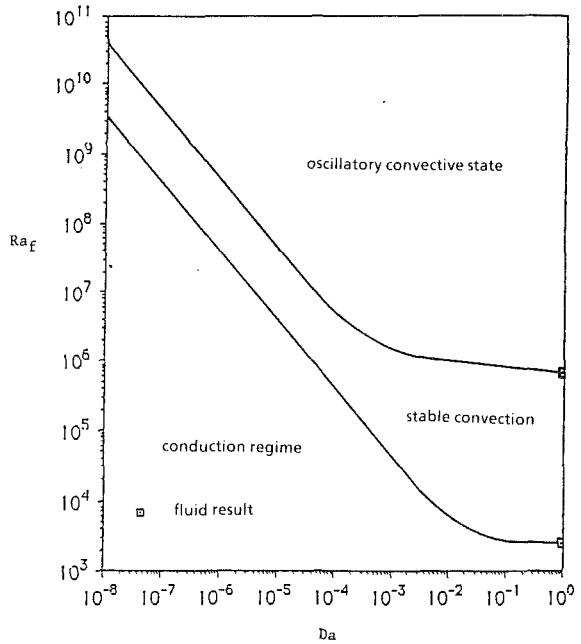

Fig. 1 Criteria for the onsets of stable and oscillatory convection regimes predicted by the Darcy-Brinkman-Forchheimer formulation; critical Rayleigh numbers obtained for the fluid layer are close to those predicted by Fromm (1965), $\text{Pr}_f = 1$, $\lambda = S = 1$

where unicellular flow is observed in the square cell. The recirculating flow then intensifies with an increase in the fluid Rayleigh number.

Periodic Oscillatory Convection. Unicellular convection in a square cell is steady for Rayleigh numbers less than a second critical value, beyond which the solution involves an oscillation in time (Fig. 1). Irrespective of the number of iterations in the calculation, both the temperature and flow fields and the heat transfer rate fluctuate with time. At the onset, the oscillatory convection has a strong periodic nature. For example, the average Nusselt number at the midheight of the cavity for $\text{Ra}_f = 4 \times 10^8$, $\text{Da} = 10^{-6}$ shows a period of $\tau = 0.016$; the fluctuation are of a single-frequency, sinusoidal character with almost equal peak heights (Fig. 2*a*). On the other hand, the period of oscillation increases to $\tau \approx 0.023$ when Darcy number increases to $\text{Da} = 10^{-4}$ (Fig. 2*c*, $\text{Ra}_f = 5 \times 10^6$).

Figures 3(*a*-*c*) show the streamlines and isotherms at successive intervals of time during one-half of an oscillation cycle for $\text{Ra}_f = 5 \times 10^6$ ($\text{Ra}^* = 500$). These figures demonstrate the periodic oscillations in temperature and velocity fields corresponding to the maximum, mean, and minimum Nusselt numbers, respectively. Periodic modulations of the depth of the thermal boundary layers are responsible for the oscillatory behavior (Howard instability). The core of the flow undergoes a significant change during the oscillation. A careful observation of the streamline patterns reveals that the axis of the convective cell swings back and forth. The axis is close to the diagonal of the cavity when the Nusselt number is minimum (Fig. 3*c*) and it makes the largest angle with the diagonal for $\overline{\text{Nu}}_{\max}$ (Fig. 3*a*). The buoyant plume then sways from right to left as $\overline{\text{Nu}}$ varies from a minimum to a maximum. It is important to note that the periodic nature of these oscillations is very strong, and the streamline and isotherm patterns are perfectly identical at the time levels of equal $\overline{\text{Nu}}$ (compare Figs. 3*a* and 3*d*). The isotherms and streamlines in Fig. 3 are very similar to those obtained by Kimura et al. (1986) for $\text{Ra}^* = 500$ (Darcy flow).

In order to compare our predictions for the onset of oscillatory convection with those reported in the literature (Darcy

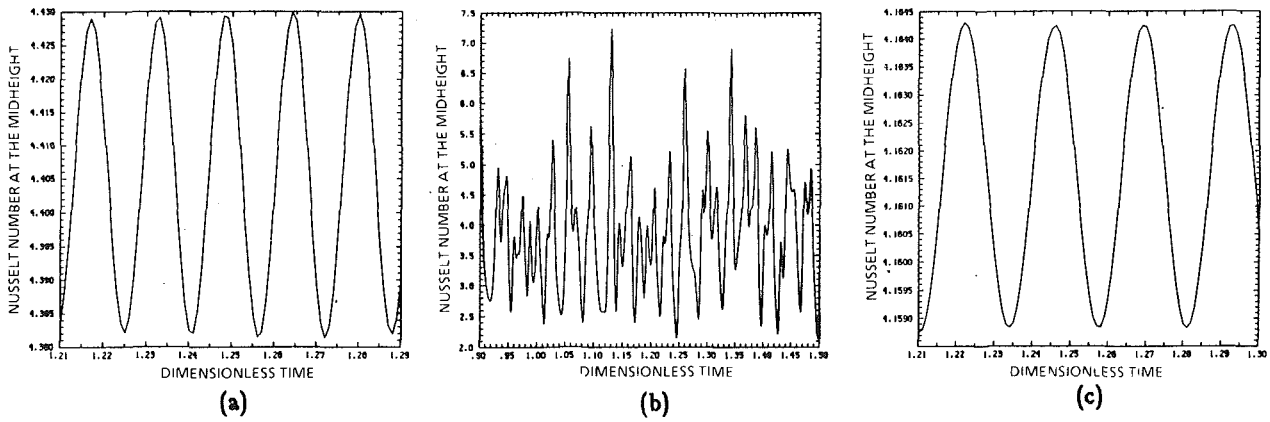

Fig. 2 Periods of oscillations: (*a*) $Ra_f = 4\times10^8$, $Da = 10^{-6}$ ($Ra^* = 400$), (*b*) $Ra_f = 5\times10^8$, $Da = 10^{-6}$ ($Ra^* = 500$), (*b*) $Ra_f = 5\times10^8$, $Da = 10^{-6}$ ($Ra^* = 500$), and (*c*) $Ra_f = 5\times10^6$, $Da = 10^{-4}$ ($Ra^* = 500$)

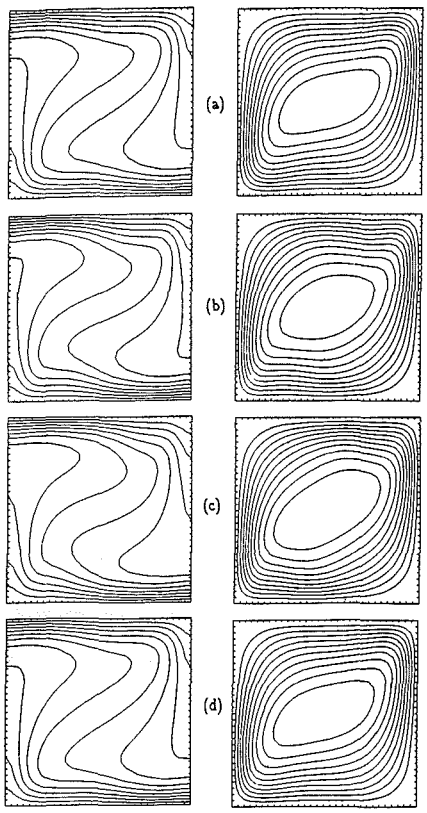

Fig. 3 Isotherms ($\Delta\theta = 0.091$) and streamlines ($\Delta\Psi \approx 1.54$) for periodic oscillations, $Ra_f = 5\times10^6$, $Da = 10^{-4}$; (*a*) $t = 1.246$, $\overline{Nu}_{max} = 4.16$; (*b*) $t = 1.252$, $\overline{Nu}_{mean} = 4.155$; (*c*) $t = 1.258$, $\overline{Nu}_{min} = 4.15$; and (*d*) $t = 1.269$, $\overline{Nu}_{max} = 4.16$

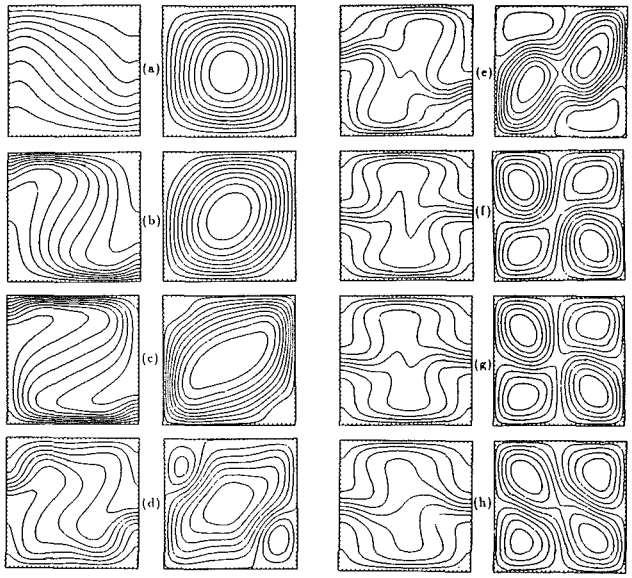

Fig. 4 Evolution and structure of random oscillatory flows: isotherms ($\Delta\theta = 0.1$) and streamlines for $Ra_f = 5\times10^8$, $Da = 10^{-6}$, $Pr_f = 1$; (*a*) $t = 0.005$, $\overline{Nu} = 4.20$ ($\Delta\psi = 1.48$), (*b*) $t = 0.010$, $\overline{Nu} = 4.45$ ($\Delta\psi = 2.62$), (*c*) $t = 0.014$, $\overline{Nu} = 4.64$ ($\Delta\psi = 1.95$), (*d*) $t = 0.420$, $\overline{Nu} = 3.84$ ($\Delta\psi = 1.85$), (*e*) $t = 0.466$, $\overline{Nu} = 4.92$ ($\Delta\psi = 1.14$), (*f*) $t = 1.108$, $\overline{Nu} = 3.04$ ($\Delta\psi = 1.26$), (*g*) $t = 1.134$, $\overline{Nu} = 2.68$ ($\Delta\psi = 1.22$), and (*h*) $t = 1.49$, $\overline{Nu} = 3.30$ ($\Delta\psi = 1.51$).

flow), a few runs were made for the Darcy flow case ($Da = 0$, $\Lambda = 0$, $Fs = 0$). We have found the onset of periodic oscillations to be at $Ra^* = 380$ with a period of $\tau = 0.016$ and Nusselt number fluctuation between $\overline{Nu}_{min} = 4.36$ and $\overline{Nu}_{max} = 4.38$. Indeed, the onset of oscillatory convection in two dimensions has been reported by Caltagirone (1975) to occur at $Ra^* = 384 \pm 5$. Horne and O'Sullivan (1974) stated that unicellular flow is oscillatory at $Ra^* \geq 280$ while Horne (1979) found oscillating single cell convection at $Ra^* = 300$. On the other hand, Schubert and Straus (1979) reported the onset of fluctuations at $Ra^* = 320$ with a period $\tau = 0.014$ and $\overline{Nu}_{min} = 4.62$ and $\overline{Nu}_{max} = 4.63$.

Moreover, experiments on horizontal porous layers by Combarnous and LeFur (1969), Caltagirone et al. (1970), and Horne and O'Sullivan (1974) show that the oscillations start at $Ra^* = 390$ in the nearly square geometry. This behavior is consistent with our findings and shows that the oscillations are physical and not simply computational. (To check further the grid independence of our calculations, the computations were performed for two cases: $Ra^* = 400$, $Da = 10^{-6}$ and $Ra^* = 500$, $Da = 10^{-4}$. Indeed, the numerical experiments yielded the same period of oscillations for grid sizes 41×41, 61×61, and 71×71, i.e., 0.016 and 0.023, respectively.)

Random Oscillatory Convection. As Ra_f increases, a transition to multiple-frequency solutions is observed, where the well-defined periodic nature of the oscillations vanishes and a highly random fluctuation in $\overline{Nu}$ is observed (Fig. 2*b*, $Ra_f = 5\times10^8$, $Da = 10^{-6}$). The corresponding modifications in the temperature and flow fields can be seen in Figs. 4(*a–h*), where the isotherm and streamlines are presented at eight time in-

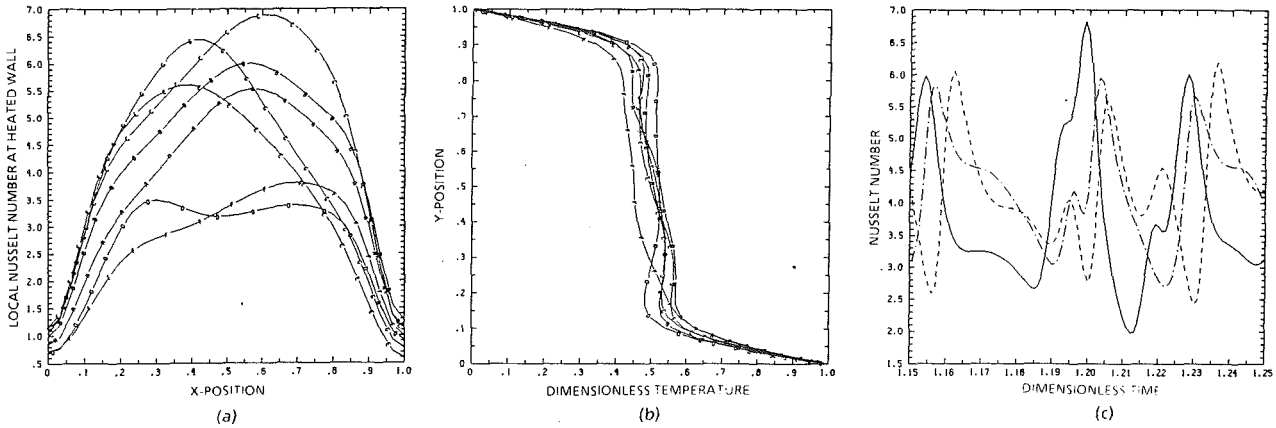

Fig. 5 (*a*)Variation in local Nusselt number on the heated wall with time for randomly oscillating convection: $Ra_f = 5 \times 10^6$, $Da = 10^{-6}$ (time, $A = 1.068$, $B = 1.094$, $C = 1.118$, $D = 1.129$, $E = 1.143$, $F = 1.155$, and $G = 1.171$), (*b*) variation in temperature distribution at the vertical middle plane for randomly oscillating convection; $Ra_f = 5 \times 10^8$, $Da = 10^{-6}$ (time: similar to (*a*)), and (*c*) average Nusselt number at bottom, midheight and top surfaces for $Ra_f = 5 \times 10^6$, $Da = 10^{-6}$ (--- :bottom, —— :midheight, -.- :top)

stants. Figure 4(*a*), $t = 0.005$, shows that a single-cell convective pattern is still dominant. However, local thermal instabilities in the areas of large temperature gradient (top left and right bottom corners in Figs. 4*b*, *c*) cause the appearance of two microvortices at $t = 0.420$ (Fig. 4*d*). These microvortices are carried away by the main circulation (Fig. 4*e*, $t = 0.466$) to produce two secondary cells with a main elongated cell encompassing two small cells along the left diagonal (Fig. 4*f*, $t = 0.497$). The two secondary cells keep growing with time, squeezing and finally breaking the main cell into two parts (Fig. 4*g*, $t = 0.5$) where a four-cell convective pattern is observed. Then, at $t = 0.504$ (Fig. 4*h*) a main cell appears along the right diagonal; the two secondary cells are located at the right top and left bottom corners, and the cycle is then repeated. The temperature field exhibits a corresponding division of the cavity into four regions with the orientation of the upward and downward buoyant flow moved in a counterclockwise direction with time.

A similar four-cell pattern was also reported by Caltagirone (1975) for Darcy porous media (for $Ra^* > 800$), and by Fromm (1965) and Muller (1982) for a fluid layer. The sequence of transitions reported here is characterized by an increasing disorder similar to what has been observed in the fluid layer heated from below. Indeed, the experiments of Gollub and Benson (1980) in a fluid-filled cavity show four paths from a state of rest to turbulence depending on the aspect ratio and the Prandtl number. All of them begin with a bifurcation from a steady-state to an oscillatory periodic flow and gradually toward more complex time-dependent flows, which end in a chaotic state. On the other hand, Kimura et al. (1986) reported a reverse transition from a more-disordered to a less-disordered state, which takes place before the transition to nonperiodic state. This discrepancy between our findings of monotonically increasing disorder and the observations of Kimura et al. may be due to the fact that we have considered the inertial effects, while the work of Kimura et al. is based on the Darcy flow model.

Further Discussion of Results

To study the effect of the grain size d/H, which is related to Darcy and Forchheimer numbers by equations (9) and (10), respectively, numerical results have been obtained for a porous medium of uniform porosity, $\epsilon = 0.4$, with fixed conductivity and specific heat ratios, $\lambda = S = 1$, while the fluid Prandtl number has been fixed to $Pr_f = 1$. The effect of these parameters is then studied separately. On the other hand, the viscosity ratio has been taken as $\Lambda = 1/\epsilon$ (see Kladias and Prasad, 1988).

Effect of Darcy Number

Stable Convection Regime. The effect of Darcy number on critical Rayleigh number, $Ra_{f,c}$, for the onset of convection can be seen in Fig. 1. As expected from the Darcy solution ($Da \leq 10^{-6}$), the Nusselt number approaches its conduction value of unity when $Ra^* = 40$. However, as Da increases, $Ra_{f,c}$ decreases. For $Da \approx 2 \times 10^{-3}$ the slope of the critical Rayleigh number changes substantially and soon it exhibits an asymptotic behavior; $Ra_{f,c}$ is independent of Da, where for $Da > 10^{-1}$ the porous medium critical Rayleigh number matches with the critical Rayleigh number for the fluid layer (Fig. 1). The above results are in excellent agreement with the findings of Walker and Homsy (1977). Indeed, their linear stability analysis based on the Rayleigh–Ritz method shows that the critical Rayleigh number for the onset of convection in a porous medium can be predicted correctly by the Darcy flow model as long as $Da < 10^{-3}$, while for $Da > 10$ the viscous fluid result is recovered. Beyond $Da > Da_c$ for a given Ra_f, the initial perturbation yields a stable solution for the convective flow (Fig. 1). The effect of Darcy number on the flow and temperature fields and the heat transfer rates in the stable convection regime has been studied extensively in our earlier paper (Kladias and Prasad, 1988). Also, a comparison between the numerical predictions and the experimental data is presented in the doctoral dissertation of Kladias (1988).

Oscillatory Convective State. The critical Rayleigh number as a function of Da, to delimit the oscillatory convective state, has been presented in Fig. 1. The straight line portion of this curve, $Ra_f = 380/\lambda Da$, indicates that for $Da < 10^{-5}$, inertia and additional viscous drag terms do not affect the critical Rayleigh number for the initiation of oscillations. When the Darcy number is increased beyond 10^{-4}, the slope of the limiting Ra_f curve changes substantially and approaches zero for $Da > 10^{-1}$. This makes it possible to recover the critical Rayleigh number for the fluid layer, $Ra_f \approx 7.5 \times 10^5$, for $\lambda = 1$ (Fromm, 1965).

As noted earlier, the oscillations are first periodic in nature and then become random with an increase in Rayleigh number for a fixed Da. On the other hand, an increase in Da for a fixed Ra* results in a reversal of the random pattern to a

Table 1 Maximum and minimum values of Nusselt number and periods of oscillations in the fluctuating convection regime: effect of Darcy and Rayleigh numbers

Da	Ra*	Ra_f	$\overline{Nu}_{max,\ min}$	Period τ
	400	4×10^8	4.43, 4.38	0.016
10^{-6}	500	5×10^8	7.23, 2.14	0.005 -0.035
	1000	10^9	13.92, 4.60	0.008 -0.028
	2000	2×10^9	24.48, 3.92	0.008 -0.023
	500	5×10^6	4.16, 4.15	0.023
10^{-4}	1000	10^7	8.12, 2.62	0.009 -0.016
	2000	2×10^7	14.76, 1.49	0.01 -0.048
10^{-3}	2000	2×10^6	9.28, 1.03	0.0047-0.015
10^{-2}	1000	10^6	8.96, 1.94	0.0062-0.053
10^{-1}	8000	8×10^5	4.10, 3.94	0.0024-0.0025

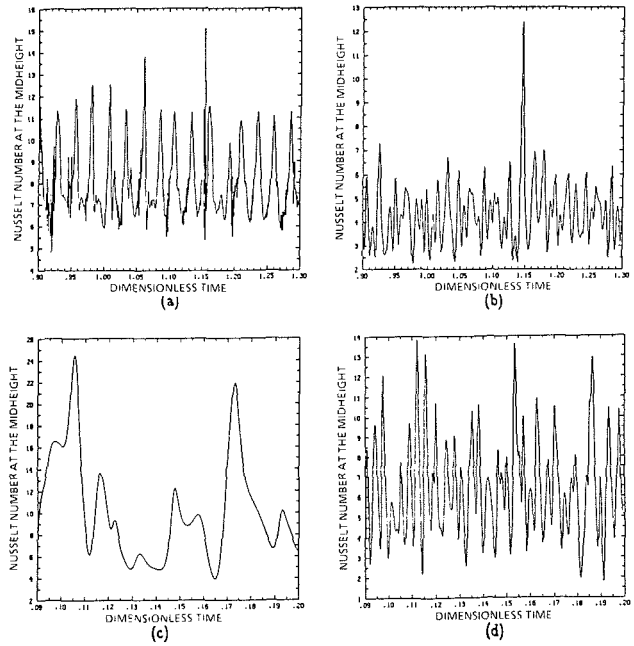

Fig. 6 Effect of Darcy and Rayleigh numbers on fluctuating Nusselt number at midheight for (*a*) $Ra_f = 10^9$ (Ra* = 1000), Da = 10^{-6}, (*b*) $Ra_f = 10^7$ (Ra* = 1000), Da = 10^{-4}, (*c*) $Ra_f = 2 \times 10^9$ (Ra* = 2000), Da = 10^{-6}, and (*d*) $Ra_f = 2 \times 10^7$ (Ra* = 2000), Da = 10^{-4}

periodic oscillation as demonstrated by the Nusselt number plots for Ra* = 500, Da = 10^{-6} (Fig. 2*b*) and Da = 10^{-4} (Fig. 2*c*). This is primarily because, for a fixed λ and Ra*, an increase in Da reduces the fluid Rayleigh number Ra_f (Fig. 2*b*, $Ra_f = 5 \times 10^8$ and Fig. 2*c*, $Ra_f = 5 \times 10^6$). Clearly, Ra* cannot be considered as a sole parameter to characterize the oscillatory state as has been done in the past.

The modifications in temperature and flow fields for the above two characteristic behaviors, i.e., periodic and random, have been demonstrated in Figs. 3 and 4, respectively. Corresponding random variations in the local heat transfer rate on the heated surface and in the temperature distribution at the midheight ($Y = 0.5$) and at different time levels can be observed in Figs. 5(*a*) and 5(*b*), respectively. It is interesting to note that the bounding walls damp the oscillations in the wall region, and the amplitude of fluctuations is largest at the midheight. This has been well demonstrated by the plots for Nu at $Y = 0$, 0.5, and 1 in Fig. 5(*c*).

To show the effect of Ra_f and Da on the nature of oscillations, $\overline{Nu}$ for Da = 10^{-6} and 10^{-4}, and Ra* = 10^3 and 2×10^3 are plotted against time in Figs. 6(*a–d*). A comparison among Figs. 2(*b*), 6(*a*), and 6(*c*) shows that the amplitude of fluctuation increases with Ra_f (also see Table 1). On the other hand, a comparison among Figs. 6(*a–d*) indicates that the Darcy number has an opposite effect; i.e., for a fixed Ra* the amplitude decreases with an increase in Da, and the oscillations become periodic at high Darcy numbers before moving into the stable convection regime. This behavior may be explained more clearly if the results are considered in terms of Ra_f and Da. It is then easy to see that the amplitude of fluctuations increases with both Rayleigh and Darcy numbers.

The quantitative results for the oscillatory convection regime are presented in Table 1. In the case of fluctuating convection, the time step in the numerical computations was at least 16 to 20 times smaller than the period of oscillations. Table 1 lists the smallest minimum and the largest maximum Nusselt numbers at the midheight observed during the extent of the calculations, together with the period of oscillations. In the case of random oscillations, the range over which the period varies has also been reported in Table 1.

In the oscillatory convection regime, the variation between $\overline{Nu}_{max}$ and $\overline{Nu}_{min}$ depends on both the Rayleigh and Darcy numbers. The further away the location of (Ra_f, Da) is from the limiting curve for the stable convection state (Fig. 1), the larger is the difference between $\overline{Nu}_{max}$ and $\overline{Nu}_{min}$. Indeed, Table 1 shows that the variation between the maximum and minimum values of Nusselt number can be highly significant.

Effect of Prandtl Number

For a detailed discussion of the effect of Prandtl number on the onset of convection, the flow and temperature fields, and the heat transfer rate in the stable convection regime, the reader is referred to Kladias and Prasad (1988). We shall present the effect of Pr_f on oscillatory flows only.

To examine the effect of fluid Prandtl number on the origin and nature of fluctuating convection, numerical results have been obtained for $Pr_f = 10^{-2}$, 10^{-1}, 1, 10 and Da = 10^{-6}, 10^{-4} (all other parameters, except Ra_f, are constant). Table 2 lists the predicted values of largest maximum and smallest minimum Nusselt numbers at the midheight together with the range over which the period varies. It is clear that the amplitude of oscillation increases as the Prandtl number increases. Another interesting aspect of the effect of Prandtl number is revealed from Figs. 7(*a–b*). It is seen that for $Ra_f = 4 \times 10^8$ and Da = 10^{-6} the single-frequency periodic oscillation for $Pr_f = 1$ reverts to a random oscillation when Pr_f is increased to 10. This can be attributed to the relative increase in the contribution of Darcy term. If equation (5) is multiplied by Pr_f throughout, we obtain

$$\mathrm{Da}\left\{\frac{1}{\epsilon}\frac{\partial \zeta}{\partial t} + \frac{1}{\epsilon^2}\left(u\frac{\partial \zeta}{\partial X} + v\frac{\partial \zeta}{\partial Y}\right)\right\} = \mathrm{Ra}_f\,\mathrm{Pr}_f\,\mathrm{Da}\frac{\partial \theta}{\partial X} - \mathrm{Pr}_f\zeta - \mathrm{Fs}|\mathbf{V}|\zeta - \mathrm{Fs}\left\{v\frac{\partial |\mathbf{V}|}{\partial X} - u\frac{\partial |\mathbf{V}|}{\partial Y}\right\} + \Lambda\,\mathrm{Pr}_f\mathrm{Da}\left\{\frac{\partial^2 \zeta}{\partial X^2} + \frac{\partial^2 \zeta}{\partial Y^2}\right\} \quad (15)$$

This equation clearly indicates that by increasing the Prandtl number, the dominance of the Darcy term in comparison with the Brinkman and Forchheimer terms is further increased. This is contrary to what happens in the fluid case where an increase in Pr_f (or an increase ν) is expected to diminish the oscillations by reducing the contribution of the convective term.

On the other hand, the amplitude of oscillation decreases and the convective flow becomes more stable with a reduction in Pr_f (Table 2). The isotherms and streamlines for $Ra_f = 5 \times 10^8$, Da = 10^{-6}, $Pr_f = 0.1$ (Figs. 8*a–f*) show that the saturating fluid now has the tendency to rise right from the heated surface instead of traveling along the hot wall before rising. Indeed, Fig. 8(*a*), $t = 1.0$, shows two main cells together with two secondary cells at the left and right bottom corners

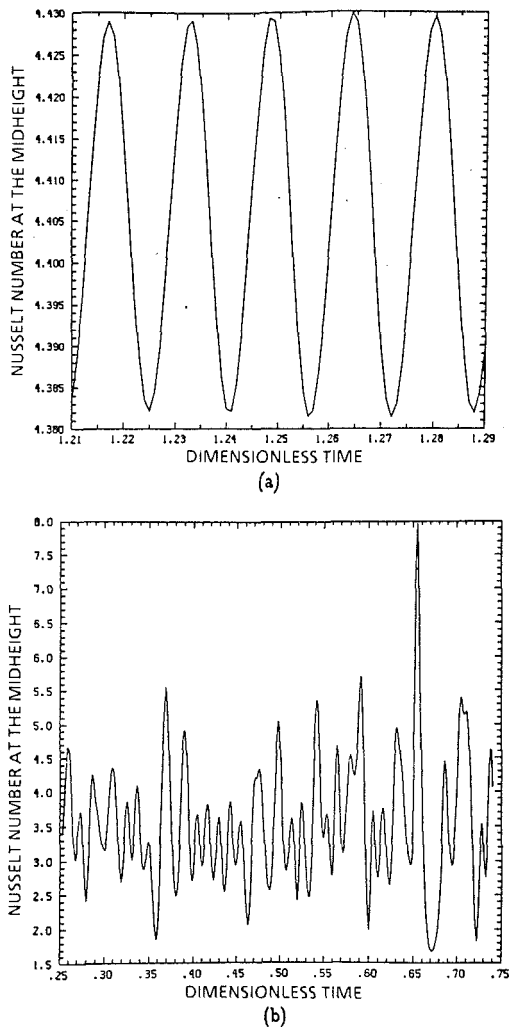

Fig. 7 Effect of Prandtl number on fluctuating Nusselt number at midheight for $Ra_f = 4 \times 10^8$, $Da = 10^{-6}$; (*a*) $Pr_f = 1$, and (*b*) $Pr_f = 10$

of the cavity. Then, at $t = 1.08$ (Fig. 8*c*) three main cells are formed with a secondary cell at the left bottom corner of the cavity (compare with Fig. 4*g*, $Pr_f = 1$) to yield finally a three-cell flow pattern at $t = 1.13$ (Fig. 8*e*) and $t = 1.3$ (Fig. 8*f*).

Table 2 further shows that for $Pr_f = 0.01$, the convective flow becomes much more stable. The oscillatory convection for a porous layer of $Da = 10^{-6}$ saturated with a liquid of Prandtl number, $Pr_f = 0.01$, is seen to start at $Ra_f = 3 \times 10^9$ instead of $Ra_f = 4 \times 10^8$ when the Prandtl number of the saturating fluid is unity. A similar effect of Pr_f can be observed at all Darcy numbers. However, the effect of low Prandtl number in stabilizing the flow is much more pronounced at high Darcy numbers. Indeed, the stable convective state is retained up to $Ra_f = 5 \times 10^7$ for $Pr_f = 0.01$ and $Da = 10^{-4}$, whereas for $Pr_f = 1$ and $Da = 10^{-4}$, the onset of oscillatory regime is at $Ra_f = 5 \times 10^6$. (Refer to Kladias, 1988, for the Pr_f effect on streamline and isotherm patterns.)

Effect of Porosity

Stable Convective State. The effect of porosity ϵ on the overall heat transfer rate in the stable convection regime has been found to be insignificant. This is clearly shown in Table 3 where $\overline{Nu}$ and ψ_{max} are presented for $\epsilon = 0.2$, 0.4, and 0.6, $Ra_f = 2 \times 10^8$, and $Da = 10^{-6}$. Although in the steady-state, stable convection regime the contribution of the first term in equation (5) is zero, a small variation in the solutions has been recorded because of $\Lambda = 1/\epsilon$, which reduces the contribution of the viscous term as ϵ is increased.

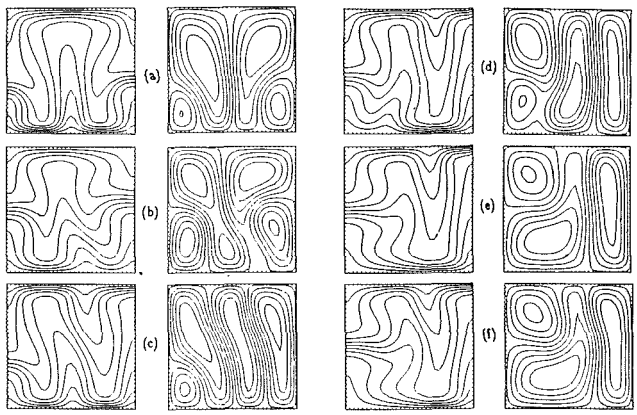

Fig. 8 Isotherms ($\Delta\theta = 0.1$) and streamlines for random fluctuations, $Ra_f = 5 \times 10^8$, $Da = 10^{-6}$, $Pr_f = 0.1$; (*a*) $t = 1.0$, $\overline{Nu} = 4.29$ ($\Delta\psi = 1.77$), (*b*) $t = 1.025$, $\overline{Nu} = 4.58$ ($\Delta\psi = 1.12$), (*c*) $t = 1.08$, $\overline{Nu} = 4.55$ ($\Delta\psi = 1.30$), (*d*) $t = 1.096$, $\overline{Nu} = 4.61$ ($\Delta\psi = 1.42$), (*e*) $t = 1.134$, $\overline{Nu} = 4.31$ ($\Delta\psi = 1.53$), and (*f*) $t = 1.30$, $\overline{Nu} = 4.30$ ($\Delta\psi = 1.48$)

Table 2 Maximum and minimum values of Nusselt number and periods of oscillations in the fluctuating convection regime: effect of Prandtl number

Da	Pr_f	Ra_f	$\overline{Nu}_{max,\ min}$	Period τ
		4×10^8	3.652	–
	0.01	5×10^8	3.929	
		10^9	5.677	
		3×10^9	21.85, 1.03	0.001–0.004
10^{-6}	0.1	4×10^8	4.61, 4.75	0.001
		5×10^8	4.63, 4.32	0.015
	1	4×10^8	4.43, 4.38	0.016
		5×10^8	7.23, 2.14	0.005–0.035
	10	4×10^8	7.98, 1.68	0.004–0.025
		5×10^8	9.37, 2.02	0.004–0.041
		5×10^6	2.178	–
	0.01	10^7	2.768	–
		3×10^7	3.810	–
		5×10^7	4.354	–
10^{-4}	0.1	5×10^6	3.385	–
		10^6	4.58	–
	1	5×10^6	4.16, 4.15	0.023
		10^7	8.12, 2.62	0.009–0.016
	10	5×10^6	4.98, 3.81	0.014–0.0025
		10^7	15.55, 1.66	0.003–0.014

Table 3 Effect of porosity on Nusselt number and maximum stream function in the stable convection regime (uniform porosity), $Ra_f = 2 \times 10^8$, $Da = 10^{-6}$

ϵ	$\overline{Nu}$	ψ_{max}
0.2	3.519	8.7216
0.4	3.556	8.8409
0.6	3.565	8.8697

Oscillatory Convective State. To study the effect of ϵ in the oscillatory convective regime, results have been obtained for $Da = 10^{-6}$, $Ra_f = 4 \times 10^7$–5×10^7, and $\epsilon = 0.2$, 0.4, and 0.6. The quantitative results of this study are presented in Table 4, where the largest maximum and smallest minimum Nusselt numbers observed during the extent of the calculations are listed together with the range over which the period varies. Also, the Nusselt number at the midheight as a function of dimensionless time is plotted in Figs. 9(*a–c*). The periodic oscillation for $Da = 10^{-6}$, $Ra_f = 4 \times 10^7$, $\epsilon = 0.4$ (Fig. 2*a*) changes to random fluctuations for $\epsilon = 0.6$ (Fig. 9*a*). On the other hand, a decrease in ϵ stabilizes the flow (Table 4). Generally, the amplitude of fluctuation increases with ϵ. This may be a result of the relative increase of buoyancy and inertia terms in equation (5).

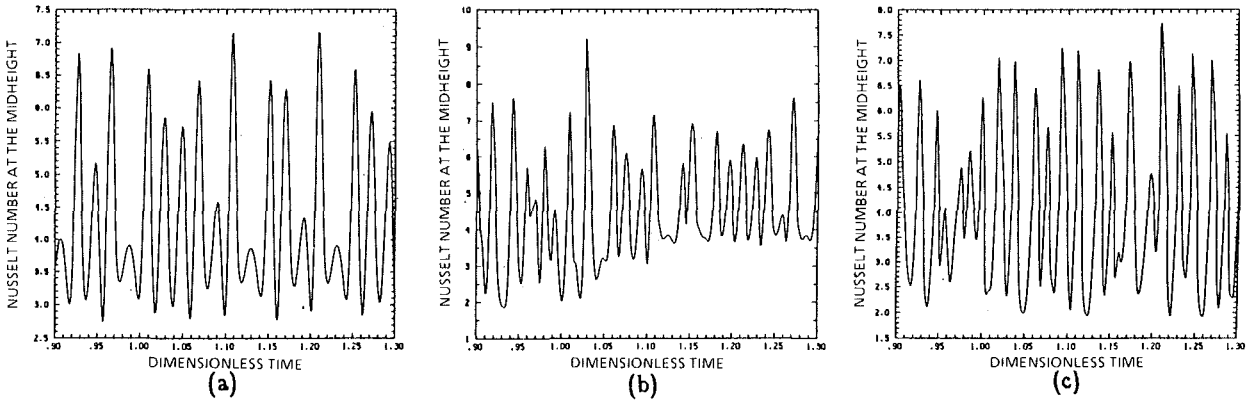

Fig. 9 Effect of porosity on fluctuating Nusselt numbers: (*a*) $Ra_f = 4 \times 10^8$, $Da = 10^{-6}$, $\epsilon = 0.6$, (*b*) $Ra_f = 5 \times 10^8$, $Da = 10^{-6}$, $\epsilon = 0.6$, and (*c*) $Ra_f = 5 \times 10^8$, $Da = 10^{-6}$, $\epsilon = 0.2$

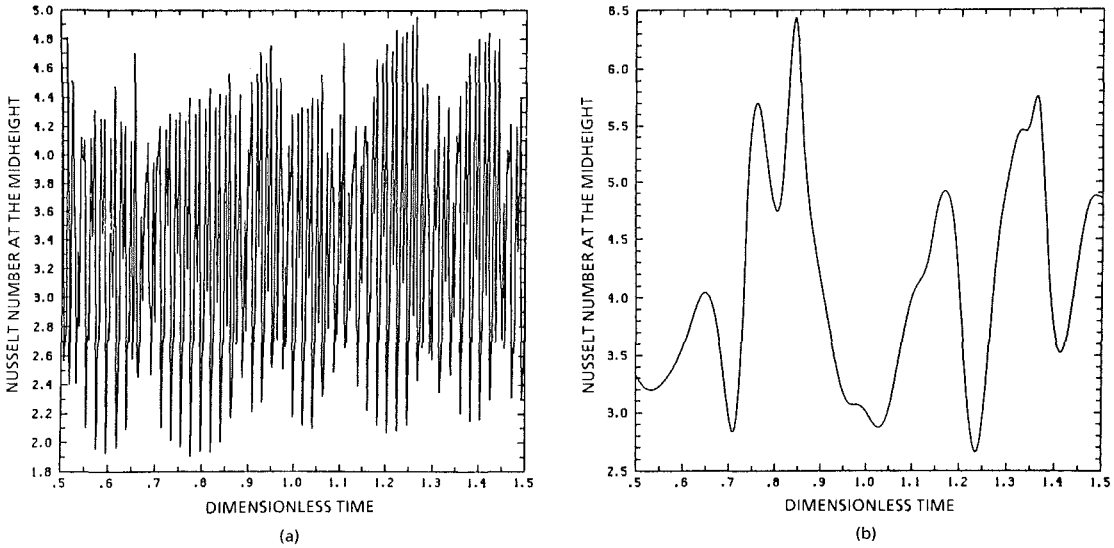

Fig. 10 Effect of specific heat ratio on fluctuating Nusselt number at midheight for $Ra_f = 5 \times 10^6$, $Da = 10^{-4}$: (*a*) $S = 0.5$, and (*b*) $S = 10$

Table 4 Maximum and minimum values of Nusselt number and periods of oscillations in the fluctuating convection regime: effect of porosity ($Da = 10^{-6}$)

Ra_f	ϵ	$\overline{Nu}_{max,\ min}$	Period τ
4×10^8	0.6	7.15, 1.61	0.005–0.049
	0.4	4.43, 4.38	0.016
	0.2	5.39	–
5×10^8	0.6	10.57, 1.70	0.012–0.024
	0.4	7.23, 2.14	0.005–0.035
	0.2	6.71, 2.32	0.007–0.025

Effect of Specific Heat Ratio

Stable Convective State. Since the specific heat ratio appears only in the time derivative term in equation (6), no effect of this parameter on the steady-state solution in the stable convection regime is expected.

Oscillatory Convective State. Table 5 presents the effect of the specific heat ratio. It is observed that the amplitude of fluctuations is minimum for $S = 1$ and is seen to increase as S increases or decreases from unity. On the other hand, the period of oscillation increases as S increases. This is obvious from a comparison between Figs. 10(*a*) ($S = 0.5$) and 10(*b*) ($S = 10$); and also between Figs. 11(*a*) ($S = 0.5$) and 11(*b*) ($S = 10$). Another interesting aspect of the specific heat ratio effect is that the periodic fluctuation in $\overline{Nu}$ for $S = 1$ always reverts to random oscillations as S decreases to 0.5 (a value that is more applicable to geothermal systems). This becomes clear from a comparison between Figs. 10(*a*), 11(*c*) and 2(*c*), 2(*a*), respectively.

Table 5 Maximum and minimum values of Nusselt number and periods of oscillation in the fluctuating convection regime: effect of specific heat ratio S

Da	Ra_f	S	$\overline{Nu}_{max,\ min}$	Period τ
10^{-6}	4×10^8	0.5	8.31, 1.48	0.005 –0.023
		1	4.43, 4.38	0.016
		10	4.69, 4.15	0.098
		100	16.88, 1.62	1.763
	10^9	0.5	13.88, 3.04	0.0006–0.003
		1	13.92, 4.60	0.008 –0.028
		10	16.56, 2.81	0.011 –0.085
		100	43.08, 1.13	0.649
10^{-4}	5×10^6	0.5	4.88, 1.92	0.005 –0.013
		1	4.16, 4.15	0.023
		10	6.63, 2.87	0.005 –0.183
		100	15.99, 1.04	1.129
	10^7	0.5	13.22, 3.90	0.002 –0.01
		1	8.12, 2.62	0.009 –0.016
		10	8.37–2.35	0.0215–0.112
		100	30.53, 1.10	1.287

Furthermore, it is interesting to observe the effect of S on the transient evolution of the oscillatory flow pattern in Figs. 12(*a–i*) ($Ra_f = 10^9$, $Da = 10^{-6}$, $S = 100$). Figures 12(*a–c*) (*t*

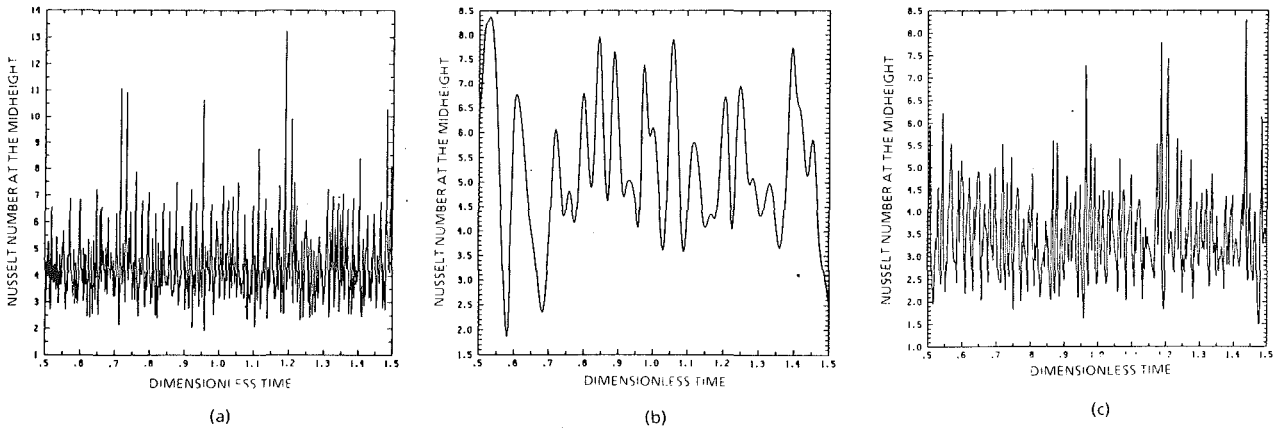

Fig. 11 Effect of specific heat ratio on fluctuating Nusselt number at midheight for $Ra_f = 10^7$, $Da = 10^{-4}$: (*a*) $S = 0.5$, (*b*) $S = 10$, and (*c*) $Ra_f = 4 \times 10^8$, $Da = 10^{-6}$, $S = 0.5$

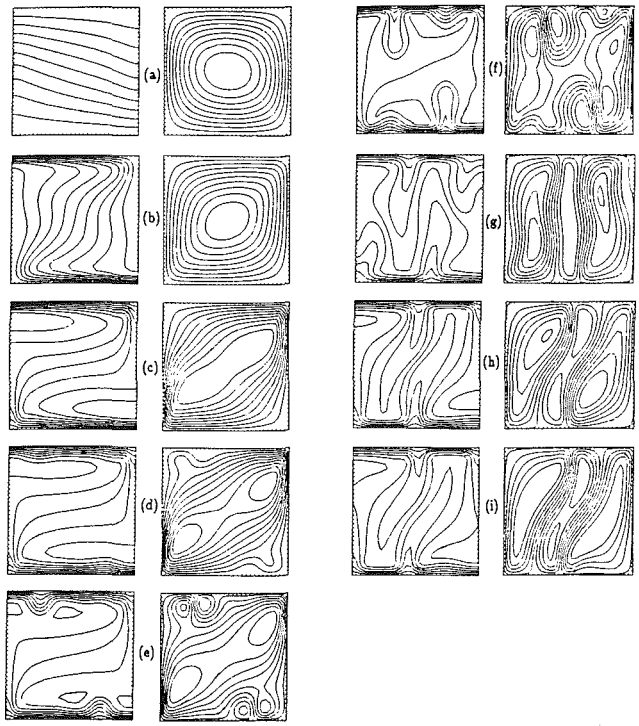

Fig. 12 Effect of specific heat ratio on the evolution and structure of oscillatory flows: isotherms ($\Delta\theta = 0.1$) and streamlines for $Ra_f = 10^9$, $Da = 10^{-6}$, $S = 100$: (*a*) $t = 0.05$, Nu = 2.68, (*b*) $t = 0.375$, Nu = 43.08, (*c*) $t = 0.630$, Nu = 2.69, (*d*) $t = 0.80$, Nu = 1.45, (*e*) $t = 0.88$, Nu = 1.38, (*f*) $t = 1.024$, Nu = 1.14, (*g*) $t = 1.418$, Nu = 8.18, (*h*) $t = 1.80$, Nu = 8.47, and (*i*) $t = 2.0$, Nu = 8.82

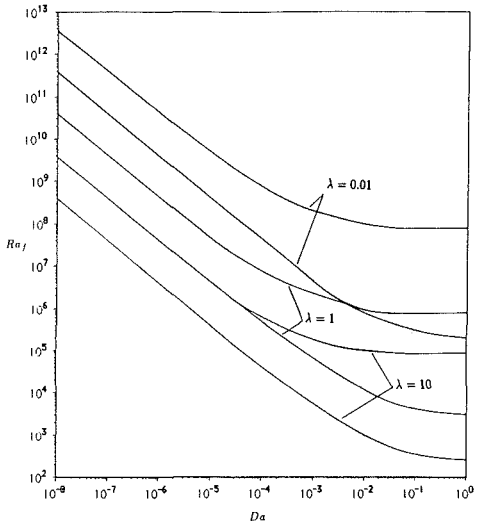

Fig. 13 Effect of conductivity ratio on critical values of Rayleigh and Darcy numbers for the onsets of stable and fluctuating convection regimes (for every λ the upper curve delimits the stable and fluctuating convection regimes while the lower curve delimits the conduction and stable convection regimes)

$= 0.05$–0.63) show that as time increases the flow is intensified and temperature gradients become steeper. Then, local instabilities develop in the areas of large temperature gradient (Fig. 12*d*, $t = 0.8$) to cause the appearance of two microvortices (Fig. 12*e*, $t = 0.88$). As time passes, the microvortices grow and the flow structure becomes highly complex (Fig. 12*f*, $t = 1.024$), giving rise to a three-cell swing from left to right (Figs. 12*h*, $t = 1.8$ and 12*i*, $t = 2.0$).

Effect of Thermal Conductivity Ratio

Onset of Convection. The effect of conductivity ratio λ on $Ra_{f,c}$ can be seen in Fig. 13. It is clear that the smaller the conductivity ratio, the higher is the Rayleigh number required for the onset of convection. The expression $\lambda = k_f/k_m$ and the fact that k_m increases with k_s implies that the onset of convection for a given saturating fluid and a porous matrix of fixed Da will be delayed with an increase in the thermal conductivity of the solid particles. This is primarily because the high-conductivity solid particles have stabilizing effect.

An interesting aspect of Fig. 13 is that the delimiting curves corresponding to different values of λ are seen to be parallel. This trend can be explained if we nondimensionalize the governing equations (1)–(3) using α_m instead of α_f. Then λ will be eliminated from the energy equation (6) and appear, on the other hand, in the vorticity transport equation (5)

$$\frac{\mathrm{Da}}{\lambda \mathrm{Pr}_f}\left[\frac{1}{\epsilon}\frac{\partial \zeta}{\partial t} + \frac{1}{\epsilon^2}\left(u\frac{\partial \zeta}{\partial X} + v\frac{\partial \zeta}{\partial Y}\right)\right] = \lambda\,\mathrm{Ra}_f\mathrm{Da}\frac{\partial \theta}{\partial X} - \frac{\mathrm{Fs}}{\lambda \mathrm{Pr}_f}|\mathbf{V}|\,\zeta - \zeta - \frac{\mathrm{Fs}}{\lambda \mathrm{Pr}_f}\left(v\frac{\partial |\mathbf{V}|}{\partial X} - u\frac{\partial |\mathbf{V}|}{\partial Y}\right) + \Lambda\mathrm{Da}\left(\frac{\partial^2 \zeta}{\partial X^2} + \frac{\partial^2 \zeta}{\partial Y^2}\right) \quad (16)$$

Equation (16) and Fig. 13 show that it is possible to use a more general Rayleigh number, λRa_f, as the parameter of interest, instead of Ra_f. Thus, solutions of Ra_f ($\lambda = 1$), reported in the previous paragraphs, are valid for corresponding values of λRa_f, which makes them more general. However, in that case λPr_f must be used as the Prandtl number rather than Pr_f.

Stable Convective State. As reported earlier (Kladias and

Prasad, 1988), the heat transfer rate for fixed values of Ra_f and Da always increases with an increase in thermal conductivity of the solid particles, k_s, and therefore, with a reduction in the conductivity ratio λ.

Oscillatory Convective State. The effect of conductivity ratio on critical Rayleigh number for the onset of oscillatory convection can also be seen in Fig. 13. It is clear that the onset of oscillations is delayed (in terms of Ra_f) with a decrease in the conductivity ratio (or an increase in the conductivity of solid particles). Again, this is due to the stabilizing effect of high conductivity solid particles. On the other hand, the effect of λ on the structure of oscillatory flows and the periods of oscillations can be studied if we present the previous results in terms of λRa_f, instead of Ra_f.

Conclusions

The Darcy–Brinkman–Forchheimer solutions support the existence of four flow regimes in the case of free convection in horizontal porous layers heated from below: conduction, stable convection, periodic oscillatory, and randomly oscillatory convection regimes. The critical Rayleigh number for the onset of convection decreases from a value predicted by the Darcy flow model, $Ra_{f,c} = 4\pi^2/\lambda Da$, as the particle diameter (or Da) and/or the conductivity ratio is increased. The heat transfer results for $\lambda = 1$ show the existence of an asymptotic convection regime where the critical Rayleigh numbers for the onsets of stable and oscillatory convection regimes are very close to those for the pure fluid layers.

At the onset the oscillatory convection is highly periodic. However, at a high Rayleigh number and/or Darcy number, this gives rise to random fluctuations where the flow structure and the temperature distributions are highly complex. The flow patterns in the randomly fluctuating convection regime show the existence of four cells in a square cavity with two cells on the diagonals being alternately attached and detached with time. This results in a large variation in Nusselt number with time. Also, the effect of Prandtl number on the amplitude and periods of fluctuations and the convective flow pattern is seen to be significant. Generally, an increase in Prandtl number (for $Pr_f > 10$) increases the amplitude of fluctuation, whereas a decrease in Pr_f (< 0.1) results in more stable flow. This behavior is contrary to what is expected in the case of pure fluid.

On the other hand, the effects of porosity (ϵ) and specific heat ratio (S) have been shown to be insignificant in the stable convection regime. The effects of specific heat ratio and porosity are, however, quite significant in the fluctuating convection flow regime. The highly complex flow structures obtained in the oscillatory regime show that all the parameters under consideration strongly affect the evolution of instabilities and emphasize the need to consider the three-dimensional effects. As shown by Schubert and Straus (1979) three-dimensional convection also becomes unsteady at approximately the same Ra^* as the one at which unicellular two-dimensional convection becomes unsteady. They also showed that at $Ra^* = 350$ the fluctuations resemble those of the unicellular oscillatory flow while at $Ra^* = 400$ the variations in Nu with time are more complex. As Ra^* increases, the Nu versus time pattern becomes more complex with larger period variations and less repeatability. Also, Horne and O'Sullivan (1979) have found unsteady three-dimensional solutions at $Ra^* = 300$ and 400, with periods of oscillation about a factor of 3 smaller than those observed for unsteady single-cell convection at comparable Ra^*. Nevertheless, considerable care must be exercised in attempting to apply the results of strictly two-dimensional studies to convection in three-dimensional geometries because the results simply may not carry over (see Straus, 1974).

Acknowledgments

This work was supported by the National Science Foundation under Grant No. CBT-85-04100.

References

Caltagirone, J. P., 1975, "Thermoconvective Instabilites in a Horizontal Porous Layer," *Journal of Fluid Mechanics*, Vol. 72, pp. 269–287.

Caltagirone, J. P., Cloupeau, M., and Combarnous, M. A., 1971, "Convection naturelle Fluctuante dans une couche poreuse horizontale," *C. R. Acad. Sci.*, Ser. B, Vol. 273, pp. 833–836.

Catton, I., 1985, "Natural Convection in Porous Media," *Natural Convection: Fundamentals and Applications*, S. Kakac et al., eds., Hemisphere, Washington, DC, pp. 514–547.

Cheng, P., 1978, "Heat Transfer in Geothermal Systems," *Advances in Heat Transfer*, Vol. 14, pp. 1–105.

Combarnous, M., 1970, "Convection naturelle et convection mixte dans une couche poreuse horizontale," *Revue Generale de Thermique*, Vol. 108, pp. 1355–1376.

Combarnous, M., and Bories, S., 1975, "Hydrothermal Convection in Saturated Porous Media," *Advances in Hydroscience*, Vol. 10, pp. 231–307.

Combarnous, M. A., and LeFur, B., 1969, "Transfer de chaleur par convection naturelle dans une couche poreuse horizontale," *C. R. Acad. Sci.*, Ser. B, Vol. 269, pp. 1009–1012.

Fromm, J. E., 1965, "Numerical Solutions of the Nonlinear Equations for a Heated Fluid Layer," *Physics of Fluids*, Vol. 8, pp. 1757–1769.

Georgiadis, J. G., and Catton, I., 1986, "Prandtl Number Effect on Bénard Convection in Porous Media," ASME JOURNAL OF HEAT TRANSFER, Vol. 108, pp. 284–290.

Gollub, J. P., and Benson, S. V., 1980, "Many Routes to Turbulent Convection," *Journal of Fluid Mechanics*, Vol. 100, pp. 449–470.

Horne, R. N., 1979, "Three-Dimensional Natural Convection in a Confined Porous Medium Heated From Below," *Journal of Fluid Mechanics*, Vol. 92, pp. 751–766.

Horne, R. N., and O'Sullivan, M. J., 1974, "Oscillatory Convection in a Porous Medium Heated From Below," *Journal of Fluid Mechanics*, Vol. 66, pp. 339–352.

Horne, R. N., and O'Sullivan, M. J., 1978, "Origin of Oscillatory Convection in a Porous Medium Heated From Below," *Physics of Fluids*, Vol. 21, pp. 1260–1264.

Jonsson, T., and Catton, I., 1987, "Prandtl Number Dependence of Natural Convection in Porous Media," ASME JOURNAL OF HEAT TRANSFER, Vol. 109, pp. 371–377.

Kimura, S., Schubert, G., and Straus, J. M., 1986, "Route to Chaos in Porous-Medium Thermal Convection," *Journal of Fluid Mechanics*, Vol. 166, pp. 305–324.

Kladias, N., 1988, "Non-Darcy Free Convection in Horizontal Porous Layers," Doctoral Dissertation, Columbia University, New York.

Kladias, N., and Prasad, V., 1987, "Numerical Study for Inertia and Viscous Diffusion Effects on Bénard Convection in Porous Media," *Proc. Fifth International Conference on Numerical Methods for Thermal Problems*, Vol. 1, pp. 797–810.

Kladias, N., and Prasad, V., 1988, "Natural Convection in Horizontal Porous Layers: Effects of Darcy and Prandtl Numbers," *Proceedings, National Heat Transfer Conference*, Houston, ASME HTD-Vol. 96, pp. 593–604; also ASME JOURNAL OF HEAT TRANSFER, Vol. 111, 1989, pp. 926–935.

Kvernvold, O., and Tyvand, P. A., 1979, "Nonlinear Thermal Convection in Anisotropic Porous Media," *Journal of Fluid Mechanics*, Vol. 90, pp. 609–624.

Muller, V., 1982, "Bénard Convection in Gaps and Cavities," *Convective Transport and Instability Phenomena*, J. Zievep and H. Oerted, Jr., eds., pp. 71–100.

Prasad, V., Lauriat, G., and Kladias, N., 1988, "Reexamination of Darcy-Brinkman Solutions for Free Convection in Porous Media," *Proceedings, National Heat Transfer Conference*, Houston, ASME HTD-Vol. 96, pp. 569–579.

Rudraiah, N., 1984, "Non-linear Convection in a Porous Medium With Convective Acceleration and Viscous Force," *Arabian Journal of Science and Engineering*, Vol. 9, pp. 153–1267.

Rudraiah, N., Veerappa, B., and Rao, S. B., 1980, "Convection in a Fluid-Saturated Porous Layer With Non-uniform Temperature Gradient," *International Journal of Heat and Mass Transfer*, Vol. 25, pp. 1147–1156.

Schubert, G., and Straus, J. M., 1979, "Three-Dimensional and Multicellular Steady and Unsteady Convection in Fluid-Saturated Porous Media at High Rayleigh Numbers," *Journal of Fluid Mechanics*, Vol. 94, pp. 25–38.

Walker, K., and Homsy, G. M., 1977, "A Note on Convective Instabilities in Boussinesq Fluids and Porous Media," ASME JOURNAL OF HEAT TRANSFER, Vol. 99, pp. 338–339.

Effect of Modulation on the Onset of Convection in a Sparsely Packed Porous Layer

N. Rudraiah[1]

M. S. Malashetty[2]

UGC-DSA Centre in Fluid Mechanics,
Central College,
Bangalore University,
Bangalore—560001, India

The stability of a Boussinesq fluid-saturated horizontal porous layer heated from below is examined when the applied temperature gradient is the sum of a steady component and a time-dependent sinusoidal component. The Brinkman model is employed and only infinitesimal disturbances are considered. A perturbation solution as a function of the applied field is obtained. The critical Rayleigh number is obtained for several cases depending on the frequency of oscillations and it is found that it is possible to advance or delay the onset of convection by thermal modulation of the wall temperature. The Darcy limit and viscous flow limit are obtained as degenerate cases.

1 Introduction

The problem of natural convection in a horizontal fluid layer driven by buoyancy and heated from below and cooled from above has been studied extensively over the years, both theoretically and experimentally. Most of the findings relevant to this problem have been compiled in the works of Combarnous (1978), Cheng (1979), Rudraiah (1984), Nield (1984), and Bejan (1984, 1987), for example. The investigations carried out so far were mainly concerned with finding the conditions for the onset of convection and the corresponding heat and mass transfer. However, a mechanism to control convection has not been given much attention in spite of its numerous practical applications, exemplified for instance by geothermal energy storage devices, thermal insulation, cooling of electronic equipment, and postaccident cooling of nuclear reactors. It is also of interest in solidifying casting processes.

One effective mechanism to control convection is by maintaining a nonuniform temperature gradient. Such a temperature gradient may be generated:

(*i*) by appropriate heating or cooling at the boundaries (Currie, 1963; Nield, 1975; Rudraiah et al., 1980, 1982);

(*ii*) by injection of fluid at one boundary and removal of the same at the other boundary (Wooding, 1960; Sutton, 1970; Homsy and Sherwood, 1976; Jones and Persichetti, 1986; Nield, 1987; Rudraiah, 1989);

(*iii*) by an appropriate distribution of heat sources (Gasser and Kazimi, 1976; Rudraiah et al., 1980, 1982; Somerton and Catton, 1982);

(*iv*) by radiative heat transfer (Vortmeyer et al., 1988).

The works cited were mainly concerned with space-dependent temperature gradients. However, in many practical situations the nonuniform temperature gradient is generally a function of both position and time, and time dependence of the same cannot altogether be neglected. Such a temperature gradient is determined by solving the energy equation under a suitable time-dependent temperature boundary condition, called thermal modulation.

The effect of thermal modulation in the case of a viscous fluid layer has been studied by Venezian (1969) and Rosenblat and Herbert (1970). They have shown that suitable thermal modulation can control convection. The equivalent of this problem in fluid-saturated porous media has, however, received only marginal attention. By employing the Darcy model, Caltagirone (1976) and Rudraiah and Malashetty (1989) studied the same effect in a densely packed fluid-saturated porous medium. In such a medium the Darcy resistance is so large that the nonlinear inertial acceleration and boundary effects can be neglected. However, many practical problems involve sparsely packed porous media of high porosity and the resistance is quite small. For example, in the solidifying casting process the mushy zone that exists due to the extended freezing temperature is a sparsely packed porous medium. In such problems the inertia and boundary effects are not negligible. One of the suitable models that accounts for inertia and boundary effects is the Darcy-Forchheimer-Brinkman (DFB) model. The results obtained from this model may play an important role in the solidification process.

The object of this paper is, therefore, to study natural convection in a sparsely packed porous medium employing the DFB model in the presence of a nonuniform temperature gradient, which is a function of both position and time. We are interested only in finding the condition for the onset of convection; hence we concentrate only on the linear theory. The findings of this study are believed, in addition to playing an important role in the solidification process, to bridge the gap between the results valid for a Darcy porous medium (low permeability) and those valid for classical viscous fluids.

2 Mathematical Formulation

We consider a fluid-saturated porous layer bounded between two horizontal free surfaces at $z=0$ and $z=d$. The wall temperatures are externally imposed and are taken as follows:

$$(\Delta T/2)[1+\epsilon\cos\Omega t] \qquad \text{at } z=0 \qquad (2.1)$$

and

$$-(\Delta T/2)[1-\epsilon\cos(\Omega t+\phi)] \qquad \text{at } z=d \qquad (2.2)$$

The amplitude ϵ of thermal modulation arises in a natural way when we use the time-dependent thermal boundary conditions of equations (2.1) and (2.2). This amplitude can also be used to control convection. If an imposed modulation can destabilize an otherwise stable system, there can be an appreciable enhancement of heat, mass, or momentum transfer. If it can stabilize an otherwise unstable system, higher efficiency can be achieved in many processing techniques, particularly in solidification processes. We therefore use the amplitude of

[1]Present Address: Vice-Chancellor, Gulbarga University, Gulbarga—585106, Karnataka, India.

[2]Present Address: Department of Mathematics, Gulbarga University, Gulbarga—585106, Karnataka, India.

Contributed by the Heat Transfer Division for publication in the JOURNAL OF HEAT TRANSFER. Manuscript received by the Heat Transfer Division November 10, 1988; revision received September 29, 1989. Keywords: Flow Instability, Geophysical Heat Transfer, Porous Media.

thermal modulation as a parameter to find the solutions of the basic equations. With the usual assumptions and approximations made in the study of thermal convection problems on a porous medium saturated with Boussinesq fluid, the governing equations are taken as follows (Rudraiah, 1984):

$$(\partial \mathbf{q}/\partial t) + (C_b/\sqrt{k})\,|\mathbf{q}|\,\mathbf{q} = -(1/\rho_R)\nabla p + (\rho/\rho_R)\mathbf{g} - (\nu/k)\mathbf{q} + \nu\nabla^2\mathbf{q} \tag{2.3}$$

$$(\rho C_p)_m(\partial T/\partial t) + (\rho C_p)_f(\mathbf{q}\cdot\nabla)T = K\nabla^2 T \tag{2.4}$$

$$\nabla\cdot\mathbf{q} = 0 \tag{2.5}$$

$$\rho = \rho_R[1-\alpha(T-T_R)] \tag{2.6}$$

Equations (2.3)–(2.6) admit an equilibrium solution in which $\mathbf{q}=0$ and $T=T_H(z,t)$ where T_H obeys the equation

$$\gamma(\partial T_H/\partial t) = \kappa(\partial^2 T_H/\partial z^2) \tag{2.7}$$

Here the subscript H refers to the temperature distribution in the basic state. Under the boundary conditions (2.1) and (2.2) one solution of equation (2.7) is

$$T_H = \frac{\Delta T}{2}\left(1-\frac{2z}{d}\right) + \epsilon\mathrm{Re}[b(\lambda)e^{\lambda z/d} + b(-\lambda)e^{-\lambda z/d}e^{-i\Omega t}] \tag{2.8}$$

where

$$\lambda = (1-i)\,(\gamma\Omega d^2/2\kappa)^{1/2}$$

$$b(\lambda) = (\Delta T/2)(e^{-i\phi}-e^{-\lambda})/(e^{\lambda}-e^{-\lambda})$$

and Re stands for the "real part of."

We assume a solution for $\mathbf{q}$, T, and p in the form

$$\mathbf{q}=\mathbf{q}', \quad T = T_H + T', \quad p = P_H + p' \tag{2.9}$$

where $\mathbf{q}'$, T', and p' are perturbations over their equilibrium counterparts. Substituting equation (2.9) into equations (2.3)–(2.5) and neglecting nonlinear terms in perturbed quantities, we get the following perturbation equations:

$$(\partial \mathbf{q}'/\partial t) = (1/\rho_R)\nabla p' + \alpha g T'\hat{k} - (\nu/\mathrm{k})\mathbf{q}' + \nu\nabla^2\mathbf{q}' \tag{2.10}$$

$$(\partial T'/\partial t) + W'(\partial T_H/\partial z) = \kappa\nabla^2 T'. \tag{2.11}$$

We eliminate p' and T' from equations (2.10) and (2.11) and render the resulting equations into dimensionless form by setting

$$(x^*, y^*, z^*) = \frac{1}{d}(x, y, z), \quad t^* = \Omega t,$$

$$\theta^* = \frac{T'}{\Delta T}, \quad W^* = (\nu/\alpha g d^2)W' \tag{2.12}$$

Then, we obtain the following equation for the vertical component of velocity on dropping asterisks:

$$\left(\frac{\omega}{\sigma}\frac{\partial}{\partial t} + Pl^{-1} - \nabla^2\right)\left(\omega\frac{\partial}{\partial t} - \nabla^2\right)\nabla^2 W + \mathrm{Ra}(\partial T_H/\partial z))\nabla_1^2 W = 0 \tag{2.13}$$

In dimensionless form the boundary conditions are

$$W = \partial^2 W/\partial z^2 = \partial^4 W/\partial z^4 = 0 \text{ at } z = 0, 1 \tag{2.14}$$

The dimensionless temperature gradient appearing in equation (2.13) is given on using equation (2.8), as follows:

$$\partial T_H/\partial z = -1 + \epsilon f \tag{2.15}$$

where

$$f = \mathrm{Re}[A(\lambda)e^{\lambda z} + A(-\lambda)e^{-\lambda z}]e^{-it}$$

with

$$A(\lambda) = (\lambda/2)(e^{-i\phi}-e^{-\lambda})/(e^{\lambda}-e^{-\lambda})$$

and

$$\lambda = (1-i)(\omega\gamma/2)^{1/2}$$

Since equation (2.13) is a linear partial differential equation, the horizontal dependence of W is factorable and we look for solutions with a single wave number a, such that

$$\nabla_1^2 W = -a^2 W$$

3 Small Amplitude Approximation

We seek the eigenvalue Ra and the eigenfunction W of equation (2.13) in the form

$$(\mathrm{Ra}, W) = (\mathrm{Ra}_0, W_0) + \epsilon(\mathrm{Ra}_1, W_1) + \epsilon^2(\mathrm{Ra}_2, W_2) + \ldots \tag{3.1}$$

Substituting this into equation (2.13) and equating the corresponding terms, we obtain the following system of equations:

$$LW_0 = 0 \tag{3.2}$$

Nomenclature

a = horizontal wave number
a_c = critical wave number
C_b = $1.75(\epsilon)^{-3/2}/175$ = drag coefficient
C_p = heat capacity at constant pressure
d = width of the porous layer
d_p = particle diameter
f = function appearing in equation (2.15)
$\mathbf{g}$ = gravitational acceleration
k = $d_p^2(\epsilon^*)^3/175(1-\epsilon^*)^2$ = permeability
K = effective thermal conductivity
p = pressure
P_H = basic state pressure
Pl = k/d^2 = porous parameter
$\mathbf{q}$ = (u, v, w) = mean filter velocity
Ra = $\alpha g\Delta T d^3/\nu\kappa$ = Rayleigh number
T = temperature
T_R = reference temperature
T_H = basic state temperature distribution
ΔT = temperature difference between the layers
t = time
(x, y, z) = Cartesian coordinates
α = coefficient of volume expansion
γ = $(\rho C_p)_m/(\rho C_p)_f$ = ratio of specific heats
ϵ = amplitude
ϵ^* = permeability
κ = $K/(\rho C_p)_f$ = thermal diffusivity
ν = kinematic viscosity
ρ = density
ρ_R = reference density
$(\rho C_p)_m$ = $(1-\epsilon^*)(\rho C_p)_s + \epsilon^*(\rho C_p)_f$ (the subscript s refers to solid and f to fluid)
σ = ν/κ = Prandtl number
ϕ = phase angle
Ω = frequency
ω = $\Omega d^2/\kappa$ = nondimensional frequency
∇_1^2 = $\partial^2/\partial x^2 + \partial^2/\partial y^2$

$$L W_1 = \mathrm{Ra}_1 \nabla_1^2 W_0 - \mathrm{Ra}_0 f \nabla_1^2 W_0 \tag{3.3}$$

$$L W_2 = \mathrm{Ra}_1 \nabla_1^2 W_1 + \mathrm{Ra}_2 \nabla_1^2 W_0 - \mathrm{Ra}_0 f \nabla_1^2 W_1 - \mathrm{Ra}_1 f \nabla_1^2 W_0 \tag{3.4}$$

Here

$$L = [(\omega/\sigma)(\partial/\partial t) + Pl^{-1} - \nabla^2](\omega(\partial/\partial t) - \nabla^2)\nabla^2 - \mathrm{Ra}_0 \nabla_1^2$$

Note that each W_0, W_1, W_2 is required to satisfy the boundary conditions of equation (2.14).

Equation (3.2) is the one used in the study of convection in a horizontal porous layer subject to uniform temperature gradient. A general solution of equation (3.2) is $W_0 = W_0^{(n)}$, $n = 1, 2, 3, \ldots$, where

$$W_0^{(n)} = \sin(n\pi z) \tag{3.5}$$

with the corresponding eigenvalues

$$\mathrm{Ra}_0^{(n)} = [(n^2\pi^2 + a^2)^3/a^2] + [(n^2\pi^2 + a^2)^2/Pla^2] \tag{3.6}$$

For a fixed wave number the least eigenvalue occurs for $n = 1$. Ra_0 assumes a minimum value for $a = a_c$ where

$$a_c^2 = \frac{1}{4}[-(\pi^2 + Pl^{-1}) + (9\pi^4 + 10\pi^2 Pl^{-1} + Pl^{-2})^{1/2}] \tag{3.7}$$

This minimum value is usually called the critical Rayleigh number $\mathrm{Ra}_{\mathrm{OC}}$. Equation (3.3) is inhomogeneous and its solution poses a problem, because of the presence of resonance terms. This is analogous to the power integral technique employed in the discussion of nonlinear natural convection problems (see Catton and Ayyaswamy, 1972). In the study of nonlinear convection problems, ϵ is usually the amplitude of perturbations, whereas in the present paper it is the amplitude of thermal modulation. In this power integral technique, the solubility condition requires that the time-independent part of the right-hand side of equation (3.3) should be orthogonal to W_0. The term independent of time in the right-hand side is $\mathrm{Ra}_1 \nabla_1^2 W_0$ so that $\mathrm{Ra}_1 = 0$. Hence it follows that Ra_3, Ra_5, ... in equation (3.1) are all zero. Expanding the right-hand side of equation (3.3) in a Fourier series of the form

$$e^{\lambda z}\sin(m\pi z) = \sum_{n=1}^{\infty} g_{nm}(\lambda)\sin(n\pi z)$$

where

$$g_{nm}(\lambda) = -\frac{4mn\pi^2[1 + (-1)^{m+n+1}e^{\lambda}]\lambda}{[\lambda^2 + (n+m)^2\pi^2][\lambda^2 + (n-m)^2\pi^2]}$$

we obtain the following expression for W_1 by inverting the operator L term by term

$$W_1 = \mathrm{Ra}_0 a^2 \mathrm{Re}\left\{ \sum \frac{B_n(\lambda)}{M(\omega, n)} \sin(n\pi z)e^{-it} \right\}, \tag{3.8}$$

where

$$B_n(\lambda) = A(\lambda)g_{n1}(\lambda) + A(-\lambda)g_{n1}(-\lambda)$$

and

$$M(\omega, n) = \frac{\omega^2}{\sigma}(n^2\pi^2 + a^2) + i\omega[[(n^2\pi^2 + a^2)^2/\sigma] + ((n^2\pi^2 + a^2) + Pl^{-1})(n^2\pi^2 + a^2)] - [(n^2\pi^2 + a^2) + Pl^{-1}](n^2\pi^2 + a^2)^2 + [(\pi^2 + a^2) + Pl^{-1}](\pi^2 + a^2)^2 \tag{3.9}$$

Similarly we can obtain higher eigenfunctions W_2 and eigenvalues Ra_2. We note that the solution equation (3.1) breaks down in the limit $\omega \to 0$. For example when $n = 1$, we get $M(\omega, n) \to 0$ and $W_1 \to \infty$ as $\omega \to 0$. Hence for our assumption to be valid, we must have $|\epsilon W_1| < |W_0|$ or equivalently that $W > \epsilon$. Since $\epsilon \ll 1$, we restrict computation only to Ra_2. Following the analysis of Venezian (1969), we obtain

$$\mathrm{Ra}_2 = \frac{1}{2}\mathrm{Ra}_0^2 a^2 \sum |B_n(\lambda)|^2 C_n \tag{3.10}$$

where

$$C_n = \frac{M(\omega, n) + M^*(\omega, n)}{2|M(\omega, n)|^2}$$

and * denotes the complex conjugate.

To the order of ϵ^2, Ra_{2c} is obtained for the cases when the oscillating temperature field is (*i*) symmetric ($\phi = 0$), (*ii*) asymmetric ($\phi = \pi$), and (*iii*) when only the lower wall temperature is oscillating while the upper wall is held at constant temperature. The last case was also discussed by Caltagirone (1976). The variation of Ra_{2c} with ω for different values of Pl is shown in Figs. 1-4 and the results are discussed in the final section.

4 Limiting Cases

Some features of the behavior of Ra_{2c} as a function of ω can be seen by examining two limiting cases.

(i) Very Low Frequency ($\omega \ll 1$). For very small frequency ($\omega \to 0$) the expression for Ra_{2c} (writing the summation for $n = 1$ and $n \neq 1$) reduces to

$$\mathrm{Ra}_{2c} = \mathrm{Ra}(\sigma, Pl) = \beta\omega^2 \tag{3.11}$$

where

$$\mathrm{Ra}(\sigma, Pl) = \frac{\mathrm{Ra}_{oc}^2 a_c^2}{2(\pi^2 + a_c^2)[(\pi^2 + a_c^2) + \sigma[(\pi^2 + a_c^2) - Pl^{-1}]]^2}$$

(for $n = 1$)

and

$$\beta = 8\mathrm{Ra}_{0c}^2 a_c^2 n^2/\mathrm{D} \text{ (for } n \neq 1),$$

with

$$D = \pi^4(n^2 - 1)^4[[(n^2\pi^2 + a_c^2)^2 - (\pi^2 + a_c^2)]Pl^{-1} - (n^2\pi^2 + a_c^2)^3 - (\pi^2 + a_c^2)^3]$$

For $n > 1$, we have $(n^2\pi^2 + a_c^2) > (\pi^2 + a_c^2)$ so that $\beta > 0$ in all cases. In the case of symmetric modulation the sum extends over even values of n so that the expression for Ra_{ac} reduces to

$$\mathrm{Ra}_{2c} = -\beta\omega^2 \tag{3.12}$$

This implies that symmetric modulation advances the onset of convection because of the reduction in the total critical Rayleigh number at low frequencies. Further, it may be noted that Ra_{2c} is independent of the Prandtl number σ.

In the asymmetric case as well as in the case in which only the lower wall temperature is modulated, Ra_{2c} is given by equation (3.10); in the former case the sum extends over only odd values of n and in the later case for all values of n. In these two cases the effect of modulation is to delay the onset of convection because of the increase in the critical Rayleigh number.

(ii) Very High Frequency ($\omega \to \infty$). For high frequency ($\omega \to \infty$), we find that Ra_{2c} tends to zero in all three cases, so that the effect of modulation disappears.

5 Discussion

The problem of linear convection in a sparsely packed horizontal porous layer subject to timewise periodic

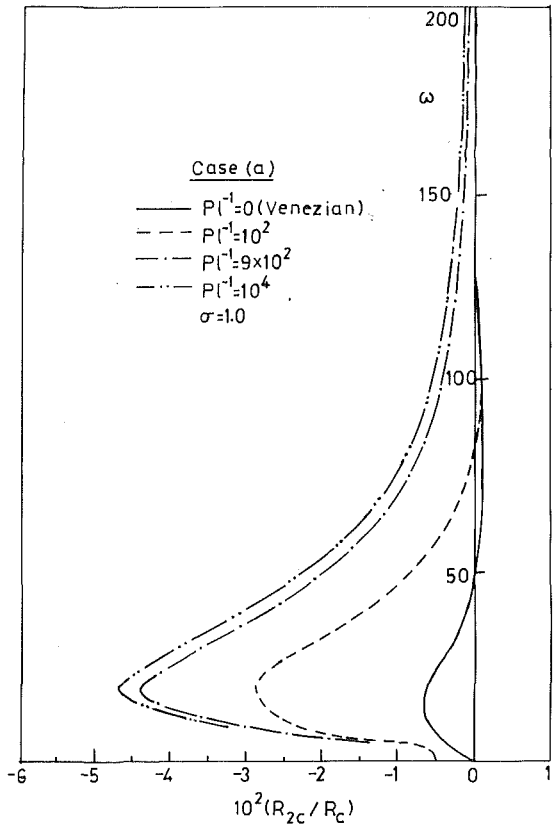

Fig. 1 Variation of Ra_{2c} with ω

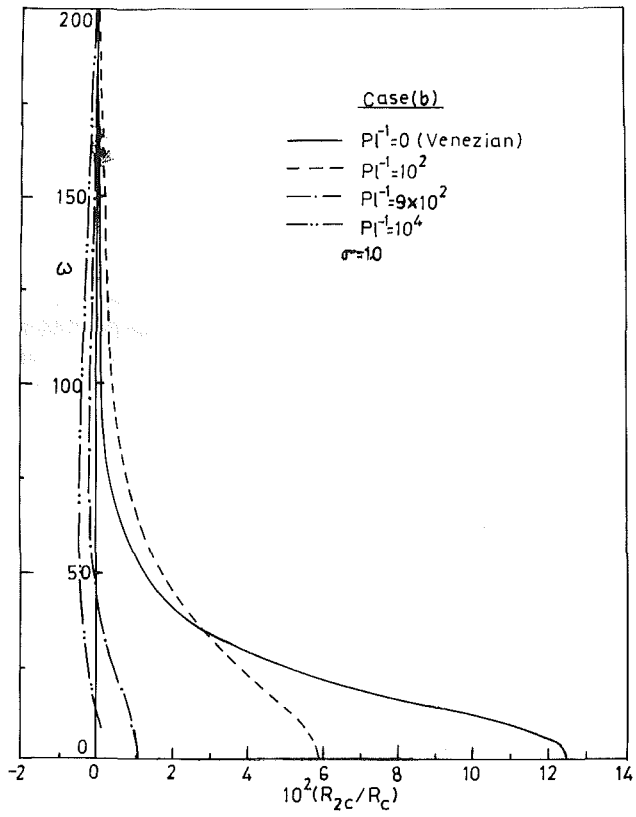

Fig. 2 Variation of Ra_{2c} with ω

temperature boundary conditions is investigated. The solution is obtained on the assumption that the amplitude of the applied temperature modulation is small. The following conclusions are drawn:

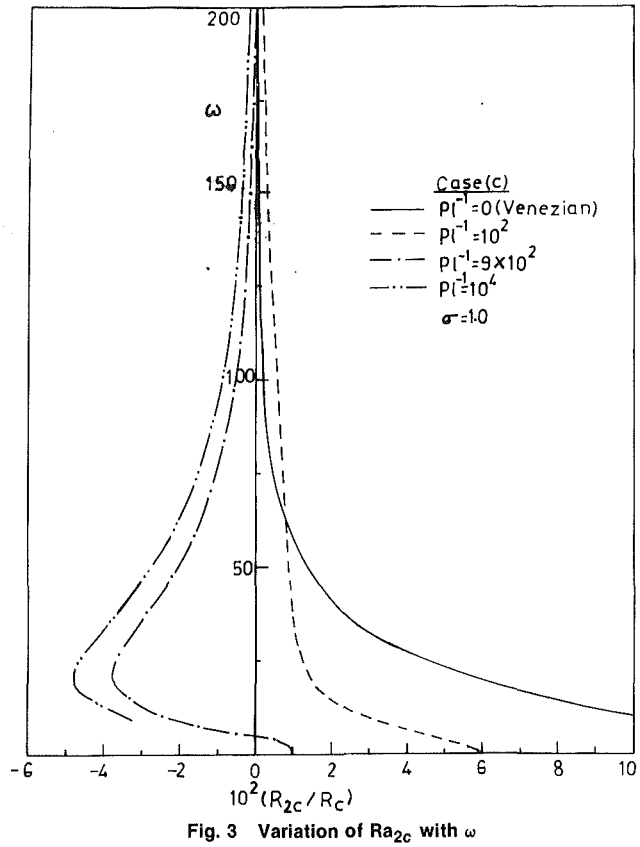

Fig. 3 Variation of Ra_{2c} with ω

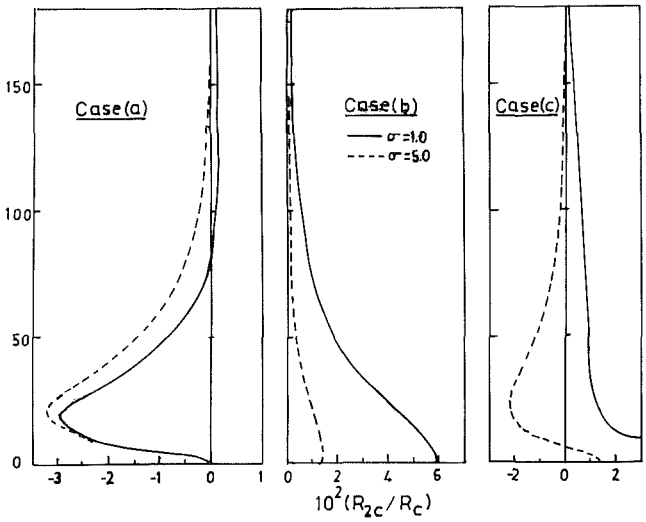

Fig. 4 Variation of Ra_{2c} with ω for different values of σ ($Pl^{-1}=10^2$)

1 In the case of symmetric modulation of the wall temperature, Ra_{2c}, which is the correction to the critical Rayleigh number, is found to be negative for all ranges of frequency except for $Pl^{-1} \leq 100$. Hence the effect is to destabilize the system. We observe, from Fig. 1, that the symmetric modulation has a mild stabilizing effect for $80 < \omega < 130$.

2 In the case of asymmetric modulation of the wall temperature, Ra_{2c} is found to be positive for small Pl^{-1} over the whole range of ω. This implies that the asymmetric modulation has a stabilizing effect (Fig. 2).

3 In the case of only lower wall temperature modulation, Ra_{2c} is positive for small Pl^{-1} and negative for large Pl^{-1}. The critical Rayleigh number increases at low frequency and hence has a stabilizing effect (Fig. 3).

4 The effect of an increase in porous parameter, Pl^{-1}, is to decrease the critical Rayleigh number (Figs. 1-3). Thus the effect of permeability is to augment the onset of convection in the presence of thermal modulation.

5 The effect of increasing Prandtl number is also to augment the onset of convection (Fig. 4).

6 The Brinkman model serves to bridge the gap between the viscous fluid limit and the Darcy limit in the sense that in the limit $Pl^{-1} \to 0$, we recover the results of viscous fluid (Venezian, 1969) and in the limit $Pl \to 0$ we recover the results of Darcy limit (Caltagirone, 1976; Malashetty, 1983). In particular, for $Pl \leq 10^{-4}$ the results of the present analysis are indistinguishable from the results for the Darcy problem.

7 The solutions obtained in the present paper, using the Power Integral technique of Malkus and Veronis (1958), are based on the assumptions that the amplitude of thermal modulation is small compared with the imposed steady temperature difference, and that the Darcy resistance dampens the convective currents so that nonlinear effects may be neglected. The validity of the results obtained here using these solutions will depend on the value of the modulating frequency. At higher frequencies, the effect of thermal modulation is confined to a narrow thermal boundary layer, of thickness $\Omega^{-1/2}$, near the boundary, and outside this thickness the basic temperature field of equation (2.8) has essentially a uniform gradient. In the absence of external constraints of rotation, magnetic field, or concentration gradient, it is known that a constant basic temperature gradient cannot generate subcritical instabilities in porous media (Rudraiah et al., 1982) even when the amplitude of thermal modulation is large. Since the amplitude of modulation is externally controlled, subcritical instabilities can be avoided by simply not allowing the amplitude to become very large. The amplitude of convection, however, cannot be controlled, but rather is determined by the nonlinear theory. On the other hand the situation is quite the opposite when the frequency of modulation is small. In this case, subcritical instabilities do exist even in the porous layer because of the same reasons given by Venezian (1969) in the study of viscous fluid layer.

The results obtained in this paper are valid only when the amplitude of the flow fields remain small throughout a cycle of modulation; otherwise the assumption of infinitesimal amplitude breaks down in the limit of $\omega \to 0$. For example when $n = 1$, the temperature $M(\omega, n)$ in equation (3.8) tends to zero and $W \to \infty$ as $\omega \to 0$. Hence, for the assumption of linear theory to be valid, we must have $|\epsilon w_1| < |W_0|$ or equivalently that $\omega > \epsilon$.

Acknowledgments

This work was sponsored by the University Grants Commission under the Departmental Special Assistance Programme.

References

Bejan, A., 1984, *Convection Heat Transfer*, Wiley, New York.

Bejan, A., 1987, in: *Convective Heat Transfer in Porous Media, Handbook of Single-Phase Convective Heat Transfer*, S. Kakac, R. K. Shah, and W. Aung, eds., Wiley, New York, Chap. XVI, pp. 1-34.

Catton, I., and Ayyaswamy, P. S., 1972, "Prediction of Momentum Transfer Between Rotating Cylinders," ASME *J. Appl. Mech.*, Vol. 39, No. 1, pp. 33-35.

Caltagirone, J. P., 1976, "Stabilite d'une Couche Poreuse Horizontale Soumise a des Conditions aux Limite periodiques," *Int. J. Heat Mass Transfer*, Vol. 19, pp. 815-820.

Cheng, P., 1979, "Heat Transfer in Geothermal Systems," *Adv. Heat Transfer*, Vol. 14, pp. 1-105.

Combarnous, M. A., 1978, "Natural Convection in Porous Media and Geothermal Systems," *Proc. VI Int. Heat Transfer Conference*, Toronto, Vol. 6, pp. 45-50.

Currie, I.G., 1967, "The Effect of Heating Rate on the Stability of Stationary Fluids," *J. Fluid Mech.*, Vol. 29, pp. 237-247.

Gasser, R. D., and Kazimi, M. S., 1976, "Onset of Convection in a Porous Medium With Internal Heat Generation," ASME JOURNAL OF HEAT TRANSFER, Vol. 98, pp. 49-54.

Homsy, G. M., and Sherwood, A. E., 1976, "Convective Instabilities in Porous Media With Through Flow." *AIChE J.*, Vol. 22, No. 1, pp. 168-174.

Jones, M. C., and Persichetti, J. M., 1986, "Convective Instability in Packed Beds With Through Flow," *AIChE J.*, Vol. 32, No. 9, pp. 1555-1557.

Joseph, D. D., 1976, *Stability of Fluid Motions I and II*, Springer Tracts in Natural Philosophy, Springer-Verlag, New York.

Lapwood, E. R., 1948, "Convection of a Fluid in a Porous Medium," *Proc. Camb. Phil. Soc.*, Vol. 44, pp. 508-521.

Malashetty, M. S., 1983, Ph. D., Thesis, Bangalore University, pp. 102-144.

Malkus, W. V. R., and Veronis, G., 1958, "Finite Amplitude Cellular Convection," *J. Fluid Mech.*, Vol. 4, Part 3, pp. 225-232.

Nield, D. A., 1968, "Onset of Thermohaline Convection in a Porous Medium," *Water Resources Research*, Vol. 4, No. 3, pp. 553-560.

Nield, D. A., 1975, "The Onset of Transient Convective Instability," *J. Fluid Mech.*, Vol. 71, Part 3, pp. 441-454.

Nield, D. A., 1984, "Convection in a Porous Medium" *Proc. CSIRO/DSIR Seminar on Convective Flows in Porous Media*, R. A. Wooding and I. White, eds., DSIR, Wellington, New Zealand, Vol. 129, pp. 5-32.

Nield, D. A., 1987, "Convective Instability in Porous Media With Through Flow," *AIChE J.*, Vol. 33, No. 7, pp. 1222-1224.

Rosenblat, S., and Herbert, D. M., 1970, "Low Frequency Modulation of Thermal Instability," *J. Fluid Mech.*, Vol. 43, pp. 385-389.

Rudraiah, N., and Srimani, P. K., 1980, "Finite Amplitude Cellular Convection in a Fluid Saturated Porous Layer," *Proc. Roy. Soc.*, Vol. A373, pp. 199-222.

Rudraiah, N., Veerappa, B., and Balachandra Rao, S., 1980, "Effects of Non-uniform Thermal Gradient and Adiabatic Boundaries on Convection in a Porous Medium," ASME JOURNAL OF HEAT TRANSFER, Vol. 102, pp. 254-260.

Rudraiah, N., Srimani, P. K., and Friedrich, R., 1982, "Finite Amplitude Convection in a Two Component Fluid-Saturated Porous Layer," *Int. J. Heat Mass Transfer*, Vol. 25, pp. 715-722.

Rudraiah, N., Veerappa, B., and Balachandra Rao, S., 1982, "Convection in a Fluid-Saturated Porous Layer With Non-uniform Temperature Gradient," *Int. J. Heat Mass Transfer*, Vol. 25, pp. 1147-1156.

Rudraiah, N., 1984, "Non-linear Convection in a Porous Medium With Convective Acceleration and Viscous Force," *Arabian J. Sci. Engg.*, Vol. 9, No. 2, pp. 153-167.

Rudraiah, N., and Malashetty, M. S., 1988, "Effect of Modulation on the Onset of Convection in a Porous Medium," *Vignana Bharathi* (a Bangalore University Journal), Vol. 11, No. 1, pp. 19-44.

Rudraiah, N., 1989, "Heat and Mass Transfer in Composite Materials," Sectional Presidential Address at the 76th Sci. Cong., Part II, pp. 1-26.

Somerton, C. W., and Catton, I., 1982, "On the Thermal Instability of Superposed Porous and Fluid Layers," ASME JOURNAL OF HEAT TRANSFER, Vol. 104, pp. 160-165.

Sutton, K. M., 1970, "Onset of Convection in a Porous Channel With Net Through Flow," *Phys. Fluids*, Vol. 13, pp. 1931-1937.

Venezian, G., 1969, "Effect of Modulation on the Onset of Thermal Convection," *J. Fluid Mech.*, Vol. 35, pp. 243-254.

Vortmeyer, D., Rudraiah, N., and Sasikumar, T. P., 1988, "Effect of Radiation on the Onset of Convection in a Porous Medium," *Int. J. Heat Mass Transfer*, in press.

Wooding, R. A., 1960, "Rayleigh Instability of a Thermal Boundary Layer in Flow Through a Porous Medium," *J. Fluid Mech.*, Vol. 9, pp. 183-192.

Analysis of Energy and Momentum Transport for Fluid Flow Through a Porous Bed

Kambiz Vafai

Mehmet Sozen

Department of Mechanical Engineering,
The Ohio State University,
Columbus, OH 43210

This paper presents an analysis for the forced convective flow of a gas through a packed bed of spherical solid particles, and the associated heat transport processes. Ergun's correlation was used as the vapor phase momentum equation in order to account for the inertia effects as well as the viscous effects. No local thermal equilibrium was assumed between the solid and the vapor phases. A thorough discussion of the thermal interactions between the solid and vapor phases and their effects on the fluid flow as well as the pressure and density fields is presented. The analysis shows that the local thermal equilibrium condition was very sensitive to the particle Reynolds number (Re_p) and the Darcy number (Da) while thermophysical properties did not have a very significant effect on this condition. On the other hand, two-dimensional behavior of certain variables was found to be very sensitive to thermophysical parameters but insensitive to Re_p and Da.

1 Introduction

Packed beds have been used very widely in the chemical industry and for energy storage purposes. Among the common applications are catalytic reactors, absorption and adsorption operations, as well as packed bed (pebble bed or rock pile) heat storage units. Due to their high performance, they are now also being considered for use in a number of applications such as fixed-bed nuclear propulsion systems and spacecraft thermal management systems. Utilization of phase-change material in microencapsulated form as the solid particles of the bed has also proved to be a promising research area. For example, Ananthanarayanan et al. (1987) have investigated numerically the utilization of encapsulated spherical Al–Si shots as the heat storage medium in a packed bed. All of these applications require a thorough understanding of the transport phenomena in packed beds, and in porous media in general. Therefore, clarification of a number of outstanding points with regard to transport phenomena in porous media needs to be undertaken. The aim of this investigation is to perform a fundamental part of this task.

A major part of the studies conducted to date on packed bed applications concentrate on utilizing incompressible fluids, liquid or gas, as the heat transfer medium. In these investigations a constant mass flow rate is assumed at every cross section of the packed bed and therefore there is no need for solving the continuity and momentum equations. The problem reduces to solving the governing energy equations for the solid and fluid phases. For this category of problems the two commonly employed models are the so-called single-phase conductivity and two-phase Schumann models. The main distinction between these two models is that whereas local thermal equilibrium is assumed to prevail in the single-phase model, no such assumption is made in the two-phase model. Therefore the single-phase conductivity model reduces to one governing energy equation, whereas in the two-phase model there are two governing energy equations with each of them possessing a fluid to solid phase heat transfer term. The origin of the two-phase models is the classical Schumann model (Schumann, 1929). Riaz (1977) presented an investigation and comparison of both models. From a practical point of view, both of these models are quite incomplete since they incorporate a number of major simplifying assumptions, such as neglecting the heat capacity and the conduction terms in the fluid phase, which may not be reasonable at all for certain cases. The additional fluid-to-solid phase heat transfer term in the two-phase model requires information about an important quantity, namely the fluid-to-particle heat transfer coefficient. A considerable amount of experimental work has been carried out for determining this quantity for packed beds using different sizes, shapes, and packing configurations of solid particles. Typical experimental investigations and some reviews on fluid-to-particle heat transfer coefficients may be found in the works of Baumeister and Bennett (1958), Bhattacharyya and Pei (1975), and Barker (1965).

The second major class of problems studied to date deals with compressible gas flow through a porous medium. To our knowledge, in this category of problems too, the complete transient, nonisothermal, and nonequilibrium flow of a compressible gas has not been studied. One-dimensional, transient, isothermal flow of an ideal gas through a porous medium has been studied analytically using the perturbation method by Kidder and La Habra (1957). Morrison (1972) also obtained analytical solutions by a perturbation method for one-dimensional isothermal and adiabatic flows of an ideal gas. In both of these investigations the Darcy formulation has been used for fluid flow. Nilson (1981), on the other hand, obtained an analytical solution for one-dimensional isothermal flow using the Ergun equation to account for the inertial effects. In all of these investigations it was assumed that the gas phase was in local thermal equilibrium with the solid phase. Goldstein and Siegel (1971) performed an analytical investigation on a steady, nonisothermal ideal gas flow in a porous medium. They also utilized the local thermal equilibrium assumption and the Darcy formulation.

As may be seen, the models used in both categories of problems described above are incomplete in one aspect or another since they concentrate on either the momentum transport in an isothermal or adiabatic flow or the energy transport in an incompressible flow. In addition they incorporate some simplifying assumptions such as local thermal equilibrium, neglect of conduction and transient terms in the gas phase energy equation, and neglect of inertial effects in momentum equa-

Contributed by the Heat Transfer Division for publication in the JOURNAL OF HEAT TRANSFER. Manuscript received by the Heat Transfer Division September 30, 1988; revision received July 21, 1989. Keywords: Packed and Fluidized Beds, Thermal Energy Storage, Transient and Unsteady Heat Transfer.

tions. Therefore their application is limited to certain special cases. Thus the need for a more rigorous formulation of the transport processes in a porous medium for establishing a more flexible and reliable model with a wide range of applicability becomes apparent. This is the main motive in undertaking the present investigation. The main objective of this study is to present a rigorous analysis and investigation for transient, non-equilibrium transport processes in a gas flow through a packed bed. The thermal interactions between the vapor and the solid phases and how the fluid flow as well as the pressure and density fields are affected by these interactions will be analyzed in detail. Another objective is to attain a better understanding of the situations under which the local thermal equilibrium assumption and one- or two-dimensional considerations of certain field variables would be justifiable. It is also aimed at investigating the effect of certain characteristic nondimensional parameters, such as the particle Reynolds number, the Darcy number, and certain thermophysical parameters, on the general qualitative behavior of the transport phenomena in packed beds.

2 Statement of the Problem and Analysis

The problem analyzed in this investigation is the transfer and storage of heat from a high-temperature reservoir into a packed bed that consists of randomly packed spherical particles of uniform size. The schematic diagram of the problem considered is depicted in Fig. 1. The extent of the packed bed in the z direction is assumed to be large enough to make the problem essentially two dimensional. Superheated Freon-12 is used as the heat transfer medium, i.e., the fluid phase flowing through the packed bed. Freon-12 was chosen as the vapor phase because it is a highly inert and stable compound whose critical point is well above the temperatures considered in this investigation. Moreover, it has a relatively high vapor density making it capable of carrying more thermal energy, and thus requiring smaller volume flow rate for a certain application, than other typical gases such as air. Three different materials have been considered for solid particles in order to determine the effect of different thermophysical parameters on the associated transport processes. The high-temperature vapor in the reservoir is suddenly allowed to flow through the packed bed initially filled by Freon-12, which is also initially at a uniform temperature and pressure throughout the packed bed. The pressure in the reservoir is higher than the initial pressure in the packed bed and it remains unchanged. A uniform pressure equal to the initial pressure in the packed bed is maintained at the right boundary of the bed so that there is always a pressure difference between the left-hand and the right-hand sides of the bed, thus sustaining the vapor flow. In essence

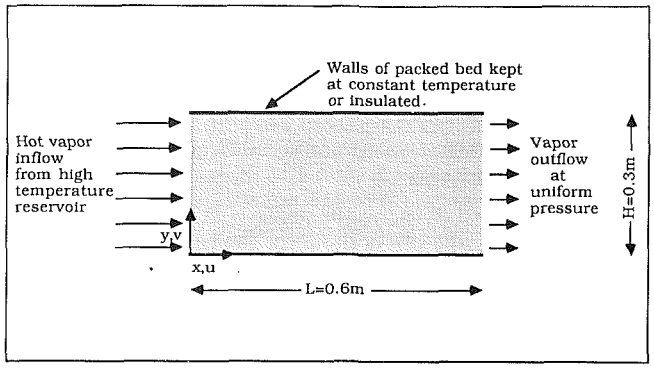

Fig. 1 Schematic diagram of the packed bed

this is a forced convection flow through a packed bed. Therefore, relatively higher particle Reynolds number flows than the Darcy regime flows are considered. Since the Darcy formulation would fail for these flows, Ergun's correlation (Ergun, 1952) is employed instead, in order to account for the inertial effects as well as the viscous effects. The problem is analyzed for the case in which the two horizontal walls of the packed bed are maintained at constant temperature.

The "local volume averaging" technique is used in developing the governing equations for the transport processes in the packed bed. The volume averaging process is performed by associating a small volume V closed by a surface S with every point in the porous medium (Vafai and Whitaker, 1986). The two important averages of a quantity frequently encountered in the governing equations are the so-called local volume average and the intrinsic phase average. The local volume average of a quantity Φ associated with phase Ψ is defined as

$$\langle \Phi \rangle = \frac{1}{V} \int_{V_\Psi} \Phi dV \tag{1}$$

while the intrinsic phase average of a quantity Φ associated with phase Ψ is defined as

$$\langle \Phi \rangle^\Psi = \frac{1}{V_\Phi} \int_{V_\Psi} \Phi \, dV \tag{2}$$

where V_Ψ is the volume associated with phase Ψ. Thus it becomes meaningful to represent the intrinsic properties such as the temperature and the density of a phase by the intrinsic volume averaged quantities and to represent the frequently used "superficial velocity" by the local volume averaged quantity.

Considerable information is available on the application of the spatial-averaging theorem for establishing the local volume

Nomenclature

a_{sv} = specific surface area, m^2/m^3
c_p = specific heat at constant pressure, J $kg^{-1}K^{-1}$
d_p = particle diameter, m
Da = Darcy number $= K/H^2$
F = geometric factor defined in equation (11)
G = mass velocity, kg $m^{-2}s^{-1}$
h_{sv} = fluid-to-particle heat transfer coefficient, $Wm^{-2}K^{-1}$
H = height of the packed bed, m
k = thermal conductivity, $Wm^{-1}K^{-1}$
K = permeability, m^2
L = length of the packed bed, m
P = pressure, N m^{-2}
R = gas constant, J $kg^{-1}K^{-1}$
Re_p = particle Reynolds number $= \rho u d_p/\mu$
T = temperature, K
u = velocity m s^{-1}
V = volume, m^3
α = thermal diffusivity, $m^2\ s^{-1}$
ϵ = porosity
Θ = dimensionless temperature $= (T-T_0)/(T_{vin}-T_0)$
μ = absolute viscosity, kg $m^{-1}s^{-1}$
ρ = density, kg m^{-3}
τ = dimensionless time $= tu^*/L$

Subscripts

0 = initial
s = solid
v = vapor
vin = vapor inlet
seff = effective property for solid
veff = effective property for vapor

Superscripts

s = solid
v = vapor
* = reference

Symbols

$\langle\ \rangle$ = "local volume average" of a quantity

averages of the conservation equations and the models formed by using this principle (Vafai and Whitaker, 1986; Whitaker, 1977; Vafai, 1984). Application of the same procedure will be used for establishing the model for analyzing the energy and momentum transfer in the packed bed with forced convective flow. The major assumptions and simplifications that are employed in this study are:

1 Freon-12 used as the vapor phase is always in the superheated form and obeys the ideal gas equation of state.
2 Natural convection effects are negligible. This assumption is based on the fact that the bed is dominated by forced convection.
3 The solid phase is incompressible. The packed bed is assumed to have uniform porosity and to be isotropic.
3 Boundary and variable permeability effects are not considered.
5 The temperature range used in the analysis of the problem is relatively small (20 K), therefore the physical properties such as thermal conductivity, viscosity, and specific heat capacity are considered to be constant.
6 Due to the relatively low temperature range in the present investigation the interparticle and intraparticle radiation heat transfer is negligible.

With these points taken into consideration the volume-averaged governing equations are derived as

Vapor phase continuity equation:

$$\frac{\partial}{\partial t}\left(\epsilon\langle\rho_v\rangle^v\right) + \nabla\cdot\left(\langle\rho_v\rangle^v\langle\mathbf{u}_v\rangle\right) = 0 \tag{3}$$

Vapor phase momentum equation:

$$\nabla\langle P_v\rangle^v = -\frac{\langle\rho_v\rangle^v F\epsilon}{K_v^{1/2}}\left[\langle\mathbf{u}_v\rangle\cdot\langle\mathbf{u}_v\rangle\right]\mathbf{j} - \frac{\mu_v}{K_v}\langle\mathbf{u}_v\rangle \tag{4}$$

Vapor phase energy equation:

$$\epsilon\langle\rho_v\rangle^v c_{pv}\frac{\partial\langle T_v\rangle^v}{\partial t} + c_{pv}\langle\rho_v\rangle^v\langle\mathbf{u}_v\rangle\cdot\nabla\langle T_v\rangle^v = \nabla\cdot\left\{k_{\text{veff}}\cdot\nabla\langle T_v\rangle^v\right\} + h_{sv}\,a_{sv}\left(\langle T_s\rangle^s - \langle T_v\rangle^v\right) \tag{5}$$

Solid phase energy equation:

$$(1-\epsilon)\rho_s c_{ps}\frac{\partial\langle T_s\rangle^s}{\partial t} = \nabla\cdot\left\{k_{\text{seff}}\cdot\nabla\langle T_s\rangle^s\right\} - h_{sv}\,a_{sv}\left(\langle T_s\rangle^s - \langle T_v\rangle^v\right) \tag{6}$$

Vapor phase equation of state:

$$\langle P_v\rangle^v = \langle\rho_v\rangle^v R\langle T_v\rangle^v \tag{7}$$

where $\langle\rho_v\rangle^v$, $\langle u_v\rangle$, $\langle T_v\rangle^v$, $\langle T_s\rangle^s$, $\langle P_v\rangle^v$, ϵ, R and $\mathbf{j}$ represent the vapor density, x component of the vapor velocity, vapor temperature, solid temperature, vapor pressure, porosity, the ideal gas constant for the vapor phase, and the unit vector oriented along the vapor velocity, respectively. The initial conditions are

$$P_v(x, y, t=0) = P_0$$
$$T_v(x, y, t=0) = T_s(x, y, t=0) = T_0 \tag{8}$$
$$u_v(x, y, t=0) = 0$$

The boundary conditions are

$$P_v(0, y, t) = P_{\text{in}},\ P_v(L, y, t) = P_0$$
$$T_v(0, y, t) = T_{\text{vin}} \tag{9}$$
$$T_v(x, 0, t) = T_v(x, H, t) = T_s(x, 0, t) = T_s(x, H, t) = T_0$$

It should be noted that the vapor phase momentum equation given above differs in nature from the usual momentum equation for regular media, and it essentially accounts for the viscous and the form drag resistances in the porous matrix. It should also be emphasized that the behavior of a real gas would be more or less the same as the ideal gas case modeled in this investigation. Replacing the ideal gas equation of state by one for a real gas taking into account the compressibility factor will result in an appropriate model for the forced convective flow of a real gas through a packed bed and the associated heat transport phenomena. The permeability of the packed bed, K_v, and the geometric function F in the vapor momentum equation can be obtained from the experimental results of Ergun (Ergun, 1952; Vafai, 1984) in terms of the porosity ϵ and the particle diameter d_p as follows:

$$K_v = \frac{\epsilon^3 d_p^2}{150(1-\epsilon)^2} \tag{10}$$

$$F = \frac{1.75}{\sqrt{150}\,\epsilon^{3/2}} \tag{11}$$

In equations (5) and (6), a_{sv} represents the specific surface area of the packed bed, i.e., the surface area per unit bulk volume of the packed bed. This ratio can be expressed in terms of the particle diameter and porosity as (Dullien, 1979)

$$a_{sv} = \frac{6(1-\epsilon)}{d_p} \tag{12}$$

For the fluid-to-particle heat transfer coefficient h_{sv}, it is necessary to choose an empirical correlation from a range of existing experimental results. Considering the ranges of the particle diameter d_p and the particle Reynolds number Re_p, used in this investigation, the empirical correlations established by Gamson et al. (1943) were found to be the most appropriate. These empirical correlations, which were presented in terms of Colburn–Chilton j_h factors, can be expressed in the following form after some manipulation:

$$h_{sv} = 1.064 c_p G\left(\frac{c_p\mu}{k}\right)^{-2/3}\left(\frac{d_p G}{\mu}\right)^{-0.41} \quad \text{for} \quad \frac{d_p G}{\mu} \geq 350 \quad \text{(turbulent)} \tag{13}$$

$$h_{sv} = 18.1 c_p G\left(\frac{c_p\mu}{k}\right)^{-2/3}\left(\frac{d_p G}{\mu}\right)^{-1} \quad \text{for} \quad \frac{d_p G}{\mu} \leq 40 \quad \text{(laminar)} \tag{14}$$

where G represents the rate of mass flow through a unit surface area perpendicular to the flow direction.

Equations (3) through (7) form the model for analyzing the energy and momentum transport in unsteady forced convection flow of a gas through a packed bed. This is a system of five highly coupled equations, which we must utilize to analyze the five pertinent variables, namely $\langle T_v\rangle^v$, $\langle T_s\rangle^s$, $\langle\rho_v\rangle^v$, $\langle u_v\rangle$, and $\langle P_v\rangle^v$. In the next section the procedure for the numerical solution of the above model will be explained.

3 Procedure and Numerical Scheme

A numerical algorithm was developed for solving the system of equations presented in the previous section. The Beam–Warming type implicit method frequently used in compressible flow problems in regular media was not applicable in this case because the nature of the equations made it impractical and inefficient to write them in the required conservative form. Therefore it was necessary to employ explicit schemes. In developing the finite difference forms of equations (3) through (7), central difference approximations were used for most of the spatial derivatives for the inner grid points. Spatial derivatives for the grid points on the left and right boundaries were formed by first-order forward and backward difference approximations, respectively. Also it was found, through extensive experimentation, that for the pressure gradient term in the vapor phase momentum equation, forward differencing was more stable and accurate then central differencing during the "*initial stage*," which will be explained later. Therefore first-order forward differencing was employed for that term in the *initial stage* and it was converted to central differencing in the "*later stage,*" which will also be discussed later. Upwind differencing was implemented for the convective terms in the vapor energy and continuity equations in order to insure the stability of the numerical scheme. It was found through numerical experimentation that using central differencing in the convective term of the continuity equation did not make any appreciable change in the results.

While the vapor density at each grid point on the left boundary was determined from the equation of state by using the boundary conditions for temperature and pressure, the density at each grid point on the right boundary was determined from the equation of state by using the vapor temperature computed from equation (5) and the pressure from the right boundary condition. For the rest of the grid points the density was computed by the vapor continuity equation. The velocity $\langle u_v \rangle$ for all the grid points except those on the right boundary was determined from the vapor phase momentum equation. The velocity at the grid points on the right boundary was computed by linear extrapolation from the preceding two grid points in the x direction. Temperatures of the solid and fluid phases were determined by the associated energy equations while the pressure was determined from the equation of state.

A number of interesting observations were made on the stability of the numerical scheme. It was found that the time step used in the *initial stage* could be increased in the *later stage* by an order of magnitude in some cases without any influence on the accuracy of the results. It was observed that for a fixed Re_p, decreasing Da consistently increased the stability of the numerical scheme in both the *initial* and *later stages*. Decreasing Da at a fixed Re_p requires using smaller particle diameter (hence smaller permeability) and a larger pressure difference across the packed bed. In other words the stability of the numerical scheme was observed to increase with an increase in the magnitude of the damping forces.

For a fixed Da, smaller value of Re_p translate into smaller mass flow rates and smaller amounts of thermal energy flowing into the packed bed per unit time. Therefore, for small values of Re_p the CPU time required for simulating the complete charging of the packed bed becomes large. For instance, for the case when lithium-nitrate-trihydrate is the solid phase and $\mathrm{Da} = 1.18 \times 10^{-8}$, the CRAY CPU time required for simulating the complete charging of the packed bed was of the order of 1 hr for $\mathrm{Re}_p = 1100$. For this specific case the Δt employed in the computations was 1.8×10^{-5} s, for the *initial stage* while it was possible to push it up to 1.8×10^{-4} s, for the *later stage*. The CPU time was estimated to increase significantly for small Reynolds numbers. Therefore full simulation of such cases is very costly on the CRAY and would be extremely tedious on regular mainframes. For this reason no attempt was made to perform the complete simulation for such cases.

To analyze the effect of different parameters on energy and momentum transport in the packed bed, different solid particle sizes and different materials for the solid phase were considered. A complete set of computations was carried out for particle diameter values of 1 mm, 2.5 mm, and 5 mm for the set of different materials considered for the solid phase. Several runs were also performed for a particle diameter of 1 cm. The three different materials considered for the solid phase in this study were lithium-nitrate-trihydrate, sandstone, and 1 percent carbon-steel. The main criterion in selecting these materials was to obtain a wide range of thermophysical properties and explore their effects on the qualitative behavior of the transport phenomena, since the properties of the bed material may differ widely from one application to another. The average porosity is chosen to be equal to the asymptotic value of 0.39 throughout the packed bed. This is a valid assumption for all cases in which the ratio of the solid particle diameter to the characteristic global dimension of the packed bed is below a certain value, as determined by Benanati and Brosilow (1962). The following physical data were used for the boundary conditions and for the properties of the materials considered in the numerical computations:

Freon-12	Lithium-nitrate-trihydrate
$R = 68.7588$ J/kg•K	$c_p = 2090$ J/kg•K
$c_p = 602$ J/kg•K	$k = 0.5$ W/m•K
$k = 0.0097$ W/m•K	$\rho = 1550$ kg/m^3
$\mu = 12.6 \times 10^{-6}$ Pa•s	
Sandstone	**1 percent carbon-steel**
$c_p = 710$ J/kg•K	$c_p = 473$ J/kg•K
$k = 1.83$ W/m•K	$k = 43$ W/m•K
$\rho = 2200$ kg/m^3	$\rho = 7800$ kg/m^3

$P_0 = 100$ kP $\quad T_{\mathrm{vin}} = 300$ K $\quad T_0 = 280$ K

The effects of three important parameters have been studied extensively in this investigation. These are the particle Reynolds number, the Darcy number, and the ratio of the solid phase thermal diffusivity to liquid thermal diffusivity. Different Reynolds numbers were obtained by varying the pressure in the reservoir, i.e., by applying different pressure gradients across the packed bed. Different Darcy numbers resulted from different particle sizes, as the permeability of the packed bed varies with the particle diameter (see equation (10)). The ratio of solid-to-vapor thermal diffusivity (α_s/α_v) was of a different order of magnitude for each of the three materials considered for the solid phase.

3.1 Numerical Accuracy. The numerical computations were performed on a CRAY XMP/28. Full vectorization was achieved in all the subroutines in the numerical code. As a result the CPU time required on the CRAY for a certain run using a grid mesh of 21×11 was more than 30 times smaller than the CPU time required for the same run on VAX 8530. Due to the nature of the governing equations, small time steps had to be employed for the stability of the numerical scheme. A systematic decrease in the grid size was carried out and the corresponding stable Δt was employed until an agreement to within 1 percent was achieved in the solutions between the consecutive grid sizes, and the effect of reducing the Δt further did not make any appreciable change in the solutions. Some other detailed features of the numerical stability have already been discussed above.

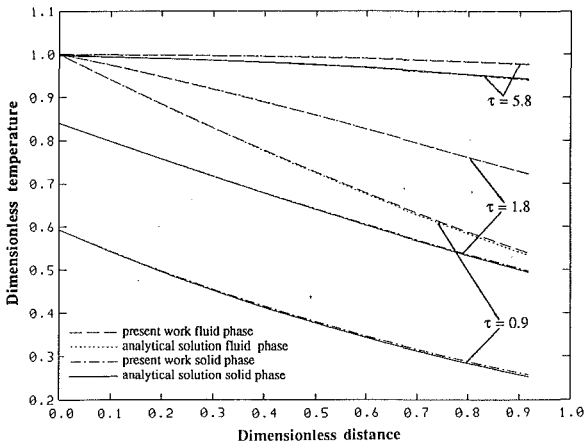

Fig. 2 Comparison of the solid and fluid phase temperature distribution generated by our numerical algorithm with the analytical solution in Riaz (1977)

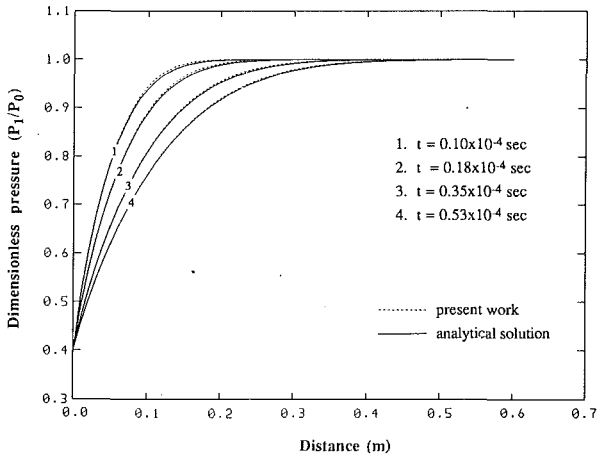

Fig. 3 Comparison of the numerical pressure solution with the analytical solution of Kidder and La Habra (1957)

Checking the reliability of a numerical analysis also requires benchmarking against some analytical solutions, experimental results, or other reliable numerical results. As mentioned earlier, no complete analysis of unsteady, nonisothermal, and nonequilibrium flow of an ideal gas through a porous medium is available in the literature. Therefore, in order to check the computational algorithm developed in this investigation, it was necessary to compare its results with different analytical solutions dealing with different aspects of energy and momentum transport in porous media. This benchmarking was performed in two main sections, namely, the comparison of momentum transport (pressure and hence velocity distributions) in an isothermal flow of an ideal gas through a porous medium, and the comparison of energy transport (temperature distribution in solid and fluid phases) of an incompressible fluid flow through a porous medium with no local thermal equilibrium between the solid and vapor phases. The two sources chosen for this benchmarking were the most relevant sources found whose parameters were translatable to those of the present numerical scheme.

The benchmarking of the energy transport was carried out by comparing the analytical solution of the simplified Schumann model presented by Riaz (1977) with the results generated by our numerical scheme. This was achieved by making the necessary adjustments to our numerical algorithm to reduce it to a system that was equivalent to the simplified Schumann model, i.e., by neglecting some of the transport terms. This comparison is depicted in Fig. 2 for the fluid phase and solid phase temperature distributions, respectively, in terms of the dimensionless variables that appear in the work of Riaz (1977). As may be seen from these figures, the agreement between our numerical results and the analytical solution is excellent. The benchmarking of the momentum transport was carried out by comparing our results with the analytical solution to a one-dimensional isothermal flow of an ideal gas through a semi-infinite porous medium presented by Kidder and La Habra (1957). Although this analytical solution was obtained for a semi-infinite porous medium, it could be safely compared with our numerical results for small times during which the information from the boundary had not reached the total length of the packed bed. The comparison of the analytical solution with the results generated by the present numerical algorithm is shown in Fig. 3 in terms of the dimensional distance and time and the dimensionless pressure that appears in the work of Kidder and La Habra (1957). Again, very good agreement can be observed between the numerical results and the analytical solution. Sixty-one grid points were used in the x direction for this computation. It should be noted that the use of a larger number of grid points would result in an even better agreement.

4 Results and Discussion

The reference quantities that are used in nondimensionalizing the variables are the reference density, reference velocity, and reference pressure denoted by ρ^*, u^*, and P^*, respectively. For convenience, the reference pressure P^* for each run was taken to be the average of the initial pressure P_0 and the pressure of the inflowing vapor from the reservoir, P_{in}. Likewise, the reference density ρ^* is computed from the equation of state by using P^* and the average value of the initial and the vapor inflow temperatures. Finally, the reference velocity, u^* is computed from equation (4) by using ρ^* and the global pressure gradient applied across the packed bed. The dimensionless time chosen for presenting the results is defined as $\tau = tu^*/L$, and the dimensionless temperature is defined as $\Theta = (T - T_0)/(T_{vin} - T_0)$.

For each of the computational runs two distinct regimes were observed. These two regimes will be referred to as the "*initial stage*" and the "*later stage.*" The *initial stage* exists for a very short period of time starting with the application of the high-temperature and high-pressure boundary conditions on the left, and ending when the pressure distribution across the packed bed becomes almost linear. This process takes place extremely quickly and afterward the pressure distribution remains in a quasi-steady state. During the *initial stage* no appreciable thermal penetration depth develops in the packed bed. The *later stage* is the period of time following this *initial stage.*

The vapor velocity, density, and pressure distributions along the x direction at the midplane of the packed bed during the *initial stage* for the case where the solid phase material was lithium-nitrate-trihydrate are depicted in Fig. 4. It turned out that for this case the variation of different variables in the y direction for the core region of the packed bed did not exceed 1 percent. Therefore, it is very reasonable to present the results for this case in one dimension only. The variation in the velocity distribution can be explained by the pressure variation. Initially when the high-pressure boundary condition is applied the large pressure gradient causes high velocities. Gradually as the pressure propagates in time and space, the large pressure gradients die away, and the velocities follow the same trend. As mentioned earlier, there is no appreciable thermal penetration depth during the *initial stage.* Therefore there is a sharp decrease in the vapor temperature near the entrance of the bed. This drop in temperature is more pronounced than the corresponding pressure drop. The resulting peak value of the vapor density

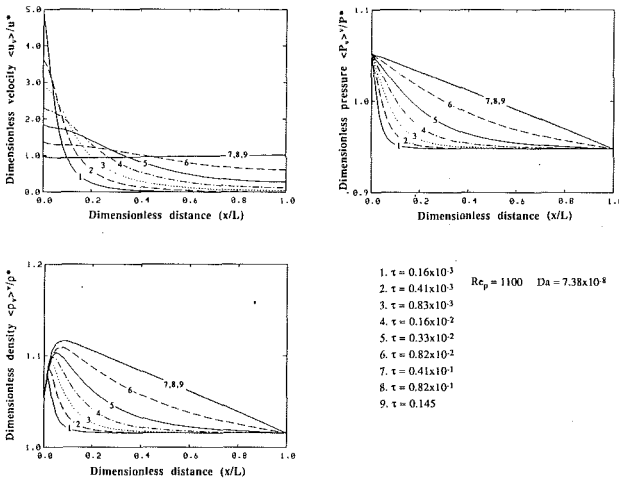

Fig. 4 Vapor velocity, density, and pressure distributions in the vapor at midplane of the packed bed in the *initial stage*

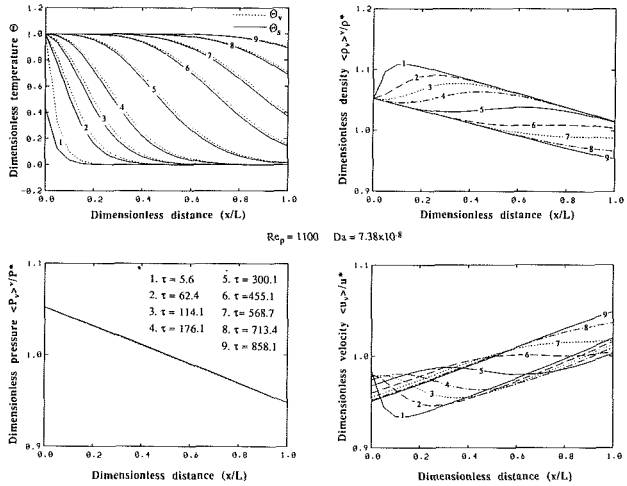

Fig. 5 Temperature distribution in the solid and vapor phases and velocity, density, and pressure distributions in the vapor phase at the midplane of the packed bed in the *later stage*

close to the entrance region, therefore, follows from the equation of state. Beyond the peak region the temperature is almost constant while the pressure decreases in the x direction. Hence, based on the equation of state the vapor density will follow the same trend as the vapor pressure. On the other hand, the temporal increase in the vapor density during the *initial stage* occurs because during this period the mass flux at any point is larger than the mass flux at a point on its right, i.e., there is a continuous net mass flux into the bed. Therefore the second term of equation (3) has a negative value. Thus the density has to increase in time during the *initial stage* in order to satisfy the continuity equation of the vapor phase.

The variations of the solid and vapor temperatures, vapor density, velocity, and pressure during the *later stage* for the above mentioned case are shown in Fig. 5. It should be noted that the *later stage* starts after the pressure distribution in the packed bed becomes almost linear and remains in that quasi-steady state thereafter. During this stage the thermal penetration depth develops as shown in the figure. Since the effect of the transient term in the vapor continuity equation essentially dies away during the *initial stage*, an almost steady-state continuity equation prevails in the *later stage*. This requires the existence of an inverse relationship between the density and velocity distributions. This behavior can be seen in the figure as almost a mirror image trend in the variations of the density and the velocity, i.e., as one increases the other one decreases. The vapor pressure distribution is almost linear in the x direction and remains almost unchanged. Furthermore, at any time before the packed bed is fully charged, the slope of the temperature profile is much steeper than the slope of the pressure profile within a major portion of the thermal penetration depth. Therefore, during such times the vapor density increases in the x direction within the zone. Beyond this zone the vapor temperature is almost constant and the vapor pressure decreases linearly, and so the vapor density also decreases linearly. The advancement of thermal penetration front, which translates into a temporal increase in temperature at a given x location, causes a decrease in density in time at that location. This of course follows from the equation of state. When ultimately a uniform temperature is reached throughout the packed bed, the density distribution becomes similar to the pressure distribution as dictated by the equation of state. From the variation of the different field variables in Fig. 5 it becomes evident that the flow field is very much influenced by the temperature field.

It should be noted that a grid mesh of 21×11 was used in all the *later stage* computations for lithium-nitrate-trihydrate runs except the *initial stage* presented here, in which a 61×11 mesh was used in order to obtain smoother variations. It was observed that, even though refining the mesh resulted in smoother graphs, it did not change the quantitative behavior or increase the accuracy of the results appreciably. However, a refined mesh greatly increased the CPU time. This was the case despite the use of a highly vectorized scheme (which indeed had a significant effect in reducing the CPU time). The reason for this was the complex nature of the equations.

A typical sample run in which two-dimensional variations are very pronounced is considered next. The solid particle material considered for this case was 1 percent carbon-steel. Figure 6(*a*) and 6(*b*) depict the distributions of the solid and vapor phase temperatures, the vapor density, and the vapor pressure. As may be seen from this figure there is considerable heat loss through the horizontal walls of the packed bed due to conduction heat transfer in the y direction and there is a strongly two-dimensional temperature distribution within the packed bed. Apparently, a one-dimensional modeling for such a case will yield erroneous results. In order to track the two-dimensional behavior of the variables better a 21×21 grid mesh was employed for the cases in which sandstone or steel was considered as solid material.

It was observed from the numerical computations that during the *later stage* of each run, the value of the vapor-to-solid heat transfer coefficient computed for each grid point at each time step was very stable and did not differ more than 2 percent from the reference vapor-to-solid heat transfer coefficient based on ρ^* and u^*. Therefore an assumption that this value is a constant for all the grid points during the *later stage* would be very reasonable. Considerable CPU time could be saved in this way by eliminating the otherwise required computations from equations (13) and (14) at each time step. However, all the runs for this investigation were performed by using the variable heat transfer coefficient.

4.1 Effect of the Darcy Number (Da). In order to determine the effect of the Darcy number on energy and momentum transport in the packed bed, different cases with different Darcy numbers were compared. These comparisons were performed for a fixed particle Reynolds number of 1100 using the same solid material. Again lithium-nitrate-trihydrate was used for convenience in presenting the results, since for this material the distribution of variables turned out to be essentially one-dimensional in all of these cases. Figure 7 depicts the temperature distributions in the solid and vapor phases along the packed bed at different time levels for Darcy numbers

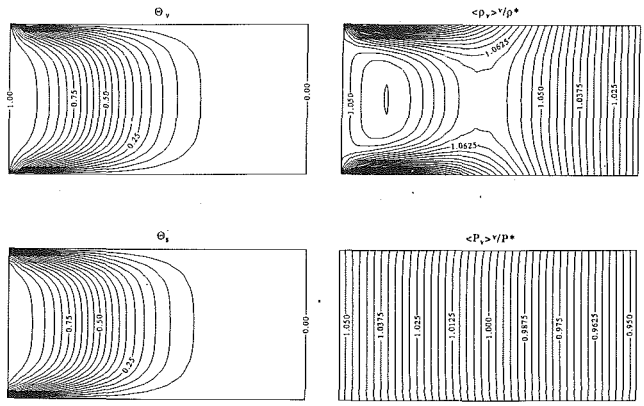

Fig. 6(*a*) Temperature, density, and pressure distribution in the packed bed for steel at $\tau = 211.4$

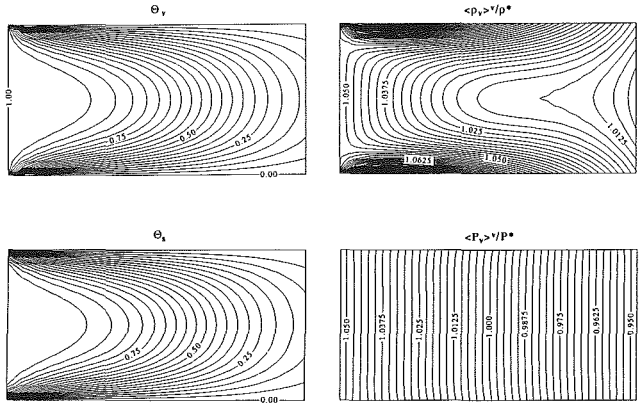

Fig. 6(*b*) Temperature, density, and pressure distribution in the packed bed for steel at $\tau = 546.2$

1.18×10^{-8}, 7.38×10^{-8}, and 2.95×10^{-7}. The time levels in this figure were chosen such that they would result in a reasonable presentation of the penetration fronts in each case. It can easily be seen that as the Darcy number decreases, the difference between the solid and vapor phase temperatures decrease. The reason for this is that a decrease in the Darcy number translates into a decrease in the particle diameter (see equation (10)). As the particle diameter decreases, the specific surface area a_{sv} of the packed bed increases, thus increasing the vapor-to-solid heat transfer interaction by offering a larger surface area. Hence the heat exchange between the solid and vapor phases becomes more efficient. Therefore the local thermal equilibrium assumption would be more justifiable at low Darcy number flows.

4.2 Effect of the Particle Reynolds Number (Re_p). The procedure followed for determing the effect of Re_p on transport phenomena was similar to the one carried out in determining the effect of the Darcy number. This time Da was fixed at 7.38×10^{-8} for the same solid phase material while Re_p was varied. The temperature distributions for the solid and vapor phases along the x direction at the horizontal midplane of the packed bed are shown in Fig. 8 for Re_p of 400, 1100, and 2126. Again, the time levels for each of these figures were chosen such that they would result in a reasonable presentation of the penetration fronts in each case. As can be seen from these figures, the difference between the temperatures of the solid and fluid phases at any point increases with an increase in Re_p. This increase should be attributed to the velocity of the flow since the specific surface area of the packed bed is the same in all of these cases. As the velocity of the flow increases the time for the solid-to-vapor heat interaction decreases. This will

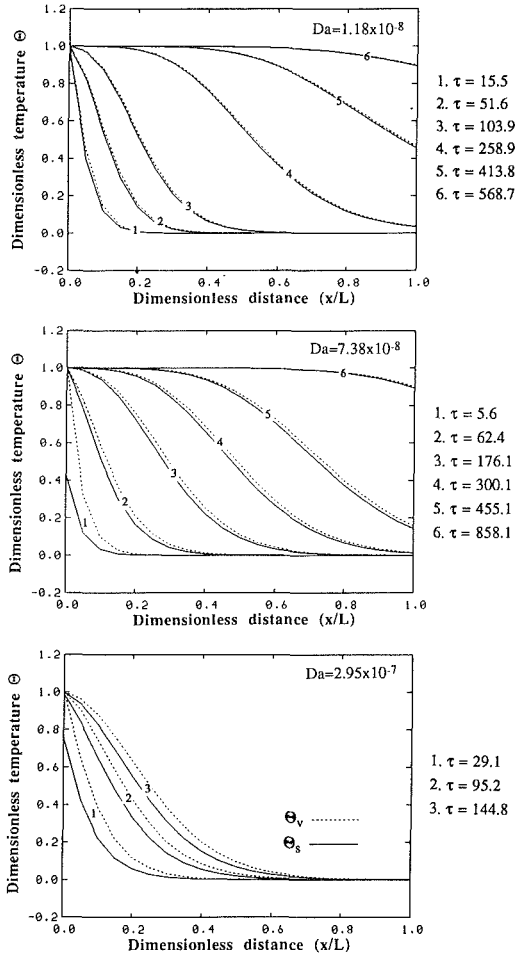

Fig. 7 Temperature distribution in the solid and vapor phases at the midplane of the packed bed for $Re_p = 1100$ and $Da = 1.18\times10^{-8}$, 7.38×10^{-8}, 2.95×10^{-7}

cause a decrease in the efficiency of heat exchange between the solid and vapor phases and hence the deviation from the local thermal equilibrium will increase.

The combined effect of increasing both Re_p and Da was found to have, as expected by now, a much more pronounced effect on the local thermal equilibrium assumption. It becomes evident that for high Re_p and Da flows the local thermal equilibrium assumption becomes very erroneous. It should be noted that the above results were also found to be valid for the cases in which sandstone or steel was used as the solid phase. Lithium-nitrate-trihydrate was chosen just for its convenience in presenting the results.

4.3 Effect of the Thermal Diffusivities Ratio (α_s/α_v). It was found through numerical experimentations that the ratio of the solid phase thermal diffusivity to liquid phase thermal diffusivity, α_s/α_v, was the most appropriate parameter to represent the combined effects of k_s/k_v, c_{ps}/c_{pv}, and ρ_s/ρ_v ratios, all of which are determining factors in the overall heat transfer process. Furthermore, from the numerical experimentation it was also found that the one-dimensional approach was very satisfactory for all cases in which lithium-nitrate-trihydrate was used as the solid phase for which α_s/α_v was of the order of 0.035 to 0.075. Therefore the effect of α_s/α_v will be shown for cases in which sandstone and steel were used as the solid phase. The temperature distributions in the solid and fluid phases for two cases in which sandstone and steel were used, respectively, are shown in Figs. 9(*a*) and 9(*b*). In both of these figures the value of Re_p was 1100 and the Darcy number was chosen to

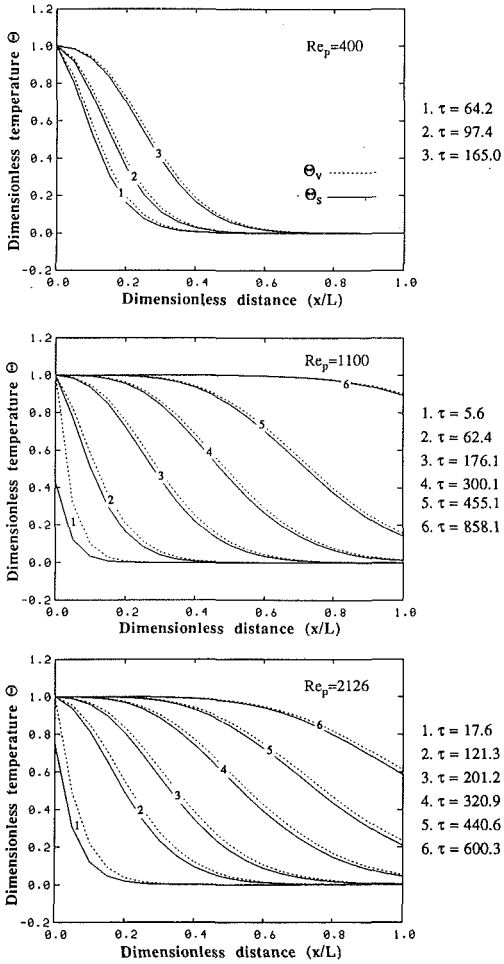

Fig. 8 Temperature distribution in the solid and vapor phases at the midplane of the packed bed for Da = 1.18×10^{-8} and Re$_p$ = 400, 1100, and 2126

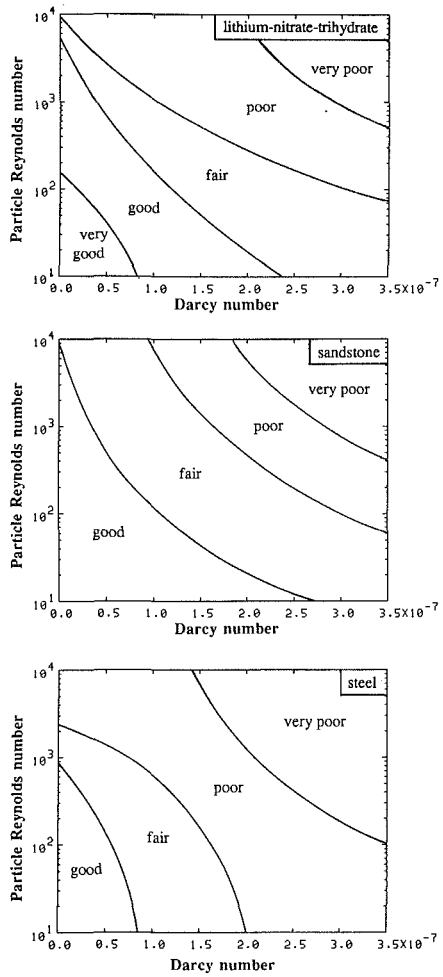

Fig. 10 Assessment of the validity of local thermal equilibrium for lithium-nitrate-trihydrate, sandstone, and steel

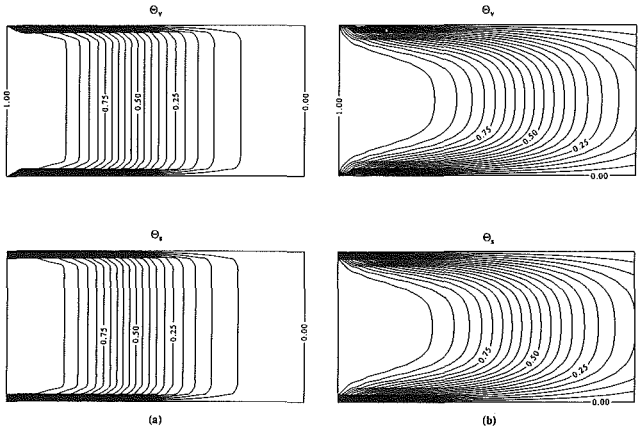

Fig. 9(a) Temperature distribution in the solid and vapor phase in the packed bed for sandstone for Re$_p$ = 1100 and Da = 1.18 × 10^{-8} at τ = 103.9; (b) temperature distribution in the solid and vapor phases in the packed bed for steel for Re$_p$ = 1100 and Da = 1.18 × 10^{-8} at τ = 568.7

be 1.18×10^{-8}. In the case of sandstone α_s/α_v was equal to 0.57, whereas in the case of steel it was 5.71. As can be seen from these figures the temperature distributions are strongly two-dimensional in the case of steel and mildly two-dimensional in the case of sandstone for which one-dimensional approach may give fair results. It should be noted that the same qualitative behavior was observed for all ranges of Re$_p$ and Da considered in this investigation, which proves that two-dimensional effects are not sensitive to the particle Reynolds and Darcy numbers.

The thermal diffusivity ratio that we have chosen as the characteristic parameter for assessing the two dimensionality gives a measure of the strength of the conduction heat loss through the walls of the packed bed. This is basically what causes the two-dimensional effects since the rate of conduction heat loss from the walls becomes comparable in magnitude to the axial convective energy flow rate and the transient energy storage rate. Since conduction heat transfer in the working fluid is usually not significant, the conduction heat loss from the walls of the packed bed is primarily the result of heat conduction in the solid phase, and for this loss to be comparable to the other modes of heat transfer the thermal diffusivity of the solid phase has to be significantly larger than that of the working fluid. This makes the choice of α_s/α_v ratio as the determining parameter of two dimensionality logical.

For a qualitative assessment of the validity of the local thermal equilibrium assumption and the strength of the two-dimensional effects in the energy and momentum transport, the findings of the numerical computations will be presented in an integrated form. Figure 10 shows this assessment for the local thermal equilibrium assumption for the case of lithium-nitrate-trihydrate, sandstone, and steel for the entire ranges of Re$_p$ and Da considered in this work. It should be noted that this qualitative assessment is based on the *later stage* during which we had appreciable thermal penetration depth in the packed bed. For all the runs performed, the *initial stage* did

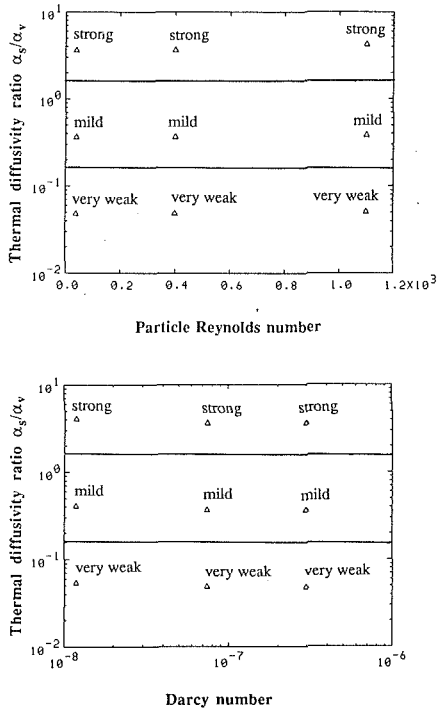

Fig. 11 Assessment of the strength of two-dimensionality effects

not last for more than one second. Since the problem considered is a step change problem in temperature, there is a sharp difference between the solid and the vapor phase temperatures at time equal to zero, and due to this large difference between the solid and vapor temperatures at the inlet of the packed bed, it becomes rather irrelevant to talk about the validity of local thermal equilibrium in the *initial stage*. It is, therefore, reasonable to analyze the degree of LTE during the *later stage*. It should be noted, however, that even though the *initial stage* lasts for a very short time, it still has a significant effect on the results of the later stage. For this reason, throughout our investigation the initial stage was fully analyzed in each run we performed. The dividing lines in Fig. 10 were decided by the maximum difference between the solid and the vapor phase temperatures relative to the overall temperature range (20 K, difference between the inlet vapor temperature and the initial temperature). For the qualitative ratings, the percentage difference relative to the overall temperature range fall into the following categories: very poor, more than 15 percent; poor, 10–15 percent; fair, 5–10 percent; good, 1–5 percent, very good, less than 1 percent. From Fig. 10 it can be concluded that Da is the most influential parameter in determining the validity of local thermal equilibrium. The Reynolds number based on particle diameter is also a very important parameter in this regard. The local thermal equilibrium assumption becomes more viable as both Re_p and Da decrease for the reasons that were explained in the sections analyzing the effects of these parameters. This is clearly seen from the lower left corner of each figure. By the same token it is reasonable to observe the opposite behavior as Re_p and Da increase, i.e., approaching the top right corners of these figures. Also it may be seen that the thermophysical parameters have a much less pronounced influence on the local thermal equilibrium condition. Only for the case of steel were the effects of the physical parameters found to be mildly significant. This is because the conduction heat transfer becomes more dominant than the vapor-to-solid convective heat transfer in this case.

In a similar manner a qualitative assessment of the strength of the two-dimensional behavior is depicted in Fig. 11. This figure shows the behavior for a fixed Re_p equal to 400 for the entire range of Da used in this investigation, and the behavior for a fixed Da of 7.38×10^{-8} for the entire range of Re_p used in this investigation. This qualitative behavior, for each case in the figure, was found to be exactly the same for the entire ranges of the corresponding Da or Re_p considered in this investigation. Therefore, for brevity only these two cases are presented. The above-mentioned fact and Fig. 11 confirm that the two-dimensionality effects are not sensitive to either Re_p or Da, but very sensitive to the α_s/α_v ratio, i.e., to the thermophysical properties of the materials that are considered for the bed.

It should be noted that choosing a representative nondimensional parameter based on a scaling analysis of the simplified form of our model, in which we assume LTE between the solid and the vapor phase, neglect conduction heat transfer in the axial direction, and base scaling on the axial convective energy flow term and the conduction term in the transverse direction, i.e., neglect the transient storage term, would result in the following criterion for the two-dimensional effects to be negligible:

$$\mathrm{Pe}_m\left(\frac{H}{L}\right)^2 \gg 1$$

where Pe_m is a modified Peclet number defined as $\mathrm{Pe}_m=\rho_v c_{p_v} u^*/k_{\mathrm{eff}}$, where k_{eff} is the effective thermal conductivity of the packed bed saturated with vapor in LTE. However, we found that this criterion was only valid for a limited range of particle Reynolds number. That is, the criterion failed at relatively large Reynolds numbers even for cases with high α_s/α_v ratios in which the two-dimensional effects were very much pronounced. Therefore, the nondimensional ratio α_s/α_v used in the presentation of the results in Fig. 11 is a much more appropriate parameter in determining the two dimensionality of the problem, because it can predict the two-dimensional effects independent of any other parameter such as Re_p and Da.

5 Conclusions

The following conclusions can be drawn from this investigation of the transport processes in forced convective flow of a gas through a packed bed:

1 Complete modeling of the unsteady flow of a gas through a porous medium is important since some of the information such as the initial velocities may be very crucial during the start-up and shut-down processes for certain applications.

2 The local thermal equilibrium assumption should not be carried out for high Re_p and/or high Da flows in a packed bed.

3 Re_p and Da were found to be very influential in determining the validity of local thermal equilibrium while thermophysical properties were much less influential in this respect.

4 The two-dimensional behavior of the transport processes was found to be very sensitive to the thermophysical properties but not sensitive to Re_p or Da.

5 The stability of the numerical scheme was found to be primarily dependent on the magnitudes of the particle Reynolds and Darcy numbers. It was found that the numerical scheme becomes more stable as the Darcy number decreases or as the particle Reynolds number increases.

6 Complete simulation of the charging process of the packed bed may require excessively large CPU times for low Re_p flows.

7 A reference vapor-to-solid heat transfer coefficient based on ρ^* and u^* was found to be within 2 percent of the actual values for all the grid points during the *later stages* in all the numerical computations performed in this investigation. Therefore it can be used safely during the *later stages* as a constant value for all the grid points rather than computing these values for each grid point at each time step. Thus con-

siderable CPU time would be conserved without significant loss of accuracy.

References

Ananthanarayanan, V., Sahai, Y., Mobley, C. E., and Rapp, R. A., 1987, "Modeling of Fixed Bed Heat Storage Units Utilizing Phase Change Materials," *Metallurgical Transactions B*, Vol. 18B, pp. 339–346.

Barker, J. J., 1965, "Heat Transfer in Packed Beds," *Industrial and Engineering Chemistry*, Vol. 57(4), pp. 43–51.

Baumeister, E. B., and Bennett, C. O., 1958, "Fluid Particle Heat Transfer in Packed Beds," *AIChE Journal*, Vol. 4(1), pp. 69–74.

Benanati, R. F., and Brosilow, C. B., 1962, "Void Fraction Distribution in Beds of Spheres," *AIChE Journal*, Vol. 8(3), pp. 359–361.

Bhattacharyya, D., and Pei, D. C. T., 1975, "Heat Transfer in Fixed Bed Gas-Solid Systems," *Chemical Engineering Science*, Vol. 30, pp. 293–300.

Dullien, F. A. L., 1979, *Porous Media Fluid Transport and Pore Structure*, Academic Press, New York.

Ergun, S., 1952, "Fluid Flow Through Packed Columns," *Chemical Engineering Progress*, Vol. 48, pp. 89–94.

Gamson, B. W., Thodos, G., and Hougen, O. A., 1943, "Heat, Mass and Momentum Transfer in the Flow of Gases Through Granular Solids," *Transactions AIChE*, Vol. 39, pp. 1–35.

Goldstein, M. E., and Siegel, R., 1971, "Analysis of Heat Transfer for Compressible Flow in Two-Dimensional Porous Media," *Int. Journal Heat Mass Transfer*, Vol. 14, pp. 1677–1699.

Kidder, R. E., and La Habra, X. X., 1957, "Unsteady Flow of Gas Through a Semi-infinite Porous Medium," ASME *Journal of Applied Mechanics*, Vol. 24, pp. 329–332.

Morrison, F. A., 1972, "Transient Gas Flow in a Porous Column," *Industrial and Engineering Chemistry Fundamentals*, Vol. 11(2), p. 191.

Nilson, R. H., 1981, "Transient Fluid Flow in Porous Media: Inertia-Dominated to Viscous Dominated Transition," ASME *Journal of Fluids Engineering*, Vol. 103, pp. 339–343.

Riaz, M., 1977, "Analytical Solution for Single- and Two-Phase Models of Packed-Bed Thermal Storage Systems," ASME JOURNAL OF HEAT TRANSFER, Vol. 99, pp. 489–492.

Schumann, T. E. W., 1929, "Heat Transfer: A Liquid Flowing Through a Porous Prism," *Journal of the Franklin Institute*, Vol. 208, pp. 405–416.

Vafai, K., 1984, "Convective Flow and Heat Transfer in Variable-Porosity Media," *Journal of Fluid Mechanics*, Vol. 147, pp. 233–259.

Vafai, K., and Whitaker, S., 1986, "Simultaneous Heat and Mass Transfer Accompanied by Phase Change in Porous Insulation," ASME JOURNAL OF HEAT TRANSFER, Vol. 108, pp. 132–140.

Whitaker, S., 1977, "Simultaneous Heat, Mass, and Momentum Transfer in Porous Media: A Theory of Drying," *Adv. Heat Transfer*, Vol. 13, pp. 119–203.

Analysis of Surface Enhancement by a Porous Substrate

Kambiz Vafai

Sung-Jin Kim

Department of Mechanical Engineering,
The Ohio State University,
Columbus, OH 43210

Convective flow and heat transfer through a composite porous/fluid system have been studied numerically. The composite medium consists of a fluid layer overlaying a porous substrate, which is attached to the surface of the plate. The numerical simulations focus primarily on flows that have the boundary layer characteristics. However, the boundary layer approximation was not used. A general flow model that accounts for the effects of the impermeable boundary and inertia is used to describe the flow inside the porous region. Several important characteristics of the flow and temperature fields in the composite layer are reported. The dependence of these characteristics on the governing parameters such as the Darcy number, the inertia parameter, the Prandtl number, and the ratio of the conductivity of the porous material to that of the fluid is also documented. The results of this investigation point out a number of interesting practical applications such as in frictional drag reduction, and heat transfer retardation or enhancement of an external boundary.

1 Introduction

The problem of convective heat transfer and fluid flow over a horizontal flat plate has received considerable attention since the early work of Blasius. The analogous problem in fluid-saturated porous media has also drawn much attention due to such diverse applications as drying processes, thermal insulation, direct contact heat exchangers, heat pipe, filtration, etc. These applications made it imperative that a deeper insight into porous media transport processes must be gained. While numerous studies have been performed in the above areas, little attention has been focused on the problem in which a porous/fluid composite system is involved. This type of composite system is encountered in various applications such as solidification of castings, crude oil extraction, thermal insulation, geophysical systems, etc.

Of the few investigations in the porous/fluid composite systems, Poulikakos's (1986) work can be cited. Poulikakos (1986) studied the buoyancy-driven flow instability numerically for a fluid layer extending over a porous substrate in a cavity heated from the bottom. Beckermann et al. (1987, 1988) and Sathe et al. (1988) performed numerical and experimental investigations on the natural convection heat transfer and fluid flow in a vertical rectangular enclosure that is partially filled with a fluid-saturated porous medium. They found that the amount of fluid penetrating from the fluid region into the porous region depends strongly on the Darcy and Rayleigh numbers. More relevant to the present study is the work of Vafai and Thiyagaraja (1987). They analytically investigated the fully developed forced convection for the interface region between a fluid layer and a porous medium. Another related problem is that of Poulikakos and Kazmierczak (1987), in which a fully developed forced convection in a channel that is partially filled with a porous matrix was investigated. They showed the existence of a critical thickness of the porous layer at which the value of Nusselt number reaches a minimum.

This paper presents a numerical study of forced convection over a fluid/porous composite system. The system is composed of a relatively thin porous substrate attached to the surface of the flat plate. Since little is known about *external* forced convection fluid flow and heat transfer in the porous/fluid composite medium (to the best of authors' knowledge the present work constitutes the first analysis in this area), the present study is aimed at a fundamental investigation of the interaction phenomena occurring in the porous substrate and the fluid layer. The effects of various parameters governing the physics of the problem on the fluid flow and heat transfer are analyzed and the interfacial effects are systematically categorized. The accumulated knowledge gained through this investigation will provide a fundamental framework for predicting heat transfer and fluid flow characteristics for more complicated configurations.

Contributed by the Heat Transfer Division for publication in the JOURNAL OF HEAT TRANSFER. Manuscript received by the Heat Transfer Division September 25, 1989; revision received February 27, 1990. Keywords: Augmentation and Enhancement, Forced Convection, Porous Media.

2 Analysis

2.1 Mathematical Formulation. The coordinate system and the corresponding physical configuration are shown in Fig. 1. The thickness of the porous substrate is H, the free-stream velocity u_∞ and temperature T_∞ are constant, and the wall is maintained at constant temperature T_w. It is assumed that the flow is steady, laminar, incompressible, and two dimensional. In addition, the thermophysical properties of the fluid and the porous matrix are assumed to be constant and the fluid-saturated porous medium is considered homogeneous and isotropic and in local thermodynamic equilibrium with the fluid. The conservation equations for mass, momentum, and energy in the fluid region are

$$\nabla \cdot \mathbf{v} = 0 \tag{1}$$

$$\mathbf{v} \cdot \nabla \mathbf{v} = -\frac{1}{\rho_f} \nabla p + \nu_f \nabla^2 \mathbf{v} \tag{2}$$

$$\mathbf{v} \cdot \nabla T = \alpha_f \nabla^2 T \tag{3}$$

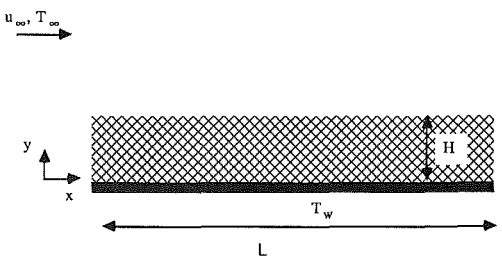

Fig. 1 Schematic of the coordinate system of the porous/fluid composite system

The conservation equations for the porous region are based on a general flow model, which includes the effects of flow inertia as well as friction caused by macroscopic shear (Vafai and Tien, 1981; Hong et al., 1985; Kaviany, 1987). This generalized flow model is also known as the Brinkman–Forchheimer-extended Darcy model. The governing equations for the porous layer are

$$\nabla \cdot \mathbf{v} = 0 \tag{4}$$

$$\mathbf{v} \cdot \nabla \mathbf{v} = -\frac{1}{\rho_f}\nabla p + \nu_{\text{eff}}\nabla^2 \mathbf{v} - \frac{\nu_f}{K}\mathbf{v} - \frac{F\delta}{\sqrt{K}}|\mathbf{v}|\mathbf{v} \tag{5}$$

$$\mathbf{v} \cdot \nabla T = \alpha_{\text{eff}}\nabla^2 T \tag{6}$$

where α_{eff} is defined as $\alpha_{\text{eff}} = k_{\text{eff}}/\delta\rho_f c_{p,f}$ and ρ_f and $c_{p,f}$ refer to the density and the heat capacity of fluid. It should be noted that the variables $\mathbf{v}$ and T are both volume-averaged quantities as described by Vafai and Tien (1981). The appropriate boundary conditions for the present problem are

$$u = u_\infty,\ v = 0,\quad p = p_\infty,\ T = T_\infty,\ \text{at } x = 0 \tag{7}$$

$$u = 0,\quad v = 0,\quad T = T_w \qquad \text{at } y = 0 \tag{8}$$

$$u = u_\infty,\ p = p_\infty,\ T = T_\infty, \qquad \text{as } y \to \infty \tag{9}$$

In addition to these the following matching conditions have to be satisfied at the interface of the porous/fluid layer:

$$u|_{y=H^-} = u|_{y=H^+},\qquad v|_{y=H^-} = v|_{y=H^+} \tag{10a}$$

$$p|_{y=H^-} = p|_{y=H^+},\qquad \mu_{\text{eff}}\left.\frac{\partial v}{\partial y}\right|_{y=H^-} = \mu_f\left.\frac{\partial v}{\partial y}\right|_{y=H^+} \tag{10b}$$

$$\mu_{\text{eff}}\left(\frac{\partial u}{\partial y}+\frac{\partial v}{\partial x}\right)\Bigg|_{y=H^-} = \mu_f\left(\frac{\partial u}{\partial y}+\frac{\partial v}{\partial x}\right)\Bigg|_{y=H^+} \tag{10c}$$

$$T|_{y=H^-} = T|_{y=H^+},\qquad k_{\text{eff}}\left.\frac{\partial T}{\partial y}\right|_{y=H^-} = k_f\left.\frac{\partial T}{\partial y}\right|_{y=H^+} \tag{10d}$$

These conditions express the continuity of longitudinal and transverse velocities, pressure, deviatoric normal and shear stresses, temperature, and the heat flux. The conditions expressed equation (10*b*) together imply matching of the total normal stress at the interface. The fifth condition in equation (10*c*) represents the matching condition for the shear stress, which is an extension of the condition used by Vafai and Thiyagaraja (1987) and Neale and Nader (1974) for flow that is not parallel to the porous/fluid interface. As rigorously proved by Vafai and Thiyagaraja (1987), matching of the stresses at the interfaces can only be accomplished if Brinkman's shear term is included in the momentum equation for the porous media.

It has been found that setting the effective viscosity of the fluid-saturated porous medium equal to the viscosity of the fluid provides good agreement with experimental data (Lundgren, 1972; Neale and Nader, 1974). This approximation is adopted in the present work. In addition the effect of thermal dispersion in the porous matrix is assumed to be constant and is incorporated in the effective thermal conductivity for simplicity in presentation of the results.

2.2 Numerical Simulations. Separate calculation schemes for the porous and fluid regions would require an involved iterative procedure for matching the interface conditions. A more efficient alternative is to combine the two sets of equations for the fluid region an the porous region into one set of conservation equations. In other words the porous substrate and the fluid region can be modeled as a single domain governed by one set of equations, the solution of which satisfies the continuity of the velocities, stresses, temperatures, and heat fluxes across the porous/fluid interface as described by equations (10*a–d*).

Introducing the stream function and the vorticity as

$$u = \frac{\partial \psi}{\partial y},\qquad v = -\frac{\partial \psi}{\partial x}$$

$$\zeta = \frac{\partial v}{\partial x} - \frac{\partial u}{\partial y}$$

yields the dimensionless vorticity transport equation, stream function equation, and energy equation. These equations are valid throughout the composite layer.

$$\frac{\partial \psi^*}{\partial y^*}\frac{\partial \zeta^*}{\partial x^*} - \frac{\partial \psi^*}{\partial x^*}\frac{\partial \zeta^*}{\partial y^*} = \frac{1}{\text{Re}_L}\nabla^2\zeta^* + S^* \tag{11}$$

$$\nabla^2\psi^* = -\zeta^* \tag{12}$$

$$\frac{\partial \psi^*}{\partial y^*}\frac{\partial \theta}{\partial x^*} - \frac{\partial \psi^*}{\partial x^*}\frac{\partial \theta}{\partial y^*} = \nabla \cdot \left(\frac{1}{\text{Pe}_L}\nabla\theta\right) \tag{13}$$

where in the fluid region

$$\text{Re}_L = \frac{u_\infty L}{\nu_f},\qquad \text{Pe}_L = \frac{u_\infty L}{\alpha_f},\qquad S^* = 0 \tag{14a}$$

and in the porous region

$$\text{Pe}_L = \frac{u_\infty L}{\alpha_{\text{eff}}},\qquad \text{Da}_L = \frac{K}{L^2},\qquad \Lambda_L = \frac{FL\delta}{K^{1/2}} \tag{14b}$$

Nomenclature

C_f = friction coefficient, equation (17)
Da_L = Darcy number, equation (14*b*)
F = a function used in expressing inertia terms
h = convective heat transfer coefficient, $\text{Wm}^{-2}\text{K}^{-1}$
H = thickness of the porous medium, m
k = thermal conductivity, $\text{Wm}^{-1}\text{K}^{-1}$
K = permeability of the porous medium, m^2
L = length of the external boundary as shown in Fig. 1, m
Nu = Nusselt number, equation (18)
P = pressure, Pa
Pe_L = Peclet number, equation (14*a*) or (14*b*)
Pr = Prandtl number
Re_L = Reynolds number defined for the fluid region, equation (14)
T = temperature, K
u = x-component velocity, ms^{-1}
v = y-component velocity, ms^{-1}
$\mathbf{v}$ = velocity vector
x = horizontal coordinate, m
y = vertical coordinate, m
α = thermal diffusivity, m^2s^{-1}
α_{eff} = effective thermal diffusivity = $k_{\text{eff}}/\rho_f c_{p,f}$, m^2s^{-1}
δ = porosity of the porous medium
ζ = vorticity
Λ_L = inertia parameter, equation (14*b*)
μ = dynamic viscosity, $\text{kgm}^{-1}\text{s}^{-1}$
ν = kinematic viscosity, m^2s^{-1}
θ = dimensionless temperature
ρ = fluid density, kgm^{-3}
ψ = stream function

Subscripts

eff = effective
f = fluid
∞ = free stream

$$S^* = -\frac{1}{\mathrm{Re}_L \mathrm{Da}_L}\zeta^* - \Lambda_L |v^*|\zeta^* - \Lambda_L\left(v^*\frac{\partial |v^*|}{\partial x^*} - u^*\frac{\partial |v^*|}{\partial y^*}\right) \quad (15)$$

$$+\frac{u^*}{\mathrm{Re}_L}\frac{\partial}{\partial y}\left(\frac{1}{\mathrm{Da}_L}\right) - \frac{v^*}{\mathrm{Re}_L}\frac{\partial}{\partial x}\left(\frac{1}{\mathrm{Da}_L}\right)$$

$$+ |v^*| u^*\frac{\partial}{\partial y}(\Lambda_L) - |v^*| v^*\frac{\partial}{\partial x}(\Lambda_L)$$

Note that all the variables have been nondimensionalized based on the following definitions:

$$x^* = \frac{x}{L}, \quad y^* = \frac{y}{L}, \quad u^* = \frac{u}{u_\infty}, \quad v^* = \frac{v}{u_\infty}$$

$$\psi^* = \frac{\psi}{u_\infty L}, \quad \zeta^* = \frac{L\zeta}{u_\infty}, \quad \theta = \frac{T - T_\infty}{T_w - T_\infty}$$

The dimensionless boundary conditions are

$$\psi^* = y^*, \quad \zeta^* = -\frac{\partial^2 \psi^*}{\partial x^{*2}}, \quad \theta = 0 \quad \text{at } x^* = 0$$

$$\psi^* = 0, \quad \zeta^* = -\frac{\partial^2 \psi^*}{\partial y^{*2}}, \quad \theta = 1 \quad \text{at } y^* = 0 \quad (16)$$

$$\frac{\partial \psi^*}{\partial y^*} = 1, \quad \zeta^* = -\frac{\partial^2 \psi^*}{\partial x^{*2}}, \quad \theta = 0 \quad \text{as } y^* \to \infty$$

It is worthwhile to note that the boundary conditions at $x^* = 0$ and $y^* \to \infty$ are the same, i.e., the only difference is that at $x^* = 0$, ψ^* is specified and for $y^* \to \infty$, the gradient of ψ^*, i.e., $\partial\psi^*/\partial y^* = 1$, is specified. The downstream boundary conditions are discussed below. A control-volume-based finite difference method is employed to solve the system of elliptic partial differential equations for the vorticity, stream function, and temperature. The control volume formulation has the attractive feature that the resulting solution would imply that the integral conservation of mass, momentum, and energy is exactly satisfied over the whole domain as well as any group of control volumes. The physical domain was covered by a rectangular grid system consisting of m horizontal and n vertical lines. Extensive tests were carried out to determine the proper value of m and n for each numerical run. Each grid point was placed at the center of the corresponding control volume. A variable grid system was employed in the y direction, in the fluid region, in order to reduce the computational time. In this system, the grid spacing was based on a constant ratio between two adjacent increments (Anderson et al., 1984; Roache, 1972). The inlet boundary conditions were applied at a short distance upstream of the leading edge of the plate. It should be noted that as long as the inlet conditions are applied sufficiently upstream, it becomes immaterial where they are applied and the location of the inlet conditions will not affect the results. This procedure virtually eliminated the errors associated with the singular point at the leading edge of the composite system. In addition, the harmonic mean formulation suggested by Patankar (1980) was used to handle abrupt variations in thermophysical properties, such as the permeability and the thermal conductivity, across the interface. This ensured the continuity of the convective and diffusive fluxes across the interface without requiring the use of an excessively fine grid structure. Therefore, in the generalized formulation for the entire composite layer, to preserve all the interface boundary conditions, Λ_L and Da_L were treated as variables. However, in presenting the results the constant values of Λ_L and Da_L for the specified porous substrate that was analyzed were used.

In the present numerical scheme the space derivatives were approximated by a central-difference form except for the convective terms, which were approximated by using a second upwind-differencing scheme. It is worth mentioning that the source terms associated with the boundary and inertia effects were linearized according to a general recommendation by Patankar (1980). The finite difference equations thus obtained were solved by the extrapolated-Jacobi scheme. This iterative scheme is based on a double cyclic routine, which translates into a sweep of only half of the grid points at each iteration step (Adams and Oretega, 1982). It is noted that this scheme is vectorizable so that it can be used quite efficiently when used on a supercomputer. It was necessary to use underrelaxation to ensure convergence.

It was found that the downstream boundary conditions had quite a limited influence on the solution because the present problem had a significant parabolic character. Hence, the type of boundary condition specification on the right-hand side of the computational domain did not have much influence on the physical domain. Therefore, by using an extended computational domain, we were able to find very accurate results for our physical domain. That is, the computational domain was always chosen to be larger than the physical domain. We ran extensive tests on the effect of varying the size of the computational domain and observed its effects on the physical domain to ensure that the boundary conditions on the downstream side of the computational domain had no influence on our results. In our work, for simplicity, the conditions at the last interior grid points from the outflow boundary condition in the previous iteration were used and yielded the same solution for the domain of interest, except for the region very close to the downstream boundary as when the other conditions were used. For this reason the boundary conditions at the right-hand side of the domain were not explicitly given in equation (16).

Additional calculations were carried out in order to evaluate the effects of the porous material on the shear stress and heat transfer rate at the wall. The results for the shear stress were cast in dimensionless form by means of the local friction coefficient as

$$C_{f,x} = \frac{\tau_{w,x}}{\rho_f u_\infty^2/2} = \frac{2}{\mathrm{Re}_L}\frac{\partial u^*}{\partial y^*}\bigg|_{y^*=0} \quad (17)$$

and the results for the heat transfer rate were represented in dimensionless form in terms of a dimensionless Nusselt number

$$\mathrm{Nu}_x = \frac{hx}{k_f} = -x^*\frac{k_e}{k_f}\frac{\partial \theta}{\partial y^*}\bigg|_{y^*=0} \quad (18)$$

It should be noted that the conductivity of the fluid was chosen in the formation of the Nusselt number. This choice resulted in more meaningful comparisons for the heat flux at the external boundary between the composite system and the case where there was no porous substrate.

2.3 Stability and Accuracy of the Numerical Scheme. The numerical integration was performed until the following convergence criterion was satisfied:

$$\max\left|\frac{\varphi_{i,j}^{n+1} - \varphi_{i,j}^{n}}{\varphi_{i,j}^{n}}\right| < 10^{-6} \quad (19)$$

where φ stands for ζ^*, ψ^*, or θ and n denotes the iteration number. The stability of the numerical scheme was found to be somewhat insensitive to the choice of Δx and Δy. We employed a proper combination of Δx and Δy to assure stability. This was done by a systematic decrease in the grid size until further refinement of the grid size showed no more than a 1 percent difference in the convergent results.

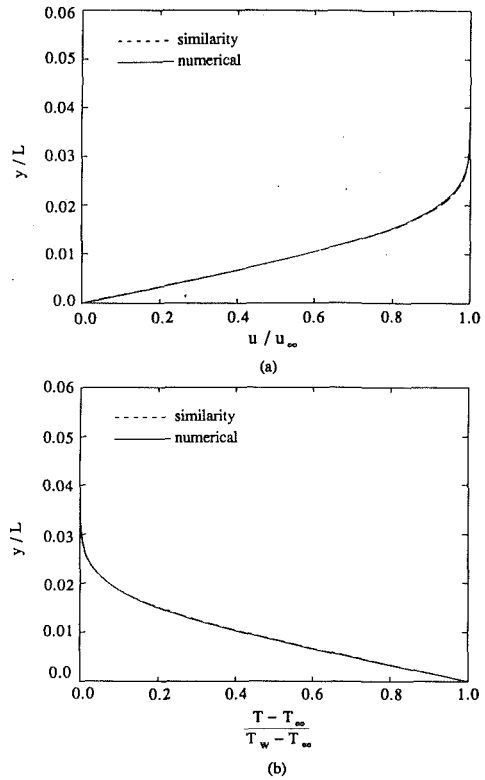

Fig. 2 Comparison of numerical solutions with the similarity solutions for convective flow over a semi-infinite flat plate: (*a*) velocity distribution, (*b*) temperature distribution

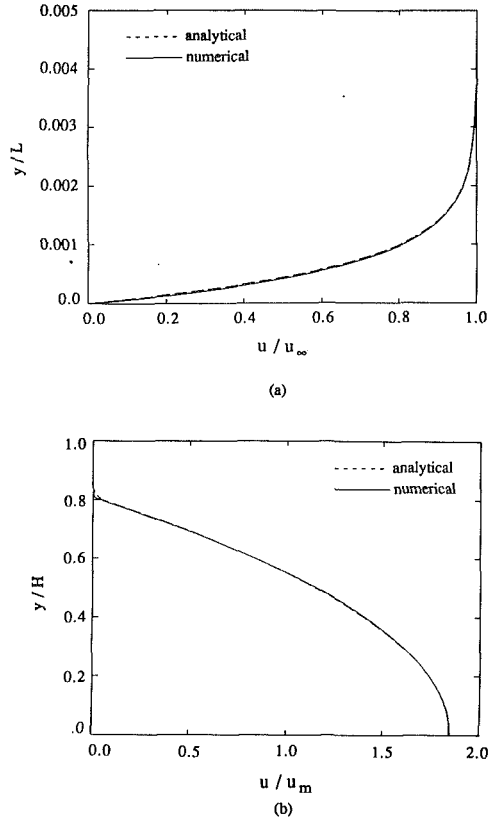

Fig. 3 Comparison of numerical solutions for the velocity with the corresponding analytical solutions: (*a*) flow over a flat plate embedded in a porous medium, (*b*) flow in a channel partially filled with a porous medium

The application of the boundary condition at infinity at a finite distance from the wall was given careful consideration. This was done through the following procedure. The length of the computational domain in the vertical direction was systematically increased until the maximum vorticity changes for two consecutive runs became less than 1 percent. Comparisons with more classical results were made in order to validate the present numerical model. The results for $H^* = 0$ (no porous substrate) agree to better than 1 percent with boundary layer similarity solutions for velocity and temperature fields as shown in Figs. 2(*a*) and 2(*b*). In these figures the Reynolds number based on the characteristic length was 3×10^5 and the Prandtl number of the fluid was taken to be 1.0. Note that this limiting case simply corresponds to forced convection over a flat plate. Also the results for $H^* \to \infty$ (full porous medium) agree to better than 1 percent with boundary layer analytical solutions by Vafai and Thiyagaraja (1987) and Beckerman et al. (1987). The results of such a comparison for a case where the product of the Reynolds number, Darcy number, and the inertia parameter was 1.0 are shown in Fig. 3(*a*). Note that this limiting case corresponds to flow over a flat plate embedded in a porous medium.

In addition to these two limiting cases, the numerical solutions for the velocity field in a porous/fluid composite medium using the present numerical code were compared with the analytical solution by Poulikakos and Kazmierczak (1987) for the problem of hydrodynamically and thermally fully developed forced convection in a channel partially filled with a porous medium. The results of this comparison for a case where the thickness ratio of the porous material to channel width is 0.2 and the Darcy number based on the channel width is 10^{-4} are presented in Fig. 3(*b*). As a final check, the problem of fully developed flow over a porous/fluid composite layer was solved using the present numerical code and compared with the analytical solution presented by Vafai and Thiyagaraja (1987). It was found that there is a very good agreement between the analytical and numerical results. Through the above-mentioned series of tests it was confirmed that the numerical model used in the present work predicts quite accurately the velocity and temperature fields in a porous/fluid composite system.

3 Results and Discussion

The effects of the porous substrate on the velocity and temperature fields are illustrated in Fig. 4 for a case where the Darcy number is 8×10^{-6}, the inertia parameter is 0.35, and the dimensionless thickness of the porous substrate is 0.02. Also shown in these figures are the velocity and temperature profiles for the case where no porous substrate is present. It should be noted that the effects of the porosity variation and the thermal dispersion in the porous region can change the results because of the channeling effect and the dynamic heat transfer mechanism (Vafai, 1986). However, the main features presented in this work will prevail even for the case where variable porosity effects are important. It can be seen that two distinct momentum boundary layers exist: one in the porous region and the other in the fluid region. Inside the porous region the velocity profile is shown to increase from zero to a certain constant value as the transverse coordinate increases. This constant value is maintained until the outer boundary layer appears. This velocity profile then goes through a smooth transition across the porous/fluid interface and approaches a free-stream value in the fluid region. As expected, the momentum boundary layers in the porous substrate as well as the fluid region grow as the streamwise coordinate increases. As a result the magnitude of the interfacial velocity decreases to accommodate this growth. Physically this is the result of a continuous displacement of fluid (or blowing) from the porous region into the fluid region due to the relatively larger resistance that the flow experiences in the porous region. This blowing

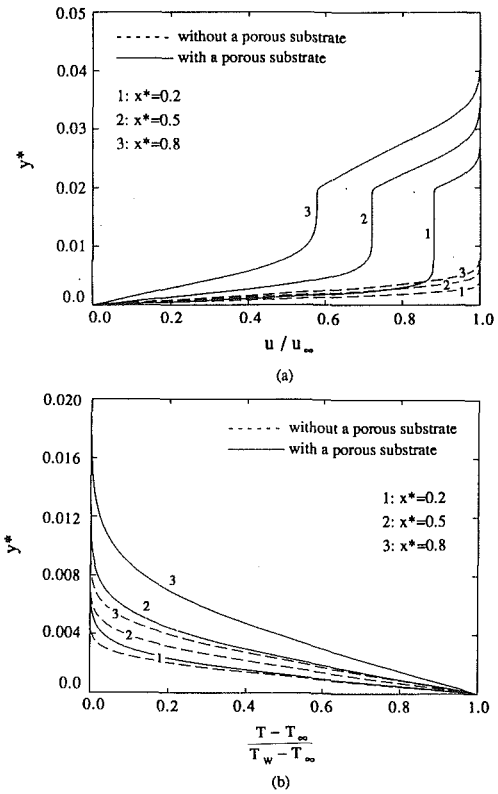

Fig. 4 (*a*) Velocity and (*b*) temperature distribution along the flat plate at three different locations, $x = 0.2$, 0.5, and 0.8, for $Da_L = 8 \times 10^{-6}$, $\Lambda_L = 0.35$, $k_e/k_f = 1.0$, $H^* = 0.02$

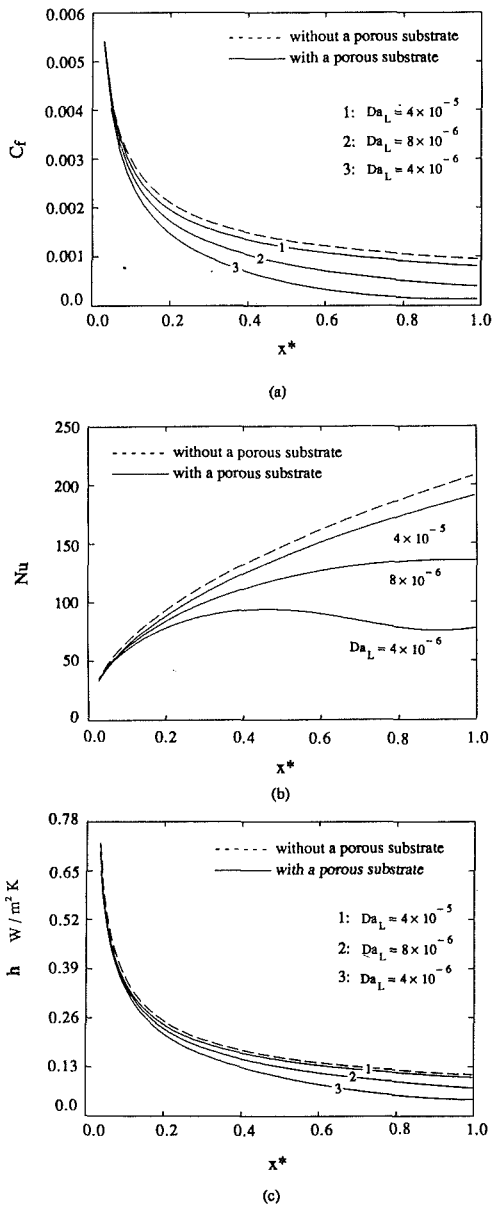

Fig. 5 Effects of the Darcy number on (*a*) friction coefficient, (*b*) Nusselt number, and (*c*) convection heat transfer coefficient variation along the flat plate for $\Lambda_L = 0.0$, $Pr = 0.7$, $k_e/k_f = 1.0$, $H^* = 0.02$

effect becomes less pronounced as the amount of flow into the porous region becomes smaller. It can be seen from Fig. 4(*a*) that the attachment of the porous substrate onto the flat plate results in a significant decrease in the frictional drag at the wall. This decrease is a direct result of the blowing effect previously discussed. It should be noted that the frictional resistance at the porous/fluid interface is essentially negligible. However, this condition of negligible frictional drag at the porous/fluid interface was not imposed in our solution scheme, it was a fact that was the outcome of our numerical results. The matching of the shear stress, equation (10*c*), will then ensure that the frictional resistance on both the fluid side and the porous side at the porous/fluid interface is negligible. This can be observed upon careful examination of Fig. 4(*a*) around the narrow interface region.

The temperature field shown in Fig. 4(*b*) corresponds to a case where the Prandtl number is 0.7 and the conductivity of the porous medium is equal to that of the fluid. It can be seen that the heat transfer rate at the wall is lower for the case in which a porous substrate is attached to the external boundary. This is due to lower velocities at the wall, which in turn diminish the convective energy transport for the case where the porous substrate is present. It is this decrease in the transport of the convective energy that causes a lower temperature gradient and heat flux at the wall for the composite system. The influence of Reynolds number comes through changes in the slopes of the curves shown in Fig. 4. However, the main feature of the results presented in Fig. 4 will also prevail for different Reynolds numbers, i.e., a decrease in the frictional drag and the heat transfer at the wall for the case where the porous substrate is attached to the wall. It should be noted that the thickness of the thermal boundary layer depends on the Prandtl number and the ratio of the conductivity of the porous material to that of the fluid. Therefore, the porous substrate could be designed such that it would either enhance or retard the transfer of energy to the impermeable boundary.

Effect of the Darcy Number. The Darcy number, as can be seen from equation (14*b*), is directly related to the permeability of the porous medium. Figure 5 shows the streamwise variations of the local friction coefficient and the Nusselt number, C_f and Nu, for various Darcy numbers. In order to concentrate only on the effects of the Darcy number the inertial effects were neglected in obtaining the results displayed in Fig. 5. As expected the local friction coefficient at the wall decreases as the Darcy number decreases. This is because smaller values of Da relate to larger bulk frictional resistance to the flow in the porous substrate. This in turn causes a lower velocity gradient at the wall. Also, as expected, the frictional drag at the wall approaches that of the case without the porous substrate for larger values of the Darcy number. As shown in Fig. 5(*b*), the Nusselt number values for the case with a porous substrate are lower than the case where no porous substrate is present. This is because the presence of the porous substrate and/or smaller value of Da translate into smaller velocities near the impermeable boundary, which in turn diminish the transfer of the convective energy. The peculiar variation in the Nusselt

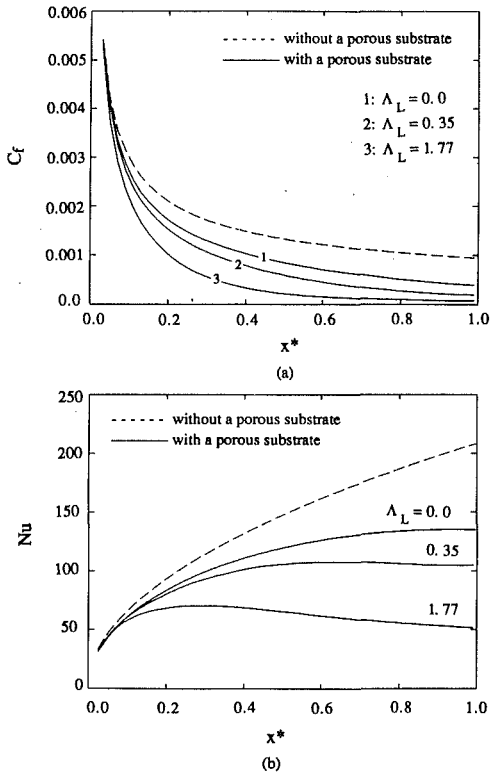

Fig. 6 Effects of the inertia parameter on the friction coefficient and the Nusselt number for $Da_L = 8 \times 10^{-6}$, Pr = 0.7, $k_e/k_f = 1.0$, $H^* = 0.02$

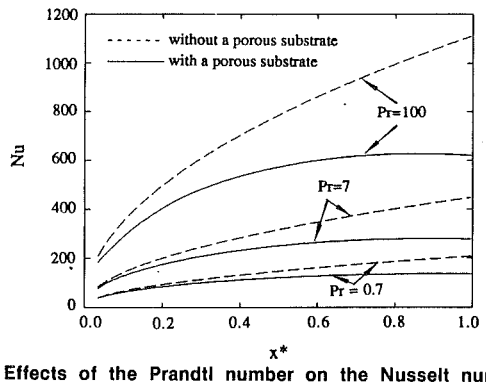

Fig. 7 Effects of the Prandtl number on the Nusselt number for $Da_L = 8 \times 10^{-6}$, $\Lambda_L = 0.0$, $k_e/k_f = 1.0$, $H^* = 0.02$

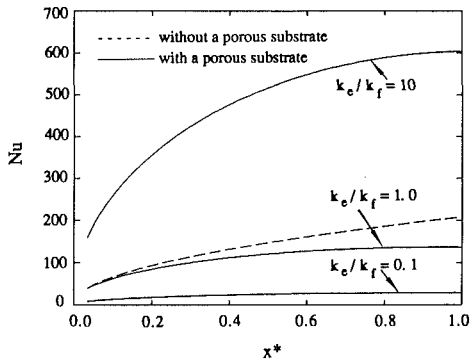

Fig. 8 Effects of the ratio of the conductivity of the porous medium to that of the fluid on the Nusselt number for $Da_L = 8 \times 10^{-6}$, $\Lambda_L = 0.0$, Pr = 0.7, $H^* = 0.02$

number distribution for smaller values of Darcy numbers is directly related to the way the Nusselt number is defined. First, it should be noted that the Nusselt number is linearly proportional to the product of the heat transfer coefficient, h, and the axial distance x. However, the heat transfer coefficient itself is also a function of x. Specifically h is a decreasing function of x. As can be clearly seen in Fig. 5(c), the rate of decrease of the heat transfer coefficient changes significantly over the length of the plate. It is exactly this nonuniform rate of decrease in h that causes the type of variation in the Nusselt number shown in Fig. 5(b). Therefore as the curvature of the heat transfer coefficient h changes at different axial locations, then depending on the rate of decrease of h at a particular axial location versus the rate of increase of the linear function x, we can get either an increasing or decreasing Nusselt number at that particular location.

Inertial Effects. As pointed out by a number of previous investigators, the inertial effects become significant when the Reynolds number based on the pore diameter becomes large. The effect of the inertial parameter is depicted in Fig. 6 for a fixed value of the Darcy number, $Da_L = 8 \times 10^{-6}$. The larger the inertial parameter, the larger will be the bulk frictional resistance that the flow will experience. Consequently the mass flow rate through the porous substrate decreases. Therefore larger value of Λ_L would result in a larger blowing effect through the porous substrate, which would consequently create thicker boundary layer thicknesses as well as a reduction in the friction coefficient and the Nusselt number values. The computed results confirm these facts and reveal that the thickness of the boundary layer increases as the inertial parameter increases. Also as expected the friction coefficient and the Nusselt number values decrease as the inertial parameter increases.

Prandtl Number Effects. The Prandtl number effects are shown in Fig. 7 for a fixed value of the Darcy number, $Da_L = 8 \times 10^{-6}$ and $\Lambda_L = = 0$. In this figure, the Nusselt number variation along the streamwise coordinate are shown for three different Prandtl numbers for two different cases. These cases refer to situations where the porous substrate is present and where it is absent. The values for the Prandtl number—0.7, 7.0, and 100—are such that they will cover a wide range of thermophysical fluid properties. So, for example, fluids such as air, water, and several different oils are well represented by the chosen values. As expected, the Nusselt numbers for both cases increase with an increase in the Prandtl number. However, there is a significant difference between the values of the Nusselt number for the two cases. The reasons for these differences were given previously when the effects of the Darcy number were discussed.

Effects of the Conductivity Ratio. The effect of the thermal conductivity ratio is shown in Fig. 8 for a fixed value of the Darcy number, $Da_L = 8 \times 10^{-6}$ and $\Lambda_L = 0$. As expected an increase in the conductivity ratio, k_e/k_f, where k_e is the effective conductivity of the porous medium and k_f is that of the fluid, results in an increase in the Nusselt number. It is important to note that the heat transfer rate at the wall for the case where a porous substrate is attached can be either greater or less than the case where no porous substrate has been used. The determining parameter as to whether the heat transfer will increase or decrease with the attachment of the porous substrate is the conductivity ratio, k_e/k_f. Therefore both the heat transfer enhancement or retardation of an external boundary can be achieved through the attachment of a porous substrate.

4 Conclusions

Forced convection over an external boundary lined with a porous substrate has been investigated in the present work. The characteristics of the velocity and temperature fields have been researched. Consideration was given to convective flows that exhibit boundary layer characteristics. However, the boundary layer approximation was not used. Comparisons of the friction coefficient and the Nusselt number between the

composite system and the case where no porous substrate was used revealed a number of physically interesting phenomena. Two distinct boundary layers were shown to exist for the velocity field while only one boundary layer was observed for the temperature field. It was shown that the porous substrate significantly reduces the frictional drag and the heat transfer rate at the wall. Therefore this configuration can be used as a frictional drag reducer for flows that have a parabolic character. It should be noted that here we are referring to the frictional drag and not the total drag. A momentum balance on a control volume extending from the plate surface out into the free stream, and accounting for pressure forces across the control volume, would provide us with the magnitude of the total drag. It has been shown that both heat transfer retardation and enhancement of an external boundary can be achieved through the attachment of a porous substrate. Furthermore, the effects of the governing parameters such as the Darcy number, inertia parameter, Prandtl number, and conductivity ratio of the porous material to the fluid were also investigated.

References

Adams, J., and Ortega, J., 1982, "A Multicolor SOR Method for Parallel Computation," *Proceedings of Int. Conf. on Parallel Processing*, pp. 53–56.

Anderson, D. A., Tannehill, J. C., and Pletcher, R. H., 1984, 1984, *Computational Fluid Mechanics and Heat Transfer*, Hemisphere Publishing Corp., New York.

Beckermann, C., Ramadhyani, S., and Viskanta, R., 1987, "Natural Convection Flow and Heat Transfer Between a Fluid Layer and a Porous Layer Inside a Rectangular Enclosure," ASME JOURNAL OF HEAT TRANSFER, Vol. 109, pp. 363–370.

Beckermann, C., Viskanta, R., and Ramadhyani, S., 1988, "Natural Convection in Vertical Enclosures Containing Simultaneously Fluid and Porous Layers," *J. Fluid Mechanics*, Vol. 186, pp. 257–284.

Hong, J. T., Tien, C. L., and Kaviany, M., 1985, "Non-Darcian Effects on Vertical-Plate Natural Convection in Porous Media With High Porosities," *Int. J. Heat Mass Transfer*, Vol. 28, pp. 2149–2157.

Kaviany, M., 1987, "Boundary-Layer Treatment of Forced Convection Heat Transfer From a Semi-infinite Flat Plate Embedded in Porous Media," ASME JOURNAL OF HEAT TRANSFER, Vol. 109, pp. 345–349.

Lundgren, T. S., 1972, "Slow Flow Through Stationary Random Beds and Suspensions of Spheres," *J. Fluid Mechanics*, Vol. 51, pp. 273–299.

Neale, G., and Nader, W., 1974, "Practical Significance of Brinkman's Extension of Darcy's Law: Coupled Parallel Flows Within a Channel and a Bounding Porous Medium," *Canadian Journal of Chemical Engineering*, Vol. 52, pp. 475–478.

Patankar, S. V., 1980, *Numerical Heat Transfer and Fluid Flow*, Hemisphere Publishing Corp., New York.

Poulikakos, D., 1986, "Buoyancy-Driven Convection in a Horizontal Fluid Layer Extending Over a Porous Substrate," *Phys. Fluids*, Vol. 29, pp. 3949–3957.

Poulikakos, D., and Kazmierczak, M., 1987, "Forced Convection in a Duct Partially Filled With a Porous Material," ASME JOURNAL OF HEAT TRANSFER, Vol. 109, pp. 653–662.

Roache, P. J., 1972, *Computational Fluid Dynamics*, Hermosa, Albuquerque, NM.

Sathe, S. B., Lin, W. Q., and Tong, T. W., 1988, "Natural Convection in Enclosures Containing an Insulation With a Permeable Fluid-Porous Interface," *Int. J. Heat Fluid Flow*, Vol. 9, pp. 389–395.

Vafai, K., 1986, "Analysis of the Channeling Effect in Variable Porosity Media," ASME *Journal of Energy Resources Technology*, Vol. 108, pp. 131–139.

Vafai, K., and Thiyagaraja, R., 1987, "Analysis of Flow and Heat Transfer at the Interface Region of a Porous Medium," *Int. J. Heat Mass Transfer*, Vol. 30, pp. 1391–1405.

Vafai, K., and Tien, C. L., 1981, "Boundary and Inertia Effects on Flow and Heat Transfer in Porous Media," *Int. J. Heat Mass Transfer*, Vol. 24, pp. 195–203.

Ice Formation and Heat Transfer With Water Flow Around Isothermally Cooled Cylinders Arranged in a Line

T. Hirata
Associate Professor.

H. Matsui
Graduate Student.

Department of Mechanical Engineering,
Faculty of Engineeering,
Shinshu University,
Nagano 380, Japan

The ice formation phenomenon and heat transfer around isothermally cooled cylinders that are lined up in the direction of flow in a crossflow of cold water were examined experimentally. Under the conditions of low Reynolds numbers and low cooling temperatures, the cylinders became linked by an ice layer. The amount of ice formed around the cylinders was much more than that for a single cylinder. A correlation equation was proposed for the amount of linked ice around the cooled cylinders. It was found that the local heat transfer coefficients on the linked ice surface showed an alternating decrease and increase in the flow direction. The mean value of the local Nusselt number showed the same characteristic as that on a flat plate in a turbulent flow. A dimensionless parameter that represents how efficiently the cylinders can work as a thermal energy storage system was introduced.

1 Introduction

Ice formation around cooled cylinders in a water flow is a basic engineering problem. It relates to many practical problems such as lowering thermal efficiency or increasing pressure drop in a water-cooled heat exchanger in a refrigeration system. It also relates many other practical applications such as ice-bank systems (Takada, 1984) and low-temperature storage systems (Taku, 1984), which utilize the latent heat of phase change. In those cases, the problems must be examined as ice formation around tube bundles; however, few such studies have been reported thus far.

For the ice formation phenomena around a single cylinder in a crossflow of cold water, Okada et al. (1978) did an analysis to derive a dimensionless parameter that governs the amount of ice formed in a steady-state condition. Inaba and Cheng (1983) and Cheng et al. (1981) obtained a correlation equation for the average heat transfer rate on the ice surface and introduced a parameter for a cooling capacity of formed ice. On the other hand, very few studies have been reported for ice formation around a bundle of cooled cylinders. Lock and Kaiser (1985) examined the ice formation phenomena around a couple of cylinders situated in a crossflow of cold water in relation to the damming of northern rivers.

Under conditions that produce thicker ice layers, the ice formation phenomena around cooled cylinders in a convective water flow become completely different from those for a single cylinder. That is, the cylinders are linked by the ice layer. In the previous study by Hirata and Matsui (1989), the ice formation phenomena around isothermally cooled cylinders arranged in a line were examined. It was found that the heat rate transferred from water to ice was controlled by a dimensionless parameter that represents the amount of heat stored by ice.

In the present study, the ice formation phenomena and heat transfer around isothermally cooled cylinders, which are lined up in the direction of flow in a crossflow of cold water, were examined. The onset conditions that describe whether the cylinders are linked by ice were discussed. A correlation equation representing the effect of cylinder pitch on the amount of linked ice was also proposed.

Contributed by the Heat Transfer Division for publication in the JOURNAL OF HEAT TRANSFER. Manuscript received by the Heat Transfer Division April 18, 1989; revision received September 11, 1989. Keywords: Forced Convection, Phase-Change Phenomena, Thermal Energy Storage.

2 Experimental Apparatus and Procedure

The experimental apparatus consisted of a calming section, a test section, a flow meter, a refrigeration unit, and two circulation systems of water and a coolant. The flow conditions at the inlet of the test section were assumed to be a laminar and a uniform velocity profile from the result of visual observations by a dye-injection method. In Fig. 1, a schematic illustration of the test section is shown. The test section had a 150 mm × 40 mm cross-sectional area and was 1000 mm length. The walls were made of transparent acrylic resin plates in order to observe the growth of the ice layer, and were installed in the vertical position to minimize the effect of the natural convection of water. Isothermally cooled cylinders with 41 mm o.d. and 40 mm in length were arranged in a line and installed in the test section. Three kinds of cylinder arrangement were chosen: 10 cylinders with $p = 60$ mm cylinder pitch, 8 cylinders with $p = 80$ mm, and 7 cylinders with $p = 100$ mm. To produce a uniform wall temperature, copper was used to fabricate the cylinders. The coolant was led directly from a constant-temperature bath to each cylinder and was circulated at a high velocity inside the cylinders. The flow of the water in the test section was in the upward vertical direction.

The wall temperatures of the cooled cylinders, T_w, were evaluated from two thermocouples located at the top and 90 deg of the third and fifth cylinders, respectively. Although a small temperature difference between the two cylinders was detected during the initial stage of ice formation, the difference became negligible with ice growth. The free-stream water temperature T_∞ was estimated from the mean value of

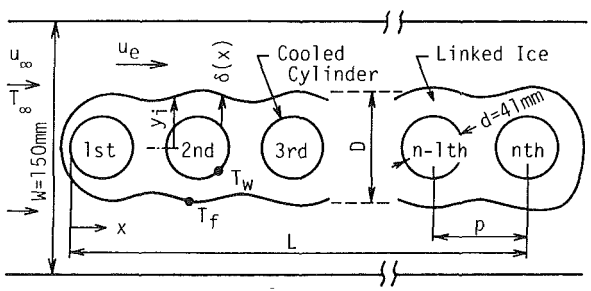

Fig. 1 Schematic illustration of test section

the inlet and outlet of the test section. An isothermal wall condition was satisfied within an error of 3 percent in T_w. The inlet water temperature variations due to the dynamics of the refrigeration system yielded a maximum error of 2 percent in T_∞. After a steady-state condition was reached, a small amount of dye was injected into the water stream to enhance the ice-water interface. To measure the thickness of the ice layer, the ice around the cylinders was photographed and the coordinates of the ice-water interface were measured. An anastigmatic lens (Nikon Micro Nikkor 200-mm F4S) was used to avoid distortion of the subject.

The flow condition around the rear surface of the last cylinder was different from others; therefore, an effective length L of the row of cylinders was defined, as shown in Fig. 1, as $L = 560.5$ mm for $p = 60$ mm, $L = 580.5$ mm for $p = 80$ mm and $L = 620.5$ mm for $p = 100$ mm. All measurements of ice thickness were done in those regions, respectively. The two dimensionality of heat flow from the water to the cylinders was confirmed by the fact that a two-dimensional ice layer was produced around the cylinders. Although the effect of heat conduction through the acrylic resin plates of the test section wall was observed at both ends of each cylinder, the region with this effect was considered to be negligible compared to the cylinder length. Experimental ranges covered in the present experiment were:

$p = 60$ mm; $u_\infty = 0.02$–0.11 m/s, $T_\infty = 1.3$–4.5°C, $\mathrm{Re_d} = 570$–3160, $\theta = 0.51$–4.93

$p = 80$ mm; $u_\infty = 0.04$–0.09 m/s, $T_\infty = 1.1$–1.9°C, $\mathrm{Re_d} = 990$–1970, $\theta = 1.5$–4.3

$p = 100$ mm; $u_\infty = 0.03$–0.08 m/s, $T_\infty = 1.0$–1.4°C, $\mathrm{Re_d} = 630$–1910, $\theta = 3.6$–6.9

where $\mathrm{Re_d}$ is a Reynolds number and θ is a cooling temperature ratio defined by $\theta = (T_f - T_w)/(T_\infty - T_f)$. A steady-state condition was confirmed by measuring ice thickness with slide calipers from outside the test section at predetermined time intervals. All measurements were done after a steady-state condition was reached. For the present experimental ranges, 8 to 12 h was needed to obtain a steady-state condition.

3 Determination of Local Heat Transfer Coefficient

For the steady-state ice layer around a single cylinder, some determination methods for the local heat transfer coefficient have been reported, such as a heat conduction analysis using a boundary-fitted coordinate system (Cheng and Sabhapathy, 1985) and a point-matching technique using an exact solution of the Laplace equation for polar coordinates (Cheng et al., 1981). In this study, the cylinders became linked by an ice layer under conditions of a thicker ice layer, so that a completely different shape of ice from that for a single cylinder was produced. Therefore, the above determination methods for the local heat transfer coefficient cannot be applied. The other method, which measures the temperature gradient in a water stream on the ice-water interface, results in a comparatively large error in measurement.

In the present study, the boundary element method (Brebbia, 1978) was used to determine the local heat transfer coefficient on the surface of the ice. For this method, the data necessary are the coordinates of the ice-water interface and the temperature boundary conditions. Figure 2 shows three patterns of ice shape expected to form around the cylinders. The effect of the number of the boundary element, m, on the accuracy of the solution was checked for the ice pattern shown in Fig. 2(*c*). It was ascertained that the effect of m is less than 5 percent for $m > 56$. The temperature boundary condition at the ice-water interface and cylinder wall was a uniform and constant temperature. At the other boundaries, a zero temperature gradient was used. The temperature gradient inside the ice layer was computed by the boundary element method. The local heat transfer coefficient h_x on the ice surface in a steady-state condition was determined by

$$h_x(T_\infty - T_f) = \lambda_i \left.\frac{\partial T}{\partial n}\right|_{y=y_i} \tag{1}$$

where T_f is the freezing temperature of water, λ_i is the thermal

Nomenclature

A_i = volume of ice per unit length of cylinder
A^* = dimensionless value of A_i, equation (12)
Cp_w = specific heat of water
d = diameter of cylinder
D = mean ice thickness, Fig. 1
g = acceleration of gravity
$\mathrm{Gr_L}$ = Grashof number $= g\beta(T_\infty - T_f)L^3/\nu_w{}^2$
h_m = mean heat transfer coefficient for $x = 0$–L
h_x = local heat transfer coefficient
H = dimensionless parameter, equation (11)
L = effective length of the row of cylinders, Fig. 1
L^* = dimensionless value of $L = L/d$
L_f = latent heat of fusion
$\mathrm{Nu}_{m,L}$ = mean Nusselt number $= h_m L/\lambda_w$
Nu_x = local Nusselt number $= h_x x/\lambda_w$
p = cylinder pitch
q_i = amount of heat rate stored per unit of time
q_w = amount of heat rate transferred from water to ice
Re_d = pipe Reynolds number $= ud/\nu_w$
Re_L = Reynolds number $= u_e L/\nu_w$
Re_x = Reynolds number $= u_e x/\nu_w$
Ste = Stefan number $= Cp_w(T_\infty - T_f)/L_f$
T_f, T_w, T_∞ = temperatures of freezing, cylinder wall, and water
u = velocity of water around the row of cylinders without ice $= u_\infty W/(W-d)$
u_e = velocity of water around the row of cylinders with ice $= u_\infty W/(W-D)$
u_∞ = free-stream velocity of water upstream of the row of cylinders
W = width of test section, Fig. 1
y_i = distance from center axis of the row of cylinders to ice water interface
β = volume expansion coefficient
$\delta(x)$ = local ice thickness
θ = dimensionless cooling temperature ratio $= (T_f - T_w)/(T_\infty - T_f)$
λ^* = thermal conductivity ratio of ice to water $= \lambda_i/\lambda_w$
ν_w = kinematic viscosity of water
ρ_i = density of ice

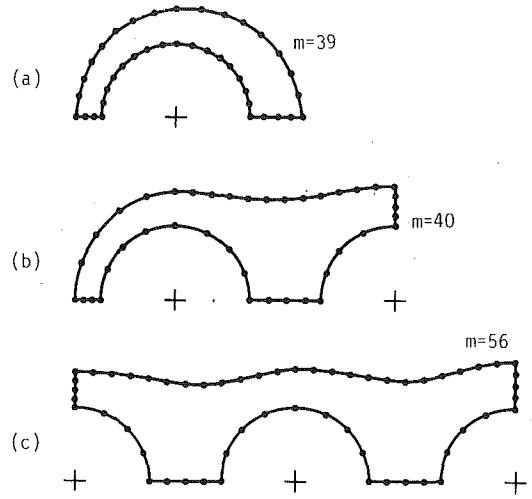

Fig. 2 Typical ice shape patterns for boundary element method

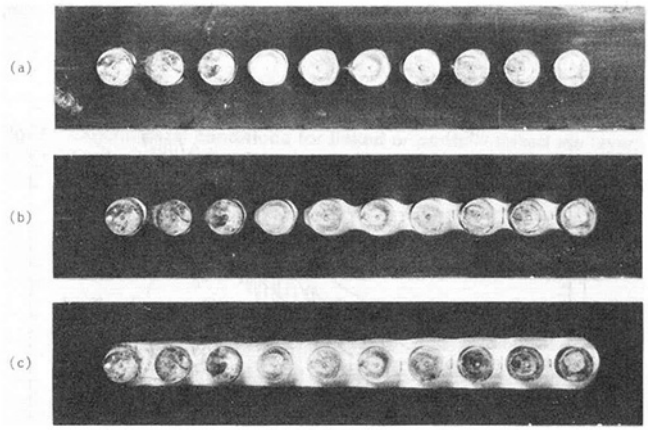

Fig. 3 Ice formation pattern for $p = 60$ mm (note: flow direction is from left to right and the actual experiments were done with the test section vertical): (a) $Re_d = 3170$, $\theta = 0.98$, (b) $Re_d = 2310$, $\theta = 1.17$, (c) $Re_d = 2060$, $\theta = 2.44$

conductivity of ice, and y_i is the coordinate of the ice–water interface. The measurement of the coordinates of the ice–water interface yielded a maximum error of 3 percent in the amount of ice and it produced an error of about 8 percent in h_x.

4 Results and Discussion

4.1 Freezing Phenomena and Local Heat Transfer. Figure 3 shows typical results of an ice shape formed in a steady-state condition for $p = 60$ mm. The flow direction is from left to right and the ice layer is shown by gray-color areas around the cylinders.

Figure 3(a) is the result for large Reynolds number and small cooling temperature ratio θ. In this case, the ice was formed around each individual cylinder. A close observation revealed that ice shape was affected by a stagnant flow resulting from the existence of neighboring cylinders; for example, the ice shape of the fifth cylinder showed that the local ice thickness at the forward stagnation region became thick. This phenomenon was due to a decrease of heat transfer rate at the stagnation region and was entirely different from that for a single cylinder (Okada et al., 1978; Inaba and Cheng, 1983). Because the ice formed in the stagnation region made its neighboring flow more stagnant, local ice growth in this region became accelerated with increasing ice thickness. The experimental conditions of Fig. 3(a) were nearly the onset conditions to produce the linked ice layer. It was also observed that the individually formed ice layer was not always symmetric about the cylinder axis.

Figure 3(b) is the result obtained under conditions that produce thicker ice layers than Fig. 3(a). Because the water temperature decreased as it flowed across the cooled cylinders, the cylinders downstream of the fifth position were finally linked by the ice layer. Under the conditions shown in Fig. 3(b), the amount of linked ice between the cylinders were comparatively small and a flow separation occurred on the linked ice surface between the cylinders. As can be seen in Fig. 3(b), the ice layer downstream of the fifth cylinder shows a narrowed shape due to the existence of the separation flow.

Figure 3(c) shows the completely linked ice layer. Under the conditions that produce thicker ice layers, a flow separation was not observed on the linked ice surface. The ice–water interface of Fig. 3(c) shows the sinuous shape of a wavelength corresponding with the cylinder pitch. This resulted from a sinuous distribution of the local heat flux at the ice–water interface. The ice layer in Fig. 3(c) became thicker downstream, which implies that the ice layer was also affected by a temperature boundary layer in the water stream. For the linked ice pattern, the symmetric ice layer was always observed. The ice formation phenomena for $p = 80$ mm and 100 mm did not differ largely from the results observed in Fig. 3. Two steady-state ice shapes obtained by growing and by melting the ice layer, respectively, were compared with each other under same steady-state conditions. A detectable difference between the final ice shapes was not observed.

Figure 4 shows the coordinate of the ice–water interface, y_i, the local ice thickness, $\delta(x)$, and the local heat transfer coefficient on the ice surface, h_x. The heavy lines in the abscissa indicate the locations of the cylinders. Figure 4(a) is the result of individually formed ice layers. In this case, the amount of ice was small. The value of h_x at the second cylinder showed a larger value than the neighboring ones, because the separated flow from the first cylinder reattached to the second one under this experimental condition. Downstream of the third cylinder, h_x increased due to the development of flow turbulence.

In Fig. 4(b), the difference in the amount of ice between the linked and the individually formed ice layers is clearly shown by $\delta(x)$. When the cylinders were linked by ice, the amount of ice between the cylinders became considerably larger. This is a characteristic of the ice formation around the cooled cylinders utilizing, for example, an ice-bank low-temperature storage system.

Figure 4(c) shows the results for the linked ice layer. It is shown that the amount of ice is large and the local heat transfer coefficient decreases in the downstream direction with the alternations of a decrease and increase corresponding with the cylinder pitch. In the present study, the discussions will be focused mainly on the case shown in Fig. 4(c).

4.2 Local Nusselt Number. When the cylinders are linked by ice, the heat transfer coefficient on the ice surface cannot be estimated from the results for a tube bank heat exchanger. In this case, the shape of the ice presents an appearance similar to that produced on a cold flat plate in a water stream. In the present study, the local heat transfer data were arranged in the same manner as those on a flat plate. The results are shown in Fig. 5 where Re_x is defined by a mean free stream velocity, u_e, over the ice layer. It is indicated that Nu_x increases with Re_x with the alternations of a decrease and increase, and that the tendency of the average value of Nu_x versus Re_x is the same as that for turbulent heat transfer on a flat plate. Even though the Reynolds number range was in a laminar flow on a flat plate, Nu_x shows the turbulent heat transfer characteristic. It was considered that alternations of acceleration and deceleration of the flow on the sinuous ice surface made the surface

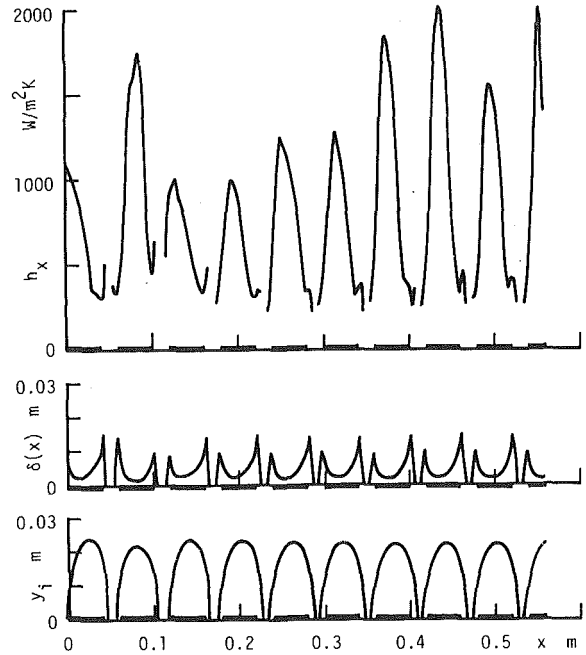

Fig. 4(*a*) Ice shape and heat transfer coefficient for $p = 60$ mm, $Re_d = 3160$, and $\theta = 0.82$

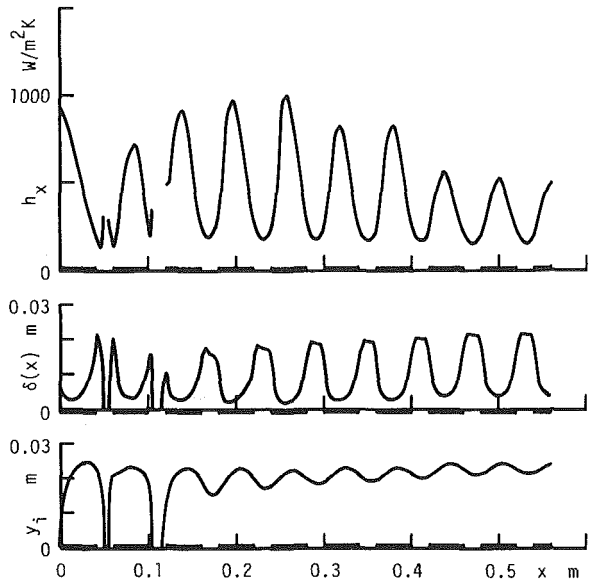

Fig. 4(*b*) Ice shape and heat transfer coefficient for $p = 60$ mm, $Re_d = 1320$, and $\theta = 0.94$

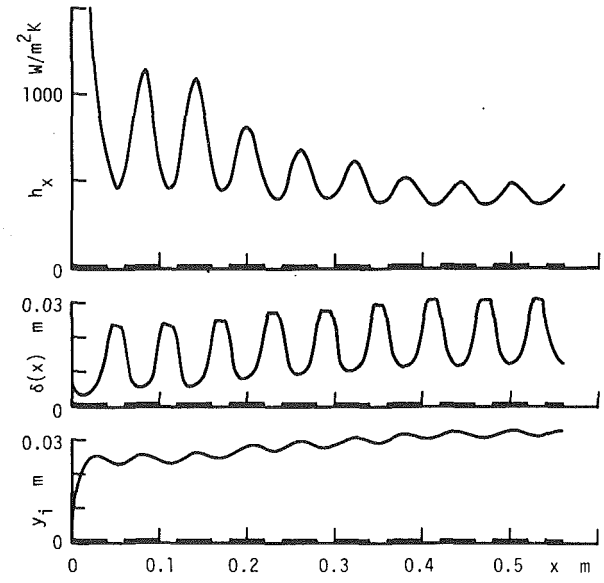

Fig. 4(*c*) Ice shape and heat transfer coefficient for $p = 60$ mm, $Re_d = 1390$, and $\theta = 3.00$.

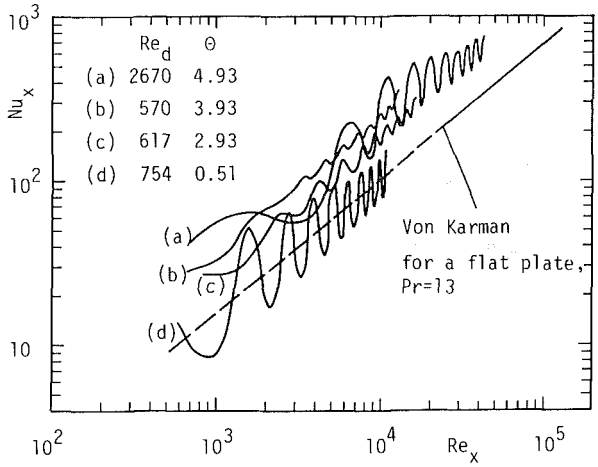

Fig. 5 Local Nusselt number for $p = 60$ mm

unstable and produced turbulence. The same results were obtained also for $p = 80$ mm and 100 mm. It should be noted that under conditions of much thicker ice layers, the area of flow passage, *W–D*, decreases in the downstream direction and the effect of acceleration of the free-stream velocity on the heat transfer rate will be involved, which is practically important for the problem of ice formation around a bundle of cooled cylinders.

In this experiment, the flow over the cylinders might be affected by the boundary layers on the side walls, because the length of the cylinder was not sufficiently long in comparison with the diameter. If it was assumed that the flow on the side walls was laminar and the boundary layers developed from the inlet of the test section (250 mm upstream of the first cylinder), the two boundary layers were estimated to merge at the sixth cylinder for $Re_d = 754$ in Fig. 5. If a turbulent flow was assumed, the boundary layers merge at the third cylinder for $Re_d = 2670$. Judging from the results in Fig. 5, the tendency of Nu_x versus Re_x was consistent over the length of lined up cylinders, and the effect of the boundary layers on the ice shape was considered to be negligible.

Gebhart (1971) noted that the effect of free convection on the local heat transfer coefficient in a turbulent flow was less than 10 percent for $Gr_x/Re_x^{2.5} < 0.0016$, where Gr_x is a Grashof number. For the present experiment, the values of $Gr_L/Re_L^{2.5}$ fell in the range from 1.45×10^{-4} to 1.67×10^{-3}; therefore, the free convection effect was considered to be less than 10 percent.

4.3 Onset Conditions for Linked Ice Layers. In the present study, the linked ice layer was defined for the case in which all the cylinders were linked by ice, and the partially linked ice layer was defined for the case in which not all cylinders were linked by ice. According to the ice formation phenomena shown in Fig. 4(*b*), the onset conditions are strongly dependent on the amount of ice around the first and the second cylinders, because the ice layers at the upstream cylinders are thin due to a high heat transfer rate. Let us suppose that the ice layer was individually formed around the cylinders in a steady-state condition. If it is assumed that the cylinder pitch

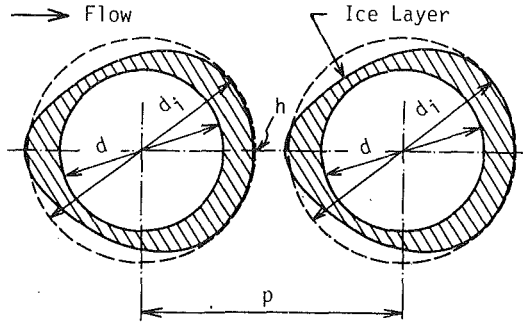

Fig. 6 Analytical model for onset conditions

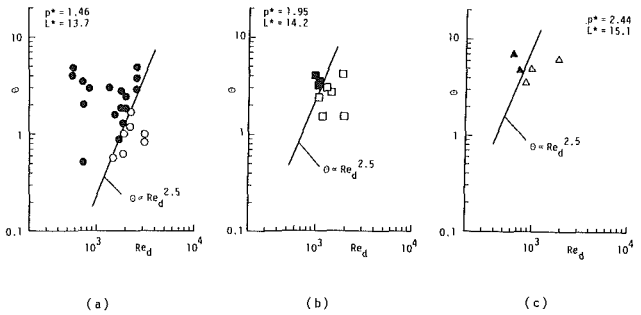

Fig. 7 Experimental conditions for linked or partially linked ice layer: (a) $p = 60$ mm, (b) $p = 80$ mm, (c) $p = 100$ mm

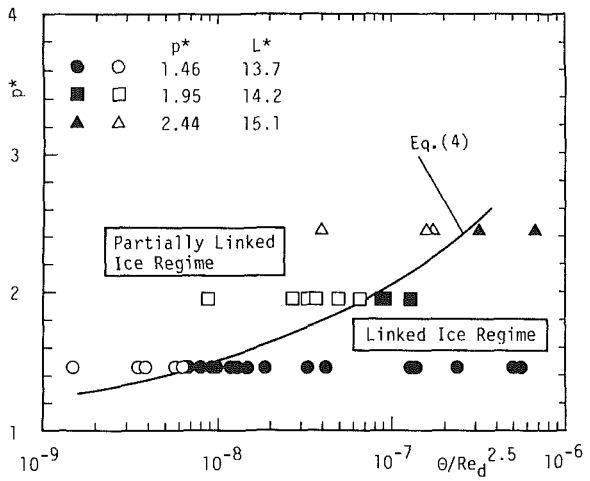

Fig. 8 Onset conditions for linked or partially linked ice layer

is comparatively small and, therefore, the ice layer for the onset conditions is also thin, the ice shape will be approximated by the cylinder with a diameter d_i, as shown in Fig. 6. Then, we have a heat balance equation at the ice-water interface in a steady-state condition as

$$\frac{d_i}{d} \ln \frac{d_i}{d} = \frac{2\lambda_i \theta}{dh} \tag{2}$$

where h is the heat transfer coefficient in the stagnation regions, λ_i is the thermal conductivity of ice, and θ is the dimensionless cooling temperature. In equation (2), the onset conditions are given by $d_i = p$. Introducing the dimensionless cylinder pitch $p^* = p/d$ and assuming that the Nusselt number $\mathrm{Nu_d} = hd/\lambda_w$ on the right-hand side in equation (2) is represented as a function of Reynolds number $\mathrm{Re}_d = ud/\nu_w$, we have

$$p^* \ln p^* = f(\theta, \mathrm{Re_d}) \tag{3}$$

Equation (3) implies that the onset conditions are represented in terms of $p^* \ln p^*$.

Figure 7 shows a map of linked and partially linked ice regimes on the θ–Re_d coordinate system for the three cylinder pitches. The solid and open circles represent linked and partially linked ice, respectively. In Fig. 7(a), for example, it is shown that linked ice was produced under larger θ and lower $\mathrm{Re_d}$, and the onset conditions for the linked ice layer were approximated by $\theta = \mathrm{const} \times \mathrm{Re_d^{2.5}}$. Although the data in Fig. 7(a) were not enough to determine the onset conditions precisely, the $\theta \propto \mathrm{Re_d^{2.5}}$ relation would be accepted at this stage of the present research. With reference to this result, the onset values for cylinder pitches of $p = 80$ mm and 100 mm can be obtained as shown in Figs. 7(b) and 7(c), respectively. The function on the right-hand side of equation (3), which governs the onset conditions is, thus, considered to be $\theta/\mathrm{Re_d^{2.5}}$.

Figure 8 shows a map of the ice formation pattern on the p^*–$\theta/\mathrm{Re_d^{2.5}}$ coordinate system. Since the dimensionless parameter $\theta/\mathrm{Re_d^{2.5}}$ means a degree of ice thickness at the stagnation regions, it is realized from Fig. 8 that when the cylinder pitch is large, the linked ice layer is produced under conditions of thicker ice layers. The experimental data are arranged well in terms of $\theta/\mathrm{Re_d^{2.5}}$ and the onset values are represented by

$$p^* \ln p^* = 731 \left(\frac{\theta}{\mathrm{Re_d^{2.5}}} \right)^{0.384} \tag{4}$$

The applicable range of equation (4) is for $p^* < 2.44$. In Fig. 8, the lower regime of equation (4) is the linked ice regime and the upper, the partially linked ice regime. It should be noted that the effective length of the row of cylinders, L, does not appear in equation (4), because the onset conditions are strongly dependent on the ice layers around the first and second cylinders.

4.4 Ice Storage Efficiency. To analyze the efficiency of low-temperature storage system utilization of cooled cylinders, the parameter that describes the ratio of stored heat around the cylinder, q_i, to removed heat from the cylinder, q_w, should be considered (Hirata and Matsui, 1989). In the present paper, q_i/q_w was defined as an ice storage efficiency.

Neglecting sensible heat as compared with latent heat, the stored heat, q_i, for a unit of time is given by

$$q_i = \rho_i L_f A_i \tag{5}$$

where ρ_i is the density of ice, L_f is the latent heat, and A_i is the volume of ice on a unit length of cylinder ($\mathrm{m^3/m}$). On the other hand, the heat removed from the cylinder for a unit of time, q_w, which is equal to the heat transferred from the water to the ice surface under steady-state conditions, is given by

$$q_w = 2 \int_0^L h_x (T_\infty - T_f) dx \tag{6}$$

where L is the effective length of the row of cylinders. Because the value of h_x on the right-hand side of equation (6) showed the same tendency as that of turbulent heat transfer on a flat plate (see Fig. 5), ice storage efficiency on a cooled flat plate was first derived to discuss a dimensionless parameter for the efficiency of the cooled cylinders. The volume of ice on both sides of a cooled flat plate in a turbulent flow is given by

$$A_i = 2 \int_0^L \delta(x) dx \tag{7}$$

where $\delta(x)$ is given by Hirata et al. (1979) as

$$\delta(x) = \lambda^* \theta x / \mathrm{Nu_x} \tag{8}$$

The local Nusselt number $\mathrm{Nu_x}$ of turbulent heat transfer on a flat plate is given by equation (9) for $5 \times 10^5 < \mathrm{Re_x} < 10^7$ (Holman, 1976).

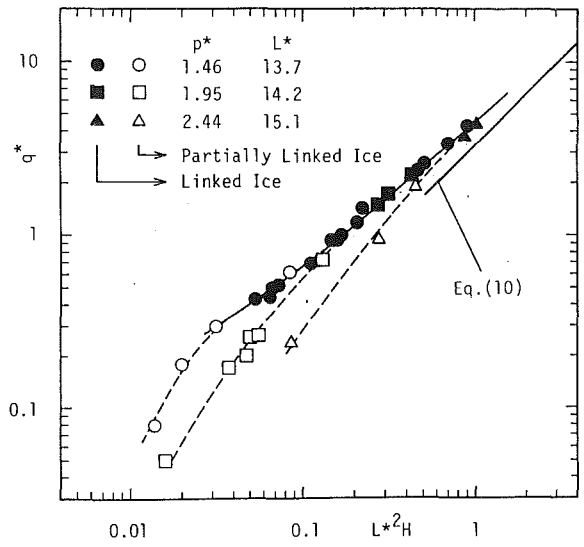

Fig. 9 Ice storage efficiency

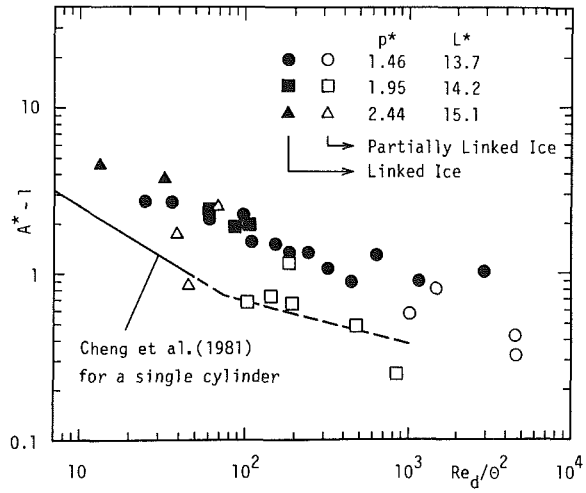

Fig. 10 Volume of ice around cooled cylinders

$$Nu_x = 0.0296\ Re_x^{0.8}\ Pr^{1/3} \tag{9}$$

The ice storage efficiency on a cooled flat plate in a turbulent flow is then obtained from equations (5)–(9) as

$$q^* = q_i/q_w = 3.32\ L^{*2}H \tag{10}$$

where L^* is a dimensionless parameter of the effective length L, and H is defined by

$$H = \frac{\lambda^*\theta}{Nu_{m,L}^2}\frac{1}{Ste} \tag{11}$$

where λ^* is the thermal conductivity ratio of ice to water, $Nu_{m,L}$ is the mean Nusselt number for $x = 0$—L, and Ste is the Stefan number. H is the dimensionless parameter representing stored heat in ice. The physical properties of water were estimated at 0°C.

In Fig. 9, the data for ice storage efficiency are plotted against the dimensionless parameter derived by equation (10). It is shown that q^*increases with the dimensionless parameter H, defined in equation (11). The results for linked ice layers (solid circles) correlate well with the parameter of $L^{*2}H$. This implies that q^* for linked ice layers is independent of cylinder pitch. On the other hand, the values of q^* for partially linked ice layers (open circles) show lower values than those for linked ice layers. This implies that linked ice conditions should

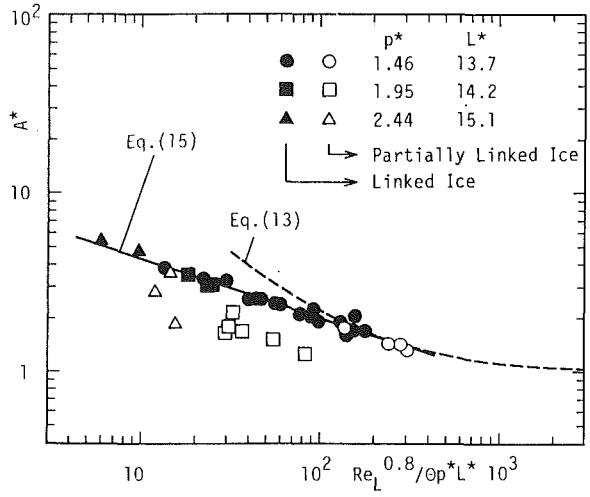

Fig. 11 Correlation of ice volume for linked ice layer

be maintained to obtain high ice-storage efficiency in an ice bank system utilizing the cooled cylinders. In Fig. 9, the result for a flat plate given by equation (10) is also shown by a solid line. If it was assumed that the length of the row of cylinders increased in comparison to the cylinder pitch, the ice layer around the cylinders can be considered from a macroscopic point of view to be that of a cooled flat plate. With increasing $L^{*2}H$, the value of q^* for the linked ice layer demonstrates a tendency to coincide with that for a flat plate.

4.5 Amount of Ice Growth Around Cylinders. In the present study, the dimensionless volume of ice was defined by

$$A^* = \frac{4pA_i}{\pi d^2 L} + 1 \tag{12}$$

In Fig. 10, the volume of ice around the cylinders under steady-state conditions is compared with the result for a single cylinder obtained by Cheng et al. (1981); the abscissa is the parameter governing the volume of ice for a single cylinder derived by Okada et al. (1978). It is shown that the volume of ice for linked ice layers is more than twice as much as that for a single cylinder. For partially linked ice layers, there are some data that show the ice volume being less than that for a single cylinder. This is caused by the high heat transfer rate due to the development of flow turbulence at the downstream cylinders. It is also shown that the present data for linked ice layers cannot be correlated with the parameter for a single cylinder, Re_d/θ^2.

From the results shown in Fig. 5, it was supposed that the heat transfer rate on the ice surface was controlled by turbulent heat transfer. Introducing the value of A_i calculated from equations (7)–(9) into equation (12) yields

$$A^* = 118\left(\frac{Re_L^{0.8}}{\theta p^* L^*}\right)^{-1} + 1 \tag{13}$$

where Pr = 13 was used. The parameter in the brackets on the right-hand side of equation (13) represents the dimensionless amount of ice for linked ice layers. The dimensionless parameter A^* given by equation (13) involves the effects of both the cylinder pitch, p^*, and the effective length of the row of cylinders, L^*. Using the relation of $Re_L = Re_d L/d$, equation (13) is transformed into

$$A^* = 118\left(\frac{Re_d^{0.8}}{\theta p^* L^{*0.2}}\right)^{-1} + 1 \tag{14}$$

Equation (14) suggests that the volume of ice A^* is a weak function of L^*. This implies that p^* rather than L^* should be taken at larger values to produce large amounts of ice.

In Fig. 11, the volume of ice is plotted on the dimensionless

coordinate system given by equation (13). The data for linked ice layers correlate well and are represented by the following empirical equation:

$$A^* = 8.89\left(\frac{\mathrm{Re}_L^{0.8}}{\theta p^* L^*}\right)^{-0.324} \tag{15}$$

where the applicable range is for $6 < \mathrm{Re}_L^{0.8}/\theta p^* L^* < 3 \times 10^2$ and the accuracy is within an error of ± 7 percent. If it is assumed that the cylinder pitch decreases to the limiting value, the row of cylinders can be considered to be a flat plate, as described above. The data in Fig. 11 clearly show a tendency to approach the values of equation (13) with increasing $\mathrm{Re}_L^{0.8}/\theta p^* L^*$. On the other hand for partially linked ice layers (open circles), it is shown that the values of A^* become small and the data cannot be correlated with equation (15). It should be noted again that the onset conditions for linked ice layers are given by equation (4).

5 Conclusions

Experimental studies were performed for ice formation and heat transfer around isothermally cooled cylinders arranged in the direction of flow in a crossflow of cold water. The following conclusions may be drawn:

1 The local Nusselt number Nu_x on the ice surface around the cylinders increased with Re_x with alternations of a decrease and increase. The tendency of the average value of Nu_x versus Re_x was the same as that for a turbulent heat transfer on a flat plate.

2 Linked ice layers were produced under conditions of larger values of $\theta/\mathrm{Re}_d^{2.5}$ and the onset conditions for linked ice layers were given by equation (4).

3 The ice storage efficiency defined by equation (10) was introduced to examine how cooled cylinders can work as a low-temperature storage system. It was shown that ice storage efficiency was controlled by the dimensionless parameter given by equation (11).

4 The volume of ice for linked ice layers was more than twice as much as that for a single cylinder and was correlated by equation (15).

The problem of ice formation and heat transfer under unsteady conditions is also important for the water-cooled heat exchanger and ice storage system, and will be a topic for future research.

References

Brebbia, C. A., 1978, *The Boundary Element Method for Engineering*, Pentech Press.

Cheng, K. C., Inaba, H., and Gilpin, R. R., 1981, "An Experimental Investigation of Ice Formation Around an Isothermally Cooled Cylinder in Crossflow," ASME JOURNAL OF HEAT TRANSFER, Vol. 103, pp. 733–738.

Cheng, K. C., and Sabhapathy, P., 1985, "Determination of Local Heat Transfer Coefficient at the Solid–Liquid Interface by Heat Conduction Analysis of the Solidified Region," ASME JOURNAL OF HEAT TRANSFER, Vol. 107, pp. 703–706.

Gebhart, B., 1971, *Heat Transfer*, McGraw-Hill, New York, p. 393.

Hirata, T., Gilpin, R. R., and Cheng, K. C., 1979, "The Steady State Ice Layer Profile on a Constant Temperature Plate in a Forced Convection Flow: II, The Transition and Turbulent Regimes," *International Journal of Heat and Mass Transfer*, Vol. 22, pp. 1435–1443.

Hirata, T., and Matsui, H., 1989, "Ice Formation Phenomena With Water Flow Around Isothermally Cooled Cylinders Arranged in a Line," *Proc. of 1989 Int. Symp. on Cold Region Heat Transfer*, N. Seki et al., eds., pp. 33–38.

Holman, J. P., 1976, *Heat Transfer*, McGraw-Hill, New York, p. 180.

Inaba, H., and Cheng, K. C., 1983, "Freezing Behaviour Around Horizontal Cylinder in Cold Water Flow," *Refrigeration* [in Japanese], Vol. 58, pp. 13–22.

Lock, G. S. H., and Kaiser, T. M. V., 1985, "Icing on Submerged Tubes: A Study of Occlusion," *International Journal of Heat and Mass Transfer*, Vol. 28, pp. 1689–1698.

Okada, M., Katayama, K., Terasaki, K., Akimoto, M., and Mafune, K., 1978, *Transactions of JSME* [in Japanese], Vol. 44, pp. 624–631.

Takada, S., 1984, "The Trends of Heat Storage Engineering Utilizing the Water–Ice Transition," *Refrigeration* [in Japanese], Vol. 59, pp. 511–518.

Taku, K., 1984, "Long Cycle Heat Storage System by Ice-Making Heat Pump," *Refrigeration* [in Japanese], Vol. 59, pp. 504–510.

Electron Beam Deflection When Welding Dissimilar Metals

P. S. Wei
Professor.

T. W. Lii
Graduate Student.

Institute of Mechanical Engineering,
National Sun Yat-Sen University,
Kaohsiung, Taiwan

High-intensity electron beam deflection due to thermoelectric magnetism generated during the welding of dissimilar metals is systematically and analytically investigated. A simple thermoelectric model is proposed and the temperature field, penetration depth of the fusion zone, magnetic field, and motion of an electron are determined. Deviation of the fused zone from a joint is affected by the incident angle of the energy beam, the difference in Seebeck coefficients of workpieces, relative magnetic permeability, beam power, welding speed, thermal and electrical conductivities, and the effective electrical contact resistance. Their effects are clearly interpreted in this study. Analytical results for the deviation of the fused zone from the joint between the materials to be welded show good agreement with available experimental data.

Introduction

The major advantage of high-intensity electron beam welding is the ability to create a deep and narrow fusion zone with depth-to-width ratios of 5 to 10 or greater (Tong and Giedt, 1971; Wei et al., 1990). Recently, Wei and Chiou (1988) provided a detailed interpretation of the formation of deep penetration obtained with a high-intensity energy beam (electron or laser beam). When the energy beam impinges on the workpieces to be joined, a thin layer of material is melted. With continued heating the reactive force of evaporating material and the force induced by surface tension cause the liquid layer to flow upward and outward continuously. A vapor-filled deep and narrow cavity is produced and results in a deep weld joint. Therefore, the electron beam can readily pass through the vapor core to the liquid layer surrounding the cavity.

Electron beam welding is a very useful process for joining a wide range of dissimilar metal combinations that are difficult or impossible to weld by other techniques. When a small-diameter electron beam is used to make a deep weld in a thick section, the beam axis must be in the same plane as the joint faces and aligned with the joint along its entire length of travel. However, even when the beam from the electron gun is properly aligned with the joint, subsequent deflection of the beam can result in nonsymmetric fusion along a joint, or the fusion zone may miss the joint completely. Electron beam deflection can be due to: (*a*) the residual magnetism of weldments in their fixtures, (*b*) electric currents on the wall of the vacuum chamber of an electron beam welding unit or the metal weldment near which the electron beam passes, and (*c*) thermoelectric magnetic fields caused by temperature gradients in dissimilar materials (Nazarenko, 1982).

The residual magnetic fields can be unexpectedly induced in ferromagnetic materials due to contact with electromagnetics during machining or welding. For example, steel may be magnetized if it is held by a magnetic chuck. Consequently, the residual magnetism in the steel distorts and deflects the electron beam. The electron beam can also be deflected as it passes close to the wall of an electron beam vacuum chamber by interaction with eddy current, with currents passing over the surface of the wall to earth, or by reflected currents at the surface of the ferromagnetic metal.

It is crucial to know that the magnetic field originating from the thermoelectric currents can induce beam deflection during the welding of dissimilar metals, as shown in Fig. 1 (Blakeley and Sanderson, 1984). In fact, the weld pool can create a hot junction around the vapor cavity, while a cold junction is formed by the much cooler joint in front and behind the beam and at the top of the fusion zone (Schauer et al., 1978; Wei et al., 1990). Due to low resistance, currents of several hundred amperes can be obtained (Blakeley and Sanderson, 1984). Such a thermoelectric current can circulate and give rise to magnetic fields of around 10 gauss. Experimental observations indicated that the lines of magnetic flux parallel to the joint line are responsible for the deflection out of the joint plane.

It is feasible to use two beams to make two joints simultaneously (Blakeley and Sanderson, 1984), so arranged that the thermoelectric current from one cancels the current from

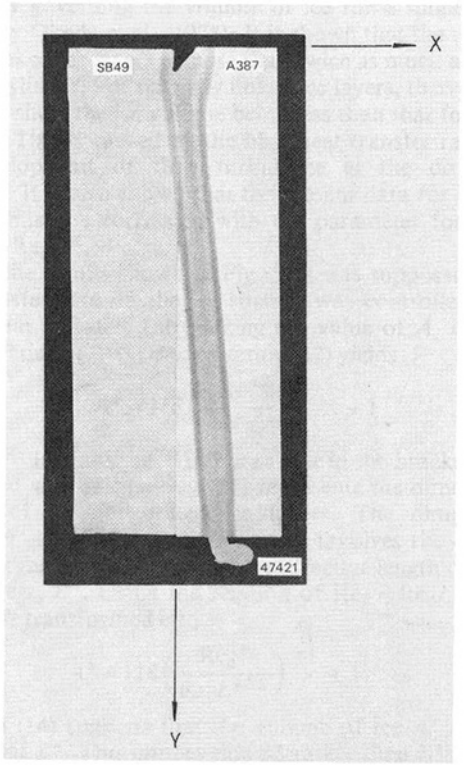

Fig. 1 Dissimilar metal electron-beam weld in 150-mm-thick SB49 (C-Mn) steel and A387 (2¼ Cr-1 Mo) steel (Blakeley and Sanderson, 1984)

Contributed by the Heat Transfer Division for publication in the JOURNAL OF HEAT TRANSFER. Manuscript received by the Heat Transfer Division June 9, 1989; revision received November 6, 1989. Keywords: Conduction, Materials Processing and Manufacturing Processes, Thermodynamics and Second Law.

the other. Since much of the damage is caused by external fields that deflect the beam before it reaches the joint, the use of a magnetic shielding plate is recommended. Tilting the workpieces is also possible to ensure that the joint is encompassed by the deflected weld pool. In order to quantify such procedures it is necessary to determine how thermoelectricity affects the beam deflection. This study was therefore undertaken to investigate the problem.

The deflection of an electron beam caused by the thermoelectric magnetic force due to a temperature gradient in dissimilar metals is investigated. The analytic results obtained will provide a systematic understanding of the deflection of the beam from the weld joint for different welding beam powers, welding speeds, and properties for both dissimilar materials.

Analysis

The dissimilar metals to be investigated are assumed to be semi-infinite in the x–z plane and finite with a thickness l in the y direction, as shown in Fig. 2. The cavity produced by the electron beam is an inverted cone. The opening radius and depth are denoted r_0 and d, respectively. Schauer et al. (1978) measured the cavity surface temperature distribution and found that the vertical temperature gradient along the cavity wall is significant. This can result in thermoelectric currents that circulate in the workpieces. The induced magnetic field above the workpiece surface deflects the electron beam from the joint plane by an incident angle of β. The electron beam can also be affected by the thermoelectric magnetism in workpieces. As a result, asymmetric fusion along a joint occurs.

In this study, the metal having the larger Seebeck coefficient

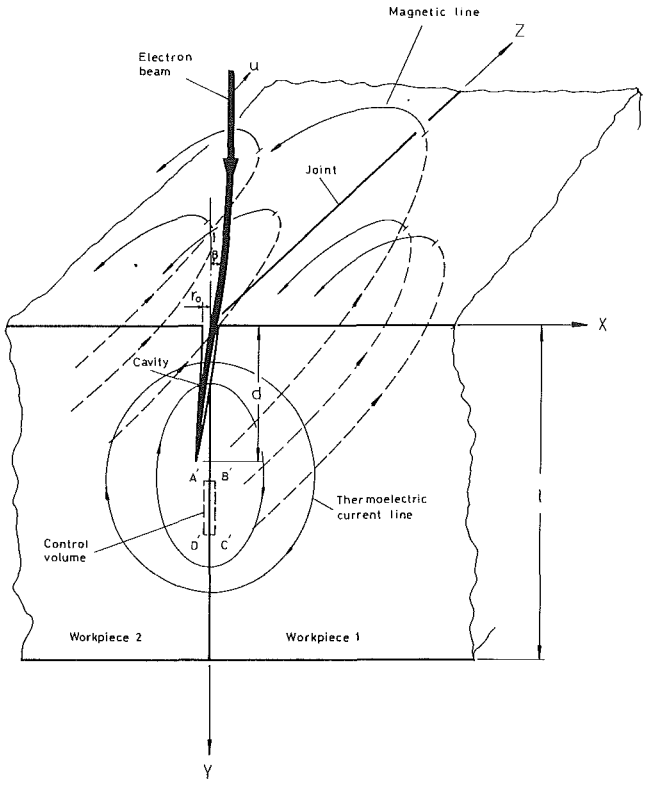

Fig. 2 System model and coordinate system

Nomenclature

B, B^* = magnetic flux density, Weber/m^2; dimensionless magnetic flux density parallel to welding direction, $B^* = B/\mu_0\mu_{r1}\sigma_1(S_1 - S_2)(T_{1m} - T_\infty)$

Bi = Biot number $= hl/k_1$

d, D = dimensional and dimensionless depth of fusion zone; $D = d/l$

e = electron charge, coulomb

E = electric field intensity, V/m

G = dimensionless effective electrical contact resistance parameter $= \sigma_1\tau/l$

h = heat convective coefficient

I = electron beam current, amp

j = electric current density, amp/m^2

j_n = electric current density normal to contact surface

k, K = dimensional and dimensionless thermal conductivity, $K = k_1/k_2$

l = dimensional weldment thickness

m = electron mass, kg

q, q' = beam energy density

Q = dimensionless beam power $= VI/lk(\bar{T}_m - T_\infty)$

r, R = dimensional and dimensionless trajectory radius of curvature, $R = r/l$

r_0, R_0 = cavity opening radius, $R_0 = r_0/l$

S = absolute thermoelectric power, V/K

T = temperature

u, U = dimensional and dimensionless welding speed; $U = 2r_0u/\tilde{\alpha}$

v = electron velocity

V = accelerating voltage, V

V_i = induced Seebeck voltage, V

x, X = coordinates as shown in Fig. 2, $X = x/l$

y, Y = coordinates as shown in Fig. 2, $Y = y/l$

α = thermal diffusivity

β = incident angle of electron beam impinging on workpiece surface

Γ = dimensionless electrical conductivty ratio $= \sigma_2/\sigma_1$

Δw = deflection of electron beam in a subdivision

Δz = distance increment following straight path of electron beam

θ_r = $(T_{1m} - T_\infty)/(T_{2m} - T_\infty)$

θ_1 = dimensionless temperature $= (T_1 - T_\infty)/(T_{1m} - T_\infty)$

θ_2 = dimensionless temperature $= (T_2 - T_\infty)/(T_{2m} - T_\infty)$

λ = eigenvalue

Λ = $(2Vm/e)^{1/2}/\mu_{r1}l\mu_0\sigma_1(S_1 - S_2)(T_{1m} - T_\infty)$

M = μ_{r2}/μ_{r1}

μ_r = relative permeability

μ_0 = free space magnetic permeability $= 4\pi \times 10^{-7}$ N/amp^2

Π = dimensionless beam energy distribution parameter $= \sigma_q/r_0$

σ = electric conductivity, ohm^{-1} m^{-1}

σ_q = beam energy flux distribution parameter

τ = effective electrical contact resistance, ohm-m^2

ϕ = electrical potential, V

ψ, Ψ = dimensional, V, and dimensionless magnetic potential, $\psi = \phi + ST$, $\Psi = \psi/(S_1 - S_2)/(T_{1m} - T_\infty)$

Subscripts and Superscripts

m = melting

∞ = ambient

1, 2 = dissimilar weldments

$\bar{}$ = average quantities for dissimilar metals

is called workpiece 1, so that the dimensional and dimensionless magnetic fields are in the same direction. Hence, workpiece 1 can be on the left or the right-hand side of workpiece 2. In order to make the analysis tractable, additional assumptions are made:

1 Thermal and thermoelectric magnetic fields are in quasi-steady states. This is appropriate for quasi-steady-state welding.

2 Heat and thermoelectric current flow are two dimensional. As mentioned previously, deflection of the electron beam out of the joint line is due to the magnetic field parallel to the welding direction (Watanabe et al., 1975; Blakeley and Sanderson, 1984). This indicates that thermoelectric currents flow mainly in a plane perpendicular to the weld line.

3 The electron beam energy flux incident on top surfaces of workpieces can be assumed to have a Gaussian distribution, as measured by Burgardt (1986).

4 Zero thermal contact resistance is assumed between dissimilar metals.

5 Thermal, physical, and thermoelectric properties are assumed to be constant and independent of the temperature range considered.

Heat Conduction Equations and Boundary Conditions. With the above assumptions, dimensionless heat conduction equations for metals 1 and 2 reduce to

$$\nabla^2\theta_1 = 0 \tag{1}$$

$$\nabla^2\theta_2 = 0 \tag{2}$$

Convective heat losses to the surroundings at the top and bottom surfaces of the workpieces give, respectively

$$\frac{\partial\theta_1}{\partial Y} = \mathrm{Bi}\theta_1 \quad \text{at } Y=0 \tag{3}$$

$$\frac{\partial\theta_2}{\partial Y} = K\mathrm{Bi}\theta_2 \quad \text{at } Y=0 \tag{4}$$

$$\frac{\partial\theta_1}{\partial Y} = -\mathrm{Bi}\theta_1 \quad \text{at } Y=1 \tag{5}$$

$$\frac{\partial\theta_2}{\partial Y} = -K\mathrm{Bi}\theta_2 \quad \text{at } Y=1 \tag{6}$$

Temperatures far from the electron beam are

$$\theta_1 = \theta_2 = 0 \quad \text{if } X \to \pm\infty \tag{7}$$

Temperatures of the workpieces are identical at the contact surface

$$\theta_1 = \frac{\theta_2}{\theta_r} \quad \text{at } X=0 \tag{8}$$

where θ_r is the ratio of the characteristic temperatures for dissimilar metals. An energy balance at $X=0$ gives

$$\frac{\partial\theta_2}{\partial X} - K\theta_r\frac{\partial\theta_1}{\partial X} = q \tag{9}$$

The energy flux incident on top of the workpiece surfaces ($Y=0$) is a Gaussian distribution and can be expressed as

$$q' = \frac{3VI}{\pi\sigma_q^2}\exp\left(-\frac{3x^2}{\sigma_q^2}\right) \tag{10}$$

The beam energy per unit area of cavity opening, given by equation (10), impinging on the cavity wall can be considered as interfacial heat generation per unit area of the contact surface. That is,

$$q = \frac{3Q(K+1)(\theta_r+1)}{4\pi\Pi^2 DR_0}\exp\left(-\frac{3\left(1-\frac{Y}{D}\right)^2}{\Pi^2}\right) \quad \text{if } Y<D$$

$$= 0 \quad \text{if } Y \geq D \tag{11}$$

where the penetration depth of a weld joint D can be determined from a general dimensionless correlation equation obtained by Giedt and Tallerico (1988)

$$D = \frac{Q}{3.33U^{0.625}} \tag{12}$$

In equation (12) the dimensionless depth of penetration D is proportional to the dimensionless beam power Q, which is normalized by heat conduction to the solid. The dimensionless variable U includes the effect of welding speed u and cavity opening radius r_0 divided by the average thermal diffusivity $\bar{\alpha}$ of workpieces. Equation (12) is acceptable for welding workpieces of the same material since the fraction of the variation in the calculated and measured depths of penetration is around 0.955 (Giedt and Tallerico, 1988). Up to now, prediction of the penetration depth for a bimetallic weld has not been provided. To a first approximation, equation (12) was used. Thermal and physical properties, however, were replaced by the average values between dissimilar metals. Energy balance at the contact surface can then be obtained by substituting equations (11) and (12) into equation (9).

Temperature fields in both dissimilar metals must satisfy equations (1) and (2) subject to boundary conditions (3)–(7). By assuming that solutions can be separated into two functions whose independent variables are X and Y, respectively, dimensionless temperatures in workpieces can then be obtained (Arpaci, 1966)

$$\theta_1 = \sum_{n=1}^{\infty} A_n e^{-\lambda_{1n}X}\left(\cos\lambda_{1n}Y + \mathrm{Bi}\frac{\sin\lambda_{1n}Y}{\lambda_{1n}}\right) \tag{13}$$

$$\theta_2 = \sum_{n=1}^{\infty} B_n e^{\lambda_{2n}X}\left(\cos\lambda_{2n}Y + K\mathrm{Bi}\frac{\sin\lambda_{2n}Y}{\lambda_{2n}}\right) \tag{14}$$

where

$$\tan\lambda_{1n} = \frac{2}{\frac{\lambda_{1n}}{\mathrm{Bi}} - \frac{\mathrm{Bi}}{\lambda_{1n}}} \tag{15}$$

$$\tan\lambda_{2n} = \frac{2}{\frac{\lambda_{2n}}{K\mathrm{Bi}} - \frac{K\mathrm{Bi}}{\lambda_{2n}}} \tag{16}$$

Substituting equations (13) and (14) into the interfacial boundary conditions given by equations (8) and (9) yields

$$\sum_{n=1}^{\infty} A_n\left(\cos\lambda_{1n}Y + \frac{\mathrm{Bi}\sin\lambda_{1n}Y}{\lambda_{1n}}\right) = \sum_{n=1}^{\infty}\frac{B_n}{\theta_r}\left(\cos\lambda_{2n}Y + \frac{K\,\mathrm{Bi}\sin\lambda_{2n}Y}{\lambda_{2n}}\right) \tag{17}$$

$$\sum_{n=1}^{\infty} B_n\lambda_{2n}\left(\cos\lambda_{2n}Y + \frac{K\mathrm{Bi}\sin\lambda_{2n}Y}{\lambda_{2n}}\right) + K\theta_r\sum_{n=1}^{\infty} A_n\lambda_{1n}\left(\cos\lambda_{1n}Y + \frac{\mathrm{Bi}\sin\lambda_{1n}Y}{\lambda_{1n}}\right) = q \tag{18}$$

Substituting equations (11), (12), (15), and (16), the coefficients A_n and B_n in equations (17) and (18) can be obtained by using the collocation method described by Villadsen and Michelsen (1978). To evaluate the A_n and B_n, the number of terms chosen for both A_n and B_n was 110. Collocation points in the fusion zone and the heat-affected zone at the contact surface were 18 and 92, respectively. A satisfactory solution for the temperature field was assumed to be obtained when the relative deviations of temperatures were less than 0.5 percent by comparing different pairs of collocation points. In most cases, collocations points of 12 and 98 in the fusion zone and the heat-affected zone, respectively, were used.

Governing Equations for Thermoelectric Magnetism. When a temperature gradient is present in dissimilar metals even with no electric current flow, an electric potential exists. This is known as the Seebeck effect and is a characteristic of thermoelectricity (Giedt, 1971). The ratio of induced voltage to temperature difference is called the absolute thermoelectric power or the Seebeck coefficient. Mathematically, the Seebeck coefficient is defined as

$$S = -\frac{dV_j}{dT} \quad \text{for } j = 0 \tag{19}$$

Values of the Seebeck coefficient for different metals and temperature ranges can be found from Shercliff (1979). The equation for Ohm's law, including the thermoelectric Seebeck effect (Shercliff, 1979), becomes

$$\frac{\mathbf{j}}{\sigma} = \mathbf{E} - S\nabla T \tag{20}$$

where the first term on the right-hand side of equation (20) is an irrotational electric field obeying Faraday's law by assuming a time-independent state

$$\nabla \times \mathbf{E} = \mathbf{0} \tag{21}$$

which leads to

$$\mathbf{E} = -\nabla\phi \tag{22}$$

The relationship between the electric current and magnetic flux densities is determined from Ampere's law

$$\mathbf{j} = \nabla \times \frac{\mathbf{B}}{\mu_0\mu_r} \tag{23}$$

Substituting equations (20) and (22) into equation (23) yields

$$\nabla \times \mathbf{B} = -\mu_0\mu_r\sigma\nabla\psi; \qquad \psi = \phi + ST \tag{24}$$

After carrying out the divergence operation, the dimensionless form of equation (24) for dissimilar metals becomes

$$\nabla^2\Psi_1 = 0 \tag{25}$$

$$\nabla^2\Psi_2 = 0 \tag{26}$$

Assuming electric currents across the contact surface are conservative, equation (23) yields

$$\frac{\partial\Psi_1}{\partial X} = \Gamma\frac{\partial\Psi_2}{\partial X} \quad \text{at} \quad X = 0 \tag{27}$$

The second boundary condition at the contact surface was derived by Shercliff (1965, 1979) by integrating equation (20) along the closed line $A'B'C'D'$, as shown in Fig. 2,

$$\oint \frac{\mathbf{j}}{\sigma}\cdot d\mathbf{r} = \oint \mathbf{E}\cdot d\mathbf{r} - \oint S\nabla T\cdot d\mathbf{r} \tag{28}$$

where the first term on the right-hand side is zero by substituting equation (22) and assuming ϕ is a single-value function. Hence equation (28) becomes

$$\frac{j_1}{\sigma_1} - \frac{j_2}{\sigma_2} - \frac{\partial\tau j_n}{\partial y} = (S_2 - S_1)\frac{\partial T}{\partial y} \tag{29}$$

The dimensionless form of equation (29) then becomes

$$\frac{\partial\Psi_1}{\partial Y} - \frac{\partial\Psi_2}{\partial Y} - G\frac{\partial^2\Psi_1}{\partial X\partial Y} = \frac{\partial\theta_1}{\partial Y} \quad \text{at } X = 0 \tag{30}$$

No electric currents are lost to the surroundings and current densities are negligibly small far from the electron beam. Hence the boundary conditions for the magnetic potentials become

$$\frac{\partial\Psi_1}{\partial X} = \frac{\partial\Psi_2}{\partial X} = 0 \qquad \text{if } X \to \pm\infty \tag{31}$$

$$\frac{\partial\Psi_1}{\partial Y}, \quad \frac{\partial\Psi_2}{\partial Y} = 0 \quad \text{at } Y = 0, 1 \tag{32}$$

Magnetic potentials can be determined from equations (25) and (26) subject to boundary conditions (31) and (32) by using the method of separation of variables (Arpaci, 1966)

$$\Psi_1 = \sum_{m=1}^{\infty} C_m e^{-m\pi X}\cos\, m\pi Y \tag{33}$$

$$\Psi_2 = \sum_{m=1}^{\infty} D_m e^{m\pi X}\cos\, m\pi Y \tag{34}$$

where the coefficients C_m and D_m can be determined by substituting equations (33) and (34) into equations (27) and (30)

$$C_m = \frac{\Gamma\sum_{n=1}^{\infty} A_n\lambda_{1n}\left[\dfrac{\sin(\lambda_{1n} - m\pi)}{\lambda_{1n} - m\pi} - \dfrac{\sin(\lambda_{1n} + m\pi)}{\lambda_{1n} + m\pi}\right]}{m\pi(1 + \Gamma + \Gamma G m\pi)} \tag{35}$$

$$D_m = -\frac{C_m}{\Gamma} \tag{36}$$

The magnetic flux densities B_1^* and B_2^* are related to the magnetic potentials according to the following relations:

$$\frac{\partial B_1^*}{\partial Y} = -\frac{\partial\Psi_1}{\partial X} \tag{37}$$

$$\frac{\partial B_1^*}{\partial X} = \frac{\partial\Psi_1}{\partial Y} \tag{38}$$

$$\frac{\partial B_2^*}{\partial Y} = -\Gamma M\frac{\partial\Psi_2}{\partial X} \tag{39}$$

$$\frac{\partial B_2^*}{\partial X} = \Gamma M\frac{\partial\Psi_2}{\partial Y} \tag{40}$$

Solutions for B_1^* and B_2^* can then be shown to be

$$B_1^* = \sum_{m=1}^{\infty} C_m e^{-m\pi X}\sin\, m\pi Y \tag{41}$$

$$B_2^* = -\Gamma M\sum_{m=1}^{\infty} D_m e^{m\pi X}\sin\, m\pi Y \tag{42}$$

Equation of Motion for Electrons. An electron traveling through a magnetic field experiences a Lorentz force eBv in a direction perpendicular to its trajectory. Applying Newton's Second Law gives

$$eBv = \frac{mv^2}{r} \tag{43}$$

Electrons are accelerated toward the workpiece by the accelerating voltage of the welder. The velocity of an electron can be determined from energy conservation

$$v = \sqrt{\frac{2eV}{m}} \tag{44}$$

Substituting equation (44) into equation (43), the radius of curvature of the deflected electron beam becomes

$$R = \frac{\Lambda}{B^*} \tag{45}$$

The trajectory of the electron beam can be approximated by a series of linear subdivisions (Blakeley and Sanderson, 1984). For one subdivision the deflection of the electron beam yields

$$\Delta z = R - \sqrt{R^2 - \Delta w^2} \tag{46}$$

In this study, the number of increments was taken as 100 within $Y = 0.05$. Relative deviations of less than 1 percent can be obtained by using 200 grid points.

Results and Discussion

As shown in Fig. 2, the electron beam has already been deflected away from the joint plane by a thermoelectric magnetic field above the joint. This magnetic field is developed by thermoelectric currents in workpieces. Therefore, a determination of the three-dimensional temperature field in the workpieces is needed in order to predict the deflection and incident angle of the electron beam. However, the two-dimensional thermal field model proposed by the present study is relevant to investigate beam deflection for a given incident angle. The reason for this is that the deflection of the beam from the weld joint is due to the magnetic field parallel to the joint line. A major contribution to this thermoelectric magnetic field will be that developed by a two-dimensional thermal field on the transverse planes perpendicular to the welding direction.

The governing equations and their associated boundary conditions involve the thermal, thermoelectric, and magnetic properties of the dissimilar metals being welded. These properties are appropriately combined into dimensionless groups. The primary dimensionless parameters to be investigated in this study are the accelerating voltage-to-Seebeck electromotive force (abbreviated e.m.f.) parameter Λ, relative magnetic permeability ratio M, effective electrical contact resistance parameter G, thermal conductivity ratio K, electrical conductivity ratio Γ, beam power-to-heat conduction parameter Q, welding speed-to-thermal diffusivity parameter U, and Biot number Bi.

A comparison between the measured and calculated beam deflection (or deviation of the fused zone from a joint) for welding nickel and copper (see Table 1 for material properties) is shown in Fig. 3. By choosing an incident angle of -7.39 deg, an agreement of 7 percent with an experimental result obtained by Nazarenko (1982) for a beam power of 2.4 kW and a welding speed of 0.7 mm/s is achieved. In order to interpret the deflection of an electron beam, calculated thermoelectric electric current lines are plotted. Thermoelectric currents induced by a positive Seebeck coefficient always flow opposite to the direction of the temperature gradient (see equation (20)). The depthwise temperature gradients near the contact surface in the heat-affected zone (Wei et al., 1990) are negative. Hence, electric currents circulate clockwise between workpiece 1 of copper and workpiece 2 of nickel. The computed induced magnetic fields (around 132 gauss in copper and 67,000 gauss in nickel) point into the plane of the figure and cause the Lorentz force to be directed toward workpiece 2. This results in the deflection to decreasing for a negative incident angle (see Fig. 4). On the contrary, the electron beam can be expected to be moved away from the contact surface and the beam deflection becomes serious for a positive incident angle. Therefore, the characteristics of beam deflection can be expected to depend on the incident directions of the electron beam.

In order to interpret the phenomena of a deflected beam, the deviation of the beam is determined by a horizontal displacement from the joint plane at a given depth, which is chosen to be $Y=0.05$ in this study. It can be seen from Fig. 4 that increasing incident angle, excluding angles between -0.05 and 0, results in a linear increase in beam deflection from the joint. Since the reciprocal of the dimensionless parameter Λ is proportional to the difference in Seebeck coefficients, failure to weld along a joint increase with the difference in Seebeck coefficients of the materials being joined for positive incident angles. An opposite phenomenon, however, can be found for negative incident angles. A sufficient condition to reduce deviation of the fused zone from the joint is, therefore, to minimize thermoelectric potential, which decreases the incident angle. In view of strong Seebeck effect (small value of Λ), beam deflection occurs even though the incident angle is zero. The beam deflection can be found to be -0.001 at $Y=0.05$ for a large value of dimensionless parameter $\Lambda=0.05$. The corresponding deflection angle is 0.02 rad, which is equal to the incident angle. This indicates that a low thermoelectric magnetism in workpieces has an insignificant effect on beam

Table 1 Properties of nickel and copper

	Ni	Cu
Thermal conductivity k, W/m-K	70	400
Thermal diffusivity α, m^2/s	1.5×10^{-5}	1×10^{-4}
Electrical conductivity σ, mho/m	1.18×10^{6}	5×10^{6}
Melting temperature T_m, K	1727	1358
Absolute thermoelectric power S, V/m	-1.5×10^{-5}	6.5×10^{-6}
Relative magnetic permeability μ_r	600	1

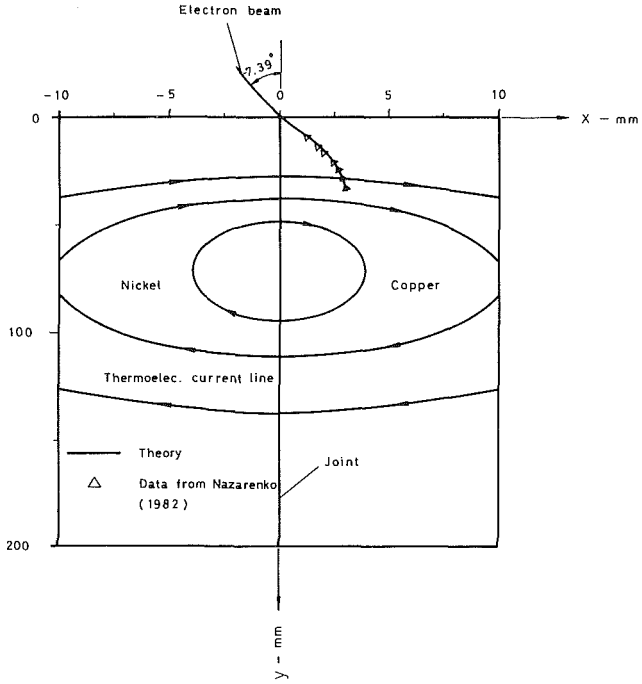

Fig. 3 Comparison between the predicted and measured deviation of the fused zone from a joint for welding nickel and copper, and prediction of thermoelectric current lines ($I=40$ mA, $V=60$ kV, $u=0.7$ mm/s, $\beta=-7.39$ deg)

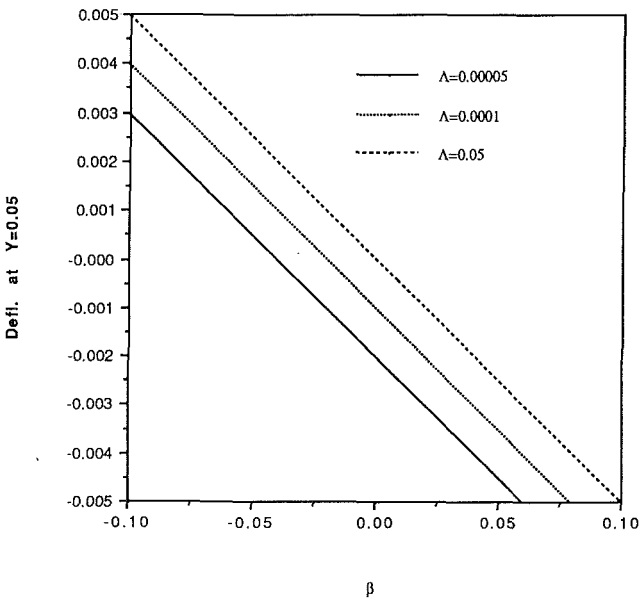

Fig. 4 Variation of beam deflection at $Y=0.05$ with incident angle (rad) for different values of dimensionless accelerating voltage-to-Seebeck e.m.f. parameter ($Q=0.0411$, $U=0.0170$, $G=250$, $\Gamma=0.235$, $M=1$, $K=5.71$, $\mathrm{Bi}=0.5$, $\Pi=1.14$, $\theta_r=0.741$)

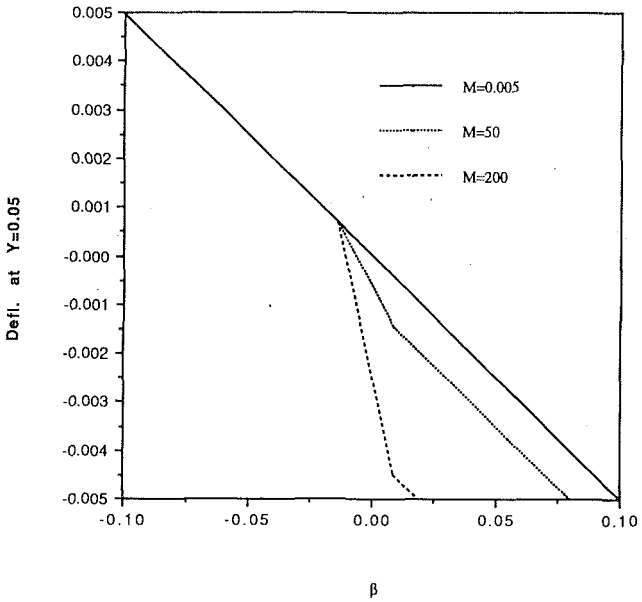

Fig. 5 Variation of beam deflection at $Y = 0.05$ with incident angle for different relative permeability ratios ($Q = 0.0411$, $U = 0.0170$, $G = 250$, $\Gamma = 0.235$, $\Lambda = 0.005$, $K = 5.71$, Bi = 0.5, $\Pi = 1.14$, $\theta_r = 0.741$)

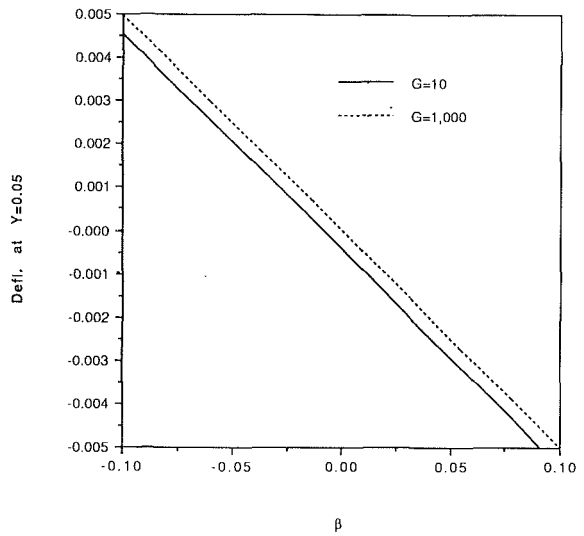

Fig. 6 Variation of beam deflection at $Y = 0.05$ with incident angle for different values of dimensionless effective electrical contact resistance parameter ($Q = 0.0411$, $U = 0.0170$, $\Gamma = 0.235$, $\Lambda = 0.005$, M = 1, $K = 5.71$, Bi = 0.5, $\Pi = 1.14$, $\theta_r = 0.741$)

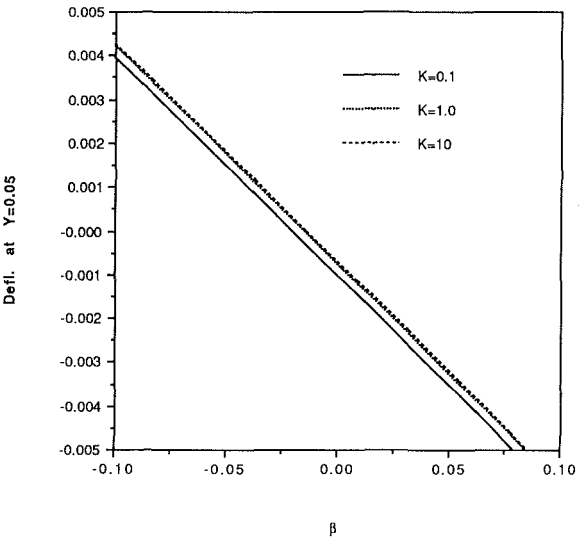

Fig. 7 Variation of beam deflection at $Y = 0.05$ with incident angle for different thermal conductivity ratios ($Q = 0.0411$, $U = 0.05$, $G = 10$, $\Gamma = 0.235$, $\Lambda = 0.005$, M = 1, Bi = 0.5, $\Pi = 1.14$, $\theta_r = 0.741$)

deflection. Effects of the thermoelectric potential were investigated by Blakeley and Sanderson (1984). They tested different dissimilar metal combinations. It was found that no deflection occurred for welding A533B and SB49 or Al-bronze and stainless steel unless a thermoelectric potential difference existed between the two different metals.

The effect of the relative magnetic permeability on beam deflection is shown in Fig. 5. Increasing the permeability ratio μ_{r2}/μ_{r1} results in the tendency for beam deflection for a positive incident angle. This is attributed to an increase in the magnetic field (see equation (24)), which increases the Lorentz force in workpiece 2. In view of high temperature gradients, which develop a strong magnetic field near the cavity wall, a sudden increase in beam deflection occurs for the beam closing to the cavity wall or the beam having a small incident angle. It can also be seen that a linear relationship between the deflection and incident angle can be obtained in the range of negative incident angles. This is because the relative permeability is small and induced internal thermoelectric magnetic fields in workpiece 1 were negligibly small as found by the authors. Therefore, the electron beam is not deflected in the metal but penetrates with the incident angle. Blakeley and Sanderson (1984) pointed out that an Al-bronze combination has permeability of 1, and no deflections were observed with this alloy even when a thermoelectric voltage was detected.

In view of the existence of the vapor-filled welding cavity or impurities at the contact surface, an accurate determination of the electrical contact resistance is impossible. Hence, an effective electrical contact resistance τ is introduced to account for the uncertainties. The effect of the effective electrical contact resistance on beam deflection is shown in Fig. 6. Due to an increase in thermoelectric currents, decreasing the contact resistance causes the electron beam to deflect from the joint plane for a positive incident angle.

Decreasing the thermal conductivity ratio k_1/k_2 gives rise to beam deflection in workpiece 2 in the range of positive incident angles, as presented in Fig. 7. The computed results are in accord with the experimental observations made by Blakeley and Sanderson (1984).

Dimensionless beam power also has an influence on the beam deflection as shown in Fig. 8. A high beam power can increase the vertical temperature gradient in the heat-affected zone (Wei et al., 1990). Therefore, deflection increases in the range of positive incident angles. Blakeley and Sanderson (1984) mentioned that the magnitude of beam deflection can be minimized by maximizing accelerating voltage. Since voltage is proportional to the power, this contradiction may be interpreted as either that the incident angle is negative or the incident angle is small due to the stiffness of a high-voltage electron beam above the workpiece surface.

The effect of dimensionless welding speed on beam deflection is shown in Fig. 9. The tendency for beam deflection in workpiece 2 is reduced for a small welding speed due to a decrease in temperature gradient (Wei et al., 1990). In view of an increase in thermoelectric currents, beam deflection in workpiece 2 is increased with the electrical conductivity ratio σ_2/σ_1, as presented in Fig. 10. In Cu-cupro nickel welding tests made by Blakeley and Sanderson (1984) a thermoelectric voltage of 21 mW was generated. Although the permeabilities are 1 for both materials, a large current was observed to flow due to low electrical resistivity. Hence the deflection increases.

Computed results also showed that the Biot number has an

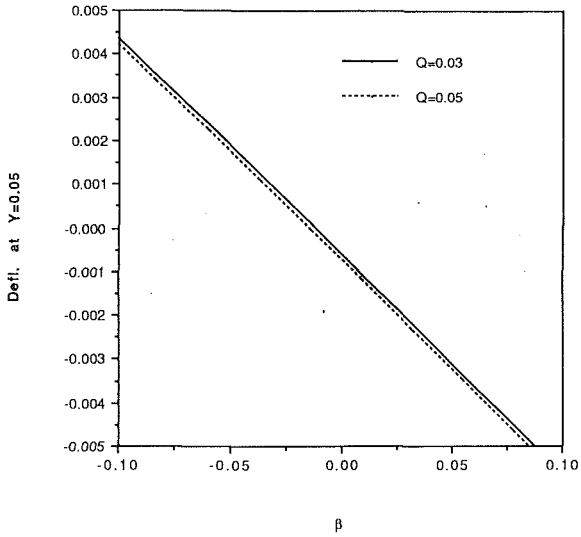

Fig. 8 Variation of beam deflection at $Y = 0.05$ with incident angle for different values of dimensionless beam power parameter ($U = 0.05$, $G = 10$, $\Gamma = 0.235$, $\Lambda = 0.005$, $M = 1$, $K = 5.71$, $Bi = 0.5$, $\Pi = 1.14$, $\theta_r = 0.741$)

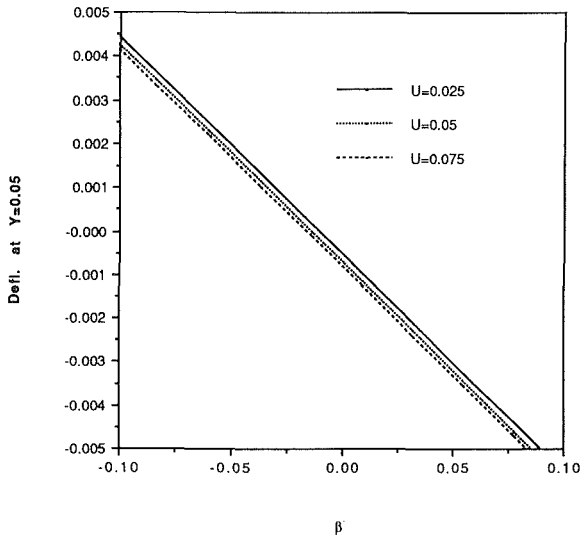

Fig. 9 Variation of beam deflection at $Y = 0.05$ with incident angle for different values of dimensionless welding speed parameter ($Q = 0.0411$, $G = 10$, $\Gamma = 0.235$, $\Lambda = 0.005$, $M = 1$, $K = 5.71$, $Bi = 0.5$, $\Pi = 1.14$, $\theta_r = 0.741$)

insignificant effect on beam deflection. The reason for this is that the heat lost to the surroundings is much smaller than the beam energy flux. Hence, the variation of temperature fields with Biot number for a deep-penetration weld is small.

Conclusions

Conclusions drawn are as follows:

1 This study provides a simple thermoelectric model to interpret the phenomena of beam deflection for welding dissimilar metals with a high-intensity electron beam. Analytical results for the deflection of the missed joint for a nickel/copper weld are found to agree with available experimental data to an accuracy of 7 percent.

2 Sufficient conditions to avoid a beam deflection are to decrease the difference in Seebeck coefficients of the workpieces, the relative magnetic permeability, and the thermal conductivity, reduce welding speed and electrical conductivity, and increase the effective electrical contact resistance as much as possible. Their effects are simply to decrease thermoelectric

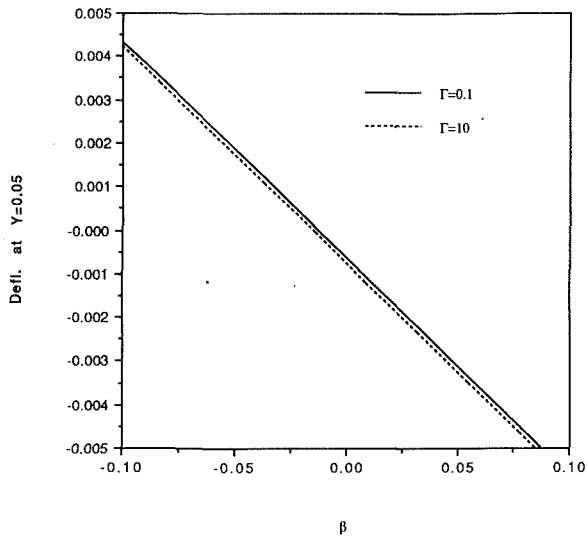

Fig. 10 Variation of beam deflection at $Y = 0.05$ with incident angle for different electrical conductivity ratios ($Q = 0.0411$, $U = 0.05$, $G = 10$, $\Lambda = 0.005$, $M = 1$, $K = 5.71$, $Bi = 0.5$, $\Pi = 1.14$, $\theta_r = 0.741$)

magnetism in dissimilar metals and the incident angle of the electron-beam. The Biot number has a minor influence on the deviation of the fused region from the joint.

3 The characteristics of beam deflection depend primarily on the incident directions of the electron beam. Even though thermoelectric magnetism is strong, deviation of the fused zone from a joint can be decreased in workpiece 1, which has a higher value of Seebeck coefficient, for an electron beam with a negative incident angle (see Fig. 2). For a positive incident angle, deflection of the beam in workpiece 2, however, is increased.

4 The most important factor affecting the deviation of the fused zone from the joint is the incident angle of the electron beam. Hence, a further investigation on characteristics of the electron beam before impinging on workpiece surfaces is required.

References

Arpaci, V. S., 1966, *Conduction Heat Transfer*, Addison-Wesley, MA, pp. 193–194.

Blakeley, P. J., and Sanderson, A., 1984, "The Origin and Effects of Magnetic Fields in Electron Beam Welding," *Welding Journal*, Vol. 63, pp. 42–49.

Burgardt, P., 1986, "Electron Beam Beam Size Calibration," *Summary of Calibration of Welding Systems Meeting*, L. N. Tallerico, ed., Sandia National Laboratories, Livermore, CA, pp. 258–266.

Giedt, W. H., 1971, *Thermophysics*, Van Nostrand Reinhold Co., New York, pp. 424–428.

Giedt, W. H., and Tallerico, L. N., 1988, "Prediction of Electron Beam Depth of Penetration," *Welding Journal*, Vol. 67, pp. 299-s–305-s.

Nazarenko, O. K., 1982, "Deflection of the Electron Beam in Electron-Beam Welding," *Avt. Svarka*, No. 1, pp. 33–39.

Schauer, D. A., Giedt, W. H., and Shintaku, S. M., 1978, "Electron Beam Welding Cavity Temperature Distributions in Pure Metals and Alloys," *Welding Journal*, Vol. 57, pp. 127-s–133-s.

Shercliff, J. A., 1965, *A Textbook of Magnetohydrodynamics*, Pergamon Press, New York, pp. 126–128.

Shercliff, J. A., 1979, "Thermoelectric Magnetohydrodynamics," *Journal of Fluid Mechanics*, Vol. 91, pp. 231–251.

Tong, H., and Giedt, W. H., 1971, "Depth of Penentration During Electron Beam Welding," ASME Journal of Heat Transfer, Vol. 93, pp. 155–163.

Villadsen, J., and Michelsen, M. L., 1978, *Solution of Differential Equation Models by Polynomial Approximation*, Prentice-Hall, Inc., NJ, p.74.

Watanabe, K., Shida, T., Suzuki, M., Okamura, H., Sejima, I., Kita, H., and Yonezawa, T., 1975, "Some Problems Associated With Deep Penetration Electron Beam Welding of Heavy Section Steels," *Proceedings of Symposium of Advanced Welding Technology*, Japan Welding Society, pp. 69–74.

Wei, P. S., and Chiou, L. R., 1988, "Molten Metal Flow Around the Base of a Cavity During a High Energy Beam Penetrating Process," ASME Journal of Heat Transfer, Vol. 110, pp. 918–923.

Wei, P. S., Wu, T. H., and Chow, Y. T., 1990, "Investigation of High-Intensity Beam Characteristics on Welding Cavity Shape and Temperature Distribution," ASME Journal of Heat Transfer, Vol. 112, pp. 163–169.

Scaled Isotropic Results for Two-Dimensional Anisotropic Scattering Media

T.-K. Kim

H. S. Lee

Department of Mechanical Engineering,
University of Minnesota,
Minneapolis, MN 55455

The full anisotropic scattering solutions of the radiative equation of transfer are compared with the scaled isotropic scattering solutions. Square enclosures with a collimated incidence, a diffuse incidence, or an isothermal emission are considered for comparison. The isotropic scaling approximation is found to predict accurately the radiative flux and the average incident radiation for the isothermal emission problem and for most diffuse incidence problems. For the collimated incidence problem, the isotropic scaling solutions are acceptable only for weakly scattering media. For large scattering albedo the error in the isotropic scaling is appreciable for the diffuse incidence problem and unacceptably large for the collimated incidence problem. The largest error in the y-direction net flux is found at the side wall regions when the medium is purely scattering. The isothermal emission problem or problems with symmetric boundary conditions can be accurately modeled by a scaled isotropic phase function, since the effect of the phase function anisotropy is negligible in such problems.

1 Introduction

Full anisotropic modeling of multidimensional radiative transfer in an anisotropic scattering medium can require large amounts of computer time and storage. For a typical forward scattering, one-dimensional, plane-parallel medium, the required cpu time is about 0.17 s on the Cray 2 with 0.5 megawords of memory. The required cpu time for the same anisotropic scattering medium in a two-dimensional rectangular geometry is about 56 s on the same machine and 6.5 megawords of memory. The S-N discrete ordinates method was used for computation, which finite differences the equation of transfer with the integral replaced by a quadrature sum over all the ordinate directions (Kim and Lee, 1988, 1989).

The treatment of the multidimensional radiation transport has therefore been frequently restricted to a simple addition of some lumped radiation effect. Many applications of the more sophisticated technology now require more accurate predictions of the radiative transfer, but the full anisotropic treatment in many dimensions is still computationally expensive. If the two-dimensional radiation heat transfer is to be combined with other heat transfer modes, the computation time given above can be expected to increase by approximately a factor of ten.

Scaling is a widely used scheme for obtaining simple, yet accurate radiative transfer results for anisotropically scattering media. The scaling laws transform the scattering phase function, optical depth, and scattering albedo of the original anisotropic system to those of a simpler system.

There are numerous ways to scale a complex anisotropic scattering problem. Many investigators have demonstrated different scaling techniques in one-dimensional plane parallel slabs. A scaling by the P_1 approximation has been reported by Lee and Buckius (1982), where the Mie anisotropic scattering phase functions are scaled to an isotropic scattering function. Wiscombe (1977) proposes a scaling technique called the δ-M method, where the scaled phase function can be changed to either isotropic or simple anisotropic scattering. A scaled linear anisotropic scattering phase function is used in the delta-Eddington approximation developed by Joseph et al. (1979). McKellar and Box (1981) present a summary of the scaling techniques for radiative transfer based on the scaling group derived by Inönü (1977).

The accuracy of the scaling laws for the one-dimensional planar layer has been demonstrated for the diffuse boundary incidence problem and the isothermally emitting media problem (Lee and Buckius, 1982). No such study has been performed for the two-dimensional geometry, although Nelson et al. (1986) used the two-dimensional isotropic scaled equation of transfer to interpret the experimental backscattering data from an anisotropic scattering cylindrical medium exposed to a collimated laser beam. They indicate a significant discrepancy between the experiment and the scaled results at small radial locations.

In this study, isotropic scaling of the equation of transfer in a two-dimensional rectangular enclosure is investigated using the S-N discrete ordinates method. Two forms of the scaled equation of transfer are presented, and the computationally more effective form is chosen for the numerical analysis. Diffuse incidence, collimated incidence, and isothermal emission problems are considered to examine the accuracy of the isotropic scaling. The participating medium in the enclosure is gray, and it absorbs, emits, and anisotropically scatters radiative energy. Approximate solutions are compared with the full anisotropic solutions presented in the previous studies (Kim and Lee, 1988, 1989). We examine the effects of scattering albedo, anisotropy of the scattering phase function, and the optical thickness on the scaling accuracy.

2 Radiative Transfer Equations

2.1 Exact Expressions. The equation of transfer describing the actual intensity in a rectangular enclosure (Fig. 1) is written in a general form as

$$\left[\mu \frac{\partial}{\partial \tau_x} + \xi \frac{\partial}{\partial \tau_y} + 1\right] I_a(\tau_x, \tau_y, \Omega) = S(\tau_x, \tau_y, \Omega) \qquad (1)$$

Contributed by the Heat Transfer Division for publication in the JOURNAL OF HEAT TRANSFER. Manuscript received by the Heat Transfer Division June 19, 1989; revision received September 15, 1989. Keywords: Radiation.

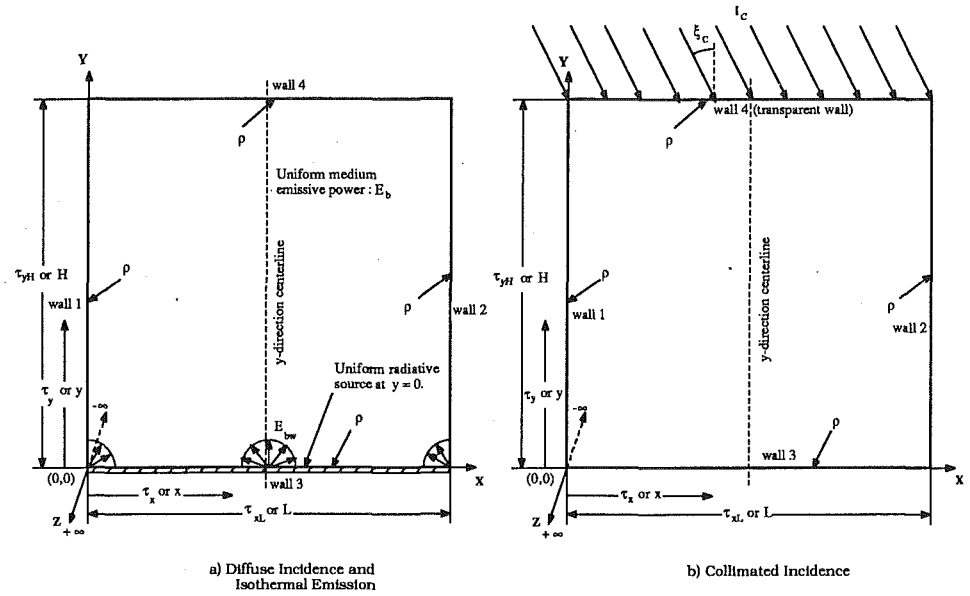

a) Diffuse Incidence and Isothermal Emission

b) Collimated Incidence

Fig. 1 System geometries

and the source function is expressed as

$$S(\tau_x, \tau_y, \Omega) = (1-\omega)I_b(\tau_x, \tau_y) + \frac{\omega}{4\pi}\int_{\Omega'} I_a(\tau_x, \tau_y, \Omega')\Phi(\Omega'; \Omega)d\Omega' \quad (2)$$

The scattering phase function is approximated by a finite series of Legendre polynomials as

$$\Phi(\Omega'; \Omega) = \Phi(\cos\psi) = \sum_{l=0}^{K} C_l P_l(\cos\psi) \quad (3)$$

The boundary condition for the top wall of Fig. 1(*b*) with collimated incidence I_c can be written in general as

$$I_{aw}(\tau_x, \tau_y, \Omega) = \epsilon_w I_{bw}(\tau_x, \tau_y) + \frac{\rho}{\pi}\int_{\mathbf{n}\cdot\Omega'<0} |\mathbf{n}\cdot\Omega'| I_{aw}(\tau_x, \tau_y, \Omega')d\Omega' + I_c(\tau_x, \tau_{yH}, \Omega_c)\delta(\Omega_c - \Omega)$$

$$\text{for } \mathbf{n}\cdot\Omega > 0 \text{ and } \mathbf{n}\cdot\Omega' < 0 \quad (4)$$

The collimated beam is incident at an angle $\Omega_c = (\mu_c, \xi_c)$. The boundary condition for the other three walls is equation (4) without the term containing I_c. All the walls of the collimated incidence problems are considered to be cold, and I_{bw}, the blackbody intensity from the walls, is zero. The boundary conditions for the diffuse incidence problem (Fig. 1*a*) contain first the wall emission and the diffuse reflection terms of the equation (4), and only the bottom wall is considered hot.

Nomenclature

C_l = expansion coefficients of phase function
E = emissive power $= \sigma T^4$
f = forward fraction for scaling
G = average incident radiation; $G^* = 4\pi G/Q_0$
H, L = height and length of the enclosure
I = radiative intensity
$K+1$ = number of terms in phase function expansion
$\mathbf{n}$ = inward normal vector to enclosure walls
$P_l(\cos\psi)$ = Legendre polynomial of order l
Q_0 = incident radiative flux $= |\xi_c I_c|$ or πI_{bw}
Q_x^+, Q_x^- = positive and negative components of $\mathbf{Q}$ in x direction
Q_y^+, Q_y^- = positive and negative components of $\mathbf{Q}$ in y direction
Q_y = net radiative heat flux in y direction
S = intensity source function
β = extinction coefficient
$\delta(\Omega_c - \Omega)$ = Dirac delta function
ϵ_w = wall emissivity
θ = polar angle
μ = direction cosine in x direction $= \cos\theta$
ξ = direction cosine in y direction $= \sin\theta\cos\varphi$
ρ = diffuse wall reflectivity
σ_s = scattering coefficient
τ = optical path length
τ_x, τ_y = optical coordinates; $\tau_x = \beta x$; $\tau_y = \beta y$
τ_{xL}, τ_{yH} = overall optical thicknesses; $\tau_{xL} = \beta L$; $\tau_{yH} = \beta H$
φ = azimuthal angle
$\Phi(\cos\psi)$ = scattering phase function
ψ = scattering angle measured between Ω' and Ω
ω = scattering albedo $= \sigma_s/\beta$
Ω = ordinate direction $= (\mu, \xi)$

Superscripts

$*$ = dimensionless variable
$'$ = incident direction
$\hat{}$ = scaled variable

Subscripts

a = actual
b = blackbody
c = collimated component
s = scattered component
w = wall

Note that the top wall boundary condition with collimated incidence contains a Dirac delta function, which is sometimes undesirable for numerical work. In the discrete ordinates method, the selection of the ordinate directions is restricted by the delta function, since the term including the function must have a nonzero value in the collimated direction Ω_c.

Once the actual intensity field is obtained, the average incident radiation and the radiative fluxes can be obtained as

$$G(\tau_x, \tau_y) = \frac{1}{4\pi}\int_{4\pi} I_a(\tau_x, \tau_y, \Omega)\, d\Omega \tag{5}$$

$$Q_x^+(\tau_x, \tau_y) = \int_{\mu>0} \mu I_a(\tau_x, \tau_y, \Omega)\, d\Omega \tag{6a}$$

$$Q_x^-(\tau_x, \tau_y) = \int_{\mu<0} \mu I_a(\tau_x, \tau_y, \Omega)\, d\Omega \tag{6b}$$

$$Q_y^+(\tau_x, \tau_y) = \int_{\xi>0} \xi I_a(\tau_x, \tau_y, \Omega)\, d\Omega \tag{7a}$$

$$Q_y^-(\tau_x, \tau_y) = \int_{\xi<0} \xi I_a(\tau_x, \tau_y, \Omega)\, d\Omega \tag{7b}$$

The net radiative fluxes are obtained by summing the positive and negative components of Q.

In the previous study (Kim and Lee, 1989), the strong peaks in the angular intensity distributions, due to a possible collimated incidence, are avoided by separating the actual intensity into two components. The actual intensity is related to the scattered component of the intensity as

$$I_a(\tau_x, \tau_y, \Omega) = I_s(\tau_x, \tau_y, \Omega) + I_c \exp(-\tau)\, \delta(\Omega_c - \Omega) \tag{8}$$

where τ is the optical path length traveled by the incident beam. For oblique collimated incidences, equation (8) applies only in the illuminated region. For the shaded region of an enclosure with a collimated incidence, as well as for the diffuse incidence problem, I_a is simply equal to I_s.

2.2 Approximate Expressions. Scaling the anisotropic scattering problem, described by equations (1) and (2), to an isotropic scattering problem involves finding the scaled parameters $\hat{\tau}$ and $\hat{\omega}$. The scaled parameters can be derived from the P_1 scaling (Lee and Buckius, 1982) or from the δ-M method (Wiscombe, 1977) with $M=1$. These are

$$\hat{\omega} = \frac{\omega(1-f)}{(1-\omega f)} \tag{9}$$

$$\hat{\tau}_x = (1-\omega f)\tau_x \tag{10}$$

$$\hat{\tau}_y = (1-\omega f)\tau_y \tag{11}$$

where f is set equal to the asymmetry factor of the original phase function, defined by $C_1/3$ (Irvine, 1963).

Using the scaled optical depths and scattering albedo, the governing equations can be transformed. The scaled equation for the actual intensity is

$$\left[\mu\frac{\partial}{\partial\hat{\tau}_x} + \xi\frac{\partial}{\partial\hat{\tau}_y} + 1\right] I_a(\hat{\tau}_x, \hat{\tau}_y, \Omega) = S(\hat{\tau}_x, \hat{\tau}_y, \Omega) \tag{12}$$

and the source function is now expressed as

$$S(\hat{\tau}_x, \hat{\tau}_y, \Omega) = (1-\hat{\omega})\, I_b(\hat{\tau}_x, \hat{\tau}_y) + \frac{\hat{\omega}}{4\pi}\int_{\Omega'} I_a(\hat{\tau}_x, \hat{\tau}_y, \Omega')d\Omega' \tag{13}$$

The Dirac delta function, which remains in the boundary condition, is avoided by further transforming the equation of transfer. Two different forms of the equation of transfer are possible for the scattered component of the intensity, depending on the relationship between I_a and I_s.

One possibility is to express the actual intensity in the scaled variables as

$$I_a(\hat{\tau}_x, \hat{\tau}_y, \Omega) = I_s(\hat{\tau}_x, \hat{\tau}_y, \Omega) + I_c \exp(-\tau)\, \delta(\Omega_c - \Omega) \tag{14}$$

where only the scattered intensity is scaled, and the τ in the exponential term is not scaled. The scaled equation of transfer then has the following form:

$$\left[\mu\frac{\partial}{\partial\hat{\tau}_x} + \xi\frac{\partial}{\partial\hat{\tau}_y} + 1\right] I_s(\hat{\tau}_x, \hat{\tau}_y, \Omega) = S(\hat{\tau}_x, \hat{\tau}_y, \Omega) \tag{15}$$

with

$$S(\hat{\tau}_x, \hat{\tau}_y, \Omega) = (1-\hat{\omega}) I_b(\hat{\tau}_x, \hat{\tau}_y) + \frac{\hat{\omega}}{4\pi}\int_{\Omega'} I_s(\hat{\tau}_x, \hat{\tau}_y, \Omega')d\Omega' + \frac{\hat{\omega}}{4\pi}\left[1 + \frac{4\pi\omega f\, \delta(\Omega_c - \Omega)}{\hat{\omega}(1-\omega f)}\right] I_c \exp(-\tau) \tag{16}$$

The boundary intensity equation (4) is now transformed to

$$I_{sw}(\hat{\tau}_x, \hat{\tau}_y, \Omega) = \epsilon_w I_{bw}(\hat{\tau}_x, \hat{\tau}_y) + \frac{\rho}{\pi}\int_{\mathbf{n}\cdot\Omega'<0} |\mathbf{n}\cdot\Omega'|\, I_{sw}(\hat{\tau}_x, \hat{\tau}_y, \Omega')d\Omega' + \frac{\rho}{\pi}|\mathbf{n}\cdot\Omega_c| I_c$$

$$\text{for } \mathbf{n}\cdot\Omega>0,\ \mathbf{n}\cdot\Omega'<0 \text{ and } \mathbf{n}\cdot\Omega_c<0 \tag{17}$$

The delta function has been removed from the boundary condition, but it is now contained in the source function. This set of scaled equations can also be derived by using the scaling group presented by Inönü (1977) and McKeller and Box (1981).

The other possibility is to express the actual intensity as

$$I_a(\hat{\tau}_x, \hat{\tau}_y, \Omega) = I_s(\hat{\tau}_x, \hat{\tau}_y, \Omega) + I_c \exp(-\hat{\tau})\, \delta(\Omega_c - \Omega) \tag{18}$$

where now the $\hat{\tau}$ in the exponential term is scaled. The scaled equation of transfer is then

$$\left[\mu\frac{\partial}{\partial\hat{\tau}_x} + \xi\frac{\partial}{\partial\hat{\tau}_y} + 1\right] I_s(\hat{\tau}_x, \hat{\tau}_y, \Omega) = S(\hat{\tau}_x, \hat{\tau}_y, \Omega) \tag{19}$$

with

$$S(\hat{\tau}_x, \hat{\tau}_y, \Omega) = (1-\hat{\omega}) I_b(\hat{\tau}_x, \hat{\tau}_y) + \frac{\hat{\omega}}{4\pi}\int_{\Omega'} I_s(\hat{\tau}_x, \hat{\tau}_y, \Omega')d\Omega' + \frac{\hat{\omega}}{4\pi} I_c \exp(-\hat{\tau}) \tag{20}$$

By using equation (18), the boundary intensity expression given in equation (4) transforms to the same form given in equation (17).

The scaled equations (17), (19), and (20) can be easily solved by the discrete ordinates method and are used for the current scaling solutions. The scattered components in these two formulations are different from each other, but the actual intensity results are equivalent.

3 Numerical Results

Three fundamental cases are considered to examine the accuracy of the isotropic scaling. These are the diffuse incidence, the collimated incidence, and the isothermal emission cases. The system geometry for the diffuse incidence and the isothermal emission problems, with the heated bottom wall or a uniform isothermal medium, is shown in Fig. 1(*a*). The system geometry for the collimated incidence problem is shown in Fig. 1(*b*), where the beam is incident through the top wall.

The dimensionless fluxes are defined with respect to the

Table 1 The phase function expansion coefficients C_l

l	$F1$	$F2$	$B1$	$B2$
0	1.00000	1.00000	1.00000	1.00000
1	2.53602	2.00917	−0.56524	−1.20000
2	3.56549	1.56339	0.29783	0.50000
3	3.97976	0.67407	0.08571	
4	4.00292	0.22215	0.01003	
5	3.66401	0.04725	0.00063	
6	3.01601	0.00671		
7	2.23304	0.00068		
8	1.30251	0.00005		
9	0.53463			
10	0.20136			
11	0.05480			
12	0.01099			
No. of terms	13	9	6	3
f	0.84534	0.66972	−0.18841	−0.40000

Note: F indicates forward scattering phase functions and B indicates backward scattering phase functions.

incident flux Q_0, where $Q_0 = |\xi_c I_c|$ for the collimated incidence, $Q_0 = E_{bw}$ for the diffuse incidence, and $Q_0 = E_b$ for the isothermal emission. The dimensionless average incident radiation has been defined to be $4\pi G/Q_0$. The dimensionless coordinates are defined as $\tau_x^* = \hat{\tau}_x/\hat{\tau}_{xL}$ and $\tau_y^* = \hat{\tau}_y/\hat{\tau}_{yH}$. The scaled results are shown compared to the full anisotropic results, which are marked as "EXACT" in the figures.

The full anisotropic scattering results for the diffuse incidence and isothermal emission problems are from Kim and Lee (1988), and the collimated incidence results are from Kim and Lee (1989). The S-14 approximation, which computes 112 fluxes over the hemisphere, is used to obtain the intensity field of both the full anisotropic and the scaled isotropic problems. All the results are for square enclosures, $\tau_{xL} = \tau_{yH}$, with nonreflecting walls ($\rho = 0$). Only normal incidence is considered. The expansion coefficients for the phase functions considered are given in Table 1.

3.1 Diffuse Incidence Problems. Solutions for the diffuse incidence cases are obtained by setting $I_c = 0$ and $I_b = 0$ in the source function expressions (2) and (20) and the boundary intensity equations (4) and (17). Only the bottom wall blackbody intensity I_{bw} remains nonzero.

The different anisotropic phase functions appear to have only a small influence on the isotropic scaling accuracy of the diffuse incidence problems. One set of comparisons for the transmitted (Q_y^{+*} at $\tau_y^* = 1$) and reflected (Q_y^{-*} at $\tau_y^* = 0$) components of the flux (Figs. 2*a* and 2*b*, respectively) shows roughly 5 percent error magnitudes for all four phase functions considered. The side wall energy losses [$Q_x^{+*}(1, \tau_y^*)$ or $-Q_x^{-*}(0, \tau_y^*)$] are also shown accurately predicted by the isotropic scaling in Fig. 2(*c*).

Note that the side wall losses from a diffuse incidence are always largest near the incident wall, regardless of the phase function. This trend is very different from the collimated incidence case, where the location of the maximum loss moves farther away from the wall of incidence, as the asymmetry factor increases to +1 (Kim and Lee, 1989).

The dominant effect of the scattering albedo on the scaling accuracy is illustrated in Figs. 3 and 4 for an enclosure of unit optical thickness and phase function $F2$. Figure 3 shows the scaled and the full anisotropic Q_y^* distributions along the edge of the enclosure ($\tau_x^* = 0$). The scaled isotropic results are very accurate for the smaller albedo cases, while a maximum error of about 12 percent is shown for the purely scattering medium ($\omega = 1$). The scaled predictions for the centerline fluxes [$Q_y^*(0.5, \tau_y^*)$] are accurate to within 5 percent for the same case shown in Fig. 3.

In Fig. 4, the scaled isotropic G^* distributions along the edge are compared with the corresponding full anisotropic

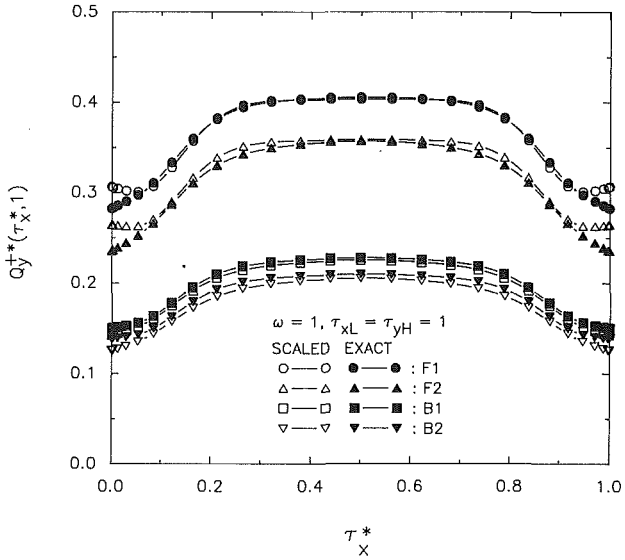

Fig. 2(*a*) Transmitted flux comparisons (diffuse incidence)

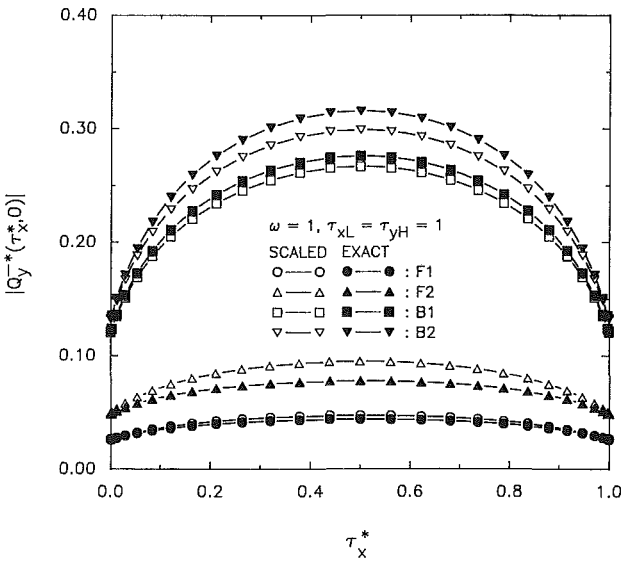

Fig. 2(*b*) Reflected flux comparisons (diffuse incidence)

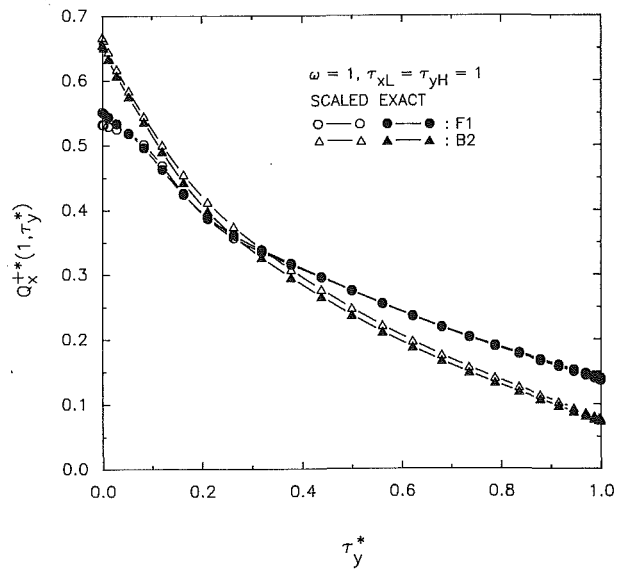

Fig. 2(*c*) Side wall energy loss comparisons (diffuse incidence)

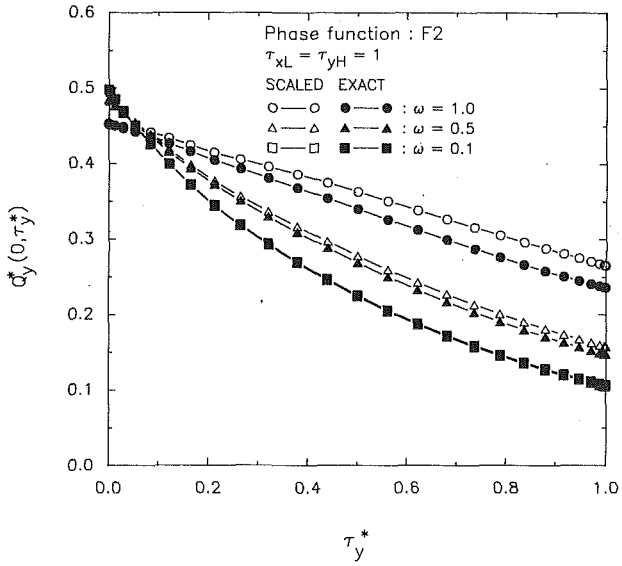

Fig. 3 Edge flux comparisons (diffuse incidence)

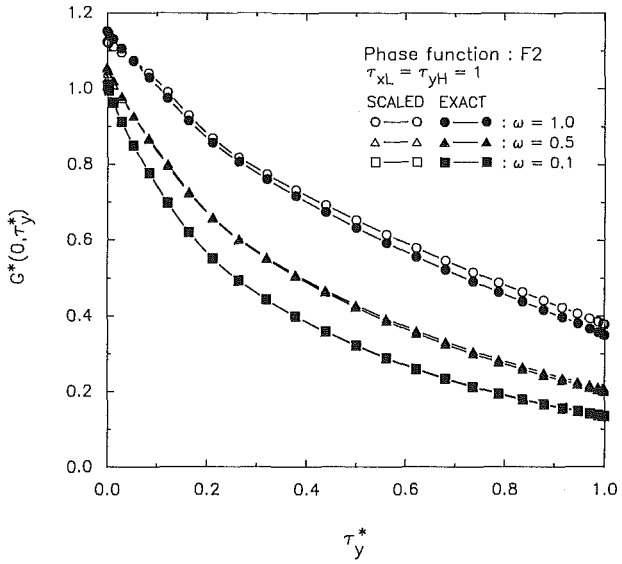

Fig. 4 Edge average incident radiation comparisons (diffuse incidence)

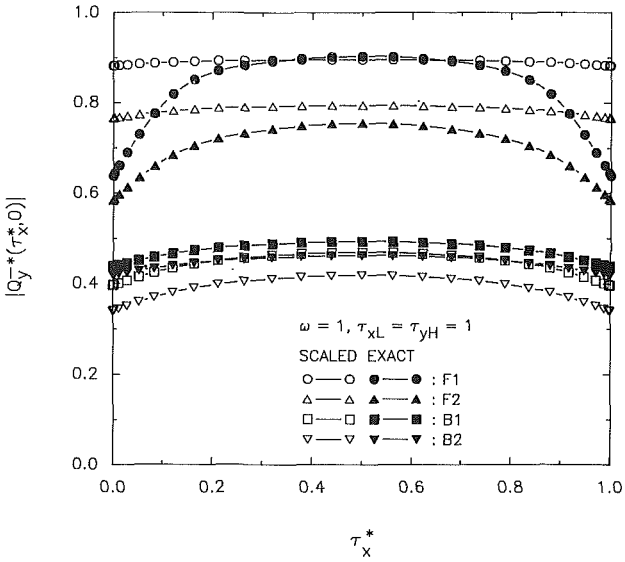

Fig. 5(*a*) Transmitted flux comparisons (collimated incidence)

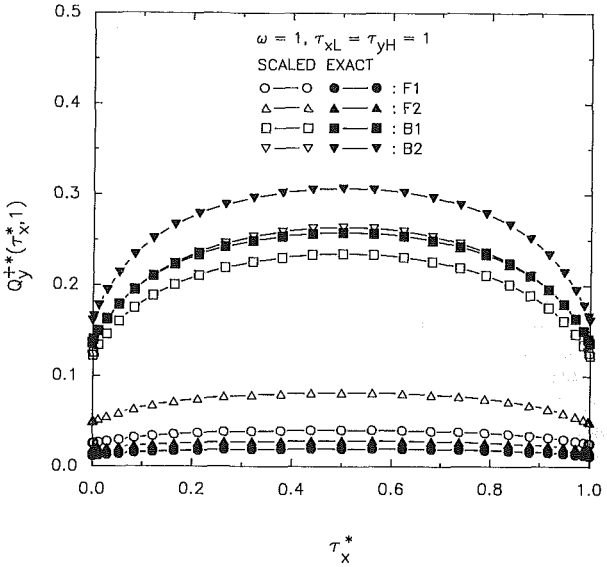

Fig. 5(*b*) Reflected flux comparisons (collimated incidence)

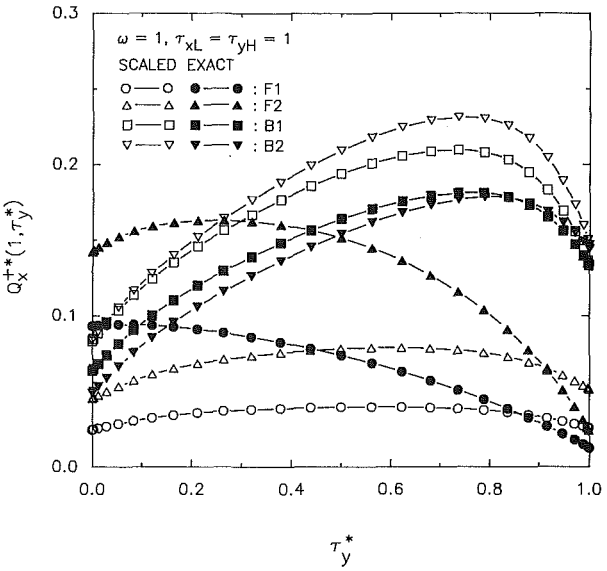

Fig. 5(*c*) Side wall energy loss comparisons (collimated incidence)

results. The comparisons show a better accuracy in G^* than in Q_y^* predictions. The maximum error in G^* shown for the purely scattering medium is 8.2 percent along the edge. Accuracy to within 3 percent is obtained along the centerline.

For every case considered, the maximum error was found when $\omega = 1.0$, where the lack of absorption in the medium accentuates the details of the angular scattering patterns. The accuracy is always significantly better along the centerlines (see Fig. 1 for location). Even along the edge, the scaling accuracy is excellent for all but the large scattering albedos. Even then, the accuracy may be acceptable for many applications. The scaling accuracy has been found not be greatly affected by the optical depth parameter.

3.2 Collimated Incidence Problems. Solutions for the collimated incidence cases are obtained by setting $I_b = 0$ and $I_{bw} = 0$ in the source function expressions (2) and (20) and the boundary intensity equations (4) and (17). Only the normal incidence through the top wall is considered in the following discussion ($I_c = \text{const}$).

The scaling accuracy is profoundly affected by the shape of

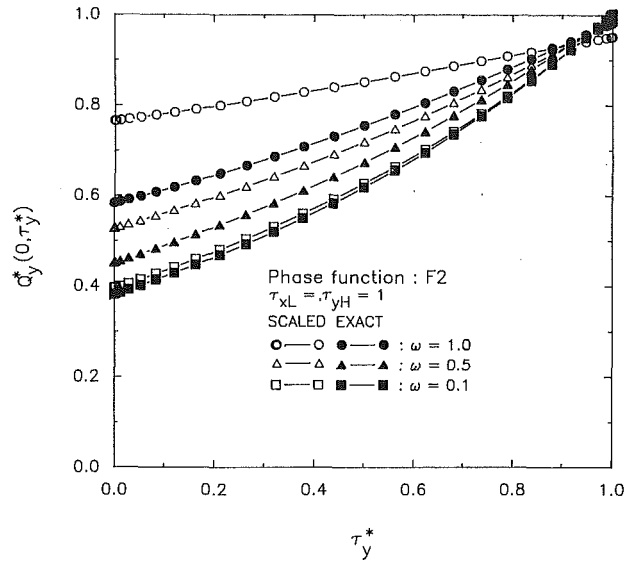

Fig. 6 Edge flux comparisons (collimated incidence)

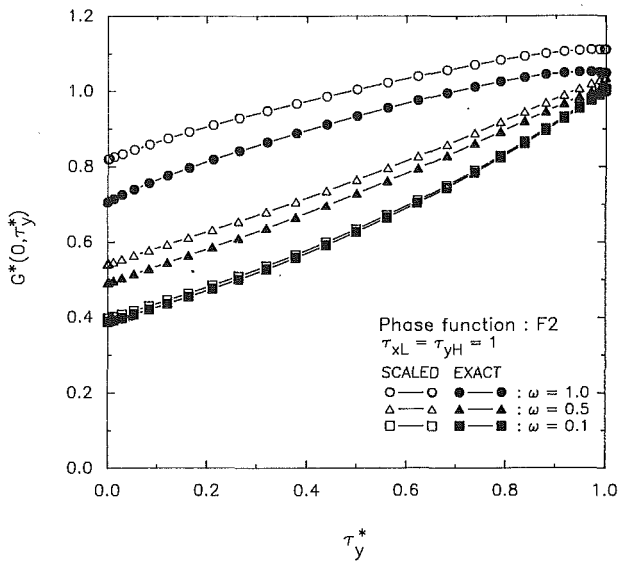

Fig. 7 Edge average incidence radiation comparisons (collimated incidence)

the phase function for the collimated incidence problems, especially for purely scattering media. For four different phase functions, comparisons of the transmitted (Q_y^{-*} and $\tau_y^* = 0$) and reflected (Q_y^{+*} at $\tau_y^* = 1$) components of the flux are shown in Figs. 5(*a*) and 5(*b*), respectively. The accuracy in the side wall losses [$Q_x^{+*}(1, \tau_y^*)$ or $-Q_x^{-*}(0, \tau_y^*)$] is also examined in Fig. 5(*c*).

The isotropic scaled predictions of the transmitted flux components (Fig. 5*a*) can be very poor. Scaling overpredicts the flux at the corners of the enclosure by 36 percent for the extremely forward peaked phase function *F*1. For the backward phase function *B*2, the predicted flux is about 12 percent average under the full anisotropic result. The reflected component is overpredicted by about 100 percent for *F*1 and underpredicted by about 15 percent for *B*2 (Fig. 5*b*). Figure 5(*c*) shows that the isotropic scaling severely underpredicts the side wall losses for the forward peaked phase functions *F*1 and *F*2 (up to 65 percent for *F*1). The scaling overpredicts the losses for the backward peaked phase functions *B*1 and *B*2 (maximum 30 percent for *B*2).

The magnitude and the location of the maximum side losses have been found to be strongly influenced by the anisotropy of the phase functions (Kim and Lee, 1989). For Fig. 5(*c*) the phase function anisotropy changes from 0.84534 for *F*1 to -0.4 for *B*2. The scaled scattering albedos for the isotropic media remain 1.0, since the anisotropic scattering media considered are pure scattering. The only variable that changes for the scaled problems is the optical depth. Since the optical depth cannot have a similar influence on the side wall losses as the phase function anisotropy, the scaled solutions are simply unable to match the trends of the full anisotropic solutions.

The errors in the side wall predictions explain the errors seen in the transmitted and reflected fluxes. The anisotropic scattering medium *F*1, for example, experiences a significant side loss at the far wall ($\tau_y^* = 0$), which results in the drop in the transmitted fluxes at the corners. The corresponding scaled isotropic medium still has $\hat{\omega} = 1.0$, but the overall optical thickness is reduced to 0.1547. The side wall losses are then significantly lower than they should be at the far wall. This results in the overly high scaled transmitted fluxes at the corners and the higher reflected fluxes.

The scattering albedo is still an important parameter for the scaling accuracy, and the enclosure of unit optical thickness and phase function *F*2 is considered for illustration. The edge flux distributions at $\tau_x^* = 0$ are presented in Fig. 6. For small ω, the *y*-direction net flux is accurately predicted over the entire enclosure by the isotropic scaling. As the ω is increased, the flux error increases, especially near the side walls. For the purely scattering medium, the maximum error from the full anisotropic solution is 31 percent at the side walls.

Comparisons for the average incident radiation at the edge of the enclosure are shown in Fig. 7. The overall scaling accuracy is better than for the radiative flux, but it is still poor for large scattering albedos (maximum error of 16 percent along the edge for $\omega = 1$).

The maximum errors for collimated incidence problems are also found along the edge for purely scattering media, and the optical depth is again not an important parameter. The scaling accuracy for the collimated incidence problem is only very good for the low albedos. The errors become unacceptably large for high albedo values, where the phase function dependent side wall loss errors become important.

3.3 Isothermal Emission Problems. Solutions for the isothermal emission cases are obtained by setting $I_c = 0$ and $I_{bw} = 0$ in the source function expressions (2) and (20) and the boundary intensity equations (4) and (17). The blackbody intensity of the isothermal medium, I_b, is set to a nonzero constant. Due to the symmetry of the isothermal emission problem, the effect of the different phase functions has been shown to be negligible in a previous study (Kim and Lee, 1988). The isotropic scaling accuracy is therefore very good for all the phase functions. For the phase function *F*2 and optical depth of unity as an example, the net radiative flux predictions at a boundary wall are within 6 percent for all albedos.

4 Conclusions

The scaled isotropic solutions of radiative transfer problems have been obtained and compared with the full anisotropic solutions. For the small scattering albedos, the scaled radiative flux and average incident radiation compare well with the full anisotropic solutions for both the diffuse and collimated incidence problems. The errors in the net *y*-direction flux for the large scattering albedos are appreciably larger. The maximum error at the side wall is 12 percent for diffuse incidence and 31 percent for collimated incidence for $\omega = 1$ with *F*2 phase function. The isotropic scaling tends to overpredict the transmitted and reflected fluxes for the forward peaked phase functions, and it tends to underpredict for the backward peaked phase functions. These error trends are reversed for the side wall losses.

The phase functions are found not to have a significant effect on the scaling accuracy of the diffuse incidence problem. The asymmetry factor does, however, play an important and complex role for the collimated incidence problem, particularly in connection with the side wall loss predictions. The isotropic scaling is very accurate for isothermal emission problems. To avoid the large flux errors of the isotropic scaling for collimated incidence problem, a modified δ–M anisotropic scaling will be examined in our next work.

Acknowledgments

This work was supported, in part, by the National Science Foundation Grant No. NSF/CBT-8451076. A grant from the Minnesota Supercomputer Institute is also gratefully acknowledged.

References

Inönü, E., 1977, "Scaling and Time Reversal for the Linear Monoenergetic Boltzmann Equation," in: *Topics in Mathematical Physics*, H. Odabasi and O. Akyuz, eds., Colorado Univ. Press, pp. 113–127.

Irvine, W. M., 1963, "The Asymmetry of the Scattering Diagram of a Spherical Particle," *Bulletin of the Astronomical Institute of Netherlands*, Vol. 17, No. 3, pp. 176–184.

Joseph, J. H., Wiscombe, W. J., and Weinman, J. A., 1979, "The Delta-Eddington Approximation for Radiative Flux Transfer," *Journal of the Atmospheric Sciences*, Vol. 33, pp. 2452–2459.

Kim, T.-K., and Lee, H., 1988, "Effect of Anisotropic Scattering on Radiative Heat Transfer in Two-Dimensional Rectangular Enclosures," *International Journal of Heat and Mass Transfer*, Vol. 31, No. 8, pp. 1711–1721.

Kim, T.-K., and Lee, H., 1989, "Radiative Transfer in Two-Dimensional Anisotropic Scattering Media With Collimated Incidence," *Journal of Quantitative Spectroscopy and Radiative Transfer*, Vol. 42, No. 3, pp. 225–238.

Lee, H., and Buckius, R. O., 1982, "Scaling Anisotropic Scattering in Radiation Heat Transfer for a Planar Medium," ASME JOURNAL OF HEAT TRANSFER, Vol. 104, pp. 68–75.

McKellar, B. H. J., and Box, M. A., 1981, "The Scaling Group of the Radiative Transfer Equation," *Journal of the Atmospheric Sciences*, Vol. 38, pp. 1063–1068.

Nelson, H. F., Look, D. C., Jr., and Crosbie, A. L., 1986, "Two-Dimensional Radiative Back-Scattering From Optically Thick Media," ASME JOURNAL OF HEAT TRANSFER, Vol. 108, pp. 619–625.

Wiscombe, W. J., 1977, "The Delta-M Method: Rapid Yet Accurate Radiative Flux Calculations for Strongly Asymmetric Phase Functions," *Journal of the Atmospheric Sciences*, Vol. 34, pp. 1408–1442.

One-Dimensional Analysis of the Hydrodynamic and Thermal Characteristics of Thin Film Flows Including the Hydraulic Jump and Rotation

S. Thomas

W. Hankey

A. Faghri

Department of Mechanical and Materials Engineering, Wright State University, Dayton, OH 45435

T. Swanson

NASA Goddard Space Flight Center, Greenbelt, MD 20771

The flow of a thin liquid film with a free surface along a horizontal plate that emanates from a pressurized vessel is examined numerically. In one g, a hydraulic jump was predicted in both plane and radial flow, which could be forced away from the inlet by increasing the inlet Froude number or Reynolds number. In zero g, the hydraulic jump was not predicted. The effect of solid-body rotation for radial flow in one g was to "wash out" the hydraulic jump and to decrease the film height on the disk. The liquid film heights under one g and zero g were equal under solid-body rotation because the effect of centrifugal force was much greater than that of the gravitational force. The heat transfer to a film on a rotating disk was predicted to be greater than that of a stationary disk because the liquid film is extremely thin and is moving with a very high velocity.

Introduction

The study of thin liquid films has been performed by many researchers in the past due to the high heat transfer rates that can be achieved. Even though the heat transfer to thin films falling down a vertical plate is quite high, much better heat transfer rates can be realized when the film is generated by the impingement of a liquid jet onto a surface that is perpendicular to the jet. This is due to the fact that in most cases the film velocities are greater than those of a falling film. Since it is difficult to examine the entire flow field from the impinging jet to the perpendicular thin film, it is proposed to study only the thin film. This is accomplished by the following mechanism: The liquid is pressurized in a container and emanates from a slot, which generates the thin film on a horizontal plate. With this situation, the height and mean velocity of the film will be known boundary conditions, which will aid in determining the characteristics of the film downstream. After the structure of the liquid film has been examined, the amount of heat that can be transferred to it can be found. Furthermore, in this study it is also desired to understand the effects of centrifugal force and zero gravity on the flow field. If the film is generated on a spinning disk, it is expected that the film will accelerate and become thinner, since the centrifugal force acts in the main direction of the flow. This acceleration of the liquid film will increase the amount of heat that can be transferred from the spinning disk to the film. The effect of zero g on the flow is also examined to determine the nature of the liquid film height when the gravitational field across the film is not present. The combined effects of centrifugal acceleration and a zero g environment on the fluid characteristics and heat transfer to a thin film are not known at present. It is felt, however, that this fundamental research will become important in the future because of programs like the space station, where improved heat exchangers will be needed. This research will also be instrumental in the development of an absorber unit for a spacecraft vapor-absorption heat pump system, which was the motivation for the present work.

Many investigations have been carried out concerning thin liquid films created by impinging jets and/or spinning disks because of the numerous applications where improved heat or mass transfer is desirable. The liquid impingement cooling of bearings and gears was studied by Carper et al. (1986). The condensation of steam onto a rotor, such as that of a steam turbine, was studied by Espig and Hoyle (1965). The heat transfer due to the condensation of steam onto a rotating disk was examined by Butuzov and Rifert (1972), where the interest in this study was related to centrifugal sea-water distillation equipment. The flow of a liquid film on a rotating disk was examined by Matsumoto et al. (1973) in connection with the atomization of a liquid for spray drying and the promotion of chemical reactions or absorption between gasses and liquids. Aroesty et al. (1967) studied the use of thin films under centrifugal force as an aid to blood oxygenation. The study of thin films in regard to spin-coating deposition of thin solid films was carried out by Jenekhe (1984). Watson (1964) analyzed a free-falling jet that impinges on a horizontal plane using a similarity solution. Rauscher et al. (1973) analyzed the laminar flow of a thin film on a rotating disk by employing the asymptotic expansion technique. Miyasaka (1974) compared the results of an experimental study with those of a theoretical study of the thickness of a thin viscous film on a rotating disk. Muzhilko et al. (1983) experimentally measured the liquid film thickness on a horizontal rotating disk where the liquid is introduced onto the center of the disk by an impinging jet. Needham and Merkin (1987) theoretically studied thin axisymmetric liquid films on a horizontally rotating disk to determine the criteria for stability of the film.

The motivation of the present work is the study of thin liquid films that will be used in space-based centrifugal heat exchangers and vapor absorption heat pumps. Since a falling film cannot be achieved in a zero g environment, it is natural to consider the possibility of using the artificial gravity created by the centrifugal force on a rotating disk to generate a thin film.

In the present study, the governing equations and boundary conditions are presented for two situations of a thin liquid

Contributed by the Heat Transfer Division and presented at the National Heat Transfer Conference, Philadelphia, Pennsylvania, August 6-9, 1989. Manuscript received by the Heat Transfer Division February 21, 1989; revision received August 10, 1989. Keywords: Evaporation, Numerical Methods, Thin Film Flow.

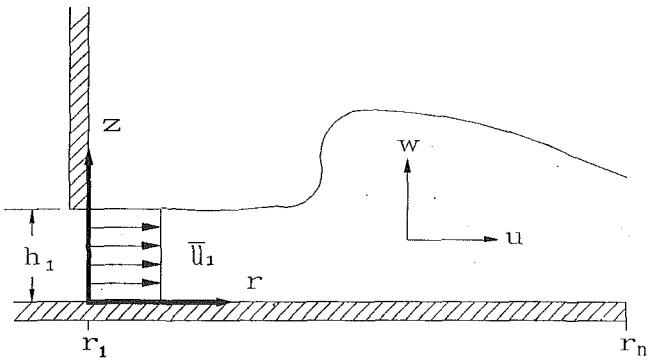

Fig. 1 The generalized coordinate system

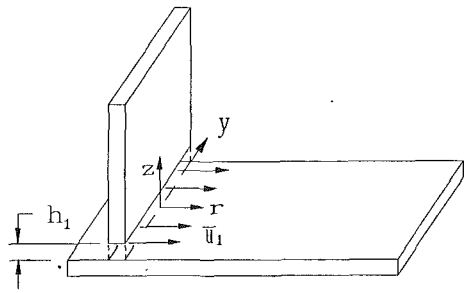

Fig. 2(*a*) The coordinate system for plane flow

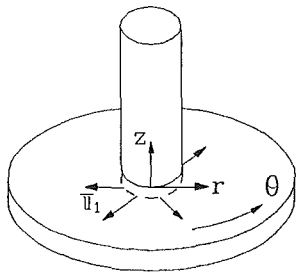

Fig. 2(*b*) The coordinate system for radial flow

layer emanating from a pressurized vessel and traveling along a horizontal plate with a constant initial height and uniform initial velocity, as shown in Fig. 1. The first case is when the liquid flows along a channel with a constant width, which is shown in Fig. 2(*a*). This situation is the same as open channel flow, but since the liquid height is very thin the effect of viscosity must be accounted for. The second case, which is shown in Fig. 2(*b*), is when the liquid originates between two parallel disks, and then spreads out radially over the bottom disk in a free surface thin film because the diameter of the upper disk is much smaller than that of the lower disk. This situation is similar to a jet of liquid impinging onto the center of a horizontal disk, except that the height and the mean velocity of the liquid film are known at a specific radial location. In the case of radial flow, the rotational acceleration will be modeled as solid-body rotation, where the centrifugal forces act only in the radial direction.

It is desired to solve numerically for the liquid height at any distance down the length of the plate for different Froude numbers and Reynolds numbers specified at the inlet. The heat transfer from the plate will also be studied for the case of simple heating with no evaporation at the free surface. Since the inlet Froude number may be greater than unity, it is possible that a hydraulic jump will occur at some point in the computational domain. A hydraulic jump is when the flow suddenly changes from supercritical ($\mathrm{Fr}>1$) to subcritical ($\mathrm{Fr}<1$) flow, which is accompanied by a sudden increase in the liquid height. This is analogous to the shock wave in gas dynamics when the flow changes from supersonic ($\mathrm{M}>1$) to subsonic ($\mathrm{M}<1$) flow in a very short distance. The similarity between the hydraulic jump and the shock wave in gas dynamics suggests using the familiar approach of modeling the flow as a transient phenomenon and allowing the solution to march in time to achieve the desired steady-state results. To the authors'

Nomenclature

C_f = skin friction coefficient $= \tau_w/(1/2\ \rho\bar{u}^2)$
C_p = constant pressure specific heat, J/kg-K
C = Courant number $= \Delta\tau/\Delta\xi$
Fr = Froude number $= \bar{u}/\sqrt{g\delta}$
$\mathbf{g}$ = gravitational acceleration, m/s^2
h = heat transfer coefficient, W/m^2-K
k = for plane flow $k=0$, for radial flow $k=1$
K = thermal conductivity, W/m-K
p = pressure, N/m^2
$\dot{q}$ = heat flux, W/m^2
Q = volumetric flow rate $= (2\pi r)^k \bar{u}\delta$
r = coordinate parallel to the plate
Re = Reynolds number $= \bar{u}\delta/\nu$
Ro = Rossby number $= \bar{u}/\omega r$
t = time, s
T = temperature, K
u = velocity in the r direction, m/s
$\bar{u}$ = mean velocity in the r direction $= \frac{1}{\delta}\int_0^\delta u\, dz$, m/s
v = velocity in the θ direction, m/s
V = dimensionless velocity in the r direction $= \bar{u}/\bar{u}_1$
$\mathbf{V}$ = velocity vector, m/s
w = velocity in the z direction, m/s
y = coordinate orthogonal to the r and z directions in plane flow
z = coordinate perpendicular to the plate
α = thermal diffusivity, m^2/s
β = artificial viscosity coefficient
δ = liquid film thickness, m
δ_B = Blasius boundary layer thickness, m
δ^+ = dimensionless film thickness $= \delta/\delta_1$
δ_B^+ = dimensionless boundary layer thickness $= \delta_B/\delta_1$
Δ = increment
θ = coordinate orthogonal to the r and z directions in radial flow
μ = dynamic viscosity, N-s/m^2
ν = kinematic viscosity, m^2/s
ξ = dimensionless coordinate parallel to the plate, r/δ_1
ρ = density, kg/m^3
τ_w = shear stress at the plate, N/m^2
τ = dimensionless time $= t\bar{u}_1/\delta_1$
ω = rotational velocity, rad/s

Subscripts

j = nodal point in the r direction
m = mixed mean
n = at the outlet
r = r direction
w = wall
z = z direction
θ = θ direction
ξ = derivative with respect to ξ
τ = derivative with respect to τ
1 = at the inlet
0 = at the initial time

Superscripts

k = for plane flow $k=0$, for radial flow $k=1$
n = nodal point in time

knowledge, this approach has not been applied to this type of problem before. It should be emphasized that conventional numerical techniques that are applied to two- or three-dimensional problems cannot be used directly to solve this particular problem because the location of the free surface is unknown prior to the start of the calculations.

Mathematical Modeling

The conservation of mass, momentum, and energy in the general coordinate system can be expressed in the following compact form for a thin incompressible liquid film with constant properties:

$$\nabla \cdot \mathbf{V} = 0$$

$$\rho \frac{D\mathbf{V}}{Dt} = -\nabla p + \mu \nabla^2 \mathbf{V} + \rho \mathbf{g} \tag{1}$$

$$\frac{DT}{Dt} = \alpha \nabla^2 T$$

In the general coordinate system given in Fig. 1, the direction that is parallel to the plate in the main direction of the flow will be denoted by r and the direction that is normal to the plate will be denoted by z. The velocity vector $\mathbf{V}$ has three components, u, v, and w, where u is in the r direction and w is in the z direction. The component of velocity in the y direction, as shown in Fig. 2(a), is set equal to zero for plane flow. The component of velocity in the θ direction, as shown in Fig. 2(b), is equal to v for radial flow.

Several assumptions are made in order to reduce the complexity of the governing equations. Any changes in the variables with respect to the θ or y directions are set to zero. In the gravitational field $\mathbf{g}$, only the component across the film thickness, g_z, is considered. The boundary layer assumptions are imposed on the governing equations, which neglect the diffusion terms in the main direction of the flow based on an order-of-magnitude analysis. At the free surface, the effects of interfacial shear stress and the surface tension are assumed to be zero. It should be noted that the effect of surface tension may be significant near the inlet and outlet of the domain. The pressure in the liquid film is defined as the difference between the actual pressure and the atmospheric pressure, so at the free surface the pressure is equal to zero. For the case of radial flow, it is assumed that the velocity component in the θ direction is $v = \omega r$, i.e., solid-body rotation. By an order-of-magnitude analysis, this assumption is valid for small values of the Rossby number ($\mathrm{Ro} < 1$).

The boundary and initial conditions for the governing equations in fixed coordinates are those on the flat plate and on the free surface of the liquid

$$\begin{aligned}
&z = 0: \quad u = 0, \quad v = \omega r, \quad w = 0 \\
&z = \delta: \quad w = \frac{\partial \delta}{\partial t} + u \frac{\partial \delta}{\partial r}, \quad p = 0, \quad \frac{\partial u}{\partial z} = 0 \\
&r = r_1: \quad u = u_1, \quad w = 0, \quad \delta = \delta_1 \\
&t = 0: \quad u = u_0, \quad w = 0
\end{aligned} \tag{2}$$

The boundary condition involving w at the free surface is the kinematic condition for time-dependent problems. The boundary condition involving $\partial u/\partial z$ at $z = \delta$ corresponds to neglecting the interfacial shear stress at the free surface.

The continuity equation and the conservation of momentum equations in the r and z directions can be integrated with respect to the z direction across the thin liquid layer by using Leibniz's rule and the kinematic condition at the free surface. Due to the boundary-layer assumptions, the conservation of momentum equation in the z direction results in a balance between the pressure gradient and the buoyancy force. This equation is then substituted into the r-direction momentum equation. It is assumed that the velocity in the main direction of the flow is constant across the thin film, so that

$$\int_0^{\delta} u^2 dz = \bar{u}^2 \delta$$

It should be noted that this is not a major assumption. For example, for a parbolic velocity profile, the left-hand side is equal to $6\bar{u}^2\delta/5$. The resulting one-dimensional time-dependent equations in the general coordinate system are given in the following form:

$$\frac{1}{r^k} \frac{\partial}{\partial r} (r^k \bar{u} \delta) + \frac{\partial \delta}{\partial t} = 0 \tag{3}$$

$$\frac{\partial}{\partial t} (\bar{u}\delta) + \frac{\partial}{\partial r} \left[\bar{u}^2 \delta + \frac{1}{2} g \delta^2 \right] = k\delta \left(r\omega^2 - \frac{\bar{u}^2}{r} \right) - \frac{1}{\rho} \mu \frac{\partial u}{\partial z} \bigg|_{z=0} \tag{4}$$

To assign the boundary conditions of the flow properly, the characteristic behavior of the flow will be examined. The governing equations can be cast in the characteristic form by the following analysis.

The governing equations (3) and (4) can be rearranged by subtracting $\bar{u}$ times the continuity equation from the momentum equation

$$\frac{1}{\delta} \frac{\partial \delta}{\partial t} + \frac{\bar{u}}{\delta} \frac{\partial \delta}{\partial r} + \frac{\partial \bar{u}}{\partial r} = -\frac{k\bar{u}}{r}$$

$$\frac{\partial \bar{u}}{\partial t} + \bar{u} \frac{\partial \bar{u}}{\partial r} + (g\delta) \frac{1}{\delta} \frac{\partial \delta}{\partial r} = r\omega^2 \left(1 - \frac{\tau_w}{\delta \rho r \omega^2} \right)$$

The characteristic form of the equations is obtained by linearizing the continuity and momentum equations

$$\left(\frac{\partial}{\partial t} + \bar{u}_1 \frac{\partial}{\partial r} \right) \frac{\delta}{\delta_1} + \frac{\partial}{\partial r} (\bar{u}) = S_1$$

$$\left(\frac{\partial}{\partial t} + \bar{u}_1 \frac{\partial}{\partial r} \right) \bar{u} + a_1^2 \frac{\partial}{\partial r} \left(\frac{\delta}{\delta_1} \right) = S_2$$

where

$$a_1^2 = g\delta_1$$

$$S_1 = -\frac{k\bar{u}}{r}$$

$$S_2 = r\omega^2 \left(1 - \frac{\tau_w}{\delta \rho r \omega^2} \right)$$

These two equations can be represented by the following characteristic equation:

$$\frac{\partial R_i}{\partial t} + c_i \frac{\partial R_i}{\partial r} = S_i$$

The Reimann invariants and the physical wave speeds are given in the following table:

R_i	c_i	S_i
$\bar{u} + a_1(\delta/\delta_1)$	$\bar{u}_1 + a_1$	$a_1 S_1 + S_2$
$\bar{u} - a_1(\delta/\delta_1)$	$\bar{u}_1 - a_1$	$-a_1 S_1 + S_2$

An examination of the characteristics reveals that the first invariant will always propagate downstream. The direction of propagation for the second invariant depends upon whether the flow is supercritical or subcritical. For supercritical flow (i.e., $\mathrm{Fr} > 1$), the second invariant propagates downstream, so the boundary conditions on $\bar{u}$ and δ will both be assigned at the inlet of the flow field. For subcritical flow (i.e., $\mathrm{Fr} < 1$), the second invariant propagates upstream, so the boundary conditions must be assigned at the inlet and the outlet of the flow field.

The following assumption is made to simplify the governing equations so that the film height can be eliminated from the equations:

$$\frac{\partial \delta}{\partial t} \simeq 0$$

This assumption results in the following quasi-steady governing equations:

$$r^k \bar{u}\delta = \frac{Q}{(2\pi)^k} = \text{const} \tag{5}$$

$$\delta \frac{\partial \bar{u}}{\partial t} + \frac{\partial}{\partial r}\left[\bar{u}^2\delta + \frac{1}{2} g\delta^2\right] = k\delta\left(r\omega^2 - \frac{\bar{u}^2}{r}\right) - \frac{1}{\rho}\mu \left.\frac{\partial u}{\partial z}\right|_{z=0} \tag{6}$$

By using this assumption, it is understood that the unsteady solutions with respect to time are not precisely accurate, but the accuracy of the steady-state solution is not affected.

The following analysis for the skin friction coefficient is given since the shear stress at the wall is not known. When the boundary layer on the plate is much smaller than the film thickness, i.e., developing flow, it is assumed that the boundary layer is the same as when there is a uniform far-field boundary. Therefore, when $\delta > \delta_B$, where δ_B is the Blasius boundary layer thickness, the Blasius skin friction coefficient will be employed to approximate the shear stress term. When the boundary layer reaches the free surface (i.e., $\delta = \delta_B$), a parabolic velocity profile is used to approximate the shear stress term. The Blasius boundary layer thickness is given by

$$\frac{\delta_B}{(r-r_1)} = \frac{5.0}{\sqrt{\frac{\bar{u}(r-r_1)}{\nu}}}$$

The Blasius skin friction coefficient is as follows:

$$C_f = \frac{0.664}{\sqrt{\frac{\bar{u}(r-r_1)}{\nu}}}$$

The Blasius skin friction coefficient can also be presented in terms of the Blasius boundary layer thickness

$$C_f(\text{Blasius}) = \frac{3.32}{\left(\frac{\bar{u}\delta_B}{\nu}\right)}$$

For $\delta = \delta_B$, it is assumed that the velocity profile is parabolic

$$u = \frac{3\bar{u}}{\delta}\left(z - \frac{z^2}{2\delta}\right) \tag{7}$$

The skin friction coefficient is

$$C_f(\text{parabolic}) = \frac{\tau_w}{\frac{1}{2}\rho\bar{u}^2} = \frac{\mu \left.\frac{\partial u}{\partial z}\right|_{z=0}}{\frac{1}{2}\rho\bar{u}^2} = \frac{6}{\left(\frac{\bar{u}\delta}{\nu}\right)}$$

The two skin friction coefficients match when

$$C_f(\text{Blasius}) = C_f(\text{parabolic})$$

or

$$\frac{\delta}{\delta_B} = 1.81$$

The value of the skin friction will be determined in the following manner:

$$\delta_B = \frac{5.0(r-r_1)}{\sqrt{\frac{\bar{u}(r-r_1)}{\nu}}}$$

$$0 < \frac{\delta}{\delta_B} < 1.81 \qquad C_f = \frac{6}{\left(\frac{\bar{u}\delta}{\nu}\right)}$$

$$\frac{\delta}{\delta_B} > 1.81 \qquad C_f = \frac{0.664}{\sqrt{\frac{\bar{u}(r-r_1)}{\nu}}}$$

The governing equations are nondimensionalized in the following manner to simplify the analysis and to generalize the results:

$$\frac{\bar{u}}{\bar{u}_1} = V \quad \frac{\delta}{\delta_1} = \delta^+ \quad \frac{r}{\delta_1} = \xi \quad t\frac{\bar{u}_1}{\delta_1} = \tau$$

$$\frac{\bar{u}_1^2}{g\delta_1} = \text{Fr}_1^2 \quad \frac{\bar{u}_1\delta_1}{\nu} = \text{Re}_1 \quad \frac{\bar{u}_1}{\omega r_1} = \text{Ro}_1 \tag{8}$$

$$\frac{\delta_B}{\delta_1} = \delta_B^+ = \text{dimensionless boundary layer thickness}$$

The Reynolds number of the flow was chosen to nondimensionalize the governing equations instead of the Ekman number because the Reynolds number is needed when the flow is stationary.

After eliminating the dimensionless film height from the momentum equation with the continuity equation, the dimensionless governing equation is as follows:

$$V_\tau + V\xi^k G_\xi = H \tag{9}$$

where

$$G = \frac{V}{\xi^k} + \frac{\xi_1^k}{2\text{Fr}_1^2}\left(\frac{1}{V\xi^k}\right)^2 - \beta V_\xi \tag{10}$$

and

$$H = k\left[\frac{\xi}{(\xi_1\text{Ro}_1)^2} - \frac{V^2}{\xi}\right] - 3\frac{V^3}{\text{Re}_1}\left(\frac{\xi}{\xi_1}\right)^{2k} \quad \text{for} \quad 0 < \frac{\delta^+}{\delta_B^+} < 1.81 \tag{11}$$

or

$$H = k\left[\frac{\xi}{(\xi_1\text{Ro}_1)^2} - \frac{V^2}{\xi}\right] - \frac{0.332V^{5/2}}{\sqrt{\text{Re}_1(\xi-\xi_1)}}\left(\frac{\xi}{\xi_1}\right)^k \quad \text{for} \quad \frac{\delta^+}{\delta_B^+} > 1.81 \tag{12}$$

where the dimensionless boundary layer thickness is given by

$$\delta_B^+ = 5.0\sqrt{\frac{(\xi-\xi_1)}{V\text{Re}_1}} \tag{13}$$

The dimensionless initial and boundary conditions are given as follows:

$$V(0, \xi) = 1$$

$$V(\tau, \xi_1) = 1$$

These conditions correspond to a constant velocity across the region at the initial time and a constant inlet velocity at all times. Since the steady-state results are the only concern due to the constraints made on the mathematical modeling ($\partial\delta/\partial t \simeq 0$), the specification of the initial condition is required only for the numerical iteration scheme.

An artificial viscosity term (βV_ξ) is included in the governing equation to dampen numerical oscillations in the solution (Anderson et al., 1984). The oscillations are commonly referred to as the Gibb phenomenon, which occurs near a double-valued point in the solution, such as a hydraulic jump or a shock wave. This term reduces the numerical oscillations in the immediate vicinity of the hydraulic jump, but does not affect the numerical solution elsewhere in the domain.

Heat Transfer Analysis

It is desired to find the amount of heat transferred from the plate or disk to the liquid when the plate is heated. This analysis assumes that the velocity of the thin film is approximated by the similarity profile presented in equation (7). The temperature profile across the thin film is assumed to be a quadratic function, with the coefficients determined by the boundary conditions imposed at the surface of the plate and the free surface. The boundary conditions are a constant heat flux at the plate and adiabatic free surface of the liquid film, which corresponds to simple heating with no evaporation at the free surface. The boundary conditions are given as

$$\left.\frac{\partial T}{\partial z}\right|_{z=\delta} = 0 \tag{14}$$

$$-K\left.\frac{\partial T}{\partial z}\right|_{z=0} = \dot{q} \tag{15}$$

The temperature distribution across the thin film is

$$T = T_w - \frac{\dot{q}}{K} z + \frac{\dot{q}}{2K\delta} z^2 \tag{16}$$

The mixed-mean temperature of the film is given by the following equation:

$$T_m = \frac{1}{\bar{u}\delta}\int_0^\delta uT\, dz = T_w - \frac{2}{5}\frac{\dot{q}\delta}{K} \tag{17}$$

The heat transfer coefficient is defined by

$$h = \frac{\dot{q}}{(T_w - T_m)} = \frac{5}{2}\frac{K}{\delta} \tag{18}$$

Therefore, the heat transfer coefficient can be found in terms of the liquid film height.

The modified Nusselt number is defined in the following manner:

$$\mathrm{Nu} = \frac{h}{K}\left(\frac{\nu^2}{g}\right)^{1/3} = \frac{2.5}{\delta}\left(\frac{\nu^2}{g}\right)^{1/3} \tag{19}$$

This definition has been used previously in the literature concerning thin falling films. For a zero g situation, the Nusselt number is defined in terms of the liquid film thickness

$$\mathrm{Nu}^* = \frac{h\delta}{K} = 2.5 \tag{20}$$

For practical applications, the mixed-mean temperature of the fluid should be known. Therefore, the following analysis is given to find the mixed-mean temperature for the case of simple heating with no evaporation at the free surface for plane and radial flow. This analysis follows the same pattern as that for the momentum equation of the problem. The conservation of energy will be integrated across the thin film in order to find the mixed-mean temperature.

The conservation of energy equation is

$$\rho C_p\left(\frac{\partial T}{\partial t} + u\frac{\partial T}{\partial r} + w\frac{\partial T}{\partial z}\right) = \frac{K}{r^k}\frac{\partial}{\partial r}\left(r^k\frac{\partial T}{\partial r}\right) + K\frac{\partial^2 T}{\partial z^2} \tag{21}$$

The assumption is made that the diffusive term in the r direction is zero.

$$\frac{\partial T}{\partial t} + u\frac{\partial T}{\partial r} + w\frac{\partial T}{\partial z} = \alpha\frac{\partial^2 T}{\partial z^2} \tag{22}$$

The conservation of energy equation is integrated across the thickness of the film by using Leibniz's rule and the kinematic condition at the free surface. Since the steady-state solution of the fluid velocity will be known from the fluid mechanics analysis, the steady solution of the conservation of energy equation will be found. The continuity equation (5) and the conservation of energy equation are

$$r^k\bar{u}\delta = \frac{Q}{(2\pi)^k} = \text{const}$$

$$\frac{\partial T_m}{\partial r} = \frac{(2\pi r)^k\alpha}{Q}\left(\left.\frac{\partial T}{\partial z}\right|_\delta - \left.\frac{\partial T}{\partial z}\right|_0\right) \tag{23}$$

Implementing the heat flux boundary conditions corresponding to simple heating with no evaporation at the free surface results in the following equation:

$$\frac{\partial T_m}{\partial r} = \frac{(2\pi r)^k\dot{q}}{Q\rho C_p} \tag{24}$$

This equation can be integrated directly to determine the difference in the mixed-mean temperature between the inlet and any point in the r direction

$$T_m - T_{m1} = \frac{\pi^k\dot{q}r}{Q\rho C_p}\left(r - \frac{r_1^2}{r}\right)^k \tag{25}$$

Numerical Solution Procedure

Due to the similarity between the hydraulic jump and the shock wave in gas dynamics, the MacCormack explicit method (Anderson et al., 1984), which is quite often used for the solution of compressible flow problems, will be used in the present numerical analysis of this incompressible film flow. Since it is an explicit method, the unknown variables are found in terms of known quantities, as opposed to implicit methods, which must solve a matrix equation to obtain the solution of the problem.

The governing equation for the present problem is equation (9):

$$V_\tau + V\xi^k G_\xi = H$$

The forward-predictor finite-difference equation for the governing equation is forward in time and space

$$\overline{V_j^{n+1}} = V_j^n\left[1 - \xi_j^k\frac{\Delta\tau}{\Delta\xi}(G_{j+1}^n - G_j^n)\right] + \Delta\tau H_j^n \tag{26}$$

The finite-difference equation based on the predicted solution using a forward-time, backward-space differencing scheme is

$$(V_j^{n+1})' = \overline{V_j^{n+1}}\left[1 - \xi_j^k\frac{\Delta\tau}{\Delta\xi}\left(\overline{G_j^{n+1}} - \overline{G_{j-1}^{n+1}}\right)\right] + \Delta\tau\overline{H_j^{n+1}}$$

The corrected solution is the arithmetic average of the past and predicted solutions

$$V_j^{n+1} = \frac{1}{2}[V_j^n + (\overline{V_j^{n+1}})']$$

$$V_j^{n+1} =$$

$$\frac{1}{2}\left\{V_j^n + \overline{V_j^{n+1}}\left[1 - \xi_j^k \frac{\Delta\tau}{\Delta\xi}\left(\overline{G_j^{n+1}} - \overline{G_{j-1}^{n+1}}\right)\right] + \Delta\tau \overline{H_j^{n+1}}\right\} \tag{27}$$

Since the foward-predictor velocity is in terms of a forward-space approximation, an outlet boundary condition on the velocity is needed. For the case of one g, it is assumed that the Froude number at the outlet is unity, which is a common boundary condition when a liquid falls over an edge because the liquid accelerates from a subcritical velocity to a supercritical velocity through the critical velocity. The Froude number at the inlet and the dimensionless velocity at the outlet are related as follows:

$$V_n = \left(\frac{\xi_1}{\xi_n}\right)^{k/3} \mathrm{Fr}_1^{-2/3} \tag{28}$$

For the zero g case and when the Rossby number is $\mathrm{Ro} < 1$, the slope of the dimensionless velocity at the last node is set equal to the slope at the next to last node for the outlet boundary condition.

The solution of the governing equation using the MacCormack explicit method proceeds as follows:

- The parameters pertaining to the numerical domain and the inlet and outlet boundary conditions are specified.
- The initial velocity distribution is input to the program.
- The variables G and H are computed using the velocity profile at the old time step.
- The velocity distribution at the midpoint time step is calculated in terms of the velocity, G, and H at the old time step. An outlet boundary condition is needed in this step because of the forward-space approximation.
- The variables G and H are computed again by using the velocity profile at the midpoint time step.
- The velocity distribution at the new time step is calculated. The inlet boundary condition is used in this step because of the backward-space approximation.
- The values of the velocity distribution at the new time step are used as the initial velocity profile for the next iteration.
- The process is repeated until steady values are reached.

In explicit schemes, the magnitude of the time step is chosen based upon a Courant number, which is defined for the present problem in the following manner:

$$C = \frac{\Delta\tau}{\Delta\xi}$$

In this study, the grid size was set to a specific value and the time step was varied to avoid convergence difficulties. The largest time step that did not lead to a divergent solution was then used in the calculations. The following table is a general guideline that was used to determine the time step size:

Flow situation	Courant number, C
Plane flow	<1.0
Radial flow	<0.5
Radial flow with rotation	$<10^{-3}$

One hundred grids were used in the plane flow calculations. For radial flow, 500 grids were used because the governing equation was very lightly damped, so that the numerical oscillations were excessive with only 100 grids. There was no significant change (<0.1 percent) in the numerical results when the aforementioned grid specifications were reduced by one-half to check the grid independence of the solution.

Results and Discussion

The thickness of free surface films in plane and radial flow have been calculated numerically. In addition, the Nusselt number was calculated for simple heating with no evaporation at the free surface with water as the working fluid. The results of the one-dimensional quasi-steady governing equation of fluid motion are given in Figs. 3–7. The heat transfer results are shown in Fig. 8 for plane and radial flow in one g and in Fig. 9 for radial flow with solid-body rotation.

Figure 3 shows the solution for plane flow as it progresses in time. It can be seen that the supercritical portion of the flow develops very quickly while the subcritical region and the exact location of the hydraulic jump take more time to reach steady state. The Gibb phenomenon can easily be noticed in the transient solutions of the governing equation, but the oscillations become more damped in the steady solution. Due to the assumptions pertaining to the governing equations, the transient solutions of the problem are not accurate, but the steady solutions should be acceptable. In the following figures, only the steady-state solutions are given. It is clear that the velocity profile in the immediate vicinity of the hydraulic jump is not a good representation of the flow field due to the transient nature of the jump. However, this does not affect the numerical results in the supercritical or subcritical regions as well as the location of the jump. In order to capture the details of the jump, a two-dimensional model using body-fitting coordinates in needed.

As can be seen in Fig. 3, the film thickness increases along the plate as the fluid travels away from the inlet of the region. The fluid is prevented from rolling back due to the action of gravity by the momentum of the fluid in the main direction of the flow. The reason that the film thickness increases with distance in the supercritical region is that the friction at the interface between the fluid and the plate slows the fluid, which translates into an increase in the film thickness due to continuity.

The effects of changing of the inlet Reynolds number and the inlet Froude number in plane flow are presented in Fig. 4. The graphs in the left-hand column of the legend show the dimensionless liquid height when the Foude number is held at $\mathrm{Fr}_1 = 10.0$ and the Reynolds number is varied for $\mathrm{Re}_1 = 25.0$, 50.0, and 75.0. By increasing the inlet Reynolds number, the location of the hydraulic jump moves downstream and the dimensionless height of the liquid at all points in the domain decreases. Physically, increasing the Reynolds number can be interpreted in increasing the inertial forces on the fluid, so one would intuitively expect that the velocity of the fluid would increase as the Reynolds number increases. This increase in the

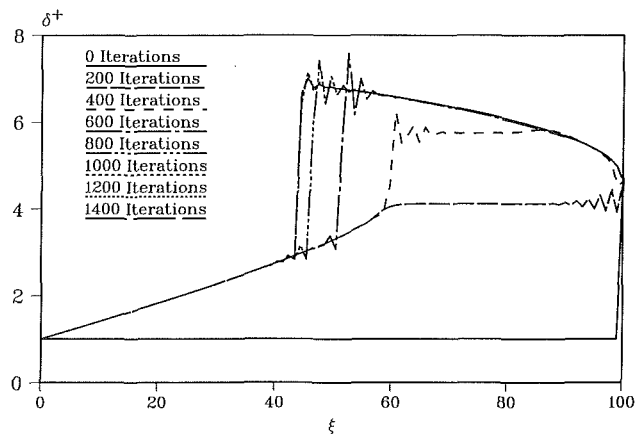

Fig. 3 Dimensionless liquid height versus dimensionless distance for plane flow with $\mathrm{Fr}_1 = 10.0$, $\mathrm{Fr}_n = 1.0$, $\mathrm{Re}_1 = 75.0$, $\xi_1 = 0.0$, and $\xi_n = 100.0$ as the solution marches in time

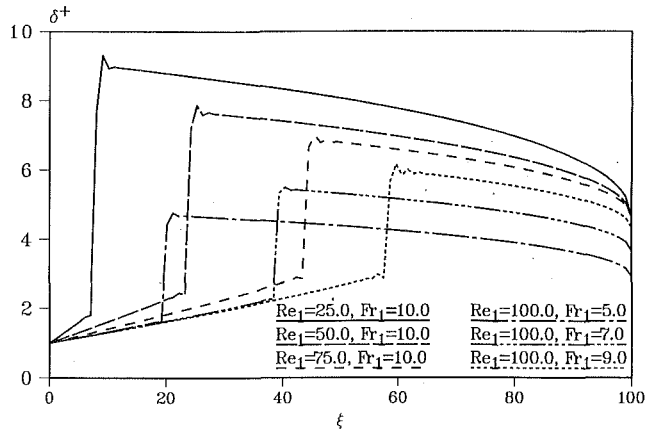

Fig. 4 Dimensionless liquid height versus dimensionless distance for plane flow with $\xi_1 = 0.0$, $\xi_n = 100.0$

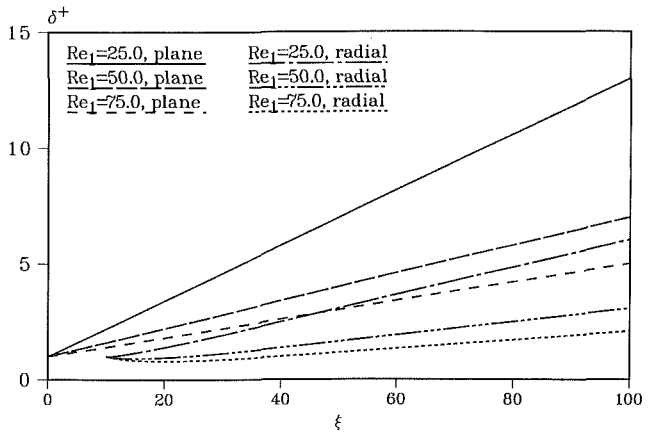

Fig. 5 Dimensionless liquid height versus dimensionless distance for plane and radial flow with $\xi_1 = 0.0$ (plane), $\xi_1 = 10.0$ (radial), and $\xi_n = 100.0$ for different values of the inlet Reynolds number in zero g

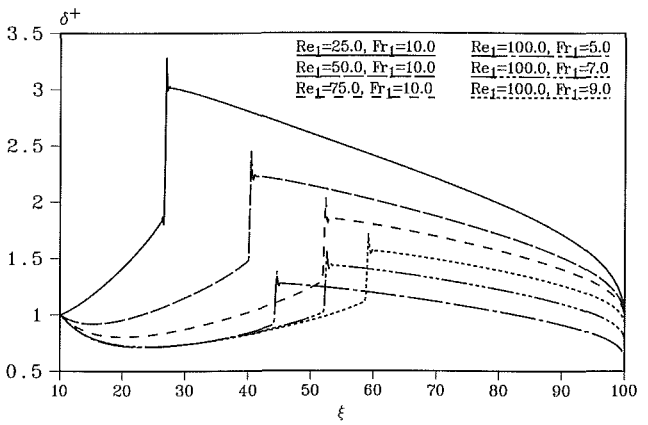

Fig. 6 Dimensionless liquid height versus dimensionless distance for radial flow with $\xi_1 = 10.0$, $\xi_n = 100.0$

fluid velocity is correlated to a decrease in the film thickness through the continuity equation.

The graphs in the right-hand column of the legend in Fig. 4 present the dimensionless liquid film height when the Reynolds number is constant at $Re_1 = 100.0$ and the Froude number is varied for $Fr_1 = 5.0$, 7.0, and 9.0. The location of the hydraulic jump moves downstream when the inlet Froude number increases, which has been seen in qualitative experiments. The dimensionless height of the liquid in the supercritical region generally lies along the same line because the viscous forces are not changing in this case. Increasing the

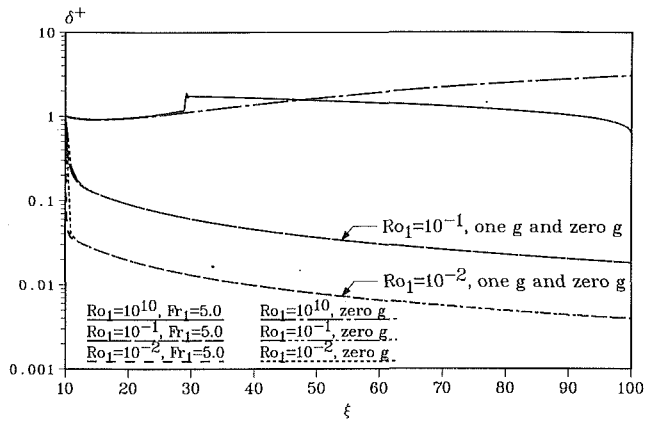

Fig. 7 Dimensionless liquid height versus dimensionless distance for radial flow with $Re_1 = 50.0$, $\xi_1 = 10.0$, and $\xi_n = 100.0$ for different values of the Rossby number in one g and zero g

Froude number can be thought of as decreasing the effect of the gravitational force, so by increasing the inlet Froude number, the flow approaches the zero g case. In the zero g situation, as shown in Fig. 5 for plane and radial flow, the hydraulic jump does not occur because the flow at all points in the domain is supercritical, since the Froude number approaches infinity in zero g. In Fig. 5, the dimensionless film height decreases as the Reynolds number increases because the inertial forces on the film flow are greater.

In Fig. 6, the inlet Froude number and the inlet Reynolds number in radial flow are varied parametrically. When the inlet Froude number is held constant and the Reynolds number is increased, the behavior of the flow is similar to plane flow in that the film thickness decreases and the hydraulic jump moves downstream. The film thickness in the supercritical region, however, decreases below the initial thickness downstream from the inlet at high Reynolds numbers. This is due to the increase in the flow area downstream as the flow spreads out radially. After this initial decrease in the film thickness, the film height increases in the supercritical region even though the flow is spreading out radially. This is due to the fact that the frictional effect is greater than the effect due to the increase in the flow area. The friction at the plate slows down the flow and increases the film thickness. As shown by Rahman et al. (1989), the liquid film height in the supercritical region may or may not have a minimum value other than the inlet height, depending upon the coefficient of friction at the plate and the inlet Froude number.

The effect of increasing the Froude number while the Reynolds number remains constant in radial flow is also shown in Fig. 6. The supercritical regions of the three cases overlap as in plane flow because the viscous forces on the liquid film are not changing. The hydraulic jump is moved downstream from the inlet as the Froude number is increased.

Figure 7 presents the effect of solid-body rotation on the dimensionless liquid film height in radial flow for one g and zero g. The Rossby number of $Ro_1 = 10^{10}$ signifies that the inertial forces are dominant in the flow, so that a profile similar to the previous results is obtained. For the other cases presented where the Rossby number is $Ro_1 = 10^{-1}$ and 10^{-2}, the hydraulic jump is completely washed out and the thickness of the fluid decreases at all points in the domain, which is physically realistic. The results for the low Rossby numbers also show that the dimensionless liquid film height is the same whether the gravitational body force is present or not. This is due to the fact that the centrifugal body force in this case is much greater than the gravitational body force.

Figure 8 presents the Nusselt number versus the dimensionless distance for plane and radial flow under one g. For these calculations, the values in equation (19) were chosen to

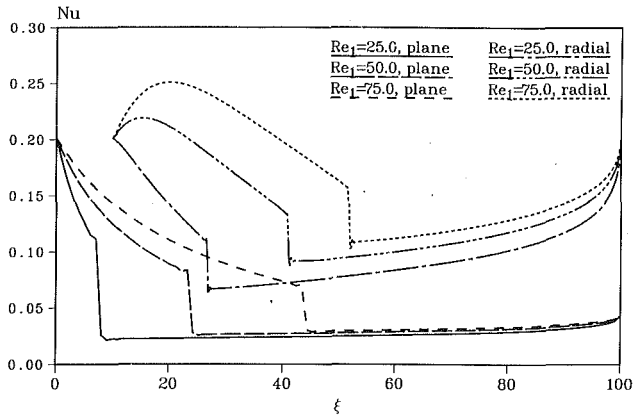

Fig. 8 Nusselt number versus the dimensionless distance for plane and radial flow with $Fr_1 = 10.0$, $\xi_1 = 0.0$ (plane), $\xi_1 = 10.0$ (radial), and $\xi_n = 100.0$ under one g

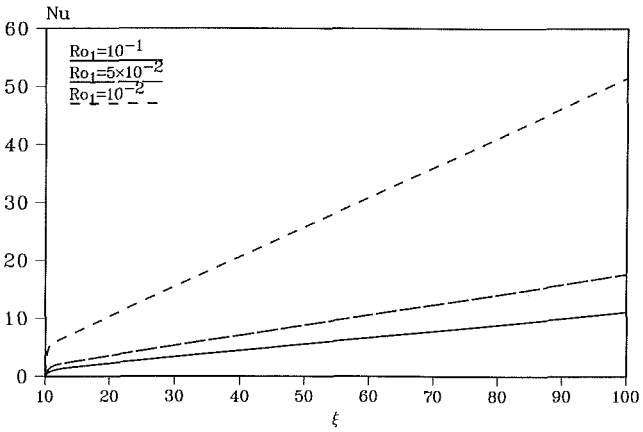

Fig. 9 Nusselt number versus the dimensionless distance for radial flow with $Fr_1 = 10.0$, $Re_1 = 50.0$, $\xi_1 = 10.0$, and $\xi_n = 100.0$, under one g

be $\delta_1 = 2.54 \times 10^{-4}$m, $K = 0.682$ W/m-K, $\nu = 2.90 \times 10^{-7}$m^2/s, and $g = 9.81$ m/s^2. The values of the thermal conductivity and the kinematic viscosity correspond to water at 373 K. As would be expected, the heat transfer increases as the Reynolds number increases because the height of the film decreases at all points along the plate.

Figure 9 presents the Nusselt number for the case of solid-body rotation in radial flow under one g. The heat transfer to the liquid in this case is two orders of magnitude higher than that without rotation because the liquid film becomes extremely thin and the velocity of the film is very high.

It should be noted that while the heat transfer results that were presented are for thin films under one g, the heat transfer to thin films in a zero g environment can also be calculated with equation (18).

Conclusions

In studying plane and radial flows experimentally, it can be seen that the flow can experience a hydraulic jump. This is a "mixed" flow situation where the flow changes from a supercritical condition to a subcritical condition with a sudden increase of the liquid height and a decrease in the velocity of the liquid. The similarity between the hydraulic jump and the shock wave in gas dynamics suggests the use of the approach where the flow is modeled as a transient phenomenon and allowed to march in time to achieve the desired steady-state results. Therefore, the equations of motion including the transient terms were integrated across the thin liquid layer, nondimensionalized, and discretized using the MacCormack explicit method to solve for the velocity and height of the liquid film in Cartesian and radial coordinates. Also, the steady-state heat transfer from the plate to the liquid was examined for the case of simple heating with no evaporation at the free surface. Since the numerical method of solution is explicit, large amounts of computer storage were not necessary.

For plane flow in one g, a hydraulic jump was predicted that could be forced away from the inlet by increasing the initial Froude number or Reynolds number, which agrees with what has been found in qualitative experiments. In zero g, the liquid film height increased monotonically, so that a hydraulic jump was not predicted.

For radial flow in one g, the liquid film height first decreased for high Reynolds numbers due to the increase of the flow area, and then increased to form a hydraulic jump. The hydraulic jump in radial flow could also be forced away from the inlet by increasing the initial Froude number or Reynolds number. In zero g, the hydraulic jump was not predicted in radial flow. The effect of solid-body rotation for radial flow in one g was found to thin the liquid film and "wash out" the hydraulic jump, which is physically realistic. The dimensionless film thickness under one g and zero g was the same for solid-body rotation because the centrifugal force was much greater than the gravitational body force. The heat transfer from the rotating disk was found to increase dramatically when under solid-body rotation compared to no rotation because the liquid film is very thin and moves with a high velocity.

Acknowledgments

Funding for this work was provided by the NASA Goddard Space Flight Center, Greenbelt, Maryland, under contract No. NAG5-956.

References

Anderson, D. A., Tannehill, J. C., and Pletcher, R. H., 1984, *Computational Fluid Mechanics and Heat Transfer*, Hemisphere Publ. Corp., New York.

Aroesty, J., et al., 1967, "Blood Oxygenation: A Study in Bioengineering Mass Transfer," The RAND Corp., Santa Monica, CA, Report P-3732.

Butuzov, A. I., and Rifert, V. F., 1972, "An Experimental Study of Heat Transfer During Condensation of Steam at a Rotating Disk," *Heat Transfer—Soviet Research*, Vol. 4, No. 6, pp. 150–153.

Carper, H. J., Jr., Saavedra, J. J., and Suwanprateep, T., 1986, "Liquid Jet Impingement Cooling of a Rotating Disk," ASME JOURNAL OF HEAT TRANSFER, Vol. 108, pp. 540–546.

Espig, H., and Hoyle, R., 1965, "Waves in a Thin Liquid Layer on a Rotating Disk," *J. Fluid Mech.*, Vol. 22, Part 4, pp. 671–677.

Jenekhe, S. A., 1984, "Effects of Solvent Mass Transfer on Flow of Polymer Solutions on a Flat Rotating Disk," *Ind. Eng. Chem. Fundam.*, Vol. 23, No. 4, pp. 425–432.

Matsumoto, S., Saito, K., and Takashima, Y., 1973, "The Thickness of a Viscous Liquid Film on a Rotating Disk," *Journal of Chemical Engineering of Japan*, Vol. 6, No. 6, pp. 503–507.

Miyasaka, Y., 1974, "On the Flow of a Viscous Free Boundary Jet on a Rotating Disk," *Bulletin of the JSME*, Vol. 17, No. 113, pp. 1475–1496.

Muzhilko, A. A., Rifert, V. G., and Barabash, P. A., 1983, "Flow of Liquid Film Over the Surface of a Rotating Disk," *Heat Transfer—Soviet Research*, Vol. 15, No. 5, pp. 1–6.

Needham, D. J., and Merkin, J. H., 1987, "The Development of Nonlinear Waves on the Surface of a Horizontally Rotating Thin Liquid Film," *J. Fluid Mech.*, Vol. 184, pp. 357–379.

Rahman, M. M., Faghri, A., Hankey, W. L., and Swanson, T. D., 1990, "Computation of the Free Surface Flow of a Thin Liquid Film at Zero and Normal Gravity," *Numerical Heat Transfer*, Part A, Vol. 17, pp. 53–71.

Rauscher, J. W., Kelly, R. E., and Cole, J. D., 1973, "An Asymptotic Solution for the Laminar Flow of a Thin Film on a Rotating Disk," ASME JOURNAL OF APPLIED MECHANICS, Vol. 40, Paper No. 72-APM-38.

Watson, E. J., 1964, "The Radial Spread of a Liquid Jet Over a Horizontal Plane," *J. Fluid Mech.*, Vol. 20, Part 3, pp. 481–499.

Experimental Study of Boiling Heat Transfer From a Sphere Embedded in a Liquid-Saturated Porous Medium

V. X. Tung[1]

V. K. Dhir

Mechanical, Aerospace and Nuclear Engineering Department,
School of Engineering and Applied Science,
University of California, Los Angeles
Los Angeles, CA 90024-1597

Boiling heat transfer from a sphere embedded in a porous medium composed of nonheated glass particles was studied under steady-state and transient quenching conditions. In the experiments, the diameter of the nonheated glass particles forming the porous layers was varied parametrically. Freon-113 was used as the test liquid. Experimental results showed that the maximum heat flux increased monotonically with increasing glass particle diameter and approached an asymptotic value corresponding to the maximum heat flux obtained in a pool free of glass particles. It was also observed that the minimum heat flux was nearly insensitive to the particle size and the film boiling heat transfer coefficient increased slightly with decreasing particle size. In the nucleate boiling region, the heat transfer coefficient showed a much weaker dependence on wall superheat in the presence of particles. Transient data indicated that the surface temperature was not uniform during quenching. Therefore, different maximum heat fluxes were obtained depending on the location of the thermocouple whose temperature history was employed in recovering the transient boiling curve. However, for some applications, cooling rates predicted by imposing the steady-state boiling curve may not be in large error.

Introduction

Understanding of boiling heat transfer from bodies submerged in liquid-saturated porous media is of interest in many nuclear, chemical, and geophysical applications. For example, in a degraded core accident, the heat-generating solidified core material may be surrounded by nonheated structural debris. In the recovery mode, the rate of cooling will depend strongly on the permeability of the surrounding debris. The objective of the present work is an experimental study of boiling heat transfer from spheres submerged in liquid-saturated porous layers composed of nonheated spherical particles.

Several studies (Bradfield, 1967; Veres and Florschuetz, 1971; Ded and Lienhard, 1972; Dhir, 1978) of pool and forced flow boiling of saturated and subcooled liquids on spheres have been reported in the past. Veres and Florschuetz (1971) compared the transient and steady-state boiling heat fluxes using oxidized copper spheres in Freon-113. Their experiments showed that the maximum and minimum heat fluxes were highly dependent upon the condition of the test surface. Heavily oxidized surfaces tended to yield higher maximum and minimum heat fluxes. On a given surface, the film boiling heat transfer coefficients obtained in steady-state tests and during quenching were about the same. However, the nucleate boiling heat fluxes in steady-state tests in which induction heating was used were much higher than those obtained during quenching. The steady-state peak heat flux was as much as 50 percent higher than the corresponding transient peak heat flux. The difference was tentatively attributed to inherent features of induction heating.

Recently, Bui and Dhir (1985) and Liaw and Dhir (1986) have conducted steady-state and quenching experiments on the same vertical surface. The magnitude of the steady-state maximum heat flux was observed to depend on the contact angle. The transient peak heat fluxes on partially wetted surfaces were found to be much lower than the steady-state heat fluxes obtained in the absence of induction heating. However, the difference between the steady-state and the transient heat fluxes decreased as the contact angle became small. In fact, with Freon-113, the steady-state and transient maximum heat fluxes were about the same. Even though the reasons for the transient heat fluxes being lower than the steady-state heat fluxes are not well understood at present, the experiments showed that the differences resulted from the manner in which the maximum heat flux condition was approached and may not be a result of induction heating as postulated by Veres and Florschuetz (1971). Bergles and Thompson (1970) also found the maximum heat fluxes obtained during quenching to be lower than those obtained in steady-state experiments. However, the experiments were not performed on the same heating surface in their work.

A hydrodynamic model for maximum heat fluxes during saturated pool boiling on spheres was developed by Ded and Lienhard (1972). The model was based on the number of jets that could be accommodated on the sphere and the velocity at which these jets became unstable. Their expression for the maximum heat flux on large spheres ($R' > 4.3$) is

$$q_{\max} = 0.11\rho_v h_{fg}[\sigma g(\rho_l - \rho_v)/\rho_v^2]^{1/4} \quad (1)$$

Subcooled pool boiling of water on a 60-mm-dia chrome-plated copper sphere was studied by Bradfield (1967). He noted a significant increase in maximum and minimum heat fluxes with liquid subcooling. Dhir (1978) investigated transition boiling of water on copper and silver spheres under saturated and subcooled forced flow conditions. He observed significant distortions in the boiling curves obtained with subcooled forced flow. The maximum heat flux obtained under transient mode showed a nonlinear dependence on liquid subcooling compared

[1]Present address: Department of Mechanical Engineering, California State University, Long Beach, CA.

Contributed by the Heat Transfer Division and presented at the 23rd National Heat Transfer Conference, Denver, Colorado, August 4–7, 1985. Manuscript received by the Heat Transfer Division April 12, 1989; revision received November 20, 1989. Keywords: Boiling, Phase-Change Phenomena, Porous Media.

to a linear dependence predicted by correlations based on steady-state data obtained on other electrically heated geometries. Here it must be mentioned that the boiling heat flux data in transient experiments reported in the above-referenced studies were reduced under the assumption that the boiling process was uniform on the surface of the sphere. However, this is generally not true, especially for large spheres, as shown by Purohit (1977), Unger (1981), and Irving and Westwater (1986).

Only a few studies of boiling heat transfer from surfaces placed in unheated liquid-saturated porous media have been reported in the literature. Schrock et al. (1970) studied boiling heat transfer from cylinders placed in water-saturated Monterey Amber (12 mesh $\simeq$ 1500 μM) and Ottawa Silica (90 mesh $\simeq$ 160 μM) sands. With particles, nucleate boiling curves were found to show hysteresis. Also, in comparison to pool boiling, a much weaker dependence of nucleate boiling heat flux on wall superheat was observed in the presence of the particles. Fukusako et al. (1986) have made an experimental investigation of transition and film boiling heat transfer from a 60-mm-dia horizontal disk supporting a liquid-saturated porous layer. In the experiments, steel, glass, and worked iron particles ranging in size from 1 to 16.5 mm in diameter were used. Freon-11 and Freon-113 were used as the test liquids and the depth of the porous layer was varied from 10 to 300 mm. Fukusako et al. found that with 1 to 2-mm-dia particles, the heat flux increased monotonically with temperature while going from nucleate to film boiling. In nucleate boiling, the slope of the boiling curve was less steep with smaller particles than that obtained with large particles or without particles. The film boiling heat transfer coefficient data were correlated with an expression for laminar film boiling on a sphere after modifying it to include the ratio of vapor to solid thermal conductivity and the ratio of particle diameter to layer height. Very recently Orozco et al. (1988) have analyzed film boiling from cylinders and spheres embedded in liquid-saturated porous media. The underlying assumption of their model is that vapor film experiences a Darcy type of flow.

In the present work, both steady-state and transient boiling heat fluxes on a 19-mm-dia stainless sphere embedded in a liquid-saturated porous medium are studied. The size of the glass particles forming the nonheated porous media is varied from 19 to 2.9 mm. In the experiments, Freon-113 is used as the test liquid. Induction heating is used in the steady-state experiments. Since the cooling process may be transient in many applications, results of a typical transient experiment are also reported.

Experimental Apparatus

A schematic diagram of the experimental apparatus is shown in Fig. 1(*a*). The main components of the experimental setup are a Pyrex beaker 87 mm in i.d., and 185 mm in height, an induction coil, a Freon-113 reservoir, and a 19-mm-dia 304 stainless steel sphere. The porous layers surrounding the stainless steel sphere were formed with glass particles varying in size from 2.9 mm to 19 mm in diameter. The Pyrex beaker and Freon reservoir were heated from below by auxiliary heaters to maintain a saturated pool of Freon-113. The vapor exiting the beaker was vented into a fume hood. The stainless steel sphere was located at the center of the Pyrex beaker 73 mm from the bottom. The sphere was instrumented with two 32-gage chromel-alumel thermocouples located at the center and at 0.76 mm from the surface of the sphere. Details of thermocouple installation are shown in Fig. 1(*b*). A third thermocouple was immersed in the beaker to determine the pool temperature. All three thermocouples had individual reference junctions placed in an ice bath. Thermocouple outputs were continuously recorded on a multichannel *x–y* recorder. The steady-state values of the thermocouple outputs were also noted on a digital voltmeter.

Power Calibration. Prior to the steady-state experiments, a power calibration was performed to determine the heat flux from the sphere corresponding to a particular setting on the Variac that controls the power input to the induction coil. By noting the rate at which the sphere temperature increased in air and using a lumped capacity method, the heat flux at a particular power setting can be obtained as

$$q = \frac{1}{6}\rho_s c_{ps} D_s \frac{dT}{dt} + q_{\text{loss}} \tag{2}$$

The heat loss, q_{loss}, due to natural convection and radiation was obtained experimentally by letting the sphere cool down after heating and noting the rate at which the sphere temperature decreased with time. In all cases, the heat loss was less than 10 percent of the total heat flux. Calibration of the surface

Nomenclature

A_s = surface area of the heated sphere, m^2
c_p = specific heat, J/kg-K
D = diameter, m
g = gravitational acceleration = 9.81 m/s^2
Gr_D = Grashof number = $g\beta\Delta T D_s^3/\nu_l^2$
h = local heat transfer coefficient, W/m^2-K
h_∞ = local heat transfer coefficient in the absence of particles
$\bar{h}$ = average heat transfer coefficient, W/m^2-K
h_{fg} = latent heat of vaporization, J/kg
j = superficial velocity, m/s
k = thermal conductivity, W/m-K
Nu = Nusselt number = hD_s/k
Pr = Prandtl number = ν/α
q = heat flux, W/m^2
R = radius of the heater, m
R' = dimensionless radius of the heater $= R/\sqrt{\dfrac{\sigma}{g(\rho_l-\rho_v)}}$
r_1, r_0 = chord radii at ϕ and ϕ_0, respectively
T_p = surface temperature of glass particles
T_s = surface temperature of heated sphere
α = thermal diffusivity, m^2/s
β = thermal expansion coefficient, K^{-1}
δ = vapor film thickness, m
ΔT = temperature difference $= T_s - T_{\text{sat}}$
ϵ = porosity of the porous layer $\approx$ 0.39
μ = dynamic viscosity, kg/m-s
ν = kinematic viscosity, m^2/s
ρ = density, kg/m^3
σ = surface tension, N/m

Subscripts

b = bubble
l = liquid
p = nonheated glass particles
s = heated sphere
v = vapor
∞ = refers to the area away from the points of contact between nonheated particles and the test sphere

heat flux as a function of surface temperature and power input to the coil could thus be made. It should be noted that the value of dT/dt employed in equation (2) was taken over a time interval during which both the center and surface thermocouples displayed the same rate of temperature rise. Observation of the same rate of temperature rise with both thermocouples indicated that the temperature profile in the sphere was fully developed.

Preparation of Sphere Surface. Three sets of experiments were performed with different surface conditions of the stainless steel sphere. In the first set of experiments, the sphere was buffed and polished to a mirrorlike surface finish at the beginning of each experiment. In the second set of experiments, the sphere was polished and then heated in air for 5 h at a temperature of 550°C to form an oxide layer on the surface of the sphere prior to the experiments. In the third set of experiments, the sphere was polished and then copper plated to form a layer of copper about 50 μm thick on the sphere surface. In all cases, the sphere was cleaned with acetone before each experiment.

Experimental Procedure. At the beginning of each experiment, the space around the stainless steel sphere was filled with uniformly sized glass particles and the porous layer was saturated with Freon-113. The power input to the auxiliary heaters was adjusted to maintain the bed at saturation temperature with a minimum level of disturbance caused by boiling at the bottom of the Pyrex beaker. Then the power input to the induction coil was gradually increased to establish the steady-state nucleate boiling curve up to the maximum heat flux. At each power setting, steady-state temperatures given by the thermocouples embedded in the sphere were recorded. The temperature given by the thermocouple located at 0.76 mm from the surface was taken to be the surface temperature. After occurrence of the maximum heat flux, the boiling process was allowed to shift to film boiling. Once the sphere surface was about 50 K above the minimum film boiling temperature, power was gradually decreased in small steps and steady-state values of temperature were recorded until the film collapsed and the process reverted to nucleate boiling. The minimum heat flux condition could thus be established to within ±6 percent. Thereafter, the power was increased again to re-establish film boiling and data at higher wall superheats were obtained. It should be noted that this procedure was designed so that the surface deposit resulting from Freon decomposition was minimized. During each run, the liquid level in the beaker was maintained at its original level by continuous addition of Freon-113 from the reservoir. The temperature of the liquid and the porous medium was brought to the saturation temperature of Freon-113 by using the auxiliary heaters.

Several quenching experiments were also performed. In these experiments, the sphere was heated to about 400°C in a Freon-saturated porous medium. Thereafter, power to the induction coil was cut off. The temperature-time traces of the thermocouple outputs were recorded on the x–y recorder. The temperature history of the thermocouple near the surface was then used as a boundary condition in the solution of the one-dimensional transient conduction equation to recover the boiling curve.

The uncertainty in the measured heat flux results from the errors in the calculation of the input heat flux and the heat loss rate. As discussed by Tung (1988), the maximum uncertainty in the heat flux is calculated to be ±6 percent. The uncertainty in the measured temperatures results from the accuracy of the multimeter and the fluctuations caused by the variation in the magnetic field. The accuracy of the multimeter readings was 0.01 mV or 0.25°C. The maximum peak-to-peak variation was found to be about 6 percent of the average emf. Thus the temperature measurements are accurate to 3 percent or 0.25°C, whichever is larger.

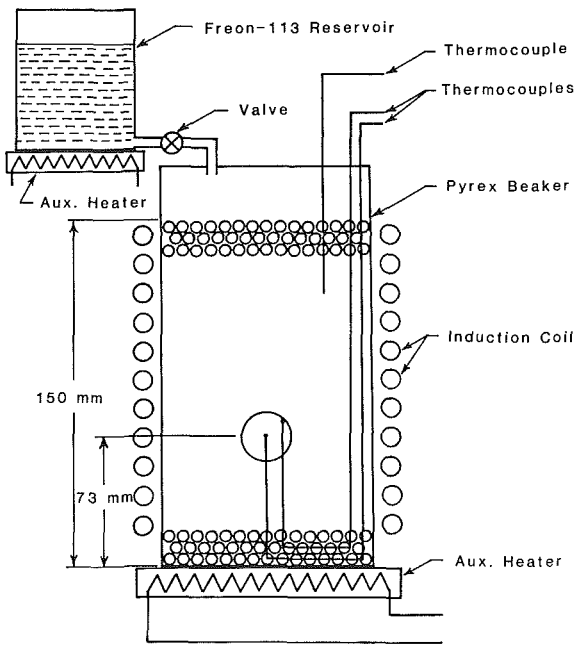

Fig. 1(*a*) Schematic diagram of experimental setup

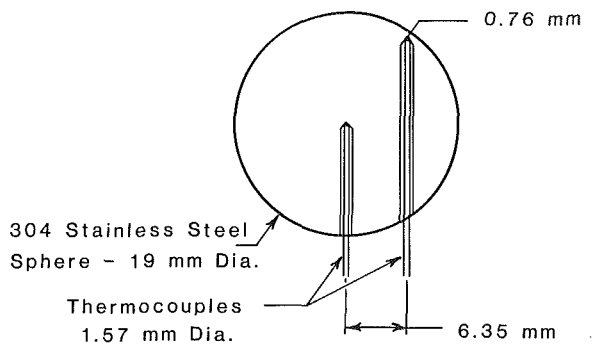

Fig. 1(*b*) Details of thermocouple installations

Results and Discussion

Steady-state and transient pool boiling data were obtained with polished and oxidized 19-mm-dia stainless steel spheres. The nonheated porous media surrounding the spheres were formed with 2.9, 5.8, 9.9, 14.6, and 19-mm-dia glass particles. The porosity of the porous layer in these experiments was about 0.39. Experiments were also conducted in a saturated pool of liquid free of particles. The data obtained in these experiments are referred to as $D_p \rightarrow \infty$. In all experiments, Freon-113 was used as the test liquid.

Boiling Curves. Figure 2 shows the steady-state nucleate and film boiling portions of the boiling curves obtained with a clean, polished test sphere. The permeability of the surrounding material appears to have little or no influence on the magnitude of the minimum wall superheat and the minimum film boiling heat flux. However, film boiling heat transfer is slightly enhanced by the particles. The enhancement is probably caused by thinning of the vapor film near the points of contact. Data obtained with a liquid pool free of particles are within 10 percent of the steady-state and transient film boiling data obtained by Veres and Florschuetz (1971) using a copper sphere. The minimum heat flux with and without surrounding particles is about 1.25 W/cm^2.

In nucleate boiling, hysteresis is observed at low wall superheats when the pool is free of particles. With increasing power, natural convection persists for wall superheats up to

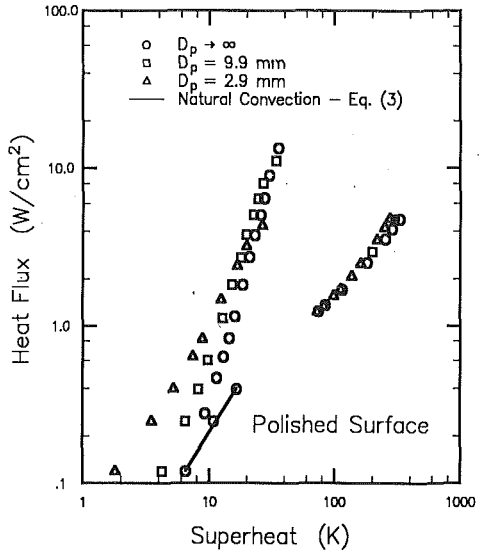

Fig. 2 Steady-state boiling curves—polished surface

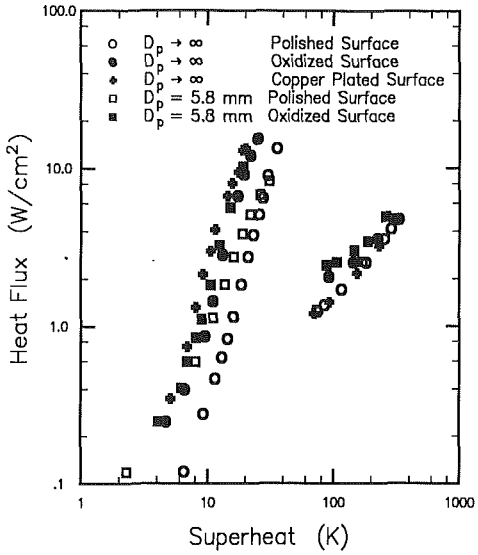

Fig. 3 Effect of surface condition on boiling heat fluxes

20 K. In the absence of particles, the observed values of natural convection heat transfer coefficients compare quite well with the correlation originally proposed by Yuge for air (1960) and as shown by the solid line

$$\mathrm{Nu} = 2 + 0.43(\mathrm{Gr}_D\mathrm{Pr})^{1/4} \tag{3}$$

Upon nucleation, the surface temperature suddenly drops. However, as the heat flux is decreased, nucleate boiling continues to prevail at much lower surface superheats. The presence of particles around the sphere results in earlier nucleation and hence a higher rate of heat transfer. The locations where the particles contact the sphere probably act as nucleation sites and these sites become activated very early. The wall superheat at which nucleation occurs with 2.9-mm particles is less than 2 K. The number of nucleation sites increases as the particle size is decreased. This in turn results in an increase in heat transfer with reduction in the size of the particles. At higher heat fluxes, when the vapor generation rate is high, the particles tend to limit the outflow of vapor. Consequently, the maximum heat flux is observed to decrease monotonically with decreasing particle size. In comparison, the fully developed nucleate boiling heat transfer coefficients obtained by Schrock et al. (1970) with cylinders embedded in 90-mesh Ottawa sand were nearly independent of wall superheat.

A comparison of the steady-state boiling curves obtained under different surface conditions is made in Fig. 3. The presence of the oxide layer is seen to shift the nucleate boiling curves to the left of those obtained with and without particles. This result is different from the findings of Bui and Dhir (1985) and Liaw and Dhir (1986). In those studies, an increase in wall superheat at a given heat flux was observed as the copper surface became more wettable. Since at low wall superheats the effect of the oxide layer on heat flux is seen to be comparable to that of the surrounding particles, it appears that the modification of the steel surface due to oxidation has overshadowed the effect of wettability on nucleation. The rough oxide layer probably has resulted in the formation of some larger cavities that nucleate at lower superheats. The improvement in surface wettability, however, has resulted in an increase of 17–20 percent in the maximum heat flux with and without particles. In the absence of particles ($D_p \to \infty$), the maximum heat flux on a polished sphere is only 13.5 W/cm^2, while that obtained with an oxidized copper sphere is about 15.5 W/cm^2. It should be pointed out, however, that Freon-113 wets oxidized copper surfaces well while the contact angle for polished stainless steel surfaces is about 25 deg. This indicates that the maximum heat flux decreases as the surface becomes non-

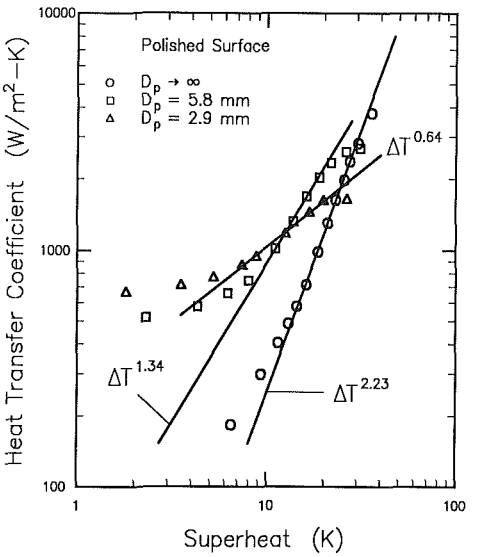

Fig. 4 Nucleate boiling heat transfer coefficient on a polished sphere

wetting. This is consistent with Bui's observations (1984). Interestingly, Bergles and Thompson (1970) obtained a steady-state maximum heat flux of 15–16 W/cm^2 on a horizontal stainless steel cylinder submerged in a pool of saturated Freon-113. Equation (1) of Ded and Lienhard (1972) predicts a maximum heat flux of 17.5 W/cm^2.

The oxide layer appears to have a strong influence on the film boiling part of the boiling curve near the minimum heat flux. The minimum heat flux in the presence of the oxide layer is about 80 percent higher than that for the polished sphere. The particles seem to magnify the effect of the oxide layer, probably by causing more liquid-solid contacts. At higher superheats, when the propensity for liquid-solid contacts diminishes, the film boiling heat fluxes on the oxidized sphere approach those for the polished sphere. The copper plating of the sphere seems to have little or no effect on film boiling heat transfer.

Correlation of Data

Nucleate Boiling. Figure 4 shows the dependence of heat transfer coefficients on wall superheat for a polished sphere with and without glass particles in the surrounding region. In fully developed nucleate boiling, the heat transfer coefficient increases with wall superheat as $\Delta T^{2.23}$. This dependence is

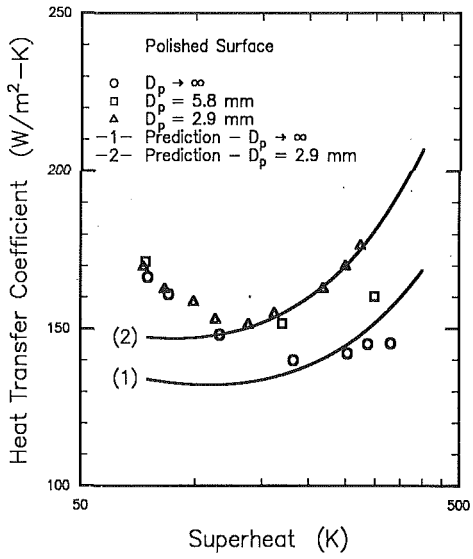

Fig. 5 Film boiling heat transfer coefficient on a polished sphere

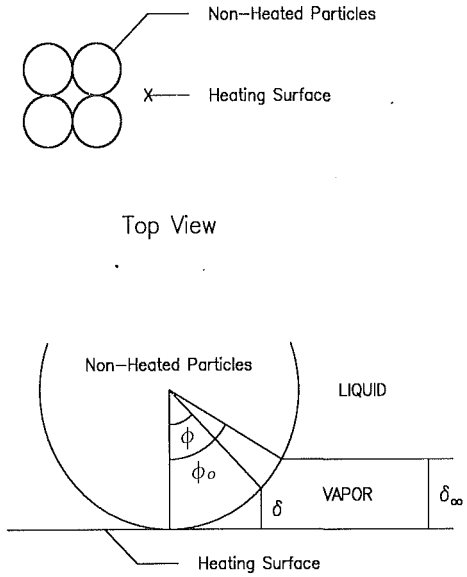

Fig. 6 Top and side views of particle-surface contact

similar to that reported in the literature for pool boiling on polished surfaces. With 2.9-mm particles in the surrounding region, the nucleate boiling heat transfer coefficient at low wall superheats is nearly independent of ΔT. This supports the argument advanced earlier that particles lead to early nucleation everywhere on the surface of the sphere. The number density of the nucleation sites appears to remain fairly constant at these superheats. At higher wall superheats, the heat transfer coefficient increases as $\Delta T^{0.64}$. This dependence is also much weaker than that observed in the absence of particles. The data clearly show that to make headway in developing a correlation for nucleate boiling, it is important to have a priori knowledge of the cavity sizes and their distribution. In the present work, no attempt is made in this direction.

Film Boiling. Film boiling heat transfer appears to be enhanced slightly by the presence of particles. At a superheat of 300 K the heat flux with 2.9-mm particles is about 20 percent higher than that obtained without particles. The film boiling heat transfer coefficients for the case of $D_p \to \infty$ and D_p = 2.9 mm are plotted in Fig. 5 as open circles and triangles, respectively. For laminar film boiling on a sphere submerged in a pool of saturated liquid, analysis such as that performed by Dhir and Lienhard (1971) for film condensation yields an expression for Nusselt number as

$$\mathrm{Nu}_\infty = \frac{\bar{h}_\infty D_s}{k_v} = 0.815 \left[\frac{\rho_v(\rho_l - \rho_v) g h_{fg}^* D_s^3}{\mu_v k_v \Delta T} \right]^{1/4} \quad (4a)$$

where

$$h_{fg}^* = h_{fg} + 0.68 C_{pv} \Delta T \quad (4b)$$

Equation (4) was derived with the assumption that inertia and convective terms can be ignored in the momentum and energy equations, respectively, and that a slip condition exists at the vapor–liquid interface. If it is assumed that the vapor dome of the upper stagnation point of the sphere occupies 15 percent of the surface area and no heat transfer takes place under this dome, the numerical constant in equation (4*a*) is reduced to 0.69. On the other hand, if the interface is assumed to be rigid, and no correction is made for the presence of a vapor dome, the numerical constant in equation (4*a*) becomes 0.68. At low pressures, the rigid interface condition is more appropriate since the ratio $\mu_v \rho_v / \mu_l \rho_l$ is very small. Generally it is agreed that the existence of ripples on the interface will enhance heat transfer and compensate for the reduction in heat transfer resulting from a partially rigid interface. When the sphere is surrounded by particles, the free area of the interface is limited by the discrete location of contacts between the heated sphere and the surrounding particles. As a result, the interfacial waves may not develop, especially if the diameter of the surrounding particles is much smaller than that of the heated sphere. Also, in the presence of particles, the area of the base of the bubbles at the bubble release sites cannot exceed the heater surface area in the pores formed at the point of contact. Thus, contrary to the case of a sphere submerged in a pool of liquid, little reduction for the insulation effect of the vapor dome needs be made in the average heat transfer coefficient. As such, a constant of 0.68 in equation (4*a*) should be employed in the presence of surrounding particles. It should also be noted that the numerical constant 0.68 does not include a correction for additional heat transfer at the points of contact between the particles and the heated sphere. Thinning of the vapor film occurs at these points of contact, resulting in a slight enhancement of heat transfer. Figure 6 shows the top and side views of four adjacent glass particles resting on the sphere surface. In carrying out calculations for the additional heat transfer, the following assumptions have been made in addition to those made in deriving equation (4):

(*i*) The vapor film thickness ($\approx 10^{-4}$ m) is much smaller than the smallest diameter of the nonheated glass particles employed in this work. With such a thin film, the Darcy effect is negligible.

(*ii*) The vapor film thickness, δ_∞, in the open area far from the points of contact is the same as that on a sphere in the absence of surrounding particles.

(*iii*) The radius of curvature of the test sphere is much larger than that of the surrounding particles.

With the angle ϕ defined in Fig. 6, the surface temperature of the nonheated glass particles is bounded by the following limits:

$$T_p(\phi = 0) = T_s \text{ and } T_p(\phi = \phi_0) = T_{\text{sat}} \quad (5)$$

Determination of the detailed variation of T_p would require a solution of the conduction equation in the glass particles. However, such a procedure is uncalled for since one is only interested in an approximate evaluation of a small increase in heat transfer coefficients. By expanding the temperature of the glass

particles in a Taylor series with respect to sin ϕ and truncating all higher order terms, the variation of T_p can be approximated as

$$T_s - T_p = (T_s - T_{sat}) \frac{\sin \phi}{\sin \phi_0} \tag{6}$$

where the angle ϕ_0 is given by

$$\phi_0 = \cos^{-1}\left(1 - 2\frac{\delta_\infty}{D_p}\right) \tag{7}$$

The film thickness near the point of contact is obtained from the geometry shown in Fig. 6 as

$$\delta = \frac{D_p}{2}(1 - \cos \phi) \tag{8}$$

The heat transfer rate near the point of contact then can be obtained as

$$Q_p = \int_0^{r0} \frac{k_v}{\delta} (T_s - T_p) 2\pi r dr \tag{9}$$

By substituting equations (6) and (8) into equation (9) one obtains

$$Q_p = \frac{\pi}{2} k_v D_p \Delta T \left[\frac{\phi_0}{\sin \phi_0} + \cos \phi_0 + 2\right] \tag{10}$$

For particles arranged in a cubic lattice, heat transfer from the heater surface area away from the point of contact can be found by

$$Q_0 = \frac{k_v}{\delta_\infty} \Delta T D_p^2 \left(1 - \frac{\pi}{4} \sin^2 \phi_0\right) \tag{11}$$

By adding the rates of heat transfer from equations (10) and (11), the average heat transfer from one cell is obtained as

$$h = \frac{\pi}{4}\frac{k_v}{\delta_\infty}(1 - \cos\phi_0)\left[\frac{\phi_0}{\sin \phi_0} + \cos \phi_0 + 2\right] + \frac{k_v}{\delta_\infty}\left(1 - \frac{\pi}{4}\sin^2\phi_0\right) \tag{12}$$

For small $\phi_0 (D_p \ll D_s)$, equation (12) reduces to

$$\frac{h}{h_\infty} = 1 + \frac{\pi}{4}(1 - \cos \phi_0)\left(1 + \frac{\phi_0}{\sin \phi_0}\right) \approx 1 + \pi \frac{\delta_\infty}{D_p} \tag{13}$$

where

$$h_\infty = \frac{k_v}{\delta_\infty}$$

If the particles are assumed to be arranged in a rhombic instead of a cubic lattice, the constant in equation (13) will change from π to $2\pi/\sqrt{3}$. It should be noted from equation (13) that the enhancement in heat transfer depends on the ratio between the vapor film thickness δ_∞ and particle diameter D_p. The enhancement increases as the film becomes thicker relative to the size of the surrounding particles. However, this enhancement should only be considered a local value since the vapor film thickness varies along the surface of the test sphere and is not a constant. In order to find the average heat transfer enhancement, the local increase in heat transfer must be integrated over the whole surface of the test sphere. In the absence of surrounding particles, the average heat transfer coefficient on the test sphere is obtained as

$$\bar{h}_\infty = \frac{1}{A_s}\int_{A_s} h_\infty dA_s \tag{14}$$

where A_s is the area of the test sphere. In the presence of the surrounding particles, the average heat transfer coefficient can be found by integrating the local value of h obtained from equation (13) as

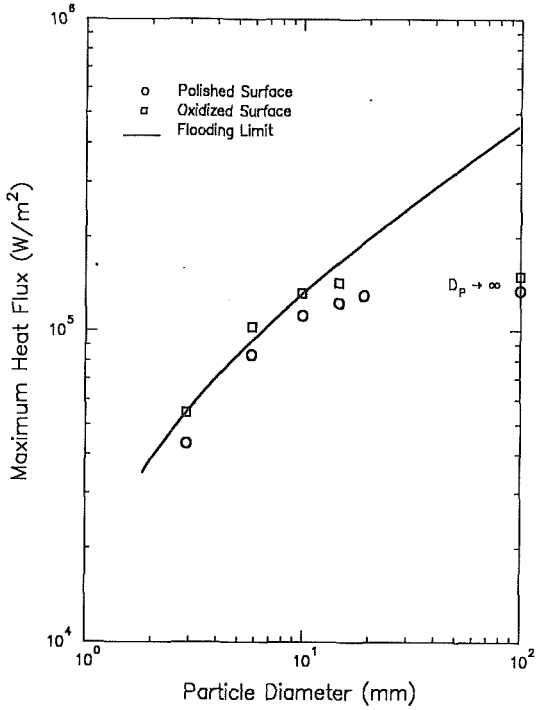

Fig. 7 Variation of maximum heat flux with particle diameter

$$\bar{h} = \frac{1}{A_s}\int_{A_s} h_\infty \left(1 + \pi\frac{\delta_\infty}{D_p}\right) dA_s = \bar{h}_\infty + \frac{1}{A_s}\int_{A_s} h_\infty \pi \frac{\delta_\infty}{D_p} dA_s \tag{15}$$

By substituting $h_\infty = k_v/\delta_\infty$ into equation (15), the average enhancement for heat transfer coefficient in the presence of particles can be obtained as

$$\bar{h} - \bar{h}_\infty = \pi \frac{k_v}{D_p} \tag{16}$$

In obtaining equation (16), k_v has been assumed to be constant and is evaluated at the mean film temperature. At a surface superheat of 300 K the heat transfer coefficient enhancement calculated by using equation (16) is about 31 W/m^2-K for 2.9-mm particles. This value corresponds almost exactly to the enhancement shown in Fig. 5. At a surface superheat of 100 K the calculated enhancement is about 15 W/m^2-K, which is also approximately the same as that shown by the data. Figure 5 also shows a comparison of the predictions with present data. It must be pointed out that the heat transfer enhancement as given by equation (16) is independent of the thermal conductivity of the nonheated particles. As long as this conductivity is larger than that of the vapor, the temperature variation in the glass particles will not be far from the first-term expansion given by equation (6) and equation (16) should hold well.

Maximum Heat Flux. Figure 7 shows the dependence of maximum heat flux obtained under steady-state conditions on the diameter of the surrounding glass particles. In Fig. 7, open circles and squares represent the maximum heat flux on polished and oxidized spheres, respectively.

It is observed that the maximum heat flux increases monotonically with particle diameter and attains an asymptotic value corresponding to that for peak heat flux in the absence of particles ($D_p \to \infty$). The present experiments are well suited to determine the location at which the limiting conditions for maximum heat flux occur. Three possible locations for the limiting conditions are:

(*i*) surface of the sphere

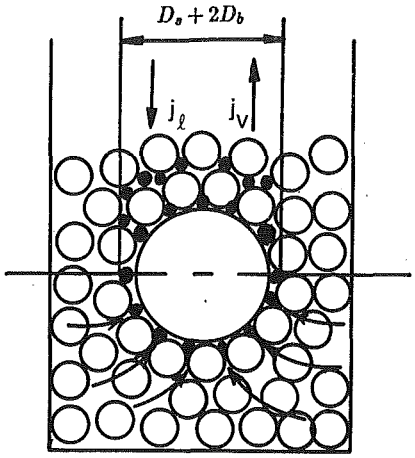

Fig. 8 Flow configuration in nucleate boiling

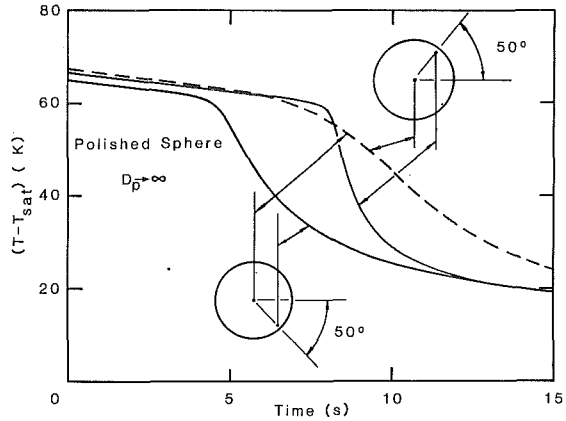

Fig. 9 Temperature of the sphere during quenching

(*ii*) the porous layer above the sphere

(*iii*) the free surface of the porous layer, i.e., the pool

The last location is easily ruled out since experiments in which a disk was placed on the free surface above the sphere showed no effect on the magnitude of the maximum heat flux. The disk simply blocked the escape of vapor from the free surface above the sphere and diverted it into the surrounding area.

To ascertain the occurrence of limiting conditions in the porous layer above the sphere, information on the countercurrent flooding limits in the porous layers is needed. Based on air-water data obtained with porous layers of several size particles, Marshall and Dhir (1984) suggested the following flooding correlation:

$$j_l^{*1/2} + j_v^{*1/2} = 0.875 \tag{17}$$

where

$$j_l^* = j_l[6\rho_l(1-\epsilon)/g(\rho_l - \rho_v)\epsilon^3 D_p]^{1/2} \tag{18a}$$

$$j_v^* = j_v[6\rho_v(1-\epsilon)/g(\rho_l - \rho_v)\epsilon^3 D_p]^{1/2} \tag{18b}$$

In equation (18), j_l and j_v are the superficial velocities of liquid and vapor, respectively, assuming that no particles are present in the flow area.

The envisioned flow configuration in the present experiments with small particles is shown in Fig. 8. If q_{max} is the heat flux on the sphere surface, the superficial velocity of the vapor can be written as

$$j_v = \frac{4q_{max}D_s^2}{\rho_v h_{fg}(D_s + 2D_b)^2} \tag{19}$$

where D_s is the diameter of the sphere and D_b is the diameter of the bubbles leaving the sphere surface. Since the lower half of the sphere has an easy access to liquid, only the upper half of the sphere needs be considered fed from the top. With this assumption, the superficial velocity of the liquid can be written as

$$j_l = \frac{2q_{max}D_s^2}{\rho_l h_{fg}(D_s + 2D_b)^2} \tag{20}$$

If countercurrent flooding is the limiting mechanism for maximum heat fluxes, the superficial velocities given in equations (19) to (20) must correspond to the flooding limit given by equation (17) or that obtained from the hydrodynamic model proposed by Tung and Dhir (1988). The resulting maximum heat fluxes are plotted in Fig. 7 as the solid line. It can be seen that, within the uncertainty of the data, maximum heat fluxes obtained at small particle diameters ($D_p \leq 10$ mm) appear to be controlled by the countercurrent flooding limit. At large particle diameters ($D_p \geq 10$ mm) the countercurrent flooding limit is much higher than the observed maximum heat fluxes. Hence it can be concluded that the limiting mechanism for this case occurs at the heated surface.

Since the maximum heat flux observed on the heated sphere with particles greater than 10 mm in diameter is about the same as that without particles and continuous vapor escape paths (jets) may not immediately form in the presence of particles, it can be inferred that maximum heat flux in the absence of particles may not be the result of instability of vapor jets away from the surface of the heated sphere.

Transient Cooling. In one of the intended applications of this work (cooling of a degraded nuclear reactor core), the sphere surface temperature will be a function of time. As such, the sphere surface will experience different modes of boiling: film boiling followed by transition boiling, nucleate boiling, and eventually single-phase convection. To assess the applicability of steady-state boiling data to a transient process, a few quenching experiments were conducted.

Figure 9 shows the time dependence of the measured center temperature and the temperature near the surface during quenching of a polished sphere. The surface thermocouples are located at an angle of 50 deg above and below the equator. It is seen that the center temperature is always higher than that given by the lower surface thermocouple. Just prior to quenching of the upper portion of the sphere, the center thermocouple drops below the value indicated by the upper surface thermocouple. This indicates that the lower part of the sphere has already been quenched and at a particular time different modes of boiling are present on the sphere surface. This is in contrast to the steady-state case for which the same boiling mode exists everywhere on the sphere. Near the occurrence of local maximum heat flux, the temperature time gradient shown by the lower surface thermocouple is much smaller than that for the upper thermocouple. This behavior suggests that the hotter portion of the sphere above the lower thermocouple tends to supply heat to the colder region, thereby reducing the observed temperature time gradient recorded by the lower thermocouple. Exactly the reverse is true for the upper surface thermocouple.

Figure 10 shows a comparison between the boiling curves obtained under steady-state and quenching conditions. The transient boiling curves are obtained by using the surface temperature data shown in Fig. 9 as a boundary condition in solving the conduction equation and assuming that the surface temperature is uniform everywhere on the sphere during quenching. Such an assumption is obviously incorrect for a relatively large sphere made of stainless steel having fairly low thermal conductivity. Hence neither of the curves by itself accurately represents the average boiling curve for the sphere. The maximum heat flux corresponding to the data for the upper surface thermocouple is 22 W/cm^2, while that corresponding to the lower thermocouple is only 10.5 W/cm^2. Such

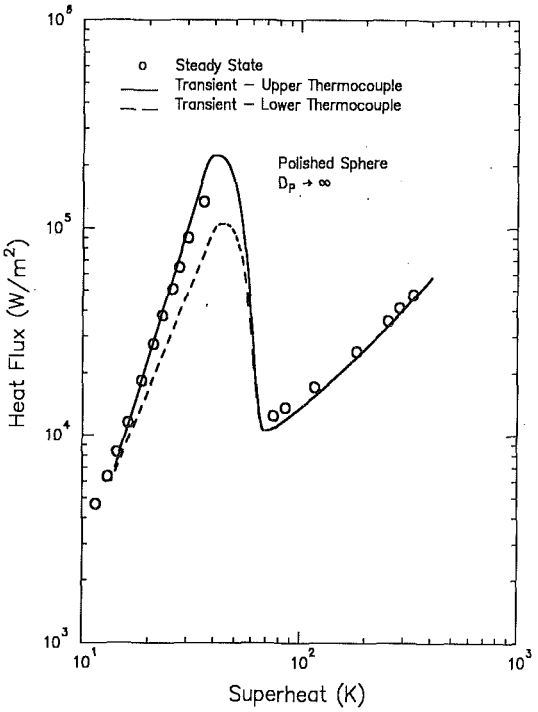

Fig. 10 Comparison of steady-state and transient boiling curves

a large difference indicates that the local and global boiling curves for the surface must not be the same. This limitation appears to be a manifestation of early quenching of the lower part of the sphere. As such, it will be most severe for large bodies made of low-thermal-conductivity materials. At very low heat fluxes typical of film boiling, data obtained under both steady-state and transient conditions seem to overlap each other. This suggests that the surface temperature is indeed uniform in film boiling. However, such a conclusion cannot be made with respect to nucleate boiling, especially at higher heat fluxes. Nevertheless, the steady-state data are approximately bounded by the transient curves obtained from the temperature histories for upper and lower thermocouples. Thus, in applications such as during quenching of a degraded nuclear reactor core, engineering estimates of the cooling rate of not very large spheres can be obtained by assuming that the sphere temperature is uniform and that the steady-state boiling curve provides the necessary boundary condition at the surface.

Finally, a few comments must be made about the use of induction heating in the present steady-state experiments. As discussed in the section on the experiments, calibration of the input heat flux was made as a function of power setting and the sphere temperature. The calibration represents the average input heat flux over the sphere since some self-shielding near the upper and lower stagnation points of the sphere can occur. The close agreement between the transient and steady-state film boiling data and between the natural convection data and existing correlation ensures that power calibration and temperature measurements are correct within a few percent of uncertainty. The induction frequency of 450 kHz is several orders of magnitude higher than the bubble frequency and should have no effect on the heat removal rate in a dielectric liquid such as Freon-113.

Conclusions

(*i*) The maximum heat flux on a sphere embedded in an unheated porous medium is observed to decrease with decreasing particle size. The minimum heat flux is found to be nearly independent of the particle size.

(*ii*) The film boiling heat transfer coefficient increases slightly with decreasing particle size. The enhancement was found to be inversely proportional to the particle size.

(*iii*) In the presence of particles, the nuclear boiling heat transfer coefficient shows a much weaker dependence on wall superheat. The heat transfer coefficient in fully developed nucleate boiling varied as $\Delta T^{0.64}$ in the presence of 2.9-mm particles. In the absence of particles it varied as $\Delta T^{2.23}$.

(*iv*) The limiting conditions for maximum heat flux were found to occur near the surface of the test sphere when the diameter of glass particles surrounding the 19-mm-dia heated sphere exceeded 10 mm. The countercurrent flooding limit in the porous layers appeared to determine the maximum heat flux for smaller diameter particles.

(*v*) The surface conditions were found to have some influence on the maximum heat flux on a sphere irrespective of the presence of particles.

Acknowledgments

The authors wish to acknowledge the Electric Power Research Institute of Palo Alto, CA, for partial financial support of this research project.

References

Bergles, A. E., and Thompson, W. G., 1970, "The Relationship of Quench Data to Steady State Pool Boiling Data," *Int. J. Heat Mass Transfer*, Vol. 13, pp. 55–68.

Bradfield, W. S., 1967, "On the Effect of Liquid Subcooling on Wall Superheat in Film Boiling," ASME JOURNAL OF HEAT TRANSFER, Vol. 89, pp. 269–270.

Bui, T. D., 1984, "Film and Transition Boiling Heat Transfer on Vertical Surfaces," Ph.D. Dissertation, University of California, Los Angeles, CA.

Bui, T. D., and Dhir, V. K., 1985, "Transition Boiling Heat Transfer on a Vertical Surface," ASME JOURNAL OF HEAT TRANSFER, Vol. 107, No. 4, pp. 756–763.

Ded, J. S., and Lienhard, J. H., 1972, "The Peak Pool Boiling Heat Flux From a Sphere," *AIChE Journal*, Vol. 18, No. 2, pp. 337–342.

Dhir, V. K., 1978, "Study of Transient Boiling Heat Fluxes From Spheres Subjected to Forced Vertical Flow," *Proc. 6th Int. Heat Transfer Conf.*, Toronto, Canada, Vol. 1, pp. 451–456.

Dhir, V. K., and Lienhard, J. H., 1971, "Laminar Film Condensation on Plane and Axisymmetric Bodies in Non-uniform Gravity," ASME JOURNAL OF HEAT TRANSFER, Vol 93, No. 1, pp. 97–100.

Fukusako, S., Komoriya, T., and Seki, N., 1986, "An Experimental Study of Transition and Film Boiling Heat Transfer in Liquid Saturated Porous Bed," ASME JOURNAL OF HEAT TRANSFER, Vol. 108, pp. 117–124.

Irving, M. E., and Westwater, J. W., 1986, "Limitations for Obtaining Boiling Curves by the Quenching Method With Spheres," *Proc. 8th Int. Heat Transfer Conf.*, San Francisco, CA, Vol. 4, pp. 2061–2066.

Liaw, S., and Dhir, V. K., 1986, "Effect of Surface Wettability on Transition Boiling Heat Transfer From a Vertical Surface," *Proc. 8th Int. Heat Transfer Conf.*, San Francisco, CA, Vol. 4, pp. 2031–2036.

Marshall, J. S., and Dhir, V. K., 1984, "Hydrodynamics of Counter-current Two-Phase Flow Through Porous Media," NUREG/CR-3995.

Orozco, J., Stellman, R., and Gutjahr, M., 1988, "Film Boiling Heat Transfer From a Sphere and a Horizontal Cylinder Embedded in a Liquid Saturated Porous Medium," ASME JOURNAL OF HEAT TRANSFER, Vol. 110, pp. 961–967.

Purohit, G. P., 1977, "Subcooled Film Boiling of Water From Spheres," M. S. Thesis, University of California, Los Angeles, CA.

Schrock, V. E., Fernandez, R. T., and Kesavan, K., 1970, "Heat Transfer From Cylinders Embedded in a Liquid Filled Porous Medium," *Proc. 4th Int. Heat Transfer Conf.*, Vol. VII, CT 3-6, pp. 1–11.

Tung, V. X., 1988, "Hydrodynamic and Thermal Aspects of Two-Phase Flow Through Porous Media," Ph.D. Dissertation, University of California, Los Angeles, CA.

Tung, V. X., and Dhir, V. K., 1988, "A Hydrodynamic Model for Two-Phase Flow Through Porous Media," *Int. J. Multiphase Flow*, Vol. 14, No. 1, pp. 47–65.

Unger, E. K., 1981, "Construction and Initial Testing of an Apparatus for Studying Boiling From a Heated Sphere," M.S. Thesis, University of Kentucky, Lexington, KY.

Veres, D. R., and Florschuetz, L. W., 1971, "A Comparison of Transient and Steady State Pool Boiling Data Using the Same Heating Surface," ASME JOURNAL OF HEAT TRANSFER, Vol. 93, No. 2, pp. 229–232.

Yuge, T., 1960, "Experiments on Heat Transfer From Spheres Including Combined Natural and Forced Convection," ASME JOURNAL OF HEAT TRANSFER, Vol. 82, pp. 214–220.

W. H. Parken[1]
Center for Building Technology,
National Bureau of Standards,
Washington, DC 20234

L. S. Fletcher
Thomas A. Dietz Professor.
Department of Mechanical Engineering,
Texas A&M University,
College Station, TX 77843-3123
Fellow ASME

V. Sernas
Professor.
Department of Mechanical
and Aerospace Engineering,
Rutgers University,
Piscataway, NJ 08855-0909
Mem. ASME

J. C. Han
Professor.
Department of Mechanical Engineering,
Texas A&M University,
College Station, TX 77843-3123
Mem. ASME

Heat Transfer Through Falling Film Evaporation and Boiling on Horizontal Tubes

Evaporation and boiling heat transfer coefficients are presented for thin, distilled water films flowing over the outside of horizontal, electrically heated brass tubes. Tests were conducted with a thin-slot water distribution system for 2.54- and 5.08-cm-dia smooth tubes. Both local and average heat transfer data were obtained for nonboiling and boiling conditions corresponding to feedwater temperatures ranging from 49 to 127°C and heat-flux values ranging from 30 to 80 kW/m². Feedwater flow rates ranged from 0.135 to 0.366 kg/s per meter length per side of the tube. Both nonboiling and boiling correlations of the average heat transfer coefficients were developed and compared.

Introduction

Heat transfer through thin liquid films has been used in distillation and desalination processes. Falling film evaporation on horizontal tubes has also been considered one of the heat transfer processes appropriate for ocean thermal energy conversion systems. In such systems, the liquid is introduced through distributors to the top of a bundle and falls from tube to tube with the thin liquid films flowing and evaporating on the outside of the tubes. Fletcher et al. (1974, 1975) studied boiling heat transfer coefficients on horizontal tube systems with a perforated-plate water distribution system for 2.54- and 5.08-cm-dia horizontal, 90/10 Cu–Ni smooth tubes. The heat transfer coefficients increased with increasing feedwater flow rate in the turbulent regime, with feedwater saturation temperature, and tube-wall heat flux for boiling conditions. They also found that heat transfer coefficients were higher for sea water films than for fresh water films.

Liu (1975) investigated nonboiling water heat transfer coefficients in the turbulent regime for 2.54- and 5.08-cm-dia horizontal, stainless steel tubes. Owens (1978) and Conti (1978) measured nonboiling ammonia heat transfer coefficients in both laminar and turbulent regimes for a 5.08-cm-dia horizontal, stainless steel tube. The data of Owens were similar to those of Liu in that the heat transfer coefficients increased with increasing feedwater temperature, but were independent of flow rate in the turbulent regime and independent of heat flux for nonboiling conditions. Lorenz and Yung (1979) developed a model for combined boiling and evaporation of liquid films on horizontal tubes. Predictions agreed favorably with the boiling data of Fletcher et al. (1974). Large-bundle test results were compared with single-tube test results by Lorenz and Yung (1982). For Reynolds numbers greater than 300, the average heat transfer coefficient of the bundle was equal to that of a single tube.

As mentioned earlier, Fletcher et al. (1974, 1975) indicated that heat transfer coefficients of thin liquid films increased with increasing feedwater flow rate for boiling conditions. They did not, however, investigate the nonboiling conditions. Liu (1975) and Owens (1978) reported that heat transfer coefficients were independent of feedwater flow rate for the nonboiling situation, but did not study the boiling case. Therefore, it is important to clarify whether or not heat transfer coefficients depend on feedwater flow rate (in the turbulent regime) for both boiling and nonboiling conditions.

Another parameter that was thought to affect heat transfer coefficients was the water distribution system at the top of the horizontal tube. Instead of the "perforated-plate" water distribution system used by Fletcher et al. (1974, 1975), the more accurately controlled "thin-slot" water distribution system was deemed more appropriate. Recently, Mitrovic (1986) has shown that the water-feed system geometry does indeed affect the heat transfer coefficient on a horizontal tube.

The present investigation is involved with the evaporation and boiling heat transfer coefficients in the turbulent regime with a thin-slot water distribution system for thin water films flowing over the outside of horizontal, electrically heated brass tubes. A well-controlled systematic study was conducted with 2.54- and 5.08-cm-dia smooth tubes. Both local and average heat transfer data were obtained for boiling and nonboiling conditions corresponding to feedwater temperatures ranging from 49°C (0.012 MPa) to 127°C (0.246 MPa) and heat-flux values ranging from 30 to 80 kW/m². Feedwater flow rates ranged from 0.135 to 0.366 kg/s per meter length per side of the tube, which corresponded to the turbulent flow regime over most of the tube surface. Correlations of average heat transfer coefficients for boiling and nonboiling conditions were developed and compared.

[1]Formerly with the Mechanical Systems Section.

Contributed by the Heat Transfer Division for publication in the JOURNAL OF HEAT TRANSFER. Manuscript received by the Heat Transfer Division October 28, 1988; revision received September 18, 1989. Keywords: Boiling, Evaporation.

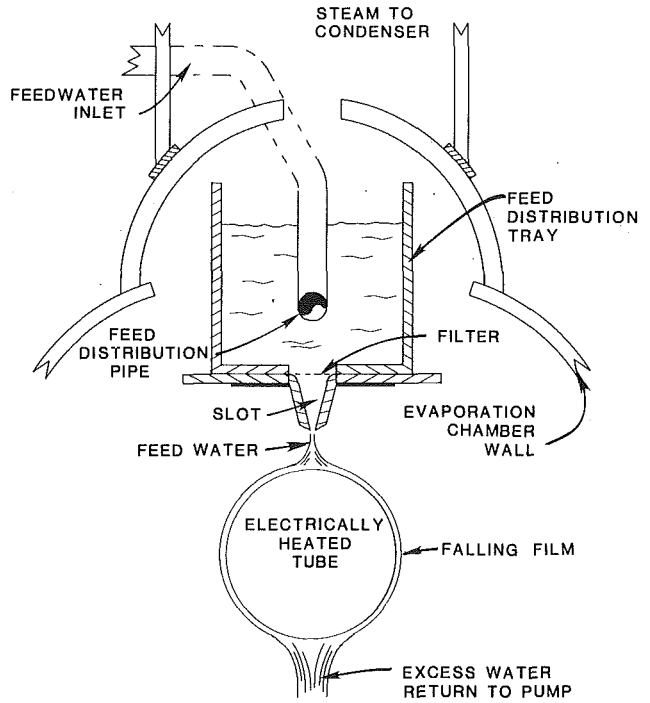

Fig. 1 Schematic of the feedwater distribution in the evaporation chamber

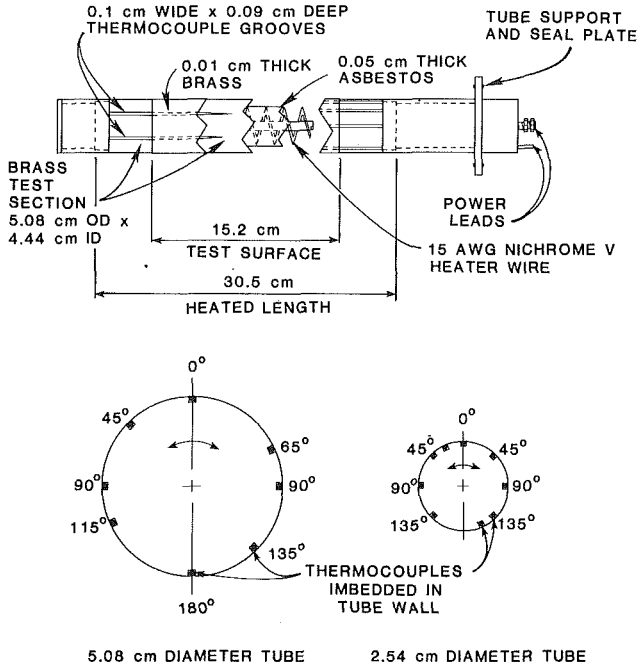

Fig. 2 Schematic of the electrically heated evaporation tube and thermocouple locations

Additional information on the investigation is provided by Parken and Fletcher (1977, 1982) and Han and Fletcher (1985, 1987).

Experimental Program

Test Facility. The experimental facility consists of an evaporation tube and surrounding chamber, a steam condenser, a recirculating feedwater system, and associated control systems. Figure 1 is a schematic of the feedwater distribution on the evaporation tube. Feedwater was distributed to the top of the tube by a thin slot at the bottom of the constant head feed tray, as shown in Fig. 1. The slot was about 0.63 cm (0.25 in.) above the heated tube. The feedwater flow rate, temperature, and tube-wall heat flux were controlled for independent variation over a wide range. To have the same feed rate over each side of the tube, the feed tray was carefully aligned with the tube.

Two electrically heated evaporation tubes were assembled and instrumented for testing, as shown in Fig. 2. The 15.2-cm-long test section consisted of a 25.4-cm brass tube with eight axially milled, thermocouple grooves around the circumference. The ends of the grooves were sloped toward the surface so that the 30-gage, copper-constantan, thermocouple junctions were located as close to the surface as possible. The test section and a 15.2-cm-wide, 0.010-cm-thick, brass shim stock were tinned with silver solder. The shim stock was wrapped tightly around the test section, and the two were soldered together in a furnace. The heating element was a spirally wound, Nichrome V wire designed to provide an approximately uniform circumferential heat flux. Circumferential conduction was estimated to be very small. To compensate for temperature error from tube wall thickness and thermocouple conduction, each evaporation tube was completely calibrated after it was assembled.

Test Procedures. The tube surface was rubbed extensively with number 3/0 steel wool and wiped with acetone. The tube was then placed into the evaporator, and preliminary runs started the next day. To "age" the surface, these runs continued intermittently for about ten hours before data were taken. Initial rms surface roughness, as indicated by a Brush indicator, was 5 to 15 μin. After aging, the surface stabilized at a much smoother value of 2 to 4 μin. A day's testing was accomplished at a set saturation pressure. The parameters varied during a day's tests were feed rate and heat flux. Sufficient time was allowed to reach equilibrium at each condition.

The characteristics of the thin film flowing around the horizontal tubes were visualized during the tests through Pyrex windows at the sides and front of the test chamber. Photographs were taken for both subcooled (inlet feedwater

Nomenclature

C_p = specific heat of the liquid film at constant pressure
D = tube outside diameter
g = acceleration due to gravity
H = distance between distribution system and tube
h_θ = local heat transfer coefficient (equation (1))
$\bar{h}$ = average heat transfer coefficient (equation (2))
k = thermal conductivity of liquid film
Nu = average Nusselt number $= \bar{h}(\nu^2/gk^3)^{1/3}$
Pr = Prandtl number $= (\mu C_p/k)$
q'' = tube wall heat flux
Re = Reynolds number $= (4\Gamma/\mu)$
T_i = inlet feedwater temperature for subcooled nonboiling conditions
T_{sat} = inlet feedwater saturation temperature for boiling conditions
$T_{w,\theta}$ = local wall temperature
Γ = mass flow rate per axial unit length flowing over one side of the horizontal tube
θ = angular location measured from the top of the tube
μ = dynamic viscosity of liquid film
ν = kinematic viscosity of liquid film $= \mu/\rho$
ρ = density of liquid film

temperature) and saturated (inlet feedwater temperature) conditions. For a majority of the subcooled tests, bubble nucleation was not visualized. For the slightly subcooled case of $T_{sat} - T_i = 6°C$, incipient nucleation was observed at the bottom surface of the 5.08-cm-dia tube (Parken and Fletcher, 1977, pp. 44–45). For all tests at saturated conditions, however, bubble nucleation was observed (Parken and Fletcher, 1977, pp. 64–66). Bubble population density was less at low heat flux values and for the smaller tube diameter. A majority of the nucleation sites appeared first at the lower portion of the tubes. As the heat flux increased, nucleation sites were seen to be distributed over the entire tube surface. The nucleated bubbles grew very rapidly to approximately 1 mm in diameter while attached to the heating surface. They were then detached from the surface and carried downward with the falling film. While moving downward the bubbles continued to grow, sometimes reaching diameters as large as 10 mm (Parken and Fletcher, 1977).

Because of the intermittent nature of the boiling process, the tube wall temperature fluctuated sharply. Fifteen to twenty temperature recordings were made over 5-s intervals for each thermocouple. The average of these readings for each thermocouple was reported. Several runs were duplicated on different days to check the data repeatability.

Data Analysis. The local heat transfer coefficients were calculated from the tube-wall heat flux (q''), the local circumferential wall temperature ($T_{w,\theta}$), and the inlet feedwater temperature (T_i) as follows:

$$h_\theta = q''/(T_{w,\theta} - T_i) \tag{1}$$

where the inlet feedwater temperature was at subcooled conditions ($T_i = T_i$) for nonboiling tests and the inlet feedwater temperature was at saturated conditions ($T_i = T_{sat}$) for the boiling tests. The feedwater temperature was measured in the bottom of the distribution tray shown in Fig. 1. The heating by heat transfer from the vapor in the enclosure, possibly occurring by the time the water impinged upon the tube surface, was estimated to be negligible.

The average evaporation heat transfer coefficients were calculated by

$$\bar{h} = \frac{1}{\pi}\int_0^\pi h_\theta d\theta \tag{2}$$

The average heat transfer coefficients ($\bar{h}$) were the averages of all the local heat transfer coefficients measured on the tube. The averaging of the tube-wall local heat transfer coefficients was area-weighted.

The maximum uncertainties in feedwater flow rate were estimated to be ±3.5 percent. The maximum uncertainty in the tube wall heat flux was estimated to be ±1.4 percent for the lowest heat flux condition of 15,800 W/m^2. The largest uncertainty in the wall temperature difference was estimated to be ±11 percent for the lowest heat flux condition. In summary, the maximum uncertainties in the heat transfer coefficient due to uncertainties in heat flux and wall temperature difference were estimated to be ±11.1 percent and ±3.7 percent for $q'' = 15{,}800$ W/m^2 and $q'' = 78{,}800$ W/m^2, respectively.

Experimental Results and Discussion

The detailed raw data for all of the 207 test runs were tabulated by Parken and Fletcher (1977). Only the most representative results are presented here.

Local Heat Transfer Coefficient. The tests were conducted with various degrees of subcooling for the inlet feedwater, ranging from approximately 55°C to just short of visible nucleation (6°C). No systematic variation of the heat transfer coefficients was observed with variations in the degree of subcooling. Consequently, the subcooled nonboiling results did not list the degree of subcooling.

Typical results to demonstrate the effects of feedwater temperature, flow rate, and tube-wall heat flux on local (subcooled) nonboiling heat transfer coefficients are shown in Figs. 3 and 4 for 2.54- and 5.08-cm-dia tubes, respectively. For the 2.54-cm-dia tube, local heat transfer coefficients are highest at the top of the tube and decrease steadily around the tube. For the 5.08-m-dia. tube, local heat transfer coefficients decrease steadily from the top of the tube until about the 90 deg location and tend to increase as the flow approaches the bottom of the tube. For both tubes, local heat transfer coefficients increase with increasing feedwater temperature and flow rate, but local heat transfer coefficients are almost independent of tube-wall heat flux for the nonboiling condition. It is noted that a laminar analysis involving both an integral approach with a cubic polynomial velocity profile and a finite difference scheme were used to determine the film thickness and nonboiling heat transfer coefficients (Parken and Fletcher, 1982). Results of these analyses were found to be in excellent agreement with the reported data similar to those in Figs. 3 and 4.

Typical results to demonstrate the effects of feedwater temperature, flow rate, and tube-wall heat flux on local (saturated) boiling heat transfer coefficients are shown in Fig. 5 for the 2.54-cm-dia tube. Local heat transfer coefficients decrease from the top of the tube until at the 45 deg location, and then tend to have a relatively uniform distribution with periodic fluctuations as the flow approaches the bottom of the tube ($\theta = 45$ to 180 deg). These fluctuations may be caused by local boiling around the tube. Local heat transfer coefficients increase with increasing feedwater temperature, flow rate, and tube-wall heat flux for boiling conditions.

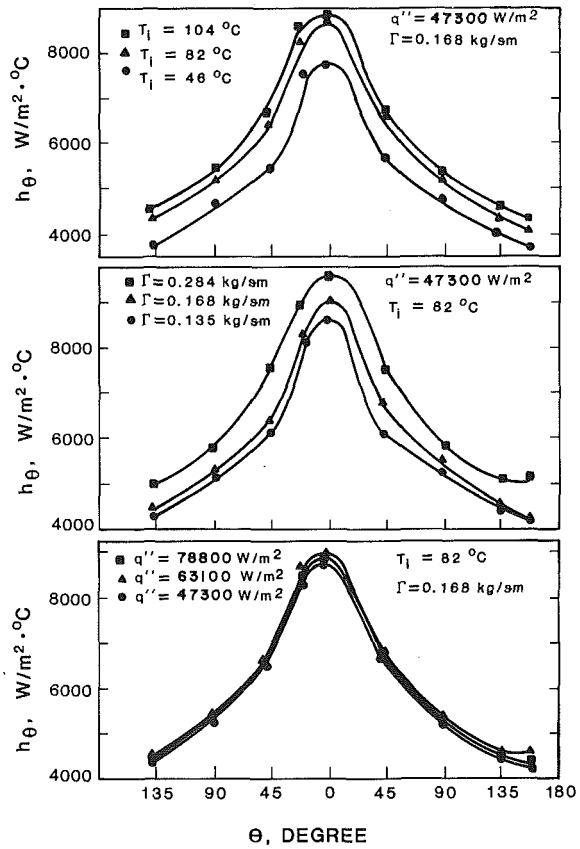

Fig. 3 Local nonboiling heat transfer coefficient for a 2.54-cm-dia smooth tube

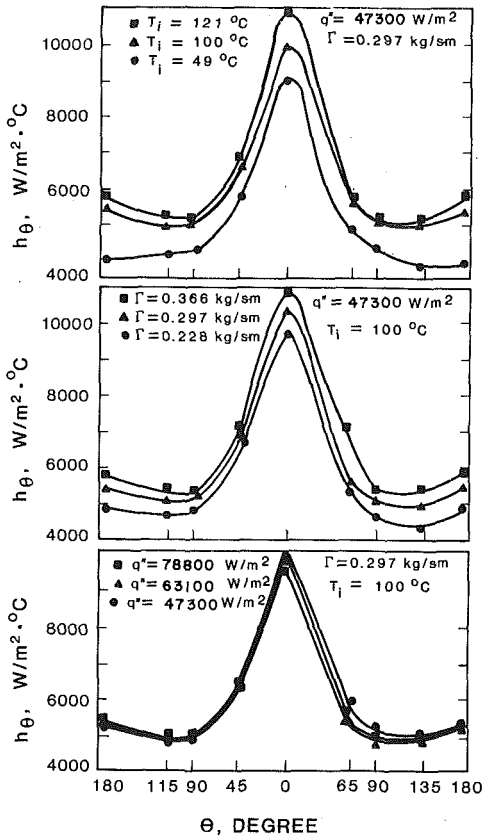

Fig. 4 Local nonboiling heat transfer coefficient for a 5.08-cm-dia smooth tube

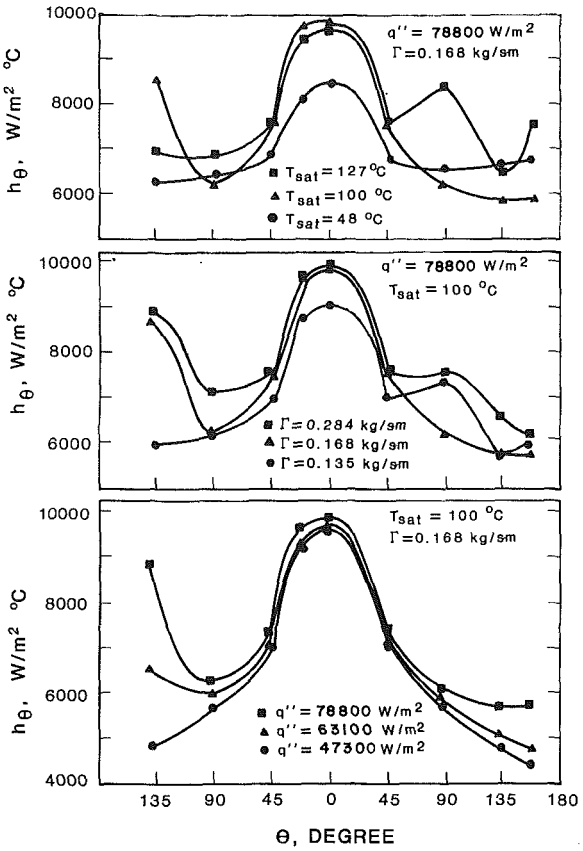

Fig. 5 Local boiling heat transfer coefficient for a 2.54-cm-dia smooth tube

Average Heat Transfer Coefficient. Typical results to show the effects of feedwater temperature, flow rate, and tube-wall heat flux on average nonboiling heat transfer coefficients are presented in Fig. 6 for 2.54- and 5.08-cm-dia tubes. As noted in Fig. 6, the data indicate an increasing average nonboiling heat transfer coefficient with increasing feedwater temperature and flow rate, while very little discernible effect on the heat transfer coefficient is shown with changes in heat flux. The average nonboiling heat transfer coefficients for the 2.54-cm-dia tube are higher than those for the 5.08-cm-dia tube. This is because the convection heat transfer coefficient decreases with distance from the top of the tube for subcooled, nonboiling tests (Cerza and Sernas, 1988). Thus, the longer the flow distance, the smaller the average heat transfer coefficient. The 5.08-cm-dia tube has twice the flow distance of the 2.54-cm-dia tube.

Selected results to show the effects of feedwater temperature, flow rate, and tube-wall heat flux on average boiling heat transfer coefficients are presented in Fig. 7. For the 2.54-cm-dia tube, average heat transfer coefficients remain about the same when feedwater saturation temperatures change from 50°C to 100°C and increase when feedwater temperatures are higher than 100°C. For the 5.08-cm-dia tube, however, average heat transfer coefficients increase with increasing feedwater temperature until 100°C and then decrease with further increases in temperature over 100°C. For a saturation temperature at 125°C, the heat flux levels of this study may not be large enough to produce as many bubble nucleations as those at 100°C. Therefore, the average heat transfer coefficients are reduced. For both tubes, average heat transfer coefficients increase with increasing feedwater flow rate and tube-wall heat flux for boiling condition. The average boiling heat transfer coefficients on the 5.08-cm-dia tube are higher than those on the 2.54-cm-dia tube. This is because the boiling heat transfer coefficients increase with increasing surface area for bubble nucleation. The falling film has to be superheated before nucleation will occur. This requires a certain circumferential distance on the tube. For a 5.08-cm-dia tube this might represent the top quarter of the tube, while for

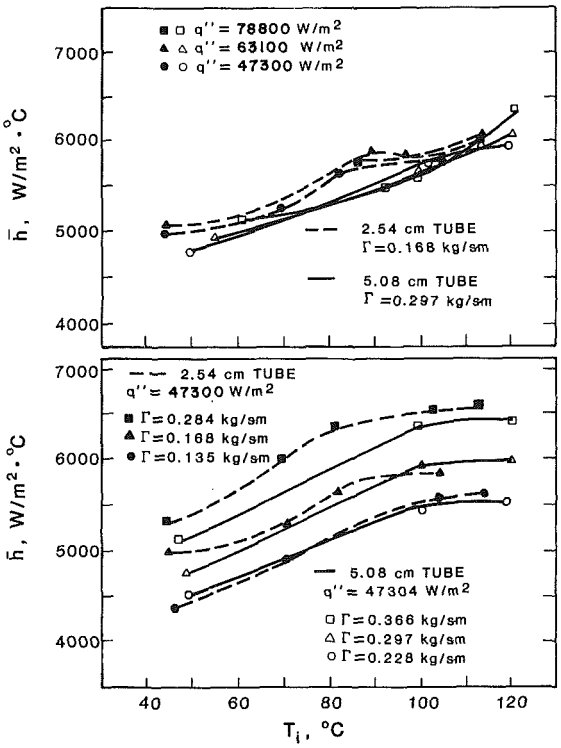

Fig. 6 Average nonboiling heat transfer coefficient for 2.54- and 5.08-cm-dia tubes

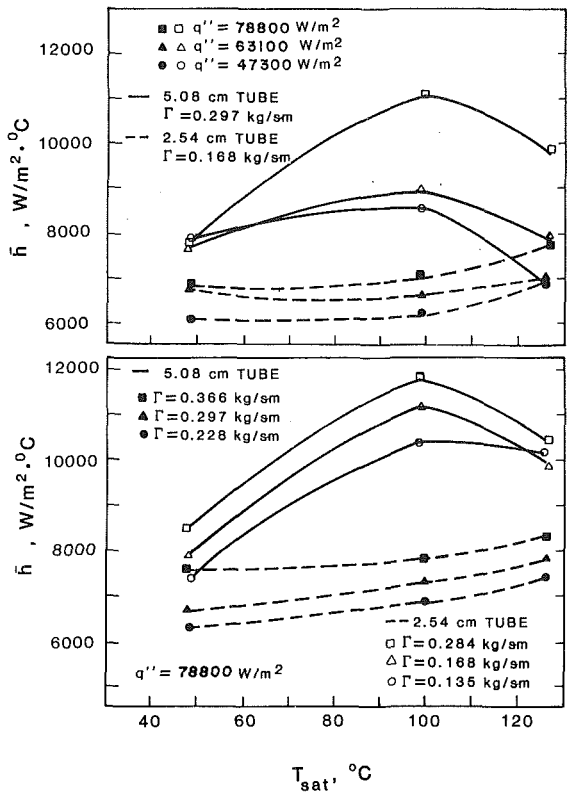

Fig. 7 Average boiling heat transfer coefficient for 2.54- and 5.08-cm-dia tubes

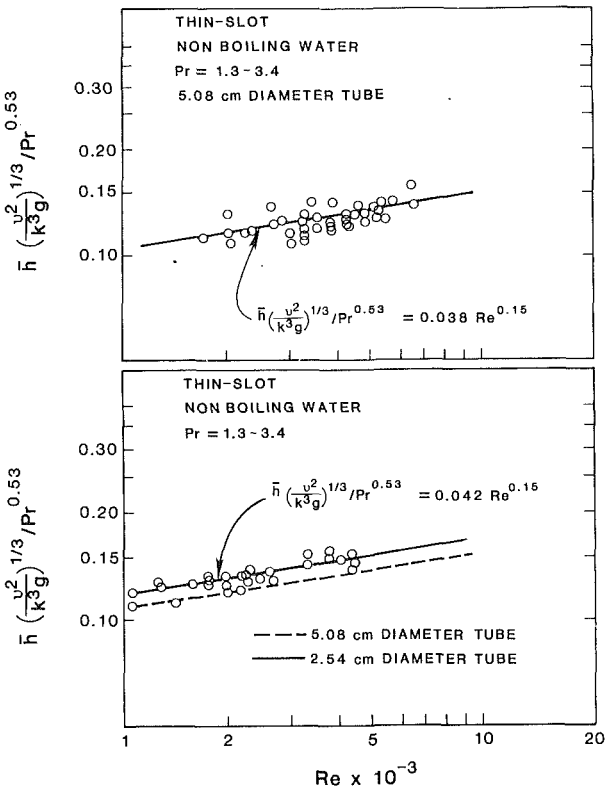

Fig. 8 Nonboiling water heat transfer correlations for 2.54- and 5.08-cm-dia tubes

the 2.54-cm-dia tube this distance would be the top half of the tube. Thus the 5.08-cm tube boils over a larger percentage of its surface (at a given heat flux and flow rate) and, as a consequence, exhibits a larger heat transfer coefficient.

Heat Transfer Data Correlations

For the results of the experimental data to be most useful, general correlations are required for average heat transfer coefficients over a wide range of test parameters. The parameters include feedwater flow rate, temperature, tube-wall heat flux, tube diameter, and water distribution method. The water flow rate may be represented by the Reynolds number, and water temperature may be represented by the Prandtl number.

Chun and Seban (1971) proposed that the nonboiling heat transfer coefficient for turbulent water film on a vertical smooth tube could be correlated as follows:

$$\bar{h}\left(\frac{\nu^2}{gk^3}\right)^{1/3} = a_1\ \mathrm{Re}^{a_2}\mathrm{Pr}^{a_3} \tag{3}$$

where a_1, a_2, and a_3 are empirical constants. Owens (1978) applied the same method to correlate data for turbulent ammonia film on a horizontal smooth stainless steel tube. He found, however, that the average nonboiling heat transfer coefficient was not Reynolds number dependent.

Nonboiling Correlations. In the present investigation, the average nonboiling heat transfer coefficient varies with feedwater flow rate (turbulent regime) and temperature, as noted above. Correlations have been developed for the present data and are shown in Fig. 8. A correlation for the 2.54-cm-dia tube data is given in equation (4), and a correlation for the 5.08-cm-dia tube data can be represented by equation (5)

$$\bar{h}\left(\frac{\nu^2}{gk^3}\right)^{1/3} = 0.042\ \mathrm{Re}^{0.15}\mathrm{Pr}^{0.53} \tag{4}$$

$$\bar{h}\left(\frac{\nu^2}{gk^3}\right)^{1/3} = 0.038\ \mathrm{Re}^{0.15}\mathrm{Pr}^{0.53} \tag{5}$$

The deviation of equation (4) from the experimental data is about 7 percent, and only seven data points (out of 52) deviate from the correlation by more than 10 percent. The maximum deviation of equation (5) from the experimental data is about 8 percent. It should be noted that in equations (4) and (5) the thermal fluid properties were to be evaluated at the film temperature, which was the average between the tube wall and the inlet (subcooled) feedwater temperature. The average Nusselt number (the average heat transfer coefficient) increases with increasing Prandtl number (feedwater temperature) and increases slightly with increasing Reynolds number (feedwater flow rate). The average Nusselt number for the 2.54-cm-dia tube is about 10 percent higher than that of the 5.08-cm-dia tube at the same Reynolds and Prandtl numbers. Sernas (1979) reported nonboiling correlations that were derived from the same experimental data. His correlations differ slightly from equations (4) and (5) because he used the inlet feedwater temperature for evaluating thermal fluid properties. It should be noted that the maximum difference between the Nusselt number calculated from the present correlations and those of Sernas is 9 percent in the range of Reynolds and Prandtl numbers used in this study.

Boiling Correlations. As mentioned earlier, the test results show that average boiling heat transfer coefficients increase with increasing feedwater temperature, flow rate, and wall heat flux. Therefore, the correlation of the average boiling heat transfer coefficient for a turbulent water film on a horizontal tube can logically be extended from equation (3) as follows:

$$\bar{h}\left(\frac{\nu^2}{gk^3}\right)^{1/3} = b_1\ \mathrm{Re}^{b_2}\mathrm{Pr}^{b_3}q''^{b_4} \tag{6}$$

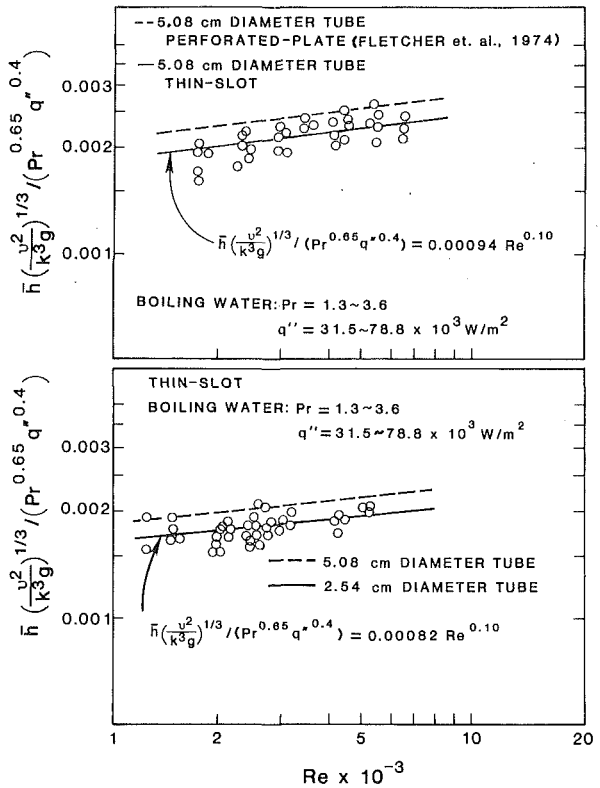

Fig. 9 Boiling water heat transfer correlations for 2.54- and 5.08-cm-dia tubes

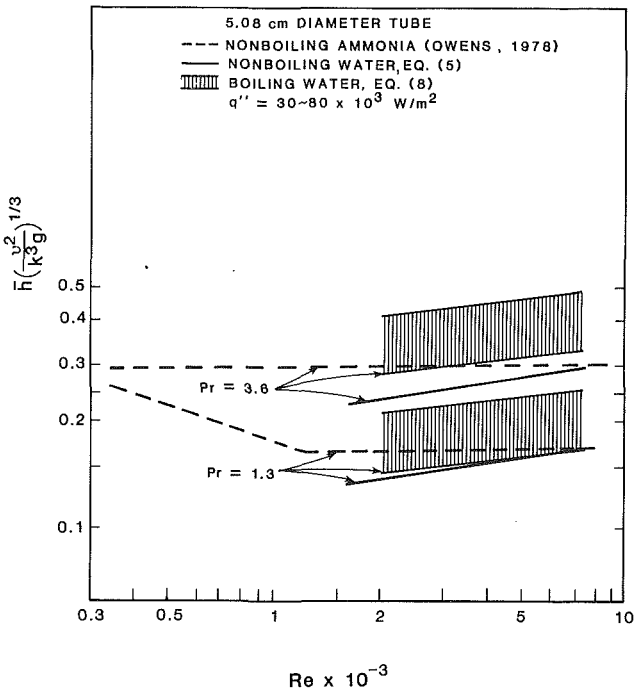

Fig. 10 Comparison of present correlations with Owens' (1978) investigation

where b_1, b_2, b_3, and b_4 are empirical constants for a given water distribution system and working fluid.

Correlations of the present data are shown in Fig. 9. A correlation for the 2.54-cm-dia tube data is shown in equation (7), and a correlation for the 5.08-cm-dia tube data can be written by equation (8)

$$\bar{h}\left(\frac{\nu^2}{gk^3}\right)^{1/3} = 0.00082\ \mathrm{Re}^{0.10}\mathrm{Pr}^{0.65}q''^{0.4} \tag{7}$$

$$\bar{h}\left(\frac{\nu^2}{gk^3}\right)^{1/3} = 0.00094\ \mathrm{Re}^{0.10}\mathrm{Pr}^{0.65}q''^{0.4} \tag{8}$$

where Re, Pr, and q'' are varied between 1000 and 7000, 1.3 and 3.6, and 30 and 80 kW/m^2, respectively. The maximum deviation of equation (7) is about 10 percent and that of equation (8) is about 12 percent. Again the properties in equations (7) and (8) were evaluated at the film temperature, which was the average between the tube wall and the inlet (saturation) feedwater temperature. The boiling Nusselt number increases with increasing Prandtl number and heat flux, and depends slightly on the Reynolds number in the turbulent regime. The average Nusselt number for the 2.54-cm-dia tube is about 13 percent lower than that of the 5.08-cm-dia tube at the same Reynolds and Prandtl numbers and the same tube-wall heat flux. The larger diameter tube with its longer film flow path produces a hotter film, which tends to boil over a larger portion of the tube. Under the same operating conditions, this produces a higher boiling heat transfer coefficient. It should be noted that the heat flux in equations (7) and (8) has units of W/m^2. Correlations were attempted using nondimensional heat fluxes, but it was found that it was not possible to correlate the data as well as equations (7) and (8).

The effect of the water distribution system on the average boiling heat transfer coefficient of the 5.08-cm tube is included in Fig. 9 for comparison. The data with a perforated-plate distribution system (Fletcher et al., 1974) are about 20 percent higher than those obtained with a thin-slot distribution system (this study) at similar conditions. These results suggest that the boundary layer on the tube surface resulting from the perforated-plate distribution system is thinner than the boundary layer resulting from the thin-slot distribution system; therefore, the heat transfer coefficient is higher at the same conditions.

Comparison With Other Investigations. Figure 10 shows a comparison of the present correlations with another investigation. The Nusselt number for nonboiling conditions on the smooth tube (equation (5)) is lower than Owens' (1978) ammonia data in the turbulent flow regime, but the discrepancy decreases with increasing Reynolds number. Although the Nusselt number for nonboiling conditions is independent of the Reynolds number in Owens' correlation, the Nusselt number increases slightly with increasing Reynolds number in this analysis. Similar conclusions regarding the sensitivity of the average heat transfer coefficient with Reynolds numbers in some Reynolds number ranges can be reached from a recent paper by Cerza and Sernas (1988), who reported solutions to the thermal entry length problem for a falling film on a vertical cylinder, and from the paper by Mitrovic (1988) who analytically solved the thermal entry length problem for a bank of horizontal tubes. Figure 10 also shows that the Nusselt number for boiling (equation (8)) is higher than the Nusselt number for nonboiling at the same Reynolds and Prandtl numbers. The Nusselt number increases with increasing heat flux level for the boiling conditions.

Conclusions

Falling thin-film heat transfer on horizontal smooth tubes has been examined. The effects of the water distribution system, tube diameter, feedwater flow rate (Reynolds number), temperature (Prandtl number), and tube-wall heat flux on local and average heat transfer coefficients at nonboiling and boiling conditions have been investigated. The following conclusions are drawn:

1 Local nonboiling heat transfer coefficients are highest at the top of the tube and decrease around the tube; local boiling

heat transfer coefficients show relatively uniform distribution with periodic fluctuations around the tube.

2 Average nonboiling heat transfer coefficients increase with increasing feedwater temperature and flow rate and remain constant with change in tube-wall heat flux; average boiling heat transfer coefficients increase with increasing feedwater temperature and tube-wall heat flux, and increase slightly with increasing flow rate.

3 With a thin-slot water distribution system, the nonboiling heat transfer coefficient on the 2.54-cm tube may be up to 10 percent higher than that on the 5.08-cm tube; the boiling heat transfer coefficient is lower by 13 percent.

4 For the 5.08-cm tube, the boiling heat transfer coefficient with the perforated-plate distribution system is about 20 percent higher than that with the thin-slot distribution system at similar conditions.

5 Equations (4) and (5) may be used to calculate the average nonboiling Nusselt number for 2.54- and 5.08-cm-dia tubes with a thin-slot distribution system; equations (7) and (8) may be used for the average boiling Nusselt number. The correlations are based on experimental data with $1000 \le \mathrm{Re} \le 8000$, $1.3 \le \mathrm{Pr} \le 3.6$, and $30 \times 10^3 \le q'' \le 80 \times 10^3$ W/m^2.

6 The correlations show that for boiling conditions, the average Nusselt numbers increase with increasing tube-wall heat flux and Prandtl number and increase slightly with Reynolds number; for nonboiling conditions, they are independent of heat flux.

Acknowledgments

The authors gratefully acknowledge the financial support of the National Science Foundation through Grant No. ENG-76-03691.

Referneces

Cerza, M., and Sernas, V., 1988, "Nucleate Boiling in Thermally Developing and Fully Developed Laminar Falling Water Film," ASME JOURNAL OF HEAT TRANSFER, Vol. 110, pp. 221–228.

Chun, K. R., and Seban, R. A., 1971, "Heat Transfer to Evaporating Liquid Films," ASME JOURNAL OF HEAT TRANSFER, Vol. 93, pp. 391–396.

Conti, R. J., 1978, "Experimental Investigation of Horizontal Tube Ammonia Film Evaporators With Small Temperature Differentials," *Proceedings of the Fifth Annual Conference on Ocean Thermal Energy Conversion*, Miami Beach, FL, Feb. 20–22.

Fletcher, L. S., Sernas, V., and Galowin, L. S., 1974, "Evaporation From Thin Water Films on Horizontal Tubes," *Industrial Engineering Chemistry—Process Design and Development*, Vol. 13, No. 3, pp. 265–269.

Fletcher, L. S., Sernas, V., and Parken, W. H., 1975, "Evaporation Heat Transfer Coefficients for Thin Sea Water Films on Horizontal Tubes," *Industrial Engineering Chemistry—Process Design and Development*, Vol. 14, No. 4, pp. 411–416.

Han, J. C., and Fletcher, L. S., 1985, "Falling Film Evaporation and Boiling in Circumferential and Axial Grooves on Horizontal Tubes," *Industrial Engineering Chemistry—Process Design and Development*, Vol. 24, No. 3, pp. 570–575.

Han, J. C., and Fletcher, L. S., 1987, "Influence of Concurrent Steam Shear Velocity on Falling Film Evaporation and Boiling on a Horizontal Tube," *Proceedings of the Joint ASME-JSME Thermal Engineering Conference*, HI, pp. 527–532.

Liu, P. J. P., 1975, "The Evaporating Falling Film on Horizontal Tubes," Ph.D. Thesis, University of Wisconsin, Madison, Wisconsin.

Lorenz, J. J., and Yung, D., 1979, "A Note on Combined Boiling and Evaporation of Liquid Films on Horizontal Tubes," ASME JOURNAL OF HEAT TRANSFER, Vol. 101, pp. 178–180.

Lorenz, J. J., and Yung, D., 1982, "Film Breakdown and Bundle-Depth Effects in Horizontal-Tube, Falling-Film Evaporators," ASME JOURNAL OF HEAT TRANSFER, Vol. 104, pp. 567–571.

Mitrovic, J., 1986, "Influence of Tube Spacing and Flow Rate on Heat Transfer From a Horizontal Tube to a Falling Liquid Film," *Proceedings, 8th International Heat Transfer Conference*, C. L. Tien et al., eds., Hemisphere Publishing Corp., Washington, DC, Vol. 4, pp. 1949–1956.

Mitrovic, J., 1988, "Der Warmeaustausch am Berieselungskuhler," *BWK*, Vol. 40, pp. 243–249.

Owens, W. L., 1978, "Correlation of Thin Film Evaporation Heat Transfer Coefficients for Horizontal Tubes," *Proceedings of the Fifth Annual Conference on Ocean Thermal Energy Conversion*, Miami Beach, FL, Feb. 20–22.

Parken, W. H., and Fletcher, L. S., 1977, "An Experimental and Analytical Investigation of Heat Transfer to Thin Water Films on Horizontal Tubes," University of Virginia, Report No. UVA-526078-MAE 77-101, Aug.

Parken, W. H., and Fletcher, L. S., 1982, "Heat Transfer in Thin Liquid Films Flowing Over Horizontal Tubes," *Proceedings of the Fifth International Heat Transfer Conference*, Munich, Federal Republic of Germany, pp. FB415-420.

Sernas, V., 1979, "Heat Transfer Correlation for Subcooled Water Films on Horizontal Tubes," ASME JOURNAL OF HEAT TRANSFER, Vol. 101, pp. 176–178.

Effects of Surface Tension on Film Condensation in a Porous Medium

A. Majumdar[1]

C. L. Tien[2]
A. Martin Berlin Professor.

Department of Mechanical Engineering,
University of California
Berkeley, CA 94720

In the process of film condensation in a porous medium, the thermodynamics of phase equilibria requires the existence of a two-phase zone lying between the liquid and the vapor regions. In the two-phase zone, solutions of the conservation equations indicate a boundary-layer profile for the capillary pressure. The liquid zone is analyzed using three models, which assume either slip or no slip at the wall and Darcy velocity or no shear at the interface with the two-phase zone. The results show that the condition of no slip at the wall must be satisfied in all cases except where the thickness of the liquid zone is much larger than the characteristic boundary layer in the porous medium. At the interface with the two-phase zone, the assumption of no shear is more realistic than that of an imposed Darcy velocity, in conjunction with no-slip condition at the wall. Comparisons with experiments suggest that the drag on the liquid film due to surface tension is significant for permeabilities lower than $10^{-7}m^2$. A dimensionless group, characterizing viscous flow due to surface tension forces, is introduced in this study.

Introduction

Vapor condensation in a porous medium has been receiving increasing attention due to its wide range of heat transfer applications. In some applications, it is a desired phenomenon, whereas in others it is detrimental. One major application of this process is in heat pipes where porous wicks are used to transfer liquid from the condenser to the evaporator section. The efficiency of the condenser is increased by augmenting the rate of condensation of the vapor. This offers a motivation to study the process of film condensation in a porous medium. Porous materials are also widely used as insulation. When this type of insulation is used to prevent heat losses from a cold wall, condensation of the vapor trapped in the porous insulation is generally undesirable, since it augments energy transport and degenerates the material. Minimizing vapor condensation in such an application provides an incentive to study this phenomenon. Other applications of this phenomenon include enhanced oil recovery by steam injection and latent heat transport in geothermal utilization.

The problem of film condensation in the absence of a porous medium has been extensively studied and is well understood. However, in the presence of a porous medium the thermodynamics governing such a process is markedly different. When both liquid and vapor phases co-exist in the presence of solid surfaces, it is natural to consider the effect of surface tension. Most of the previous theoretical investigations (Cheng, 1981; Cheng and Chui, 1984; Kaviany, 1986; Poulikakos and Orozco, 1986; Nelson and Romero, 1980; White and Tien, 1987a) do not consider this effect. Udell (1983, 1985) analyzed a one-dimensional porous heat pipe by including surface tension forces, which are responsible for the transport of vapor and liquid across the heat pipe. Shekarriz and Plumb (1986) studied the effect of surface tension on film condensation on a vertical wall, entrapped in a porous medium, by adopting a three-zone model.

The present study considers film condensation of a slightly superheated vapor on a vertical wall, embedded in a porous medium and maintained at a constant temperature. Based on the thermodynamics of phase equilibria, a logical explanation for the existence of a two-phase zone is presented. This zone, along with the liquid zone, is then analyzed by solving conservation equations.

Thermodynamics

An analysis of the process of change of phase of a fluid in the presence of a porous matrix needs an understanding of the thermodynamics (Udell, 1983; Callen, 1985) that govern such a process. It is assumed that the fluid is pure. Figure 1 shows a μ–P plot at a constant temperature. When phase change occurs at a flat interface, the pressures across the interface are equal. Therefore, phase change occurs at points B and F in Fig. 1, where both μ and P are equal for both phases.

For a transition of phase to occur at a curved boundary, the pressures in the two phases will be different, whereas μ and T would be equal. The difference in pressures balances the surface tension forces existing at the interface. In the following discussion only a wetting liquid is considered. Although some liquids are nonwetting when in contact with certain solids, it is assumed that the impurities present on the solid surface would eventually make the liquid wetting. For a wetting liquid the

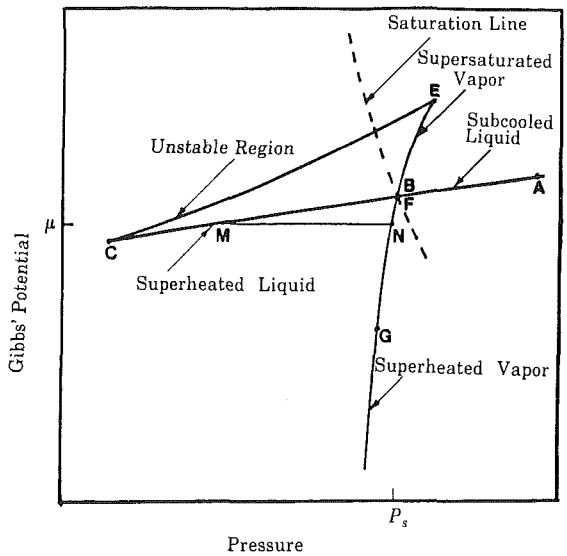

Fig. 1 Schematic diagram of Gibbs' potential for a pure fluid

[1]Currently Assistant Professor, Department of Mechanical and Aerospace Engineering, Arizona State University, Tempe, AZ 85287-6106.

[2]Current address: Office of the Chancellor, University of California, Berkeley, CA 94720.

Contributed by the Heat Transfer Division and presented at the 25th National Heat Transfer Conference, Houston, Texas, July 24–27, 1988. Manuscript received by the Heat Transfer Division August 11, 1988; revision received October 2, 1989. Keywords: Condensation, Porous Media, Thermocapillary Flows.

contact angle between the liquid-vapor interface and the solid surface is acute. Therefore the vapor pressure P_v has to be greater than the liquid pressure P_l. The difference between the pressures is attributed to the effect of surface tension, which is expressed as follows:

$$P_c = P_v - P_l = \frac{2\sigma}{r_e} \tag{1}$$

where r_e is the effective radius of curvature of the interface and P_c is the capillary pressure. The thermodynamic state of each phase can be determined from Fig. 1, where points M and N represent the liquid and the vapor, respectively. Thus both the vapor and the liquid are in superheated states.

Consider a slightly superheated vapor condensing in a porous matrix. It is extremely difficult to have a perfectly saturated vapor and invariably a slight degree of superheat would exist. Thus, the presence of solid surfaces and superheated vapor makes it possible for the liquid to exist in a metastable state. The relationship between P_c and the relevant thermodynamic variables are given by the Kelvin equation (Udell, 1983).

With this background of the thermodynamics governing the process of condensation in the presence of a porous matrix, a model (Shekarriz and Plumb, 1986) is considered for the analysis of such a problem. Consider an impermeable vertical wall embedded in a porous matrix. Let the temperature of the wall T_w be maintained below the saturation temperature T_s of the vapor present in the matrix. Condensation will occur at the cold wall as well as in the porous matrix and a liquid film will develop along the wall. In this liquid film the temperature will vary from T_w to T_s. Adjacent to this film, there will be a region where the vapor and the liquid will co-exist to form a two-phase zone and where the vapor will be in a superheated state and the liquid in a metastable state. At the interface of the two zones saturation conditions will exist and hence the capillary pressure P_c will be zero. The degree of superheat of the vapor will increase away from the wall and hence P_c will also increase until it reaches its maximum limit at the edge of the two-phase zone. The size of the two-phase zone will depend on the type of porous matrix and also on the fluid used. Beyond this region a superheated vapor zone will exist. A schematic diagram of such a model is shown in Fig. 2.

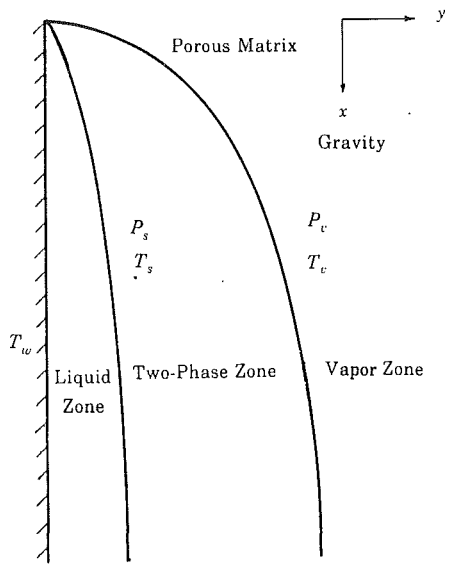

Fig. 2 Schematic diagram of three-zone model

Nomenclature

Bo = Bond number = $\Delta\rho g K/\sigma\sqrt{\epsilon}$
C_p = specific heat of liquid, J/kg-K
$f(s)$ = function, defined in equation (10)
g = gravity, m/s^2
G = dimensionless group, defined in equation (34)
h = heat transfer coefficient, W/m^2-K
h_{fg} = heat of vaporization, J/kg
Ja = Jakob number = $C_p\Delta T/h_{fg}$
K = permeability, m^2
$m(\delta^+)$ = function, defined in equation (32)
$\dot{\mathbf{m}}$ = mass flux vector, kg/s
$n(\delta^+)$ = function, defined in equation (32)
Nu_x = Nusselt number = hx/λ_e
P = pressure, N/m^2
Pr_e = Prandtl number = ν_l/α_e
r = radius of curvature, m
R = dimensionless group, defined in equation (33)
Ra_k = Rayleigh number based on permeability = $K^{3/2}\Delta\rho g/\mu_l\alpha_e$
Ra_x = Rayleigh number based on x and permeability = $Kx\Delta\rho g/\mu_l\alpha_e$
s = dimensionless saturation, defined in equation (9)
T = temperature, K
ΔT = temperature difference = $T_s - T_w$
u = velocity in x direction, m/s
$\bar{u}$ = dimensionless velocity = u/U_D
$\mathbf{u}$ = velocity vector, m/s
U_D = Darcy velocity = $K\Delta\rho g/\mu_l$, m/s
v = velocity in y direction, m/s
$\bar{v}$ = dimensionless velocity = v/U_D
x = distance in direction of gravity, m
$\bar{x}$ = dimensionless distance in x direction = $x/\sqrt{K}$
x^+ = dimensionless distance in x direction = $x/\mathrm{Ra}_k\sqrt{K}$
y = distance in direction perpendicular to gravity, m
$\bar{y}$ = dimensionless distance in y direction = $y/\sqrt{K}$
α_e = effective thermal diffusivity = $\lambda_e/\rho_l C_p$, m^2/s
δ = thickness of condensation zones, m
δ^+ = dimensionless $\delta = \delta/\sqrt{K}$
ϵ = porosity
η = similarity variable, defined in equation (14)
θ = dimensionless temperature = $(T-T_w)/(T_s-T_w)$
λ_e = effective thermal conductivity = $\epsilon\lambda_{\text{liquid}} + (1-\epsilon)\lambda_{\text{solid}}$, W/m-K
μ = Gibbs' potential, J/kg
ν = kinematic viscosity, m^2/s
ρ = density, kg/m^3
$\Delta\rho$ = difference in densities = $\rho_l - \rho_v$
σ = surface tension, N/m
v = specific volume, m^3/kg
ϕ = function defined in equation (37)
ψ = function defined in equation (36)

Subscripts

2 = two-phase zone
c = capillary
e = effective
i = irreducible
l = liquid or liquid zone
r = for relative permeability, defined in equation (11)
s = saturated condition
v = vapor
w = wall

Analysis of the Two-Phase Zone

The two-phase zone is a region where liquid and vapor coexist at conditions of local equilibrium. Although locally, the temperatures as well as the Gibbs' potential are equal, global gradients of thermodynamic state variables will exist. The capillary pressure and the temperature fully determine the thermodynamic state of each phase. It is thus necessary to determine their respective fields in this region and so conservation equations need to be solved.

The mass continuity equation is

$$\rho_l\left[\frac{\partial u_l}{\partial x}+\frac{\partial v_l}{\partial y_2}\right]+\rho_v\left[\frac{\partial u_v}{\partial x}+\frac{\partial v_v}{\partial y_2}\right]=0 \tag{2}$$

It is assumed that the mass fluxes are governed by Darcy's law

$$\dot{\mathbf{m}}_l=-\frac{KK_{rl}}{\nu_l}\nabla P_l \tag{3}$$

$$\dot{\mathbf{m}}_v=-\frac{KK_{rv}}{\nu_v}\nabla P_v \tag{4}$$

The specific volume of the vapor is usually much greater than that of the liquid, $\nu_v >> \nu_l$. Therefore, the relation $\nu=(\partial\mu/\partial P)_T$ suggests that the slope of the superheated vapor curve will be far greater than that of the liquid in a μ–P diagram. Thus it is reasonable to assume that any change in capillary pressure is mainly due to a change in liquid pressure and that $P_v \sim P_s$. This implies that vapor pressure gradients depend on the temperature gradients through the Clausius-Clapeyron equation (Callen, 1985). For most fluids in engineering applications $P_c << h_{fg}\rho_l/T_s$, and so the temperature in the two-phase zone (Udell, 1985) is assumed constant. Therefore, the continuity equation is reduced to the following form:

$$\frac{\partial u_l}{\partial x}+\frac{\partial v_l}{\partial y_2}=0 \tag{5}$$

Shekarriz and Plumb (1986) simplified this equation further by assuming $u_l = U_D$. This eliminates the first term from equation (5) and hence fails to account for the change of mass flux along the x direction. In the present analysis, the following expressions for velocity are assumed:

$$u_l=\frac{KK_{rl}\Delta\rho g}{\mu_l}=U_D K_{rl} \tag{6}$$

$$v_l=-\frac{KK_{rl}}{\mu_l}\frac{\partial P_l}{\partial y_2}=\frac{KK_{rl}}{\mu_l}\frac{\partial P_c}{\partial y_2} \tag{7}$$

Udell (1983) showed that the capillary pressure can be written in the following form:

$$P_c=\frac{\sigma}{\sqrt{K/\epsilon}}f(s) \tag{8}$$

where $f(s)$ is a function only of the nondimensional saturation, defined as follows:

$$s=\frac{s_l-s_{li}}{1-s_{li}} \tag{9}$$

The function $f(s)$ can be obtained by correlating Leverett's (1941) experimental data as follows (Udell, 1983):

$$f(s)=1.417(1-s)-2.120(1-s)^2+1.263(1-s)^3 \tag{10}$$

The vapor and liquid relative permeabilities can be correlated as functions of the liquid saturation (Fatt and Klikoff, 1959), as

$$K_{rl}=s^3 \qquad K_{rv}=(1-s)^3 \tag{11}$$

Substituting equations (6)–(11) into equation (5), the continuity equation is reduced to the following form:

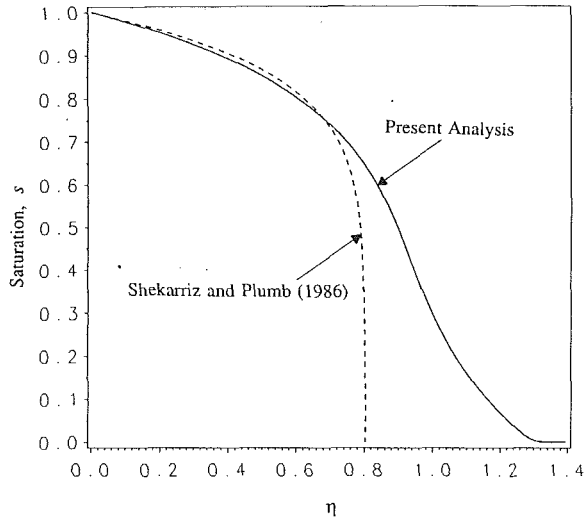

Fig. 3 Saturation profile in two-phase zone

$$3\frac{\partial s}{\partial x}+\left(\frac{\sigma/\sqrt{K/\epsilon}}{\Delta\rho g}\right)\left[(3f'+sf'')\left(\frac{\partial s}{\partial y_2}\right)^2+sf'\frac{\partial^2 s}{\partial y_2^2}\right]=0 \tag{12}$$

with boundary conditions

$$s=0 \text{ at } x=0; \quad s=1 \text{ at } y_2=0; \quad s=0 \text{ at } y_2\to\infty \tag{13}$$

In the above conditions, $y_2=0$ corresponds to the interface of the two-phase zone with the liquid zone.

The nature of equation (12), along with the boundary conditions, enables the use of a similarity transformation, the similarity variable being

$$\eta=\frac{y_2}{\left(\frac{(\sigma/\sqrt{K/\epsilon})x}{\Delta\rho g}\right)^2} \tag{14}$$

Using this similarity variable, equation (12) is transformed into the following form:

$$s''=\frac{\frac{3}{2}\eta s'-(3f'+sf'')s'^2}{sf'} \tag{15}$$

with boundary conditions

$$s(\eta=0)=1; \quad s(\eta\to\infty)=0 \tag{16}$$

Equation (16) is solved numerically using a fourth-order Runge-Kutta scheme to obtain the saturation profile, as shown in Fig. 3. It can be observed that the two-phase zone is a boundary layer, in which the saturation gradients disappear at large distances away from the origin, in the η plane. The boundary layer thickness is chosen to be at $\eta=1.296$. This is based on the fact that s^3 or the liquid velocity changes by less than one percent. The saturation gradient at $\eta=0$ is responsible for the mass flux of liquid from the liquid zone into the two-phase zone, thus reducing the liquid film thickness in the process. This increases the rate of heat transfer as compared to the case in the absence of a porous matrix. In Shekarriz and Plumb's (1986) analysis the saturation profile obtained had an infinite slope at $y_2=\delta$, that is at the interface with the vapor zone. This is due to the fact that the $\partial u_l/\partial x$ term was neglected in their analysis. The present analysis shows that the inclusion of this term has a significant effect on the saturation profile and hence would be incorrect to neglect. However, when $\eta\to 0$, $\partial u_l/\partial x$ goes to zero, as indicated by equation (15). Therefore, the results of the two analyses tend to coincide for small values of η.

Analysis of the Liquid Zone

The liquid zone consists of a thin film of liquid falling due to gravity along the wall. As shown in Fig. 2, the liquid zone lies between the cold wall and the two-phase zone. At the interface with the two-phase zone, saturation conditions exist. The temperature of the wall T_w is assumed to be less than the saturation temperature T_s. Consequently, heat is transferred from the liquid to the wall. The rate of the heat transfer depends on the temperature gradient in the liquid at the wall. In order to find this gradient, the temperature field in the liquid film needs to be determined.

The laws that govern the process of heat transfer in film condensation are those of mass, momentum, and energy conservation, and are given as

Mass

$$\nabla \cdot \dot{\mathbf{m}}_l = 0 \tag{17}$$

Momentum

$$\mathbf{u}_l \cdot \nabla \mathbf{u}_l = \left(\frac{\rho_l - \rho_g}{\rho_l}\right)\mathbf{g} - \frac{\nu_l}{K}\mathbf{u}_l + \nu_l \nabla^2 \mathbf{u}_l \tag{18}$$

Energy

$$\mathbf{u}_l \cdot \nabla T = \alpha_e \nabla^2 T \tag{19}$$

In the present literature various simplifications have been introduced to make these equations tractable. A common assumption is that the film is a thin boundary layer and hence diffusion of heat and momentum are predominantly in the y direction. In addition, Cheng (1981) neglected the convection and diffusion terms in equation (18) and thus reduced the momentum equation to Darcy's law, and allowed for a slip in velocity at the wall. Using U_D as the velocity, equation (19) was solved. The results of Cheng (1981) showed that although the convective terms were included in equation (19), the temperature profile was almost linear for small values of the Jakob number, $Ja < 1$. Shekarriz and Plumb (1986) also assumed $u_l = U_D$ as a solution of equation (18) and a linear temperature profile as a solution of equation (19), by neglecting the convective term. White and Tien (1987a) solved the complete momentum equation and used a linear temperature profile for their analysis.

From the results of Cheng (1981), it can be concluded that the convective terms in equation (19) are negligible for $Ja < 1$ and that a linear temperature profile is a reasonable assumption. However, slip in velocity at the wall (Cheng, 1981; Shekarriz and Plumb, 1986) overpredicts the heat transfer to the wall since it amounts to a higher condensate flux. In view of these facts, the present analysis incorporates the following assumptions: (*i*) The liquid film is a boundary layer, (*ii*) convection effects in equations (18) and (19) are negligible, (*iii*) subcooling of the liquid film is negligible compared to the energy transferred during phase change, and (*iv*) fluid has constant properties.

These assumptions reduce the conservation equations to

$$\frac{\partial \bar{u}_l}{\partial \bar{x}} + \frac{\partial \bar{v}_l}{\partial \bar{y}_l} = 0 \tag{20}$$

$$\frac{\partial^2 \bar{u}_l}{\partial \bar{y}_l^2} + 1 - \bar{u}_l = 0 \tag{21}$$

$$\frac{\partial^2 \theta}{\partial \bar{y}_l^2} = 0 \tag{22}$$

Equation (21) is Brinkman's (1947) equation, which was obtained by neglecting convection as a mechanism of momentum transfer.

The boundary conditions at the wall, that is at $\bar{y}_l = 0$, are

$$\bar{u}_l = \bar{v}_l = \theta = 0 \tag{23}$$

The boundary conditions at $\bar{y}_l = \delta_l^+$ correspond to that of the interface with the two-phase zone where the liquid velocities and shears need to be matched. The shear corresponds to the drag imposed on the liquid film by the surface tension forces in the two-phase zone. This matching procedure has inherent complexities, which make the system of equations extremely cumbersome to solve. This difficulty is circumvented by making certain assumptions. Three models are suggested in the present analysis. The equations of these models are analyzed and compared to bring out the characteristic features of each model.

Model 1. In this model a no-shear boundary condition, $\partial \bar{u}_l / \partial \bar{y}_l = 0$, is used for the momentum equation in the liquid zone at $\bar{y}_l = \delta_l^+$ and is the same as the assumption in the classical Nusselt analysis. This model would give accurate predictions whenever the porous matrix plays a minor role in the condensation process. This occurs when the two-phase zone, created solely due to the presence of the porous matrix, has negligible effect. The thickness of the two-phase zone depends on the parameter $\sigma\sqrt{\epsilon}/\Delta\rho g K$. Hence, for porous media with high permeabilities or with liquids of low surface tension, this model would produce accurate results.

Using this assumption, equation (21) is solved to obtain the velocity profile

$$\bar{u}_l = 1 - \cosh \bar{y}_l + \tanh \delta_l^+ \sinh \bar{y}_l \tag{24}$$

At the boundary $\bar{y}_l = \delta_l^+$, the velocity is $\bar{u}_l = 1 - \operatorname{sech} \delta_l^+$. To show the nature of this solution, two limiting cases are considered here. Firstly, as $K \to \infty$, that is in the absence of any porous matrix, equation (24) reduces to

$$u = \frac{\Delta\rho g}{\mu_l}\left(\delta y - \frac{y^2}{2}\right) \tag{25}$$

which is the same as Nusselt's solution for the velocity profile. Secondly, when δ_l^+ is small the velocity at the interface will be less than U_D. From a physical viewpoint the surface tension, which is active in the two-phase zone, will retard the liquid film from falling due to gravity. This is because the shear stress at the interface, $\partial u_l / \partial y_2$ at $y_2 = 0$, is negative due to the nature of the saturation gradient at this location. The drag of the two-phase zone will be more pronounced when the liquid film is thin. This will result in a velocity less than U_D, which incorporates only the effect of gravity. As the liquid film starts growing, the velocity at the interface will increase asymptotically from zero to U_D. This model shows the same trend although the drag due to the two-phase zone is neglected. This causes the mass flux to be higher in the liquid zone and can lead to overpredictions.

The overall energy balance in the liquid and the two-phase zones can be written as

$$h_{fg}\frac{d}{dx}\int_0^{\delta_l} \rho_l u_l dy_l + h_{fg}\rho_l U_D (1 - \operatorname{sech} \delta_l^+)\frac{d}{dx}\int_0^{\delta_2} s^3 dy_2 = \frac{\lambda_e \Delta T}{\delta_l} \tag{26}$$

In the analysis of the two-phase zone, it was shown that the temperature drop across it is negligible, and hence it is assumed that the temperature drop from the vapor to the wall occurs mainly in the liquid film. In equation (26) the first term corresponds to the contribution of energy transfer due to condensed liquid in the liquid zone, whereas the second term represents a similar contribution from the two-phase zone. The energy transfer during change of phase is conducted to the wall and is accounted for by the right-hand side of equation (26). The value of the integral of s^3 in the two-phase zone is computed numerically. In a nondimensional form the energy balance equation is

$$(1 - \operatorname{sech}^2 \delta_l^+)\frac{d\delta_l^+}{d\bar{x}} + (1 - \operatorname{sech} \delta_l^+)\frac{0.373}{\sqrt{\mathrm{Bo}\bar{x}}} = \frac{Ja}{\delta_l^+ \mathrm{Ra}_k} \tag{27}$$

Equation (27) is a nonlinear equation and needs to be solved numerically.

Model 2. The second model suggested in the present analysis is less rigorous than model 1, although more fundamental than previous works of Cheng (1981) and Shekarriz and Plumb (1986). Similar to the previous model, equation (21) is adopted as the momentum equation. The boundary condition, at $\bar{y}_l = \delta_l^+$, used for this equation is $\bar{u}_l = 1$. This model is an improvement over the previous works since it uses a no-slip condition at the wall. However, this model will overpredict the heat transfer rates since the velocity at the interface is forced to be U_D even for small values of δ_l^+. This will increase the flow rate of liquid in the liquid zone and hence enhance the condensate flux. So this model has its limitation for small values of δ_l^+, although for large values, the results should show trends similar to that of model 1 and would be accurate. The reason this model is introduced is to show the effect of the diffusion term in equation (21), which allows for a no-slip condition at the wall, in comparison with previous works where only a Darcy velocity was assumed.

Equation (21) is solved with the appropriate boundary conditions to get a velocity profile of the following form:

$$\bar{u}_l = 1 - \cosh \bar{y}_l + \coth \delta_l^+ \sinh \bar{y}_l \tag{28}$$

The overall energy balance equation can be written in a non-dimensional form as

$$\left(1 - \frac{1}{1+\cosh \delta_l^+}\right)\frac{d\delta_l^+}{d\bar{x}} + \frac{0.373}{\sqrt{\mathrm{Bo}\bar{x}}} = \frac{Ja}{\delta_l^+ \mathrm{Ra}_k} \tag{29}$$

Model 3. The only previous work on film condensation in a porous medium that recognized the presence of the two-phase zone was that of Shekarriz and Plumb (1986). The present analysis of the two-phase zone is more refined than theirs and hence the impact of only this refinement on the heat transfer results needs to be shown. Since they had assumed Darcy's law for the momentum equation in the liquid zone, model 3 is proposed to include the same assumption for the liquid zone but use the present two-phase zone analysis. This model is also useful to illustrate the effect of the two-phase zone in comparison with the work of Cheng (1981), in which this effect was not considered.

The overall energy balance equation in non-dimensional form is

$$\frac{d\delta_l^+}{d\bar{x}} + \frac{0.373}{\sqrt{\mathrm{Bo}\bar{x}}} = \frac{Ja}{\delta_l^+ \mathrm{Ra}_k} \tag{30}$$

This equation can be solved analytically to obtain the following result:

$$\frac{\delta_l^+}{\sqrt{\bar{x}}} = -\frac{0.373}{\sqrt{\mathrm{Bo}}} + \left(\left(\frac{0.373}{\sqrt{\mathrm{Bo}}}\right)^2 + \frac{2Ja}{\mathrm{Ra}_k}\right)^{1/2} \tag{31}$$

The Bond number Bo plays an important role in this analysis. It is a ratio of gravity and surface tension forces and is pertinent to the two-phase zone where surface tension forces are active. It shows the effect of the two-phase zone on the thickness of the liquid film and hence the rate of condensation. If Bo is small then the surface tension forces are dominant and hence contribution of the two-phase zone to the total liquid flow is large. This implies that, for a particular value of ΔT, the liquid zone is thin and so the heat transfer rate is high. For model 1, in the limiting case when Bo is very large, equation (27) reduces to that of Nusselt's analysis. Typical values of Bo, for a porous matrix with $K = 10^{-8}$ m^2 and for various fluids (Vargaftik, 1983), are given in Table 1. The porosity ϵ is assumed to be 0.5.

Results and Discussion

In the preceding section, three analytical models were introduced to solve the problem of film condensation in a porous medium. The last step in the analysis is to solve the overall energy balance equation, which, in a general form, is

$$m(\delta_l^+)\frac{d\delta_l^+}{dx^+} + 0.373n(\delta_l^+)\left(\frac{R}{x^+}\right)^{1/2} = \frac{Ja}{\delta_l^+} \tag{32}$$

where $x^+ = x/\mathrm{Ra}_k K^{1/2}$.

Equation (32) introduces a dimensionless group R, which is defined as

$$R = \frac{\mathrm{Ra}_k}{\mathrm{Bo}} = \frac{\sigma\sqrt{K\epsilon}}{\mu_l \alpha_e} \tag{33}$$

The physical meaning of R can be better understood when it is written in the following form:

$$R = \left(\frac{\sigma\sqrt{K\epsilon}}{\rho_l \nu_l^2}\right)\mathrm{Pr}_e = G\mathrm{Pr}_e \tag{34}$$

The parameter G in equation (34) is the ratio of surface tension and viscous forces. Since both these forces exist during a surface tension driven flow in any unsaturated porous medium, this parameter will usually appear in such a situation. A comparison of this type of flow with that of free convection will show that the parameter R is analogous to the Rayleigh number and that G is analogous to the Grashof number, which represents the ratio of buoyancy and viscous forces. Typical values of R, for various combinations of fibrous porous media and liquids, are given in Table 1.

In the liquid zone, a linear temperature profile was assumed. Consequently, the local Nusselt number is

$$\mathrm{Nu}_x = \frac{\bar{x}}{\delta_l^+} \tag{35}$$

In general, the liquid film thickness varies with distance x as $\delta_l \sim x^a$. For models 2 and 3, $a = 0.5$, hence the heat transfer results can be represented as

$$\frac{\mathrm{Nu}_x}{\sqrt{\mathrm{Ra}_x}} = \psi(R, Ja) = \frac{\sqrt{x^+}}{\delta_l^+} \tag{36}$$

This type of relation makes it convenient to compare models 2 and 3 with the results of Cheng (1981) and Shekarriz and Plumb (1986), which are also in a similar form.

For model 1, a varies from 0.15 to 0.25 with increasing values of x, and hence cannot be cast in the form of equation (36). In order to compare the results of model 1 with those of other models, the equation is presented in the following form:

$$\frac{\mathrm{Nu}_x}{\mathrm{Ra}_k} = \phi(x^+, R, Ja) = \frac{x^+}{\delta_l^+} \tag{37}$$

For models 1 and 2, equation (32) is a nonlinear equation and hence has to be solved numerically. For model 3, the heat transfer result is

$$\frac{\mathrm{Nu}_x}{\sqrt{\mathrm{Ra}_x}} = [-0.373\sqrt{R} + ((0.373\sqrt{R})^2 + 2Ja)^{1/2}]^{-1} \tag{38}$$

Table 1 Typical values of Bo and R for various fluids and porous media

Fluids	T °C	Bo $\times 10^3$	R			
			Vitreous Carbon	Aluminum	Glass	Nickel
Water	25	1.85	7191	244	35328	538
Freon113	25	11.36	1079	34	7985	76
Freon12	25	20.09	1188	38	8849	84
Ammonia	11.1	3.87	8342	273	51345	605

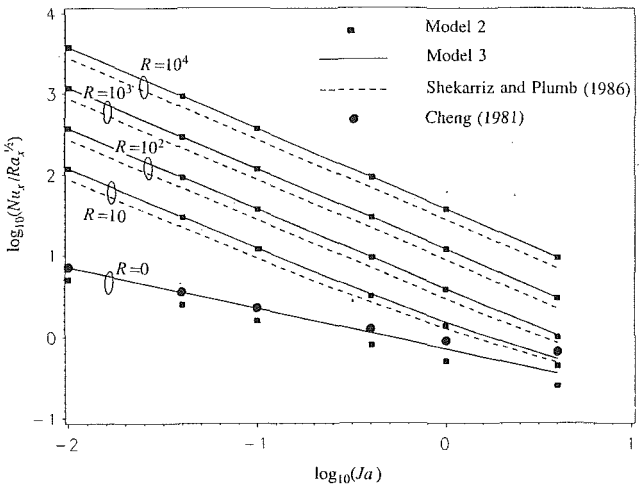

Fig. 4 Heat transfer results for models 2 and 3

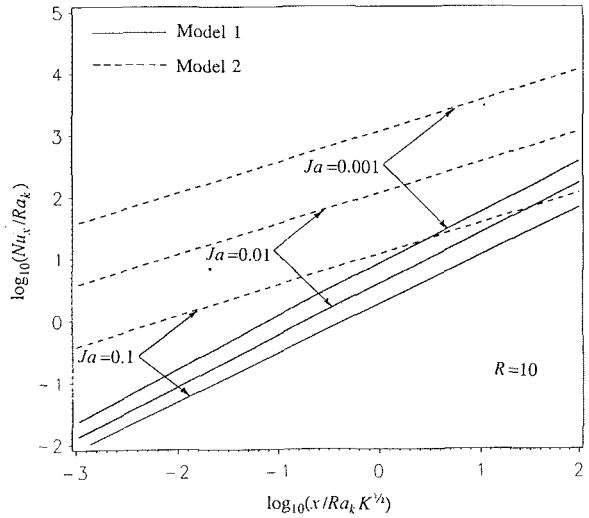

Fig. 5 Heat transfer results of models 1 and 2 for $R=10$

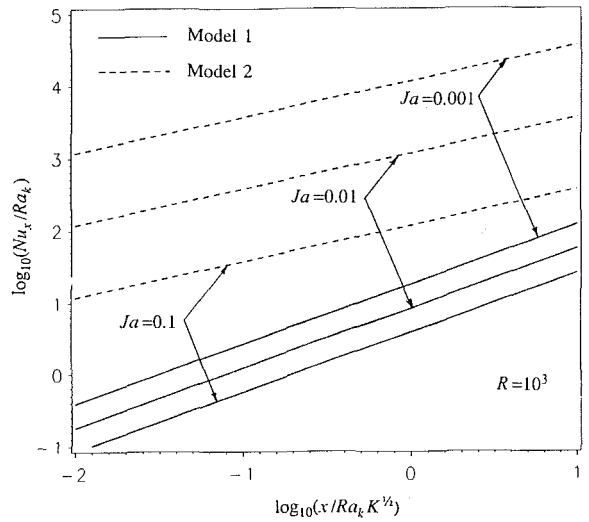

Fig. 6 Heat transfer results of models 1 and 2 for $R=1000$

The results of models 2 and 3, along with those of Cheng (1981) and Shekarriz and Plumb (1986), are shown in Fig. 4, for varying values of Ja and R. It can be observed that for increasing values of R, the rate of heat transfer goes up. The physical reason underlying this is that higher values of R imply stronger surface tension forces, which result in a two-phase zone, dominant in size over the liquid zone. This creates sharper temperature gradients in the liquid film, which result in higher heat transfer rates. A comparison of results for $R=0$ shows that for $Ja<1$, the predictions of Cheng (1981), Shekarriz and Plumb (1986), and model 3 coincide. This is as expected, since for $R=0$ the two-phase zone does not exist and hence plays no role in the condensation process. Only the liquid zone, for which all three models assume Darcy velocity, affects the condensation. For $Ja>1$, the nonlinearity of the temperature profile is significant and hence the results of Cheng (1981) diverge from those of the other two models. The heat transfer rates, as predicted by model 2, are always lower than that of Cheng (1981), Shekarriz and Plumb (1986), and model 3. This is because the no-slip condition at the wall in model 2 results in a lower liquid flux and hence a lower condensation rate. With increasing values of R, the liquid zone becomes thinner to the point where the liquid flux is predominantly in the two-phase zone. Thus the no-slip condition at the wall does not account for much of a change in the liquid flux. Consequently, the results of models 2 and 3 coincide for higher values of R. The heat transfer results of model 3 are always higher than those of Shekarriz and Plumb (1986). This is because the two-phase zone analysis of Shekarriz and Plumb (1986) underpredicts the size and the liquid flux of this zone and hence shows a lower heat transfer rate. The differences are more pronounced for higher values of R, for which the two-phase zone plays a more significant role, whereas for $R=0$ the results coincide.

To obtain the heat transfer results for model 1, equation (32) is solved numerically by a second-order Runge-Kutta method, with appropriate $m(\delta_l^+)$ and $n(\delta_l^+)$. To avoid the singularity in equation (32) at $x^+=\delta_l^+=0$, some assumptions based on physical reasoning have been made. For x^+, $\delta_l^+ \to 0$ the liquid film is much thinner than the typical pore size of the porous matrix, which is of the order of $K^{1/2}$. Hence it is reasonable to assume that for $\delta_l^+ \to 0$ the liquid film does not feel the presence of the porous matrix. Thus one can use the Nusselt analysis, which is a limiting case of model 1, to obtain the solution for the first grid point. For subsequent grid points equation (32) is fully solved.

The results of model 1 are shown in Figs. 5 and 6, each for a different value of R. The comparison is done only with model 2, and in turn with other models through Fig. 4. In the preceding section, it was pointed out that due to the no-shear condition at the liquid zone interface the condensate flux in the liquid zone in model 1 is less than that of model 2. This results in a lower heat transfer rate, as can be observed in Figs. 5 and 6. It is evident that as Ja is increased, the discrepancies in the results of models 1 and 2 decrease. This is because a higher value of Ja would result in a thicker liquid zone. As the thickness of the liquid zone is increased, the velocity profile of model 1 tends to that of model 2. However, an increase in R decreases the liquid zone thickness and increases the discrepancies between the results of models 1 and 2. Both these trends can be observed in Figs. 5 and 6.

Figures 7(a, b) show comparisons between the predictions of models 1 and 2 and experimental results of White and Tien (1987b) for constant-porosity media. The parameters for the experiments of Fig. 7(a) are $K=0.97\times10^{-7}$ m^2 and $\epsilon=0.97$ for an aluminum foam metal, $\mathrm{Ra}_k=153.22$, $Ja=0.642$, and $R=1862.1$. The results show that there is good agreement between the predictions of model 1 and the experiments, whereas model 2 severely overpredicts the heat transfer rate. The slight overprediction by model 1 is probably due to its no-shear condition, which implies a higher condensate flux than actual. The experiments of Fig. 7(b) correspond to $K=1.2\times10^{-8}$ m^2 and $\epsilon=0.97$ for a polyurethane form, $\mathrm{Ra}_k=254.73$, $Ja=0.007$, and $R=25{,}021.7$. For this case model 1 over-

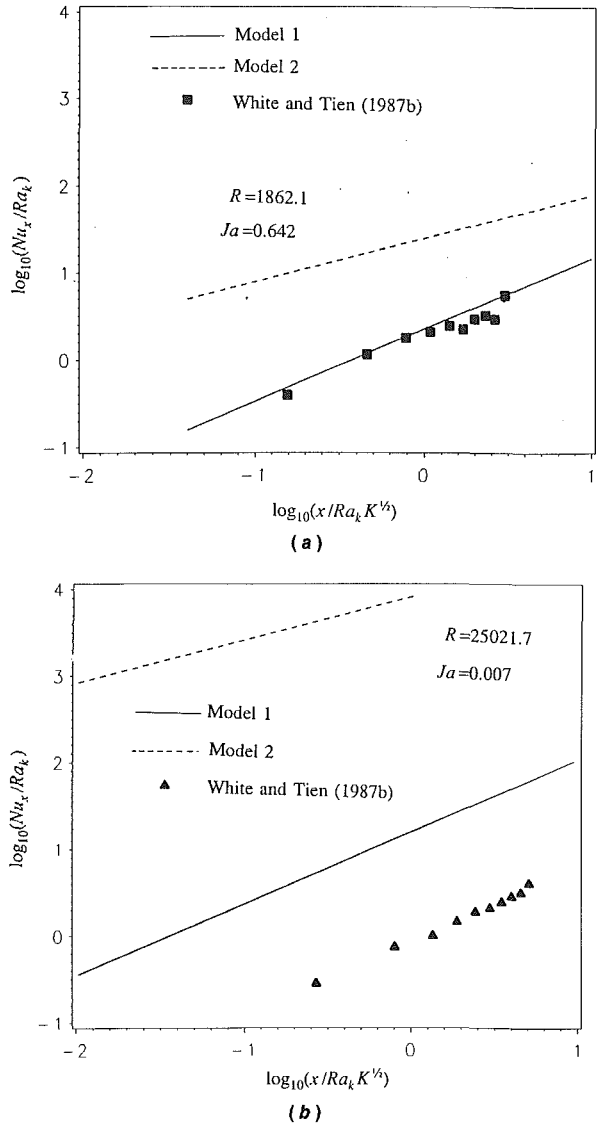

Fig. 7 Comparison of results of models 1 and 2 with experiments (White and Tien, 1987b) for different porous media: *(a)* aluminum foam metal; *(b)* polyurethane foam

predicts the experiments, although the trends of the Nu_x/Ra_k with x^+ appear similar. The overprediction is probably due to the effect of the surface tension drag at the liquid zone interface, which is neglected in model 1. As discussed earlier, this effect is more pronounced when the two-phase zone plays a more dominant role in the condensation, that is for higher σ and lower values of K. This explains why even though there is good agreement in Fig. 7(a), model 1 overpredicts in Fig. 7(b).

Conclusion

This study presents an analysis of the problem of film condensation in porous media. Based on the thermodynamics of phase equilibria, the presence of a two-phase zone during film condensation in porous media is explained. The analysis of the two-phase zone shows that the inclusion of a term representing change in liquid flux in the direction of gravity produces a boundary layer profile for the saturation. This is an improvement over the previous model in which this term was neglected.

A dimensionless group R is introduced to characterize viscous flows driven by surface tension forces. The physical meaning of this parameter is explained with an analogy of free convection. The heat transfer results are presented as a function of R, and it is observed that at higher values of R, the heat transferred is higher. It is shown that model 3, which assumes velocity slip at the wall, overpredicts the heat transfer since the slip velocity at the wall amounts to a larger liquid flux. Model 2, which assumes no slip at the wall and Darcy velocity at the liquid zone interface, produces heat transfer rates higher than those resulting from model 1, which assumes no slip at the wall and no shear at the interface. This occurs because in model 2 the Darcy velocity at the interface is an unreasonable assumption since it implies a larger liquid flux. Model 1 produces the most realistic predictions out of all three models and is compared with previous experiments. The comparison shows that model 1, however, overpredicts the experiments for low-permeability porous media. This is probably due to the drag imposed on the liquid zone due to surface tension forces in the two-phase zone, which results in a liquid flux lower than that of model 1. The porous medium imposes two competing effects during film condensation: (i) enhancement by the capillary suction of the two-phase zone, which results in thinner liquid films, and (ii) reduction due to flow retardation caused by surface tension forces of the two-phase zone and the form drag of the porous medium, which increase the liquid film thickness.

Acknowledgments

The authors would like to thank Susan White and Julia Usher for their comments and Makrand Kulkarni for his help with the graphics.

References

Brinkman, H. C., 1947, "A Calculation of the Viscous Force Exerted by a Flowing Fluid on a Dense Swarm of Particles," *Applied Science Research*, pp. 27–34.

Callen, H. B., 1985, *Thermodynamics and an Introduction to Thermostatics*, 2nd ed., Wiley, New York.

Cheng, P., 1981, "Film Condensation Along an Inclined Surface in a Porous Medium," *International Journal of Heat and Mass Transfer*, Vol. 24, pp. 983–989.

Cheng, P., and Chui, D. K., 1984, "Transient Film Condensation on a Vertical Surface in a Porous Medium," *International Journal of Heat and Mass Transfer*, Vol. 27, pp. 795–798.

Fatt, I., and Klikoff, W. A., 1959, "Effect of Fractional Wettability on Multiphase Flow Through Porous Media," AIME Technical Note No. 2043, *AIME Transactions*, Vol. 216, p. 246.

Kaviany, M., 1986, "Boundary Layer Treatment of Film Condensation in the Presence of a Solid Matrix," *International Journal of Heat and Mass Transfer*, Vol. 29, pp. 951–954.

Leverett, M. C., 1941, "Capillary Behavior in Porous Solids," *ASME Transactions*, Vol. 142, pp. 152–169.

Nilson, R. H., and Romero, L. A., 1980, "Self-Similar Condensing Films in Porous Media," *International Journal of Heat and Mass Transfer*, Vol. 23, pp. 1461–1470.

Poulikakos, D., and Orozco, J., 1986, "A Study of Condensation on a Vertical Internally Cooled Pipe Embedded in a Porous Medium," *International Communications in Heat and Mass Transfer*, Vol. 13, pp. 181–192.

Shekarriz, A., and Plumb, O. A., 1986, "A Theoretical Study of the Enhancement of Filmwise Condensation Using Porous Fins," presented at the AIAA-ASME 4th Joint Conference, Boston, June 1–4, Paper No. 86-HT-31.

Udell, K. S., 1983, "Heat Transfer in Porous Media Heated From Above With Evaporation, Condensation, and Capillary Effects," ASME JOURNAL OF HEAT TRANSFER, Vol. 105, pp. 485–492.

Udell, K. S., 1985, "Heat Transfer in Porous Media Considering Phase Change and Capillarity—the Heat Pipe Effect," *International Journal of Heat and Mass Transfer*, Vol. 28, pp. 485–495.

Vafai, K., and Tien, C. L., 1981, "Boundary and Inertia Effects on Flow and Heat Transfer in Porous Media," *International Journal of Heat and Mass Transfer*, Vol. 24, pp. 195–203.

Vargaftik, N. B., 1983, *Tables on Thermophysical Properties of Liquids and Gases*, 2nd ed., Hemisphere, Washington, DC.

White, S. M., and Tien, C. L., 1987a, "Analysis of Laminar Film Condensation in a Porous Medium," *Proceedings of the ASME-JSME Thermal Joint Engineering Conference*, Mar. 22–27, Vol. 2, pp. 401–406.

White, S. M., and Tien, C. L., 1987b, "An Experimental Investigation of Film Condensation in Porous Structures," presented at the 6th International Heat Pipe Conference, Grenoble, France.

P. J. Marto
Fellow ASME

D. Zebrowski

A. S. Wanniarachchi[1]
Mem. ASME

Department of Mechanical Engineering,
Naval Postgraduate School,
Monterey, CA 93943-5100

J. W. Rose
Mem. ASME

Department of Mechanical Engineering,
Queen Mary College,
University of London,
London, United Kingdom

An Experimental Study of R-113 Film Condensation on Horizontal Integral-Fin Tubes

Heat transfer measurements were made at near-atmospheric pressure on a smooth tube, on 24 integral-fin tubes having machined, rectangular-shaped fins, and on a commercial integral-fin tube. All tubes were made of copper. The vapor flowed vertically downward with a nominal velocity of 0.4 m/s. Vapor-side heat transfer coefficients were determined with a typical uncertainty of ± 7 percent using a "modified Wilson plot" technique. The vapor-side heat transfer coefficient of the integral-fin tubes (based upon the outside surface area of the smooth tube) was enhanced considerably more than the surface area enhancement provided by the fins. Heat transfer enhancements (for the same vapor-to-wall temperature difference) up to around 7 were measured for a corresponding area enhancement of only 3.9. The optimum fin spacing was found to lie between 0.2 and 0.5 mm, depending upon fin thickness and height. The data were compared with those of other investigations and with several existing theoretical models. Visual observations of condensate drainage patterns from the finned tubes were also made.

Introduction

Integral-fin tubes have been used in the refrigeration and process industries for many years. Although early theoretical models to predict the thermal performance of these tubes neglected surface tension effects, it is now evident that these effects are important in two distinct ways. First, surface tension causes the condensate to fill the interfin spaces between fins on the bottom part of the tube (i.e., condensate retention or "flooding" occurs) and this reduces the heat transfer. Second, on the top, "unflooded" part of the tube, surface tension thins portions of the condensate film beyond what would be expected by gravity alone and this increases the heat transfer. Although these two opposing mechanisms add to the complexity of any theoretical analysis of this heat transfer situation, promising new models have been developed (see Marto, 1988; Webb, 1988), which require validation using accurate experimental data.

This paper provides new data for R-113 condensing on a family of specially manufactured integral-fin tubes. The data are part of a systematic experimental program to assist in the validation of existing heat transfer models so that accurate generalized design equations may be developed. This program has earlier provided similar data for steam (Wanniarachchi et al., 1985, 1986; Marto et al., 1986).

Previous Investigations

Beatty and Katz (1948) measured condensing heat transfer coefficients for several refrigerants on a commercially available, horizontal, integral-fin, copper tube having 630 fins/meter (16 fins/in.). The tube had a fin root diameter of 15.88 mm and a fin height of 1.46 mm. For R-22, data were also obtained for several special tubes of different fin height and thermal conductivity.

They proposed a theoretical model that considered only gravity-driven, Nusselt-type condensation on both the vertical fin flanks and the cylindrical tube surface in the interfin spaces. Their expression for the average heat transfer coefficient (based upon an effective finned-tube surface area A_{ef}), which correlated all their data to within 10 percent, is

$$\bar{\alpha}_e = 0.689\left\{\frac{k^3\rho^2 g\ h_{fg}}{\mu\Delta T D_{eq}}\right\}^{1/4} \tag{1}$$

where the equivalent tube diameter is calculated from

$$\left\{\frac{1}{D_{eq}}\right\}^{1/4} = 1.30\ \eta_f \frac{A_f}{A_{ef}}\frac{1}{\tilde{L}^{1/4}} + \frac{A_u}{A_{ef}}\frac{1}{D_r^{1/4}} \tag{2}$$

where

$$\tilde{L} = \pi(D_o^2 - D_r^2)/4D_o \text{ and} \tag{3}$$

$$A_{ef} = \eta_f A_f + A_u \tag{4}$$

Beatty and Katz (1948) did not distinguish between fin tips and fin flanks in the above equations, presumably because commercially finned tubes have fins with no appreciable fin-tip thickness. As a consequence, the above equations must be modified for trapezoidal or rectangular-shaped fins.

Katz and Geist (1948) measured R-12 condensing film coefficients for six horizontal integral-fin tubes in a vertical row, using a tube similar to the one used by Beatty and Katz (1948). The difference between their experimental coefficient for the top tube and the predicted coefficient using equation (1) was less than 14 percent. Pearson and Withers (1969) obtained data for R-22 condensing on a bundle of 60 similar integral-fin tubes within a 40-ton refrigeration condenser. They showed that by increasing the fin density from 748 to 1024 fins/meter, the condenser heat duty was increased up to 25 percent at the same vapor-to-coolant log-mean-temperature difference.

Karkhu and Borovkov (1971) obtained data for R-113 condensing on three different integral-fin tubes. The tubes were brass and had a root diameter of 18 mm. They had either 782 or 1238 trapezoidal-shaped fins/meter. Each fin had a tip thickness of 0.14 mm, a fin base spacing of 0.14 mm, and a fin-tip half angle of between 10 and 30 deg. Heat transfer coefficients were between 50 and 100 percent higher than for a smooth tube. Smirnov and Lukanov (1972) obtained data for R-11 condensing on a bundle of finned tubes with 472 thick, trapezoidal-shaped fins/meter. Their data for the top tube in

[1]Present address: Heat Transfer Research Inc., 1000 S. Fremont Ave., Alhambra, CA 91802.

Contributed by the Heat Transfer Division and presented at the National Heat Transfer Conference, Houston, Texas, July 24-27, 1988. Manuscript received by the Heat Transfer Division April 3, 1989; revision received September 26, 1989. Keywords: Augmentation and Enhancement, Condensation, Finned Surfaces.

the bundle agreed with equation (1), provided that the expression for equivalent diameter (equation (2)) was modified to

$$\left\{\frac{1}{D_{eq}}\right\}^{1/4} = 1.30\,\eta_f \frac{A_{fs}}{A_{ef}} \frac{1}{\bar{L}^{1/4}} + \eta_f \frac{A_{ft}}{A_{ef}} \frac{1}{D_o^{1/4}} + \frac{A_u}{A_{ef}} \frac{1}{D_r^{1/4}} \quad (5)$$

where the total effective surface area includes the fin sides, the fin tips, and the unfinned root

$$A_{ef} = \eta_f A_{fs} + \eta_f A_{ft} + A_u \quad (6)$$

Equation (5) is different from equation (2) in that it subdivides the fin surface into flanks and tips, which influence the heat transfer process differently.

Enya and Kisaragi (1977) condensed R-113 on copper low-fin and high-fin tubes having 748, 1024, and 1378 fins/meter, as well as on several specially prepared, spiral-groove tubes and porous-coated, finned tubes. Using the thermal conductance per unit length of tube (i.e., the heat transfer rate per unit vapor-to-wall temperature difference and per unit length), they reported remarkable improvements over the standard 748 fins/meter tube. In particular, they found that a twofold enhancement in the conductance is possible with the grooved tubes and a fourfold enhancement is possible with the porous-coated finned tubes, presumably due to the thinning of the condensate film near the fin tips. Carnavos (1980) measured R-11 condensing heat transfer coefficients on eleven different augmented tubes and on a smooth tube. The augmented tubes included flat-sided finned surfaces, fluted surfaces, and knurled surfaces. Heat transfer enhancements (based upon the "envelope" outside surface area A) over the smooth tube at the same condensing film temperature difference were about 4–6.

Rudy (1982) obtained data for R-11 condensing on four copper, integral-fin tubes. Three of the tubes were commercially available with 748, 1024, and 1378 fins/meter. The fourth tube was a 748 fins/meter tube machined down in diameter to reduce the fin height from 1.53 to 0.85 mm. Based upon the "envelope" outside surface area A, the 1378 fins/meter tube showed a heat transfer coefficient 71 percent higher than the 748 fins/meter tube and 49 percent higher than the 1024 fins/meter tube. Webb et al. (1985) used these data to establish a theoretical model to predict condensation on horizontal integral-fin tubes. Their model includes surface-tension-driven drainage on the fin flanks as well as condensate retention between fins on the lower part of the tube. On the fin flanks, they used the heat transfer coefficient proposed by Adamek (1981), who analyzed surface-tension-driven condensation on a family of condensate surface profiles with local radius of curvature given by

$$\frac{1}{R} = \frac{\theta_m}{S_m} \frac{(\zeta+1)}{\zeta}\left[1 - \left(\frac{s}{S_m}\right)^{\zeta}\right] \quad (7)$$

for $-1 \le \zeta < \infty$.

In equation (7), ζ is a parameter that characterizes the aspect ratio of the condensate surface. A large positive value of ζ (e.g., $\zeta = 10$) corresponds to a well-rounded, thick condensate film, whereas a negative value of ζ (e.g., $\zeta = -0.5$) corresponds to a very thin condensate film with a sharply defined tip. Webb et al. (1985) arrived at an expression for the average heat transfer coefficient (based upon the envelope outside surface area A)

$$\bar{\alpha}_o \eta = (1 - C_b)\left\{\alpha_h \frac{A_r}{A} + \eta_f \alpha_f \frac{A_f}{A}\right\} + C_b \alpha_b \quad (8)$$

where C_b is the fraction of the tube flooded by condensate, α_h is the heat transfer coefficient on the unflooded root surface of the tube between fins, α_f is the heat transfer coefficient on the unflooded fin flanks, and α_b is the heat transfer coefficient in the condensate flooded zone. Using this model (with values of ζ between -0.77 and -0.85), the predicted heat transfer coefficients were within ± 20 percent of their R-11 experimental values.

In a study of augmentation of condensation on horizontal, integral-fin tubes by attaching porous drainage plates, Honda et al. (1983) obtained condensing data for R-113 on several copper tubes. The geometry of these tubes is provided in Table 1. Two of the tubes (B, C) had trapezoidal-shaped fins (fin-tip

Nomenclature

a = coefficient defined in equation (12)
A = "envelope" outside surface area $= \pi D_o L$
A_{ef} = effective finned-tube surface area defined in equations (4) and (6)
A_f = surface area of fins
A_{fs} = surface area of fin sides
A_{ft} = surface area of fin tips
A_i = inside surface area $= \pi D_i L$
A_r = smooth tube surface area having diameter of fin root $= \pi D_r L$
A_u = surface area of interfin tube space
b = fin spacing; see Table 1
C_b = fraction of a finned tube surface "flooded" by condensate $= 1 - \Phi_f/\pi$
D_{eq} = equivalent diameter defined in equations (2) and (5)
D_i = inside diameter of tube
D_o = diameter to the outside of the fin tips
D_r = diameter to the fin roots, see Table 1 (or smooth tube outside diameter)
f_f = proportion of rectangular fin flanks blanked by retained liquid, defined in equation (19)
f_t = proportion of interfin tube surface of rectangular fin tube blanked by retained liquid, defined in equation (18)
g = gravitational acceleration
h_{fg} = specific enthalpy of vaporization
h = fin height; see Table 1
k = thermal conductivity of the liquid
L = condensing length of tube
$\bar{L}$ = effective condensing length on the side of a fin, defined as $\pi(D_o^2 - D_r^2)/4D_o$
Q = heat transfer rate to coolant
q = heat flux $= Q/A_r$
r = radius of curvature of condensate meniscus between fins, defined in equation (16)
R = radius of curvature of condensate film profile around a fin, defined in equation (7)
R_o = radius to the outside of the fins
R_w = wall resistance
s = distance along the condensate film surface measured from the fin tip
S_m = length of the convex condensate surface on a fin measured from the fin tip
t = fin thickness; see Table 1
T_{ci} = inlet temperature of cooling water
T_{co} = outlet temperature of cooling water
T_s = vapor saturation temperature
$\bar{T}_{wo}$ = average outside wall temperature at the root of the fins

half angle less than 5 deg) while the third (D) had rectangular ones. Tube D exhibited the best performance, showing an enhancement factor over a smooth tube (based upon the envelope outside surface area and at the same vapor-to-wall temperature difference) of 8.9. Honda et al. (1987) developed a generalized model to predict condensation heat transfer on horizontal, finned tubes. Their model is the most comprehensive approach to the problem. They divide the tube into unflooded and flooded regions where the flooding angle Φ_f is given by

$$\Phi_f = \cos^{-1}\left\{\frac{2\sigma \cos\theta}{gbR_o} - 1\right\} \tag{9}$$

Their model includes both surface tension and gravity forces as well as variable wall temperature both circumferentially around the tube and axially between fins. When compared to their earlier data obtained for R-113, agreement to within ±10 percent was obtained.

Kabov (1984) measured condensing heat transfer coefficients for R-12 and R-21 on several families of tubes having different fin spacings and heights. One family had a fin root diameter of 17.7 mm, a fin height of 1.0 mm, a fin thickness of 0.5 mm, and spacings of 0.25, 0.4, 1.0, and 2.1 mm. He determined that fin spacing is an important parameter. Masuda and Rose (1985) tested another family of copper tubes using R-113. All tubes had a fin root diameter of 12.7 mm, and had rectangular shape fins with a height of 1.59 mm, a thickness of 0.5 mm, and variable spacings from 0.25 mm to 2.0 mm. The geometry of five of these tubes is listed in Table 1. All tests were made near atmospheric pressure with a downward-flowing vapor velocity of 0.2 m/s. They found that the best performing tube had a fin spacing of 0.5 mm and exhibited a heat transfer enhancement ratio $\epsilon_{\Delta T}$ (finned tube to smooth tube vapor-side heat transfer coefficient ratio at the same vapor-to-wall temperature difference and based upon the smooth tube surface area A_r) of 7.3. Sukhatme et al. (1989) measured the heat transfer performance of R-11 condensing on horizontal, integral-fin tubes having trapezoidal-shaped fins of outside diameter near 24 mm. They systematically varied the fin density, fin height, and fin-tip half angle. The best performing tube had a fin density of 1417 fins/meter (fin spacing about 0.35 mm), a fin-tip half angle of 10 deg, and a fin height of 1.22 mm. This tube had an enhancement ratio compared to a smooth tube of the same outside diameter (at the same condensing film temperature difference) of about 10. The performance of this tube was improved another 20 percent by cutting trapezoidal-shaped axial grooves along the length of the tube, thus creating numerous three-dimensional pyramidal-shape fins. Condensation of refrigerants on three-dimensional fins has also been studied by Webb et al. (1982), Lin and Berghmans (1986), and Honda et al. (1989).

Apparatus and Procedure

Figure 1 shows a schematic of the test apparatus used during this investigation. It was the same as that used in earlier tests for steam and described in detail by Wanniarachchi et al. (1985, 1986). Vapor was generated in an electrically heated, pyrex glass boiler. The vapor flowed vertically upward through glass piping and then downward over the test tube, which was mounted horizontally within a stainless steel test section. A portion of the vapor condensed on the test tube, while the remainder was condensed on copper coils mounted inside a pyrex glass secondary condenser. The condensate returned to the boiler by gravity.

Cooling water was pumped through the test tube via a calibrated rotameter. Its inlet and outlet temperatures were measured very accurately using quartz-crystal thermometers as well as a ten-junction, series connected, copper-constantan thermopile. These two independent techniques resulted in temperature-rise measurements within about ±0.03 K of one another. The inlet and outlet bushings, which were used to mount the test tube, were made of nylon and Teflon to prevent heat transfer between the cooling water and the test section walls. A nylon mixing chamber was used at the tube outlet to ensure a good mixed bulk temperature was being measured. Two calibrated, copper-constantan thermocouples were used for vapor temperature measurements and a mercury-in-glass manometer was used to measure the absolute pressure in the

Nomenclature (cont.)

ΔT = temperature difference $= T_s - \bar{T}_{wo}$
ΔT_{LM} = log mean temperature difference $= (T_{co} - T_{ci})/\ln[(T_s - T_{ci})/(T_s - T_{co})]$
U_r = overall heat transfer coefficient based upon root area A_r
z = vertical distance from the bottom of tube to a point on the tube surface in the interfin space
α_b = vapor-side heat transfer coefficient in the "flooded" region as used by Webb et al. (1985)
α_f = vapor-side heat transfer coefficient on the "unflooded" fin flanks as used by Webb et al. (1985)
α_h = vapor-side heat transfer coefficient on the "unflooded" root surface of a tube between fins as used by Webb et al. (1985)
α_i = inside heat transfer coefficient
$\bar{\alpha}$ = average vapor-side heat transfer coefficient based upon the root surface area A_r $= q/(T_s - \bar{T}_{wo})$
$\bar{\alpha}_e$ = average vapor-side heat transfer coefficient based upon effective finned-tube surface area A_{ef}
$\bar{\alpha}_o$ = average vapor-side heat transfer coefficient based upon "envelope" outside surface area A
ϵ_A = area ratio, defined in equation (14)
ϵ'_A = "unflooded" area ratio, defined in equation (15)
$\epsilon_{\Delta T}$ = heat transfer enhancement ratio, defined as the ratio of finned-tube vapor-side coefficient to smooth-tube value at the same vapor-to-wall temperature difference and based upon the smooth tube surface area A_r
ζ = fin surface profile parameter; see equation (7)
η_f = fin efficiency
η = total surface efficiency as used by Webb et al. (1985)
θ = fin-tip half angle
θ_m = angle through which a normal to the fin surface rotates in going from the fin tip ($s=0$) to the end of the convex surface ($s=S_m$)
λ = Taylor instability wavelength, defined in equation (20)
μ = viscosity of the liquid
ξ = "active" area enhancement, defined in equation (17)
ρ = density of liquid
ρ_v = density of vapor
σ = surface tension
Φ = angle measured from the top of the tube
Φ_f = "flooding" angle, defined in equation (9)

Table 1 Geometry of finned tubes

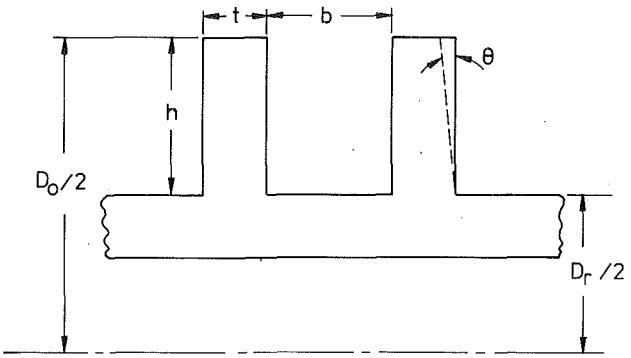

Tube No.	Outside diameter D_o, mm	Fin height h, mm	Fin thickness t, mm	Fin spacing b, mm
		Present Investigation		
		Smooth tube		
S01	19.05	–	–	–
		Machined tubes		
D02	21.05	1.0	1.0	0.25
F04				0.5
F05				1.0
F06				1.5
F07				2.0
F08				4.0
F10	21.05	1.0	0.75	0.5
F11				1.0
F12				1.5
F13				2.0
D01	21.05	1.0	0.5	0.25
F15				0.5
F16				1.0
F17				1.5
F18				2.0
F22	23.05	2.0	1.0	1.0
F23				1.5
F24				2.0
F26	20.05	0.5	1.0	1.0
F27				1.5
F28				2.0
F30	22.05	1.5	1.0	1.0
F31				1.5
F32				2.0
		Commercial tube		
	19.0	0.8	0.3	0.6
		Honda et al. (1983)		
B[a]	18.7	1.46	0.27	0.7
C[a]	18.9	0.92	0.18	0.5
D	19.4	1.13	0.11	0.4
		Masuda and Rose (1985)		
1	15.9	1.59	0.5	0.25
2				0.5
3				1.0
4				1.5
5				2.0

[a]Tubes B and C had trapezoidal shape fins with fin tip half angles of 4.5 and 5.0 deg, respectively.

test section. The saturation temperature corresponding to the measured vapor pressure agreed with the measured vapor temperature typically to within 0.3 K.

To ensure system integrity, leak tests were carried out both under vacuum and at a positive pressure. The leak rate at an absolute pressure of 45 mm Hg was estimated to be less than that corresponding to a pressure rise of 6 mm Hg in 24 hours. Under positive pressure, an automatic halogen leak detector was used to detect any leaks. Once the system was tight and the R-113 had been introduced, the immersion heaters in the boiler were energized to degas the test fluid. During this time,

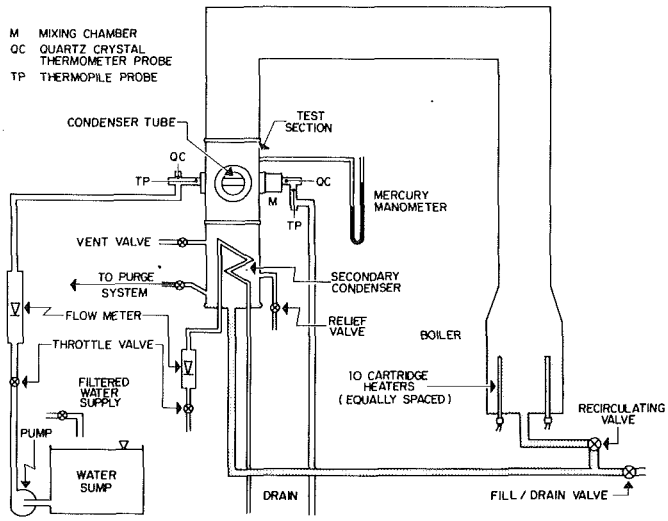

Fig. 1 Schematic of test apparatus

a vacuum pump was used intermittently to purge the system of any noncondensing gases. After several purgings, each about 60 seconds in duration, the system pressure was allowed to rise above atmospheric by adjusting the power to the boiler and the cooling water flow rate to the secondary condenser.

Data were taken for several cooling water flow rates through the test tube. At a given flow rate, once steady-state conditions were reached, the following data were recorded and read into a digital computer: cooling water velocity, inlet temperature and temperature rise, vapor temperature, and vapor pressure. These data were used to calculate an overall thermal resistance

$$\frac{1}{U_r A_r} = \frac{\Delta T_{\mathrm{LM}}}{Q} \tag{10}$$

Assuming uniform radial conduction within the tube wall, separate thermal resistances are related by

$$\frac{1}{U_r A_r} = \frac{1}{\alpha_i A_i} + \frac{R_w}{A_r} + \frac{1}{\bar{\alpha} A_r} \tag{11}$$

A "modified Wilson plot" method was used to process the data in order to arrive at vapor-side coefficients. This method is described in detail by Wanniarachchi et al. (1986). Basically, it involves choosing suitable equations for the inside and outside heat transfer coefficients, which involve unknown constants. The constants are found by using a least-squares minimization technique. In this study, a Sieder–Tate-type expression was used on the inside and a Nusselt-type expression was used on the outside. Ideally, in order to incorporate vapor velocity effects, a theoretical result such as that of Shekriladze and Gomelauri (1966) should be used. However, because of the relatively small approach vapor velocity obtained in the present work (about 0.4 m/s), a Nusselt-type expression was considered adequate

$$\bar{\alpha} = a\left\{\frac{\rho(\rho-\rho_v)gh_{fg}k^3}{\mu\Delta TD_r}\right\}^{1/4} \tag{12}$$

This modified Wilson plot technique has the advantage that direct wall temperature measurements are not required. Both Wanniarachchi et al. (1986) and Masuda and Rose (1988) have shown that this method gives comparable results to direct wall-temperature measurement methods. Using this technique, the estimated uncertainty in the measured vapor-side heat transfer coefficient was about ±7 percent.

Tests were conducted with a smooth tube and 24 integral-fin tubes, which were machined from a thick-walled copper tube. Each tube had an inside diameter of 12.7 mm and a condens-

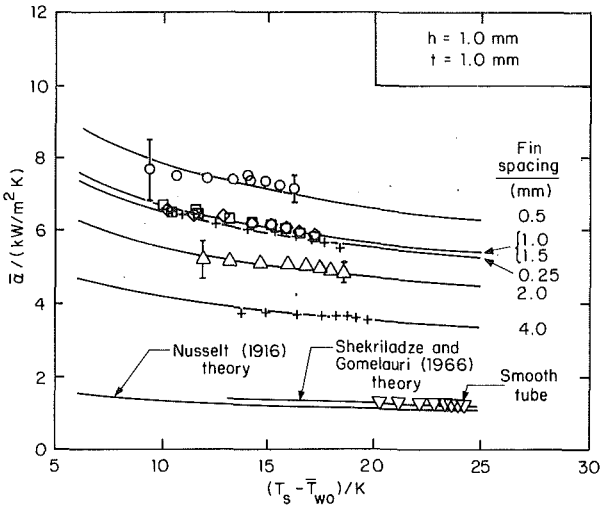

Fig. 2 Variation of vapor-side heat transfer coefficient with wall subcooling

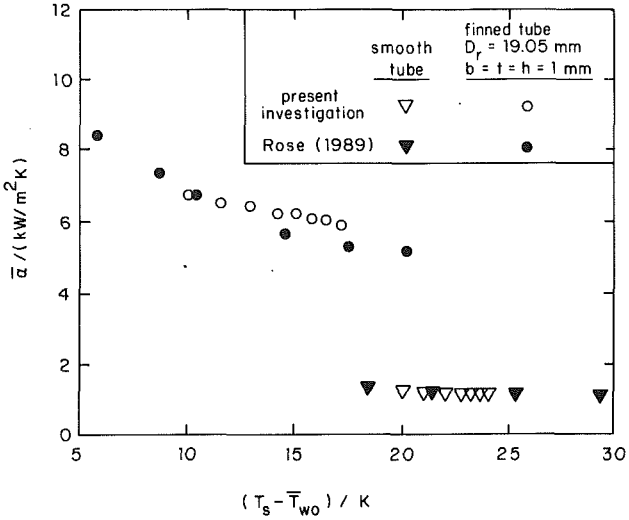

Fig. 3 Comparison of data from this investigation using the "modified Wilson plot" method to the data of Rose and Briggs (1989) for tubes with the same geometry, but using the direct wall temperature measurement method

ing length of 133 mm. All the fins were rectangular in shape. The fin dimensions (along with those of Honda et al., 1983, and Masuda and Rose, 1985) are listed in Table 1. The tubes had three different fin thicknesses (0.5, 0.75, and 1.0 mm), four fin heights (0.5, 1.0, 1.5, and 2.0 mm) and six fin spacings (0.25, 0.5, 1.0, 1.5, 2.0, and 4.0 mm). It may be noted that tubes F22–F32 had relatively large fin spacings. This is due to the fact that these tubes were originally manufactured for testing with steam, which needs an optimum fin spacing of 1.5 mm as reported by Yau et al. (1985) and Wanniarachchi et al. (1986). Table 1 also includes the geometric data for a commercially finned tube, which was tested for comparison with the specially machined tubes.

Results and Discussion

All the data were taken at a pressure slightly above atmospheric (about 765 mm Hg), which corresponds to a nominal saturation temperature of 48°C. The approach velocity of the downward-flowing vapor was near 0.4 m/s. Extreme care was taken in obtaining the data. Since noncondensing gases were removed effectively before collecting data and dropwise condensation of R-113 on copper does not occur, the measurements were highly repeatable. For example, data were taken on a few of the tubes on different days and the values of $\bar{\alpha}$ agreed to within 3 percent.

The vapor-side heat transfer coefficient measured during this investigation, $\bar{\alpha}$, was calculated based upon the outside surface area of a smooth tube having a diameter equal to the root diameter of the finned tube (i.e., $\pi D_r L$). Previous investigators have based their heat transfer coefficients upon a smooth tube area with the same overall outside diameter (i.e., $\pi D_o L$). In comparing the results of this investigation with those of earlier investigations, care was taken to convert the previous data using an appropriate area ratio.

Figure 2 shows the vapor-side heat transfer coefficient $\bar{\alpha}$ versus the wall temperature difference $(T_s - \bar{T}_{wo})$ for the family of tubes D02, F04–08, which had a fin thickness and height of 1.0 mm and spacings of 0.25, 0.5, 1.0, 1.5, 2.0, and 4.0 mm. Data for a smooth tube are also shown. Typical uncertainty bands at both low and high heat flux are provided, reflecting that the uncertainty of the data increases at lower vapor-side temperature differences. The Nusselt theory is included to confirm the accuracy of the instrumentation and the data reduction scheme. The smooth tube data lie slightly above the Nusselt theory due to the small downward vapor velocity. If vapor velocity effects are included in the theory, using the model of Shekriladze and Gomelauri (1966), excellent agreement with the data is found. The finned tube data are strongly dependent on fin spacing. As the spacing decreases to 0.5 mm, the heat transfer coefficient continues to increase. However, a further reduction in spacing to 0.25 mm decreases the heat transfer, indicating that an optimum spacing exists, presumably due to increased condensate "flooding" between fins as the fin spacing decreases.

Figure 3 compares the data obtained for one finned tube (tube F05, $b = t = h = 1.0$ mm) and the smooth tube (tube S01) to the independently acquired data of Rose and Briggs (1989) for tubes with the same geometry. Their data were obtained by *direct wall temperature measurement* (i.e., thermocouples were installed in the walls of both the finned tube and smooth tube). The agreement between these two independent sets of data is excellent, indicating that the modified Wilson plot method used during this investigation yields accurate results.

Table 2 gives the measured heat transfer enhancement ratio $\epsilon_{\Delta T}$ for all the tubes tested in this investigation, as well as those obtained by Honda et al. (1983) and Masuda and Rose (1985). Since, as noted by Masuda and Rose (1985), the dependence of q on ΔT for finned tubes at low vapor velocity is close to that for smooth tubes, i.e., $q \propto \Delta T^{3/4}$ (use was made of this fact in adopting equation (12) for the vapor side in the modified Wilson plot), $\epsilon_{\Delta T}$ is independent of ΔT and is given by

$$\epsilon_{\Delta T} = \frac{a_f}{a_s} \tag{13}$$

where a_f and a_s are the coefficients of equation (12) for the finned and smooth tubes respectively. Several additional geometric quantities are also tabulated. The flooding angle Φ_f was calculated using equation (9). The area ratio ϵ_A was calculated (see Table 1) as

$$\epsilon_A = \frac{(D_r + 2h)t + D_r b + 2h(D_r + h)}{D_r(b+t)} \tag{14}$$

This ratio represents the entire area enhancement by adding fins to a smooth tube of diameter D_r. The "unflooded" area ratio ϵ'_A was calculated as

$$\epsilon'_A = \frac{\pi(D_r + 2h)t + \Phi_f[D_r b + 2h(D_r + h)]}{\pi D_r(b+t)} \tag{15}$$

Notice that ϵ'_A includes the fin tips for the whole tube and the unflooded portion of both the fin flanks and the cylindrical,

Table 2 Heat transfer enhancement for condensation of R-113 on integral-fin tubes

Tube No. (see Table 1)	"Flooding" angle Φ_f, deg	Area ratio ϵ_A	"Unflooded" area ratio ϵ_A'	"Active" area ratio ξ	Heat transfer enhancement $\epsilon_{\Delta T}$
			Present Investigation		
D02	100	2.77	1.93	1.78	4.4
F04	126	2.47	1.95	1.75	5.3
F05	142	2.10	1.78	1.56	4.5
F06	149	1.88	1.64	1.42	4.5
F07	154	1.74	1.54	1.32	3.7
F08	161	1.44	1.32	1.13	2.8
F10	126	2.75	2.12	1.88	6.1
F11	142	2.25	1.88	1.62	4.9
F12	149	1.97	1.70	1.45	4.9
F13	154	1.79	1.58	1.34	4.1
D01	100	3.88	2.47	2.24	7.0
F15	126	3.16	2.37	2.08	6.7
F16	142	2.44	2.00	1.71	5.2
F17	149	2.08	1.77	1.50	4.7
F18	154	1.86	1.62	1.37	4.2
F22	144	3.31	2.77	2.54	6.0
F23	151	2.85	2.47	2.23	5.8
F24	155	2.54	2.24	2.01	5.2
F26	141	1.54	1.32	1.11	3.5
F27	149	1.43	1.26	1.04	3.2
F28	153	1.36	1.21	1.00	2.9
F30	143	2.70	2.26	2.03	5.3
F31	150	2.36	2.04	1.81	5.1
F32	154	2.13	1.88	1.66	4.6
			Honda et al. (1983)		
B	132 (130)[a]	4.34 (3.94)[b]	3.26	2.84	6.9[c]
C	122 (118)	3.88 (3.68)	2.73	2.28	8.9[c]
D	116 (114)	5.75 (5.64)	3.78	3.26	9.8[c]
			Masuda and Rose (1985)		
1	84	5.94	3.21	2.93	6.5
2	117	4.70	3.27	2.89	7.3
3	136	3.47	2.73	2.34	6.1
4	145	2.85	2.35	1.99	5.6
5	150	2.48	2.10	1.76	4.8

[a] Values in parentheses are experimentally determined values obtained by Honda et al. (1983).
[b] Values in parentheses have been provided by Honda (1987). They reflect the presence of a 2-mm-wide longitudinal slit in the fin to accommodate a drainage strip at the bottom of the tube.
[c] Value reflects a slight correction provided by Honda (1987).

interfin tube. It represents the surface area available for "thin-film" condensation in contrast to the flooded interfin space on the bottom part of the tube. Recently, Masuda and Rose (1987) have shown that a wetting liquid is retained on the upper parts of a finned tube surface previously regarded as unflooded. Surface tension forces cause the wetting liquid to form a meniscus at the base of the fin flanks and the surface of the tube in the interfin space. The radius of curvature of this meniscus, r, varies with vertical distance (or circumferential position) around the tube

$$r = \sigma/\rho g z \tag{16}$$

If this additional liquid film is included, then an "active" area enhancement ξ can be defined as the *unblanked* area of a finned tube (i.e., the area of the fin tips together with the *unblanked* portions of the fin flanks and the interfin tube surface) divided by the area of a smooth tube of diameter D_r. This ratio can be expressed as

$$\xi = \frac{\pi(D_r+2h)t + \Phi_f D_r b(1-f_t) + 2h(D_r+h)\Phi_f(1-f_f)}{\pi D_r(b+t)} \tag{17}$$

where

$$f_t = (2\sigma/\rho g R_r b)\,(\tan(\Phi_f/2)/\Phi_f) \tag{18}$$

$$f_f = (\sigma/\rho g R_r h)\,(\tan(\Phi_f/2)/\Phi_f) \tag{19}$$

This "active" area enhancement is therefore the smallest of the area ratios defined above. In comparing the area enhancements to the heat transfer enhancement in Table 2, several conclusions can be reached. First, the heat transfer enhancement is always significantly larger than any of the area enhancements. Second, while no systematic trend is obvious at present, the degree of improvement in heat transfer relative to the area enhancement seems to vary with fin geometry.

Figure 4 compares the heat transfer enhancement ratio for selected tubes of this investigation and those of Honda et al. (1983) and Masuda and Rose (1985) as a function of fin spacing. The enhancement ratio for the commercially finned tube is also provided. Unfortunately, because of the different geometries used, it is difficult to assess completely the significance of the results. However, it appears that the enhancement ratio increases as fin thickness decreases. This is readily evident in comparing the two families of tubes used during this investigation where the fin thickness was 0.5 and 1.0 mm. Also, the Honda et al. (1983) data give the highest enhancements and their tubes had the thinnest fins. This trend is primarily due to an increase in surface area as fin thickness decreases since, for a given spacing, more fins can be accommodated in a given tube length as fin thickness decreases.

Surface area by itself, however, is not the entire answer, as

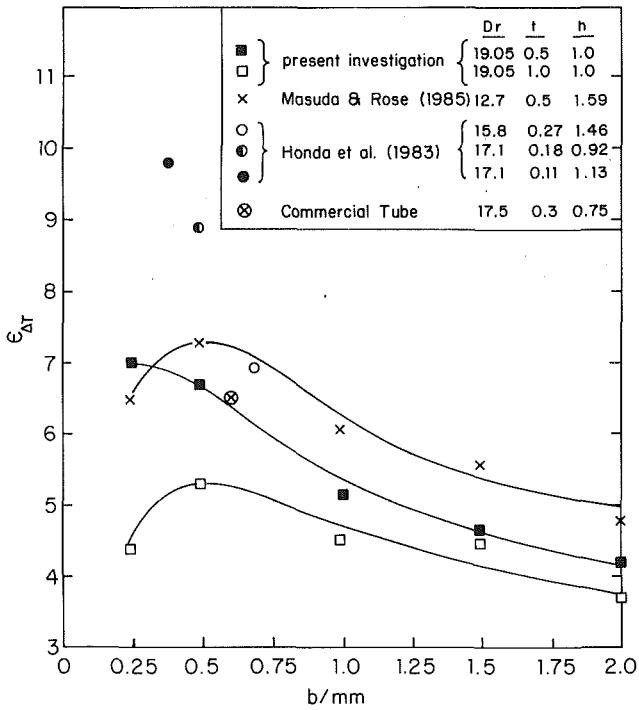

Fig. 4 Dependence of heat transfer enhancement upon fin geometry

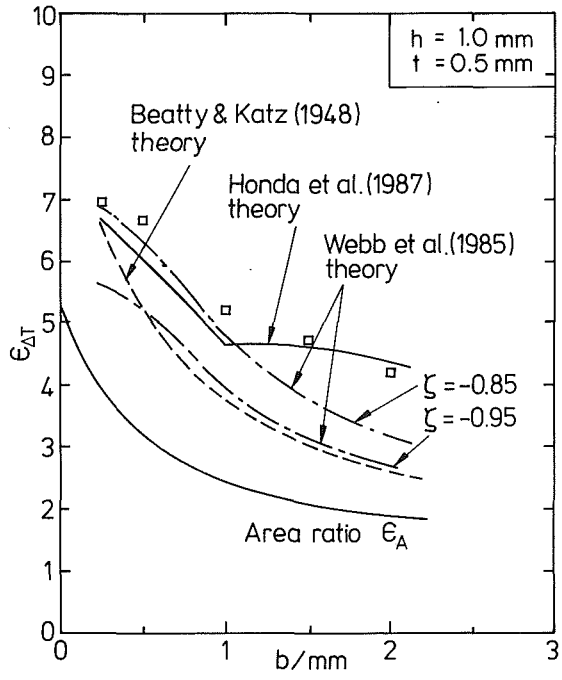

Fig. 6 Comparison of measured heat transfer enhancement to existing theoretical models for 0.5-mm-thick fins

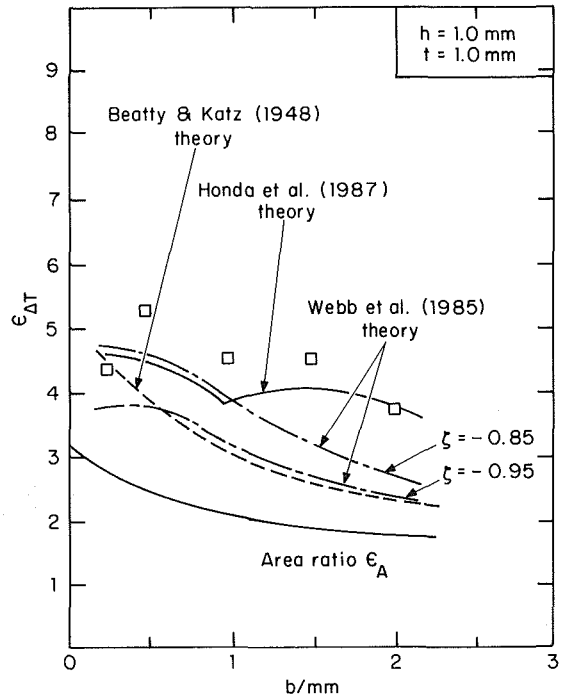

Fig. 5 Comparison of measured heat transfer enhancement to existing theoretical models for 1-mm-thick fins

can be seen by comparing (see Table 2) tube D of Honda et al. (1983) with tube 1 of Masuda and Rose (1985). Both of these tubes have a surface area ratio of about 5.8 but the heat transfer enhancement of tube D is almost 10 compared to the value of 6.5 for tube 1. Notice that tube D has a flooding angle of 116 deg versus a value of 84 deg for tube 1. Thus, although the total surface areas are about the same, tube 1 is more flooded than tube D. Also, the ratio of fin height to tube root diameter, h/D_r, may be an important variable since this ratio is about twice as large for tube 1 as for tube D.

Two of the data sets (Masuda and Rose, 1985, and the 1.0 mm fin thickness data of this investigation) indicate that, for a given fin thickness and height, an optimum fin spacing exists near 0.5 mm. The 0.5 mm fin thickness data of this investigation indicate an optimum fin spacing of about 0.25 mm. No optimum is shown by the Honda et al. (1983) data because, in addition to fin spacing, their tubes had different fin thicknesses and heights. Therefore, while the exact value of the optimum fin spacing is probably dependent upon fin geometry, it appears to lie between 0.25 and 0.5 mm. This range agrees with the observed result of 0.35 for Sukhatme et al. (1989).

Figures 5 and 6 compare the measured heat transfer enhancement ratio $\epsilon_{\Delta T}$ for two families of tubes with several theoretical models and the area ratio ϵ_A. The data fall significantly above the area ratio. The Beatty and Katz (1948) model[3], which neglects surface tension effects, falls significantly short of predicting the experimental results, except at the lowest fin spacing, and is therefore a conservative prediction. The Webb et al. (1985) model, which corrects the Beatty and Katz (1948) model for condensate flooding[4] (reducing the heat transfer) and for surface tension effects in the unflooded region (increasing the heat transfer), appears to be very sensitive to the fin-shape parameter ζ. It is interesting to note that $\zeta = -0.85$ results in a better prediction than $\zeta = -0.95$. As explained by Webb et al. (1985), as the value of ζ becomes more negative, the condensate profile becomes more "flat-sided" over a larger fraction of its length, which leads to a smaller surface-tension-driven pressure gradient in the condensate film over most of its length. Other possible sources of error discussed by Webb et al. (1985) include the assumption that gravity is negligible compared to surface tension on the fin surface and that concave curvature effects of the condensate film at the root of the fin are small. The best

[3]This model has been modified to include both the fin tips and the fin flanks in the calculation of tube equivalent diameter D_{eq}. Thus, equation (5) was used instead of equation (2).

[4]Webb et al. (1985) used a two-dimensional conduction analysis to calculate the heat transfer in the flooded region. In the present investigation, a one-dimensional conduction model, similar to that used by Owen et al. (1983), was used instead.

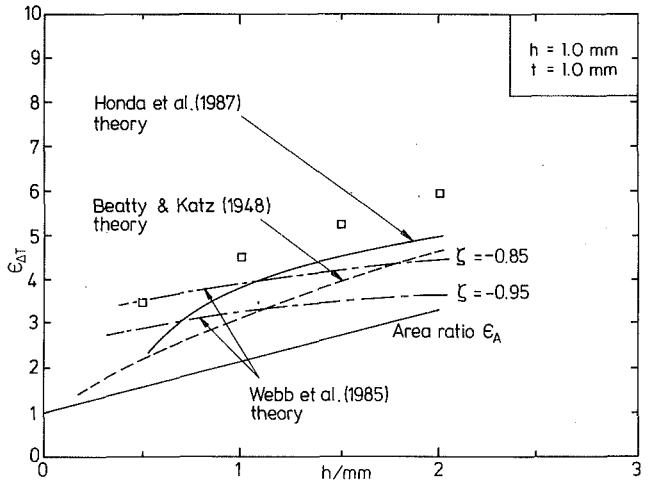

Fig. 7 Comparison of measured heat transfer enhancement to existing theoretical models for various fin heights

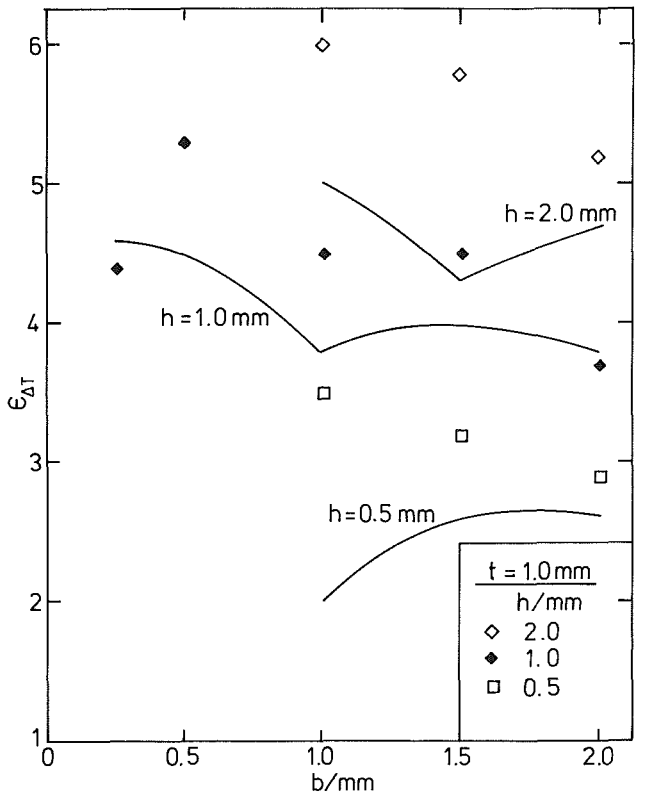

Fig. 8 Comparison of measured heat transfer enhancement to the theory of Honda et al. (1987) for various fin spacings and heights

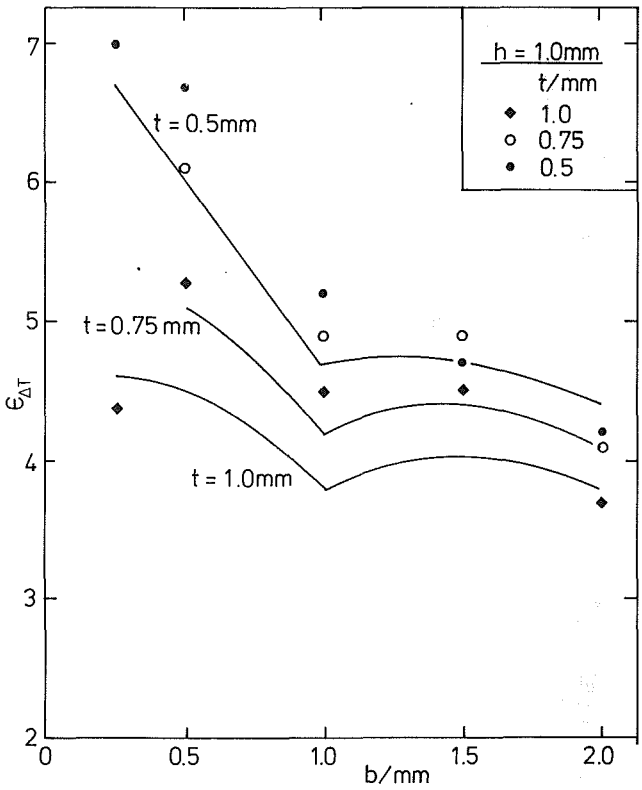

Fig. 9 Comparison of measured heat transfer enhancement to the thoery of Honda et al. (1987) for various fin spacings and thicknesses

agreement is with the model of Honda et al. (1987), which represents the data of both families of tubes to within about ±15 percent. The slope discontinuity in their theoretical curve, which occurs for a fin spacing of 1 mm, is due to a change in the treatment of the condensate film between fins in going from large to small fin spacings. It is interesting to note that this behavior is to some extent reflected in the experimental data as well. Figure 7 gives a similar comparison, showing the effect of fin height. While the three models show the correct trend, all of them underpredict the data. Once again, the Honda et al. (1987) model is best, predicting values about 20 percent less than the data, except for the lowest fin height of 0.5 mm, where the error is about 75 percent. Figures 8 and 9 provide a further comparison of the data and the theoretical model of Honda et al. (1987). Figure 8 shows the comparison for various fin heights and spacings, whereas Fig. 9 is for various fin thicknesses and spacings. The trend with fin height appears to be correctly predicted by the model; however, because of the slope discontinuity in the theoretical predictions as described above, the agreement is sensitive to fin spacing and the worst agreement appears to be for the short fin ($h = 0.5$ mm) at a small fin spacing ($b = 1.0$ mm). With regard to fin thickness, Fig. 9 shows that the theory correctly predicts an increase in enhancement as fin thickness decreases at all fin spacings.

Figures 10(a) and 10(b) are photographs of condensation showing the mode of condensate drainage for tubes F08 and F15, respectively. Notice that for large fin spacing ($b = 4.0$ mm for tube F08), the condensate drains off the tube from the bottom of each fin in discrete columns. As seen from the reflection of the light, a thin condensate film appears to exist on the entire tube surface, giving evidence that no condensate "flooding" exists. On the other hand, for small fin spacing ($b = 0.5$ mm for the tube F15), the tube is partially "flooded" (Φ_f is about 130 deg) and the condensate drainage columns are spaced wider apart at a spacing of approximately 8.5 mm, which agrees to within 10 percent of the well-known expression for the Taylor instability wavelength

$$\lambda = 2\pi\sqrt{2\sigma/\rho g} \tag{20}$$

discussed by Yung et al. (1980). This difference in drainage characteristics, while perhaps not important for a single tube, may affect the thermal performance in a tube bundle due to condensate inundation effects, and more information is therefore needed, especially at intermediate fin spacings.

Conclusions

Experiments have been conducted with R-113 condensing on several families of copper integral-fin tubes having

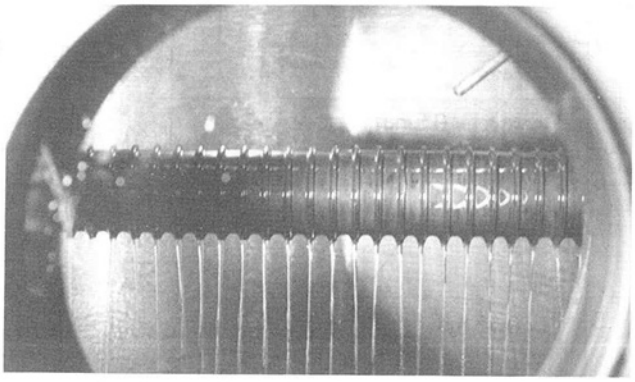

Fig. 10(a) Tube F08 at a heat flux of 70 kW/m^2

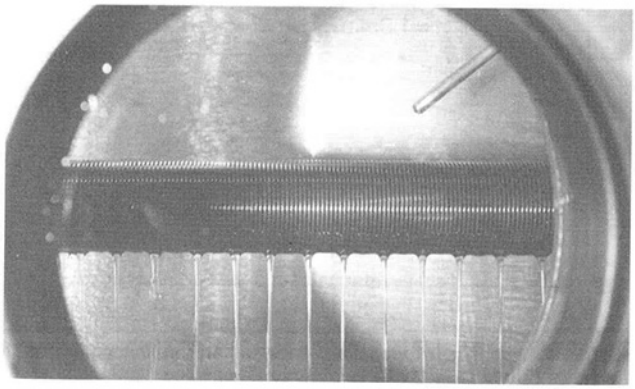

Fig. 10(b) Tube F15 at a heat flux of 128 kW/m^2

Fig. 10 Photographs showing condensate drainage from finned tubes

rectangular-shaped fins. These data have been compared with those from other investigations and with theoretical models. The following conclusions can be made:

1 When R-113 condenses on copper tubes of fixed diameter and with rectangular-shaped fins of fixed thickness and height, an optimum fin spacing occurs, which yields maximum heat transfer. This optimum spacing lies between 0.25 and 0.5 mm (in close agreement with Masuda and Rose, 1985, and Sukhatme et al., 1989) and is dependent upon fin thickness and height as well as on tube root diameter.

2 At the optimum fin spacing mentioned above, the vapor-side heat transfer coefficient is enhanced over the smooth tube value (for the same ΔT) by a factor of approximately 4 to 7. The heat transfer enhancement is always considerably more than the corresponding area enhancement that occurs when fins are present on a smooth tube of diameter equal to the fin root diameter. The ratio of heat transfer to area enhancement depends upon the geometric characteristics of the tube and the fins.

3 The vapor-side, heat transfer enhancement increases with fin height, but the rate of increase decreases with increasing fin height. This trend is in agreement with the measurements of Wanniarachchi et al. (1985) for steam.

4 The vapor-side heat transfer enhancement increases as the fin thickness decreases (for the same fin spacing), and the optimum thickness is expected to be less than 0.5 mm.

5 The existing theoretical models of Beatty and Katz (1948), Webb et al. (1985), and Honda et al. (1987) are, in general, conservative with respect to the experimental data. The Honda et al. (1987) model gives the best agreement with the data, which, except for a few tubes, is within ± 20 percent.

In addition to the above conclusions, visual observations of condensate drainage from the finned tubes indicated that the condensate drained by discrete columns for all the tubes and at all heat fluxes encountered during this investigation. For widely spaced fins, these columns formed at the bottom of each fin. On the other hand, for closely spaced fins, the columns formed with a spacing approximately equal to the Taylor instability wavelength. The exact spacing where one mode of drainage shifts to the other has not been determined.

Acknowledgments

This work was supported by the National Science Foundation through Grant No. CBT-8603582. The authors are deeply indebted to Professor H. Honda for providing the numerical results of his theoretical model. The first author would like to acknowledge also the financial assistance of the U. K. Science and Engineering Research Council.

References

Adamek, T., 1981, "Bestimmung der Kondensationgrossen auf feingewellten Oberflachen zur Auslegun optimaler Wandprofile," *Wärme- und Stoffübertragung*, Vol. 15, pp. 255–270.

Beatty, K. O., and Katz, D. L., 1948, "Condensation of Vapors on Outside of Finned Tubes," *Chem. Eng. Prog.*, Vol. 44, No. 1, pp. 55–70.

Carnavos, T. C., 1980, "An Experimental Study: Condensing R-11 on Augmented Tubes," ASME Paper No. 80-HT-54.

Enya, S., and Kisaragi, T., 1977, "Improvements of Condenser Tubes," Ishikawajima-Harima Heavy Industries Ltd., Report No. IHI/FWDC 77 014.

Honda, H., 1987, Private Communication.

Honda, H., Nozu, S., and Mitsumori, K., 1983, "Augmentation of Condensation on Horizontal Finned Tubes by Attaching a Porous Drainage Plate," *Proc. ASME-JSME Thermal Engineering Joint Conference*, Honolulu, HI, Vol. 3, pp. 289–296.

Honda, H., Nozu, S., and Uchima, B., 1987, "A Generalized Prediction Method for Heat Transfer During Film Condensation on a Horizontal Low Finned Tube," *Proc. ASME-JSME Thermal Engineering Joint Conference*, Honolulu, HI, Vol. 4, pp. 385–392.

Honda, H., Uchima, B., Nozu, S., Nakata, H., and Torigoe, E., 1989, "Film Condensation of Downward Flowing R-113 Vapor on In-Line Bundles of Horizontal Finned Tubes," *Heat Transfer Equipment Fundamentals, Design, Applications and Operating Problems*, ASME HTD-Vol. 108, pp. 117–125.

Kabov, O. A., 1984, "Film Condensation of Immobile Vapor on a Horizontal Finned Cylinder," *Heat Transfer—Soviet Research*, Vol. 16, No. 6, pp. 76–83.

Karkhu, V. A., and Borovkov, V. P., 1971, "Film Condensation of Vapor at Finely-Finned Horizontal Tubes," *Heat Transfer—Soviet Research*, Vol. 3, No. 2, pp. 183–191.

Katz, D. L., and Geist, J. M., 1984, "Condensation on Six Finned Tubes in a Vertical Row," *Trans. of the ASME*, Vol. 70, pp. 907–914.

Lin, C. C., and Berghmans, J., 1986, "R-11, R-113 and R-114 Condensation on an Enhanced Tube," *Proc. 4th International Symp. on Multiphase Transport and Particulate Phenomena*, Miami, FL.

Marto, P. J., 1988, "An Evaluation of Film Condensation on Horizontal Integral-Fin Tubes," ASME JOURNAL OF HEAT TRANSFER, Vol. 110, No. 4(B), pp. 1287–1305.

Marto, P. J., Mitrou, E., Wanniarachchi, A. S., and Rose, J. W., 1986, "Film Condensation of Steam on Horizontal Finned Tubes: Effect of Fin Shape," *Proc. 8th International Heat Transfer Conf.*, Vol. 4, pp. 1695–1700.

Masuda, H., and Rose, J. W., 1985, "An Experimental Study of Condensatoin of Refrigerant 113 on Low Integral-Fin Tubes," in: *Heat Transfer Science and Technology*, Bu-Xuan Wang, ed., Hemisphere, pp. 480–487.

Masuda, H., and Rose, J. W., 1987, "Static Configuration of Liquid Films on Horizontal Tubes With Low Radial Fins: Implications for Condensation Heat Transfer," *Proc. R. Soc.*, A410, pp. 125–139.

Masuda, H., and Rose, J. W., 1988, "Condensation of Ethylene Glycol on Horizontal Integral Fin Tubes," ASME JOURNAL OF HEAT TRANSFER, Vol. 110, pp. 1019–1022.

Nusselt, W., 1916, "Die Oberflachen-Kondensation des Wasserdampfes," *VDI Zeitung*, Vol. 60, pp. 541–546, 569–575.

Owen, R. G., Sardesai, R. G., Smith, R. A., and Lee, W. C., 1983, "Gravity Controlled Condensation on a Horizontal Low-Fin Tube," *Condensers: Theory and Practice*, Inst. Chem. Eng. Symp. Ser., No. 75, pp. 415–428.

Pearson, J. F., and Withers, J. G., 1969, "New Finned Tube Configuration Improves Refrigerant Condensing," *ASHRAE J.*, Vol. 11, pp. 77–82.

Rose, J. W., and Briggs, A., 1989, Private Communication.

Rudy, T. M., 1982, "A Theoretical and Experimental Study of Condensation on Single, Integral-Fin Tubes," Ph.D. Thesis, The Pennsylvania State University, University Park, PA.

Shekriladze, I. G., and Gomelauri, V. I., 1966, "Theoretical Study of Laminar Film Condensation of Flowing Vapour," *Int. J. Heat Mass Transfer*, Vol. 9, pp. 581–591.

Smirnov, G. F., and Lukanov, I. I., 1972, "Study of Heat Transfer From Freon-11 Condensing on a Bundle of Finned Tubes," *Heat Transfer—Soviet Research*, Vol. 4, No. 3, pp. 51–56.

Sukhatme, S. P., Jagadish, B. S., and Prabhakaran, P., 1990, "Film Condensation of R-11 Vapor on Single Horizontal Enhanced Condenser Tubes," ASME JOURNAL OF HEAT TRANSFER, Vol. 112, pp. 229–234.

Wanniarachchi, A. S., Marto, P. J., and Rose, J. W., 1985, "Film Condensation of Steam on Horizontal Finned Tubes: Effect of Fin Spacing, Thickness and Height," *Multiphase Flow and Heat Transfer*, ASME HTD-Vol. 47, pp. 93–99.

Wanniarachchi, A. S., Marto, P. J., and Rose, J. W., 1986, "Film Condensation of Steam on Horizontal Finned Tubes: Effect of Fin Spacing," ASME JOURNAL OF HEAT TRANSFER, Vol. 108, pp. 960–966.

Webb, R. L., 1988, "Enhancement of Film Condensation," *Int. Comm. Heat Mass Transfer*, Vol. 15, pp. 475–507.

Webb, R. L., Keswani, S. T., and Rudy, T. M., 1982, "Investigation of Surface Tension and Gravity Effects in Film Condensation," *Proc. 7th International Heat Transfer Conf.*, Vol. 5, pp. 175–180.

Webb, R. L., Rudy, T. M., and Kedzierski, M. A., 1985, "Prediction of the Condensation Coefficient on Horizontal Integral-Fin Tubes," ASME JOURNAL OF HEAT TRANSFER, Vol. 107, pp. 369–376.

Yau, K. K., Cooper, J. R., and Rose, J. W., 1985, "Effect of Fin Spacing on the Performance of Horizontal Integral-Fin Condenser Tubes," ASME JOURNAL OF HEAT TRANSFER, Vol. 107, pp. 377–383.

Yung, D., Lorenz, J. J., and Ganic, E. N., 1980, "Vapor/Liquid Interaction and Entrainment in Falling Film Evaporators," ASME JOURNAL OF HEAT TRANSFER, Vol. 102, pp. 20–25.

Row Effect for R-11 Condensation on Enhanced Tubes

R. L. Webb
Fellow ASME

C. G. Murawski

Department of Mechanical Engineering,
The Pennsylvania State University,
University Park, PA 16802

Experimental results of a condensation row effect study on enhanced tubes are presented. A test cell was constructed to condense Refrigerant-11 on the shell side of a vertical bank of five horizontal tubes. Four distinctly different commercially available tubes were tested. The tubes are a 1024-fpm integral fin, the Wolverine Turbo-C, Wieland GEWA-SC, and the Tred-D. A modified Turbo-C tube was also tested. Experimental and visual observations are used to understand the row effect due to condensate loading. By plotting the data in the form of the local condensation coefficient versus condensate Reynolds number, the results may be interpreted for any number of tube rows, up to the maximum Reynolds numbers tested. Bundle average condensation coefficients may be established by integrating the h versus Re values over the number of tube rows.

Introduction

Nusselt (1916) was the first to theorize laminar film condensation of vapor on a smooth solid surface. Nusselt was able to solve for the local condensate film thickness by using a momentum and energy balance on a vertical flat plate. He then integrated over $0 \le x \le L$, to obtain the average film thickness δ. In laminar film condensation, the condensation coefficient is given by k/δ, where k is the thermal conductivity of the condensate. Thus the average condensation coefficient for a vertical flat plate can be calculated. Nusselt extended the analysis to a horizontal smooth tube. Nusselt's equation for condensation on a single horizontal tube is

$$h_1 = 0.725(k^3 \rho \lambda / \nu D \Delta T_{sw})^{1/4} \quad (1)$$

where $\Delta T_{sw} \equiv (T_{sat} - T_w)$. Assuming constant wall temperature and a laminar film, he also showed that

$$h_{av}/h_1 = N^{-m} \quad (2)$$

where N is the number of vertical tube rows. Nusselt's analysis theoretical analysis showed that $m = 1/4$. Practical measurements have found that $m < 1/4$. For example, Kern (1958) recommends $m = 1/6$. Webb (1984b) surveys row effect data for refrigerants.

Assuming that the correct row effect exponent is known, a precise application of equation (1) requires constant wall temperature on all tube rows, which results in $\Delta T_{sw} = \text{const}$. This will probably never be attained in practice, since the heat flux and the condensation coefficient will decrease with increasing rows. If the water side coefficient is constant, ΔT_{sw} will increase with tube rows. Hence, the average condensation coefficient will drop faster than indicated by Nusselt's equation (2).

Horizontal, integral fin tubes were introduced in the late 1940s for use in shell-and-tube heat exchangers. These tubes were not developed for condensation service, but were used for condensation because they performed better than plain tubes. Beatty and Katz (1948) proposed that the integral fin tube could be modeled using the Nusselt theory of condensation on vertical plates and horizontal tubes. They calculated the condensation coefficients as the area-weighted average of the condensation coefficient on the finned surface, and on the tube surface between the fins. The Beatty and Katz model assumes that gravity force drains the condensate from the integral finned surfaces and that no condensate is retained between the fins. The Beatty and Katz (1948) model assumes that surface tension plays no role in the condensation process. Katz and Geist (1948) measured the row effect exponent of equation (2) for 630-fpm integral fin tubes. Their work was done by condensing R-11 on a vertical bank of six horizontal tubes, and they found $m = 0.04$.

Gregorig (1954) proposed that surface tension forces may play a major role in the condensation process. His work dealt with condensation on vertical fluted tubes. Gregorig showed that, if the fin profile had the proper curvature, surface tension forces would drain the condensate along the fin profile. Then, gravity force drains the accumulated condensate from the channel between the fins. Kedzierski and Webb (1987) have proven experimentally that surface tension forces plays an important role in condensate drainage on flat plates with special fin profiles on the surface. The surface tension forces can increase heat transfer by ensuring that the film thickness is small on the surface of an enhanced tube. If $h = k/\delta$, and δ is small, then the local heat transfer coefficient will be large.

Surface tension can also be detrimental to the condensation process. Rudy and Webb (1985) have shown that condensate is retained between the fins of integral fin tubes. For a 1024-fpm tube Rudy and Webb showed that R-11 can be retained in the lower 25 percent of the integral fin tube. The same tube was totally flooded when water was the condensing vapor. Totally flooded means that the whole interfin region retained liquid. Rudy and Webb proposed a theoretical model to predict the liquid holdup angle for integral fin tubes using a force balance on the retained condensate. Surface tension forces act to retain condensate, and gravity forces act to remove it. The retained condensate creates a large film thickness. This large film thickness greatly increases the heat transfer resistance in the lower portion of the tube. This will decrease the overall condensation coefficient.

Many new manufacturing techniques have evolved since Beatty and Katz carried out their experiments in 1948, and new shell side enhancement geometries have been introduced for use in condensers. These new enhancement geometries have typically been tested as single tubes, with almost no work done to determine the row effect.

Carnavos (1980) condensed R-11 on the shell side of numerous enhanced tubes. Masuda and Rose (1985) have condensed R-113 on the shell side of low integral-fin tubes. Rudy and Webb (1985) conducted experiments to understand and model the liquid holdup angle on integral fin tubes by condensing water, R-11, and pentane on the shell side. Wanniarachchi et al. (1986) have condensed steam on the shell side of integral fin tubes to determine the effect of fin spacing.

Contributed by the Heat Transfer Division for publication in the JOURNAL OF HEAT TRANSFER. Manuscript received by the Heat Transfer Division April 26, 1989; revision received October 1, 1989. Keywords: Condensation, Finned Surfaces, Heat Exchangers.

Webb (1984a) provides a survey of enhanced condenser tubes developed for refrigeration service.

Beatty and Katz (1948) were the first to propose a condensation model for integral fin tubes. Their model did not account for surface tension drainage forces or liquid holdup between the fins. Webb et al. (1985) developed a model for single horizontal integral fin tubes, which accounted for the surface tension drainage on the fin flanks, gravity drainage in the interfin tube surface, and heat transfer in the flooded regions. Honda et al. (1987a) have developed a complex model to predict the performance of a vertical row of horizontal integral fins tubes. Honda et al. (1987b) used trapezoidal fin shapes with rounded corners near the fin tips. They divided the tubes into flooded and unflooded regions. On the fin surface, it was assumed that the condensate flow was driven by surface tension and gravity. In the interfin space between the fins only gravity was acting on drainage. The fin surface was divided into thin and thick film regions around the tube circumference. They neglected the heat transfer in the thick-film regions, and numerically solved for the heat transfer in the thin film regions.

Between 1948 and 1984 very little work was done to quantify the row effect of enhanced tubes. Marto and Wanniarachchi (1984) have condensed steam on the shell side of five horizontal tubes in a vertical row. Marto et al. (1984) were able to simulate thirty rows of tubes by placing a distributor tube above the column of five tubes. The distributor tube was a tube whose top was perforated with small holes. The tube was fed with condensate from one end and the perforation holes were spaced properly to ensure uniform flooding along its length. Marto et al. (1984) measured the row effect for steam condensation on plain and robed tubes, and the same having a helical wire wrap. Honda et al. (1987b) observed the condensate drainage characteristics from a bank of 1024-fpm integral fin tubes. They also developed a theoretically based model to predict the row-by-row condensation coefficient. Honda et al. (1987a) condensed R-113, methanol, and *n*-propanol on two active tubes. A distributor tube was placed above the two active tubes. The distributor tube had a smaller tube fitted concentrically through an outer tube. A series of perforations facing downward were drilled in the inner tube. The outer tube had a small slit running the length of the tube facing upward. The test liquid was fed from one end and exited through the holes of the inner tube and the slit in the outer tube.

Because so little is known of the row effect on recently developed enhanced condenser tubes, experiments have been conducted for condensing R-11 on a vertical rank of five horizontal tubes rows. Four different surface geometries were selected for testing.

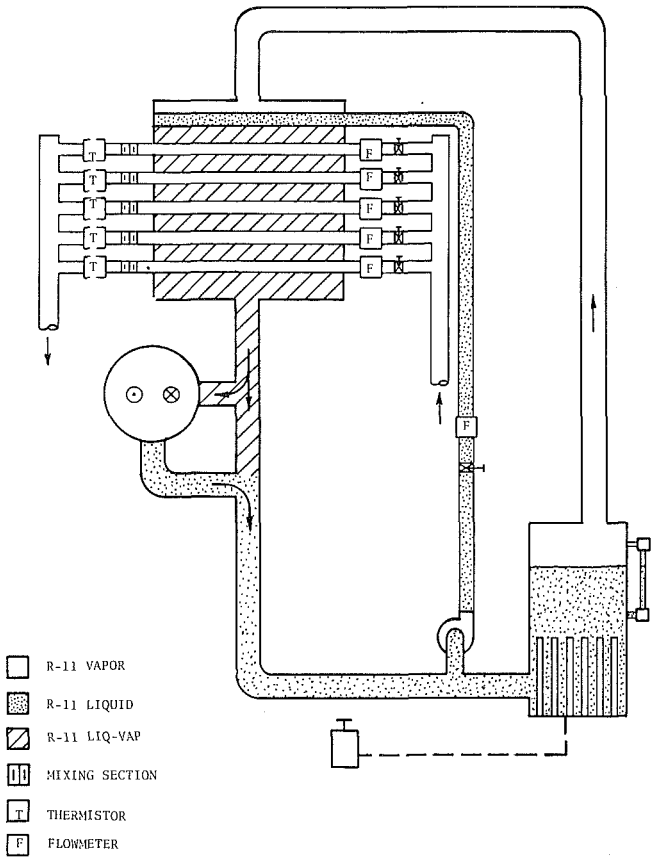

Fig. 1 Schematic of test apparatus

Experimental Apparatus

The test chamber allowed R-11 to condense on the shell side of a vertical rank of five horizontal tubes, each 305 mm long. Figure 1 shows a schematic of the apparatus. A window on the front of the test chamber allows visual observation of the condensate drainage from each tube. The vertical tube pitch is

Nomenclature

A = surface area = $\pi D_o L$, m^2
c_p = specific heat of cooling water, J/kg-°C
D = diameter of plain tube, m
D_o = diameter over fins, m
fpm = fins per meter, m^{-1}
h = average condensation coefficient for a tube h_1 (on top row); h_n (on Nth tube row), W/m^2-°C
h_{av} = average condensation coefficient for a row of tubes, W/m^2-°C
h_{ref} = condensation coefficient on the 1024-fpm tube as used on Fig. 13, W/m^2-°C
k = thermal conductivity of condensate liquid, W/m-°C
L = length of tube, m
m = row effect exponent in equation (2)
m = mass flow rate, kg/s; m_c is for coolant; m_r is for refrigerant condensate
N = Number of rows measured from top row
q = heat transfer rate, W
Re = condensate Reynolds number (equation (5))
T_b = bottom wall temperature on a tube, °C
T_c = cooling water temperature, °C; T_{c1} is for inlet; T_{c2} is for outlet
T_s = side wall temperature on a tube, °C
T_{sat} = saturation temperature, °C
T_t = top wall temperature on a tube, °C
T_w = average wall temperature on a tube, °C
ΔT = water temperature rise in each tube, °C
ΔT_{sw} = $T_{\text{sat}} - T_w$, °C
μ = dynamic viscosity of condensate, kg/m-s
λ = latent heat of vapor, J/kg
ρ = density of condensate, kg/m^3
ρ_v = density of vapor, kg/m^3

44.5 mm. The test cell is supplied with saturated vapor by an electrically heated R-11 boiler.The boiler contains six immersion heaters, one of which is controlled by an autotransformer. Noncondensibles are prevented from accumulating near the test section by use of a postcondenser installed downstream from the test chamber. Equilibrium between the vapor produced by the boiler and vapor condensed by the test section and post-condenser establishes the operating pressure of the apparatus. The condensing pressure was held at 1220 ± 5 mm Hg. Vapor pressure in the boiler, the postcondenser, and at one location in the test chamber were measured with an absolute mercury manometer. The saturation temperature of the vapor was obtained from the measured pressure in the test chamber and saturation properties of R-11.

Each tube consisted of a 305-mm-long fully finned tube length with plain stainless steel end sections. The end sections were soldered to the finned tube. The 305-mm-long tube precisely matched the 305-mm interior width of stainless steel test chamber. The end pieces contained double O-rings that sealed against the holes drilled in the end walls of the test chamber. Thermocouples were installed on the external surface of tubes at the top, side, and bottom of the tubes in rows 1, 3, and 5. The thermocouples were made of 0.13-mm-dia copper-constantan wire, and were located at the middle of the tube length. The thermocouples were attached to the tube surface by bending the copper fins over the thermocouple, and held in place by preening the copper on top of the thermocouple.

Three thermocouples were used to measure vapor temperature in the test apparatus. One thermocouple measured the vapor temperature in the boiler, and one was used to measure the vapor temperature in the post condenser. The vapor temperature obtained from the thermocouples was checked against the vapor temperature obtained from the manometer reading. Two thermocouples were used to measure the inlet and outlet water temperature of the post condenser. A Fluke 2200B data logger was used to measure the voltage output of the thermocouples.

Rotameters were used to measure the water flow rate through each test tube. Each test tube contained a 9.5-mm-dia rod insert to increase the tube side water velocity and provide a water temperature rise of 1.6–3.2°C. The water inlet and outlet temperatures were measured using six linear thermistors. One thermistor measured the inlet water temperature of all five testing tubes, and five thermistors independently measured the outlet temperature from each test tube. A mixing section was installed between the tube exit and the thermistor. The thermistor outputs were read using an Omega Model 5830 Precision Thermistor Thermometer. A weight tank was used to measure the water flow rate through the postcondenser.

The mass flow rate of the condensate from the test chamber and the post-condenser was determined by measuring the time required for the condensate to fill a known volume in a liquid level gage.

In order to distribute the vapor evenly within the test section, a tight mesh screen was installed at the top of the test cell. A liquid distributor tube was also installed in the test chamber above the five test tubes to simulate drainage for more than five tube rows. The distributor flow circuit consisted of a refrigerant line from the bottom of the boiler, a centrifugal pump, a valve, and a flowmeter. The distributor tube was constructed as a tube within a tube. The inner tube had 2.5-mm-dia holes drilled in it facing downward. The outer tube had an axial slit 2.5 mm wide along its length at the top of the tube. A nylon mesh was inserted in the annulus slit to even the flow as it exited the annulus. A small circular rod was attached at the bottom of the drainage tube to aid in stabilizing the flow drainage.

Table 1 Table of tube geometries (all dimensions in mm)

Tube Type	Outside Diameter		Inside Diameter		FPM
	Fin Tip	Fin Base	Fin Tip	Fin Base	
1024 fpm	18.9	16.3	--	14.4	1024
Turbo-C	18.9	16.7	14.4	15.1	1575
GEWA-SC	18.9	16.4	14.0	15.1	1024
Tred-D	18.9	16.3	13.3	14.0	1024

Enhancement Geometries Tested

Five tube geometries were tested. Table 1 describes the geometry of each tube, and Fig. 2 shows a photo of each tube tested. All tubes had 1024 fins/m (fpm), except the Turbo-C, which had 1575 fpm. The standard 1024-fpm tube has vertical fins of a trapezoidal cross section. The GEWA-SC tube has a fin shape similar to the standard 1024-fpm tube, except that these fins have a Y-shaped cross section. The Turbo-C and Tred-D tube fins are similar to those of the standard 1024-fpm tube, except the fin tips have been knurled in the circumferential direction. The knurling produces a saw-tooth fin shape. Table 1 shows all dimensions in mm.

A modified Turbo-C was also tested. A tube cutter was used to form a helical groove along the length of the three-start fin geometry. A 0.5-mm-dia nylon cord was wrapped in the groove. The nylon cord projected approximately 0.35 mm above the top of the fins. The wrap of the nylon cord was in every third fin groove.

Test Procedure

After the system was leak free, it was again evacuated using a vacuum pump. The pump was left on for one hour after the manometer read 0 mm Hg to ensure that the system contained no noncondensible gases. The boiler was then filled with R-11 liquid while the vacuum pump was left running for a short time. Further purging was done by running the system and operating the postcondenser only. The postcondenser was then vented to the atmosphere to remove any noncondensibles. Since room temperature was always kept above 24°C, the system was above ambient pressure, so no air could leak into the system. A post condenser purge was done before every test series to remove noncondensible gasses.

A series of three tests was done for each tube. First, a purge test was done to evacuate noncondensibles from the system. Second, regular tests were run, for which the water flow rate through all tubes was equal. Test data on the top tube provided single tube performance. Finally, the distributor tube test was operated to obtain data for more than five tube rows.

Data Reduction

The data were reduced in the following manner. The thermocouple readings were averaged and converted to temperature using NBS copper-constantan thermocouple tables. The average wall temperature was determined using $(T_t + 2T_s + T_b)/4$, where T_t, T_s, and T_b are the top, side, and bottom thermocouples, respectively. The saturation temperature is calculated by converting the test cell pressure to temperature using R-11 property tables. The heat load (q) on each tube is calculated using

$$q = m_c c_p (T_{c2} - T_{c1}) \tag{3}$$

The condensation coefficient (h) was calculated by

$$h = q/[\pi D_o L (T_{\text{sat}} - T_w)] \tag{4}$$

As shown by equation (4) , h is based on the envelope area of the tube. A heat balance was calculated to determine the accuracy of the test run. The heat balance is defined as the heat received by the water (five tubes) minus the heat transfer rate

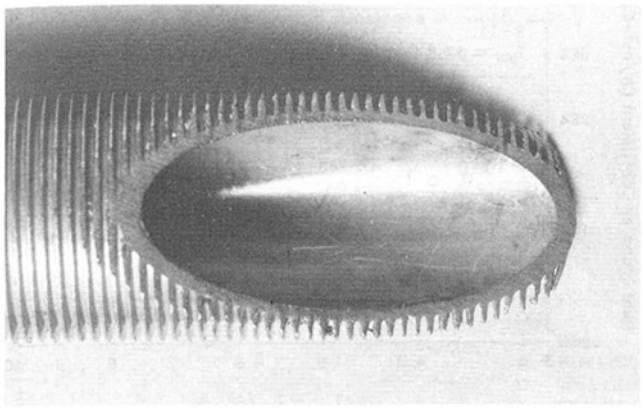

(a) 26 fpi

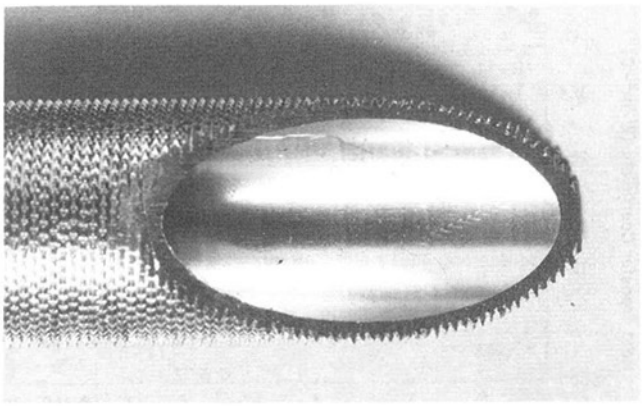

(b) Turbo-C

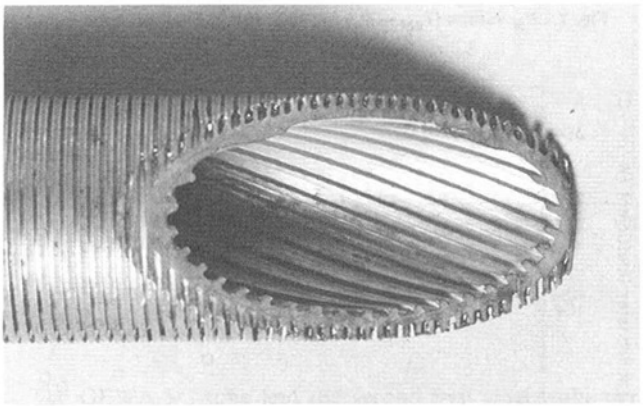

(c) GEWA-SC

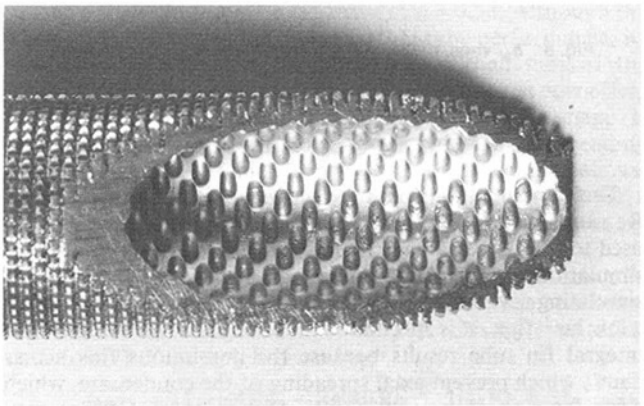

(d) Tred-D

Fig. 2 Photograph of tubes tested

from the condensate catch method, divided by the heat received by the water. The condensate Reynolds number is defined as

$$\mathrm{Re} = 4m_r/L\mu \tag{5}$$

where m_r is the condensate draining from the tube, for which the Reynolds number is desired. m_r is the total condensate draining from this tube, and is calculated by summing the heat load on all tubes above and including the tube of interest, and dividing by the latent heat λ.

The data were reduced to determine the row effect exponent of equation (2). Since the measurements provided the condensation coefficient on each tube, rather than the average value over N-rows, it was necessary to manipulate equation (1) to derive the row effect exponent. This derivation is shown in the appendix. The result is

$$h_N/h_1 = N^{1-m} - (N-1)^{1-m} \tag{6}$$

Thus, for row 5 ($N=5$) one uses the condensation coefficients for rows 1 and 5 in equation (6) and solves for the exponent, m.

As previously discussed, Nusselt's classic definition for the row effect exponent (equation (2)) assumes $(T_{sat} - T_w) = \text{const}$. This boundary condition cannot be achieved in practical systems. Our row effect exponent is based on data for constant inlet water temperature and water flow rate in each tube, at a given value of T_{sat}. The value of the exponent m in equation (6) was determined using the lowest heat load data for the top tube (h_1) and the fifth tube row ($N=5$).

The reduced data are portrayed in the form of h_N versus $(T_{sat} - T_w)$ and as h_N versus Re, where Re is the condensate Reynolds number leaving row N.

Experimental Results

The data reduction was performed using a computer program. Heat balances were calculated, and experiments were conducted over the course of several days to verify system accuracy and repeatability. The maximum test chamber heat balances are as follows: Turbo-C (+16/0%), 1024-fpm (+14/0%), GEWA-SC (+9/+3%), Tred-D (+9/0%), and Modified Turbo-C (+6/0%). A "+" error means the heat received by the water is greater than that calculated by the condensate catch method. The Turbo-C tube geometry yield the largest heat balance error. The Turbo-C tube was the first tube to be tested in the experimental study, and an error found in the condensate catch method was later corrected. The condensate catch does not affect the calculation of the condensate coefficients, and the Turbo-C results were repeatable. Hence, the Turbo-C results are believed to correct. The heat balances are felt to be more accurate after the Turbo-C testing series. An error analysis showed that the error associated with the condensation coefficient is ±5 percent.

Figure 3 shows h versus $(T_{sat} - T_w)$ for the top tube for the enhanced tube geometries tested. Figures 4–8 show curves of h_N versus $(T_{sat} - T_w)$ for all tubes tested. Figures 9–11 show the same results plotted in the format h_N versus Re. Figure 12 shows a map of the condensate drainage patterns observed for each tube.

Single Tube Test Results. Figure 3 compares the single tube performance of all the geometries tested. These data are for the top tube in the five-row tube bank. This figure shows that the highest single-tube performance is provided by the Turbo-C tube, and the lowest by the standard 1024-fpm tube. The condensation coefficient of the standard 1024-fpm tube is 60 percent that of the Turbo-C. The second and third best performance is given by the GEWA-SC (80 percent of Turbo-C) and Tred-D (72 percent of Turbo-C) tubes, respectively.

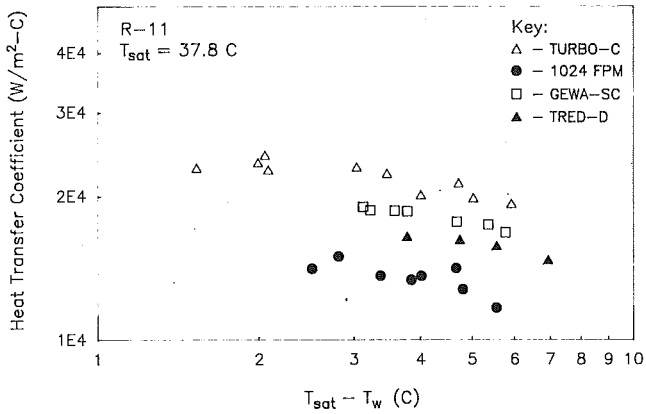

Fig. 3 h_1 versus $(T_{sat}-T_w)$ for single tubes

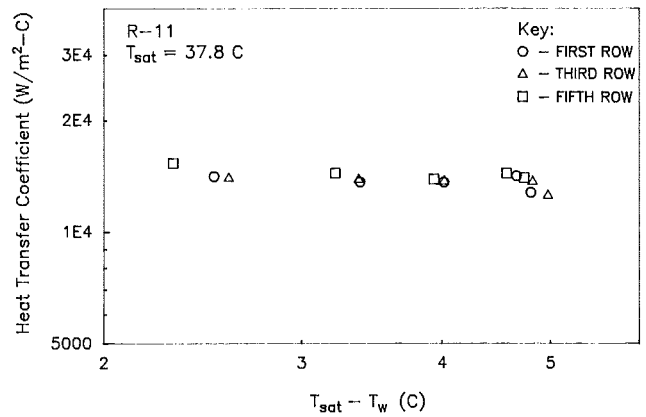

Fig. 4 h_N versus $(T_{sat}-T_w)$ for 1024-fpm tube

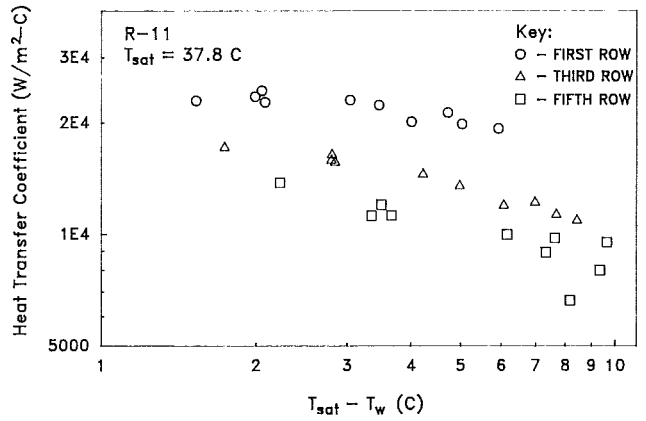

Fig. 5 h_N versus $(T_{sat}-T_w)$ for 1575-fpm Turbo-C tube bank

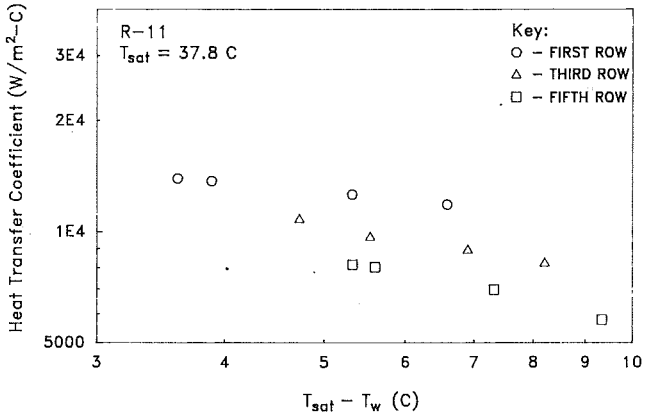

Fig. 6 h_N versus $(T_{sat}-T_w)$ for modified Turbo-C tube banks

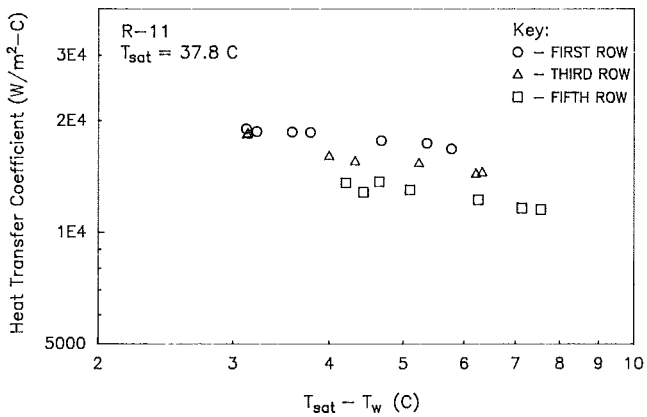

Fig. 7 h_N versus $(T_{sat}-T_w)$ for 1024-fpm GEWA-SC tube bank

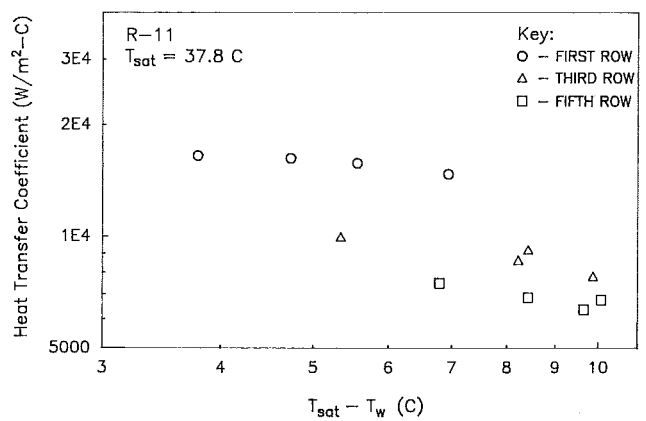

Fig. 8 h_N versus $(T_{sat}-T_w)$ for 1024-fpm Tred-D tube bank

h_N versus Re for Table 1 Geometries. Figure 9 shows how h_N varies with the condensate Reynolds number leaving the tube row in question. The data for all tubes, except the standard 1024-fpm tube, were taken for five tube rows. Up to seven tube rows were simulated for the standard 1024-fpm tube. Figure 9 shows that the data for all tube rows fall on a single curve, when plotted in the h_N versus Re format. Because the h_N depends only on Re, and not on tube rows, Fig. 9 may be interpreted for any number of tube rows, within the Re range of the data.

Table 2 gives curve fits of straight lines drawn through the h_N versus Re curves of Fig. 9. These straight line curve fits yield equations of the form

$$h_N = a\mathrm{Re}^{-n} \tag{7}$$

The standard 1024-fpm tube shows no row effect within the Re range tested. This was also true when the drip tube was used to simulate drainage from two tube rows, which allowed simulation of seven tube rows. Figure 10 shows the result of simulating seven tube rows for the standard 1024-fpm tube at a low heat flux. It is speculated that the good row effect of the integral fin tube results because the continuous fins act as dams, which prevent axial spreading of the condensate, which drips from the tube row above. Honda et al. (1987a) condensed R-113 on a rank of standard 1024-fpm tubes, and found zero row effect.

Table 2 Exponent n and constant a in equation (7)

Geometry	a x 10^{-3}	n
1024 fpm	13.90	0.000
GEWA-SC	54.14	0.220
Turbo-C	257.80	0.507
Tred-D	269.90	0.576
Mod. Turbo-C	113.30	0.446

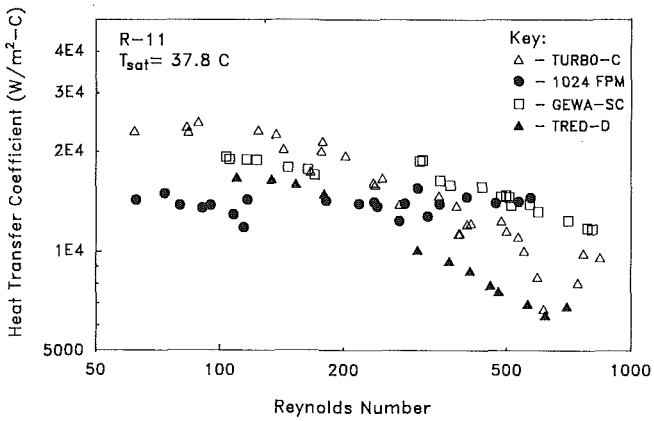

Fig. 9 h_N versus Re Table 1 tube geometries

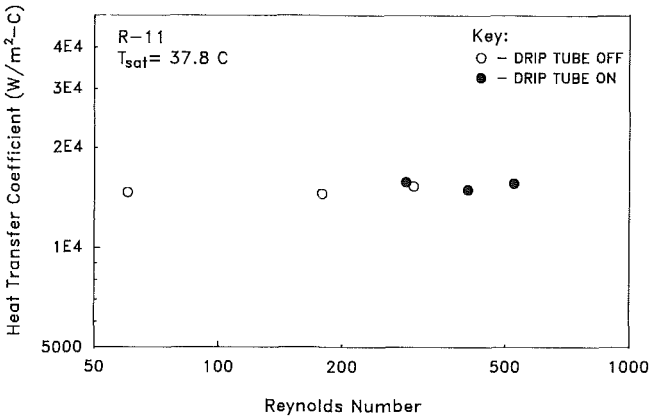

Fig. 10 h_N versus Re for 1024-fpm tube using drip tube

The GEWA-SC tube had the second best single-tube performance, and the second best row effect ($n = 0.22$).

The greatest row effect was displayed by the Tred-D tube, having a Reynolds number exponent of $n = 0.58$. Although the Turbo-C tube showed the highest single-tube performance, its row effect ($n = 0.51$) is only little better than that of the Tred-D. It is interesting to observe that the poorest row effect was yielded by the geometries having a sawtooth fin shape. It appears that the sawtooth cuts in the fins allow axial spreading of the condensate, which drops from the tube row above. These row effect exponents may be compared to that for a plain tube, which has $n = 1/3$, according to the Nusselt theory and given by Holman (1986).

If the condensate Reynolds number leaving the last row of a bank of tubes is known, one may find the average condensation coefficient on the bank of N-tube rows by integrating equation (7). The result is given by

$$h_{av} = [a/(1-n)(\mathrm{Re}_N - \mathrm{Re}_1][(\mathrm{Re}_N)^{-n} - (\mathrm{Re}_1)^{-n}] \qquad (8)$$

where Re_N and Re_1 are the Reynolds numbers leaving the Nth and the first tube rows, respectively. An example is given later,

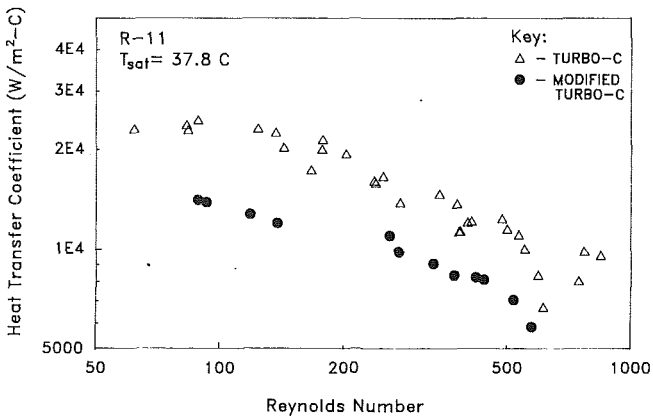

Fig. 11 h_N versus Re for standard and modified Turbo-C tube banks

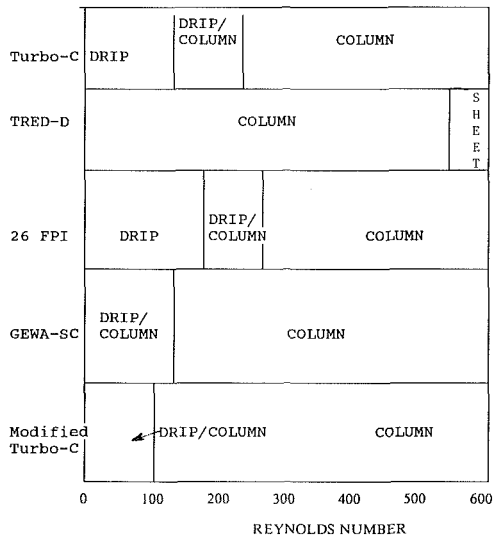

Fig. 12 Observed condensate drainage patterns versus condensate Reynolds number for all tubes tested

which shows how the bundle average condensation coefficient may be calculated using equation (8).

Observed Drainage Pattern. Figure 12 shows the results of visual observations of the condensate drainage patterns. For all tests conducted, four flow patterns were observed. They are "drip," "drip/column," "column," and "sheet" modes, as defined by Honda et al. (1987a). The drip mode refers to a flow pattern in which condensate drips from tube to tube, like a dripping faucet. The drip/column mode is a flow pattern that appears to be dripping columns. Unlike the dripping mode, which has distinct, separate drops, the drip/column mode appears an interrupted columns. The column mode is a continuous jet from the bottom of a testing tube.

The condensate drainage pattern from the Turbo-C tube became very unstable after the third tube. Unstable means the condensate did not flow vertically downward, but sometimes oscillated lateral to the tube axis. The columns draining from the Turbo-C did not have a constant spacing or fixed drainage points along the tube axis. The axial distance between jets was typically 6–12 mm. When condensate impinged on the Turbo-C tube at one axial position, the condensate would not leave the tube at the same axial position. The shape slows the circumferential condensate drainage, and allows it to spread in the axial direction. The time between condensate impingement to condensate separation appears to be considerably longer on the Turbo-C tube compared to the standard 1024-fpm tube.

The flow patterns were more stable for the 1024-fpm and GEWA-SC tubes.

A small liquid meniscus was observed between some of the fins, in the unflooded regions of the Turbo-C tube. The meniscus appeared to cling to the contours of the interfin spaces. This meniscus was also observed on the Tred-D tube. These meniscus regions may be partially responsible for the poor row effect performance of the tube. However, its existence is contrary to the good single-tube performance of the Turbo-C.

We conclude that the Turbo-C tube shows a high row effect because of the flow pattern of condensate on the tube. The geometry impedes circumferential condensate flow and does not establish any axial regions that are clear of condensate for any extended time period. This will reduce active heat transfer area that would otherwise condense R-11 vapor.

The standard 1024-fpm tube showed a very distinctive flow pattern relative to the other geometries. The flow clearly channeled between the fins. Channeling is defined as flow impinging on and flowing from the tube at the same axial location. The condensate drainage appeared to be confined between two and three fin spacings. The tube surface between the drainage regions was virtually condensate free. These unflooded regions experience a high condensation rate, which explains the negligible row effect.

Only the drip mode was observed to occur from the top tube. The spacing between droplets appeared to oscillate with a maximum spacing of 10 mm. As seen in Fig. 12, the standard 1024-fpm tube is the last tube to enter the column mode. It appeared that the diameter of the draining droplets and columns was larger than from the other geometries. The diameter of the droplets and columns from the standard 1024-fpm tube was approximately 50 percent larger than those of the Turbo-C tube. The GEWA-SC drop diameters were intermediate to those of the standard 1024-fpm and the Turbo-C tubes. The liquid holdup angle, within the flooded region, appeared to fluctuate as the condensate left the tube. The axial location of the condensate drainage points was nearly constant from the top to the bottom tube row. The condensate appeared to drain in the circumferential direction faster than was observed for the Turbo-C tube.

A drip drainage mode was not observed for the GEWA-SC tube. As seen in Fig. 12, the GEWA-SC tube entered the column mode at a lower Reynolds number than was observed for the other tubes. This tube geometry did appear to channel the flow. It was observed that a portion of the condensate was caught by the Y-shaped fin and carried around the tube circumference. The time of condensate impingement to dripoff was very short. The holdup angle did not appear to fluctuate significantly when the condensate drained from the tube. The spacing between columns fluctuatedfrom 6 to 10 mm. If the distance became less than 6 mm, the columns would merge. Even at high condensate flow rates, the draining condensate did not fluctuate significantly in the lateral direction.

The nylon wrapping on the modified Turbo-C tube greatly affected the flow pattern from the tube. As seen in Fig. 12, the modified Turbo-C tube had a transition from the drip/column mode to the column mode at a condensate Reynolds number of 100. A drop mode was not observed on the modified Turbo-C tube. The column mode was very stable and the condensate channeled from tube to tube. The channeling effect constrained the condensate within two or three nylon wraps. The nylon cord was wrapped between every third fin. In the column mode, the condensate totally flooded the region, in which it was flowing. A small retention angle of about 30 deg measured from the bottom of the tube was observed. The retention angle did not vary much as the condensate left the tube, unlike the standard 1024-fpm tube. The spacing between columns fluctuated from 6 to 10 mm, and behaved the same as the column mode on the standard 1024-fpm tube. The spacing between columns fluctuated from 6 to 10 mm, and behaved the same as the column mode on the standard 1024-fpm and GEWA-SC tubes.

Table 3 Row effect exponent for $\Delta T_{sw} = 5.55°C$ (based on rows 1 and 5)

Geometry	m
1024 fpm	0.00
GEWA-SC	0.12
Turbo-C	0.23
Tred-D	0.26
Mod. Turbo-C	0.17

As noted above, the Tred-D geometry had the highest row effect of all the geometries tested. The draining columns were steady, and without lateral oscillation. The condensate appeared to channel from row to row. However, this was accompanied by more axial spreading than was observed for the standard 1024-fpm tube. As seen on Fig. 12, Tred-D is the only tube to attain the sheet mode. The axial location of the columns fluctuated slightly; from tube to tube, the axial column location varied only one or two fin spacings. Like the Turbo-C tube, the Tred-D tube had a low condensate retention angle. Retention angle refers to the region at the bottom of a tube, in which the fin spaces are completely filled with condensate from fin root to fin tip. A thick liquid meniscus could be seen in the interfin regions of the Tred-D tube. There was so much liquid between the fins that only the upper half of every fin was exposed to the condensing vapor. The liquid meniscus may significantly decrease the heat transfer rate.

Test Results for Individual Tube Rows. Figures 4–7 show h_N versus $(T_{sat} - T_w)$ for the different enhanced tubes and are discussed in this section. The h_N data are shown for rows 1, 3, and 5. These figures show two salient features: the single tube performance of the top tube, which has been discussed, and the decreasing peformance of the lower tube rows, due to condensate loading. The information presented on these figures has basically the same content as the h_N versus Re format (Fig. 9). However, Fig. 4–7 clearly show the decrease of h_N with rows. Examination of these figures shows that the slope of the h_N versus $(T_{sat} - T_w)$ curves increases with increasing number of rows. The row effect exponent would be constant if the curves for the different tube rows were parallel. This means the row effect exponent, as defined by equation (6), is not constant. We feel that the h_N versus Re format for plotting the data is preferred, since the data for the different rows collapse to fall on one curve.

We have used equation (6) to define the row effect exponent (n) for the four enhanced surfaces. These results are given in Table 3 for $(T_{sat} - T_w) = 5.55°C$ based on data for rows 1 and 5. Except for the standard 1024-fpm tube, the exponent n becomes larger as $(T_{sat} - T_w)$ is increased. Figure 4 shows the condensation coefficient of the standard 1024-fpm tube plotted against $(T_{sat} - T_w)$ for rows 1, 3, and 5. This graph shows that the there is no row effect for five tube rows.

The distributor tube was modified several times and drip tests were conducted for several heat loads. At low heat loads the drip tube does a good job of simulating condensation flow. At higher heat loads, the flow from the drip tube becomes "unstable." By "unstable," we mean that some of the condensate drained to the side wall, rather than to the tube below. The drip tube was able to simulate only two tube rows before the flow pattern became unstable. As shown in Fig. 10, the drip tube results were consistent with test results of higher Reynolds number flow for five flow rows. The effective simulation of two tube rows supports the previous conclusion

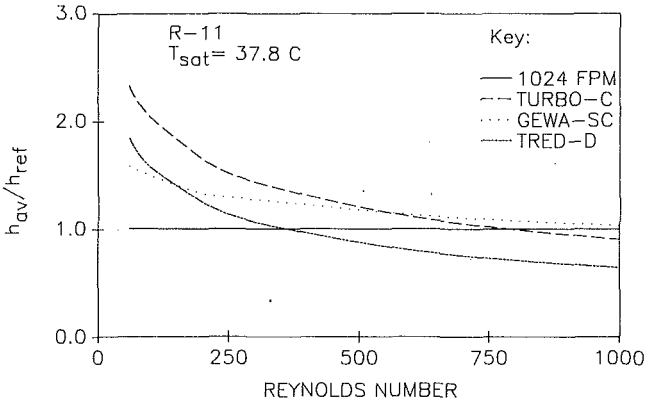

Fig. 13 h_{av}/h_{ref} versus Re for tubes tested

that the zero row effect exponent is applicable over the tested Reynolds number range, independent of the actual number of tube rows. After the standard 1024-fpm test series, the distributor tube was no longer used to simulate vertical tube rows.

Figure 5 shows the individual row results for the Turbo-C tube. It is normally assumed that $h_N \propto (T_{sat} - T_w)^{-0.25}$ in accordance with Nusselt's theory, equation (1). This is approximately true for the top tube row. However, the slope of h_N versus $(T_{sat} - T_w)$ increases with row number, and was sensitive to $(T_{sat} - T_w)$. At low heat loads the row effect exponent of equation (6) is 0.20. At high heat loads the row effect exponent changes to 0.28. The scatter of the row 5 data at high $(T_{sat} - T_w)$ is believed to be due to condensate splashing from the tube.

Comparison of Figs. 5 and 6 shows that the heat transfer coefficient for the modified Turbo-C tube is less than the standard Turbo-C tube. The nylon wrap apparently reduced the effective heat transfer surface area. Since the thermal conductivity of nylon is much less than that of copper it can be assumed that no condensation takes place on the nylon cord. It was intended that the nylon cord would promote condensate channeling, as occurred on the standard 1024-fpm tube. This should reduce the row effect. However, Fig. 11 shows the slope of the modified Turbo-C is slightly less than that of the standard Turbo-C geometry (0.37 versus 0.43). Visual observation showed that the nylon wrap did improve the channeling. The small improvement in row effect provided by the nylon wrap was disappointing.

Figure 7 shows the heat transfer coefficient versus $(T_{sat} - T_w)$ for the GEWA-SC tube. This tube has a smaller row effect than Turbo-C or Tred-D. The row effect exponent (as defined by equation (6)) is 0.12 for $(T_{sat} - T_w) = 5.55°C$. At the higher heat loads, the row effect exponent is 0.15.

Figure 8 shows h_N versus $(T_s - T_w)$ for the Tred-D tube. This tube shows the greatest row effect of all tubes tested. At $(T_{sat} - T_w) = 10°F$, Table 3 shows that the row effect exponent is 0.26. It is interesting to note that the Tred-D and Turbo-C tubes both have the sawtooth fin design. These two tubes show a higher row effect than the other tubes. The fin height of Tred-D is greater than that of Turbo-C (1.3 versus 0.095 mm). However, the higher fins do not enhance its row effect performance, relative to Turbo-C.

Average Condensation Coefficient for N-Rows

Equation (8) may be used to define the average condensation coefficient for a bank of tubes. We have evaluated equation (8) for the case of $Re_1 = 60$ for four tube goemetries. Re_1 is the condensate Reynolds number leaving the first tube row. Figure 13 shows the ratio h_{av}/h_{ref}, where:

1 h_{av} is for each of the several enhanced tubes tested.

2 h_{ref} is for the 1024-fpm standard integral fin tube, which shows no row effect exponent.

The ordinate h_{av}/h_{ref} on Fig. 13 shows the ratio of average condensation coefficient on N-rows to that provided by the 1024-fpm tube, which shows no row effect. The bottom rows of typical R-11 condensers have $200 \le Re_N \le 500$. For $Re_N = 300$, Fig. 13 shows that the Tred-D provides approximately the same average condensation coefficient as that of the 1024-fpm tube. The average condensation coefficients of the GEWA-SC tubes are 27 percent higher than that of the 1024-fpm tube, and the Turbo-C provides a 43 percent higher average condensation coefficient than the 1024 fpm tube. It is unlikely that the tubes would be used in a condenser for $Re_N > 600$. However, if they were, only the GEWA-SC would provide an average condensation coefficient comparable to that of the 1024 fpm tube.

Conclusions

1 The Turbo-C tube shows the highest single-tube performance, but its poor row effect substantially decreases its performance in a tube bundle.

2 The standard 1024-fpm tube showed virtually no row effect.

3 The GEWA-SC single tube condensation coefficient is 80 percent that of the Turbo-C, but its lower row effect may make it attractive for use in a tube bundle.

4 The Tred-D tube has lower single-tube performance than the GEWA-SC, and the largest row effect on all tubes tested.

5 Attempts to improve the row effect of the Turbo-C tube using a nylon wrap decreased the row effect (relative to the original Turbo-C) by only 10 percent. The single-tube performance also dropped.

6 The test results were presented in two formats: h_N versus $(T_{sat} - T_w)$, and h_N versus Re. The second format is superior, because the data for all tube rows collapse to a single line.

7 When presented in the h_N versus $(T_{sat} - T_w)$ plot, the row effect exponent is not constant. It is a function of $(T_{sat} - T_w)$ and increases with increasing $(T_{sat} - T_w)$.

8 The superior row effect of the standard 1024-fpm tube is believed to result because the solid fins channel the condensate as it drains downward across successive tube rows. This leaves condensate free regions between drainage points, which have the same performance as a single tube.

Acknowledgments

Funding for this work was provided by York International, Inc., and the Commonwealth of Pennsylvania Ben Franklin Program.

References

Beatty, K . O., Jr., and Katz, D. L., 1948, "Condensation of Vapors on Outside of Finned Tubes," *Chemical Engineering Progress*, Vol. 44, No. 1, pp. 908-914.

Carnavos, T. C., 1980, "An Experimental Study: Condensing R-11 Augmented Tubes," ASME Paper No. 80-HT-54.

Gregorig, R., 1954, "Film Condensation on Finely Rippled Surfaces With Consideration of Surface Tension," *Z. Angew, Math. Phys.*, Vol. V, pp. 36-49.

Holman, J. P., 1986, *Heat Transfer*, 6th ed., McGraw-Hill, New York, p. 497.

Honda, H., Nozu, S., and Takeda, Y., 1987a, "A Theoretical Model of Film Condensation in a Bundle of Horizontal Low Finned Tubes," *Boiling and Condensing in Process Heat Exchangers*, ASME HTD-Vol. 85, pp. 79-85.

Honda, H., Nozu, S., and Takeda, Y., 1987b, "Flow Characteristics of Condensate on a Vertical Column of Horizontal Low Finned Tubes," *ASME-JSME Thermal Eng. Joint Cong.*, Vol. 1, pp. 517-524.

Katz, D. L., and Geist, J. M., 1948, "Condensation of Six Finned Tubes in a Vertical Row," *Trans. ASME*, Vol. 70, pp. 907-914.

Kedzierski, M. A., and Webb, R. L., 1987, "Experimental Measurements of Condensation on Vertical Plates With Enhanced Fins," *Boiling and Condensation in Heat Transfer Equipment*, ASME HTD-Vol. 85 pp. 87-95.

Marto, P. J., and Wanniarachchi, A. S., 1984, "The Use of Wire-Wrapped Tubing to Enhance Steam Condensation in Tube Bundles," *Heat Transfer in Heat Rejection Systems*, ASME HTD-Vol. 37, S. Sengupta and Y. G. Mussalli, eds., pp. 9–16.

Marto, P. J., 1986, "Recent Progress in Enhancing Film Condensation Heat Transfer on Horizontal Tubes," *Heat Transfer 1986—Proceeding of the Eighth International Heat Transfer Conference*, Vol. 1, pp. 161–170.

Masuda, H., and Rose, J. W., 1985, "An Experimental Study of Condensation of Refrigerant R-113 on Low Integral-Fin Tubes," *Proceedings, International Symposium on Heat Transfer*, Tsinghua Univ. Press, Vol. 2, Paper 32.

Nusselt, W., 1916, "Die Oberflachenkondensation des Wasserdampfes," *Z. Ver. Deut. Ing.*, Vol. 60, pp. 541–569.

Rudy, T. M., and Webb, R. L., 1985, "An Analytical Model to Predict Condensate Retention on Horizontal Integral-Fin Tubes," ASME JOURNAL OF HEAT TRANSFER, Vol. 107, pp. 361–368.

Wanniarachchi, A. S., Marto, P. J., and Rose, J. W., 1986, "Film Condensation of Steam on Horizontal Finned Tubes: Effect of Fin Spacing," ASME JOURNAL OF HEAT TRANSFER, Vol. 108, pp. 960–966.

Webb, R. L., 1984a, "Shell-Side Condensation in Refrigerant Condensers," *ASHRAE Trans.*, Vol. 90, Part 1B, pp. 5–25.

Webb, R. L., 1984b, "The Effects of Vapor Velocity and Tube Bundle Geometry on Condensation in Shell-Side Refrigeration Condensers," *ASHRAE Trans.*, Vol. 90, Part 1B, pp. 39–59.

Webb, R. L., and Rudy, T. M., and Kedzierski, M. A., 1985, "Prediction of the Condensation Coefficient on Horizontal Integral-Fin Tubes," ASME JOURNAL OF HEAT TRANSFER, Vol. 107, pp. 369–376.

APPENDIX

Development of Equations (2) and (6)

The classical Nusselt (1916) equation for the condensation coefficient for a smooth horizontal tube may be expressed as

$$h_1 = 0.725\left(\frac{k^3\lambda\rho(\rho-\rho_v)g}{\mu(T_{\text{sat}}-T_w)D}\right)^m \tag{10}$$

Nusselt's theory shows $m=1/4$. For a vertical tier of N horizontal tubes, the average condensation coefficient may be expressed as

$$h_{av,n} = 0.725\left(\frac{k^3\lambda\rho(\rho-\rho_v)g}{\mu(T_{\text{sat}}-T_w)DN}\right)^m \tag{11}$$

where N is the number of tube rows. Equations (A1) and (A2) are the same equation except for the appearance of N in equation (A2). Equation (A2) can be rewritten as

$$h_{av,N} = h_1 N^{-m} \tag{12}$$

Therefore:

$$h_{av,N}/h_1 = \mathrm{N}^{-\mathrm{m}} \tag{13}$$

Equation (A4) states that the average condensate coefficient for N rows of tubes divided by the condensation coefficient on the first row is equal to the number of rows raised to the negative m power. In this experimental study, the condensation coefficient is measured on three out of the five rows in the test chamber. If equation (A4) is applied to this experiment, some error may occur when we assume the average condensation coefficient for the five rows is equal to the average of rows 1, 3, and 5. Therefore, it is necessary to develop an equation that defines the row effect exponent in equation (A4) without averaging the condensate coefficients. The average condensation coefficient for N rows of tubes can be written as

$$h_{av,N} = [h_{av,N-1}(N-1) + h_N]/N \tag{14}$$

Equation (A5) may be rewritten as

$$h_N = Nh_{av,N} - (N-1)h_{av,N-1} \tag{15}$$

Substituting equation (A3) into equation (A6) yields

$$h_N = Nh_1 N^{-m} - (N-1)h_1(N-1)^{-m} \tag{16}$$

Equation (A7) simplifies to

$$h_N/h_1 = N^{(1-m)} - (N-1)^{(1-m)} \tag{17}$$

Equation (A8) enables us to take the ratio of the condensation coefficients of the first and fifth row and get the same row effect exponent as in equation (A4).

Journal of Heat Transfer

Technical Notes

This section contains shorter technical papers. These shorter papers will be subjected to the same review process as that for full papers.

Non-Quasi-Steady Analysis of Heat Conduction From a Moving Heat Source

H. J. Zhang[1]

Nomenclature

a = thermal diffusivity, m^2/s
A = section area, m^2
C_p = specific heat at constant pressure, J/kg-K
F = dimensionless time
h = heat transfer coefficient, W/m^2-K
m = fin parameter, m^{-1}
M = dimensionless parameter
p = perimeter, m
q = plane heat source, W/m^2
Q = point heat source, W
t = temperature, K
U = moving velocity, m/s
x = stationary space coordinate, m
X = moving space coordinate, m
θ = temperature rise, K
Θ = dimensionless temperature rise
ξ, η, ζ = transformed variables, dimensionless coordinates
ρ = density, kg/m^3
τ = time, s

Subscripts

c = constant
i = initial state
s = steady state

Introduction

The problem of heat conduction resulting from a moving heat source applies to many fields of engineering such as arc welding, surface hardening, continuous casting, metal material treatment, moving friction between mechanical parts, laser machining, and even in nucleate boiling theory. Many investigations of this problem have been performed.

Earlier work is based on the principle of a quasi-steady state, that is, if the heat source with constant power moves with a constant velocity in a medium of sufficiently large dimensions, then the temperature field appears to be at steady state with respect to the moving coordinate system after quite a long time. The origin of this coordinate system is placed on the heat source and moves with it. Such a steady temperature field is called quasi-steady. Rosenthal (1946) derived appropriate exact solutions for point, linear, and plane sources in a medium of infinite size by using the transformation of the moving coordinate. Carslaw and Jaeger (1959) obtained the same solution using the heat source method.

Although the quasi-steady solution has been widely used in engineering, there are some rigid limits to it. First, the power in the moving heat source must be constant, otherwise the quasi-steady state cannot appear even if the medium is large. Next, the medium itself must be large, so that the quasi-steady state can be reached. Both of these conditions must be simultaneously satisfied. In developing high technologies such as laser, plasma, and others, greater importance is given to research into heat conduction in bodies with finite size resulting from a moving heat source. For these bodies, the temperature distribution is non-quasi-steady, not only for the moving heat source with variable power, but also for those with constant power. Thus, the investigation of non-quasi-steady heat conduction resulting from the moving heat source is of importance in engineering. Carslaw and Jaeger (1959) gave an integral expression for the non-quasi-steady temperature distribution in an infinite medium due to a moving point source. Modest and Abakians (1986) considered heat conduction in a moving semi-infinite medium subject to laser irradiation. They expanded the body of knowledge of exact analytical solutions for Gaussian laser irradiation to include pulsed lasers and laser beams, and also found a simple approximate solution, which is easily applied to complicated geometries. However, the investigation of non-quasi-steady heat conduction resulting from a moving heat source is still limited, and this form of heat conduction requires further study.

The present note considers heat conduction in a finite medium or a thin rod with heat loss from the rod surface resulting from a moving plane source through the use of a heat source method and presents the appropriate exact analytical solutions.

Non-Quasi-Steady Analysis of Heat Conduction

In order to understand clearly the characteristics of heat conduction resulting from a moving heat source, the heat conduction caused by the moving plane heat source in the infinite medium is first analyzed. Suppose that the initial temperature of the medium is t_i. When $\tau > 0$, the plane source with power $q(\tau)$ at $x = 0$ releases heat and moves at a constant velocity U along the x axis as shown in Fig. 1. For simplicity, the moving coordinate system $0X$ is taken relative to the moving heat source. For the point source with constant power Q_c located at the origin, the temperature distribution in an infinite medium that moves past the origin with constant velocity U along the x axis is given by Carslaw and Jaeger (1959). In the moving coordinate system, as shown in Fig. 1, the elevated temperature distribution, $\theta = t - t_i$, is given by

[1]Department of Heat Power Engineering, Chongqing University, Chongqing, People's Republic of China.

Contributed by the Heat Transfer Division for publication in the JOURNAL OF HEAT TRANSFER. Manuscript received by the Heat Transfer Division September 20, 1988; revision received September 27, 1989. Keywords: Conduction, Moving Boundaries, Transient and Unsteady Heat Transfer.

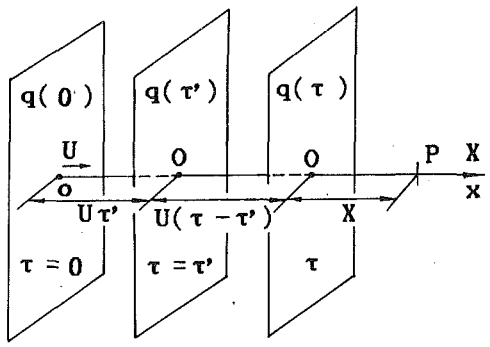

Fig. 1 Coordinate system of a moving plane source

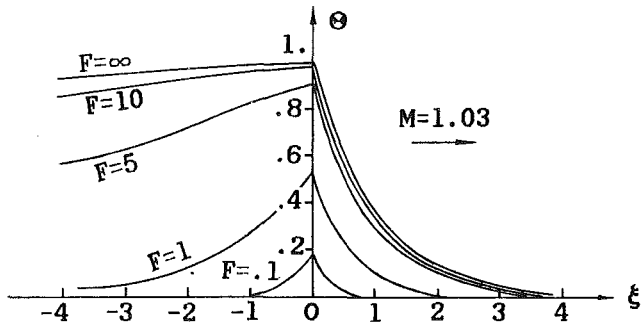

Fig. 2 Temperature distribution in the thin rod

$$\theta(X,0,0,\tau)=\frac{Q_c}{8\rho C_p(\pi a)^{3/2}}\int_0^{\tau}(\tau-\tau')^{-3/2}\cdot\exp\left\{-\frac{[X+U(\tau-\tau')]^2+y'^2+z'^2}{4a(\tau-\tau')}\right\}d\tau' \tag{1}$$

As shown in Fig. 1, the elevated temperature distribution in the infinite medium resulting from a moving plane heat source with constant power q_c can be obtained by integrating equation (1) with respect to the variables y' and z' between the limits $-\infty$ and ∞, respectively. As a result, we find

$$\theta(X,\tau)=\frac{q_c}{2\rho C_p(\pi a)^{1/2}}\int_0^{\tau}(\tau-\tau')^{-1/2}\cdot\exp\left\{-\frac{[X+U(\tau-\tau')]^2}{4a(\tau-\tau')}\right\}d\tau' \tag{2}$$

Denoting $(\tau-\tau')^{-1/2}$ by η, equation (2) becomes

$$\theta(X,\tau)=\frac{q_c}{\rho C_p(\pi a)^{1/2}}\exp\left(-\frac{UX}{2a}\right)\cdot\int_{1/\sqrt{\tau}}^{\infty}\exp\left[-\frac{X^2}{4a}\eta^2-\frac{U^2}{4a}\eta^{-2}\right]\eta^{-2}d\eta \tag{3}$$

For a long thin rod with heat loss from its surface, the heat conduction equation is

$$\frac{1}{a}\frac{\partial\theta}{\partial\tau}=\frac{\partial^2\theta}{\partial x^2}-m^2\theta \tag{4}$$

where $\theta(x,\tau)=t(x,\tau)-t_\infty$ is the excess temperature of the thin rod compared with ambient temperature t_∞; $m^2=hp/(kA)$; p, A, k, and h are the perimeter, cross sectional area, thermal conductivity, and heat transfer coefficient, respectively. The difference between equation (4) and the heat conduction equation in an infinite medium is only in the source term $-m^2\theta$. By use of the transformation $\theta(x,\tau)=\phi(x,\tau)\cdot\exp(-m^2\theta)$, equation (4) reduces to

$$\frac{1}{a}\frac{\partial\phi}{\partial\tau}=\frac{\partial^2\phi}{\partial x^2} \tag{5}$$

which is the same as the conduction equation in an infinite medium. Thus the temperature distribution of the thin rod resulting from the moving plane heat source with constant power, Q_c, can be obtained as

$$\theta(X,\tau)=\frac{Q_c/A}{\rho C_p(\pi a)^{1/2}}\exp\left(-\frac{UX}{2a}\right)\cdot\int_{1/\sqrt{\tau}}^{\infty}\exp\left[-\frac{X^2}{4a}\eta^2-\left(am^2+\frac{U^2}{4a}\right)\eta^{-2}\right]\eta^{-2}d\eta \tag{6}$$

When the surface of the thin rod is insulated, $h=0$, $m^2=0$, and equation (6) reduces to equation (3).

Exact Analytical Solutions

In order to obtain the exact solutions of the two foregoing unsteady problems, the key is to find the analytic expression of the definite integral with an infinite limit in equations (3) and (6). For this purpose, the definite integral in equation (6) is transformed as

$$\left[\int_{1/\sqrt{\tau}}^{\infty}\exp\left[-\frac{X^2}{4a}\eta^2-\left(am^2+\frac{U^2}{4a}\right)\eta^{-2}\right]\eta^{-2}d\eta\right]=\frac{1}{2}\exp\left[\sqrt{m^2+\left(\frac{U}{2a}\right)^2}\,|X|\right]\cdot\int_{1/\sqrt{\tau}}^{\infty}\exp\left[-\frac{|X|}{2\sqrt{a}}\eta+\sqrt{a}\sqrt{m^2+\left(\frac{U}{2a}\right)^2}\,\eta^{-1}\right]^2\eta^{-2}d\eta+\frac{1}{2}\exp\left[-\sqrt{m^2+\left(\frac{U}{2a}\right)^2}\,|X|\right]\cdot\int_{1/\sqrt{\tau}}^{\infty}\exp\left[-\frac{|X|}{2\sqrt{a}}\eta-\sqrt{a}\sqrt{m^2+\left(\frac{U}{2a}\right)^2}\,\eta^{-1}\right]^2\eta^{-2}d\eta \tag{7a}$$

In the two integrands of the right-hand side of equation (7*a*), let $\zeta=\frac{|X|}{2\sqrt{a}}\eta-\sqrt{a}\sqrt{m^2+\left(\frac{U}{2a}\right)^2}\,\eta^{-1}$, and $\xi=\frac{|X|}{2\sqrt{a}}\eta+\sqrt{a}\sqrt{m^2+\left(\frac{U}{2a}\right)^2}\,\eta^{-1}$, respectively; then the following analytical expression is obtained:

$$\int_{1/\sqrt{\tau}}^{\infty}\exp\left[-\frac{X^2}{4a}\eta^2-\left(am^2+\frac{U^2}{4a}\right)\eta^{-2}\right]\eta^{-2}d\eta=\frac{\sqrt{\pi}}{4\sqrt{a}\sqrt{m^2-[U/(2a)]^2}}\left\{\exp\left[-\sqrt{m^2+\left(\frac{U}{2a}\right)^2}\,|X|\operatorname{erfc}\left[\frac{|X|}{2\sqrt{a\tau}}-\sqrt{m^2+\left(\frac{U}{2a}\right)^2}\,\sqrt{a\tau}\right]\right]-\exp\left[\sqrt{m^2+\left(\frac{U}{2a}\right)^2}\,|X|\right]\operatorname{erfc}\left[\frac{|X|}{2\sqrt{a\tau}}+\sqrt{m^2+\left(\frac{U}{2a}\right)^2}\,\sqrt{a\tau}\right]\right\} \tag{7b}$$

Substituting equation (7*b*) into equation (6), the exact solution of the unsteady temperature distribution caused by a constant-power plane heat source moving in the thin rod with heat loss is obtained as

$$\theta(X,\tau)=\frac{q_c}{4k\sqrt{m^2+[U/(2a)]^2}}\left\{\exp\left[-\frac{UX}{2a}-\sqrt{m^2+\left(\frac{U}{2a}\right)^2}\,|X|\right]\operatorname{erfc}\left[\frac{|X|}{2\sqrt{a\tau}}-\sqrt{m^2+\left(\frac{U}{2a}\right)^2}\sqrt{a\tau}\right]\right.$$
$$\left.-\exp\left[-\frac{U}{2a}X+\sqrt{m^2+\left(\frac{U}{2a}\right)^2}\,|X|\right]\operatorname{erfc}\left[\frac{|X|}{2\sqrt{a\tau}}+\sqrt{m^2+\left(\frac{U}{2a}\right)^2}\sqrt{a\tau}\right]\right\} \quad (8a)$$

When the surface of the thin rod is insulated, $h=0$, $m^2=0$, equation (8*a*) reduces to

$$\theta(X,\tau)=\frac{q_c a}{2kU}\left\{\exp\left[-\frac{UX}{2a}-\frac{U}{2a}|X|\right]\operatorname{erfc}\left[\frac{|X|}{2\sqrt{a\tau}}-\frac{U}{2a}\sqrt{a\tau}\right]-\exp\left[-\frac{U}{2a}X+\frac{U}{2a}|X|\right]\operatorname{erfc}\left[\frac{|X|}{2\sqrt{a\tau}}+\frac{U}{2a}\sqrt{a\tau}\right]\right\} \quad (8b)$$

When $\tau\to\infty$, the process of heat conduction reaches its quasi-steady state in the moving coordinate, and equations (8*a*) and (8*b*) reduce to the corresponding quasi-steady solutions. This shows that the exact solutions developed in the present paper are the universal solutions applicable for both the non-quasi-steady and quasi-steady state.

The following dimensionless variables and parameters are defined:

$$\Theta=kMu\theta/(aq_c),\quad \xi=UX/a,\quad F=U^2\tau/a,$$
$$M=\sqrt{1+4m^2a^2/U^2}\geq 1$$

Substituting these parameters into equations (8*a*) and (8*b*), we obtain the corresponding dimensionless solutions:

$$\Theta=0.5\{\exp[-0.5(\xi+M|\xi|)]\operatorname{erfc}[0.5(|\xi|F^{-1/2}-MF^{1/2})]-\exp[-0.5(\xi-M|\xi|)]\operatorname{erfc}[0.5(|\xi|F^{-1/2}+MF^{1/2})]\} \quad (9a)$$

and

$$\Theta=0.5\{\exp[-0.5(\xi+|\xi|)]\operatorname{erfc}[0.5(|\xi|F^{-1/2}-F^{1/2})]-\exp[-0.5(\xi-|\xi|)]\operatorname{erfc}[0.5(|\xi|F^{-1/2}+F^{1/2})]\} \quad (9b)$$

When the dimensionless time $F\to\infty$, we approach a quasi-steady state. Then equations (9*a*) and (9*b*) reduce to

$$\Theta=\exp[-0.5(\xi+M|\xi|)] \quad (10a)$$

and

$$\Theta=\exp[-0.5(\xi+|\xi|)] \quad (10b)$$

In order to reveal the difference between non-quasi-steady and quasi-steady solutions, Fig. 2 illustrates the temperature distribution of the thin rod at $M=1.03$. It can be seen that there is a large difference between them. Heat conduction tends to quasi-steady state with time. For example, for the time $F=0.1$, 1, 5, 10, and ∞, Θ at the location of $\xi=1$ is equal to 0, 0.1, 0.3, 0.34, and 0.36, respectively. Thus the conventional quasi-steady solution cannot be used to predict the temperature distribution of the thin rod in the non-quasi-steady state. Otherwise the computation of the temperature distribution will give a low accuracy, and the smaller the time F, the larger the error of the computed results.

It is expected that the tendency of the temperature change for the infinite medium is the same as that in the thin rod. However, the time interval required to reach the quasi-steady state is larger than that for the thin rod under the same condition because of no heat loss. Meantime the moving velocity has a large effect on the temperature distribution: the larger the value of U, the smaller the value of M. Then a shorter time is required to reach the quasi-steady state.

The exact analytical solutions above can be expanded to include the variable power source employing Duhamel's superposition integral.

References

Rosenthal, D., 1946, "The Theory of Moving Sources of Heat and Its Application to Metal Treatments," *Trans. ASME*, Vol. 68, p. 849.

Carslaw, H. S., and Jaeger, J. C., 1959, *Conduction of Heat in Solids*, 2nd ed., Oxford University Press, United Kingdom.

Modest, M. F., and Abakians, H., 1986, "Heat Conduction in a Moving Semi-infinite Solid Subjected to Pulsed Laser Irradiation," ASME JOURNAL OF HEAT TRANSFER, Vol. 108, p. 597.

A Note on the Gas Distribution in a Cylindrical Gas-Loaded Heat Pipe

W. S. Chang[1] and J. S. Yu[2]

1 Introduction

A gas-loaded heat pipe, which contains a fixed quantity of noncondensible gas in addition to the primary heat transfer fluid, is known to have distinct advantages over conventional fixed-conductance heat pipes for thermal control under variable evaporator load conditions (Brennan and Kroliczek, 1979). In order to predict the thermal performance of such a heat pipe, it is necessary to determine the concentration distribution of the noncondensible gas inside the pipe, which is governed by the intricate balance between convective flow and mass diffusion. For the simplest pipe circular in geometry, a two-dimensional configuration must be employed for its analysis. The flat-front model, though extensively used for the initial design of variable-conductance heat pipes (Marcus, 1972), represents the simplest of all approaches by ignoring diffusion altogether. The one-dimensional model of Edwards and Marcus (1972) takes into account diffusion in the axial direction but neglects the effect on the gas distribution due to radial diffusion. The partial solution to the exact two-dimensional formulation given by Peterson and Tien (1989) has emphati-

[1]Wright Research and Development Center, Wright-Patterson AFB, OH 45433; Mem. ASME.

[2]Department of Mechanical Engineering, West Virginia Institute of Technology, Montgomery, WV 25136; Mem. ASME.

Contributed by the Heat Transfer Division for publication in the JOURNAL OF HEAT TRANSFER. Manuscript received by the Heat Transfer Division February 8, 1989; revision received January 4, 1990. Keywords: Heat Pipes and Thermosyphons, Mass Transfer.

Substituting equation (7*b*) into equation (6), the exact solution of the unsteady temperature distribution caused by a constant-power plane heat source moving in the thin rod with heat loss is obtained as

$$\theta(X,\tau)=\frac{q_c}{4k\sqrt{m^2+[U/(2a)]^2}}\left\{\exp\left[-\frac{UX}{2a}-\sqrt{m^2+\left(\frac{U}{2a}\right)^2}\,|X|\right]\operatorname{erfc}\left[\frac{|X|}{2\sqrt{a\tau}}-\sqrt{m^2+\left(\frac{U}{2a}\right)^2}\sqrt{a\tau}\right]\right.$$
$$\left.-\exp\left[-\frac{U}{2a}X+\sqrt{m^2+\left(\frac{U}{2a}\right)^2}\,|X|\right]\operatorname{erfc}\left[\frac{|X|}{2\sqrt{a\tau}}+\sqrt{m^2+\left(\frac{U}{2a}\right)^2}\sqrt{a\tau}\right]\right\} \quad (8a)$$

When the surface of the thin rod is insulated, $h=0$, $m^2=0$, equation (8*a*) reduces to

$$\theta(X,\tau)=\frac{q_c a}{2kU}\left\{\exp\left[-\frac{UX}{2a}-\frac{U}{2a}|X|\right]\operatorname{erfc}\left[\frac{|X|}{2\sqrt{a\tau}}-\frac{U}{2a}\sqrt{a\tau}\right]-\exp\left[-\frac{U}{2a}X+\frac{U}{2a}|X|\right]\operatorname{erfc}\left[\frac{|X|}{2\sqrt{a\tau}}+\frac{U}{2a}\sqrt{a\tau}\right]\right\} \quad (8b)$$

When $\tau\to\infty$, the process of heat conduction reaches its quasi-steady state in the moving coordinate, and equations (8*a*) and (8*b*) reduce to the corresponding quasi-steady solutions. This shows that the exact solutions developed in the present paper are the universal solutions applicable for both the non-quasi-steady and quasi-steady state.

The following dimensionless variables and parameters are defined:

$$\Theta=kMu\theta/(aq_c),\quad \xi=UX/a,\quad F=U^2\tau/a,$$
$$M=\sqrt{1+4m^2a^2/U^2}\geq 1$$

Substituting these parameters into equations (8*a*) and (8*b*), we obtain the corresponding dimensionless solutions:

$$\Theta=0.5\{\exp[-0.5(\xi+M|\xi|)]\operatorname{erfc}[0.5(|\xi|F^{-1/2}-MF^{1/2})]-\exp[-0.5(\xi-M|\xi|)]\operatorname{erfc}[0.5(|\xi|F^{-1/2}+MF^{1/2})]\} \quad (9a)$$

and

$$\Theta=0.5\{\exp[-0.5(\xi+|\xi|)]\operatorname{erfc}[0.5(|\xi|F^{-1/2}-F^{1/2})]-\exp[-0.5(\xi-|\xi|)]\operatorname{erfc}[0.5(|\xi|F^{-1/2}+F^{1/2})]\} \quad (9b)$$

When the dimensionless time $F\to\infty$, we approach a quasi-steady state. Then equations (9*a*) and (9*b*) reduce to

$$\Theta=\exp[-0.5(\xi+M|\xi|)] \quad (10a)$$

and

$$\Theta=\exp[-0.5(\xi+|\xi|)] \quad (10b)$$

In order to reveal the difference between non-quasi-steady and quasi-steady solutions, Fig. 2 illustrates the temperature distribution of the thin rod at $M=1.03$. It can be seen that there is a large difference between them. Heat conduction tends to quasi-steady state with time. For example, for the time $F=0.1$, 1, 5, 10, and ∞, Θ at the location of $\xi=1$ is equal to 0, 0.1, 0.3, 0.34, and 0.36, respectively. Thus the conventional quasi-steady solution cannot be used to predict the temperature distribution of the thin rod in the non-quasi-steady state. Otherwise the computation of the temperature distribution will give a low accuracy, and the smaller the time F, the larger the error of the computed results.

It is expected that the tendency of the temperature change for the infinite medium is the same as that in the thin rod. However, the time interval required to reach the quasi-steady state is larger than that for the thin rod under the same condition because of no heat loss. Meantime the moving velocity has a large effect on the temperature distribution: the larger the value of U, the smaller the value of M. Then a shorter time is required to reach the quasi-steady state.

The exact analytical solutions above can be expanded to include the variable power source employing Duhamel's superposition integral.

References

Rosenthal, D., 1946, "The Theory of Moving Sources of Heat and Its Application to Metal Treatments," *Trans. ASME*, Vol. 68, p. 849.

Carslaw, H. S., and Jaeger, J. C., 1959, *Conduction of Heat in Solids*, 2nd ed., Oxford University Press, United Kingdom.

Modest, M. F., and Abakians, H., 1986, "Heat Conduction in a Moving Semi-infinite Solid Subjected to Pulsed Laser Irradiation," ASME JOURNAL OF HEAT TRANSFER, Vol. 108, p. 597.

A Note on the Gas Distribution in a Cylindrical Gas-Loaded Heat Pipe

W. S. Chang[1] and J. S. Yu[2]

1 Introduction

A gas-loaded heat pipe, which contains a fixed quantity of noncondensible gas in addition to the primary heat transfer fluid, is known to have distinct advantages over conventional fixed-conductance heat pipes for thermal control under variable evaporator load conditions (Brennan and Kroliczek, 1979). In order to predict the thermal performance of such a heat pipe, it is necessary to determine the concentration distribution of the noncondensible gas inside the pipe, which is governed by the intricate balance between convective flow and mass diffusion. For the simplest pipe circular in geometry, a two-dimensional configuration must be employed for its analysis. The flat-front model, though extensively used for the initial design of variable-conductance heat pipes (Marcus, 1972), represents the simplest of all approaches by ignoring diffusion altogether. The one-dimensional model of Edwards and Marcus (1972) takes into account diffusion in the axial direction but neglects the effect on the gas distribution due to radial diffusion. The partial solution to the exact two-dimensional formulation given by Peterson and Tien (1989) has emphati-

[1]Wright Research and Development Center, Wright-Patterson AFB, OH 45433; Mem. ASME.

[2]Department of Mechanical Engineering, West Virginia Institute of Technology, Montgomery, WV 25136; Mem. ASME.

Contributed by the Heat Transfer Division for publication in the JOURNAL OF HEAT TRANSFER. Manuscript received by the Heat Transfer Division February 8, 1989; revision received January 4, 1990. Keywords: Heat Pipes and Thermosyphons, Mass Transfer.

cally revealed the importance of the radial dependence of the gas distribution on the condenser performance of the heat pipe. As a first step directed toward solving the steady-state two-dimensional problem of simultaneous heat and mass transfer at the presence of diffusion within a gas-loaded heat pipe of circular cross section, this brief note reports a consistent method for determining the radial dependence of the noncondensible gas concentration distribution. Following the authors of the last two references cited above, we shall present our discussions in the context of heat pipes having a sealed condenser end and a uniform circumferential wick.

Under conditions where thermal and pressure diffusion and the effects due to gravity can be neglected, it has been shown, under the assumption that the vapor–gas molar density and the diffusion coefficient are treated as constant system operating parameters, that the steady-state noncondensible gas concentration distribution is governed by the equation (Peterson and Tien, 1989)

$$\nabla^2 \ln x_g = 0 \tag{1}$$

where x_g is the mole fraction of the noncondensible gas. For cylindrical heat pipes with a circumferential wick, x_g is axisymmetric and equation (1) becomes

$$\frac{1}{r}\frac{\partial}{\partial r}\left(r\frac{\partial F}{\partial r}\right) + \frac{\partial^2 F}{\partial z^2} = 0 \tag{2}$$

where (z, r) are the dimensionless coordinates measured in units of the radius of the vapor–gas transverse flow area or, for all practical purposes, simply the inner radius of the wick structure, and, following the notations of Peterson and Tien (1989)

$$F = \ln x_g(z, r) \tag{3}$$

Conservation of the gas inventory in the heat pipe can be written in the form

$$\int_0^1 r dr \int_0^L \exp[F(z, r)] dz = \text{const} \tag{4}$$

where L is the dimensionless length of the heat pipe and the constant at the end is proportional to the gas inventory in moles.

2 Radial Coefficient Functions

To investigate the radial dependence of the function $F(z, r)$, we recognize that equation (2) admits a general solution of the form

$$F(z, r) = F_m(z) + \sum_{k=1}^{\infty} f_k(r) \frac{d^k F_m}{dz^k} \tag{5}$$

Here we call $f_k(r)$ the kth order radial coefficient function and $F_m(z)$, termed here as the axial distribution function, is defined as the transverse average of $F(z, r)$ over the vapor–gas flow area within the heat pipe, that is,

$$F_m(z) = 2\int_0^1 F(z, r) r dr \tag{6}$$

It is of interest to note here that the flat-front model is prescribed by equation (5) with an F_m that is constant over a certain distance satisfying equation (4) upstream of the condenser end and $-\infty$ elsewhere. For this singular case, diffusion is totally absent in the process and a sharp interface therefore would be required to exist between the condensing vapor and the noncondensible gas. Substitution of equation (5) into equation (2) gives

$$\sum_{k=1}^{\infty} \frac{d^k F_m}{dz^k} \frac{1}{r}\frac{d}{dr}\left(r\frac{df_k}{dr}\right) + \frac{d^2 F_m}{dz^2} + \sum_{k=1}^{\infty} f_k \frac{d^{k+2} F_m}{dz^{k+2}} = 0 \tag{7}$$

The z derivatives cannot be identically zero because of axial diffusion. By collecting the coefficients of $d^k F_m/dz^k$ of equal order in the above equation and equating the results to zero, the following equations are obtained for the radial coefficient functions:

$$\frac{1}{r}\frac{d}{dr}\left(r\frac{df_1}{dr}\right) = 0, \tag{8a}$$

$$\frac{1}{r}\frac{d}{dr}\left(r\frac{df_2}{dr}\right) + 1 = 0 \tag{8b}$$

and

$$\frac{1}{r}\frac{d}{dr}\left(r\frac{df_k}{dr}\right) + f_{k-2} = 0, \qquad k = 3, 4, \ldots \tag{8c}$$

Integrating equation (5) over the vapor–gas flow area and making use of the definition of $F_m(z)$ given by equation (6), we obtain

$$\sum_{k=1}^{\infty} \frac{d^k F_m}{dz^k} \int_0^1 r f_k(r) dr = 0 \tag{9}$$

The z derivatives, as before, are not identically zero due to the existence of axial diffusion. It therefore follows that the radial coefficient functions must satisfy the condition

$$\int_0^1 r f_k(r) dr = 0, \qquad k = 1, 2, \ldots \tag{10}$$

Axial symmetry also requires that

$$df_k/dr = 0 \text{ at } r = 0 \tag{11}$$

The solutions of equations (8a–c) subject to the conditions given by equations (10) and (11) are

$$f_{2k+1}(r) = 0, \qquad k = 0, 1, \ldots \tag{12}$$

and

$$f_{2k}(r) = \sum_{j=0}^{k} a_j^{(2k)} r^{2j}, \qquad k = 1, 2, \ldots \tag{13}$$

where the coefficients $a_j^{(2k)}$ are given by the recurrence relations

$$a_0^{(2k)} = \sum_{j=1}^{k} \frac{a_{j-1}^{(2k-2)}}{4j^2(j+1)}, \tag{14a}$$

and

$$a_j^{(2k)} = -\frac{a_{j-1}^{(2k-2)}}{4j^2}, \qquad 1 \le j \le k \tag{14b}$$

with $a_0^{(0)} = 1$.

Since the odd order radial coefficient functions all vanish identically, equation (5) can therefore be written as

$$F(z, r) = F_m(z) + \sum_{k=1}^{\infty} f_{2k}(r) \frac{d^{2k} F_m}{dz^{2k}} \tag{15}$$

where the first two radial coefficient functions have the explicit expressions

$$f_2 = -\frac{1}{4}\left(r^2 - \frac{1}{2}\right), \quad f_4 = \frac{1}{32}\left(\frac{1}{2}r^4 - r^2 + \frac{1}{3}\right) \tag{16}$$

and functions of higher orders also can be readily determined by using the above recurrence relations. It can easily be deduced from these recurrence relations that

$$\frac{\partial f_{2k}}{\partial r} = -\frac{1}{2}\delta_{k1} \text{ at } r = 1 \tag{17}$$

where δ_{k1} is the Kronecker delta. Thus

$$\frac{\partial F}{\partial r} = -\frac{1}{2}\frac{\partial^2 F_m}{\partial z^2} \text{ at } r = 1 \tag{18}$$

which can also be obtained by integrating equation (2) over the vapor–gas flow area.

The significance of the present solution lies in that it places the currently existing models of analysis on a mathematically consistent basis. The flat-front model, as noted before, represents a singular case. The one-dimensional diffusion model of Edwards and Marcus (1972) assumes $F = F_m(z)$, which is given by equation (15) by ignoring all the radial terms. Peterson and Tien (1989) in their two-dimensional analysis, through physical arguments, arrived at the particular form

$$F(z, r) = F_m(z) - \frac{1}{4}\left(r^2 - \frac{1}{2}\right)\frac{d^2F_m}{dz^2} \tag{19}$$

($A = F_m(z)$, $B = -\frac{1}{4}\frac{d^2F_m}{dz^2}$ in the authors' notation besides the omission of a constant of proportionality), which is seen to represent the lowest order approximation given by equation (15) for including radial diffusion. Arbitrary truncation of equation (15) at fixed orders cannot *a priori* be justified. It is apparently necessary, at least in principle as can be perceived in the sense of convergence in the mean, that additional higher order terms should be included for a consistent description of the concentration distribution.

3 Remarks on the Axial Distribution Function

To predict the performance characteristics of heat and mass transfer along the heat pipe, it is necessary to determine the axial distribution function $F_m(z)$. Peterson and Tien (1989) analyzed the problem with the use of the approximation given by equation (19). The basic governing equations entail the coupling between $F_m(z)$ and the liquid–vapor interface temperature $\theta(z)$. Specifically, under simplifying assumptions, these are established by (*i*) a local overall energy balance across the wick/shell structure of the condenser section and (*ii*) the specification of the liquid–vapor interface mole fractions based on local saturation equilibrium of the condensing vapor. The correct solutions $F_m(z)$ and $\theta(z)$ of these equations obtained under specified boundary conditions must satisfy equation (4) for the conservation of the noncondensible gas in the pipe. The energy equation, because of equation (18) and axial wall conduction, is second order in both F_m and θ (equation (25) of Peterson and Tien). With additional radial terms included in $F(z, r)$, however, the equation specifying interface equilibrium takes on the form

$$F_m + \sum_{k=1}^{N} f_{2k}(1)\frac{d^{2k}F_m}{dz^{2k}} = \ln x_{gi}(\theta) \tag{20}$$

Here $N \geq 1$, $x_{gi}(\theta)$, being exclusively a thermodynamic function of θ based on the assumption of constant mixture molar density in the pipe, is the interface mole fraction of the gas, and

$$f_2(1) = -\frac{1}{8}, \quad f_4(1) = -\frac{1}{192}, \quad f_6(1) = -\frac{1}{3072}, \quad \text{etc.} \tag{21}$$

are the values of $f_{2k}(r)$ at the liquid–vapor interface where $r = 1$. Peterson and Tien revealed the existence of the first term under the summation. The problem for $N \geq 2$ awaits an effective method of solution.

References

Brennan, P. J., and Kroliczek, E. J., 1979, *Heat Pipe Design Handbook*, Vol. I, B & K Engineering, Inc., Towson, MD.

Edwards, D. K., and Marcus, B. D., 1972, "Heat and Mass Transfer in the Vicinity of the Vapor–Gas Front in a Gas-Loaded Heat Pipe," ASME JOURNAL OF HEAT TRANSFER, Vol. 94, pp. 155–162.

Marcus, B. D., 1972, "The Theory and Design of Variable Conductance Heat Pipes," NASA CR-2019.

Peterson, P. F., and Tien, C. L., 1989, "Numerical and Analytical Solutions for Two-Dimensional Gas Distribution in Gas-Loaded Heat Pipes," ASME JOURNAL OF HEAT TRANSFER, Vol. 111, pp. 598–604.

Forced Convection From a Nonisothermal Cylinder in Crossflow

Wongee Chun[1] and R. F. Boehm[2]

Nomenclature

- Nu = Nusselt number
- Nu_{av} = average Nusselt number
- Re = Reynolds number based on cylinder diameter and free-stream velocity
- T_w = wall temperature, K
- $T_{w,\,av}$ = average wall temperature, K
- T_∞ = bulk fluid temperature, K
- UWT = uniform wall temperature boundary condition
- UHF = uniform heat flux boundary condition
- θ = angle measured from the front stagnation point of a cylinder, deg
- Θ_w = dimensionless wall temperature = $[T_w(\theta) - T_\infty]/[T_{w,\,av} - T_\infty]$

Introduction

When nonuniform thermal boundary conditions are imposed on the surface of a circular cylinder in crossflow, the heat transfer characteristics can be quite different compared to what is found for isothermal or constant heat flux boundary conditions. In the present analysis, two kinds of nonuniform boundary condition along the circumference of the cylinder are considered in a uniform stream of air: step changes and linear profiles. To cite only one motiviating application, step changes in temperature can arise on the surface of an external, cylindrical, solar central receiver. As the working fluid (water) flows through the vertical tubes that ring the circumference of Solar One (a solar central receiver in Barstow, CA), the solar flux on the receiver heats the water from a liquid to a superheated state. In this process, portions of the receiver panels, and thus portions of the circumference of the cylinder, function as a preheater, boiler, or superheater. Hence the surface temperature can vary significantly around the cylinder. Common engineering practice has been to use an average wall temperature with an isothermal cylinder heat transfer coefficient when estimating the convective loss in these kinds of situation.

To simulate the convective phenomena numerically can be quite difficult, particularly at Reynolds numbers over a few hundred, due to the complex transient flow behind the cylinder. Our desire is to obtain solutions numerically over a wide range of Reynolds numbers for the nonisothermal conditions with rather simplified boundary conditions and to examine how closely they approximate the long-term averaged heat transfer behavior in the real situation. This was done in

[1]Graduate Research Assistant, Department of Mechanical Engineering, University of Utah, Salt Lake City, UT 84112; current address: Energy Laboratory, Korea Institute of Energy and Resources, Chungnam, Korea.

[2]Professor, Department of Mechanical Engineering, University of Utah, Salt Lake City, UT 84112; Fellow ASME.

Contributed by the Heat Transfer Division for publication in the JOURNAL OF HEAT TRANSFER. Manuscript received by the Heat Transfer Division July 30, 1987; revision received August 10, 1989. Keywords: Forced Convection, Numerical Methods.

which can also be obtained by integrating equation (2) over the vapor–gas flow area.

The significance of the present solution lies in that it places the currently existing models of analysis on a mathematically consistent basis. The flat-front model, as noted before, represents a singular case. The one-dimensional diffusion model of Edwards and Marcus (1972) assumes $F = F_m(z)$, which is given by equation (15) by ignoring all the radial terms. Peterson and Tien (1989) in their two-dimensional analysis, through physical arguments, arrived at the particular form

$$F(z, r) = F_m(z) - \frac{1}{4}\left(r^2 - \frac{1}{2}\right)\frac{d^2F_m}{dz^2} \tag{19}$$

($A = F_m(z)$, $B = -\frac{1}{4}\frac{d^2F_m}{dz^2}$ in the authors' notation besides the omission of a constant of proportionality), which is seen to represent the lowest order approximation given by equation (15) for including radial diffusion. Arbitrary truncation of equation (15) at fixed orders cannot *a priori* be justified. It is apparently necessary, at least in principle as can be perceived in the sense of convergence in the mean, that additional higher order terms should be included for a consistent description of the concentration distribution.

3 Remarks on the Axial Distribution Function

To predict the performance characteristics of heat and mass transfer along the heat pipe, it is necessary to determine the axial distribution function $F_m(z)$. Peterson and Tien (1989) analyzed the problem with the use of the approximation given by equation (19). The basic governing equations entail the coupling between $F_m(z)$ and the liquid–vapor interface temperature $\theta(z)$. Specifically, under simplifying assumptions, these are established by (*i*) a local overall energy balance across the wick/shell structure of the condenser section and (*ii*) the specification of the liquid–vapor interface mole fractions based on local saturation equilibrium of the condensing vapor. The correct solutions $F_m(z)$ and $\theta(z)$ of these equations obtained under specified boundary conditions must satisfy equation (4) for the conservation of the noncondensible gas in the pipe. The energy equation, because of equation (18) and axial wall conduction, is second order in both F_m and θ (equation (25) of Peterson and Tien). With additional radial terms included in $F(z, r)$, however, the equation specifying interface equilibrium takes on the form

$$F_m + \sum_{k=1}^{N} f_{2k}(1)\frac{d^{2k}F_m}{dz^{2k}} = \ln x_{gi}(\theta) \tag{20}$$

Here $N \geq 1$, $x_{gi}(\theta)$, being exclusively a thermodynamic function of θ based on the assumption of constant mixture molar density in the pipe, is the interface mole fraction of the gas, and

$$f_2(1) = -\frac{1}{8}, \quad f_4(1) = -\frac{1}{192}, \quad f_6(1) = -\frac{1}{3072}, \quad \text{etc.} \tag{21}$$

are the values of $f_{2k}(r)$ at the liquid–vapor interface where $r = 1$. Peterson and Tien revealed the existence of the first term under the summation. The problem for $N \geq 2$ awaits an effective method of solution.

References

Brennan, P. J., and Kroliczek, E. J., 1979, *Heat Pipe Design Handbook*, Vol. I, B & K Engineering, Inc., Towson, MD.

Edwards, D. K., and Marcus, B. D., 1972, "Heat and Mass Transfer in the Vicinity of the Vapor–Gas Front in a Gas-Loaded Heat Pipe," ASME JOURNAL OF HEAT TRANSFER, Vol. 94, pp. 155–162.

Marcus, B. D., 1972, "The Theory and Design of Variable Conductance Heat Pipes," NASA CR-2019.

Peterson, P. F., and Tien, C. L., 1989, "Numerical and Analytical Solutions for Two-Dimensional Gas Distribution in Gas-Loaded Heat Pipes," ASME JOURNAL OF HEAT TRANSFER, Vol. 111, pp. 598–604.

Forced Convection From a Nonisothermal Cylinder in Crossflow

Wongee Chun[1] and R. F. Boehm[2]

Nomenclature

- Nu = Nusselt number
- Nu_{av} = average Nusselt number
- Re = Reynolds number based on cylinder diameter and free-stream velocity
- T_w = wall temperature, K
- $T_{w,\,av}$ = average wall temperature, K
- T_∞ = bulk fluid temperature, K
- UWT = uniform wall temperature boundary condition
- UHF = uniform heat flux boundary condition
- θ = angle measured from the front stagnation point of a cylinder, deg
- Θ_w = dimensionless wall temperature = $[T_w(\theta) - T_\infty]/[T_{w,\,av} - T_\infty]$

Introduction

When nonuniform thermal boundary conditions are imposed on the surface of a circular cylinder in crossflow, the heat transfer characteristics can be quite different compared to what is found for isothermal or constant heat flux boundary conditions. In the present analysis, two kinds of nonuniform boundary condition along the circumference of the cylinder are considered in a uniform stream of air: step changes and linear profiles. To cite only one motiviating application, step changes in temperature can arise on the surface of an external, cylindrical, solar central receiver. As the working fluid (water) flows through the vertical tubes that ring the circumference of Solar One (a solar central receiver in Barstow, CA), the solar flux on the receiver heats the water from a liquid to a superheated state. In this process, portions of the receiver panels, and thus portions of the circumference of the cylinder, function as a preheater, boiler, or superheater. Hence the surface temperature can vary significantly around the cylinder. Common engineering practice has been to use an average wall temperature with an isothermal cylinder heat transfer coefficient when estimating the convective loss in these kinds of situation.

To simulate the convective phenomena numerically can be quite difficult, particularly at Reynolds numbers over a few hundred, due to the complex transient flow behind the cylinder. Our desire is to obtain solutions numerically over a wide range of Reynolds numbers for the nonisothermal conditions with rather simplified boundary conditions and to examine how closely they approximate the long-term averaged heat transfer behavior in the real situation. This was done in

[1]Graduate Research Assistant, Department of Mechanical Engineering, University of Utah, Salt Lake City, UT 84112; current address: Energy Laboratory, Korea Institute of Energy and Resources, Chungnam, Korea.

[2]Professor, Department of Mechanical Engineering, University of Utah, Salt Lake City, UT 84112; Fellow ASME.

Contributed by the Heat Transfer Division for publication in the JOURNAL OF HEAT TRANSFER. Manuscript received by the Heat Transfer Division July 30, 1987; revision received August 10, 1989. Keywords: Forced Convection, Numerical Methods.

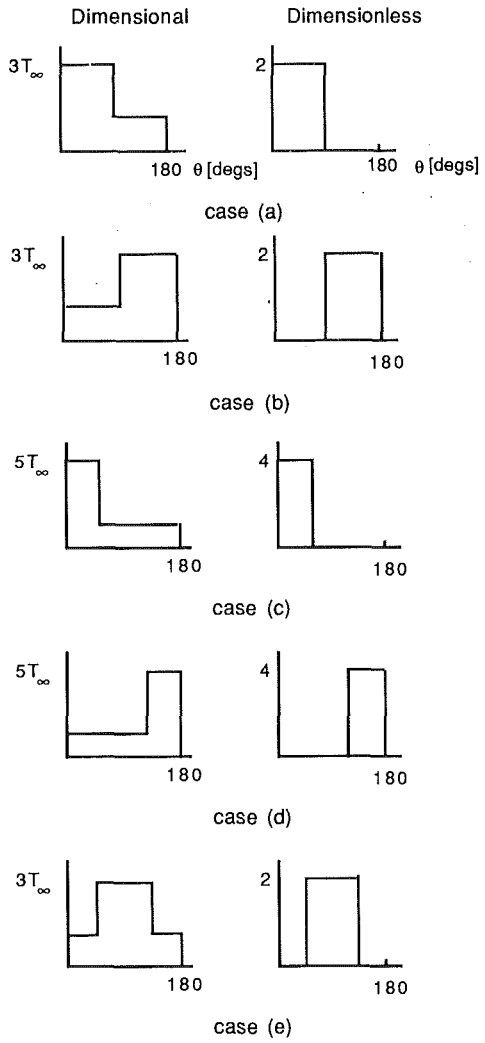

Fig. 1 Step changes in wall temperature assumed in this analysis; note that all cases have the same average temperature

an earlier paper (Chun and Boehm, 1989) for both the uniform wall temperature (UWT) and the uniform heat flux (UHF) conditions. Excellent agreement was found between calculations and experimental values for wall shear and heat transfer, the latter being for both local and average values. Included were comparisons to the work or summaries of Eckert and Soehngen (1952), Krall and Eckert (1973), Sarma and Sukhatme (1977), and Zukauskas and Ziugzda (1985). For detailed comparisons, see our earlier paper (Chun and Boehm, 1989). In this paper we use this approach for predicting nonisothermal convection from cylinders.

Method of Analysis

The analysis is carried out as described in the earlier paper noted above. Surface temperature variations as a function of the angle from the front stagnation point were assumed as shown in Fig. 1. In addition, two cases were considered where a linear variation in surface temperature was assumed. One started at zero at the front stagnation point and increased, while a second started high and decreased to zero at the rear stagnation point. Note that *all* of these distributions are carefully chosen to yield the same *average* wall temperature, *except* for the UHF condition discussed in the Results section. Local Nusselt numbers were determined from numerically computed temperature gradients at the wall for the range of Re between 200 and 3480 for each wall temperature distribution. This included the UWT and UHF cases described in the earlier paper. Local values of Nusselt number were then averaged according to the following:

$$\mathrm{Nu}_{av} = \left[\int_0^{180} \mathrm{Nu}(\theta)d\theta\right]/180$$

Results and Discussion

Results for a number of nonisothermal cases are given in Figs. 2 and 3. As anticipated, cases that have higher temperatures over the front portion of the cylinder demonstrate higher average heat transfer.

In Fig. 2, each plot shows the angular distribution of the local Nusselt number for the corresponding boundary conditions in Fig. 1 at Re = 200 and 1000. Although such conditions could be difficult to realize in practice, some detailed discussions are given here regarding discontinuities in heat transfer, as they display distinct characteristics with the location of step changes in wall temperature.

Figure 2(*a*) shows, for Re = 200, a small peak at $\theta = 90$ and makes a sharp decrease to Nu = −52. The sudden small increase in heat transfer might be the effect of upstream diffusion, which subcools the oncoming fluid. This enhances the heat transfer. The negative Nusselt number observed here indicates a reversal in heat transfer direction. That is, heat flows from the fluid to surface. As the fluid flow proceeds farther downstream toward the rear stagnation point, the Nusselt number asymptotically approaches zero.

Figure 2(*b*) displays an opposite picture to the case discussed above. For Re = 200, a small decrease and then a large increase in heat transfer is shown. The local Nusselt number is practically zero until it reaches the neighborhood of the discontinuity. Compared to Fig. 2(*a*), the portion that is heated at a constant temperature of $\Theta_w = 2$ gives lower heat transfer for the most part except near the peak (from 90 to 100 deg). This would definitely result in a lower average Nusselt number.

Figures 2(*c*) and 2(*d*) exhibit even larger increases and decreases at the point of discontinuity. This is due to a larger temperature change there. In Fig. 1, cases (*c*) and (*d*) have a step change in temperature that is twice as large as cases (*a*) and (*b*). Plot (*e*) corresponds to case (*e*) in Fig. 1. It shows all the characteristics at the point of discontinuity, which are observed separately in each of the four cases discussed above.

The results for Re = 1000 in each case show the augmentation in heat transfer. This is due to the convection dominance in heat transfer phenomena at higher Reynolds number. Diffusion becomes less important as expected. In Figs. 2(*a*, *b*, *c*, *e*), there is no increase or decrease due to upstream diffusion. These should have been washed away by the convective fluxes.

Different nonuniform boundary conditions have produced different results, even though they all have the same mean wall temperature. Some of the cases studied here have shown a significant change in the overall heat transfer in comparison to UWT or UHF boundary conditions. They also have revealed some dependency on the Reynolds number, which measures the relative importance of convection and diffusion fluxes in the heat transfer processes for a fluid stream.

Figure 3(*a*) shows the calculated average Nusselt numbers for both the UWT and UHF cases, as found in our earlier study. (As noted before, the UHF case does not have the same average wall temperatures as the other cases). The experimental UHF results of Krall and Eckert (1973) and the correlation of extensive data for the UWT case given by Morgan (1975) are compared to our results. Extremely good agreement is shown. Figure 3(*a*) also compares UWT and UHF boundary conditions with the linear profiles in wall temperature. Differences between the curves grow as the Reynolds number is increased. The linear profile, which locates the maximum temperature in the rear stagnation point, gives the least heat transfer throughout. This is to be expected since the wake itself imposes a resistance to transfer phenomena. The UWT

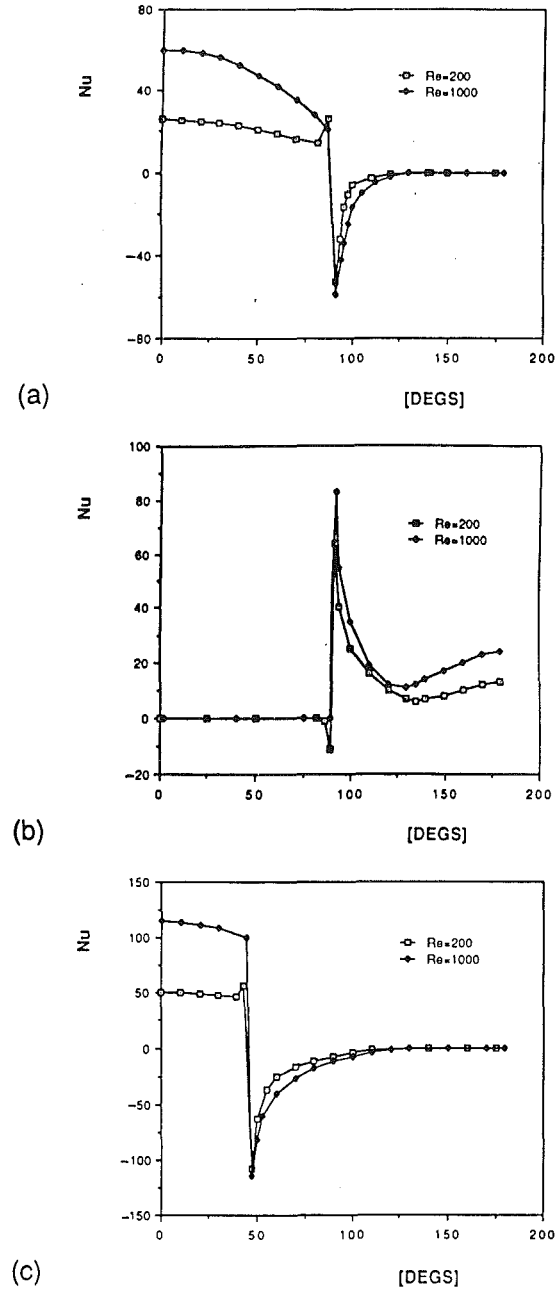

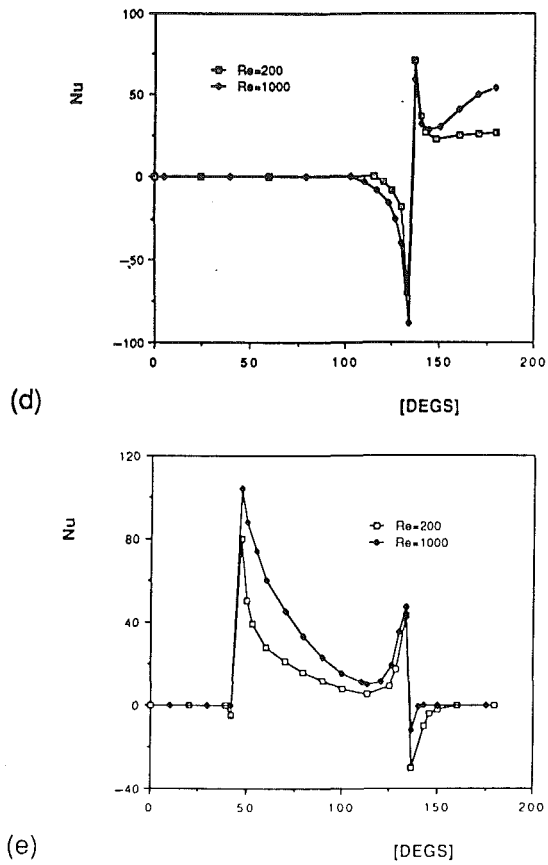

Fig. 2 Effects of the step change in wall temperature on local heat transfer in air; these cases compare to those shown in Fig. 1

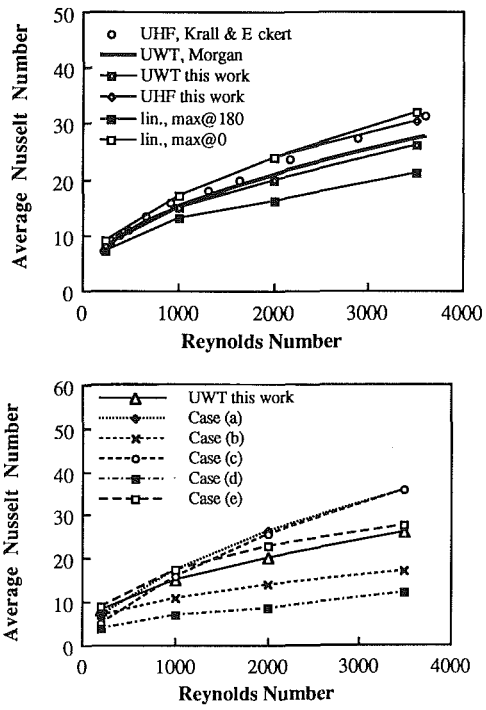

Fig. 3 Average heat transfer for (a) UWT and UHF data and calculations compared with the linear variation calculations and (b) UWT calculations compared to step cases shown in Fig. 1; these results are for air

case lies between the upper and lower limits of heat transfer. A linear profile, which locates the maximum at the front stagnation point, shows the highest heat transfer of these cases in the range of Reynolds number covered here. However, no differences are detected between this linear profile and the UHF boundary condition up to Re = 2000. Even at Re = 3480, the differences are minute.

Step changes in wall temperature show profound effects on the average Nusselt number for the cases examined here; see Fig. 3(*b*). The UWT boundary condition is compared in this figure with the cases of step change in wall temperature. Again differences grow percentagewise and in absolute magnitude as the Reynolds number increase. For example, the case (*b*) in Fig. 1 shows 12.5 percent difference with the UWT case at Re = 200. This becomes 34.6 percent at Re = 3480. Beyond Re = 1000, maximum heat transfer is attained when the front half is heated to maintain the dimensionless surface temperature at 2(case (*a*) in Fig. 1). It also shows a rapid improvement in heat transfer for case (*c*) in Fig. 1. This represents the case where the first quadrant is heated. At Re = 3480, the value converges with that of the maximum case. Unless the rear half or quadrant is heated at a constant temperature, heat transfer is improved over the UWT case.

Although our analysis has ignored the unsteady nature of the flow on the rear portion of the cylinder, this does not render the solution insensitive to the boundary conditions in that region. This was shown in the earlier paper (Chun and Boehm, 1989). It can be seen by comparing the average heat transfer variation for cases where temperature changes occur on the downstream portion of the cylinder; see cases (*b*) and (*d*) in Figs. 1 and 3(*b*).

Conclusions

A numerical study is presented of forced convection heat transfer over a very long circular cylinder in a uniform stream of air. Results are found using the stream function-vorticity approach. A series of situations was investigated where the surface temperature varied with angle around the cylinder. Included in this were linearly varying temperatures and other situations where the surface temperature varied in a step-change manner. In all cases the variations were set so that the mean surface temperature remained the same. This allowed easy comparisons between nonisothermal and isothermal cases for the same Reynolds number.

Some of the nonuniform surface temperature cases showed considerable differences in total heat transfer between one another. Differences between the various cases did not remain in the same relationships as the Reynolds number changed.

The practice used by some analysts when calculating nonisothermal heat transfer of invoking an average surface temperature with an isothermal correlation could be considerably in error. From the cases considered here the magnitude of this error could be on the order of 50 percent.

Acknowledgments

This work was sponsored in part by Sandia National Laboratories, Livermore, CA.

References

Chun, W., and Boehm, R. F., 1989, "Calculation of Forced Flow and Heat Transfer Around a Cylinder in Crossflow," *Num. Heat Transfer, Part A, Applications*, Vol. 15, pp. 101–122.

Eckert, E. R. G., and Soehngen, E., 1952, "Distribution of Heat Transfer Coefficients Around Circular Cylinders in Crossflow at Reynolds Numbers From 20 to 500," *Trans. ASME*, Vol. 74, pp. 343–347.

Krall, K. M., and Eckert, E. R. G., 1973, "Local Heat Transfer Around a Cylinder at Low Reynolds Number," ASME JOURNAL OF HEAT TRANSFER, Vol. 95, pp. 273–275.

Morgan, V. T., 1975, "The Overall Convective Heat Transfer From Smooth Circular Cylinders," *Advances in Heat Transfer*, Vol. 11, p. 234.

Sarma, T. S., and Sukhatme, S. P., 1977, "Local Heat Transfer From a Horizontal Cylinder to Air in Crossflow: Influence of Free Convection and Free Stream Turbulence," *Int. J. Heat Mass Transfer*, Vol. 20, pp. 51–56.

Zukauskas, A., and Ziugzda, J., 1985, *Heat Transfer of a Cylinder in Crossflow*, Hemisphere Publishing Corp., Washington, DC, pp. 1–165.

Flow Visualization Studies of Natural Convective Flow in a Horizontal Cylindrical Annulus

R. Kumar[1] and M. Keyhani[2]

Nomenclature

a = wave number
d_i = inner diameter
L = gap width = $r_o - r_i$
Nu_L = Nusselt number = $\bar{h}L/k$
Nu = Nusselt number = $\bar{h}d_i/k$
Pr = Prandtl number = ν/α
r = radial coordinate
Ra_L^* = Rayleigh number = $\beta g\left(\frac{qL}{k}\right)L^3/\alpha\nu$
Ra = Rayleigh number = $\beta g(\Delta T)L^3/\alpha\nu$
Ra_L = $\mathrm{Ra}_L^*/\mathrm{Nu}$
z = axial coordinate
κ = radius ratio = r_o/r_i
λ' = dimensional wavelength, cm
λ = nondimensional wavelength

Subscripts

C = conduction
cr = critical
i = inner wall
L = based on gap width

Introduction

Natural convection in horizontal annuli has been extensively studied by several investigators, mostly for isothermal cylinders. Only a few papers deal with a constant heat flux boundary condition on the inner wall. Natural convection of gases and liquids within horizontal cylinders has applications in thermal storage systems and transmission cables.

Experimental results of natural convection within horizontal isothermal cylinders were reported by Liu et al. (1961), Grigull and Hauf (1966), Bishop and Carley (1966), Lis (1966), and Bishop et al. (1968). The work of Bishop and Carley (1966) was extended by Powe et al. (1969) and a chart was presented for the prediction of the nature of the flow for various diameter ratios. Kuehn and Goldstein (1976a, 1976b, 1980) determined flow structure and heat transfer results experimentally and numerically up to a Rayleigh number of 10^5 and also presented a correlation equation. The effects of variable property and diameter ratio on the heat transfer results were determined by Mahony et al. (1986).

Van de Sande and Hamer (1979) determined experimentally the heat transfer between horizontal cylinders with the inner wall maintained at constant heat flux. Their results focused mainly on eccentric cylinders for Rayleigh numbers greater than 2×10^6. Kumar (1988) provided detailed numerical results for various diameter ratios for natural convection in horizontal annuli with isoflux inner wall. Based on the data of Petavel (1901) for the isothermal case, and those of Dyer (1965) for the constant heat flux boundary condition, Morgan (1975) presented heat transfer correlation equations for a horizontal cylinder in an infinite medium as

$$\mathrm{Nu} = 1.05\ \mathrm{Ra}^{0.14} \qquad 0.1 \le \mathrm{Ra} \le 300$$
$$= 0.562\ \mathrm{Ra}^{0.25} \qquad 300 < \mathrm{Ra} < 2 \times 10^5 \text{ (isothermal)} \quad (1)$$
$$\mathrm{Nu} = 0.55\ \mathrm{Ra}^{0.233} \qquad 10^5 < \mathrm{Ra} < 4 \times 10^6 \text{ (isoflux)} \quad (2)$$

The present study reports numerical and experimental heat transfer results and flow structure in horizontal annuli with the inner wall maintained at constant heat flux and the outer wall at constant temperature. Flow visualizations investigate the metastability and the three-dimensionality of the flow in the annulus.

Experimental Apparatus and Procedure

The experimental annulus consisted of an acrylic outer cylinder with an inside diameter of 13.97 cm and a thickness of 3.18 mm; a Watlow cartridge heater rod with a diameter of 1.27 cm as the inner cylinder; and two square (30.48 cm ×

[1]Clemson University, Clemson, SC 29634-0921.
[2]University of Tennessee, Knoxville, TN 37996-2110.

Contributed by the Heat Transfer Division for publication in the JOURNAL OF HEAT TRANSFER. Manuscript received by the Heat Transfer Division May 18, 1989; revision received November 8, 1989. Keywords: Flow Visualization, Natural Convection, Numerical Methods.

Although our analysis has ignored the unsteady nature of the flow on the rear portion of the cylinder, this does not render the solution insensitive to the boundary conditions in that region. This was shown in the earlier paper (Chun and Boehm, 1989). It can be seen by comparing the average heat transfer variation for cases where temperature changes occur on the downstream portion of the cylinder; see cases (*b*) and (*d*) in Figs. 1 and 3(*b*).

Conclusions

A numerical study is presented of forced convection heat transfer over a very long circular cylinder in a uniform stream of air. Results are found using the stream function-vorticity approach. A series of situations was investigated where the surface temperature varied with angle around the cylinder. Included in this were linearly varying temperatures and other situations where the surface temperature varied in a step-change manner. In all cases the variations were set so that the mean surface temperature remained the same. This allowed easy comparisons between nonisothermal and isothermal cases for the same Reynolds number.

Some of the nonuniform surface temperature cases showed considerable differences in total heat transfer between one another. Differences between the various cases did not remain in the same relationships as the Reynolds number changed.

The practice used by some analysts when calculating nonisothermal heat transfer of invoking an average surface temperature with an isothermal correlation could be considerably in error. From the cases considered here the magnitude of this error could be on the order of 50 percent.

Acknowledgments

This work was sponsored in part by Sandia National Laboratories, Livermore, CA.

References

Chun, W., and Boehm, R. F., 1989, "Calculation of Forced Flow and Heat Transfer Around a Cylinder in Crossflow," *Num. Heat Transfer, Part A, Applications*, Vol. 15, pp. 101–122.

Eckert, E. R. G., and Soehngen, E., 1952, "Distribution of Heat Transfer Coefficients Around Circular Cylinders in Crossflow at Reynolds Numbers From 20 to 500," *Trans. ASME*, Vol. 74, pp. 343–347.

Krall, K. M., and Eckert, E. R. G., 1973, "Local Heat Transfer Around a Cylinder at Low Reynolds Number," ASME JOURNAL OF HEAT TRANSFER, Vol. 95, pp. 273–275.

Morgan, V. T., 1975, "The Overall Convective Heat Transfer From Smooth Circular Cylinders," *Advances in Heat Transfer*, Vol. 11, p. 234.

Sarma, T. S., and Sukhatme, S. P., 1977, "Local Heat Transfer From a Horizontal Cylinder to Air in Crossflow: Influence of Free Convection and Free Stream Turbulence," *Int. J. Heat Mass Transfer*, Vol. 20, pp. 51–56.

Zukauskas, A., and Ziugzda, J., 1985, *Heat Transfer of a Cylinder in Crossflow*, Hemisphere Publishing Corp., Washington, DC, pp. 1–165.

Flow Visualization Studies of Natural Convective Flow in a Horizontal Cylindrical Annulus

R. Kumar[1] and M. Keyhani[2]

Nomenclature

a = wave number
d_i = inner diameter
L = gap width = $r_o - r_i$
Nu_L = Nusselt number = $\bar{h}L/k$
Nu = Nusselt number = $\bar{h}d_i/k$
Pr = Prandtl number = ν/α
r = radial coordinate
Ra_L^* = Rayleigh number = $\beta g\left(\frac{qL}{k}\right)L^3/\alpha\nu$
Ra = Rayleigh number = $\beta g(\Delta T)L^3/\alpha\nu$
Ra_L = $\mathrm{Ra}_L^*/\mathrm{Nu}$
z = axial coordinate
κ = radius ratio = r_o/r_i
λ' = dimensional wavelength, cm
λ = nondimensional wavelength

Subscripts

C = conduction
cr = critical
i = inner wall
L = based on gap width

Introduction

Natural convection in horizontal annuli has been extensively studied by several investigators, mostly for isothermal cylinders. Only a few papers deal with a constant heat flux boundary condition on the inner wall. Natural convection of gases and liquids within horizontal cylinders has applications in thermal storage systems and transmission cables.

Experimental results of natural convection within horizontal isothermal cylinders were reported by Liu et al. (1961), Grigull and Hauf (1966), Bishop and Carley (1966), Lis (1966), and Bishop et al. (1968). The work of Bishop and Carley (1966) was extended by Powe et al. (1969) and a chart was presented for the prediction of the nature of the flow for various diameter ratios. Kuehn and Goldstein (1976a, 1976b, 1980) determined flow structure and heat transfer results experimentally and numerically up to a Rayleigh number of 10^5 and also presented a correlation equation. The effects of variable property and diameter ratio on the heat transfer results were determined by Mahony et al. (1986).

Van de Sande and Hamer (1979) determined experimentally the heat transfer between horizontal cylinders with the inner wall maintained at constant heat flux. Their results focused mainly on eccentric cylinders for Rayleigh numbers greater than 2×10^6. Kumar (1988) provided detailed numerical results for various diameter ratios for natural convection in horizontal annuli with isoflux inner wall. Based on the data of Petavel (1901) for the isothermal case, and those of Dyer (1965) for the constant heat flux boundary condition, Morgan (1975) presented heat transfer correlation equations for a horizontal cylinder in an infinite medium as

$$\mathrm{Nu} = 1.05\ \mathrm{Ra}^{0.14} \qquad 0.1 \le \mathrm{Ra} \le 300$$
$$= 0.562\ \mathrm{Ra}^{0.25} \qquad 300 < \mathrm{Ra} < 2 \times 10^5 \text{ (isothermal)} \quad (1)$$
$$\mathrm{Nu} = 0.55\ \mathrm{Ra}^{0.233} \qquad 10^5 < \mathrm{Ra} < 4 \times 10^6 \text{ (isoflux)} \quad (2)$$

The present study reports numerical and experimental heat transfer results and flow structure in horizontal annuli with the inner wall maintained at constant heat flux and the outer wall at constant temperature. Flow visualizations investigate the metastability and the three-dimensionality of the flow in the annulus.

Experimental Apparatus and Procedure

The experimental annulus consisted of an acrylic outer cylinder with an inside diameter of 13.97 cm and a thickness of 3.18 mm; a Watlow cartridge heater rod with a diameter of 1.27 cm as the inner cylinder; and two square (30.48 cm ×

[1]Clemson University, Clemson, SC 29634-0921.
[2]University of Tennessee, Knoxville, TN 37996-2110.

Contributed by the Heat Transfer Division for publication in the JOURNAL OF HEAT TRANSFER. Manuscript received by the Heat Transfer Division May 18, 1989; revision received November 8, 1989. Keywords: Flow Visualization, Natural Convection, Numerical Methods.

30.48 cm) end plates (one made of aluminum and the other plexiglass) with a thickness of 1.91 cm. The horizontal annulus had a radius ratio of 11 and an inside length-to-annular gap width ratio of 18.85.

The Watlow cartridge heater rod (the inner cylinder) consists of a nickel–chromium wire wound around a magnesium oxide core, which is covered by a 0.05 cm sheath of incoloy to assure constant heat flux at the surface. To ensure that the temperature distribution on the outer cylinder is as uniform as possible, a fan positioned 50 cm above the annulus with a high volumetric flow rate was used. The difference between the maximum temperature on the outer cylinder and its mean value was 10 percent of the mean temperature difference across the annulus.

A total of eighteen 30 gage copper-constantan thermocouples were used. Two sets of three equally spaced thermocouples along the length of the annulus were glued to the surface of the heater rod at angular positions of 0 and 180 deg, i.e., at the top and bottom of the annulus, respectively. Six thermocouples, whose positions corresponded to the ones on the inner cylinder, were attached to the outer cylinder 1.5 mm from its inner surface. At the midlength of the annulus, two additional thermocouples were glued to the inner surface of the outer cylinder at 0 and 180 deg, respectively. The temperatures of the inner and outer cylinders were calculated as the average value of the reading of their respective thermocouples. Each end plate was instrumented with two thermocouples 6.4 mm apart in-depth. These measurements were used to estimate the conduction losses.

To examine the flow structure, flow visualization experiments were conducted for several power inputs. Neutrally buoyant aluminum powder (5 to 20 μm in size) in ethylene glycol served as the convection medium to visualize the flow. The aluminum particles were illuminated to obtain still and video photographs.

The thermocouples outputs were measured to 0.1 μV with a sensitivity of 0.0025°C. A conservative estimate of the accuracy of the temperature measurements is ± 0.1°C. The uncertainty associated with the length scale used in the data reduction was ± 0.25 mm. The overall uncertainty in the Nusselt and Rayleigh numbers varies with the power input. Smaller power input resulted in a larger uncertainty due to a relatively lower temperature difference across the annulus. The estimated uncertainties in Nu and Ra were 3.3 to 12.2, and 4.0 to 12.6 percentages, respectively. More details of the experimental procedure are given by Kumar and Keyhani (1988).

Mathematical Formulation and Numerical Procedure

The governing conservation equations for a steady laminar flow using the Boussinesq approximation were recast in terms of vorticity and stream function equations. The boundary conditions on the walls were evaluated using no-slip conditions for velocity, constant heat flux on the inner wall, constant temperature on the outer wall, and no crossflow in vertical lines of symmetry. The vorticity transport equation and the energy equation were numerically solved by the false transient Alternating Direction Implicit (ADI) method, and the stream function equation was solved by the successive overrelaxation (SOR) method. The numerical procedures are standard and more details are given by Mahony et al. (1986) and Kumar (1988).

Results and Discussion

The heat transfer results of natural convection are discussed in this section for a constant heat flux boundary on the inner cylinder of the horizontal annulus. Flow visualization photographs for Ra = 3.6×10^4 and 1.06×10^5 with $\kappa = 11$ are presented in Figs. 1(*a*) and 1(*b*). These photographs indicate asymmetric flow behavior with virtually no detectable

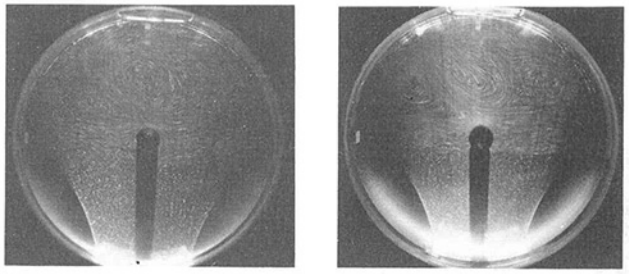

Fig. 1 Flow visualization photographs for $\kappa = 11$, and Ra of (*a*) 3.596×10^4; (*b*) 1.063×10^5

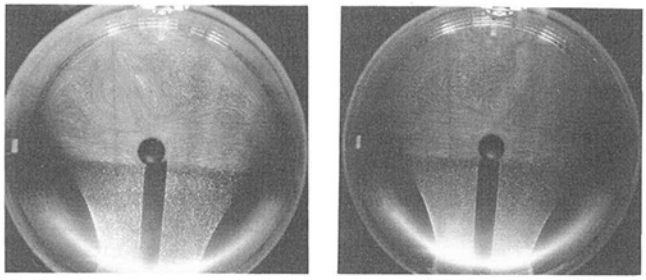

Fig. 2 Flow visualization photographs for $\kappa = 11$ and Ra = 3.029×10^5

flow pattern at the bottom half of the annulus. Two major vortical cells are evident from Fig. 1(*a*). As Ra increases, the right vortex increases in intensity and eventually breaks into two cells, as seen in Fig. 1(*b*) for Ra = 1.06×10^5. As the Rayleigh number increases to Ra = 3.03×10^5, the three-cell structure becomes stronger, and the centers of rotation come closer together and shift toward one side of the top half of the annulus, as shown in Fig. 2(*a*). Such a shift toward any one side does not seem to have a preference in direction. The structure of the flow shown in Fig. 2(*a*) was observed to be consistently the same for a long period of time (several days, as long as the power input and outer cylinder temperature remained the same). However, when the experiment was repeated, from an initial state of a motionless fluid layer and for identical thermal boundary conditions, a mirror image of the flow structure about the vertical plane was observed, as seen in Fig. 2(*b*). The probability of the occurrence of this metastable behavior at other Ra was not investigated. Several photographs were taken once in five minutes over a 2-hour period to check for the steady nature of the flow. These photographs showed identical flow fields.

In order to investigate the three dimensionality of the flow, several flow visualization experiments were conducted with photographs taken in the r–z plane. The cylinder was divided into six equal segments lengthwise and marked for identification in the photographs.

The photographs of two adjacent segments of Ra = 1.06×10^5 are presented in Fig. 3. The arrows indicate the location where one vortex cell ends and another begins in the axial direction. Several other photographs were taken that covered the entire length of the annulus. Careful analysis of these photographs at Ra = 1.06×10^5 revealed a total of eight cells in the axial direction, resulting in a nondimensional wavelength λ of 2.22 and a wave number a of 2.83. As the Ra was increased to 5.72×10^5, the observed number of cells increased to 12, corresponding to $\lambda = 1.548$ and $a = 4.06$ (see Table 1).

Heat Transfer Results

In order to reveal the different aspects of natural convection heat transfer in a horizontal annulus, the results will be pre-

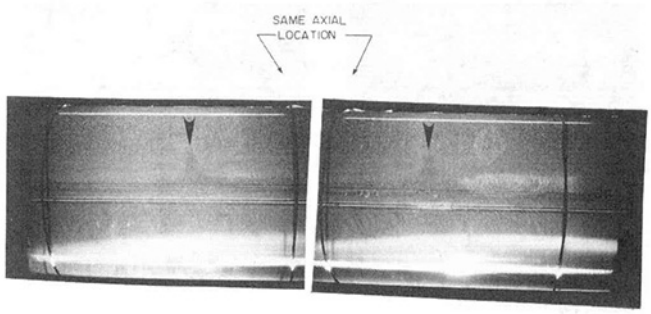

Fig. 3 Flow visualization photographs along the length of the annulus for $\kappa = 11$ and $Ra = 1.06 \times 10^5$

Table 1

Power input, W	Nu	Pr	Ra	λ' cm	λ	a
80	8.07	144	1.06×10^5	14.10	2.220	2.83
350	11.79	75	5.72×10^5	9.83	1.548	4.06

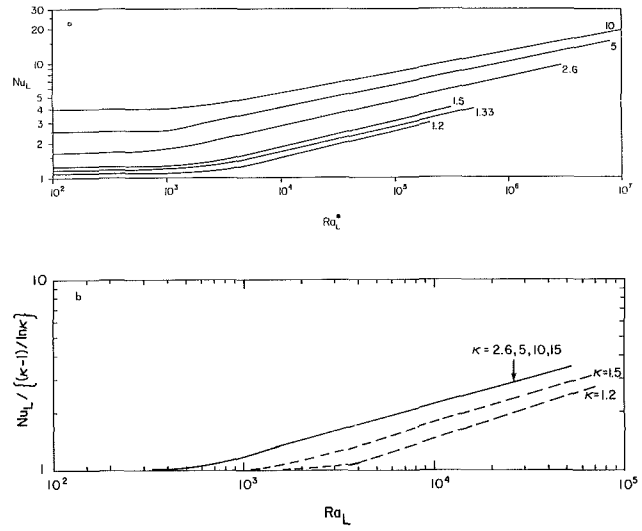

Fig. 4 Numerical heat transfer results: (*a*) Nu_L versus Ra_L^*; (*b*) Nu_L/Nu_C versus Ra_L

sented in terms of Nu_L versus Ra_L, Nu_L/Nu_C versus Ra_L, and finally Nu versus Ra. The numerical results for various radius ratios are given in Figs. 4(*a*) and 4(*b*). Figure 4(*a*) [Nu_L versus Ra_L^*] suggests that convection heat transfer is a function of κ for $2.6 < \kappa < 10$. However, when the same results are normalized with respect to conduction heat transfer (i.e., Nu_L/Nu_C) and presented as a function of Ra_L in Fig. 4(*b*), the contribution to heat transfer due to convection alone is no longer dependent on the radius ratio for $\kappa \geq 2.6$. The limiting line for $\kappa \geq 2.6$ represents an average of numerical heat transfer results for diameter ratios of 2.6, 5, 10, and 15, and Prandtl numbers of 0.7, 5, and 100 within an error of 2 percent. For diameter ratios of less than 2.6, the conduction regime is extended further as κ is decreased.

The critical Ra_L at which the conduction flow regime ceases and the convection motion begins has been calculated based on the criterion $Nu_L/Nu_C = 1.1$ used by Thomas and de Vahl Davis (1970). The critical values of Ra_L for $\kappa = 1.2$, 1.5, 1.8, 2.6, 5, 10, and 15 have been calculated and given in Table 2. The critical Rayleigh number Ra_{cr} for $\kappa \geq 2.6$ is found to be nearly constant at 740 ± 45. On a log–log scale, the data points for $\kappa \leq 1.8$ suggest a linear variation and hence, the critical Ra_L may take the form $Ra_{cr} = 6735\ \kappa^{-2.89}$.

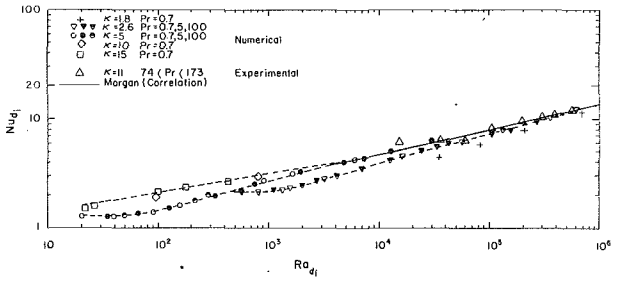

Fig. 5 Comparison of experimental and numerical heat transfer results, Nu versus Ra

Table 2 *Critical Rayleigh number Ra_L for transition*

κ	1.2	1.33	1.5	1.8	2.6	5	10	15
Ra_L	4144	2357	1954	1270	782	760	717	703

Table 3 Comparison of heat transfer results with correlation for a single cylinder

κ	Ra	Nu (annulus)	Nu (Morgan)
15.0	100.25	2.075	2.001
10.0	807.50	2.972	2.995
5.0	5945.00	4.205	4.166
2.6	5.81×10^5	12.040	12.118
1.8	6.88×10^5	11.040	12.604

The numerical results for $\kappa = 1.8$–15 for Pr = 0.7, 5, and 100 along with the experimental data for $\kappa = 11$ and Pr = 74 to 173 are presented in terms of Nu versus Ra in Fig. 5. The correlation proposed in equation (2) by Morgan (1975) for a single horizontal cylinder in an infinite medium is also plotted in Fig. 5 for comparison purposes. The numerical results are presented in symbols for Pr = 0.7, 5, and 100, and dashed lines are drawn through the symbols representing fixed diameter ratios. It is evident that the Prandtl number effect is insignificant. For a given diameter ratio, as Ra is increased the Nusselt number approaches a single-cylinder solution. The Rayleigh number Ra at which the annulus Nu is equivalent to that of a single cylinder increases as κ is reduced. The present values of Nu at corresponding Ra are compared with Morgan's (1975) single-cylinder correlation at various diameter ratios and are given in Table 3. Although our results are compared with the correlation given for isothermal cylinders (equation (1)) for the first two points in Table 3 (isoflux data are not available) for $\kappa \geq 10$, the agreement is excellent and is within 4 percent. The correlation (equation (2)) is extended to lower Ra and compared with the present results for $\kappa = 5$ and, once again, the data are in good agreement. At $Ra = 6.88 \times 10^5$ for $\kappa = 1.8$, an aymptotic value is reached; however, the Nusselt number is within 14 percent of Morgan's (1975) value. The eight experimental data points compare very well with the single-cylinder solution, with six of them being within 3 percent of the correlation. Thus, it is seen that d_i is the appropriate length scale for correct interpretation of heat transfer results for large diameter ratios. The asymmetry could not be predicted by the numerical investigation since the vertical symmetry was forced in the model. Nonetheless, despite significant differences between the predicted and observed flow fields, the average Nusselt numbers are remarkably close. Thus, it is believed that the numerical results are acceptable in predicting average heat transfer results.

Summary and Conclusions

The effects of natural convection due to a constant heat flux boundary condition on the inner wall of a horizontal annulus have been quantified both experimentally and numerically.

Numerical data have been generated for diameter ratios in the range $1.8 \leq \kappa \leq 15$, and Prandtl numbers of 0.7, 5.0, and 100, and the results have been compared with the experimental data for $\kappa = 11$ and $74 < \mathrm{Pr} < 173$. Moreover, flow visualization studies have been performed. The following conclusions may be drawn:

1 The appropriate flow parameter for the analysis of heat transfer due to convection only is the conventional Rayleigh number.

2 The appropriate length scale for the representation of the Rayleigh number in the conduction flow regime is the annular gap width.

3 The numerical and experimental results suggest that at a sufficiently high Ra and/or κ, the convection heat transfer from the inner cylinder is nearly the same as that of a single horizontal cylinder in an infinite medium. Thus, it is suggested that for high Rayleigh number flow and/or large radius ratios, the appropriate length scale is the diameter of the inner cylinder.

4 Flow visualization studies for $\kappa = 11$, $74 < \mathrm{Pr} < 173$, and $1 \times 10^4 < \mathrm{Ra} < 6 \times 10^5$ indicate an asymmetric, metastable, steady flow behavior. The three-dimensionality of the flow was investigated with observed wavelengths and wave numbers reported at two Rayleigh numbers.

5 Prandtl number effects in the horizontal annuli were found to be insignificant for $\mathrm{Pr} > 0.7$.

References

Bishop, E. H., and Carley, C. T., 1966, "Photographic Studies of Natural Convection Between Concentric Cylinders," *Proc. Heat Transfer Fluid Mech. Inst.*, pp. 63–78.

Bishop, E. H., Carley, C. T., and Powe, R. E., 1968, "Natural Convective Oscillatory Flow in Cylindrical Annuli," *Int. J. Heat Mass Transfer*, Vol. 11, pp. 1741–1752.

Dyer, J. R., 1965, "Laminar Natural Convection From a Horizontal Cylinder With a Uniform Convective Heat Flux," *Trans. Inst. Eng.*, Aust. MC1, pp. 125–128.

Grigull, U., and Hauf, W., 1966, "Natural Convection in Horizontal Cylindrical Annuli," *Proc. Third Int. Heat Transfer Conf.*, Paper No. 60, Vol. 2, pp. 182–195.

Kuehn, T. H., and Goldstein, R. J., 1976a, "An Experimental and Theoretical Study of Natural Convection in the Annulus Between Horizontal Concentric Cylinders," *J. Fluid Mech.*, Vol. 74, pp. 695–719.

Kuehn, T. H., and Goldstein, R. J., 1976b, "Correlating Equations for Natural Convection Heat Transfer Between Horizontal Circular Cylinders," *Int. J. Heat Mass Transfer*, Vol. 19, pp. 1127–1134.

Kuehn, T. H., and Goldstein, R. J., 1980, "A Parametric Study of Prandtl Number and Diameter Ratio Effects on Natural Convection Heat Transfer in Horizontal Cylindrical Annuli," ASME JOURNAL OF HEAT TRANSFER, Vol. 102, pp. 768–770.

Kumar, R., 1988, "Study of Natural Convection in Horizontal Annuli," *Int. J. Heat Mass Transfer*, Vol. 31, No. 6, pp. 1137–1148.

Kumar, R., and Keyhani, M., 1988, "Experimental and Numerical Investigation of Natural Convective Flow in a Horizontal Cylindrical Annulus," *Proceedings of the ASME National Heat Transfer Conference*, Houston, July, Vol. 3, pp. 391–401.

Lis, J., 1966, "Experimental Investigation of Natural Convection Heat Transfer in Simple and Obstructed Horizontal Annuli," *Proc. 3rd Int. Heat Transfer Conf.*, Vol. 2, AIChE, New York, Vol. 2, pp. 196–204.

Liu, C. Y., Mueller, W. K., and Landis, F., 1961, "Natural Convection Heat Transfer in Long Horizontal Cylindrical Annuli," *International Developments in Heat Transfer*, Paper No. 117, Part V, pp. 976–984.

Mahony, D. N., Kumar, R., and Bishop, E. H., 1986, "Numerical Investigation of Variable Property Effects on Laminar Natural Convection of Gases Between Two Horizontal Isothermal Concentric Cylinders," ASME JOURNAL OF HEAT TRANSFER, Vol. 108, pp. 783–789.

Morgan, V. T., 1975, "The Overall Convective Heat Transfer From Smooth Circular Cylinders," *Advances in Heat Transfer*, T. F. Irvine and J. P. Hartnett, eds., Vol. 11, Academic Press, New York, pp. 199–265.

Petavel, J. E., 1901, "The Heat Dissipated by a Platinum Surface at High Temperature," *Phil. Trans. Roy. Soc. London*, Vol. 197, pp. 229–254.

Powe, R. E., Carley, C. T., and Bishop, E. H., 1969, "Free Convective Flow Patterns in Cylindrical Annuli," ASME JOURNAL OF HEAT TRANSFER, Vol. 91, No. 3, pp. 310–314.

Thomas, R. W., and de Vahl Davis, G., 1970, "Natural Convection in Annular and Rectangular Cavities: A Numerical Study," *Proc. 4th Int. Heat Transfer Conf.*, Paris, Vol. 4, Paper No. NC 2.4, Elsevier, Amsterdam.

Van de Sande, E., and Hamer, B. J. G., 1979, "Steady and Transient Natural Convection in Enclosures Between Horizontal Circular Cylinders (Constant Heat Flux)," *Int. J. Heat Mass Transfer*, Vol. 22, pp. 361–370.

The Prandtl Number Effect on the Transition in Natural Convection Along a Vertical Surface

A. Bejan[1,2] and J. L. Lage[1]

Nomenclature

- Bo = Boussinesq number $= g\beta H^3 \Delta T/\alpha^2$
- Bo* = modified Boussinesq number $= g\beta H^4 q''/\alpha^2 k$
- D = local transverse length scale of straight flow, m
- g = gravitational acceleration, m/s^2
- Gr = Grashof number $= g\beta H^3 \Delta T/\nu^2$
- Gr* = modified Grashof number $= g\beta H^4 q''/\nu^2 k$
- H = height of vertical wall, m
- k = thermal conductivity, W/m•K
- Nu = average Nusselt number $= q'' H/k\Delta T$
- Pr = Prandtl number $= \nu/\alpha$
- q'' = heat flux, W/m^2
- Ra = Rayleigh number $= g\beta H^3 \Delta T/\alpha\nu$
- v = local longitudinal velocity scale of straight flow, m/s
- ΔT = wall–fluid temperature difference, K
- α = thermal diffusivity, m^2/s
- β = coefficient of volumetric thermal expansion, K^{-1}
- ν = kinematic viscosity, m^2/s
- $( )_i$ = inner
- $( )_o$ = outer

Introduction

During the last two decades we have witnessed intense activity on natural (free) convection, from air convection in rooms to the spreading of pollutants in the environment. This activity has been the subject of many reviews, recent book-size examples of which are Jaluria (1980), Bejan (1984), and Gebhart et al. (1988). One impression that may be left by scanning these reviews is that most of the fundamental questions in natural convection have been answered, especially with regard to *laminar* natural convection.

On this extensive background of published research, it may seem redundant to undertake one more fundamental study into the basics of natural convection. As is often the case, the decision to embark on a new project was triggered by a set of coincidental and mutually reinforcing observations:

(*i*) There is a definite lack of information (theoretical, numerical, experimental) on natural convection in low-Pr fluids (Lykoudis, 1989). This observation was stressed recently also by Wolff et al. (1988).

(*ii*) Georgiadis (1989) drew our attention to the line of work represented by Chao et al. (1982) and Bertin and Ozoe (1986), who showed numerically that the onset of Bénard convection appears to be influenced by the Prandtl number in the $\mathrm{Pr} < 1$ range.

(*iii*) We were struck by Bertin and Ozoe's (1986) discovery that they were unable to obtain numerically a steady flow below a certain Prandtl number ($\mathrm{Pr} = 0.001$), even though the

[1]Department of Mechanical Engineering and Materials Science, Duke University, Durham, NC 27706.

[2]J. A. Jones Professor of Mechanical Engineering; Fellow ASME.

Contributed by the Heat Transfer Division for publication in the JOURNAL OF HEAT TRANSFER. Manuscript received by the Heat Transfer Division September 25, 1989; revision received January 4, 1990. Keywords: Liquid Metals, Natural Convection, Turbulence.

Numerical data have been generated for diameter ratios in the range $1.8 \leq \kappa \leq 15$, and Prandtl numbers of 0.7, 5.0, and 100, and the results have been compared with the experimental data for $\kappa = 11$ and $74 < Pr < 173$. Moreover, flow visualization studies have been performed. The following conclusions may be drawn:

1 The appropriate flow parameter for the analysis of heat transfer due to convection only is the conventional Rayleigh number.

2 The appropriate length scale for the representation of the Rayleigh number in the conduction flow regime is the annular gap width.

3 The numerical and experimental results suggest that at a sufficiently high Ra and/or κ, the convection heat transfer from the inner cylinder is nearly the same as that of a single horizontal cylinder in an infinite medium. Thus, it is suggested that for high Rayleigh number flow and/or large radius ratios, the appropriate length scale is the diameter of the inner cylinder.

4 Flow visualization studies for $\kappa = 11$, $74 < Pr < 173$, and $1 \times 10^4 < Ra < 6 \times 10^5$ indicate an asymmetric, metastable, steady flow behavior. The three-dimensionality of the flow was investigated with observed wavelengths and wave numbers reported at two Rayleigh numbers.

5 Prandtl number effects in the horizontal annuli were found to be insignificant for $Pr > 0.7$.

References

Bishop, E. H., and Carley, C. T., 1966, "Photographic Studies of Natural Convection Between Concentric Cylinders," *Proc. Heat Transfer Fluid Mech. Inst.*, pp. 63–78.

Bishop, E. H., Carley, C. T., and Powe, R. E., 1968, "Natural Convective Oscillatory Flow in Cylindrical Annuli," *Int. J. Heat Mass Transfer*, Vol. 11, pp. 1741–1752.

Dyer, J. R., 1965, "Laminar Natural Convection From a Horizontal Cylinder With a Uniform Convective Heat Flux," *Trans. Inst. Eng.*, Aust. MC1, pp. 125–128.

Grigull, U., and Hauf, W., 1966, "Natural Convection in Horizontal Cylindrical Annuli," *Proc. Third Int. Heat Transfer Conf.*, Paper No. 60, Vol. 2, pp. 182–195.

Kuehn, T. H., and Goldstein, R. J., 1976a, "An Experimental and Theoretical Study of Natural Convection in the Annulus Between Horizontal Concentric Cylinders," *J. Fluid Mech.*, Vol. 74, pp. 695–719.

Kuehn, T. H., and Goldstein, R. J., 1976b, "Correlating Equations for Natural Convection Heat Transfer Between Horizontal Circular Cylinders," *Int. J. Heat Mass Transfer*, Vol. 19, pp. 1127–1134.

Kuehn, T. H., and Goldstein, R. J., 1980, "A Parametric Study of Prandtl Number and Diameter Ratio Effects on Natural Convection Heat Transfer in Horizontal Cylindrical Annuli," ASME JOURNAL OF HEAT TRANSFER, Vol. 102, pp. 768–770.

Kumar, R., 1988, "Study of Natural Convection in Horizontal Annuli," *Int. J. Heat Mass Transfer*, Vol. 31, No. 6, pp. 1137–1148.

Kumar, R., and Keyhani, M., 1988, "Experimental and Numerical Investigation of Natural Convective Flow in a Horizontal Cylindrical Annulus," *Proceedings of the ASME National Heat Transfer Conference*, Houston, July, Vol. 3, pp. 391–401.

Lis, J., 1966, "Experimental Investigation of Natural Convection Heat Transfer in Simple and Obstructed Horizontal Annuli," *Proc. 3rd Int. Heat Transfer Conf.*, Vol. 2, AIChE, New York, Vol. 2, pp. 196–204.

Liu, C. Y., Mueller, W. K., and Landis, F., 1961, "Natural Convection Heat Transfer in Long Horizontal Cylindrical Annuli," *International Developments in Heat Transfer*, Paper No. 117, Part V, pp. 976–984.

Mahony, D. N., Kumar, R., and Bishop, E. H., 1986, "Numerical Investigation of Variable Property Effects on Laminar Natural Convection of Gases Between Two Horizontal Isothermal Concentric Cylinders," ASME JOURNAL OF HEAT TRANSFER, Vol. 108, pp. 783–789.

Morgan, V. T., 1975, "The Overall Convective Heat Transfer From Smooth Circular Cylinders," *Advances in Heat Transfer*, T. F. Irvine and J. P. Hartnett, eds., Vol. 11, Academic Press, New York, pp. 199–265.

Petavel, J. E., 1901, "The Heat Dissipated by a Platinum Surface at High Temperature," *Phil. Trans. Roy. Soc. London*, Vol. 197, pp. 229–254.

Powe, R. E., Carley, C. T., and Bishop, E. H., 1969, "Free Convective Flow Patterns in Cylindrical Annuli," ASME JOURNAL OF HEAT TRANSFER, Vol. 91, No. 3, pp. 310–314.

Thomas, R. W., and de Vahl Davis, G., 1970, "Natural Convection in Annular and Rectangular Cavities: A Numerical Study," *Proc. 4th Int. Heat Transfer Conf.*, Paris, Vol. 4, Paper No. NC 2.4, Elsevier, Amsterdam.

Van de Sande, E., and Hamer, B. J. G., 1979, "Steady and Transient Natural Convection in Enclosures Between Horizontal Circular Cylinders (Constant Heat Flux)," *Int. J. Heat Mass Transfer*, Vol. 22, pp. 361–370.

The Prandtl Number Effect on the Transition in Natural Convection Along a Vertical Surface

A. Bejan[1,2] and J. L. Lage[1]

Nomenclature

- Bo = Boussinesq number $= g\beta H^3 \Delta T/\alpha^2$
- Bo* = modified Boussinesq number $= g\beta H^4 q''/\alpha^2 k$
- D = local transverse length scale of straight flow, m
- g = gravitational acceleration, m/s^2
- Gr = Grashof number $= g\beta H^3 \Delta T/\nu^2$
- Gr* = modified Grashof number $= g\beta H^4 q''/\nu^2 k$
- H = height of vertical wall, m
- k = thermal conductivity, W/m•K
- Nu = average Nusselt number $= q'' H/k\Delta T$
- Pr = Prandtl number $= \nu/\alpha$
- q'' = heat flux, W/m^2
- Ra = Rayleigh number $= g\beta H^3 \Delta T/\alpha\nu$
- v = local longitudinal velocity scale of straight flow, m/s
- ΔT = wall–fluid temperature difference, K
- α = thermal diffusivity, m^2/s
- β = coefficient of volumetric thermal expansion, K^{-1}
- ν = kinematic viscosity, m^2/s
- $( )_i$ = inner
- $( )_o$ = outer

Introduction

During the last two decades we have witnessed intense activity on natural (free) convection, from air convection in rooms to the spreading of pollutants in the environment. This activity has been the subject of many reviews, recent book-size examples of which are Jaluria (1980), Bejan (1984), and Gebhart et al. (1988). One impression that may be left by scanning these reviews is that most of the fundamental questions in natural convection have been answered, especially with regard to *laminar* natural convection.

On this extensive background of published research, it may seem redundant to undertake one more fundamental study into the basics of natural convection. As is often the case, the decision to embark on a new project was triggered by a set of coincidental and mutually reinforcing observations:

(*i*) There is a definite lack of information (theoretical, numerical, experimental) on natural convection in low-Pr fluids (Lykoudis, 1989). This observation was stressed recently also by Wolff et al. (1988).

(*ii*) Georgiadis (1989) drew our attention to the line of work represented by Chao et al. (1982) and Bertin and Ozoe (1986), who showed numerically that the onset of Bénard convection appears to be influenced by the Prandtl number in the $Pr < 1$ range.

(*iii*) We were struck by Bertin and Ozoe's (1986) discovery that they were unable to obtain numerically a steady flow below a certain Prandtl number ($Pr = 0.001$), even though the

[1]Department of Mechanical Engineering and Materials Science, Duke University, Durham, NC 27706.

[2]J. A. Jones Professor of Mechanical Engineering; Fellow ASME.

Contributed by the Heat Transfer Division for publication in the JOURNAL OF HEAT TRANSFER. Manuscript received by the Heat Transfer Division September 25, 1989; revision received January 4, 1990. Keywords: Liquid Metals, Natural Convection, Turbulence.

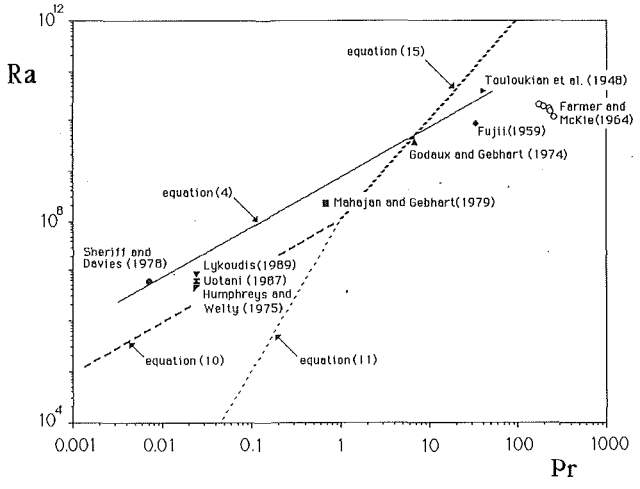

Fig. 1 The effect of Prandtl number on the Rayleigh number of transition to turbulence in the natural convection boundary layer near a vertical surface

Rayleigh number based on height seemed sufficiently low (Ra = 2800).

The present study was motivated by these observations and the apparent suggestion that in low-Pr fluids the laminar flow expires at unexpectedly low Rayleigh numbers. This idea is particularly intersting if we think of the natural convection boundary layer near a vertical wall, for which the textbook teaches us to associate the constant $Ra \approx 10^9$ with the height of transition to the turbulent flow, *regardless* of the Prandtl number (e.g., Incropera and DeWitt, 1985, p. 427).

In order to test this idea, we re-examined the experimental record of observations on transition in vertical natural convection boundary layer flow. Indeed, the empirical data described next show that the Prandtl number has a strong influence on the transition Rayleigh number. In low-Pr fluids the transition occurs at Rayleigh numbers much lower than the oftenmentioned $Ra \approx 10^9$, while in high-Pr fluids the transition Rayleigh number is higher than 10^9. It appears that the constant *Grashof number* $Gr \approx 10^9$ (i.e., not $Ra \approx 10^9$) marks the transition in the wide Pr range 0.001–1000.

Experimental Observations

The results of our survey of experimental observations of transition are summarized in Fig. 1. The Rayleigh number Ra is based on the temperature difference between the vertical surface and the surrounding fluid. In the case of experiments in which the surface was heated with uniform flux, Ra is based on the height-averaged temperature difference between surface and fluid. What follows is an explanation of how each (Pr, Ra) point was plotted on Fig. 1.

The first point counted from the left in Fig. 1 is based on the work of Sheriff and Davies (1978). For natural convection heat transfer from a uniform-flux wall to sodium (Pr = 0.007), these authors reported that the transition occurs in the vicinity of $Bo^* \approx 10^7$, where Bo* is the modified (i.e., flux based) Boussinesq number. They had drawn this conclusion by looking at the growing discrepancy between their measurements of the Nusselt number and the theoretical Nu curve known for the laminar regime. A more careful reading of Sheriff and Davies' heat transfer data (Fig. 4 in their paper) suggests that the Nu measurements depart from the laminar curve at smaller Boussinesq numbers, namely $Bo^* \approx 4 \times 10^5$ (Lykoudis, 1989). In view of the relationship

$$Bo = \frac{Bo^*}{Nu} \tag{1}$$

in which Bo is the Boussinesq number based on the average wall-fluid temperature difference, we found that $Bo^* \approx 4 \times 10^5$ corresponds to $Bo \approx 4.2 \times 10^4$, and to a Rayleigh number

$$Ra = \frac{Bo}{Pr} \tag{2}$$

of approximately $Ra \approx 6 \times 10^6$. This Rayleigh number of transition was plotted in Fig. 1. Worth noting is that if we use Sheriff and Davies' original conclusion, $Bo^* \approx 10^7$, we obtain $Ra \approx 7.8 \times 10^7$, which would still be a considerably lower Rayleigh number than in the traditional $Ra \approx 10^9$ criterion.

Sheriff and Davies' correlation for heat transfer in the turbulent regime was confirmed and extended by Uotani (1987). Experimenting with a vertical uniform-flux surface in an isothermal mixture of lead and bismuth (Pr = 0.023), Uotani obtained Nu data that fall above the laminar curve, suggesting the presence of turbulence. The lowest Bo* run of this kind was for $Bo^* \approx 2.9 \times 10^6$, which corresponds to the $Ra \approx 7.8 \times 10^6$ point plotted in Fig. 1.

Additional support for this last conclusion is provided by two experiments involving mercury (Pr = 0.023). Humphreys and Welty's (1975) measurements of the instantaneous velocity show that chaotic oscillations occur somewhere between $Gr^* = 2.5 \times 10^8$ and $Gr^* = 4 \times 10^9$ (see the lowest two traces in their Fig. 8). Taking $Gr^* \approx 4 \times 10^9$ as a conservative report of the height of transition, and recognizing Gr* as the modified (flux based) Grashof number

$$Gr^* = Nu\ Gr = Nu \frac{Ra}{Pr} \tag{3}$$

we obtained and plotted the point $Ra \approx 7.1 \times 10^6$.

In a more recent study of natural convection in mercury, Lykoudis (1989) found that the transition to turbulence occurs in the vicinity of $Ra \approx 10^7$. The apparatus was a modified version of the one described earlier in Papailiou and Lykoudis (1974). Both Humphreys and Welty's and Lykoudis' mercury results agree very well with Uotani's Pb–Bi experiments.

In the case of vertical boundary layer natural convection in air (Pr = 0.71), Mahajan and Gebhart (1979) found that the transition begins at $Gr^* \approx 1.6 \times 10^{10}$. This observation corresponds to the temperature-difference Rayleigh number $Ra \approx 2.1 \times 10^8$.

For natural convection in water (Pr = 6.7), Godaux and Gebhart (1974) reported that the beginning of transition is located at $Gr^* \approx 6.6 \times 10^{10}$, which corresponds to $Ra \approx 3.4 \times 10^9$. It is worth noting that although the transition Rayleigh number for both air and water is of order 10^9, the Ra value *increases* as Pr increases. Furthermore, this trend is consistent with the discovery that Ra is much smaller (10^7 or less) in the liquid-metals range of Prandtl numbers.

Very few observations of transition have been reported for high-Pr fluids. Fujii (1959) shows that in ethylene glycol (Pr = 28–33) the transition is located at $Ra \approx 8.5 \times 10^9$. Touloukian et al. (1948) also experimented with ethylene glycol (Pr = 40) and chose $Ra \approx 4 \times 10^{10}$ as the demarcation between the Ra ranges covered by their heat transfer correlations for the laminar and turbulent regimes.

At still higher Prandtl numbers, Pr ~ 200, we have Farmer and McKie's (1964) study of natural convection in oil. The flow was reported laminar throughout the Ra range 10^8–2.2×10^{10}. The (Pr, Ra) points that correspond to the five highest Ra experiments in Farmer and McKie's study are marked with empty circles in Fig. 1. The still unknown Rayleigh number of transition must be located somewhere *above* these circles, i.e., at Rayleigh numbers considerably greater than the $Ra \approx 10^9$ criterion.

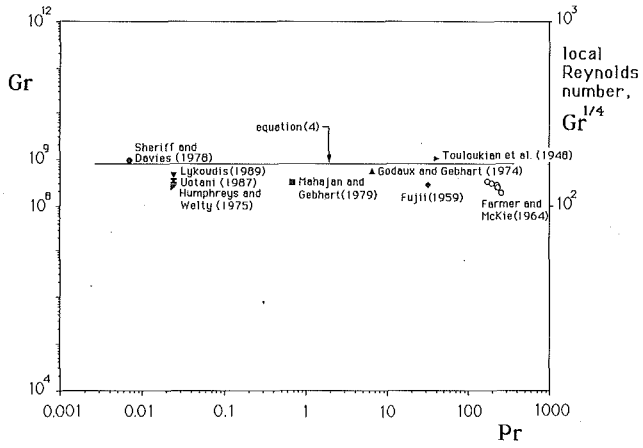

Fig. 2 The Grashof number of order 10^9 as a universal criterion for transition to turbulence near a vertical surface with natural convection

Discussion

The empirical data assembled in Fig. 1 demonstrate that the Prandtl number influences strongly the transition Rayleigh number. The transition Ra increases by four orders of magnitude as Pr increases from 10^{-2} to 10^2. An adequate, order-of-magnitude summary of the alignment of these empirical data is

$$\mathrm{Ra} \sim 8 \times 10^8 \mathrm{Pr} \tag{4}$$

This empirical criterion states that, at transition, it is the temperature-difference Grashof number $\mathrm{Gr} = \mathrm{Ra}/\mathrm{Pr}$ that is of order 10^9 throughout the Prandtl number range covered by Fig. 1,

$$\mathrm{Gr} \sim 10^9 \qquad (10^{-3} < \mathrm{Pr} < 10^3) \tag{5}$$

Finally, it is worth pointing out that there is a theoretical basis for the *monotonic* relationship between the transition Rayleigh number and the Prandtl number. This is provided by the comparison of time scales that lead to the conclusion that a straight flow becomes nonlaminar when its local Reynolds number exceeds the order of 10^2

$$\frac{vD}{\nu} \sim O(10^2) \tag{6}$$

In the construction of this Reynolds number, v is the longitudinal velocity scale of the flow, and D is the transverse length scale. The applicability of the transition criterion (6) has been tested extensively (Bejan, 1984, 1989). This criterion is presented also in the newest natural convection treatise (Gebhart et al., 1988, pp. 630–632). A local Reynolds number criterion similar to equation (6) was derived subsequently by Mikic (1988).

For vertical boundary layer natural convection in the $\mathrm{Pr} < 1$ range, the proper v scale is (see, for example, Bejan, 1984, p. 118)

$$v \sim \frac{\alpha}{H} (\mathrm{Ra\ Pr})^{1/2} \tag{7}$$

The velocity profile has two thicknesses, the inner thickness D_i (wall shear layer ruled by a balance between buoyancy and friction)

$$D_i \sim H\ \mathrm{Gr}^{-1/4} \tag{8}$$

and the outer thickness D_o of the flow driven by buoyancy and restrained by inertia

$$D_o \sim H(\mathrm{Ra\ Pr})^{-1/4} \tag{9}$$

Substituting the scales (7) and (8) into equation (6) leads to the constant-Gr transition criterion

$$\mathrm{Gr}^{1/2} \sim O(10^2) \tag{10}$$

This agrees well with the empirical criterion represented by equation (5); see the right side of Fig. 2.

Alternatively, if we use the outer thickness (9) instead of the inner thickness (8), the local Reynolds number criterion (6) becomes

$$\mathrm{Ra}^{1/4} \sim \mathrm{Pr}^{3/4} \cdot O(10^2) \tag{11}$$

or

$$\mathrm{Gr}^{1/4} \sim \mathrm{Pr}^{1/2} \cdot O(10^2) \tag{12}$$

The transition Ra predicted by this alternative falls considerably below the empirical data of Fig. 1. One possible explanation for the much better agreement that we see between the empirical data and the inner-thickness criterion (10) is that the empirical data represent the observed transition from laminar to turbulent *heat transfer*. The heat transfer through the wall is a quantity that is affected directly by the buckling of the inner shear layer D_i. The buckling of the outer flow is harder to detect, especially in opaque fluids such as liquid metals. Future numerical experiments based on the full (time-dependent) Navier-Stokes equations can shed new light on whether the criterion (12) is supported by the observed fluctuations of the outer flow.

A similar scale analysis can be carried out for the $\mathrm{Pr} > 1$ half of the Prandtl number range. For example, the vertical velocity scale and the thickness of the outer flow are (Bejan 1984, p. 116):

$$v \sim \frac{\alpha}{H} \mathrm{Ra}^{1/2} \tag{13}$$

$$D_o \sim H\ \mathrm{Ra}^{-1/4}\ \mathrm{Pr}^{1/2} \tag{14}$$

The local Reynolds number criterion (6) becomes

$$\mathrm{Ra}^{1/4} \sim \mathrm{Pr}^{1/2} \cdot O(10^2) \tag{15}$$

or, in terms of the Grashof number

$$\mathrm{Gr}^{1/4} \sim \mathrm{Pr}^{1/4} \cdot O(10^2) \tag{16}$$

Taken together, the theoretical equations (10) and (16) anticipate the monotonic relationship between the transition Rayleigh number and the Prandtl number. The agreement between this theory and the empirical data of Fig. 1 is quantitative as well: note that theoretical results such as equation (10) are correct in an order of magnitude sense, and that a factor-of-10 error in the $\mathrm{Gr}^{1/4}$ of equation (10) translates into a factor-of-10^4 error in the Ra and Gr values plotted on the ordinates of Figs. 1 and 2.

There have been several other attempts to anticipate theoretically the transition in natural convection on a vertical wall (e.g., Klyachko, 1962; Sparrow and Tsou, 1965). Many of these have been discussed by Gebhart et al. (1988). A worthwhle direction for the future would be to review the theoretical work in light of the $\mathrm{Gr} \approx 10^9$ criterion and the scale analysis advanced in this paper.

Acknowledgments

We wish to thank Prof. Paul S. Lykoudis and Dr. Akira Tokuhiro for sharing with us their 1989 observations of transition to turbulence in mercury. Professor Lykoudis' continued advice has been very valuable.

References

Bejan, A., 1984, *Convection Heat Transfer*, Wiley, New York.

Bejan, A., 1989, "Buckling Flows: Exploring the Origins and Structure of Turbulence," *Mechanical Engineering*, Vol. 111, Nov., pp. 70–74.

Bertin, H., and Ozoe, H., 1986, "Numerical Study of Two-Dimensional Natural Convection in a Horizontal Fluid Layer Heated From Below, by Finite-Element Method: Influence of Prandtl Number," *Int. J. Heat Mass Transfer*, Vol. 29, pp. 439–449.

Chao, P., Churchill, S. W., and Ozoe, H., 1982, "The Dependence of the Critical Rayleigh Number on the Prandtl Number," in: *Convection Transport and Instability Phenomena*, J. Zierep, and H. Oertel, Jr., eds., G. Braun, Karlsruhe, Federal Republic of Germany, pp. 55–70.

Farmer, W. P., and McKie, W. T., "Natural Convection From a Vertical Isothermal Surface in Oil," ASME Paper No. 64-WA/HT-12.

Fujii, T., 1959, "Experimental Studies of Free Convection Heat Transfer," *Bulletin of JSME*, Vol. 2, No. 8, pp. 555–558.

Gebhart, B., Jaluria, Y., Mahajan, R. L., and B. Sammakia, 1988, *Buoyancy-Induced Flows and Transport*, Hemisphere, New York.

Georgiadis, J., 1989, Private Communication to A. Bejan.

Godaux, R., and Gebhart, B., 1974, "An Experimental Study of the Transition of Natural Convection Flow Adjacent to a Vertical Surface," *Int. J. Heat Mass Transfer*, Vol. 17, pp. 93–107.

Humphreys, W. W., and Welty, J. R., 1975, "Natural Convection With Mercury in a Uniformly Heated Vertical Channel During Unstable Laminar and Transitional Flow," *AIChE Journal*, Vol. 21, pp. 268–274.

Incropera, F. P., and DeWitt, D. P., 1985, *Fundamentals of Heat and Mass Transfer*, 2nd ed., Wiley, New York, p. 427.

Jaluria, Y., 1980, *Natural Convection Heat and Mass Transfer*, Pergamon, Oxford, United Kingdom.

Klyachko, L. S., 1962, "Relations for the Critical State Describing Transition From Laminar to Turbulent Flow in Free Convection," *Int. J. Heat Mass Transfer*, Vol. 5, pp. 763–764.

Lykoudis, P. S., 1989, Private Communication to A. Bejan.

Mahajan, R. L., and Gebhart, B., 1979, "An Experimental Determination of Transition Limits in a Vertical Natural Convection Flow Adjacent to a Surface," *J. Fluid Mechanics*, Vol. 91, pp. 131–154.

Mikic, B. B., 1988, "On Destabilization of Shear Flows: Concept of Admissible System Perturbations," *International Communications in Heat and Mass Transfer*, Vol. 15, pp. 799–811.

Papailiou, D. D., and Lykoudis, P. R., 1974, "Turbulent Free Convection Flow," *Int. J. Heat Mass Transfer*, Vol. 17, pp. 161–172.

Sheriff, N., and Davies, N. W., 1978, "Sodium Natural Convection From a Vertical Plate," *Heat Transfer 1978*, Hemisphere, Washington, DC, Vol. 5, pp. 131–136.

Sparrow, E. M., and Tsou, F. K., 1965, "Stability of Laminar Free-Convection Flow on a Vertical Plate," *Physics of Fluids*, Vol. 8, pp. 1559–1561.

Touloukian, Y. S., Hawkins, G. A., and Jakob, M., 1948, "Heat Transfer by Free Convection From Heated Vertical Surfaces to Liquids," *Trans. ASME*, Vol. 70, pp. 13–23.

Uotani, M., 1987, "Natural Convection Heat Transfer in Thermally Stratified Liquid Metal," *J. Nuclear Science and Technology*, Vol. 24, No. 6, pp. 442–451.

Wolff, F., Beckermann, C., and Viskanta, R., 1988, "Natural Convection of Liquid Metals in Vertical Cavities," *Experimental Thermal and Fluid Science*, Vol. 1, pp. 83–91.

Natural Convection in a Vertical Heated Tube Attached to a Thermally Insulated Chimney of a Different Diameter

Y. Asako,[1,3] H. Nakamura,[2,3] and M. Faghri[4]

Nomenclature

Ra = Rayleigh number = $g\beta r_1^3(t_w - t_\infty)/\alpha\nu$
t_w = tube temperature
t_∞ = ambient temperature
u = velocity component in x direction
α = thermal diffusivity
Ψ_w = dimensionless stream function at tube = $\int_0^{r1} ru\, dr/\alpha r_1$

[1]Associate Professor.
[2]Professor.
[3]Department of Mechanical Engineering, Tokyo Metropolitan University, Setagaya, Tokyo 158, Japan.
[4]Professor, Department of Mechanical Engineering and Applied Mechanics, University of Rhode Island, Kingston, Rhode Island 02881.

Contributed by the Heat Transfer Division for publication in the JOURNAL OF HEAT TRANSFER. Manuscript received by the Heat Transfer Division December 12, 1988; revision received November 28, 1989. Keywords: Environmental Heat Transfer, Natural Convection, Numerical Methods.

Introduction

Natural convection is often a convenient and inexpensive mode of heat transfer. It is commonly employed in the cooling of electronic equipment and many other applications. Since the initial work by Bodoia and Osterle (1962) on finite difference solutions of natural convection between vertical isothermal plates, many other researchers have studied natural convection in vertical channels. Specifically Davis and Perona (1971) studied natural convection in vertical heated tubes.

A thermally insulated chimney attached to a vertical heated channel induces an increase in the natural convection in the channel and leads to a higher heat transfer rate. This is the well-known chimney effect discussed in the paper by Haaland and Sparrow (1983). If the chimney diameter is larger than the heated tube diameter, the friction loss in the chimney region decreases with increasing chimney diameter. This induces an increase in the mass flow rate and leads to a higher heat transfer rate than the case for a chimney of the same diameter. However, from a geometric consideration it is evident that the chimney effect diminishes in the limiting case of an extremely large chimney diameter compared with its height. Therefore, there exists an optimum diameter where the heat transfer is maximum. To investigate the chimney effect computations are carried out for a Rayleigh number of 12.5, based on the heated tube radius, and for a Prandtl number of 0.7. The numerical results are based on a control volume finite difference method. The average Nusselt number results are compared with the numerical results obtained for a chimney attached to a tube of the same diameter.

Formulation

Description of the Problem. The problem to be considered in this study is schematically depicted in Fig. 1. It involves the determination of two-dimensional heat transfer for laminar natural convection in a vertical heated tube at a uniform temperature t_w attached to a thermally insulated chimney of different diameter. The geometry of the heated tube is specified by the height h_1 and radius r_1 and that of the chimney by the height h_2 and radius r_2. This is a two-dimensional problem and because of the symmetry only half of the domain needs to be considered for the numerical analysis.

Conservation Equations. The governing equations to be considered are the continuity, momentum, and energy equations. Laminar flow is assumed to prevail and the only fluid property variation considered is the density difference needed to establish the buoyancy term for which the Boussinesq density-tem-

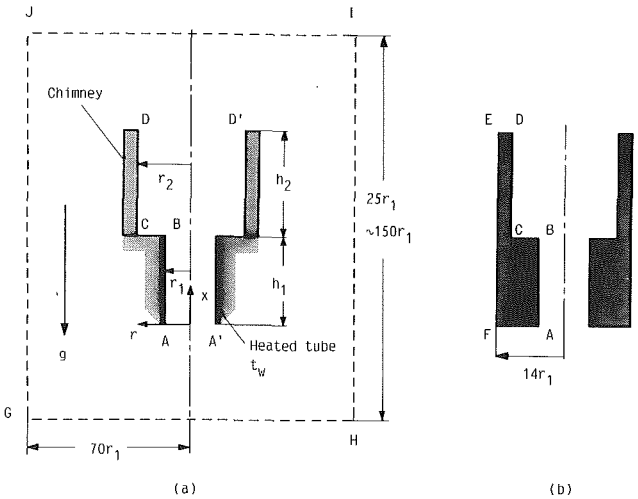

Fig. 1 A schematic diagram of a heated vertical tube with a chimney

Chao, P., Churchill, S. W., and Ozoe, H., 1982, "The Dependence of the Critical Rayleigh Number on the Prandtl Number," in: *Convection Transport and Instability Phenomena*, J. Zierep, and H. Oertel, Jr., eds., G. Braun, Karlsruhe, Federal Republic of Germany, pp. 55–70.

Farmer, W. P., and McKie, W. T., "Natural Convection From a Vertical Isothermal Surface in Oil," ASME Paper No. 64-WA/HT-12.

Fujii, T., 1959, "Experimental Studies of Free Convection Heat Transfer," *Bulletin of JSME*, Vol. 2, No. 8, pp. 555–558.

Gebhart, B., Jaluria, Y., Mahajan, R. L., and B. Sammakia, 1988, *Buoyancy-Induced Flows and Transport*, Hemisphere, New York.

Georgiadis, J., 1989, Private Communication to A. Bejan.

Godaux, R., and Gebhart, B., 1974, "An Experimental Study of the Transition of Natural Convection Flow Adjacent to a Vertical Surface," *Int. J. Heat Mass Transfer*, Vol. 17, pp. 93–107.

Humphreys, W. W., and Welty, J. R., 1975, "Natural Convection With Mercury in a Uniformly Heated Vertical Channel During Unstable Laminar and Transitional Flow," *AIChE Journal*, Vol. 21, pp. 268–274.

Incropera, F. P., and DeWitt, D. P., 1985, *Fundamentals of Heat and Mass Transfer*, 2nd ed., Wiley, New York, p. 427.

Jaluria, Y., 1980, *Natural Convection Heat and Mass Transfer*, Pergamon, Oxford, United Kingdom.

Klyachko, L. S., 1962, "Relations for the Critical State Describing Transition From Laminar to Turbulent Flow in Free Convection," *Int. J. Heat Mass Transfer*, Vol. 5, pp. 763–764.

Lykoudis, P. S., 1989, Private Communication to A. Bejan.

Mahajan, R. L., and Gebhart, B., 1979, "An Experimental Determination of Transition Limits in a Vertical Natural Convection Flow Adjacent to a Surface," *J. Fluid Mechanics*, Vol. 91, pp. 131–154.

Mikic, B. B., 1988, "On Destabilization of Shear Flows: Concept of Admissible System Perturbations," *International Communications in Heat and Mass Transfer*, Vol. 15, pp. 799–811.

Papailiou, D. D., and Lykoudis, P. R., 1974, "Turbulent Free Convection Flow," *Int. J. Heat Mass Transfer*, Vol. 17, pp. 161–172.

Sheriff, N., and Davies, N. W., 1978, "Sodium Natural Convection From a Vertical Plate," *Heat Transfer 1978*, Hemisphere, Washington, DC, Vol. 5, pp. 131–136.

Sparrow, E. M., and Tsou, F. K., 1965, "Stability of Laminar Free-Convection Flow on a Vertical Plate," *Physics of Fluids*, Vol. 8, pp. 1559–1561.

Touloukian, Y. S., Hawkins, G. A., and Jakob, M., 1948, "Heat Transfer by Free Convection From Heated Vertical Surfaces to Liquids," *Trans. ASME*, Vol. 70, pp. 13–23.

Uotani, M., 1987, "Natural Convection Heat Transfer in Thermally Stratified Liquid Metal," *J. Nuclear Science and Technology*, Vol. 24, No. 6, pp. 442–451.

Wolff, F., Beckermann, C., and Viskanta, R., 1988, "Natural Convection of Liquid Metals in Vertical Cavities," *Experimental Thermal and Fluid Science*, Vol. 1, pp. 83–91.

Natural Convection in a Vertical Heated Tube Attached to a Thermally Insulated Chimney of a Different Diameter

Y. Asako,[1,3] H. Nakamura,[2,3] and M. Faghri[4]

Nomenclature

Ra = Rayleigh number = $g\beta r_1^3(t_w - t_\infty)/\alpha\nu$
t_w = tube temperature
t_∞ = ambient temperature
u = velocity component in x direction
α = thermal diffusivity
Ψ_w = dimensionless stream function at tube = $\int_0^{r1} ru\, dr/\alpha r_1$

[1]Associate Professor.
[2]Professor.
[3]Department of Mechanical Engineering, Tokyo Metropolitan University, Setagaya, Tokyo 158, Japan.
[4]Professor, Department of Mechanical Engineering and Applied Mechanics, University of Rhode Island, Kingston, Rhode Island 02881.

Contributed by the Heat Transfer Division for publication in the JOURNAL OF HEAT TRANSFER. Manuscript received by the Heat Transfer Division December 12, 1988; revision received November 28, 1989. Keywords: Environmental Heat Transfer, Natural Convection, Numerical Methods.

Introduction

Natural convection is often a convenient and inexpensive mode of heat transfer. It is commonly employed in the cooling of electronic equipment and many other applications. Since the initial work by Bodoia and Osterle (1962) on finite difference solutions of natural convection between vertical isothermal plates, many other researchers have studied natural convection in vertical channels. Specifically Davis and Perona (1971) studied natural convection in vertical heated tubes.

A thermally insulated chimney attached to a vertical heated channel induces an increase in the natural convection in the channel and leads to a higher heat transfer rate. This is the well-known chimney effect discussed in the paper by Haaland and Sparrow (1983). If the chimney diameter is larger than the heated tube diameter, the friction loss in the chimney region decreases with increasing chimney diameter. This induces an increase in the mass flow rate and leads to a higher heat transfer rate than the case for a chimney of the same diameter. However, from a geometric consideration it is evident that the chimney effect diminishes in the limiting case of an extremely large chimney diameter compared with its height. Therefore, there exists an optimum diameter where the heat transfer is maximum. To investigate the chimney effect computations are carried out for a Rayleigh number of 12.5, based on the heated tube radius, and for a Prandtl number of 0.7. The numerical results are based on a control volume finite difference method. The average Nusselt number results are compared with the numerical results obtained for a chimney attached to a tube of the same diameter.

Formulation

Description of the Problem. The problem to be considered in this study is schematically depicted in Fig. 1. It involves the determination of two-dimensional heat transfer for laminar natural convection in a vertical heated tube at a uniform temperature t_w attached to a thermally insulated chimney of different diameter. The geometry of the heated tube is specified by the height h_1 and radius r_1 and that of the chimney by the height h_2 and radius r_2. This is a two-dimensional problem and because of the symmetry only half of the domain needs to be considered for the numerical analysis.

Conservation Equations. The governing equations to be considered are the continuity, momentum, and energy equations. Laminar flow is assumed to prevail and the only fluid property variation considered is the density difference needed to establish the buoyancy term for which the Boussinesq density-tem-

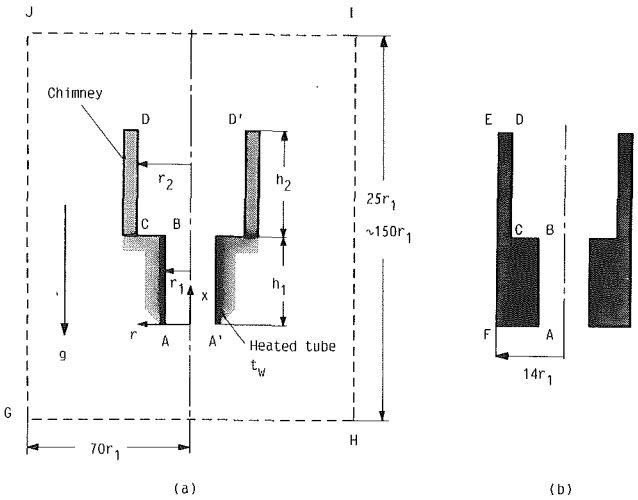

Fig. 1 A schematic diagram of a heated vertical tube with a chimney

perature relation is employed. Then, the governing equations will be the conventional natural convection differential equations.

Numerical Solutions. To avoid the specification of the inflow (A-A') and outflow (D-D') boundaries, which are not known, the solution domain is extended from $25r_1$ to $150r_1$ in the X direction and $70r_1$ in the R direction as depicted in Fig. 1(a). The boundary of this domain is denoted by GHIJ and is maintained at an ambient temperature t_∞. Numerical experimentation for a tube without a chimney for $h_1/r_1 = 10$, Ra = 12.5 and for a number of extended solution domains (height × radius: $25r_1 \times 70r_1$, $50r_1 \times 85r_1$, and $82r_1 \times 105r_1$) were performed to investigate the size of the solution domain. The change in the average Nusselt number between the narrow domain ($25r_1 \times 70r_1$) and the intermediate domain ($50r_1 \times 85r_1$) was 0.9 percent, and that between the narrow domain and the wide domain ($82r_1 \times 105r_1$) was 1.4 percent. Thus, the solution domain ($25r_1 \times 70r_1$) is considered to be large enough for all computations to maintain relatively moderate computing cost.

The shaded domain ABCDEF in Fig. 1(b) consists of the heated tube and the chimney. The boundaries AB and CD are the inner surfaces of the heated tube and the chimney, respectively. For the application of the computer program in cylindrical coordinates, the viscosity is taken to have a large value and the thermal conductivity is taken to be zero. These choices ensure that the shaded domain ABCDEF acts as a solid wall, the inside of which is thermally insulated. Only the boundary AB adjacent control volumes are maintained at constant temperature t_w. Note that the boundary EF is fixed to $14r_1$ for all computations. The large step change in the fluid properties is handled by using harmonic-mean practice by Patankar (1980). The discretization procedure of the equations is based on the SIMPLER algorithm of Patankar (1980). The underrelaxation factors for the velocity and pressure are set to 0.2 and 1, respectively. About 400 to 600 iterations are required to obtain a converged solution.

The final computations were carried out for a grid containing 28×25 nodal points. The points in the X and R coordinate directions are distributed in a nonuniform manner with a higher concentration of grids closer to the center of the solution domain except in the tube. The grid points in the tube are distributed with a higher concentration of grids closer to the wall. Numerical experimentation for a tube without chimney, for $h_1/r_1 = 10$ and Ra = 12.5, with the grid points of (36×34), (44×40), (52×46), (60×52), (68×58), and (76×58), were also performed to investigate the grid size effect. The Nusselt numbers are plotted as a function of the total number of grid points in Fig. 2. The change in the average Nusselt number between the coarse mesh (28×25) and the finest mesh (76×58) was 10.7 percent. The (28×25) mesh is chosen for all computations to maintain relatively moderate computing time. The prediction of Nu by Davis and Perona (1971) who solved the boundary layer form of the conservation equations, is 0.0781. The present analytical value is 10 percent higher.

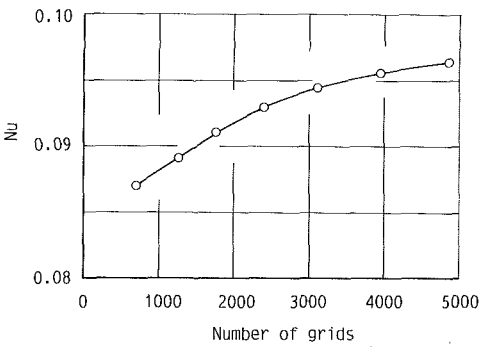

Fig. 2 Grid size effect on the average Nusselt number

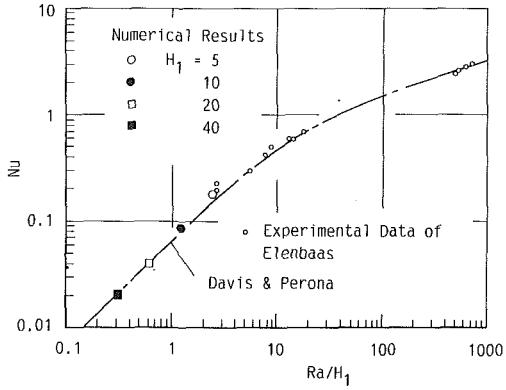

Fig. 3 Comparison of Nusselt number for a heated tube without a chimney

Since higher values of Ra may require a finer mesh size than the one tested for Ra = 12.5, a value of 12.5 is chosen for Ra, and a value of 0.7 is chosen for Pr. Aside from Pr and Ra, there are four geometric parameters that have to be specified. These are the radii of the heated tube and the chimney, r_1 and r_2, and heights of the heated tube and the chimney, h_1 and h_2. If the r_1 is used as a reference length, then $H_1 = h_1/r_1$, $H_2 = h_2/r_1$, and r_2/r_1 needs to be specified as a geometric parameter. The selected values of H_1 are 5, 10, 20, and 40 and those of H_2 are 5, 10, and 20. The radius ratio r_2/r_1 ranges from 1 to 10.7.

Nusselt Numbers. The average heat transfer coefficient on the heated wall is defined as

$$h = Q/[A(t_w - t_\infty)] \tag{1}$$

where A is the area of the heated wall, $2\pi r_1 h_1$, and Q is the total heat transfer rate from the heated wall. It can be expressed as

$$Q = 2\pi\rho C_p \left[\int_{\text{exit}} rut\, dr - \int_{\text{ent.}} rut\, dr\right] + 2\pi \left[\int_{\text{ent.}} rk(\partial t/\partial x)\, dr - \int_{\text{exit}} rk(\partial t/\partial x) dr\right] \tag{2}$$

where ρ is the density of the fluid, C_p is the specific heat of the fluid, and k is the thermal conductivity. The average Nusselt number is defined as

$$\text{Nu} = hr_1/k \tag{3}$$

The total heat transfer rate calculated from equation (2) agrees well with the calculated value from the temperature gradient at the heated wall.

Results and Discussion

Nusselt Number for Channel Without Chimney. The Nusselt numbers for a channel without a chimney for $H_1 = 5$, 10, 20, and 40 are plotted as a function of Ra/H_1 in Fig. 3. The experimental data of Elenbaas (1942) and the analytical data of Davis and Perona (1971) are also depicted in this figure for comparison. The latter authors solved the boundary layer form of the conservation equations and also plotted their Nusselt number results as a function of Ra/H_1. As seen from this figure, slight discrepancies exist between the experimental and numerical results.

Effect of Radius Ratio on Nusselt Number. The representative Nusselt number ratios, Nu/Nu_0, for the nondimensional heated tube height, $H_1 = 10$, are plotted as a function of the radius ratio, r_2/r_1, in Fig. 4 with the nondimensional chimney height H_2 as a curve parameter. Nu_0 represents the value of the Nusselt number for a channel without a chimney. The present analytical value of Nu_0 is 0.0870. As seen from this

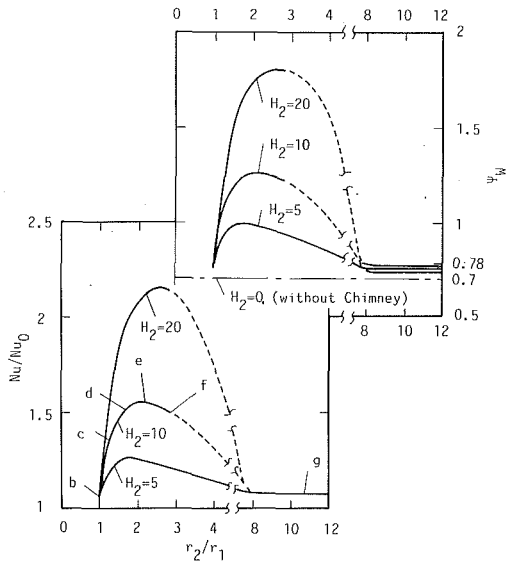

Fig. 4 Nusselt number ratio Nu/Nu$_0$, and flow rate Ψ_w, for $H_1 = 10$, Ra = 12.5, as a function of radius ratio r_2/r_1

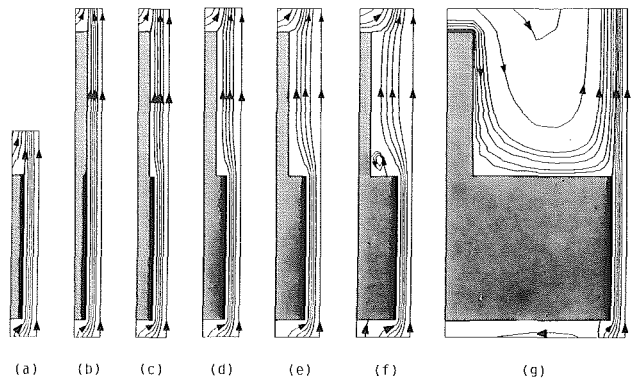

Fig. 5 Streamline diagrams for $H_1 = 10$, $H_2 = 10$, Ra = 12.5, and radius ratio, r_2/r_1, as parameter: (*a*) ($H_2 = 0$), (*b*) $r_2/r_1 = 1$, (*c*) $r_2/r_1 = 1.3$, (*d*) $r_2/r_1 = 1.7$, (*e*) $r_2/r_1 = 2.2$, (*f*) $r_2/r_1 = 2.9$, (*g*) $r_2/r_1 = 10.7$

figure, the Nusselt number ratio increases with increasing radius ratio until it reaches a peak value. Then, it decreases with increasing radius ratio until it approaches the value for the channel without a chimney. In the computations, in the range of $r_2/r_1 = 3$ to 8, it was hard to obtain a converged solution. Therefore, the converged values outside this range are connected by dashed lines.

Streamline Diagrams. The representative streamline maps obtained from the numerical solutions for $H_1 = 10$ and $H_2 = 10$ are presented in Fig. 5. Figures 5(*b–g*) are for $r_2/r_1 = 1$, 1.3, 1.7, 2.2, 2.9, and 10.7, respectively. The streamline map for the channel without a chimney is presented in Fig. 5(*a*). The streamlines Ψ/Ψ_w are spaced in increments of 0.2 and their values on the symmetric axis and on the wall are 0 and 1, respectively. The line for $H_2 = 10$ in Fig. 4 is marked with the letters *b*, *c*, *d*, *g*. These letters correspond to radius ratios in Figs. 5(*b–g*). That is, Fig. 5(*b*) represents the streamline for a channel with a chimney of same diameter. Figure 5(*e*) represents the streamlines for the case where maximum heat is transferred. In Fig. 5(*f*), a separation bubble can be seen at the bottom of the chimney. Figure 5(*g*) represents a streamline for the channel with a large radius chimney, where the inflow from the upper end of the chimney can be seen. The chimney effect diminishes for such an extremely large radius ratio.

Flow Rate. The flow rate obtained by the evaluation of the dimensionless stream function at the heated tube, Ψ_w, is also

Table 1 Optimum radius ratio $(r_2/r_1)_{opt}$

H_1	$(r_2/r_1)_{opt}$		
	H_2=5	H_2=10	H_2=20
5	1.95	2.41	2.73
10	1.90	2.24	2.63
20	1.84	2.05	2.51
40	1.77	1.95	2.08

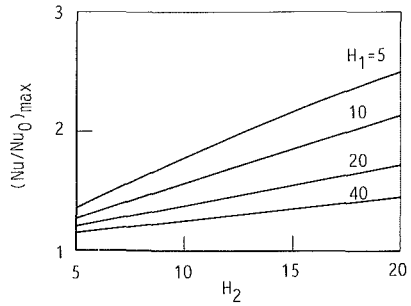

Fig. 6 Maximum Nusselt number ratio $(Nu/Nu_0)_{max}$ as a function of H_2

plotted as a function of the radius ratio, r_2/r_1 in Fig. 4 with the nondimensional chimney height H_2 as a curve parameter for the case of $H_1 = 10$. The dashed line in the figure represents the value for the channel without the chimney. In case of an infinitely long heated tube, the stream function Ψ_w can be analytically obtained as

$$\Psi_w = (1/16)\ \mathrm{Ra} \tag{4}$$

The stream function for Ra = 12.5 takes a value of 0.781. The stream function for the channel with a chimney of the same diameter cannot exceed this value. However, as seen from Fig. 4, the maximum value of the stream function for the channel with the chimney for $H_2 = 20$ is about 2.5 times higher than this value.

Optimum Diameter. As seen from Fig. 4, there exists an optimum diameter where the heat transfer is maximum. The optimum radius ratio, $(r_2/r_1)_{opt}$, is listed in Table 1, and was obtained by a curve-fitting technique. Three numerically obtained values near the maximum are chosen for the curve fittings. A parabolic curve that passes through these three points is obtained. The optimum radius ratio decreases with increasing nondimensional heated tube height H_1, and it increases with an increase in the nondimensional chimney height H_2.

Maximum Heat Transfer Rate. The maximum value of the Nusselt number ratio, $(Nu/Nu_0)_{max}$, is plotted as a function of the nondimensional chimney height H_2 in Fig. 6 with the nondimensional heated tube height H_1 as a curve parameter. Nu_0 represents the value for the channel without the chimney. As seen from the figure, the chimney effect is accentuated for a lower Rayleigh number, for lower H_1, and for a higher H_2. In the range of the present computations, the maximum Nusselt number ratio reaches about 2.5. This value is for the case of Ra = 12.5, $H_1 = 5$, and $H_2 = 20$.

Concluding Remarks

The heat transfer characteristics for natural convection in a vertical heated tube attached to a thermally insulated chimney of a different diameter has been investigated by a numerical study to find the optimum chimney diameter where the maximum amount of heat is transferred. The optimum diameter

ratio r_2/r_1 ranges from 1.4 to 2.7 depending on the geometric parameters, H_1 and H_2. The heat transfer rate for the channel with a chimney of optimum diameter is about 2.5 higher than the rate for the channel without a chimney.

References

Bodoia, J. R., and Osterle, J. F., 1962, "The Development of Free Convection Between Heated Vertical Plates," ASME JOURNAL OF HEAT TRANSFER, Vol. 84, pp. 40–44.

Davis, L. P., and Perona, J. J., 1971, "Development of Free Convection Flow of a Gas in a Heated Vertical Open Tube," *International Journal of Heat and Mass Transfer*, Vol. 14, pp. 889–903.

Elenbaas, W., 1942, "The Dissipation of Heat by Free Convection. The Inner Surface of Vertical Tubes of Different Shapes of Cross-Section," *Physica*, Vol. 9, pp. 865–874.

Haaland, S. E., and Sparrow, E. M., 1983, "Solutions for the Channel Plume and the Parallel-Walled Chimney," *Numerical Heat Transfer*, Vol. 6, pp. 155–172.

Patankar, S. V., 1980, *Numerical Heat Transfer and Fluid Flow*, Hemisphere, New York.

An Experimental Investigation of Heat Transfer in Enclosures Filled or Partially Filled With a Fibrous Insulation

K. Vafai[1] and J. Belwafa[1]

Nomenclature

A = aspect ratio = H/L
A_c = cross-sectional area of enclosure, m^2
g = gravitational acceleration, m/s^2
Gr_L = Grashof number
H = height of enclosure, m
k = thermal conductivity, W/mK
K = permeability of the fibrous insulation, m^2
L = width of enclosure, m
Nu, Nu* = Nusselt number for unobstructed and partially filled enclosures, respectively
Q_{tot} = total heat transfer, W
Ra_L = Rayleigh number = $g\beta\Delta TL^3/\alpha_f\nu_f$
Ra_L^* = Darcy–Rayleigh number = $Kg\beta\Delta TL/\alpha_{eff}\nu_f$
t = air gap thickness, m
S = dimensionless air gap thickness = s/L
T = temperature, K
α = thermal diffusivity, m^2/s
β = coefficient of thermal expansion, K^{-1}
ΔT = temperature difference, K
ϵ = porosity
ν = kinematic viscosity, m^2/s

Subscripts

C = cold
eff = effective
f = fluid
H = hot
M = mean
r = radiation
s = solid matrix

1 Introduction

Recently, the subject of partially filled enclosures has received considerable attention. The main reason for this interest is the possibility of attaining an R-value for a partially filled enclosure that may be the same or even higher than the R-value of an enclosure that is completely filled with a porous medium. Obviously in a partial enclosure the overall convection process is going to be more vigorous; that is, the removal of a portion of the porous medium removes part of the convective suppression by the porous matrix. However, at the same time the introduced air gap has a lower thermal conductivity than the combined stagnant effective thermal conductivity of the porous and air media that used to occupy that gap. The idea here is that *maybe* under some circumstances lowering the thermal conductivity in the gap region will make up for the augmentation in natural convection that is experienced as a result of the introduction of the air gap. One of the first publications dealing with an investigation of partial enclosures was that of Tong and Subramanian (1986). They numerically analyzed the steady-state natural convection heat transfer in rectangular enclosures partially filled with a porous medium, where the porous medium was separated from the air gap by an impermeable interface. In their study, it was found that under many circumstances (depending on the thermal conductivity of the layers), to achieve the best insulating effect, there was no need to fill an enclosure completely with the porous insulation. Later, Sathe et al. (1987) presented their experimental results for the same problem that was analyzed by Tong and Subramanian. They found good agreement with the numerical results presented in the latter work. Beckermann et al. (1987) performed a numerical and experimental study to analyze the steady-state natural convection fluid flow and heat transfer in a vertical rectangular enclosure that is partially filled with a porous medium using a permeable interface. They found that it was possible to obtain the same heat transfer values for a partially insulated enclosure as it is for a fully insulated enclosure. However, their results showed that it is not possible to get lower heat transfer values when a partial insulation arrangement is used. It should be noted that while there are some experimental results available for an enclosure filled with a porous medium, the ones with air as the working fluid are very limited in number. Seki et al. (1978b) presented results for an enclosure totally filled with fibrous insulation saturated with air, while to the authors' knowledge no experimental results are available for partially filled enclosures in which air is used as the working fluid. This fact is very important since the use of liquids in previous experiments produces Darcy–Rayleigh numbers much higher than any that can be associated with the use of fibrous insulation in realistic situations.

The main purpose of this work is to present an experimental investigation dealing specifically and explicitly with different and widely used forms of fibrous insulation for both partially and fully insulated situations. Furthermore, the experimental investigations have been performed under conditions that will closely simulate some realistic situations under which these fibrous insulations are used. The present investigation reveals a number of different and interesting results, which clarify some distinct similarities and differences between heat transfer results at high Ra_L^* values and the very low Ra_L^* values that

[1]Department of Mechanical Engineering, The Ohio State University, Columbus, OH 43210.

Contributed by the Heat Transfer Division for publication in the JOURNAL OF HEAT TRANSFER. Manuscript received by the Heat Transfer Division April 16, 1989; revision received October 2, 1989. Keywords: Building Heat Transfer, Enclosure Flows, Natural Convection.

ratio r_2/r_1 ranges from 1.4 to 2.7 depending on the geometric parameters, H_1 and H_2. The heat transfer rate for the channel with a chimney of optimum diameter is about 2.5 higher than the rate for the channel without a chimney.

References

Bodoia, J. R., and Osterle, J. F., 1962, "The Development of Free Convection Between Heated Vertical Plates," ASME JOURNAL OF HEAT TRANSFER, Vol. 84, pp. 40–44.

Davis, L. P., and Perona, J. J., 1971, "Development of Free Convection Flow of a Gas in a Heated Vertical Open Tube," *International Journal of Heat and Mass Transfer*, Vol. 14, pp. 889–903.

Elenbaas, W., 1942, "The Dissipation of Heat by Free Convection. The Inner Surface of Vertical Tubes of Different Shapes of Cross-Section," *Physica*, Vol. 9, pp. 865–874.

Haaland, S. E., and Sparrow, E. M., 1983, "Solutions for the Channel Plume and the Parallel-Walled Chimney," *Numerical Heat Transfer*, Vol. 6, pp. 155–172.

Patankar, S. V., 1980, *Numerical Heat Transfer and Fluid Flow*, Hemisphere, New York.

An Experimental Investigation of Heat Transfer in Enclosures Filled or Partially Filled With a Fibrous Insulation

K. Vafai[1] and J. Belwafa[1]

Nomenclature

A = aspect ratio = H/L
A_c = cross-sectional area of enclosure, m^2
g = gravitational acceleration, m/s^2
Gr_L = Grashof number
H = height of enclosure, m
k = thermal conductivity, W/mK
K = permeability of the fibrous insulation, m^2
L = width of enclosure, m
Nu, Nu* = Nusselt number for unobstructed and partially filled enclosures, respectively
Q_{tot} = total heat transfer, W
Ra_L = Rayleigh number = $g\beta\Delta TL^3/\alpha_f\nu_f$
Ra_L^* = Darcy–Rayleigh number = $Kg\beta\Delta TL/\alpha_{eff}\nu_f$
t = air gap thickness, m
S = dimensionless air gap thickness = s/L
T = temperature, K
α = thermal diffusivity, m^2/s
β = coefficient of thermal expansion, K^{-1}
ΔT = temperature difference, K
ϵ = porosity
ν = kinematic viscosity, m^2/s

Subscripts

C = cold
eff = effective
f = fluid
H = hot
M = mean
r = radiation
s = solid matrix

1 Introduction

Recently, the subject of partially filled enclosures has received considerable attention. The main reason for this interest is the possibility of attaining an R-value for a partially filled enclosure that may be the same or even higher than the R-value of an enclosure that is completely filled with a porous medium. Obviously in a partial enclosure the overall convection process is going to be more vigorous; that is, the removal of a portion of the porous medium removes part of the convective suppression by the porous matrix. However, at the same time the introduced air gap has a lower thermal conductivity than the combined stagnant effective thermal conductivity of the porous and air media that used to occupy that gap. The idea here is that *maybe* under some circumstances lowering the thermal conductivity in the gap region will make up for the augmentation in natural convection that is experienced as a result of the introduction of the air gap. One of the first publications dealing with an investigation of partial enclosures was that of Tong and Subramanian (1986). They numerically analyzed the steady-state natural convection heat transfer in rectangular enclosures partially filled with a porous medium, where the porous medium was separated from the air gap by an impermeable interface. In their study, it was found that under many circumstances (depending on the thermal conductivity of the layers), to achieve the best insulating effect, there was no need to fill an enclosure completely with the porous insulation. Later, Sathe et al. (1987) presented their experimental results for the same problem that was analyzed by Tong and Subramanian. They found good agreement with the numerical results presented in the latter work. Beckermann et al. (1987) performed a numerical and experimental study to analyze the steady-state natural convection fluid flow and heat transfer in a vertical rectangular enclosure that is partially filled with a porous medium using a permeable interface. They found that it was possible to obtain the same heat transfer values for a partially insulated enclosure as it is for a fully insulated enclosure. However, their results showed that it is not possible to get lower heat transfer values when a partial insulation arrangement is used. It should be noted that while there are some experimental results available for an enclosure filled with a porous medium, the ones with air as the working fluid are very limited in number. Seki et al. (1978b) presented results for an enclosure totally filled with fibrous insulation saturated with air, while to the authors' knowledge no experimental results are available for partially filled enclosures in which air is used as the working fluid. This fact is very important since the use of liquids in previous experiments produces Darcy–Rayleigh numbers much higher than any that can be associated with the use of fibrous insulation in realistic situations.

The main purpose of this work is to present an experimental investigation dealing specifically and explicitly with different and widely used forms of fibrous insulation for both partially and fully insulated situations. Furthermore, the experimental investigations have been performed under conditions that will closely simulate some realistic situations under which these fibrous insulations are used. The present investigation reveals a number of different and interesting results, which clarify some distinct similarities and differences between heat transfer results at high Ra_L^* values and the very low Ra_L^* values that

[1]Department of Mechanical Engineering, The Ohio State University, Columbus, OH 43210.

Contributed by the Heat Transfer Division for publication in the JOURNAL OF HEAT TRANSFER. Manuscript received by the Heat Transfer Division April 16, 1989; revision received October 2, 1989. Keywords: Building Heat Transfer, Enclosure Flows, Natural Convection.

characterize the realistic conditions under which fibrous insulation is used in buildings.

2 Experimental Apparatus and Procedure

The apparatus used in our experimental investigation is depicted in Fig. 1. At all times the quantities of interest in our experimental runs were the input heat flux and the temperatures of the hot and the cold walls. The experimental setup was designed so as to ensure a unidirectional heat transfer from the hot wall into the enclosure. The apparatus consists of three major parts: the cold plate, hot plate, and the backside (guard heater system). The cold plate was made of a 12 in. × 12 in. × 1¼ in. hollow aluminum plate. The hollow part of the plate was composed of six bypass tubes. Water was passed through these tubes to obtain a uniform wall temperature. This arrangement created a very uniform cold wall temperature. The hollow aluminum plate was designed such that it could slide easily inside the test section. The position of the cold plate with respect to the hot plate would provide us with a control over different air gap thicknesses as well as different overall aspect ratios. The hot plate was made of a 12 in. × 12 in. × 1/4 in. aluminum plate heated by two independently controlled 6 in. × 12 in. Chromalox (240 V, 142 W) strip heaters. On the other side of the heaters a 12 in. × 12 in. × 1/16 in. aluminum sheet was placed so that accurate and uniform temperature data could be collected. A 2-in.-thick high-density Fiberglas insulation (96 kg/m^3) was placed behind the 12 in. × 12 in. × 1/16 in. aluminum sheet in order to control the backward heat losses from the main heaters. To reduce the backward heat transfer losses a guard heater arrangement was used. First, an 18 in. × 18 in. × 1/16 in. aluminum sheet was placed against the high-density Fiberglas insulation (again to obtain accurate and uniform temperature data), then four independently controlled 6 in. × 6 in. Chromalox (240 V, 72 W) strip heaters were placed right after this 18 in. × 18 in. × 1/16 in. aluminum sheet. The objective here was to heat the 18 in. × 18 in. × 1/16 in. aluminum sheet to the same temperature as the 12 in. × 12 in. × 1/16 in. aluminum sheet, which was on the back side of the main heaters. This would of course ensure that there are no backward losses and consequently the heat out of the main heaters would essentially flow toward the hot plate. The whole system was then insulated using a high-density Fiberglas.

The temperatures were recorded by a digital thermometer (Fluke 2190A) using thermocouple selectors (Fluke Y2001). Gage 24 copper-constantan thermocouples were used. Five of them were attached to the cold plate, six were attached to the hot plate, and four thermocouples were attached on each of the two aluminum sheets that were used in controlling the backward losses (away from the test section). In all of the experimental runs the maximum temperature gradient measured on any of the plates was less than 0.1 °C when the enclosure was filled with a porous medium and less than 0.3 °C when the enclosure was filled with air. The heat input into the hot plate was measured by using a watt transducer and a digital multimeter. The accuracy of the power read was within 1/10 of a watt. The depth of the enclosure was chosen to be 12 in. and was found to be deep enough to reduce the end effects. Based on some preliminary calculations the total heat losses for all cases were estimated to be less than 5 percent. The power input to the heaters was controlled by a set of variacs. Once the heaters were turned on, the temperatures on the 18 in. × 18 in. × 1/16 in. and 12 in. × 12 in. × 1/16 in. aluminum sheets were compared and then the power going to the guard heaters was adjusted so that temperatures on both sides of the aluminum sheets would match to within 1 °C. It was assumed that steady-state conditions prevailed when the temperature change for any of the thermocouples was less than 0.05 °C within one hour. It took about 7 hours to reach steady state when the enclosure was totally filled with air and about 15 hours when the enclosure was filled with Fiberglas insulation. The discrepancy in reproducing the results for the Nusselt number was found to be within 3 percent. The experimental uncertainties in the measurements reported were found to range from 0.5 to 7 percent for the Nusselt number and about 10 percent for the Rayleigh number.

The dimensionless parameters were calculated using thermophysical properties evaluated at the mean temperature, which was calculated as $(T_H + T_C)/2$. Table 1 lists the properties of four different types of fibrous insulation that are commonly used in building and industrial applications. These samples, which present a good cross section of different types of fibrous insulations currently in use, were obtained from Owens-Corning Fiberglas Company (1986).

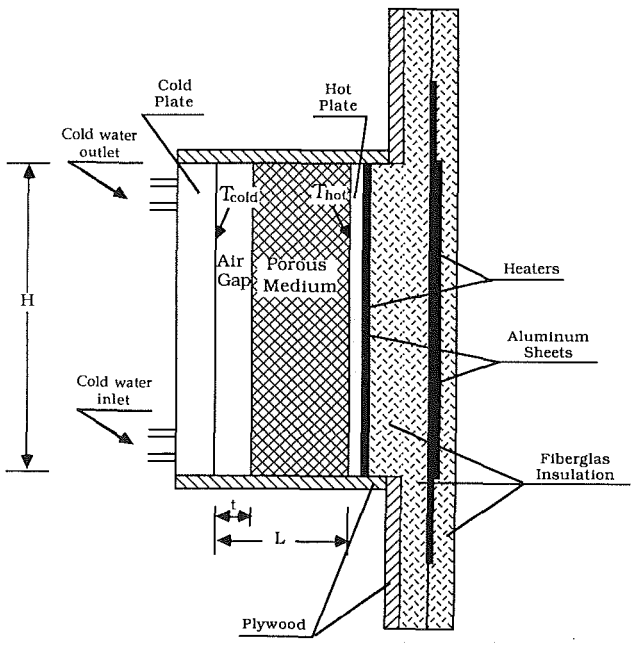

Fig. 1 Schematic diagram of the test section

3 Results and Discussion

3.1 Enclosure Totally Filled With Air. The first set of experiments was based on investigating heat transfer in an enclosure that contained only air. This set of experiments was used to benchmark our experimental results against the existing experimental data in this area. The agreement between the results obtained from this first set of experiments and the

Table 1 Characteristics of the fibrous insulation samples used in the experiments

	Type	Density	Permeability
Sample A	RA-24 insulation high-density wool	32 kg/m^3	1.8×10^{-9}m^2
Sample B	RA-22 insulation low-density board	43 kg/m^3	1.3×10^{-9}m^2
Sample C	R-11 Batt insulation low-density wool	10 kg/m^3	5.9×10^{-9}m^2
Sample D	Roof deck insulation high-density board	112 kg/m^3	4.9×10^{-10} m^2

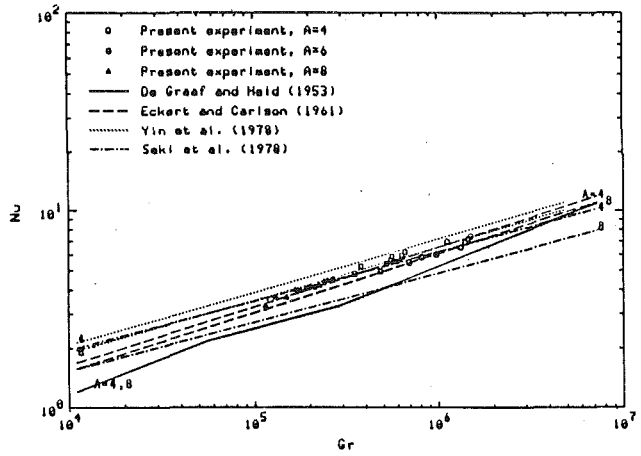

(a)

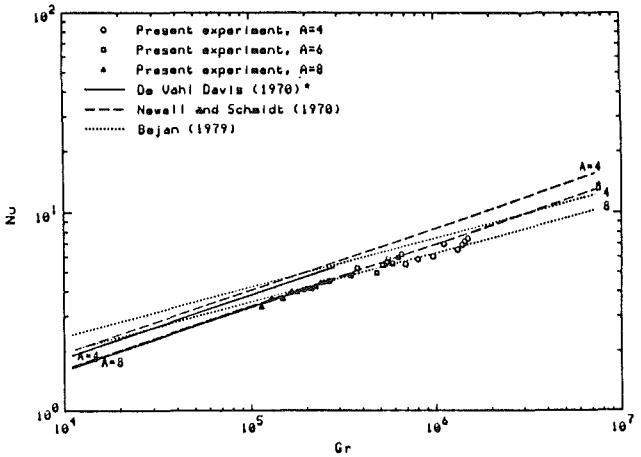

(b)

Fig. 2 Results for an unobstructed enclosure: (*a*) comparison of present experimental results with previous experimental investigations; (*b*) comparison of present experimental results with previous numerical and analytical investigations; *results presented by Landis and Rubel in Newell and Schmidt (1970)

previous experimental results was found to be quite good. These results are shown in Fig. 2, where Nu is plotted versus Gr_L for various values of the aspect ratio A. As can be seen in Fig. 2 the best agreements were with the analytical results of Bejan (1979) and with the experimental work of Eckert and Carlson (1961). In the Nusselt number calculations the radiation contribution was calculated and was subtracted from the overall heat transfer. The Nusselt number Nu and the Grashof number Gr_L, were defined respectively as

$$\mathrm{Nu} = \frac{\text{Total heat transfer}}{\text{Heat transfer by conduction when the cavity is totally filled with air}} = \frac{Q_{tot}L}{k_f A_c \Delta T} \quad (1)$$

$$\mathrm{Gr_L} = \frac{g\beta\Delta T L^3}{\nu_f^2} \quad (2)$$

where Q_{tot} is the total heat transfer into the test section. All of the earlier investigators except De Graaf and Van Der Held (1953) had found that the heat transfer is dependent on the aspect ratio A. De Graaf and Van Der Held found the aspect ratio to be an irrelevant parameter in the presentation of their results. In the present study it was observed that the heat transfer in air layers has a very weak dependence on A for $1\times10^5 < \mathrm{Gr_L} < 2\times10^6$, which constituted the range in which our experimental runs were performed. This observation was also noted by Yin et al. (1978), who found a weak dependence on the aspect ratio. In all of the reported experimental studies, different cold wall temperatures were used during the experiments. In this study it was noted that when a different cold wall temperature is used for the same Grashof number, the Nusselt number will increase or decrease somewhat depending on whether T_c has increased or decreased. The above fact could be partially responsible for some of the scatter observed in the experimental data that are available in the literature. Furthermore this fact could also explain why differences between experimental results were larger than differences between numerical and analytical results.

3.2 Enclosures Totally Filled With Insulation. Although this case has been investigated extensively, limited experimental studies have been reported in which fibrous insulation has been used as the porous matrix and air as the working fluid. The work of Seki et al. (1978b) is one of the very few studies addressing this problem. In most of the other previous investigations the test section was filled with either glass or metallic beads saturated with a liquid. The use of a liquid in these experiments would naturally lead to larger values of the Darcy-Rayleigh number. The range of the Darcy-Rayleigh numbers used in most of the prior experiments was approximately from 40 to 500. This range is very high compared to the actual range of $\mathrm{Ra_L^*}$ in fibrous insulation applications for buildings, which is usually somewhere between 0.1 and 1. A numerical solution by Tong and Subramanian (1986) dealt with such low values of $\mathrm{Ra_L^*}$; however, they assume an impermeable membrane between the porous medium and the neighboring fluid chamber. Furthermore, most of the numerical studies reported only cases with high values of $\mathrm{Ra_L^*}$. These numerical results were in turn used for comparison with those previous experimental results. Also in some previous investigations it was estimated, mainly by extrapolation, that for values of $\mathrm{Ra_L^*}$ below 20, conduction will be the dominant heat transfer mode. In the present investigation, it was found that there is still some convection present even for values of $\mathrm{Ra_L^*}$ below 1. Seki et al. (1978b) reported that there was convection at $\mathrm{Ra_L^*}=1$; however, below that range they found that conduction was dominant. In the present experiments results indicate greater heat transfer than by conduction alone. Since possible error due to heat losses was estimated to be less than 5 percent, any greater deviation had to have been due to convection. The discrepancy between the results of Seki et al. (1978b) and the present results is believed to be due mainly to the permeability values used in those investigations. To determine the permeability values of the fibrous insulation, Seki et al. used values of permeabilities that agreed with the results of the work of Castinel and Combarnous (1977), while in this paper the permeability values were determined by the Owens-Corning Fiberglas Company. The permeability values for samples A, B, and D used in this investigation, which were provided by O.C.F. (1986) for randomly oriented fibers, agreed with Bankvall's data (1978) for flow parallel to the fiber axis to within 3 percent. For sample C, the permeability value given by O.C.F. agreed with Bankvall's result for flow perpendicular to the fiber axis to within 1 percent. The permeability values reported by Castinel and Combarnous (1977) were four to five times larger than the ones reported by Bankvall (1978) or O.C.F. For instance, if Seki et al. used Bankvall's data for permeability, they would have concluded that there was convection at $\mathrm{Ra_L^*}=0.25$. Since most of the other investigators claimed that there is no significant convection for a small Darcy-Rayleigh number range, this paper along with that of Seki et al. is then among the very few that have reported the existence of convective currents at low $\mathrm{Ra_L^*}$.

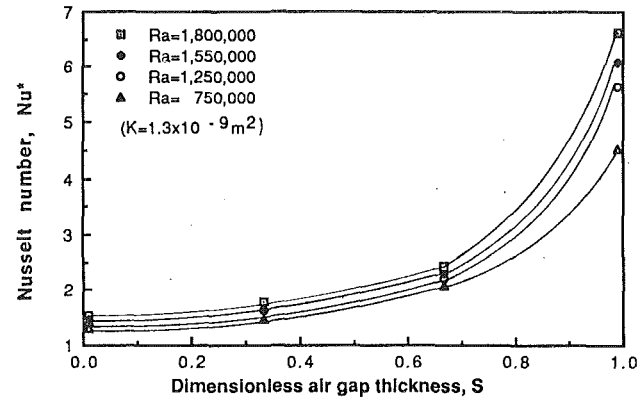

(a)

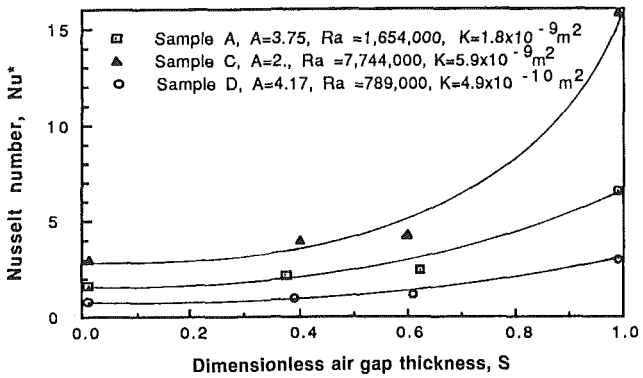

(b)

Fig. 3 Effects of the air layer thickness on the heat transfer rate across the enclosure: (*a*) sample B, $A = 4$; (*b*) samples A, C, and D

In the formation of the Nusselt number the radiation contribution was estimated using the work of Bankvall (1973) and was then subtracted from the overall heat transfer. Both the Nusselt number and the Darcy-Rayleigh number were formulated based on the effective thermal conductivity for the stagnant matrix-air system given by the following expression:

$$k_{\text{eff}} = \epsilon\, k_f + (1-\epsilon)k_s \tag{3}$$

The values of the porosity ϵ for samples A, B, C, and D were found to be 0.956, 0.967, 0.860, and 0.987, respectively. The values of the effective thermal conductivity for samples A, B, C, and D were 0.043, 0.049, 0.031, and 0.086 W/mK, respectively.

3.3 Partially Filled Enclosures. Here, the experiments were performed using four different Fiberglas insulations. The effects of the driving force (temperature difference) as well as the dimensionless thickness ratio S on the Nusselt number are illustrated in Fig. 3. We have also looked at the heat transfer in partial enclosures for the case where the air gap was separated from the porous matrix by an impermeable interface (by using aluminum foil). No measurable differences were obtained from those results where no impermeable interface was used. This is due to the presence of relatively small buoyancy forces. Since different air gap thicknesses were investigated, we had to come up with a consistent reference value for the nondimensionalization of the Nusselt numbers. For convenience this reference value was based on conduction heat transfer across an enclosure that has the same thickness, L, as the partially filled enclosure but is completely filled with the porous matrix. therefore, the Nusselt number used in Figs. 3 is as follows:

$$\text{Nu}^* = \frac{\text{Total heat transfer}}{\text{Heat transfer by conduction when the cavity is totally filled with insulation}} = \frac{Q_{\text{tot}} L}{k_{\text{eff}} A_c \Delta T} \tag{4}$$

Also to avoid defining a new effective thermal conductivity for the partially filled cavity, the regular Rayleigh number was used in presenting the results in Fig. 3. In presenting these results the radiation contribution was included in the total heat transfer. The reasons for inclusion of the radiation contribution in this part were twofold. First and foremost, since one of the aims of this investigation was to look at the feasibility of using partial insulations, it was therefore desirable to account for the total heat transfer rate, which is after all what counts in a practical situation for building insulation. Secondly, there was no reliable method available for calculating the radiation contribution in this case. It should be noted that for each type of fibrous insulation used in the present investigation, several samples with different thicknesses were used. This way in studying heat transfer in partial enclosures, different air gap ratios were created by using samples of the same type but different thicknesses.

It can be observed in Fig. 3(*a*), which shows the effect of the air layer thickness on the Nusselt number, that reducing the insulation thickness (and thereby increasing the air gap thickness) causes an increase in the total heat transfer rate. The increase in Nu was not very sharp for small air gap thicknesses. For example, the heat transfer rate increased by only 12 percent for a 34 percent decrease in insulation. For higher values of S the increase was more pronounced; for instance, for an increase in S from 0.34 to 0.66 the Nusselt number increased by about 37 percent. As expected, further reductions in the insulation thickness caused a sharp increase in the value of the Nusselt number. Figure 3(*b*) shows the same trends for samples A, C, and D as was seen in Fig. 3(*a*) for sample B.

The above results clarify two main objectives. First, for practical applications of the fibrous insulation in buildings, the possibility of actually reducing the heat transfer rate by using a partial insulation does not exist. Secondly, while the heat transfer rate certainly increases as soon as an air gap is introduced, for some circumstances, as can be seen in Fig. 3, there might be some benefits in reducing the insulation by as much as 1/3 at the expense of a modest increase in the heat transfer rate across the enclosure.

4 Conclusions

The results of an experimental investigation on heat transfer in an enclosure that is partially or fully filled with a fibrous insulation were presented. The experiments were tailored such that they reflect realistic situations under which these insulations are used in practice. The present experimental results were first compared with prior experimental and numerical results for the case of an unobstructed enclosure. The experimental results were then presented for two cases. The first case corresponded to an enclosure that was totally filled with insulation. The second case was for partially filled enclosures. Four different samples provided by the Owens-Corning Fiberglas Company were used in these investigations. Even though the case of a totally filled enclosure has been investigated in the past, very limited experimental studies have been reported in which fibrous insulation has been used as the porous matrix and air as the working fluid. This fact is very important, since the use of liquids in previous experiments produces Darcy-Rayleigh numbers that are much higher than any that can be associated with the use of fibrous insulations in realistic situations.

In the present investigation it was found that for values of

Ra_L^* below 1, there is still some convection in the enclosure. It was found that, at all times for all of the samples, reducing the insulation thickness and thereby increasing the air gap thickness causes a definite increase in the total heat transfer rate. However, for some circumstances there might be some benefits in reducing the insulation by as much as 1/3 at the expense of a modest increase in the heat transfer rate across the enclosure.

Acknowledgments

A grant from Owens Corning Fiberglas Company is gratefully acknowledged.

References

Bankvall, C., 1973, "Heat Transfer in Fibrous Materials," *Journal of Testing and Evaluation*, Vol. 1, No. 3, pp. 235–243.

Bankvall, C. G., 1978, "Natural Convective Heat Transfer in Permeable Insulation," *Thermal Transmission Measurements of Insulation*, American Society for Testing and Materials, pp. 73–81.

Bejan, A., 1979, "Note on Gill's Solution for Free Convection in a Vertical Enclosure," *Journal of Fluid Mechanics*, Vol. 90, Part 3, pp. 561–568.

Beckermann, C., Ramadhyani, S., and Viskanta, R., 1987, "Natural Convection Flow and Heat Transfer Between a Fluid Layer and a Porous Layer Inside a Rectangular Enclosure," ASME JOURNAL OF HEAT TRANSFER, Vol. 109, pp. 363–370.

Castinel, G., and Combarnous, M., 1977, "Natural Convection in an Anisotropic Porous Layer," *International Chemical Engineering*, Vol. 17, No. 4, pp. 605–612.

DeGraaf, J. G. A., and Van Der Held, E. F. M., 1953, "The Relation Between the Heat Transfer and the Convection Phenomena in Enclosed Plane Air Layers," *Applied Scientific Research*, Vol. 3, Section A, pp. 393–409.

Eckert, E. R. G., and Carlson, W. O., 1961, "Natural Convection in an Air Layer Enclosed Between Two Vertical Plates With Different Temperatures," *International Journal of Heat and Mass Transfer*, Vol. 2, pp. 106–120.

Holman, J. P., 1971, "Experimental Methods for Engineers," 2nd ed., McGraw-Hill-Kogakusha, p. 37.

Newell, M. E., and Schmidt, F. W., 1970, "Heat Transfer by Laminar Natural Convection within Rectangular Enclosures," ASME JOURNAL OF HEAT TRANSFER, Vol. 92, pp. 159–168.

Owens Corning Fiberglas Company, 1986, Internal Communications.

Sathe, S. B., Tong, T. W., and Faruque, M. A., 1987, "Experimental Study of Natural Convection in a Partially Porous Enclosure," *Journal of Thermophysics*, Vol. 1, No. 3, pp. 260–267.

Seki, N., Fukusako, S., and Inaba, H., 1978a, "Visual Observation of Natural Convective Flow in a Narrow Vertical Cavity," *Journal of Fluid Mechanics*, Vol. 84, Part 4, pp. 695–704.

Seki, N., Fukusako, S., and Inaba, H., 1978b, "Heat Transfer in a Cavity Packed With Fibrous Glass," ASME JOURNAL OF HEAT TRANSFER, Vol. 100, pp. 748–750.

Tong, T. W., and Subramanian, E., 1986, "Natural Convection in Rectangular Enclosures Partially Filled With a Porous Medium," *International Journal of Heat and Fluid Flow*, Vol. 7, No. 1, pp. 3–10.

Yin, S. H., Wung, T. Y., and Chen, K., 1978, "Natural Convection in an Air Layer Enclosed Within Rectangular Cavities," *International Journal of Heat and Mass Transfer*, Vol. 21, pp. 307–315.

Parallel-Flow and Counterflow Conjugate Convection in a Vertical Pipe

J. Libera[1] and D. Poulikakos[1]

Nomenclature

- A = dimensionless group, equation (20)
- B = dimensionless group, equation (6)
- c_{p1} = specific heat of pipe fluid
- g = acceleration of gravity
- h = heat transfer coefficient
- H = length of pipe
- k = thermal conductivity
- Nu = Nusselt number, equation (7)
- Pe = Peclet number, equation (8)
- Pr = Prandtl number
- q = heat flux perpendicular to flow direction
- R = radius of pipe
- Ra = Rayleigh number, equation (13)
- T = temperature
- u = reservoir velocity component in the x direction
- U = mean velocity of pipe fluid
- v = reservoir velocity component in the y direction
- x = coordinate parallel to flow direction
- y = coordinate perpendicular to flow direction
- α = thermal diffusivity of pipe fluid
- β = coefficient of thermal expansion
- θ = dimensionless temperature
- λ = Oseen function
- ν = kinematic viscosity
- ρ = fluid density

Subscripts

- $*$ = dimensional variable
- ∞ = reservoir condition far away from the pipe
- 1 = pipe fluid
- 2 = reservoir fluid
- c = cold
- i = inner surface of pipe
- o = outer surface of pipe
- w = pipe wall

1 Introduction

Conjugate heat transfer in general finds numerous applications in thermal engineering. It is because of this reason that conjugate heat transfer has been the main focal point of several investigations over the past few decades. Since convection is a common heat transfer mode, it is reasonable to expect that it often constitutes one of the two or more interweaving modes (mechanisms) in conjugate heat transfer applications. For example, Poulikakos (1986) studied theoretically the problem of natural convection along a vertical conductive wall coupled with film condensation on the other side of this wall. He determined the parametric domain over which the two phenomena (natural convection and condensation) seriously affected each other, as well as the overall heat transfer through the wall. In a related study, Poulikakos and Sura (1986) investigated the effect of condensation inside a vertical layer of insulation, and natural convection at the surface of the insulation. Faghri and Sparrow (1980) examined theoretically the coupling of condensation on a pipe and forced convection of a fluid inside the pipe. Also theoretical is the work of Bejan and Anderson (1980, 1983), who investigated the problem of natural convection along the impermeable interface of two fluid reservoirs and of a porous and a fluid reservoir, respectively. In the work of Bejan and Anderson the coupling was between two different counterflowing boundary layers.

The present paper investigates the problem of interaction (coupling) of forced convection inside a vertical pipe and natural convection outside the pipe. Both the cases of

[1]Department of Mechanical Engineering, University of Illinois at Chicago, Chicago, IL 60680.

Contributed by the Heat Transfer Division for publication in the JOURNAL OF HEAT TRANSFER. Manuscript received by the Heat Transfer Division November 22, 1988; revision received October 2, 1989. Keywords: Conjugate Heat Transfer, Heat Exchangers.

Ra_L^* below 1, there is still some convection in the enclosure. It was found that, at all times for all of the samples, reducing the insulation thickness and thereby increasing the air gap thickness causes a definite increase in the total heat transfer rate. However, for some circumstances there might be some benefits in reducing the insulation by as much as 1/3 at the expense of a modest increase in the heat transfer rate across the enclosure.

Acknowledgments

A grant from Owens Corning Fiberglas Company is gratefully acknowledged.

References

Bankvall, C., 1973, "Heat Transfer in Fibrous Materials," *Journal of Testing and Evaluation*, Vol. 1, No. 3, pp. 235–243.

Bankvall, C. G., 1978, "Natural Convective Heat Transfer in Permeable Insulation," *Thermal Transmission Measurements of Insulation*, American Society for Testing and Materials, pp. 73–81.

Bejan, A., 1979, "Note on Gill's Solution for Free Convection in a Vertical Enclosure," *Journal of Fluid Mechanics*, Vol. 90, Part 3, pp. 561–568.

Beckermann, C., Ramadhyani, S., and Viskanta, R., 1987, "Natural Convection Flow and Heat Transfer Between a Fluid Layer and a Porous Layer Inside a Rectangular Enclosure," ASME JOURNAL OF HEAT TRANSFER, Vol. 109, pp. 363–370.

Castinel, G., and Combarnous, M., 1977, "Natural Convection in an Anisotropic Porous Layer," *International Chemical Engineering*, Vol. 17, No. 4, pp. 605–612.

DeGraaf, J. G. A., and Van Der Held, E. F. M., 1953, "The Relation Between the Heat Transfer and the Convection Phenomena in Enclosed Plane Air Layers," *Applied Scientific Research*, Vol. 3, Section A, pp. 393–409.

Eckert, E. R. G., and Carlson, W. O., 1961, "Natural Convection in an Air Layer Enclosed Between Two Vertical Plates With Different Temperatures," *International Journal of Heat and Mass Transfer*, Vol. 2, pp. 106–120.

Holman, J. P., 1971, "Experimental Methods for Engineers," 2nd ed., McGraw-Hill-Kogakusha, p. 37.

Newell, M. E., and Schmidt, F. W., 1970, "Heat Transfer by Laminar Natural Convection within Rectangular Enclosures," ASME JOURNAL OF HEAT TRANSFER, Vol. 92, pp. 159–168.

Owens Corning Fiberglas Company, 1986, Internal Communications.

Sathe, S. B., Tong, T. W., and Faruque, M. A., 1987, "Experimental Study of Natural Convection in a Partially Porous Enclosure," *Journal of Thermophysics*, Vol. 1, No. 3, pp. 260–267.

Seki, N., Fukusako, S., and Inaba, H., 1978a, "Visual Observation of Natural Convective Flow in a Narrow Vertical Cavity," *Journal of Fluid Mechanics*, Vol. 84, Part 4, pp. 695–704.

Seki, N., Fukusako, S., and Inaba, H., 1978b, "Heat Transfer in a Cavity Packed With Fibrous Glass," ASME JOURNAL OF HEAT TRANSFER, Vol. 100, pp. 748–750.

Tong, T. W., and Subramanian, E., 1986, "Natural Convection in Rectangular Enclosures Partially Filled With a Porous Medium," *International Journal of Heat and Fluid Flow*, Vol. 7, No. 1, pp. 3–10.

Yin, S. H., Wung, T. Y., and Chen, K., 1978, "Natural Convection in an Air Layer Enclosed Within Rectangular Cavities," *International Journal of Heat and Mass Transfer*, Vol. 21, pp. 307–315.

Parallel-Flow and Counterflow Conjugate Convection in a Vertical Pipe

J. Libera[1] and D. Poulikakos[1]

Nomenclature

A = dimensionless group, equation (20)
B = dimensionless group, equation (6)
c_{p1} = specific heat of pipe fluid
g = acceleration of gravity
h = heat transfer coefficient
H = length of pipe
k = thermal conductivity
Nu = Nusselt number, equation (7)
Pe = Peclet number, equation (8)
Pr = Prandtl number
q = heat flux perpendicular to flow direction
R = radius of pipe
Ra = Rayleigh number, equation (13)
T = temperature
u = reservoir velocity component in the x direction
U = mean velocity of pipe fluid
v = reservoir velocity component in the y direction
x = coordinate parallel to flow direction
y = coordinate perpendicular to flow direction
α = thermal diffusivity of pipe fluid
β = coefficient of thermal expansion
θ = dimensionless temperature
λ = Oseen function
ν = kinematic viscosity
ρ = fluid density

Subscripts

$*$ = dimensional variable
∞ = reservoir condition far away from the pipe
1 = pipe fluid
2 = reservoir fluid
c = cold
i = inner surface of pipe
o = outer surface of pipe
w = pipe wall

1 Introduction

Conjugate heat transfer in general finds numerous applications in thermal engineering. It is because of this reason that conjugate heat transfer has been the main focal point of several investigations over the past few decades. Since convection is a common heat transfer mode, it is reasonable to expect that it often constitutes one of the two or more interweaving modes (mechanisms) in conjugate heat transfer applications. For example, Poulikakos (1986) studied theoretically the problem of natural convection along a vertical conductive wall coupled with film condensation on the other side of this wall. He determined the parametric domain over which the two phenomena (natural convection and condensation) seriously affected each other, as well as the overall heat transfer through the wall. In a related study, Poulikakos and Sura (1986) investigated the effect of condensation inside a vertical layer of insulation, and natural convection at the surface of the insulation. Faghri and Sparrow (1980) examined theoretically the coupling of condensation on a pipe and forced convection of a fluid inside the pipe. Also theoretical is the work of Bejan and Anderson (1980, 1983), who investigated the problem of natural convection along the impermeable interface of two fluid reservoirs and of a porous and a fluid reservoir, respectively. In the work of Bejan and Anderson the coupling was between two different counterflowing boundary layers.

The present paper investigates the problem of interaction (coupling) of forced convection inside a vertical pipe and natural convection outside the pipe. Both the cases of

[1]Department of Mechanical Engineering, University of Illinois at Chicago, Chicago, IL 60680.

Contributed by the Heat Transfer Division for publication in the JOURNAL OF HEAT TRANSFER. Manuscript received by the Heat Transfer Division November 22, 1988; revision received October 2, 1989. Keywords: Conjugate Heat Transfer, Heat Exchangers.

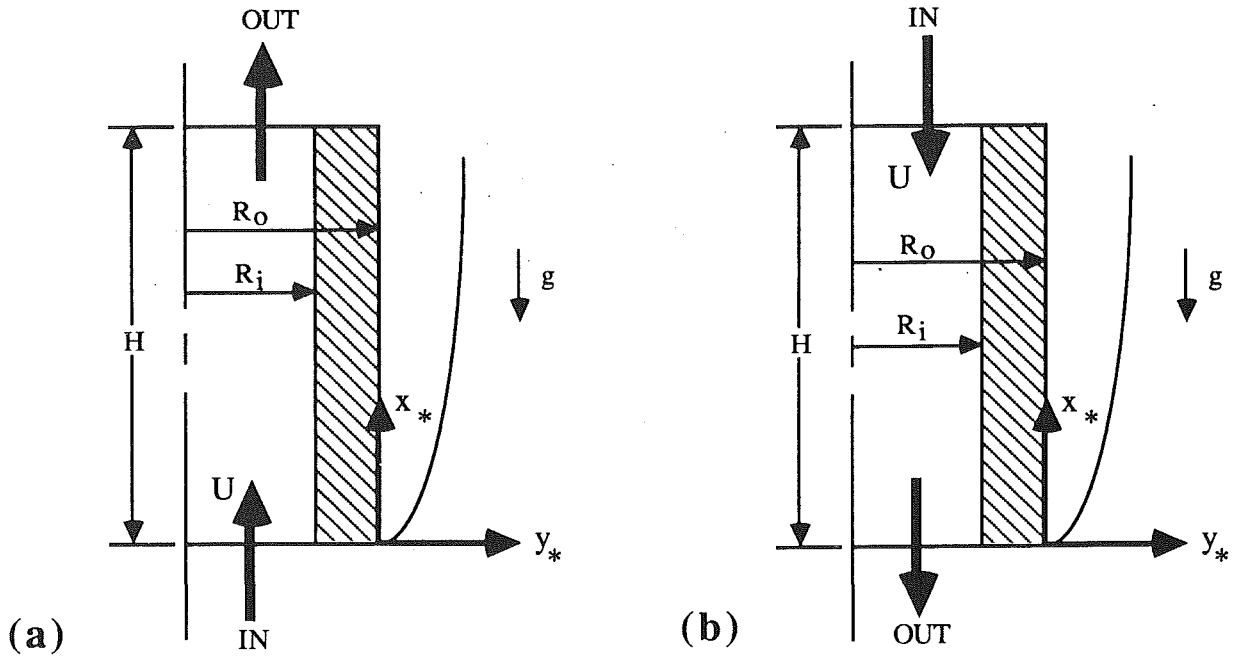

Fig. 1 Schematic of the system of interest: (*a*) cross section of the parallel-flow configuration; (*b*) cross section of the counterflow configuration

counterflow and parallel flow are considered. The problem finds applications in heat exchanger apparatuses of various types where a warm (cold) fluid is flowing inside a conductive pipe bathed in or surrounded by a colder (warmer) fluid. Clearly, the heat transfer through the pipe wall is a direct result of the interaction between the forced convection inside the pipe and the natural convection outside the pipe.

2 Formulation and Analysis

Consider the system shown in Fig. 1(*a*). A warm fluid is flowing inside a vertical conductive pipe opposite to the direction of gravity. The pipe is immersed in a reservoir of colder fluid. The heating effect of the forced convection in the pipe is responsible for the establishment of temperature gradients inside the reservoir. These gradients in turn trigger a natural convection flow in the direction opposite to gravity. Clearly, the temperature of the fluid in the pipe varies along the flow passage, and so does the wall temperature and the temperature difference across the natural convection current, which is assumed to be of the boundary layer type. Therefore, the local and overall heat transfer from the fluid in the pipe to the fluid in the reservoir depends on the aforementioned conjugate heat transfer mechanisms (natural convection and forced convection). Figure 1(*b*) pertains to the same phenomenon explained above with the difference that the fluid in the pipe and the fluid in the reservoir are flowing in the opposite direction (counterflow configuration).

A paper related to the parallel-flow part of the present study has been published by Sparrow and Faghri (1980). This paper was brought to our attention by an anonymous reviewer. It is important to state clearly the differences between our work and that of Sparrow and Faghri (1980). First, our work pertains to turbulent flow in the pipe. Since we are dealing with turbulent flow in the pipe, we assume that the inner heat transfer coefficient of the pipe is approximately constant, as also discussed by Faghri and Sparrow (1980). On the other hand, Sparrow and Faghri (1980) consider the case of hydrodynamically fully developed but thermally developing laminar flow in the pipe and obtain the heat transfer coefficient at the inner pipe wall as part of their solution. Note that for laminar flow, because of the considerable extent of the entrance region, assuming that the inner heat transfer coefficient is constant is not as good an approximation as it is for turbulent flow. Second, in our work, we account for the thermal resistance of the pipe wall, which was neglected for simplicity in the work of Sparrow and Faghri. Third, we consider both the parallel-flow and counterflow configurations while Sparrow and Faghri focus on the former. Fourth, our solution is based on the linearization method proposed by Gill (1966), while Sparrow and Faghri use finite differencing of the governing partial differential equations. Fifth, Sparrow and Faghri (1980) are interested in the local heat transfer coefficient and present their results in terms of the local Nusselt number. The present paper, on the other hand, documents the dependence of the overall heat transfer coefficient (Nusselt number) on problem parameters. Because of the above differences, no direct quantitative comparisons between the two studies are possible.

To formulate the problem mathematically, we will focus first on the forced convection side, and next on the natural convection side of the parallel-flow configuration in Fig. 1(*a*).

Forced Convection Inside the Pipe. At any axial position the heat transfer rate from the forced convection side through the pipe wall to the natural convection side is

$$dq = \frac{2\pi k_w}{\ln(R_i/R_o)} (T_{w_i} - T_{w_o}) dx_* \tag{1}$$

The heat transfer rate convected to the inner surface of the pipe over a length dx_* is

$$dq = 2\pi R_i h_i (T_1 - T_{w_i}) dx_* \tag{2}$$

Next, stating that the heat transfer rate leaving a volume of fluid of length dx_* in the pipe equals the heat transfer rate convected to the inner surface of the pipe of length dx_* yields

$$m_1 c_{p1} \frac{dT_1}{dx_*} dx_* = 2\pi R_i h_i (T_1 - T_{w_i}) dx_* \tag{3}$$

In the formulation above, the axial conduction in the fluid and the pipe wall have been neglected as customarily done in pipe flow analyses. Neglecting the axial conduction through the pipe wall is justified, for example, when the length of the pipe is considerably larger than the thickness of the pipe. Such is the case in many practical applications. Clearly, the accuracy of the predictions of the present model will deteriorate if the axial conduction through the pipe wall becomes important. In addition, the turbulent heat transfer coefficient for pipe flow, h_i, is assumed constant because of the fact that for turbulent pipe flows the thermal entrance length is very short and the coefficient is rather insensitive to the thermal boundary condition at the wall (Faghri and Sparrow, 1980). The above stated assumption is not recommended for laminar pipe flow. Therefore, the results of the present study are pertinent to turbulent flow in the pipe. All of the quantities in equations (1)-(3) as well as in all the equations to follow are clearly defined in the nomenclature. Eliminating T_{w_i} from equations (1)-(3) and casting the resulting equation in dimensionless form yields

$$\frac{d\theta_1}{dx} = -B(\theta_1 - \theta_0) \tag{4}$$

The nondimensionalization was carried out utilizing the following definitions:

$$x = \frac{x_*}{H}, \qquad \theta_1 = \frac{T_1 - T_c}{T_{1_i} - T_c}, \qquad \theta_0 = \frac{T_{w_o} - T_c}{T_{1_i} - T_c} \tag{5}$$

A dimensionless group appeared as a result of the nondimensionalization

$$B = \left[\mathrm{Pe}\left(\frac{R_i}{2H\mathrm{Nu}_i} + \frac{R_i}{4H}\,\frac{k_1}{k_w}\ln(R_o/R_i)\right)\right]^{-1} \tag{6}$$

In equation (6) the Nusselt and the Peclet numbers are defined as

$$\mathrm{Nu}_i = \frac{2h_iR_i}{k_1} \tag{7}$$

$$\mathrm{Pe} = \frac{2UR_i}{\alpha_1} \tag{8}$$

Note that the definition of group B is rather complex and its physical meaning is not straightforward to deduce. By inspection of equation (6) it appears that B is inversely proportional to both the Peclet number and the thermal resistance between the fluid in the pipe and the outer surface of the pipe.

Natural Convection in the Reservoir. The pertinent dimensionless boundary boundary layer equations for the natural convection side of the system shown in Fig. 1 are (Poulikakos, 1986; Bejan and Anderson, 1980, 1983)

$$\frac{\partial u}{\partial x} + \frac{\partial v}{\partial y} = 0 \tag{9}$$

$$\frac{1}{\mathrm{Pr}}\,\frac{\partial}{\partial y}\left(u\,\frac{\partial u}{\partial x} + v\,\frac{\partial u}{\partial y}\right) = \frac{\partial^3 u}{\partial y^3} + \frac{\partial \theta_2}{\partial y} \tag{10}$$

$$u\,\frac{\partial \theta_2}{\partial x} + v\,\frac{\partial \theta_2}{\partial y} = \frac{\partial^2 \theta_2}{\partial y^2} \tag{11}$$

In writing equations (9)-(11) it was assumed that the natural convection boundary layer is thin compared to the outer diameter of the pipe. Therefore, curvature effects were neglected and the governing equations were written in Cartesian coordinates. For the nondimensionalization, the following definitions were used in addition to those already defined in equation (5)

$$y = \frac{y_*}{H\mathrm{Ra}^{-1/4}}, \qquad u = \frac{u_*}{\alpha_2 H/(H\mathrm{Ra}^{-1/4})^2}, \quad v = \frac{v_*}{\alpha_2/(H\mathrm{Ra}^{-1/4})}$$

$$\theta_2 = \frac{T_2 - T_c}{T_{1_i} - T_c}. \tag{12}$$

where

$$\mathrm{Ra} = \frac{g\beta_2(T_{1_i} - T_c)H^3}{\nu_2\alpha_2} \tag{13}$$

is the Rayleigh number based on the pipe height H, and the temperature difference between the pipe fluid inlet temperature and the reservoir temperature far from the pipe, $T_{w_i} - T_c$. The above nondimensionalization was based on boundary layer scaling. Note that the boundary layer thickness scale ($\delta \sim H\mathrm{Ra}^{-1/4}$) was used as the reference for the horizontal coordinate y_*. Note further that in order to arrive at equation (10), the pressure gradients in the horizontal and vertical momentum equations were eliminated and that the Boussinesq approximation was utilized. According to the Boussinesq approximation, the density of the fluid is constant everywhere except in the buoyancy term of the momentum equation where it depends linearly on the temperature ($\rho = \rho_c[1 - \beta(T_2 - T_c)]$). The boundary conditions for the natural convection side are

$$y = 0, \quad u = 0, \quad v = 0, \quad \theta_2 = \theta_0(x)$$

$$y \to \infty \quad u = 0, \quad \theta_2 = 0 \tag{14}$$

As mentioned earlier, the wall temperature variation with x is unknown as it is dictated by the degree of coupling of the two sides.

To obtain solutions for the natural convection side we follow the Oseen linearization procedure used first by Gill (1966) in natural convection analysis. No details are shown here for brevity. All the details are reported in references such as Poulikakos (1986), Poulikakos and Sura (1986), Bejan and Anderson (1983), and Libera (1989). The final expressions for the temperature and velocity distributions read

$$u = \frac{\theta_0}{2\lambda}\,e^{-\lambda y}\sin\lambda y \tag{15}$$

$$\theta_2 = \theta_0 e^{-\lambda y}\cos\lambda y \tag{16}$$

where λ is an unknown function of x connected to θ_0 by the following equation:

$$\frac{d}{dx}\left(\frac{\theta_o^2}{16\lambda^3}\right) - \lambda\theta_o = 0 \tag{17}$$

To complete the analysis we invoke the heat flux matching condition through the outer surface of the pipe

$$\frac{2\pi k_w dx_*}{\ln(R_o/R_i)}\,(T_{w_i} - T_{w_o}) = -2\pi R_o dx_* k_2\left(\frac{\partial T_2}{\partial y_*}\right)_{y_*=0} \tag{18}$$

Eliminating T_{w_i} from equation (18) using equations (1) and (2) and casting the result into dimensionless form yields

$$\frac{1}{A}\,(\theta_1 - \theta_0) = \lambda\theta_0 \tag{19}$$

where we have introduced a second dimensionless group A defined as

$$A = \left(\frac{4R_0}{R_i}\,\frac{k_2}{k_1}\,\mathrm{Ra}^{-1/4}\right)\left[\frac{R_i}{2H\mathrm{Nu}_i} + \frac{R_i}{4Hk_w}\ln\left(\frac{R_o}{R_i}\right)\right] \tag{20}$$

As in the case of group B, the physical meaning of group A is not straightforward to deduce because it depends on several factors. Group A is proportional to the thermal resistance between the pipe fluid and the outer pipe wall, as well as the ratio of the thermal conductivity of the reservoir fluid to that of the

pipe fluid. In addition, group A is inversely proportional to the Rayleigh number raised to the one fourth power. If the flow in the pipe is fixed, small values of A represent the existence of strong natural convection flow in the surroundings. As A increases the natural convection flow weakens. Combining equations (4), (17), and (19) yields

$$\frac{d\theta_0}{dx} = -B\frac{\theta_0(\theta_1-\theta_0)}{(5\theta_1-2\theta_0)} + \frac{16}{A^4}\frac{(\theta_1-\theta_0)^5}{\theta_0^4(5\theta_1-2\theta_0)} \tag{21}$$

We now have attained a relationship between θ_0 and θ_1 in terms a set of two first-order nonlinear differential equations (4) and (21). The dimensionless boundary conditions necessary to complete the problem formulation are

$$\text{at } x=0 \quad \theta_0=0, \quad \theta_1=1 \tag{22}$$

The system of equations (4), (21), and (22) was solved numerically yielding $\theta_0(x)$ and $\theta_1(x)$. For the numerical solution the fourth-order Runge-Kutta method was used. However, inspecting the right-hand side of equation (21) shows that the second term has a singularity for $\theta_0=0$. To deal with this situation, a very small value of θ_0 was used to approximate zero. Regarding the increments in x, it was found necessary to begin the integration with an x increment as small as $\Delta x=10^{-10}$. As the value of θ_0 increased, the effects of the singularity on the stability of the integration process disappeared and the value of the x increment was increased to speed up the integration process.

The analysis for the counterflow configuration is nearly identical to that of the parallel-flow configuration, the only difference being the addition of a minus sign on the left-hand side of the equation (3). As a result, in the dimensionless equations (4) and (21), the parameter B needs to be replaced by $-B$ to obtain the equations for θ_0 and θ_1 in the counterflow case. The boundary conditions for the counterflow case are

$$x=0, \qquad \theta_0=0$$

$$x=1, \qquad \theta_1=1 \tag{23}$$

To start the numerical integration, two boundary conditions are needed at one x position. However, equation (23) provides us with one boundary condition at each end of the interval. This necessitates the use of a shooting scheme. The value of θ_0 at $x=1$ was guessed and the integration was performed starting from $x=1$ and proceeding to $x=0$. The value of θ_0 was checked and the process was repeated by adjusting the guessed value of $\theta_0(1)$ until condition (23) for θ_0 was satisfied. It was found that 1000 equal increments of x between 0 and 1 were sufficient to provide accurate results in the integration.

3 Results and Discussion

The main results document the effect of the two dimensionless groups of the problem, A and B, on the temperature field and the heat transfer through the pipe. Figure 2(*a*) pertains to the counterflow case and shows the variation of the mean temperature of the fluid in the pipe (θ_1) as well as the variation of the temperature of the outer surface of the pipe (θ_0) with the distance (x), for characteristic values of B. As we move from the pipe inlet ($x=1$) to the pipe exit ($x=0$), θ_1 decreases monotonically. This decrease becomes drastic as the parameter B increases. On the other hand, as B decreases, the dependence of θ_1 on x weakens up to the point where for $B\sim 0.01$, the mean temperature of the fluid in the pipe is practically independent of x and equal to the inlet temperature. By examining equations (6) and (20) one realizes that decreasing B while keeping A constant is equivalent to increasing the Peclet number or the flow rate in the pipe while keeping all of the remaining parameters constant. Increasing the flow rate is then responsible for the reduction of the drop in the fluid temperature along the pipe.

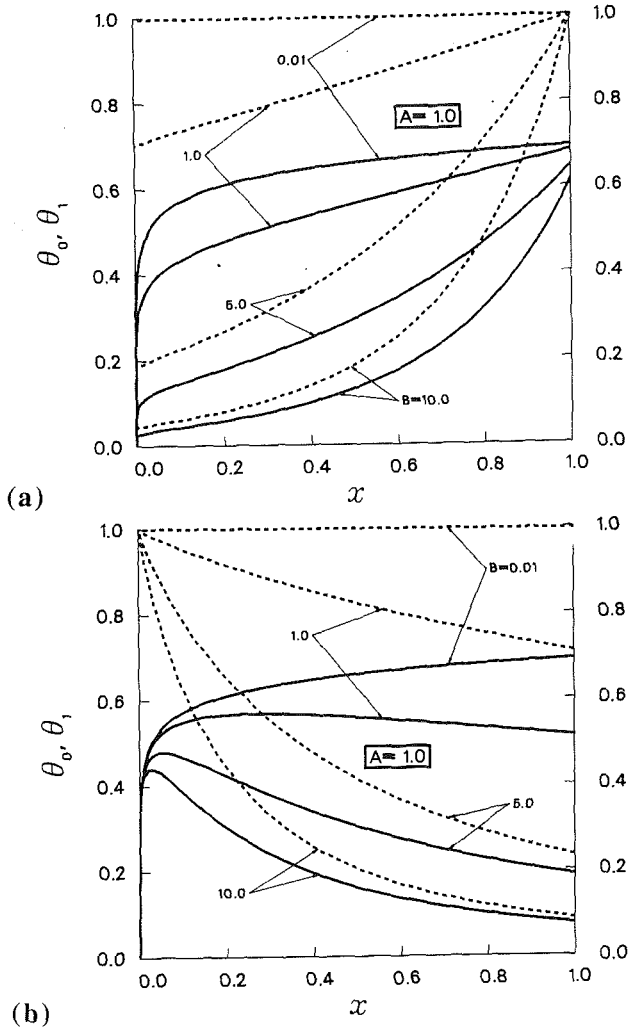

Fig. 2 Temperature profiles for $\theta_0(x)$_____, and $\theta_1(x)$----for characteristic values of B: (*a*) counterflow, (*b*) parallel flow

The wall temperature θ_0 decreases monotonically from inlet to outlet (Fig. 2*a*). As B decreases, the wall temperature increases rapidly (exponentially) over a small distance near the pipe exit ($x=0$) and weakly thereafter. The local temperature difference between the mean fluid temperature in the pipe (θ_1) and the outer wall temperature (θ_0) increases at any x as the parameter B decreases. Therefore, the local heat transfer is expected to increase with decreasing parameter B.

Figure 2(*b*) shows the effect of parameter B for the parallel-flow case. All the observations made above regarding the counterflow case are valid here as well and will not be repeated for brevity. A new feature however, is that the dependence of θ_0 on x is not monotonic, i.e., θ_0 increases as we move away from the inlet, attains a maximum value, and thereafter decreases. This maximum occurs closer to the inlet as the value of B decreases. The reason for the existence of the maximum of θ_0 is that the temperature of the outer wall surface has to increase initially to respond to the heating effect of the fluid in the pipe. As we move downstream, the fluid in the pipe gradually loses its energy, until at "infinity" it attains the temperature of the cold reservoir ($\theta_1=0$). Naturally, the temperature of the pipe wall also shows this trend by starting to decrease until very far from the inlet it also approaches the reservoir temperature.

Figure 3 illustrates the effect of the parameter A. In the counterflow case (Fig. 3*a*), increasing A decreases both the mean fluid temperature (θ_1) and the wall temperature (θ_0) at

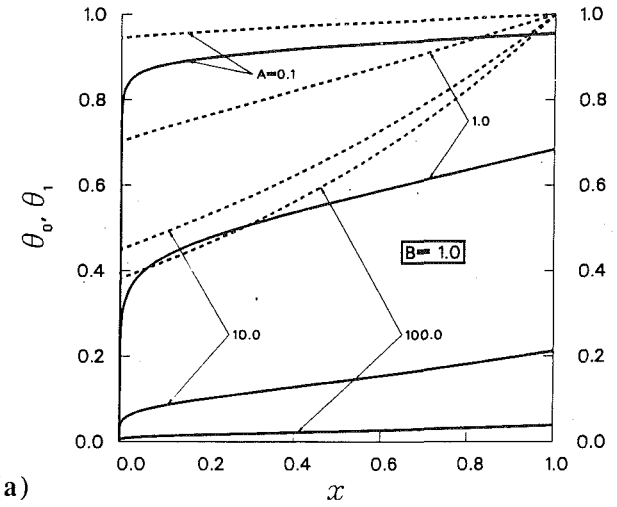

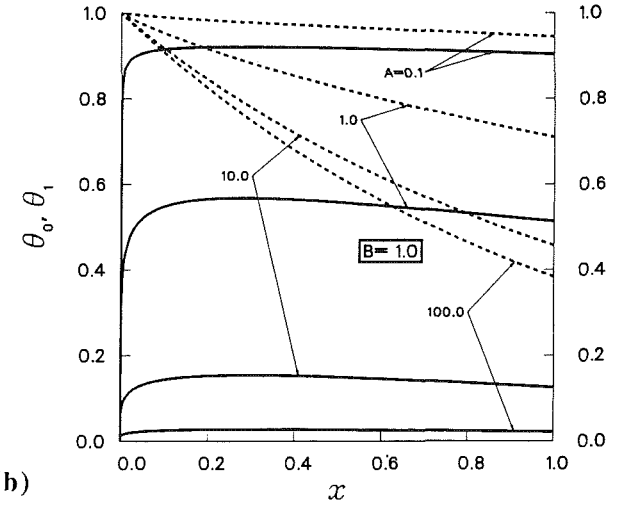

Fig. 3 Temperature profiles for $\theta_0(x)$_____, and $\theta_1(x)$----for characteristic values of A: (*a*) counterflow, (*b*) parallel flow

any given location. As A approaches zero, both θ_0 and θ_1 become constant, retaining the value $\theta_1 = 1$. From equations (6) and (20) we see that decreasing parameter A while keeping B constant is equivalent to decreasing the ratio k_2/k_1 or the conductivity of the naturally convecting fluid, thus explaining the observed trend. Similar observations are made in Fig. 3(*b*) relevant to the parallel-flow case. The maxima on the θ_0 curves, discussed earlier with reference to Fig. 2(*b*), are again observed. Decreasing A gradually renders both θ_0 and θ_1 practically constant.

It is of engineering interest to calculate the effect of both the dimensionless groups in the problem (A and B) on the overall heat flux from the pipe to the surrounding fluid. This is achieved with help of the overall Nusselt number

$$\mathrm{Nu} = \frac{h_o H}{k_2} \tag{24}$$

where the average outer heat transfer coefficient h_o is defined by

$$h_o = \frac{1}{H}\int_0^H \frac{-k_2\left(\frac{\partial T_2}{\partial y_*}\right)_{y_*=0}}{(T_0 - T_c)}\, dx_* \tag{25}$$

In dimensionless form, after combining equations (24) and (25) the expression for the Nusselt number is

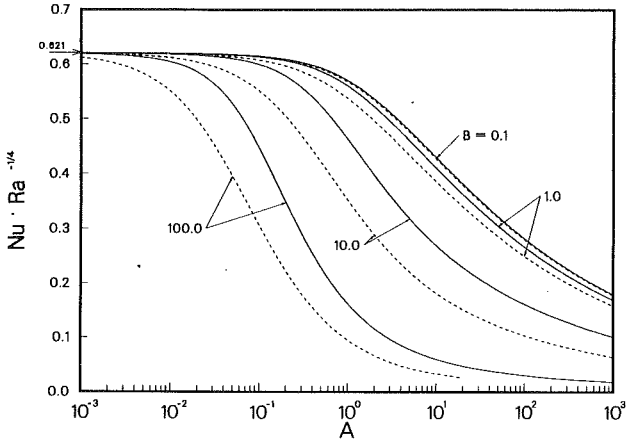

Fig. 4 Heat transfer results showing the dependence of Nu on the parameters A and B for both counterflow _____ and parallel flow----

$$\mathrm{Nu} = \frac{\mathrm{Ra}^{1/4}}{A}\int_0^1 \frac{(\theta_1 - \theta_0)}{\theta_0}\, dx \tag{26}$$

After $\theta_0(x)$ and $\theta_1(x)$ were obtained, equation (26) was integrated numerically to yield the value of Nu.

Figure 4 shows that Nu decreases as the parameter A increases. As A approaches zero, the value $\mathrm{Nu} = 0.621\ \mathrm{Ra}^{1/4}$ is attained in both the parallel and counterflow cases for all values of B. This value corresponds to natural convection from an isothermal flat plate (Poulikakos, 1986; Bejan and Anderson, 1980, 1983) and is consistent with the earlier observation that the outer wall temperature approaches a constant value as the parameter A becomes small. The trend of the results in Fig. 4 also shows the other extreme of the value of Nu, namely, as A approaches infinity, Nu approaches zero, indicating that the overall heat flux through the wall diminishes. The very definition of parameter A (equation (20)) offers an explanation for this fact. Increasing A can be obtained, for example, by decreasing the wall thermal conductivity or the outer radius R_o (and therefore the thickness, if R_i is fixed) of the pipe. In both cases, the expected result is a decrease in thermal communication between the warm and the cold side. The thermal communication ceases to exist as A becomes infinity. Hence, the heat transfer through the wall (Nu) becomes zero. In summary, the heat transfer results in Fig. 4 feature two limits: an upper limit corresponding to natural convection from a vertical wall and a lower limit corresponding to an insulated wall (zero heat transfer though the wall).

In all cases the counterflow configuration yields a higher overall heat flux than the parallel-flow configuration. This effect, however, weakens as the parameter B decreases, such that for values of $B < 0.1$ the overall heat transfer through the pipe is identical for both cases. Note that decreasing B while keeping A constant is equivalent to increasing the flow rate in the pipe.

4 Conclusions

In this technical note a simple yet reliable analysis was presented for the problem of counterflow and parallel-flow convection in a vertical pipe immersed in a fluid reservoir. Important results were found revealing interesting features of the temperature distribution of the pipe outer surface, of the mean fluid temperature in the pipe, and of the overall heat flux from the pipe to the fluid reservoir. As the values of parameters A and B approach zero, the outer pipe surface approached an isothermal condition. A maximum was observed in the θ_0 distribution in the parallel-flow case. This maximum is more pronounced and occurs closer to the pipe inlet for larger values of B.

The overall heat flux through the pipe reaches a plateau as A decreases. This plateau corresponds to natural convection from an isothermal vertical wall. The counterflow configuration yields higher overall heat transfer than for the parallel-flow configuration. This feature diminishes as the pipe flow rate is increased (or the parameter B is decreased).

Finally, Fig. 4 illustrates the usefulness (from the standpoint of a thermal engineering application) of the formulation of the problem that resulted in the two dimensionless groups, A and B. These groups are not as easy to interpret physically as, for instance, a ratio of thermal conductivities or diameters, but they are the sole reason why we are able to present the heat transfer results in a compact and easy-to-use manner (a single figure). Clearly, for any combination of fluids, pipe geometry and pipe material, the values of the parameters A and B can be evaluated from equations (6) and (20) and used in Fig. 4 to provide directly the overall heat transfer (leak) from the pipe to the reservoir. In alternative formulations, numerous figures, each of limited applicability, would be required to show the effects of the various physical parameters contained in the "aggregate" groups A and B.

Acknowledgments

Support for the authors while this research was conducted was provided by the National Science Foundation and by the Microswitch Division of the Honeywell Co.

References

Bejan, A., and Anderson, R., 1980, "Heat Transfer Across a Vertical Impermeable Partition Imbedded in Porous Medium," *International Journal of Heat and Mass Transfer*, Vol. 24, pp. 1237–1245.

Bejan, A., and Anderson, R., 1983, "Natural Convection at the Interface Between a Vertical Porous Layer and an Open Space," ASME JOURNAL OF HEAT TRANSFER, Vol. 105, pp. 124–129.

Faghri, M., and Sparrow, E. M., 1980, "Parallel-Flow and Counter-Flow Condensation on an Internally Cooled Vertical Tube," *International Journal of Heat and Mass Transfer*, Vol. 23, pp. 559–562.

Gill, A. E., 1966, "The Boundary-Layer Regime for Convection in a Rectangular Cavity," *Journal of Fluid Mechanics*, Vol. 26, pp. 515–536.

Libera, J., 1989, "Parallel-Flow and Counter-Flow Conjugate Convection From a Vertical Pipe," M.S. Thesis, University of Illinois at Chicago.

Poulikakos, D., 1986, "Interaction Between Film Condensation on One Side of a Vertical Wall and Natural Convection on the Other Side," ASME JOURNAL OF HEAT TRANSFER, Vol. 108, pp. 560–566.

Poulikakos, D., and Sura, P., 1986, "Conjugate Film Condensation and Natural Convection Along the Interface Between a Porous and an Open Space," *International Journal of Heat and Mass Transfer*, Vol. 29, pp. 1747–1758.

Sparrow, E. M., and Faghri, M., 1980, "Fluid-to-Fluid Conjugate Heat Transfer for a Vertical Pipe—Internal Forced Convection and External Natural Convection," ASME JOURNAL OF HEAT TRANSFER, Vol. 102, pp. 402–407.

A Computational and Experimental Study of Natural Convection and Surface/Gas Radiation Interactions in a Square Cavity

T. Fusegi[1,2] and B. Farouk[1]

Introduction

Interaction of natural convection and radiation within enclosures occurs in various thermal engineering systems. The analysis, however, requires considerable computational effort, particularly with gas radiation due to its integro-differential nature. Exact treatment of the convection–radiation interaction is not practical and engineering analysis must resort to approximate methods for the radiative transfer equation and nongray gas radiation models (Yang, 1986). In addition to being accurate, a desirable method should be compatible with flow field prediction methods. These considerations may be fulfilled with the spherical harmonics (P_N) differential approximation method, which converts the radiative transfer equation for the intensity to a set of differential equations for moments of the intensity. To handle nongray gas radiation efficiently, the Weighted Sum of Gray Gas model can be incorporated into the P_N method. Song and Viskanta (1987) have studied turbulent interactions of flow and radiation in a furnace by employing the first-order (P_1) approximation method with the WSGG model. The method has satisfactorily predicted field characteristics in the flow domain filled with nongray combustion gas mixtures.

Interactions of natural convection and surface/gas radiation in a nongray gas filled square cavity are investigated in the present paper, both computationally and experimentally. A schematic of the cross sectional view of the cavity is depicted in Fig. 1. The cavity is heated from the isothermal side wall located at $x = H$, which is maintained at a temperature of T_H, and cooled from the opposing side wall with a temperature T_C located at $x = 0$. All the interior surfaces are assumed to be nonslip and radiatively black for the computations. Various thermal boundary conditions are specified for the horizontal walls. Carbon dioxide gas is considered as the medium.

The overheat ratio δ (defined as $(T_H - T_C)/T_o$, where T_o is the reference film temperature, $(T_C + T_H)/2$) has been limited to small values ($\delta < 0.2$) in the experimental study of natural convection–radiation interactions in the past (Kurosaki et al., 1982). In the present investigation, significantly higher values of δ are used in the computations and experiments.

Computational Study

The governing equations consist of the variable-property Navier–Stokes and energy conservation equations along with the transfer equation for the radiative intensity (Fusegi and Farouk, 1989). The last equation is replaced with a set of differential equations for the irradiance of component gray gases by applying the P_1-approximation method and the WSGG model. Three component gray gases are considered to characterize the radiative properties of carbon dioxide, following Smith et al. (1982). Since the complete governing equations can be found elsewhere (Fusegi, 1988; Fusegi and Farouk, 1989), they are not repeated here. It suffices to mention that all the governing equations can be cast in the following general equation form:

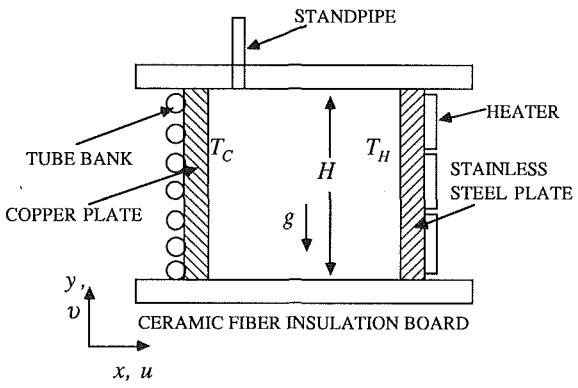

Fig. 1 Cross-sectional view of the test section

[1]Department of Mechanical Engineering and Mechanics, Drexel University, Philadelphia, PA 19104.

[2]Present address: Institute of Computational Fluid Dynamics, 1-22-3, Haramachi, Meguro-ku, Tokyo 152, Japan.

Contributed by the Heat Transfer Division for publication in the JOURNAL OF HEAT TRANSFER. Manuscript received by the Heat Transfer Division March 13, 1989; revision received November 29, 1989. Keywords: Enclosure Flows, Natural Convection, Radiation Interactions.

The overall heat flux through the pipe reaches a plateau as A decreases. This plateau corresponds to natural convection from an isothermal vertical wall. The counterflow configuration yields higher overall heat transfer than for the parallel-flow configuration. This feature diminishes as the pipe flow rate is increased (or the parameter B is decreased).

Finally, Fig. 4 illustrates the usefulness (from the standpoint of a thermal engineering application) of the formulation of the problem that resulted in the two dimensionless groups, A and B. These groups are not as easy to interpret physically as, for instance, a ratio of thermal conductivities or diameters, but they are the sole reason why we are able to present the heat transfer results in a compact and easy-to-use manner (a single figure). Clearly, for any combination of fluids, pipe geometry and pipe material, the values of the parameters A and B can be evaluated from equations (6) and (20) and used in Fig. 4 to provide directly the overall heat transfer (leak) from the pipe to the reservoir. In alternative formulations, numerous figures, each of limited applicability, would be required to show the effects of the various physical parameters contained in the "aggregate" groups A and B.

Acknowledgments

Support for the authors while this research was conducted was provided by the National Science Foundation and by the Microswitch Division of the Honeywell Co.

References

Bejan, A., and Anderson, R., 1980, "Heat Transfer Across a Vertical Impermeable Partition Imbedded in Porous Medium," *International Journal of Heat and Mass Transfer*, Vol. 24, pp. 1237–1245.

Bejan, A., and Anderson, R., 1983, "Natural Convection at the Interface Between a Vertical Porous Layer and an Open Space," ASME JOURNAL OF HEAT TRANSFER, Vol. 105, pp. 124–129.

Faghri, M., and Sparrow, E. M., 1980, "Parallel-Flow and Counter-Flow Condensation on an Internally Cooled Vertical Tube," *International Journal of Heat and Mass Transfer*, Vol. 23, pp. 559–562.

Gill, A. E., 1966, "The Boundary-Layer Regime for Convection in a Rectangular Cavity," *Journal of Fluid Mechanics*, Vol. 26, pp. 515–536.

Libera, J., 1989, "Parallel-Flow and Counter-Flow Conjugate Convection From a Vertical Pipe," M.S. Thesis, University of Illinois at Chicago.

Poulikakos, D., 1986, "Interaction Between Film Condensation on One Side of a Vertical Wall and Natural Convection on the Other Side," ASME JOURNAL OF HEAT TRANSFER, Vol. 108, pp. 560–566.

Poulikakos, D., and Sura, P., 1986, "Conjugate Film Condensation and Natural Convection Along the Interface Between a Porous and an Open Space," *International Journal of Heat and Mass Transfer*, Vol. 29, pp. 1747–1758.

Sparrow, E. M., and Faghri, M., 1980, "Fluid-to-Fluid Conjugate Heat Transfer for a Vertical Pipe—Internal Forced Convection and External Natural Convection," ASME JOURNAL OF HEAT TRANSFER, Vol. 102, pp. 402–407.

A Computational and Experimental Study of Natural Convection and Surface/Gas Radiation Interactions in a Square Cavity

T. Fusegi[1,2] and B. Farouk[1]

Introduction

Interaction of natural convection and radiation within enclosures occurs in various thermal engineering systems. The analysis, however, requires considerable computational effort, particularly with gas radiation due to its integro-differential nature. Exact treatment of the convection–radiation interaction is not practical and engineering analysis must resort to approximate methods for the radiative transfer equation and nongray gas radiation models (Yang, 1986). In addition to being accurate, a desirable method should be compatible with flow field prediction methods. These considerations may be fulfilled with the spherical harmonics (P_N) differential approximation method, which converts the radiative transfer equation for the intensity to a set of differential equations for moments of the intensity. To handle nongray gas radiation efficiently, the Weighted Sum of Gray Gas model can be incorporated into the P_N method. Song and Viskanta (1987) have studied turbulent interactions of flow and radiation in a furnace by employing the first-order (P_1) approximation method with the WSGG model. The method has satisfactorily predicted field characteristics in the flow domain filled with nongray combustion gas mixtures.

Interactions of natural convection and surface/gas radiation in a nongray gas filled square cavity are investigated in the present paper, both computationally and experimentally. A schematic of the cross sectional view of the cavity is depicted in Fig. 1. The cavity is heated from the isothermal side wall located at $x = H$, which is maintained at a temperature of T_H, and cooled from the opposing side wall with a temperature T_C located at $x = 0$. All the interior surfaces are assumed to be nonslip and radiatively black for the computations. Various thermal boundary conditions are specified for the horizontal walls. Carbon dioxide gas is considered as the medium.

The overheat ratio δ (defined as $(T_H - T_C)/T_o$, where T_o is the reference film temperature, $(T_C + T_H)/2$) has been limited to small values ($\delta < 0.2$) in the experimental study of natural convection–radiation interactions in the past (Kurosaki et al., 1982). In the present investigation, significantly higher values of δ are used in the computations and experiments.

Computational Study

The governing equations consist of the variable-property Navier–Stokes and energy conservation equations along with the transfer equation for the radiative intensity (Fusegi and Farouk, 1989). The last equation is replaced with a set of differential equations for the irradiance of component gray gases by applying the P_1-approximation method and the WSGG model. Three component gray gases are considered to characterize the radiative properties of carbon dioxide, following Smith et al. (1982). Since the complete governing equations can be found elsewhere (Fusegi, 1988; Fusegi and Farouk, 1989), they are not repeated here. It suffices to mention that all the governing equations can be cast in the following general equation form:

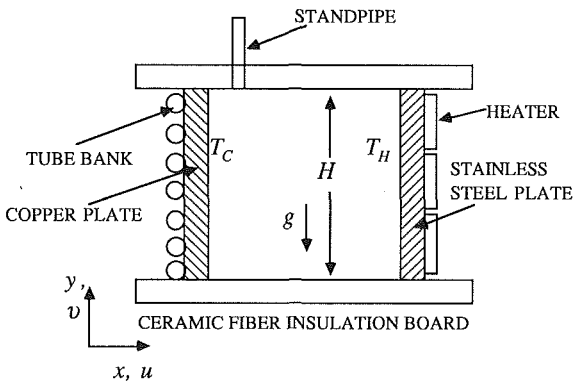

Fig. 1 Cross-sectional view of the test section

[1]Department of Mechanical Engineering and Mechanics, Drexel University, Philadelphia, PA 19104.

[2]Present address: Institute of Computational Fluid Dynamics, 1-22-3, Haramachi, Meguro-ku, Tokyo 152, Japan.

Contributed by the Heat Transfer Division for publication in the JOURNAL OF HEAT TRANSFER. Manuscript received by the Heat Transfer Division March 13, 1989; revision received November 29, 1989. Keywords: Enclosure Flows, Natural Convection, Radiation Interactions.

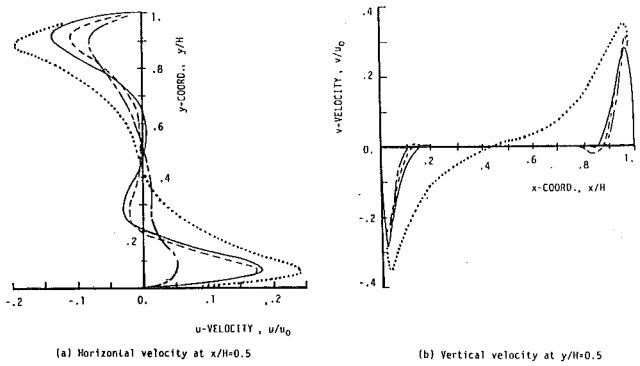

Fig. 2 Velocity profiles along the cavity midplanes (Gr = 6.6 × 10^6, Pr = 0.69; thermally insulated horizontal walls; T_C = 278 K, T_H = 833 K, δ = 1); —·— no radiation, ----- surface radiation, ——— surface/gas radiation, ••••• rectangular band model (Fusegi and Farouk, 1987)

$$\alpha\left\{\frac{\partial}{\partial t}(\rho\phi)+\frac{\partial}{\partial x}(\rho u\,\phi)+\frac{\partial}{\partial y}(\rho v\,\phi)\right\}$$
$$=\frac{\partial}{\partial x}\left(\Gamma\frac{\partial\phi}{\partial x}\right)+\frac{\partial}{\partial y}\left(\Gamma\frac{\partial\phi}{\partial y}\right)+S \qquad (1)$$

where ϕ denotes any dependent variable, α is a coefficient (1 or 0), Γ represents an exchange coefficient, and S is the source term. The gas is assumed ideal and its density is computed from the ideal-gas law. The absorption coefficient of carbon dioxide gas is represented by a function of temperature in the WSGG model. The model considers specifically the 2.7, 4.3, and 15-μm absorption bands of the gas.

Approximate solutions of the governing equations under appropriate boundary conditions (Fusegi and Farouk, 1989) are obtained by a control-volume based finite difference method. The convection-diffusion terms are discretized by the hybrid scheme (Patankar, 1980). The SIMPLE algorithm is employed as the iterative solution method. Finite difference equations are solved by a multidimensional simultaneous algebraic equation solver, the Strongly Implicit Scheme (Stone, 1968). The shape factor for radiation between any two control volume faces located on the boundary is obtained from the shape factor between differential elements taken on the control volumes. Simpson's rule is used for the numerical integration of the formula for the shape factor.

Results are obtained for the Grashof number Gr (defined with the cavity height, H, and the overall temperature difference, $T_H - T_C$), of 1.5 × 10^4, 2.4 × 10^5, and 6.6 × 10^6 with unity overheat ratio (δ = 1) and the overall temperature difference of 555 K. The corresponding enclosure length for each Grashof number is 0.01, 0.026, and 0.077 m, respectively. The optical thickness of the gas is roughly one order of magnitude smaller than the cavity height for each case. The Boltzmann number varies between 30 and 90 accordingly. The reference Prandtl number of the fluid, Pr, is held fixed at 0.69. These parameters are computed from fluid properties at the reference temperature. The horizontal walls are assumed to be thermally insulated.

Steady-state velocity profiles along the midplanes of the enclosure at Gr = 6.6 × 10^6 are depicted in Fig. 2. The coordinate and the velocity are normalized by the cavity height, H, and a reference convective velocity, $u_o = [g\,\beta_o\,H(T_H - T_C)]^{1/2}$, where g is the gravitational acceleration and β is the volumetric thermal expansion coefficient. Three different radiation modes are considered: no radiation (natural convection), surface radiation only, and surface/gas radiation. Results for the first two cases are obtained by selectively turning off surface and gas radiation calculations. Predictions obtained by the rectangular band model (Fusegi and Farouk, 1987) are also plotted in these figures for comparison. As shown in the horizontal (u-) velocity profiles, intense flows are induced near the insulated surfaces when radiation is taken into account. This change is caused by the steep temperature gradients near the horizontal walls due to the interaction of natural convection and radiation. On the other hand, surface radiation thickens the boundary layers formed along the isothermal surfaces as seen in the vertical (v-) velocity profiles. Gas radiation enhances these changes particularly for the boundary layer at the heated wall since the overall fluid temperature increases in the region due to absorption. Results obtained by the band model overestimate gas radiation and predict radical changes in the velocity profiles.

The heat transfer rate is presented in Table 1. For comparison, the results of the previous computational studies (Chang et al., 1983; Zhong et al., 1985; Fusegi and Farouk, 1987) are also included. With surface radiation, the heat transfer rate increases by five to seven times the values obtained by natural convection alone. This is primarily due to the large temperature difference considered between the isothermal walls. In the surface/gas radiation mode, the energy absorption by the gas slightly reduces the Nusselt number relative to the surface radiation cases.

In the surface/gas radiation mode, agreement is good among the predictions. In gray gas radiation analysis, the P_1-approximation method has been found to overestimate radiative transfer and to be inaccurate in small optical thickness ranges ($\tau \leq 5$, where τ is optical thickness). However, these drawbacks are not critical for nongray gas radiation analysis since surface radiation predominates at small optical thicknesses, as shown in the present results.

Experimental Study

The temperature field in a test cavity (Fig. 1) is visualized by a holographic interferometry technique. Details of the experimental procedure are available from Fusegi (1988). The thermal boundary condition of the horizontal walls is not ideal (perfectly insulated) during an experimental run. Soot is coated over the inner surfaces of the cavity to simulate black walls. The endwalls are made of silica-glass plates to allow optical access to the temperature field inside the test section. Carbon dioxide gas is introduced from one of the two standpipes. The entire assembly is covered with a layer of bulk ceramic fibers to minimize heat loss to the ambient.

Figure 3 depicts a representative interferogram obtained in the present study. Steady state was reached at the side wall temperatures of 300 (T_C) and 755 K (T_H). With this large temperature difference (δ = 0.86), refraction effects cannot be eliminated from the measurement (Gebhart, 1988). Therefore, regions near the surfaces cannot be clearly seen due to strong bending of the beam by refraction. The boundary layers formed along the walls are not apparent in the obtained fringe field. In the calculation, boundary layers are clearly seen along the side walls. The indicated Grashof number (Gr = 5.8 × 10^6) is computed from the temperature difference. Computational results are shown in Fig. 3(b) for the present values of the isothermal wall temperatures with insulated horizontal walls. The significant difference is attributed to unavoidable heat losses from the horizontal walls in the test cavity. Another computation (Fig. 3(c)) assumes a linear profile for heat loss from the horizontal walls as $q_{\text{loss}}(x) = C\,q_{in}\,(x/H + 1)$, where C is a constant, q_{loss} is the heat loss from one horizontal plate in W/m^2, and q_{in} is the average value of the energy supplied to the flow field through the heated wall (total energy divided by the cavity height). For the case in Fig. 3(c), the constant C is set at 0.05 at the top wall located at $y = H$ and 0.1 for the bottom wall at $y = 0$.

In both the experimental and computational results (Figs. 3(a, c)), isotherms are skewed in the central core region of the cavity. At the top left corner, closed isotherms appear in the

Table 1 Nusselt number at the isothermal wall (thermally insulated horizontal walls, $\delta = 1$)

Gr	NC*	Surface/gas radiation			
		Present	Chang et al.	Zhong et al.	Fusegi and Farouk
1.5×10^4	2.21	12.0 (1.6%)**	-	11.9	-
2.4×10^5	5.04	26.4 (1.5%)	24.5 (3.9%)	26.5	24.0 (9.0%)
6.6×10^6	12.4	75.5 (3.8%)	70.0 (6.7%)	-	67.9 (15%)

Notes: * NC = Natural Convection
** The data in the parentheses are *percent* reduction of the Nusselt number with respect to the surface radiation mode.

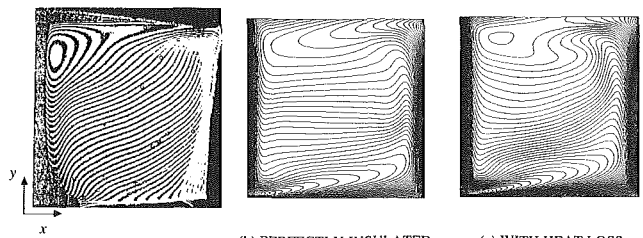

Fig. 3 Measured and computed temperature fields in the cavity (surface/gas radiation; heat loss from the horizontal walls; $\Delta T = 3$ K; Gr = 5.8×10^6, Pr = 0.69, $T_C = 300$ K, $T_H = 755$ K, $\delta = 0.86$)

interferogram, although the computationally predicted loops are smaller than those appearing in the fringe field. This discrepancy is due to differences in the thermal boundary conditions between the computation and the experiment. Due to the refraction effect, little information is available from the fringe field on thermal boundary conditions realized at the horizontal walls. Hence, several boundary conditions (with varying amounts of heat loss for the horizontal walls) were also considered in the computations. The result presented in Fig. 3(*c*) was the most satisfactory prediction among those considered.

Conclusions

The interactions of natural convection and radiation in a closed cavity have been studied computationally and by holographic interferometry. The mathematical model has successfully predicted changes in field characteristics due to surface and gas radiation.

In spite of the imperfection in the experimental setup and difficulties associated with interferometric measurements with large temperature differences, qualitative agreement was obtained between the experimental and computational results.

Comparison of the experiment with the prediction suggests that the temperature field is sensitive to the imposed boundary condition. Improved experiments are suggested for validation of complex numerical models for radiation–natural convection interaction analysis.

Acknowledgments

The computational resources were provided by the Office of Computing Service of Drexel University on the PRIME 9950 system and by the Institute of Computational Fluid Dynamics on the HITAC S820 system. The experimental program was partially funded by the National Science Foundation through Grant No. CBT-8505815.

References

Chang, L. C., Yang, K. T., and Lloyd, J. R., 1983, "Radiation-Natural Convection Interaction in Two-Dimensional Complex Enclosures," ASME JOURNAL OF HEAT TRANSFER, Vol. 105, pp. 89–95.

Fusegi, T., 1988, "Interaction Analysis of Turbulent Natural Convection and Radiation in Compartment Fires," Ph.D. Thesis, Drexel University, Philadelphia, PA.

Fusegi, T., and Farouk, B., 1987, "Radiation-Convection Interactions of a Non-gray Gas in a Square Enclosure," *Heat Transfer in Fire*, A. K. Kulkarni and Y. Jaluria, eds., ASME HTD-Vol. 73, pp. 63–68.

Fusegi, T., and Farouk, B., 1989, "Laminar and Turbulent Natural Convection-Radiation Interactions in a Square Enclosure Filled With a Nongray Gas," *Numerical Heat Transfer*, Part A, Vol. 15, pp. 303–322.

Gebhart, B., 1988, Private Communication, University of Pennsylvania, Philadelphia, PA.

Kurosaki, Y., Mishima, H., and Kashiwagi, T., 1982, "Heat Transfer Combined With Radiation and Natural Convection in a Rectangular Enclosure," *Proceedings, 7th International Heat Transfer Conference*, U. Grigull et al., eds., Hemisphere Publishing Corp., Washington, DC, Vol. 2, pp. 215–220.

Patankar, S. V., 1980, *Numerical Heat Transfer and Fluid Flow*, Hemisphere Publishing Corp., Washington, DC, Chap. 6.

Smith, T. F., Shen, Z. F., and Friedman, J. N., 1982, "Evaluation of Coefficients for the Weighted Sum of Gray Gases Model," ASME JOURNAL OF HEAT TRANSFER, Vol. 104, pp. 602–608.

Song, T. H., and Viskanta, R., 1987, "Interaction of Radiation With Turbulence: Application to a Combustion System," *Journal of Thermophysics and Heat Transfer*, Vol. 1, pp. 56–62.

Stone, H. L., 1968, "Iterative Solution of Implicit Approximations of Multidimensional Partial Differential Equations," *Journal of Numerical Analysis*, Vol. 5, pp. 530–558.

Yang, K. T., 1986, "Numerical Modeling of Natural Convection-Radiation Interactions in Enclosures," *Proceedings, 8th International Heat Transfer Conference*, C. L. Tien, ed., Vol. 1, pp. 131–140.

Zhong, Z. Y., Yang, K. T., and Lloyd, J. R., 1985, "Variable-Property Natural Convection in Tilted Enclosures With Thermal Radiation," *Numerical Methods in Heat Transfer*, R. W. Lewis and K. Morgan, eds., Vol. III, pp. 195–214.

A Generalized Model for Gravity-Assisted Melting in Enclosures

S. K. Roy[1] and S. Sengupta[1]

Introduction

Thermal energy storage devices using phase-change materials have some advantages that make them extremely attractive for certain applications. These include a high energy storage density and uniform temperature at which the energy is released or absorbed. A variety of applications at different temperatures are possible since different materials can be used as required. However, before a latent heat storage can be designed, the melt time required must be known, and given a certain phase-change material, operating conditions, and storage configuration, one must be able to predict the heat transfer coefficient

[1]Department of Mechanical Engineering, University of Miami, Coral Gables, FL 33124.

Contributed by the Heat Transfer Division for publication in the JOURNAL OF HEAT TRANSFER. Manuscript received by the Heat Transfer Division January 20, 1989; revision received June 27, 1989. Keywords: Modeling and Scaling, Moving Boundaries, Phase-Change Phenomena.

Table 1 Nusselt number at the isothermal wall (thermally insulated horizontal walls, $\delta = 1$)

Gr	NC*	Surface/gas radiation			
		Present	Chang et al.	Zhong et al.	Fusegi and Farouk
1.5×10^4	2.21	12.0 (1.6%)**	-	11.9	-
2.4×10^5	5.04	26.4 (1.5%)	24.5 (3.9%)	26.5	24.0 (9.0%)
6.6×10^6	12.4	75.5 (3.8%)	70.0 (6.7%)	-	67.9 (15%)

Notes: * NC = Natural Convection
** The data in the parentheses are *percent* reduction of the Nusselt number with respect to the surface radiation mode.

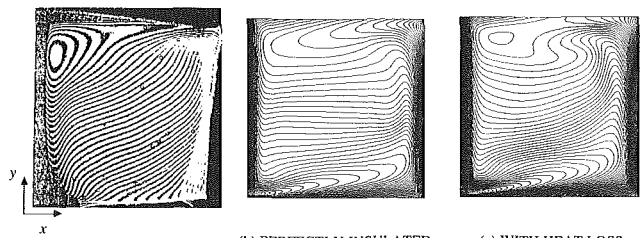

Fig. 3 Measured and computed temperature fields in the cavity (surface/gas radiation; heat loss from the horizontal walls; $\Delta T = 3$ K; Gr = 5.8×10^6, Pr = 0.69, $T_C = 300$ K, $T_H = 755$ K, $\delta = 0.86$)

interferogram, although the computationally predicted loops are smaller than those appearing in the fringe field. This discrepancy is due to differences in the thermal boundary conditions between the computation and the experiment. Due to the refraction effect, little information is available from the fringe field on thermal boundary conditions realized at the horizontal walls. Hence, several boundary conditions (with varying amounts of heat loss for the horizontal walls) were also considered in the computations. The result presented in Fig. 3(*c*) was the most satisfactory prediction among those considered.

Conclusions

The interactions of natural convection and radiation in a closed cavity have been studied computationally and by holographic interferometry. The mathematical model has successfully predicted changes in field characteristics due to surface and gas radiation.

In spite of the imperfection in the experimental setup and difficulties associated with interferometric measurements with large temperature differences, qualitative agreement was obtained between the experimental and computational results.

Comparison of the experiment with the prediction suggests that the temperature field is sensitive to the imposed boundary condition. Improved experiments are suggested for validation of complex numerical models for radiation–natural convection interaction analysis.

Acknowledgments

The computational resources were provided by the Office of Computing Service of Drexel University on the PRIME 9950 system and by the Institute of Computational Fluid Dynamics on the HITAC S820 system. The experimental program was partially funded by the National Science Foundation through Grant No. CBT-8505815.

References

Chang, L. C., Yang, K. T., and Lloyd, J. R., 1983, "Radiation-Natural Convection Interaction in Two-Dimensional Complex Enclosures," ASME JOURNAL OF HEAT TRANSFER, Vol. 105, pp. 89–95.

Fusegi, T., 1988, "Interaction Analysis of Turbulent Natural Convection and Radiation in Compartment Fires," Ph.D. Thesis, Drexel University, Philadelphia, PA.

Fusegi, T., and Farouk, B., 1987, "Radiation-Convection Interactions of a Non-gray Gas in a Square Enclosure," *Heat Transfer in Fire*, A. K. Kulkarni and Y. Jaluria, eds., ASME HTD-Vol. 73, pp. 63–68.

Fusegi, T., and Farouk, B., 1989, "Laminar and Turbulent Natural Convection-Radiation Interactions in a Square Enclosure Filled With a Nongray Gas," *Numerical Heat Transfer*, Part A, Vol. 15, pp. 303–322.

Gebhart, B., 1988, Private Communication, University of Pennsylvania, Philadelphia, PA.

Kurosaki, Y., Mishima, H., and Kashiwagi, T., 1982, "Heat Transfer Combined With Radiation and Natural Convection in a Rectangular Enclosure," *Proceedings, 7th International Heat Transfer Conference*, U. Grigull et al., eds., Hemisphere Publishing Corp., Washington, DC, Vol. 2, pp. 215–220.

Patankar, S. V., 1980, *Numerical Heat Transfer and Fluid Flow*, Hemisphere Publishing Corp., Washington, DC, Chap. 6.

Smith, T. F., Shen, Z. F., and Friedman, J. N., 1982, "Evaluation of Coefficients for the Weighted Sum of Gray Gases Model," ASME JOURNAL OF HEAT TRANSFER, Vol. 104, pp. 602–608.

Song, T. H., and Viskanta, R., 1987, "Interaction of Radiation With Turbulence: Application to a Combustion System," *Journal of Thermophysics and Heat Transfer*, Vol. 1, pp. 56–62.

Stone, H. L., 1968, "Iterative Solution of Implicit Approximations of Multidimensional Partial Differential Equations," *Journal of Numerical Analysis*, Vol. 5, pp. 530–558.

Yang, K. T., 1986, "Numerical Modeling of Natural Convection-Radiation Interactions in Enclosures," *Proceedings, 8th International Heat Transfer Conference*, C. L. Tien, ed., Vol. 1, pp. 131–140.

Zhong, Z. Y., Yang, K. T., and Lloyd, J. R., 1985, "Variable-Property Natural Convection in Tilted Enclosures With Thermal Radiation," *Numerical Methods in Heat Transfer*, R. W. Lewis and K. Morgan, eds., Vol. III, pp. 195–214.

A Generalized Model for Gravity-Assisted Melting in Enclosures

S. K. Roy[1] and S. Sengupta[1]

Introduction

Thermal energy storage devices using phase-change materials have some advantages that make them extremely attractive for certain applications. These include a high energy storage density and uniform temperature at which the energy is released or absorbed. A variety of applications at different temperatures are possible since different materials can be used as required. However, before a latent heat storage can be designed, the melt time required must be known, and given a certain phase-change material, operating conditions, and storage configuration, one must be able to predict the heat transfer coefficient

[1]Department of Mechanical Engineering, University of Miami, Coral Gables, FL 33124.

Contributed by the Heat Transfer Division for publication in the JOURNAL OF HEAT TRANSFER. Manuscript received by the Heat Transfer Division January 20, 1989; revision received June 27, 1989. Keywords: Modeling and Scaling, Moving Boundaries, Phase-Change Phenomena.

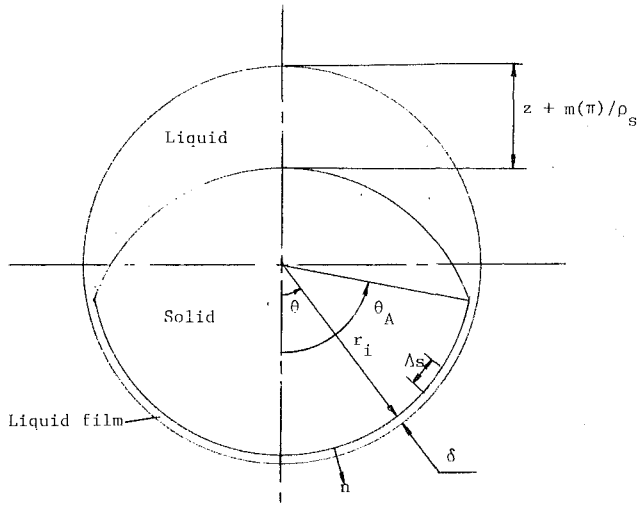

Fig. 1 Geometry

throughout the melting process. A number of reviews in this area have been published recently (Viskanta, 1983, 1985; Sengupta and Roy, 1988).

Gravity-assisted melting in cylindrical and spherical capsules has been studied over the past decade. However, none of these earlier analyses are truly complete. All are based on a number of simplifying assumptions, and have been developed from the studies of Moore and Bayazitoglu (1981, 1982), Emmerman and Turcotte (1983), and Bareiss and Beer (1984). As a consequence, there is a notion that gravity-assisted melting is always dominated by conduction, with natural convection having a minor effect on the overall melting. In the absence of a generalized model for the melting process, there has also been a lack of proper scaling of the governing variables resulting in a proliferation of parameters, and ultimately unnecessary experimentation. In addition, correlations have been presented for different geometries often without any mention of the parameter ranges over which these are valid.

In order to provide a stronger basis for the numerous analyses published previously, a more generalized model is presented in this paper. Since this model is based on fewer preliminary assumptions, it can be used to describe a wider variety of engineering problems than was possible with earlier models. Based on the observation that most of the heat transfer occurs through the liquid film (Fig. 1), a scaling analysis is then done to derive the nondimensional equations and finally the nondimensional numbers governing the process.

Problem Definition

For convenience in presenting the analysis, the spherical geometry will be considered in this paper. However, the analysis is valid for any similar axisymmetric case. Figure 1 shows the geometry of the problem. A sphere with a phase-change material initially in the solid phase, which may be initially subcooled or at its melting temperature, is instantaneously exposed to a uniform temperature, greater than the melting temperature, at the wall. Heat transfer to the solid core is primarily by conduction where the liquid layer is thin, whereas natural convection plays an important role in other regions. If the solid phase is subcooled at the start of the process, some of the heat transferred to the core is used to raise its temperature and only part of the energy is used in melting the solid. The following conditions describe the physical phenomenon:

1 The melting process is assumed to be axisymmetric as seen in previous experiments of Moore and Bayazitoglu (1982) and Bareiss and Beer (1984).

2 The phase-change material has constant properties, except for density in the body force term, which is assumed to vary linearly with temperature.

3 No mushy region is formed during the melting process.

4 The solid core remains as one piece and does not deform while melting.

5 For convenience in presenting the analysis, the solid phase density is assumed to be greater than the liquid phase density. The solid will therefore tend to drop down as it melts.

Given the above conditions, the governing equations describing the melting process can be formulated. These are applicable throughout the domain, including the solid core, the lower liquid film, and the upper liquid zone:

Interface Mass Balance Equation

$$\frac{\partial r_i}{\partial t}\,\bar{r}\cdot\bar{n} = -m + \frac{dz}{dt}\,\bar{k}\cdot\bar{n} \tag{1}$$

with $r_i = r_o$, $z = 0$ at $t = 0$. r_i is the location of the interface, r_o the location of the enclosure wall, m the mass of solid melting per unit time per unit area, and dz/dt is the drop rate of the solid core (i.e., Δz gives the distance that a point in the solid core has moved relative to its original position at $t = 0$).

Interface Energy Equation

$$m\bar{n}\,(l + c_{ps}(T_F - \bar{T}_s)) = -k\bar{\nabla}T|_l + k\bar{\nabla}T|_s \tag{2}$$

where $\bar{T}_s$ is the temperature of that portion of the solid that actually melts at any instant, and T_F is the melting temperature of the phase-change material. The term $c_{ps}(T_F - \bar{T}_s)$ is usually very small and is neglected.

Force Balance on Solid Core

$$\left[\frac{d^2z}{dt^2} - g\right]\int_0^{\pi}\int_0^{r_i} \rho_s 2\pi r \sin\theta\, r d\theta dr =$$

$$-\int_0^{\pi} (P\bar{n} + \tau\bar{s})\cdot\bar{k}\, 2\pi r_i \sin\theta r_i d\theta \tag{3}$$

where P is the pressure (including the hydrostatic pressure), and τ the shear stress at the interface. On integration, the vertical velocity of the core can be obtained. However, the initial condition is not known exactly in this case, and a suitable assumption is required.

Liquid Zone Equations

Continuity Equation

$$\bar{\nabla}\cdot\bar{v} = 0 \tag{4}$$

Navier–Stokes Equations

$$\frac{\partial\bar{v}}{\partial t} + \bar{v}\cdot\overline{\nabla v} = \nu\bar{\nabla}^2\bar{v} - \frac{1}{\rho}\,\bar{\nabla}P + \bar{g} \tag{5}$$

Energy Equation

$$\frac{\partial T}{\partial t} + \bar{v}\cdot\bar{\nabla}T = \alpha\bar{\nabla}^2 T \tag{6}$$

with the initial and boundary conditions

$$t = 0: \quad \bar{v} = 0, \quad T = T_C \qquad \theta = 0, \quad \pi: \quad \frac{\partial\bar{v}}{\partial\theta} = 0, \quad \frac{\partial\bar{T}}{\partial\theta} = 0$$

$$r = r_i: \; v_n = \left[\frac{\rho_s}{\rho} - 1\right]\frac{m}{\rho_s}\,\bar{n} + \frac{dz}{dt}\bar{k}\cdot\bar{m}, \quad T = T_F$$

$$r = r_o: \quad \bar{v} = 0, \quad T = T_H$$

where T_c is the initial temperature of the solid core and T_H is the temperature of the enclosure wall.

Solid Energy Equation

$$\frac{\partial T}{\partial t}=\alpha_s \bar{\nabla}^2 T \tag{7}$$

with the initial and boundary conditions

$$t=0: \quad T=T_C \qquad \theta=0,\ \pi: \quad \frac{\partial T}{\partial \theta}=0$$

$$r=0: \quad T \text{ is finite} \qquad r=r_i: \quad T=T_F$$

It should be noted that the obvious assumption of zero velocity at the enclosure wall, when taken together with the fixed enclosure size and a velocity boundary condition at the interface accounting for the density difference between the solid and liquid phases, results in violation of "volume balance." In actual experiments, a small opening with a riser is usually made at the highest elevation where the excess liquid volume may be accommodated.

Analysis

A scaling analysis is done to obtain the above equations in the nondimensional form. This analysis is based both on assumptions made in the previous section, as well as experimental observations, which show that most of the heat transfer takes place through the liquid film (e.g., Moore and Bayazitoglu, 1982). Complete details are given by Roy (1988). The nondimensional variables, and the nondimensional equations (after dropping the superscript *) for the film, along with the order of magnitude of each of the terms, are given below:

Nondimensional Variables

$$r^*, z^*=r/D, z/D \quad t^*=\frac{\nu t}{MtD^2} \qquad T^*=\frac{T-T_C}{T_H-T_C}$$

$$v^*=\frac{Mt\ Md\ \rho^\circ D}{\nu}v \quad m^*=\frac{Dm}{Mt\rho_s \nu}$$

$$p^*=\frac{p}{\Delta\rho g D} \quad \text{or} \quad P^*=\frac{p-p_{hs}}{\Delta\rho g D}$$

- **Interface Mass Balance Equation**

$$\frac{\partial r_i}{\partial t}\ \bar{r}\cdot\bar{n} = -m+\frac{dz}{dt}\bar{k}\cdot\bar{n} \tag{8}$$

$$(Md) \qquad (1) \quad (1)$$

- **Interface Energy Equation**

$$m=\frac{-Md}{1-Sb}\left[\left.\frac{\partial T}{\partial n}\right|_l-\frac{1}{Md}\frac{\mathrm{Ste}}{c_p^\circ}\frac{Mt}{\mathrm{Pr}\alpha^\circ}\left.\frac{\partial T}{\partial n}\right|_s\right] \tag{9}$$

$$(1) \qquad (1) \qquad ((\mathrm{Ste}/c_p^\circ)\,(Mt/\mathrm{Pr}\alpha^\circ(Sb/(1-Sb)))$$

- **Force Balance on Solid Core**

$$\frac{1}{ArMt^2}\frac{d^2z}{dt^2}\int_0^\pi\int_0^{r_i} r^2\sin\theta\ dr\ d\theta =$$

$$(1/ArMt^2)$$

$$-\int_0^\pi \left(p\,\bar{n}+\frac{Md^2}{r}\frac{\partial v/r}{\partial r}\bar{t}\right)\cdot\bar{k}\ r_i\sin\theta\ ds +$$

$$(1) \qquad (Md)$$

$$\int_0^\pi\int_0^{r_i} r^2\sin\theta\ dr\ d\theta \tag{10}$$

$$(1)$$

- **Film Equations**

Continuity Equation

$$\bar{\nabla}\cdot\bar{v}=0 \tag{11}$$

Both terms are of the same order.

Navier-Stokes Equations

$$\frac{Md^2}{Mt}\frac{\partial\bar{v}}{\partial t}+\frac{1}{\rho^\circ}\frac{Md}{Mt}\bar{v}\cdot\overline{\nabla v}\ \Big|_r = -\bar{\nabla}p +$$

$$(Md^3/Mt) \quad (Md^2/\rho^\circ Mt) \qquad --$$

$$Md^2\left[\bar{\nabla}^2 v_r-\frac{2}{r^2\sin\theta}\frac{\partial}{\partial\theta}v_\theta\sin\theta\right]+\frac{\mathrm{Gr}}{\mathrm{Ar}}(T-Sb)g_r$$

$$(Md,\ Md^3) \qquad (Md^2) \qquad (\mathrm{Gr}(1-Sb)/Ar) \tag{12a}$$

$$\frac{Md^2}{Mt}\frac{\partial\bar{v}}{\partial t}+\frac{1}{\rho^\circ}\frac{Md}{Mt}\bar{v}\cdot\overline{\nabla v}\ \Big|_\theta =$$

$$(Md^2/Mt) \quad (Md/\rho^\circ Mt) \qquad --$$

$$-\bar{\nabla}p+Md^2\left[\bar{\nabla}^2 v_\theta-\frac{2}{r^2}\frac{\partial v_r}{\partial\theta}\right]+\frac{\mathrm{Gr}}{Ar}(T-Sb)g_\theta$$

$$(1,\ Md^2) \quad (Md) \quad (\mathrm{Gr}(1-Sb)/Ar) \tag{12b}$$

Energy Equation

$$\mathrm{Pr}\frac{Md^2}{Mt}\frac{\partial T}{\partial t}+\frac{\mathrm{Pr}}{\rho^\circ}\frac{Md}{Mt}\bar{v}\cdot\bar{\nabla}T = Md^2\,\bar{\nabla}^2 T \tag{13}$$

$$\mathrm{Pr}Md^2/Mt \quad \mathrm{Pr}Md/\rho^\circ Mt \quad (\mathrm{Pr},\ \mathrm{Pr}Md^2)$$

where

$$\bar{\nabla}^2_- = \frac{\partial}{\partial r}\left[\frac{1}{r^2}\frac{\partial}{\partial r}(r^2_-)\right]+\frac{1}{r^2\sin\theta}\frac{\partial}{\partial\theta}\left[\sin\theta\frac{\partial}{\partial\theta}\right]$$

in equations (12) and (13) above.

- *Solid Energy Equation*

$$\frac{\partial T}{\partial t}=\frac{Mt}{\mathrm{Pr}\alpha^\circ}\bar{\nabla}^2 T \tag{14}$$

$$(Sb) \quad (SbMt/\mathrm{Pr}\alpha^\circ)$$

with the boundary conditions

$$t=0; \quad r_i=r_o, \quad z=0, \quad \bar{v}=0, \quad T=0$$

$$\theta=0, \quad \pi: \quad \frac{\partial\bar{v}}{\partial\theta}=0, \quad \frac{\partial T}{\partial\theta}=0$$

$$r=r_i: \quad v_n=\rho^\circ Md\left[\left[\frac{1}{\rho^\circ}-1\right]m+\frac{dz}{dt}\bar{k}\cdot\bar{n}\right], \quad T=Sb$$

$$r=r_o: \quad \bar{v}=0, \quad T=1$$

where

$$Md=\left(\frac{\mathrm{Ste}\rho^\circ}{\mathrm{Pr}}\Big/Ar_s\right)^{0.25}=\left[\frac{k\Delta T\nu}{l\Delta\rho g D^3}\right]^{0.25}$$

$$Mt=\left(\left[\frac{\mathrm{Ste}\rho^\circ}{\mathrm{Pr}}\right]^3 Ar_s\right)^{-0.25}=\left(\left[\frac{k\Delta T}{l}\right]^3\frac{\Delta\rho g D^3}{\rho_s^4\nu^5}\right)^{-0.25}$$

$$\mathrm{Ste}=c_p(T_H-T_F)/\rho \quad Ar=(\rho_s-\rho_l)gD^3/\rho_l\nu^2$$

$$\mathrm{Gr}=g\beta(T_H-T_F)D^3/\nu^2$$

$$Sb=(T_F-T_C)/(T_H-T_C)$$

and the superscript ° refers to liquid-to-solid property ratio.

Discussion

Three points need consideration. These are discussed separately below:

Analysis of Nondimensional Equations. The importance of the different terms in the governing equations can be readily judged from their relative magnitudes in the above equations. These equations are greatly simplified and natural convection effects are small when Md, Gr/Ar, $Sb \ll 1$, and Ar, $\mathrm{Gr} \gg 1$, i.e., for parameters values typical of solar thermal energy applications. However, under certain conditions, such simplifications may not be possible. For example, for materials where the density difference between the solid and liquid phase is small, or when the temperature difference between the wall and the melting point is large, Gr/Ar will be of order (1) (equation (12)). Under these circumstances, natural convection in the film can no longer be ignored.

The importance of deriving and analyzing the generalized governing equations before undertaking extensive experimental or numerical work can be further appreciated by considering two more cases. First, when the Stefan number is high, it can be seen that the convective terms in the energy equation become important (equation (13)). This has been previously reported by Bayazitoglu and Moore (1982) from their numerical results. As a second case, subcooling can be seen to have negligible effects on the melt time (equation (9)) only if (Ste/c_p^*) $(Mt/\mathrm{Pr}\alpha^*(Sb/(1-Sb)) \ll 1$. Previous studies also confirm this point (Roy and Sengupta, 1988).

Derivation of Simplified Models. For typical solar energy applications, the above equations reduce to the forms used in earlier studies (Bareiss and Beer, 1984; Roy and Sengupta, 1987; Bahrami and Wang, 1987) only if a few additional assumptions, which are valid only when $Md \ll 1$ (Roy, 1988), are made:

(*a*) The flow field in the liquid film is "fully developed" (e.g., Roy, 1988):

$$\frac{\partial}{\partial \theta}(v_\theta \sin\theta) = 0 \tag{15}$$

(*b*) The lower surface area of the solid core is approximately equal to the surface area of the sphere covering the same solid angle.

(*c*) The pressure at the interface in the upper zone is assumed to be equal to the hydrostatic pressure:

$$p(\theta - \theta_A) = 0 \tag{16}$$

The importance of Md is discussed further in the following section.

Nondimensional Numbers. The nondimensional governing equations show that two nondimensional parameters, Mt and Md, completely characterize the melting process in the absence of subcooling and natural convection. In comparison, in earlier studies, the nondimensional drop height and Nusselt number were typically presented as a function of nondimensional time and at least two additional parameters (some combination of Ste, Pr, ρ^*, and Ar).

The parameter Mt is associated with the melt time scale and its importance with this analysis. In Fig. 2, the experimental data of Moore and Bayazitoglu (1981) have been presented using the nondimensional time derived in this study. All data points collapse approximately onto a single curve with a maximum deviation of about ±5 percent. The slight difference between the data for $\mathrm{Ste} = 0.05$ and $\mathrm{Ste} = 0.1$ can be attributed to the melting taking place at the upper surface.

The significance of Mt can also be noted by considering the melt rate and the overall melt time in the absence of subcooling and natural convection. By using the nondimensional melt time

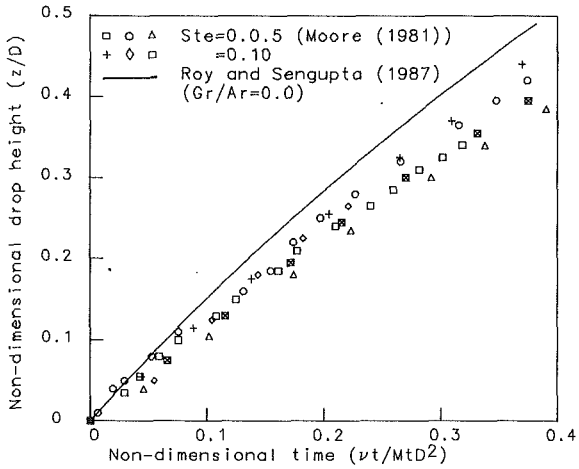

Fig. 2 Variation of drop height with time

used in this study (MtD^2/ν), for the cylindrical case (Bareiss and Beer, 1984), these become

$$\frac{dz}{dt} = \left[\frac{5 \arccos z - z\sqrt{1-z^2}}{6((1-z^2)(2/3+z^2/3-z^4))^{1/2}}\right]^{1/4} \tag{17}$$

and $t(z=1) = 1.05$.

From equation (17), the melt rate is found to depend only on the drop height z, and after integration, the drop height will be solely a function of time. This is also true for the spherical geometry (Sengupta and Roy, 1988). The overall melt time for the spherical case comes out as:

$t(z=1) = 1.06$ (Roy and Sengupta, 1987), and

$= 1.03$ (Bahrami and Wang, 1987).

Thus, Mt characterizes the time required for melting with the reference time for gravity-assisted melting given by MtD^2/ν. In contrast, three different nondimensional times have been used in the earlier analyses: Fourier number Fo (based on conduction heat transfer), the product of the Fourier number and the Prandtl number PrFo (since specific heat is not a parameter in the melting problem when there is no subcooling), and the product of the Fourier number and Stefan number SteFo (to account for the phase-change phenomenon) with the total nondimensional melt time in these analyses lying between 10^{-1} and 10^{1} depending on the actual parameter values.

The second nondimensional parameter obtained during this analysis is the film thickness ("Melt-distance") parameter Md. On integrating the simplified energy equation in the film, it can be seen that the film thickness δ is of order Md. Further, the interface Nusselt number is also found to be inversely proportional to δ. Thus, the nondimensional parameter Md ultimately determines the melt rate and Nusselt number during gravity-assisted melting.

Conclusions

A general model for axisymmetric melting in an enclosure with constant wall temperature has been presented in this paper. Based on this model, a scaling analysis has been done to obtain the orders of magnitude of the different terms and to derive the characteristic nondimensional parameters associated with gravity-assisted melting. In the absence of subcooling and natural convection, two nondimensional parameters, Mt and Md, are found completely to characterize the melting process. The melt time parameter Mt is related to the melting time scale given by MtD^2/ν. The melt distance parameter Md determines the order of the liquid film thickness and thus governs the heat transfer and Nusselt number during the melting process.

References

Bahrami, P. A., and Wang, T. G., 1987, "Analysis of Gravity and Conduction-Driven Melting in a Sphere," ASME JOURNAL OF HEAT TRANSFER, Vol. 109, pp. 806–809.

Bareiss, M., and Beer, H., 1984, "An Analytical Solution of the Heat Transfer Process During Melting of an Unfixed Solid Phase Change Material Inside a Horizontal Enclosure," *Int. J. Heat Mass Transfer*, Vol. 27, pp. 739–746.

Emmerman, M. K., and Turcotte, D. L., 1983, "Stoke's Problem With Melting," *Int. J. Heat Mass Transfer*, Vol. 26, pp. 1625–1630.

Moore, F., and Bayazitoglu, Y., 1982, "Melting Within a Spherical Enclosure," ASME JOURNAL OF HEAT TRANSFER, Vol. 104, pp. 19–23.

Moore, F., 1981, "Melting Within a Spherical Enclosure," M.S. Thesis, Rice University, TX.

Roy, S. K., 1988, "Melting in Spherical Enclosures," Ph.D. Dissertation, Department of Mechanical Engineering, University of Miami, FL.

Roy, S. K., and Sengupta, S., 1987, "The Melting Process in Spherical Enclosures," ASME JOURNAL OF HEAT TRANSFER, Vol. 109, pp. 460–462.

Roy, S. K., and Sengupta, S., 1989, "Melting of a Free Solid in a Spherical Enclosure: Effect of Subcooling," ASME *Journal of Solar Energy Engineering*, Vol. 110, pp. 32–36.

Sengupta, S., and Roy, S. K., 1989, "Gravity-Assisted Melting in Enclosures," *Energy Storage Systems*, NATO ASI Publ. Ser. E., B. Kilkis and S. Kakac, eds., Kluwer Acad. Pub., Dordrecht, pp. 721–752.

Viskanta, R., 1983, "Phase-Change Heat Transfer," *Solar Heat Storage: Latent Heat Materials*, Vol. 1, G. Lane, ed., CRC Press, Inc., FL, pp. 153–222.

Viskanta, R., 1985, "Natural Convection in Melting and Solidification," *Natural Convection: Fundamentals and Applications*, S. Kakac et al., eds., Hemisphere Pub. Corp., Washington, DC, pp. 845–877.

Sliding Contact Melting: The Effect of Heat Transfer in the Solid Parts

P. A. Litsek[1] and A. Bejan[1,2]

Nomenclature

- c_0 = specific heat of solid phase-change material
- F_n = normal force per unit width, Fig. 1
- $\tilde{F}_n$ = dimensionless normal force $= F_n/\mu U$
- F_t = tangential force per unit width, Fig. 1
- $\tilde{F}_t$ = dimensionless tangential force $= F_t/\mu U$
- h = liquid gap thickness, Fig. 1
- $\tilde{h}$ = dimensionless liquid gap thickness, equation (1)
- h_{sf} = latent heat of melting
- k_f = thermal conductivity of liquid phase-change material
- k_s = thermal conductivity of solid slider (heater), Fig. 1
- k_0 = thermal conductivity of solid phase-change material
- L = length of sliding contact, Fig. 1
- p = dimensionless group, equation (12)
- P = pressure
- $\tilde{P}$ = dimensionless pressure $= PL/\mu U$
- q = dimensionless group, equation (13)
- q_0'' = heat flux on the solid side of the two-phase interface, Fig. 1
- q_w'' = heat flux along the surface of the solid slider, Fig. 1
- Q = longitudinal liquid flow rate, equation (16)
- Q_0 = constant
- $\tilde{Q}_0$ = dimensionless constant $= Q_0/VL$
- Ste = solid subcooling Stefan number $= c_0(T_m - T_0)/h_{sf}$
- T = temperature
- T_m = melting point, Fig. 1
- T_s = solid slider temperature, Fig. 1
- T_w = temperature of the solid slider surface, Fig. 1
- T_0 = temperature of solid phase-change material, Fig. 1
- u = longitudinal liquid velocity
- U = solid slider velocity, Fig. 1
- V = melting velocity, Fig. 1
- $\tilde{V}$ = dimensionless melting velocity, equation (11)
- x = longitudinal position, Fig. 1
- y = transversal position, Fig. 1
- α_s = thermal diffusivity of solid slider
- α_0 = thermal diffusivity of solid phase-change material
- δ_s = thickness of slider boundary layer, Fig. 1
- δ_0 = thickness of boundary layer in solid phase-change material, Fig. 1
- μ = viscosity
- ξ = dimensionless longitudinal coordinate $= x/L$
- ρ_0 = density of phase-change material
- Φ = normal force correction factor, equation (22)
- Ψ = tangential force correction factor, equation (26)

1 Introduction

In an earlier paper (Bejan, 1989), the phenomenon of steady melting and lubrication by sliding contact was studied based on a model in which:

(*a*) the block of phase-change material was isothermal and at its melting point, and

(*b*) the solid slider (heater) was either isothermal or adiabatic.

These simplifying assumptions had the purpose of decoupling the liquid-film phenomenon (melting and lubrication) from the heat transfer processes that can occur in the two solid bodies. The objective of the present note is to relax the assumptions (*a*) and (*b*), and to document the effect of peripheral heat transfer on the sliding-contact melting phenomenon.

Consider the two-body configuration sketched in Fig. 1. The block of phase-change material (i.e., the body that melts) is

[1]Department of Mechanical Engineering and Materials Science, Duke University, Durham, NC 27706.

[2]J. A. Jones Professor of Mechanical Engineering; Fellow ASME.

Contributed by the Heat Transfer Division for publication in the JOURNAL OF HEAT TRANSFER. Manuscript received by the Heat Transfer Division September 8, 1988; revision received September 5, 1989. Keywords: Conduction, Materials Processing and Manufacturing Process, Phase-Change Phenomena.

References

Bahrami, P. A., and Wang, T. G., 1987, "Analysis of Gravity and Conduction-Driven Melting in a Sphere," ASME JOURNAL OF HEAT TRANSFER, Vol. 109, pp. 806–809.

Bareiss, M., and Beer, H., 1984, "An Analytical Solution of the Heat Transfer Process During Melting of an Unfixed Solid Phase Change Material Inside a Horizontal Enclosure," *Int. J. Heat Mass Transfer*, Vol. 27, pp. 739–746.

Emmerman, M. K., and Turcotte, D. L., 1983, "Stoke's Problem With Melting," *Int. J. Heat Mass Transfer*, Vol. 26, pp. 1625–1630.

Moore, F., and Bayazitoglu, Y., 1982, "Melting Within a Spherical Enclosure," ASME JOURNAL OF HEAT TRANSFER, Vol. 104, pp. 19–23.

Moore, F., 1981, "Melting Within a Spherical Enclosure," M.S. Thesis, Rice University, TX.

Roy, S. K., 1988, "Melting in Spherical Enclosures," Ph.D. Dissertation, Department of Mechanical Engineering, University of Miami, FL.

Roy, S. K., and Sengupta, S., 1987, "The Melting Process in Spherical Enclosures," ASME JOURNAL OF HEAT TRANSFER, Vol. 109, pp. 460–462.

Roy, S. K., and Sengupta, S., 1989, "Melting of a Free Solid in a Spherical Enclosure: Effect of Subcooling," ASME *Journal of Solar Energy Engineering*, Vol. 110, pp. 32–36.

Sengupta, S., and Roy, S. K., 1989, "Gravity-Assisted Melting in Enclosures," *Energy Storage Systems*, NATO ASI Publ. Ser. E., B. Kilkis and S. Kakac, eds., Kluwer Acad. Pub., Dordrecht, pp. 721–752.

Viskanta, R., 1983, "Phase-Change Heat Transfer," *Solar Heat Storage: Latent Heat Materials*, Vol. 1, G. Lane, ed., CRC Press, Inc., FL, pp. 153–222.

Viskanta, R., 1985, "Natural Convection in Melting and Solidification," *Natural Convection: Fundamentals and Applications*, S. Kakac et al., eds., Hemisphere Pub. Corp., Washington, DC, pp. 845–877.

Sliding Contact Melting: The Effect of Heat Transfer in the Solid Parts

P. A. Litsek[1] and A. Bejan[1,2]

Nomenclature

- c_0 = specific heat of solid phase-change material
- F_n = normal force per unit width, Fig. 1
- $\tilde{F}_n$ = dimensionless normal force $= F_n/\mu U$
- F_t = tangential force per unit width, Fig. 1
- $\tilde{F}_t$ = dimensionless tangential force $= F_t/\mu U$
- h = liquid gap thickness, Fig. 1
- $\tilde{h}$ = dimensionless liquid gap thickness, equation (1)
- h_{sf} = latent heat of melting
- k_f = thermal conductivity of liquid phase-change material
- k_s = thermal conductivity of solid slider (heater), Fig. 1
- k_0 = thermal conductivity of solid phase-change material
- L = length of sliding contact, Fig. 1
- p = dimensionless group, equation (12)
- P = pressure
- $\tilde{P}$ = dimensionless pressure $= PL/\mu U$
- q = dimensionless group, equation (13)
- q_0'' = heat flux on the solid side of the two-phase interface, Fig. 1
- q_w'' = heat flux along the surface of the solid slider, Fig. 1
- Q = longitudinal liquid flow rate, equation (16)
- Q_0 = constant
- $\tilde{Q}_0$ = dimensionless constant $= Q_0/VL$
- Ste = solid subcooling Stefan number $= c_0(T_m - T_0)/h_{sf}$
- T = temperature
- T_m = melting point, Fig. 1
- T_s = solid slider temperature, Fig. 1
- T_w = temperature of the solid slider surface, Fig. 1
- T_0 = temperature of solid phase-change material, Fig. 1
- u = longitudinal liquid velocity
- U = solid slider velocity, Fig. 1
- V = melting velocity, Fig. 1
- $\tilde{V}$ = dimensionless melting velocity, equation (11)
- x = longitudinal position, Fig. 1
- y = transversal position, Fig. 1
- α_s = thermal diffusivity of solid slider
- α_0 = thermal diffusivity of solid phase-change material
- δ_s = thickness of slider boundary layer, Fig. 1
- δ_0 = thickness of boundary layer in solid phase-change material, Fig. 1
- μ = viscosity
- ξ = dimensionless longitudinal coordinate $= x/L$
- ρ_0 = density of phase-change material
- Φ = normal force correction factor, equation (22)
- Ψ = tangential force correction factor, equation (26)

1 Introduction

In an earlier paper (Bejan, 1989), the phenomenon of steady melting and lubrication by sliding contact was studied based on a model in which:

(*a*) the block of phase-change material was isothermal and at its melting point, and

(*b*) the solid slider (heater) was either isothermal or adiabatic.

These simplifying assumptions had the purpose of decoupling the liquid-film phenomenon (melting and lubrication) from the heat transfer processes that can occur in the two solid bodies. The objective of the present note is to relax the assumptions (*a*) and (*b*), and to document the effect of peripheral heat transfer on the sliding-contact melting phenomenon.

Consider the two-body configuration sketched in Fig. 1. The block of phase-change material (i.e., the body that melts) is

[1]Department of Mechanical Engineering and Materials Science, Duke University, Durham, NC 27706.

[2]J. A. Jones Professor of Mechanical Engineering; Fellow ASME.

Contributed by the Heat Transfer Division for publication in the JOURNAL OF HEAT TRANSFER. Manuscript received by the Heat Transfer Division September 8, 1988; revision received September 5, 1989. Keywords: Conduction, Materials Processing and Manufacturing Process, Phase-Change Phenomena.

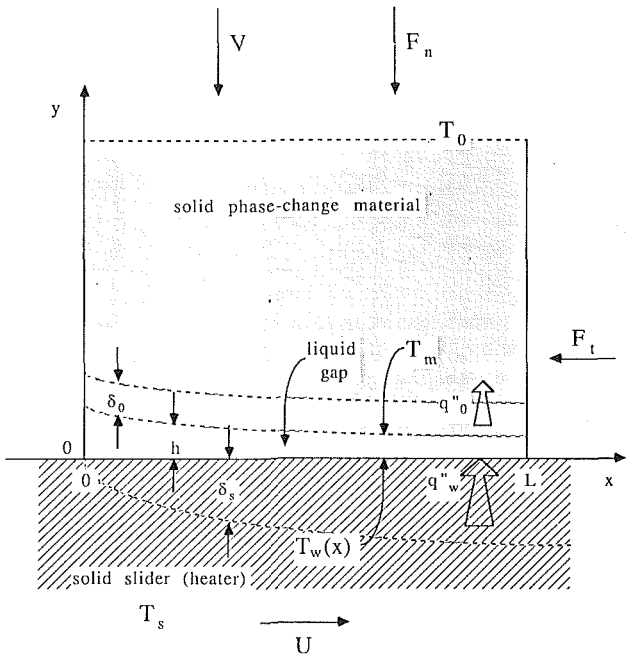

Fig. 1 Melting by sliding contact, and the boundary-layer temperature fields formed in the two solid parts

pressed against a warmer solid that slides to the right with the velocity U. The melting body advances into the melt-lubricated region with the "melting" velocity V. The key thermal engineering question relative to this very basic process is "What is the relationship between the melting rate V and the mechanical loading (F_n, F_t) of the two-body arrangement?"

The answer depends on the thermophysical properties of the two solids and the liquid that is steadily generated in the relative-motion gap of thickness $h(x)$. There is also conduction heat transfer on both sides of the liquid film, because

(*i*) the upper solid is subcooled, $T_0 < T_m$,

(*ii*) the lower solid is warmer than the melting point of the phase-change material, $T_s > T_m$, and

(*iii*) the thermal diffusivities of the upper solid (α_0) and lower solid (α_s) are finite.

In what follows, we consider separately the upper solid, the liquid film, and the lower solid, and then mesh the three by invoking appropriate matching conditions along the interfaces that define the liquid film.

2 Conduction in the Upper (Melting) Solid

Let δ_0 be the thickness of the solid layer that makes the transition from the melting point (T_m) of the solid–liquid interface, to the rest of the solid phase, the temperature of which is T_0. If we assume that the boundary layer thickness δ_0 is smaller than the length L.

$$\delta_0 << L \tag{1}$$

and that in the x-y frame the interface shape is sufficiently "flat" such that

$$\left|\frac{dh}{dx}\right| < 1 \tag{2}$$

then the phenomenon of steady conduction in the $\delta_0 \times L$ region is governed by

$$-V\frac{\partial T}{\partial y} = \alpha_0 \frac{\partial^2 T}{\partial y^2} \tag{3}$$

In this equation, the melting rate V is an unknown constant. Integrated twice in y and subjected to the boundary conditions $T(y=h) = T_m$ and $T(y \to \infty) = T_0$, equation (3) yields the temperature distribution across the δ_0 thin layer:

$$T = T_0 + (T_m - T_0)\exp\left[-\frac{V}{\alpha_0}(y-h)\right] \tag{4}$$

This result shows that the temperature of the upper solid decreases exponentially from the melting front (T_m) to the temperature (T_0) found sufficiently above the melting front. The bulk of the decrease from T_m to T_0 occurs over a vertical distance $(y-h)$ large enough so that the argument of the exponential[3] in equation (4) is of order 1, i.e., when $(y-h)V/\alpha_0 \sim 1$. In the first sentence of this section, this vertical distance $(y-h)$ was called δ_0; therefore, we conclude that $\delta_0 V/\alpha_0 \sim 1$, and that the inequality (1) is the same as writing $VL/\alpha_0 >> 1$.

A direct consequence of the fact that V is a constant in equation (3) is that the melting-front heat flux that enters the upper solid, q''_0, is independent of longitudinal position:

$$q''_0 = -k_0\left(\frac{\partial T}{\partial y}\right)_{y=h} = \rho_0 c_0 V(T_m - T_0) \tag{5}$$

The fact that q''_0 is not a function of x is essential to being able to continue this solution analytically.

3 Energy Conservation in the Liquid Film

There are four effects that compete in an energy balance at every point in the liquid film, namely, longitudinal convection, transversal conduction, longitudinal conduction, and frictional heat generation. The scale analysis and resulting criteria for properly neglecting one or more effects in the energy balance have been presented in the first part of this work (Bejan, 1989), and are not repeated. Therefore, we place the present study in the domain where the liquid film is sufficiently thin and the liquid viscosity sufficiently small so that the effect of transversal conduction overwhelms all the other effects in the energy balance. What is left of the energy conservation equation is the statement that the liquid temperature varies linearly in y, or that the vertical heat flux is conserved across the liquid film.

The heat flux that crosses the liquid film is equal to the heat flux q''_w absorbed by the film from the surface of the lower (sliding) solid. This heat flux arrives at the solid–liquid interface and drives both the melting process and the conduction heat transfer into the upper solid

$$q''_w = \rho_0 h_{sf} V + q''_0 \tag{6}$$

Since q''_0 is independent of x [equation (5)], we reach the important conclusion that the heat flux drawn from the lower solid is also independent of x. Furthermore, since $q''_w = k_f(T_w - T_m)/h$, where $T_w(x)$ is the base surface temperature (Fig. 1), equation (6) provides a relationship between melting rate and liquid film thickness

$$h = \frac{k_f(T_w - T_m)}{\rho_0 h_{sf} V(1 + \mathrm{Ste})} \tag{7}$$

In this expression, Ste is the Stefan number that accounts for the degree of subcooling of the upper solid, $\mathrm{Ste} = c_0(T_m - T_0)/h_{sf}$.

4 Convection in the Lower (Sliding) Solid

The heat transfer process beneath the $y=0$ plane is one of constant-flux convection in a solid that moves with the velocity U. Assuming that the respective thermal penetration region is slender (Fig. 1)

$$\delta_s << L \tag{8}$$

the temperature distribution in that region is the same as in the forced-convection thermal boundary layer solution in the

[3]The knee (bend) in the exponential temperature profile (4) is located (roughly) where the argument of the exponential is of order 1.

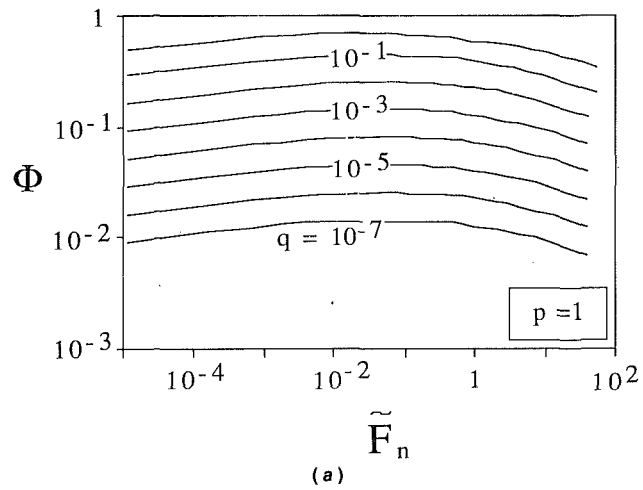

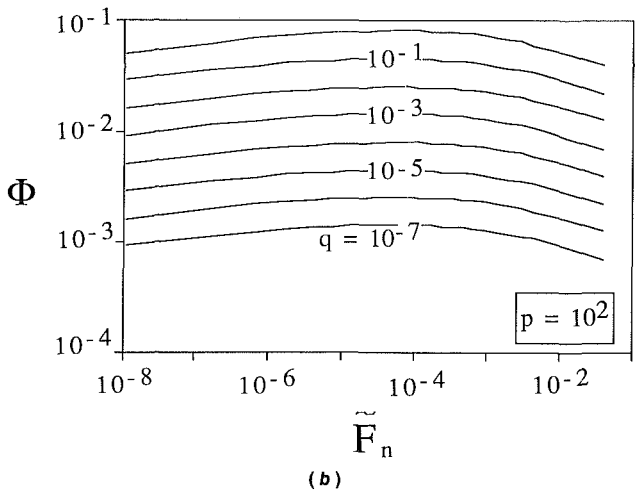

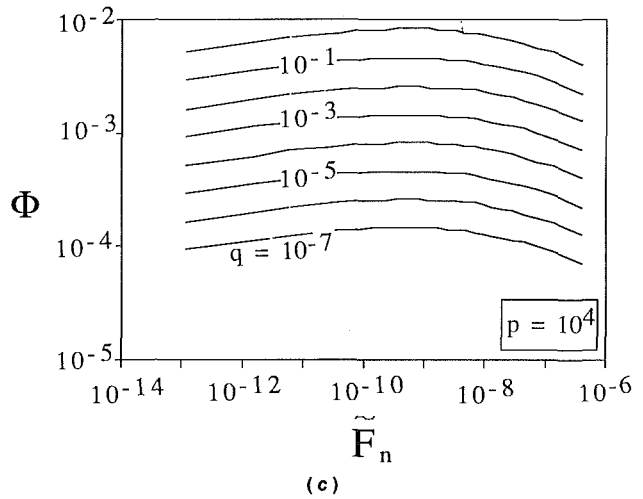

Fig. 2 The correction factor Φ, or the effect of lateral conduction on the melting velocity, equation (22)

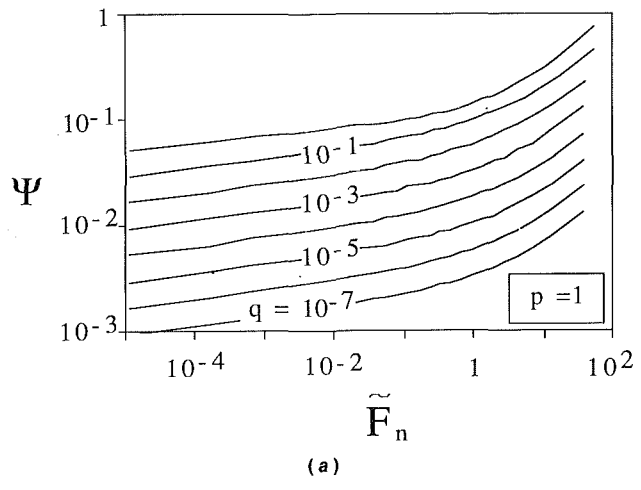

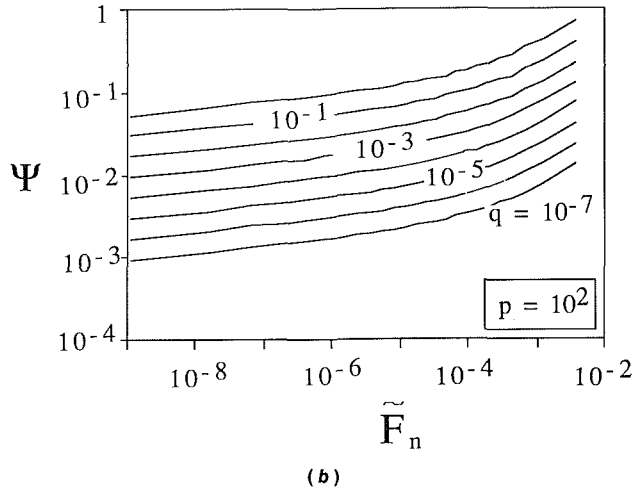

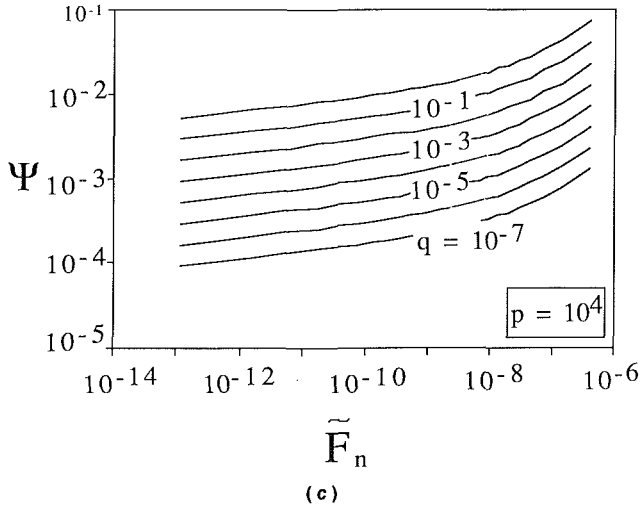

Fig. 3 The correction factor Ψ, or the effect of lateral conduction on the tangential force, equation (26)

slug flow limit. In particular, the relationship between the surface heat flux q''_w and the temperature difference that drives it $[T_s - T_w(x)]$ is (see, for example, Bejan, 1984)

$$T_s - T_w(x) = \frac{q''_w / k_s}{0.886} \left(\frac{\alpha_s x}{U} \right)^{1/2} \tag{9}$$

The corresponding form of the slenderness condition (8) is therefore the high Peclet number condition $UL/\alpha_s \gg 1$.

Eliminating the intermediate temperature T_w between equations (7) and (9), we obtain an expression that spells out the manner in which the film thickness varies with the longitudinal position. In dimensionless terms, this expression is

$$\tilde{h} = \frac{q}{\tilde{V}} - p\xi^{1/2} \tag{10}$$

where

$$\tilde{h}=\frac{h}{L},\qquad \tilde{V}=\frac{V}{U},\qquad \xi=\frac{x}{L} \tag{11}$$

$$p=\frac{k_f}{0.886k_s}\left(\frac{UL}{\alpha_s}\right)^{1/2} \tag{12}$$

$$q=\frac{k_f(T_s-T_m)}{\rho_0 h_{sf} UL\,(1+\mathrm{Ste})} \tag{13}$$

In this formulation, $\tilde{V}$ is the unknown dimensionless melting rate, while p and q are two presumably known physical parameters. Equation (10) shows that the film thickness decreases monotonically in the downstream direction, in the manner illustrated in Fig. 1. Note also that equation (10) does not hold near $\xi=0$, because in that region the smooth melting front assumption (2) breaks down. The same can be said about the boundary layer solution (9), on which equation (10) is based.

The "convection" terminology used starting with the title of this section may be misleading because in solids we are used to encountering problems of pure conduction. From the point of view of an observer who rides on the block of phase-change material, the lower solid is a conducting medium that "flows" to the right with the uniform velocity U. Relative to this observer then, the heat transfer in the lower solid may be termed as one of "convection." In the eyes of a different observer who would ride on the lower solid, however, the same heat transfer phenomenon would be one of time-dependent conduction, triggered by the short contact with the liquid gap.

5 Lubrication Effect

The heat transfer conclusions condensed in equations (10)–(13) account for the two heat transfer effects associated with the solid parts [note the role played by Ste and (T_s-T_m)]. The melting rate V, which is still an unknown, can be determined by considering the mechanical equilibrium of the upper body. This step consists of analyzing the lubrication effect and pressure distribution along the liquid film. Since this analysis can be found in most fluid mechanics textbooks (e.g., Batchelor, 1967), we omit its detail and focus only on the features that make the present application special.

The analysis is based on Reynolds' simplified momentum equation for the liquid film

$$\frac{dP}{dx}=\mu\frac{\partial^2 u}{\partial y^2} \tag{14}$$

which can be integrated across the film (subject to $u=U$ at $y=0$, and $u=0$ at $y=h$) to yield the longitudinal velocity profile

$$u=\frac{1}{2\mu}\frac{dP}{dx}y(y-h)+U\left(1-\frac{y}{h}\right) \tag{15}$$

and, in particular, the longitudinal flow rate

$$Q=\int_0^h u\,dy=\frac{h^2}{12\mu}\left(-\frac{dP}{dx}\right)+\frac{1}{2}Uh \tag{16}$$

It can be shown further that the across-the-film integral of the mass conservation equation yields

$$Q=-Q_0+Vx \tag{17}$$

regardless of the shape of the liquid gap $h(x)$. The constant of integration Q_0 is determined in two steps. First, the elimination of Q between equations (16) and (17) leads to an equation for dP/dx. Second, by integrating this equation over the entire length of the film, and by imposing the end conditions $P=0$ at $x=0$ and $x=L$, one obtains a single equation (an integral condition) whose only unknown is Q_0. In the dimensionless notation defined in equations (11)–(13), that integral condition is

$$\int_0^1\left[\frac{6}{\tilde{h}^2}+12\frac{\tilde{V}}{\tilde{h}^3}(\tilde{Q}_0-\xi)\right]d\xi=0 \tag{18}$$

in which the new dimensionless constant $\tilde{Q}_0$ is defined as $\tilde{Q}_0=Q_0/VL$. Equation (18) delivers $\tilde{Q}_0$ as a function of p, q, and $\tilde{V}$.

A step that precedes equation (18) in the analysis is the pressure distribution along the film

$$\tilde{P}(\xi)=\int_0^\xi\left[\frac{6}{\tilde{h}^2(\beta)}+12\frac{\tilde{V}}{\tilde{h}^3(\beta)}(\tilde{Q}_0-\beta)\right]d\beta \tag{19}$$

where the dimensionless pressure is defined as $\tilde{P}=PL/\mu U$. This leads immediately to the net vertical load per unit length normal to the plane of Fig. 1

$$\tilde{F}_n=\int_0^1\tilde{P}(\xi)\,d\xi \tag{20}$$

Table 1 Numerical examples of sliding-melting configurations, and the order of magnitude of the dimensionless parameters p and q (in all the examples, $U=1$ cm/s and $L=10$ cm)

Property	(Units)	Ice on steel	Polymer on steel	Zinc on steel	Tin on steel
k_f	(W/m°C)	0.55	0.178	56.9	33.5
h_{sf}	(J/kg)	334,944	130,000	102,138	60,697
α_0	(m^2/s)	4.7×10^{-5}	9×10^{-8}	4.2×10^{-5}	6.3×10^{-5}
ρ_0	(kg/m^3)	922	760	7140	7304
c_0	(J/kg°C)	2009.7	2600	388	139
k_0	(W/m°C)	87.44	0.178	116	64
α_s	(m^2/s)	1.5×10^{-5}	1.5×10^{-5}	1.5×10^{-5}	1.5×10^{-5}
k_s	(W/m°C)	55	55	55	55
T_s	(°C)	30	180→280	450→500	250→350
T_m	(°C)	0	110	419	231
T_0	(°C)	−30	20→80	30→400	30→200
p		29	9.4	3001	1775
q		4.5×10^{-6}	4.5×10^{-6}→ 6.6×10^{-5}	1.3×10^{-4}→ 5.8×10^{-4}	1×10^{-6}→ 8.4×10^{-6}
References		Brown and Marco (1958), Shortley and Williams (1959) Eckert and Drake (1959)	Shapiro et al. (1976)	Mantell (1958)	Mantell (1958)

in which the dimensionless normal force is now defined as $\tilde{F}_n = F_n/\mu U$. The pressure integral depends on p, q, and $\tilde{V}$; therefore, equation (20) is an implicit relation for the unknown $\tilde{V}$ as a function of $\tilde{F}_n$, p, and q.

In the limit where the thermal conductivity of the lower solid is sufficiently large so that the slider surface is practically isothermal ($p \to 0$), equation (20) reduces to

$$\tilde{V} = \tilde{F}_n^{1/4} q^{3/4} \tag{21}$$

In general, the $\tilde{V}$ ($\tilde{F}_n$, p, q) surface resulting from equation (20) is represented by

$$\tilde{V} = \tilde{F}_n^{1/4} q^{3/4} \Phi \tag{22}$$

in which the new factor $\Phi(\tilde{F}_n, p, q)$ satisfies the condition $\Phi(\tilde{F}_n, 0, q) = 1$. Figure 2 shows the values that can be taken by the Φ factor, and how these values are affected by the independent parameters $\tilde{F}_n$, p, and q. The figure was constructed by first performing the integrals (18) and (19) analytically, and then calculating the $\tilde{F}_n$ integral (20) numerically. Together, equation (22) and Fig. 2 constitute the solution to the problem of calculating the melting rate when the conduction effects on both sides the liquid film are not negligible.

The net tangential force between the two solid bodies can be evaluated by performing the integral

$$F_t = -\int_0^L \mu \left(\frac{\partial u}{\partial y}\right)_{y=0} dx \tag{23}$$

or, in the dimensionless terms,

$$\tilde{F}_t = \int_0^1 \left[\frac{4}{\tilde{h}} + 6\frac{\tilde{V}}{\tilde{h}^2}(\tilde{Q}_0 - \xi)\right] d\xi \tag{24}$$

where $\tilde{F}_t = F_t/\mu U$. Employing the calculus of limits, one can show that in the isothermal-slider limit ($p = 0$), equation (24) becomes

$$\tilde{F}_t = \left(\frac{\tilde{F}_n}{q}\right)^{1/4} \tag{25}$$

Therefore, a reasonable closed-form substitute for the general version of equation (24) is

$$\tilde{F}_t = \left(\frac{\tilde{F}_n}{q}\right)^{1/4} \Psi \tag{26}$$

where the correction factor Ψ ($\tilde{F}_n$, p, q) satisfies the condition Ψ ($\tilde{F}_n$, 0, q) = 1. The impact of $\tilde{F}_n$, p, and q on the correction factor Ψ is documented in Fig. 3.

6 Conclusion

The effect of solid-body heat transfer on the phenomenon of melting by sliding contact is condensed in Figs. 2 and 3. The (p, q) domain that is covered by these figures was chosen based on numerical examples such as those exhibited in Table 1. The entire solution is "referenced" to the simpler case in which the base heater is isothermal ($p = 0$): This reference case is represented by $\Phi = 1$ in Fig. 2 and $\Psi = 1$ in Fig. 3.

The present results can be compared with the conclusions of the earlier study (Bejan, 1989) in which the lower solid was modeled as isothermal, and the upper solid was assumed isothermal and at the melting point. This earlier model fits the ($p = 0$, Ste = 0) limit of the present study.

The chief conclusion of this note is that the lateral conduction heat transfer can have a significant effect on the melting velocity. The correction factor Φ decreases steadily as p increases, i.e., as the slider departs from the isothermal-wall description. According to equation (22), as Φ becomes considerably smaller than 1, the melting velocity becomes considerably smaller than the value that prevails in the isothermal-slider limit.

Similar conclusions apply to the secondary result of the analysis, the tangential force F_t. Since the correction factor Φ is smaller than 1, the tangential force is smaller than the value predicted by the isothermal-slider limit of the same problem (Bejan, 1989).

Acknowledgments

The support received from the National Science Foundation through Grant No. CBT-8711369 is gratefully acknowledged. Pedro A. Litsek acknowledges also the support received from his home company, Promon Engenharia, S.A., Brazil.

References

Batchelor, G. K., 1967, *An Introduction to Fluid Dynamics*, Cambridge University Press, Cambridge, pp. 219–222.

Bejan, A., 1984, *Convection Heat Transfer*, Wiley, New York, pp. 358, 384–385.

Bejan, A., 1989, "The Fundamentals of Sliding Contact Melting and Friction," ASME JOURNAL OF HEAT TRANSFER, Vol. 111, pp. 13–20.

Brown, A. I., and Marco, S. M., 1958, *Introduction to Heat Transfer*, 3rd ed., McGraw-Hill, New York.

Eckert, E. R. G., and Drake, R. M., 1959, *Heat and Mass Transfer*, 2nd ed., McGraw-Hill, New York.

Mantell, C., 1958, *Engineering Materials Handbook*, McGraw-Hill, New York.

Shapiro, J., Halmos, A. L., and Pearson, J. R. A., 1976, "Melting in Single Extruders," *Polymer*, Vol. 17, pp. 905–918.

Shortley, G., and Williams, D., 1959, *Principles of College Physics*, Prentice-Hall, Englewood Cliffs, NJ.

A Numerical Analysis of Phase-Change Problems Including Natural Convection

Y. Cao[1,3] and A. Faghri[2,3]

Nomenclature

c = specific heat, J/(kg-K)
c_p^* = equivalent specific heat, J/(kg-K)
D = diagonal distance, m
E = enthalpy, J/kg
g = gravitational acceleration, m/s^2
H = height of the vertical wall, m
k = thermal conductivity, W/(m-K)
L = latent heat, J/kg
l^2 = cross-sectional area of square bar in Fig. 2(a), m^2
p = pressure, N/m^2
s = interface position along the diagonal, m
T^o = temperature, K
T = dimensionless temperature = $(T^o - T_m^o)/(T_h^o - T_c^o)$
t = time, s
u, v, w = velocities, m/s
x, y, z = coordinate directions
α = thermal diffusivity, m^2/s
β = coefficient of volumetric thermal expansion, K^{-1}
μ = dynamic viscosity, kg/(m-s)
ν = kinematic viscosity, m^2/s
ρ = density, kg/m^3

[1]Graduate Research Assistant.

[2]Brage Golding Distinguished Professor.

[3]Department of Mechanical and Materials Engineering, Wright State University, Dayton, OH 45435.

Contributed by the Heat Transfer Division and presented at the National Heat Transfer Conference, Philadelphia, Pennsylvania, August 6–9, 1989. Manuscript received by the Heat Transfer Division July 24, 1989; revision received November 28, 1989. Keywords: Natural Convection, Numerical Methods, Phase-Change Phenomena.

in which the dimensionless normal force is now defined as $\tilde{F}_n = F_n/\mu U$. The pressure integral depends on p, q, and $\tilde{V}$; therefore, equation (20) is an implicit relation for the unknown $\tilde{V}$ as a function of $\tilde{F}_n$, p, and q.

In the limit where the thermal conductivity of the lower solid is sufficiently large so that the slider surface is practically isothermal ($p \to 0$), equation (20) reduces to

$$\tilde{V} = \tilde{F}_n^{1/4} q^{3/4} \tag{21}$$

In general, the $\tilde{V}$ ($\tilde{F}_n$, p, q) surface resulting from equation (20) is represented by

$$\tilde{V} = \tilde{F}_n^{1/4} q^{3/4} \Phi \tag{22}$$

in which the new factor $\Phi(\tilde{F}_n, p, q)$ satisfies the condition $\Phi(\tilde{F}_n, 0, q) = 1$. Figure 2 shows the values that can be taken by the Φ factor, and how these values are affected by the independent parameters $\tilde{F}_n$, p, and q. The figure was constructed by first performing the integrals (18) and (19) analytically, and then calculating the $\tilde{F}_n$ integral (20) numerically. Together, equation (22) and Fig. 2 constitute the solution to the problem of calculating the melting rate when the conduction effects on both sides the liquid film are not negligible.

The net tangential force between the two solid bodies can be evaluated by performing the integral

$$F_t = -\int_0^L \mu \left(\frac{\partial u}{\partial y}\right)_{y=0} dx \tag{23}$$

or, in the dimensionless terms,

$$\tilde{F}_t = \int_0^1 \left[\frac{4}{\tilde{h}} + 6\frac{\tilde{V}}{\tilde{h}^2}(\tilde{Q}_0 - \xi)\right] d\xi \tag{24}$$

where $\tilde{F}_t = F_t/\mu U$. Employing the calculus of limits, one can show that in the isothermal-slider limit ($p = 0$), equation (24) becomes

$$\tilde{F}_t = \left(\frac{\tilde{F}_n}{q}\right)^{1/4} \tag{25}$$

Therefore, a reasonable closed-form substitute for the general version of equation (24) is

$$\tilde{F}_t = \left(\frac{\tilde{F}_n}{q}\right)^{1/4} \Psi \tag{26}$$

where the correction factor Ψ ($\tilde{F}_n$, p, q) satisfies the condition Ψ ($\tilde{F}_n$, 0, q) = 1. The impact of $\tilde{F}_n$, p, and q on the correction factor Ψ is documented in Fig. 3.

6 Conclusion

The effect of solid-body heat transfer on the phenomenon of melting by sliding contact is condensed in Figs. 2 and 3. The (p, q) domain that is covered by these figures was chosen based on numerical examples such as those exhibited in Table 1. The entire solution is "referenced" to the simpler case in which the base heater is isothermal ($p = 0$): This reference case is represented by $\Phi = 1$ in Fig. 2 and $\Psi = 1$ in Fig. 3.

The present results can be compared with the conclusions of the earlier study (Bejan, 1989) in which the lower solid was modeled as isothermal, and the upper solid was assumed isothermal and at the melting point. This earlier model fits the ($p = 0$, Ste = 0) limit of the present study.

The chief conclusion of this note is that the lateral conduction heat transfer can have a significant effect on the melting velocity. The correction factor Φ decreases steadily as p increases, i.e., as the slider departs from the isothermal-wall description. According to equation (22), as Φ becomes considerably smaller than 1, the melting velocity becomes considerably smaller than the value that prevails in the isothermal-slider limit.

Similar conclusions apply to the secondary result of the analysis, the tangential force F_t. Since the correction factor Φ is smaller than 1, the tangential force is smaller than the value predicted by the isothermal-slider limit of the same problem (Bejan, 1989).

Acknowledgments

The support received from the National Science Foundation through Grant No. CBT-8711369 is gratefully acknowledged. Pedro A. Litsek acknowledges also the support received from his home company, Promon Engenharia, S.A., Brazil.

References

Batchelor, G. K., 1967, *An Introduction to Fluid Dynamics*, Cambridge University Press, Cambridge, pp. 219–222.

Bejan, A., 1984, *Convection Heat Transfer*, Wiley, New York, pp. 358, 384–385.

Bejan, A., 1989, "The Fundamentals of Sliding Contact Melting and Friction," ASME JOURNAL OF HEAT TRANSFER, Vol. 111, pp. 13–20.

Brown, A. I., and Marco, S. M., 1958, *Introduction to Heat Transfer*, 3rd ed., McGraw-Hill, New York.

Eckert, E. R. G., and Drake, R. M., 1959, *Heat and Mass Transfer*, 2nd ed., McGraw-Hill, New York.

Mantell, C., 1958, *Engineering Materials Handbook*, McGraw-Hill, New York.

Shapiro, J., Halmos, A. L., and Pearson, J. R. A., 1976, "Melting in Single Extruders," *Polymer*, Vol. 17, pp. 905–918.

Shortley, G., and Williams, D., 1959, *Principles of College Physics*, Prentice-Hall, Englewood Cliffs, NJ.

A Numerical Analysis of Phase-Change Problems Including Natural Convection

Y. Cao[1,3] and A. Faghri[2,3]

Nomenclature

c = specific heat, J/(kg-K)
c_p^* = equivalent specific heat, J/(kg-K)
D = diagonal distance, m
E = enthalpy, J/kg
g = gravitational acceleration, m/s^2
H = height of the vertical wall, m
k = thermal conductivity, W/(m-K)
L = latent heat, J/kg
l^2 = cross-sectional area of square bar in Fig. 2(a), m^2
p = pressure, N/m^2
s = interface position along the diagonal, m
T^o = temperature, K
T = dimensionless temperature = $(T^o - T_m^o)/(T_h^o - T_c^o)$
t = time, s
u, v, w = velocities, m/s
x, y, z = coordinate directions
α = thermal diffusivity, m^2/s
β = coefficient of volumetric thermal expansion, K^{-1}
μ = dynamic viscosity, kg/(m-s)
ν = kinematic viscosity, m^2/s
ρ = density, kg/m^3

[1]Graduate Research Assistant.

[2]Brage Golding Distinguished Professor.

[3]Department of Mechanical and Materials Engineering, Wright State University, Dayton, OH 45435.

Contributed by the Heat Transfer Division and presented at the National Heat Transfer Conference, Philadelphia, Pennsylvania, August 6–9, 1989. Manuscript received by the Heat Transfer Division July 24, 1989; revision received November 28, 1989. Keywords: Natural Convection, Numerical Methods, Phase-Change Phenomena.

Subscripts

i = initial condition
l = liquid phase
m = mushy phase
s = solid phase
w = wall

Introduction

Fixed grid solutions for phase-change problems remove the need to satisfy conditions at the phase-change front and can be easily extended to multidimensional problems. The two most important and widely used methods are enthalpy methods and temperature-based equivalent heat capacity methods. Both methods in this group have advantages and disadvantages. Enthalpy methods (Shamsundar and Sparrow, 1975; Voller and Prakash, 1987; Cao et al., 1989) are flexible and can handle phase-change problems occurring both at a single temperature and over a temperature range. The drawback of this method is that although the predicted temperature distributions and melting fronts are reasonable, the predicted time history of the temperature at a typical grid point may have some oscillations. The temperature-based fixed grid methods (Morgan, 1981; Hsiao and Chung, 1984) have no such time history problems and are more convenient with conjugate problems involving an adjacent wall, but have to deal with the severe nonlinearity of the governing equations when the phase-change temperature range is small. Since the objective of this paper is to improve the temperature-based fixed-grid methods, the equivalent heat capacity model is briefly described below. The energy equation including convective terms is given by Morgan (1981) and Hsiao and Chung (1984)

$$\rho c_p^* \left(\frac{\partial T^o}{\partial t} + u\frac{\partial T^o}{\partial x} + v\frac{\partial T^o}{\partial y} + w\frac{\partial T^o}{\partial z} \right) = \nabla \cdot k \nabla T^o \tag{1}$$

To account for the latent heat effect on the liquid–solid interface, an equivalent heat capacity is introduced assuming that phase change occurs over a temperature range

$$c_p^* = \begin{cases} c_s & (T^o < T_m^o - \delta T^o) \\ \dfrac{L}{2\delta T^o} + \dfrac{c_l + c_s}{2} & (T_m^o - \delta T^o \le T^o \le T_m^o + \delta T^o) \\ c_l & (T^o > T_m^o + \delta T^o) \end{cases} \tag{2}$$

Although the equivalent heat capacity formulation has the advantage of being simple to program, many studies have revealed difficulties in the selection of the time step, mesh size, and the phase-change temperature range, $2\delta T^o$. The predicted phase-change interface location advances frequently in an unrealistic oscillatory fashion and this is accompanied by distortion of the temperature profile in the region undergoing phase change. In this paper, a new temperature-based fixed-grid formulation is proposed, and the reason that the original equivalent heat capacity model is subject to such restrictions on the time step, mesh size, and the phase-change temperature range will also be discussed.

Numerical Formulation and Modeling

The continuity, momentum, and energy equations governing three-dimensional transient laminar flows with no viscous dissipation in the Cartesian coordinate system are

$$\frac{\partial \rho}{\partial t} + \frac{\partial}{\partial x}(\rho u) + \frac{\partial}{\partial y}(\rho v) + \frac{\partial}{\partial z}(\rho w) = 0 \tag{3a}$$

$$\rho \frac{D\mathbf{V}}{Dt} = -\nabla p + \mu \nabla^2 \mathbf{V} + \rho \mathbf{g} \tag{3b}$$

$$\frac{\partial(\rho E)}{\partial t} + \frac{\partial}{\partial x}(\rho u E) + \frac{\partial}{\partial y}(\rho v E) + \frac{\partial}{\partial z}(\rho w E) = \nabla \cdot k \nabla T^o \tag{3c}$$

$$\frac{dE}{dT^o} = c(T^o) \tag{4}$$

For the phase change occurring over a temperature range and in the case of constant specific heats for each phase, the relation between enthalpy and temperature can be expressed as

$$E(T^*) = \begin{cases} c_s T^* + c_s \delta T^o & \\ \left(c_m + \dfrac{L}{2\delta T^o} \right) T^* + c_m \delta T^o + \dfrac{L}{2} & \\ c_l T^* + c_s \delta T^o + L & \end{cases}$$

$$\begin{array}{ll} (T^* < -\delta T^o) & \text{(solid phase)} \\ (-\delta T^o \le T^* \le \delta T^o) & \text{(mushy phase)} \\ (T^* > \delta T^o) & \text{(liquid phase)} \end{array} \tag{5}$$

where $T^* = T^o - T_m^o$, and T_m^o is the melting or freezing temperature, which is defined as the center of the phase-change temperature range. In the above relation, we have selected $E = 0$ to correspond to phase-change materials in the solid state at $T^o = T_m^o - \delta T^o$. The specific heat of the mushy phase has been taken as the average of those of the solid and liquid phases; i.e., $c_m = (c_s + c_l)/2$.

A temperature function is introduced as follows:

$$E(T^*) = C^o(T^*) T^* + S^o(T^*) \tag{6}$$

where $C^o(T^*)$ and $S^o(T^*)$ are determined from equation (5)

$$C^o(T^*) = \begin{cases} c_s & (T^* < -\delta T^o) \\ c_m + \dfrac{L}{2\delta T^o} & (-\delta T^o \le T^* \le \delta T^o) \\ c_l & (T^* > \delta T^o) \end{cases} \tag{7}$$

$$S^o(T^*) = \begin{cases} c_s \delta T^o & (T^* < -\delta T^o) \\ c_m \delta T^o + \dfrac{L}{2} & (-\delta T^o \le T^* \le \delta T^o) \\ c_s \delta T^o + L & (T^* > \delta T^o) \end{cases} \tag{8}$$

Upon substituting equation (6) into equation (3c)

$$\frac{\partial(\rho C^o T^*)}{\partial t} + \frac{\partial}{\partial x}(\rho u C^o T^*) + \frac{\partial}{\partial y}(\rho v C^o T^*) + \frac{\partial}{\partial z}(\rho w C^o T^*) = \nabla \cdot k \nabla T^* + B \tag{9}$$

with $B = -\left[\dfrac{\partial(\rho S^o)}{\partial t} + \dfrac{\partial(\rho u S^o)}{\partial x} + \dfrac{\partial(\rho v S^o)}{\partial y} + \dfrac{\partial(\rho w S^o)}{\partial z} \right]$, and $C^o = C^o(T^*)$, $S^o = S^o(T^*)$ given by equations (7) and (8), respectively.

It can be seen that equation (7) is identical to equation (2), and that when the density ρ is constant the equivalent heat capacity model is a special case of equation (9) with $B = 0$ and C^o independent of the space variables x, y, z, and time. This is why many studies using the equivalent capacity model found difficulties in selecting the time step and mesh sizes and have often encountered physically unrealistic oscillatory results. In order for $\dfrac{\partial(\rho C^o T^*)}{\partial t} = C^o \dfrac{\partial(\rho T^*)}{\partial t}$, and $\dfrac{\partial(\rho S^o)}{\partial t} = 0$, the time step must be small enough that the temperature change is so small that values of C^o and S^o will not change from one phase to another within the time step. Special care must also be taken for the selection of grid sizes to make C^o and S^o

independent of the space variables. In fact, the above conditions are so severe that it is very difficult to satisfy them.

The following nondimensionalized variables are introduced:

$$X=\frac{x}{H},\quad Y=\frac{y}{H},\quad Z=\frac{z}{H},\quad U=u\frac{H}{\alpha_l},\quad V=v\frac{H}{\alpha_l},\quad W=w\frac{H}{\alpha_l},$$

$$\tau=\frac{\alpha_l}{H^2}t,\quad T=\frac{T^o-T_m^o}{T_h^o-T_c^o},\quad C=\frac{C^o}{c_l},\quad S=\frac{S^o}{c_l(T_h^o-T_c^o)},\quad K=\frac{k}{k_l},$$

$$\delta T^*=\frac{\delta T^o}{T_h^o-T_c^o},\quad \mathrm{St}=\frac{c_l(T_h^o-T_c^o)}{L},\quad C_{sl}=\frac{c_s}{c_l},\quad K_{sl}=\frac{k_s}{k_l} \tag{10}$$

It should be noted that the superscript o is used for variables that have units, while dimensionless terms do not have superscripts. The governing equation is nondimensionalized as

$$\frac{\partial(CT)}{\partial\tau}+\frac{\partial}{\partial X}(UCT)+\frac{\partial}{\partial Y}(VCT)+\frac{\partial}{\partial Z}(WCT)=\nabla\cdot K\nabla T+B^* \tag{11}$$

with

$$B^*=-\left[\frac{\partial S}{\partial\tau}+\frac{\partial}{\partial X}(US)+\frac{\partial}{\partial Y}(VS)+\frac{\partial}{\partial Z}(WS)\right]$$

$$C(T)=\begin{cases} C_{sl} & (T<-\delta T^*)\\ \dfrac{1}{2}(1+C_{sl})+\dfrac{1}{2\ \mathrm{St}\ \delta T^*} & (-\delta T^*\le T\le\delta T^*)\\ 1 & (T>\delta T^*)\end{cases} \tag{12}$$

$$S(T)=\begin{cases} C_{sl}\delta T^* & (T<-\delta T^*)\\ \dfrac{1}{2}\delta T^*(1+C_{sl})+\dfrac{1}{2\ \mathrm{St}} & (-\delta T^*\le T\le\delta T^*)\\ C_{sl}\delta T^*+\dfrac{1}{\mathrm{St}} & (T>\delta T^*)\end{cases} \tag{13}$$

The conductivity k is a function of T^*. With the assumption of a linear change in the mushy phase, $K=k/k_l$ can be written as

$$K(T)=\begin{cases} K_{sl} & (T<-\delta T^*)\\ K_{sl}+(1-K_{sl})(T+\delta T^*)/2\delta T^* & (-\delta T^*\le T\le\delta T^*)\\ 1 & (T>\delta T^*)\end{cases} \tag{14}$$

The discretization of the above equation employs the control-volume finite-difference approach described by Patankar (1980). Since equation (11) is nonlinear, iterations are needed at each time step. For the dimensionless thermal conductivity K, it is important to use the harmonic mean described by Patankar (1980) at the faces of the control volume.

Numerical Results and Discussion

Consider first a one-dimensional melting problem in a half-space (one-region problem). A solid at the solidification (or melting) temperature T_m^o is confined to a half-space $x>0$. At time $t=0$, the temperature of the boundary surface at $x=0$ is raised to T_h^o, which is higher than T_m^o and maintained at that temperature for $t>0$.

Figure 1 shows the comparison between the exact solution and the present numerical solution with a grid size $\Delta X=0.05$ for the location of the melting front as a function of the square root of the dimensionless time τ. In order to simulate the sharp melting front, a small temperature range $\delta T^*=0.001$ is used in the calculation and the initial temperature is set to $T=-0.001$ instead of $T=0$. As can be seen from Fig. 1, the present solution is in agreement with the exact solution.

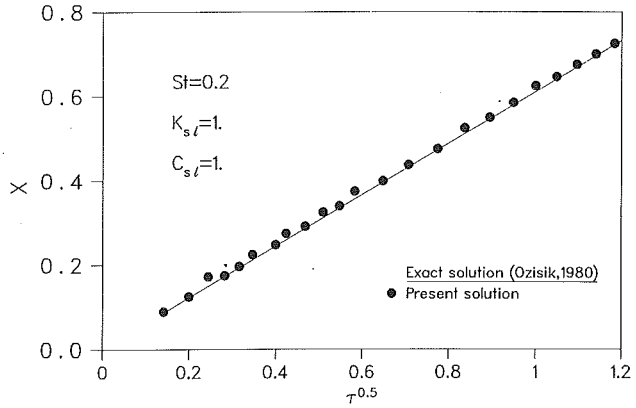

Fig. 1 The exact and numerical solutions of the melting front in a half-space

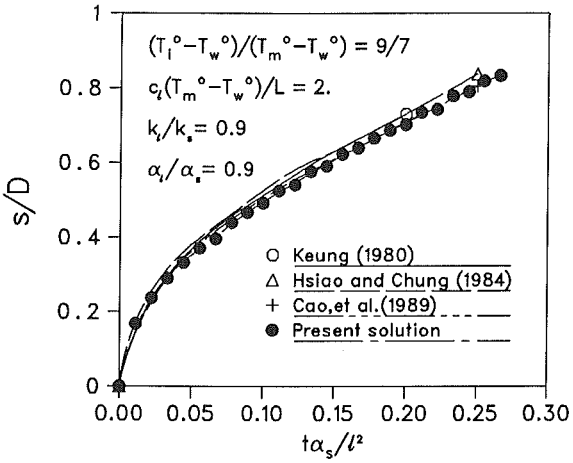

Fig. 2(*a*) Interface position along the diagonal

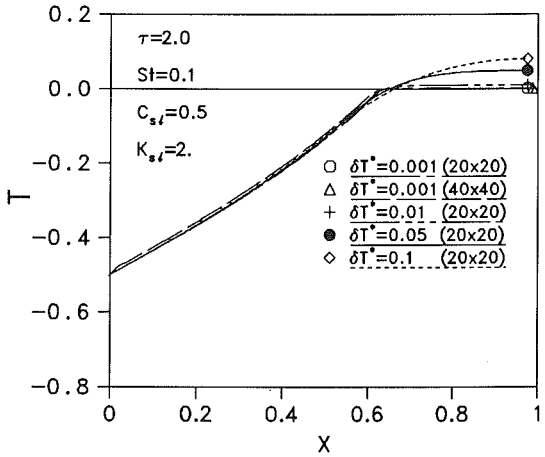

Fig. 2(*b*) Temperature profiles along an adiabatic line

Fig. 2 Interface position along the diagonal and temperature profiles along the adiabatic line

The accuracy of the present model will now be tested with a two-dimensional freezing problem. Consider a liquid initially at temperature T_i^o in a bar with a uniform square cross section and adiabatic ends. The surface is suddenly exposed to a uniform wall temperature below the fusion temperature and freezing takes place immediately. Because of the symmetry of the geometry, only a quarter of the bar is considered. Figure 2(*a*) shows the interface position as a function of dimensionless

time along the diagonal with a grid size of 20×20 and a time step $\Delta\tau=0.01$. It took about 40 s to run the case on a VAX 8550. Also included in Fig. 2(*a*) are solutions obtained by Hsiao and Chung (1984), Keung (1980), and Cao et al. (1989) using the enthalpy-transforming model. It can be seen that the present two-dimensional solution agrees well with the results of those studies.

Calculations were also made with different phase-change temperature ranges and physical property ratios between the solid and liquid phases. Figure 2(*b*) shows temperature distributions along the adiabatic line of the cross section for different values of δT^*. The initial dimensionless temperature of the liquid was set to $T_i=0.5$ and the dimensionless surface temperature was set to $T_w=-0.5$. It can be seen that the present scheme is insensitive to the phase-change temperature range. The temperature distributions in the solid region and phase-change interfaces ($T=0$) are almost identical with slight differences of the temperature distribution in the liquid region. It can also be seen that the curve with $\delta T^*=0.01$ is almost the same as that with $\delta T^*=0.001$. This means that a moderately small phase-change temperature range is enough to simulate the phase-change problem occurring at a single temperature.

Time step and grid size limits were not encountered in the above calculations. The dimensionless time step $\Delta\tau$ can be on the order of 0.1–1.0 and the real time step Δt can be as large as several days. The model is also independent of grid sizes. The curve with a grid size of 40×40 is almost identical to that of 20×20 with the same δT^*. It should be pointed out that due to the severe nonlinearity of phase-change problems, underrelaxation is needed during the iterations for C, S and K in equation (11) when δT^* is very small. The normal underrelaxation parameters are 0.1–0.5 for small values of δT^*. For a moderate value of δT^*, underrelaxation is not needed.

To further demonstrate the present model, the phase change with natural convection in a two-dimensional cavity was studied. The dimensionless governing equations with parameters introduced in equation (10) and the Boussinesq approximation are as follows:

$$\frac{\partial U}{\partial X}+\frac{\partial V}{\partial Y}=0 \tag{15}$$

$$\frac{\partial U}{\partial \tau}+\frac{\partial (U^2)}{\partial X}+\frac{\partial (UV)}{\partial Y}=-\frac{\partial P}{\partial X}+\frac{\partial}{\partial X}\left(\mathrm{Pr}\frac{\partial U}{\partial X}\right)+\frac{\partial}{\partial Y}\left(\mathrm{Pr}\frac{\partial V}{\partial Y}\right) \tag{16}$$

$$\frac{\partial V}{\partial \tau}+\frac{\partial (UV)}{\partial X}+\frac{\partial (V^2)}{\partial Y}=-\frac{\partial P}{\partial Y}+\mathrm{RaPr}_l\mathrm{T}+\frac{\partial}{\partial X}\left(\mathrm{Pr}\frac{\partial V}{\partial X}\right)+\frac{\partial}{\partial Y}\left(\mathrm{Pr}\frac{\partial V}{\partial Y}\right) \tag{17}$$

$$\frac{\partial (CT)}{\partial \tau}+\frac{\partial}{\partial X}(UCT)+\frac{\partial}{\partial Y}(VCT)=\nabla\cdot K\nabla T-\left[\frac{\partial S}{\partial \tau}+\frac{\partial}{\partial X}(US)+\frac{\partial}{\partial Y}(VS)\right] \tag{18}$$

where $\mathrm{Ra}=g\beta H^3(T_h^o-T_c^o)/\nu_l\alpha_l$, $\mathrm{Pr}_l=\nu_l/\alpha_l$, $\mathrm{Pr}=\nu/\alpha_l$, $P=(p+\rho gy)H^2/\rho\alpha_l^2$, and C, S, and K are given by equations (12), (13), and (14), respectively. Equations (15)–(18) were solved numerically using the iterative SIMPLER algorithm (Patankar, 1980) with the numerical modeling in the previous section of this paper used for the energy equation.

At the solid–liquid interface or in the mushy region, the velocities U and V go to zero. A commonly used procedure is to prescribe a fluid viscosity that is equal to the liquid viscosity in the liquid region and increases gradually over the mushy zone to a large value in the solid. Therefore, the viscosity is expressed as

$$\nu=\begin{cases}\nu_l & (T>\delta T^*)\\ \nu_l+(\mathrm{T}-\delta\mathrm{T}^*)(\nu_l-\mathrm{N})/2\delta\mathrm{T}^* & (-\delta T^*\le T\le\delta T^*)\\ N & (T<-\delta T^*)\end{cases} \tag{19}$$

where N takes a sufficiently large value such as 10^{10}.

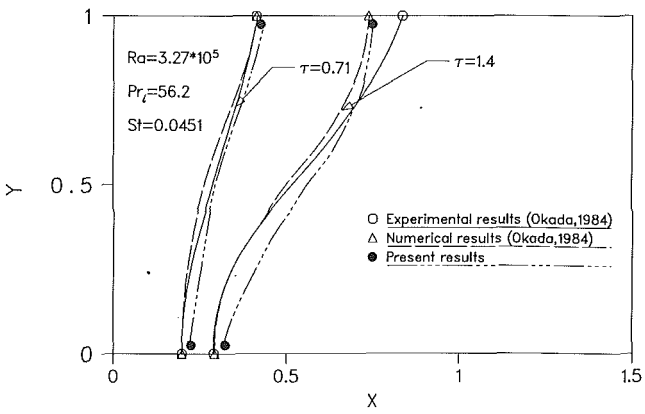

Fig. 3 Comparison of the locations of the melting front

Calculations were conducted with a melting problem occurring at a single temperature (Okada, 1984). The initial and boundary conditions for this problem are $T_i=0$; $T_h=1$ at $X=0$; $T_c=0$ at $X=1$, and $\partial T/\partial Y=0$ at $Y=0$ and $Y=1$. In order to simulate the phase change having a sharp interface with the present model, δT^* was taken as 0.01 and T_i and T_c were set to -0.01 in the calculations. Figure 3 shows the calculated results with a 20×20 grid size compared with the experimental results given by Okada (1984). Also included in the figure are the numerical results with the coordinate transforming method and the quasi-steady assumption. It can be seen that the present results are in agreement with the past experimental and numerical results. The CPU time for running the case is about three hours on the VAX 8550, which is much higher than those of purely diffusive phase-change problems.

Conclusions

The temperature transforming model and the numerical scheme proposed in this paper prove to be flexible, easy to implement, and able to handle three-dimensional phase-change problems, including those with large specific heat and thermal conductivity differences between the solid and liquid phases. For diffusion-controlled phase-change problems, the model eliminates the time step and grid size limitations that the equivalent heat capacity model usually encounters and is insensitive to phase-change temperature ranges. The model can also deal properly with convective-diffusive phase-change problems in a fixed grid system.

Acknowledgments

Funding for this work was provided by a joint effort of NASA Lewis Research Center and the Thermal Energy Group of the Aero Propulsion Laboratory of the U.S. Air Force under contract No. F33615-88-C-2820.

References

Cao, Y., Faghri, A., and Chang, W. S., 1989, "A Numerical Analysis of Stefan Problems for Generalized Multi-dimensional Phase-Change Structures Using the Enthalpy Transforming Model," *Int. J. Heat Mass Transfer*, Vol. 32, No. 7, pp. 1289–1298.

Hsiao, J. S., and Chung, B. T. F., 1984, "An Efficient Algorithm for Finite Element Solution to Two-Dimensional Heat Transfer With Melting and Freezing," ASME Paper No. 84-HT-2.

Keung, C. S., 1980, "The Use of Source and Sink in Solving Two-Dimensional Heat Conduction Problems With Change of Phase in Arbitrary Domains," Ph.D. dissertation, Columbia University, New York.
Morgan, K., 1981, "A Numerical Analysis of Freezing and Melting With Convection," *Computer Methods in Applied Mechanics and Engineering*, Vol. 28, No. 3, pp. 275–284.
Okada, M., 1984, "Analysis of Heat Transfer During Melting From a Vertical Wall," *Int. J. Heat Mass Transfer*, Vol. 27, No. 11, pp. 2057–2066.
Ozisik, M. N., 1980 , *Heat Conduction*, Wiley, New York.
Patankar, S. V., 1980, *Numerical Heat Transfer and Fluid Flow*, McGraw-Hill, New York.
Shamsundar, N., and Sparrow, E. M., 1975, "Analysis of Multidimensional Conduction Phase Change via the Enthalpy Model," ASME JOURNAL OF HEAT TRANSFER, Vol. 97, No. 3, pp. 333–340.
Voller, V. R., and Prakash, C., 1987, "A Fixed Grid Numerical Modeling Methodology for Convection-Diffusion Mushy Region Phase-Change Problems," *Int. J. Heat Mass Transfer*, Vol. 30, No. 8, pp. 1709–1718.

View Factors for Wall to Random Dispersed Solid Bed Transport

J. W. C. Tseng[1] and W. Strieder[2]

Introduction

Radiant heat transfer in fluidized beds (Brewster 1986; Grace, 1982) or dispersed solid insulation involves energy exchange between a well-defined wall surface and a random bed of solid particles whose geometry is known only in a statistical sense. In instances where the walls and bed can be considered gray-diffuse surfaces, the temperatures of each are nearly uniform, and particle dimensions (Grace, 1982) are much larger than the thermal radiation wavelength, the view factor and straightforward (Siegel and Howell, 1981) net-radiation methods can be applied to calculate radiant heat transport rates. Beyond radiation, the wall-to-random bed view factors have additional applications where the characteristic dimensions of the dispersed solid need not be large. Barron (1985) has pointed out that view factors can be used in low-pressure cryogenic insulation for Knudsen void gas heat transfer. Wall-to-bed view factors will also predict mass transfer deposition rates into random fibrous or particulate supports, for low-pressure sputtering processes (Wehner and Anderson, 1970).

Wall-to-bed view factors are calculated and plotted versus bed void fraction and thickness for several model dispersed solids—overlapping, equisized spheres and overlapping, identical, parallel long cylinders (parallel both to the wall and to each other)—randomly placed in the volume between two infinite parallel planes.

View Factors and Void Fractions

(i) Bed of Aligned, Overlapping Fibers. It seems reasonable to model a fibrous material as a bed of very long right circular cylinders of radius ω placed at random between the planes $x = 0$ and $x = L$. All cylinders are given the same orientation mutually parallel to each other and parallel to the bounding planes. Viewed from a plane perpendicular to the fiber axis (Fig. 1), the cross sections appear as circles with an average density of circle centers n per unit area of the plane. Those points lying on the perimeter of a circle, but not in the interior of an overlapping circle, make up the fiber bed surface; the solid regions of the fiber bed consist of all points lying in the interior of one or more circles. The planes Σ_0 and Σ_L located at $x = 0$ and $x = L$ in Fig. 1 each have a wall surface area A_w. The exposed, nonoverlapped surface Σ_b has an area A_b. As the fibers will not penetrate the wall, the circle centers are restricted to a distance ω from the bounding planes, i.e., the centers are placed completely at random but within the interval $x = \omega$ to $x = L - \omega$. The statistics of this geometry are sufficiently straightforward to allow closed expressions (Faley and Strieder, 1987) for the necessary probabilities. The probability P_a that no circle center lies within an area a can be written in terms of the density of circle centers n in the plane

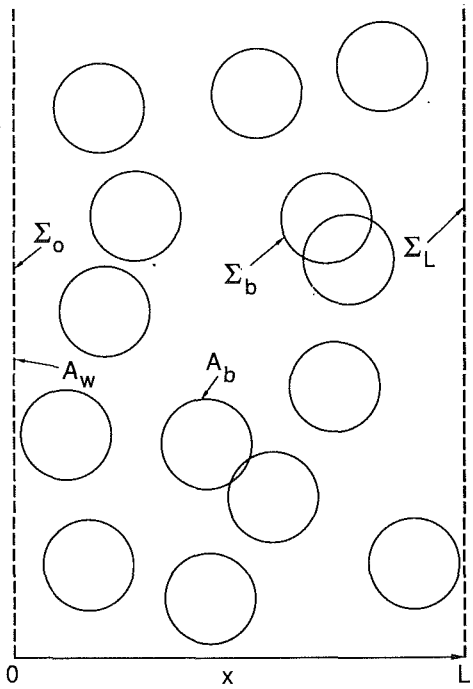

Fig. 1 Bed of fibers

$$P_a = \exp(-n\,a) \tag{1}$$

The void volume fraction can be interpreted as the probability that a randomly chosen point in the material falls in the void, or the probability that no circle has its center within a distance ω of the random point. Within the central region $(2\omega < x < L - 2\omega)$ of a sufficiently wide system $(L > 4\omega)$, the void fraction ϕ_2 is given by equation (1) as $\exp[-\pi\omega^2 n]$. However, fibers cannot penetrate the bounding walls and as no circle centers may lie within a distance ω of $x = 0$ or $x = L$, it is not necessary to exclude centers from these regions. Only that portion of the circle lying within the interval from $x = \omega$ to $x = L - \omega$ need be considered in any exclusion area. In a slab of thickness $L \geq 4\omega$, we have from equation (1) and some straightforward geometry, the bed void fraction

$$\phi_1(x) = \exp\left[-\left\{\omega^2 \arccos\left(\frac{\omega - x}{\omega}\right) - (\omega - x)\,[2\omega x - x^2]^{1/2}\right\} n\right],$$
$$0 \leq x \leq 2\omega \quad \text{for} \quad L \geq 4\omega \tag{2}$$

and

[1]Graduate Student, Department of Chemical Engineering, University of Notre Dame, Notre Dame, IN 46556.
[2]Professor, Department of Chemical Engineering, University of Notre Dame, Notre Dame, IN 46556.

Contributed by the Heat Transfer Division for publication in the JOURNAL OF HEAT TRANSFER. Manuscript received by the Heat Transfer Division September 7, 1988; revision received October 10, 1989. Keywords: Packed and Fluidized Beds, Porous Media, Radiation.

Keung, C. S., 1980, "The Use of Source and Sink in Solving Two-Dimensional Heat Conduction Problems With Change of Phase in Arbitrary Domains," Ph.D. dissertation, Columbia University, New York.
Morgan, K., 1981, "A Numerical Analysis of Freezing and Melting With Convection," *Computer Methods in Applied Mechanics and Engineering*, Vol. 28, No. 3, pp. 275–284.
Okada, M., 1984, "Analysis of Heat Transfer During Melting From a Vertical Wall," *Int. J. Heat Mass Transfer*, Vol. 27, No. 11, pp. 2057–2066.
Ozisik, M. N., 1980 , *Heat Conduction*, Wiley, New York.
Patankar, S. V., 1980, *Numerical Heat Transfer and Fluid Flow*, McGraw-Hill, New York.
Shamsundar, N., and Sparrow, E. M., 1975, "Analysis of Multidimensional Conduction Phase Change via the Enthalpy Model," ASME JOURNAL OF HEAT TRANSFER, Vol. 97, No. 3, pp. 333–340.
Voller, V. R., and Prakash, C., 1987, "A Fixed Grid Numerical Modeling Methodology for Convection-Diffusion Mushy Region Phase-Change Problems," *Int. J. Heat Mass Transfer*, Vol. 30, No. 8, pp. 1709–1718.

View Factors for Wall to Random Dispersed Solid Bed Transport

J. W. C. Tseng[1] and W. Strieder[2]

Introduction

Radiant heat transfer in fluidized beds (Brewster 1986; Grace, 1982) or dispersed solid insulation involves energy exchange between a well-defined wall surface and a random bed of solid particles whose geometry is known only in a statistical sense. In instances where the walls and bed can be considered gray-diffuse surfaces, the temperatures of each are nearly uniform, and particle dimensions (Grace, 1982) are much larger than the thermal radiation wavelength, the view factor and straightforward (Siegel and Howell, 1981) net-radiation methods can be applied to calculate radiant heat transport rates. Beyond radiation, the wall-to-random bed view factors have additional applications where the characteristic dimensions of the dispersed solid need not be large. Barron (1985) has pointed out that view factors can be used in low-pressure cryogenic insulation for Knudsen void gas heat transfer. Wall-to-bed view factors will also predict mass transfer deposition rates into random fibrous or particulate supports, for low-pressure sputtering processes (Wehner and Anderson, 1970).

Wall-to-bed view factors are calculated and plotted versus bed void fraction and thickness for several model dispersed solids—overlapping, equisized spheres and overlapping, identical, parallel long cylinders (parallel both to the wall and to each other)—randomly placed in the volume between two infinite parallel planes.

View Factors and Void Fractions

(i) Bed of Aligned, Overlapping Fibers. It seems reasonable to model a fibrous material as a bed of very long right circular cylinders of radius ω placed at random between the planes $x = 0$ and $x = L$. All cylinders are given the same orientation mutually parallel to each other and parallel to the bounding planes. Viewed from a plane perpendicular to the fiber axis (Fig. 1), the cross sections appear as circles with an average density of circle centers n per unit area of the plane. Those points lying on the perimeter of a circle, but not in the interior of an overlapping circle, make up the fiber bed surface; the solid regions of the fiber bed consist of all points lying in the interior of one or more circles. The planes Σ_0 and Σ_L located at $x = 0$ and $x = L$ in Fig. 1 each have a wall surface area A_w. The exposed, nonoverlapped surface Σ_b has an area A_b. As the fibers will not penetrate the wall, the circle centers are restricted to a distance ω from the bounding planes, i.e., the centers are placed completely at random but within the interval $x = \omega$ to $x = L - \omega$. The statistics of this geometry are sufficiently straightforward to allow closed expressions (Faley and Strieder, 1987) for the necessary probabilities. The probability P_a that no circle center lies within an area a can be written in terms of the density of circle centers n in the plane

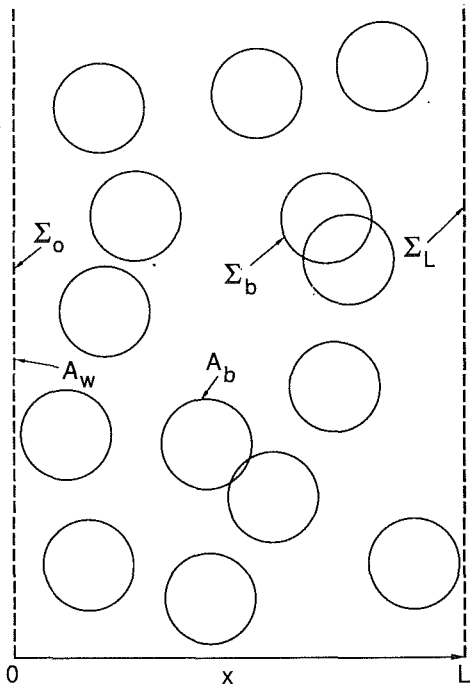

Fig. 1 Bed of fibers

$$P_a = \exp(-n\,a) \tag{1}$$

The void volume fraction can be interpreted as the probability that a randomly chosen point in the material falls in the void, or the probability that no circle has its center within a distance ω of the random point. Within the central region $(2\omega < x < L - 2\omega)$ of a sufficiently wide system $(L > 4\omega)$, the void fraction ϕ_2 is given by equation (1) as $\exp[-\pi\omega^2 n]$. However, fibers cannot penetrate the bounding walls and as no circle centers may lie within a distance ω of $x = 0$ or $x = L$, it is not necessary to exclude centers from these regions. Only that portion of the circle lying within the interval from $x = \omega$ to $x = L - \omega$ need be considered in any exclusion area. In a slab of thickness $L \geq 4\omega$, we have from equation (1) and some straightforward geometry, the bed void fraction

$$\phi_1(x) = \exp\left[-\left\{\omega^2 \arccos\left(\frac{\omega - x}{\omega}\right) - (\omega - x)\,[2\omega x - x^2]^{1/2}\right\} n\right],$$
$$0 \leq x \leq 2\omega \quad \text{for} \quad L \geq 4\omega \tag{2}$$

and

[1]Graduate Student, Department of Chemical Engineering, University of Notre Dame, Notre Dame, IN 46556.
[2]Professor, Department of Chemical Engineering, University of Notre Dame, Notre Dame, IN 46556.

Contributed by the Heat Transfer Division for publication in the JOURNAL OF HEAT TRANSFER. Manuscript received by the Heat Transfer Division September 7, 1988; revision received October 10, 1989. Keywords: Packed and Fluidized Beds, Porous Media, Radiation.

$$\phi_2 = \exp[-\pi\omega^2 n], \qquad 2\omega < x < L - 2\omega \quad \text{for} \quad L \geq 4\omega \tag{3}$$

Utilizing the slab symmetry, we find the void fraction is $\phi_1(L-x)$ in the interval $L - 2\omega \leq x \leq L$ and $L \geq 4\omega$. For those cases where $2\omega \leq L < 4\omega$, the void fraction ϕ_1 is given by equation (2) for the region $0 \leq x \leq L - 2\omega$, by symmetry in $2\omega \leq x \leq L$, and in the intermediate region by

$$\phi_2(x) = \phi_1(x)/\phi_1(x - L + 2\omega) \tag{4}$$
$$L - 2\omega < x < 2\omega \quad \text{and} \quad 2\omega \leq L < 4\omega$$

The void fraction of the entire symmetric bed is

$$\phi = \left[2\int_0^e \phi_1\, dx + \int_e^{L-e} \phi_2\, dx\right] \Big/ L \tag{5}$$

where depending on the bed thickness, the appropriate ϕ_2, either equation (3) or (4), is used and the limit e of the integrals corresponds to the region of the bed where each term applies.

View factors from the wall Σ_0 located at $x = 0$ to the wall Σ_L at $x = L$ or from Σ_0 to the exposed surface Σ_b of the dispersed solid, respectively, F_{0L} and F_{0b}, are given by

$$F_{0\,i} = A_w^{-1}\int_{\Sigma_0} d^2\mathbf{r} \int_{\Sigma_i} d^2\mathbf{r}'\, K(\mathbf{r}, \mathbf{r}'), \qquad i = b, L \tag{6}$$

where $K(\mathbf{r}, \mathbf{r}')\, d^2\mathbf{r}'$, the fraction of radiation leaving a unit surface at $\mathbf{r}$ on the wall Σ_0, that will travel an unobstructed straight line and reach the surface element $d^2\mathbf{r}'$ located at $\mathbf{r}'$ on Σ_b or Σ_L, from the cosine law is

$$K(\mathbf{r}, \mathbf{r}') = -\frac{[\rho \cdot \eta(\mathbf{r})][\rho \cdot \eta(\mathbf{r}')]}{\pi\rho^4} \qquad (\mathbf{r} \text{ can see } \mathbf{r}') \tag{7a}$$

$$= 0 \text{ (otherwise)} \tag{7b}$$

$\rho = (\mathbf{r}' - \mathbf{r})$, and $\eta(\mathbf{r})$ is the unit normal at $\mathbf{r}$ pointing into the void. Note from its definition that the view factor F_{0b} is simply

$$F_{0b} = 1 - F_{0L} \tag{8}$$

The integral, equation (6), for the view factor F_{0L} can be expressed in a form appropriate for a bed of aligned, overlapping fibers. For a given ρ, the operation $A_w^{-1}\int_{\Sigma_0} d^2\mathbf{r}$ is an average over the Σ_0 plane that, along with equation (7*b*) of $K(\mathbf{r}, \mathbf{r}')\, d^2\mathbf{r}'$, generates the probability P_ω that two points, $\mathbf{r}$ on Σ_0 and $\mathbf{r}'$ on Σ_L, can see one another, or that the vector ρ across the bed is free of obstruction. The event to accomplish this requires that circle centers be excluded from an area within the plane (Fig. 1) perpendicular to the fiber axes. The centerline of the area of exclusion is the projection ρ_ω of the ρ vector onto the plane of Fig. 1. The area extends a distance ω to either side and as circle centers must all lie between $x = \omega$ and $x = L - \omega$, the exclusion area is $2\omega(L - 2\omega)/\cos\theta$. The angle θ, between ρ_ω and the unit vector $\mathbf{i}$ pointing from $x = 0$ to $x = L$ directly across the slab, can take on values from 0 to $\pi/2$, the magnitude of ρ_ω is $L/\cos\theta$, and from equation (1) the probability is

$$P_\omega = \exp\{-n2\omega(L - 2\omega)/\cos\theta\} \tag{9}$$

The view factor for a bed of fibers from equations (6) and (7) is

$$F_{0L} = \int P_\omega(\mathbf{i} \cdot \rho)^2/(\pi\rho^4)\, d^2\rho \tag{10}$$

where the integration $d^2\rho$ is over elements of the plane wall Σ_l and includes all the possible vector lengths ρ between the planes $x = 0$ and $x = L$, or after a straightforward integration

$$F_{0L} = \int_0^{\pi/2} \cos\theta\, P_\omega d\theta \tag{11}$$

Both ϕ from equations (2), (3), (4), and (5) and F_{0L} depend only on L/ω and $n\omega^2$. The integrals are readily evaluated by the three-point Newton–Cotes composite method (Ralston and Rabinowitz, 1978) and $n\omega^2$ is numerically eliminated between the void fraction and view factor; then F_{0L} is subtracted from unity to give F_{0b} from equation (8). The wall-to-bed view factor F_{0b} is plotted versus the void fraction for various thicknesses in Fig. 2. For any thickness, F_{0b} decreases with increasing void fraction, and for any porosity the fiber bed becomes optically thick as the bed thickness is increased. In practice, fiber bed void fractions usually range from about 0.8 to unity. For these higher void fractions, overlap is not a dominant factor in the model. On the other hand, the overlapping models provide analytical forms for F_{0b} and ϕ not available from other random dispersed solid models such as those generated by direct simulation.

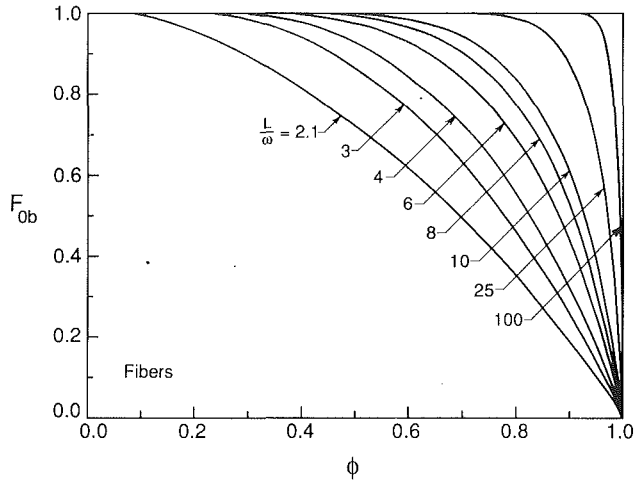

Fig. 2 View factor F_{0b} for radiant heat transport from an infinite plane wall to an adjacent bed of infinitely long, solid right circular cylinders all of the same radius ω. The cylinders are randomly placed, but aligned with their central axes parallel to the plane and mutually parallel to each other, and allowed to overlap each other. The view factors are plotted versus the bed void fraction ϕ for various bed thicknesses L/ω.

Jakob (1957) has considered radiation from an infinite plane wall to a parallel bank of tubes (parallel both to the infinite wall and to each other) and has presented view factor curves for radiation to one row and to two staggered rows of tubes arranged with equal center-to-center spacing along the wall. Because of the regular geometry of Jakob's beds, specifying the void fraction sets the value of both the tube diameter to center-to-center distance ratio, and the dimensionless bed thickness L/ω. For a given void fraction, Fig. 3 contains view factors for the one- and two-row regular geometries and the corresponding random bed view factors for the same thickness and void fraction from Fig. 2. We note that the comparisons start at the lowest close packed void fractions of the regular arrangements, 0.215 for one row and 0.158 for two rows. The regular geometries always give a larger view factor. If placed randomly, a second row cylinder can be placed behind the first, so the two-row staggered array gives greater blockage. Overlap also allows the construction of solid shapes, that for a given solid volume will block less. For example, the single-row, regular array completely blocks at 0.215, but as a result of overlap some of the void spaces between the cylinders are filled in the random volume, generating open spaces, and, for the same void fraction, and F_{0b} less than unity.

(ii) Bed of Overlapping Solid Spheres. One simple model of a particulate or granular random solid void system was proposed by Weissberg (1963). A random suspension is obtained when spheres all of the same radius ξ are placed between the planes $x = 0$ and $x = L$ without any correlation between the positions of different spheres. The final result of this process will be a random distribution of spheres, some isolated and some overlapping one another. All those points lying on a sphere surface but not in the interior of an overlapping sphere

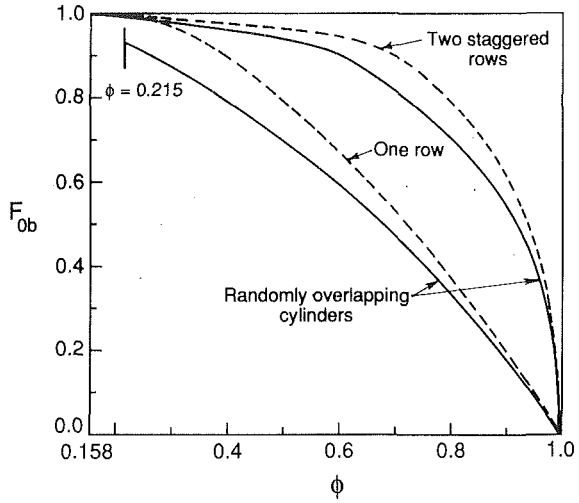

Fig. 3 View factors F_{0b} for radiant heat transport from an infinite plane wall to one row and two staggered rows of tubes arranged with equal center-to-center spacing along the wall - - - - and view factors F_{0b} to corresponding beds of randomly overlapping tubes with the same bed thickness, tube radius and void fraction ———, versus the void fraction ϕ

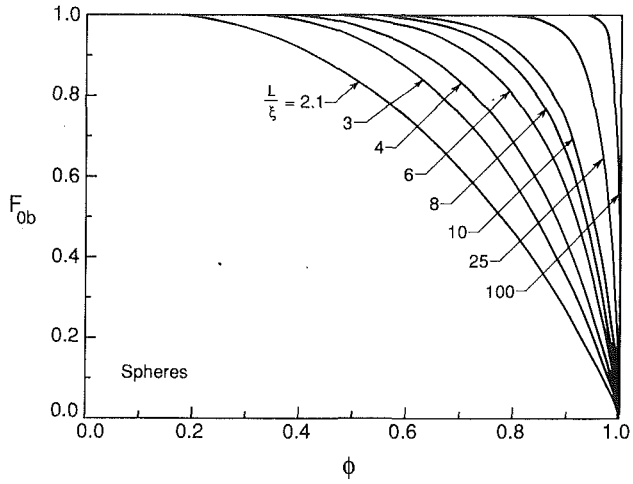

Fig. 4 View factors F_{0b} for radiant heat transport from an infinite plane wall to an adjacent bed of randomly overlapping solid spheres all of the same radius ξ. The view factors are plotted versus the bed void fraction ϕ for various bed thicknesses L/ξ.

make up the dispersed solid exposed surface; points within the interior of one or more spheres make up the solid. The statistics of an unbounded (Strieder and Aris, 1973) random bed of overlapping spheres are well known and can be applied here for an average density of sphere centers ν per unit total volume of bed with the restriction that the spheres cannot penetrate the walls on either side of the bed. The derivations of void fraction and view factor expressions, similar to those of overlapping, aligned fibers, are omitted for brevity, and can be found from Tseng (1989). The results for ϕ_1 and both forms of ϕ_2 are summarized in equations (12)–(14). In a slab of thickness $L \geq 2\xi$, the void fractions within their respective x intervals are given by

$$\phi_1(x) = \exp[-\pi\xi x^2\nu + \frac{1}{3}\pi x^3\nu] \tag{12}$$

$$0 \leq x \leq 2\xi \quad \text{for} \quad L \geq 4\xi$$

and

$$\phi_2 = \exp[-\frac{4}{3}\pi\xi^3\nu] \tag{13}$$

$$2\xi < x < L - 2\xi \quad \text{for} \quad L \geq 4\xi$$

In those cases where $2\xi \leq L < 4\xi$, the void fraction ϕ_1 is given by equation (12) within the region $0 \leq x \leq L - 2\xi$, and

$$\phi_2(x) = \phi_1(x)/\phi_1(x - L + 2\xi) \tag{14}$$

$$L - 2\xi < x < 2\xi \quad \text{for} \quad 2\xi \leq L < 4\xi$$

These forms can be used directly in equation (5) to obtain the net bed void fraction in terms of $\nu\xi^3$ and L/ξ. The wall to bed view factor F_{0b} for a bed of overlapping spheres is given by

$$F_{0b} = 1 - (1 - \mu)\exp(-\mu) - \mu E_1(\mu) \tag{15a}$$

where

$$\mu = \pi\xi^2\nu(L - 2\xi) \tag{15b}$$

and E_1 is the exponential integral (Abramowitz and Stegun, 1964). As the view factor also depends only on $\nu\xi^3$ and ξ/L, we can eliminate $\nu\xi^3$ between the void fraction and view factor. The view factor F_{0b} for a bed of randomly placed, identical, overlapping spheres is plotted versus the void fraction for several thicknesses in Fig. 4. View factors for wall-to-bed transport in Figs. 2 and 4 for overlapping fibers and spheres have the same general characteristics.

In its usual form, Bouguer's law (Saatdjian, 1987) applies only to very small particles. Writing the exponential form of Bouguer's law along a path length from the plane wall and integrating over the hemisphere of possible directions, it is straightforward to show that equation (15) has the exact form of Bouguer's law, but it contains a correction for finite sphere size. An alternative equation for F_{0b} can be obtained when the two-flux model (Brewster, 1984; 1986) is applied to calculate the radiation from a plane black wall to a black bed of spheres at zero temperature. At void fractions of 0.90 and above, sphere overlap can be neglected, and plots to compare the exact view factors from Fig. 4 to the approximate two-flux model F_{0b}, versus the bed thickness for several void fractions, have been constructed by Tseng (1989). Although both curves are of the same shape, the two-flux model always overestimates the blocking effect of the bed, giving maximum errors of 12.7 percent at $L = 7.50\xi$ and 14.6 percent at $L = 15.0\xi$, respectively, for void fractions of 0.90 and 0.97.

Illustrations by Tseng (1989) of the use of the view factors and the network method, as well as the calculation of the necessary bed surface areas, to obtain the radiant heat transport from plane parallel gray walls to a dilute, well-mixed bed of gray spheres have been omitted for brevity.

Acknowledgments

Acknowledgment is made to the Donors of the Petroleum Research Fund administered by the American Chemical Society, for support of this research.

References

Abramowitz, M., and Stegun, I. A., 1964, *Handbook of Mathematical Functions*, National Bureau of Standards, Washington, DC, p. 228.

Barron, R. F., 1985, *Cryogenic Systems*, 2nd ed., Clarendon Press, Oxford, United Kingdom, p. 388.

Brewster, M. Q., 1984, "Effective Emissivity of a Fluidized Bed," presented at the ASME Winter Annual Meeting, New Orleans, LA, HTD-40, pp. 7-13.

Brewster, M. Q., 1986, "Effective Absorptivity and Emissivity of Particulate Media With Application to a Fluidized Bed," ASME JOURNAL OF HEAT TRANSFER, Vol. 108, pp. 710-712.

Faley, T. L., and Strieder, W., 1987, "Knudsen Flow Through a Random Bed of Unidirectional Fibers," *J. Appl. Phys.*, Vol. 62, pp. 4394-4397.

Grace, J. R., 1982, "Fluidized-Bed Heat Transfer," *Handbook of Multiphase Systems*, G. Hestroni, ed., Hemisphere Publishing, New York, pp. 8-72, 8-52, and 8-53.

Jakob, M., 1957, *Heat Transfer*, Vol. 2, Wiley, New York, p. 64.

Ralson, A., and Rabinowitz, P., 1978, *A First Course in Numerical Analysis*, McGraw-Hill, New York.

Saatdjian, E., 1987, "A Cell Model That Estimates Radiative Heat Transfer in a Nonscattering, Particle Laden Flow," ASME JOURNAL OF HEAT TRANSFER, Vol. 109, pp. 756-758.

Siegel, R., and Howell, J. R., 1981, *Thermal Radiation Heat Transfer*, Hemisphere Publishing Co., New York, pp. 236–246.

Strieder, W., and Aris, R., 1973, *Variational Methods Applied to Problems of Diffusion and Reaction*, Springer-Verlag, Berlin, pp. 4–11.

Tseng, J. W. C., 1989, "Radiant Heat Transfer in Porous Media," Ph.D. Thesis, University of Notre Dame, Notre Dame, IN.

Wehner, G. K., and Anderson, G. S., 1970, "The Nature of Physical Sputtering," *Handbook of Thin Film Technology*, L. I. Maissel and R. Glang, eds., McGraw-Hill, pp. 3-25, 3-26.

Weissberg, H. L., 1963, "Effective Diffusion Coefficient in Porous Media," *J. Appl. Phys.*, Vol. 34, pp. 2636–2639.

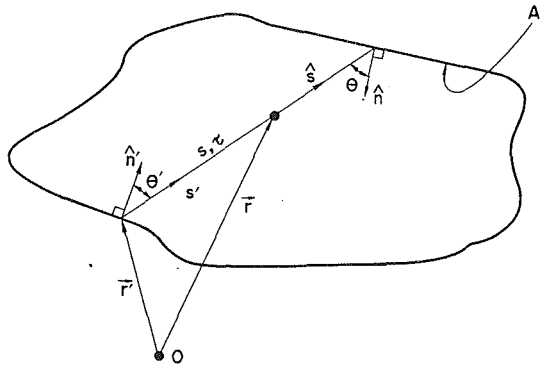

Fig. 1 Radiative intensity within an arbitrary three-dimensional enclosure

The Improved Differential Approximation for Radiative Transfer in Multidimensional Media

M. F. Modest[1]

1 Introduction

One particularly popular approximate method for radiative transfer in participating media is the so-called *differential approximation* or *P-1 approximation*. Unfortunately, the differential approximation is accurate only in optically thick media, and may become very inaccurate in optically thin situations, in particular in two- and three-dimensional geometries. To increase the accuracy, a number of improvements have been proposed. Olfe (1967, 1968) separated wall emission from medium emission in what he called the *modified differential approximation* (*MDA*). Modest (1974, 1975) combined the *P-1 approximation* with an optically thin correction term in what he called the *improved differential approximation* (*IDA*). While very accurate, both models were limited to relatively simple situations. Recently, Modest (1989) demonstrated that Olfe's MDA may be formulated for a general three-dimensional case with an absorbing/emitting, anisotropically scattering medium bounded by gray, diffusely emitting and reflecting walls.

It is the purpose of the present note to show that the *improved differential approximation* (*MDA*) may also be extended to the most general case, reducing to the correct optically thin and optically thick limits for all situations, resulting in accuracy similar to that of the MDA, but being computationally more efficient.

2 Analysis

The equation of radiative transfer for an absorbing, emitting, and scattering medium may be written as

$$\frac{dI}{d\tau}(\mathbf{r}, \hat{\mathbf{s}}) = S(\mathbf{r}, \hat{\mathbf{s}}) - I(\mathbf{r}, \hat{\mathbf{s}}) \tag{1}$$

where I is radiative intensity, τ is optical distance along the ray traveling into a direction $\hat{\mathbf{s}}$ as indicated in Fig. 1, and S is the radiative source term given by

$$S(\mathbf{r}, \hat{\mathbf{s}}) = (1-\omega)I_b(\mathbf{r}) + \frac{\omega}{4\pi}\int_{4\pi} I(\mathbf{r}, \hat{\mathbf{s}}')\Phi(\hat{\mathbf{s}}\cdot\hat{\mathbf{s}}')d\Omega' \tag{2}$$

Here ω is the single scattering albedo, I_b is the black body intensity (Planck function), Φ is the scattering phase function, and Ω denotes a solid angle.

Equation (1) may be solved along a pencil of rays

$$I(\mathbf{r}, \hat{\mathbf{s}}) = \frac{J_w}{\pi}(\mathbf{r}')e^{-\tau_s} + \int_0^{\tau_s} S(\mathbf{r}' + s'\hat{\mathbf{s}}, \hat{\mathbf{s}})e^{-(\tau_s - \tau_{s'})}d\tau_{s'} \tag{3}$$

where $\tau_s = \int_0^s \beta ds'$ is the optical distance between that point on the wall from which the beam emanates and the point under consideration, β is the radiative extinction coefficient, and J_w is the radiosity at the wall.

The problem with equation (3) is, of course, that for scattering media and/or for radiative equilibrium the radiative source S is not known *a priori* and depends on the intensity I itself. The intensity consists of two components, one related to radiosity leaving the walls (I_w), the other related to medium emission and in-scattering (I_m). We approximate I_m from the *P-1* approximation (ODA) by setting

$$I_m(\mathbf{r}, \hat{\mathbf{s}}) \simeq \int_0^{\tau_s} S^*(\mathbf{r}' + s'\hat{\mathbf{s}}, \hat{\mathbf{s}})e^{-(\tau_s - \tau_{s'})}d\tau_{s'} \tag{4}$$

where

$$S^*(\mathbf{r}, \hat{\mathbf{s}}) = (1-\omega)I_b^*(\mathbf{r}) + \frac{\omega}{4\pi}[G^*(\mathbf{r}) + A_1\mathbf{q}^*(\mathbf{r})\cdot\hat{\mathbf{s}}] \tag{5}$$

is the source term evaluated from the ODA. Here we have assumed scattering to be linear-anisotropic, with a phase function

$$\Phi(\hat{\mathbf{s}}\cdot\hat{\mathbf{s}}') = 1 + A_1\hat{\mathbf{s}}\cdot\hat{\mathbf{s}}' \tag{6}$$

The asterisks have been added to distinguish the differential approximation results from the improved values, i.e., in equation (5) the radiative flux $\mathbf{q}^*$ and incident radiation G^* (as well as the Planck function I_b^* for the case of radiative equilibrium) are evaluated approximately from (e.g., Modest and Azad, 1980)

$$\nabla_\tau \cdot \mathbf{q}^* = (1-\omega)(4\pi I_b^* - G) \tag{7}$$

$$\nabla_\tau G^* = -(3 - A_1\omega)\mathbf{q}^* \tag{8}$$

(with operators ∇_τ based on optical coordinates), subject to the boundary condition

$$2\mathbf{q}^*\cdot\hat{\mathbf{n}} = 4J_w - G^* = \frac{\epsilon}{2-\epsilon}(4\pi I_{bw} - G^*) \tag{9}$$

This approximation goes to the correct optically thin limit ($I_m \to 0$ as $\tau_s \to 0$) as well as the correct optically thick limit (where the *P-1* approximation predicts the correct radiative source, $I_m \to S^* \to S$ as $\tau_s \to \infty$). It should be noted that, in the optically thick limit, the *P-1* approximation will *always* predict

[1]Professor of Mechanical Engineering, Department of Mechanical Engineering, The Pennsylvania State University, University Park, PA 16802; Fellow ASME.

Contributed by the Heat Transfer Division for publication in the JOURNAL OF HEAT TRANSFER. Manuscript received by the Heat Transfer Division April 7, 1989; revision received January 11, 1990. Keywords: Numerical Methods, Radiation, Radiation Interactions.

Siegel, R., and Howell, J. R., 1981, *Thermal Radiation Heat Transfer*, Hemisphere Publishing Co., New York, pp. 236–246.

Strieder, W., and Aris, R., 1973, *Variational Methods Applied to Problems of Diffusion and Reaction*, Springer-Verlag, Berlin, pp. 4–11.

Tseng, J. W. C., 1989, "Radiant Heat Transfer in Porous Media," Ph.D. Thesis, University of Notre Dame, Notre Dame, IN.

Wehner, G. K., and Anderson, G. S., 1970, "The Nature of Physical Sputtering," *Handbook of Thin Film Technology*, L. I. Maissel and R. Glang, eds., McGraw-Hill, pp. 3-25, 3-26.

Weissberg, H. L., 1963, "Effective Diffusion Coefficient in Porous Media," *J. Appl. Phys.*, Vol. 34, pp. 2636–2639.

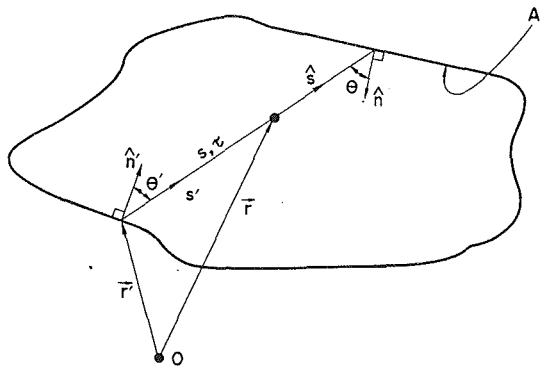

Fig. 1 Radiative intensity within an arbitrary three-dimensional enclosure

The Improved Differential Approximation for Radiative Transfer in Multidimensional Media

M. F. Modest[1]

1 Introduction

One particularly popular approximate method for radiative transfer in participating media is the so-called *differential approximation* or *P-1 approximation*. Unfortunately, the differential approximation is accurate only in optically thick media, and may become very inaccurate in optically thin situations, in particular in two- and three-dimensional geometries. To increase the accuracy, a number of improvements have been proposed. Olfe (1967, 1968) separated wall emission from medium emission in what he called the *modified differential approximation* (*MDA*). Modest (1974, 1975) combined the *P-1 approximation* with an optically thin correction term in what he called the *improved differential approximation* (*IDA*). While very accurate, both models were limited to relatively simple situations. Recently, Modest (1989) demonstrated that Olfe's MDA may be formulated for a general three-dimensional case with an absorbing/emitting, anisotropically scattering medium bounded by gray, diffusely emitting and reflecting walls.

It is the purpose of the present note to show that the *improved differential approximation* (*MDA*) may also be extended to the most general case, reducing to the correct optically thin and optically thick limits for all situations, resulting in accuracy similar to that of the MDA, but being computationally more efficient.

2 Analysis

The equation of radiative transfer for an absorbing, emitting, and scattering medium may be written as

$$\frac{dI}{d\tau}(\mathbf{r}, \hat{\mathbf{s}}) = S(\mathbf{r}, \hat{\mathbf{s}}) - I(\mathbf{r}, \hat{\mathbf{s}}) \tag{1}$$

where I is radiative intensity, τ is optical distance along the ray traveling into a direction $\hat{\mathbf{s}}$ as indicated in Fig. 1, and S is the radiative source term given by

$$S(\mathbf{r}, \hat{\mathbf{s}}) = (1-\omega)I_b(\mathbf{r}) + \frac{\omega}{4\pi}\int_{4\pi} I(\mathbf{r}, \hat{\mathbf{s}}')\Phi(\hat{\mathbf{s}}\cdot\hat{\mathbf{s}}')d\Omega' \tag{2}$$

Here ω is the single scattering albedo, I_b is the black body intensity (Planck function), Φ is the scattering phase function, and Ω denotes a solid angle.

Equation (1) may be solved along a pencil of rays

$$I(\mathbf{r}, \hat{\mathbf{s}}) = \frac{J_w}{\pi}(\mathbf{r}')e^{-\tau_s} + \int_0^{\tau_s} S(\mathbf{r}' + s'\hat{\mathbf{s}}, \hat{\mathbf{s}})e^{-(\tau_s - \tau_{s'})}d\tau_s' \tag{3}$$

where $\tau_s = \int_0^s \beta ds'$ is the optical distance between that point on the wall from which the beam emanates and the point under consideration, β is the radiative extinction coefficient, and J_w is the radiosity at the wall.

The problem with equation (3) is, of course, that for scattering media and/or for radiative equilibrium the radiative source S is not known *a priori* and depends on the intensity I itself. The intensity consists of two components, one related to radiosity leaving the walls (I_w), the other related to medium emission and in-scattering (I_m). We approximate I_m from the *P-1* approximation (ODA) by setting

$$I_m(\mathbf{r}, \hat{\mathbf{s}}) \simeq \int_0^{\tau_s} S^*(\mathbf{r}' + s'\hat{\mathbf{s}}, \hat{\mathbf{s}})e^{-(\tau_s - \tau_{s'})}d\tau_s' \tag{4}$$

where

$$S^*(\mathbf{r}, \hat{\mathbf{s}}) = (1-\omega)I_b^*(\mathbf{r}) + \frac{\omega}{4\pi}[G^*(\mathbf{r}) + A_1\mathbf{q}^*(\mathbf{r})\cdot\hat{\mathbf{s}}] \tag{5}$$

is the source term evaluated from the ODA. Here we have assumed scattering to be linear-anisotropic, with a phase function

$$\Phi(\hat{\mathbf{s}}\cdot\hat{\mathbf{s}}') = 1 + A_1\hat{\mathbf{s}}\cdot\hat{\mathbf{s}}' \tag{6}$$

The asterisks have been added to distinguish the differential approximation results from the improved values, i.e., in equation (5) the radiative flux $\mathbf{q}^*$ and incident radiation G^* (as well as the Planck function I_b^* for the case of radiative equilibrium) are evaluated approximately from (e.g., Modest and Azad, 1980)

$$\nabla_\tau\cdot\mathbf{q}^* = (1-\omega)(4\pi I_b^* - G) \tag{7}$$

$$\nabla_\tau G^* = -(3 - A_1\omega)\mathbf{q}^* \tag{8}$$

(with operators ∇_τ based on optical coordinates), subject to the boundary condition

$$2\mathbf{q}^*\cdot\hat{\mathbf{n}} = 4J_w - G^* = \frac{\epsilon}{2-\epsilon}(4\pi I_{bw} - G^*) \tag{9}$$

This approximation goes to the correct optically thin limit ($I_m \to 0$ as $\tau_s \to 0$) as well as the correct optically thick limit (where the *P-1* approximation predicts the correct radiative source, $I_m \to S^* \to S$ as $\tau_s \to \infty$). It should be noted that, in the optically thick limit, the *P-1* approximation will *always* predict

[1]Professor of Mechanical Engineering, Department of Mechanical Engineering, The Pennsylvania State University, University Park, PA 16802; Fellow ASME.

Contributed by the Heat Transfer Division for publication in the JOURNAL OF HEAT TRANSFER. Manuscript received by the Heat Transfer Division April 7, 1989; revision received January 11, 1990. Keywords: Numerical Methods, Radiation, Radiation Interactions.

the correct *radiative source*, but not necessarily the correct *radiative flux* (in the presence of temperature steps), which was found to be a minor shortcoming of the MDA. Since for optically thin media the accuracy of S^* is irrelevant, and for optically thick media only $S^*(\mathbf{r})$ is of importance (rather than the integral over it), it may be justified to further approximate equation (4). To this effect we will assume that the radiative source varies linearly from the point under consideration, $\mathbf{r}$, toward the point at the wall, $\mathbf{r}'$ (i.e., into the $-\hat{\mathbf{s}}$ direction), or

$$S^*(\mathbf{r}'+s'\hat{\mathbf{s}},\ \hat{\mathbf{s}}) \simeq S^*(r,\ \hat{\mathbf{s}}) - (\tau_s - \tau_s')\frac{dS^*}{d\tau_s}(\mathbf{r},\ \hat{\mathbf{s}}) \tag{10}$$

Substituting this into equation (4) then leads to

$$\int_0^{\tau_s} S^*(\mathbf{r}'+s'\hat{\mathbf{s}},\ \hat{\mathbf{s}})e^{-(\tau_s-\tau_s')}d\tau_s' = S^*(\mathbf{r},\ \hat{\mathbf{s}})(1-e^{-\tau_s}) - \frac{dS^*}{d\tau_s}(\mathbf{r},\ \hat{\mathbf{s}})[1-(1+\tau_s)e^{-\tau_s}] \tag{11}$$

To eliminate $dS^*/d\tau_s$ from equation (11), we use the assumed linearity of the source function in reverse, i.e., we set

$$\int_0^{\tau_s} S^*(\mathbf{r}'+s'\hat{\mathbf{s}},\ \hat{\mathbf{s}})e^{-(\tau_s-\tau_s')}d\tau_s' \simeq S^*(\mathbf{r}-s_0\hat{\mathbf{s}},\ \hat{\mathbf{s}})(1-e^{-\tau_s}) \tag{12}$$

where the geometric distance s_0 is related to the optical distance

$$\tau_0 = \int_0^{s_0} \beta(\mathbf{r}-s''\hat{\mathbf{s}})ds'' = 1 - \frac{\tau_s e^{-\tau_s}}{1-e^{-\tau_s}} \tag{13}$$

Thus, for a linearly varying source the integral is easily evaluated from equation (11), using a representative value for the source evaluated an optical distance τ_0 away [$0 < \tau_0 < \min(1,\ \tau_s)$]. We note that equations (11) and (12) also reduce to the correct optically thick and thin limits. Equation (12) is preferable over equation (11) since, at moderate optical thicknesses, it can account for nonlinear variation of the source term to a certain degree.

Now substituting equation (12) into equation (3) leads to

$$I(\mathbf{r},\ \hat{\mathbf{s}}) \simeq \frac{J_w}{\pi}(\mathbf{r}')e^{-\tau_s} + S^*(\mathbf{r}-s_0\hat{\mathbf{s}},\ \hat{\mathbf{s}})(1-e^{-\tau_s}) \tag{14}$$

The wall radiosities are found by invoking their definition, i.e.,

$$J_w(\mathbf{r}) = \epsilon\pi I_{bw}(\mathbf{r}) + (1-\epsilon)\int_{\hat{\mathbf{s}}\cdot\hat{\mathbf{n}}<0} I(\mathbf{r},\ \hat{\mathbf{s}})\,|\hat{\mathbf{s}}\cdot\hat{\mathbf{n}}|\,d\Omega \tag{15}$$

Equation (15) may be solved by standard surface transport methods, such as small zones (with little variation of J_w, τ_s, and $\hat{\mathbf{s}}$), to give

$$J_i = \epsilon_i\pi I_{bi} + (1-\epsilon_i)\sum_{j=1}^{N}[J_j\, e^{-\tau_{ij}} + \pi S_{ij}^*(1-e^{-\tau_{ij}})]F_{i-j},$$
$$i = 1,\ \ldots,\ N \tag{16}$$

Once the radiosities are known, the improved values for incident radiation and radiative flux anywhere inside the medium follow from their definition as

$$\begin{Bmatrix} G(\mathbf{r}) \\ \mathbf{q}(\mathbf{r}) \end{Bmatrix} = \int_{4\pi} I(\mathbf{r},\ \hat{\mathbf{s}}) \begin{Bmatrix} 1 \\ \hat{\mathbf{s}} \end{Bmatrix} d\Omega = \int_A I(\mathbf{r},\ \hat{\mathbf{s}}) \begin{Bmatrix} 1 \\ \hat{\mathbf{s}} \end{Bmatrix} \frac{\cos\theta'\, dA}{\pi s^2} \tag{17}$$

Thus the improved differential approximation requires: (*i*) the solution to the ordinary *P-1* approximation, (*ii*) the solution to a surface integral equation (or the evaluation of configuration factors) for the determination of radiosities, and (*iii*) the evaluation of a surface integral for any point inside the medium, for which flux or incident radiation is desired.

3 Illustrative Examples

One-Dimensional Slab at Radiative Equilibrium. We will first consider the very simple case of a one-dimensional gray absorbing/emitting and isotropically scattering slab at radiative equilibrium between two isothermal black walls, since this example is a standard by which the accuracy of many models has been assessed. The local flux is readily calculated as

$$\frac{q(\tau)}{\sigma(T_1^4 - T_2^4)} = \frac{1 + E_3(\tau) + E_3(\tau_L - \tau) - \frac{3}{2}E_4(\tau) - \frac{3}{2}E_4(\tau_L - \tau)}{1 + \frac{3\tau_L}{4}} \tag{18}$$

where the E_n are exponential integrals and τ_L is the optical distance between the two plates. At the walls equation (18) is identical to the solution given by Olfe (1967). However, equation (18) is not constant across the gap as radiative equilibrium would dictate, but varies slightly between the walls (where the flux is slightly overpredicted) and the centerline (where the flux is slightly underpredicted). The ordinary differential approximation has a maximum error of ≈ 3.3 percent as compared to ≈ 1.3 percent for the IDA (both at $\tau_L = 1$). This, however, in no way demonstrates the power of the present method since this problem is one of the very few where the ordinary differential approximation actually reduces to the correct optically thin limit.

Two-Dimensional Cold Cylinder With Isotropic Scattering. As a second example, we will consider a cold gray cylindrical medium of radius R and length L, which absorbs and isotropically scatters radiation, bounded radially and at one of the flat faces by cold black walls. The second face is isothermal at temperature T and has an emissivity of ϵ.

For comparison of the IDA with *Monte Carlo* results and the MDA (Modest, 1989) the average flux at the two faces of the cylinder, i.e., at $\tau_z = 0$ and $\tau_z = \tau_L$, is evaluated. Initially the radiosity at all three surfaces must be determined. Since the periphery and the face at $\tau_z = \tau_L$ are cold and black, the radiosities are zero there. The radiosity at $\tau_z = 0$ follows from equation (15) as

$$J_{w0}(\tau_r) = \epsilon\sigma T^4 + (1-\epsilon)H_0(\tau_r) \tag{19}$$

where

$$H_0(\tau_r) \simeq \frac{\omega}{2\pi}\int_0^{\pi/2}\int_0^{\pi} G^* \left(\tau_r' = \sqrt{\tau_0\sin\theta(\tau_0\sin\theta + 2\tau_r\cos\psi) + \tau_r^2},\quad \tau_z' = \tau_0\cos\theta\right) \times (1-e^{-\tau})\,d\psi\,\sin\theta\cos\theta\,d\theta \tag{20}$$

with

$$\tau = \begin{cases} [\sqrt{\tau_R^2 - \tau_r^2\sin^2\psi} - \tau_r\cos\psi]/\sin\theta, & \psi < \psi_{RL} \\ \tau_L/\cos\theta, & \psi > \psi_{RL} \end{cases} \tag{21}$$

and

$$\psi_{RL} = \cos^{-1}\left\{\frac{\tau_R^2 - \tau_r^2 - \tau_L^2\tan^2\theta}{2\tau_L\tau_R\tan\theta}\right\} \tag{22}$$

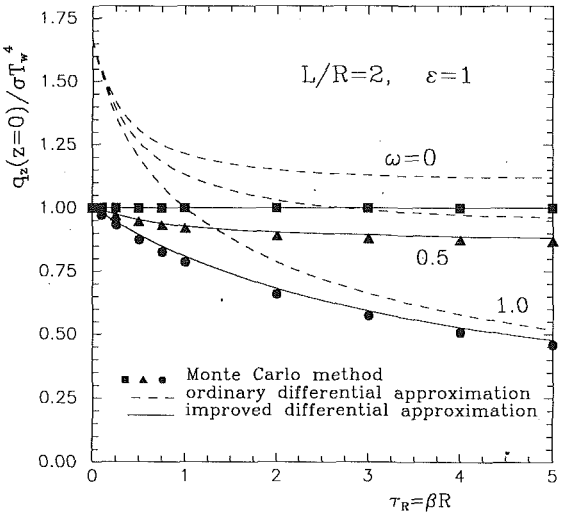

Fig. 2 Normalized flux for cold cylinder enclosed by cold, black liner, one cold face plate and one hot face plate; influence of optical depth and scattering albedo on average flux at hot face plate

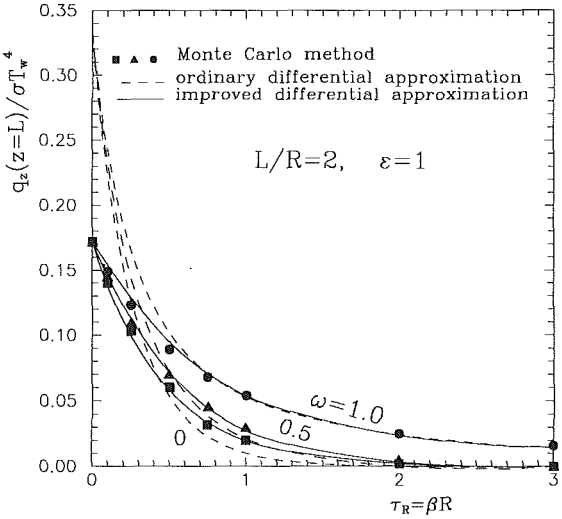

Fig. 3 Normalized flux for cold cylinder enclosed by cold, black liner, one cold face plate, and one hot face plate; influence of optical depth and scattering albedo on average flux at cold face plate

The irradiation onto the cold face consists of two terms, i.e., the contribution from the medium plus that from the hot face. The contribution from the medium, $H_{Lm}(\tau_r)$, is found by evaluating G^* in equation (20) at $\tau_L - \tau_z$ instead of at τ_z. The hot-surface contribution is readily calculated as

$$H_{Lw}(\tau_r) = \frac{2}{\pi} \int_0^{\tan^{-1}[(\tau_R+\tau_r)/\tau_L]} \int_{\psi_{RL}}^{\pi} J_{w0}\left(\tau_r' = \sqrt{\tau_L \tan\theta(\tau_L \tan\theta + 2\tau_r \cos\psi) + \tau_r^2}\right) \times e^{-\tau_L/\cos\theta} d\psi \sin\theta \cos\theta d\theta \tag{23}$$

Since the wall is cold and black, its flux follows as

$$\frac{q_z}{\sigma T^4}(\tau_\tau, \tau_L) = H_{Lm}(\tau_r) + H_{Lw}(\tau_r) \tag{24}$$

Some sample results are shown in Figs. 2 and 3.

Figure 2 shows the total normalized flux from the hot surface as a function of optical thickness (based on radius) $\tau_R = \beta R$ and scattering albedo ω, i.e., the radiative flux integrated over the entire hot surface. In this figure the hot wall is assumed to be black ($\epsilon = 1$) and the length-to-radius ratio is kept constant at $L/R = 2$. Figure 3 shows the identical case for the opposite (cold) face plate. It is observed that the IDA follows the Monte Carlo results very closely for all optical thicknesses and scattering albedos, while the ordinary *P-1* approximation displays serious errors for optically thin situations.

The results are virtually identical to those from the MDA, and have been discussed in detail by Modest (1989). Typical CPU times for the IDA on a VAX 11/780 are 30 s for the case of $L/R = 2$, $\tau_R = 1$, $\omega = 0.5$ and a 16 × 32 nodal system. This should be compared with 3:06 min for the MDA (Modest, 1989).

4 Conclusions

The improved differential approximation first proposed by Modest (1974) for nonscattering media at radiative equilibrium has been extended to the more general case of a three-dimensional, absorbing/emitting and anisotropically scattering medium bounded by gray-diffuse walls. The present model reduces to the correct optically thin and optically thick limits for all situations. Comparison with exact solutions obtained from Monte Carlo calculations demonstrates that, unlike the standard *P-1* approximation, the present method gives results of excellent accuracy for all optical conditions.

Since the present IDA competes directly with the MDA as originally presented by Olfe (1967) and generalized by Modest (1989), a comparison between the two methods is in order:

- both methods yield approximately the same (superb) accuracy;
- the MDA requires the evaluation of one surface integral for each internal and external nodal point for non- or isotropically scattering media, and three additional surface integrals for anisotropic scattering; thus, if only the flux at selected locations is desired, the IDA is computationally considerably more efficient; if flux (or its divergence) is needed at every nodal point, the MDA tends to become equally efficient for isotropic scattering, but remains less efficient for anisotropic scattering;
- since the IDA is based on *P-1* approximation results, no iterations are necessary for temperature-dependent properties (as is the case for the MDA).

Both methods give excellent results, with a moderate increase in computer time as compared to the ODA, and it will depend on the problem at hand to determine which method is preferable under what conditions.

References

Modest, M. F., 1974, "Two-Dimensional Radiative Equilibrium of a Gray Medium in a Plane Layer Bounded by Gray Non-isothermal Walls," ASME JOURNAL OF HEAT TRANSFER, Vol. 96, pp. 483–488.

Modest, M. F., 1975, "Radiative Equilibrium in a Rectangular Enclosure Bounded by Gray Non-isothermal Walls," *Journal of Quantitative Spectroscopy and Radiative Transfer*, Vol. 15, pp. 445–461.

Modest, M. F., 1989, "The Modified Differential Approximation for Radiative Transfer in General Three-Dimensional Media," *Journal of Thermophysics and Heat Transfer*, Vol. 3, No. 3, pp. 283–288.

Modest, M. F., and Azad, F. H., 1980, "The Differential Approximation for Radiative Transfer in an Emitting, Absorbing and Anisotropically Scattering Medium," *Journal of Quantitative Spectroscopy and Radiative Transfer*, Vol. 23, pp. 117–120.

Olfe, D. B., 1967, "A Modification of the Differential Approximation for Radiative Transfer," *AIAA Journal*, Vol. 5, No. 4, pp. 638–643.

Olfe, D. B., 1968, "Application of a Modified Differential Approximation to Radiative Transfer in a Gray Medium Between Concentric Sphere and Cylinders," *Journal of Quantitative Spectroscopy and Radiative Transfer*, Vol. 8, pp. 899–907.

Prediction of Heat Transfer to a Thin Liquid Film in Plane and Radially Spreading Flows

M. M. Rahman,[1] A. Faghri,[1] W. L. Hankey,[1] and T. D. Swanson[2]

Nomenclature

Fr = Froude number $= W/\sqrt{g\delta}$
g = acceleration due to gravity
h = heat transfer coefficient $= q_w/(T_w - T_b)$, for heating; $q_w/(T_w - T_{sat})$, for evaporation
k = thermal conductivity
L = length of the plate
Nu = Nusselt number $= h(\nu^2/g)^{1/3}/k$
Nu* = Nusselt number in terms of film height $= h\delta/k$
p = difference between fluid and ambient pressures
q = heat flux
r = radial coordinate
Re = Reynolds number $= 4W\delta/\nu$
T = temperature
$\mathbf{V}$ = velocity vector
W = average velocity along the plate
α = thermal diffusivity
δ = film thickness
Δ = dimensionless film height $= \delta/\delta_{in}$
ν = kinematic viscosity
ξ = dimensionless distance $= z/L$ or $(r - r_{in})/(r_{out} - r_{in})$
ρ = density
τ = tangential shear stress

Subscripts

b = mixed-mean (bulk) condition
in = condition at entrance
out = condition at exit
sat = saturation condition
w = condition on solid wall

Introduction

The numerical solution of a thin film flow is difficult since the free surface geometry changes along the path of the flow, is unknown ahead of time, and cannot be fitted in a regular Cartesian or cylindrical coordinate system. Therefore, most theoretical studies in this area were related to the development of approximate analytical models (Faghri and Seban, 1981; Chaudhury, 1964). The finite-difference solution was attempted only for a falling film (Faghri and Payvar, 1979) where the film thickness could be approximated to be uniform.

Recently, Rahman et al. (1990a) have developed a finite-difference solution method applicable for the fluid mechanics of thin film flows under zero and normal gravity. A body-fitted coordinate system was used where the free surface was approximated by a curve and iterated for the best possible solution. The present study is intended to incorporate the energy equation in the solution algorithm of Rahman et al. (1990a) to compute the heat transfer to a thin film in the presence or absence of gravity. In addition to the enhancement of our knowledge of thin film heat transfer, the results of the present study may be directly applicable to the design of space-based cooling systems.

Mathematical Model

The flow systems considered here are:

(1P) Plane film flow under zero gravity
(1R) Radial film flow under zero gravity
(2P) Plane film flow along a horizontal plate in the presence of gravity
(2R) Radial film flow along a horizontal plate in the presence of gravity

The variation of the flow parameters is denoted by A, B, etc. Two different heating conditions are considered: an isothermally heated plate (denoted by the symbol T), and a uniform heat flux on the plate (denoted by H). The thermal conditions on the free surface of the film are heating and evaporation. In the case of simple heating with no evaporation, the free surface may be assumed to be adiabatic in nature. In the case of evaporation, the free surface temperature is the same as the equilibrium temperature corresponding to the ambient vapor pressure. In the present study, the evaporation is assumed to be small so that the loss of fluid at the free surface is negligible compared to the mainstream flow. This assumption of a small evaporation rate was checked from the computed results and was found to be very adequate for the flow and heating conditions presented here. In fact, the rate of evaporation was always less than 0.002 percent of the mainstream flow.

The equations governing the conservation of mass, momentum, and energy in a thin film may be written as

$$\nabla \cdot \mathbf{V} = 0 \tag{1}$$

$$\frac{D\mathbf{V}}{Dt} = -\frac{1}{\rho}\nabla p + \nu \nabla^2 \mathbf{V} + \mathbf{g} \tag{2}$$

$$\frac{DT}{Dt} = \alpha \nabla^2 T \tag{3}$$

The fluid is assumed to be Newtonian with constant properties over the range of temperatures encountered in the problem.

A curvilinear body-fitted coordinate system is used. The local coordinate axes are directed along the lines joining the centers of adjacent grid cells. The z axis is directed in the streamline direction and the y axis across the thickness of the film. The velocity resolutes in the z and y directions are w and v, respectively. The boundary conditions are given by

At $y = 0$:

$$v = w = 0$$

$$\begin{cases} T = T_w, \text{ for isothermal wall} \\ -k\dfrac{\partial T}{\partial y} = q_w, \text{ for constant flux wall} \end{cases} \tag{4}$$

At $y = \delta$:

$$\tau = 0, \quad v = 0, \quad p = 0$$

$$\begin{cases} q = 0, \text{ for heating} \\ T = T_{sat}, \text{ for evaporation} \end{cases} \tag{5}$$

[1]Department of Mechanical and Materials Engineering, Wright State University, Dayton, OH 45435.
[2]Advanced Development, NASA Goddard Space Flight Center, Greenbelt, MD 20771.

Contributed by the Heat Transfer Division and presented at the National Heat Transfer Conference, Philadelphia, Pennsylvania, August 6–9, 1989. Manuscript received by the Heat Transfer Division February 21, 1989; revision received November 8, 1989. Keywords: Evaporation, Numerical Methods, Thin Film Flow.

Table 1 Flow parameters and free surface geometry

Case 0:	$\delta_{in}=0.000595$ m, Re = 50, Pr = 7, $L=0.03$m Free surface: $\Delta=1$
Case 1P:	$\delta_{in}=0.000595$ m, Re = 50, Pr = 7, $L=0.03$ m Free surface: $\Delta=(1+10\ \xi)^{0.93}$
Case 1R:	$\delta_{in}=0.005$ m, $\mathrm{Re}_{in}=1616$, Pr = 7, $r_{in}=0.0508$ m, $r_{out}=0.1953$ m Free surface: $\Delta=(1+1.43\ \xi)^{-0.64}$
Case 2PA:	$\mathrm{Fr}_{in}=5.7$, $\mathrm{Fr}_{out}=1.0$, Re = 355, Pr = 7, $L=0.1445$ m Free surface: $\Delta=(1+1.47\ \xi)^{1.52}$, supercritical $\Delta=8.42\ [2-(1.04+0.29\ \xi)^{1.5}]$, subcritical ($\xi<1$)
Case 2PB:	$\mathrm{Fr}_{in}=8.6$, $\mathrm{Fr}_{out}=1.0$, Re = 355, Pr = 7, $L=0.1445$ m Free surface: $\Delta=(1+1.47\ \xi)^{1.83}$, supercritical $\Delta=11.11\ [2-(1.04+0.29\ \xi)^{1.5}]$, subcritical ($\xi<1$)
Case 2RA:	$\mathrm{Fr}_{in}=7.4$, $\mathrm{Fr}_{out}=1.0$ $\mathrm{Re}_{in}=202$, Pr = 7, $r_{in}=0.0639$ m, $r_{out}=0.1953$ m Free surface: $\Delta=(1+2.05\ \xi)^{2.2}$, supercritical $\Delta=8.51\ [2-(1.04+0.37\ \xi)^{1.4}]$, subcritical ($\xi<1$)
Case 2RB:	$\mathrm{Fr}_{in}=11.0$, $\mathrm{Fr}_{out}=1.0$ $\mathrm{Re}_{in}=202$, Pr = 7, $r_{in}=0.0639$ m, $r_{out}=0.1953$ m Free surface: $\Delta=(1+2.05\ \xi)^{2.7}$, supercritical $\Delta=11.01\ [2-(1.04+0.37\ \xi)^{1.4}]$, subcritical ($\xi<1$)

At $z=0$ or r_{in}:

$$\begin{cases} w=W_{in}, \text{ for uniform entrance} \\ w=1.5\ W_{in}\left[2\left(\frac{y}{\delta}\right)-\left(\frac{y}{\delta}\right)^2\right], \text{ for parabolic entrance} \end{cases} \tag{6}$$

$$T=T_{in}$$

At $z=L$ or r_{out}:

$$\frac{\partial w}{\partial z}=0, \quad \frac{\partial T}{\partial z}=0$$

$$\begin{cases} p=0, \text{ for cases 0 and 1} \\ p=\rho g(\delta-y), \text{ for case 2} \end{cases} \tag{7}$$

Here p is the difference between the static pressure in the flow and the ambient pressure. In the absence of any significant surface tension this quantity has to be zero on the free surface.

Numerical Solution Procedure

The governing conservation equations (1)–(3) along with the appropriate boundary conditions (4)–(7) were solved numerically using a boundary-fitted curvilinear coordinate system. The velocity and force vectors were resolved into covariant components and the problem was solved in its physical domain. The details of the grid generation, the discretization of the governing equations, and the algorithm for determining the free surface height distribution are given by Rahman et al. (1990a). The optimum location of the free surface was determined by minimizing the error in the free surface pressure distribution. The final solutions corresponding to the different flow conditions considered here are listed in Table 1.

A systematic study of grid independence was made. A series of runs for the same problem with different combinations of grids in the z and y directions was performed, and the relevant results were plotted out. For radial flow, it was found that the free surface height and other computed quantities do not change any further if the computational mesh is refined beyond 50×25 grids in the z–y direction. For plane flow, 40×20 grids in the z–y plane were found to be adequate, which precisely predicted the analytical friction and heat transfer coefficients and the velocity profile for the fully developed falling film test case. Therefore, all of the computations were carried out using 40×20 grid for plane flow and 50×25 grids for radial flow.

When a jump was present, the two regimes of the flow (i.e., supercritical and subcritical) were computed separately, and the conditions were matched at the jump interface. The heat transfer coefficient for the supercritical part of the flow was determined from the supercritical temperature field, where the inlet temperature to the control volume corresponded to the actual inlet temperature. The inlet temperature for the subcritical flow was determined from the exit bulk temperature corresponding to the supercritical solution. By imposing this condition, the energy balance at the jump was automatically attained. The heat transfer coefficient in the subcritical flow was then determined from the subcritical temperature field.

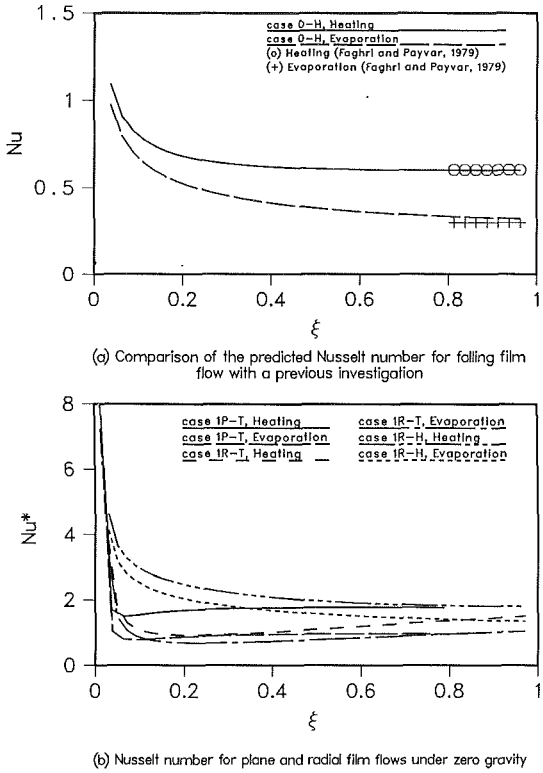

(a) Comparison of the predicted Nusselt number for falling film flow with a previous investigation

(b) Nusselt number for plane and radial film flows under zero gravity

Fig. 1 Nusselt number distributions for a falling film and for plane and radial flows under zero gravity

Results and Discussion

In order to check the accuracy of the present computational procedure, the method was first applied to the test problem of a film falling down a vertical wall (case 0 in Table 1). It was found that both the velocity and temperature fields attain the fully developed condition some distance downstream of the entrance. As shown in Fig. 1(*a*), the heat transfer coefficient approached the fully developed analytical solutions presented by Faghri and Payvar (1979).

For plane flow under zero gravity, the film height increases monotonically with distance. The variations of the Nusselt number for an isothermal wall condition for this case are shown in Fig. 1(*b*). The shapes of the curves appear to be similar for pure heating and evaporation and differ only in values. The Nusselt number considered here is Nu*, which depends on two parameters, namely, the film height and the heat transfer coefficient. As expected in any developing flow, the heat transfer coefficient is maximum at the entrance and decreases downstream. The film height, however, has the opposite trend. The net result is the variation presented in Fig. 1(*b*). The sudden drop of the Nusselt number near the entrance is due to the rapid change of the heat transfer coefficient as the thermal boundary layer develops from the leading edge at the entrance section. Moreover, when there is evaporation over an isothermal surface, Nu* is approximately unity. This shows that

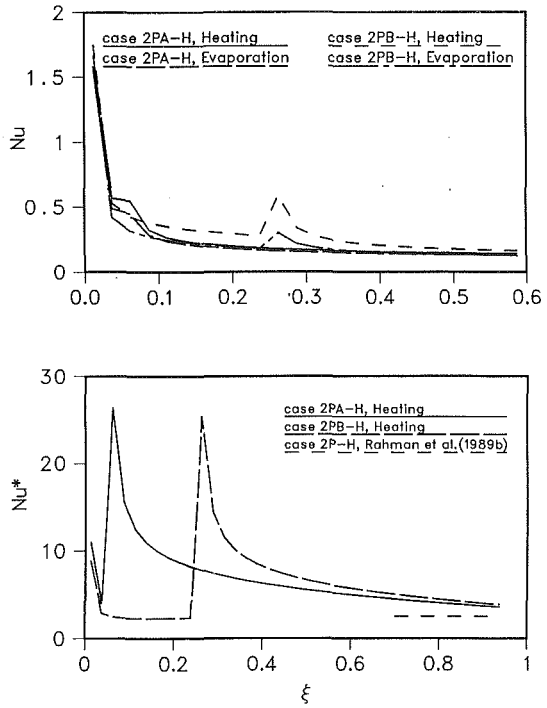

Fig. 2 Nusselt number for plane horizontal flow in the presence of gravity

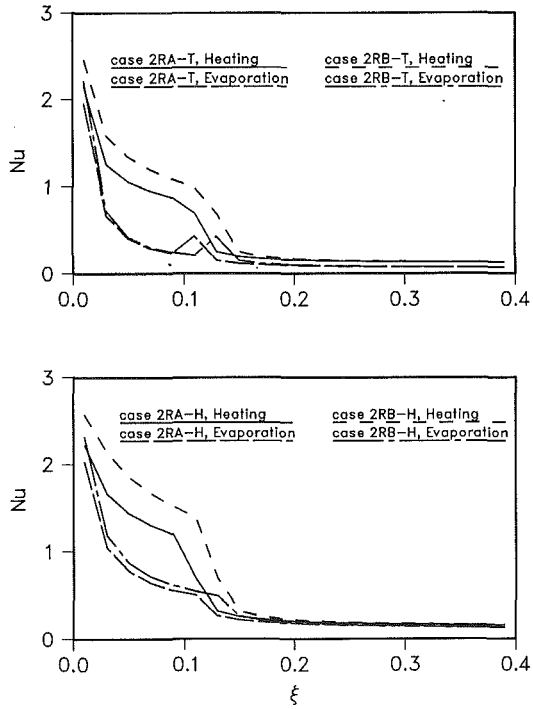

Fig. 3 Nusselt number for radial horizontal flow in the presence of gravity

the heat transfer process becomes primarily diffusive after a short distance from the entrance.

In a radially spreading flow, the area available for the fluid increases downstream and acts as an added mechanism to control the film height and the associated transport phenomena. The Nusselt number variations for radial flow under zero gravity are also shown in Fig. 1(*b*). Analogous to the plane flow case, there is a sudden drop in Nu* close to the entrance. For a uniformly heated surface, the Nusselt number keeps decreasing downstream for the heating and evaporation situations. In most developing flows, the heat transfer coefficient is maximum at the entrance and decreases with the growth of the thermal boundary layer. In this case, the film height also decreases downstream, so this trend in the Nusselt number is expected. For an isothermal surface, however, the Nusselt number drops to a minimum at an intermediate location on the plate and then gradually increases as the flow moves farther downstream. This trend also indicates that, for an isothermal surface, the heat transfer coefficient has to have a minimum at an intermediate location on the plate. In the results of the heat transfer coefficient, it was found that a minimum is indeed present for both isothermal and uniformly heated surfaces. This phenomenon can be explained by the fact that in a radially spreading flow with a rapid reduction of the film thickness, the thermal boundary layer engulfs the entire film downstream from the entrance for the moderate Prandtl number fluid considered here. Therefore, with a further reduction of film thickness, the thermal boundary layer thickness also decreases and results in a reduction of the resistance to heat transfer from the wall.

Two different flow regimes, namely supercritical and subcritical, are encountered for horizontal flow in the presence of gravity. These regimes are separated by a hydraulic jump. The distributions of the heat transfer coefficient for plane and radial flows are plotted in Figs. 2 and 3, respectively. It appears that Nu decreases rapidly close to the entrance as the thermal boundary layer develops. Also, the Nusselt number increases at the location of the jump. A sudden transition of the flow happens at the jump, and the thermal boundary layer starts growing again after the jump. In the present study, the heat transfer in the supercritical and subcritical flow was computed separately by matching the temperature and heat flux at the jump location. Therefore the heat transfer coefficient at the jump location may not be correct. Except for the jump and leading edge of the boundary layer, Nu decreases slowly with the horizontal distance in the supercritical part of the flow and remains approximately constant in the subcritical stem of the flow. In the supercritical regime the film height increases with distance, whereas in the subcritical regime it decreases with distance. When the height of the free surface increases and the fluid velocity decreases, the heat transfer from the plate to the fluid is expected to decrease downstream. In subcritical flow, however, the fluid velocity itself is smaller, and a balance is established between the thickness of the thermal layer and the velocity of the fluid near the wall. Figure 2 also shows a plot of Nu* for the case of heating on a horizontal surface with a uniform heat flux. The rapid rise of Nu* at the jump location is due to the sudden rise of the film height. The figure also shows that the numerical value of Nu* approaches the fully developed value predicted by the analysis of Rahman et al. (1990b).

Conclusions

For a plane flow under zero gravity, it was found that for both isothermal and uniformly heated walls, the heat transfer coefficient gradually decreases downstream. The Nu* in this situation was approximately constant except for regions very close to the entrance. In the case of radial flow under zero gravity, Nu* was found to decrease monotonically when the plate is uniformly heated. For an isothermal wall, however, Nu* reached a minimum and then slowly increased downstream. This behavior of the heat transfer is related to the thinning of the film and simultaneous growth of the thermal boundary layer in a diffusion-dominated heat transfer process. For both plane flow and radial flow on a horizontal plate in the presence of gravity, two different flow regimes (i.e., supercritical and subcritical) are found to be present. In the supercritical region, the heat transfer coefficient decreases

gradually downstream, whereas in the subcritical region, it remains approximately uniform at most locations on the plate.

Acknowledgments

Funding for this work was provided by the NASA Goddard Space Flight Center, Greenbelt, MD, under contract No. NAG-5-956.

References

Chaudhury, Z. H., 1964, "Heat Transfer in a Radial Liquid Jet," *J. Fluid Mechanics*, Vol. 20, Part 3, pp. 501–511.

Faghri, A., and Payvar, P., 1979, "Transport to Thin Falling Liquid Films," *Reg. J. Energy Heat Mass Transfer*, Vol. 1, No. 2, pp. 153–173.

Faghri, A., and Seban, R. A., 1981, "Heat Transfer in Wavy Liquid Film," *Int. J. Heat Mass Transfer*, Vol. 28, No. 2, pp. 506–508.

Rahman, M. M., Faghri, A., Hankey, W. L., and Swanson, T. D., 1990a, "Computation of the Free Surface Flow of a Liquid Film at Zero and Normal Gravity," *Numerical Heat Transfer*, Vol. 17, Part A, pp. 53–71.

Rahman, M. M., Hankey, W. L., and Faghri, A., 1990b, "Analysis of Fluid Flow and Heat Transfer in a Thin Liquid Film in the Presence and Absence of Gravity," to appear in *Int. J. Heat Mass Transfer*.

Dynamics of Condensing Bubbles at Intermediate Frequencies of Injection

Y. Lerner[1] and R. Letan[1]

Nomenclature

C_D = drag coefficient
CER = condensation experiments with R113
E = eccentricity, ratio of vertical to horizontal diameters
f = frequency of injection, bubbles/s
H = position above nozzle, m or cm
R = radius of bubble, mm
R_o = initial radius of bubble, mm
$\bar{R}$ = normalized radius $= R/R_o$
T = temperature, °C
t = time, s
U = instantaneous velocity of rise, m/s
ΔT = difference between the saturation temperature and the cooling liquid temperature, °C
Re = Reynolds number referred to bubble diameter

Subscripts

f = at termination of collapse
max = at the instant of maximum velocity

[1]Department of Mechanical Engineering, Ben-Gurion University of the Negev, Beer-Sheva, Israel.

Contributed by the Heat Transfer Division for publication in the JOURNAL OF HEAT TRANSFER. Manuscript received by the Heat Transfer Division August 12, 1989; revision received September 11, 1989. Keywords: Condensation, Direct-Contact Heat Transfer, Multiphase Flows.

Introduction

Our previous studies focused on a single bubble (Lerner et al., 1987; Kalman et al., 1986, 1987; Kalman and Letan, 1987). In the present study an attempt is made to define quantitatively how far the single-bubble model is obeyed.

The bubbles constitute a "train" if interaction between bubbles takes place on the same path. Each bubble in a train interacts with the wake of the leading bubble, and exerts its own wake on the trailing bubble. Moalem et al. (1973) studied trains theoretically and experimentally. The wakes were mathematically defined, and the initiation of interaction was predicted for much higher frequencies than those usually applied in dilute systems of bubbles.

The shedding and motion of bubbles and their wakes as visualized by shadowgraphing (Lerner et al., 1987), and by color entrainment (Kalman et al., 1986, 1987) have illustrated that these phenomena are still not easily defined analytically. Therefore the interaction must also be established experimentally; that is, the range of frequencies has to be defined by measurements.

In general four regions of injection frequencies can be distinguished: the region of a single bubble in an infinite medium; the intermediate region, which corresponds to a dilute system of bubbles; the train region, which corresponds to a dense system of bubbles; and the region of slugging.

The range of frequencies of injection within which a single bubble moves and condenses on its path is theoretically the one close to zero bubbles per second. Practically in this range, the frequency is expected to be lower than the collapse time of a single bubble, $1/t_f$.

The intermediate range of frequencies relates to a system where several bubbles rise on the same path, but do not interact, being adequately separated. This is a dilute system of bubbles. The frequency in this region is higher than $1/t_f$, but lower than f_t, the frequency corresponding to train initiation.

The train region relates to the range of frequencies where bubbles on the same path interact through their wakes, and each bubble preserves its identity. The resulting system contains a large volumetric fraction of bubbles; that is, it is a bubble-dense system.

The region of slugging relates to higher frequencies, f_s, at which the injected bubbles coalesce, forming slugs. These frequencies are higher than the velocity of rise of the injected bubbles, $f_s > U/2R_o$.

The experimental results presented here were obtained in the intermediate region in order to establish experimentally the upper limit of frequency below which the bubbles could be described by the single-bubble models. The regions of trains and slugging are being investigated and will be described in subsequent works.

The previously developed model for collapse of a single bubble (Lerner et al., 1987) is presently used within the intermediate range of frequencies. The deviation of the predicted collapse curve from the experimental points would serve to define the upper bound of this region, and the initiation of the train region.

Bubble Velocity

The rate of bubble collapse as formulated in our previous work (Lerner et al., 1987) involves the instantaneous velocity of the bubble. Videotaping of closely spaced images of pentane bubbles in water (Kalman et al., 1986) has illustrated that even these bubbles—droplets lighter than water—accelerate/decelerate on their path of collapse. These phenomena of acceleration/deceleration are even more accentuated in a system of freon-113 bubbles, which condense in water to the heavier droplets.

gradually downstream, whereas in the subcritical region, it remains approximately uniform at most locations on the plate.

Acknowledgments

Funding for this work was provided by the NASA Goddard Space Flight Center, Greenbelt, MD, under contract No. NAG-5-956.

References

Chaudhury, Z. H., 1964, "Heat Transfer in a Radial Liquid Jet," *J. Fluid Mechanics*, Vol. 20, Part 3, pp. 501–511.

Faghri, A., and Payvar, P., 1979, "Transport to Thin Falling Liquid Films," *Reg. J. Energy Heat Mass Transfer*, Vol. 1, No. 2, pp. 153–173.

Faghri, A., and Seban, R. A., 1981, "Heat Transfer in Wavy Liquid Film," *Int. J. Heat Mass Transfer*, Vol. 28, No. 2, pp. 506–508.

Rahman, M. M., Faghri, A., Hankey, W. L., and Swanson, T. D., 1990a, "Computation of the Free Surface Flow of a Liquid Film at Zero and Normal Gravity," *Numerical Heat Transfer*, Vol. 17, Part A, pp. 53–71.

Rahman, M. M., Hankey, W. L., and Faghri, A., 1990b, "Analysis of Fluid Flow and Heat Transfer in a Thin Liquid Film in the Presence and Absence of Gravity," to appear in *Int. J. Heat Mass Transfer*.

Dynamics of Condensing Bubbles at Intermediate Frequencies of Injection

Y. Lerner[1] and R. Letan[1]

Nomenclature

C_D = drag coefficient
CER = condensation experiments with R113
E = eccentricity, ratio of vertical to horizontal diameters
f = frequency of injection, bubbles/s
H = position above nozzle, m or cm
R = radius of bubble, mm
R_o = initial radius of bubble, mm
$\bar{R}$ = normalized radius $= R/R_o$
T = temperature, °C
t = time, s
U = instantaneous velocity of rise, m/s
ΔT = difference between the saturation temperature and the cooling liquid temperature, °C
Re = Reynolds number referred to bubble diameter

Subscripts

f = at termination of collapse
max = at the instant of maximum velocity

[1]Department of Mechanical Engineering, Ben-Gurion University of the Negev, Beer-Sheva, Israel.

Contributed by the Heat Transfer Division for publication in the JOURNAL OF HEAT TRANSFER. Manuscript received by the Heat Transfer Division August 12, 1989; revision received September 11, 1989. Keywords: Condensation, Direct-Contact Heat Transfer, Multiphase Flows.

Introduction

Our previous studies focused on a single bubble (Lerner et al., 1987; Kalman et al., 1986, 1987; Kalman and Letan, 1987). In the present study an attempt is made to define quantitatively how far the single-bubble model is obeyed.

The bubbles constitute a "train" if interaction between bubbles takes place on the same path. Each bubble in a train interacts with the wake of the leading bubble, and exerts its own wake on the trailing bubble. Moalem et al. (1973) studied trains theoretically and experimentally. The wakes were mathematically defined, and the initiation of interaction was predicted for much higher frequencies than those usually applied in dilute systems of bubbles.

The shedding and motion of bubbles and their wakes as visualized by shadowgraphing (Lerner et al., 1987), and by color entrainment (Kalman et al., 1986, 1987) have illustrated that these phenomena are still not easily defined analytically. Therefore the interaction must also be established experimentally; that is, the range of frequencies has to be defined by measurements.

In general four regions of injection frequencies can be distinguished: the region of a single bubble in an infinite medium; the intermediate region, which corresponds to a dilute system of bubbles; the train region, which corresponds to a dense system of bubbles; and the region of slugging.

The range of frequencies of injection within which a single bubble moves and condenses on its path is theoretically the one close to zero bubbles per second. Practically in this range, the frequency is expected to be lower than the collapse time of a single bubble, $1/t_f$.

The intermediate range of frequencies relates to a system where several bubbles rise on the same path, but do not interact, being adequately separated. This is a dilute system of bubbles. The frequency in this region is higher than $1/t_f$, but lower than f_t, the frequency corresponding to train initiation.

The train region relates to the range of frequencies where bubbles on the same path interact through their wakes, and each bubble preserves its identity. The resulting system contains a large volumetric fraction of bubbles; that is, it is a bubble-dense system.

The region of slugging relates to higher frequencies, f_s, at which the injected bubbles coalesce, forming slugs. These frequencies are higher than the velocity of rise of the injected bubbles, $f_s > U/2R_o$.

The experimental results presented here were obtained in the intermediate region in order to establish experimentally the upper limit of frequency below which the bubbles could be described by the single-bubble models. The regions of trains and slugging are being investigated and will be described in subsequent works.

The previously developed model for collapse of a single bubble (Lerner et al., 1987) is presently used within the intermediate range of frequencies. The deviation of the predicted collapse curve from the experimental points would serve to define the upper bound of this region, and the initiation of the train region.

Bubble Velocity

The rate of bubble collapse as formulated in our previous work (Lerner et al., 1987) involves the instantaneous velocity of the bubble. Videotaping of closely spaced images of pentane bubbles in water (Kalman et al., 1986) has illustrated that even these bubbles—droplets lighter than water—accelerate/decelerate on their path of collapse. These phenomena of acceleration/deceleration are even more accentuated in a system of freon-113 bubbles, which condense in water to the heavier droplets.

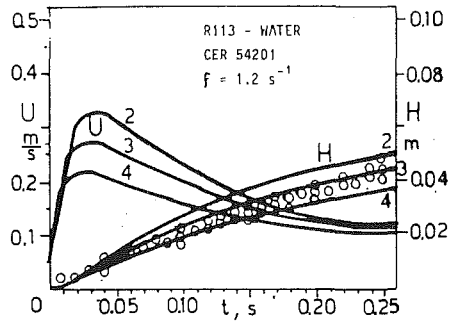

Fig. 1 Bubble velocity and path curves at $f = 1.2\ s^{-1}$

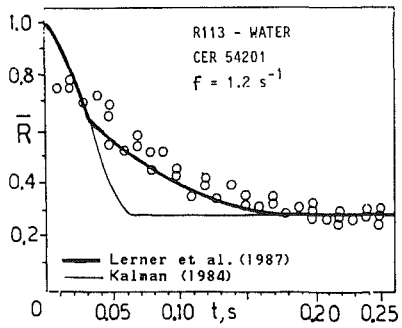

Fig. 2 Bubble collapse rate at $f = 1.2\ s^{-1}$: predicted curves and experimental points

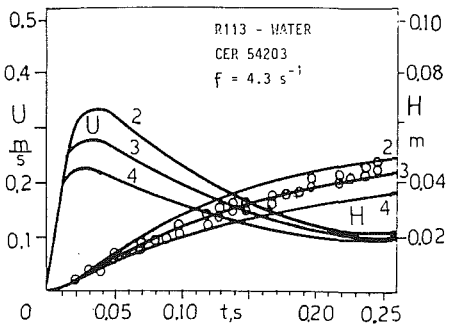

Fig. 3 Bubble velocity and path at $f = 4.3\ s^{-1}$: predicted curves and experimental points

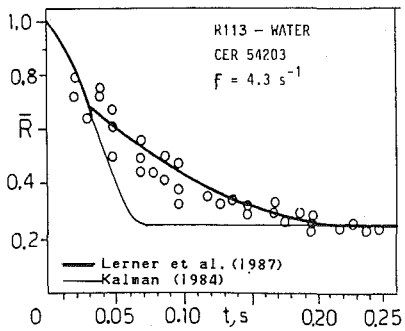

Fig. 4 Bubble collapse rate at $f = 4.3\ s^{-1}$: predicted curves and experimental points

The terminal velocity of a steadily rising bubble is calculated by conventional methods. The instantaneous velocity of an accelerating/decelerating bubble involves additional terms. In our previous works the effect of "added mass" was accounted for. The choice of the appropriate drag coefficient is also a complex matter. Three relations have been now utilized for the drag coefficient C_D in calculating the instantaneous velocity.

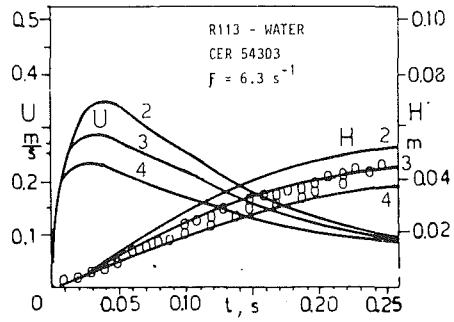

Fig. 5 Bubble velocity and path at $f = 6.3\ s^{-1}$: predicted curves and experimental points

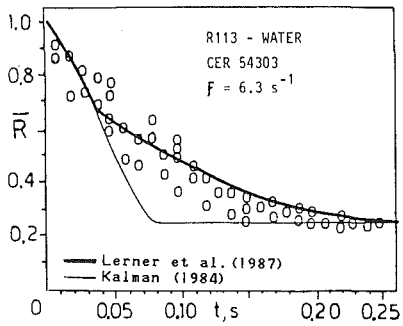

Fig. 6 Bubble collapse rate at $f = 6.3\ s^{-1}$: predicted curves and experimental points

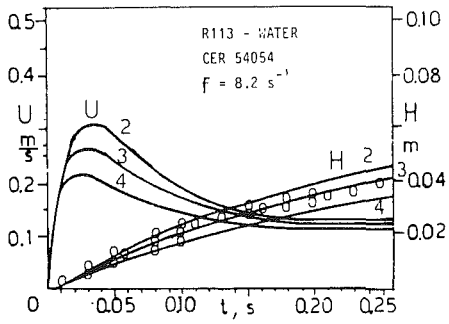

Fig. 7 Bubble velocity and path at $f = 8.2\ s^{-1}$: predicted curves and experimental points

For distorted droplets

$$C_D = 1 \tag{1}$$

as quoted by Wallis (1969).

For a spheroid of an eccentricity $E = 0.5$ in the range of $100 < \mathrm{Re} < 1000$,

$$\log_{10} C_D = 2.035 - 1.66 \log_{10}\mathrm{Re} + 0.396 (\log_{10}\mathrm{Re})^2 - 0.0306 (\log_{10}\mathrm{Re})^3 \tag{2}$$

as presented by Clift et al. (1978).

For a rigid sphere

$$C_D = \frac{24}{\mathrm{Re}} + \frac{6}{1+\sqrt{\mathrm{Re}}} + 0.4 \tag{3}$$

All the three curves were drawn for each experiment, using in each curve one of the above drag coefficients (Ullmann, 1984). The comparison of the experimental points with the three curves was made to illustrate the variation of size and shape of the condensing bubble along its path.

Results

The experimental work presented in Figs. 1–14 was con-

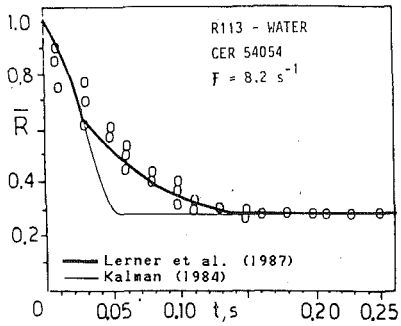

Fig. 8 Bubble collapse rate at $f = 8.2\ s^{-1}$: predicted curves and experimental points

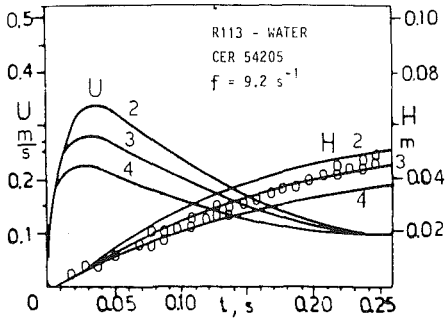

Fig. 9 Bubble velocity and path at $f = 9.2\ s^{-1}$: predicted curves and experimental points

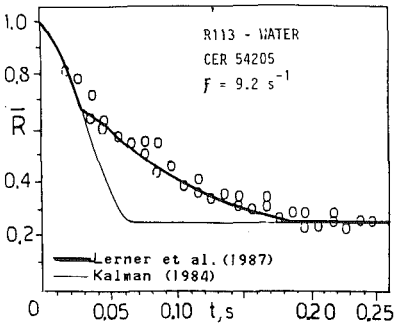

Fig. 10 Bubble collapse rate at $f = 9.2\ s^{-1}$: predicted curves and experimental points

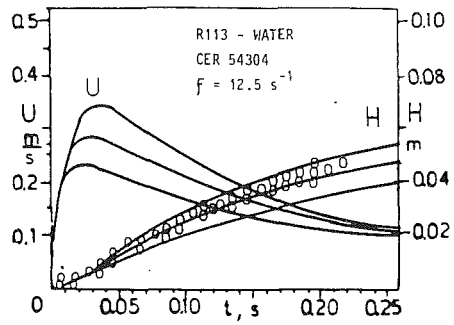

Fig. 11 Bubble velocity and path at $f = 12.5\ s^{-1}$: predicted curves and experimental points

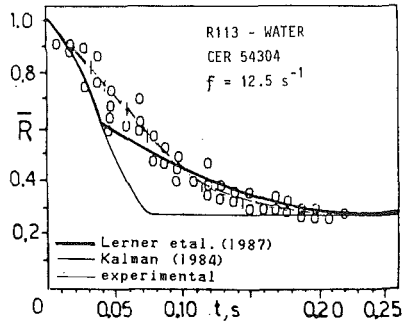

Fig. 12 Bubble collapse rate at $f = 12.5\ s^{-1}$: predicted curves and experimental points

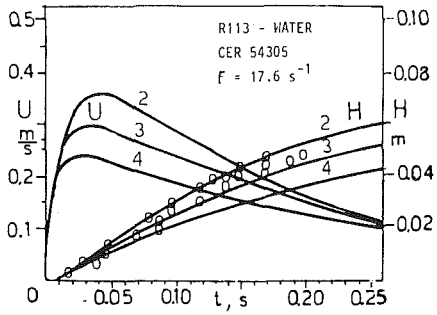

Fig. 13 Bubble velocity and path at $f = 17.6\ s^{-1}$: predicted curves and experimental points

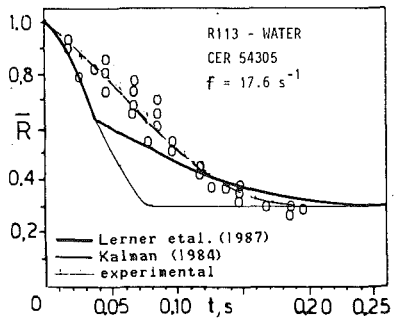

Fig. 14 Bubble collapse rate at $f = 17.6\ s^{-1}$: predicted curves and experimental points

ducted with freon-113 bubbles collapsing in water. The apparatus was the same as in our previous work (Lerner et al., 1987).

The frequency of injection of the bubbles was increased from 1.2 bubbles/s to 17.6 bubbles/s. The bubbles at all frequencies were formed at the nozzle and detached from it. The time-dependent size of the bubble, and the corresponding position (path) were recorded in each experiment. Two to four bubbles were recorded for each collapse curve $R(t)$. Videotaping and subsequent screen-tracing were applied in measurements of bubble size, shape, position, and instantaneous velocity.

The images projected on the screen were timed, and the time was digitally exposed with an accuracy of 0.01 s. The time lapse between images corresponded to 0.0166 s. At least ten images were counted, noting the time lapse of their appearance. That provided an accuracy of 0.001 s. The width of the graphic symbols in Figs. 1–14 corresponds to 0.005 s, i.e., the indicated error is five times larger than the uncertainty in measurement.

For size and shape of the bubble, the horizontal and vertical diameters of each image were measured on an enlarged scale about four times the actual size. The error in these length measurements was about 0.5 mm, i.e., 0.12 mm of the actual diameter, or 0.06 mm of the actual radius. The error expressed in a nondimensional form is $\Delta\bar{R} = 0.02$–0.03 for $R_o = 2$–3 mm. The height of the graphic symbols in Figs. 1–14 is also 0.05. Thus, the size of the graphic points also represents the uncertainty in measurements.

The position of the bubble along its path is measured from the position of the initial bubble. The error in length

measurements is again 0.5 mm on the enlarged scale, and 0.12 mm on the actual scale. The graphic symbols correspond to a height of about 1 mm, and are therefore about ten times larger than the actual experimental error in bubble position.

In the experiments performed, the bubbles were of an initial radius of $R_o = 2.3$–2.5 mm, final radius, $\bar{R}_f = 0.25$–0.30, and collapsed at a temperature difference of $\Delta T = 4.8$–7.3°C. The measured radii of the collapsing bubble have been plotted elsewhere (Ullmann, 1984), and a least-squares curve was fitted to obtain the polynomial function of $R(t)$ used in turn for the velocity curves.

Two figures are presented for each frequency of injection. One figure illustrates the collapse curve $R(t)$. The other figure shows the measured location of the collapsing bubble, and three theoretical path curves calculated for the bubble as sphere, spheroid, and a distorted droplet. The theoretical velocity also has the same three variations. The three distinct curves of velocity, $U(t)$, in each figure are designated as 2, 3, and 4. The instantaneous position $H(t)$ is marked in the same way. Curve 2 is obtained using the drag coefficient of a rigid sphere, 3 of a spheroid, and 4 that of a deformed droplet. These velocity curves are integrated to yield the three path curves for the duration of collapse.

The experimental points are found between the curves or on them. The experimental path indicates the real path curve. It illustrates clearly how the points cross the theoretical curves, indicating this way the variations in size, shape, and the respective drag on the collapsing bubble. The actual velocity curve $U(t)$ can then be interpreted from the path curve $H(t)$. Furthermore, the point of maximum velocity U_{max}, and the respective instant t_{max}, can be determined. This point is of importance in prediction of the collapse curve, because it defines the termination of the acceleration zone, and initiation of the deceleration zone.

The collapse curves, evenly numbered in Figs. 2–14, are described by two curves: The thin curve corresponds to the mobility model (Lerner, 1983; Kalman, 1984; Lerner and Letan, 1985). The solid curve represents the model of a boundary layer and wake over the accelerating bubble, and the vorticular "envelope" around the decelerating bubble (Lerner et al., 1987).

Identifying the actual $H(t)$ curve, and projecting on the $U(t)$ curve, yields the point of U_{max}, and the respective instant t_{max}. The crossing of the acceleration/deceleration zones was determined at the experimental point of t_{max} in five experiments. In two other experiments this point was chosen within the range of three t_{max} values to fit more closely the curve of collapse $R(t)$.

The following steps were applied to the seven experiments summarized in Table 1, and presented in Figs. 1–14: The final radius $\bar{R}_f$ of the condensed bubble-droplet was obtained from the experimental data. The time interval t_f, required to reach the size $\bar{R}_f$, was determined. The height $H_f = H(t_f)$, which was required to reach size $\bar{R}_f$, was identified.

The graphic presentations illuminate very clearly that the single-bubble model of boundary layer and wake, and that of the envelope fit well the experimental rate of collapse up to a frequency of 9.2 bubbles/s. A slight deviation appears at $f = 12.5\ s^{-1}$. This deviation is largest in the region of the maximum velocity (Fig. 12). The measured radii are larger than the predicted values, indicating a slower rate of collapse of the more closely spaced bubbles.

The deviation increases further as the frequency reaches 17.6 bubbles/s (Fig. 14). There, the deviation extends over the whole zone of acceleration, and over most of the deceleration zone. The experimental radii are much larger than those predicted by the single-bubble model. The experimental points appear to form a continuous curve over the entire collapse interval, indicating the same mechanism of condensation from its initiation to its termination.

The closer spacing of bubbles at the higher frequency of injection also affects the path of collapse. At lower frequencies and larger spacing between the bubbles as at $f = 1.2$–$6.3\ s^{-1}$ (Figs. 1–5), most of the experimental points are allocated between curves 4 and 3, which correspond to the larger drag coefficients. As the frequency increases to $8.2\ s^{-1}$ (Fig. 7), a shift towards curve 3 takes place. It relates to a lower drag coefficient and a higher velocity. The same effect is illustrated at the frequency of $9.2\ s^{-1}$. With an additional increase in frequency to $12.5\ s^{-1}$ (Fig. 11), the experimental points drift further to the higher velocity, and accumulate between curves 3 and 2. This drift is further accentuated at the highest frequency of $17.6\ s^{-1}$ (Fig. 13).

The higher velocity apparently does not affect the time of collapse t_f (Figs. 2–14). It does however affect the length of the collapse path $H(t_f)$, as illustrated in Figs. 7, 9, 11, and 13. It varies from 3 cm to 5 cm, as the frequency increases from $8.2\ s^{-1}$ to $17.6\ s^{-1}$. Thus, with the closer spacing of bubbles, the time of collapse appears to be unchanged, but the path is elongated.

Another effect of the higher injection frequency is pronounced in the more spherical shape of the bubbles. The ratio of the vertical/horizontal diameters was measured on screen-traced images of the bubbles and is presented as eccentricity in Table 2. The smaller deformation of the bubbles expressed itself also in the drift toward the smaller drag and higher velocity, as seen above.

A maximum velocity $U_{max} = 0.25$–0.27 m/s was obtained in the range of $f = 1.2$–$9.2\ s^{-1}$ (Figs. 1–9 and Table 1). It increased to 0.31 m/s at $f = 12.5\ s^{-1}$, and to 0.40 m/s at $f = 17.6\ s^{-1}$. The time of collapse t_f remained 0.18–0.20 s, at a temperature difference of 4.8–5.8°C.

The effect of the higher injection frequency seemingly becomes apparent at about $f > 1/(t_f/2)$. The time of collapse, frequency-independent, may be due to the present specific operating conditions: the bubble size or the small temperature difference. However, obviously the closer spacing of bubbles makes them move faster. It also makes the bubbles collapse more slowly at the initial stages, and faster at the final stages, as compared to a single bubble. A possible interpretation of these results may be the following: The close spacing of bubbles causes envelopment of the trailing bubble in the wake of the leading bubble, instantly at the point of injection. That prevents the formation of the boundary layer on the bubble. Consequently the heat transfer rates are lower in comparison to a single bubble in the zone of acceleration. However the faster velocity of the bubble makes the circulation in the wake more effective, and the heat transfer rates to the vortices are higher than those to the "envelope" of a single bubble. Quantitative local measurements in the wake would contribute to a better understanding of these phenomena.

Conclusions

The single-bubble model of acceleration/deceleration zones describes satisfactorily the noninteracting bubbles rising on the same path. The predicted rates of collapse showed good agreement with experiment up to an injection frequency of about 9 bubbles/s.

A deviation of the predicted curve from experiment was first noticed in the region of the peak velocity at the injection frequency of 12.5 bubbles/s. The deviation increased considerably at the frequency of 17.6 bubbles/s.

Apparently at the operating conditions of this study the initiation of interaction between bubbles corresponds to a frequency of about $1/(t_f/2)$, which is in this case about 10 bubbles/s.

At the higher frequencies of injection the drag upon the bubbles was reduced, their velocity increased, and the shape became more spherical. The time required for collapse ap-

Table 1 Freon-113 in water

Exp. No. CER	54201	54203	54303	54054	54205	54304	54305
Figs.	1, 2	3, 4	5, 6	7, 8	9, 10	11, 12	13, 14
f, s^{-1}	1.2	4.3	6.3	8.2	9.2	12.5	17.6
R_o, mm	2.3	2.5	2.8	2.3	2.4	2.4	2.5
$\bar{R}_f$	0.28	0.25	0.25	0.29	0.25	0.25	0.30
ΔT, °C	5.8	5.8	4.8	7.3	5.8	4.8	4.8
U_{max}, exp., m/s	0.27	0.27	0.27	0.27	0.25	0.31	0.40
t_{max}, exp., s	0.032	0.030	0.030	0.028	0.030	0.035	0.040
t_{max}, th curve 2, s	0.034	0.034	0.037	0.031	0.035	0.038	0.042
t_{max}, th., s curve 3	0.029	0.029	0.032	0.027	0.030	0.032	0.036
t_{max}, th., s curve 4	0.024	0.024	0.026	0.026	0.025	0.027	0.030
t_f, exp., s	0.175	0.215	0.195	0.150	0.20	0.20	0.19
H_f, cm	3.3	3.9	3.8	2.9	3.9	4.2	4.8

Table 2 Examples of bubble eccentricity E

t, s / f, s^{-1}	0	0.02	0.04	0.05	0.07	0.08	0.09
1.2	0.66	0.73	0.38	0.54	1.0	0.86	—
17.6	0.85	0.86	0.76	0.80	0.95	—	0.81

peared unaffected by the bubble spacing. The height of collapse increased with the bubble velocity.

References

Clift, R., Grace, J. R., and Weber, M. E., 1978, *Bubbles, Drops and Particles*, Academic Press, New York, p. 296.

Kalman, H., 1984, "Condensation of Bubbles," Preparatory Report for Ph.D. Candidacy, Ben-Gurion University, Beer-Sheva, Israel.

Kalman, H., Ullmann, A., and Letan, R., 1986, "Dynamics of a Condensing Bubble in Zones of Time-Dependent Velocity," *Proc. 8th Int. Heat Transfer Conf.*, Vol. 4, pp. 1925–1930.

Kalman, H., and Letan, R., 1987, "Condensation of a Bubble in an Immiscible Liquid: Characteristics of the Thermal Resistance," AIChE Symposium Series, Vol. 83, No. 257, pp. 128–133.

Kalman, H., Ullmann, A., and Letan, R., 1987, "Visualization Studies of a Freon-113 Bubble Condensing in Water," ASME JOURNAL OF HEAT TRANSFER, Vol. 109, pp. 543–545.

Lerner, Y., 1983, "Condensation of Bubbles," M.Sc. Thesis, Ben-Gurion University, Beer-Sheva, Israel.

Lerner, Y., and Letan, R., 1985, "Dynamics of Condensing Bubbles: Effects of Injection Frequency," ASME Paper No. 85-HT-47.

Lerner, Y., Kalman, H., and Letan, R., 1987, "Condensation of an Accelerating-Decelerating Bubble: Experimental and Phenomenological Analysis," ASME JOURNAL OF HEAT TRANSFER, Vol. 109, pp. 509–517.

Moalem, D., Sideman, S., Orell, A., and Hetsroni, G., 1973, "Direct Contact Heat Transfer With Change of Phase: Condensation of Bubble Train," *Int. Journal of Heat and Mass Transfer*, Vol. 16, pp. 2305–2319.

Ullmann, A., 1984, Internal Report for M.Sc., Ben-Gurion University, Beer-Sheva, Israel.

Wallis, G. B., 1969, *One Dimensional Two-Phase Flow*, McGraw-Hill, New York, p. 381.